BRIDGING THE GAP IN NEUROELECTRONIC INTERFACES

EDITED BY: Jeffrey R. Capadona and Ulrich G. Hofmann
PUBLISHED IN: Frontiers in Neuroscience, Frontiers in Materials, and Frontiers in Bioengineering and Biotechnology

frontiers Research Topics

frontiers

Frontiers eBook Copyright Statement

The copyright in the text of individual articles in this eBook is the property of their respective authors or their respective institutions or funders. The copyright in graphics and images within each article may be subject to copyright of other parties. In both cases this is subject to a license granted to Frontiers.

The compilation of articles constituting this eBook is the property of Frontiers.

Each article within this eBook, and the eBook itself, are published under the most recent version of the Creative Commons CC-BY licence. The version current at the date of publication of this eBook is CC-BY 4.0. If the CC-BY licence is updated, the licence granted by Frontiers is automatically updated to the new version.

When exercising any right under the CC-BY licence, Frontiers must be attributed as the original publisher of the article or eBook, as applicable.

Authors have the responsibility of ensuring that any graphics or other materials which are the property of others may be included in the CC-BY licence, but this should be checked before relying on the CC-BY licence to reproduce those materials. Any copyright notices relating to those materials must be complied with.

Copyright and source acknowledgement notices may not be removed and must be displayed in any copy, derivative work or partial copy which includes the elements in question.

All copyright, and all rights therein, are protected by national and international copyright laws. The above represents a summary only. For further information please read Frontiers' Conditions for Website Use and Copyright Statement, and the applicable CC-BY licence.

ISSN 1664-8714
ISBN 978-2-88963-850-5
DOI 10.3389/978-2-88963-850-5

About Frontiers

Frontiers is more than just an open-access publisher of scholarly articles: it is a pioneering approach to the world of academia, radically improving the way scholarly research is managed. The grand vision of Frontiers is a world where all people have an equal opportunity to seek, share and generate knowledge. Frontiers provides immediate and permanent online open access to all its publications, but this alone is not enough to realize our grand goals.

Frontiers Journal Series

The Frontiers Journal Series is a multi-tier and interdisciplinary set of open-access, online journals, promising a paradigm shift from the current review, selection and dissemination processes in academic publishing. All Frontiers journals are driven by researchers for researchers; therefore, they constitute a service to the scholarly community. At the same time, the Frontiers Journal Series operates on a revolutionary invention, the tiered publishing system, initially addressing specific communities of scholars, and gradually climbing up to broader public understanding, thus serving the interests of the lay society, too.

Dedication to Quality

Each Frontiers article is a landmark of the highest quality, thanks to genuinely collaborative interactions between authors and review editors, who include some of the world's best academicians. Research must be certified by peers before entering a stream of knowledge that may eventually reach the public - and shape society; therefore, Frontiers only applies the most rigorous and unbiased reviews.
Frontiers revolutionizes research publishing by freely delivering the most outstanding research, evaluated with no bias from both the academic and social point of view. By applying the most advanced information technologies, Frontiers is catapulting scholarly publishing into a new generation.

What are Frontiers Research Topics?

Frontiers Research Topics are very popular trademarks of the Frontiers Journals Series: they are collections of at least ten articles, all centered on a particular subject. With their unique mix of varied contributions from Original Research to Review Articles, Frontiers Research Topics unify the most influential researchers, the latest key findings and historical advances in a hot research area! Find out more on how to host your own Frontiers Research Topic or contribute to one as an author by contacting the Frontiers Editorial Office: researchtopics@frontiersin.org

BRIDGING THE GAP IN NEUROELECTRONIC INTERFACES

Topic Editors:
Jeffrey R. Capadona, Case Western Reserve University, United States
Ulrich G. Hofmann, University of Freiburg, Germany

Citation: Capadona, J. R., Hofmann, U. G., eds. (2020). Bridging the Gap in Neuroelectronic Interfaces. Lausanne: Frontiers Media SA.
doi: 10.3389/978-2-88963-850-5

Table of Contents

06 ***Editorial: Bridging the Gap in Neuroelectronic Interfaces***
Ulrich G. Hofmann and Jeffrey R. Capadonat

09 ***The Role of Toll-Like Receptor 2 and 4 Innate Immunity Pathways in Intracortical Microelectrode-Induced Neuroinflammation***
John K. Hermann, Shushen Lin, Arielle Soffer, Chun Wong, A. Ali, Jeremy Chang, Smrithi Sunil, Shruti Sudhakar, William H. Tomaszewski, Grace Protasiewicz, Stephen M. Selkirk, Robert H. Miller and Jeffrey R. Capadona

26 ***Development and Characterization of PEDOT:PSS/Alginate Soft Microelectrodes for Application in Neuroprosthetics***
Laura Ferlauto, Antonio Nunzio D'Angelo, Paola Vagni, Marta Jole Ildelfonsa Airaghi Leccardi, Flavio Maurizio Mor, Estelle Annick Cuttaz, Marc Olivier Heuschkel, Luc Stoppini and Diego Ghezzi

36 ***Does Impedance Matter When Recording Spikes With Polytrodes?***
Joana P. Neto, Pedro Baião, Gonçalo Lopes, João Frazão, Joana Nogueira, Elvira Fortunato, Pedro Barquinha and Adam R. Kampff

45 ***Understanding the Effects of Both CD14-Mediated Innate Immunity and Device/Tissue Mechanical Mismatch in the Neuroinflammatory Response to Intracortical Microelectrodes***
Hillary W. Bedell, Sydney Song, Xujia Li, Emily Molinich, Shushen Lin, Allison Stiller, Vindhya Danda, Melanie Ecker, Andrew J. Shoffstall, Walter E. Voit, Joseph J. Pancrazio and Jeffrey R. Capadona

58 ***Diamond/Porous Titanium Nitride Electrodes With Superior Electrochemical Performance for Neural Interfacing***
Suzan Meijs, Matthew McDonald, Søren Sørensen, Kristian Rechendorff, Ladislav Fekete, Ladislav Klimša, Václav Petrák, Nico Rijkhoff, Andrew Taylor, Miloš Nesládek and Cristian P. Pennisi

68 ***Softening Shape Memory Polymer Substrates for Bioelectronic Devices With Improved Hydrolytic Stability***
Seyed Mahmoud Hosseini, Rashed Rihani, Benjamin Batchelor, Allison M. Stiller, Joseph J. Pancrazio, Walter E. Voit and Melanie Ecker

80 ***Quantification of Signal-to-Noise Ratio in Cerebral Cortex Recordings Using Flexible MEAs With Co-localized Platinum Black, Carbon Nanotubes, and Gold Electrodes***
Alex Suarez-Perez, Gemma Gabriel, Beatriz Rebollo, Xavi Illa, Anton Guimerà-Brunet, Javier Hernández-Ferrer, Maria Teresa Martínez, Rosa Villa and Maria V. Sanchez-Vives

92 ***Bioactive Neuroelectronic Interfaces***
Dayo O. Adewole, Mijail D. Serruya, John A. Wolf and D. Kacy Cullen

103 ***Response of Mouse Visual Cortical Neurons to Electric Stimulation of the Retina***
Sang Baek Ryu, Paul Werginz and Shelley I. Fried

121 ***Implantable Direct Current Neural Modulation: Theory, Feasibility, and Efficacy***
Felix P. Aplin and Gene Y. Fridman

140 ***Isolated Murine Brain Model for Large-Scale Optoacoustic Calcium Imaging***
Sven Gottschalk, Oleksiy Degtyaruk, Benedict Mc Larney, Johannes Rebling, Xosé Luis Deán-Ben, Shy Shoham and Daniel Razansky

151 ***Using Chronopotentiometry to Better Characterize the Charge Injection Mechanisms of Platinum Electrodes Used in Bionic Devices***
Alexander R. Harris, Carrie Newbold, Paul Carter, Robert Cowan and Gordon G. Wallace

164 ***3D Reconstruction of the Intracortical Volume Around a Hybrid Microelectrode Array***
Aparna Nambiar, Nicholas F. Nolta and Martin Han

178 ***Multichannel Silicon Probes for Awake Hippocampal Recordings in Large Animals***
Alexandra V. Ulyanova, Carlo Cottone, Christopher D. Adam, Kimberly G. Gagnon, D. Kacy Cullen, Tahl Holtzman, Brian G. Jamieson, Paul F. Koch, H. Isaac Chen, Victoria E. Johnson and John A. Wolf

194 ***Toward a Bidirectional Communication Between Retinal Cells and a Prosthetic Device – A Proof of Concept***
Viviana Rincón Montes, Jana Gehlen, Stefan Lück, Wilfried Mokwa, Frank Müller, Peter Walter and Andreas Offenhäusser

213 ***Mediating Retinal Ganglion Cell Spike Rates Using High-Frequency Electrical Stimulation***
Tianruo Guo, David Tsai, Chih Yu Yang, Amr Al Abed, Perry Twyford, Shelley I. Fried, John W. Morley, Gregg J. Suaning, Socrates Dokos and Nigel H. Lovell

225 ***Erratum: Mediating Retinal Ganglion Cell Spike Rates Using High-Frequency Electrical Stimulation***
Frontiers Production Office

227 ***Revealing Spatial and Temporal Patterns of Cell Death, Glial Proliferation, and Blood-Brain Barrier Dysfunction Around Implanted Intracortical Neural Interfaces***
Steven M. Wellman, Lehong Li, Yalikun Yaxiaer, Ingrid McNamara and Takashi D. Y. Kozai

244 ***Design and Development of Microscale Thickness Shear Mode (TSM) Resonators for Sensing Neuronal Adhesion***
Massoud L. Khraiche, Jonathan Rogul and Jit Muthuswamy

259 ***Mechanics of Brain Tissues Studied by Atomic Force Microscopy: A Perspective***
Prem Kumar Viji Babu and Manfred Radmacher

268 ***Tissue Response to Neural Implants: The Use of Model Systems Toward New Design Solutions of Implantable Microelectrodes***
Maurizio Gulino, Donghoon Kim, Salvador Pané, Sofia Duque Santos and Ana Paula Pêgo

292 ***Insights From Dynamic Neuro-Immune Imaging on Murine Immune Responses to CNS Damage***
R. Dixon Dorand, Bryan L. Benson, Lauren F. Huang, Agne Petrosiute and Alex Y. Huang

301 ***Viral-Mediated Optogenetic Stimulation of Peripheral Motor Nerves in Non-human Primates***
Jordan J. Williams, Alan M. Watson, Alberto L. Vazquez and Andrew B. Schwartz

317 ***Computational Simulation Expands Understanding of Electrotransfer-Based Gene Augmentation for Enhancement of Neural Interfaces***
Amr Al Abed, Jeremy L. Pinyon, Evelyn Foster, Frederik Crous, Gary J. Cowin, Gary D. Housley and Nigel H. Lovell

329 ***High Density, Double-Sided, Flexible Optoelectronic Neural Probes With Embedded μLEDs***
Jay W. Reddy, Ibrahim Kimukin, Luke T. Stewart, Zabir Ahmed, Alison L. Barth, Elias Towe and Maysamreza Chamanzar

344 ***Protuberant Electrode Structures for Subretinal Electrical Stimulation: Modeling, Fabrication and* in vivo *Evaluation***
Pedro González Losada, Lionel Rousseau, Marjorie Grzeskowiak, Manon Valet, Diep Nguyen, Julie Dégardin, Elisabeth Dubus, Serge Picaud and Gaelle Lissorgues

358 ***Chronically Implanted Microelectrodes Cause c-fos Expression Along Their Trajectory***
Patrick Pflüger, Richard C. Pinnell, Nadja Martini and Ulrich G. Hofmann

369 ***Second Harmonic Generation Imaging of Collagen in Chronically Implantable Electrodes in Brain Tissue***
Corinne R. Esquibel, Kristy D. Wendt, Heui C. Lee, Janak Gaire, Andrew Shoffstall, Morgan E. Urdaneta, Jenu V. Chacko, Sarah K. Brodnick, Kevin J. Otto, Jeffrey R. Capadona, Justin C. Williams and K. W. Eliceiri

frontiers in Neuroscience

EDITORIAL
published: 03 June 2020
doi: 10.3389/fnins.2020.00457

Editorial: Bridging the Gap in Neuroelectronic Interfaces

Ulrich G. Hofmann[1]* *and Jeffrey R. Capadona*[2,3]

[1] Medical Center, University of Freiburg, Freiburg, Germany, [2] Department of Biomedical Engineering, Case Western Reserve University, Cleveland, OH, United States, [3] Advanced Platform Technology Center, Louis Stokes Cleveland Veterans Affairs Medical Center, Cleveland, OH, United States

Keywords: brain-machine interfaces, brain implantable devices, brain stimulation, brain recordings, chronic implants, flexible substrate, BBB rupturing, neuroprotection

Editorial on the Research Topic

Bridging the Gap in Neuroelectronic Interfaces

In the field of Neuroelectronic Interfaces it seems as though the lines between reality and science-fiction/fantasy are often blurred. One of the inspirations for our most recent Gordon Research Conference in March 2018 aimed at "Bridging the Gap in Neuroelectronic Interfaces" dates back to 1999 when Chapin et al. (1999) described their ability to predict movement trajectories of rodents and non-human primates by "eavesdropping" on groups of neurons. Many in the field felt that science fiction seemed to become reality and the future of prosthetics appeared on the horizon. Less than a decade later invasive micro-electrode arrays and the latest jewels of micro-machining found their way into the brains of a few human patients as well (Hochberg et al., 2006), very much triggering expectations of a coming Golden Age of Brain-Machine-Interfacing for severely handicapped patients.

Unfortunately, after this very promising start two decades ago, these technologies were "lost in translation" (Ryu and Shenoy, 2009) on the way to clinical applications and widespread use. The unclear path through this first Valley of Death toward true chronic BMIs caused despair in patients and funders as well. It became clear a deterioration of signal quality largely due to the brain's fierce response to foreign bodies leads to a loss in high quality, wide-band signals meant to control any artifact or prosthetic device. One major obstacle thought to limit practical clinical translation is the poor understanding of failure modes of all types of high channel count implanted microelectrode arrays and how to counteract them. Besides fabrication and handling related failures (abiotic), several classes of multi-modal problems were encountered (biotic). The strong sterile inflammation and thus an electrical decoupling of implanted devices from the brain were identified as the major obstacle on the path to chronic applications in humans. However, where were the ideas to overcome this hurdle?

Such was the frustrating situation in our field when we were honored in 2016 by the Gordon Research Organisation to organize and run their inaugural conference dedicated to the unexpectedly complex neuro-electronic interface. Our intention was to look beyond the usual trinity of neurons, astrocytes, and microglia and provide some type of common knowledge in the surrounding of our challenge. The conference took place in 2018 in Galveston, Texas, and was attended by almost 200 researchers. It had an exquisite line-up of excellent speakers, motivated discussion leaders and curious audience—in short, it was a full week of intense discussion, collective brainstorming and shared experience—it was truly a success!

OPEN ACCESS

Edited and reviewed by:
Michele Giugliano, International School for Advanced Studies (SISSA), Italy

***Correspondence:**
Ulrich G. Hofmann
ulrich.hofmann@coregen.uni-freiburg.de

Specialty section:
This article was submitted to Neural Technology, a section of the journal Frontiers in Neuroscience

Received: *01 April 2020*
Accepted: *15 April 2020*
Published: *03 June 2020*

Citation:
Hofmann UG and Capadona JR (2020) Editorial: Bridging the Gap in Neuroelectronic Interfaces. Front. Neurosci. 14:457. doi: 10.3389/fnins.2020.00457

However, rules of the Gordon Research Conferences series prohibits documentation in any form, no photos, no abstracts were published—only paper and pencil are welcome. Therefore, this Special Research Topic is supposed to partially remedy this lack of collected knowledge and provide the multi-disciplinary audience of leading experts in micro-technology, cellular neuroscience, brain pathology, neuro-engineering, and materials science a platform to present their cutting edge solutions after peer review. We surely believe that this collection will progress the quest for a chronically useful and reliable neural interface.

Several insightful reviews support our conference's look outside the box and give an overview into microfluidic based model systems (Gulino et al.) useful to further explore the foreign body responses or nano-particle based stimulations. The prospects of bioactive, so called "living electrodes" were discussed by Adewole et al., who points out several differing approaches to "trick" the brain into incorporating artificial implants. The biomechanics of neuronal adhesion may play an important role in this context and can be assessed by frequency analysis of quartz crystal oscillators, as is pointed out by Khraiche et al.. As important as microscopic biomechanics is in our field of research, it is equally difficult to quantify in brain tissue. Help is offered from localized probing of biomechanics by Atomic Force Microscopy (AFM) as is briefly reviewed by Viji Babu and Radmacher. Another exciting review by Aplin and Fridman extensively discusses the rarely used constant current (DC) stimulation of neural tissue, a potential new field of neuromodulation enabled by recent developments in microfluidics.

As one common denominator, several groups reported on recent approaches to a long-standing idea to use of flexible or compliant substrates. For example, Hosseini et al. went so far as to present a novel, more stable, shape-memory polymer, able to soften in an aqueous environment. Materials of this type are designed to remain stiff during implantation, but compliant when deployed in the brain. Implantation of a stiff microelectrode may suffice to express c-Fos, a popular early marker for neuron activation, as found by Pflüger et al.. Flexible substrates were also presented by Dorand et al. and Reddy et al., exhibiting double sided electrodes to create novel micro-LEDs toward optogenetic applications. Optogenetic applications were the focus of another study that reported on an important milestone toward clinical use (Williams et al.). They were able to show optogenetic stimulation of muscles in non-human primates! It goes without saying, flexibility was not a feature expected from silicon probes successfully used in large animals as reported by Ulyanova et al..

Electrode composition and performance was an issue investigated in several articles.

Meijs et al. deposited different layers of Boron Doped Diamond (BDD) on TiN electrodes and compared them electrochemically, identifying good candidates for further *in vivo* testing. The article from Ferlauto et al. demonstrates a reduction of electrical noise by inserting conductive polymers as compliant intermediary on Pt-electrodes. Whereas, the work by Neto et al. informed us to stop worrying about impedances—at least of recording micro-electrodes in the usual range (0.1 to 2 MΩ)—as long as they exhibit a low shunting capacity. In contrast, potentiostatic experiments done by Harris et al. concluded that the use of Ohm's law to describe electrical stimulation over Pt-electrodes is an unwarranted oversimplification, ignoring the electrically complex, spatially varying tissue-electrode interface. In order to further the quality control with MEAs Suarez-Perez et al. introduced spectral definitions of SNR based on cortical slow oscillations (SO) providing a less disputable "signal" (LFP UP state) over a "noise" state.

Several articles dealt with improvements for artificial sensing front ends:

Losada et al. took the well-known mushroom electrodes (Spira and Hai, 2013) to a new level, by placing them on a flexible substrate inside a cavity, improving the stimulation efficacy to bipolar retinal cells. A more traditional approach to the retina was taken by Rincon Montes et al. who used custom designed, laminar and penetrating silicon probes to assess stimulation effects on other retinal layers in an attempt to close the stimulation loop. Ryu et al. went in a similar direction, but separated retinal electrical stimulation from laminar visual cortex recordings. Stimulation of retinal ganglion cells was investigated both by simulation and *in vitro* experiments to shed light on their non-monotonic response profile to high-frequency stimuli (Guo et al.). A novel simulation tool was presented by Al Abed et al. to shed light on *in vivo* electroporation in context of gene therapeutic improvements of the cochlea-electrode-interface.

Improvements of optical techniques were presented by several other articles.

Nambiar et al. demonstrated an algorithmic pipeline to reconstruct brain tissue surrounding explanted "hybrid" array electrodes. Esquibel et al. employed the label free, optical sectioning method of second harmonic generation to examine implanted brain slices and showed unusual collagen fiber patterns not found in normal brains. Quite remarkably, by applying a custom made optoacoustic imaging setup Gottschalk et al. monitored neuronal calcium dynamics under blood-free conditions deep in an *ex vivo* maintained whole mouse brain. It will not be the last we are going to hear from genetically encoded calcium indicators (GECI). Improvements in 2-photon imaging presented in the review by Dorand et al. show a complicated and dynamic response to BBB-rupturing, substantial immune activation and microglia participation which might warrant a systematic application of different medications. Wellman et al. further supports the quest to widen the circle of usual suspects around brain implanted devices as they reveal an involvement of a wealth of other players like oligodendrocytes or even pericytes. A view shared by Bedell et al. and Hermann et al. poihc who not only vote for minimizing the cross sectional area of implants, but propose benefits from targeting the TLR/CD14 pathway as a therapeutic mechanism—in particular focusing on infiltrating peripheral immune cells, while allowing the resident microglia to facilitate neuroprotection.

As hoped for while organizing the conference, several overarching cutting-edge topics were presented to the

community for the first time. The conference organizers then crystalized the momentum from the meeting into in the subsequent articles reported in this virtual issue. Unfortunately, the COVID-19 pandemic postponed the most recent installment of our meeting. Please continue to check the Gordon Research Conference website for information about the rescheduled conference.

AUTHOR CONTRIBUTIONS

UH and JC both wrote and edited this article.

REFERENCES

Chapin, J. K., Moxon, K. A., Markowitz R. S., and Nicolelis, M. A. L. (1999). Real-time control of a robot arm using simultaneously recorded neurons in the motor cortex. *Nat. Neurosci.* 2, 664–670. doi: 10.1038/10223

Hochberg, L. R., Serruya, M. D., Friehs, G. M., Mukand, J. A., Saleh, M., Caplan, A. H., et al. (2006). Neuronal ensemble control of prosthetic devices by a human with tetraplegia. *Nature* 442, 164–171. doi: 10.1038/nature04970

Ryu, S. I., and Shenoy, K. V. (2009). Human cortical prostheses: lost in translation? *Neurosurg. Focus* 27:E5. doi: 10.3171/2009.4.FOCUS0987

Spira, M. E., and Hai, A. (2013). Multi-electrode array technologies for neuroscience and cardiology. *Nat. Nanotechnol.* 8, 83–94. doi: 10.1038/nnano.2012.265

FUNDING

This work was supported by the Research Career Scientist Award # GRANT12635707 (Capadona) from the United States (US) Department of Veterans Affairs Rehabilitation Research and Development Service.

ACKNOWLEDGMENTS

Special thanks to the Gordon Research Organisation and all the sponsors of the 2018 meeting.

Conflict of Interest: The authors declare that the research was conducted in the absence of any commercial or financial relationships that could be construed as a potential conflict of interest.

Copyright © 2020 Hofmann and Capadona. This is an open-access article distributed under the terms of the Creative Commons Attribution License (CC BY). The use, distribution or reproduction in other forums is permitted, provided the original author(s) and the copyright owner(s) are credited and that the original publication in this journal is cited, in accordance with accepted academic practice. No use, distribution or reproduction is permitted which does not comply with these terms.

frontiers in Bioengineering and Biotechnology

ORIGINAL RESEARCH
published: 14 August 2018
doi: 10.3389/fbioe.2018.00113

The Role of Toll-Like Receptor 2 and 4 Innate Immunity Pathways in Intracortical Microelectrode-Induced Neuroinflammation

*John K. Hermann[1,2], Shushen Lin[1,2], Arielle Soffer[1,2], Chun Wong[1,2], A. Ali[1,2], Jeremy Chang[1,2], Smrithi Sunil[1,2], Shruti Sudhakar[1,2], William H. Tomaszewski[1,2], Grace Protasiewicz[1,2], Stephen M. Selkirk[2,3,4], Robert H. Miller[5] and Jeffrey R. Capadona[1,2]**

[1] Department of Biomedical Engineering, Case Western Reserve University, Cleveland, OH, United States, [2] Advanced Platform Technology Center, Louis Stokes Cleveland Veterans Affairs Medical Center, Cleveland, OH, United States, [3] Department of Neurology, Case Western Reserve University, Cleveland, OH, United States, [4] Spinal Cord Injury Division, Louis Stokes Cleveland Veterans Affairs Medical Center, Cleveland, OH, United States, [5] Neurosciences, George Washington University, Washington, DC, United States

OPEN ACCESS

Edited by:
Nihal Engin Vrana,
Protip Medical, France

Reviewed by:
Helena Knopf-Marques,
INSERM U1121 Biomatériaux et Bioingénierie, France
Cristian Pablo Pennisi,
Aalborg University, Denmark

***Correspondence:**
Jeffrey R. Capadona
jeffrey.capadona@case.edu

Specialty section:
This article was submitted to Biomaterials, a section of the journal Frontiers in Bioengineering and Biotechnology

Received: 05 June 2018
Accepted: 19 July 2018
Published: 14 August 2018

Citation:
Hermann JK, Lin S, Soffer A, Wong C, Ali A, Chang J, Sunil S, Sudhakar S, Tomaszewski WH, Protasiewicz G, Selkirk SM, Miller RH and Capadona JR (2018) The Role of Toll-Like Receptor 2 and 4 Innate Immunity Pathways in Intracortical Microelectrode-Induced Neuroinflammation. Front. Bioeng. Biotechnol. 6:113. doi: 10.3389/fbioe.2018.00113

We have recently demonstrated that partial inhibition of the cluster of differentiation 14 (CD14) innate immunity co-receptor pathway improves the long-term performance of intracortical microelectrodes better than complete inhibition. We hypothesized that partial activation of the CD14 pathway was critical to a neuroprotective response to the injury associated with initial and sustained device implantation. Therefore, here we investigated the role of two innate immunity receptors that closely interact with CD14 in inflammatory activation. We implanted silicon planar non-recording neural probes into knockout mice lacking Toll-like receptor 2 (*Tlr2*$^{-/-}$), knockout mice lacking Toll-like receptor 4 (*Tlr4*$^{-/-}$), and wildtype (WT) control mice, and evaluated endpoint histology at 2 and 16 weeks after implantation. *Tlr4*$^{-/-}$ mice exhibited significantly lower BBB permeability at acute and chronic time points, but also demonstrated significantly lower neuronal survival at the chronic time point. Inhibition of the Toll-like receptor 2 (TLR2) pathway had no significant effect compared to control animals. Additionally, when investigating the maturation of the neuroinflammatory response from 2 to 16 weeks, transgenic knockout mice exhibited similar histological trends to WT controls, except that knockout mice did not exhibit changes in microglia and macrophage activation over time. Together, our results indicate that complete genetic removal of Toll-like receptor 4 (TLR4) was detrimental to the integration of intracortical neural probes, while inhibition of TLR2 had no impact within the tests performed in this study. Therefore, approaches focusing on incomplete or acute inhibition of TLR4 may still improve intracortical microelectrode integration and long term recording performance.

Keywords: BCI, intracortical microelectrode, neuroinflammation, innate immunity, Toll-like receptors

INTRODUCTION

Brain machine interfaces are a growing area of interest for basic research, rehabilitation, and commercial applications (Winkler, 2017; Wu and Rao, 2017; Savage, 2018). Intracortical microelectrodes remain a high-resolution tool for extracting information from the brain (Ajiboye et al., 2017), critical for current and future applications. Unfortunately, inconsistent recording performance remains a barrier to long-term utilization in any animal model, including humans (Gunasekera et al., 2015; Patel et al., 2016; Wellman et al., 2018).

The correlation between the neuroinflammatory response to intracortical microelectrodes and recording performance remains a commonly debated topic for over a decade (Szarowski et al., 2003; Biran et al., 2005; Jorfi et al., 2015). The consensus of the field is that in order to maintain viable recordings, the integrity of both the implanted electrodes and the neural tissue must remain intact. Several labs have shown that delamination of the insulation layers or corrosion of the electrode contacts are common in both accelerated aging and upon explanting of a variety of microelectrode types (Prasad et al., 2012, 2014; Barrese et al., 2013; Jorfi et al., 2015; Kozai et al., 2015; Takmakov et al., 2015). Additionally, the loss of neuronal cell bodies and dendrites within the distance required for single unit detection (Buzsáki, 2004) is well documented (Jorfi et al., 2015). While subtle difference exist across all microelectrode types, the typical response to intracortical microelectrodes can be generalized (Jorfi et al., 2015); upon implantation of the microelectrodes, tissue and cells are damaged resulting in both wound healing and scar formation. Most importantly, the robust response from microglia and macrophages leads to neuronal dieback, astrocytic encapsulation, and blood-brain barrier permeability, each of which have been implicated in biological failure mechanisms of single unit recordings from intracortical microelectrodes (Polikov et al., 2005; McConnell et al., 2009; Saxena et al., 2013; Jorfi et al., 2015).

As the failure modes of intracortical microelectrodes are further elucidated, one mechanism that has been suggested to play a key role in several failure modes is oxidative stress and/or Fenton chemical reactions (iron catalyzed peroxide formation) at the microelectrode-tissue interface (Prasad et al., 2012, 2014; Barrese et al., 2013; Potter et al., 2013, 2014; Potter-Baker et al., 2014a, 2015; Potter-Baker and Capadona, 2015; Ereifej et al., 2018). Pro-inflammatory cells (activated microglia, macrophages and astrocytes) remain reactive on and around the intracortical microelectrodes for the duration of implantation (McConnell et al., 2009; Ravikumar et al., 2014b; Nguyen et al., 2016). Furthermore, it is understood that these pro-inflammatory cells release cytokines (Polikov et al., 2005), free radicals, reactive oxygen species (ROS) and reactive nitrogen species (RNS) when activated (Streit et al., 1999; Abbott et al., 2006; Kettenmann et al., 2011).

Many attempts have been made to alter the design or materials properties of the intracortical microelectrodes to minimize the neuroinflammatory response (for review see Jorfi et al., 2015). We have utilized many antioxidative strategies to specifically attenuate oxidative damage, resulting in higher densities of neuronal nuclei and more viable neurons at the intracortical microelectrode / tissue interface (Potter et al., 2013, 2014; Potter-Baker et al., 2014a; Jorfi et al., 2015; Nguyen et al., 2016). In parallel, we have also attempted to understand the subcellular mechanisms at play in the initiation of reactive oxygen species generation, in response to the implantation and chronic indwelling of intracortical microelectrodes (Ereifej et al., 2018).

In that respect, we have identified the innate immunity receptor CD14 as a molecule of interest in the chronic neuroinflammatory response to implanted intracortical microelectrodes (Bedell et al., 2018; Hermann et al., 2018). CD14 is a molecule associated with the recognition of pathogen associated molecular patterns (PAMPs) and damage associated molecular patterns (DAMPs) to promote inflammation, including the release of numerous cytokines, chemokines, and reactive oxygen species (Reed-Geaghan et al., 2009; Janova et al., 2015). Hermann et al. first observed acute but not chronic improvements in intracortical microelectrode recording performance in knockout mice lacking CD14, and chronic improvements in recording performance in mice receiving a small-molecule inhibitor to the CD14 pathway (Hermann et al., 2018). More recently, using a bone marrow chimera model, Bedell et al. demonstrated that inhibiting CD14 from only the blood-derived macrophages, and not resident brain derived glial cells improves recording quality over the 16 week long study (Bedell et al., 2018). Together, these two studies indicated that partial inhibition of CD14 pathways resulted in a greater improvement to microelectrode performance than complete inhibition. Therefore, we are interested in developing a better understanding of the mechanism, to optimize the natural wound healing response, yet still inhibit the over-excitation of the pathway that can lead to decreased microelectrode performance.

In the current study, we will focus on the complementary receptors associated with CD14 activation, Toll-like receptors 2 and 4 (TLR2 and TLR4). TLR4 is an innate immunity receptor closely associated with CD14 that is involved in the recognition of PAMPs and DAMPs to promote inflammation (Asea et al., 2002; Reed-Geaghan et al., 2009; Trotta et al., 2014). TLR2 is another innate immunity receptor closely associated with CD14 that is involved in the recognition of PAMPs and DAMPs to promote inflammation (Asea et al., 2002; Reed-Geaghan et al., 2009; Piccinini and Midwood, 2010; Kong and Le, 2011). Both TLR2 and TLR4 have been associated with neurodegenerative disorders (Landreth and Reed-Geaghan, 2009; Arroyo et al., 2011; Casula et al., 2011; Kong and Le, 2011; Trotta et al., 2014). Of note, the small molecule inhibitor to CD14 (IAXO-101, Innaxon) is also listed as a TLR4 inhibitor. Thus, we hypothesize that TLR2 and TLR4 differentially play a role in the neuroinflammatory response to implanted intracortical microelectrodes. To test this hypothesis, we implanted silicon planar non-recording neural probes in the shape of Michigan-style intracortical microelectrode arrays into knockout mice lacking TLR2 ($Tlr2^{-/-}$), knockout mice lacking TLR4 ($Tlr4^{-/-}$), and WT control mice, and evaluated endpoint histology at 2 and 16 weeks after implantation. Gaining a more detailed understanding of innate immunity receptors associated with

the CD14 pathway should further our understanding of CD14 mediated neuroinflammation to intracortical microelectrodes.

MATERIALS AND METHODS

Animal Model

Tlr2$^{-/-}$ mice (B6.129-Tlr2^{tm1Kir}/J, stock no. 004650), *Tlr4*$^{-/-}$ mice (B6.B10ScN-Tlr4$^{lps-del}$/JthJ, stock no. 007227), and WT mice (C57BL/6J, stock no. 000664) were acquired from the Jackson laboratory and bred in-house. Both male and female mice were used as to not bias the results based on sex. Mice were handled according to the approved Case Western Reserve University IACUC protocol and the NIH Guide for Care and Use of Laboratory Animals.

Genotyping

Strains of mice were verified prior to surgery by extracting DNA from tail snips, running PCR, and running gel electrophoresis. Genotyping protocols were performed as suggested by the mouse vendor (Jackson Laboratories), following similar protocols described in previous studies within the lab (Bedell et al., 2018).

Probe Implantation Surgery

Mice were implanted with neural probes (described in detail below) using methods adapted from Ravikumar et al. (2014a,b) and Potter-Baker et al. (2014b). Mice were aged to between 5 and 9 weeks; and weighed between 14 and 29 grams at the time of surgery. Each mouse was induced with 3% isoflurane in an induction chamber. While under anesthesia, mice were mounted to the ear bars of the stereotaxic frame, and anesthesia was lowered to 1% isoflurane for maintenance. Mice were kept on a heating pad while under anesthesia to maintain body temperature. Ophthalmic ointment was applied to the eyes of the mouse to prevent drying, followed by shaving of the scalp with a hand-held beard trimmer. The scalp of the mouse was sterilized with three applications of betadine alternated with 70% isopropanol. Marcaine (0.02 ml, 0.25%) was injected below the scalp, at the surgical site, as a local anesthetic. Either buprenorphine (0.1 mg/kg) or meloxicam (0.07 ml, 1.5 mg/mL) were administered subcutaneously as an analgesic. Choice of analgesic changed during the study due to availability from the vendor at the time. Substitutions were chosen following consultation with staff veterinarian. Additionally, cefazolin (0.2 mL, 2 mg/mL) was injected subcutaneously as an antibiotic, to prevent post-operative infection. The proper surgical plane of anesthesia was verified using a toe pinch throughout the surgery.

Mouse skulls were exposed by a midline incision on the scalp and retraction of the skin using tissue spreaders. Craniotomies were carried out using a 3 mm biopsy punch (PSS select) lateral to midline, and between lambda and bregma, to minimize heat associated with drilling (Shoffstall et al., 2017). One alcohol cleaned, ethylene oxide-sterilized silicon probe in the shape of a Michigan-style microelectrode array (2 mm long × 123 μm wide (tapered) × 15 μm thick, 1 mm x 1 mm bond tab) was inserted 2 mm into the craniotomy via forceps to avoid vasculature. Prior to sterilization, electrodes were cleaned in 70% ethanol and de-ionized water. Craniotomies were sealed with a biocompatible silicone elastomer (Kwik-sil) and closed with a UV-cured liquid dentin (Fusio/Flow-it ALC, Pentron dental). Protruding bond tabs were encased in the liquid dentin to anchor the implant. Incisions were sutured closed with 5-0 monofilament polypropylene suture (Butler Schein). Antibiotic ointment was applied to the incision to prevent infection.

Mice were administered cefazolin (0.2 mL, 2 mg/mL) subcutaneously twice on the first day after surgery. Mice were administered meloxicam (0.07 ml, 1.5 mg/mL) once or buprenorphine (0.1 mg/kg) twice on the first day after surgery and as needed thereafter. Mice were monitored daily for 5 days after the operation for signs of pain and distress and then weekly thereafter.

Tissue Processing

Mice were transcardially perfused 2 or 16 weeks after probe implantation using protocols adapted from Ravikumar et al. (2014a). Prior to transcardial perfusion, mice were anesthetized with 0.3 ml of a 10 mg ml^{-1} ketamine, 1 mg ml^{-1} xylazine solution, administered subcutaneously. Additional ketamine-xylazine solution was administered as needed. Following perfusions, the mouse heads were removed and post-fixed in 4% paraformaldehyde dissolved in 1xPBS overnight. Liquid dentin skull caps were carefully removed up from the skulls to remove implanted electrodes and minimize damage to the tissue. Brains were gently extracted from skulls and transferred to a series of sucrose solutions with concentrations of 10%, 20%, and two rounds of 30% in 1xPBS for cryoprotection. Upon equilibration (typically overnight), brains were advanced to the next solution in the series and stored at 4°C. Next, brains were frozen in blocks of Optical Cutting Temperature gel over dry ice and moved to a −80°C freezer. Finally, brains were cryostat sectioned into 16 μm horizontal slices and directly mounted to slides at a ∼ −20 to −25°C, and stored at −80°C until removed for immunohistochemical staining.

Endpoint Histology

Two cohorts of animals were implanted with neural probes to assess both the acute and chronic neuroinflammatory response to implanted intracortical microelectrodes. For the purposes of this study, four histological markers were investigated. First, since neurons are the source of electrical signals recorded by intracortical microelectrodes, sections of cortical tissue were stained with an antibody directed against NeuN, a nuclear protein specific to neurons (Mullen et al., 1992). Neuronal dieback around implanted intracortical microelectrode arrays is commonly attributed to the release of soluble factors by inflammatory activated microglia and macrophages (Polikov et al., 2005). Therefore, to understand how the absences of TLR2 and TLR4 affect inflammatory activation of microglia and macrophages in response to implanted neural probes, sections of cortical tissue were stained with an antibody directed against CD68 (macrosialin), a sialoglycoprotein found in activated microglia and macrophages (Rabinowitz and Gordon, 1991). Another byproduct of chronic inflammatory mechanisms potentially detrimental to intracortical microelectrode activation is astrocytic encapsulation. Astrocytes may become hypertrophic

in response to implanted microelectrode arrays and encase the array in a sheath that impedes electrical signals (Burns et al., 1974). Therefore, to understand how the absences of TLR2 and TLR4 affect astrocytic encapsulation in response to implanted neural probes, sections of cortical tissue were stained with an antibody directed against glial fibrillary acidic protein (GFAP), an astrocytic intermediate filament that is upregulated during inflammatory activation (Eddleston and Mucke, 1993). Finally, another component of chronic inflammatory mechanisms correlated to poor recording performance is blood-brain barrier permeability (Saxena et al., 2013). To understand how the absences of TLR2 and TLR4 affect blood-brain barrier permeability in response to implanted neural probes, sections of cortical tissue were stained with an antibody directed against IgG, a blood protein not normally found in healthy brain tissue.

Immunohistochemical Staining

Staining protocols were adapted from Ravikumar et al. (2014a). Microscope slides were removed from the freezer and equilibrated to room temperature in a humidity chamber. Brain slices were blocked in buffers composed of 4% goat or chicken serum, 0.3% Triton-X 100, and 0.1% sodium azide dissolved in 1x PBS for 1 h at room temperature. Primary and secondary stain selections and dilutions are summarized in **Table 1**. Brain slices were incubated in primary antibody solutions dissolved in blocking buffers containing serum matching the species of secondary antibody. Brain slices were incubated in secondary antibody solutions for 2 h at room temperature. Tissue autofluorescence was reduced via the application of a copper sulfate solution, as described by Potter et al. (2012b). Microscope slides of brain slices were coverslipped using fluromount-G mounting medium.

DAB Staining for Neuronal Nuclei

A majority of the tissue slices stained for neuronal nuclei using NeuN were followed with a DAB chromogen to make the cells visible under brightfield light. Protocols to stain neuronal nuclei were adapted from Ravikumar et al. (2014a). Brain slices were blocked in goat blocking buffer for 1 h at room temperature. Slices were then incubated in blocking buffer solutions containing NeuN antibodies (Millipore MAB377) diluted 1:250 for 1 h at room temperature. Horseradish peroxidase polymer and DAB chromogen were added to the brain slices according to the manufacturer protocols (Life Technologies Super PicTure Polymer Detection Kit, Ref 879163). Hematoxylin was applied to the brain slices as a counter stain for all cell nuclei. Slides were coverslipped with Histomount mounting medium.

Additional NeuN sections were added using a superior protocol involving a fluorescent secondary antibody. These sections were stained following the protocols established in section Endpoint Histology. Since NeuN was quantified by hand, regardless of the protocol, no difference in results were achieved with the two protocols, just ease of quantification for the counter.

Imaging

Fluorescent images were captured using a Zeiss AxioObserver Z1 inverted fluorescent microscope with a 10x objective and an AxioCam MRm monochrome camera. As described in Hermann et al. 4 × 4 mosaic images centered on the probe hole were assembled using AxioVision and Zen software (Hermann et al., 2018).

Color images were captured for NeuN stains utilizing a DAB chromogen, as described by Ravikumar et al. (2014a). The same AxioObserver Z1 inverted microscope was used with a 10x objective and an Erc5 color camera. As described by Ravikumar et al. 4 × 4 mosaic images were assembled using Axiovision software (Ravikumar et al., 2014a).

Representative images of sham animals not implanted with neural probes are displayed in **Figure 1**. Sham animals were age matched to the 16 week group and underwent the same perfusion, tissue processing, and staining protocols as described above. This figure demonstrates constitutive expression of NeuN, CD68, GFAP, and IgG in *Tlr2*$^{-/-}$, *Tlr4*$^{-/-}$, and WT mice. No differences were seen in control, non-implanted shams.

The brightness and color balance of representative images were adjusted to enhance visibility.

Neuronal Nuclei Counting

Neuronal nuclei counts were obtained using our freely available custom Matlab scripts Second and AfterNeuN as described in Hermann et al. (2018). A user traced the outline of the probe hole and defined artifacts (tissue edge, etc) using Second and subsequently defined NeuN positive cell positions using AfterNeuN. Users counted out to a background defined as 400 μm from the probe hole plus a 50 μm buffer zone. Neuronal density was quantified as cell count per area, in concentric 50 μm bins extending from the probe hole. Percent of background density was quantified as bin neuronal density divided by the neuronal density of the 300–400 μm region times 100. Average percent of background was assessed for each animal using 3–7 slices. Mean and standard error were defined for each group based on animal averages from 4 to 7 mice per group. Statistics are calculated using animal averages.

TABLE 1 | Summary of immunohistochemical reagents used in histology.

Target	Antigen	1° Antibody	Concentration	2° Antibody/Detection Kit	Concentration
Neurons (DAB)	NeuN	Millipore MAB377	1:250	Life Technologies 879163	N/A
Neurons (Fluorescent)	NeuN	Millipore MAB377	1:250	Thermo Fisher Scientific A21121	1:1,000
Astrocytes	GFAP	Neuromics RA22101	1:500	Thermo Fisher Scientific A11012	1:1,000
Activated Microglia/Macrophages	CD68	Abcam ab53444	1:500	Thermo Fisher Scientific A21470	1:1,000
Extravasated Blood Proteins	IgG	AbD Serotec STAR26B	1:500	Thermo Fisher Scientific A21442	1:1,000

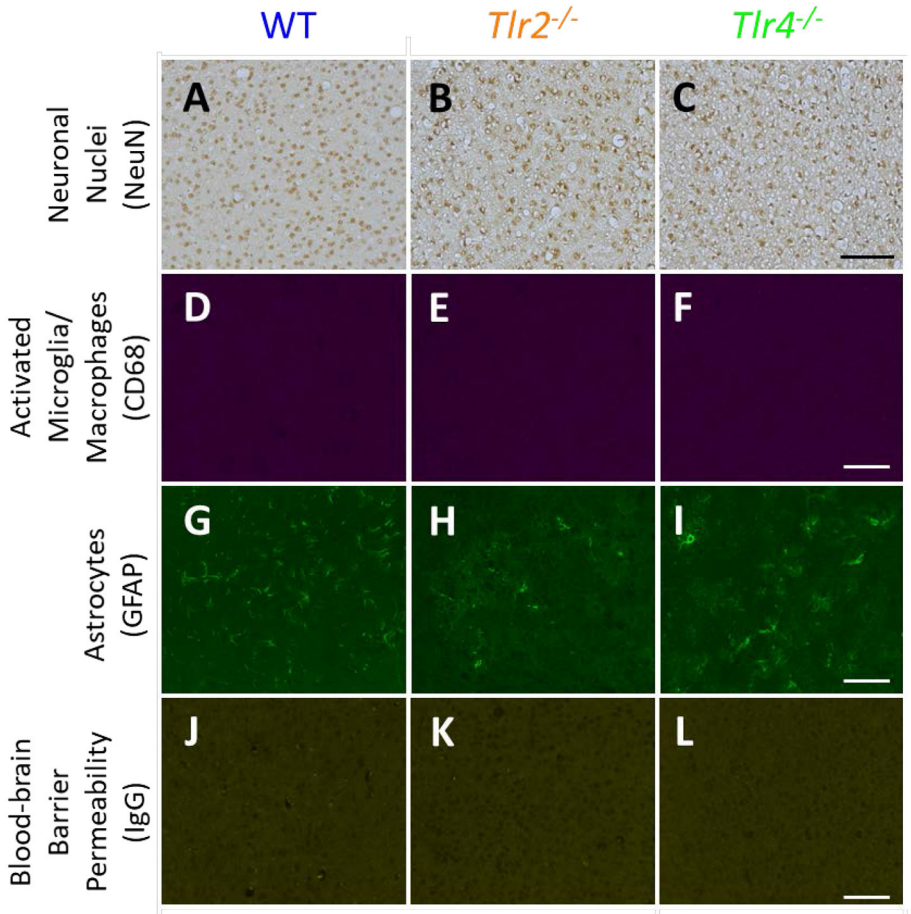

FIGURE 1 | Immunohistochemical staining in sham animals. WT **(A,D,G,J)**, *Tlr2*$^{-/-}$ **(B,E,H,K)**, and *Tlr4*$^{-/-}$ **(C,F,I,L)** mice without implanted probes were stained for neuronal nuclei (NeuN, **A-C**), activated microglia and macrophages (CD68, **D–F**), astrocytes (GFAP, **G–I**), and blood-brain barrier permeability (IgG, **J–L**). Scale bars are provided for each row of images, scale = 100 μm.

Immunohistochemical Marker Quantification

Immunohistochemical markers were quantified using the Matlab script Second, as described in Hermann et al. (2018). A user traced the outline of the probe hole and defined artifacts using Second. Second calculated fluorescence intensity in 5 μm concentric bins out to a distance of 650 μm from the probe. Background intensity was defined as the fluorescence intensity in the 600–650 μm region. Fluorescence intensity was normalized to a value of 0 at background for CD68 and IgG as no CD68 or IgG expression is seen in the non-implanted sham (**Figure 1**), and normalized to a value of 1 at background for GFAP, as GFAP is expressed in native tissue (**Figure 1**). Area under the curve was calculated for 50 μm bins extending away from the probe hole; 5 μm normalized intensity bins and 50 μm area under the curve bins were averaged by animal across 3–6 slices. Mean and standard error for each group were based on animal averages from 4 to 8 mice per group. Statistics were calculated using animal averages of 50 μm area under the curve bins.

Statistics

All statistical comparisons were carried out using Minitab software. For each time point neuronal nuclei percent background density and normalized fluorescence intensity area under the curve animal averages are compared between knockout mice and WT controls. Animal average values for a given stain were entered into a general linear model with animal average values from other strains at the same time point. Comparisons are made between *Tlr2*$^{-/-}$ and WT mice and between *Tlr4*$^{-/-}$ and WT mice using a Bonferroni test. Significance was defined as a p value less than 0.05.

Additionally, statistical comparisons were made between mice of the same strain at different time points. Neuronal nuclei percent background density and normalized fluorescence intensity area under the curve animal averages are compared between 2 and 16 week time points. Animal average values from a given strain and time point are entered into a general linear model with animal average values from the same strain at the opposite time point. Comparisons are made between 2 and 16

week mice for a given strain using a Bonferroni test. Significance was defined as a p value less than 0.05.

RESULTS

Acute (2-Week) Neuroinflammatory Response to Implanted Intracortical Probes in *Tlr2*$^{-/-}$, *Tlr4*$^{-/-}$, and WT Mice

Plots of percentage of background neuronal density (Neuronal survival) or normalized fluorescence intensity (microglia/macrophage activation, astrocytic encapsulation, blood-brain barrier permeability) with respect to distance from probe hole for *Tlr2*$^{-/-}$, *Tlr4*$^{-/-}$, and WT are shown in **Figure 2**. All three strains of mice exhibited trends of increasing neuronal density, decreasing microglia/macrophage activation, decreasing astrocytic encapsulation, and decreasing blood-brain barrier permeability with increasing distance from the probe hole at the acute 2-week time point. Examination of neuronal survival via the NeuN stain in *Tlr2*$^{-/-}$, *Tlr4*$^{-/-}$, and WT mice (**Figure 2A**) revealed no statistical differences between groups at the counted distance intervals (*Tlr2*$^{-/-}$: $N = 7$; *Tlr4*$^{-/-}$: $N = 5$; WT: $N = 5$). Similarly, examination of the accumulation of inflammatory activated microglia and macrophages via CD68 revealed no significant differences between either of the knockout conditions and WT mice (*Tlr2*$^{-/-}$: $N = 8$; *Tlr4*$^{-/-}$: $N = 4$; WT: $N = 6$). Additionally, examination of the chronic glial scar as a function of GFAP expression also indicated no significant differences were observed between either of the knockout conditions and WT mice (**Figure 2C**). Unlike glial cell density, blood-brain barrier permeability (as a function of IgG expression) indicated significant differences between experimental and control group at the acute 2-week time point (**Figure 2D**). Specifically, *Tlr4*$^{-/-}$ mice exhibit significantly less IgG expression compared to WT mice at the distance intervals 0–50 and 550–600 μm from the probe hole, indicating reduced blood-brain barrier permeability, $\$p < 0.05$ (*Tlr2*$^{-/-}$: $N = 5$; *Tlr4*$^{-/-}$: $N = 4$; WT: $N = 6$). *Tlr2*$^{-/-}$ mice did not exhibit any differences in IgG expression from WT controls.

Chronic (16-Week) Neuroinflammatory Response to Implanted Intracortical Probes in *Tlr2*$^{-/-}$, *Tlr4*$^{-/-}$, and WT Mice

An additional cohort of animals was implanted with identical non-functional probes for 16 weeks, to assess the chronic neuroinflammatory response (Potter et al., 2012a). Examination of neuronal density via the NeuN stain in *Tlr2*$^{-/-}$, *Tlr4*$^{-/-}$, and WT mice revealed a trend of increasing neuronal survival with distance from the probe at the 16 week time point (**Figure 3A**). Neuronal survival in *Tlr4*$^{-/-}$ mice was significantly lower than neuronal survival in WT mice in the distance interval 0–50 μm from the probe hole. Neuronal survival in *Tlr2*$^{-/-}$ mice was significantly higher than neuronal survival in WT mice in the distance intervals 200–250 and 250–300 μm from the probe hole (*Tlr2*$^{-/-}$: $N = 5$; *Tlr4*$^{-/-}$: $N = 5$; WT: $N = 7$). Examination of the accumulation of inflammatory activated microglia and macrophages via CD68 expression indicated that *Tlr2*$^{-/-}$, *Tlr4*$^{-/-}$, and WT mice all exhibit a trend of decreasing CD68 expression with distance from the probe hole at the chronic 16 week time point (**Figure 3B**). However, no significant differences were observed between either of the knockout conditions and WT mice (*Tlr2*$^{-/-}$: $N = 5$; *Tlr4*$^{-/-}$: $N = 5$; WT: $N = 7$). Similarly, examination of the chronic glial scar as a function of GFAP expression also indicated no significant differences between either of the knockout conditions and WT mice (*Tlr2*$^{-/-}$: $N = 8$; *Tlr4*$^{-/-}$: $N = 4$; WT: $N = 6$) (**Figure 3C**). Unlike glial cell density, blood-brain barrier permeability as a function of IgG expression indicated significant differences between experimental and control group at 16 weeks post-implantation (**Figure 3D**). Specifically, *Tlr4*$^{-/-}$ mice exhibit significantly less IgG expression compared to WT mice at each of the interval examined from 0 to 350 μm from the probe hole, indicating reduced blood-brain barrier permeability, $\$p < 0.05$. Additionally, *Tlr2*$^{-/-}$ mice exhibit significantly less IgG expression within a distance of 450–500 μm from the probe hole, indicating reduced blood-brain barrier permeability, $^*p < 0.05$ (*Tlr2*$^{-/-}$: $N = 5$; *Tlr4*$^{-/-}$: $N = 4$; WT: $N = 6$).

The Progression of Neuroinflammation and Neurodegeneration Following Intracortical Microelectrode Implantation

It is also important to understand how the progression of the neuroinflammatory and neurodegenerative response to intracortical microelectrodes is effected by the removal of either TLR2 or TLR4 from the innate immunity process. Therefore, expression of immunohistochemical markers for neuronal survival, microglia and macrophage activation, astrocytic encapsulation, and blood brain barrier permeability were compared between the 2 week and 16 week time points for WT (**Figure 4**), *Tlr2*$^{-/-}$ (**Figure 5**), and *Tlr4*$^{-/-}$ mice (**Figure 6**), independent of each other.

The Progression of Neuroinflammation and Neurodegeneration in WT Mice

Changes in immunohistochemical markers between the acute 2-week and chronic 16-week time points in WT mice will indicate the standard progression of chronic neuroinflammatory mechanisms in response to implanted neural probes in mice. Examination of neuronal density via the NeuN stain in WT mice exhibited significantly higher neuronal density at 2 weeks after probe implantation in distance intervals between 150 and 300 μm from the probe hole, $^*p < 0.05$ (2 wk WT: $N = 5$; 16 wk WT: $N = 7$) (**Figure 4A**). Additionally, examination of the accumulation of inflammatory activated microglia and macrophages via CD68 expression indicated WT mice exhibit significantly higher CD68 expression at 2 weeks after probe implantation in distance intervals between 0 and 100 μm from the probe hole, $^*p < 0.05$ (2 wk WT: $N = 6$; 16 wk WT: $N = 7$) (**Figure 4B**). In contrast, examination of the chronic glial scar as a function of GFAP expression revealed WT mice exhibit significantly higher GFAP expression at 16 weeks after probe implantation in distance intervals between 0 and 200 μm from the probe hole, $^*p < 0.05$ (2 wk WT: $N = 6$; 16 wk WT: N

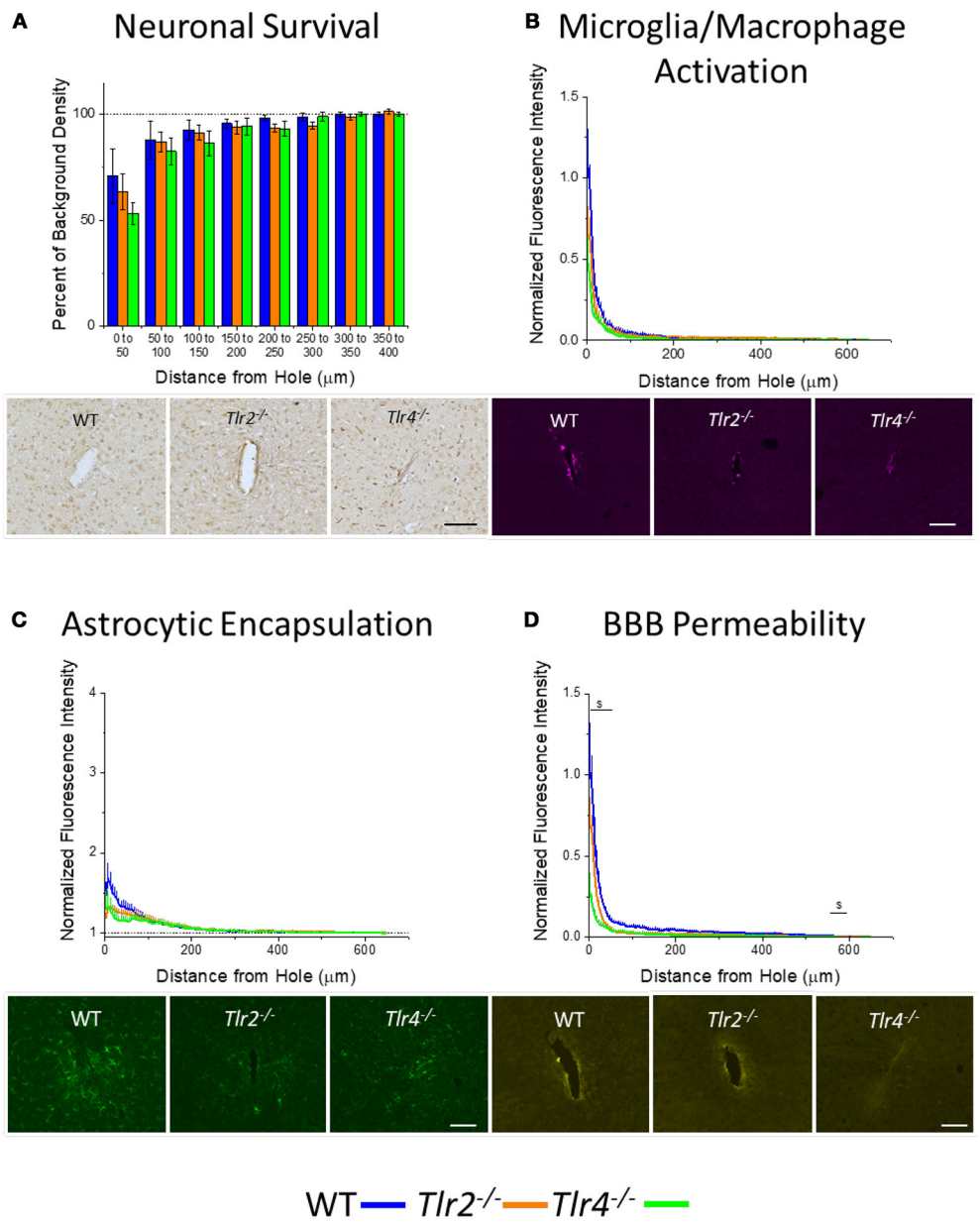

FIGURE 2 | Acute immunohistochemical evaluation of *Tlr2*$^{-/-}$, *Tlr4*$^{-/-}$, and wildtype mice two weeks after probe implantation. **(A)** Neuronal survival in cortical tissue around implanted probes presented as percent of background density with respect to distance from probe hole (μm). No significant differences were observed between either of the knockout conditions and wildtype mice. *Tlr2*$^{-/-}$: $N = 7$; *Tlr4*$^{-/-}$: $N = 5$; WT: $N = 5$. **(B)** Microglia and macrophage activation in cortical tissue around implanted probes presented as normalized fluorescence intensity with respect to distance from probe hole (μm). Normalized fluorescence intensity indicates expression of CD68. No significant differences were observed between either of the knockout conditions and wildtype mice. *Tlr2*$^{-/-}$: $N = 8$; *Tlr4*$^{-/-}$: $N = 4$; WT: $N = 6$. **(C)** Astrocyte encapsulation in cortical tissue around implanted probes presented as normalized fluorescence intensity with respect to distance from probe hole (μm). Normalized fluorescence intensity indicates expression of GFAP. No significant differences were observed between either of the knockout conditions and wildtype mice. *Tlr2*$^{-/-}$: $N = 8$; *Tlr4*$^{-/-}$: $N = 4$; WT: $N = 6$. **(D)** Blood-brain barrier permeability presented as normalized fluorescence intensity with respect to distance from probe hole (μm). Normalized fluorescence intensity indicates expression of IgG. *Tlr4*$^{-/-}$ mice exhibited significantly less IgG expression within distances of 0–50 and 550–600 μm from the probe hole, indicating reduced blood-brain barrier permeability, $\$ p < 0.05$. *Tlr2*$^{-/-}$: $N = 5$; *Tlr4*$^{-/-}$: $N = 4$; WT: $N = 6$. Orange = *Tlr2*$^{-/-}$, Green = *Tlr4*$^{-/-}$, and Blue = WT. Scale bars are provided for each set of images, scale = 100 μm.

= 7) (**Figure 4C**). Similar to microglia/macrophage activation, blood-brain barrier permeability as a function of IgG expression revealed WT mice exhibit significantly higher IgG expression at 2 weeks after probe implantation in distance intervals 0–50 and between 400 and 600 μm from the probe hole, $^{*}p < 0.05$ (2 wk WT: $N = 6$; 16 wk WT: $N = 7$) (**Figure 4D**).

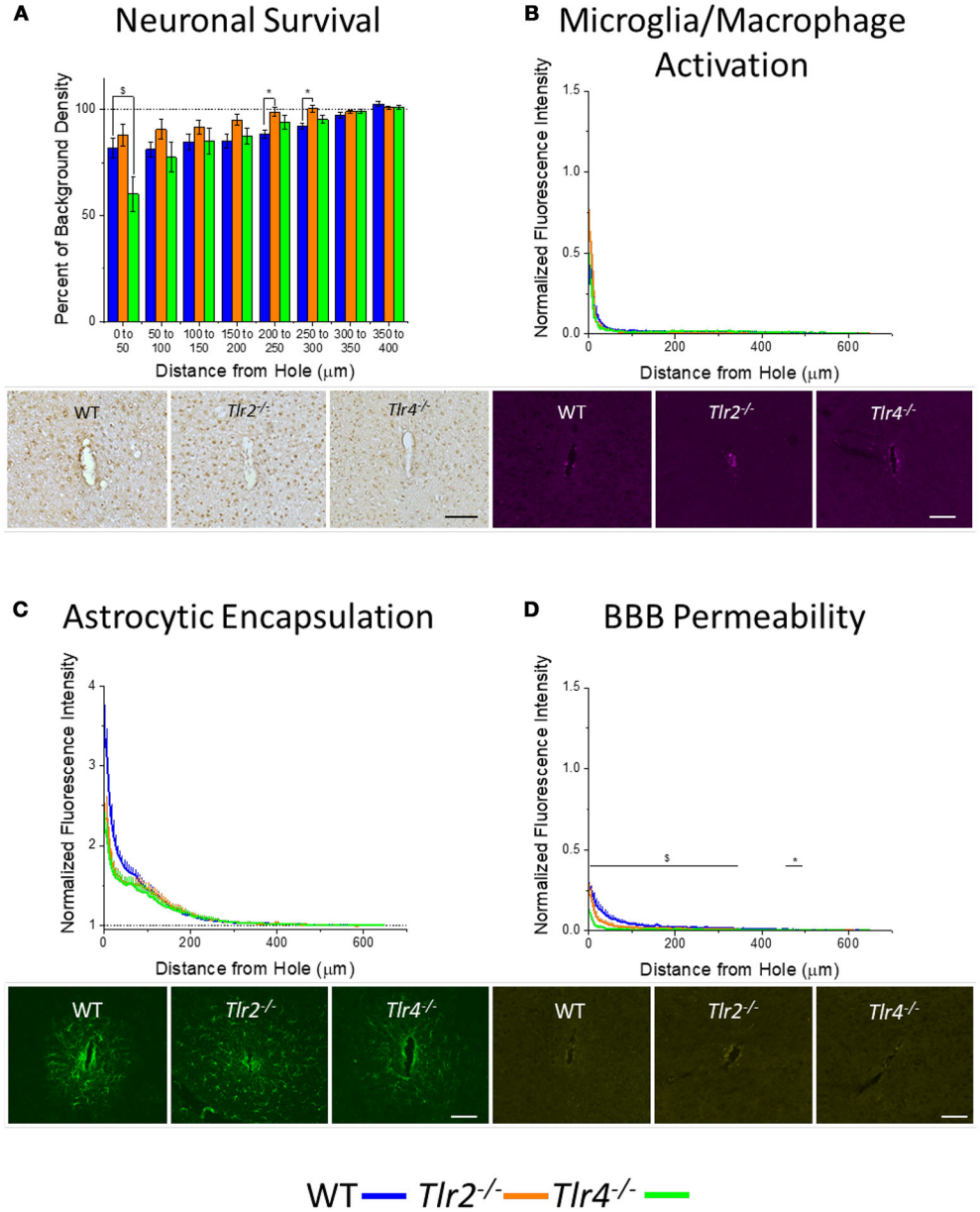

FIGURE 3 | Chronic immunohistochemical evaluation of $Tlr2^{-/-}$, $Tlr4^{-/-}$, and *wildtype* mice 16 weeks after probe implantation. **(A)** Neuronal survival in cortical tissue around implanted probes presented as percent of background density with respect to distance from probe hole (μm). Neuronal survival in $Tlr4^{-/-}$ mice was significantly lower than neuronal survival in wildtype mice in the distance interval 0–50 μm from the probe hole. Neuronal survival in $Tlr2^{-/-}$ mice was significantly higher than neuronal survival in wildtype mice in the distance intervals 200–250 and 250–300 μm from the probe hole. $Tlr2^{-/-}$: $N = 5$; $Tlr4^{-/-}$: $N = 5$; WT: $N = 7$. **(B)** Microglia and macrophage activation in cortical tissue around implanted probes presented as normalized fluorescence intensity with respect to distance from probe hole (μm). Normalized fluorescence intensity indicates expression of CD68. No significant differences were observed between either of the knockout conditions and wildtype mice. $Tlr2^{-/-}$: $N = 5$; $Tlr4^{-/-}$: $N = 5$; WT: $N = 7$. **(C)** Astrocyte encapsulation in cortical tissue around implanted probes presented as normalized fluorescence intensity with respect to distance from probe hole (μm). Normalized fluorescence intensity indicates expression of GFAP. No significant differences were observed between either of the knockout conditions and wildtype mice. $Tlr2^{-/-}$: $N = 5$; $Tlr4^{-/-}$: $N = 5$; WT: $N = 7$. **(D)** Blood-brain barrier permeability presented as normalized fluorescence intensity with respect to distance from probe hole (μm). Normalized fluorescence intensity indicates expression of IgG. $Tlr4^{-/-}$ mice exhibited significantly less IgG expression within each distance interval examined from of 0-350 μm from the probe hole, indicating reduced blood-brain barrier permeability, $\$ p < 0.05$. Additionally, $Tlr2^{-/-}$ mice exhibited significantly less IgG expression within a distance of 450–500 μm from the probe hole, indicating reduced blood-brain barrier permeability, $*p < 0.05$. $Tlr2^{-/-}$: $N = 5$; $Tlr4^{-/-}$: $N = 5$; WT: $N = 7$. $Tlr2^{-/-}$: $N = 5$; $Tlr4^{-/-}$: $N = 4$; WT: $N = 6$. Orange = $Tlr2^{-/-}$, Green = $Tlr4^{-/-}$, and Blue = WT. Scale bars are provided for each set of images, scale = 100 μm.

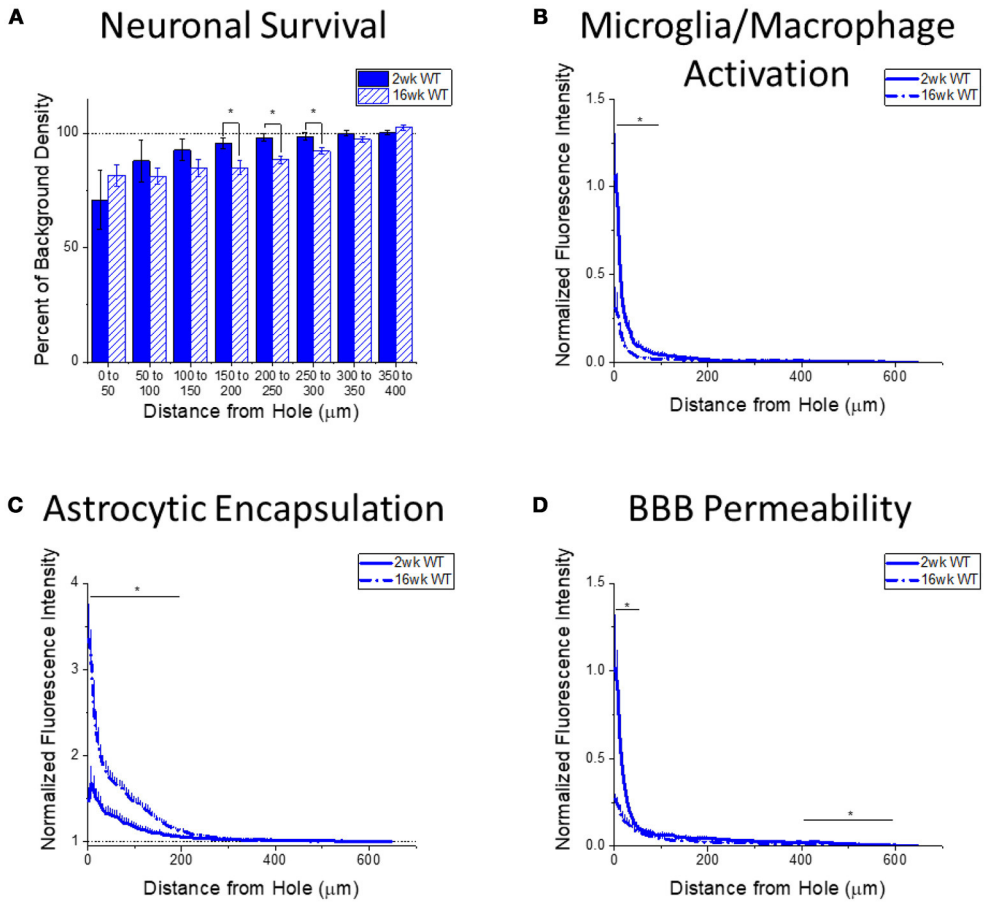

FIGURE 4 | Changes in immunohistochemical markers in wildtype mice over time. **(A–D)** Show immunohistochemical marker expression in WT mice at 2 and 16 weeks after probe implantation. **(A)** Neuronal survival displayed as percent of background neuronal density with respect to distance from the probe hole (μm). Wildtype mice exhibit significantly higher neuronal survival at 2 weeks after implantation in distance intervals 150–200, 200–250, and 250–300 μm from the probe hole, $^*p < 0.05$. 2 wk WT: $N = 5$; 16 wk WT: $N = 7$. **(B)** Microglia and macrophage activation (CD68) displayed as normalized fluorescence intensity with respect to distance from the probe hole (μm). Wildtype mice exhibited significantly higher microglia and macrophage activation at 2 weeks after probe implantation at distance intervals 0–50 and 50–100 μm from the probe hole, $^*p < 0.05$. 2 wk WT: $N = 6$; 16 wk WT: $N = 7$. **(C)** Astrocytic encapsulation (GFAP) displayed as normalized fluorescence intensity with respect to distance from the probe hole (μm). Wildtype mice exhibit significantly higher astrocytic encapsulation at 16 weeks after probe implantation at distance intervals 0–50, 50–100, 100–150, and 150–200 μm from the probe hole, $^*p < 0.05$. 2 wk WT: $N = 6$; 16 wk WT: $N = 7$. **(D)** Blood-brain barrier permeability (IgG) as normalized fluorescence intensity with respect to distance from the probe hole (μm). Wildtype mice exhibit significantly higher blood-brain barrier permeability at 2 weeks after probe implantation at distance intervals 0–50, 400–450, 450–500, 500–550, and 550–600 μm from the probe hole, $^*p < 0.05$. 2 wk WT: $N = 6$; 16 wk WT: $N = 7$.

The Progression of Neuroinflammation and Neurodegeneration in *Tlr2*$^{-/-}$ Mice

Examining the time course of immunohistochemical markers in *Tlr2*$^{-/-}$ mice will identify potential effects of TLR2 removal on the standard progression of chronic neuroinflammatory mechanisms in response to implanted neural probes. Contrary to the trend in WT mice, examination of neuronal density in *Tlr2*$^{-/-}$ mice exhibited significantly higher neuronal density at 16 weeks than 2 weeks after probe implantation in the distance interval 250–300 μm from the probe hole, $^*p < 0.05$ (2 wk *Tlr2*$^{-/-}$: $N = 7$; 16 wk *Tlr2*$^{-/-}$: $N = 5$); (**Figure 5A**). While this is a significant finding, it is likely not appreciable for electrode performance. Similar to the trend observed in WT mice, the accumulation of inflammatory activated microglia and macrophages in *Tlr2*$^{-/-}$ mice exhibited significantly higher CD68 expression at 2 weeks than 16 weeks after probe implantation. However, the distance intervals with higher CD68 expression were between 500 and 600 μm from the probe hole, $^*p < 0.05$ (2 wk *Tlr2*$^{-/-}$: $N = 8$; 16 wk *Tlr2*$^{-/-}$: $N = 5$) (**Figure 5B**), which likely does not impact device performance. Similar to the trend observed in WT mice, examination of the chronic glial scar as a function of GFAP expression exhibited significantly higher GFAP expression at 16 weeks after probe implantation at distance intervals between 0 and 200 μm from the probe hole, $^*p < 0.05$ (2 wk *Tlr2*$^{-/-}$: $N = 8$; 16 wk *Tlr2*$^{-/-}$: $N = 5$) (**Figure 5C**). Astrocytic encapsulation increases over time in *Tlr2*$^{-/-}$ mice in similar distance ranges as WT mice. As seen in WT mice, blood-brain barrier permeability as a function of

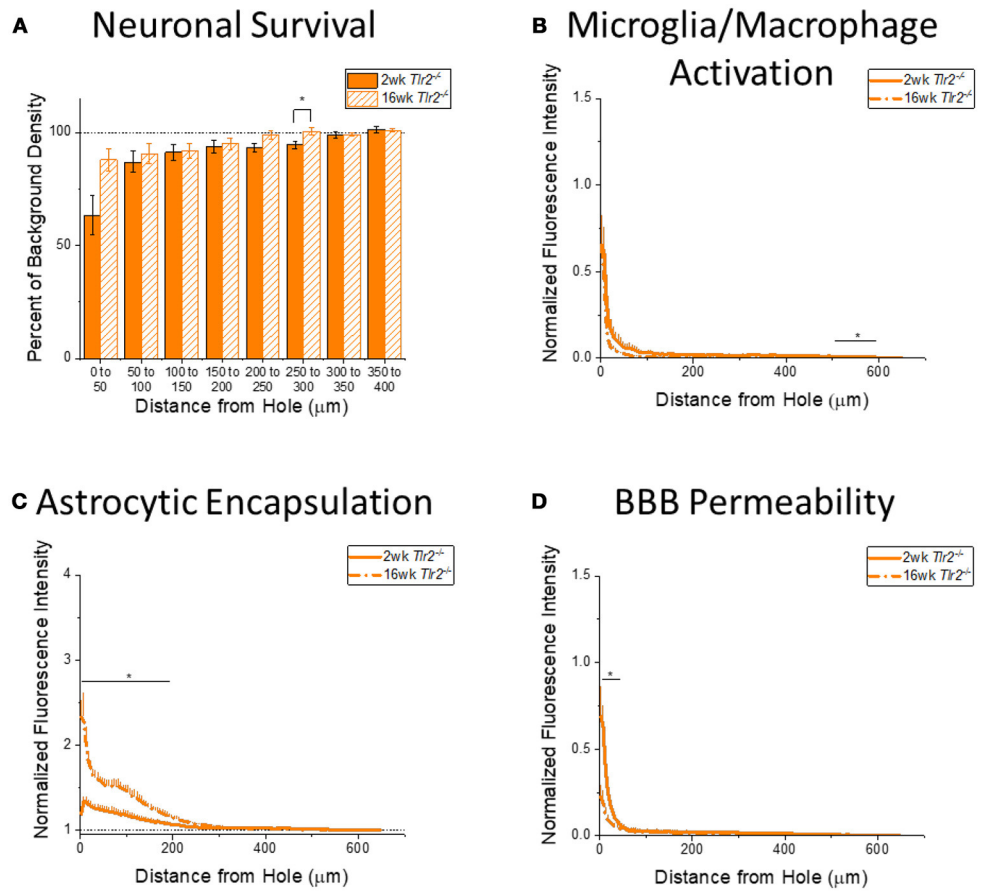

FIGURE 5 | Changes in immunohistochemical markers in $Tlr2^{-/-}$ mice over time. **(A–D)** Show immunohistochemical marker expression in $Tlr2^{-/-}$ mice at 2 and 16 weeks after probe implantation. **(A)** Neuronal survival displayed as percent of background neuronal density with respect to distance from the probe hole (μm). $Tlr2^{-/-}$ mice exhibit significantly higher neuronal survival at 16 weeks after probe implantation in the distance interval 250–300 μm from the probe hole. 2 wk $Tlr2^{-/-}$: $N = 7$; 16 wk $Tlr2^{-/-}$: $N = 5$. **(B)** Microglia and macrophage activation (CD68) displayed as normalized fluorescence intensity with respect to distance from the probe hole (μm). $Tlr2^{-/-}$ mice exhibit significantly higher microglia and macrophage activation at 2 weeks after probe implantation at the distance interval 550–600 μm from the probe hole $^*p < 0.05$. 2 wk $Tlr2^{-/-}$: $N = 8$; 16 wk $Tlr2^{-/-}$: $N = 5$. **(C)** Astrocytic encapsulation (GFAP) displayed as normalized fluorescence intensity with respect to distance from the probe hole (μm). $Tlr2^{-/-}$ mice exhibit significantly higher astrocytic encapsulation at 16 weeks after probe implantation at distance intervals 0–50, 50–100, 100–150, and 150–200 μm from the probe hole, $^*p < 0.05$. 2 wk $Tlr2^{-/-}$: $N = 8$; 16 wk $Tlr2^{-/-}$: $N = 5$. **(D)** Blood-brain barrier permeability (IgG) as normalized fluorescence intensity with respect to distance from the probe hole (μm). $Tlr2^{-/-}$ mice exhibit significantly higher blood-brain barrier permeability at 2 weeks after probe implantation at the distance interval 0–50 μm from the probe hole, $^*p < 0.05$. 2 wk $Tlr2^{-/-}$: $N = 5$; 16 wk $Tlr2^{-/-}$: $N = 5$.

IgG in $Tlr2^{-/-}$ mice revealed significantly higher IgG expression at 2 weeks after probe implantation compared to 16 weeks after probe implantation at the distance intervals 0–50 μm from the probe hole, $^*p < 0.05$ (**Figure 5D**) (2 wk $Tlr2^{-/-}$: $N = 5$; 16 wk $Tlr2^{-/-}$: $N = 5$).

The Progression of Neuroinflammation and Neurodegeneration in *Tlr4*$^{-/-}$ Mice

Examining the time course of immunohistochemical markers in $Tlr4^{-/-}$ mice will identify potential effects of TLR4 removal on the standard progression of chronic neuroinflammatory mechanisms in response to implanted neural probes. Unlike WT mice and $Tlr2^{-/-}$ mice, examination of neuronal density and accumulation of inflammatory activated microglia and macrophages in $Tlr4^{-/-}$ mice exhibited no significant differences between time points (2 wk $Tlr4^{-/-}$: $N = 5$; 16 wk $Tlr4^{-/-}$: $N = 5$) (**Figures 6A,B**). Similar to trends observed in WT and $Tlr2^{-/-}$ mice, examination of the chronic glial scar in $Tlr4^{-/-}$ mice exhibited significantly higher GFAP expression at 16 weeks than 2 weeks after probe implantation. Unlike WT and $Tlr2^{-/-}$ mice, significantly higher GFAP expression only occurred in the distance interval 0-50 μm from the probe hole, $^*p < 0.05$ (2 wk $Tlr4^{-/-}$: $N = 4$; 16 wk $Tlr4^{-/-}$: $N = 5$) (**Figure 6C**). Similar to WT and $Tlr2^{-/-}$ mice, blood-brain barrier permeability as a function of IgG expression in $Tlr4^{-/-}$ mice exhibited significantly higher IgG expression at 2 weeks than at 16 weeks after probe implantation. Unlike WT and $Tlr2^{-/-}$ mice, significant differences occurred over the distance intervals between 0 and 150 μm from the probe hole, $^*p < 0.05$ (2 wk $Tlr4^{-/-}$: $N = 4$; 16 wk $Tlr4^{-/-}$: $N = 5$) (**Figure 6D**).

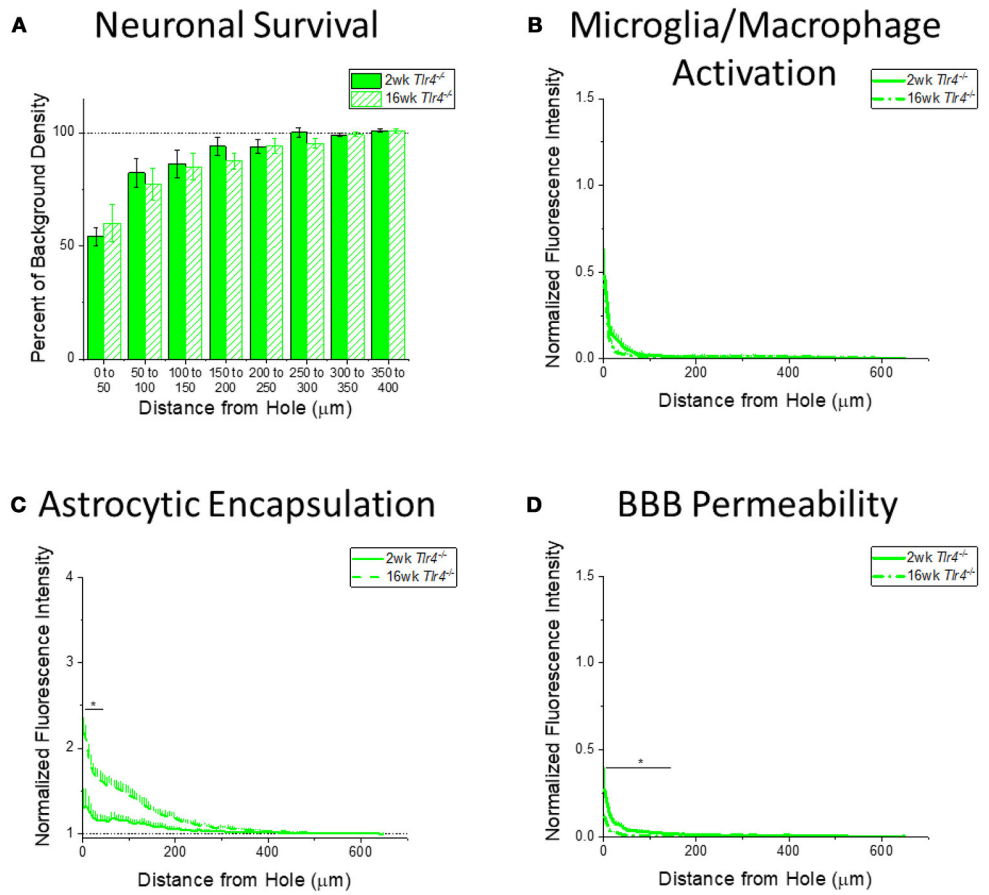

FIGURE 6 | Changes in immunohistochemical markers in $Tlr4^{-/-}$ mice over time. **(A–D)** Show immunohistochemical marker expression in $Tlr4^{-/-}$ mice at 2 and 16 weeks after probe implantation. **(A)** Neuronal survival displayed as percent of background neuronal density with respect to distance from the probe hole (μm). $Tlr4^{-/-}$ mice exhibit no significant difference in neuronal survival between two and 16 weeks after probe implantation. 2 wk $Tlr4^{-/-}$: $N = 5$; 16 wk $Tlr4^{-/-}$: $N = 5$. **(B)** Microglia and macrophage activation (CD68) displayed as normalized fluorescence intensity with respect to distance from the probe hole (μm). $Tlr4^{-/-}$ mice exhibit no significant differences in microglia and macrophage activation between time points. 2 wk $Tlr4^{-/-}$: $N = 4$; 16 wk $Tlr4^{-/-}$: $N = 5$. **(C)** Astrocytic encapsulation (GFAP) displayed as normalized fluorescence intensity with respect to distance from the probe hole (μm). $Tlr4^{-/-}$ mice exhibit significantly higher astrocytic encapsulation at 16 weeks after probe implantation the distance intervals 0–50 μm from the probe hole, $^*p < 0.05$. 2 wk $Tlr4^{-/-}$: $N = 4$; 16 wk $Tlr4^{-/-}$: $N = 5$. **(D)** Blood-brain barrier permeability (IgG) as normalized fluorescence intensity with respect to distance from the probe hole (μm). $Tlr4^{-/-}$ mice exhibit significantly higher blood-brain barrier permeability at 2 weeks after probe implantation at the distance intervals 0–50, 50–100, and100–150 μm from the probe hole, $^*p < 0.05$. 2 wk $Tlr4^{-/-}$: $N = 4$; 16 wk $Tlr4^{-/-}$: $N = 5$.

DISCUSSION

This study sought to interpret the roles of TLR2 and TLR4 in the neuroinflammatory response to implanted intracortical microelectrodes. Overall, this study reveals that full removal of TLR4 results in reduced blood-brain barrier permeability at an acute (2 weeks) and chronic time points (16 weeks), and reduced neuronal survival at chronic time points, compared to WT animals. Further, microglia/macrophage activation and blood-brain barrier permeability significantly decreased from acute to chronic time points, whereas astrocytic encapsulation significantly increased from acute to chronic time points in WT mice. Mice lacking TLR2 or TLR4 exhibited similar trends in decreasing blood-brain barrier permeability and increasing astrocytic encapsulation, but significant changes in microglia/macrophage activation close to the electrode-tissue interface from 2 to 16 weeks post-implantation. The findings presented here introduce more questions regarding the role of innate immunity receptors in the neuroinflammatory response to intracortical microelectrodes.

The first major finding of this study indicated that knocking out TLR4 resulted in decreased blood-brain barrier permeability around implanted intracortical microelectrode at both acute and chronic time points. The blood-brain barrier is a network of endothelial cells with tight junctions that protects parenchymal brain tissue from neurotoxic molecules and infiltrating inflammatory cells. Damage to the blood-brain barrier following intracortical microelectrode implantation has been linked to poor recording performance (Saxena et al., 2013), potentially through neuronal damage, altered extracellular ionic

concentrations, or propagation of inflammatory mechanisms (Jorfi et al., 2015). It is important to note that improved blood-brain barrier permeability alone may not lead to improved intracortical microelectrode performance. Blood-brain permeability in response to implanted neural probes may be related to TLR4 signaling on several levels: TLR4 signaling in endothelial cells, release of cytokines in response to TLR4 activation, and oxidative damage caused by factors released in response to TLR4 activation. An upregulation of TLR4 has been observed in vascular endothelial cells in response to renal ischemia reperfusion injuries, and an increase in co-localization of TLR4 and vascular endothelial cells was observed in response to subarachnoid hemorrhages (Zhao et al., 2014; Zhang et al., 2015). Ischemic injury has been tied to neurodegeneration around implanted intracortical microelectrodes (Kozai et al., 2014). It is possible that signaling of TLR4 on vascular endothelial cells in response to the implanted intracortical microelectrodes contributes to permeability of the blood-brain barrier.

Activation of TLR4 on secondary cells may also be responsible for increased permeability of the blood-brain barrier. In addition to vascular endothelial cells, neurons and microglia also exhibited elevated co-localization with TLR4 in response to subarachnoid hemorrhages (Zhang et al., 2015). Leow-Dyke et al. demonstrated that factors released by neurons conditioned with the TLR4 ligand lipopolysaccharide (LPS), including RANTES (CCL5), KC (CXCL1), tumor necrosis factor-α (TNFα), and IL-6, promoted the migration of neutrophils across an endothelial monolayer *in vitro*, and prior application of a TLR4 antagonist to the neurons significantly reduced this effect (Leow-Dyke et al., 2012). Additionally, activation of TLR4 on microglia may lead to activation of the inflammatory NFκB pathway, which can induce the release of pro-inflammatory cytokines, such as TNFα, IL-6, IL1-β (O'Neill and Kaltschmidt, 1997; Pineau and Lacroix, 2009). TNF-α and IL1-β have been shown to increase permeability of the blood-brain barrier (Ballabh et al., 2004). Bennett et al. recently detected upregulation of genes encoding pro-inflammatory cytokines paired with downregulation of genes encoding junction proteins of the blood-brain barrier at acute time points following intracortical microelectrode implantation (Bennett et al., 2018). Coincidentally, Bennett et al identified enhanced expression of TNFα, IL-6, and KC (CXCL1) following intracortical microelectrode implantation, potentially indicating a role of neuronal cytokine and chemokine release (Leow-Dyke et al., 2012; Bennett et al., 2018). Activation of TLR4 on microglia may also lead to the release of reactive oxygen species (Reed-Geaghan et al., 2009). Reactive oxygen species can promote leakiness of the blood-brain barrier (Merrill and Murphy, 1997; Lehner et al., 2011). In the absence of TLR4, less pro-inflammatory cytokines and reactive oxygen species are likely released, and thus less damage to the blood brain barrier occurs. Conversely, *Tlr4*$^{-/-}$ mice did not exhibit any significant differences in microglia/macrophage activation. Differences in CD68 expression may not be sensitive enough to confer differences in cytokine and ROS release by activated microglia and macrophages, other infiltrating myeloid cells or neurons may be driving the release of factors damaging the blood-brain barrier, or TLR4 signaling on endothelial cells may facilitate blood-brain barrier permeability.

The next major finding of this study, indicating a reduction in neuronal survival around implanted intracortical microelectrodes in mice lacking TLR4, is more difficult to explain. Neurons are the source of signals recorded by intracortical microelectrodes and hypothesized to be needed within 50 μm of the microelectrode to record single units (Buzsáki, 2004). Although neuronal dieback has frequently been observed around implanted intracortical microelecrodes (Biran et al., 2005; McConnell et al., 2009; Potter et al., 2012a) and neuronal dieback has been hypothesized to cause intracortical microelectrode failure (Biran et al., 2005), the relationship between neuronal dieback and recording performance has not been fully elucidated (Jorfi et al., 2015). Typically, knocking out TLR4 results in neuroprotective effects (Tang et al., 2007; Hyakkoku et al., 2010). Here the opposite trend is observed. Perhaps the reduced capability to detect and fight pathogens makes mice more susceptible to localized infections; however, no indications of localized infection were seen in this study. Robust sterilization methods such as ethylene oxide sterilization do not always reduce endotoxin levels below the FDA requirement for devices implanted in the brain (Ravikumar et al., 2014a). Hermann et al. proposed that the reduced capability to detect and respond to tissue damage may hinder wound healing mechanisms beneficial to integrating devices into the brain (Hermann et al., 2018). Studies investigating the role of TLRs in neurodegenerative disorders such as Alzheimer's and synucleinopathies suggested that some amount of TLR signaling was necessary to clean up the accumulation of abnormal protein deposits (Tahara et al., 2006; Stefanova et al., 2011; Fellner et al., 2013) and neurons damaged by the proteins (Bate et al., 2004). Damaged matrix proteins and necrotic cells resulting from the implantation and chronic presence of an intracortical microelectrode that are normally recognized and disposed of by TLR4 mediated pathways may be detrimental to neurons directly or through the activation of redundant inflammatory mechanisms.

The third major finding of this study identified differences in the time course of the foreign body response to implanted intracortical microelectrodes in the absence of TLR2 and TLR4. *Tlr2*$^{-/-}$ and *Tlr4*$^{-/-}$ mice exhibited most of the same trends as WT mice between the 2 and 16 week time points, except for microglia/macrophage activation. WT mice exhibit a significant reduction in microglia and macrophage activation whereas *Tlr2*$^{-/-}$ and Tlr4$^{-/-}$ mice do not exhibit significant changes close to the electrode-tissue interface over time. The trend in WT mice indicate that TLR2 and/or TLR4 may play an important role in the activation of microglia and macrophages at the acute time point, despite the lack of significant differences between either *Tlr2*$^{-/-}$ or *Tlr4*$^{-/-}$ mice and WT mice. *Tlr2*$^{-/-}$ or *Tlr4*$^{-/-}$ mice both demonstrated lower peak CD68 intensities, but the intensities decayed to similar values over a short span of distance (∼10 μm). Differences in CD68 expression may be limited to the first layer of cells around the neural probe hole. The decrease in CD68 expression in WT mice over time may indicate a diminishing importance of TLR2 and TLR4 in the chronic

neuroinflammatory response to intracortical microelectrodes over time, or that lacking either TLR2 or TLR4 retards the rate of wound healing / scar progression. For example, TLR4 deficient mice exhibited delayed skin wound closure paired with decreased Il-1β and IL-6 production (Chen et al., 2013), indicating the importance of TLR4 activation and subsequent cytokine release in wound healing. Similarly, $Tlr2^{-/-}$, $Tlr4^{-/-}$, and $Tlr2/4^{-/-}$ mice exhibited larger skin wound areas paired with a reduction in infiltrating macrophages and decreased expression of TGF-β and CCL5 (RANTES) (Suga et al., 2014). On the contrary, $Tlr2^{-/-}$ and $Tlr4^{-/-}$ mice exhibited improved wound healing in response to diabetic skin injuries (Dasu et al., 2010). Opposing outcomes of knocking out TLRs have been attributed to differences in acute and chronic injures, where chronic inflammation, as found in diabetic injuries, may hinder wound healing (Dasu and Jialal, 2013; Portou et al., 2015). The unresolved presence of an implanted intracortical microelectrode would likely behave like other chronic injuries. The role of TLR2 and TLR4 on wound healing in the brain would be difficult to predict, since activation of TLRs promotes injury or wound healing in a variety of injuries throughout the body (Kluwe et al., 2009), and the effects are hypothesized to be dose dependent (Strbo et al., 2014), timing dependent (Dasu and Rivkah Isseroff, 2012), and location dependent (Kluwe et al., 2009; Dasu and Rivkah Isseroff, 2012). In the context of spinal cord injury, $Tlr4^{-/-}$ mice exhibited deficits in locomotor recovery and elevated demyelination, astrogliosis, and macrophage activation, and $Tlr2^{-/-}$ mice exhibited deficits in locomotor recovery paired with abnormal myelin patterning (Kigerl et al., 2007). These findings suggest that TLR2 and TLR4 may play a beneficial role in the recovery of CNS injuries. However, the exact role of TLR2 and TLR4 in wound healing of the CNS remains to be elucidated.

Another interpretation of the time course of CD68 expression suggests that the enhanced CD68 expression in the WT group at 2 weeks post-implantation may be, in part, due to a higher infiltration of activated macrophages at the electrode tissue interface, considering the enhanced permeability of the blood-brain barrier at that time point. The contribution of infiltrating macrophages is important to consider since infiltrating macrophages have been shown to induce detrimental effects on neurons following central nervous system injuries (Horn et al., 2008; Busch et al., 2009). In contrast to the WT group, the $Tlr4^{-/-}$ mice did not exhibit enhanced CD68 expression at 2 weeks post implantation and blood-brain barrier permeability was significantly lower than in WT mice at that time point. Lower BBB permeability at 2 weeks post-implantation may lead to less activated macrophage infiltration, resulting in CD68 expression comparable to 16 weeks post-implantation in $Tlr4^{-/-}$ mice. On the other hand, $Tlr2^{-/-}$ mice, which exhibited similar BBB permeability to WT mice did not exhibit elevated CD68 expression close to the electrode-tissue interface at 2 weeks after implantation. Regardless, assessing the contributions of microglia and macrophages require alternate methods, such as bone marrow chimeras with labeled blood-derived cells (Ravikumar et al., 2014b).

Comparing the findings of this study to previous studies in our lab, inhibiting the TLR co-receptor will provide a greater understanding of the role of innate immunity receptors in the chronic inflammatory response to intracortical microelectrodes. Hermann et al. previously observed that knockout mice lacking CD14 exhibited enhanced recording performance over the acute (0–2 weeks) but not chronic (2–16 weeks) time range, with no differences in neuronal survival, microglia/macrophage activation, astrocytic encapsulation, or blood-brain barrier permeability at 16 weeks after implantation (Hermann et al., 2018). Here we observe that knockout mice completely lacking TLR4 exhibit significantly reduced blood-brain barrier permeability at both acute and chronic time points. Although TLR4 and CD14 are closely associated in the recognition of ligands, knocking out TLR4 but not CD14 resulted in reduced blood-brain barrier permeability. Activation of TLR4 to promote blood-brain barrier permeability does not require CD14. TLR4 is able to bind and respond to its ligand LPS in the absence of CD14, although with drastically less sensitivity (Janova et al., 2015). There is evidence that TLR4 may bind and respond to DAMPs without CD14 (Allam et al., 2012), but the exact role of CD14 in the recognition of structurally diverse DAMPs by TLR4 remains to be elucidated. Further, knocking out TLR4 but not CD14 resulted in significantly lower neuronal survival (Hermann et al., 2018). It appears that fully removing TLR4 exhibits a beneficial effect at acute time points, as with CD14, but fully removing TLR4 at chronic time points is also detrimental. The presence of functioning TLR4 signaling may be more critical for long-term wound healing than CD14, since $Tlr4^{-/-}$ mice exhibited significantly decreased neuronal survival and $Cd14^{-/-}$ mice exhibited no differences from wildtype mice at the chronic time point. Alternatively, chronic decreases in neuronal survival in $Tlr4^{-/-}$ mice may be a carry-over effect from improper wound healing at earlier time points. Experiments stopping and starting or delaying the administration of TLR4 antagonists to mice with implanted intracortical microelectrodes could potentially delineate the time-dependent role of TLR4 in the neuroinflammatory response. TLR4 and CD14 play related but independent roles that vary over time in the foreign body response to intracortical microelectrodes.

In addition to investigating the complete removal of CD14 via a knockout mouse, Hermann et al. observed that administering a small molecule inhibitor to the CD14-TLR4 complex improved recording performance at acute time points and out to chronic time points (16 weeks), without any differences in 16 week endpoint histology. Inhibition via a small molecule antagonist is less complete as full removal of a receptor via knockout. Residual TLR4 signaling from incomplete inhibition may protect neurons from the processes detrimental to neuronal survival in $Tlr4^{-/-}$ mice at chronic time points after intracortical electrode implantation. The role of innate immunity signaling in the foreign body response to intracortical microelectrodes is dependent on the degree of receptor inhibition.

Further studies by Bedell et al. investigated the effects of knocking out CD14 in specific cell populations on intracortical microelectrode recording performance (Bedell et al., 2018). Mice with infiltrating blood-derived cells lacking CD14 and resident cells featuring intact CD14 exhibited significantly improved recording performance over wildtype mice over the 16-week

study without any differences in 16-week endpoint histology. TLR4 signaling may have different roles on resident cells than on infiltrating myeloid cells. Since TLR4 is constitutively expressed in parenchymal microglia as opposed to CD14, knocking out TLR4 on resident or infiltrating cells only may produce vastly different results from CD14. The roles of innate immunity signaling are cell-specific.

Initially, we hypothesized that TLR2 and TLR4 play a role in the neuroinflammatory response to implanted intracortical microelectrodes. Although $Tlr2^{-/-}$ mice did not exhibit any significant differences in endpoint histology, changes in blood-brain barrier permeability and neuronal survival in $Tlr4^{-/-}$ mice would suggest a role of TLR4 in the neuroinflammatory response to intracortical microelectrodes. Differences in the time course of microglia/macrophage activation observed in $Tlr2^{-/-}$ mice suggest a subtler role in the neuroinflammatory response to intracortical microelectrodes. Further, we proposed TLR2 and TLR4 signaling as a mechanism for the activation of microglia and macrophages and subsequent release of pro-inflammatory cytokines, ROS, and RNS in response to an implanted intracortical microelectrode. Here, we did not observe significant changes in microglia/macrophage activation via expression of CD68 in ether $Tlr2^{-/-}$ or $Tlr4^{-/-}$ mice at acute or chronic time points. However, the paradoxical decrease in blood-brain barrier permeability and decrease in neuronal survival observed in $Tlr4^{-/-}$ mice may be affected by decreased or increased release of pro-inflammatory factors. As stated earlier, differences in expression of CD68 may not be sensitive enough to detect functional differences in cytokine, ROS, and NOS release. Alternatively, activation of TLR4 on other infiltrating myeloid cells not expressing CD68, endothelial cells, or neurons may be responsible for the observed histological changes (Ravikumar et al., 2014b). Future studies investigating the effects of innate immunity inhibition on gene and mRNA expression following the implantation of intracortical microelectrodes may elucidate changes in the production of cytokines, ROS, and NOS (He et al., 2006; Ereifej et al., 2018). Since this study employed intracortical microelectrode arrays without functional recording sites, conductive traces, and insulating layers, the effects of knocking out TLR2 and TLR4 on oxidative damage to these structures could not be determined via SEM. Much remains to be learned about the specific roles of TLR2 and TLR4 in the neuroinflammatory response to intracortical microelectrodes.

Building off of the previous studies of Hermann et al. and Bedell et al. innate immunity signaling pathways appear to play a role in the neuroinflammatory response against intracortical microelectrodes (Bedell et al., 2018; Hermann et al., 2018). The findings of this study suggest that fully removing TLR4 is beneficial at acute time points and fully removing TLR4 at chronic time points is detrimental. Based off the success of cell-specific CD14 inhibition exhibited by Bedell et al. (2018), incomplete inhibition of TLR4 and its co-receptors via small molecule antagonists or antibodies may be of further interest for improving the long-term performance of intracortical microelectrodes. Delaying or stopping and starting the administration of TLR4 inhibitors may be more appropriate to address the time variant role in the foreign body response to implanted intracortical microelectrodes. Targeting TLR4 on specific cell populations may be more beneficial than inhibiting TLR4 in the whole body. The Toll-like receptors and their adapter molecules affect the foreign body response in a time, method/extent of inhibition, and cellular subset –dependent manner. Future strategies to integrate intracortical microelectrodes using modulation of innate immunity signaling pathways should consider these parameters to optimize the preservation of electrode and tissue integrity.

CONCLUSIONS

Complete removal of TLR2 via genetic knockout did not result in meaningful changes in the expression of the markers stained for in this study. Thus, TLR2 does not likely play a significant role in the foreign body response to intracortical microelectrodes. Complete removal of TLR4 via genetic knockout results in reduced blood brain barrier permeability in response to implanted neural probes at acute and chronic time points, as well as reduced neuronal survival around implanted neural probes. Benefits of fully removing TLR4 are overshadowed by detrimental effects on neuronal survival. Inhibition of TLR4 without complete removal of the pathway or for intermittent time courses may still be worth investigating as an intervention for improving intracortical microelectrode integration.

AUTHOR CONTRIBUTIONS

JH, SMS, RM, and JRC contributed substantially to the conception or design of the work, analysis, and interpretation of data for the work, drafting, and revising the manuscript for important intellectual content, approved the final version to be published, and agreed to be accountable for all aspects of the work. SL, AS, CW, AA, JC, SmS, ShS, WT, and GP aided in the collection and analysis of histological data. JH, SL, AS, CW, AA, JC, SmS, ShS, WT, GP, SMS, RM, and JRC approved the final version to be published and agreed to be accountable for all aspects of the work.

FUNDING

This work was supported in part by the Department of Biomedical Engineering and Case School of Engineering at Case Western Reserve University through laboratory start-up funds, the National Institute of Health, National Institute of Neurological Disorders and Stroke, (Grant # 1R01NS082404-01A1), the NIH Neuroengineering Training Grant 5T- 32EB004314-14. Additional support was provided by the Presidential Early Career Award for Scientists and Engineers (PECASE, JR. Capadona) and by Merit Review Awards B1495-R and B2611 from the United States (US) Department of Veterans Affairs Rehabilitation Research and Development Service. None of the funding sources aided in

collection, analysis and interpretation of the data, in writing of the manuscript, or in the decision to submit the manuscript for publication. The authors have no conflict of interest related to this work to disclose. The contents do not represent the views of the U.S. Department of Veterans Affairs or the United States Government.

ACKNOWLEDGMENTS

We would like to thank Jessica Nguyen, Kelly Buchanan, Monika Goss, Seth Meade, Emily Molinich, Jacob Rayyan, Andres Robert, Zishen Zhuang, Cara Smith, and Keying Chen for their help in earlier iterations of the project.

REFERENCES

Abbott, N. J., Rönnbäck, L., and Hansson, E. (2006). Astrocyte–endothelial interactions at the blood–brain barrier. *Nat. Rev. Neurosci.* 7, 41–53. doi: 10.1038/nrn1824

Ajiboye, A. B., Willett, F. R., Young, D. R., Memberg, W. D., Murphy, B. A., Miller, J. P., et al. (2017). Restoration of reaching and grasping movements through brain-controlled muscle stimulation in a person with tetraplegia: a proof-of-concept demonstration. *Lancet* 389, 1821–1830. doi: 10.1016/S0140-6736(17)30601-3

Allam, R., Scherbaum, C. R., Darisipudi, M. N., Mulay, S. R., Hägele, H., Lichtnekert, J., et al. (2012). Histones from dying renal cells aggravate kidney injury via TLR2 and TLR4. *J. Am. Soc. Nephrol.* 23, 1375–1388. doi: 10.1681/ASN.2011111077

Arroyo, D. S., Soria, J. A., Gaviglio, E. A., Rodriguez-Galan, M. C., and Iribarren, P. (2011). Toll-like receptors are key players in neurodegeneration. *Int. Immunopharmacol.* 11, 1415–1421. doi: 10.1016/j.intimp.2011.05.006

Asea, A., Rehli, M., Kabingu, E., Boch, J. A., Bare, O., Auron, P. E., et al. (2002). Novel signal transduction pathway utilized by extracellular HSP70 role of Toll-like receptor (TLR) 2 and TLR4. *J. Biol. Chem.* 277, 15028–15034. doi: 10.1074/jbc.M200497200

Ballabh, P., Braun, A., and Nedergaard, M. (2004). The blood–brain barrier: an overview: structure, regulation, and clinical implications. *Neurobiol. Dis.* 16, 1–13. doi: 10.1016/j.nbd.2003.12.016

Barrese, J. C., Rao, N., Paroo, K., Triebwasser, C., Vargas-Irwin, C., Franquemont, L., et al. (2013). Failure mode analysis of silicon-based intracortical microelectrode arrays in non-human primates. *J. Neural Eng.* 10:066014. doi: 10.1088/1741-2560/10/6/066014

Bate, C., Veerhuis, R., Eikelenboom, P., and Williams, A. (2004). Microglia kill amyloid-β1-42 damaged neurons by a CD14-dependent process. *Neuroreport* 15, 1427–1430. doi: 10.1097/01.wnr.0000132203.76836.16

Bedell, H. W., Hermann, J. K., Ravikumar, M., Lin, S., Rein, A., Li, X., et al. (2018). Targeting CD14 on blood derived cells improves intracortical microelectrode performance. *Biomaterials* 163, 163–173. doi: 10.1016/j.biomaterials.2018.02.014

Bennett, C., Samikkannu, M., Mohammed, F., Dietrich, W. D., Rajguru, S. M., and Prasad, A. (2018). Blood brain barrier (BBB)-disruption in intracortical silicon microelectrode implants. *Biomaterials* 164, 1–10. doi: 10.1016/j.biomaterials.2018.02.036

Biran, R., Martin, D. C., and Tresco, P. A. (2005). Neuronal cell loss accompanies the brain tissue response to chronically implanted silicon microelectrode arrays. *Exp. Neurol.* 195, 115–126. doi: 10.1016/j.expneurol.2005.04.020

Burns, B. D., Stean, J. P., and Webb, A. C. (1974). Recording for several days from single cortical neurons in completely unrestrained cats. *Electroencephalogr. Clin. Neurophysiol.* 36, 314–318. doi: 10.1016/0013-4694(74)90175-8

Busch, S. A., Horn, K. P., Silver, D. J., and Silver, J. (2009). Overcoming macrophage-mediated axonal dieback following CNS injury. *J. Neurosci.* 29, 9967–9976. doi: 10.1523/JNEUROSCI.1151-09.2009

Buzsáki, G. (2004). Large-scale recording of neuronal ensembles. *Nat. Neurosci.* 7, 446–451. doi: 10.1038/nn1233

Casula, M., Iyer, A. M., Spliet, W. G., Anink, J. J., Steentjes, K., Sta, M., et al. (2011). Toll-like receptor signaling in amyotrophic lateral sclerosis spinal cord tissue. *Neuroscience* 179, 233–243. doi: 10.1016/j.neuroscience.2011.02.001

Chen, L., Guo, S., Ranzer, M. J., and DiPietro, L. A. (2013). Toll-like receptor 4 has an essential role in early skin wound healing. *J. Invest. Dermatol.* 133, 258–267. doi: 10.1038/jid.2012.267

Dasu, M. R., and Jialal, I. (2013). Amelioration in wound healing in diabetic toll-like receptor-4 knockout mice. *J. Diabet. Complic.* 27, 417–421. doi: 10.1016/j.jdiacomp.2013.05.002

Dasu, M. R., and Rivkah Isseroff, R. (2012). Toll-like receptors in wound healing: location, accessibility, and timing. *J. Invest. Dermatol.* 132, 1955–1958. doi: 10.1038/jid.2012.208

Dasu, M. R., Thangappan, R. K., Bourgette, A., DiPietro, L. A., Isseroff, R., and Jialal, I. (2010). TLR2 expression and signaling-dependent inflammation impair wound healing in diabetic mice. *Lab. Invest.* 90:1628. doi: 10.1038/labinvest.2010.158

Eddleston, M., and Mucke, L. (1993). Molecular profile of reactive astrocytes-implications for their role in neurologic disease. *Neuroscience* 54, 15–36. doi: 10.1016/0306-4522(93)90380-X

Ereifej, E. S., Rial, G. M., Hermann, J. K., Smith, C. S., Meade, S. M., Rayyan, J. M., et al. (2018). Implantation of neural probes in the brain elicits oxidative stress. *Front. Bioeng. Biotechnol.* 6:9. doi: 10.3389/fbioe.2018.00009

Fellner, L., Irschick, R., Schanda, K., Reindl, M., Klimaschewski, L., Poewe, W., et al. (2013). Toll-like receptor 4 is required for α-synuclein dependent activation of microglia and astroglia. *Glia* 61, 349–360. doi: 10.1002/glia.22437

Gunasekera, B., Saxena, T., Bellamkonda, R., and Karumbaiah, L. (2015). Intracortical recording interfaces: current challenges to chronic recording function. *ACS Chem. Neurosci.* 6, 68–83. doi: 10.1021/cn5002864

He, W., McConnell, G. C., and Bellamkonda, R. V. (2006). Nanoscale laminin coating modulates cortical scarring response around implanted silicon microelectrode arrays. *J. Neural Eng.* 3, 316–326. doi: 10.1088/1741-2560/3/4/009

Hermann, J. K., Ravikumar, M., Shoffstall, A., Ereifej, E. S., Kovach, K. M., Chang, J., et al. (2018). Inhibition of the cluster of differentiation 14 innate immunity pathway with IAXO-101 improves chronic microelectrode performance. *J. Neural Eng.* 15:025002. doi: 10.1088/1741-2552/aaa03e

Horn, K. P., Busch, S. A., Hawthorne, A. L., van Rooijen, N., and Silver, J. (2008). Another barrier to regeneration in the CNS: activated macrophages induce extensive retraction of dystrophic axons through direct physical interactions. *J. Neurosci.* 28, 9330–9341. doi: 10.1523/JNEUROSCI.2488-08.2008

Hyakkoku, K., Hamanaka, J., Tsuruma, K., Shimazawa, M., Tanaka, H., Uematsu, S., et al. (2010). Toll-like receptor 4 (TLR4), but not TLR3 or TLR9, knock-out mice have neuroprotective effects against focal cerebral ischemia. *Neuroscience* 171, 258–267. doi: 10.1016/j.neuroscience.2010.08.054

Janova, H., Böttcher, C., Holtman, I. R., Regen, T., van Rossum, D., Götz, A., et al. (2015). CD14 is a key organizer of microglial responses to CNS infection and injury. *Glia* 64, 635–649. doi: 10.1002/glia.22955

Jorfi, M., Skousen, J. L., Weder, C., and Capadona, J. R. (2015). Progress towards biocompatible intracortical microelectrodes for neural interfacing applications. *J. Neural Eng.* 12:011001. doi: 10.1088/1741-2560/12/1/011001

Kettenmann, H., Hanisch, U. K., Noda, M., and Verkhratsky, A. (2011). Physiology of microglia. *Physiol. Rev.* 91, 461–553. doi: 10.1152/physrev.00011.2010

Kigerl, K. A., Lai, W., Rivest, S., Hart, R. P., Satoskar, A. R., and Popovich, P. G. (2007). Toll-like receptor (TLR)-2 and TLR-4 regulate inflammation, gliosis, and myelin sparing after spinal cord injury. *J. Neurochem.* 102, 37–50. doi: 10.1111/j.1471-4159.2007.04524.x

Kluwe, J., Mencin, A., and Schwabe, R. F. (2009). Toll-like receptors, wound healing, and carcinogenesis. *J. Mol. Med.* 87:125. doi: 10.1007/s00109-008-0426-z

Kong, Y., and Le, Y. (2011). Toll-like receptors in inflammation of the central nervous system. *Int. Immunopharmacol.* 11, 1407–1414. doi: 10.1016/j.intimp.2011.04.025

Kozai, T. D., Catt, K., Li, X., Gugel, Z. V., Olafsson, V. T., Vazquez, A. L., et al. (2015). Mechanical failure modes of chronically implanted planar

silicon-based neural probes for laminar recording. *Biomaterials* 37, 25–39. doi: 10.1016/j.biomaterials.2014.10.040

Kozai, T. D., Li, X., Bodily, L. M., Caparosa, E. M., Zenonos, G. A., Carlisle, D. L., et al. (2014). Effects of caspase-1 knockout on chronic neural recording quality and longevity: insight into cellular and molecular mechanisms of the reactive tissue response. *Biomaterials* 35, 9620–9634. doi: 10.1016/j.biomaterials.2014.08.006

Landreth G. E., and Reed-Geaghan E. G. (2009). "Toll-like receptors in Alzheimer's disease," in *Toll-like Receptors: Roles in Infection and Neuropathology, Current Topics in Microbiology and Immunology,* Vol. 336, ed T. Kielian (Berlin; Heidelberg: Springer).

Lehner, C., Gehwolf, R., Tempfer, H., Krizbai, I., Hennig, B., Bauer, H. C., et al. (2011). Oxidative stress and blood–brain barrier dysfunction under particular consideration of matrix metalloproteinases. *Antioxid. Redox Signal.* 15, 1305–1323. doi: 10.1089/ars.2011.3923

Leow-Dyke, S., Allen, C., Denes, A., Nilsson, O., Maysami, S., Bowie, A. G., et al. (2012). Neuronal toll-like receptor 4 signaling induces brain endothelial activation and neutrophil transmigration *in vitro*. *J. Neuroinflamm.* 9:230. doi: 10.1186/1742-2094-9-230

McConnell, G. C., Rees, H. D., Levey, A. I., Gutekunst, C. A., Gross, R. E., and Bellamkonda, R. V. (2009). Implanted neural electrodes cause chronic, local inflammation that is correlated with local neurodegeneration. *J. Neural Eng.* 6:056003. doi: 10.1088/1741-2560/6/5/056003

Merrill, J. E., and Murphy, S. P. (1997). Inflammatory events at the blood brain barrier: regulation of adhesion molecules, cytokines, and chemokines by reactive nitrogen and oxygen species. *Brain Behav. Immun.* 11, 245–263. doi: 10.1006/brbi.1997.0496

Mullen, R. J., Buck, C. R., and Smith, A. M. (1992). NeuN, a neuronal specific nuclear protein in vertebrates. *Development* 116, 201–211.

Nguyen, J. K., Jorfi, M., Buchanan, K. L., Park, D. J., Foster, E. J., Tyler, D. J., et al. (2016). Influence of resveratrol release on the tissue response to mechanically adaptive cortical implants. *Acta Biomater.* 29, 81–93. doi: 10.1016/j.actbio.2015.11.001

O'Neill, L. A., and Kaltschmidt, C. (1997). NF-kB: a crucial transcription factor for glial and neuronal cell function. *Trends Neurosci.* 20, 252–258. doi: 10.1016/S0166-2236(96)01035-1

Patel, P. R., Zhang, H., Robbins, M. T., Nofar, J. B., Marshall, S. P., Kobylarek, M. J., et al. (2016). Chronic *in vivo* stability assessment of carbon fiber microelectrode arrays. *J. Neural Eng.* 13:066002. doi: 10.1088/1741-2560/13/6/066002

Piccinini, A. M., and Midwood, K. S. (2010). DAMPening inflammation by modulating TLR signalling. *Mediat. Inflamm.* 2010:672395. doi: 10.1155/2010/672395

Pineau, I., and Lacroix, S. (2009). Endogenous signals initiating inflammation in the injured nervous system. *Glia* 57, 351–361. doi: 10.1002/glia.20763

Polikov, V. S., Tresco, P. A., and Reichert, W. M. (2005). Response of brain tissue to chronically implanted neural electrodes. *J. Neurosci. Methods* 148, 1–18. doi: 10.1016/j.jneumeth.2005.08.015

Portou, M. J., Baker, D., Abraham, D., and Tsui, J. (2015). The innate immune system, toll-like receptors and dermal wound healing: a review. *Vasc. Pharmacol.* 71, 31–36. doi: 10.1016/j.vph.2015.02.007

Potter, K. A., Buck, A. C., Self, W. K., Callanan, M. E., Sunil, S., and Capadona, J. R. (2013). The effect of resveratrol on neurodegeneration and blood brain barrier stability surrounding intracortical microelectrodes. *Biomaterials* 34, 7001–7015. doi: 10.1016/j.biomaterials.2013.05.035

Potter, K. A., Buck, A. C., Self, W. K., and Capadona, J. R. (2012a). Stab injury and device implantation within the brain results in inversely multiphasic neuroinflammatory and neurodegenerative responses. *J. Neural Eng.* 9:046020. doi: 10.1088/1741-2560/9/4/046020

Potter, K. A., Jorfi, M., Householder, K. T., Foster, E. J., Weder, C., and Capadona, J. R. (2014). Curcumin-releasing mechanically-adaptive intracortical implants improve the proximal neuronal density and blood-brain barrier stability. *Acta Biomater.* 10, 2209–2222. doi: 10.1016/j.actbio.2014.01.018

Potter, K. A., Simon, J. S., Velagapudi, B., and Capadona, J. R. (2012b). Reduction of autofluorescence at the microelectrode-cortical tissue interface improves antibody detection. *J. Neurosci. Methods* 203, 96–105. doi: 10.1016/j.jneumeth.2011.09.024

Potter-Baker, K. A., and Capadona, J. R. (2015). Reducing the "stress": antioxidative therapeutic and material approaches may prevent intracortical microelectrode failure. *ACS Macro Lett.* 4, 275–279. doi: 10.1021/mz500743a

Potter-Baker, K. A., Nguyen, J. K., Kovach, K. M., Gitomer, M. M., Srail, T. W., Stewart, W. G., et al. (2014a). Development of superoxide dismutase mimetic surfaces to reduce accumulation of reactive oxygen species surrounding intracortical microelectrodes. *J. Mater. Chem. B* 2, 2248–2258. doi: 10.1039/C4TB00125G

Potter-Baker, K. A., Ravikumar, M., Burke, A. A., Meador, W. D., Householder, K. T., Buck, A. C., et al. (2014b). A comparison of neuroinflammation to implanted microelectrodes in rat and mouse models. *Biomaterials* 34, 5637–5646. doi: 10.1016/j.biomaterials.2014.03.076

Potter-Baker, K. A., Stewart, W. G., Tomaszewski, W. H., Wong, C. T., Meador, W. D., Ziats, N. P., et al. (2015). Implications of chronic daily anti-oxidant administration on the inflammatory response to intracortical microelectrodes. *J. Neural Eng.* 12:046002. doi: 10.1088/1741-2560/12/4/046002

Prasad, A., Xue, Q. S., Dieme, R., Sankar, V., Mayrand, R., Nishida, T., et al. (2014). Abiotic-biotic characterization of Pt/Ir microelectrode arrays in chronic implants. *Front. Neurosci.* 4:72. doi: 10.3389/fneng.2014.00002

Prasad, A., Xue, Q. S., Sankar, V., Nishida, T., Shaw, G., Streit, W. J., et al. (2012). Comprehensive characterization and failure modes of tungsten microwire arrays in chronic neural implants. *J. Neural Eng.* 9:056015. doi: 10.1088/1741-2560/9/5/056015

Rabinowitz, S. S., and Gordon, S. (1991). Macrosialin, a macrophage-restricted membrane sialoprotein differentially glycosylated in response to inflammatory stimuli. *J. Exp. Med.* 174, 827–836. doi: 10.1084/jem.174.4.827

Ravikumar, M., Hageman, D. J., Tomaszewski, W. H., Chandra, G. M., Skousen, J. L., and Capadona, J. R. (2014a). The effect of residual endotoxin contamination on the neuroinflammatory response to sterilized intracortical microelectrodes. *J. Mater. Chem. B* 2, 2517–2529. doi: 10.1039/C3TB21453B

Ravikumar, M., Sunil, S., Black, J., Barkauskas, D., Haung, A. Y., Miller, R. H., et al. (2014b). The roles of blood-derived macrophages and resident microglia in the neuroinflammatory response to implanted intracortical microelectrodes. *Biomaterials* S0142-9612, 8049–8064. doi: 10.1016/j.biomaterials.2014.05.084

Reed-Geaghan, E. G., Savage, J. C., Hise, A. G., and Landreth, G. E. (2009). CD14 and toll-like receptors 2 and 4 are required for Fibrillar Aß -stimulated microglial activation. *J. Neurosci.* 29, 11982–11992. doi: 10.1523/JNEUROSCI.3158-09.2009

Savage, N. (2018). The mind-reading devices that can free paralysed muscles. *Nature* 555, S12–S14. doi: 10.1038/d41586-018-02478-0

Saxena, T., Karumbaiah, L., Gaupp, E. A., Patkar, R., Patil, K., Betancur, M., et al. (2013). The impact of chronic blood–brain barrier breach on intracortical electrode function. *Biomaterials* 34, 4703–4713. doi: 10.1016/j.biomaterials.2013.03.007

Shoffstall, A. J., Paiz, J., Miller, D., Rial, G., Willis, M., Mendez, D., et al. (2017). Potential for thermal damage to the blood-brain barrier during craniotomy procedure: implications for intracortical recording microelectrodes. *J. Neural Eng.* 15:034001. doi: 10.1088/1741-2552/aa9f32

Stefanova, N., Fellner, L., Reindl, M., Masliah, E., Poewe, W., and Wenning, G. K. (2011). Toll-like receptor 4 promotes α-synuclein clearance and survival of nigral dopaminergic neurons. *Am. J. Pathol.* 179, 954–963. doi: 10.1016/j.ajpath.2011.04.013

Strbo, N., Yin, N., and Stojadinovic, O. (2014). Innate and adaptive immune responses in wound epithelialization. *Adv. Wound Care* 3, 492–501. doi: 10.1089/wound.2012.0435

Streit, W. J., Walter, S. A., and Pennell, N. A. (1999). Reactive microgliosis. *Prog. Neurobiol.* 57, 563–581. doi: 10.1016/S0301-0082(98)00069-0

Suga, H., Sugaya, M., Fujita, H., Asano, Y., Tada, Y., Kadono, T., et al. (2014). TLR4, rather than TLR2, regulates wound healing through TGF-β and CCL5 expression. *J. Dermatol. Sci.* 73, 117–124. doi: 10.1016/j.jdermsci.2013.10.009

Szarowski, D. H., Andersen, M. D., Retterer, S., Spence, A. J., Isaacson, M., Craighead, H. G., et al. (2003). Brain responses to micro-machined silicon devices. *Brain Res.* 983, 23–35. doi: 10.1016/S0006-8993(03)03023-3

Tahara, K., Kim, H. D., Jin, J. J., Maxwell, J. A., Li, L., and Fukuchi, K. (2006). Role of toll-like receptor signalling in Aβ uptake and clearance. *Brain* 129, 3006–3019. doi: 10.1093/brain/awl249

Takmakov, P., Ruda, K., Scott Phillips, K., Isayeva, I. S., Krauthamer, V., and Welle, C. G. (2015). Rapid evaluation of the durability of cortical neural implants

using accelerated aging with reactive oxygen species. *J. Neural Eng.* 12:026003. doi: 10.1088/1741-2560/12/2/026003

Tang, S. C., Arumugam, T. V., Xu, X., Cheng, A., Mughal, M. R., Jo, D. G., et al. (2007). Pivotal role for neuronal Toll-like receptors in ischemic brain injury and functional deficits. *Proc. Natl. Acad. Sci. U.S.A.* 104, 13798–13803. doi: 10.1073/pnas.0702553104

Trotta, T., Porro, C., Calvello, R., and Panaro, M. A. (2014). Biological role of Toll-like receptor-4 in the brain. *J. Neuroimmunol.* 268, 1–12. doi: 10.1016/j.jneuroim.2014.01.014

Wellman, S. M., Eles, J. R., Ludwig, K. A., Seymour, J. P., Michelson, N. J., McFadden, W. E., et al. (2018). A Materials Roadmap to Functional Neural Interface Design. *Adv. Funct. Mater.* 28:1701269. doi: 10.1002/adfm.201701269

Winkler, R. (2017). *Elon Musk Launches Neuralink to Connect Brains With Computers [Online].* The Wall Street Journal. Available Online at: https://www.wsj.com/articles/elon-musk-launches-neuralink-to-connect-brains-with-computers-1490642652 (Accessed April 25, 2017).

Wu, J., and Rao, R. P. N. (2017). *How Close are We to Elon Musk's Brain-Computer Interface*? [Online]. Available online at: http://www.cnn.com/2017/04/12/health/brain-computer-interface-partner/ (Accessed).

Zhang, T., Su, J., Guo, B., Wang, K., Li, X., and Liang, G. (2015). Apigenin protects blood–brain barrier and ameliorates early brain injury by inhibiting TLR4-mediated inflammatory pathway in subarachnoid hemorrhage rats. *Int. Immunopharmacol.* 28, 79–87. doi: 10.1016/j.intimp.2015.05.024

Zhao, H., Perez, J. S., Lu, K., George, A. J., and Ma, D. (2014). Role of Toll-like receptor-4 in renal graft ischemia-reperfusion injury. *Am. J. Physiol. Renal Physiol.* 306, F801–F811. doi: 10.1152/ajprenal.00469.2013

Conflict of Interest Statement: The authors declare that the research was conducted in the absence of any commercial or financial relationships that could be construed as a potential conflict of interest.

Copyright © 2018 Hermann, Lin, Soffer, Wong, Ali, Chang, Sunil, Sudhakar, Tomaszewski, Protasiewicz, Selkirk, Miller and Capadona. This is an open-access article distributed under the terms of the Creative Commons Attribution License (CC BY). The use, distribution or reproduction in other forums is permitted, provided the original author(s) and the copyright owner(s) are credited and that the original publication in this journal is cited, in accordance with accepted academic practice. No use, distribution or reproduction is permitted which does not comply with these terms.

frontiers in Neuroscience

ORIGINAL RESEARCH
published: 19 September 2018
doi: 10.3389/fnins.2018.00648

Development and Characterization of PEDOT:PSS/Alginate Soft Microelectrodes for Application in Neuroprosthetics

*Laura Ferlauto[1], Antonio Nunzio D'Angelo[1], Paola Vagni[1], Marta Jole Ildelfonsa Airaghi Leccardi[1], Flavio Maurizio Mor[2], Estelle Annick Cuttaz[1], Marc Olivier Heuschkel[2], Luc Stoppini[2] and Diego Ghezzi[1]**

[1] Medtronic Chair in Neuroengineering, Center for Neuroprosthetics and Institute of Bioengineering, School of Engineering, École Polytechnique Fédérale de Lausanne, Geneva, Switzerland, [2] Tissue Engineering Laboratory, HEPIA, University of Applied Sciences and Arts Western Switzerland (HES-SO), Geneva, Switzerland

Reducing the mechanical mismatch between the stiffness of a neural implant and the softness of the neural tissue is still an open challenge in neuroprosthetics. The emergence of conductive hydrogels in the last few years has considerably widened the spectrum of possibilities to tackle this issue. Nevertheless, despite the advancements in this field, further improvements in the fabrication of conductive hydrogel-based electrodes are still required. In this work, we report the fabrication of a conductive hydrogel-based microelectrode array for neural recording using a hybrid material composed of poly(3,4-ethylenedioxythiophene)-poly(styrenesulfonate), and alginate. The mechanical properties of the conductive hydrogel have been investigated using imaging techniques, while the electrode arrays have been electrochemically characterized at each fabrication step, and successfully validated both *in vitro* and *in vivo*. The presence of the conductive hydrogel, selectively electrodeposited onto the platinum microelectrodes, allowed achieving superior electrochemical characteristics, leading to a lower electrical noise during recordings. These findings represent an advancement in the design of soft conductive electrodes for neuroprosthetic applications.

Keywords: conductive hydrogel, conjugated polymers, electrode array, electrochemistry, neural recordings

OPEN ACCESS

Edited by:
Jeffrey R. Capadona, Case Western Reserve University, United States

Reviewed by:
David Martin, University of Delaware, United States
Jit Muthuswamy, Arizona State University, United States

****Correspondence:***
Diego Ghezzi
diego.ghezzi@epfl.ch

Specialty section:
This article was submitted to Neural Technology, a section of the journal Frontiers in Neuroscience

Received: *26 May 2018*
Accepted: *30 August 2018*
Published: *19 September 2018*

Citation:
Ferlauto L, D'Angelo AN, Vagni P, Airaghi Leccardi MJI, Mor FM, Cuttaz EA, Heuschkel MO, Stoppini L and Ghezzi D (2018) Development and Characterization of PEDOT:PSS/Alginate Soft Microelectrodes for Application in Neuroprosthetics. Front. Neurosci. 12:648. doi: 10.3389/fnins.2018.00648

INTRODUCTION

In neuroprosthetics, the realization of a performing interface between an implant and the soft tissue is of primary importance for both the preservation of the neuronal environment, and the correct functioning of the device (Lacour et al., 2016). The main approaches taken into consideration for this purpose are essentially two: the modification of the electrode surface with conductive polymers (CPs) or carbon nanotubes (CNTs) (Abidian et al., 2010; Guex et al., 2015; Charkhkar et al., 2016) and the encapsulation of the device in a hydrogel matrix (Kim et al., 2010; Heo et al., 2016). CPs and CNTs are versatile carbon-based materials already exploited in the fabrication of several neuroprosthetic devices (Antognazza et al., 2015; Khodagholy et al., 2015; Feyen et al., 2016; Xiang et al., 2016; Ferlauto et al., 2018). In particular, their incorporation in the active sites of recording or

stimulating neural devices is known to lower the impedance and the stiffness of metal electrodes, to allow both electronic and ionic charge transport, and to promote cell adhesion and proliferation (Abidian et al., 2010; Harris et al., 2013; Balint et al., 2014; Martin and Malliaras, 2016; Rivnay et al., 2016; Simon et al., 2016). Despite these attractive properties, these materials still suffer from a Young's modulus far higher than the one of the tissue they are in contact with, potentially leading to important implications in terms of foreign body reaction and ultimately to the device failure (Salatino et al., 2017).

On the other hand, hydrogels are natural, or synthetic materials based on a three-dimensional network of polymer chains that can retain a large amount of water and are already used in a variety of biomedical applications, ranging from contact lenses to wound healing, and drug delivery (Buwalda et al., 2014; Caló and Khutoryanskiy, 2015; Ullah et al., 2015; Bryant and Vernerey, 2018). Their tunable mechanical properties, high water content, high porosity, and soft consistency mimic the ones of living tissues; this makes hydrogels extremely attractive for neural prostheses.

To combine the strengths of these two approaches, the exploitation of conductive hydrogels (CHs) as coatings for microelectrodes in neural implants has recently emerged as a promising strategy (Green et al., 2012, 2016; Goding et al., 2017; Staples et al., 2017; Spencer et al., 2017). A CH on the electrodes could in fact simultaneously guarantee appropriate electrochemical and mechanical properties for the interaction with the neural tissue.

To our knowledge, despite recent progress in this field, a selective micro-sized confinement of CHs, with a thorough electrochemical characterization at each fabrication step, followed by *in vitro* and *in vivo* validation, is still missing (Kleber et al., 2017; Staples et al., 2017). The aim of this work is therefore to provide a comprehensive characterization of a CH-based microelectrode array, consisting of a poly (3,4-ethylenedioxythiophene)-poly(styrenesulfonate; PEDOT:PSS) and alginate (A) coating (called conductive alginate, CA) selectively electrodeposited on platinum (Pt) microelectrodes to reduce the mismatch of the material properties at the electrode-tissue interface.

MATERIALS AND METHODS

Electrode Arrays Used in the Study

Pt-based microelectrode arrays (MEAs) with various geometries (linear or grid), electrode diameters (30, 100, or 400 μm), and electrode coatings (PEDOT:PSS, PEDOT:PSS/A, PEDOT:PSS/CA, and Pt Black) have been fabricated and used in this study. For structural and electrochemical characterization, planar grid MEAs (g-MEAs) with 16 electrodes (4 × 4) of 400 μm in diameter and a center-to-center distance of 1 mm were used. Electrodes were bare Pt, or Pt-coated with PEDOT:PSS, PEDOT:PSS/A, and PEDOT:PSS/CA. For *in vitro* validation, two planar MEAs with eight electrodes of 30 μm in diameter were used: a bottom porous MEA (p-MEA) and a top strip MEA (s-MEA). Pt electrodes were coated with Pt black or with PEDOT:PSS/CA. For *in vivo* validation, penetrating linear MEAs (l-MEAs) with 16 electrodes of 100 μm in diameter and a center-to-center distance of 200 μm were used. Electrodes were bare Pt or Pt-coated with PEDOT:PSS/CA.

Electrode Array Fabrication

Microelectrode arrays were fabricated on 4-inch silicon (Si) wafers (thickness 525 μm) with a titanium-tungsten alloy/aluminum release layer (TiW/Al, 200 nm/1 μm). A polyimide (PI) layer (HD MicroSystems PI2611, 10 μm) was spin-coated (1,400 rpm for 40 s) and then cured by a soft bake (5 min at 65°C and 5 min at 95°C) followed by a hard bake (1 h at 300°C with nitrogen from 190°C). A titanium/platinum (Ti/Pt, 5 nm/150 nm) adhesive/conductive layer was deposited by sputtering (Alliance Concept AC450). A positive photoresist (AZ1512, 2 μm) was deposited by spin-coating and soft baked at 110°C for 2 min before direct exposure (Heidelberg Instruments MLA150, 405 nm) and development. Electrode shaping and photoresist removal were performed by chlorine dry etching (Corial 210IL) followed by oxygen plasma (500 W for 30 s). MEAs were encapsulated by spin-coating an adhesion promoter (VM651, 1,000 rpm for 10 s + 3,000 rpm for 30 s), spin-coating and soft baking a first PI layer (PI2611, 10 μm) followed by a second layer (10 μm), and curing (soft and hard bake). Then, a Si hard mask (1 μm) was deposited by sputtering (Alliance Concept AC450) and the photolithography was repeated. Dry etching (Corial 210IL) of Si and eventually PI and photoresist (respectively, chlorine and oxygen chemistries) allowed the exposure of Pt pads and electrodes. A final Si dry etching removed the remaining hard mask. An extra etching step was performed on p-MEAs to fabricate a porous substrate (7.5 μm diameters holes with a pitch of 20 μm). The MEAs were cut by a laser cutter (Optec MM200-USP) and released by Al anodic dissolution for 15 h.

PEDOT:PSS Coating

An aqueous solution of 0.1 wt% 3,4-ethylenedioxythiophene (EDOT 97%, 483028, Sigma) and 4 wt% poly(4-styrenesulfonic acid) solution (PSS, M_W ~75,000, 561223, Sigma) in deionized water was mixed by ultrasonication for 5 min before being filtered with 0.2 μm PTFE filters (431229, Corning). The electropolymerization of PEDOT:PSS was obtained using a potentiostat (Compact Stat, Ivium). MEAs were immersed in the solution together with a silver/silver-chloride (Ag/AgCl) reference electrode and a Pt counter electrode. The potential was increased from 0.4 to 0.9 V in 5 steps of 0.1 V and 2 s in duration. Then, the potential was held at 0.9 V for 40 s. The protocol was repeated twice and MEAs were finally cured at 65°C for 3 h.

Alginate and Conductive Alginate Coating

1% Alginate mother solution was prepared by dissolving 1 wt% of alginic acid from brown algae (A2033, Sigma) and 0.5 wt% of calcium carbonate ($CaCO_3$ −99%, C5929, Sigma) in phosphate-buffered saline (PBS). The solution was then stirred and heated at

100°C for 1 h and all further alginate deposition solutions with different concentrations were obtained by its dilution (Cheng et al., 2011). First, an adhesion layer composed of 0.1 wt% EDOT and 4 wt% PSS in alginate deposition solution was prepared, ultrasonicated for 5 min, and electropolymerized (as in section "PEDOT:PSS coating"). Then, alginate was electropolymerized from the alginate deposition solution with a voltage increase from 0 to 2 V without any intermediate step and kept constant for 2 s. MEAs were then stored in a hardening solution consisting of 1 wt% of calcium chloride ($CaCl_2$, C7902, Sigma) in PBS for at least 30 min. To obtain a CA, the electropolymerization of PEDOT:PSS was then repeated twice (as in section "PEDOT:PSS Coating").

Platinum Black Coating

Platinum electrodes were coated with platinum black using a platinum solution made of: 2 g $H_2PtCl_6 \cdot xH_2O$, 16 mg $C_4H_6O_4Pb \cdot 3H_2O$, and 58 g of H_2O (Sigma). A 700 mV signal at 300 Hz was applied via a 4,284A Precision LCR Meter (Keysight Technologies) until the electrode impedance reached a magnitude of 8 kΩ and a phase of −45°. About 10–15 s were required to achieve sufficient plating corresponding to a black platinum coating thickness of 300 to 400 nm.

PEGDMA Coating

The 5 wt% of Poly(ethylene glycol) dimethacrylate (PEGDMA, M_n 20,000, 25406-5, Polysciences), 5 wt% of PEGDMA (M_n 550, 409510, Sigma), and 0.5 wt% of 2-hydroxy-4′-(2-hydroxyethoxy)-2-methylpropiophenone photoinitiator (IRGACURE 2959, 410896, Sigma) were mixed in PBS and ultrasonicated until complete dissolution. MEAs were dipped in this solution for 3 s and then exposed to UV light (365 nm, Thorlabs) for 15 min. Afterward, MEAs were stored inside the hardening solution (1 wt% of $CaCl_2$ in PBS).

Microscopic Characterization

The thickness of the PEDOT:PSS double layer was measured using a Bruker's DektakXT Stylus Profiler. The topography and the elastic modulus surface map were taken using a Dimension Icon atomic force microscope (AFM, Bruker); measurements were performed in liquid (1 wt% of $CaCl_2$ in PBS), with a ScanAsyst Fluid + probe (Bruker, nominal spring constant 0.7 N m^{-1}). Each scan contains 512 lines of 512 data points across a 3 μm × 3 μm surface. Images were analyzed using Gwyddion software. For each map, the average stiffness value with its SD was obtained. The variance of the stiffness was calculated as the square of the standard deviation.

Electrochemistry

Electrochemical characterizations were performed with a three-electrode (Ag/AgCl reference electrode, Pt counter electrode) potentiostat (Compact Stat, Ivium) in PBS (pH 7.4) at room temperature. Impedance spectroscopy (IS) was performed between 1 Hz and 1 MHz with an AC voltage of 50 mV. Cyclic voltammetry (CV) was obtained by sweeping a cyclic potential at a speed of 50 mV s^{-1} between −0.6 and 0.8 V for Pt electrodes and between −0.9 and 0.8 V for coated electrodes. For each electrode, the average response over 5 cycles was calculated; the anodic and cathodic charge storage capacities (CSCs) were extrapolated from the integration of the respective currents.

Cell Culture

Human neural stem cells from induced pluripotent stem cells (iPSCs) were obtained from MTI-Globalstem (GSC-4301, Thermo Fisher Scientific). They were cultured and maintained on 1:200 GelTrex LDEV-free hESC quality (A1413302, Thermo Fisher Scientific) coated flask in a proliferation medium composed of neurobasal™ medium (21103049, Thermo Fisher Scientific) supplemented with 2% B-27™ supplement (17504001, Thermo Fisher Scientific), MEM non-essential amino acids (11140050, Thermo Fisher Scientific), 1% Glutamax™ supplement (35050061, Thermo Fisher Scientific), and 20 ng ml^{-1} FGF-2 (100-18B, PeproTech). For the generation of three-dimensional neurospheres (NSs), cells were detached at approximately 80% confluence with pre-warmed StemPro™ Accutase™ (A1110501, Thermo Fisher Scientific) for 1–2 min. The single cell suspension was centrifuged for 3 min at 320 g, suspended in proliferation medium and cells were counted. 500,000 cells in 3 ml proliferating medium were added into a non-treated six-well plate. The plate was left under orbital agitation (80 rpm) for 4 days in a cell culture incubator at 37°C (100% humidity, 5% CO_2). 24 h later, the free-floating three-dimensional NSs were formed by aggregation. Four days after seeding, the NS size was checked and switched to a differentiation medium composed of NeuralQ™ Basal Medium (GSM9420, GlobalStem), GS21T Supplement (GSM3100, GlobalStem), and 1% Glutamax™ supplement (35050061, Thermo Fisher Scientific). Cultures were maintained in orbital agitation (80 rpm) for 6 weeks. A breathable plate sealer was added in order to reduce medium evaporation. The medium was changed once a week (3 ml). Mature NSs were then transferred to a 6 mm patch of pre-cut circular hydrophilic membrane supported by a six well insert (PICMORG50, Merck-Millipore) and kept in the incubator for 1 week. The use of membrane pre-cut patches facilitates the NS manipulation.

Electrophysiology *in vitro*

Neurospheres on membranes were transferred with forceps under a dissection microscope (Leica Microsystems) onto the center of a p-MEA device. After 1 day of recovery, NSs top surface was put in contact with an s-MEA device (coated with platinum black or conductive alginate) and electrophysiological recordings were performed using an amplifier (W2100-HS32, Multi Channel Systems) and a data acquisition system (W2100, Multi Channel Systems). The signal-to-noise ratio (SNR) was evaluated as follow: for each electrode, the noise was quantified as the standard deviation of the voltage during a 5 min recording, while the signal was the average peak-to-peak voltage of the spikes recorded in the same 5 min period. For each electrode, the SNR was computed as the signal divided by the noise. Therefore, electrodes unable to detect neural spikes have been excluded (n = 11 out of 16 and n = 4 out of 21, respectively, for s-MEA with Pt black and s-MEA-CA).

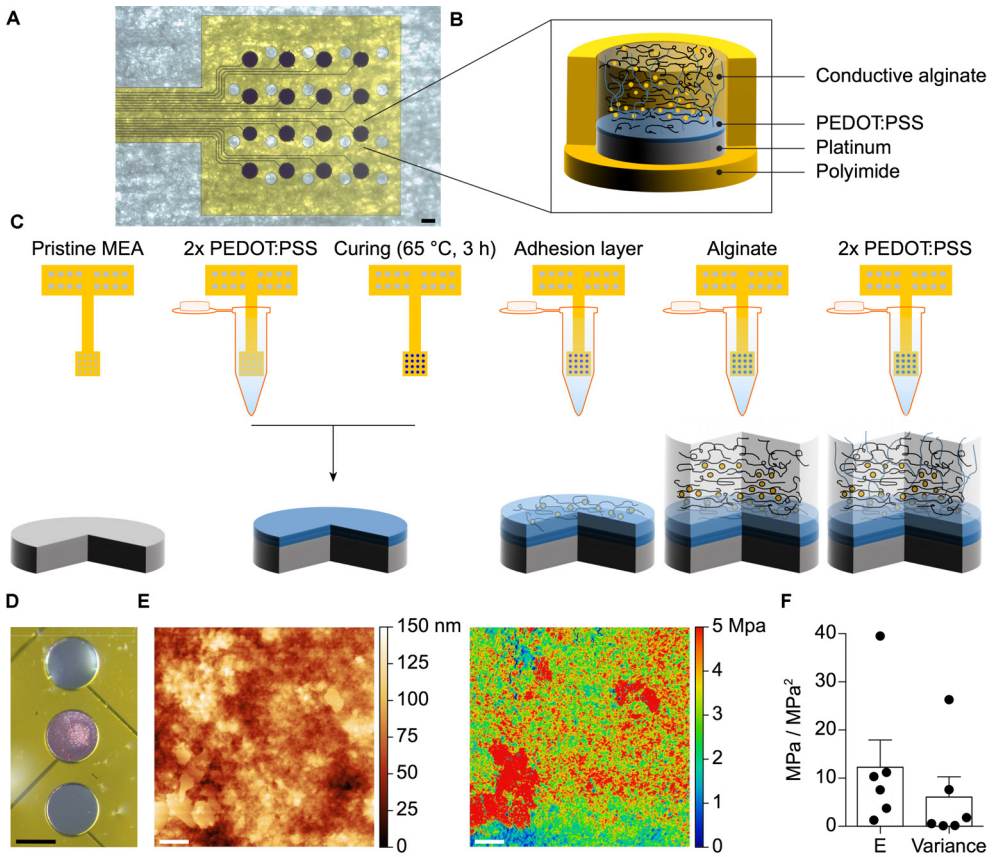

FIGURE 1 | (A) Pictures of a fabricated g-MEA with 400 μm diameter electrodes. The scale bar is 400 μm. **(B)** Schematic of the soft CA-based electrode structure. **(C)** Step-by-step coating process of the CA-based electrodes. **(D)** Selective electroplating of alginate with added Rhodamine B on the central Pt electrode only. The scale bar is 150 μm. **(E)** AFM topography map of a 3 × 3 μm surface area of the CA (left) and the corresponding elastic modulus surface map (right). The scale bar is 400 nm. **(F)** Quantification of the mean (± SEM) stiffness and variance (n = 6 electrodes, 1 map per electrode).

Electrophysiology *in vivo*

Animal experiments were performed according to the animal authorization GE13416 issued by the Département de l'emploi, des affaires sociales et de la santé (DEAS), Direction générale de la santé of the Republique et Canton de Geneve, Switzerland. Two months old C57BL6J mice were anesthetized with isoflurane inhalation (induction 0.8–1.5 l min^{-1}, 4–5%; maintenance 0.8–1.5 l min^{-1}, 1–2%). A 0.5 mm small craniotomy was opened in the correspondence of the visual cortex (identified by stereotaxic coordinates). MEAs were implanted in the cortical layers using a micromanipulator (SM-15R, Narishige). Light flashes (4 ms, 30 cd s m^{-2}) were delivered using a Ganzfeld stimulator (Biomedica Mangoni) positioned close to the contralateral eye and visually evoked cortical potentials (VEPs) were recorded and filtered (0.1–300 Hz).

Statistical Analysis and Graphical Representation

Statistical analysis and graphical representation were performed on Prism (GraphPad Software Inc.). The normality test (D'Agostino & Pearson omnibus normality test) was performed in each dataset to justify the use of a parametric or non-parametric test. In each figure p-values were represented as: $^{*}p < 0.05$, $^{**}p < 0.01$, $^{***}p < 0.001$, and $^{****}p < 0.0001$. Data were always reported as mean ± SD or ± SEM; n identifies the number of electrodes.

RESULTS

Microelectrode arrays with various geometries (linear or grid) and electrode diameters (30, 100, or 400 μm) have been fabricated using PI as substrate and superstrate and Pt for the electrodes, traces, and pads (**Figure 1A**). Soft electrodes consisting of a first layer of PEDOT:PSS and a second layer of CA have been then electrodeposited on top of the Pt electrodes (**Figures 1B,C**). With a mechanical profilometer the average (± SD, n = 12) thickness of the PEDOT:PSS layer has been quantified as 1.18 ± 0.69 μm. The sharp confinement of the conductive alginate coating on top of the electrodes has been obtained by ionic crosslinking via electroplating (Cheng et al., 2011). This has been experimentally visualized and validated by adding Rhodamine B to the hydrogel (**Figure 1D**). The map of

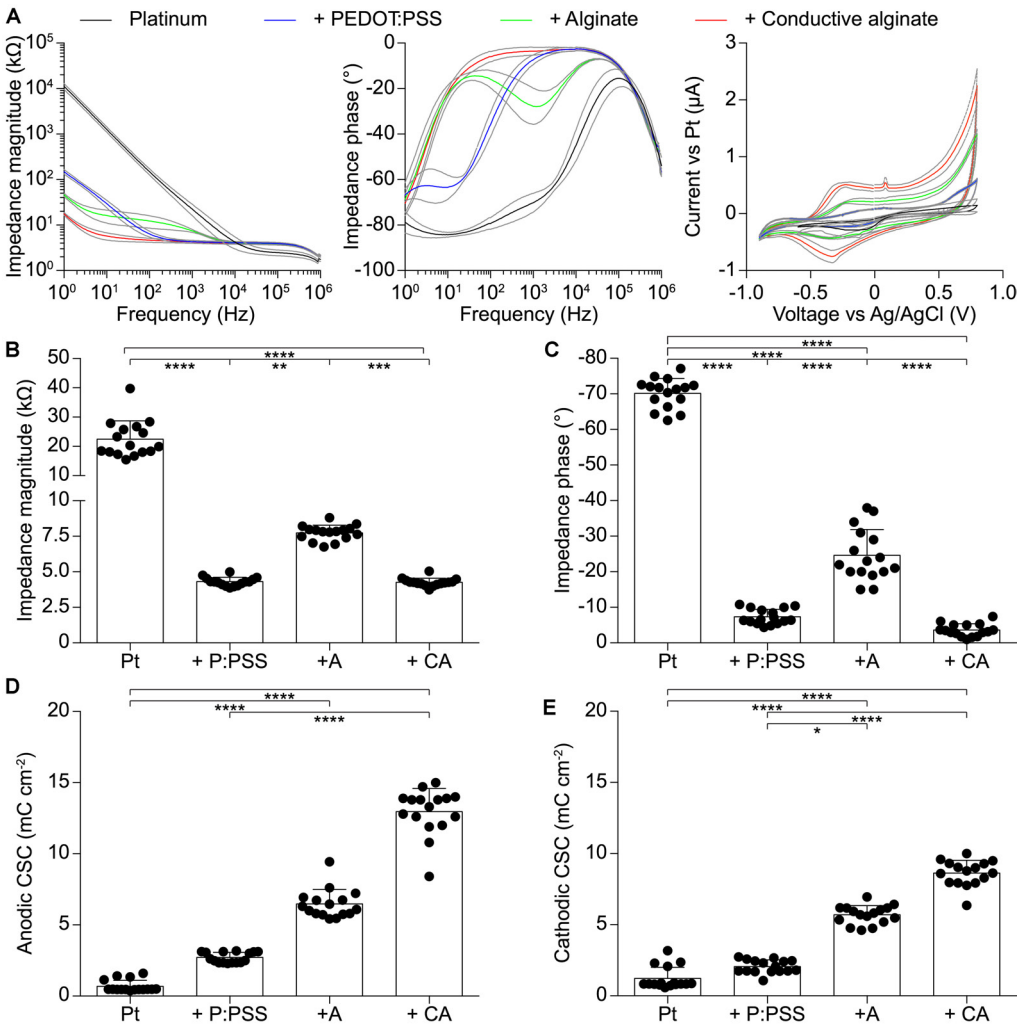

FIGURE 2 | Quantification of the electrochemical characteristics of g-MEA with 400-μm diameter electrodes (n = 16) at each fabrication step. **(A)** IS (magnitude and phase) and CV performed at each fabrication step. Colored lines represent average values and gray lines the ± SD. **(B)** Impedance magnitude at 1 kHz ($p < 0.0001$, Kruskal–Wallis test with Dunn's multiple comparisons test). **(C)** Impedance phase at 1 kHz ($p < 0.0001$, one-way ANOVA with Tukey's multiple comparisons test). **(D)** Anodic CSC ($p < 0.0001$, Kruskal–Wallis test with Dunn's multiple comparisons test). **(E)** Cathodic CSC ($p < 0.0001$, Kruskal–Wallis test with Dunn's multiple comparisons test). In all panels P:PSS means PEDOT:PSS.

the elastic modulus on the surface of the CA (**Figure 1E**) has been obtained through peak-force quantitative nanomechanical mapping atomic force microscopy (PF-QNM AFM) of the hydrated sample. The variability of the modulus values points out the presence of an interpenetrating network of a stiffer material within a softer embedding, thus revealing the co-presence of the two components of the CA. The mean (± SEM) elastic modulus measured from various electrodes (n = 6) has been quantified in 12.29 ± 5.67 MPa with a mean (± SEM) variance of 6.10 ± 4.21 MPa^2 (**Figure 1F**).

IS and CV have been performed at each fabrication step on g-MEAs with 400 μm electrodes to evaluate their electrochemical characteristics (**Figure 2**). In agreement with the literature (Staples et al., 2017), CA-based electrodes showed (mean ± SD, n = 16) a lower impedance magnitude (4.26 ± 0.29 kΩ at 1 kHz), a resistive behavior (−3.59 ± 1.71° at 1 kHz), and a larger charge storage capacity (CSC, anodic: 12.96 ± 1.63 mC cm^{-2}, cathodic: 8.62 ± 0.90 mC cm^{-2}) in comparison with the other conditions tested (bare Pt, Pt-coated with PEDOT:PSS, and Pt-coated with PEDOT:PSS and pure alginate). Amongst the different concentrations of alginate within the conductive hydrogel, the lowest (0.125%) has been chosen due to its effectiveness in constraining the gel on the electrode sites. In fact, higher gel concentrations will form a continuous layer over the entire electrode array due to the higher viscosity of the solution. From the electrochemical point of view, an improvement of impedance magnitude and phase of bare alginate coated electrodes was observed by lowering the alginate concentration, while no effect was appreciable on CA-based electrodes (**Figure 3**).

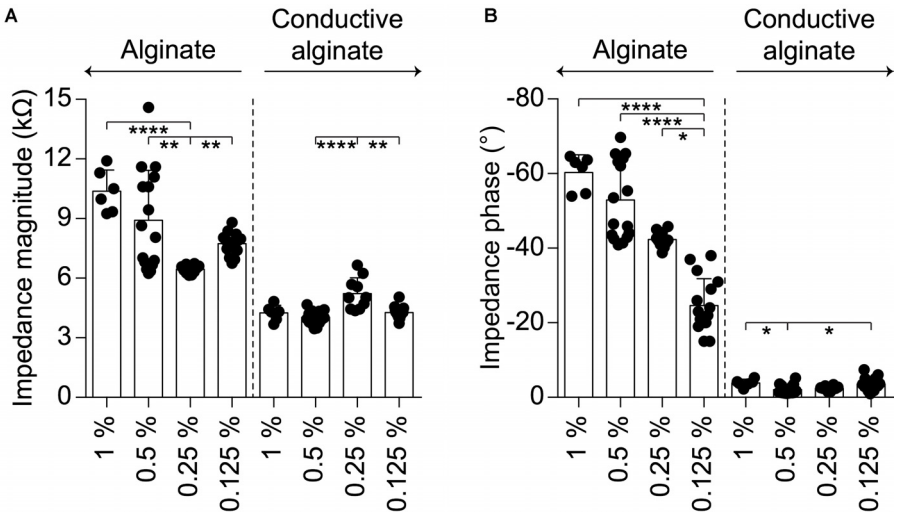

FIGURE 3 | Quantification of the electrochemical characteristics of g-MEA with 400-μm diameter electrodes at different alginate concentrations (1%, $n = 6$; 0.5%, $n = 16$; 0.25%, $n = 10$; 0.125% $n = 16$); bare alginate on the left and CA on the right. **(A)** Impedance magnitude at 1 kHz (alginate $p < 0.0001$, CA $p < 0.001$, Kruskal–Wallis test with Dunn's multiple comparisons test). **(B)** Impedance phase at 1 kHz (alginate $p < 0.0001$, CA $p < 0.01$, one-way ANOVA with Tukey's multiple comparisons test).

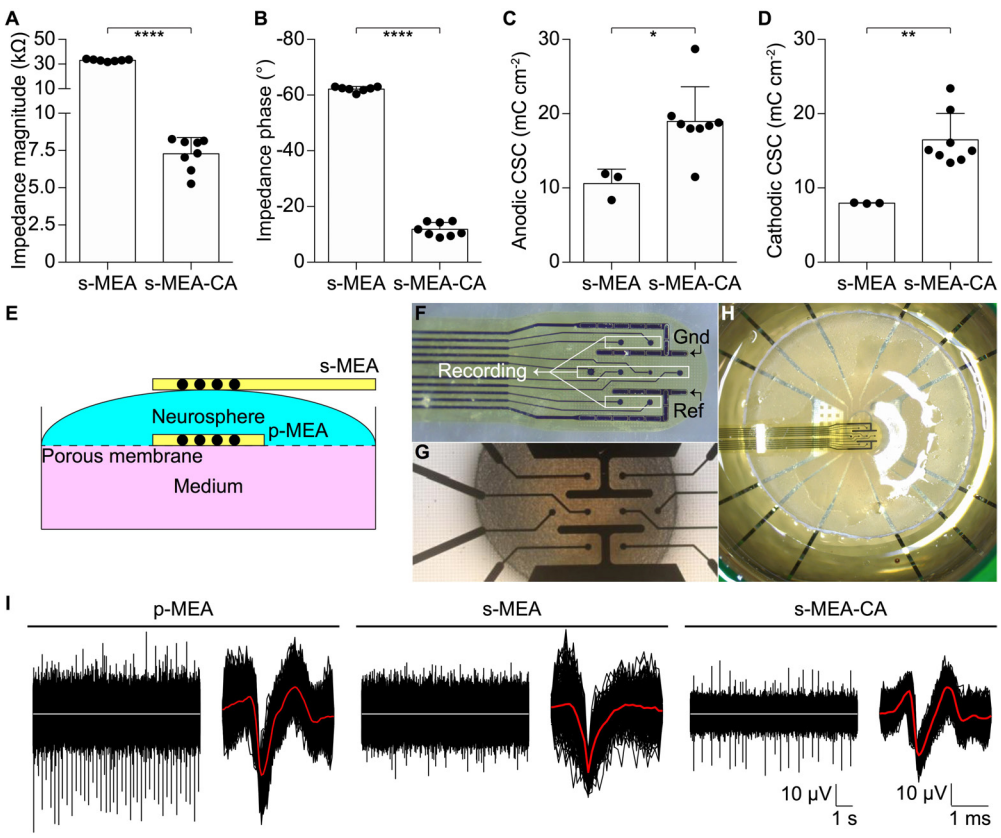

FIGURE 4 | Validation *in vitro*. **(A–D)** Quantification of the impedance magnitude at 1 kHz ($p < 0.0001$, *t*-test), impedance phase at 1 kHz ($p < 0.0001$, *t*-test), anodic CSC ($p < 0.05$, *t*-test), cathodic CSC ($p < 0.01$, *t*-test) of s-MEA ($n = 7$ for IS and $n = 3$ for CV) and s-MEA-CA ($n = 8$). The electrode diameter is 30 μm. **(E)** Sketch of the recording set-up. **(F)** Picture of an s-MEA. **(G)** Picture of a p-MEA with the NS on top. **(H)** Picture of the set-up with p-MEA, NS, and s-MEA. **(I)** Representative recordings from a p-MEA, an s-MEA, and an s-MEA-CA. For each, on the left is a representative raw trace and on the right the overlay of the spike waveform from the same electrode. The white traces represent the baseline (0 μV), while the red lines are the averages of the spike waveforms.

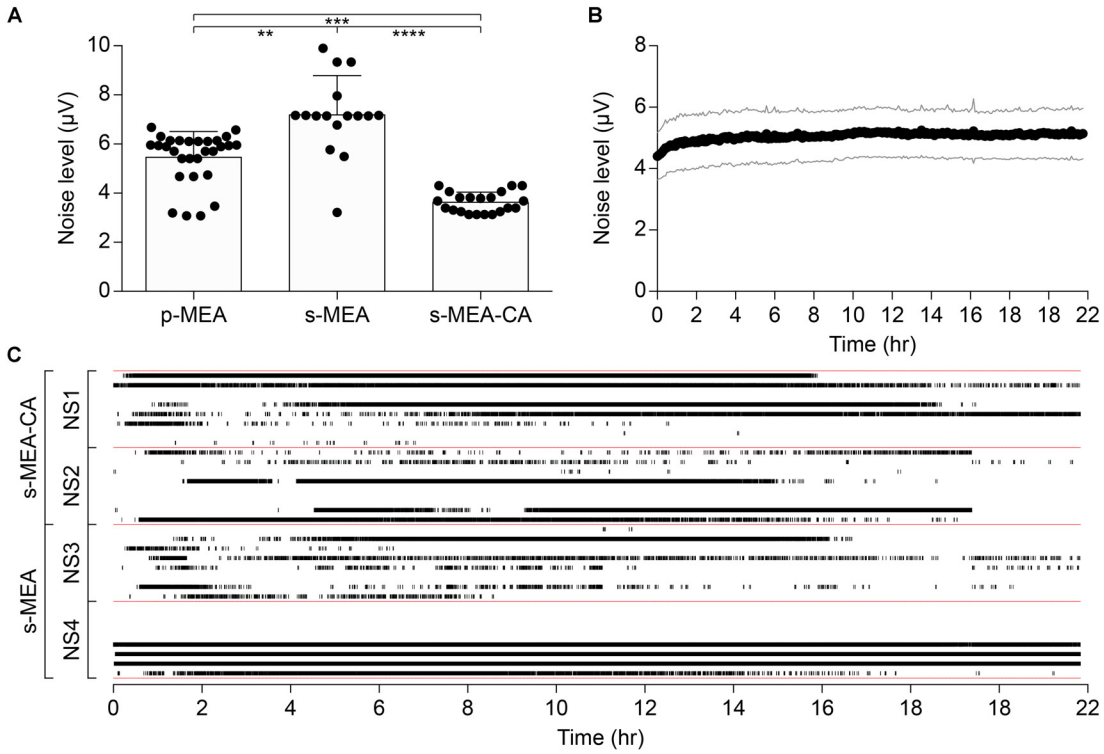

FIGURE 5 | Noise performance of CA-based electrodes. **(A)** Mean (± SD) of the noise level between p-MEA (n = 29), s-MEA (n = 16), and s-MEA-CA (n = 21); $p < 0.0001$ Kruskal–Wallis test with Dunn's multiple comparisons test. **(B)** Mean (± SD) noise level over the time of s-MEA-CA (n = 21). **(C)** Spike raster plot of four NSs over 22 h of recordings. s-MEA (two NSs) and s-MEA-CA (two NSs) have eight electrodes each.

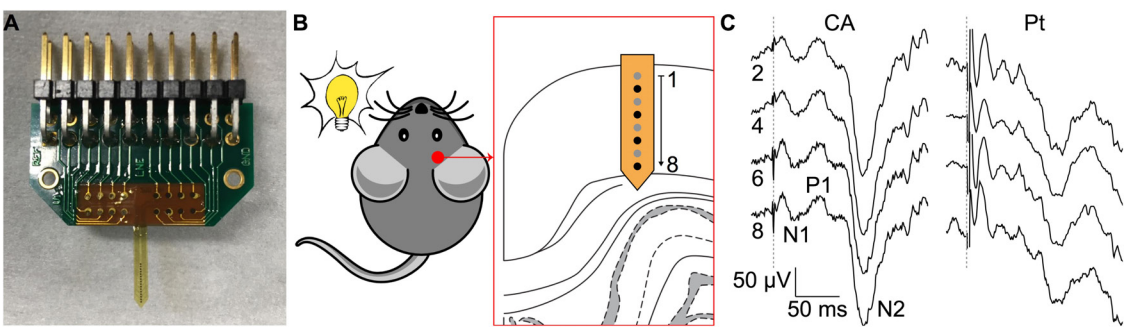

FIGURE 6 | Validation *in vivo*. **(A)** Picture of a penetrating MEA with CA electrodes. **(B)** Experiment sketch. **(C)** Representative single-sweep recordings from 4 (out of 8) CA-based electrodes (diameter 100 μm, black electrodes in **B** from an implanted array on the left and representative averaged recordings (average of 10 consecutive sweeps) from 4 (out of 8) bare Pt electrodes (diameter 100 μm) on the right. The dotted gray line represents the flash occurrence (4 ms, 30 cd s m^{-2}). The main peaks of the VEP are highlighted in the trace of electrode 8.

The detailed characterization of the CA-based electrodes has been performed at 1 kHz since this frequency is a standard reference for application in neuroprosthetics. It should be noted (**Figure 2A**), that at lower frequencies (<100 Hz), the mean impedance magnitude of PEDOT:PSS coated electrodes starts to increase, while the mean impedance magnitude of CA-based electrodes remains remarkably low till a frequency of 10 Hz. Below 10 Hz, it starts to increase but remains at values which are 10 times lower than those of PEDOT:PSS coated electrodes. This could be very relevant for several biomedical applications in which low-frequency signals are collected, such as for electrocardiographic and electromyographic tattoo skin sensors (Zucca et al., 2015; Wang et al., 2018).

The performance of the CA-based electrode array in recording neuronal signals has been tested *in vitro* on NSs formed by human neural stem cells derived from iPSCs. CA-based electrodes (30 μm in diameter) have been compared to Pt/Pt black ones, which represent the standard reference in neuronal recordings.

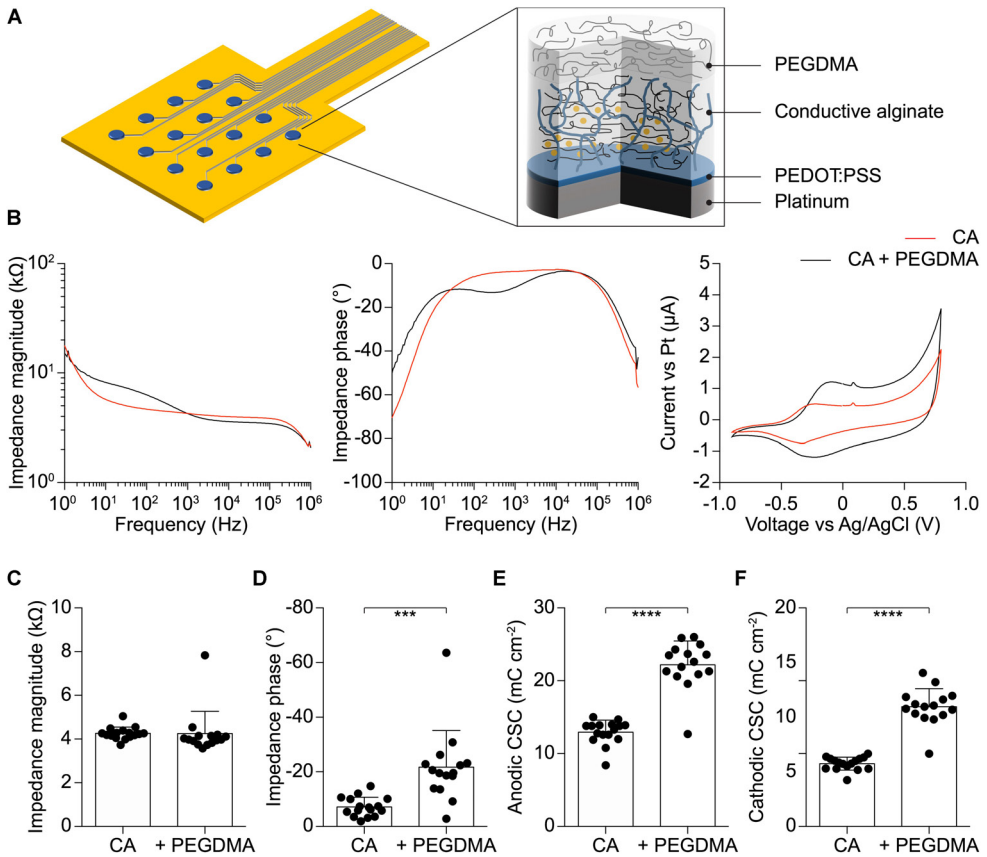

FIGURE 7 | (A) Schematic of the soft electrode structure coated with PEGDMA. **(B)** Mean impedance magnitude, phase, and cyclic voltammetry for CA (red) and PEGDMA (black) 400 μm diameter electrodes (n = 15). **(C)** Quantification of the impedance magnitude at 1 kHz (p = 0.9568, t-test, n = 15). **(D)** Quantification of the impedance phase at 1 kHz ($p < 0.001$, t-test, n = 15). **(E)** Quantification of the anodic CSC ($p < 0.0001$, t-test, n = 15). **(F)** Quantification of the cathodic CSC ($p < 0.0001$, t-test, n = 15).

As in the previous case, the electrochemical characterization of CA-based electrodes showed (mean ± SD, n = 8) a lower impedance magnitude (7.29 ± 1.09 kΩ at 1 kHz), a more resistive behavior (−11.82 ± 2.46° at 1 kHz), and an increase in the CSC values (anodic: 18.96 ± 4.68 mC cm^{-2}, cathodic: 16.46 ± 3.57 mC cm^{-2}) with respect to Pt/Pt black electrodes (**Figures 4A–D**). For *in vitro* validation, four NSs have been placed onto four p-MEAs with 30 μm Pt/Pt black electrodes, used as a reference for tissue viability. The top side of each NS has been contacted with an s-MEA embedding either 30 μm Pt/Pt black (s-MEA) or 30 μm CA-based (s-MEA-CA) electrodes (**Figures 4E–H**). Both p-MEA and s-MEA showed a noise level larger than s-MEA-CA (**Figure 4I**), that has been quantified as the standard deviation of the voltage recordings. In agreement with IS (**Figure 4A**), CA-based electrodes (s-MEA-CA) showed a better noise level (**Figure 5A**) compared to Pt/Pt black electrodes (p-MEA and s-MEA). Since NSs are seeded on top of the p-MEA, they had a stronger adhesion to the tissue, which translated into the detection of spikes with a higher peak-to-peak voltage with respect to any s-MEA (with or without CA). On the contrary, the s-MEA suffered from a weak contact to the NSs due to their spherical surface and the flexibility of the PI strip; this resulted in the detection of spikes with a lower peak-to-peak voltage (**Figure 4I**). However, regardless of the weaker contact, the s-MEA-CA devices presented a lower noise level in comparison with the s-MEA and p-MEA (**Figure 5A**), which turned into a better SNR with respect to the equivalent condition with s-MEAs: mean SNRs (± SD) are 6.75 ± 0.87 (n = 5) and 8.20 ± 1.35 (n = 17), respectively, for s-MEA with Pt black and s-MEA-CA ($p < 0.05$, unpaired t-test). Moreover, the noise level of s-MEA-CA devices was not affected over a time-period of 22 h (**Figure 5B**), in which neuronal spikes have been detected (**Figure 5C**). The frequency of the detected spikes decreases after about 16 h of recordings. This effect has not been associated with a deterioration of the CA-based electrodes since both electrode types (s-MEA and s-MEA-CA) showed a similar reduction. On the contrary, it could be owed to a reduction of the NS viability.

The ability of CA-based electrodes to detect neuronal activity has also been proven *in vivo*. Penetrating CA-based MEAs with linear geometry and electrode diameters of 100 μm have been implanted in the visual cortex of mice (**Figure 6A**). Due to the thin thickness of the mouse visual cortex, only the first eight electrodes of the probe (16 in total) have been inserted over the entire cortical thickness (**Figure 6B**).

VEPs have been successfully recorded upon light stimulation of the contralateral eye (**Figure 6C**, left). Because of the low impedance of the CA electrodes, individual responses to a single flash highlighted all main components (positive and negative peaks, respectively, P and N) of the cortical VEP, without synchronous averaging. As a qualitative comparison, the cortical VEP recorded with bare Pt electrodes (diameter of 100 μm) upon synchronous averaging of 10 consecutive responses have been shown (**Figure 6C**, right). Qualitatively, it is visible that CA-based electrodes have better performances even without synchronous averaging. Lastly, taking into consideration the possibility of the alginate to dissolve with time during chronic implantation (Lee and Mooney, 2012), we also verified that a protective coating of the probe with Poly(ethylene glycol) dimethacrylate (PEGDMA), created by dip-coating, would not alter the electrochemical properties of the CA-based electrodes (**Figure 7**).

CONCLUSION

The use of CA as a soft coating of MEAs is an attractive strategy to both reduce the mechanical mismatch at the electrode-tissue interface and improve the electrochemical properties of microelectrodes (Green et al., 2012, 2016; Goding et al., 2017). Our results showed a selective and sharp micro-sized confinement of CA onto the metallic electrodes of MEAs, which is one of the open challenges in the field. In addition, we provided a comprehensive and complete characterization of CA-based MEAs via electrochemical, mechanical, and electrophysiological analyses. With respect to Pt and Pt/Pt black electrodes, which are the standard materials employed in clinical devices, the soft CA-based microelectrodes presented in this work demonstrated lower impedance magnitude, higher CSCs, and a more resistive behavior. This turns into an improved SNR during neuronal recordings. These results represent an important advancement for the fabrication of performing neuroprosthetic devices able to reduce the mechanical and electrical mismatch at the electrode-tissue interface.

DATA AVAILABILITY STATEMENT

The authors declare that all the data supporting the findings of the study are available in this article. Access to our raw data can be obtained from the corresponding author upon reasonable request.

AUTHOR CONTRIBUTIONS

LF designed, fabricated, and tested the MEAs, co-supervised the study, and wrote the manuscript. AD optimized the conductive hydrogel coating and performed the electrochemical characterizations. PV performed the *in vivo* electrophysiology. MA fabricated the MEAs and optimized the electrodeposition of the PEDOT:PSS. FM performed and analyzed the *in vitro* electrophysiology. EC contributed to the electrochemical characterization. MH fabricated the Pt-black MEAs. LS designed the *in vitro* assay. DG designed and led the study, validate the data analysis, and wrote the manuscript. All the authors read and accepted the manuscript.

FUNDING

This work was supported by École Polytechnique Fédérale de Lausanne, Medtronic, and European Commission (EU project 701632). The Tissue Engineering Laboratory received support from the Wyss Center for Bio- and Neuro-Engineering, Geneva, and HES-SO for the cell culture assay.

REFERENCES

Abidian, M., Corey, J., Kipke, D., and Martin, D. (2010). Conducting-polymer nanotubes improve electrical properties, mechanical adhesion, neural attachment, and neurite outgrowth of neural electrodes. *Small* 6, 421–429. doi: 10.1002/smll.200901868

Antognazza, M. R., Martino, N., Ghezzi, D., Feyen, P., Colombo, E., Endeman, D., et al. (2015). Shedding light on living cells. *Adv. Mater.* 27, 7662–7669. doi: 10.1002/adma.201403513

Balint, R., Cassidy, N., and Cartmell, S. (2014). Conductive polymers: towards a smart biomaterial for tissue engineering. *Acta Biomater.* 10, 2341–2353. doi: 10.1016/j.actbio.2014.02.015

Bryant, S., and Vernerey, F. (2018). Programmable hydrogels for cell encapsulation and neo-tissue growth to enable personalized tissue engineering. *Adv. Healthc. Mater.* 7:1700605. doi: 10.1002/adhm.201700605

Buwalda, S., Boere, K., Dijkstra, P., Feijen, J., Vermonden, T., and Hennink, W. (2014). Hydrogels in a historical perspective: from simple networks to smart materials. *J. Control Release* 190, 254–273. doi: 10.1016/j.jconrel.2014.03.052

Caló, E., and Khutoryanskiy, V. (2015). Biomedical applications of hydrogels: a review of patents and commercial products. *Eur. Polym. J.* 65, 252–267.

Charkhkar, H., Knaack, G., McHail, D., Mandal, H., Peixoto, N., Rubinson, J., et al. (2016). Chronic intracortical neural recordings using microelectrode arrays coated with PEDOT–TFB. *Acta Biomater.* 32, 57–67.

Cheng, Y., Luo, X., Betz, J., Payne, G., Bentley, W., and Rubloff, G. (2011). Mechanism of anodic electrodeposition of calcium alginate. *Soft Matter* 7, 5677–5684.

Ferlauto, L., Leccardi, M., Chenais, N., Gilliéron, S., Vagni, P., Bevilacqua, M., et al. (2018). Design and validation of a foldable and photovoltaic wide-field epiretinal prosthesis. *Nat. Commun.* 9:992. doi: 10.1038/s41467-018-03386-7

Feyen, P., Colombo, E., Endeman, D., Nova, M., Laudato, L., Martino, N., et al. (2016). Light-evoked hyperpolarization and silencing of neurons by conjugated polymers. *Sci. Rep.* 6:22718. doi: 10.1038/srep22718

Goding, J., Gilmour, A., Martens, P., Poole-Warren, L., and Green, R. (2017). Interpenetrating conducting hydrogel materials for neural interfacing electrodes. *Adv. Healthc. Mater.* 6:1601177. doi: 10.1002/adhm.201601177

Green, R., Baek, S., Poole-Warren, L., and Martens, P. (2016). Conducting polymer-hydrogels for medical electrode applications. *Sci. Technol. Adv. Mater.* 11:014107.

Green, R., Hassarati, R., Goding, J., Baek, S., Lovell, N., Martens, P., et al. (2012). Conductive hydrogels: mechanically robust hybrids for use as biomaterials. *Macromol. Biosci.* 12, 494–501. doi: 10.1002/mabi.201100490

Guex, A. A. A., Vachicouras, N., Hight, A. E., Brown, M. C., Lee, D. J., and Lacour, S. P. P. (2015). Conducting polymer electrodes for auditory brainstem implants. *J. Mater. Chem. B Mater. Biol. Med.* 3, 5021–5027.

Harris, A., Morgan, S., Chen, J., Kapsa, R., Wallace, G., and Paolini, A. (2013). Conducting polymer coated neural recording electrodes. *J. Neural Eng.* 10:016004. doi: 10.1088/1741-2560/10/1/016004

Heo, D., Song, S.-J., Kim, H.-J., Lee, Y., Ko, W.-K., Lee, S., et al. (2016). Multifunctional hydrogel coatings on the surface of neural cuff electrode for improving electrode-nerve tissue interfaces. *Acta Biomater.* 39, 25–33. doi: 10.1016/j.actbio.2016.05.009

Khodagholy, D., Gelinas, J. N., Thesen, T., Doyle, W., Devinsky, O., Malliaras, G. G., et al. (2015). NeuroGrid: recording action potentials from the surface of the brain. *Nat. Neurosci.* 18, 310–315. doi: 10.1038/nn.3905

Kim, D.-H., Wiler, J., Anderson, D., Kipke, D., and Martin, D. (2010). Conducting polymers on hydrogel-coated neural electrode provide sensitive neural recordings in auditory cortex. *Acta Biomater.* 6, 57–62. doi: 10.1016/j.actbio.2009.07.034

Kleber, C., Bruns, M., Lienkamp, K., Rühe, J., and Asplund, M. (2017). An interpenetrating, microstructurable and covalently attached conducting polymer hydrogel for neural interfaces. *Acta Biomater.* 58, 365–375. doi: 10.1016/j.actbio.2017.05.056

Lacour, S., Courtine, G., and Guck, J. (2016). Materials and technologies for soft implantable neuroprostheses. *Nat. Rev. Mater.* 1:16063.

Lee, K., and Mooney, D. (2012). Alginate: properties and biomedical applications. *Prog. Polym. Sci.* 37, 106–126.

Martin, D. C., and Malliaras, G. G. (2016). Interfacing electronic and ionic charge transport in bioelectronics. *ChemElectroChem* 3, 686–688.

Rivnay, J., Inal, S., Collins, B. A., Sessolo, M., Stavrinidou, E., Strakosas, X., et al. (2016). Structural control of mixed ionic and electronic transport in conducting polymers. *Nat. Commun.* 7:11287. doi: 10.1038/ncomms11287

Salatino, J., Ludwig, K., Kozai, T., and Purcell, E. (2017). Glial responses to implanted electrodes in the brain. *Nat. Biomed. Eng.* 1, 862–877.

Simon, D. T., Gabrielsson, E. O., Tybrandt, K., and Berggren, M. (2016). Organic bioelectronics: bridging the signaling gap between biology and technology. *Chem. Rev.* 116, 13009–13041.

Spencer, K., Sy, J., Ramadi, K., Graybiel, A., Langer, R., and Cima, M. (2017). Characterization of mechanically matched hydrogel coatings to improve the biocompatibility of neural implants. *Sci. Rep.* 7:1952. doi: 10.1038/s41598-017-02107-2

Staples, N., Goding, J., Gilmour, A., Aristovich, K., Byrnes-Preston, P., Holder, D., et al. (2017). Conductive hydrogel electrodes for delivery of long-term high frequency pulses. *Front. Neurosci.* 11:748. doi: 10.3389/fnins.2017.00748

Ullah, F., Othman, M., Javed, F., Ahmad, Z., and Akil, H. (2015). Classification, processing and application of hydrogels: a review. *Mater. Sci. Eng. C* 57, 414–433. doi: 10.1016/j.msec.2015.07.053

Wang, Y., Qiu, Y., Ameri, S., Jang, H., Dai, Z., Huang, Y., et al. (2018). Low-cost, μm-thick, tape-free electronic tattoo sensors with minimized motion and sweat artifacts. *NPJ Flexible Electron.* 2:6.

Xiang, Z., Yen, S., Sheshadri, S., Wang, J., Lee, S., Liu, Y., et al. (2016). Progress of flexible electronics in neural interfacing – a self-adaptive non-invasive neural ribbon electrode for small nerves recording. *Adv. Mater.* 28, 4472–4479. doi: 10.1002/adma.201503423

Zucca, A., Cipriani, C., Sudha, Tarantino, S., Ricci, D., Mattoli, V., et al. (2015). Tattoo conductive polymer nanosheets for skin-contact applications. *Adv. Healthc. Mater.* 4, 983–990. doi: 10.1002/adhm.201400761

Conflict of Interest Statement: The authors declare that the research was conducted in the absence of any commercial or financial relationships that could be construed as a potential conflict of interest.

Copyright © 2018 Ferlauto, D'Angelo, Vagni, Airaghi Leccardi, Mor, Cuttaz, Heuschkel, Stoppini and Ghezzi. This is an open-access article distributed under the terms of the Creative Commons Attribution License (CC BY). The use, distribution or reproduction in other forums is permitted, provided the original author(s) and the copyright owner(s) are credited and that the original publication in this journal is cited, in accordance with accepted academic practice. No use, distribution or reproduction is permitted which does not comply with these terms.

frontiers in Neuroscience

ORIGINAL RESEARCH
published: 08 October 2018
doi: 10.3389/fnins.2018.00715

Does Impedance Matter When Recording Spikes With Polytrodes?

Joana P. Neto[1,2,3], Pedro Baião[1], Gonçalo Lopes[2], João Frazão[2], Joana Nogueira[2], Elvira Fortunato[1], Pedro Barquinha[1] and Adam R. Kampff[2,3]*

[1] CENIMAT/I3N and CEMOP/Uninova, Departamento de Ciência dos Materiais, Faculdade de Ciências e Tecnologia, Universidade Nova de Lisboa, Caparica, Portugal, [2] Champalimaud Neuroscience Programme, Champalimaud Centre for the Unknown, Lisbon, Portugal, [3] Sainsbury Wellcome Centre, University College London, London, United Kingdom

Extracellular microelectrodes have been widely used to measure brain activity, yet there are still basic questions about the requirements for a good extracellular microelectrode. One common source of confusion is how much an electrode's impedance affects the amplitude of extracellular spikes and background noise. Here we quantify the effect of an electrode's impedance on data quality in extracellular recordings, which is crucial for both the detection of spikes and their assignment to the correct neurons. This study employs commercial polytrodes containing 32 electrodes (177 μm^2) arranged in a dense array. This allowed us to directly compare, side-by-side, the same extracellular signals measured by modified low impedance (~100 kΩ) microelectrodes with unmodified high impedance (~1 MΩ) microelectrodes. We begin with an evaluation of existing protocols to lower the impedance of the electrodes. The poly (3,4-ethylenedioxythiophene)-polystyrene sulfonate (PEDOT-PSS) electrodeposition protocol is a simple, stable, and reliable method for decreasing the impedance of a microelectrode up to 10-fold. We next record *in vivo* using polytrodes that are modified in a 'chess board' pattern, such that the signal of one neuron is detected by multiple coated and non-coated electrodes. The performance of the coated and non-coated electrodes is then compared on measures of background noise and amplitude of the detected action potentials. If the proper recording system is used, then the impedance of a microelectrode within the range of standard polytrodes (~0.1 to 2 MΩ) does not greatly affect data quality and spike sorting. This study should encourage neuroscientists to stop worrying about one more unknown.

Keywords: microelectrodes, impedance, spikes, noise, coating

OPEN ACCESS

Edited by:
Ulrich G. Hofmann, Universitätsklinikum Freiburg, Germany

Reviewed by:
Abhishek Prasad, University of Miami, United States
Kevin J. Otto, University of Florida, United States

****Correspondence:***
Joana P. Neto
j.neto@ucl.ac.uk;
joana.neto@neuro.fchampalimaud.org

Specialty section:
This article was submitted to Neural Technology, a section of the journal Frontiers in Neuroscience

Received: *14 June 2018*
Accepted: *19 September 2018*
Published: *08 October 2018*

Citation:
Neto JP, Baião P, Lopes G, Frazão J, Nogueira J, Fortunato E, Barquinha P and Kampff AR (2018) Does Impedance Matter When Recording Spikes With Polytrodes? Front. Neurosci. 12:715. doi: 10.3389/fnins.2018.00715

INTRODUCTION

Throughout the electrophysiology literature, an electrode's impedance magnitude measured at 1 kHz in a saline solution is regularly used as a proxy for its ability to detect the activity of individual neurons (Nam, 2012; Alivisatos et al., 2013; Won et al., 2018). Actually, the impedance is a measure of the ability of the solution-electrode interface circuit to resist the flow of charge across the interface's phases (i.e., from the ionic to electronic conductor).

How much does an electrode's impedance affect its signal-to-noise ratio (SNR) and thus ability to detect spikes? Several studies suggest that electrode impedance has a major impact on SNR (Ludwig et al., 2006; Keefer et al., 2008; Ferguson et al., 2009; Ansaldo et al., 2011; Baranauskas et al., 2011; Du et al., 2011; Ludwig et al., 2011; Scott et al., 2012; Chung et al., 2015; Kozai et al., 2015; Zhao et al., 2016). However, there is also literature showing that electrode impedance does not greatly affect SNR (Cui et al., 2001; Suner et al., 2005; Desai et al., 2010). Commercially available silicon probes, also called polytrodes, have relatively high impedance electrodes due to their low surface area and small diameters (<50 μm), which are suitable for recording single unit activity. Materials such as Au, Pt, and Ir are often used as the electrode material in polytrodes, and lowering the electrode impedance prior to recording is a 'standard' step in various laboratories (Desai et al., 2010). How does one lower the impedance of commercial polytrodes? Electrodeposition is a simple and reproducible technique, yet has great flexibility to produce a variety of coatings (Ferguson et al., 2009). For more details about electrodeposition techniques see (Santos et al., 2015). By electroplating Au or Pt, the surface roughness increases and the electrode impedance decreases (Cui and Martin, 2003; Ferguson et al., 2009; Desai et al., 2010; Márton et al., 2014). Over the last decade, conductive polymers, particularly poly(3,4-ethylenedioxythiophene) (PEDOT), have been electrodeposited onto electrodes due to their chemical stability and mechanical integrity when implanted in the brain (Ludwig et al., 2006; Ludwig et al., 2011; Kozai et al., 2016). Moreover, when compared to metals, these polymers are typically softer materials offering a more intimate contact between the electrode surface and brain tissue (Green et al., 2008). Prior to the electrodeposition, a dopant is added to the synthesis solution to improve conductivity; the most common dopant molecule is polystyrene sulfonate (PSS) (Guimard et al., 2007; Aregueta-Robles et al., 2014).

Our goal was simply to answer the question: 'should I reduce the impedance of my polytrode electrodes'? Despite the prevalence of this question in the field, a definitive answer is still lacking. It is important to quantify the impact of an electrode's impedance on the background noise and amplitude of extracellular spikes to determine if the effort to reduce impedance by electrodeposition is necessary.

MATERIALS AND METHODS

Polytrodes

All experiments were performed with a commercially available 32-channel probe (A1x32-Poly3-5mm-25s-177-CM32, NeuroNexus), with 177 μm^2 area electrodes (iridium) and an inter-site pitch of 22–25 μm (see **Supplementary Figure S1**).

Coatings

NanoZ hardware and software (Neuralynx) was used to perform gold and PEDOT-PSS electrodepositions. Moreover, both coatings were galvanostatically deposited in a two electrode cell configuration consisting of the probe microelectrodes individually selected as the working electrode and a platinum wire as the reference electrode. The reference wire was placed around the deposition cup while the probe was maintained at a fixed and equal distance to all points of the reference wire. By selecting 'Manual Control' from the NanoZ software it is possible to select individual electrodes.

For gold coatings, a commercial non-cyanide gold solution was obtained from Neuralynx. The deposition solution for PEDOT-PSS consisted of 0.01 M of EDOT (Sigma-Aldrich, 97%, Mw = 142.18) and 0.1 M of PSS (Sigma-Aldrich, Mw = 1000000) dissolved in deionized water. The optimal deposition parameters were -30 nA during 120 s for gold and +30 nA during 5 s for PEDOT-PSS (Baião, 2014). Before and after the deposition, electrode impedance magnitude at 1 kHz was measured in sterile phosphate buffer saline solution (PBS, 1 mM, pH 7.4) with NanoZ. Post-deposition assessment of coating morphology was performed by scanning electron microscopy (SEM-FIB, Zeiss Auriga).

Electrochemical Characterization

The electrochemical behavior of microelectrodes was studied in PBS (1 mM, pH 7.4) by electrochemical impedance spectroscopy (EIS). For the electrochemical characterization, a potentiostat (Reference 600, Gamry Instruments) was used with a three electrode cell configuration where probe microelectrodes were connected individually as the working electrode, a platinum wire served as the counter electrode, and an Ag-AgCl (3 M KCl, Gamry Instruments) as the reference electrode. The impedance was measured in a frequency range from 1 Hz to 100 kHz by applying a sinusoidal signal with an amplitude of 10 mV.

In vivo Acute Recordings

Before and after each acute recording, the impedance magnitude of each electrode was measured using a protocol implemented by the RHD2000 series chip (Intan Technologies), with the probe microelectrodes placed in a dish with sterile PBS (1 mM, pH 7.4) and a reference electrode, Ag-AgCl wire (Science Products GmbH, E-255). Following each surgery, cleaning was performed by immersing the probe in a trypsin solution (Trypsin-EDTA (0.25%), phenol red, TermoFisher Scientific) for 30–120 min and rinsing with distilled water (Neto et al., 2016).

For the surgeries under ketamine, Long Evans rats (400–700 g, both sexes) were anesthetized with a mixture of ketamine (60 mg/kg) and medetomidine (0.5 mg/kg), and placed in a stereotaxic frame. At the initial stage of each ketamine surgery, atropine was given to suppress mucus secretion (0.1 mg/kg, atropine methyl nitrate, Sigma-Aldrich). For the surgeries under urethane, rats (400–700 g, both sexes) of the Lister Hooded strain were anesthetized with urethane (1.6 g/kg) and placed in a stereotaxic frame. At the initial stage of each urethane surgery, the animal was injected with atropine (0.05 mg/kg), temgesic (20 μg/kg), and

rimadyl (5 mg/kg). Ketamine, medetomidine and urethane were administered by intraperitoneal injection, while temgesic and rimadyl were administered by subcutaneous injection. Atropine was administered by intramuscular injection.

Anesthetized rodents then underwent a surgical procedure to remove the skin and expose the skull above the targeted brain region. Small craniotomies (2 mm medial-lateral and 2 mm anterior-posterior) were performed above the target area. The acute recordings were conducted in different brain regions and at different depths (for more details see **Supplementary Figure S2** and **Supplementary Table S1**). The reference electrode Ag-AgCl wire (Science Products GmbH, E-255) was inserted at the posterior part of the skin incision. Equipment for monitoring body temperature as well as a live video system for performing probe insertion were integrated into the setup. For the extracellular recordings we used the Open Ephys [27] acquisition board along with the RHD2000 series interface chip that amplifies and digitally multiplexes the signal from the 32 extracellular electrodes (Intan Technologies). Extracellular signals in a frequency band of 0.1–7,500 Hz were sampled at 20 or 30 kHz with 16-bit resolution and were saved in a raw binary format for subsequent offline analysis using the Bonsai framework (Lopes et al., 2015; Bonsai, 2017).

Animal experiments under urethane were approved by the local ethical review committee and conducted in accordance with Home Office personal and project (I67952617; 70/8116) licenses under the UK Animals (Scientific Procedures) 1986 Act. Animal experiments under ketamine were approved by the Champalimaud Foundation Bioethics Committee and the Portuguese National Authority for Animal Health, Direcção-Geral de Alimentação e Veterinária.

Analysis

For the noise and signal (spikes amplitude) characterization, a third order Butterworth filter with a band-pass of 250–9,500 or 14,250 Hz (95% of the Nyquist frequency) was used in the forward-backward mode in all datasets.

The magnitude of the background noise was estimated from the median absolute signal, assuming a normal noise distribution, σ_{Median} = median(|signal(t)|/0.6745) avoiding contamination by spike waveforms (Quiroga et al., 2004). Alternatively, the noise was defined as the standard deviation (σ_{RMS}) of the signal (Scott et al., 2012).

We ran Kilosort (Pachitariu et al., 2016) for spike sorting on all the datasets with the maximum number of templates set to 128 (four times the number of electrodes on our probe). This algorithm iteratively generates templates and then uses these templates to detect and classify the individual spikes. Each spike is assigned to the template that matches it best. Afterward, we used Phy (Rossant et al., 2016) to check the automatically generated clusters. Phy is a graphical user interface for refining the results of spike sorting. After the manual sorting we used functions to assess cluster quality[1]. The "well isolated" units considered for the signal analysis have simultaneously low interspike interval (ISI) violations and contamination rates, and high isolation distances values. Neurons with more than 200 spikes were considered for further analyses. The average spike waveform of all spikes from each unit on a given recording site was plotted and the respective peak-to-peak (P2P) amplitude was computed (see **Supplementary Figure S3**).

Some results are presented as mean ± standard deviation. Impedance magnitude, background noise and spikes amplitude from pristine and PEDOT coated electrodes were compared for significance using the Mann-Whitney test. Moreover, to evaluate coating stability the impedance magnitude from electrodes after the electrodeposition and after acute surgeries were also compared for significance using the Mann-Whitney test.

[1]https://github.com/cortex-lab/sortingQuality

RESULTS

Microelectrode Coating

This study begins with an evaluation of existing electrodeposition protocols to reduce impedance of microelectrode. **Figures 1A–C** reveals the morphological differences between a pristine iridium electrode, PEDOT-PSS coated electrode, and gold coated electrode (**Figures 1A–C**, respectively). Pristine electrodes typically display a smooth surface with almost no irregularities (although some might occur due to the microfabrication process). Gold coating creates a rough structure on the electrode, which leads to an increase in surface area, one of the key factors in lowering the impedance magnitude at 1 kHz in saline solution (Rivnay et al., 2017). However, in **Figure 1D** we observe that even though the impedance after coating is lower when compared to the pristine counter-part, these values tend to increase following an acute surgery. This may reflect the poor adhesion of the gold coating to the iridium electrodes (**Figure 1D**). The gold instability and delamination was also observed in some previous studies (Scott et al., 2012). In the case of PEDOT-PSS coated electrodes (**Figures 1B,E**), they have a 'fuzzy' coating and the impedance values after the deposition remained stable for a long period of time, allowing for repeated acute surgeries (1 week, 3 weeks, and 6 months after the deposition). Therefore, taking into account the impedance value of PEDOT-PSS coated electrodes (values under 100 kΩ) and its stability, this coating was considered ideal for reducing the polytrode microelectrodes impedance.

Figure 2A illustrates the polytrode microelectrode array design employed to assess the impact of impedance on data quality. Electrodes from three polytrodes were coated in a 'chess board' pattern such that the signal of one neuron is detected by both coated and non-coated electrodes. In each polytrode 16 electrodes were coated with PEDOT-PSS. In **Figure 2B** the impedance at 1 kHz for three polytrodes was 1.1 ± 0.4 MΩ for pristine electrodes (n = 48) and 0.084 ± 0.015 MΩ for PEDOT coated electrodes (n = 48). As can be seen from the figure, the PEDOT-PSS electrodeposition protocol is reliable across probes and electrodes (3 polytrodes, $n_{pristine}$ = 48 and n_{PEDOT} = 48).

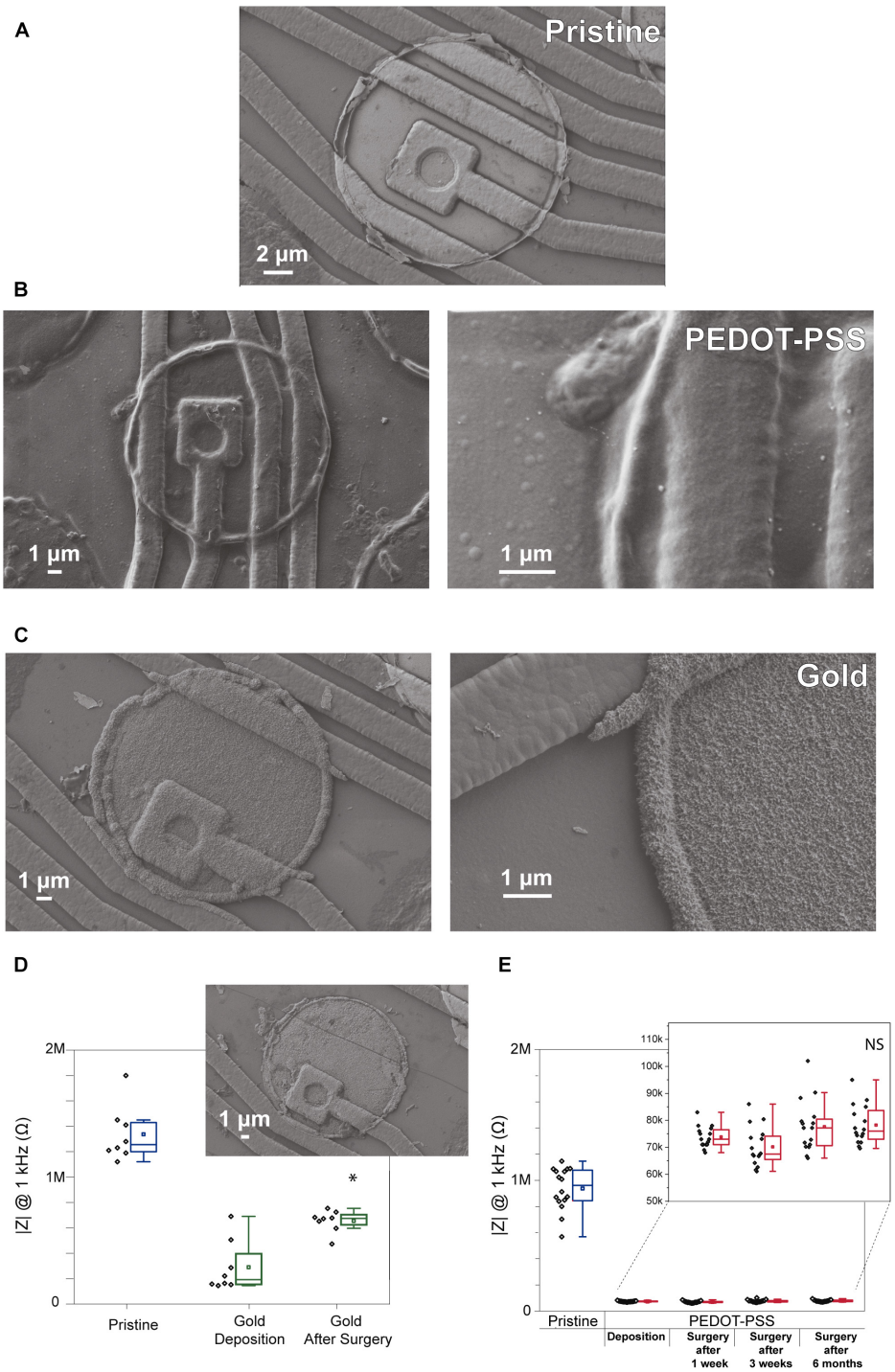

FIGURE 1 | Comparison of gold coated electrodes and PEDOT-PSS coated electrodes. SEM images showing the surface morphology of electrodes from a commercial polytrode in their original state, and after the coatings. **(A)** Pristine electrode, **(B)** PEDOT-PSS coated electrode, and **(C)** gold coated electrode. **(D)** Impedance stability of gold coating for 8 electrodes from one polytrode before, after the deposition and after one acute surgery. SEM image insert of the gold coating from one electrode after the surgery. **(E)** Impedance stability of PEDOT-PSS coating for 16 electrodes from one polytrode before, after the deposition, and after acute surgeries performed 1 week, 3 weeks, and 6 months after the deposition. Black points denote impedance magnitude measured at 1 kHz in saline solution for individual electrodes, and boxplots show the distribution of these values. In the boxplots, line: median, square: mean, box: 1st quartile–3rd quartile, and whiskers: 1.5× interquartile range above and below the box. *$p < 0.001$ when compared with electrodes after deposition. 'NS' not significant ($p > 0.05$) when compared with electrodes after deposition.

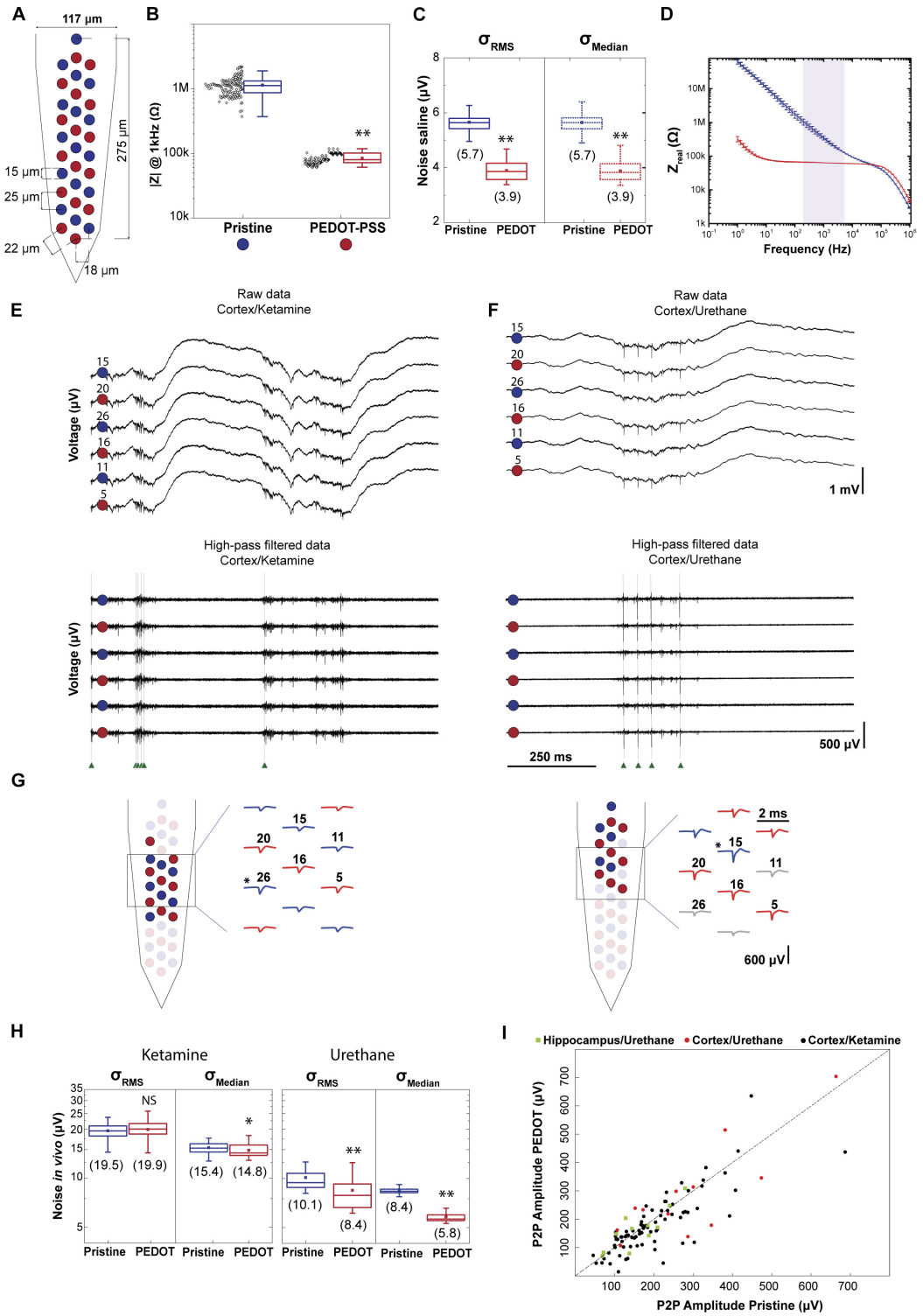

FIGURE 2 | Impact of impedance on data quality. **(A)** Schematic of a polytrode where electrodes were modified in a 'chess board' pattern. Red circles represent PEDOT-PSS coated electrodes and blue circles represent pristine electrodes. **(B)** Reliability of PEDOT-PSS electrodeposition protocol. Impedance magnitude measured at 1 kHz in saline solution for 3 polytrodes ($n_{pristine}$ = 48 and n_{PEDOT} = 48). Black points denote individual measurement for each electrode (3 measurements for each electrode). **(C)** Noise σ_{RMS} and σ_{Median} of recordings performed in saline solution ($n_{pristine}$ = 48 and n_{PEDOT} = 48). Values in parentheses show mean value. **(D)** Impedance spectroscopy of PEDOT-PSS coated (n = 3) and pristine (n = 3) electrodes shows a significant decrease in the impedance real value. The light purple shaded area corresponds to the frequency range in which the thermal noise was computed. **(E)** 1 s-long raw data traces from 6 electrodes, 3 coated

(Continued)

FIGURE 2 | Continued
and 3 non-coated, from the recording '*amplifier2014_11_25T23_00_08.bin*'. This recording was carried out in cortex under ketamine anesthesia. Top: signals correspond to the 0.1–7.5 kHz frequency band. Bottom: high-pass filtered traces to highlight spontaneous spiking activity. Green arrows indicate the time of spikes identified for a putative neuron. **(F)** The same representation as in **(E)** for the recording '*amplifier2017_02_02T15_49_35.bin*'. This recording was carried out in cortex under urethane anesthesia. **(G)** Representative putative neurons from each of the recordings shown above. Left panel corresponds to the cortex/ketamine recording and right panel to the cortex/urethane recording. Schematic of two polytrodes with red and blue colored waveforms and circles denoting the electrodes with the highest peak-to-peak amplitudes from each unit, respectively. The asterisks indicates the electrode with the maximum amplitude P2P. **(H)** σ_{RMS} and σ_{Median} of 9 acute recordings performed in rat cortex, 6 of which under ketamine, and 3 under urethane (n_{PEDOT_ket} = 96, $n_{Pristine_ket}$ = 96, n_{PEDOT_ure} = 48 and $n_{Pristine_ure}$ = 48). Values in parentheses show mean value. **(I)** The maximum P2P amplitude average for coated electrodes and for non-coated is plotted for 103 sorted neurons. In the boxplots, line: median, square: mean, box: 1st quartile–3rd quartile, and whiskers: 1.5× interquartile range above and below the box. *$p < 0.001$ when compared with pristine electrodes. **$p < 0.0001$ when compared with pristine electrodes. 'NS' not significant ($p > 0.05$) when compared with pristine electrodes.

Noise Characterization: In Saline

First, the performance of PEDOT-PSS coated electrodes was compared to pristine electrodes in terms of noise, both in saline solution and during *in vivo* recordings. The contribution of all non-biological noise sources was measured by recording signals from microelectrodes immersed in a saline solution. The non-biological sources include the electronic noise due to the amplifier, thermal noise, and noise associated with the double layer interface (Hassibi et al., 2004; Baranauskas et al., 2011). At room temperature, the actual noise measured in saline solution for pristine and PEDOT coated microelectrodes is shown in **Figure 2C**. The σ_{Median} noise value in saline, for pristine electrodes was 5.7 ± 0.4 μV and for PEDOT coated electrodes was 3.9 ± 0.4 μV, which represents a reduction of about 30%. Additionally, the σ_{RMS} and σ_{Median} values are similar in saline solution.

The thermal noise depends on the real part of the measured impedance. The thermal noise computed in the 200–8,000 Hz frequency band for pristine (n = 3) microelectrodes was 5.0 μV and for PEDOT coated (n = 3) microelectrodes was 2.8 μV (**Figure 2D** and for a detailed description see **Supplementary Material**). Additionally, the electronic noise due to the amplifier in our system, measured by shorting the headstage inputs, was 2.0 ± 0.1 μV. We can predict the non-biological noise value as the square root of the sum of the squared thermal noise (5.0 μV and 2.8 μV for pristine and coated microelectrodes, respectively) with the squared electronic noise (∼2.0 μV). The predicted values for the noise in saline (5.4 μV in non-coated and 3.4 μV in coated) were similar to the measured noise values (5.6 μV in non-coated and 3.9 μV in coated).

Noise Characterization: *In vivo*

We next recorded *in vivo* using the same polytrodes with the 'chess board' pattern described in **Figure 2A**. These recordings were conducted in different brain regions and at different depths (**Supplementary Figure S2** and **Supplementary Table S1**). Also, ketamine and urethane anesthesia was used to compare noise and signal magnitude recorded during different brain states (Hildebrandt et al., 2017; **Figures 2E,F**). Under ketamine, the cortex switches between periods of higher neuronal activity and periods of much lower activity (up and down states) (Ruiz-Mejias et al., 2011). Under urethane anesthesia, the activity is similar to natural brain activity during sleep (Clement et al., 2008; Pagliardini et al., 2013).

Figures 2E,F highlight the variability of noise *in vivo* (i.e., biological noise magnitude is highly variable due to variations in background neural firing rate). Note that, in general, the magnitude of noise under ketamine is higher compared to urethane, due to the increase in this background activity. Moreover, the values of noise vary with the method used to compute the noise magnitude. Higher values for the noise *in vivo* were found when taking into consideration σ_{RMS} values, probably due to the contribution of spikes. The σ_{RMS} value is based on the standard deviation of the signal, which increases with the firing rate (Quiroga et al., 2004). Therefore, the σ_{Median} noise values were used to compare the noise between experiments, and within an experiment. Under urethane, the σ_{Median} values from coated electrodes are smaller compared to the non-coated electrodes. On average, the σ_{Median} value was reduced from 8.4 ± 0.4 μV in non-coated to 5.8 ± 0.5 μV in PEDOT coated microelectrodes, a 30% reduction. Under ketamine the σ_{Median} noise was 15.4 ± 1.2 μV in non-coated and 14.8 ± 1.3 μV in PEDOT coated microelectrodes.

The noise values found for *in vivo* recordings are highly variable (**Figure 2H**) and the noise reduction observed in saline is likely preserved *in vivo*, yet masked by the much larger variation in background spiking activity. Does the difference in noise observed between coated and non-coated electrodes matter for detecting spikes? Usually, the negative voltage deflection of a well isolated unit exceeds 40–70 μV. Therefore, the benefits resulting from the ∼2 μV noise reduction achieved by coating electrodes would be irrelevant for detecting spikes.

Signal Characterization: Amplitude of Action Potentials

Although not resulting in a major reduction of noise at relevant frequencies, it is still possible that coating electrodes might increase the amplitude of each spike (see **Supplementary Figure S5** for more details about attenuation of signal). **Figure 2G** shows two examples of putative neurons where each waveform corresponds to the average of all the spikes from the respective neuron on a given recording electrode. Additionally, red and blue colored waveforms and circles denote electrodes where the peak-to-peak average amplitude is larger than half of the maximum peak-to-peak average amplitude of the isolated neuron. Therefore, they represent the electrodes with the highest peak-to-peak amplitude from each neuron.

For each of the 103 putative neurons sorted from 11 recordings, the largest average peak-to-peak amplitudes from the pristine and PEDOT electrode groups were plotted (**Figure 2I**). Therefore, for each neuron, two values are plotted in **Figure 2I**, corresponding to the pristine and PEDOT electrode with the largest average peak-to-peak amplitude. If the largest peak-to-peak amplitude spikes are detected by the PEDOT coated electrodes (low impedance electrodes), then the scatter points would fall above the unity line. However, if the largest peak-to-peak amplitude spikes are detected in the pristine electrodes (high impedance electrodes), the scatter points would fall below the line. Our results show that the probability of recording the largest peak-to-peak amplitude spikes is similar for coated and non-coated electrodes and the peak-to-peak amplitude values from the pristine and PEDOT electrode groups are similar (see **Supplementary Figure S6**). Therefore, there is no obvious relationship between impedance and the peak-to-peak amplitude of sorted neurons in this impedance range.

DISCUSSION

Side-by-Side Impedance Comparison

The ability to record from closely spaced electrodes permitted accurate comparisons between electrodes with two very different impedance values. The PEDOT-PSS electrodeposition protocol made it possible to decrease impedance up to 10-fold on average, from 1.1 ± 0.4 MΩ to 0.084 ± 0.015 MΩ. We divided our noise analysis into non-biological noise (noise measured in saline solution) and biological noise, where the level of noise was assessed during acute recordings within the cortex of anesthetized rats. As expected with the impedance reduction, we found a reduction in noise magnitude in saline after coating, since the thermal noise is proportional to the square root of the real part of the impedance (Baranauskas et al., 2011). The reduction in impedance resulted in ∼30% decrease in the non-biological noise. Nevertheless, when using electrodes *in vivo*, this reduction in the thermal noise is largely overwhelmed by the much larger biological noise and would not improve the detection of spikes with commercial polytrodes. Moreover, we found no significant effect of impedance on spike peak-to-peak amplitude and detection probability on both coated and non-coated electrodes. In summary, the impedance values found at 1 kHz in commercial silicon polytrode microelectrodes don't seem to affect data quality during spike recording. Moreover, the entire dataset used to quantify the effect of an electrode's impedance on data quality is available online[2] and summarized in **Supplementary Table S1**.

But Why Different Views About the Impact of Impedance?

Electrophysiological studies report different views of the impedance impact on data quality. Many studies show that decreasing the impedance improves the signal-to-noise ratio because of thermal noise reduction, while others find that impedance reduction did not affect greatly the signal-to-noise ratio.

In studies where researchers use tetrodes and single microwires, lowering the impedance is beneficial because a low-impedance electrode minimizes signal loss through shunt pathways (usually capacitive coupling to ground). Shunt capacitance can be significant in long, thinly insulated electrode wires (Robinson, 1968). Thus, for tetrodes and microwires, lowering impedance will result in a larger signal for both local field potentials and spikes (Ferguson et al., 2009). However, with silicon polytrodes, shunt capacitance is much smaller and does not appear to cause signal attenuation for typical values of polytrode electrodes impedance (Obien et al., 2015).

However, if polytrodes, particularly those with higher impedance values (>2 MΩ), are used with a differential amplifier that has a (relatively) low input impedance, then a voltage-divider is formed between the electrode and amplifier. The amplifier from Intan Technologies has an input impedance of 13 MΩ, and with electrode impedances of 1 MΩ and 100 kΩ, the signal loss is around 7% and 1%, respectively, which may be negligible, but for an electrode with 3 MΩ impedance, this signal loss is around 20%. For more details about the voltage divider occurrence, see **Supplementary Figure S5**.

Do we need to coat our polytrode electrodes? No, assuming we have a good amplifier and low shunt capacitance. But we propose that microelectrode coatings, in chronic applications, may do more than just reduce the impedance. Some coatings may help to promote cell health at the electrode surface and minimize the immune response of surrounding brain tissue. Strong neural attachment to implanted electrodes is desirable as it increases interface stability and improves electrical transfer across the tissue-electrode interface (Green et al., 2008; Nam, 2012; Jorfi et al., 2015; Kook et al., 2016). We thus propose that we stop worrying about impedance magnitude (as long as it stays well below the input impedance of the amplifier) and start focusing on bio-compatible materials (Bellamkonda et al., 2012; Chen and Allen, 2012; Jorfi et al., 2015).

DATA AVAILABILITY

The datasets generated for this study can be found in the http://www.kampff-lab.org/polytrode-impedance/.

AUTHOR CONTRIBUTIONS

JPN, GL, JF, and AK conceived and designed the research. JPN, JF, JN, and PBa performed the experiments. JPN and AK analyzed the data. JPN, JF, PBar, EF, and AK interpreted the results of experiments. JN and AK prepared the figures. JN and AK drafted the manuscript. All authors read and approved the submitted version of the manuscript.

[2]http://www.kampff-lab.org/polytrode-impedance/

FUNDING

This work was supported by funding from the European Union's Seventh Framework Programme (FP7/2007–2013) Grant Agreement 600925, the Bial Foundation Grant 190/12 and the FCT-MCTES Doctoral Grant SFRH/BD/76004/2011 (to JN).

ACKNOWLEDGMENTS

We would like to thank the institutional support and funding provided by the Champalimaud Foundation, CENIMAT/I3N and Sainsbury Wellcome Centre (funded by the Gatsby Charitable Foundation and the Wellcome Trust). An earlier version of this work has been released as a preprint (Neto et al., 2018).

SUPPLEMENTARY MATERIAL

The Supplementary Material for this article can be found online at: https://www.frontiersin.org/articles/10.3389/fnins.2018.00715/full#supplementary-material

REFERENCES

Alivisatos, A. P., Andrews, A. M., Boyden, E. S., Chun, M., Church, G. M., Deisseroth, K., et al. (2013). Nanotools for neuroscience and brain activity mapping. *ACS Nano* 7, 1850–1866. doi: 10.1021/nn4012847

Ansaldo, A., Castagnola, E., Maggiolini, E., Fadiga, L., and Ricci, D. (2011). Superior electrochemical performance of carbon nanotubes directly grown on sharp microelectrodes. *ACS Nano* 5, 2206–2214. doi: 10.1021/nn103445d

Aregueta-Robles, U. A., Woolley, A. J., Poole-Warren, L. A., Lovell, N. H., and Green, R. A. (2014). Organic electrode coatings for next-generation neural interfaces. *Front. Neuroeng.* 7:15. doi: 10.3389/fneng.2014.00015

Baião, P. (2014). *Nanostructuring Silicon Probes via Electrodeposition?: Characterization of Electrode Coatings for Acute in Vivo*. Available at: https://run.unl.pt/handle/10362/14666

Baranauskas, G., Maggiolini, E., Castagnola, E., Ansaldo, A., Mazzoni, A., and Angotzi, G. N. (2011). Carbon nanotube composite coating of neural microelectrodes preferentially improves the multiunit signal-to-noise ratio. *J. Neural Eng.* 8:066013. doi: 10.1088/1741-2560/8/6/066013

Bellamkonda, R. V., Balakrishna Pai, S., and Renaud, P. (2012). Materials for neural interfaces. *MRS Bull.* 37, 557–561. doi: 10.1557/mrs.2012.122

Bonsai (2017). *Bonsai*. Available at: http://bonsai-rx.org/

Chen, S., and Allen, M. G. (2012). Extracellular matrix-based materials for neural interfacing. *MRS Bull.* 37, 606–613. doi: 10.1557/mrs.2012.120

Chung, T., Wang, J. Q., Wang, J., Cao, B., Li, Y., and Pang, S. W. (2015). Electrode modifications to lower electrode impedance and improve neural signal recording sensitivity. *J. Neural Eng.* 12:056018. doi: 10.1088/1741-2560/12/5/056018

Clement, E. A., Richard, A., Thwaites, M., Ailon, J., Peters, S., and Dickson, C. T. (2008). Cyclic and sleep-like spontaneous alternations of brain state under urethane Anaesthesia. *PLoS One* 3:e2004. doi: 10.1371/journal.pone.0002004

Cui, X., Hetke, J. F., Wiler, J. A., Anderson, D. J., and Martin, D. C. (2001). Electrochemical deposition and characterization of conducting polymer polypyrrole/pss on multichannel neural probes. *Sens. Actuators A Phys.* 93, 8–18. doi: 10.1016/S0924-4247(01)00637-9

Cui, X., and Martin, D. C. (2003). Fuzzy gold electrodes for lowering impedance and improving adhesion with electrodeposited conducting polymer. *Most* 103, 384–394.

Desai, S. A., Rolston, J. D., Guo, L., and Potter, S. M. (2010). Improving impedance of implantable microwire multi-electrode arrays by ultrasonic electroplating of durable platinum black. *Front. Neuroeng.* 3:5. doi: 10.3389/fneng.2010.00005

Du, J., Blanche, T. J., Harrison, R. R., Lester, H. A., and Masmanidis, S. C. (2011). Multiplexed, high density electrophysiology with nanofabricated neural probes. *PLoS One* 6:e26204. doi: 10.1371/journal.pone.0026204

Ferguson, J. E., Boldt, C., and David Redish, A. (2009). Creating low-impedance tetrodes by electroplating with additives. *Sens. Actuators A Phys.* 156, 388–393. doi: 10.1016/j.sna.2009.10.001

Green, R. A., Lovell, N. H., Wallace, G. G., and Poole-Warren, L. A. (2008). Conducting polymers for neural interfaces: challenges in developing an effective long-term implant. *Biomaterials* 29, 3393–3399. doi: 10.1016/j.biomaterials.2008.04.047

Guimard, N. K., Gomez, N., and Schmidt, C. E. (2007). Conducting polymers in biomedical engineering. *Prog. Polym. Sci.* 32, 876–921. doi: 10.1016/J.PROGPOLYMSCI.2007.05.012

Hassibi, A., Navid, R., Dutton, R. W., and Lee, T. H. (2004). Comprehensive study of noise processes in electrode electrolyte interfaces. *J. Appl. Phys.* 96, 1074–1082. doi: 10.1063/1.1755429

Hildebrandt, K. J., Sahani, M., and Linden, J. F. (2017). The impact of anesthetic state on spike-sorting success in the cortex: a comparison of Ketamine and urethane Anesthesia. *Front. Neural Circuits* 11:95. doi: 10.3389/fncir.2017.00095

Jorfi, M., Skousen, J. L., Weder, C., and Capadona, J. R. (2015). Progress towards biocompatible intracortical microelectrodes for neural interfacing applications. *J. Neural Eng.* 12:011001. doi: 10.1088/1741-2560/12/1/011001

Keefer, E. W., Botterman, B. R., Romero, M. I., Rossi, A. F., and Gross, G. W. (2008). Carbon nanotube coating improves neuronal recordings. *Nat. Nanotechnol.* 3, 434–439. doi: 10.1038/nnano.2008.174

Kook, G., Lee, S., Lee, H., Cho, I. J., and Lee, H. (2016). Neural probes for chronic applications. *Micromachines* 7:179. doi: 10.3390/mi7100179

Kozai, T. D. Y., Catt, K., Du, Z., Na, K., Srivannavit, O., Haque, R. U., et al. (2016). Chronic in vivo evaluation of pedot/cnt for stable neural recordings. *IEEE Trans. Bio Med. Eng.* 63, 111–119. doi: 10.1109/TBME.2015.2445713

Kozai, T. D. Y., Du, Z., Gugel, Z. V., Smith, M. A., Chase, S. M., and Bodily, L. M. (2015). Comprehensive chronic laminar single-unit, multi-unit, and local field potential recording performance with planar single shank electrode arrays. *J. Neurosci. Methods* 242, 15–40. doi: 10.1016/j.jneumeth.2014.12.010

Lopes, G., Bonacchi, N., Frazão, J., Neto, J. P., Atallah, B. V., Soares, S., et al. (2015). Bonsai: an event-based framework for processing and controlling data streams. *Front. Neuroinform.* 9:7. doi: 10.3389/fninf.2015.00007

Ludwig, K. A., Langhals, N. B., Joseph, M. D., Richardson-Burns, S. M., Hendricks, J. L., and Kipke, D. R. (2011). Poly(3,4-Ethylenedioxythiophene) (PEDOT) polymer coatings facilitate smaller neural recording electrodes. *J. Neural Eng.* 8:014001. doi: 10.1088/1741-2560/8/1/014001

Ludwig, K. A., Uram, J. D., Yang, J., Martin, D. C., and Kipke, D. R. (2006). Chronic neural recordings using silicon microelectrode arrays electrochemically deposited with a poly(3,4-Ethylenedioxythiophene) (PEDOT) film. *J. Neural Eng.* 3, 59–70. doi: 10.1088/1741-2560/3/1/007

Márton, G., Bakos, I., Fekete, Z., Ulbert, I., and Pongrácz, A. (2014). Durability of high surface area platinum deposits on microelectrode arrays for acute neural recordings. *J. Mater. Sci. Mater. Med.* 25, 931–940. doi: 10.1007/s10856-013-5114-z

Nam, Y. (2012). Material considerations for in vitro neural interface technology. *MRS Bull.* 37, 566–572. doi: 10.1557/mrs.2012.98

Neto, J. P., Baião, P., Lopes, G., Frazão, J., Nogueira, J., Fortunato, E., et al. (2018). Does impedance matter when recording spikes with polytrodes? *bioRxiv* [Preprint]. doi: 10.1101/270058

Neto, J. P., Lopes, G., Frazão, J., Nogueira, J., Lacerda, P., Baião, P., et al. (2016). Validating silicon polytrodes with paired juxtacellular recordings: method and dataset. *J. Neurophysiol.* 116, 892–903. doi: 10.1152/jn.00103.2016

Obien, M. E. J., Deligkaris, K., Bullmann, T., Bakkum, D. J., and Frey, U. (2015). Revealing neuronal function through microelectrode array recordings. *Front. Neurosci.* 8:423. doi: 10.3389/fnins.2014.00423

Pachitariu, M., Steinmetz, N., Kadir, S., Carandini, M., and Harris, K. D. (2016). Kilosort: realtime spike-sorting for extracellular electrophysiology with hundreds of channels. *bioRxiv* [Preprint]. doi: 10.1101/061481

Pagliardini, S., Gosgnach, S., and Dickson, C. T. (2013). Spontaneous sleep-like brain state alternations and breathing characteristics in urethane anesthetized mice. *PLoS One* 8:e70411. doi: 10.1371/journal.pone.0070411

Quiroga, R. Q., Nadasdy, Z., and Ben-Shaul, Y. (2004). Unsupervised spike detection and sorting with wavelets and superparamagnetic clustering. *Neural Comput.* 16, 1661–1687. doi: 10.1162/089976604774201631

Rivnay, J., Wang, H., Fenno, L., Deisseroth, K., and Malliaras, K. (2017). Next-generation probes, particles, and proteins for neural interfacing. *Sci. Adv.* 3:e1601649. doi: 10.1126/sciadv.1601649

Robinson, D. A. (1968). The electrical properties of metal microelectrodes. *Proc. IEEE* 56, 1065–1071. doi: 10.1109/PROC.1968.6458

Rossant, C., Kadir, S. N., Goodman, D. F. M., Schulman, J., Hunter, M. L. D., Saleem, A. B., et al. (2016). Spike sorting for large, dense electrode arrays. *Nat. Neurosci.* 19, 634–641. doi: 10.1038/nn.4268

Ruiz-Mejias, M., Ciria-Suarez, L., Mattia, M., and Sanchez-Vives, M. V. (2011). Slow and fast rhythms generated in the cerebral cortex of the anesthetized mouse. *J. Neurophysiol.* 106, 2910–2921. doi: 10.1152/jn.00440.2011

Santos, L., Neto, J. P., Crespo, A., Baião, P., Barquinha, P., Pereira, L., et al. (2015). "Electrodeposition of WO3 nanoparticles for sensing applications," in *Electroplating of Nanostructures*, ed. M. Aliofkhazraei (London: InTech), 1–22. doi: 10.5772/61216

Scott, K. M., Du, J., Lester, H. A., and Masmanidis, S. C. (2012). Variability of acute extracellular action potential measurements with multisite silicon probes. *J. Neurosci. Methods* 211, 22–30. doi: 10.1016/j.jneumeth.2012.08.005

Suner, S., Fellows, M. R., Vargas-Irwin, C., Nakata, G. K., and Donoghue, J. P. (2005). Reliability of signals from a chronically implanted, silicon-based electrode array in non-human primate primary motor cortex. *IEEE Trans. Neural Syst. Rehabil. Eng.* 13, 524–541. doi: 10.1109/TNSRE.2005.857687

Won, S. M., Song, E., Zhao, J., Li, J., Rivnay, J., and Rogers, J. A. (2018). Recent advances in materials, devices, and systems for neural interfaces. *Adv. Mater.* 30:e1800534. doi: 10.1002/adma.201800534

Zhao, Z., Gong, R., Zheng, L., and Wang, J. (2016). In vivo neural recording and electrochemical performance of microelectrode arrays modified by rough-surfaced aupt alloy nanoparticles with nanoporosity. *Sensors* 16:1851. doi: 10.3390/s16111851

Conflict of Interest Statement: The authors declare that the research was conducted in the absence of any commercial or financial relationships that could be construed as a potential conflict of interest.

Copyright © 2018 Neto, Baião, Lopes, Frazão, Nogueira, Fortunato, Barquinha and Kampff. This is an open-access article distributed under the terms of the Creative Commons Attribution License (CC BY). The use, distribution or reproduction in other forums is permitted, provided the original author(s) and the copyright owner(s) are credited and that the original publication in this journal is cited, in accordance with accepted academic practice. No use, distribution or reproduction is permitted which does not comply with these terms.

frontiers in Neuroscience

ORIGINAL RESEARCH
published: 31 October 2018
doi: 10.3389/fnins.2018.00772

Understanding the Effects of Both CD14-Mediated Innate Immunity and Device/Tissue Mechanical Mismatch in the Neuroinflammatory Response to Intracortical Microelectrodes

*Hillary W. Bedell[1,2], Sydney Song[1,2], Xujia Li[1], Emily Molinich[1], Shushen Lin[1], Allison Stiller[3], Vindhya Danda[3,4], Melanie Ecker[3,4,5], Andrew J. Shoffstall[1,2], Walter E. Voit[3,4,5,6], Joseph J. Pancrazio[3] and Jeffrey R. Capadona[1,2]**

[1] Department of Biomedical Engineering, School of Engineering, Case Western Reserve University, Cleveland, OH, United States, [2] Advanced Platform Technology Center, L. Stokes Cleveland VA Medical Center, Rehab. R&D, Cleveland, OH, United States, [3] Department of Bioengineering, The University of Texas at Dallas, Richardson, TX, United States, [4] Center for Engineering Innovation, The University of Texas at Dallas, Richardson, TX, United States, [5] Department of Materials Science and Engineering, The University of Texas at Dallas, Richardson, TX, United States, [6] Department of Mechanical Engineering, The University of Texas at Dallas, Richardson, TX, United States

OPEN ACCESS

Edited by:
Mikhail Lebedev,
Duke University, United States

Reviewed by:
Takashi D. Y. Kozai,
University of Pittsburgh, United States
Erkin Seker,
University of California, Davis, United States

***Correspondence:**
Jeffrey R. Capadona
jrc35@case.edu

Specialty section:
This article was submitted to Neural Technology, a section of the journal Frontiers in Neuroscience

Received: *26 July 2018*
Accepted: *04 October 2018*
Published: *31 October 2018*

Citation:
Bedell HW, Song S, Li X, Molinich E, Lin S, Stiller A, Danda V, Ecker M, Shoffstall AJ, Voit WE, Pancrazio JJ and Capadona JR (2018) Understanding the Effects of Both CD14-Mediated Innate Immunity and Device/Tissue Mechanical Mismatch in the Neuroinflammatory Response to Intracortical Microelectrodes. Front. Neurosci. 12:772. doi: 10.3389/fnins.2018.00772

Intracortical microelectrodes record neuronal activity of individual neurons within the brain, which can be used to bridge communication between the biological system and computer hardware for both research and rehabilitation purposes. However, long-term consistent neural recordings are difficult to achieve, in large part due to the neuroinflammatory tissue response to the microelectrodes. Prior studies have identified many factors that may contribute to the neuroinflammatory response to intracortical microelectrodes. Unfortunately, each proposed mechanism for the prolonged neuroinflammatory response has been investigated independently, while it is clear that mechanisms can overlap and be difficult to isolate. Therefore, we aimed to determine whether the dual targeting of the innate immune response by inhibiting innate immunity pathways associated with cluster of differentiation 14 (CD14), and the mechanical mismatch could improve the neuroinflammatory response to intracortical microelectrodes. A thiol-ene probe that softens on contact with the physiological environment was used to reduce mechanical mismatch. The thiol-ene probe was both softer and larger in size than the uncoated silicon control probe. *Cd14*$^{-/-}$ mice were used to completely inhibit contribution of CD14 to the neuroinflammatory response. Contrary to the initial hypothesis, dual targeting worsened the neuroinflammatory response to intracortical probes. Therefore, probe material and CD14 deficiency were independently assessed for their effect on inflammation and neuronal density by implanting each microelectrode type in both wild-type control and *Cd14*$^{-/-}$ mice. Histology results show that 2 weeks after implantation, targeting CD14 results in higher neuronal density and decreased glial scar around the probe, whereas the thiol-ene probe results in more microglia/macrophage activation and greater blood–brain barrier (BBB) disruption around the probe. Chronic histology demonstrate no differences in

the inflammatory response at 16 weeks. Over acute time points, results also suggest immunomodulatory approaches such as targeting CD14 can be utilized to decrease inflammation to intracortical microelectrodes. The results obtained in the current study highlight the importance of not only probe material, but probe size, in regard to neuroinflammation.

Keywords: intracortical microelectrodes, neuroinflammation, innate immunity, softening electrode, shape memory polymer

INTRODUCTION

Intracortical microelectrodes allow researchers to record single-unit and multi-unit activity from individual or groups of neurons by detecting changes to the extracellular potential as a result of neurons generating action potentials (Renshaw et al., 1940; Wessberg et al., 2000). Recorded neural signals afford neuroscientists insight into the activity of specific populations of neurons. Thus, intracortical microelectrodes provide a valuable research tool to the field of cognitive and sensorimotor neuroscience. Intracortical microelectrodes are also utilized in brain–computer interfacing (BCI) applications to record neural activity as an input signal to decode and extract motor intent (Schwartz, 2004; Hochberg et al., 2012). Recorded neural signal informs the generation of a desired action for an external device, prosthetic, or muscles (*via* muscle stimulators) for a patient suffering from paralysis or limb loss. Thus, intracortical microelectrodes are a promising technology for both basic research and the development of clinical neuroprosthetic devices.

For both clinical and research applications, intracortical microelectrodes must be able to record from single cortical neurons for long periods (months to years). Unfortunately, there are limitations to intracortical microelectrodes that impede device reliability. Many studies document the failure of intracortical microelectrodes exemplified by both decrease of signal to noise ratio and loss of number of channels detecting single units (Polikov et al., 2005; Liu et al., 2006; Rennaker et al., 2007; Barrese et al., 2013). There are multiple factors that contribute to the failure of intracortical microelectrodes, including but not limited to a biological response to chronically implanted intracortical microelectrodes (Rennaker et al., 2007; Saxena et al., 2013; Kozai et al., 2014b; Hermann et al., 2017).

Inflammation ensues after the device damages tissue during implantation when blood vessels are unavoidably severed leading to blood infiltration and serum protein adsorption onto the device. Implantation results in the release of endogenous damage signals such as high mobility growth box 1 (HMGB1) and inflammatory lipids from damaged cells (Potter et al., 2014). Plasma proteins and damage-associated molecular patterns (DAMPs) are recognized by cellular receptors such as the toll-like receptor (TLR)/cluster of differentiation 14 (CD14) complex. As a result, microglial and infiltrating macrophage cells become inflammatory or "activated" and subsequently release of pro-inflammatory molecules (Kim S. et al., 2013; Zanoni et al., 2017). Glial encapsulation, neurodegeneration, and neuronal death follow this inflammatory cascade. Since the long-term success of the devices depends on the presence of healthy, active neurons immediately adjacent to the recording sites of the probe, the inflammatory process leads to a reduction of detectable signals necessary for BCI and other neuroscience research applications (Schwartz, 2004; Bjornsson et al., 2006; Jorfi et al., 2015).

In addition to the primary injurious events caused by the initial implantation, a persistent inflammatory response is present at the probe–tissue interface under chronic conditions. The pro-inflammatory microenvironment resulting from probe implantation leads to further breakdown of the blood–brain barrier (BBB) and increased vascular permeability perpetuating the inflammatory cascade (Abdul-Muneer et al., 2015).

Furthermore, the mechanical mismatch between a traditional probe (with a metal or silicon substrate) and the brain can exacerbate inflammation (Harris et al., 2011; Moshayedi et al., 2014; Nguyen et al., 2014; Du et al., 2017; Lee et al., 2017a). The mechanical discrepancy in modulus between the non-compliant probe and the pliant brain results in tissue strain and compression at the tissue–device interface. We have shown that reducing the modulus of the probe from 100 to 1000 s of GPa, to 1–10 s of MPa to more closely match that of gray matter in brain tissue (E = ∼3–6 kPa (Green et al., 2008)) reduces the micromotion-induced strain (Sridharan et al., 2015). As a result, after implantation of such relatively compliant materials, the inflammatory response to intracortical microelectrodes is significantly reduced, but not completely eliminated, providing neuroprotection and a more stable BBB (Harris et al., 2011; Nguyen et al., 2014).

Increased BBB permeability can facilitate the infiltration of myeloid cells into the injured brain tissue. These peripheral immune cells become activated and perpetuate the inflammatory response leading to neuronal death by the probe–tissue interface (Ravikumar et al., 2014). To combat the inflammatory response from microglia and infiltrating myeloid cells triggered by recognition of DAMPs and serum proteins, our lab has explored targeting the TLR/CD14 pathway involved in the recognition of DAMPs as a method to improve the chronic recording performance and reduce inflammation around the brain–electrode interface (Hermann et al., 2017). More recently, we have also shown that targeting the TLR/CD14 pathway in only infiltrating blood-derived cells leads to an improvement in chronic recording quality (Bedell et al., 2018).

Our initial softening probes used in the Capadona Lab yielded desirable mitigation of the neuroinflammatory response to

intracortical microelectrodes (Capadona et al., 2008; Nguyen et al., 2014). However, these initial materials swelled up to 70% in aqueous conditions, making fabrication into functional electrodes problematic. In collaboration with the Voit and Pancrazio labs, we have begun exploring similar softening materials, thiol-ene and thiol-ene/acrylate shape memory polymers (softening from ∼1.7 GPa down to ∼35 MPa (Ecker et al., 2017)) that possess fabrication benefits over the initial nanocomposite softening probes. These polymers soften under physiological conditions due to plasticization effects, but swell only up to 3%. The strong interaction between thiols and noble metals commonly used for electrodes yields improved adhesion between substrate and thin film metals (Nuzzo et al., 1987). Moreover, thiol-ene and thiol-ene/acrylates are more compatible with high yield, high-resolution photolithographic processes enabling manufacturability. Most importantly, a functional device, comprised of a thiol-ene/acrylate substrate, has been synthesized which was able to record single units for more than 2 months (Simon et al., 2017). Therefore, in the current study, thiol-ene was used as a probe substrate material that more closely matches the modulus of the brain to reduce BBB breakdown while also targeting an innate immune pathway involved in the recognition of serum proteins. Our work combines these approaches using a softening material and targeting CD14 through $Cd14^{-/-}$ mice, to reduce neuroinflammation in response to single-shank intracortical microelectrode probes.

RESULTS

The current study aimed to determine whether the dual targeting of the innate immune response and the mechanical mismatch between tissue and a single-shank probe, which generates tissue damage, results in combinatorial or synergistic effects to improve neuronal density and reduce inflammation at the probe–tissue interface. We utilized a thiol-ene probe, which is stiff when inserted, but softens at physiological temperatures as the probe that more closely matches the brain tissue modulus. A $Cd14^{-/-}$ knock-out model was used to target the innate immune response while immunohistochemistry was used to evaluate the neuroinflammatory response. A neuronal nuclear protein, NeuN, was used as an immunohistochemical marker for cortical neurons around the probe (Mullen et al., 1992). The glial scar is an indicator of neuroinflammation, so glial fibrillary acidic protein (GFAP), a type of intermediate filament protein upregulated by reactive astrocytes, was examined *via* immunohistochemistry (Landis, 1994). To explore microglia and macrophage activation, an antibody to CD68, was used to detect activated microglia/macrophages around the probe interface. CD68 is an lysosomal-associated membrane protein which may play a role in antigen processing and presenting (Song et al., 2011). Furthermore, BBB dysfunction characterizes inflammation resulting from a neural implant such as an intracortical probe. BBB disruption was evaluated by quantifying the presence of IgG, a prolific plasma protein not found in the brain parenchyma under normal conditions, using an anti-IgG antibody (Potter et al., 2012a).

Comparing Dual Innate Immune Response and Mechanical Mismatch to Control

We first aimed to determine whether knocking out CD14 while using a softening probe would lead to reduced neuroinflammation and improved neuronal density around the probe at 2 weeks post implantation. For both experimental and control conditions, neuronal density at 0–50 μm from the implant surface was significantly lower than that at the background (300–350 μm from probe surface). Additionally, neuronal density surrounding softening (thiol-ene) probes in $Cd14^{-/-}$ animals was significantly higher than control animals at each 50 μm interval from 100 to 250 μm from the probe surface (**Figure 1A**). There was no difference in glial scar between these two conditions at any distance interval from the probe (**Figure 1B**). However, the combinatorial targeting approach increases BBB disruption and activated macrophages and microglia at each 50 μm interval from 0 to 150 μm from the probe (**Figures 1C,D**). Altogether, these data suggest that dual targeting the innate immune response while using the thiol-ene softening probe actually worsens the neuroinflammatory response. Thus, subsequent experiments were conducted to delineate the role of each strategy – targeting CD14 versus using a thiol-ene probe.

Delineating Effect of Each Variable – Probe Stiffness and CD14 Expression

To elucidate if either factor (probe stiffness or CD14 expression) drove the increased neuroinflammatory response of the combinatorial targeting, additional animals were set up as controls for each factor resulting in four different conditions (silicon shank + WT, silicon shank + $Cd14^{-/-}$, thiol-ene + WT, thiol-ene + $Cd14^{-/-}$). Additional animals were also set up to examine more chronic (16 weeks post-implantation) time points for each of the four experimental conditions. Comparisons were made between levels of each independent variable – responses of softening thiol-ene probes versus stiff silicon probes and comparisons between $Cd14^{-/-}$ and wild-type animals.

Neuronal Density

At both 2 and 16 weeks post implant, neuronal density at 0–50 μm from the electrode surface was significantly lower than that at the background for all conditions regardless of substrate material or genotype (**Figures 2A,B**). In the absence of CD14, neuronal density at each interval from 0 to 300 μm was significantly higher than that of wild-type at 2 weeks post implant (**Figures 2A,C**). However, at the chronic time point, 16 weeks, CD14 deficiency seemed to play a lesser role as there were no significant differences between wild-type and $Cd14^{-/-}$ animals (**Figures 2B,D**). At both 2 and 16 weeks post implant, the thiol-ene probe did not result in increased neuronal density compared to the control silicon probe (**Figure 2**). Furthermore, the combinatorial approach of using a softening substrate and targeting CD14 did not significantly improve neuronal density over the other conditions (**Figure 2**). Thus, targeting CD14 results in higher neuronal density around the probe at 2 weeks,

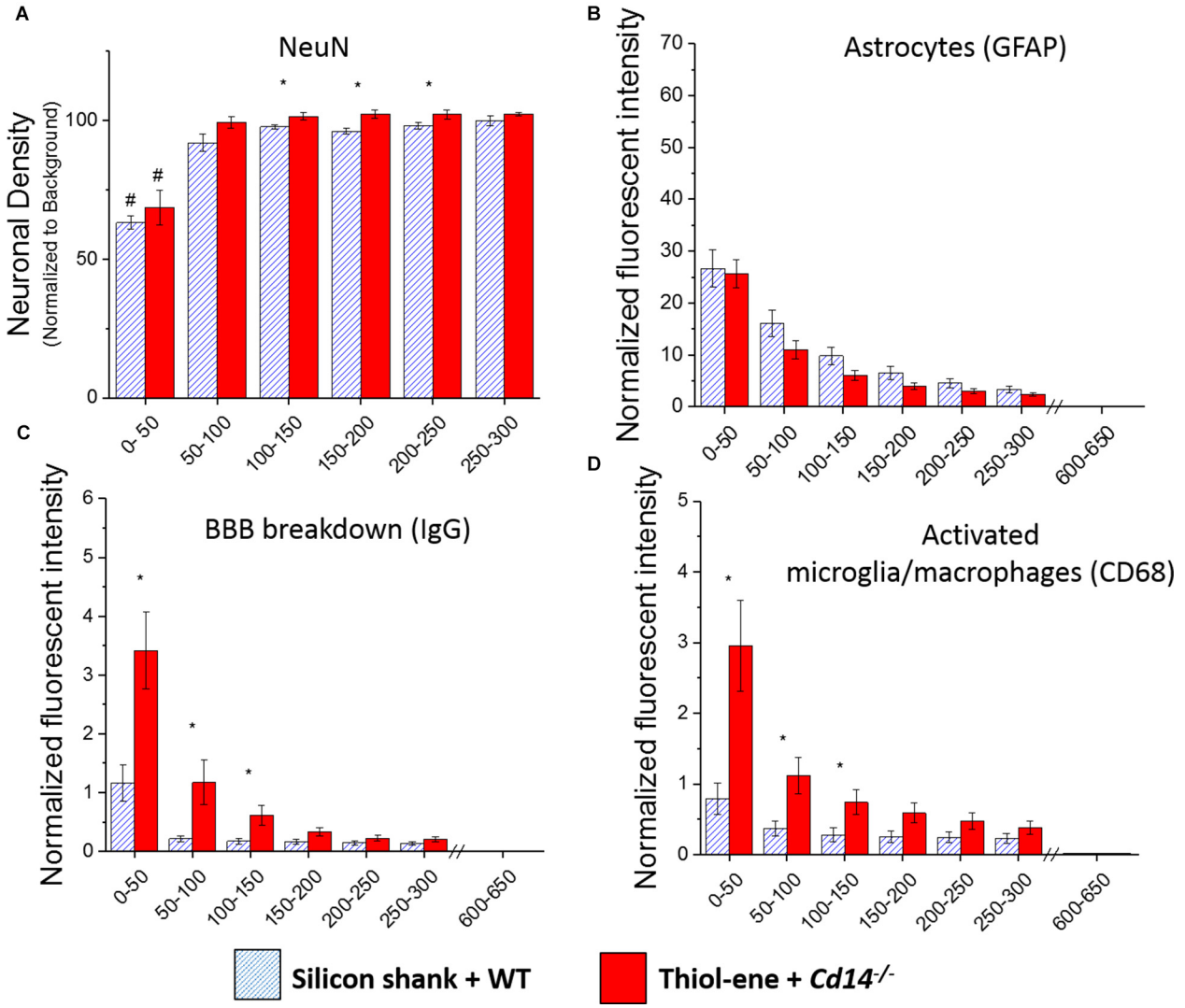

FIGURE 1 | Immunohistochemical evaluation comparing the dual targeting of the innate immune response and mechanical mismatch to control at 2 weeks after implantation. All analyses were evaluated with respect to distance from the explanted microelectrode hole (μm). **(A)** Neuronal density evaluated as NeuN$^+$ cells. **(B)** Astrocyte encapsulation evaluated as GFAP expression. **(C)** Blood-brain barrier permeability evaluated as IgG expression. **(D)** Microglial and macrophage activation evaluated as CD68 expression. * Denotes significance between silicon shank + WT and thiol-ene + *Cd14*$^{-/-}$; $^{\#}$ denotes significant difference from background neuronal density.

but combining CD14 inhibition with a reduction in probe stiffness was counterproductive.

Glial Scarring

In all conditions, the glial scar was the densest closest to the probe and decreased as a function of distance from the probe–tissue interface (**Figure 3**). The glial scar became denser from 2 to 16 weeks post-implantation for all conditions (**Figure 3**), indicated by more intense GFAP staining from 0 to 50 μm from the surface of the implants. In animals that do not express CD14, there is less glial scar compared to wild-type animals at each 50 μm interval from 100 to 300 μm from the probe-tissue interface at 2 weeks post-implantation (**Figures 3A,C**), but not 16 weeks post-implantation (**Figures 3B,D**). Notably, there were no significant differences in the glial scar between the thiol-ene probe and control silicon probe at either time point (**Figure 3**).To summarize, targeting CD14 decreases glial scar around probe at 2 weeks.

Microglia/Macrophage Expression

Overall, microglial/macrophage activation as assessed *via* CD68 expression was heavily increased at the probe–tissue interface, and declined to background levels (zero expression) as a function of distance from the interface (**Figure 4**). The thiol-ene probes resulted in more activated microglia/macrophages than the silicon probes at 2 weeks post-implantation at each interval 0–200 μm from the probe–tissue interface (**Figures 4A,C**). However, there were no significant differences

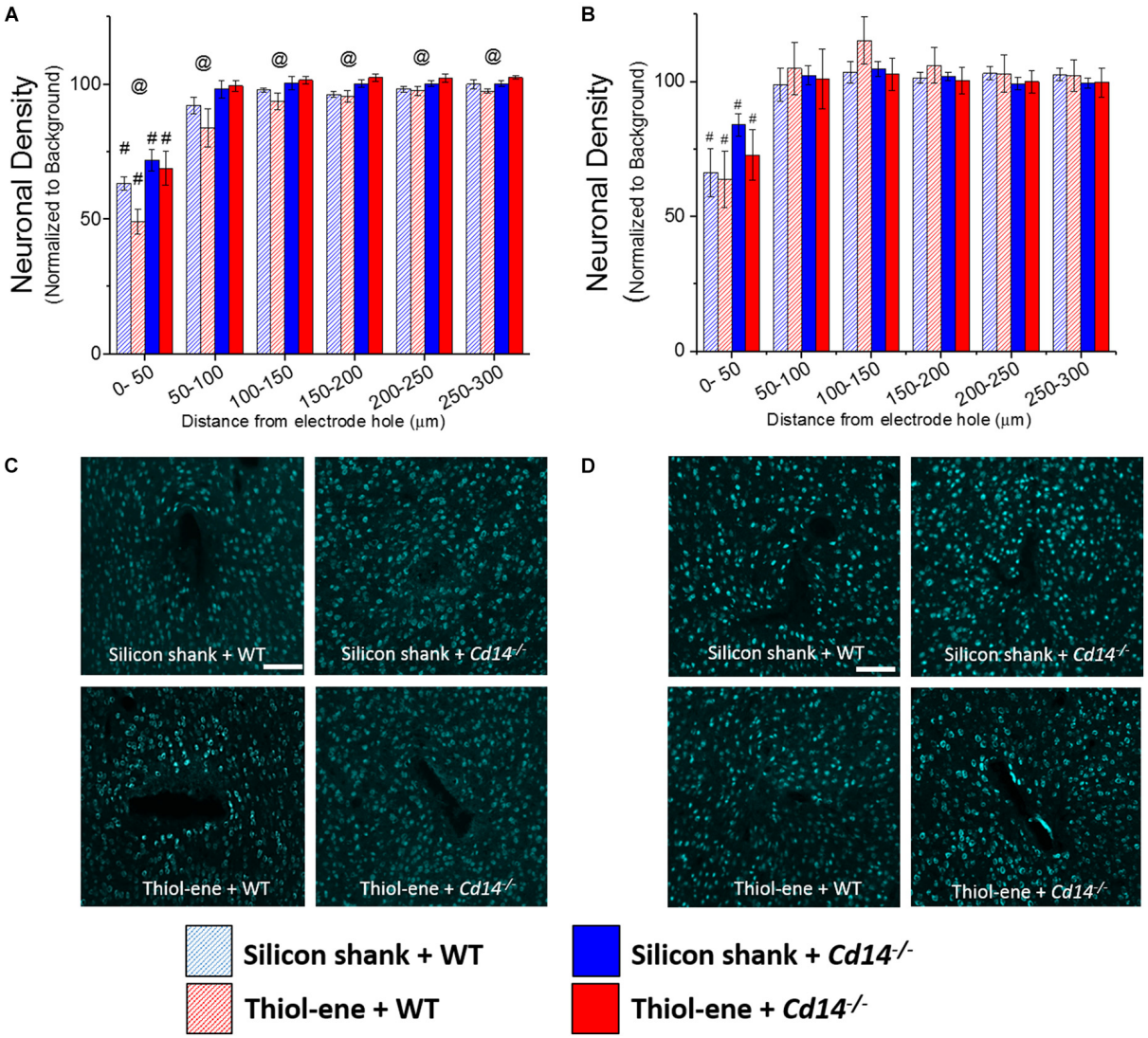

FIGURE 2 | Immunohistochemical evaluation of neuronal density. Neuronal density evaluated as $NeuN^+$ cells with respect to distance from the explanted microelectrode hole (μm). **(A)** 2 weeks. **(B)** 16 weeks. **(C)** Representative images of 2 weeks neuronal density. **(D)** Representative images of 16 weeks neuronal density. Scale bar: 100 μm. $^{@}$ Denotes significance between WT and $Cd14^{-/-}$; $^{\#}$ denotes significant difference from background neuronal density.

between wild-type and $Cd14^{-/-}$ groups at 2 weeks post-implantation (**Figures 4A,C**). By 16 weeks post-implant, activated microglia/macrophages for all groups had decreased compared to 2 weeks post-implantation (**Figures 4A,B**). Additionally, there were no differences in activation of microglia/macrophages among the conditions at 16 weeks (**Figures 4B,D**). Altogether, thiol-ene probe results in more microglia/macrophage activation around the probe at 2 weeks, but not 16 weeks post-implantation.

BBB Disruption

Similar to the glial scar and activated microglia/macrophages, BBB disruption (IgG expression) was found to be greatest at the probe-tissue interface and decreased in intensity as distance from probe-tissue interface increased (**Figure 5**). The only significant differences found between the groups were at 2 weeks post-implantation (**Figures 5A,C**). At 2 weeks post-implantation, the softer thiol-ene probes yielded significantly greater BBB breakdown compared to the stiff silicon probes (at each interval examined between 0 and 250 μm from probe interface, **Figures 5A,C**). In summary, thiol-ene probe results in greater BBB disruption around the probe at 2 weeks.

DISCUSSION

The current study explores how a softening thiol-ene probe and/or targeting the TLR/CD14 innate immune pathway affects inflammation and neuronal density at both 2 and 16 weeks post-implantation of intracortical microelectrode probes. Because

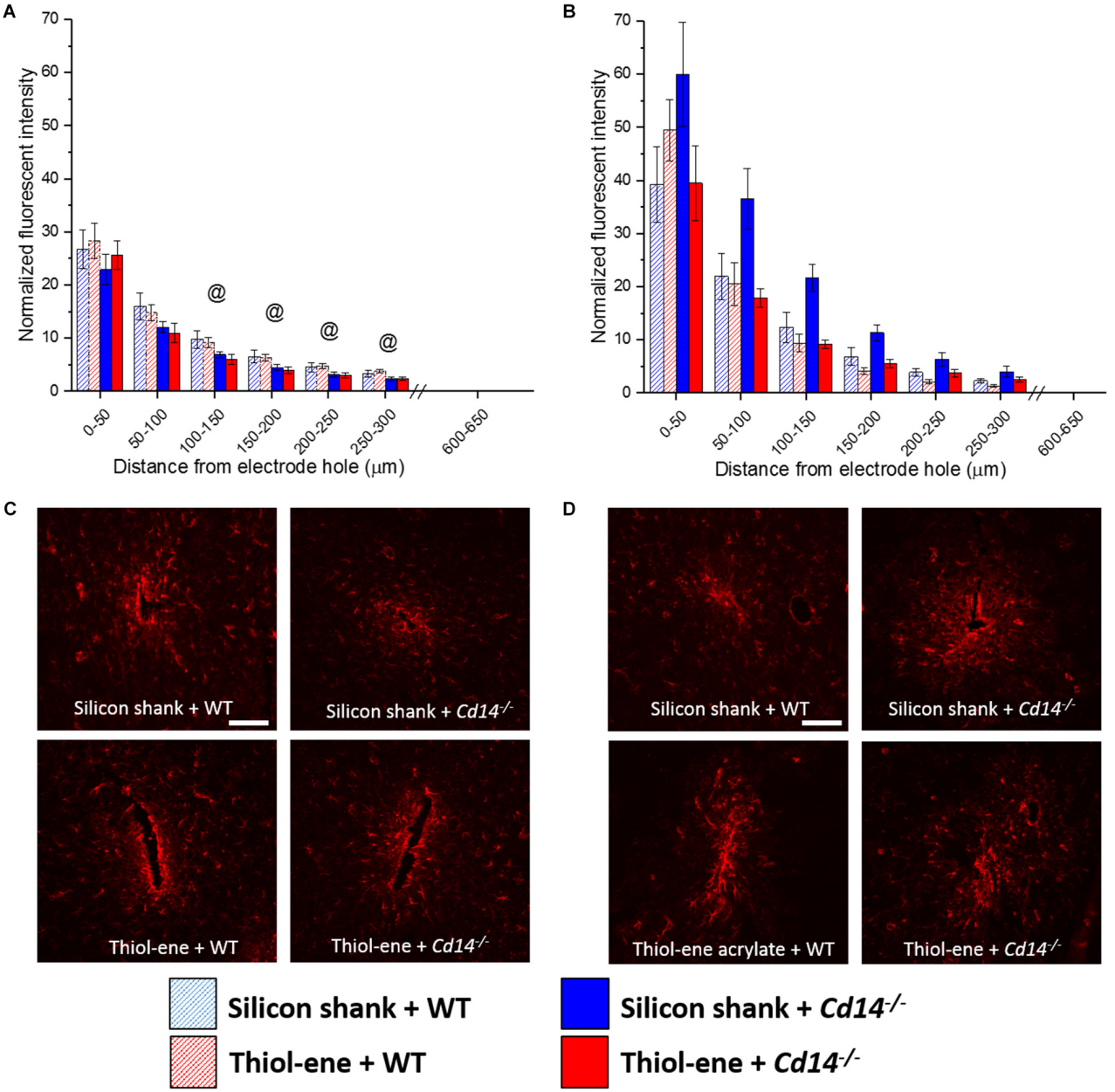

FIGURE 3 | Immunohistochemical evaluation of glial scarring assessed *via* astrocyte encapsulation. Astrocyte encapsulation evaluated as GFAP expression with respect to distance from the explanted microelectrode hole (μm). **(A)** 2 weeks. **(B)** 16 weeks. **(C)** Representative images of 2 weeks glial scar. **(D)** Representative images of 16 weeks glial scar. Scale bar: 100 μm. [@] Denotes significance between WT and $Cd14^{-/-}$.

initial results exploring synergistic effects of two different approaches resulted in increased neuroinflammation, we set out to parse out the response of each variable to gain a better understanding of each strategy alone. Our results demonstrate targeting CD14 results in higher neuronal density and decreased astroglial scarring around the probe at 2 weeks (**Figures 2A,C**, **3A,C**). We also describe the use of the thiol-ene probe with a modulus 3 orders of magnitude lower and a cross-sectional area 4× greater than the control silicon probes. Our observations demonstrate that a probe with a lower modulus but larger implantation footprint resulted in more BBB breakdown and activated microglia/macrophages than the control silicon probes. However, in spite of these markers of inflammation, the softening thiol-ene probes did not result in significantly decreased neuronal density or increased astroglial scarring around the implant at either acute (2 weeks) or chronic (16 weeks) time points.

Physiological sources such as respiration and vascular pulsations result in micromotion of an intracortical probe against brain tissue resulting in strain on brain tissue which can induce tissue damage (Subbaroyan et al., 2005; Gilletti

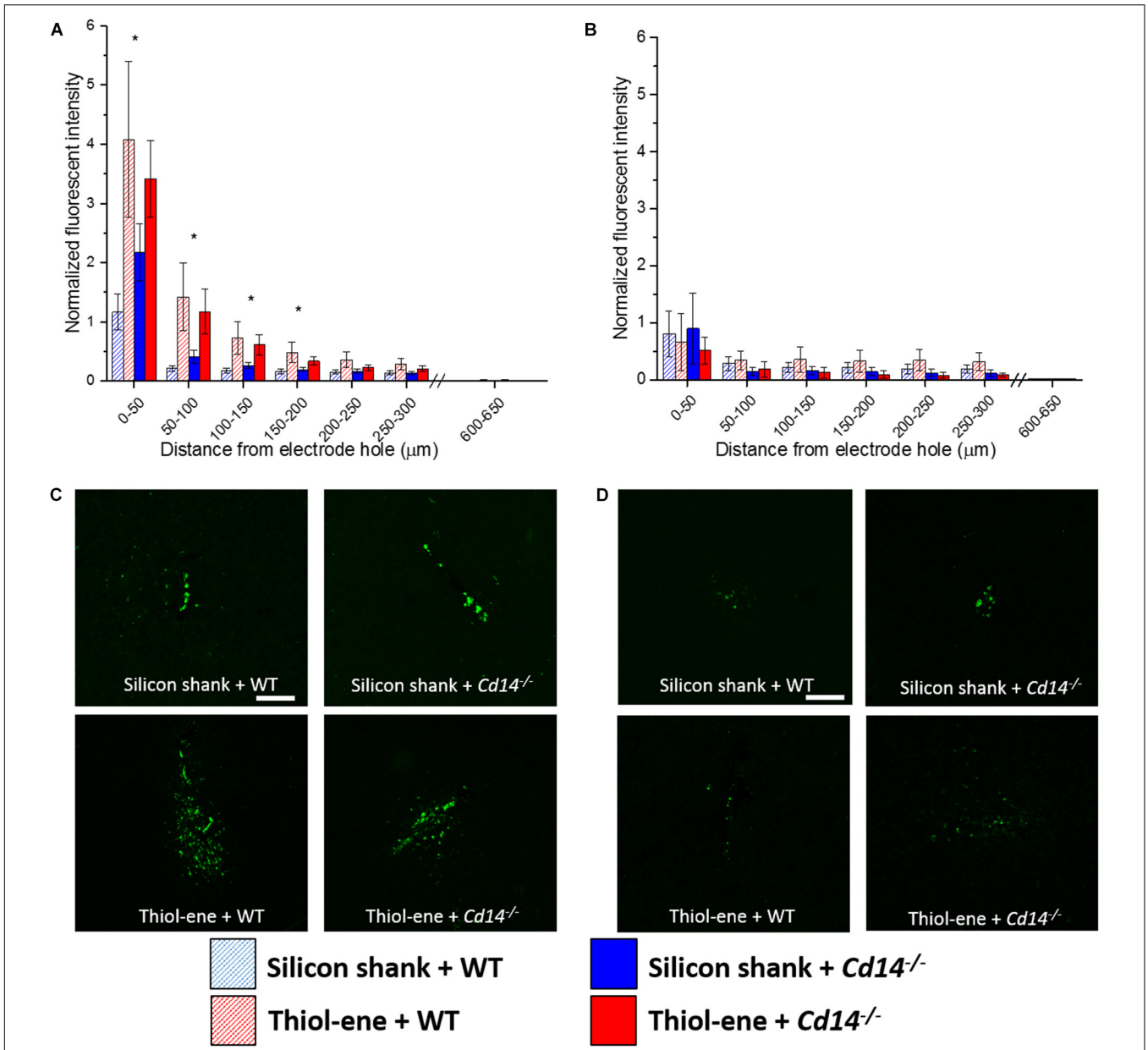

FIGURE 4 | Immunohistochemical evaluation of activated microglia and macrophages. Microglial and macrophage activation evaluated as CD68 expression with respect to distance from the explanted probe hole (μm). **(A)** 2 weeks. **(B)** 16 weeks. **(C)** Representative images of 2 weeks activated microglia and macrophages. **(D)** Representative images of 16 weeks activated microglia and macrophages. Scale bar: 100 μm. * Denotes significance between silicon and thiol-ene probes.

and Muthuswamy, 2006). One of the approaches to reduce the effects of micromotion is to increase probe flexibility. Decreasing the modulus of the probe material is one commonly explored/hypothesized methods to increase flexibility of the device. Probes made of polymers with a modulus or overall stiffness closer to brain tissue such as PDMS, polyimide, and SU-8 have been explored (Rousche et al., 2001; McClain et al., 2011; Altuna et al., 2013). However, implanting such soft probes present challenges with their insertion into the brain. A probe with too soft of a modulus will buckle during insertion and compress the brain tissue during the insertion process (Hess et al., 2013; Jorfi et al., 2015). Current methods used to implant soft electrodes while avoiding buckling include temporarily increasing the stiffness of the probe by use of a coating that dissolves after implantation or a stiff shuttle that accompanies the soft probe and is later removed (Lewitus et al., 2011; Kim B.J. et al., 2013; Kozai et al., 2014a; Vitale et al., 2015). Unfortunately, both approaches increase the footprint of the primary implant which can exacerbate the acute damage to brain tissue during implantation and lead to an increase in inflammation.

Materials which are innately stiff enough to implant, but soften while residing in tissue minimize the modulus

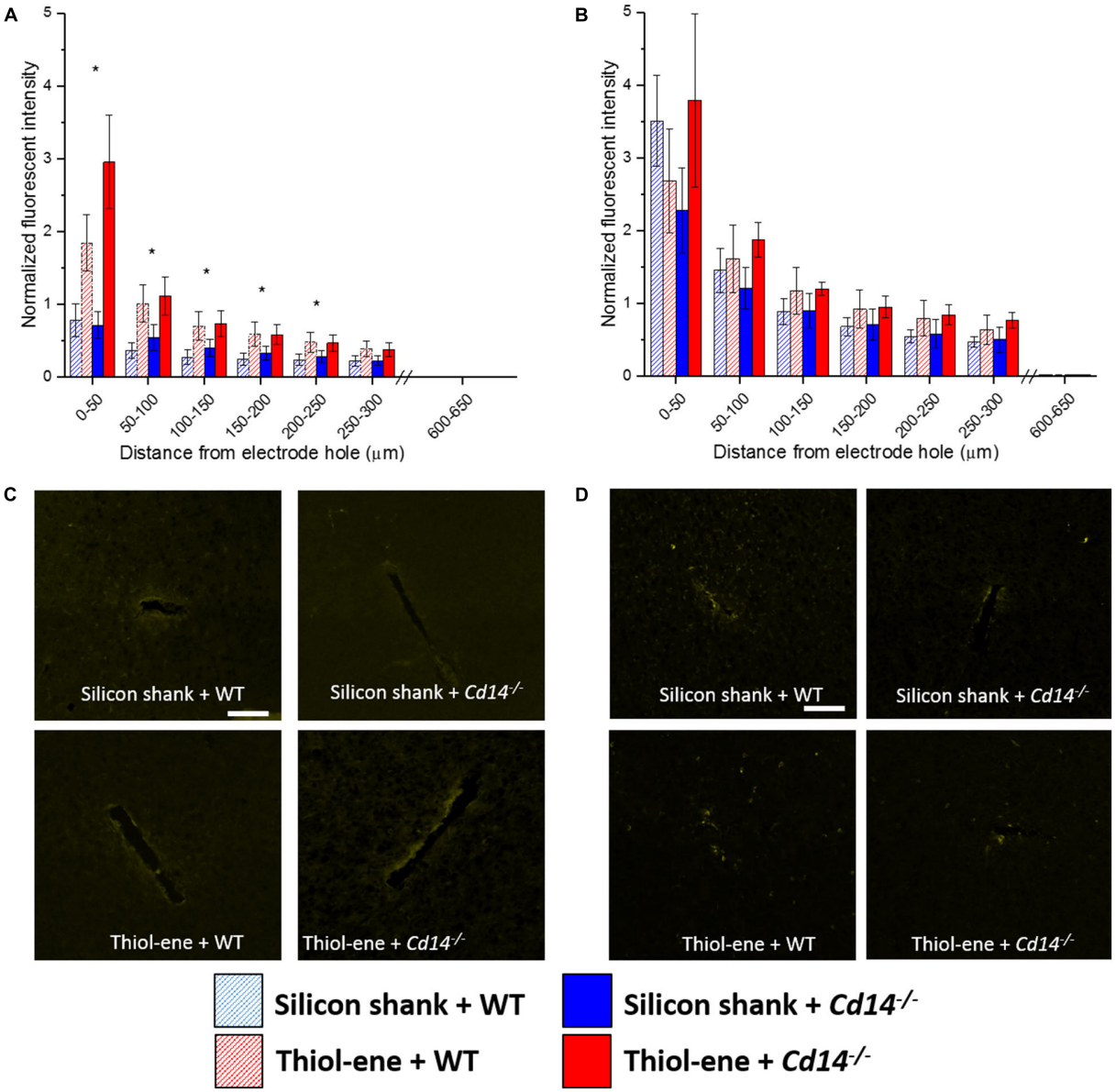

FIGURE 5 | Immunohistochemical evaluation of blood-brain barrier permeability. Blood–brain barrier permeability evaluated as IgG expression with respect to distance from the explanted microelectrode hole (μm). **(A)** 2 weeks. **(B)** 16 weeks. **(C)** Representative images of 2 weeks BBB permeability. **(D)** Representative images of 16 weeks BBB permeability. Scale bar: 100 μm. * Denotes significance between silicon and thiol-ene probes.

difference between probe and brain tissue. Previous literature has suggested that a softening material can compensate for increased damage footprint generated by a device with a larger cross-sectional area compared to a stiff silicon control probe (Nguyen et al., 2014). However, we found this phenomenon to be inconsistent in the current study as the larger thiol-ene probes had a larger cross-sectional area and resulted in more activated microglia/macrophages and increased evidence of BBB breakdown at 2 weeks compared to the smaller, stiffer silicon probes (**Figures 4A,C**, **5A,C**).

The thiol-ene probes used in the current study had a cross-sectional area of about 9000 μm^2, which is a 4× increase over the silicon probes utilized. The bending stiffness of the probe is determined by both the Young's modulus (E) and the probe dimensions. Although modulus of the probe material affects flexibility of the device, the probe dimensions play more of a role in reducing stiffness; bending stiffness is proportional to Et^3, where t is the cross-sectional area of the probe (Salatino et al., 2017).

A larger implant confers more acute tissue damage during implantation leading to greater extravasation of blood cells and proteins (Saxena et al., 2013). However, Nguyen et al. showed that a polyvinyl acetate, another softening material, can overcome increased inflammation induced by a slightly larger penetration

profile. The polyvinyl acetate probes used in Nguyen et al. (2014) had a pre-implant cross-sectional area that was 1.5× larger than control polyvinyl acetate dip-coated silicon probes. However, findings by Nguyen et al. (2014) were not recapitulated with thiol-ene, as the thiol-ene resulted in more activated microglia and macrophages and increased BBB permeability compared to the silicon probes (**Figures 4**, **5**). Therefore, there might be a size threshold to where a probe comprised of a softer material cannot overcome the increased inflammation resulting from an increased penetration profile.

The results from the current study suggest that the degree of initial trauma influences acute but not chronic inflammatory response, as there were significant results at 2 weeks post implantation, but there were no differences in the inflammatory response or neuronal density at 16 weeks between implants of different sizes (**Figures 2B**, **3B**, **4B**, **5B**). Current findings are consistent with Szarowski et al. (2003) which suggests initial glial response is correlated with the cross-sectional area of the electrode; however, sustained response of the implant was independent of probe size.

The different swelling properties of thiol-ene and polyvinyl acetate could also elicit differences in inflammation. The polyvinyl acetate swells ∼70% by volume under physiological conditions (Nguyen et al., 2014), while the thiol-ene substrate yields very minimal (<3%) swelling in physiologic environment (Ware et al., 2014). From a fabrication standpoint, minimal swelling is desirable as fluid uptake from the substrate results in cracking of thin film conductors used for the electrodes. However, as posited by Skousen et al. (2015), the thick hydrogel formed by the swollen polyvinyl acetate could have functioned as a sink for pro-inflammatory cytokines and chemokines at the probe–tissue interface, both of which facilitate inflammation. Reduced pro-inflammatory molecules at the device interface can lead to decreased inflammation and neuronal death. Future studies will need to explore the aforementioned theory.

In the current study, the thiol-ene probe resulted in an increased inflammatory response, likely because of its greater surface area and vascular damage during implantation, consistent with previously published research (Karumbaiah et al., 2013; Lee et al., 2017b; Spencer et al., 2017). The thiol-ene materials utilized in the present study have previously undergone testing to control for material surface chemistry. Shoffstall et al. (2018a) demonstrated that intracortical silicon probes dip-coated with the SMP material (SI, Section "Materials and Methods") generated similar histological responses (with respect to neuronal survival, activated microglia/macrophages, and BBB permeability) as compared to size-matched bare-silicon probes. While there was a statistically significant reduction in reactive astrocyte staining (GFAP) with the dip-coated probes, taken by itself it is unclear if the effects are substantially different from the bare silicon probes. Similar results suggestive of the effects of cross-sectional dimensions are found using a chemistry-controlled experiment (**Supplementary Figure S1**). Thiol-ene probes with larger cross-sectional width were compared to silicon probes dip-coated with the thiol-ene material, hereby setting up a chemistry-controlled comparison. Neuronal survival around the larger thiol-ene probes appears to be consistently lower compared to the smaller dip-coated probes, at both 2 and 16 weeks after implantation. Thus, the differences in size of the two probes in the current study are the most likely driver for the heightened inflammatory response of the thiol-ene probes.

Our study adds to the current body of research which suggests that size of the implant is a very important consideration in intracortical microelectrode design and too large of an implant can counteract benefit conferred by improved material selection or approaches to target the biology (Seymour and Kipke, 2007). Based on these and other findings from the field, size of the implant needs to be a major consideration for electrode design.

The current study further highlights the importance of CD14 for microglial and macrophage responses to DAMPs. As previously reported, CD14 is central for microglial responses to damage signals in the brain (Janova et al., 2016). In this current study, $Cd14^{-/-}$ resulted in higher neuronal density (**Figures 2A,C**) and decreased glial scar (**Figures 3A,C**) at 2 weeks post implantation, further revealing the importance of CD14 as a molecular target to reduce neuroinflammation. In our past work, we have demonstrated that partial inhibition of CD14 (in myeloid cells) was shown to improve single-shank, multi-channel electrode performance over time, whereas a complete CD14 inhibition did not result in such promising electrode performance (Bedell et al., 2018). In the current study, coupling complete inhibition of CD14 with the thiol-ene probe not only prevented exaggerated frustrated phagocytosis but also inhibited proper wound healing; the promising effects afforded by targeting CD14 were not able overcome the detriments of a larger probe size. However, the promising results of partial CD14 inhibition suggest that controlled of the thiol-ene inhibition of CD14 with a drug may still be promising for the integration of softer probes.

The dimensions of the thiol-ene probe are larger than that of the silicon probe, likely contributing to the increased inflammation seen on the thiol-ene probes compared to the uncoated silicon probes. The length of the thiol-ene probe taper (1.4 mm) is greater than that of the uncoated silicon probe taper (0.6 mm). However, the angle of their tips are similar, at 41.6° and 47°, respectively. As such, the differences in the angle between the tips are not expected to contribute significantly to vascular damage and hence tissue response; it is unlikely to affect our study. It also should be noted that there are conflicting reports in the literature to the benefits/disadvantages of different insertion speeds. Although Bjornsson et al. (2006) report that *fast* insertion (2 mm/s) results in less vascular damage and tissue strain, there are other reports indicating that slower insertion speeds afford time for tissue to adapt to probe thus decreasing compressive forces (Edell et al., 1992; Andrei et al., 2011).

Together, the results found in the current study suggest that large cross-sectional area probes comprised of a minimally swelling, yet softening material cannot overcome inflammation driven by large penetration profile differences. Accordingly, the differences in the size of the electrodes is a major limitation of our study. Overall, the results presented here highlight the detriment of only considering one or two aspects of probe design and mitigation of biological response. When approaching translatable strategies to improve chronic intracortical microelectrode

performance by decreasing inflammation, one needs to consider many characteristics in tandem.

CONCLUSION

The current manuscript demonstrates the impact of size of the probe on the initial stages of inflammation. To reduce inflammation, the cross-sectional area of the probe should be minimized. The current study also characterizes the acute benefits of targeting CD14 and further confirms the TLR/CD14 pathway as a mechanism amenable for therapeutic targeting. In the initial weeks after probe implantation, the benefits a minimally swelling soft probe affords does not exceed the inflammation driven by a probe with 4× the cross-sectional area. When optimizing probe design for intracortical microelectrodes, many elements of the probe need to be carefully considered, especially size.

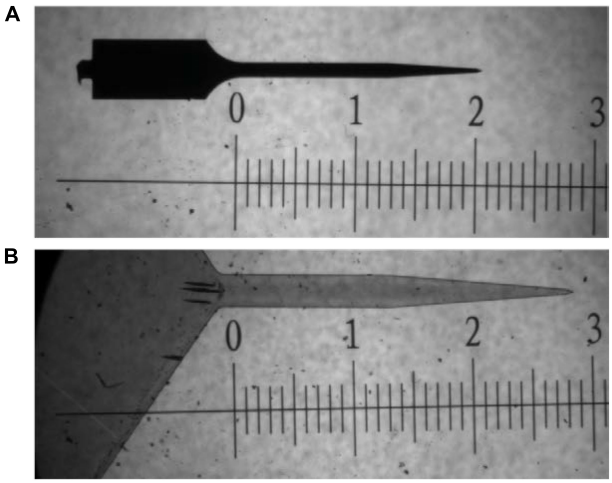

FIGURE 6 | Bright field microscope image comparing dimensions of probes used in study. **(A)** uncoated silicon probe and **(B)** thiol-ene probe. Both images are taken at 5× magnification. Scale is in mm.

MATERIALS AND METHODS

Electrodes

Single shank, uncoated, Michigan style silicon probes (2 mm × 15 μm × 123 μm; 47° taper angle) and thiol-ene based shape memory polymer (SMP) probes (3 mm × 30 μm × 290 μm; 41.6° taper angle) were used as intracortical probes (**Figure 6**). Polymer films were fabricated as previously described (Ecker et al., 2017). Briefly, 0.5 mol% 1,3,5-triallyl-1,3,5-triazine-2,4,6(1H,3H,5H)-trione (TATATO), 0.45 mol% trimethylolpropane tris(3-mercaptopropionate) (TMTMP), and 0.05 mol% Tris[2-mercaptopropionyloxy)ethyl] isocyanurate (TMICN) were mixed with 0.1 wt% of photoinitiator 2,2-dimethoxy-2-phenylacetophenone (DMPA). The polymer solution was then spin coated on glass slides using a spin coater (Laurell WS-650-23B) to receive ∼33 μm films before they were cured for 2 h at 254 nm (UVP CL-1000 cross-linking chamber) followed by an overnight post-cure at 120 °C under vacuum. Dummy probes were fabricated in the UT Dallas Class 10000 cleanroom facility. The 33-μm SMP-on-glass substrates were used as the starting substrates in the cleanroom. Low temperature silicon nitride (using PlasmaTherm-790 PECVD) was deposited to act as a hard mask for the following plasma etching processes. The device outline/shape was then patterned using standard lithography techniques. The hard mask and the SMP layer were plasma etched in Technics RIE using SF_6 and O_2 plasma, respectively. After the 30-μm SMP layer was plasma etched down to the glass slide, the remaining silicon nitride hard mask was etched away in diluted 10:1 HF dip. A ∼3 μm SMP layer from the surface of these devices was etched in Technics RIE using O_2 plasma. The devices were then released by soaking in DIW. The material is characterized by a glass transition temperature (T_g) of 52°C before, and 35 °C after softening under physiological conditions as measured by dynamic mechanical analysis (TA RSA-G2). The storage modulus E' at 37°C (measured in tension) changes from 1.2 GPa (dry) to 35 MPa (soaked). Stainless-steel wires (∼3 mm length) were used as dummy ground and reference wires to mimic the implants involved with functional probes. Probes and wires were sterilized *via* a cold ethylene oxide gas cycle as previously described.

Animals

C57/BL6 (strain #000664) and $Cd14^{-/-}$ (C57/BL6 background) (strain #003726) were bred in-house. Strain of $Cd14^{-/-}$ mice was verified *via* genotyping according to the protocols established by the vendor (Jackson Laboratories). Both male and female mice between 8 and 12 weeks of age were used for surgeries. Prior to surgery, mice were group housed with food and water *ad libitium* while maintained on a 12-h light/dark cycle. After surgery, mice were individually housed. All animal handling was performed in a class II sterile hood using microisolator techniques. All procedures and animal care practices comply with the protocol approved by the Case Western Reserve University Institutional Animal Care and Use Committee.

Surgical Implantation of Electrodes

A total of three holes were drilled in the exposed skull using a 0.45 mm size bit (Stoetling Co.) with adequate breaks in the drilling pulses to prevent overheating of the skull (Shoffstall et al., 2018b). The probe hole was created in the skull over the motor region of the brain (1.5 mm lateral and 0.5 mm anterior to bregma) (Tennant et al., 2011). Two additional craniotomies were conducted for dummy ground and reference wires which were implanted in the contralateral hemisphere to the probe (∼2 mm lateral, ∼2 mm rostral and caudal to bregma). The dummy probes and dummy wires were manually inserted (∼2–3 mm/s) into the cortex. Silicone elastomer (Kwik-Sil, World Precision Instruments) and dental acrylic (Fusio/Flow-it ALC, Patterson Dental) tethered the probe and wires to the skull. The incision site was then sutured closed using 5-0 monofilment polypropylene suture. To minimize variability, the same surgeon performed all implantation surgeries.

TABLE 1 | Number of experimental animals for each condition at each time point.

	2 weeks post implantation	16 weeks post implantation
Silicon shank + WT	10	6
Thiol-ene + WT	10	4
Silicon shank + *Cd14*$^{-/-}$	8	6
Thiol-ene + *Cd14*$^{-/-}$	9	4

Immunohistochemistry

At each 2 and 16 weeks post-implantation, mice were sacrificed and brain tissue was harvested. At the respective time point, mice were anesthetized with an intraperitoneal injection of ketamine/xylazine cocktail. Each animal was then transcardially perfused with phosphate buffered saline (PBS) followed by 4% paraformaldehyde (PFA) to fix the tissue. Mouse heads were post-fixed for an additional 2 days in 4% PFA at 4°C. After fixation, brains were extracted and immersed in 30% sucrose for at least 48 h. After dummy electrodes and wires were removed, brain tissue was cryopreserved in optimal cutting temperature compound (OCT) (Tissue-Tek). Horizontal brain tissue sections (16 μm thick) were obtained using a cryostat and stored at −80°C.

To compare neuroinflammation and neuronal density in the area adjacent the implanted dummy shank among conditions, immunohistochemistry was utilized using previously established methodology (Potter et al., 2014). Only tissue slices between ∼320 and 1000 μm from the surface of the cortex were used as this depth corresponds with Layers III–VI of the mouse motor cortex, the layers from which functional probes aim to record (Oswald et al., 2013). After blocking the tissue (4% chicken serum, 0.3% Trition-X-100 in 1× PBS), the following primary antibodies (in 4% chicken serum, 0.3% Trition-X-100 in 1× PBS) were added to incubate overnight at 4 °C: Rabbit anti-GFAP (1:500, Z0334, Dako), mouse anti-neuronal nuclei (NeuN) (1:250, MAB377, Millipore), rat anti-CD68 (1:500, ab53444, Abcam), and rabbit anti-immunoglobulin G (IgG) (1:500, STAR26B, Bio-Rad). Visualization of the inflammatory and neuronal markers was achieved with respective Alexa Fluor® secondary antibodies (1:1000) (in 4% chicken serum, 0.3% Trition-X-100 in 1× PBS). DAPI (Molecular Probes D3571) was incorporated in secondary antibody solution to visualize cell nuclei. Furthermore, tissue autofluorescence was reduced by incubating tissue sections with of 0.5 mM copper sulfate buffer solution for 10 min (Potter et al., 2012b). Finally, copper sulfate buffer was washed off thoroughly with MilliQ H_2O, and slides were coverslipped using Fluoromount-G. Slides were stored in the dark at 4 °C until imaged.

Imaging and Quantitative Analysis

Images were acquired using a 10× objective on a Carl Zeiss AxioObserver.Z1 (Zeiss Inc.) inverted epifluorescence microscope. Fluorescent markers were imaged on single optical sections using an AxioCam MRm monochrome camera with fixed exposure times for each marker.

Images of fluorescent markers were analyzed using SECOND, a custom-written MATLAB program previously used in the Capadona lab (Goss-Varley et al., 2017). The fluorescent intensity of each marker in concentric rings at fixed distances (normalized by area) from the probe–tissue interface was measured as a function of distance from the implant. Prior to measurement, the user defines the implant hole and any imperfections in the brain slice to omit from the analysis. For each slice, raw fluorescent intensities were then normalized to background signal, defined as the fluorescent intensity of the concentric ring 600–650 μm from the interface. The area under the curve (AUC) was calculated from the intensity profile.

Neuronal densities at the interface were determined using AfterNeuN, another custom-written MATLAB program. Using AfterNeuN, the user manually defines the electrode implant region, any areas to be excluded from analysis, and neuronal cell bodies. The program then outputs the density of neurons at fixed radial distances from the electrode interface. Neuronal densities at uniform binned distances (50 μm bins) were then normalized to background counts from the same brain tissue slice 300–350 μm away from the interface.

Immunohistochemistry Statistical Analysis

Table 1 indicates number of animals for each condition at each time point. Measurements from all brain tissue slices for a given animal were first averaged together (four to six brain slices per animal, average of 5.29 ± 0.87). Average intensity or count for a given condition was calculated using independent animal averages. Statistical analyses for the first experiment, comparing thiol-ene + *Cd14*$^{-/-}$ to silicon shank + WT were performed using unpaired *t*-tests. All statistical analyses assessing immunohistochemical results comparing all four conditions were performed using a general linear model with a two-way analysis of variance (ANOVA) using Minitab software with genotype (WT or *Cd14*$^{-/-}$) and electrode material (uncoated silicon or thiol-ene) as separate factors. Results were considered significant at $p < 0.05$ and expressed as mean ± standard error of mean.

AUTHOR CONTRIBUTIONS

HB, WV, JP, and JC contributed substantially to the conception or design of the work, analysis, and interpretation of data for the work, drafting, and revising the manuscript for important intellectual content, approved the final version to be published, and agreed to be accountable for all aspects of the work. HB, SS, XL, EM, AJS, and SL aided in the collection and analysis of histological data. AS, ME, and VD fabricated and characterized the SMP probes. All authors approved the final version to be published and agreed to be accountable for all aspects of the work.

FUNDING

The current work was supported in part by the Department of Biomedical Engineering and Case School of Engineering at

Case Western Reserve University through laboratory start-up funds, the National Institute of Health, National Institute of Neurological Disorders and Stroke (Grant # 1R01NS082404-01A1), and the NIH Neuroengineering Training Grant 5T-32EB004314-16. Additional support was provided by the Presidential Early Career Award for Scientists and Engineers (PECASE, JR. Capadona), by Merit Review Awards B1495-R and B2611-R from the United States Department of Veterans Affairs Rehabilitation Research and Development Service, and in part by the Office of the Assistant Secretary of Defense for Health Affairs through the Peer Reviewed Medical Research Program under Award no. W81XWH-15-1-0607 and W81XWH-15-1-0608. None of the funding sources aided in collection, analysis, and interpretation of the data, in writing of the manuscript, or in the decision to submit the manuscript for publication. The contents do not represent the views of the U.S. Department of Veterans Affairs or the United States Government.

SUPPLEMENTARY MATERIAL

The Supplementary Material for this article can be found online at: https://www.frontiersin.org/articles/10.3389/fnins.2018.00772/full#supplementary-material

REFERENCES

Abdul-Muneer, P., Chandra, N., and Haorah, J. (2015). Interactions of oxidative stress and neurovascular inflammation in the pathogenesis of traumatic brain injury. *Mol. Neurobiol.* 51, 966–979. doi: 10.1007/s12035-014-8752-3

Altuna, A., Bellistri, E., Cid, E., Aivar, P., Gal, B., Berganzo, J., et al. (2013). SU-8 based microprobes for simultaneous neural depth recording and drug delivery in the brain. *Lab Chip* 13, 1422–1430. doi: 10.1039/c3lc41364k

Andrei, A., Welkenhuysen, M., Nuttin, B., and Eberle, W. (2011). A response surface model predicting the in vivo insertion behavior of micromachined neural implants. *J. Neural Eng.* 9:016005. doi: 10.1088/1741-2560/9/1/016005

Barrese, J. C., Rao, N., Paroo, K., Triebwasser, C., Vargas-Irwin, C., Franquemont, L., et al. (2013). Failure mode analysis of silicon-based intracortical microelectrode arrays in non-human primates. *J. Neural Eng.* 10:066014. doi: 10.1088/1741-2560/10/6/066014

Bedell, H. W., Hermann, J. K., Ravikumar, M., Lin, S., Rein, A., Li, X., et al. (2018). Targeting CD14 on blood derived cells improves intracortical microelectrode performance. *Biomaterials* 163, 163–173. doi: 10.1016/j.biomaterials.2018.02.014

Bjornsson, C. S., Oh, S. J., Al-Kofahi, Y. A., Lim, Y. J., Smith, K. L., Turner, J. N., et al. (2006). Effects of insertion conditions on tissue strain and vascular damage during neuroprosthetic device insertion. *J. Neural Eng.* 3, 196–207. doi: 10.1088/1741-2560/3/3/002

Capadona, J. R., Shanmuganathan, K., Tyler, D. J., Rowan, S. J., and Weder, C. (2008). Stimuli-responsive polymer nanocomposites inspired by the sea cucumber dermis. *Science* 319, 1370–1374. doi: 10.1126/science.1153307

Du, Z. J., Kolarcik, C. L., Kozai, T. D., Luebben, S. D., Sapp, S. A., Zheng, X. S., et al. (2017). Ultrasoft microwire neural electrodes improve chronic tissue integration. *Acta Biomater.* 53, 46–58. doi: 10.1016/j.actbio.2017.02.010

Ecker, M., Danda, V., Shoffstall, A. J., Mahmood, S. F., Joshi-Imre, A., Frewin, C. L., et al. (2017). Sterilization of Thiol-ene/Acrylate based shape memory polymers for biomedical applications. *Macromol. Mater. Eng.* 302:1600331. doi: 10.1002/mame.201600331

Edell, D. J., Toi, V., McNeil, V. M., and Clark, L. (1992). Factors influencing the biocompatibility of insertable silicon microshafts in cerebral cortex. *IEEE Trans. Biomed. Eng.* 39, 635–643. doi: 10.1109/10.141202

Gilletti, A., and Muthuswamy, J. (2006). Brain micromotion around implants in the rodent somatosensory cortex. *J. Neural Eng.* 3, 189–195. doi: 10.1088/1741-2560/3/3/001

Goss-Varley, M., Dona, K. R., McMahon, J. A., Shoffstall, A. J., Ereifej, E. S., Lindner, S. C., et al. (2017). Microelectrode implantation in motor cortex causes fine motor deficit: implications on potential considerations to brain computer interfacing and human augmentation. *Sci. Rep.* 7:15254. doi: 10.1038/s41598-017-15623-y

Green, M. A., Bilston, L. E., and Sinkus, R. (2008). In vivo brain viscoelastic properties measured by magnetic resonance elastography. *NMR Biomed.* 21, 755–764. doi: 10.1002/nbm.1254

Harris, J., Hess, A. E., Rowan, S. J., Weder, C., Zorman, C., Tyler, D., et al. (2011). In vivo deployment of mechanically adaptive nanocomposites for intracortical microelectrodes. *J. Neural Eng.* 8:046010. doi: 10.1088/1741-2560/8/4/046010

Hermann, J. K., Ravikumar, M., Shoffstall, A., Ereifej, E. S., Kovach, K., Chang, J., et al. (2017). Inhibition of the cluster of differentiation 14 innate immunity pathway with IAXO-101 improves chronic microelectrode performance. *J. Neural Eng.* 15:025002. doi: 10.1088/1741-2552/aaa03e

Hess, A. E., Potter, K. A., Tyler, D. J., Zorman, C. A., and Capadona, J. R. (2013). Environmentally-controlled microtensile testing of mechanically-adaptive polymer nanocomposites for ex vivo characterization. *J. Vis. Exp.* 78:e50078. doi: 10.3791/50078

Hochberg, L. R., Bacher, D., Jarosiewicz, B., Masse, N. Y., Simeral, J. D., Vogel, J., et al. (2012). Reach and grasp by people with tetraplegia using a neurally controlled robotic arm. *Nature* 485, 372–375. doi: 10.1038/nature11076

Janova, H., Böttcher, C., Holtman, I. R., Regen, T., van Rossum, D., Götz, A., et al. (2016). CD14 is a key organizer of microglial responses to CNS infection and injury. *Glia* 64, 635–649. doi: 10.1002/glia.22955

Jorfi, M., Skousen, J. L., Weder, C., and Capadona, J. R. (2015). Progress towards biocompatible intracortical microelectrodes for neural interfacing applications. *J. Neural Eng.* 12:011001. doi: 10.1088/1741-2560/12/1/011001

Karumbaiah, L., Saxena, T., Carlson, D., Patil, K., Patkar, R., Gaupp, E. A., et al. (2013). Relationship between intracortical electrode design and chronic recording function. *Biomaterials* 34, 8061–8074. doi: 10.1016/j.biomaterials.2013.07.016

Kim, B. J., Kuo, J. T., Hara, S. A., Lee, C. D., Yu, L., Gutierrez, C., et al. (2013). 3D Parylene sheath neural probe for chronic recordings. *J. Neural Eng.* 10:045002. doi: 10.1088/1741-2560/10/4/045002

Kim, S., Kim, S. Y., Pribis, J. P., Lotze, M., Mollen, K. P., Shapiro, R., et al. (2013). Signaling of high mobility group box 1 (HMGB1) through toll-like receptor 4 in macrophages requires CD14. *Mol. Med.* 19, 88–98. doi: 10.2119/molmed.2012.00306

Kozai, T. D., Gugel, Z., Li, X., Gilgunn, P. J., Khilwani, R., Ozdoganlar, O. B., et al. (2014a). Chronic tissue response to carboxymethyl cellulose based dissolvable insertion needle for ultra-small neural probes. *Biomaterials* 35, 9255–9268. doi: 10.1016/j.biomaterials.2014.07.039

Kozai, T. D., Li, X., Bodily, L. M., Caparosa, E. M., Zenonos, G. A., Carlisle, D. L., et al. (2014b). Effects of caspase-1 knockout on chronic neural recording quality and longevity: insight into cellular and molecular mechanisms of the reactive tissue response. *Biomaterials* 35, 9620–9634. doi: 10.1016/j.biomaterials.2014.08.006

Landis, D. M. D. (1994). The early reactions of nonneuronal cells to brain injury. *Annu. Rev. Neurosci.* 17, 133–151. doi: 10.1146/annurev.ne.17.030194.001025

Lee, H. C., Ejserholm, F., Gaire, J., Currlin, S., Schouenborg, J., Wallman, L., et al. (2017a). Histological evaluation of flexible neural implants; flexibility limit for reducing the tissue response? *J. Neural Eng.* 14:036026. doi: 10.1088/1741-2552/aa68f0

Lee, H. C., Gaire, J., Currlin, S. W., McDermott, M. D., Park, K., and Otto, K. J. (2017b). Foreign body response to intracortical microelectrodes is not altered with dip-coating of polyethylene glycol (PEG). *Front. Neurosci.* 11:513. doi: 10.3389/fnins.2017.00513

Lewitus, D., Smith, K. L., Shain, W., and Kohn, J. (2011). Ultrafast resorbing polymers for use as carriers for cortical neural probes. *Acta Biomater.* 7, 2483–2491. doi: 10.1016/j.actbio.2011.02.027

Liu, X., McCreery, D. B., Bullara, L. A., and Agnew, W. F. (2006). "Evaluation of the stability of intracortical microelectrode arrays," in *Proceedings of the IEEE Transactions on Neural Systems and Rehabilitation Engineering*, Vol. 14, (Piscataway, NJ: IEEE), 91–100.

McClain, M. A., Clements, I. P., Shafer, R. H., Bellamkonda, R. V., LaPlaca, M. C., and Allen, M. G. (2011). Highly-compliant, microcable neuroelectrodes fabricated from thin-film gold and PDMS. *Biomed. Microdevices* 13, 361–373. doi: 10.1007/s10544-010-9505-3

Moshayedi, P., Ng, G., Kwok, J. C., Yeo, G. S., Bryant, C. E., Fawcett, J. W., et al. (2014). The relationship between glial cell mechanosensitivity and foreign body reactions in the central nervous system. *Biomaterials* 35, 3919–3925. doi: 10.1016/j.biomaterials.2014.01.038

Mullen, R. J., Buck, C. R., and Smith, A. M. (1992). NeuN, a neuronal specific nuclear protein in vertebrates. *Development* 116, 201–211.

Nguyen, J. K., Park, D. J., Skousen, J. L., Hess-Dunning, A., Tyler, D. J., Rowan, S. J., et al. (2014). Mechanically-compliant intracortical implants reduce the neuroinflammatory response. *J. Neural Eng.* 11:056014. doi: 10.1088/1741-2560/11/5/056014

Nuzzo, R. G., Fusco, F. A., and Allara, D. L. (1987). Spontaneously organized molecular assemblies. 3. Preparation and properties of solution adsorbed monolayers of organic disulfides on gold surfaces. *J. Am. Chem. Soc.* 109, 2358–2368. doi: 10.1021/ja00242a020

Oswald, M. J., Tantirigama, M. L., Sonntag, I., Hughes, S. M., and Empson, R. M. (2013). Diversity of layer 5 projection neurons in the mouse motor cortex. *Front. Cell. Neurosci.* 7:174. doi: 10.3389/fncel.2013.00174

Polikov, V. S., Tresco, P. A., and Reichert, W. M. (2005). Response of brain tissue to chronically implanted neural electrodes. *J. Neurosci. Methods* 148, 1–18. doi: 10.1016/j.jneumeth.2005.08.015

Potter, K. A., Buck, A. C., Self, W. K., and Capadona, J. R. (2012a). Stab injury and device implantation within the brain results in inversely multiphasic neuroinflammatory and neurodegenerative responses. *J. Neural Eng.* 9:046020. doi: 10.1088/1741-2560/9/4/046020

Potter, K. A., Simon, J. S., Velagapudi, B., and Capadona, J. R. (2012b). Reduction of autofluorescence at the microelectrode-cortical tissue interface improves antibody detection. *J. Neurosci. Methods* 203, 96–105. doi: 10.1016/j.jneumeth.2011.09.024

Potter, K. A., Jorfi, M., Householder, K. T., Foster, E. J., Weder, C., and Capadona, J. R. (2014). Curcumin-releasing mechanically adaptive intracortical implants improve the proximal neuronal density and blood–brain barrier stability. *Acta Biomater.* 10, 2209–2222. doi: 10.1016/j.actbio.2014.01.018

Ravikumar, M., Sunil, S., Black, J., Barkauskas, D., Haung, A. Y., Miller, R. H., et al. (2014). The roles of blood-derived macrophages and resident microglia in the neuroinflammatory response to implanted intracortical microelectrodes. *Biomaterials* 35, 8049–8064. doi: 10.1016/j.biomaterials.2014.05.084

Rennaker, R. L., Miller, J., Tang, H., and Wilson, D. A. (2007). Minocycline increases quality and longevity of chronic neural recordings. *J. Neural Eng.* 4, L1–L5.

Renshaw, B., Forbes, A., and Morison, B. (1940). Activity of isocortex and hippocampus: electrical studies with micro-electrodes. *J. Neurophysiol.* 3, 74–105. doi: 10.1152/jn.1940.3.1.74

Rousche, P. J., Pellinen, D. S., Pivin, D. P., Williams, J. C., Vetter, R. J., and Kipke, D. R. (2001). Flexible polyimide-based intracortical electrode arrays with bioactive capability. *IEEE Trans. Biomed. Eng.* 48, 361–371. doi: 10.1109/10.914800

Salatino, J. W., Ludwig, K. A., Kozai, T. D., and Purcell, E. K. (2017). Glial responses to implanted electrodes in the brain. *Nat. Biomed. Eng.* 1, 862–877. doi: 10.1038/s41551-017-0154-1

Saxena, T., Karumbaiah, L., Gaupp, E. A., Patkar, R., Patil, K., Betancur, M., et al. (2013). The impact of chronic blood–brain barrier breach on intracortical electrode function. *Biomaterials* 34, 4703–4713. doi: 10.1016/j.biomaterials.2013.03.007

Schwartz, A. B. (2004). Cortical neural prosthetics. *Annu. Rev. Neurosci.* 27, 487–507. doi: 10.1146/annurev.neuro.27.070203.144233

Seymour, J. P., and Kipke, D. R. (2007). Neural probe design for reduced tissue encapsulation in CNS. *Biomaterials* 28, 3594–3607. doi: 10.1016/j.biomaterials.2007.03.024

Shoffstall, A. J., Danda, V., Joshi-Imre, A., Stiller, A., Yu, M., Paiz, J., et al. (2018a). Characterization of the neuroinflammatory response to thiol-ene shape memory polymer coated intracortical microelectrodes. *Micromachines* 9:486. doi: 10.3390/mi9100486

Shoffstall, A. J., Paiz, J. E., Miller, D. M., Rial, G. M., Willis, M. T., Menendez, D. M., et al. (2018b). Potential for thermal damage to the blood–brain barrier during craniotomy: implications for intracortical recording microelectrodes. *J. Neural Eng.* 15:034001. doi: 10.1088/1741-2552/aa9f32

Simon, D. M., Charkhkar, H., St John, C., Rajendran, S., Kang, T., Reit, R., et al. (2017). Design and demonstration of an intracortical probe technology with tunable modulus. *J. Biomed. Mater. Res. A* 105, 159–168. doi: 10.1002/jbm.a.35896

Skousen, J. L., Bridge, M. J., and Tresco, P. A. (2015). A strategy to passively reduce neuroinflammation surrounding devices implanted chronically in brain tissue by manipulating device surface permeability. *Biomaterials* 36, 33–43. doi: 10.1016/j.biomaterials.2014.08.039

Song, L., Lee, C., and Schindler, C. (2011). Deletion of the murine scavenger receptor CD68. *J. Lipid Res.* 52, 1542–1550. doi: 10.1194/jlr.M015412

Spencer, K. C., Sy, J. C., Ramadi, K. B., Graybiel, A. M., Langer, R., and Cima, M. J. (2017). Characterization of mechanically matched hydrogel coatings to improve the biocompatibility of neural implants. *Sci. Rep.* 7:1952. doi: 10.1038/s41598-017-02107-2

Sridharan, A., Nguyen, J. K., Capadona, J. R., and Muthuswamy, J. (2015). Compliant intracortical implants reduce strains and strain rates in brain tissue in vivo. *J. Neural Eng.* 12:036002. doi: 10.1088/1741-2560/12/3/036002

Subbaroyan, J., Martin, D. C., and Kipke, D. R. (2005). A finite-element model of the mechanical effects of implantable microelectrodes in the cerebral cortex. *J. Neural Eng.* 2, 103–113. doi: 10.1088/1741-2560/2/4/006

Szarowski, D., Andersen, M., Retterer, S., Spence, A., Isaacson, M., Craighead, H., et al. (2003). Brain responses to micro-machined silicon devices. *Brain Res.* 983, 23–35. doi: 10.1016/S0006-8993(03)03023-3

Tennant, K. A., Adkins, D. L., Donlan, N. A., Asay, A. L., Thomas, N., Kleim, J. A., et al. (2011). The organization of the forelimb representation of the C57BL/6 mouse motor cortex as defined by intracortical microstimulation and cytoarchitecture. *Cereb. Cortex* 21, 865–876. doi: 10.1093/cercor/bhq159

Vitale, F., Summerson, S. R., Aazhang, B., Kemere, C., and Pasquali, M. (2015). Neural stimulation and recording with bidirectional, soft carbon nanotube fiber microelectrodes. *ACS Nano* 9, 4465–4474. doi: 10.1021/acsnano.5b01060

Ware, T., Simon, D., Liu, C., Musa, T., Vasudevan, S., Sloan, A., et al. (2014). Thiol-ene/acrylate substrates for softening intracortical electrodes. *J. Biomed. Mater. Res. B Appl. Biomater.* 102, 1–11. doi: 10.1002/jbmb.32946

Wessberg, J., Stambaugh, C. R., Kralik, J. D., Beck, P. D., Laubach, M., Chapin, J. K., et al. (2000). Real-time prediction of hand trajectory by ensembles of cortical neurons in primates. *Nature* 408, 361–365. doi: 10.1038/35042582

Zanoni, I., Tan, Y., Di Gioia, M., Springstead, J. R., and Kagan, J. C. (2017). By capturing inflammatory lipids released from dying cells, the receptor CD14 induces inflammasome-dependent phagocyte hyperactivation. *Immunity* 47, 697.e3–709.e3. doi: 10.1016/j.immuni.2017.09.010

Conflict of Interest Statement: The authors declare that the research was conducted in the absence of any commercial or financial relationships that could be construed as a potential conflict of interest.

Copyright © 2018 Bedell, Song, Li, Molinich, Lin, Stiller, Danda, Ecker, Shoffstall, Voit, Pancrazio and Capadona. This is an open-access article distributed under the terms of the Creative Commons Attribution License (CC BY). The use, distribution or reproduction in other forums is permitted, provided the original author(s) and the copyright owner(s) are credited and that the original publication in this journal is cited, in accordance with accepted academic practice. No use, distribution or reproduction is permitted which does not comply with these terms.

frontiers in Bioengineering and Biotechnology

ORIGINAL RESEARCH
published: 15 November 2018
doi: 10.3389/fbioe.2018.00171

Diamond/Porous Titanium Nitride Electrodes With Superior Electrochemical Performance for Neural Interfacing

Suzan Meijs[1], Matthew McDonald[2], Søren Sørensen[3], Kristian Rechendorff[3], Ladislav Fekete[4], Ladislav Klimša[4], Václav Petrák[4†], Nico Rijkhoff[1], Andrew Taylor[4], Miloš Nesládek[2] and Cristian P. Pennisi[5]*

[1] SMI, Department of Health, Science and Technology, Aalborg University, Aalborg, Denmark, [2] Institute for Materials Research, University of Hasselt, Diepenbeek, Belgium, [3] Materials Division, Danish Technological Institute, Århus, Denmark, [4] Department of Functional Materials, Institute of Physics of the Czech Academy of Sciences, Prague, Czechia, [5] Laboratory for Stem Cell Research, Department of Health Science and Technology, Aalborg University, Aalborg, Denmark

OPEN ACCESS

Edited by:
Jeffrey R. Capadona, Case Western Reserve University, United States

Reviewed by:
Diego Mantovani, Laval University, Canada
Rajendra K. Singh, Institute of Tissue Regeneration Engineering (ITREN), South Korea

***Correspondence:**
Cristian P. Pennisi
cpennisi@hst.aau.dk

†Present Address:
Václav Petrák, Faculty of Biomedical Engineering, Department of Natural Sciences, Czech Technical University, Kladno, Czechia

Specialty section:
This article was submitted to Biomaterials, a section of the journal Frontiers in Bioengineering and Biotechnology

Received: *29 June 2018*
Accepted: *25 October 2018*
Published: *15 November 2018*

Citation:
Meijs S, McDonald M, Sørensen S, Rechendorff K, Fekete L, Klimša L, Petrák V, Rijkhoff N, Taylor A, Nesládek M and Pennisi CP (2018) Diamond/Porous Titanium Nitride Electrodes With Superior Electrochemical Performance for Neural Interfacing. Front. Bioeng. Biotechnol. 6:171. doi: 10.3389/fbioe.2018.00171

Robust devices for chronic neural stimulation demand electrode materials which exhibit high charge injection (Q_{inj}) capacity and long-term stability. Boron-doped diamond (BDD) electrodes have shown promise for neural stimulation applications, but their practical applications remain limited due to the poor charge transfer capability of diamond. In this work, we present an attractive approach to produce BDD electrodes with exceptionally high surface area using porous titanium nitride (TiN) as interlayer template. The TiN deposition parameters were systematically varied to fabricate a range of porous electrodes, which were subsequently coated by a BDD thin-film. The electrodes were investigated by surface analysis methods and electrochemical techniques before and after BDD deposition. Cyclic voltammetry (CV) measurements showed a wide potential window in saline solution (between −1.3 and 1.2 V vs. Ag/AgCl). Electrodes with the highest thickness and porosity exhibited the lowest impedance magnitude and a charge storage capacity (CSC) of 253 mC/cm^2, which largely exceeds the values previously reported for porous BDD electrodes. Electrodes with relatively thinner and less porous coatings displayed the highest pulsing capacitances (C_{pulse}), which would be more favorable for stimulation applications. Although BDD/TiN electrodes displayed a higher impedance magnitude and a lower C_{pulse} as compared to the bare TiN electrodes, the wider potential window likely allows for higher Q_{inj} without reaching unsafe potentials. The remarkable reduction in the impedance and improvement in the charge transfer capacity, together with the known properties of BDD films, makes this type of coating as an ideal candidate for development of reliable devices for chronic neural interfacing.

Keywords: neural prosthesis, neural interfaces, implantable electrodes, electrical stimulation, boron-doped diamond, porous diamond, titanium nitride, electrochemistry

INTRODUCTION

Nanocrystalline diamond films synthesized by means of chemical vapor deposition (CVD) represent a unique class of materials with outstanding physical and chemical properties, including superior hardness and the ability to resist extreme corrosive environments (Williams, 2011). Besides these features, electrically conductive boron-doped diamond (BDD) exhibits a wide potential window and low background currents, which make it a fascinating material for electrochemical applications (Rao and Fujishima, 2000). During the last few decades, BDD has been employed for the fabrication of electrodes for a wide range of applications, including electroanalysis (Compton et al., 2003; Suzuki et al., 2007; Schwarzová-Pecková et al., 2017), electrosynthesis (Kraft, 2007; Ivandini and Einaga, 2017; Ashcheulov et al., 2018), and biosensing (Vermeeren et al., 2009; Zhou and Zhi, 2009; Qureshi et al., 2010; Svítková et al., 2016). More recently, BDD attracted attention as electrode material for neurochemical sensing, neural recording, and neural stimulation applications, both *in vitro* and *in vivo* (Hébert et al., 2014b; Garrett et al., 2016). Studies have shown that BDD microelectrodes are suitable for the measurement of bioelectric potentials from cultured mammalian neural cells (Ariano et al., 2005; McDonald et al., 2017) and from neural tissue in acute settings (Ho-Yin et al., 2009). BDD holds also great promise for the fabrication of implantable electrodes for chronic application, as the material exhibits extraordinary physical stability, biocompatibility, and resistance to protein biofouling *in vivo* (Alcaide et al., 2016b; Meijs et al., 2016a). However, in contrast to conventional electrode materials, planar BDD films display relatively lower double layer capacitance, and high impedance (Swain, 1994; Alehashem et al., 1995). This is a drawback for neural stimulation applications, as the amount of charge that can be effectively injected through electrodes with relatively small contact sites is quite limited.

Several approaches have been proposed to increase the effective electrochemical area of BDD films as means to boost the amount of charge that could be transferred through the interface. In classical top-down strategies, diamond films are typically etched under a reactive plasma atmosphere to increase their porosity (Yu et al., 2014). In this direction, Kiran et al. have demonstrated successful *in vitro* recording and stimulation of neural preparations using microelectrode arrays (MEAs) comprising "nanograss" BDD contact sites (Kiran et al., 2013). Although this approach has shown to achieve a moderate increase in the electrode capacitance, the fabrication method remains complex and time-consuming, compromising its industrial viability. Alternatively, in bottom-up strategies, a highly porous substrate is used as a template onto which thin diamond films are deposited. Some examples within the various types of porous templates include vertically aligned carbon nanotubes (Hébert et al., 2014a; Zanin et al., 2014), TiO_2 nanostructures (Siuzdak et al., 2015), and SiO_2 fibers (Petrák et al., 2017; Vlčková Živcová et al., 2018). Accordingly, BDD electrodes using 3 μm-long vertically aligned carbon nanotubes as an interlayer template have displayed a significant increase in charge storage capacity (CSC) and reduction in the impedance. This improvement in the electrochemical properties allowed successful stimulation and recording of electrical activity in excised mouse hindbrain preparations (Piret et al., 2015). However, integration of carbon nanotubes in implantable neural probes still faces some concerns, due to the risks of long-term cytotoxic effects and the mechanical damage that might occur during implantation (Musa et al., 2012; Liu et al., 2013).

Titanium nitride (TiN) is an attractive material, which can be applied for the fabrication of porous templates with high electrochemical surface area (ESA) by simple physical vapor deposition techniques. Porous TiN coatings have long been employed for pacemaker electrodes and have also been used for fabrication of neural stimulation and recording electrodes (Norlin et al., 2005; Specht et al., 2006; Meijs et al., 2015a). The porosity of TiN films can be easily controlled by adjusting the deposition parameters, such as gas composition, flow rate, and deposition time (Norlin et al., 2005; Cunha et al., 2009). The pores extend deep into the coating, resulting in a high ESA and a high CSC (Cunha et al., 2009). In a preliminary study, we have confirmed the feasibility of fabricating electrodes based on a thin-film BDD deposited on TiN and shown that these electrodes exhibited a relatively high CSC due to the wide potential window typical for BDD (Meijs et al., 2015b).

In this work, the aim is to identify deposition conditions that would allow fabricating BDD electrodes suitable for neural stimulation applications. A range of porous TiN electrodes was fabricated and subsequently deposited with a BDD thin-film. The morphology, quality, and surface properties of the resulting BDD/TiN films were characterized. In addition, we assessed the influence of the underlying TiN film parameters on the electrochemical performance of the electrodes by means of cyclic voltammetry (CV), voltage transient (VT) measurements, and electrochemical impedance spectroscopy (EIS).

MATERIALS AND METHODS

Electrode Fabrication

The test samples were fabricated using a monopolar Ti_6Al_4V electrode pin, which belongs to a system intended for genital nerve stimulation (Martens et al., 2011). Seven types of TiN coatings were evaluated, which were deposited on the electrodes' contact sites by reactive DC magnetron sputtering. Deposition was carried out using an industrial coating unit (CC800, CemeCon AG, Germany) from two Ti targets (88 × 200 mm) with 99.5% purity in a mixed Ar/N_2 atmosphere. In one set of samples (designated as samples I to V), the N_2 flow was varied from 30 to 300 standard cubic centimeters per min (sccm), while the deposition time was kept constant at 27.5×10^3 s. In another set of samples (designated as samples III, VI, and VII), the flow rate of N_2 was kept at 180 sccm while the deposition time was modified. In both cases, the Ar flow was kept constant at 180 sccm.

BDD thin films were synthesized on the TiN layers using an Astex AX6500 microwave plasma enhanced CVD system. The TiN-coated electrodes were first immersed in a 0.33 g/L solution of diamond nanoparticles (3.8 ± 0.7 nm) from Shinshu University to seed the surface for diamond growth. Hydrogen gas

with an addition of 1% CH_4 was added to the chamber at a total flow rate of 500 sccm. Tri-methyl boron was added to the gas as the dopant source, at boron to carbon concentrations of 10,000 ppm. The substrate temperature was maintained at ∼750°C by using a pressure of 25 Torr (3.33 kPa) and a microwave power of 2,500 W.

Surface Characterization

The TiN thin-films were investigated using scanning electron microscopy (SEM) (Nova 600, FEI, The Netherlands). Detailed images of all electrodes were recorded at 80,000× magnification. For the assessment of film thickness, flat substrates (10 × 10 mm) obtained from silicon wafers were coated during deposition of each batch of electrodes. The silicon substrates were placed in a manner that ensured an even coating thickness. The coated substrates were subsequently broken and analyzed by cross sectional SEM. The thickness was measured via analysis of the SEM micrographs using Image J (NIH, Bethesda, MD). Each sample was measured at several locations along the cleavage to assess for thickness variations. Only small variations were observed and a unique thickness could unambiguously be assigned to each sample. The surface morphology of the BDD/TiN films was analyzed by a FERA3 GM SEM (Tescan, Czech Republic) with Schottky field emission cathode (FEG-SEM). Images were taken in the high-resolution mode at the accelerating voltage of 5 kV to minimize the interaction volume.

Raman spectroscopy of BDD/TiN films was carried out at room temperature using an InVia Raman Microscope (Renishaw ApS, Denmark) with the following conditions: wavelength = 325 nm, ×40 Olympus objective, 65 μm slits, spot focus, grating = 2,400 L/mm. A high pressure, high temperature Ib single crystal diamond was used as a reference for the sp^3 Raman peak position.

Topography and surface roughness over a large area (220 × 280 μm^2) was investigated by an optical profilometer (NewView 7200, ZYGO, Middlefield, CT). In addition, surface roughness and topography over a small area (5 × 5 μm^2) were investigated by atomic force microscopy (AFM) using a Dimension Icon ambient AFM (Bruker, Germany) in peak force tapping mode using Tap150AL-g tips (BudgetSensors, Innovative Solutions Bulgaria).

Electrochemical Measurements

All electrochemical measurements were carried out in a three-electrode set-up, using the either the TiN or the BDD/TiN electrodes as working electrodes (0.06 cm^2), a platinum foil counter electrode (50 cm^2), and a Ag|AgCl reference electrode (1.6 cm^2). Measurements were performed in Ringer's solution at room temperature.

Cyclic voltammetry was performed by cycling the electrode potential between the water window limits. These limits were determined by increasing and decreasing the electrode potential until an exponentially increasing current was observed using a sweep rate of 0.05 V/s. Measurements were made at 0.05, 0.1, 0.5, and 1.0 V/s; 10 cycles were recorded at each sweep rate. The cathodic CSC of the electrodes was found by calculating the surface area under the zero current axis. The electrochemical surface area to geometrical surface area (ESA/GSA) ratio was calculated by dividing the CSC of the porous coatings by the CSC of the corresponding smooth coating at a sweep rate of 0.05 V/s.

Voltage transient measurements were made using a cathodic-first bipolar symmetric current pulse with an interphase, during which no current was applied. Each phase had a phase width of 200 μs and the duration of the inter-phase was 40 μs. For analysis of the VTs, the OCP was set to 0 V and the IR drop was subtracted. The IR-drop was calculated for each phase by subtracting the potential at 20 μs after pulse cessation from the last data point of the respective phase. The pulsing capacitance (C_{pulse}) was calculated for each pulse using the following equation:

$$I_{stim} = C_{pulse} \times \frac{dV}{dt}$$

where I_{stim} is the stimulation current and dV/dt is the slope of the last 90% of the cathodic phase of the VT. The C_{pulse} of the type I TiN electrodes was determined at a current at which safe potential limits were reached. The C_{pulse} of the other electrodes was determined at a stimulation current of 20 mA.

Cyclic voltammetry and VT measurements were performed with VersaSTAT 3 potentio-galvanostat (Princeton Applied Research, USA). The impedance spectrum was measured from 0.1 Hz to 100 kHz, five points/decade using a sinusoidal measurement current of 5.0 μA. Impedance spectroscopy was performed using Solartron, Model 1294 in conjunction with 1260 Impedance/gain-phase Analyzer (Solartron Analytical, UK). Linear regression analyses of the CSC and C_{pulse}-values were performed in Prism 7 (GraphPad Software Inc, La Jolla, CA).

RESULTS

Effect of Deposition Conditions on the Surface Properties of TiN Films

The influence of deposition parameters on thickness and morphology of the TiN films was investigated by depositing films at different partial pressures of N_2 while keeping the deposition time at 27.5 × 10^3 s. The partial pressure of N_2 in the deposition chamber was modified by varying the N_2 flow rate. At the lowest flow rate, the TiN films displayed a relatively smooth surface (**Figure 1A**). These samples, designated as type I, were used as substrates for the planar reference coatings throughout the study. The remaining films, deposited at N_2 flow rates ranging from 120 sccm and above, consisted of rough surfaces displaying pyramidal-like features whose lateral dimensions decreased at higher N_2 flow rates (Samples II–V, **Figure 1A**). The porous TiN films comprise of a highly dense columnar-type structure, with pyramidal features at the top of the columns. The typical cross-section profile of porous TiN films is shown in the **Supplementary Figure 1**. Thickness displayed a non-monotonic dependence on the N_2 flow rate (**Figure 1C**). The maximum film thickness was obtained at 180 sccm (sample type III), where the partial pressures of N_2 and Ar are equal. Subsequently, the effect of deposition time on thickness and morphology of films was assessed by depositing films at a shorter and a longer time interval in relation to sample III (samples VI

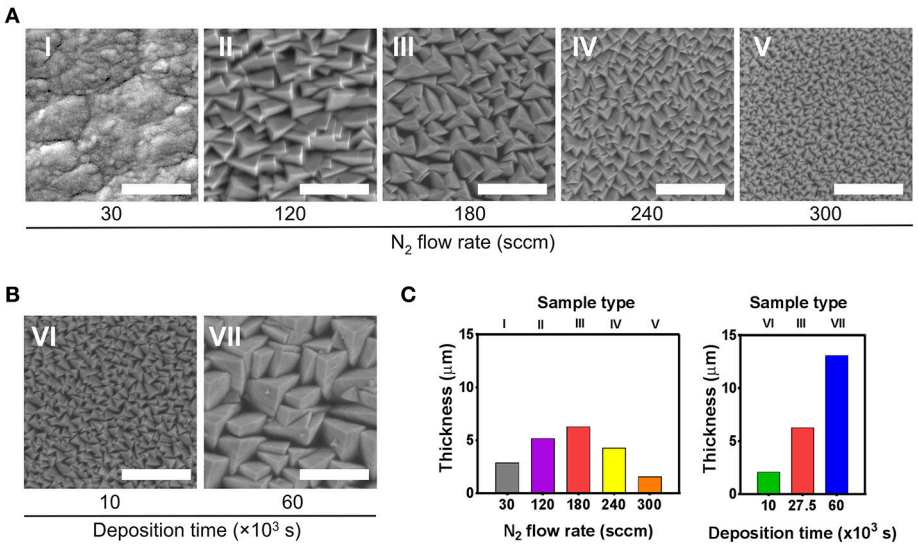

FIGURE 1 | Scanning electron microscopy (SEM) analysis of the seven types of prepared TiN films (I–VII). **(A)** Effect of varying the N_2 flow rate on film morphology. For this set of samples (I–V), the deposition time was kept at 27.5 × 10^3 s. Films type I were used as smooth reference coatings. **(B)** Effect of varying the deposition time on film morphology, while keeping the N_2 flow rate at 180 sccm. **(C)** Thickness of the films displayed in **(A,B)**. Scale bar in SEM images represents 1 μm.

and VII). The column size (**Figure 1B**) as well as film thickness (**Figure 1C**) correlated directly to the deposition time.

Assessment of the Surface Properties of BDD/TiN Films

Diamond thin-films were synthesized on all types of TiN coating (I–VII). SEM images (**Figure 2A**) along with AFM images (**Figure 2B**) show the morphology of BDD films grown on four representative substrates: smooth TiN (type I), and the three electrodes grown at a growth rate of 180 sccm (types III, VI, and VI). SEM images revealed that the BDD films had a uniform coverage on the TiN and displayed a nanocrystalline structure with a grain size of ∼50 nm. Due to the electrode geometry, *in situ* BDD-film thickness measurements were not possible, however, deposition onto silicon substrates at identical conditions resulted in film thicknesses in the order of the grain size (i.e., ∼50–70 nm).

The large-scale topography of the diamond films, as measured using an optical profilometer over an area of 220 × 280 μm^2, was governed by grooves on the underlying TiAlV substrate, which are ∼20 μm wide and up to 400 nm high. The roughness on this scale was around 200–350 nm and it was not significantly influenced by the TiN or the BDD coating. However, the small-scale topography measured by AFM over an area of 5 × 5 μm^2 was mostly governed by the topography of the TiN pyramidal structure. The roughness of the diamond layer, which measured on a flat surface was around 30 nm, had only a minimal influence on the topography of the BDD/TiN films. **Figure 2C** shows the RMS surface roughness of the selected sample types before and after BDD deposition. As the electrode surface is not flat the error in the estimation of the roughness is ∼20% when measured on different areas on the pin.

Raman spectroscopy confirmed the synthesis of diamond films in all TiN substrates. **Figure 2D** displays the Raman spectra of BDD films grown on the selected sample types. In all spectra, a shifted diamond peak is observed at 1,320–1,328 cm^{-1} as well as broad features related to sp^2 at 1,360 and 1,585 cm^{-1}, i.e., the D and G bands.

Electrochemical Characterization

The water window potentials were obtained by CV and their values were typically −0.6 to 0.9 V for TiN and −1.3 to 1.2 V for BDD/TiN electrodes (vs. Ag|AgCl). **Table 1** summarizes the cathodic CSC-values which were obtained at a sweep rate of 0.05 V/s. The CSC obtained at a slow sweep rate gives an insight into the entire ESA of the porous electrodes. Due to the wide potential window brought by the BDD coating, the CSC of the BDD/TiN electrodes was consistently higher than the CSC of bare TiN electrodes. The CSC-values pre- and post-BDD deposition followed a linear relationship with a slope of 2.2, indicating that the CSC-values of the electrodes doubled upon BDD deposition (**Supplementary Figure 2**). It was also noticed that the CSC-values were drastically increased in all porous samples as compared to the smooth reference electrodes, for which the CSC-values were 0.36 and 7.74 mC/cm^2, respectively. **Table 1** includes the ESA/GSA ratio, which reflects the relative increase in the ESA for each of the porous samples, before and after BDD deposition. **Figure 3A** displays representative CV curves from electrodes type III, VI, and VI, before and after BDD deposition, where it is possible to observe the relative increase in the CSC when TiN films become deposited with BDD. As shown in **Figure 3B**, the CSC of these electrodes appears to increase linearly with an increase in the TiN coating thickness. The CSC-values fit a linear regression with a slope of 6.7 $mC/cm^2.\mu m$ for

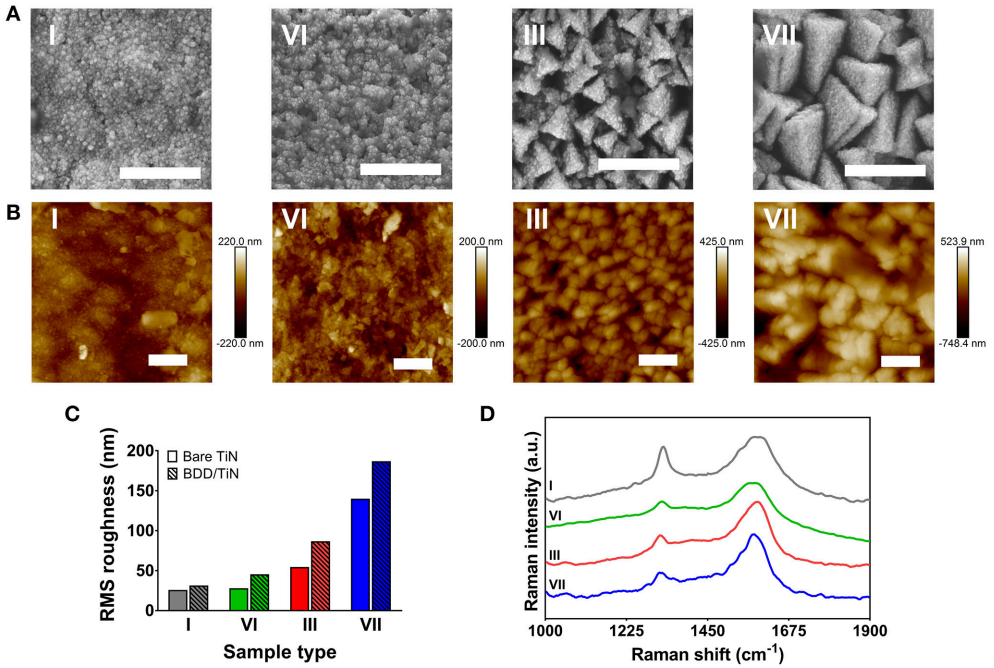

FIGURE 2 | Surface analysis of four representative electrodes (type I, III, VI, and VII). **(A)** Scanning electron microscopy (SEM) images displaying the uniform coverage of the nanocrystalline diamond layer. Scale bar represents 1 μm. **(B)** Atomic force microscopy (AFM) height images. Scale bar represents 1 μm. **(C)** AFM surface roughness measurements from the films displayed in **(B)** before (bare TiN) and after diamond deposition (BDD/TiN). **(D)** 325-nm Raman spectra showing the diamond-related peak between 1,320 and 1,328 cm^{-1}. The spectra have been offset for clarity.

TABLE 1 | Cathodic CSC of the bare TiN and BDD/TiN electrodes obtained at 0.05 V/s.

	TiN		BDD/TiN	
Sample type	**CSC (mC/cm^2)**	**ESA/GSA ratio**	**CSC (mC/cm^2)**	**ESA/GSA ratio**
I	0.36	–	7.74	–
II	54	150	105	14
III	69	190	143	19
IV	86	238	177	23
V	58	159	136	18
VI	32	89	99	13
VII	107	295	253	33

The ESA/GSA ratios were calculated by dividing the CSC of each of the porous coatings by the CSC of the smooth reference coatings.

the bare TiN films ($r^2 = 0.98$) and 14.2 $mC/cm^2.\mu m$ for the BDD/TiN films ($r^2 = 0.99$), but the slopes are not significantly different ($P > 0.05$).

Table 2 summarizes the C_{pulse} for all electrode types, which was derived from the VT measurements. Except for electrode type I, the C_{pulse} of the BDD/TiN electrodes was consistently lower than the C_{pulse} of the corresponding TiN electrodes. **Figure 4A** shows representative VT measurements on electrodes type III, VI, and VII, before and after BDD coating. As compared to the bare TiN electrodes, the lower C_{pulse} of BDD/TiN electrodes leads to larger electrode potentials. However, as the safe potential window for BDD is larger than for TiN, the amount of charge that can safely be injected will be higher for BDD/TiN than for TiN. C_{pulse} displays a negative trend for both TiN and BDD/TiN electrodes as a function of TiN coating thickness (**Figure 4B**). The C_{pulse}-values fit similar linear regressions, with a slope of -0.051 $mF/cm^2.\mu m$ for the bare TiN films ($r^2 = 0.82$) and -0.052 $mF/cm^2.\mu m$ for the BDD/TiN films ($r^2 = 0.77$).

As anticipated, increased film porosity significantly reduced the impedance of the electrodes (**Figure 5**). The impedance magnitudes of the TiN and BDD/TiN porous electrodes were only different at frequencies below 10 Hz. The greatest difference in impedance magnitude between TiN and BDD/TiN was at 100 mHz, where the BDD electrodes consistently had a higher impedance than the TiN electrodes. The impedance magnitude of both BDD and TiN electrodes decreased with increasing thickness. The lowest impedance magnitude for TiN with and without BDD coating were obtained using the electrode with the thickest TiN coating (type VII).

DISCUSSION

A range of porous TiN films, to be used as templates, was deposited onto test electrodes by means of a physical vapor deposition. The smooth TiN reference films were fabricated using a low partial pressure of N_2 to ensure a stoichiometric Ti/N ratio below 0.6, which has been shown to be unfavorable for columnar growth (Igasaki et al., 1978; Cunha et al., 2009). Formation of

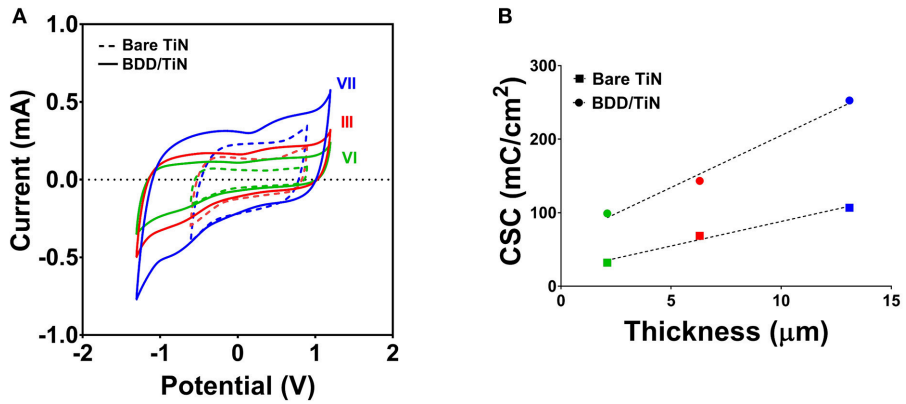

FIGURE 3 | Cyclic voltammetry measurements of electrodes type III, VI, and VII before (bare TiN) and after BDD deposition (BDD/TiN). **(A)** Cyclic voltammograms showing that the safe potential limits are increased in BDD/TiN electrodes as compared to the bare counterparts. The potential limits are the same within the two electrode groups. **(B)** Cathodic charge storage capacity (CSC) of the electrodes as a function of the underlying TiN film thickness, showing that CSC-values were consistently increased after BDD deposition. Data from samples type III, VI, and VII are shown in red, green, and blue, respectively. Dotted lines represent the linear regression of the CSC-values.

TABLE 2 | Pulsing capacitance of the bare TiN and BDD/TiN electrodes.

Sample type	TiN (mF/cm^2)	BDD/TiN (mF/cm^2)
I	0.024	0.059
II	1.6	1.6
III	2.2	1.4
IV	1.9	1.5
V	2.0	1.5
VI	2.1	1.8
VII	1.6	1.2

Values are derived from the voltage transient measurements.

the columnar, highly porous structures was favored using N_2 flow rates of 120 sccm and above. For the set of samples II–V, higher N_2 flow rates resulted in decreased film columnar width. This effect has been associated to a reduced mobility of the deposited atoms as a consequence of a weakening in the argon bombardment (Arshi et al., 2012). Furthermore, increasing the N_2 flow poisons the Ti targets to the extent where the entire target surface is covered in TiN. This effect decreases the deposition rate as the sputter yield is lower for TiN than for Ti (Berg and Nyberg, 2005), which also results in thinner films with smaller columns. The deposition rate appeared to be maximal at a N_2 flow rate of 180 sccm, where the N_2 flow rate equals that of Ar and it is assumed that deposition occurs at a stoichiometric Ti/N ratio. TiN films with stoichiometric Ti/N composition are usually preferred due to their optimal mechanical and electrical properties (Kang and Kim, 1999; Martinez et al., 2014). Samples III, VI, and VII were therefore deposited keeping the N_2 flow constant and varying the deposition time to obtain porous films with similar crystalline composition but different thickness. A longer deposition time increased the columnar width, which is a result of the competitive growth where some columns grow at the expense of others. Such a growth is typically observed for coatings deposited at a relatively low temperature compared to the melting temperature of the coating material (Ohring, 2002). For the TiN films, increasing the N_2 flow (in samples I–III) led to higher thickness and higher porosity, which was reflected as an increased ESA/GSA ratio. Further increase in N_2 (sample IV) still gave an increase in area due to increased porosity, although the thickness was smaller. Going to higher N_2 the growth rate was slower, so that the lower thickness dominated over the increased porosity and an overall decrease in the ESA/GSA was obtained. For the samples grown at constant gas flow rate (III, VI, and VII), film thickness, and ESA/GSA ratio were directly correlated.

Surface analysis of the BDD/TiN samples by SEM and AFM revealed homogeneous and high quality BDD films. The overall structure and topography of the films appeared similar to the bare TiN samples, suggesting that CVD deposition did not significantly affect the morphology of the TiN template. The uniform coverage of diamond crystallites indicates a highly cohesive diamond film. This is in agreement with previous studies, which have shown that TiN possesses several favorable properties for nucleation and growth of good quality CVD diamond films, including low diffusivity of carbon, compatible interatomic potential, and small lattice mismatch (Weiser et al., 1992; Kumar et al., 1997; Polini et al., 2006). In addition, since TiN exhibits a moderate interface reactivity, its surface is stable under high-temperature diamond–CVD deposition (Contreras et al., 2000). Moreover, given the similar thermal expansion coefficient of both materials, the interlayer stresses are minimal, which ensures the synthesis of highly adherent diamond layers (Kumar et al., 1997). Although we did not encounter any evidence of cracks or film delamination, future studies should further investigate the nature the BDD/TiN interlayer by appropriate techniques, as for instance transmission electronic microscopy (TEM). Concerning the Raman analysis, the shifts in diamond's Raman peak can be related to a variation

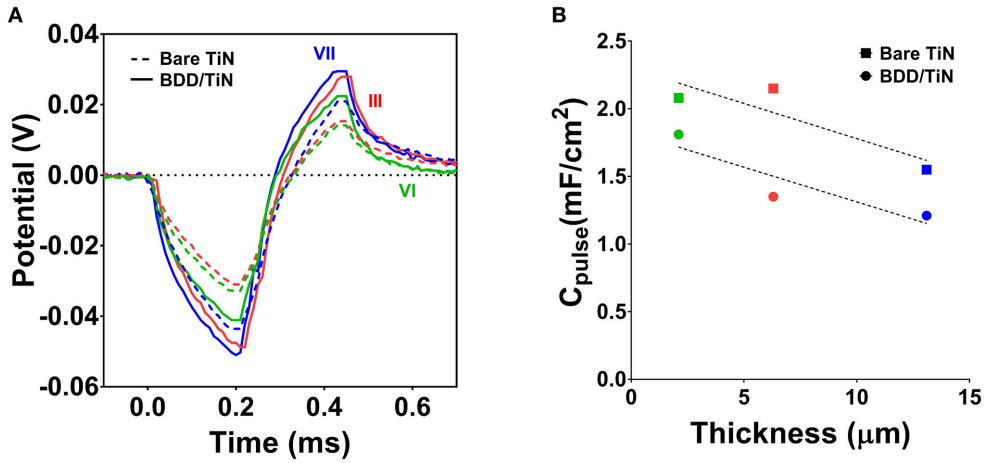

FIGURE 4 | Voltage transient measurements of electrodes type III, VI, and VII before (bare TiN) and after BDD deposition (BDD/TiN). **(A)** The voltage transients of the BDD/TiN electrodes were larger than those of the bare TiN electrodes, evidencing a decrease in the pulsing capacitance (C_{pulse}). **(B)** C_{pulse} of the electrodes as a function of the underlying TiN film thickness, showing that C_{pulse}-values were decreased after BDD deposition. Data from samples type III, VI, and VII are shown in red, green, and blue, respectively. Dotted lines represent the linear regression of the C_{pulse}-values.

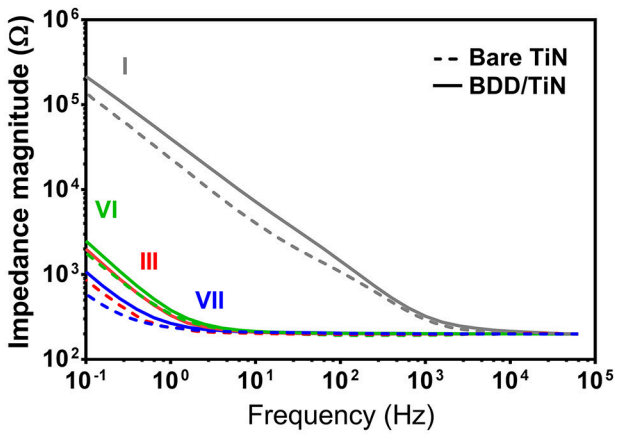

FIGURE 5 | Impedance magnitude spectra of electrodes type I, III, VI, and VII before (bare TiN) and after BDD deposition (BDD/TiN). Data from electrodes type I, III, VI, and VII are shown in gray, red, green, and blue, respectively.

of stress in layers, nonetheless its shift to lower wavenumbers is associated with increasing B incorporation in the lattice (Prawer and Nemanich, 2004). It is worth noting that the spectra in **Figure 2D** are representative only, i.e., the ratio of sp^3/sp^2 changes with measurement position. This apparent variation in sp^3/sp^2 is related to the fact that the BDD coating is very thin and therefore the grain boundary content is high.

The superior ESA of the TiN coatings used as porous templates is evident from the high ESA/GSA ratios and the drastic reduction in the impedance magnitudes. Thicker films had a consistently higher CSC, suggesting that pores extend into the entire depth of the coating, which is in agreement with previous studies (Norlin et al., 2005; Cunha et al., 2009). BDD deposition onto the TiN coatings significantly increased the CSC of the electrodes due to the wide potential window of diamond. The linear correlation between the CSC of the TiN and the BDD/TiN electrodes indicates that the diamond films did not block the pores. On the other hand, the C_{pulse} showed a negative correlation with film thickness, as the highest C_{pulse}-values were obtained with thinner coatings and smaller column width. The BDD films might therefore cause narrowing of the pores, with a consequent increase in the pore resistance. This effect decreases the pore depth that can be used under pulsing conditions (Cogan, 2008). Thus, increasing the coating thickness beyond a certain level would be less advantageous for electrical stimulation purposes. While C_{pulse} is decreased for BDD/TiN as compared to bare TiN electrodes, it is important to view this result in the light of the wide safe potential window of BDD (Garrett et al., 2011). The decrease in C_{pulse} after depositing BDD ranged from 67% to <1%, while the cathodic potential limit was more than doubled (−0.6 V for TiN vs. −1.3 for BDD/TiN). This means that the amount of charge that can be injected without reaching unsafe potentials is doubled by applying a BDD thin-film onto a porous TiN coating. It is important to view these results in the light of the intended application of the BDD/TiN electrodes, which is *in vivo* chronic neurostimulation. It has been shown that the stimulation performance of TiN electrodes deteriorates after implantation (Meijs et al., 2015a, 2016b,c). This is not the case for BDD electrodes, which display a remarkable resistance to protein biofouling (Trouillon and O'Hare, 2010; Alcaide et al., 2016a; Meijs et al., 2016a). Nevertheless, protein adsorption is influenced by surface topography, which warrants further investigation of the electrochemical performance of porous BDD/TiN electrodes in protein-rich environments.

The relatively low C_{pulse} and high impedance shown by the smooth BDD electrodes was evident and corresponds well to what has been shown in previous studies (Garrett et al., 2011; Meijs et al., 2013). Remarkably, the electrochemical performance of BDD displayed a significant improvement thanks to the

large ESA gained by using the porous TiN templates. As previous studies have shown, other porous templates have been instrumental in enhancing the electrochemical performance of BDD (Bonnauron et al., 2008; Kiran et al., 2013; Hébert et al., 2014a). A notable example is the growth of BDD on vertically aligned nanotubes, which has shown to increase the CSC of BDD up to 10 mC/cm^2 (Piret et al., 2015). The BDD/TiN electrodes in the current, however, displayed CSC-values up to 253 mC/cm^2 for the type VII electrode. Furthermore, while the use of carbon nanotube based materials for human implants remains controversial due to evidence of cytotoxic effects (Smart et al., 2006; Liu et al., 2013), both TiN and BDD have demonstrated low risk of cytotoxicity and excellent biocompatibility in diverse applications. TiN is well known for improving the electrochemical and biocompatibility properties of various materials (Subramanian et al., 2011) and represents one of the coatings with a long history of clinical use for orthopedic implants (Gotman et al., 2014; van Hove et al., 2015). Data from implantation studies revealed that BDD electrodes are associated with no signs of chronic inflammation and a very thin fibrous capsule (Alcaide et al., 2016b). Taken together, these results indicate that this novel type of combined coating may be used to fabricate safe implants for clinical use. Furthermore, the method can be easily scaled-up, making the production process fast and cost-effective (Taylor et al., 2014, 2018). The production process is reproducible and clean, as both coatings are deposited under vacuum conditions. Overall, these factors make this novel type of coating particularly attractive for the development of commercially viable electrodes for neural interfacing.

To achieve an increased charge injection (Q_{inj}), the production parameters are of critical importance, as the extra coating increases the pore resistance, which may deteriorate Q_{inj}. This study suggests that specific deposition parameters are optimal for stimulation electrodes, as increased thickness and N_2 flow only result to a certain extent in larger C_{pulse} and Q_{inj}. The data suggests that BDD deposited onto thinner coatings with smaller columnar size results in better stimulation performance. A thicker coating, however, results in a high CSC and low impedance, which could be exploited for other purposes, such as electrical and electrochemical sensing. This highlights the versatility of the novel coating combination presented in this work.

CONCLUSION

In this work, we have fabricated a range of BDD/porous TiN electrodes with very high surface area, which exhibit a broad safe potential window and CSC-values which are superior to those reported in the literature for porous BDD electrodes. Electrodes with more porous and thick coatings were associated with higher CSC and lower impedance magnitudes, but the relatively limited C_{pulse} would make them more suited for sensing applications. On the other hand, relatively higher C_{pulse} were obtained with thinner films with small column size, which would result more favorable for stimulation applications. Although BDD/TiN electrodes displayed a higher impedance magnitude and a lower C_{pulse} as compared to the bare TiN electrodes, the wider potential window likely allows for higher Q_{inj} without reaching unsafe potentials. These remarkable improvements, together with the known mechanical stability, resistance to biofouling and long-term *in vivo* stability of BDD films, makes this coating combination an ideal candidate for development of reliable devices for chronic neural interfacing. This novel type of coating is particularly attractive for the development of commercially viable electrodes due to the simplicity and the scalability of the approach.

AUTHOR CONTRIBUTIONS

AT, MN, and CP conceived and designed the study. SM, MM, SS, and KR prepared the samples. MM, SS, KR, LF, LK, and AT obtained the data and performed the surface analysis of the films. SM and VP acquired and analyzed the electrochemistry data under supervision of NR. SM and CP drafted the manuscript and designed the figures. All authors contributed to the critical revision of the draft and approved the submitted version.

FUNDING

This work was supported by the EU through the project MERIDIAN (Micro and Nano Engineered Bi-Directional Carbon Interfaces for Advanced Peripheral Nervous System Prosthetics and Hybrid Bionics), contract number 280778-02, by the Danish National Advanced Technology Foundation, and by the Czech Science Foundation (contract 17-15319S). AFM and SEM equipment were partially funded by projects LM2016088 and LO1409, Ministry of Education, Youth and Sports, Czech Republic.

SUPPLEMENTARY MATERIAL

The Supplementary Material for this article can be found online at: https://www.frontiersin.org/articles/10.3389/fbioe.2018.00171/full#supplementary-material

REFERENCES

Alcaide, M., Papaioannou, S., Taylor, A., Fekete, L., Gurevich, L., Zachar, V., et al. (2016a). Resistance to protein adsorption and adhesion of fibroblasts on nanocrystalline diamond films: the role of topography and boron doping. *J. Mater. Sci. Mater. Med.* 27:90. doi: 10.1007/s10856-016-5696-3

Alcaide, M., Taylor, A., Fjorback, M., Zachar, V., and Pennisi, C. P. (2016b). Boron-doped nanocrystalline diamond electrodes for neural interfaces: *in vivo* biocompatibility evaluation. *Front. Neurosci.* 10:87. doi: 10.3389/fnins.2016.00087

Alehashem, S., Chambers, F., Strojek, J. W., Swain, G. M., and Ramesham, R. (1995). Cyclic voltammetric studies of charge transfer reactions at highly boron-doped polycrystalline diamond thin-film electrodes. *Anal. Chem.* 67, 2812–2821. doi: 10.1021/ac00113a014

Ariano, P., Baldelli, P., Carbone, E., Gilardino, A., Lo Giudice, A., Lovisolo, D., et al. (2005). Cellular adhesion and neuronal excitability on functionalised diamond

surfaces. *Diam. Relat. Mater.* 14, 669–674. doi: 10.1016/j.diamond.2004.11.021

Arshi, N., Lu, J., Joo, Y. K., Lee, C. G., Yoon, J. H., and Ahmed, F. (2012). Study on structural, morphological and electrical properties of sputtered titanium nitride films under different argon gas flow. *Mater. Chem. Phys.* 134, 839–844. doi: 10.1016/j.matchemphys.2012.03.078

Ashcheulov, P., Taylor, A., Mortet, V., Poruba, A., Le Formal, F., Krýsová, H., et al. (2018). Nanocrystalline boron-doped diamond as a corrosion resistant anode for water oxidation via si photoelectrodes. *ACS Appl. Mater. Interfaces* 10, 29552–29564. doi: 10.1021/acsami.8b08714

Berg, S., and Nyberg, T. (2005). Fundamental understanding and modeling of reactive sputtering processes. *Thin Solid Films* 476, 215–230. doi: 10.1016/j.tsf.2004.10.051

Bonnauron, M., Saada, S., Rousseau, L., Lissorgues, G., Mer, C., and Bergonzo, P. (2008). High aspect ratio diamond microelectrode array for neuronal activity measurements. *Diam. Rel. Mat.* 17, 1399–1404. doi: 10.1016/j.diamond.2007.12.065

Cogan, S. F. (2008). Neural stimulation and recording electrodes. *Annu. Rev. Biomed. Eng.* 10, 275–309. doi: 10.1146/annurev.bioeng.10.061807.160518

Compton, R. G., Foord, J. S., and Marken, F. (2003). Electroanalysis at diamond-like and doped-diamond electrodes. *Electroanalysis* 15, 1349–1363. doi: 10.1002/elan.200302830

Contreras, O., Hirata, G. A., and Avalos-Borja, M. (2000). Interface analysis of CVD diamond on TiN surfaces. *Appl. Surf. Sci.* 158, 236–245. doi: 10.1016/S0169-4332(00)00014-3

Cunha, L. T., Pedrosa, P., Tavares, C. J., Alves, E., Vaz, F., and Fonseca, C. (2009). The role of composition, morphology and crystalline structure in the electrochemical behaviour of TiNx thin films for dry electrode sensor materials. *Electrochim. Acta* 55, 59–67. doi: 10.1016/j.electacta.2009.08.004

Garrett, D. J., Ganesan, K., Stacey, A., Fox, K., Meffin, H., and Prawer, S. (2011). Ultra-nanocrystalline diamond electrodes: optimization towards neural stimulation applications. *J. Neural Eng.* 9:016002. doi: 10.1088/1741-2560/9/1/016002

Garrett, D. J., Tong, W., Simpson, D. A., and Meffin, H. (2016). Diamond for neural interfacing: a review. *Carbon* 102, 437–454. doi: 10.1016/j.carbon.2016.02.059

Gotman, I., Gutmanas, E. Y., and Gotman, I. (2014). Titanium nitride-based coatings on implantable medical devices. *Adv. Biomater. Devices Med.* 1, 53–73.

Hébert, C., Mazellier, J. P., Scorsone, E., Mermoux, M., and Bergonzo, P. (2014a). Boosting the electrochemical properties of diamond electrodes using carbon nanotube scaffolds. *Carbon* 71, 27–33. doi: 10.1016/j.carbon.2013.12.083

Hébert, C., Scorsone, E., Bendali, A., Kiran, R., Cottance, M., Girard, H. A., et al. (2014b). Boron doped diamond biotechnology: from sensors to neurointerfaces. *Faraday Discuss.* 172, 47–59. doi: 10.1039/C4FD00040D

Ho-Yin, C., Aslam, D. M., Wiler, J. A., and Casey, B. (2009). A novel diamond microprobe for neuro-chemical and -electrical recording in neural prosthesis. *J. Microelectromech. Syst.* 18, 511–521. doi: 10.1109/JMEMS.2009.2015493

Igasaki, Y., Mitsuhashi, H., Azuma, K., and Muto, T. (1978). Structure and electrical properties of titanium nitride films. *Jpn. J. Appl. Phys.* 17, 85–96. doi: 10.1143/JJAP.17.85

Ivandini, T. A., and Einaga, Y. (2017). Polycrystalline boron-doped diamond electrodes for electrocatalytic and electrosynthetic applications. *Chem. Commun.* 53, 1338–1347. doi: 10.1039/C6CC08681K

Kang, J. H., and Kim, K. J. (1999). Structural, optical, and electronic properties of cubic TiNx compounds. *J. Appl. Phys.* 86:346. doi: 10.1063/1.370736

Kiran, R., Cottance, M., Joucla, S., Rousseau, L., Bongrain, A., Yvert, B., et al. (2013). "Nanograss boron doped diamond microelectrode arrays for recording and stimulating neuronal tissues," in *Transducers & Eurosensors XXVII: The 17th International Conference on Solid-State Sensors, Actuators and Microsystems* (Barcelona: IEEE), 748–751.

Kraft, A. (2007). Doped diamond: a compact review on a new, versatile electrode material. *Int. J. Electrochem. Sci.* 2, 355–385.

Kumar, A., You, Q., Kapat, J., Mangiaracina, A., Catletge, A., and Vohra, Y. (1997). Evaluation of buffer layers for hot filament chemical vapor deposition diamond films on silicon substrates. *Thin Solid Films* 308–309, 209–214. doi: 10.1016/S0040-6090(97)00669-X

Liu, Y., Zhao, Y., Sun, B., and Chen, C. (2013). Understanding the toxicity of carbon nanotubes. *Acc. Chem. Res.* 46, 702–713. doi: 10.1021/ar300028m

Martens, F. M., Heesakkers, J. P., and Rijkhoff, N. J. (2011). Minimal invasive electrode implantation for conditional stimulation of the dorsal genital nerve in neurogenic detrusor overactivity. *Spinal Cord* 49, 566–572. doi: 10.1038/sc.2010.134

Martinez, G., Shutthanandan, V., Thevuthasan, S., Chessa, J. F., and Ramana, C. V. (2014). Effect of thickness on the structure, composition and properties of titanium nitride nano-coatings. *Ceram. Int.* 40, 5757–5764. doi: 10.1016/j.ceramint.2013.11.014

McDonald, M., Monaco, A., Vahidpour, F., Haenen, K., Giugliano, M., and Nesladek, M. (2017). Diamond microelectrode arrays for *in vitro* neuronal recordings. *MRS Commun.* 7, 683–690. doi: 10.1557/mrc.2017.62

Meijs, S., Alcaide, M., Sørensen, C., McDonald, M., Sørensen, S., Rechendorff, K., et al. (2016a). Biofouling resistance of boron-doped diamond neural stimulation electrodes is superior to titanium nitride electrodes *in vivo*. *J. Neural Eng.* 13:056011. doi: 10.1088/1741-2560/13/5/056011

Meijs, S., Fjorback, M., Jensen, C., Sørensen, S., Rechendorff, K., and Rijkhoff, N. J. (2015a). Electrochemical properties of titanium nitride nerve stimulation electrodes: an *in vitro* and *in vivo* study. *Front. Neurosci.* 9:268. doi: 10.3389/fnins.2015.00268

Meijs, S., Fjorback, M., Jensen, C., Sørensen, S., Rechendorff, K., and Rijkhoff, N. J. M. (2016b). Influence of fibrous encapsulation on electrochemical properties of TiN electrodes. *Med. Eng. Phys.* 38, 468–476. doi: 10.1016/j.medengphy.2016.02.010

Meijs, S., McDonald, M., Sørensen, S., Rechendorff, K., Petrák, V., Nesládek, M., et al. (2015b). "Increased charge storage capacity of titanium nitride electrodes by deposition of boron-doped nanocrystalline diamond films," in *NEUROTECHNIX 2015 - Proceedings of the 3rd International Congress on Neurotechnology, Electronics and Informatics* (Lisbon).

Meijs, S., Sørensen, C., Sørensen, S., Rechendorff, K., Fjorback, M., and Rijkhoff, N. J. (2016c). Influence of implantation on the electrochemical properties of smooth and porous TiN coatings for stimulation electrodes. *J. Neural Eng.* 13:026011. doi: 10.1088/1741-2560/13/2/026011

Meijs, S., Taylor, A., Pennisi, C. P., and Rijkhoff, N. J. M. (2013). "Electrochemical characterization of boron-doped nanocrystalline diamond electrodes for neural stimulation," in *6th Annual International IEEE EMBS Conference on Neural Engineering* (San Diego, CA).

Musa, S., Rand, D. R., Cott, D. J., Loo, J., Bartic, C., Eberle, W., et al. (2012). Bottom-Up SiO_2 embedded carbon nanotube electrodes with superior performance for integration in implantable neural microsystems. *ACS Nano* 6, 4615–4628. doi: 10.1021/nn201609u

Norlin, A., Pan, J., and Leygraf, C. (2005). Investigation of electrochemical behavior of stimulation sensing materials for pacemaker electrode applications. *J. Electrochem. Soc.* 152, J85–J92. doi: 10.1149/1.1933372

Ohring, M.(ed.). (2002). "Substrate surfaces and thin-film nucleation," in *Materials Science of Thin Films* (San Diego, CA: Academic Press), 357–415. doi: 10.1016/B978-012524975-1/50010-0

Petrák, V., Vlčková Živcová, Z., Krýsová, H., Frank, O., Zukal, A., Klimša, L., et al. (2017). Fabrication of porous boron-doped diamond on SiO_2 fiber templates. *Carbon* 114, 457–464. doi: 10.1016/j.carbon.2016.12.012

Piret, G., Hébert, C., Mazellier, J.-P., Rousseau, L., Scorsone, E., Cottance, M., et al. (2015). 3D-nanostructured boron-doped diamond for microelectrode array neural interfacing. *Biomaterials* 53, 173–183. doi: 10.1016/j.biomaterials.2015.02.021

Polini, R., Kumashiro, S., Jackson, M. J., Amar, M., Ahmed, W., and Sein, H. (2006). A study of diamond synthesis by hot filament chemical vapor deposition on Nc coatings. *J. Mater. Eng. Perform.* 15, 218–222. doi: 10.1361/105994906X95913

Prawer, S., and Nemanich, R. J. (2004). Raman spectroscopy of diamond and doped diamond. *Philos. Trans. A Math. Phys. Eng. Sci.* 362, 2537–2565. doi: 10.1098/rsta.2004.1451

Qureshi, A., Gurbuz, Y., Howell, M., Kang, W. P., and Davidson, J. L. (2010). Nanocrystalline diamond film for biosensor applications. *Diam. Relat. Mater.* 19, 457–461. doi: 10.1016/j.diamond.2010.01.012

Rao, T. N., and Fujishima, A. (2000). Recent advances in electrochemistry of diamond. *Diam. Relat. Mater.* 9, 384–389. doi: 10.1016/S0925-9635(99)00234-4

Schwarzová-Pecková, K., Vosáhlová, J., Barek, J., Šloufová, I., Pavlova, E., Petrák, V., et al. (2017). Influence of boron content on the morphological, spectral, and electroanalytical characteristics of anodically oxidized boron-doped diamond

electrodes. *Electrochim. Acta* 243, 170–182. doi: 10.1016/j.electacta.2017.05.006

Siuzdak, K., Bogdanowicz, R., Sawczak, M., and Sobaszek, M. (2015). Enhanced capacitance of composite TiO 2 nanotube/boron-doped diamond electrodes studied by impedance spectroscopy. *Nanoscale* 7, 551–558. doi: 10.1039/C4NR04417G

Smart, S. K., Cassady, A. I., Lu, G. Q., and Martin, D. J. (2006). The biocompatibility of carbon nanotubes. *Carbon* 44, 1034–1047. doi: 10.1016/j.carbon.2005.10.011

Specht, H., Krüger, F., Wachter, H. J., Keitel, O., Leitold, C., and Frericks, M. (2006). "Electrochemical properties and stability of PVD coatings for the application in cardiac and neurological stimulation," in *Medical Device Materials III - Proceedings of the Materials and Processes for Medical Devices Conference* 2005 (Boston, MA), 169–173.

Subramanian, B., Muraleedharan, C. V., Ananthakumar, R., and Jayachandran, M. (2011). A comparative study of titanium nitride (TiN), titanium oxy nitride (TiON) and titanium aluminum nitride (TiAlN), as surface coatings for bio implants. *Surf. Coat. Technol.* 205, 5014–5020. doi: 10.1016/j.surfcoat.2011.05.004

Suzuki, A., Ivandini, T. A., Yoshimi, K., Fujishima, A., Oyama, G., Nakazato, T., et al. (2007). Fabrication, characterization, and application of boron-doped diamond microelectrodes for *in vivo* dopamine detection. *Anal. Chem.* 79, 8608–8615. doi: 10.1021/ac071519h

Svítková, J., Ignat, T., Švorc, L., Labuda, J., and Barek, J. (2016). Chemical modification of boron-doped diamond electrodes for applications to biosensors and biosensing. *Crit. Rev. Anal. Chem.* 46, 248–256. doi: 10.1080/10408347.2015.1082125

Swain, G. M. (1994). The Susceptibility to surface corrosion in acidic fluoride media: a comparison of diamond, HOPG, and glassy carbon electrodes. *J. Electrochem. Soc.* 141, 3382. doi: 10.1149/1.2059343

Taylor, A., Ashcheulov, P., Hubík, P., Klimša, L., Kopeček, J., Remeš, Z., et al. (2018). Precursor gas composition optimisation for large area boron doped nano-crystalline diamond growth by MW-LA-PECVD. *Carbon* 128, 164–171. doi: 10.1016/j.carbon.2017.11.063

Taylor, A., Fekete, L., Hubík, P., Jäger, A., Janíček, P., Mortet, V., et al. (2014). Large area deposition of boron doped nano-crystalline diamond films at low temperatures using microwave plasma enhanced chemical vapour deposition with linear antenna delivery. *Diam. Relat. Mater.* 47, 27–34. doi: 10.1016/j.diamond.2014.05.002

Trouillon, R., and O'Hare, D. (2010). Comparison of glassy carbon and boron doped diamond electrodes: resistance to biofouling. *Electrochim. Acta* 55, 6586–6595. doi: 10.1016/j.electacta.2010.06.016

van Hove, R. P., Sierevelt, I. N., van Royen, B. J., and Nolte, P. A. (2015). Titanium-nitride coating of orthopaedic implants: a review of the literature. *Biomed Res. Int.* 2015:485975. doi: 10.1155/2015/485975

Vermeeren, V., Wenmackers, S., Wagner, P., and Michiels, L. (2009). DNA sensors with diamond as a promising alternative transducer material. *Sensors* 9, 5600–5636. doi: 10.3390/s90705600

Vlčková Živcová, Z., Mortet, V., Taylor, A., Zukal, A., Frank, O., and Kavan, L. (2018). Electrochemical characterization of porous boron-doped diamond prepared using SiO_2 fiber template. *Diam. Relat. Mater.* 87, 61–69. doi: 10.1016/j.diamond.2018.05.007

Weiser, P. S., Prawer, S., Hoffman, A., Manory, R. R., Paterson, P. J. K., and Stuart, S. (1992). Carbon diffusion in uncoated and titanium nitride coated iron substrates during microwave plasma assisted chemical vapor deposition of diamond. *J. Appl. Phys.* 72, 4643–4647. doi: 10.1063/1.352119

Williams, O. A. (2011). Nanocrystalline diamond. *Diam. Relat. Mater.* 20, 621–640. doi: 10.1016/j.diamond.2011.02.015

Yu, Y., Wu, L., and Zhi, J. (2014). Diamond nanowires: fabrication, structure, properties, and applications. *Angew. Chem. Int. Ed. Engl.* 53, 14326–14351. doi: 10.1002/anie.201310803

Zanin, H., May, P. W., Fermin, D. J., Plana, D., Vieira, S. M., Milne, W. I., et al. (2014). Porous boron-doped diamond/carbon nanotube electrodes. *ACS Appl. Mater. Interfaces* 6, 990–995. doi: 10.1021/am4044344

Zhou, Y., and Zhi, J. (2009). The application of boron-doped diamond electrodes in amperometric biosensors. *Talanta* 79, 1189–1196. doi: 10.1016/j.talanta.2009.05.026

Conflict of Interest Statement: The authors declare that the research was conducted in the absence of any commercial or financial relationships that could be construed as a potential conflict of interest.

Copyright © 2018 Meijs, McDonald, Sørensen, Rechendorff, Fekete, Klimša, Petrák, Rijkhoff, Taylor, Nesládek and Pennisi. This is an open-access article distributed under the terms of the Creative Commons Attribution License (CC BY). The use, distribution or reproduction in other forums is permitted, provided the original author(s) and the copyright owner(s) are credited and that the original publication in this journal is cited, in accordance with accepted academic practice. No use, distribution or reproduction is permitted which does not comply with these terms.

frontiers in Materials

ORIGINAL RESEARCH
published: 15 November 2018
doi: 10.3389/fmats.2018.00066

Softening Shape Memory Polymer Substrates for Bioelectronic Devices With Improved Hydrolytic Stability

*Seyed Mahmoud Hosseini[1], Rashed Rihani[2], Benjamin Batchelor[3], Allison M. Stiller[2], Joseph J. Pancrazio[2], Walter E. Voit[2,3,4] and Melanie Ecker[2,3,4]**

[1] Department of Chemistry and Biochemistry, The University of Texas at Dallas, Dallas, TX, United States, [2] Department of Bioengineering, The University of Texas at Dallas, Dallas, TX, United States, [3] Center for Engineering Innovation, The University of Texas at Dallas, Dallas, TX, United States, [4] Department of Materials Science and Engineering, The University of Texas at Dallas, Dallas, TX, United States

Candidate materials for next generation neural recording electrodes include shape memory polymers (SMPs). These materials have the capability to undergo softening after insertion in the body, and therefore reduce the mismatch in modulus that usually exists between the device and the tissue. Current SMP formulations, which have shown promise for neural implants, contain ester groups within the main chain of the polymer and are therefore prone to hydrolytic decomposition under physiological conditions over periods of 11–13 months *in vivo*, thus limiting the utility for chronic applications. Ester free polymers are stable in harsh condition (PBS at 75°C or NaOH at 37°C) and accelerated aging results suggest that ester free SMPs are projected to be stable under physiological condition for at least 7 years. In addition, the ester free SMP is compatible with microfabrication processes needed for device fabrication. Furthermore, they demonstrate *in vitro* biocompatibility as demonstrated by high levels of cell viability from ISO 10993 testing.

Keywords: neural interfaces, softening behavior, accelerated aging, hydrolytic stable, shape memory polymer, thiol-ene degradation, chronic viable polymer

OPEN ACCESS

Edited by:
Ulrich G. Hofmann, Universitätsklinikum Freiburg, Germany

Reviewed by:
Ahmed El-Fiqi, Dankook University, South Korea
Ajay Devidas Padsalgikar, St. Jude Medical, United States

***Correspondence:**
Melanie Ecker
melanie.ecker@utdallas.edu

Specialty section:
This article was submitted to Biomaterials, a section of the journal Frontiers in Materials

Received: *09 August 2018*
Accepted: *24 October 2018*
Published: *15 November 2018*

Citation:
Hosseini SM, Rihani R, Batchelor B, Stiller AM, Pancrazio JJ, Voit WE and Ecker M (2018) Softening Shape Memory Polymer Substrates for Bioelectronic Devices With Improved Hydrolytic Stability. Front. Mater. 5:66. doi: 10.3389/fmats.2018.00066

INTRODUCTION

Shape memory polymers (SMPs) are an emerging class of materials. Their capability to restore their original shape after being deformed is outstanding (Dietsch and Tong, 2007; Liu et al., 2007; Mather et al., 2009; Lendlein, 2010; Hu et al., 2012b; Hager et al., 2015) and these materials have found utility in a variety of potential applications, including airspace, (Ishizawa et al., 2003; Barrett et al., 2006; Rory Barrett et al., 2006; Yanju and Jinsong, 2010; Yanju et al., 2014) anti-counterfeiting technology, (Pretsch et al., 2012; Ecker and Pretsch, 2013, 2014a,b) textile industry, (Matilla, 2006; Hu and Chen, 2010; Hu et al., 2012a) and as medical devices (Feninat et al., 2002; Buckley et al., 2006; Baer et al., 2007; Kulshrestha and Mahapatro, 2008; Lendlein and Behl, 2008; Baudis et al., 2014; Wang et al., 2017). The triggers for SMPs to recover to their permanent shape are diverse and include direct heating above the transition temperature of the polymer, indirect heating through electric or magnetic activation, and less commonly, chemical modification including plasticization. The plasticization of the SMP with solvent molecules, e.g., water, leads to a lowering of the glass transition temperature (T_g) of the polymer due to swelling and the resulting increased free volume of the polymer chains

(Immergut and Mark, 1965; Singhal et al., 2013). When the T_g of a polymer is above room temperature (RT) before, but below after plasticization, the SMP may recover its permanent shape upon immersion in aqueous solutions at ambient temperatures. At the same time, the polymer changes from a glassy (stiff) materials to a rubbery (soft) material. This behavior of SMPs is what is of interest for the development of (self)-softening SMP substrates for bioelectronics devices. Especially for cortical neural interfaces, there is a need for devices which are stiff enough during the implantation to enable a sufficient penetration of the tissue with least possible trauma. However, after implantation, materials that soften to a modulus that is much closer to the tissue modulus offer the promise of decreasing the foreign body response and micromotion effects. Previously, the Voit Lab has presented a new generation of neural implants comprising of softening thiol-ene/acrylate polymers used as substrates (Ware et al., 2013, 2014; Do et al., 2017; Ecker et al., 2017; Simon et al., 2017). These devices work well for acute experiments and for chronic experiments on the order of 1–3 months. At least one factor limiting the long term stability of current SMP devices may be the fact that these polymers contain ester groups in their backbone which are vulnerable to hydrolytic degradation under moist conditions. For future applications, including translation to the clinic, it is necessary to have substrate materials with increased durability under *in vivo* conditions to enable chronic experiments over the course of years (Ryu and Shenoy, 2009; Rubehn and Stieglitz, 2010; Takmakov et al., 2015; Teo et al., 2016; Lecomte et al., 2017; ASTM, 2018), Reit et al. (2015) have demonstrated, that the use of ester free thiol-monomers significantly increases the durability of thiol-ene networks while it still allows to tune the glass transition temperature and cross-link density.

Here, we present a thiol-ene SMP formulation that is chemically and structurally similar to the most recent ones, but does not contain any ester groups (Do et al., 2017; Ecker et al., 2017; Simon et al., 2017; Garcia-Sandoval et al., 2018; Shoffstall et al., 2018). We have optimized the synthesis of a new monomer and tailored the polymer composition to have similar *in vivo* softening capabilities as previous reported SMPs. Dynamic mechanical analysis (DMA) of the hydrolytically stable SMP revealed that the SMP has a glass transition temperature above body temperature when dry, but below body temperature after being soaked in phosphate buffered saline (PBS). Thus, the novel SMP is also able to soften under physiological conditions to a modulus that is much closer to the tissue. To verify the improved stability of the new material against hydrolysis, we have performed accelerated aging tests in PBS at elevated temperatures (75°C) for 8 weeks and in one molar sodium hydroxide (NaOH) solution at body temperature over the course of 4 weeks. Weight loss and mechanical properties were determined and compared to a SMP composition that contains ester groups in the main chain. Our results demonstrate that the ester free SMP remained stable over the course of the study whereas the ester-containing counterpart lost about 15% of mass after aging in PBS and even 39% after aging in NaOH. We have also demonstrated that the new softening polymer is biocompatible, can be sterilized, and is compatible with microfabrication methods. That makes this polymer an ideal substrate candidate for future neural implants.

MATERIALS AND METHODS

Synthesis of 1,3,5-tris(3-mercaptopropyl)-1,3,5-triazinane-2,4,6-trione (TTTSH)

Trithiol monomer TTTSH was synthesized following previously reported method (Lundberg et al., 2010) with minor modifications (**Scheme 1**). Briefly, 30 g (120.4 mmol) 1, 3, 5-triallyl-1, 3, 5-triazine-2, 4, 6-trione (TATATO), 82.40 g (1,080 mmol) thioacetic acid, and 1.98 g (12.04 mmol) 2, 2′-azobis (2-methylpropionnitrile) (AIBN) were placed in a 500 mL three-neck round-bottom flask which was equipped with condenser and nitrogen inlet. Afterward, the reaction mixture was stirred at 65°C for 24 h under a nitrogen atmosphere. Excess thioacetic acid was removed by reduced pressure and then was reacted with methanol (100 ml) and concentrated hydrochloric acid (50 ml) at 65°C for 36 h to cleave the thioester bond. After cooling down to room temperature, water was added (300 ml) and extracted for three times with methylene chloride (300 ml). The organic mixture was washed with sodium hydrogen carbonate solution (5%), dried over $MgSO_4$, and concentrated with reduced pressure. After purification by column chromatography with gradient hexane: ethyl acetate mixtures 1:0 to 1:4 yellowish viscous liquid was obtained.

Fabrication of Polymers

1,3,5-Triallyl- 1,3,5-triazine-2,4,6(1H,3H,5H)-trione (TATATO), Trimethylolpropane tris(3-mercaptopropionate) (TMTMP), and 2,2-Dimethoxy-2-phenylacetophenone (DMPA) were purchased from Sigma Aldrich, whereas Tris [2-(3-mercaptopropionyloxy) ethyl] isocyanurate (TMICN) was purchased from Evans Chemicals, and 1,10-Decanedithiol (DDT) from TCI Chemicals. All the chemicals were used as received without further purification. TTTSH was synthesized as described under section Synthesis of 1,3,5-tris(3-mercaptopropyl)-1,3,5-triazinane-2,4,6-trione (TTTSH). Two thiol-ene SMP compositions were prepared, an ester-free (SMP-A) and an ester containing (SMP-B) formulation, each consisting of stoichiometric quantities of thiol to alkene functionalities. Exact mole fractions are: TTTSH/DDT-TATATO = 0.3/0.2–0.5 (SMP-A) and TMTMP/TMICN-TATATO = 0.45/0.05–0.5 (SMP-B) (**Figure 1**). A total of 0.1 wt% DMPA of total monomer weight was dissolved in the solution for the initiation of the photopolymerization of the monomer solution. The vial was covered in aluminum foil to prevent incident light from contacting the monomer solution and kept at room temperature. Without exposing the solution to light, the vial was mixed thoroughly by planetary speed mixing.

The polymer solutions were spin cast on 75 × 50 mm glass microscope slides using a Laurell WS-650-8B spin coater. Spin speed was 350 rpm and time was 45 s for SMP-A and 600 rpm and 25 s for SMP-B in order to achieve thicknesses of about 30 μm, respectively. Polymerization was performed at ambient temperature using an UVP CL-1000 crosslinking chamber with five overhead 365 nm UV bulbs for 60 min under air. Cured

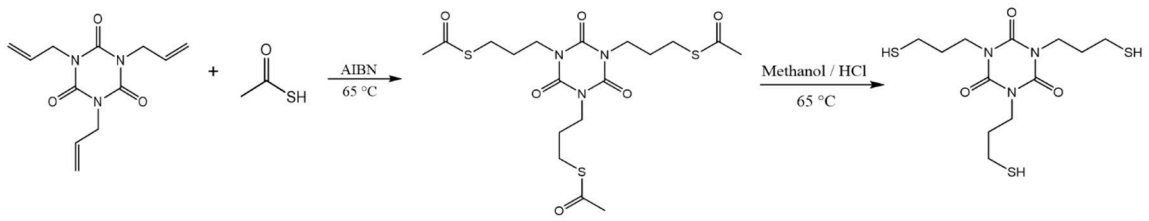

SCHEME 1 | Reaction scheme of the TTT-SH synthesis.

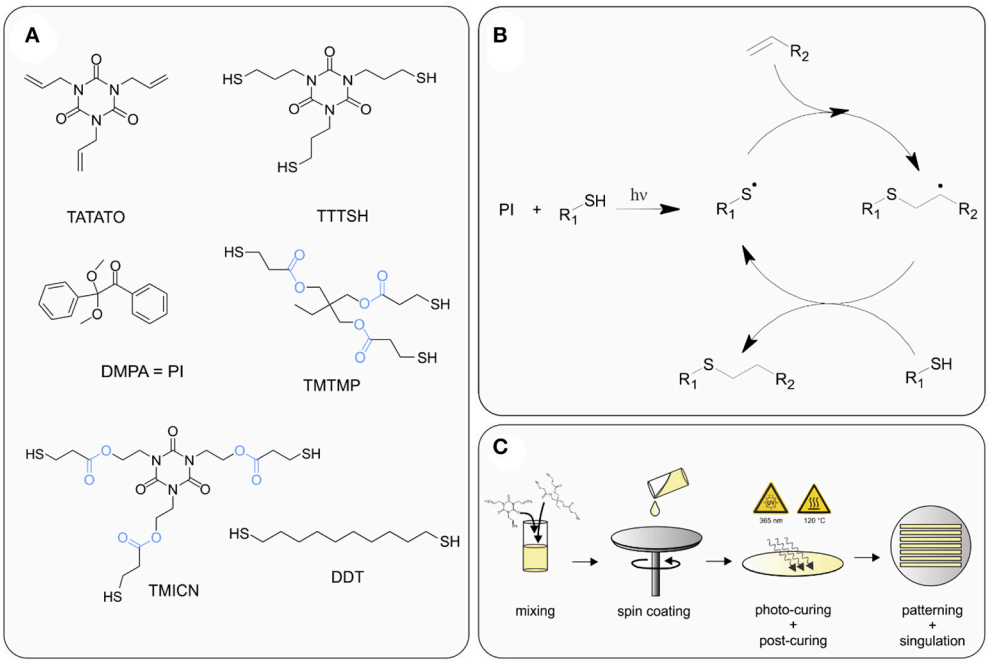

FIGURE 1 | (A) Chemical structures of monomers and photoinitiator (PI) used for synthesis of polymers SMP-A and SMP-B. Ester groups are highlighted in blue, **(B)** reaction mechanism of thiol-ene click reaction, and **(C)** schematic of polymer fabrication.

samples were then placed in a vacuum oven at 120°C and 5 inHg (∼16.9 kPa) for 24 h to further complete network conversion.

Test devices were either fabricated using a CO_2 laser or were fabricated in the UT Dallas Class 10,000 cleanroom facility. The above SMP-on-glass substrates were used as the starting substrates in the cleanroom. Low temperature silicon nitride (using PlasmaTherm-790 PECVD) was deposited to act as a hard mask for the following plasma etching processes in which the device outline/shape was patterned. Adjacently, the nitride hard mask was etched away in the 1:10 HF dip. For some SMP samples top 4 μm thick crust was etched away in oxygen plasma (Technics RIE). In a final step, the test devices having dimensions of 4.5 × 50 mm × 30 μm were delaminated from the glass slide by soaking in water.

Accelerated Aging

SMP-A and B were subjected to two different accelerated aging scenarios; test samples were either immersed in 20 ml phosphate buffered saline (PBS) at 75°C or in 1 M sodium hydroxide (NaOH) solution at 37°C, respectively. A number of $N = 3$ samples were removed after 7, 14, 21, and 28 days immersion in NaOH and after 7, 14, 21, 28, 35, 42, 49, and 56 days after immersion in PBS. After removal, the samples were rinsed in de-ionized water before they were dried with a lint-free cloth. The accelerated aging in PBS follows the Arrhenius equation under the conservative assumption for biomedical polymers (Hemmerich, 1998) that $Q_{10} = 2$:

$$Accelerated\ Aging\ Time\ (t_{AA}) = \frac{Real\ Aging\ Time\ (t_{RT})}{Q_{10}^{\frac{(T_{AA}-T_{RT})}{10}}} \quad (1)$$

where t_{AA} is the accelerated aging time, t_{RT} the real aging time, T_{AA} temperature for accelerated aging, T_{RT} temperature for real time aging and Q_{10} the temperature coefficient. According to the Q_{10} temperature coefficient, which is a derivation of the Arrhenius equation, 1 week in PBS at 75°C is equal to 14 weeks at 37°C.

Weight and Thickness Loss

The dry weight of all samples was determined with 0.01 mg precision before and after aging. The weight loss was calculated according the following equation:

$$mass\ loss\ (\%) = \frac{m_0 - m_T}{m_0} \times 100 \quad (2)$$

where m_0 is the weight of the neat samples and m_T is the weight of the samples after aging. A Marathon micrometer with 0.001 mm precision was applied to determine thickness of samples before and after the aging study. The mean value and standard deviation was calculated for $N = 3$ samples per aging time.

Dynamic Mechanical Analysis (DMA)

DMA was performed using a TA Instruments RSA-G2 Solids Analyzer with the immersion system in tension mode in order to quantify the storage modulus *E*' and tan δ of dry or in PBS soaked samples. All measurements were performed on rectangular samples as received after the clean room processing or CO_2 laser cutting, having a width of 4.5 ± 0.1 mm and thicknesses of 30 ± 3 μm. The following parameters were selected: clamping distance of 15 mm, a preload force of 0.1 N, a frequency of 1 Hz, and a deformation amplitude of 0.275% strain. Dry experiments were run from 10 to 100°C or from 20 to 120°C using a heating rate of 2°C min^{-1}. Soaking experiments were performed using the immersion system of the RSA-G2 filled with PBS. The first step (the soaking) included the heating from room temperature to 37°C followed by isothermal oscillating for 60 or 120 min. The second step comprised first cooling down to the start temperature with a rate of 3 C min^{-1} followed by heating from 10 to 80°C applying a heating rate of 2°C min^{-1}. All measurements were performed on three independent specimens in order to gather statistical results. Graphics show representative measurements only.

Termogravimetric Analysis (TGA)

A Mettler Toledo TGA/DSC 1 was used to perform Thermal Gravimetric Analysis on $N = 3$ samples before and after accelerated aging. The polymer samples were heated from 25 to 700°C at a heating rate of 20°C/min and flow of 50 ml/min nitrogen gas. Samples were approximately 5 mg each.

Cytotoxicity Test

Cytotoxicity assays were carried out as previously described (Black et al., 2018) and in accordance with the International Organization for Standards (ISO) protocol "10993-5: Biological evaluation of medical devices"(ISO, 2008). Briefly, 50% and 100% concentration shape-memory polymer (SMP-A) extract was evaluated against Tygon-F-4040-Lubricant Tubing extract (positive control) and cell medium (negative control). Material extracts which reduced normalized cell viability percentages below 70% were considered cytotoxic in accordance with the ISO protocol (ISO, 2008).

Material extracts were made by soaking 3 cm^2/ml of positive control and SMP A in Dulbecco's Modified Eagle Medium (DMEM) at 37°C, 5% CO_2, and 95% relative humidity for 24 h in a polystyrene, glass-bottom 24 well plate (Greiner Bio-One, Austria). NCTC clone 929 fibroblasts (ATCC, USA) were routinely sub-cultured and seeded in a separate 24 well plate at a density of 100,000 cells per well in complete cell medium (DMEM with 10% horse serum) and allowed to incubate at 37°C, 5% CO_2, and 95% relative humidity for 24 h until a semi-confluent monolayer of cells was formed. Cell media was replaced with the respective material extract for 24 h before being stained using a LIVE/DEAD Cytotoxicity kit for mammalian cells (Thermo Fisher, L3324) using manufacturer protocol. Briefly, Cells were washed three times with sterile PBS and incubated at 37°C with 2 μM Calcein AM (CaAM) and 4 μM Ethidium Homodimer (EthD-1) for 15 min. CaAM dye stained the cytoplasm of live cells while EthD-1 stained the nucleus of apoptotic cells. 2 × 2 field stitched fluorescent images (10x objective) were taken in each well using an inverted microscope (Nikon Ti eclipse).

Live/dead cell counts were quantified using ImageJ (NIH). Briefly, images were treated with a 2.0 Gaussian Blur then automatically counted based on local intensity maxima. Further analysis using a MATLAB program identified cells that exhibited both live and dead stains based on cell-to-cell proximity through and were removed from the live count. Cell viability percentage was defined as the ratio of live cells to the total number of cells. Cell viability percentages reported were normalized to the negative control.

RESULTS

Synthesis of Ester Free Monomer

Trifunctional thiol (TTTSH) was synthesized by radical addition reaction between TATATO and thioacetic acid followed by hydrolysis in acidic media. Column chromatography was applied to remove byproducts. Yield: 30 g (71%). ^{1}H NMR, ^{13}C NMR and FTIR, support the successful synthesis (detailed plots are shown in SI, **Supplementary Figures 1–3**). ^{1}H NMR [600 MHz, $CDCl_3$, δ (ppm)]: 3.98 (t, $J = 7$ Hz, 6H, -N-C**H2**-CH2-), 2.54 (dt, $J = 7$ Hz/ $J = 8$ Hz, -C**H2**-SH), 1.94 (quintet, $J = 7$ Hz, 6H, -CH2-C**H2**-CH2-), 1.52 (t, 3H, $J = 8$ Hz, -S**H**).^{13}C NMR [150 MHz, $CDCl_3$, δ (ppm)]: 149.03(–**C**=O), 41.84 (–N**C**H_2–), 31.87 (–**C**H2–), 21.95 (–**C**H_2SH). FT-IR (cm^{-1}): 2962, 2933, 2854, 2566 (ν_{S-H}), 1671 ($\nu_{C=O}$), 1454, 1423, 1373, 1334, 1288, 1230, 759.

Softening Effect on Pristine SMPs

Our aim was to synthesize an ester free SMP formulation with similar softening properties as previously used ester-containing thiol-ene and thiol-ene/acrylate polymer compositions. In order to mimic the effect of body fluids on mechanical properties of the polymer SMP-A, dynamic mechanical analysis was performed in dry and soaked conditions (**Figure 2A**). The glass transition temperature (T_g) and storage modulus (*E*') in the glassy and rubbery state was tuned to be similar to the previously used SMP-B (**Figure 2B**). Soaked conditions were achieved by immersing the polymers in phosphate buffered saline (PBS) at 37°C and monitoring the storage modulus loss until the modulus no longer decreases. We determined that the composition consisting of TTTSH/DDT-TATATO = 0.3/0.2–0.5 had comparable values.

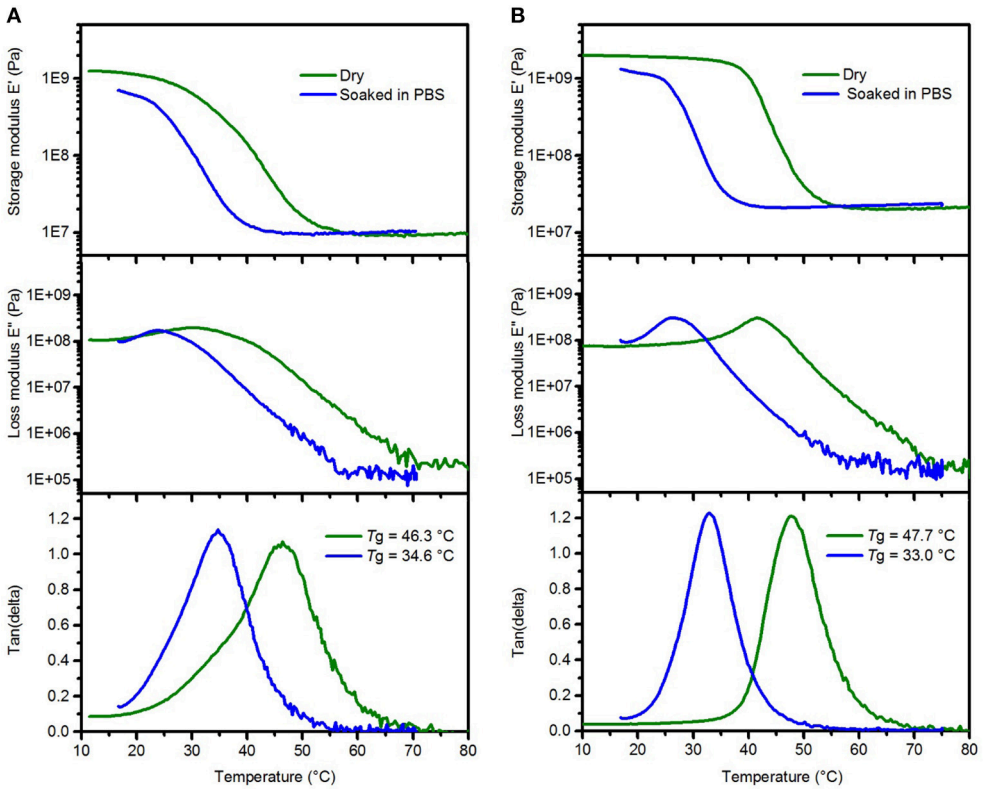

FIGURE 2 | Representative DMA data of SMP-A **(A)** and SMP-B **(B)** showing the changes in the storage modulus (top), loss modulus (center), and tan delta (bottom) after softening in PBS, respectively.

Soaking in PBS led to a modulus decrease for SMP-A from 1,020 ± 67 MPa at room temperature (23°C) to 22.1 ± 0.3 MPa after 20 min at 37°C, while the modulus of SMP-B dropped from 2,187 ± 98 MPa to 28.8 ± 0.4 MPa. After soaking in PBS, the peaks of loss modulus and tan (delta) which show the glass transition temperature of both SMPs decreased by 12–14°C compared to the dry values (**Figure 2**). For SMP-A, T_g dropped from 46.3 ± 0.7 to 34.6 ± 0.8°C and for the SMP-B, fell from 47.8 ± 0.4 to 33.0 ± 0.6°C.

Accelerating Aging Test in PBS at 75°C

Chronic implantable bioelectronic devices must consist of stable substrate materials in biological environment to enable operation for many years *in vivo* (Lyu and Untereker, 2009). To compare the hydrolytic stability of the sample's network in physiological conditions, aging in PBS was performed. In order to accelerate the aging process, the temperature was increased to 75°C. The effect of the aging conditions on mass change (**Figure 3**) and viscoelastic behavior (**Figure 4**) of the samples were then assessed. As shown in **Figure 3A**, the SMP-B was stable for nearly 4 weeks, but thereafter began to continually lose mass until the test was stopped. After 8 weeks at elevated temperature, SMP-B lost 14.7 ± 0.9% of its original mass. On the other hand, SMP-A exhibited no weight loss. A similar trend is seen in **Figure 3B**, where SMP-A displayed no change in thickness over the testing period, whereas SMP-B began to thin after 5 weeks. At the end of 8 weeks SMP-B lost 9.8 ± 1.6% of its original thickness.

The DMA data of the SMPs aged in PBS indicates that T_g increased each week, which can be seen in the peak shifts of tan delta and the loss modulus, respectively. As seen in **Figure 4**, the $T_g$for both SMP-A and SMP-B displayed higher glass transition temperatures after soaking in PBS at 75°C (shifting from 47 to∼61°C). **Figure 4B** indicates that rubbery modulus of SMP-B decreases gradually and tan delta peak is getting wider and asymmetric with increasing aging time. On the other hand SMP-A does not show any changes in the shape of graphs.

Accelerated Aging Test in 1 M NaOH Solution

The effect of harsh conditions (1.0 M NaOH, 37°C) on our two different polymers (SMP-A and B) was investigated. Mass and thickness changes (**Figure 5**) and mechanical properties (**Figure 6**) of the polymers were compared to the initial pristine and dry polymers. **Figure 5A** shows the change in polymer mass over time. Over the course of the 4 weeks investigation, SMP-A had no appreciable loss of mass, whereas SMP-B showed remarkable mass change during 4 weeks with a final mass loss of 38.7 ±

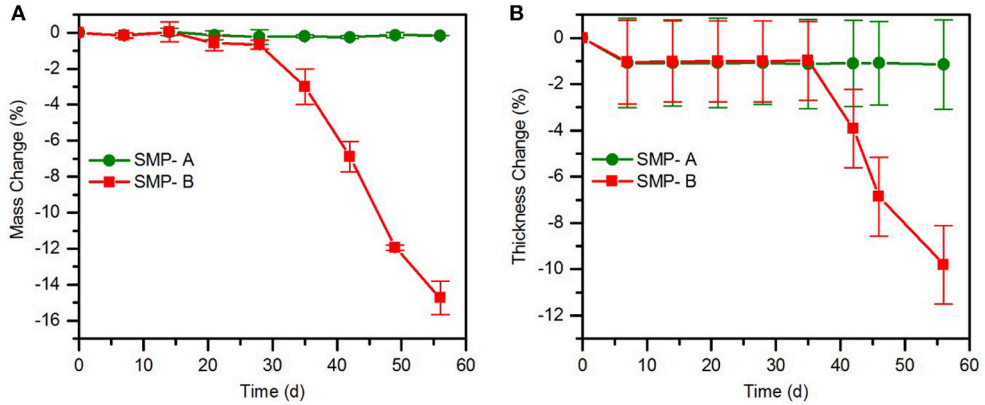

FIGURE 3 | Mass change **(A)** and thickness change **(B)** of SMP-A and SMP-B after various aging times in PBS at 75°C.

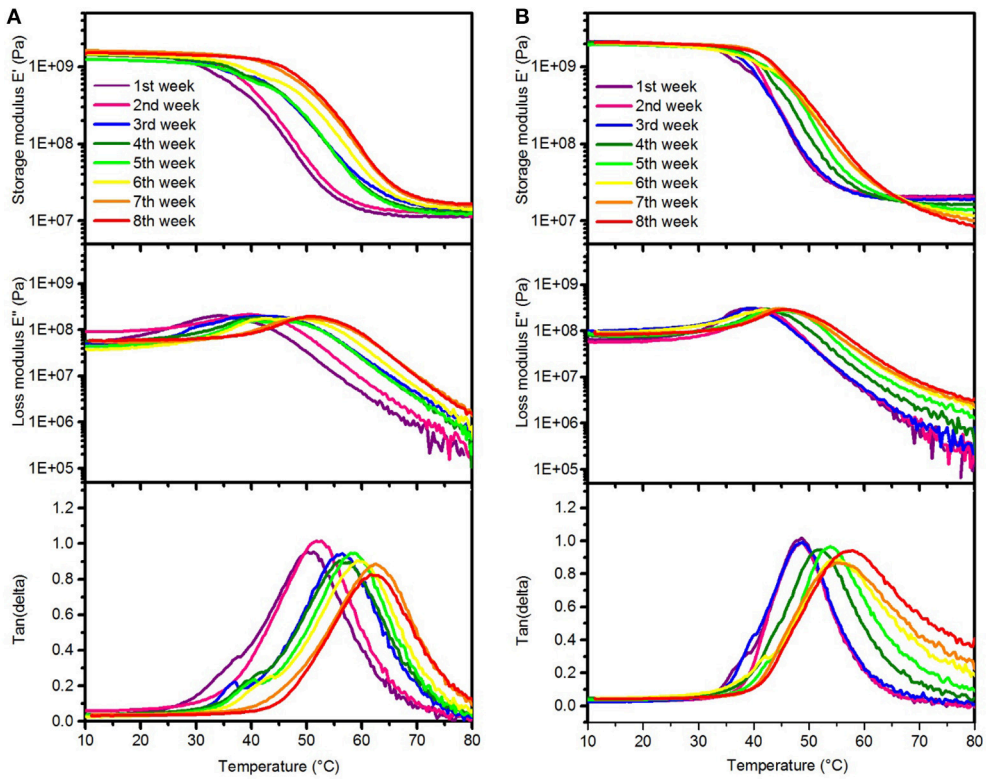

FIGURE 4 | Representative DMA measurements of SMP-A **(A)** and SMP-B **(B)** showing changes in the storage modulus (top), loss modulus (center), and tan delta (bottom) after various aging times in PBS at 75°C, respectively.

0.3%. In addition to the weight loss study, the thickness of each polymer was monitored during the aging. **Figure 5B** indicates significant thickness loss (42.1 ± 1.7%) for SMP-B over the course of the aging test, while SMP-A was stable.

Dynamic mechanical analysis (DMA) was performed to investigate the stability of thermomechanical properties of both SMPs after aging in NaOH (**Figure 6**). It can be seen that there are no changes in the profiles of the storage/loss moduli, and tan delta. We could not measure the thermomechanical properties of SMP-B after 4 weeks of aging in NaOH, since the polymers were already too degraded and the specimen were brittle and ruptured (see **Supplementary Figure 4** in SI). These findings are in line with the weight loss and thickness measurements, which also revealed drastic changes. Thermal gravimetric analysis (TGA) was performed in order to compare

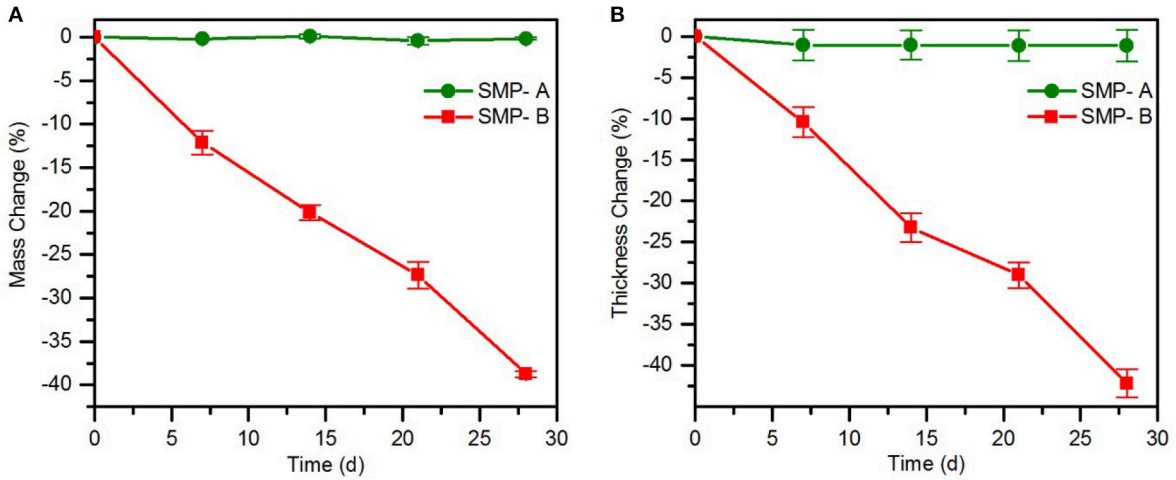

FIGURE 5 | (A) Mass change of SMP-A and SMP-B in 1 M NaOH with **(B)** corresponding thickness loss.

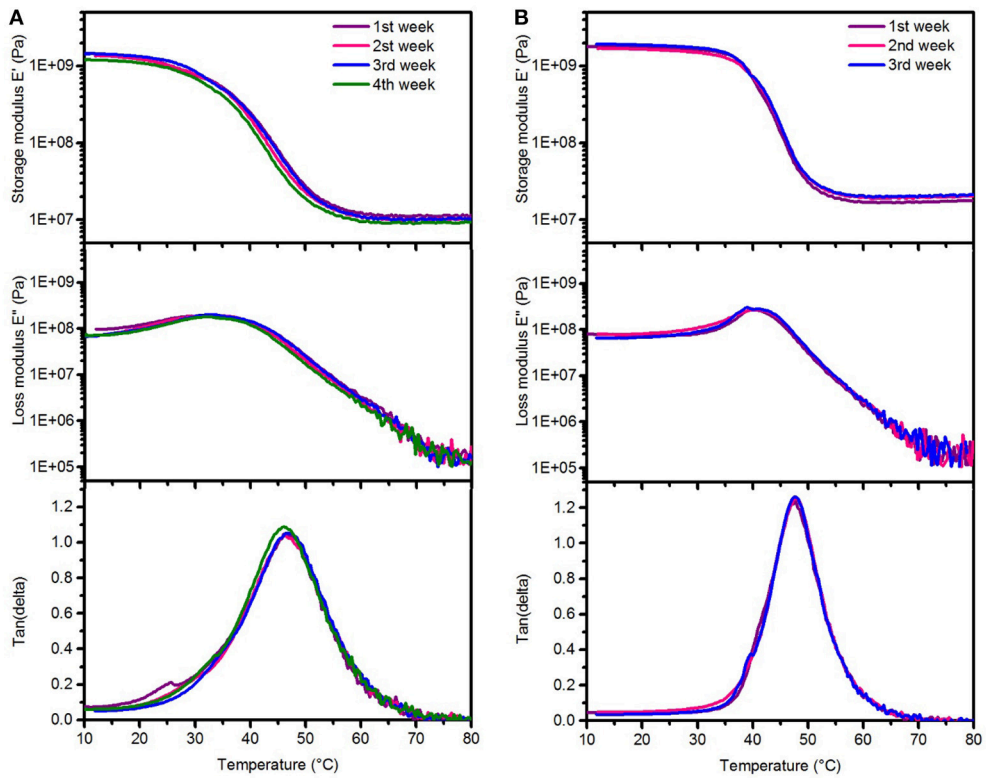

FIGURE 6 | Representative dynamic mechanical analysis after aging test in 1 M NaOH solution showing changes in the storage modulus (top), loss modulus (center), and tan delta (bottom) after various aging times at 37°C **(A)** SMP-A **(B)** SMP-B.

thermal stability of materials before and after the aging study in NaOH and PBS (**Figure 7**). It can be seen in **Figure 7A** that SMP-A (top) was not affected by the aging study in both media and degradation temperature and mass loss rate did not change. However, SMP-B (bottom) displays a slightly lower onset in the decomposition temperature after 4 weeks in NaOH (from 320 to 300°C) and even larger shift (from 320 to 250°C) after 8 weeks in PBS media. **Figure 7B** displays a more detailed view on the aging effects of 75°C PBS on SMP-B. The onset of the decomposition temperature shifts downward

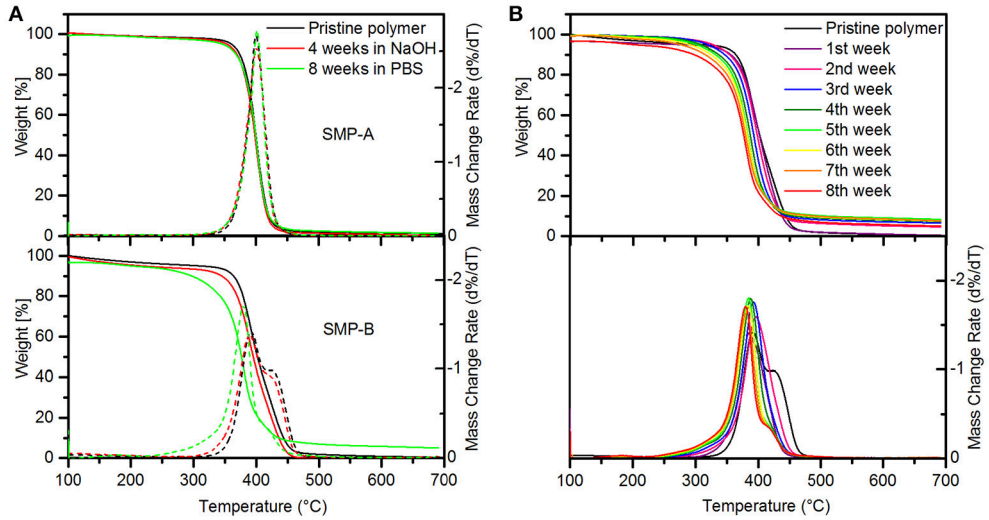

FIGURE 7 | Thermal gravimetric analysis of SMPs. **(A)** Showing weight loss and mass change rate of SMP-A (top) and SMP-B (bottom) after 4 weeks in 1 M NaOH solution at 37°C (red line) and 8 weeks in PBS at 75°C (green line). **(B)** Weight loss (top) and mass change rate (bottom) of SMP-B in PBS over 8 weeks.

about 8–10°C per week. In addition, the mass loss rate pattern changes over time, in detail the shoulder at higher temperature diminishes.

Cytotoxicity Test

To evaluate the cytotoxicity of SMP-A *in vitro*, we carried out live/dead assays based on material extract treatments in accordance with ISO protocol 10993-5. After fibroblasts were incubated for 24 h in the material extract, cell viability percentages were calculated and normalized to the negative control (**Figure 8**). SMP A at 50 and 100% concentrations had normalized viability percentages of 97.8 ± 0.8% (mean ± SEM, $n = 6$) and 93.6 ± 1% (mean ± SEM, $n = 6$), respectively. The positive control had a significantly lower viability percentage of 21.8 ± 4.7% (mean ± SEM, $n = 6$) (**Figure 8B**). Normalized viability percentages for SMP A at both 50 and 100% concentrations were both above the 70% threshold and deemed non-cytotoxic in accordance with ISO protocol 10993-5.(ISO, 2008) The *in vitro* cytotoxicity of SMP-B was evaluated in a different study (Black et al., 2018) and is therefore not shown detailed herein. The other study revealed that SMP-B (which was named FS SMP in the other study) had normalized viability percentages of 99.1 ± 0.7 % in the case of NCTC fibroblasts.

DISCUSSION

The focus of this study was to compare the stability of two types of SMPs that are applicable for flexible bioelectronic devices. Finding the appropriate substrate for the use in self-softening bioelectronic devices requires an understanding of the chemical structure and composition of the monomers for fine-tuning of the glass transition temperature of the final polymer. Glass transition (T_g) is critical to designing polymeric substrates for softening bioelectronic devices, since the T_g must be higher than body temperature prior to insertion for easy handling. After insertion however, a T_g higher than body temperature may cause an inflammatory response because the polymer is still in its glassy (stiff) state. Both SMP-A and SMP-B were synthesized utilizing a thiol-click polymerization mechanism and the glass transitions were tuned to be between 42 and 46°C in dry conditions and around 34°C when immersed in PBS. The mechanical properties of the SMPs change in the aqueous environments due to the plasticization effect of water molecules on polymer films. The storage modulus E' decreased significantly after 25 and 10 min immersion in PBS at 37°C, for SMP-A and SMP-B, respectively. Therefore, the glass transition in dry condition is high enough for handling during insertion and low enough to minimize an inflammatory response under physiological conditions. After finding the proper composition for both SMPs, the polymers were evaluated for long-term stability in two different media; PBS to mimic the aqueous environment *in vivo* at elevated temperature (75°C) and a harsher alkaline solution (NaOH) at 37°C. Afterward, the weight loss and thermomechanical properties of the SMPs were investigated.

The weight loss and thickness loss data of polymers in PBS (**Figure 3**) indicates that SMP-B is stable until the fourth week but thereafter begins to continually lose weight and thickness up to 15 and 10%, respectively. According to equation 1, aging test at 75°C for 1 week is equivalent to 14 weeks at body temperature. Therefore, SMP-B is expected to start to degrade after about 56 weeks (14 months) under physiological conditions. While this time span might be long enough for many chronic and sub-chronic studies on animals, which usually last 3 months to a year, it would not be sufficient for long-term chronic applications, which may take several years to decades. In contrast, SMP-A data shows that ester-free polymers are stable under these conditions until the end of this study, which was 8 weeks (projected to ∼26 months under physiological conditions) without any signs of

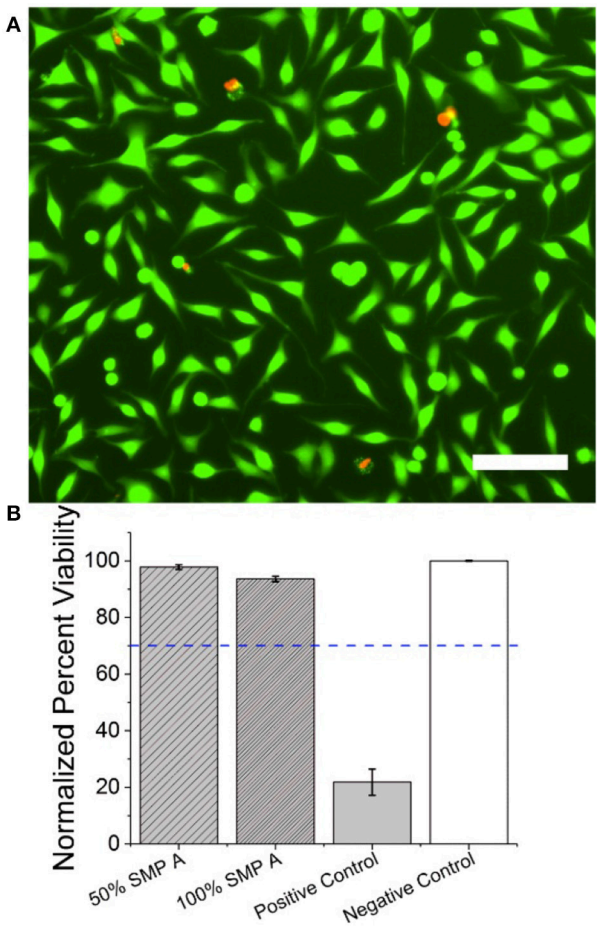

FIGURE 8 | SMP-A Cytotoxicity assays using NCTC fibroblasts (A) Fluorescent image of NCTC fibroblasts stained with CaAM (green) and EthD-1 (red). Green cells represent live cells while red cells represent apoptotic cells. Scale bar represents 100 μ m (B) Mean normalized cell viability percentage of SMP A at 50 and 100% concentrations, positive control, and negative control. Blue dotted line represents the 70% threshold based on ISO protocols (ISO, 2008) needed to pass for non-cytotoxic materials.

degradation. Harsh conditions (1 M NaOH) were used to further accelerate aging, which will be discussed later.

DMA data (**Figure 4**) reveals that the glass transition temperature of both polymers shifts to a higher temperature with increasing aging time, which is indicated by shifted loss modulus and tan delta peaks. In order to investigate whether this effect is due to the PBS or due to the relatively high temperature (this effect was not seen upon aging on NaOH at 37°C), additional experiments were performed. We aged SMP-A samples in de-ionized (DI) water at 75°C for up to 3 weeks, respectively, before DMA measurements were conducted and compared to the aging study in PBS at the same temperature. DMA data (shown in SI, **Supplementary Figure 5**) revealed that the samples aged in water showed similar shifting in T_g, which shows that the elevated temperature causes annealing effects. We do not expect to see such effects at body temperature. In addition, the DMA data shows that after 4 weeks of aging test in PBS, the rubbery storage modulus started to decrease and tan delta got wider which means the SMP-B started to lose the crosslink density. Since accelerating aging test was performed at 75°C (above the glass transition of the polymer), the mobility of polymer chains and diffusion of water molecules were increased. Therefore, the water migration into the polymer was faster than the reaction rate of the hydrolysis, which leads to bulk degradation (Lyu and Untereker, 2009). TGA data (**Figure 7B**) also confirms that at higher temperature water molecules can diffuse into the polymer structure and hydrolize ester functional groups. That causes a loss in the crosslink density of polymer. With that, the thermal stability of the polymer was reduced as shown by decreased decomposition temperatures. The diminishing shoulder at higher temperatures can be attributed to the fact that the polymer network got already broken down by hydrolysis. Fragments of the hydrolyzed TMICN and TMTMP monomers have already left the polymeric network and therefore do no longer contribute to the thermal decomposition profile of the polymer. To further investigate the degradation of the polymers, gas chromatography-mass spectroscopy (GS-MS) was applied on the PBS solution after aging. GC-MS data (shown in SI, **Supplementary Figure 7**) indicates that tris(hydroxymethyl)propane was released from SMP-B. In contrast, however, SMP-A did not reveal any degradation products in the PBS after aging. That confirms our assumption that the ester-containing SMP-B undergoes hydrolysis since tris(hydroxymethyl)propane is a fragment of the monomer TMTMP, which used for the synthesis of this polymer (**Supplementary Scheme 1**).

Figure 5 shows the weight loss and thickness loss of SMP-A and SMP-B in NaOH solution. According to the graphs, SMP-A, which does not contain ester groups, is completely stable and the weight and thickness did not change over the course of the aging study. On the other hand, ester-group containing SMP-B started to hydrolize which leads to a 38% and 42% decrease in weight and thickness, respectively after 4 weeks. It was seen that SMP-B had a maximum weight loss of 15% after 8 weeks in PBS at 75°C, which was approximately the same as for aging in NaOH for 9 days. Therefore, we assume that the aging in NaOH at 37°C is roughly six times faster than in PBS at 75°C. Based on the equation 1, 1 week in PBS at 75°C is equal to 14 weeks at 37°C. Taking both considerations into account, we estimate that 4 weeks degradation in NaOH at 37°C is equal to 24 weeks at 75°C. Therefore, it could be concluded that SMP-A is projected to be completely stable for at least 7 years under physiological conditions.

The DMA data of SMP-A and SMP-B after aging in NaOH (**Figure 6**) indicates that T_g, loss and storage moduli of SMP-A are completely conserved, while SMP-B degrades too rapidly for data collection after 4 weeks. All of the SMP-B samples tore apart during testing before obtaining a glass transition temperature (see **Supplementary Figure 4** in SI). Since salts and ions have low solubility in polymer chains, hydroxide ions did not diffuse into the polymer structure and hydrolysis took place on the surface (Lyu and Untereker, 2009). Therefore, erosion of the polymer occurred from the outside to the inside of the film. Another finding was, that in contrast to the aging in

PBS, the rubbery modulus of SMP-B did not decrease. That indicates that there are no changes in the polymeric network and the crosslink density. These findings support the hypothesis that aging in NaOH follows surface erosion rather than bulk degradation. We have also noticed, that the aging at 37°C was not affecting the T_g of the polymers, which indicates that no annealing took place at this temperature. Additionally, we have performed ATR-FTIR of polymers SMP-A and SMP-B before and after both aging scenarios (**Supplementary Figure 8** in SI). SMP-A shows as expected no changes in surface chemistries after both aging studies. SMP-B however has shown only minor changes after 4 weeks in NaOH, wheras it shows more distinct changes after aging for 8 weeks in PBS. It can be seen for example a broad peak appearing between 2,500 and 3,500 cm^{-1}, which can be assigned to the hydroxyl (OH) and carboxyl (OH) streching vibration signatures, which is due to hydrolized polymer fragments. These measurements support the bulk vs. surface erosion theory further. Even if ATR is a surface method, the penetration depth of the IR beam is between 0.5 and 5 μm into the bulk of the sample. Therefore, the bulk degraded sample (PBS aged) shows a higher number of degraded moieties per volume measured.

Thermogravimetric analysis graph (**Figure 7**) displays SMP data before and after aging in NaOH. **Figure 7A** indicates that SMP-A is completely stable, while for SMP-B the onset of decomposition shifts about 30–40°C toward lower temperatures after aging. In general, polymers with decomposition temperatures higher than ∼300°C are favorable for the fabrication of bioelectronic devices. The micro-fabrication of such devices uses processes such as photolithography, metal deposition, reactive ion etching, and chemical etching.

It should be noted that long term implants are not only subjected to hydrolytic degradation in an *in vivo* environment. Takmakov et al. (2015) pointed out that hydrolytic degradation alone may not adequately capture the aggressive chemical environment that is created by activated immune cells, which release digestive enzymes and reactive oxygen species (ROS). They have developed an *in vitro* system to simulate degradation of neural implants that can occur in a stressful environment by using hydrogen peroxide to mimic the effect of ROS generation during the brain's injury response. While this presents an important part of real live conditions, the focus of the present study is on the hydrolytic degradation only, because we wanted to demonstrate the improved durability of the ester free SMP-A against the ester containing SMP-B. In future studies however, we will perform experiments to evaluate the durability of thiol-ene and thiol-ene/acrylate formulations against oxidative species such as hydrogen peroxide. We do not expect to see any differences between ester containing and ester free versions because the ester groups are reported in literature to be not susceptible for oxidation (Lyu and Untereker, 2009). The sulfide groups however, may undergo oxidation to sulfoxides and sulfones using 30% aqueous hydrogen peroxide (Jeyakumar and Chand, 2006; Gregori et al., 2008).

The ultimate goal is to utilize the hydrolytically stable SMP-A as a substrate for neural interfaces and therefore have an alternative to the currently used softeing SMP versions (Simon et al., 2017; Garcia-Sandoval et al., 2018). To validate that the polymer is compatible with microfabrication processes, SMP-A was spin-coated on silicon wafers and subjected to photolithography as previously decribed (Ecker et al., 2017). Briefly, the polymer was covered by a silicon nitride (SiN) hard mask before it was coated with positive photoresist. Afterward, a photomask was used to pattern the pacifier probe through the photoresist by exposure to UV light. Next, the probe was subjected to dry etch with SF_6 to remove unpatterned hard mask. Subsequently, oxygen plasma was applied to remove excess polymer and patterned photoresist. Finally, the sample was etched with hydrofluoric acid to remove SiN that was on the SMP (Garcia-Sandoval et al., 2018). The micro-fabricated pacifier probes were also used for the *in vitro* cytotoxicity test.

Another important aspect is that materials for biomedical applications should be biocompatible and sterilizable. The materials need to be able to show a desirable performance with respect to a specific medical treatment, without any unwanted effects on the tissues (Johnson and Shiraishi, 2014; Huang et al., 2017). One of the tests for evaluating prospective biocompatibility of biomedical devices before clinical survey is *in vitro* cytotoxicity (Johnson and Shiraishi, 2014). To investigate the potential toxicity without affecting the mechanical or chemical properties of the polymer, cytotoxicity tests were performed on pacifier probes by incubating fibroblasts with extract of SMP-A for 24 h. **Figure 8** confirms that the extract of the polymer at both concentrations is reliable and the polymer is expected to be safe for biomedical applications. We have seen, that SMP-B produces some water soluble byproducts after hydrolysis. These byproducts may undergo some deleterious reactions including oxidation *in vivo*. Therefore, the degraded polymer may not prove to be as biocompatible as the original polymer. Additional studies, such as functional neurotoxicity or cytotoxicity assays using primary cortical neurons, (Charkhkar et al., 2014) need to be performed to further investigate potential harm of degradation product. On the other hand, SMP-A sustained even in harsh conditions without any signs of degradation and therefore is less of a biocompatibility concern. Biomedical devices need to be sterilized properly for *in vivo* studies. To inquire the effect of sterilization on mechanical properties, SMP-A was subjected to sterilization with ethylene oxide (EtO) as previously described (Ecker et al., 2017). Since the sterilization with EtO was performed at a low temperature, it has negligible effects on the mechanical properties of SMPs. DMA data (shown in SI, **Supplementary Figure 6**) before and after sterilization shows that storage modulus and glass transition did not change remarkably.

CONCLUSION

Ester free (SMP-A) and ester containing (SMP-B) polymers with comparable thermomechanical properties and softening capabilities were prepared and their stability *in vitro* was evaluated. Accelerated aging tests were performed on both polymers and their stability was compared. According to the test

results, ester free polymers are projected to be stable for at least 7 years in the biological environment, whereas the ester containing polymer should be stable for approximately 1 year. Therefore, the new ester-free polymer (SMP-A) is a good candidate for future devices. It was stable under the tested conditions and is therefore much more reliable and robust than SMP-B, but still biocompatible. Furthermore, fabrication of pacifier probes demonstrated that SMP-A was stable in cleanroom processes and conserved its mechanical properties. Next steps will include the fabrication of fully functional neural interfaces and their testing *in vitro* as well as *in vivo*.

AUTHOR CONTRIBUTIONS

SH and ME: Conceptualization; SH, RR, BB, and AS: Methodology; SH, RR, BB, and ME: Formal Analysis; SH, RR, and BB: Data Curation; SH and ME: Writing–Original Draft Preparation; SH and ME: Writing–Review and Editing; SH, RR, and BB: Visualization; ME: Supervision; ME: Project Administration; WV and JP: Resources; JP and WV: Funding Acquisition; All authors approved the final version to be published and agreed to be accountable for all aspects of the work.

ACKNOWLEDGMENTS

This work was supported by the Center for Engineering Innovation and in parts by the Office of the Assistant Secretary of Defense for Health Affairs through the Peer Reviewed Medical Research Program under Award No. W81XWH-15-1-0607. Opinions, interpretations, conclusions and recommendations are those of the authors and are not necessarily endorsed by the Department of Defense. Additionally, the contents do not represent the views of the U.S. Department of Veterans Affairs or the United States Government. The authors want to thank Dr. Taylor Ware for allowing us to use the environmental DMA.

SUPPLEMENTARY MATERIAL

The Supplementary Material for this article can be found online at: https://www.frontiersin.org/articles/10.3389/fmats.2018.00066/full#supplementary-material

REFERENCES

ASTM (2018). *Standard Guide for Accelerated Aging of Sterile Barrier Systems for Medical Devices*. ASTM F1980–07.

Baer, G., Wilson, T. S., Matthews, D. L., Maitland, D. (2007). Shape-memory behavior of thermally stimulated polyurethane for medical applications. *J. Appl. Polym. Sci.* 103, 3882–3892. doi: 10.1002/app.25567

Barrett, R., Francis, W., Abrahamson, E., Lake, M. S., and Scherbarth, M. (2006). "Qualification of elastic memory composite hinges for spaceflight applications," in *47th AIAA/ASME/ASCE/AHS/ASC Structures, Structural Dynamics, and Materials Conference* (Newport, RI). doi: 10.2514/6.2006-2039

Baudis, S., Behl, M., and Lendlein, A. (2014). Smart polymers for biomedical applications. *Macromol. Chem. Phys.* 215, 2399–2402. doi: 10.1002/macp.201400561

Black, B. J., Ecker, M., Stiller, A., Rihani, R., Danda, V. R., Reed I., et al. (2018). *In vitro* compatibility testing of thiol-ene/acrylate-based shape memory polymers for use in implantable neural interfaces. *J. Biomed. Mater. Res. A* doi: 10.1002/jbm.a.36478. [Epub ahead of print].

Buckley, P. R., McKinley, G. H., Wilson, T. S., Small, W., Benett W.J., Bearinger J.P., et al. (2006). Inductively heated shape memory polymer for the magnetic actuation of medical devices. *IEEE Transac. Biomed. Eng.* 53, 2075–2083. doi: 10.1109/TBME.2006.877113

Charkhkar, H., Frewin, C., Nezafati, M., Knaack, G. L., Peixoto, N., Saddow S. E., et al. (2014). Use of cortical neuronal networks for *in vitro* material biocompatibility testing. *Biosensors Bioelectron.* 53, 316–323. doi: 10.1016/j.bios.2013.10.002

Dietsch, B., and Tong, T. (2007). A review - Features and benefits of shape memory polymers (SMPs). *J. Adv. Mater.* 39, 3–12. Available online at: http://apps.webofknowledge.com/full_record.do?product=WOS&search_mode=GeneralSearch&qid=8&SID=8BSUhmnqWxNvZmIqxlx&page=1&doc=1

Do, D. H., Ecker, M., and Voit, W. E. (2017). Characterization of a Thiol-Ene/acrylate-based polymer for neuroprosthetic implants. *ACS Omega* 2, 4604–4611. doi: 10.1021/acsomega.7b00834

Ecker, M., Danda, V., Shoffstall, A. J., Mahmood, S. F., Joshi-Imre A., Frewin C. L., et al. (2017). Sterilization of Thiol-ene/Acrylate based shape memory polymers for biomedical applications. *Macromol. Mater. Eng.* 302:1600331. doi: 10.1002/mame.201600331

Ecker, M., and Pretsch, T. (2013). Durability of switchable QR code carriers under hydrolytic and photolytic conditions. *Smart Mater. Struct.* 22:094005. doi: 10.1088/0964-1726/22/9/094005

Ecker, M., and Pretsch, T. (2014a). Multifunctional poly(ester urethane) laminates with encoded information. *RSC Adv.* 4, 286–292. doi: 10.1039/C3RA45651J

Ecker, M., and Pretsch, T. (2014b). Novel design approaches for multifunctional information carriers. *RSC Adv.* 4, 46680–46688. doi: 10.1039/C4RA08977D

Feninat, F. E., Laroche, G., Fiset, M., and Mantovani, D. (2002). Shape Memory materials for biomedical applications. *Adv. Eng. Mater.* 4, 91–104. doi: 10.1002/1527-2648(200203)4:3<91::AID-ADEM91>3.0.CO;2-B

Garcia-Sandoval, A., Pal, A., Mishra, A. M., Sherman, S., Parikh, A., Joshi-Imre A., et al. (2018). Chronic softening spinal cord stimulation arrays. *J. Neural Eng.* 15:045002. doi: 10.1088/1741-2552/aab90d

Gregori, F., Nobili, I., Bigi, F., Maggi, R., Predieri, G., and Sartori, G. (2008). Selective oxidation of sulfides to sulfoxides and sulfones using 30% aqueous hydrogen peroxide and silica-vanadia catalyst. *J. Mol. Catal. A Chem.* 286, 124–7. doi: 10.1016/j.molcata.2008.02.004

Hager, M. D., Bode, S., Weber, C., and Schubert, U. S. (2015). Shape memory polymers: past, present and future developments. *Prog. Polym. Sci.* 49–50, 3–33. doi: 10.1016/j.progpolymsci.2015.04.002

Hemmerich, K. J. (1998). General aging theory and simplified protocol for accelerated aging of medical devices. *Medi. Plastic Biomater.* 5, 16–23.

Hu, J., and Chen, S. (2010). A review of actively moving polymers in textile applications. *J. Mater. Chem.* 20, 3346–3355. doi: 10.1039/b922872a

Hu, J., Meng, H., Li, G., and Ibekwe, S. I. (2012a). A review of stimuli-responsive polymers for smart textile applications. *Smart Mater. Struct.* 21:053001. doi: 10.1088/0964-1726/21/5/053001

Hu, J., Zhu, Y., Huang, H., and Lu, J. (2012b). Recent advances in shape memory polymers: structure, mechanism, functionality, modeling and applications. *Prog. Polym. Sci.* 37, 1720–1763. doi: 10.1016/j.progpolymsci.2012.06.001

Huang, Y., Zhou, J., Hakamivala, A., Wu, J., Hong, Y., Borrelli, J., et al. (2017). An optical probe for detecting chondrocyte apoptosis in response to mechanical injury. *Sci. Rep.* 7:10906. doi: 10.1038/s41598-017-10653-y

Immergut, E. H., and Mark, H. F. (1965). Principles of plasticization. plasticization and plasticizer processes. *Am. Chem. Soc.* 48, 1–26. doi: 10.1021/ba-1965-0048.ch001

Ishizawa, J., Imagawa, K., Minami, S., Hayashi, S., and Miwa, N. (2003). "Research on Application of Shape Memory Polymers to Space Inflatable Systems," in

Proceeding of the 7th International Symposium on Artificial Intelligence, Robotics and Automation in Space: i-SAIRAS (Nara).

ISO (2008). *ISO 10993-5 Biological Valuation of Medical Devices, Part 5: Tests for in vitro Cytotoxicity*. Geneva: International Organization for Standardization.

Jeyakumar, K., and Chand, D. K. (2006). Selective oxidation of sulfides to sulfoxides and sulfones at room temperature using H_2O_2 and a Mo(VI) salt as catalyst. *Tetrahedron Lett.* 47, 4573–4576. doi: 10.1016/j.tetlet.2006.04.153

Johnson, A. and Shiraishi, T. (2014). "Biocompatibility of precious metals for medical applications," in *Precious Metals for Biomedical Applications*, eds N. Baltzer and T. Copponnex (Woodhead Publishing), 37–55. doi: 10.1533/9780857099051.1.37

Kulshrestha, A. S., and Mahapatro, A. (2008). Polymers for biomedical applications. *Polym. Biomed. Appl.* 977, 1–7. doi: 10.1021/bk-2008-0977.ch001

Lecomte, A., Degache, A., Descamps, E., Dahan, L., and Bergaud, C. (2017). *In vitro* and *in vivo* biostability assessment of chronically-implanted Parylene C neural sensors. *Sensors Actuators B Chemical* 251(Suppl. C):1001–8. doi: 10.1016/j.snb.2017.05.057

Lendlein, A. (2010). *Shape-Memory Polymers*. Berlin; Heidelberg: Springer.

Lendlein, A., and Behl, M. (2008). "Shape-memory polymers for biomedical applications," in *CIMTEC 2008 - Proceedings of the 3rd International Conference on Smart Materials, Structures and Systems - Smart Materials and Micro/Nanosystems* (Acireale), 96–102.

Liu, C., Qin, H., and Mather, P. T. (2007). Review of progress in shape-memory polymers. *J. Mater. Chem.* 17, 1543–1558. doi: 10.1039/b615954k

Lundberg, P., Bruin, A., Klijnstra, J. W., Nystrom, A. M., Johansson M., Malkoch M., et al. (2010). Poly(ethylene glycol)-based thiol-ene hydrogel coatings-curing chemistry, aqueous stability, and potential marine antifouling applications. *ACS Appl. Mater. Interfaces* 2, 903–912. doi: 10.1021/am900875g

Lyu, S., and Untereker, D. (2009). Degradability of polymers for implantable biomedical devices. *Int. J. Mol. Sci.* 10:4033. doi: 10.3390/ijms10094033

Mather, P. T., Luo, X., and Rousseau, I. A. (2009). Shape memory polymer research. *Annu. Rev. Mater. Res.* 39, 445–471. doi: 10.1146/annurev-matsci-082908-145419

Matilla, H. R. (2006). *Intelligent Textiles and Clothing*. Cambridge, UK: Woodhead Publishing in Textiles.

Pretsch, T., Ecker, M., Schildhauer, M., and Maskos, M. (2012). Switchable information carriers based on shape memory polymer. *J. Mater. Chem.* 22, 7757–7766. doi: 10.1039/c2jm16204k

Reit, R., Zamorano, D., Parker, S., Simon, D., Lund, B., Voit, W., et al. (2015). Hydrolytically stable thiol–ene networks for flexible bioelectronics. *ACS Appl. Mater. Interfaces* 7, 28673–28681. doi: 10.1021/acsami.5b10593

Rory Barrett, W. F., Erik, A., Mark Lake, S., and Mark, S. (2006). "Qualification of elastic memory composite hinges for spaceflight applications,"in *47nd IAA/ASME/ASCE/AHS/ASC SDM Conference*. (Newport, RI: AIAA-2006-2039).

Rubehn, B., and Stieglitz, T. (2010). In vitro evaluation of the long-term stability of polyimide as a material for neural implants. *Biomaterials* 31, 3449–3458. doi: 10.1016/j.biomaterials.2010.01.053

Ryu, S. I., and Shenoy, K. V. (2009). Human cortical prostheses: lost in translation? *Neurosurg. Focus* 27:E5. doi: 10.3171/2009.4.FOCUS0987

Shoffstall, A. J., Srinivasan, S., Willis, M., Stiller, A. M., Ecker, M., Voit W. E., et al. (2018). A mosquito inspired strategy to implant microprobes into the brain. *Sci. Rep.* 8:122. doi: 10.1038/s41598-017-18522-4

Simon, D. M., Charkhkar, H. C., St John, Rajendran, S., Kang, T., Reit, R., et al. (2017). Design and demonstration of an intracortical probe technology with tunable modulus. *J. Biomed. Mater. Res. A* 105, 159–168. doi: 10.1002/jbm.a.35896

Singhal, P., Boyle, A., Brooks, M. L., Infanger, S., Letts, S., Small W., et al. (2013). Controlling the actuation rate of low-density shape-memory polymer foams in water. *Macromol. Chem. Phys.* 214, 1204–1214. doi: 10.1002/macp.201200342

Takmakov, P., Ruda, K., Scott Phillips, K., Isayeva, I. S., Krauthamer, V., and Welle C. G., (2015). Rapid evaluation of the durability of cortical neural implants using accelerated aging with reactive oxygen species. *J. Neural Eng.* 12:026003. doi: 10.1088/1741-2560/12/2/026003

Teo, A. J. T., Mishra, A., Park, I., Kim, J., Park, T., and, Yoon, J. (2016). Polymeric biomaterials for medical implants and devices. *ACS Biomater. Sci. Eng.* 2, 454–472. doi: 10.1021/acsbiomaterials.5b00429

Wang, K., Strandman, S., and Zhu, X. X. (2017). A mini review: shape memory polymers for biomedical applications. *Front. Chem. Sci. Eng.* 11, 143–153. doi: 10.1007/s11705-017-1632-4

Ware, T., Simon, D., Hearon, K., Kang, T. H., Maitland, D., et al. (2013). Thiol-click chemistries for responsive neural interfaces. *Macromol. Biosci.* 13, 1640–1647. doi: 10.1002/mabi.201300272

Ware, T., Simon, D., Liu, C., Musa, T., Vasudevan, S., Sloan, A., et al. (2014). Thiol-ene/acrylate substrates for softening intracortical electrodes. *J. Biomed. Mater. Res. B Appl. Biomater.* 102, 1–11. doi: 10.1002/jbmb.32946

Yanju, L., Haiyang, D., Liwu, L., and Jinsong, L. (2014). Shape memory polymers and their composites in aerospace applications: a review. *Smart Mater. Struct.* 23:23001. doi: 10.1088/0964-1726/23/2/023001

Yanju, L., and Jinsong, L. (2010). "Applications of shape-memory polymers in aerospace," in *Shape-Memory Polymers and Multifunctional Composites*, eds J. Leng and S. Du (Boca Raton, FL: CRC Press), 233–266. doi: 10.1201/9781420090208-c8

Conflict of Interest Statement: The authors declare that the research was conducted in the absence of any commercial or financial relationships that could be construed as a potential conflict of interest.

Copyright © 2018 Hosseini, Rihani, Batchelor, Stiller, Pancrazio, Voit and Ecker. This is an open-access article distributed under the terms of the Creative Commons Attribution License (CC BY). The use, distribution or reproduction in other forums is permitted, provided the original author(s) and the copyright owner(s) are credited and that the original publication in this journal is cited, in accordance with accepted academic practice. No use, distribution or reproduction is permitted which does not comply with these terms.

frontiers in Neuroscience

ORIGINAL RESEARCH
published: 29 November 2018
doi: 10.3389/fnins.2018.00862

Quantification of Signal-to-Noise Ratio in Cerebral Cortex Recordings Using Flexible MEAs With Co-localized Platinum Black, Carbon Nanotubes, and Gold Electrodes

*Alex Suarez-Perez[1], Gemma Gabriel[2,3], Beatriz Rebollo[1], Xavi Illa[2,3], Anton Guimerà-Brunet[2,3], Javier Hernández-Ferrer[4], Maria Teresa Martínez[4], Rosa Villa[2,3] and Maria V. Sanchez-Vives[1,5]**

[1] Systems Neuroscience, Institut d'Investigacions Biomèdiques August Pi i Sunyer (IDIBAPS), Barcelona, Spain, [2] Instituto de Microelectrónica de Barcelona, Centro Nacional de Microelectrónica, Consejo Superior de Investigaciones Científicas, Barcelona, Spain, [3] Centro de Investigación Biomédica en Red en Bioingeniería, Biomateriales y Nanomedicina, Madrid, Spain, [4] Instituto de Carboquímica, Consejo Superior de Investigaciones Científicas, Zaragoza, Spain, [5] ICREA, Barcelona, Spain

Developing new standardized tools to characterize brain recording devices is critical to evaluate neural probes and for translation to clinical use. The signal-to-noise ratio (SNR) measurement is the gold standard for quantifying the performance of brain recording devices. Given the drawbacks with the SNR measure, our first objective was to devise a new method to calculate the SNR of neural signals to distinguish signal from noise. Our second objective was to apply this new SNR method to evaluate electrodes of three different materials (platinum black, Pt; carbon nanotubes, CNTs; and gold, Au) co-localized in tritrodes to record from the same cortical area using specifically designed multielectrode arrays. Hence, we devised an approach to calculate SNR at different frequencies based on the features of cortical slow oscillations (SO). Since SO consist in the alternation of silent periods (Down states) and active periods (Up states) of neuronal activity, we used these as noise and signal, respectively. The spectral SNR was computed as the power spectral density (PSD) of Up states (signal) divided by the PSD of Down states (noise). We found that Pt and CNTs electrodes have better recording performance than Au electrodes for the explored frequency range (5–1500 Hz). Together with two proposed SNR estimators for the lower and upper frequency limits, these results substantiate our SNR calculation at different frequency bands. Our results provide a new validated SNR measure that provides rich information of the performance of recording devices at different brain activity frequency bands (<1500 Hz).

Keywords: SNR, neural recording, slow oscillations, low impedance, neural interfaces

OPEN ACCESS

Edited by:
Ulrich G. Hofmann, Universitätsklinikum Freiburg, Germany

Reviewed by:
Luca Berdondini, Fondazione Istituto Italiano di Tecnologia, Italy
Sara L. Gonzalez Andino, Geneva University Hospitals (HUG), Switzerland

***Correspondence:**
Maria V. Sanchez-Vives
msanche3@clinic.ub.es; sanchez.vives@gmail.com

Specialty section:
This article was submitted to Neural Technology, a section of the journal Frontiers in Neuroscience

Received: *28 May 2018*
Accepted: *05 November 2018*
Published: *29 November 2018*

Citation:
Suarez-Perez A, Gabriel G, Rebollo B, Illa X, Guimerà-Brunet A, Hernández-Ferrer J, Martínez MT, Villa R and Sanchez-Vives MV (2018) Quantification of Signal-to-Noise Ratio in Cerebral Cortex Recordings Using Flexible MEAs With Co-localized Platinum Black, Carbon Nanotubes, and Gold Electrodes. Front. Neurosci. 12:862. doi: 10.3389/fnins.2018.00862

INTRODUCTION

Interfacing the brain using electrodes to record from and stimulate it is a standard approach for investigating brain function. Multielectrode arrays (MEAs) in particular are widely used devices, both in basic research and in the clinic, that can record electrophysiological signals simultaneously from different neuronal populations. MEAs have been used in basic research to study brain function in *in vitro* experiments (Berdondini et al., 2006; Taketani and Baudry, 2006; D'Andola et al., 2017) as well as in anesthetized and in chronically implanted behaving animals (Nicolelis et al., 2003; Dickey et al., 2009; Khodagholy et al., 2015). Furthermore, the use of chronic implants based on MEA technology has increased in the last few decades with the development of brain-computer interfaces (BCIs) to compensate for lost neural functions (Hochberg et al., 2006; Lebedev and Nicolelis, 2006; Donoghue, 2008). An important group of BCIs is based on the recording of the local neuronal population such as local field potentials (LFPs) and on multi-unit activity (MUA) (Lebedev and Nicolelis, 2006). An important drawback of this group of BCIs is their limitations on obtaining brain signals within a large bandwidth, especially high-frequency signals such as MUA. These limitations are not only a feature of the electrodes themselves, but also a feature of the design of the recording system and the filtering procedure. Hence, one of the strategies to overcome this frequency limitation consists in increasing the ability of the recording system to accurately sense and record biological signals in their whole frequency range in order to detect as many frequency bands as possible. The main feature that characterizes an ideal extracellular microelectrode for recording brain signals is a high signal-to-noise ratio (SNR), which is a measure of the fidelity of the received message for the whole frequency band containing useful neural information (Baranauskas et al., 2011). SNR is usually assessed using saline-measured electrode impedances. Typically, electrodes are made of metallic conductors such as gold (Au), and since the electrodes used in MEAs are on the micrometer scale, it is a challenge to achieve low electrode impedance with plain conductors only (Obien et al., 2015). It is generally assumed that higher SNR values can be achieved by lowering the electrode impedance, which decreases with increasing active surface area. Thus, recent research has pursued new materials and fabrication techniques aimed at increasing as much as possible the active surface area. Two particularly appealing approaches to increasing the active surface area of electrodes are: (1) platinum black coating electroplated on metallic electrodes (Pt) (Desai et al., 2010; Zhang et al., 2013); and (2) polypyrrole/carbon nanotubes composite electrodeposited on metal electrodes (CNTs) (Keefer et al., 2008; Baranauskas et al., 2011). Whereas the quantitative characterization of the working performance of electrodes is usually achieved by using electrochemical impedance spectroscopy (EIS), this measure is useful to predict some electrode properties but does not assess the entire electrode performance while measuring biological signals (Ludwig et al., 2006; Ferguson et al., 2009; Baranauskas et al., 2011). On the other hand, the SNR of the signal recorded through the electrode allows the quantification of the recording performance of the electrode and therefore contrasting electrodes of different types.

Besides electrode limitations, it is important to consider that recording systems have to ensure an amplification stage as close as possible to the recording site by means of a high common mode rejection (the ability to reject common noise in the active and reference electrode) in order to reduce external noise and ensure stable recordings. This can be achieved by a large input impedance in the amplifier (normally in the order of TΩ at 1 kHz) (Nelson et al., 2008). The recorded frequency band is also limited by the filters of the amplifiers, which have to ensure the same amplification value for all the frequencies of interest (Kappenman and Luck, 2010).

Current approaches for assessing SNR in brain recordings rely mostly on the amplitude of the signal. For instance, some reported methodologies are based on the recording of evoked (Kuzum et al., 2014) or spontaneous epileptic activity (Khodagholy et al., 2013) and the SNR is calculated by taking the highest peak during a period of epileptic activity and dividing it by the standard deviation (SD) of the background signal during a period of low biological activity. Recently, a similar procedure was performed by calculating the SNR of slow oscillations—an activity pattern that alternates between periods of neuronal firing, or Up states, and periods of almost neuronal silence, or Down states (Steriade et al., 1993)—as the ratio of the Up state amplitude to the Down state SD (Blaschke et al., 2017). Since these SNR approaches are based on the amplitude of the signal, the calculated SNR values only evaluate the behavior of the devices at the frequency of the recorded events. Nonetheless, obtaining information about the SNR at different frequency ranges of the brain signals is a relevant step in the characterization of recording devices. To overcome the limitations of the current SNR approaches, new methodologies to quantify the SNR in brain recordings are needed.

In brain recordings, the frequency bands of interest include the LFP (<500 Hz), MUA (200–1500 Hz) (Mattia and Del Giudice, 2002) and single-unit activity (>1000 Hz). Within the LFP band are the slow oscillations, which constitute a good model to study the SNR of brain signals because they encompass different frequency bands: from <1 Hz (frequency of Up and Down state alternation) to high-frequency synchronization in the β/γ range (15–100 Hz) (Steriade et al., 1996; Compte et al., 2008) and population spiking activity (MUA) above 200 Hz during Up states (Steriade et al., 1993). Slow oscillations spontaneously arise during slow wave sleep and under anesthesia *in vivo* (Steriade et al., 1993), and also in *in vitro* brain slices (Sanchez-Vives and McCormick, 2000), granting the possibility of exploring them in distinct experimental conditions.

The aims of this study were: (1) to develop and validate a new approach to quantify the SNR of brain recording devices; and (2) to compare the throughput of co-localized electrodes of different materials, namely Au, CNTs and Pt. For these purposes, we used an adaptation of the SNR calculation based on the features of the slow oscillations, which we recorded using MEAs with electrodes of the three aforementioned materials distributed in tritrodes and stereotrodes. The integration of three materials in close vicinity within the same MEA allowed the direct comparison between

them, thereby avoiding the problem of comparing electrodes from different probes and/or electronic systems, and avoiding recording different neural activity patterns coming from distant neuronal populations.

MATERIALS AND METHODS

SNR Calculation

Signal-to-noise ratio is defined as the ratio of the power spectral density (PSD) of a signal (meaningful information) with respect to the power of the background noise. In the analysis of brain recordings, this measure is commonly applied in spike sorting to select the best recording location, and also to characterize the reliability of neural information transmission (Schultz, 2007). The SNR can be calculated from spontaneous or evoked neural responses to different types of stimuli (electrical, sensory, etc.). For example, in the calculation of the SNR from a time-dependent signal in single cell recordings, the action potentials are considered "signal" and the inter-spike intervals the "noise." Then, following the description from Rieke et al. (1997), the SNR is calculated as follows:

$$SNR(f) = \frac{S(f)}{N(f)} \tag{1}$$

Where $S(f)$ is the PSD of the signal and $N(f)$ is the PSD of the noise. In our study, we obtained extracellular LFP recordings from active cortical slices that spontaneously generated slow oscillations (Sanchez-Vives and McCormick, 2000). Since Up states are the consequence of a population of neurons firing, we considered Up states the "signal." As described above, Up states contain a broad band of frequencies; that is, they contain meaningful information. On the other hand, we considered Down states the "noise" because they are mostly silent periods. In order to quantify the SNR at different frequencies, the spectral SNR (in dB) becomes:

$$= 10\ \log_{10} \frac{\frac{1}{N}\sum_{i=1}^{N}(PSD_{Up})_i}{\frac{1}{N'}\sum_{j=1}^{N'}(PSD_{Down})_j}[dB] \tag{2}$$

where N is the total number of Up states and N' is the total number of Down states.

SNR Estimators

To easily quantify the performance of each material, thereby avoiding the vast amounts of information obtained through the spectral analysis, we proposed and validated a set of SNR estimators. The advantage of using these SNR estimators is that they reduce and summarize the large amount of information provided by the spectral SNR, since the spectral SNR gives a value of SNR at each different frequency. These estimators are derived from the spectral SNR curve (Eq. 2), or directly from the LFP signal.

Area Under the Curve (AUC)

The area under the spectral SNR curve within the frequency range from 5 to 1500 Hz, where 5 Hz is the minimum frequency allowed by the PSD and 1500 Hz is the upper limit of the MUA band. It is calculated as follows:

$$AUC = \int_{fl}^{fu} SNR_{Spectral}(f)df \tag{3}$$

where *fl* is the lower integration limit (5 Hz in this case) and *fu* is the upper integration limit (1500 Hz). However, when AUC is computed in frequency bands, these limits change, being f_0 the lowest frequency of the band and f the highest frequency of the band.

The AUC can also be calculated for defined frequency bands. In our case, we chose three frequency bands of interest: low (5–30 Hz), middle (30–200 Hz), and high (200–1500 Hz). The low band ranges from the limit of resolution of the PSD (5 Hz) to the upper limit of the β band (30 Hz). The middle band ranges from the lower limit of the γ band (30 Hz) to the lower limit of the MUA band (200 Hz). Finally, the high band corresponds to a part of the MUA band (> 200 Hz).

Frequency Limit of Detection (FLOD)

Frequency at which the spectral SNR equals zero. At this point, the power of the signal is exactly the same as the power of the noise.

Voltage SNR (vSNR)

This is the most widely reported approach to compute the SNR in LFP recordings in animals under anesthesia (Kuzum et al., 2014; Blaschke et al., 2017). The vSNR is calculated as the ratio between the mean of the peak-to-peak amplitude of all the Up states and the mean of the SD of all the Down states:

$$SNR_{Voltage} = \frac{\frac{1}{N}\sum_{i=1}^{N}(P2P_{Up})_i}{\frac{1}{N'}\sum_{j=1}^{N'}(STD_{Down})_j} \tag{4}$$

Fabrication and Characterization of the MEAs

Flexible microprobes integrating 16 Au microelectrodes were fabricated using SU-8 negative photoresist as flexible substrate as previously described (Gabriel et al., 2013; Illa et al., 2015). The fabricated MEA has dimensions of approximately 32 mm long (**Figure 1A**). The tip, where the array of distributed microelectrodes is, covers 6.00 mm × 1.55 mm. The microelectrodes are distributed in tritrodes and stereotrodes. They are 50 μm in diameter and the center-to-center distance with neighboring electrodes is 200 μm. The rest of the tip is provided with holes to enhance tissue oxygenation. To facilitate the use of the fabricated microprobes, these were connected to a printed circuit board (PCB) with a proper pin output by means of a 16-channel zero insertion force (ZIF) connector. For this, the connecting pads of the microprobe were designed to match the specifications of the desired ZIF connector and, additionally, a spacer was used to ensure good contact between the probe and the connector.

Platinum Black (Pt) Electrodeposition

Au electrodes on individual devices were electrochemically coated with a porous layer of platinum black to reduce

their impedance through a customized process of platinization (Gabriel et al., 2007). More specifically, electrodeposition was performed using a platinum chloride solution [0.1 M hydrochloric acid, 2.3% platinum (IV) chloride and 0.023% lead (IV) acetate 99%] at −0.2 V for 20 s. The electrodes modified with platinum black correspond to numbers 3, 4, 7, 10, 13, and 14 in **Figure 1A**, depicted in black. In **Figure 1B**, a scanning electron microscopy image shows the rough morphology that is achieved by electrodepositing this material.

Single-Walled Carbon Nanotubes/Polypyrrole Composite (CNTs) Electrodeposition

Carbon nanotubes were synthesized by the arc-discharge method using graphite electrodes and a Ni/Y 4/1% metal catalyst mixture. As-grown single-walled carbon nanotubes (agSWCNTs; initial nanotube concentration: 4 mg/ml) were dispersed ultrasonically in aqueous 1% sodium dodecylbenzenesulfonates (SDBS) solution. Afterward, the dispersion was centrifuged at 13,000 rpm for 30 min (Hermle Z383, Hermle Labortechnik, Wehingen, Germany) in order to increase their purity and decrease their metal content (Ansón-Casaos et al., 2014), achieving a final nanotube concentration of 1.3 mg/ml.

Electrodeposition of the composite material was carried out in galvanostatic conditions (0.13 mg/ml gSWCNTs, buffer phosphate with 0.05 M dihydrogen phosphate and 0.05 M monohydrogen phosphate solutions, 3.2 mM SDBS and 0.14 M pyrrole) using a constant current value of 3 mA $\cdot$ cm^{-2} during 120 s. An Ag/AgCl (3 M NaCl) electrode was used as a reference electrode, and a graphite bar was used as a counter electrode.

Figure 1A depicts the electrodes modified with the CNTs composite with the numbers 1, 2, 5, 12, 15, and 16, shown in green. In **Figure 1B**, a scanning electron microscopy image also shows the rough morphology that is obtained with this coating, and even the tubes can be observed in a random distribution (for further information about the fabrication of the MEAs, see Gabriel et al. (2013).

In vitro Recordings

Slice Preparation

This study was carried out in accordance with Spanish regulatory laws (BOE-A-2013-6271), which comply with the European Union guidelines on protection of vertebrates used for experimentation (Directive 2010/63/EU of the European Parliament and the Council of September 22, 2010). The protocol was approved by the ethics committee of Hospital Clinic Barcelona. Two ferrets (5-month-old, male) were anesthetized with sodium pentobarbital and decapitated. The entire forebrain was rapidly removed and placed in oxygenated cold (4–10°C) bathing medium. Coronal slices (0.4-mm thick) from the occipital cortex containing primary and secondary visual cortical areas (areas 17, 18, and 19) were used (Innocenti et al., 2002). A modification of the sucrose-substitution was used to increase tissue viability (Aghajanian and Rasmussen, 1989). Briefly, during the preparation of slices, the tissue was placed in a solution in which NaCl was replaced with sucrose. After the preparation, slices were placed in an interface style recording chamber (Fine Sciences Tools, Foster City, CA, United States). During the first 15 min, cortical slices were superfused with an equal mixture in volume of the normal bathing medium and the sucrose-substituted solution. Next, normal bathing medium was added to the chamber and the slices were superfused for 1–2 h. The modified slice solution was used throughout the rest of the experiment. Bath temperature was maintained at 36°C. The artificial cerebrospinal fluid (ACSF) bathing medium contained (in mM): NaCl, 126; KCl, 2.5; $MgSO_4$, 2; NaH_2PO_4, 1.25; $CaCl_2$, 2; $NaHCO_3$, 26; dextrose, 10, and was aerated with 95% O_2, 5% CO_2 to a final pH of 7.4. The modified solution had the same ionic composition except for different levels of (in mM): KCl, 4; $MgSO_4$, 1 and $CaCl_2$, 1–1.2 (Sanchez-Vives and McCormick, 2000). Electrophysiological recordings started after allowing at least 2 h of recovery.

Recording Set-Up

Multielectrode arrays attached to a ZIF connector were placed on the slices. The data acquisition system comprised a 16-channel preamplifier (μPA16, Multichannel Systems, Germany) and amplifier (PGA16, Multichannel Systems, Germany) with a 100× gain factor, and a CED 1401 digitizer and Spike 2 software (Cambridge Electronic Design, United Kingdom). The sampling frequency of the recordings was set to 5 kHz.

Data Analysis

Recordings of 20–60 s duration only from operative tritrodes and stereotrodes were selected for the analysis. From optical imaging and EIS characterization (**Figure 1** and **Supplementary Figure S1**), exclusion criteria were defined: only tritrodes and stereotrodes with the three or two electrodes, respectively, well fabricated and operative were selected for the comparison analysis (some of them were short-circuited or the material was not well deposited). In addition, only recordings with detectable Up states were used. Five MEAs containing four different tritrodes and two different stereotrodes were tested in seven cortical slices. After excluding non-operative tritrodes and stereotrodes (usually a very noisy electrode recording), we ended up with the following sample sizes: $N_{Pt} = N_{CNTs} = 102$ and $N_{Au} = 67$ recordings.

Signal analysis was performed using MATLAB 2012a (The MathWorks Inc., Natick, MA, United States). Up and Down state detection was performed as in Castano-Prat et al. (2017). Detection of Up and Down states from the recorded signals was based on three main fingerprints of the Up states: the slow LFP deflection, the gamma rhythm, and the neuronal firing. These three features are reflected in three different time series: (1) the slow oscillation envelope (smoothing filter with a 5-ms moving window), (2) the envelope of the variance of the gamma-filtered LFP (15–100 Hz) (Mukovski et al., 2007), and (3) the estimation of the MUA, which was bandpass filtered from 200 to 1500 Hz (Mattia and Sanchez-Vives, 2012). From each LFP we obtained a highly processed time series as a linear combination of these three features. The contribution of each one was weighted by principal component analysis (PCA). As the three signals correspond to three different frequency bands, this method is very robust against colored noise or band-limited electrode malfunction. Up and Down states were singled out by setting a threshold in

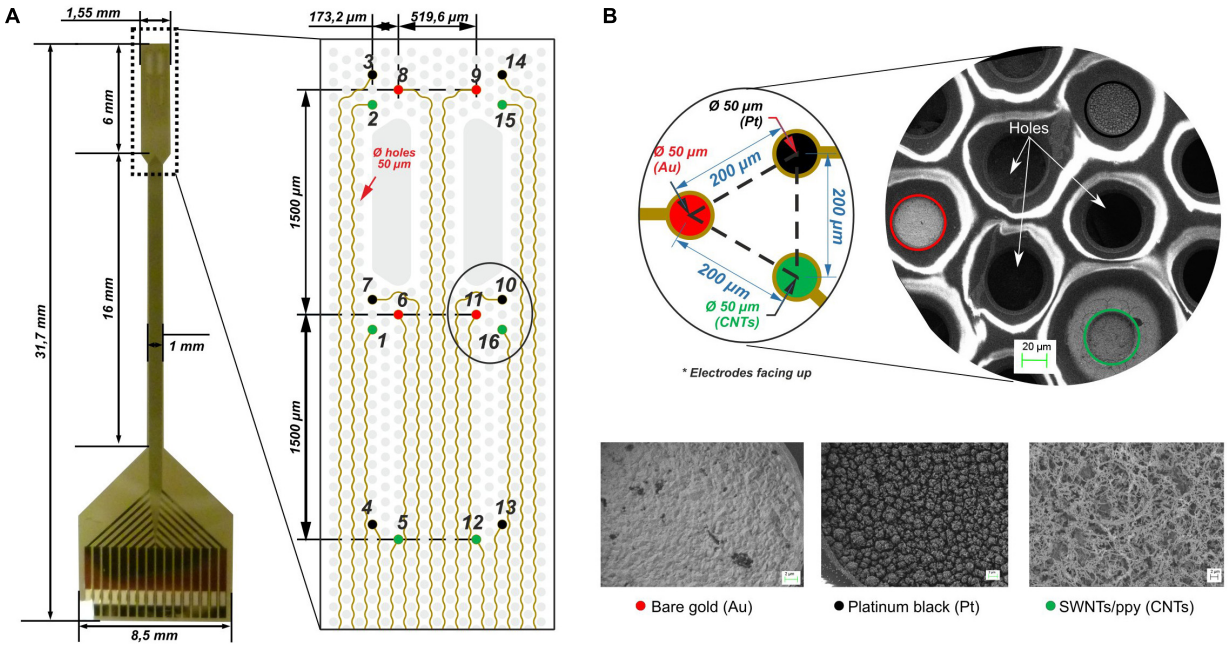

FIGURE 1 | Cortical multielectrode arrays (MEAs). **(A)** Overview of the microfabricated device. Optical microscopy image of the MEA including dimensions and layout in detail of the microelectrodes disposition (tritrodes and stereotrodes) and holes (gray). **(B)** Tritrodes distribution in detail and scanning electron micrographs (SEM) showing 50-µm bare gold microelectrodes before the modification (Au in red), after the modification with platinum black (Pt in black) and the single-walled carbon nanotubes/polypyrrole composite electrode (CNTs in green).

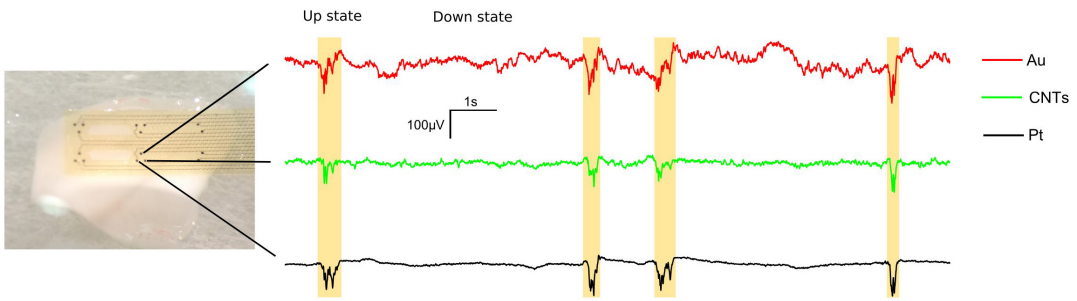

FIGURE 2 | Local field potential (LFP) traces from a representative tritrode showing the recording of spontaneous cortical slow oscillations *in vitro* for the three co-localized electrodes of different materials (Au, CNTs and Pt). For this figure, the LFP signals were filtered by applying Notch filters at 50 and 150 Hz and a smoothing filter using 10-ms sliding windows with 5-ms steps. Up states are shown in yellow.

this highly processed time series. A threshold calculated from the bimodal distribution of Up and Down states duration was set on the reconstructed signal to classify the parts of the recording with more frequency content (Up states) and less frequency content (Down states). For electrodes where the detection did not work, we used the detection times from the nearest electrode.

Once the detection was performed, the PSD with a resolution of 1024 points of the fast Fourier transform (FFT) was calculated for every Up and Down state separately using Welch's method (window size 1024 time bins with an overlap of 512 time bins). The mean PSD of the Up states and Down states in the recording fragment were calculated. The same approach was employed to calculate the mean peak-to-peak amplitude of all the Up states and the mean SD of all the Down states.

The Spectral SNR was calculated for every electrode recording using Eq. (2). From the Spectral SNR, AUC was calculated by a trapezoidal numerical integration along the three different defined frequency bands. FLOD was estimated by smoothing the spectral SNR curve to easily find the intersection with zero. The smoothing filter we used is based on a moving average method with a span of 10 ms. vSNR was calculated as the mean peak-to-peak amplitude of Up states divided by the mean SD of the Down states.

For the statistical analyses, the Kolmogorov–Smirnov test was performed for every SNR estimator distribution separately for each material to test the normality. Because none of the distributions was normal, non-parametric tests were applied to assess statistical differences between materials. More specifically,

we used the Wilcoxon signed-rank test to compare the SNR distributions of different materials at every frequency, the Mann–Whitney test to assess differences in estimator distributions between different materials, and Pearson correlation coefficient to quantify the degree of association between SNR estimators. A non-parametric ANOVA test equivalent for independent samples (Kruskal–Wallis test) was performed for all the data separately for each MEA, tritrode/stereotrode and material using IBM SPSS 22 statistics software.

RESULTS

Five MEAs with electrodes of the three different materials (Au, CNTs and Pt) arranged in tritrodes and stereotrodes were tested on seven different visual cortical slices that generated spontaneous slow oscillations (**Figure 2**). From the LFP recordings of every electrode, the SNR was calculated using the different methods described above: the spectral SNR, the vSNR estimator, and the estimators derived from the spectral SNR: AUC and FLOD. The proposed SNR analysis was aimed at characterizing the behavior of the three electrode materials while recording brain signals. Moreover, the results themselves validate the proposed SNR analysis as a methodology for characterizing the SNR using biological signals.

Spectral SNR and AUC Estimator

Since the electrode SNR depends, among other things, on the impedance, the SNR is frequency-dependent. For this reason, measuring the SNR at different biological frequencies is crucial in electrode characterization. The spectral SNR curve was computed for each electrode recording and the results were grouped into materials in order to compare them. Overall, from the spectral SNR analysis, we found that Pt as well as CNTs electrodes showed significantly higher SNR values than Au electrodes for all the functional frequencies (frequencies with SNR $>$ 0 dB) (**Figure 3**). Moreover, Pt electrodes presented a slightly higher SNR than CNTs electrodes but this difference was not statistically significant for frequencies below 400 Hz. Nevertheless, for certain frequencies above 400 Hz, significant differences appeared between Pt and CNTs electrodes, Pt electrodes having higher SNR values. Regarding the MUA frequency range (200–1500 Hz), Au electrodes showed SNR values very close to zero while Pt and CNTs electrodes had SNR values of approximately 4 dB at 200 Hz (**Figure 3**). Negative SNR values at higher frequencies are caused because the Down PSD values lightly exceed Up PSD values. This effect may be caused by certain noise artifacts; since Down states have a larger duration than Up states, the probability of having some artifactual noise in Down states is also larger.

More specifically, SNR values for the low-frequency band (5–30 Hz) were almost constant for the three materials (**Figure 3**). At this frequency range, Pt and CNTs electrodes had SNR values around 9 dB while that of Au was around 4 dB. These values indicate that the power of the signal was around eight times greater than the power of the noise in recordings obtained with Pt and CNTs electrodes and 2.5 times in the case of Au electrodes ($Up_{\mathrm{PSD}}/Down_{\mathrm{PSD}} = 10^{\mathrm{SNR}/10}$). For frequencies over 50 Hz, the SNR decayed almost linearly following the typical $1/f$ decay (**Figure 3**). The PSD of the Up and Down states (inset in **Figure 3**) revealed that the power of the Up state was almost the same for Pt and CNTs electrodes while the power of the Down state was lower in Pt electrodes, resulting in better SNR values. The signals recorded by the Au electrodes showed similar powers of Up and Down states, leading to low SNR values.

The SNR distribution curves represent the mean behavior of different stereotrodes and tritrodes (**Figure 4A**). For the lower frequency band (5–30 Hz), the distributions were very wide and chi-square shaped while as the frequency increased, the distributions became narrower and closer to SNR = 0, indicating that the recording performance of the electrodes was reduced when the frequency of the signal increased (**Figure 4B**). In particular, the maximum SNR values in the low frequency band (5–30 Hz) were slightly above 20 dB for Pt and CNTs electrodes, and around 15 dB for Au (**Figure 4A**, left). While Au SNR distribution peaked at around 2 dB, the peak for Pt was about 5 dB. On the other hand, CNTs electrodes showed a bimodal SNR distribution. The results from the Kruskal–Wallis test ($p < 0.05$) suggest that this bimodality in the SNR value distribution for CNTs electrodes was due to the variability in the fabrication process since significant differences in variances are given by the distribution of SNR values sorted by the tritrode location inside the probe (**Supplementary Figure S2**). The SNR distribution in the 30–200 Hz frequency range became more similar between Pt and CNTs electrodes, although CNTs distribution was slightly broader (**Figure 4A**, middle). The distribution for these two materials was wider than that of Au, which was narrow and centered at zero. At the 200–1500 Hz frequency range, the distributions were very similar since most electrodes had their SNR around zero (**Figure 4A**, right).

The area under the spectral SNR curve (AUC) was calculated as an SNR estimator, and the distributions of normalized AUC values for the three defined frequency bands (low: 5–30 Hz, middle: 30–200 Hz, high: 200–1500 Hz) were represented in boxplots for the three different materials. For the three frequency bands, the AUC for the Pt and CNTs electrodes was significantly higher than for the Au electrodes ($p < 0.001$ for the low and middle frequency bands; $p < 0.05$ for the high frequency band) (**Figure 4B**). In the 5–30 Hz frequency range, the AUC mean value was equal for Pt and CNTs electrodes but the median was higher for CNTs. On the other hand, for the 200–1500 Hz frequency range, AUC mean values for Pt were greater. At this high-frequency range, the significance values between Pt-Au and CNTs-Au decreased from $p < 0.001$ to $p < 0.05$ because most AUC values were very close to zero, but the difference was still significant.

The results from the spectral SNR analysis shed light on the recording performance of the electrodes for the whole spectral range from 5 to 1500 Hz. The analyzed data show significant differences between Au and Pt, and between Au and CNTs electrodes, indicating that Pt and CNTs electrodes record the brain signals better than Au electrodes for the whole range of studied frequencies. No significant differences were found between Pt and CNTs electrodes but our results suggest that Pt electrodes had a slightly better performance

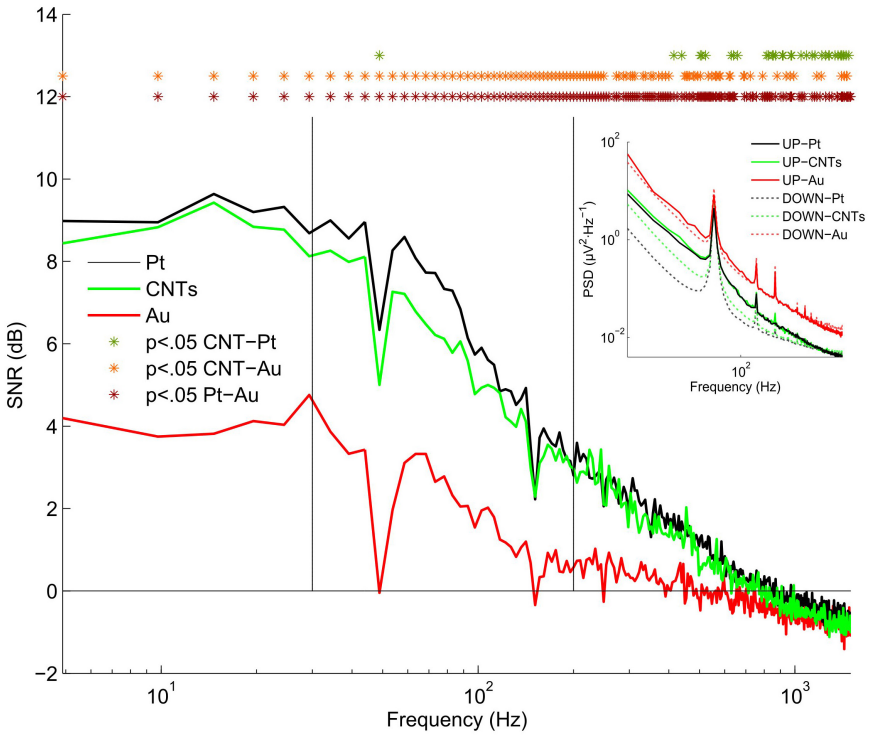

FIGURE 3 | Spectral signal-to-noise ratio (SNR). SNR was calculated as in Eq. (2) giving a SNR value for each frequency ranging from 5 to 1500 Hz. The spectral SNR curve was calculated for the electrodes of the three different materials and the mean SNR curve of the five MEAs was tested in seven slices. The horizontal line at zero represents $SNR = 0$ ($Up_{PSD} = Down_{PSD}$). Vertical lines separate the three frequency bands: low, 5–30; medium, 30–200; and high, 200–1500 Hz. Inset; Mean power spectral density of Up and Down states (solid and dotted lines, respectively). $^*p < 0.05$ by Wilcoxon signed-rank test.

than CNTs electrodes. Finally, our findings validate that the AUC estimator, computed at different selected frequency bands, properly describes the overall behavior of the electrodes in terms of SNR for low, middle, and high frequency ranges.

vSNR and FLOD as SNR Estimators for Lower and Higher Frequencies, Respectively

As described above, vSNR and FLOD were calculated as estimators to complement and validate the results obtained with the spectral SNR analysis. Our findings show that vSNR, FLOD, and AUC show the same qualitative results, reinforcing the outcome of the previous SNR analysis (**Figure 5**).

As vSNR is calculated using the amplitude of the signal during Up states and the SD of the Down states, vSNR values are expected to describe the SNR at frequencies related to the slow oscillations (>1 Hz); that is, very low frequencies. In agreement with this, the results shown in the vSNR boxplot (**Figure 5A**) match the results obtained with the AUC estimator (**Figure 4B**) for the low frequency band (5–30 Hz). In addition, the expected tendency of CNTs electrodes to have higher and lower AUC values for lower frequencies and higher frequencies, respectively, than Pt electrodes (**Figure 4B**) was detected in the vSNR boxplot as well as in the FLOD boxplot (**Figures 5A,C**).

To confirm that vSNR is related to the SNR at lower frequencies, a linear correlation was performed with the different AUC distributions at the three frequency bands (**Figure 6**). Since the larger correlation coefficient was for the vSNR-AUC (5–30 Hz), our findings indicate that vSNR better describes the SNR at lower frequencies (**Supplementary Figure S3A**). Furthermore, vSNR complements our analysis by providing new information regarding the behavior at frequencies that are too low to be obtained with the spectral SNR.

Since FLOD is the value of the frequency at which the SNR is zero, it is easy to relate this estimator to the SNR value at the highest frequencies. Comparing the results of FLOD distributions for each material (**Figure 5C**) with the distributions of AUC (**Figure 4B**), one can see that the FLOD estimator has a greater Pearson correlation with AUC at the high frequency range (200–1500 Hz) (**Figure 6B**) than with AUC at low and middle frequency ranges (**Supplementary Figure S3B**) Thus, FLOD can be interpreted as an estimator for high frequencies.

The total AUC distribution is dominated by high frequencies (200–1500 Hz) since there are more frequency points within this range and, despite the SNR values being low, the AUC is large due to the frequency variable (note that in the spectral SNR in **Figure 3**, the frequency axis is in a logarithmic scale). Thus, the total AUC describes the SNR for the middle and high frequencies (**Figures 6C,D** and **Supplementary Figure S3C**).

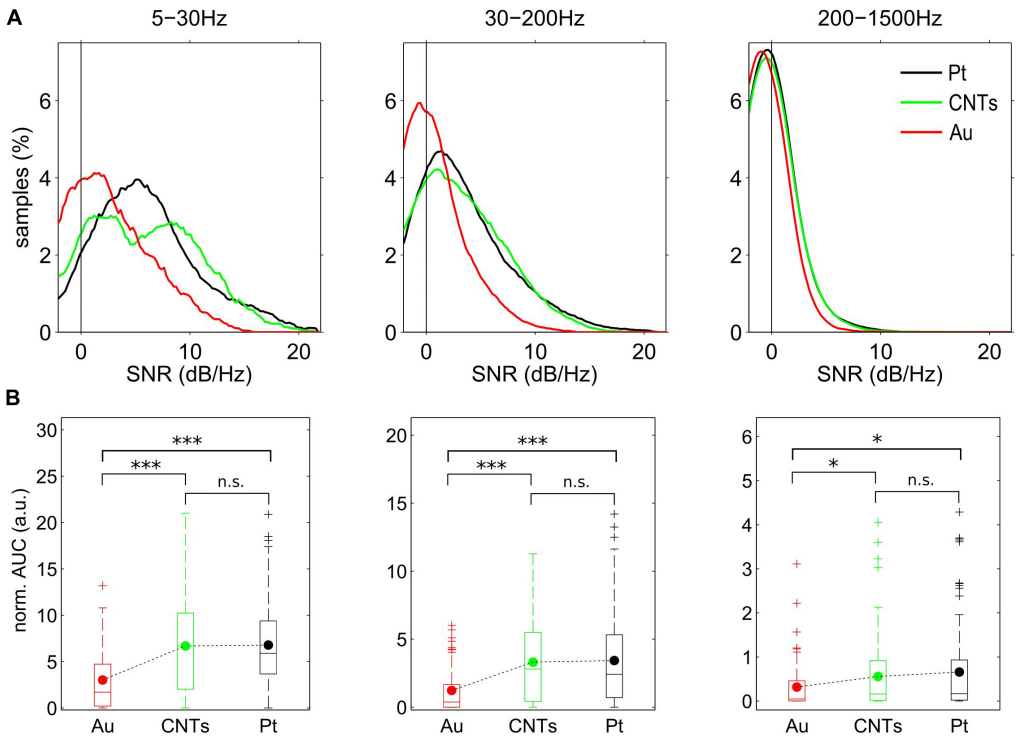

FIGURE 4 | Spectral SNR distribution and area under the spectral SNR curve (AUC) for three different frequency bands. **(A)** Distribution of mean SNR values for the electrodes of the three different materials for the three frequency bands defined in **Figure 3**. **(B)** Boxplots of AUC in the three frequency bands for the three materials. $^{*}p < 0.05$, $^{***}p < 0.001$ by Mann–Whitney test. $N_{Pt} = N_{CNTs} = 102$ and $N_{Au} = 67$ electrode recordings.

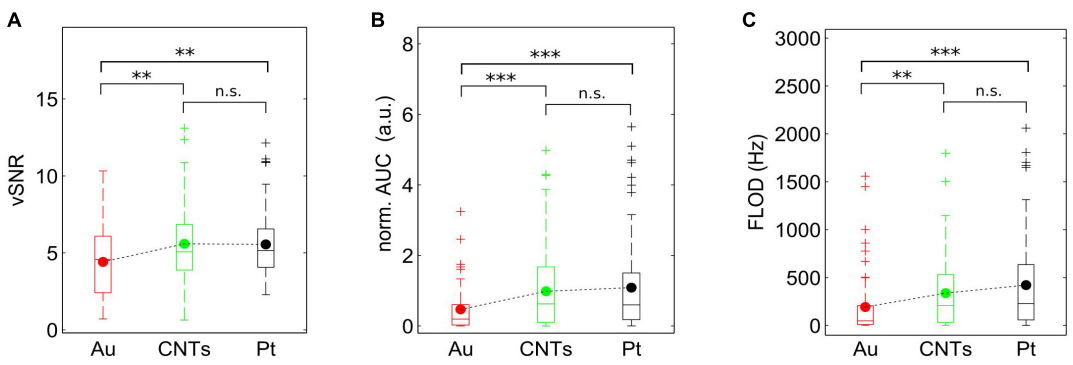

FIGURE 5 | vSNR and FLOD estimators for lower and higher frequencies, respectively. **(A)** Boxplots of the voltage SNR (vSNR) for Au, CNT and PT electrodes. **(B)** Boxplots of the area under the spectral SNR curve (AUC) for the three materials. **(C)** Boxplots of the frequency limit of detection (FLOD) for the three materials. Note the similarities with **Figure 4B**. $^{**}p < 0.01$, $^{***}p < 0.001$ by Mann–Whitney test.

DISCUSSION

In this work, we have developed and validated a novel method for characterizing the performance of brain recording devices based on a spectral SNR analysis using cortical slow oscillations. The validation was performed by applying this method to characterize and compare electrodes made of three different materials (Au, CNTs and Pt) organized in tritrodes. We also report here that electrodes made of platinum black and carbon nanotubes have better recording performance than electrodes made of gold for the whole functional frequency range that we explored (from 5 to 1500 Hz). Furthermore, Pt electrodes showed a trend toward working better than CNTs electrodes even though the difference did not reach statistical significance. Although these results can be qualitatively predicted from impedance characterization (i.e., directly related to the specific surface area of the electrode site; see **Supplementary Figure S1**), a quantitative measure of the entire electrode performance can only be assessed by SNR analysis (Ludwig et al., 2006; Baranauskas et al., 2011). We have seen that both functionalized

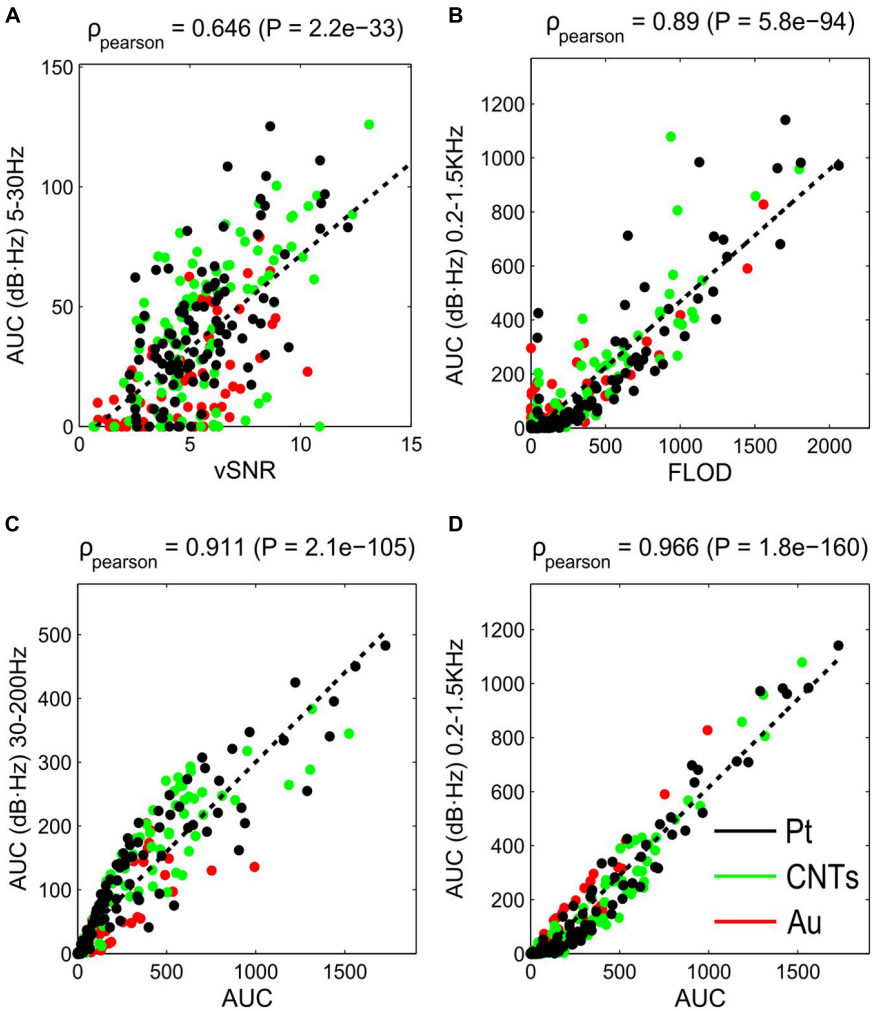

FIGURE 6 | Correlation between SNR estimators (vSNR, FLOD and total AUC) and AUC for different frequency ranges. **(A)** Linear correlation between vSNR and AUC at 5–30 Hz; **(B)** between FLOD and AUC at 200–1500 Hz; **(C,D)** between total AUC and AUC at 30–200 Hz **(C)** and 200–1500 Hz **(D)**. ρ, Pearson correlation coefficient.

electrodes (CNTs and Pt) displayed lower background noise during the Down states (inset **Figure 3**); this behavior is due to the reduction of both the root mean square and the thermal noise that are both directly related to the real part of the impedance of the electrode material (**Supplementary Table S1**). Similar results have already been published describing the improvement in the SNR by using electrodes of electrodeposited platinum black (Desai et al., 2010; Zhang et al., 2013) and carbon nanotubes (Mazzatenta et al., 2007; Keefer et al., 2008; Lu et al., 2010; Baranauskas et al., 2011; Castagnola et al., 2014), reinforcing the validation of our SNR methodology. Nevertheless, a quantitative SNR comparison of the different electrodes recording simultaneously from the same location and using the same recording system has, to our knowledge, not been done before. This novel SNR calculation has also been used recently in the characterization of graphene FET (field effect transistor) arrays in *in vivo* brain recordings, proving the potential of this measure to give information of the recoding capabilities of graphene FET in a broad biological frequency band (Hébert et al., 2017).

The design of the probes was intended to compare the materials while minimizing the interferences derived from recording from different neuronal populations by using co-localized electrodes arranged in tritrodes and stereotrodes. Because our *in vitro* experiments in cortical slices allow the recording of slow oscillations, the intrinsic characteristics of this activity pattern make it suitable for developing a SNR analysis using Up-Down states as Signal-Noise signals, thus overcoming the complexity of the SNR calculation in biological signals that usually arises from the difficulty in separating signal from noise. One could argue that Down states are not totally silent but relatively silent states and therefore that they contain neuronal information (e.g., Reig et al., 2009), such that referring to them as "noise" is not quite accurate. However, notice that in this paradigm there are no experimental manipulations that act on the neuronal firing at any point

of the experiment, plus the recordings from closely located electrodes of different materials are compared. Under these conditions, it seems reasonable to assume that Down states be considered "noise" with respect to Up states. Thus, the probes design, as well as the experimental approach, allowed the development of this SNR analysis to be able to compare quantitatively the behavior of electrodes made of different materials.

There are some differences between measurements carried out by injecting artificial currents in saline solution electrolyte (as in EIS; see **Supplementary Figure S1**) in contrast to *in vivo* and *in vitro* measurements. Measurements in saline solution display lower impedance values and larger capacitive charge capacity in comparison with the measures where the electrodes are in contact with tissue (Wei and Grill, 2009). This effect can be attributed to the differences in the composition between both electrolytes (saline solutions and brain tissue) and the difference in the electrode-reference path. When using saline solution as an electrolyte both electrode and reference are soaked in the same electrolyte. In an *in vitro* preparation, the electrode is placed over the slice of brain tissue and the reference is placed in the ACSF bath. In this case the path is composed of the brain slice and the ACSF bath. Finally, in an *in vivo* preparation, the electrode contacts the brain and the reference can be placed in different locations, such as the nearby muscles. In this case, the path is composed of the brain, the skull and the muscle. Normally, as the electrode-reference path increases, so does the number of different electrolytes (with different electrical properties), and the noise of the measured signal increases. In conclusion, both electrode–electrolyte interaction and electrode–reference path, determine the impedance-frequency dependence and the level of noise (both thermal and RMS – root mean square).

The results from the spectral SNR analysis provide a large amount of data since they give an SNR value for each frequency. Therefore, the use of SNR estimators that give an overall idea of the behavior under certain conditions is especially helpful. Because of this, we defined and validated some SNR estimators extracted from the spectral SNR analysis. On the one hand, we defined several SNR estimators from the spectral SNR analysis: total AUC, the AUC for different frequency bands of biological interest (5–30 Hz, 30–200 Hz and 200–1500 Hz), and the FLOD. On the other hand, we also calculated the vSNR, which is the standard approach to calculating SNR in LFP recordings (Khodagholy et al., 2013; Kuzum et al., 2014; Blaschke et al., 2017). AUC values defined in frequency bands of interest are very useful estimators for describing and quantifying the behavior of the electrodes (**Figure 3**). FLOD and vSNR estimators were compared with the AUC at different frequency bands and we found that while FLOD describes very well the SNR at high frequencies, the vSNR describes the SNR better at lower frequencies. Proving our hypothesis that vSNR applied to these slow oscillation signals describes the SNR at the slow oscillations frequency ($<$1 Hz), the correlation of this estimator with AUC at different frequencies is highest for the lower frequencies. On the other hand, vSNR can give more information of the SNR values at lower frequencies where spectral SNR cannot reach enough frequency resolution due to the short duration of Up states ($\sim$200 ms). Furthermore, we observed that the total AUC describes the SNR behavior at middle-high frequencies. This can be explained because, given the nature of the spectral analysis, the AUC is more weighted toward higher frequencies. Since we defined lower frequencies as 5–30 Hz, only six frequency values were considered, while for the 200–1500 Hz range, 266 frequency values were considered. This is why we normalized the AUC in different frequency bands by the number of frequency values.

Searching in the literature for SNR calculation methods, we found two different methodologies estimating the SNR at different frequencies that we consider to be worthy of note. The first one involved estimating the SNR from recordings of spike and wave discharges (SWDs) during spontaneous epileptiform activity in an animal model of absence epilepsy (Khodagholy et al., 2013). The authors of this study calculated the SNR as the ratio between the power spectra of the recording during ictal seizure in SWDs and the power spectra of the recording during inter-ictal activity (period of low biological activity) (Khodagholy et al., 2013). The second methodology implied the calculation of the SNR as the ratio between the power of the signal from the recording of rapid-eye movement (REM) sleep and the power of the signal from post-mortem recordings (Khodagholy et al., 2015). The main drawback of the first approach is the need for a specific transgenic animal model in order to have a signal of large enough amplitude, which will nevertheless be a pathological one. The possible changes that arise due to obtaining the ictal and the inter-ictal activity recordings at different time periods and the variability of SWDs activity across different animal subjects and levels of anesthesia makes this approach less robust. One of the drawbacks of the second approach is that REM activity is very similar to activity during wakefulness and the only way to distinguish one from the other is by means of an electromyogram (EMG) recording. Furthermore, in contrast to the recording of a live animal, in a post-mortem recording there is no respiration or heartbeat; finally, other biological changes related to the cessation of the homeostatic equilibrium occur. Therefore, these changes could lead to a bias in the SNR calculation.

In order to overcome these drawbacks, we propose a SNR methodology based on the slow oscillatory state that arises during anesthesia and during non-REM sleep in typical *in vivo* conditions and can be also reproduced in the *in vitro* preparations. The SNR can be assessed at different frequencies since we are applying a spectral analysis, considering the signal in the Up states (given that they contain different biological frequency rhythms caused by the firing of populations of neurons), and the noise in the Down states (since they are periods of almost silent neuronal firing). The alternation between these two states in short time periods make the approach more robust than the two approaches described above. In addition, the spectral SNR analysis was performed using the mean PSD from different Up and Down states occurring in less than 1 min,

conferring higher statistical reliability than the other methods that only used one large period as signal and one large period as noise, with both periods being very separated in time from each other. In other words, the proposed SNR methodology has the advantage of allowing the quantification of the SNR for different frequencies by using the Up and Down states of the well-known slow oscillations, which are the default neural activity pattern during sleep and anesthesia and are reproducible in *in vitro* preparations. To sum up, we have developed a novel and robust method to quantify the performance of electrodes in brain recordings by a novel SNR approach adapted to cortical slow oscillations. Additionally, we have validated the approach by quantifying the performance of electrodes made of three different materials by recording electrophysiological signals from the brain, showing that platinum black as well as carbon nanotubes electrodes have better working performance than gold electrodes.

To sum up, we present a detailed SNR analysis to quantify and compare the performance of different devices to record brain activity. Neural MEAs with electrodes of different materials arranged in co-localized tritrodes and stereotrodes were used to record slow oscillations from the cerebral cortex network. This approach was designed to avoid the interferences from external variables and thus enable a proper comparison between electrodes. The results shed light on the recording behavior of electrodes made of different materials in a broad range of biological frequencies showing that platinum black as well as carbon nanotubes electrodes have better working performance than gold electrodes. Furthermore, the results obtained here parallel previous studies involving some of the tested materials, hence reinforcing the validation of the proposed SNR approach. The work here exposed is also intended to validate and standardize a methodology for quantifying the SNR in different types of brain recording devices such as electrodes or transistors.

AUTHOR CONTRIBUTIONS

GG and MVSV designed the MEA and tritrodes. GG, XI, AGB, JHF, MM, and RV fabricated and characterized the MEAs. BR and MVSV designed and performed the *in vitro* experiments. AS-P developed the SNR measure and performed the data analysis. All authors wrote the paper.

FUNDING

This work was supported by Ministerio de Ciencia, Innovación y Universidades (Spain), BFU2017-85048-R and PCIN-2015-162-C02-01 (FLAG ERA) to MVSV, and by CERCA Programme/Generalitat de Catalunya.

ACKNOWLEDGMENTS

We would like to thank Núria Tort-Colet for suggestions for data analysis and Cristina Gonzalez-Liencres and Tony Donegan for editing assistance. This work has made use of the Spanish ICTS Network MICRONANOFABS partially supported by MINECO and the ICTS 'NANBIOSIS', more specifically by the Micro-NanoTechnology Unit of the CIBER in Bioengineering, Biomaterials & Nanomedicne (CIBER-BBN) at the IMB-CNM.

SUPPLEMENTARY MATERIAL

The Supplementary Material for this article can be found online at: https://www.frontiersin.org/articles/10.3389/fnins.2018.00862/full#supplementary-material

REFERENCES

Aghajanian, G. K., and Rasmussen, K. (1989). Intracellular studies in the facial nucleus illustrating a simple new method for obtaining viable motoneurons in adult rat brain slices. *Synapse* 3, 331–338. doi: 10.1002/syn.890030406

Ansón-Casaos, A., González-Domínguez, J. M., Lafragüeta, I., Carrodeguas, J. A., and Teresa Martínez, M. (2014). Optical absorption response of chemically modified single-walled carbon nanotubes upon ultracentrifugation in various dispersants. *Carbon N. Y.* 66, 105–118. doi: 10.1016/j.carbon.2013.08.048

Baranauskas, G., Maggiolini, E., Castagnola, E., Ansaldo, A., Mazzoni, A., Angotzi, G. N., et al. (2011). Carbon nanotube composite coating of neural microelectrodes preferentially improves the multiunit signal-to-noise ratio. *J. Neural Eng.* 8:066013. doi: 10.1088/1741-2560/8/6/066013

Berdondini, L., Chiappalone, M., Van Der Wal, P. D., Imfeld, K., De Rooij, N. F., Koudelka-Hep, M., et al. (2006). A microelectrode array (MEA) integrated with clustering structures for investigating in vitro neurodynamics in confined interconnected sub-populations of neurons. *Sensors Actuators B Chem.* 114, 530–541. doi: 10.1016/j.snb.2005.04.042

Blaschke, B. M., Tort-Colet, N., Guimerà-Brunet, A., Weinert, J., Rousseau, L., Heimann, A., et al. (2017). Mapping brain activity with flexible graphene micro-transistors. *2D Mater.* 4:025040. doi: 10.1088/2053-1583/aa5eff

Castagnola, E., Ansaldo, A., Maggiolini, E., Ius, T., Skrap, M., Ricci, D., et al. (2014). Smaller, softer, lower-impedance electrodes for human neuroprosthesis: a pragmatic approach. *Front. Neuroeng.* 7:8. doi: 10.3389/fneng.2014.00008

Castano-Prat, P., Perez-Zabalza, M., Perez-Mendez, L., Escorihuela, R. M., and Sanchez-Vives, M. V. (2017). Slow and fast neocortical oscillations in the senescence-accelerated mouse model SAMP8. *Front. Aging Neurosci.* 9:141. doi: 10.3389/fnagi.2017.00141

Compte, A., Reig, R., Descalzo, V. F., Harvey, M. A., Puccini, G. D., and Sanchez-Vives, M. V. (2008). Spontaneous high-frequency (10-80 Hz) oscillations during up states in the cerebral cortex in vitro. *J. Neurosci.* 28, 13828–13844. doi: 10.1523/JNEUROSCI.2684-08.2008

D'Andola, M., Rebollo, B., Casali, A. G., Weinert, J. F., Pigorini, A., Villa, R., et al. (2017). Bistability, causality, and complexity in cortical networks: an in vitro perturbational study. *Cereb. Cortex* 91, 1–10. doi: 10.1093/cercor/bhx122

Desai, S. A., Rolston, J. D., Guo, L., and Potter, S. M. (2010). Improving impedance of implantable microwire multi-electrode arrays by ultrasonic electroplating of durable platinum black. *Front. Neuroeng.* 3:5. doi: 10.3389/fneng.2010.00005

Dickey, A. S., Suminski, A., Amit, Y., and Hatsopoulos, N. G. (2009). Single-unit stability using chronically implanted multielectrode arrays. *J. Neurophysiol.* 102, 1331–1339. doi: 10.1152/jn.90920.2008

Donoghue, J. P. (2008). Bridging the brain to the world: a perspective on neural interface systems. *Neuron* 60, 511–521. doi: 10.1016/j.neuron.2008.10.037

Ferguson, J. E., Boldt, C., and Redish, A. D. (2009). Creating low-impedance tetrodes by electroplating with additives. *Sensors Actuators A Phys.* 156, 388–393. doi: 10.1016/j.sna.2009.10.001

Gabriel, G., Erill, I., Caro, J., Gómez, R., Riera, D., Villa, R., et al. (2007). Manufacturing and full characterization of silicon carbide-based multi-sensor

micro-probes for biomedical applications. *Microelectronics J.* 38, 406–415. doi: 10.1016/j.mejo.2006.11.008

Gabriel, G., Illa, X., Guimera, A., Rebollo, B., Hernandez-Ferrer, J., Martin-Fernandez, I., et al. (2013). "Carbon Nanotubes as suitable interface for improving neural recordings," in *Physical and Chemical Properties of Carbon Nanotubes*, ed. H. F. Han (Valley Cottage: Scitus Academics LLC).

Hébert, C., Masvidal-Codina, E., Suarez-Perez, A., Calia, A. B., Piret, G., Garcia-Cortadella, R., et al. (2017). Flexible graphene solution-gated field-effect transistors: efficient transducers for micro-electrocorticography. *Adv. Funct. Mater.* 28:1703976. doi: 10.1002/adfm.201703976

Hochberg, L. R., Serruya, M. D., Friehs, G. M., Mukand, J. A., Saleh, M., Caplan, A. H., et al. (2006). Neuronal ensemble control of prosthetic devices by a human with tetraplegia. *Nature* 442, 164–171. doi: 10.1038/nature04970

Illa, X., Rebollo, B., Gabriel, G., Sánchez-Vives, M. V., and Villa, R. (2015). "A SU-8-based flexible microprobe for close and distal recordings from the cortical network," in *Proceedings of the International Society for Optics and Photonics*, ed. S. van den Driesche, Bellingham WA.

Innocenti, G. M., Manger, P. R., Masiello, I., Colin, I., and Tettoni, L. (2002). Architecture and callosal connections of visual areas 17, 18, 19 and 21 in the ferret (*Mustela putorius*). *Cereb. Cortex* 12, 411–422. doi: 10.1093/cercor/12.4.411

Kappenman, E. S., and Luck, S. J. (2010). The effects of electrode impedance on data quality and statistical significance in ERP recordings. *Psychophysiology* 47, 888–904. doi: 10.1111/j.1469-8986.2010.01009.x

Keefer, E. W., Botterman, B. R., Romero, M. I., Rossi, A. F., and Gross, G. W. (2008). Carbon nanotube coating improves neuronal recordings. *Nat. Nanotechnol.* 3, 434–439. doi: 10.1038/nnano.2008.174

Khodagholy, D., Doublet, T., Quilichini, P., Gurfinkel, M., Leleux, P., Ghestem, A., et al. (2013). Supplementary information in vivo recordings of brain activity using organic transistors. *Nat. Commun.* 4:1575. doi: 10.1038/ncomms2573

Khodagholy, D., Gelinas, J. N., Thesen, T., Doyle, W., Devinsky, O., Malliaras, G. G., et al. (2015). NeuroGrid: recording action potentials from the surface of the brain. *Nat. Neurosci.* 18, 310–315. doi: 10.1038/nn.3905

Kuzum, D., Takano, H., Shim, E., Reed, J. C., Juul, H., Richardson, A. G., et al. (2014). Transparent and flexible low noise graphene electrodes for simultaneous electrophysiology and neuroimaging. *Nat. Commun.* 5:5259. doi: 10.1038/ncomms6259

Lebedev, M. A., and Nicolelis, M. A. L. (2006). Brain-machine interfaces: past, present and future. *Trends Neurosci.* 29, 536–546. doi: 10.1016/j.tins.2006.07.004

Lu, Y., Li, T., Zhao, X., Li, M., Cao, Y., Yang, H., et al. (2010). Electrodeposited polypyrrole/carbon nanotubes composite films electrodes for neural interfaces. *Biomaterials* 31, 5169–5181. doi: 10.1016/j.biomaterials.2010.03.022

Ludwig, K. A., Uram, J. D., Yang, J., Martin, D. C., and Kipke, D. R. (2006). Chronic neural recordings using silicon microelectrode arrays electrochemically deposited with a poly(3,4-ethylenedioxythiophene) (PEDOT) film. *J. Neural Eng.* 3, 59–70. doi: 10.1088/1741-2560/3/1/007

Mattia, M., and Del Giudice, P. (2002). Population dynamics of interacting spiking neurons. *Phys. Rev. E Stat. Nonlin. Soft Matter Phys.* 66(5 Pt 1):51917. doi: 10.1103/PhysRevE.66.051917

Mattia, M., and Sanchez-Vives, M. V. (2012). Exploring the spectrum of dynamical regimes and timescales in spontaneous cortical activity. *Cogn. Neurodyn.* 6, 239–250. doi: 10.1007/s11571-011-9179-4

Mazzatenta, A., Giugliano, M., Campidelli, S., Gambazzi, L., Businaro, L., Markram, H., et al. (2007). Interfacing neurons with carbon nanotubes: electrical signal transfer and synaptic stimulation in cultured brain circuits. *J. Neurosci.* 27, 6931–6936. doi: 10.1523/JNEUROSCI.1051-07.2007

Mukovski, M., Chauvette, S., Timofeev, I., and Volgushev, M. (2007). Detection of active and silent states in neocortical neurons from the field potential signal during slow-wave sleep. *Cereb. Cortex* 17, 400–414. doi: 10.1093/cercor/bhj157

Nelson, M. J., Pouget, P., Nilsen, E. A., Patten, C. D., and Schall, J. D. (2008). Review of signal distortion through metal microelectrode recording circuits and filters. *J. Neurosci. Methods* 169, 141–157. doi: 10.1016/J.JNEUMETH.2007.12.010

Nicolelis, M. A. L., Dimitrov, D., Carmena, J. M., Crist, R., Lehew, G., Kralik, J. D., et al. (2003). Chronic, multisite, multielectrode recordings in macaque monkeys. *Proc. Natl. Acad. Sci. U.S.A.* 100, 11041–11046. doi: 10.1073/pnas.1934665100

Obien, M. E. J., Deligkaris, K., Bullmann, T., Bakkum, D. J., and Frey, U. (2015). Revealing neuronal function through microelectrode array recordings. *Front. Neurosci.* 9:423. doi: 10.3389/fnins.2014.00423

Reig, R., Mattia, M., Compte, A., Belmonte, C., and Sanchez-Vives, M. V. (2009). Temperature modulation of slow and fast cortical rhythms. *J. Neurophysiol.* 103, 1253–1261. doi: 10.1152/jn.00890.2009

Rieke, F., Warland, D., De Ruyter Van Steveninck, R., and Bialek, W. (1997). *Spikes: Exploring the Neural Code*, ed. F. Rieke, Cambridge, MA: MIT Press.

Sanchez-Vives, M. V., and McCormick, D. A. (2000). Cellular and network mechanisms of rhythmic recurrent activity in neocortex. *Nat. Neurosci.* 3, 1027–1034. doi: 10.1038/79848

Schultz, S. (2007). Signal-to-noise ratio in neuroscience. *Scholarpedia* 2:2046. doi: 10.4249/scholarpedia.2046

Steriade, M., Amzica, F., and Contreras, D. (1996). Synchronization of fast (30-40 Hz) spontaneous cortical rhythms during brain activation. *J. Neurosci.* 16, 392–417. doi: 10.1523/JNEUROSCI.16-01-00392.1996

Steriade, M., McCormick, D. A., and Sejnowski, T. J. (1993). Thalamocortical oscillations in the sleeping and aroused brain. *Science* 262, 679–685. doi: 10.1126/science.8235588

Taketani, M., and Baudry, M. (2006). *Advances in Network Electrophysiology?: Using Multi-Electrode Arrays*. Berlin: Springer. doi: 10.1007/b136263

Wei, X. F., and Grill, W. M. (2009). Impedance characteristics of deep brain stimulation electrodes in vitro and in vivo. *J. Neural Eng.* 6, 046008. doi: 10.1088/1741-2560/6/4/046008

Zhang, C., Liu, J. Q., Tian, H. C., Kang, X. Y., Du, J. C., Rui, Y. F., et al. (2013). Implantable electrode array with platinum black coating for brain stimulation in fish. *Microsyst. Technol.* 21, 139–145. doi: 10.1007/s00542-013-2017-3

Conflict of Interest Statement: The authors declare that the research was conducted in the absence of any commercial or financial relationships that could be construed as a potential conflict of interest.

Copyright © 2018 Suarez-Perez, Gabriel, Rebollo, Illa, Guimerà-Brunet, Hernández-Ferrer, Martínez, Villa and Sanchez-Vives. This is an open-access article distributed under the terms of the Creative Commons Attribution License (CC BY). The use, distribution or reproduction in other forums is permitted, provided the original author(s) and the copyright owner(s) are credited and that the original publication in this journal is cited, in accordance with accepted academic practice. No use, distribution or reproduction is permitted which does not comply with these terms.

frontiers in Neuroscience

REVIEW
published: 29 March 2019
doi: 10.3389/fnins.2019.00269

Bioactive Neuroelectronic Interfaces

*Dayo O. Adewole[1,2,3], Mijail D. Serruya[4], John A. Wolf[1,3] and D. Kacy Cullen[1,2,3]**

[1] Center for Brain Injury and Repair, Department of Neurosurgery, Perelman School of Medicine, University of Pennsylvania, Philadelphia, PA, United States, [2] Department of Bioengineering, School of Engineering and Applied Science, University of Pennsylvania, Philadelphia, PA, United States, [3] Center for Neurotrauma, Neurodegeneration and Restoration, Corporal Michael J. Crescenz Veterans Affairs Medical Center, Philadelphia, PA, United States, [4] Department of Neurology, Thomas Jefferson University, Philadelphia, PA, United States

Within the neural engineering field, next-generation implantable neuroelectronic interfaces are being developed using biologically-inspired and/or biologically-derived materials to improve upon the stability and functional lifetime of current interfaces. These technologies use biomaterials, bioactive molecules, living cells, or some combination of these, to promote host neuronal survival, reduce the foreign body response, and improve chronic device-tissue integration. This article provides a general overview of the different strategies, milestones, and evolution of bioactive neural interfaces including electrode material properties, biological coatings, and "decoration" with living cells. Another such biohybrid approach developed in our lab uses preformed implantable micro-tissue featuring long-projecting axonal tracts encased within carrier biomaterial micro-columns. These so-called "living electrodes" have been engineered with carefully tailored material, mechanical, and biological properties to enable natural, synaptic based modulation of specific host circuitry while ultimately being under computer control. This article provides an overview of these living electrodes, including design and fabrication, performance attributes, as well as findings to date characterizing *in vitro* and *in vivo* functionality.

Keywords: neurotechnology and brain-machine interface, tissue engineering, biomaterials, neural engineering, neuroprosthetics

OPEN ACCESS

Edited by:
Jeffrey R. Capadona, Case Western Reserve University, United States

Reviewed by:
Stuart Cogan, The University of Texas at Dallas, United States
Andrew J. Shoffstall, Case Western Reserve University, United States

***Correspondence:**
D. Kacy Cullen
dkacy@pennmedicine.upenn.edu

Specialty section:
This article was submitted to Neuroprosthetics, a section of the journal Frontiers in Neuroscience

Received: *14 December 2018*
Accepted: *07 March 2019*
Published: *29 March 2019*

Citation:
Adewole DO, Serruya MD, Wolf JA and Cullen DK (2019) Bioactive Neuroelectronic Interfaces. Front. Neurosci. 13:269. doi: 10.3389/fnins.2019.00269

INTRODUCTION

Neuroelectronic interfaces, also commonly referred to as neural or brain-computer interfaces, enable the transfer of information between the nervous system and an external device (Hatsopoulos and Donoghue, 2009; Wolpaw, 2013; Adewole et al., 2016). Generally, these devices take the form of electrodes to record or modulate neuronal activity through transducing cellular activity into actionable information (recording) or delivering current into tissue (stimulation) (Cogan, 2008; Grill et al., 2009). Neural interfaces are currently applied in both investigative and clinical contexts, from answering basic neuroscience questions about behavior, information encoding, and mechanisms of injury, to cochlear implants to restore hearing loss, deep brain stimulation to treat Parkinson's disease, and the direct control of prosthetic limbs or other peripheral devices (Shih et al., 2012; Adewole et al., 2016).

A fundamental design objective for implantable neural interfaces is the maintenance of long-term function *in vivo* (Grill et al., 2009; Harris and Tyler, 2013; Adewole et al., 2016). This article focuses on interfaces for the brain, wherein the dynamic, aqueous environment presents a host

of significant obstacles that have, to date, limited the chronic performance of neural interfaces (Harris and Tyler, 2013; Fattahi et al., 2014). The most prevalent of these obstacles may be collectively summarized as a multimodal, sustained foreign body response (FBR) to the implant, which degrades the efficacy of the interface over time (Polikov et al., 2005; Tresco and Winslow, 2011). The FBR has motivated a vast body of research focused on developing electrodes and implant strategies that either address specific elements of the FBR or limit its effects on device performance, with distinct approaches offering discrete improvements. Here we provide a brief overview of the FBR and its implications for neural interface design before exploring strategies for biologically active interfaces, which use biologically-derived and/or biologically-inspired materials to promote greater host-implant integration and more consistent long-term electrode performance.

THE FOREIGN BODY RESPONSE

The FBR is a neuroinflammatory reaction to the disruption of healthy tissue and continued presence of a foreign body in the brain (**Figure 1**) (Polikov et al., 2005; Harris and Tyler, 2013). It begins at implantation, which itself causes physical trauma as the electrode(s) displaces and damages vasculature and the blood–brain barrier (BBB), cells, and extracellular matrix (ECM) on its path to the intended target (Sommakia et al., 2014). Subsequently, blood-borne macrophages and other foreign plasma components enter the area, while local microglia and astrocytes begin to transition from resting to active/phagocytic phenotypes as part of the brain's normal response to injury (Polikov et al., 2005; Harris and Tyler, 2013). Microglia have been observed responding as quickly as 30 min post-delivery, extending processes toward the implant and transitioning to an active phenotype over the course of a few hours (Neumann et al., 2009; Kozai et al., 2012). Activated microglia and macrophages release a battery of pro-inflammatory chemokines, cytokines, and other factors into the damaged area (e.g., tumor necrosis factor, interleukin-1, nitric oxide); while these factors are associated with remodeling tissue and degrading foreign materials following injury, they also cause neurodegeneration (Neumann et al., 2009; Harris and Tyler, 2013).

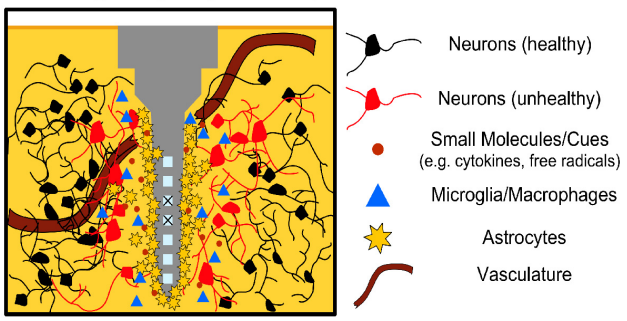

FIGURE 1 | The FBR to Neural Interfaces. Neural interfaces disrupt local tissue triggering an acute immune response wherein local immune cells (microglia, astrocytes) migrate to the injury site and begin secreting pro-inflammatory factors (e.g., cytokines, nitric oxide, free radicals). Astrocytes begin forming a glial scar around the implant over the course of a few weeks, increasing tissue impedance, while disruption of the BBB allows blood-borne macrophages to infiltrate the area. Prolonged inflammation leads to neuronal degeneration and may corrode the implant ("X" over active sites), further limiting electrode function. Note that although the microelectrode depicted represents a silicon shank (i.e., Michigan-style electrode), the concept applies similarly to other microelectrode types, such as the Blackrock Utah array.

In the weeks following implantation, a fibrous envelope of reactive astrocytes, connective tissue and ECM, commonly referred to as the glial scar, gradually forms around the device, insulating the foreign body from the surrounding brain tissue (Harris and Tyler, 2013; Sridharan et al., 2013). This glial scar has been a hallmark of neural interfaces in the brain, with experimental strategies often using the extent or thickness of the scar as a measurement for the effectiveness of mitigating the FBR (Sridharan et al., 2013). Growth-inhibiting molecules, such as chondroitin sulfate proteoglycans, also populate the glial scar, further reducing the potential for neuronal growth and recovery in the implant site (Zhong and Bellamkonda, 2007). The presence of the implant in the brain generally causes a sustained inflammatory response, with both astrocytes and microglia remaining in the area in a pro-inflammatory state in an attempt to eliminate the foreign body (Polikov et al., 2005; Harris and Tyler, 2013; Woeppel et al., 2017). The continued release of neurotoxic factors from the active microglia/astrocytes is detrimental to local neurons, with many studies reporting a decrease in the neuronal density surrounding the implant (Polikov et al., 2005).

To date, the mechanisms of the FBR are still not completely understood. As such, the relationship between various elements of the FBR and failure modes of chronically-implanted neuroelectronic interfaces is still an area of active study (Polikov et al., 2005; Winslow and Tresco, 2010; Jorfi et al., 2015; Sahyouni et al., 2017; Woeppel et al., 2017). What is known is that the introduction of any such interface to the CNS induces multi-phase tissue remodeling that results in glial scarring, prolonged BBB disruption, and the persistent presence of pro-inflammatory elements that collectively form an adverse microenvironment for neural interfacing (**Figure 1**). This microenvironment poses several active challenges to both the device and the neurons of interest (Groothuis et al., 2014; Nolta et al., 2015; Woeppel et al., 2017). The biostability of the former is continually challenged by reactive oxygen species, which corrode active electrode sites and gradually degrade insulating layers and device interconnects (Groothuis et al., 2014; Nolta et al., 2015; Woeppel et al., 2017). Other failure modes, such as mechanical failure and micromotion-induced shear as the brain shifts, may further drive inflammation in a positive feedback manner (Polikov et al., 2005; Jorfi et al., 2015). As noted above, local astrocytes around the implant eventually form the glial scar, which physically separates the device from the neurons of interest and increases the electrical impedance of local tissue. Moreover, the continued presence of reactive immune cells, cytokines, and other inflammatory factors at recording/stimulation sites induce neuronal death and/or prevent the restoration of healthy neural

tissue (McConnell et al., 2009; Winslow and Tresco, 2010; Fattahi et al., 2014; Shoffstall and Capadona, 2018). Disruption of the BBB has also been implicated as a significant link between the FBR and the decline in interface performance over chronic periods, with "leakiness" of the BBB allowing peripheral immune cells to enter the brain parenchyma and accumulate in the lesion to exacerbate neurotoxic effects at longer timepoints (Saxena et al., 2013; Woeppel et al., 2017; Bennett et al., 2018).

THE CHALLENGE OF BIOLOGICAL COMPLIANCE

The complex and multi-faceted challenge of designing long-acting neural interfaces has engendered an ongoing, cross-disciplinary mission to improve their biological compliance, defined as their ability to induce favorable – or at least not disrupt – cell- and tissue-level interactions. These strategies span mechanical design, materials science (across nano to macro scales), immunology, neurobiology, electrical engineering, and tissue engineering, among others; a subset of the milestones in the field are summarized below and are referenced in more in-depth analyses (Schmidt and Leach, 2003; Cullen et al., 2011; Jorfi et al., 2015; Sahyouni et al., 2017).

ELECTRODE MATERIAL PROPERTIES AND GEOMETRY

It has been shown that reducing electrode size minimizes the trauma of insertion and can reduce the severity of the glial scar in chronic implants (Stice et al., 2007; Karumbaiah et al., 2013). Similarly, electrodes with open-faced geometries (e.g., lattices, meshes) minimize the total surface area of the interface, while permitting diffusion throughout the area, with rodent models showing reduced microglial reactivity and higher neuronal density out to at least 1 month (Seymour and Kipke, 2007; Sommakia et al., 2014). Further, the lattice topography has been shown to influence not only the extent but the distribution of scarring around the implant, potentially leveraging it to improve contact with brain tissue (Schendel et al., 2014a,b). One such mesh electrode comprised of flexible nanowire transistors assembled in a flexible, lightweight sheet was able to record both single units and field potentials in mice for several months; histological assays showed both a lack of glial proliferation and neuronal attrition surrounding the implant for at least 1 year, suggesting that the unique geometry leaves the host tissue relatively unperturbed (Hong et al., 2018). Notably, this mesh leverages conductive ink and computer-controlled stereotactic injection to enable connection to standard electrophysiological equipment and reproducible targeting of brain regions, respectively (Hong et al., 2018).

In addition to geometric changes, reducing the stiffness of the implant minimizes the mechanical discrepancy between the device and host tissue; the use of polymers or "mechanically adaptive" materials which are stiff enough for insertion but soften upon implantation has demonstrated significant reductions in long-term neuroinflammation, immune cell activation, and neurodegeneration (Harris et al., 2011; Jeon et al., 2014; Nguyen et al., 2014; Sridharan et al., 2015; Lecomte et al., 2018). Materials science approaches to biological compliance include the patterning of nanoscale topography to better integrate with features of local tissue, increasing the effective surface area of the implant, and development of electrodes with new materials such as carbon nanotubes, which have demonstrated favorable electrochemical properties and reduced immunoreactivity compared to traditional probes (Webster et al., 2004; Saito et al., 2009; Heim et al., 2012; Vitale et al., 2015; Jalili et al., 2017; Scaini and Ballerini, 2018). Manipulating the surface chemistry of implanted materials may also improve biological compliance; certain hydrophilic or negatively-charged functional groups such as -COOH may reduce glial scarring, depending on their affinity for protein binding or cell membranes (Christo et al., 2015; Yu et al., 2015). Increasing the surface permeability of implant coatings to serve as "diffusion sinks" for pro-inflammatory molecules has also reduced immunoreactivity around the electrode (Skousen et al., 2015).

BIOACTIVE ELECTRODES

Improving biological compliance can be described as minimizing the degree of discrepancy between the self (host tissue) and not-self (foreign implants). In this context, the more closely a given interface approximates properties of biological tissue ("self"), the higher the chances of chronic stability and integration with the tissue of interest. This principle motivates the development of bioactive neural interfaces, which attempt to improve biological compliance through the elicitation, suppression, or otherwise modulation of specific biological phenomena. Broadly, this class of interfaces is designed to incorporate, mimic, or draw inspiration from pre-existing, biologically-derived materials; candidate materials are selected for their effects on cellular or physiological processes (e.g., attenuation of the immune response, promotion of neuron attachment, and growth) (Shoffstall and Capadona, 2018). These strategies are designed to improve the prospects of long-term function while reducing the complications from the presence of a foreign body. Bioactive interfaces may be visualized as a spectrum ranging from completely inorganic, non-biological devices to living engineered constructs (**Figure 2**). They may incorporate proteins or drugs that downregulate specific mechanisms of immunoreactivity (e.g., microglial activation), inflammation (e.g., cytokine release, glial scar formation), promote neuronal attachment or neurite outgrowth, recruit endogenous neuroprotective mechanisms, or present *de novo* cells or tissue to replace lost neurons and supporting architecture (Shain et al., 2003; Zhong and Bellamkonda, 2007; Purcell et al., 2009; Cullen et al., 2011; Taub et al., 2012). Most current bioactive interfaces take the form of traditional inorganic electrode materials (e.g., platinum, tungsten, silicon) surrounded by coatings that contain or are comprised of biomolecules as described below (Aregueta-Robles et al., 2014; Szostak et al., 2017). These biomaterial coatings are generally several orders of magnitude softer than the

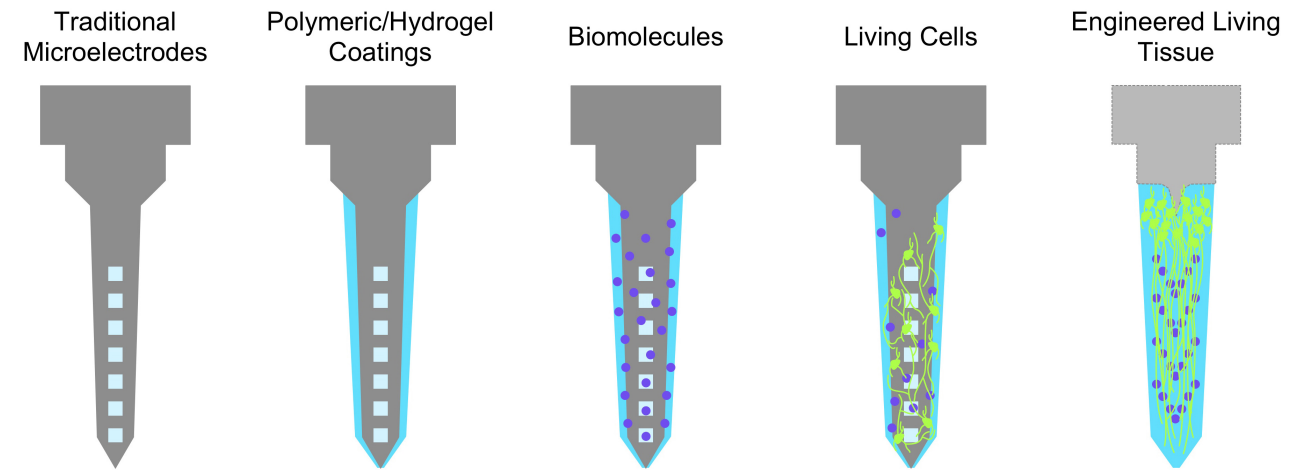

FIGURE 2 | The spectrum of bioactive neuroelectronic interfaces. Non-organic electrodes may be coated with soft biomaterials of hydrogels for better mechanical parity, which may in turn be functionalized with various biological molecules (e.g., soluble factors, ECM proteins) to transiently reduce inflammatory phenomena or provide support for neuronal growth and attachment. The incorporation of living cells may further provide sustained trophic support and a more biofidelic interface, while engineered tissue (i.e., with an organized structure, as an electrode coating or a self-contained implant) may be the closest representation of "self" attainable with respect to native tissue.

enclosed material to provide better mechanical parity with the brain; common coatings include silk, polyimide, and parylene, and various hydrogels or synthetic polymers (Zhong and Bellamkonda, 2008; Green et al., 2009; Chen and Allen, 2012; Balint et al., 2014; Mario Cheong et al., 2014).

Anti-inflammatory agents such as the steroid dexamethasone or α-MSH have been incorporated into electrode coatings to limit the production of inflammatory cytokines and other glial by-products; these approaches generally result in reduced glial scarring around neural implants in animal models, although they are limited by the release and eventual depletion of the agent in use (Zhong and Bellamkonda, 2005; Abidian and Martin, 2009; Kim et al., 2010; Aregueta-Robles et al., 2014; Boehler et al., 2017). Other biological molecules associated with neuronal attachment, structural support, or migration (e.g., laminin, L1, collagen), may be entrapped or immobilized through covalent bonding to both natural and synthetic polymer coatings to present a more attractive surface for neurons; a common strategy is the doping of conductive polymers (of which the most prevalent for neural interfacing are PEDOT and polypyrrole) with biomolecules to improve their biocompatibility (Green et al., 2008; Azemi et al., 2010, 2011; Bendrea et al., 2011; Chen and Allen, 2012; Hardy et al., 2013; Balint et al., 2014; Sommakia et al., 2014; Green and Abidian, 2015). A wealth of *in vitro* studies have demonstrated neural cell survival and process outgrowth on substrates functionalized with growth factors (i.e., NGF, NT3, BDNF) and ECM proteins (laminin, collagen); *in vivo*, histological analyses of these bioactive coatings reveal attenuation of the glial response 4–8 weeks post-implant, with some studies reporting higher local neuronal survival compared to uncoated electrodes (He and Bellamkonda, 2005; Green et al., 2008; Thompson et al., 2010; Azemi et al., 2011; Liu et al., 2011; Chen and Allen, 2012; Fattahi et al., 2014; Mario Cheong et al., 2014; Sommakia et al., 2014; Kozai et al., 2015; Shen et al., 2018; Shoffstall and Capadona, 2018; Vitale et al., 2018). However, while bioactive materials provide greater biocompatibility to these devices, ongoing challenges for these strategies include limited duration of effect as biomolecules diffuse away from the implant (with no mechanism for replenishment), are removed by local microglia or competitive binding, or undergo undesired modification (e.g., pH-driven conformational changes), which collectively result in poor translation of results from *in vitro* assays to *in vivo* implants (Aregueta-Robles et al., 2014; Kozai et al., 2015). Further, the benefits borne out by histological studies vary – e.g., diminished glial scarring with no evidence of improved neuronal survival – and have largely not yet been tied to improved functional outcomes (He et al., 2006; Aregueta-Robles et al., 2014; Jorfi et al., 2015; Michelson et al., 2018). Validating the clinical potential of these bioactive implants requires meeting the benchmarks set by current interfaces in both non-human primates and humans. For instance, despite well-known limitations in their long-term biostability, inorganic electrodes such as the Blackrock microelectrode array provide the clinical performance foundation and have been the source of significant milestones in neuroprosthesis research (Hochberg et al., 2012; Klaes et al., 2014; Gilja et al., 2015). As such, these existing devices set the standard by which bioactive interfaces will be evaluated as they evolve from a growing body of promising results *in vitro*, to improved performance and reproducibility in model systems *in vivo*, and, potentially, in clinical applications.

ELECTRODES DECORATED WITH LIVING CELLS OR TISSUE

There are clear, data-driven benefits to engineering neural interfaces as bioactive devices. Increasing similarities between the implant and tissue create further opportunities for greater

neuronal contact, reduced chronic inflammation, and more stable long-term function. However, bioactive interfaces to date are introduced to the brain with fixed quantities of biomolecules, which may become depleted or removed due to natural biological processes. Toward this end, new research efforts have begun to explore whether living cells may act as active elements of a neuroelectronic interface, potentially matching the dynamic nature of brain tissue (Cullen et al., 2011; Shoffstall and Capadona, 2018). Cell-based interfaces may leverage the self-driven machinery of living cells to actively produce neuroprotective factors while presenting a material that mimics the "self" enough to downregulate chronic inflammation, although these potential advantages must be developed and validated *in vivo*. One such study coated microelectrodes with a fibrin hydrogel containing primary astrocytes and neurons; although the fibrin was resorbed within one week following implant in rat cortex, astrocyte reactivity was diminished out to at least 30 days post-implant compared to bare electrodes (De Faveri et al., 2014). Further, the inclusion of a cell layer did not significantly affect recordings from the electrodes themselves, although effects on the survival of host neurons were not reported (De Faveri et al., 2014). Other studies have trapped live neurons within conductive polymers; although residual monomers have proven cytotoxic and negatively impacted cell survival beyond a few days, the polymerized network may serve as a three-dimensional, electrically functional scaffold (Richardson-Burns et al., 2007a). A similar approach polymerized *in vivo* the conductive polymer PEDOT within the brain, resulting in a network of conductive filaments surrounding neurons and tracking white matter (Richardson-Burns et al., 2007b). Although the network was electrochemically validated as a functional electrode, further work is required to determine effects on cellular viability, network behavior, and whether the distribution of the polymer can be controlled for precise stimulation or recording. Green et al. (2013) demonstrated a multi-layer biohybrid interface consisting of platinum electrodes, conductive polymer-hydrogel blend, and PC12 cells within a biodegradable hydrogel layer; cells survived out to 12 days *in vitro* and extended neuritic processes upon the addition of NGF. Potential future development would interrogate whether such embedded neural cells are capable of synaptogenesis, forming a functional neuronal layer around the electrode (Green et al., 2013; Aregueta-Robles et al., 2014).

In addition to dissociated or embedded cells, the combination of living tissue and neuroelectronics may further leverage the functional benefits of the ECM surrounding the neurons, including the presence of signaling molecules, structural support, tissue-level organization, and the dynamic remodeling of the matrix to facilitate growth or stabilize neuronal networks (Cullen et al., 2011). Further, the introduction of support cells (e.g., glia) in pro-regenerative states may provide sufficient cues to prevent or ameliorate the neurodegenerative outcomes present in the chronic inflammatory response (Aregueta-Robles et al., 2014). The first such interface, a "neurotrophic electrode," was reported by Dr. Philip Kennedy in a 1989 paper, where a glass pipette electrode was seeded with a piece of sciatic nerve and implanted into rat and later monkey cortex (Kennedy, 1989; Kennedy et al., 1992). Neurites grew into the tip, while the extent of growth correlated with tip diameter; recordings from these early living, biohybrid devices lasted over a year (Kennedy et al., 1992). Notably, a solution of NGF in the same pipette had the opposite effect, with a cystic cavity forming around the implant; these results suggest that the benefits of soluble factors may be further improved with the innate, dynamic regulation present in the nerve explant and/or host tissue (Kennedy, 1989). Thus, leveraging robust and multi-faceted biological mechanisms from living tissue may enhance electrode performance in the brain. However, as a relatively new evolution in the neuroengineering field, the advantages of cell- and tissue-seeded electrodes are still largely under active exploration in *in vitro* assays and rodent models (Jorfi et al., 2015; Shoffstall and Capadona, 2018). As with bioactive material-based interfaces, translating these presumed advantages into better interface performance and functional outcomes requires further validation.

MICRO-TISSUE ENGINEERED "LIVING ELECTRODES"

A recent potential neuroelectronic interface strategy developed by our research group involves the engineering of self-contained, functional neural tissue preformed *in vitro* that may be applied toward a myriad of regenerative and neuroprosthetic functions. These micro-tissue engineered neural networks (micro-TENNs) consist of microscopic hydrogel cylinders (micro-columns) with ECM optimized for axonal growth within the central lumen (Struzyna et al., 2015; Adewole et al., 2018; Serruya et al., 2018). Spherical aggregates of primary neurons placed at the micro-column terminals extend neurites through the ECM lumen over time, forming a three-dimensional network of aligned axonal tracts spanning one (unidirectional) or two (bidirectional) neuronal populations (**Figure 3**). Following network formation, these constructs may be precisely implanted in the brain to enable synaptic integration with target regions. Micro-TENNs were originally developed to replace long axonal brain pathways that are often compromised or lost due to traumatic brain injury or neurodegenerative disease, with an anatomically-inspired distribution of discrete cell body aggregates and axon tracts designed to recreate the segregation of gray and white matter in the mammalian brain (Cullen et al., 2012; Struzyna et al., 2015, 2017).

As engineered micro-tissue, micro-TENNs are unique in that their design enables a high level of control over their mechanical, material, and biological properties, while their structure mimics the natural network-level architecture of the brain. The hydrogel micro-column provides a structure to coax the neuronal and axonal growth into the desired architecture, and may be made from a range of biomaterials with varying porosity, stiffness, degradation kinetics, or similar properties as needed. The ECM in the lumen is tailored to support neuronal growth and maturation, and may be modified to contain additional structural proteins and/or chemotactic cues for axonal support and guidance.

After the desired growth and maturation are achieved, the micro-column allows for manipulation of the preformed neural

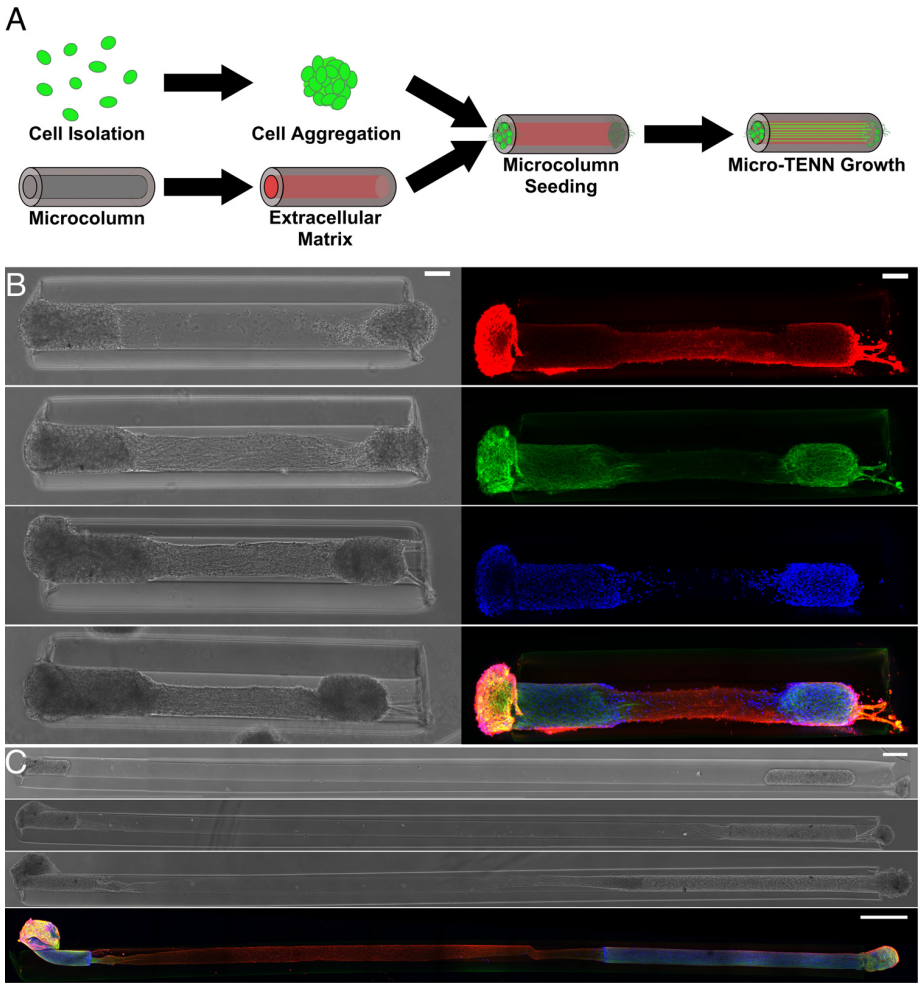

FIGURE 3 | Micro-TENNs as living, 3D constructs. **(A)** Neurons are isolated to form spheroid aggregates that are placed within hydrogel microcolumns filled with ECM. Micro-TENNs are then grown *in vitro*. Either 1 aggregate or 2 aggregates to form either unidirectional or bidirectional micro-TENNs, respectively. **(B)** Left: phase microscopy images of a 1.5 mm bidirectional micro-TENN at 1, 3, 4, and 7 days *in vitro* (DIV). Right: confocal reconstructions of the same micro-TENN stained to identify axons (Tuj-1; red), cell soma/dendrites (MAP-2; green), and cell nuclei (Hoechst; blue). Scale bars: 100 μm. **(C)** Phase microscopy images of a 9 mm bidirectional micro-TENN at 1, 3, and 7 DIV. The bottom image is a confocal reconstruction of this micro-TENN with the same labeling as in **(B)**. Scale bars: 500 μm. Adapted with permission of IOP Publishing from Dhobale et al. (2018).

network as a single unit and serves as a protective encasement to chaperone microinjection into the brain. Within the context of the FBR, the micro-column and luminal ECM also protect the neurons and axonal tracts against the potentially inflammatory post-injection microenvironment. The smallest micro-TENNs to date are only ∼320 μm in diameter, permitting minimally-invasive delivery to the brain; simultaneously, they may be made to different lengths (from 100s of microns to centimeter-scale constructs) to span large deficits or tap into deeper brain structures (Struzyna et al., 2017; Adewole et al., 2018).

In addition, the scalable bio-fabrication process is amenable to isolating precise neuronal subtypes to maintain control of the effects of micro-TENN synaptic inputs on host circuitry. To date, micro-TENNs have been fabricated using cerebral cortical neurons (e.g., mixed glutamatergic and GABAergic), dorsal root ganglia neurons (e.g., sensory), ventral mesencephalic neurons (e.g., dopaminergic), and medial ganglionic eminence neurons (e.g., GABAergic), amongst other neuronal subtypes, from a range of species including rodent, porcine, and human sources. Moreover, the process of engineering neuronal aggregates creates the opportunity for viral transduction based on neuronal phenotype and protein expression profiles. For example, functionalization of the micro-TENNs with optogenetic actuators (e.g., channelrhodopsin) and optical reporters such as GCaMP allow for light-driven control and monitoring of the constructs for *in vitro* or *in vivo* applications (Struzyna et al., 2017; Adewole et al., 2018). Thus, axon-based living electrodes provide an ability for natural, synaptic-based excitation, inhibition, and/or modulation of host circuitry under optical control.

Indeed, within the context of neuroelectronic interfaces, micro-TENNs may serve as a living information relay (or "living electrode") between deep targets in the brain and an apparatus

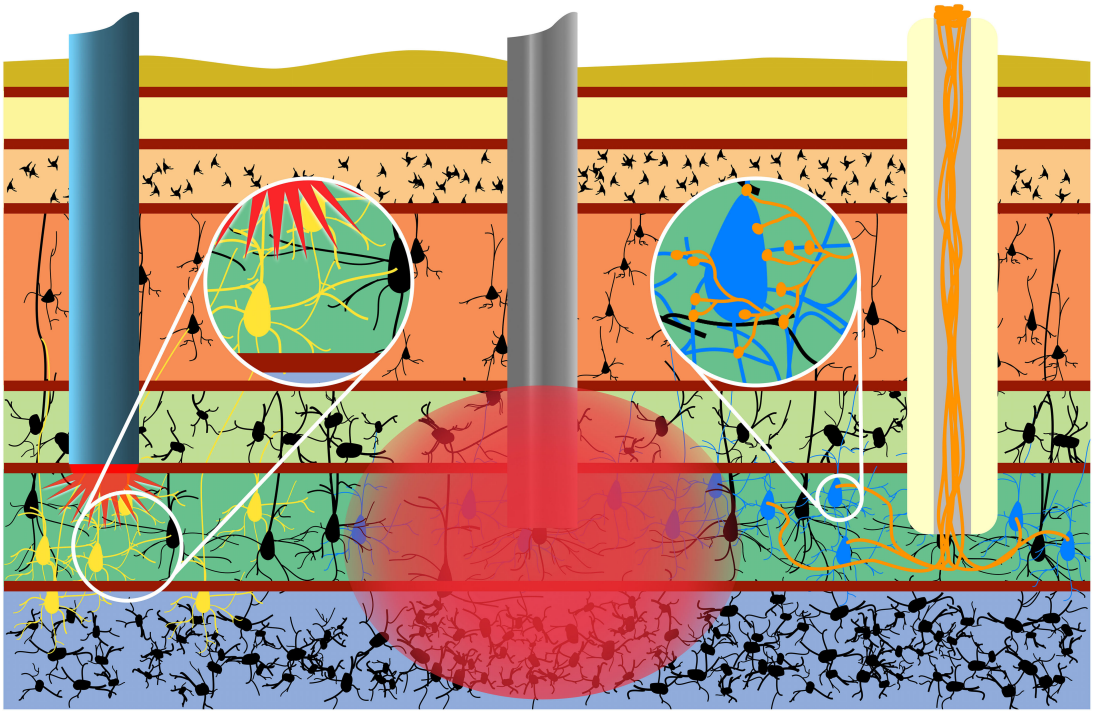

FIGURE 4 | Micro-TENNs applied to neural interface as living electrodes. Living electrodes (right) may provide engineered axonal tracts in a controlled 3D cytoarchitecture to relay signals to/from the brain. Designing constructs to synapse with specific neuronal subtypes (blue neurons) may offer higher specificity than conventional electrodes (middle), which stimulate/record from a 3D volume (red), or than optical stimulation methods (left), wherein the introduction of virus to target neurons (yellow) may spread to non-target regions (e.g., yellow neurons across multiple cortical layers). Reprinted with permission of John Wiley and Sons from Serruya et al. (2018).

on the brain surface (**Figure 4**). In this paradigm, these living electrodes may be stereotactically microinjected such that the deep axon tracts may form synapses with targeted areas of the brain while the neuronal cell bodies remain at the brain surface, allowing for signal propagation along the internal axonal tracts either from the brain surface to the host tissue or vice versa (Serruya et al., 2018). An appropriate electrical (e.g., micro-ECOG) or optical (e.g., LED array) apparatus may then be mounted on or directly above the brain surface, providing computer-controlled modulation or monitoring of the neural targets through stimulation or recording of the dorsal micro-TENN aggregate, respectively.

One significant advantage of this approach is that the non-organic stimulation or recording device is isolated to the brain surface or outside the skull entirely, while only the living electrode (comprised solely of soft biomaterials, ECM, and neurons) penetrates the parenchyma (Serruya et al., 2018). Moreover, the creation of optogenetically-active constructs *in vitro* prior to *in vivo* delivery obviates the need to inject viral components directly into the brain (as is the case with conventional optogenetic approaches). Overall, the presentation of exclusively biocompatible materials may curtail the chronic inflammatory response experienced by non-organic implants, while the hydrogel micro-column protecting the axons may be tuned to degrade at an optimal rate such that the axons are gradually introduced to the microenvironment as the tissue recovers. Additionally, as an alternative to microinjection, living electrodes may be encased in a secondary biomaterial sheath that is stiff enough to penetrate the brain and softens when hydrated, eliminating the need for needle delivery and further minimizing the severity of the tissue disruption upon initial delivery (Harris et al., 2016). Functional studies *in vitro* have shown that these constructs are capable of signal propagation through both electrical and optical stimulation, while implants in a rat model have survived out to at least 1 month with evidence of synaptogenesis and confirmation of transplant activity via intravital calcium imaging (Adewole et al., 2018; Struzyna et al., 2018). Finally, control over the neuronal subtype and protein expression prior to implant as described above may provide the opportunity for precise neuromodulation or therapeutic intervention, such as a computer-controlled "living DBS" electrode made using dopaminergic neurons for controlled dopamine replacement/inputs into the striatum for treatment of Parkinson's disease (**Figure 5**). Similarly, computer-controlled inhibitory living electrodes may be applied to seizure foci in cases of intractable epilepsy, where detection of early epileptiform activity triggers release of copious GABA to extinguish activity in hyperexcitable circuitry (**Figure 5**).

While this living electrode strategy is promising and addresses a number of major challenges in the field, there are a

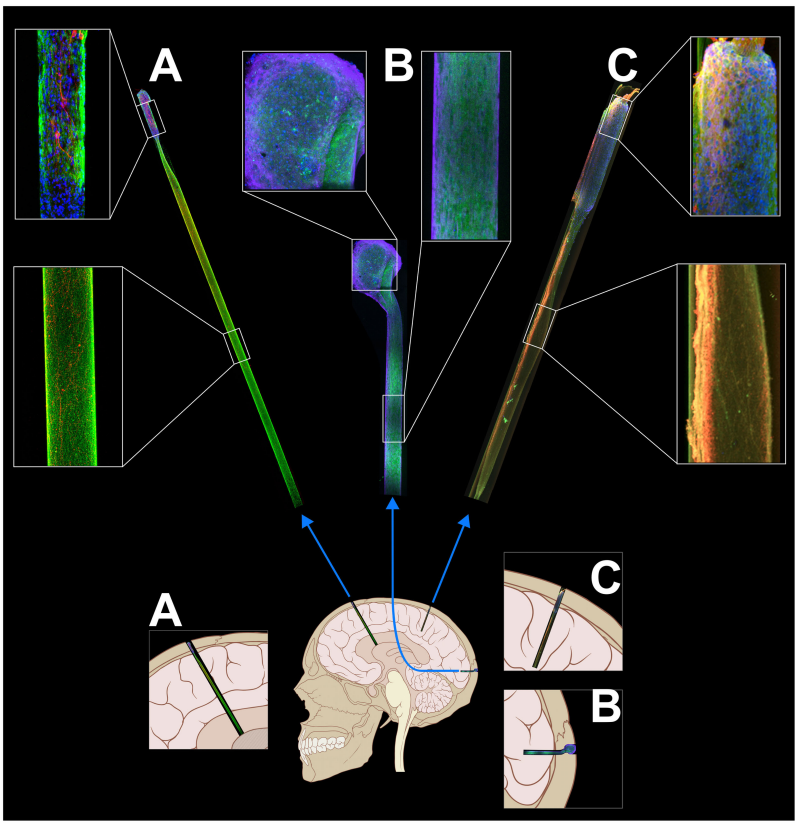

FIGURE 5 | Tissue-engineered living electrodes may be tailored to various applications for neuromodulation. **(A)** Dopaminergic constructs may provide "living deep brain stimulation" for Parkinson's disease through restoration of dopaminergic inputs to the striatum. **(B)** Living electrodes with GABAergic neurons may inhibit epileptic brain activity. **(C)** Glutamatergic constructs could serve as a means to relay sensory feedback, e.g., from prosthetic limbs. Adapted with permission of John Wiley and Sons from Serruya et al. (2018).

several non-trivial challenges to translation that underscore the increased complexity of engineering a biohybrid interface for reproducible function. For instance, as the living electrode concept is based on synapse formation between the implant and brain, the effective stimulation/recording density is dictated primarily by the extent and specificity of synaptogenesis. As such, one significant translational challenge is control over the degree and targeting of synaptogenesis upon implantation. Constructs may be seeded with neurons that preferentially synapse with specific subtypes for more targeted interfacing, although the proportion of desired to aberrant connections is an ongoing area of investigation. Further, migration of living electrode neurons from the construct over time has been observed in early-stage implants, potentially necessitating a mesh or similar barrier to prevent neuronal migration away from the target stimulation/recording site at the brain surface. In the case of bidirectional living electrodes for recording, activity from host neurons must be conveyed across at least two synapses, making them potentially useful for recording local fields but likely hindering the ability to isolate single neurons from the output activity at the brain surface. Computer models of living electrodes may provide predictions of synaptogenesis and signal propagation to better inform design choices and interpret neuronal activity (Dhobale et al., 2018). Clinical bio-fabrication will also be a significant challenge for translation, including starting biomass, quality assurance, and safety monitoring. Here, the use of autologous, stem cell derived neurons would mitigate the need for immune suppression, although personalized living electrodes would be more expensive to build and more challenging to validate than allogeneic living electrodes from a standardized neuronal source. Finally, the input/output behavior of the living electrode under external control must be characterized to (1) compare the living electrode behavior to current clinical benchmarks for neuronal interfacing, and (2) determine the best method of external control at the brain surface. The choice of electrical (e.g., μECOG) or optical interfacing (e.g., LED array) will also likely need further optimization depending on the target application.

SUMMARY

Despite decades of significant effort, to date there is no single ideal neuroelectronic interface for long-term applications. While the definition of an ideal set of properties for a given interface

is determined by the intended application, the clinical viability of these technologies is largely determined by their ability to function stably and predictably over long-term periods, which may, for several applications, span the course of the user's life. Current interfaces are limited by the multi-phasic FBR, a series of prolonged inflammatory processes that lead to neuronal attrition at the implant site and inhibit the chronic utility of recording or stimulation electrodes. Years of natural selection have provided a vast library of mechanisms for directing neuronal growth, migration, and immunoreactivity; a common design feature of bioactive interfaces is the recruitment or partial recreation of these systems to influence local biological activity for better integration. Currently, bioactive interfaces largely use a combination of minimally invasive, soft material coatings, soluble factors and other biomolecules to limit the implant footprint, curb inflammation, and promote neuronal survival, although sustaining this bioactivity over long periods of time remains a significant design challenge. As such, it is necessary that the next generation of implantable, bioactive interfaces maintain a microenvironment that enables chronically stable performance, potentially through the introduction of living cells or tissue to further minimize the disparity between the implant and host brain. Ultimately, fully biological interfaces, such as living electrodes, may allow for a seamless integration with the host circuitry for controlled neuromodulation, feedback, and, ideally, functional restoration.

AUTHOR CONTRIBUTIONS

DKC outlined, edited drafts, and finalized the manuscript. DA performed the literature search, wrote the initial draft, made revisions, and prepared all of the figures. JW and MS made additions and edits to the manuscript.

FUNDING

Financial support was provided by the National Institutes of Health [BRAIN Initiative U01-NS094340 (DKC) & T32-NS091006 (DA)], the National Science Foundation [Graduate Research Fellowship DGE-1321851 (DA)], and the Department of Veterans Affairs [Merit Review I01-BX003748 (DKC)]. Any opinion, findings, and conclusions or recommendations expressed in this material are those of the authors(s) and do not necessarily reflect the views of the National Institutes of Health, National Science Foundation, or Department of Veterans Affairs.

ACKNOWLEDGMENTS

The authors thank James P. Harris, Laura A. Struzyna, Wisberty J. Gordian-Velez, H. Isaac Chen, and Reuben H. Kraft for technical contributions.

REFERENCES

Abidian, M. R., and Martin, D. C. (2009). Multifunctional nanobiomaterials for neural interfaces. *Adv. Funct. Mater.* 19, 573–585. doi: 10.1002/adfm.200801473

Adewole, D. O., Serruya, M. D., Harris, J. P., Burrell, J. C., Petrov, D., Chen, H. I., et al. (2016). The evolution of neuroprosthetic interfaces. *Crit. Rev. Biomed. Eng.* 44, 123–152. doi: 10.1615/CritRevBiomedEng.2016017198

Adewole, D. O., Struzyna, L. A., Harris, J. P., Nemes, A. D., Burrell, J. C., Petrov, D., et al. (2018). Optically-controlled 'living electrodes' with long-projecting axon tracts for a synaptic brain-machine interface. *bioRxiv* doi: 10.2139/ssrn.3189383

Aregueta-Robles, U. A., Woolley, A. J., Poole-Warren, L. A., Lovell, N. H., and Green, R. A. (2014). Organic electrode coatings for next-generation neural interfaces. *Front. Neuroeng.* 7:15. doi: 10.3389/fneng.2014.00015

Azemi, E., Gobbel, G. T., and Cui, X. T. (2010). Seeding neural progenitor cells on silicon-based neural probes. *J. Neurosurg.* 113, 673–681. doi: 10.3171/2010.1.JNS09313

Azemi, E., Lagenaur, C. F., and Cui, X. T. (2011). The surface immobilization of the neural adhesion molecule l1 on neural probes and its effect on neuronal density and gliosis at the probe/tissue interface. *Biomaterials* 32, 681–692. doi: 10.1016/j.biomaterials.2010.09.033

Balint, R., Cassidy, N. J., and Cartmell, S. H. (2014). Conductive polymers: towards a smart biomaterial for tissue engineering. *Acta Biomater.* 10, 2341–2353. doi: 10.1016/j.actbio.2014.02.015

Bendrea, A. D., Cianga, L., and Cianga, I. (2011). Review paper: progress in the field of conducting polymers for tissue engineering applications. *J. Biomater. Appl.* 26, 3–84. doi: 10.1177/0885328211402704

Bennett, C., Samikkannu, M., Mohammed, F., Dietrich, W. D., Rajguru, S. M., and Prasad, A. (2018). Blood brain barrier (bbb)-disruption in intracortical silicon microelectrode implants. *Biomaterials* 164, 1–10. doi: 10.1016/j.biomaterials.2018.02.036

Boehler, C., Kleber, C., Martini, N., Xie, Y., Dryg, I., Stieglitz, T., et al. (2017). Actively controlled release of dexamethasone from neural microelectrodes in a chronic in vivo study. *Biomaterials* 129, 176–187. doi: 10.1016/j.biomaterials.2017.03.019

Chen, S., and Allen, M. G. (2012). Extracellular matrix-based materials for neural interfacing. *MRS Bull.* 37, 606–613. doi: 10.1557/mrs.2012.120

Christo, S. N., Diener, K. R., Bachhuka, A., Vasilev, K., and Hayball, J. D. (2015). Innate immunity and biomaterials at the nexus: friends or foes. *Biomed Res. Int.* 2015:342304. doi: 10.1155/2015/342304

Cogan, S. F. (2008). Neural stimulation and recording electrodes. *Annu. Rev. Biomed. Eng.* 10, 275–309. doi: 10.1146/annurev.bioeng.10.061807.160518

Cullen, D. K., Tang-Schomer, M. D., Struzyna, L. A., Patel, A. R., Johnson, V. E., Wolf, J. A., et al. (2012). Microtissue engineered constructs with living axons for targeted nervous system reconstruction. *Tissue Eng. Part A* 18, 2280–2289. doi: 10.1089/ten.TEA.2011.0534

Cullen, D. K., Wolf, J. A., Smith, D. H., and Pfister, B. J. (2011). Neural tissue engineering for neuroregeneration and biohybridized interface microsystems in vivo (part 2). *Crit. Rev. Biomed. Eng.* 39, 241–259. doi: 10.1615/CritRevBiomedEng.v39.i3.40

De Faveri, S., Maggiolini, E., Miele, E., De Angelis, F., Cesca, F., Benfenati, F., et al. (2014). Bio-inspired hybrid microelectrodes: a hybrid solution to improve long-term performance of chronic intracortical implants. *Front. Neuroeng.* 7:7. doi: 10.3389/fneng.2014.00007

Dhobale, A. V., Adewole, D. O., Chan, A. H. W., Marinov, T., Serruya, M. D., Kraft, R. H., et al. (2018). Assessing functional connectivity across three-dimensional tissue engineered axonal tracts using calcium fluorescence imaging. *J. Neural Eng.* 15:056008. doi: 10.1088/1741-2552/aac96d

Fattahi, P., Yang, G., Kim, G., and Abidian, M. R. (2014). A review of organic and inorganic biomaterials for neural interfaces. *Adv. Mater.* 26, 1846–1885. doi: 10.1002/adma.201304496

Gilja, V., Pandarinath, C., Blabe, C. H., Nuyujukian, P., Simeral, J. D., Sarma, J. D., et al. (2015). Clinical translation of a high-performance neural prosthesis. *Nat. Med.* 21, 6–8. doi: 10.1038/nm.3953

Green, R., and Abidian, M. R. (2015). Conducting polymers for neural prosthetic and neural interface applications. *Adv. Mater.* 27, 7620–7637. doi: 10.1002/adma.201501810

Green, R. A., Lim, K. S., Henderson, W. C., Hassarati, R. T., Martens, P. J., Lovell, N. H., et al. (2013). Living electrodes: tissue engineering the neural interface. *Conf. Proc. IEEE Eng. Med. Biol. Soc.* 2013, 6957–6960. doi: 10.1109/EMBC.2013.6611158

Green, R. A., Lovell, N. H., and Poole-Warren, L. A. (2009). Cell attachment functionality of bioactive conducting polymers for neural interfaces. *Biomaterials* 30, 3637–3644. doi: 10.1016/j.biomaterials.2009.03.043

Green, R. A., Lovell, N. H., Wallace, G. G., and Poole-Warren, L. A. (2008). Conducting polymers for neural interfaces: challenges in developing an effective long-term implant. *Biomaterials* 29, 3393–3399. doi: 10.1016/j.biomaterials.2008.04.047

Grill, W. M., Norman, S. E., and Bellamkonda, R. V. (2009). Implanted neural interfaces: biochallenges and engineered solutions. *Annu. Rev. Biomed. Eng.* 11, 1–24. doi: 10.1146/annurev-bioeng-061008-124927

Groothuis, J., Ramsey, N. F., Ramakers, G. M. J., and Van Der Plasse, G. (2014). Physiological challenges for intracortical electrodes. *Brain Stimul.* 7, 1–6. doi: 10.1016/j.brs.2013.07.001

Hardy, J. G., Lee, J. Y., and Schmidt, C. E. (2013). Biomimetic conducting polymer-based tissue scaffolds. *Curr. Opin. Biotechnol.* 24, 847–854. doi: 10.1016/j.copbio.2013.03.011

Harris, J. P., Capadona, J. R., Miller, R. H., Healy, B. C., Shanmuganathan, K., Rowan, S. J., et al. (2011). Mechanically adaptive intracortical implants improve the proximity of neuronal cell bodies. *J. Neural Eng* 8:066011. doi: 10.1088/1741-2560/8/6/066011

Harris, J. P., Struzyna, L. A., Murphy, P. L., Adewole, D. O., Kuo, E., and Cullen, D. K. (2016). Advanced biomaterial strategies to transplant preformed micro-tissue engineered neural networks into the brain. *J. Neural Eng.* 13:016019. doi: 10.1088/1741-2560/13/1/016019

Harris, J. P., and Tyler, D. J. (2013). Biological, mechanical, and technological considerations affecting the longevity of intracortical electrode recordings. *Crit. Rev. Biomed. Eng.* 41, 435–456.

Hatsopoulos, N., and Donoghue, J. (2009). The science of neural interface systems. *Annu. Rev. Neurosci.* 32, 249–266. doi: 10.1146/annurev.neuro.051508.135241

He, W., and Bellamkonda, R. V. (2005). Nanoscale neuro-integrative coatings for neural implants. *Biomaterials* 26, 2983–2990. doi: 10.1016/j.biomaterials.2004.08.021

He, W., McConnell, G. C., and Bellamkonda, R. V. (2006). Nanoscale laminin coating modulates cortical scarring response around implanted silicon microelectrode arrays. *J. Neural Eng.* 3, 316–326. doi: 10.1088/1741-2560/3/4/009

Heim, M., Yvert, B., and Kuhn, A. (2012). Nanostructuration strategies to enhance microelectrode array (mea) performance for neuronal recording and stimulation. *J. Physiol. Paris* 106, 137–145. doi: 10.1016/j.jphysparis.2011.10.001

Hochberg, L. R., Bacher, D., Jarosiewicz, B., Masse, N. Y., Simeral, J. D., Vogel, J., et al. (2012). Reach and grasp by people with tetraplegia using a neurally controlled robotic arm. *Nature* 485, 372–375. doi: 10.1038/nature11076

Hong, G., Yang, X., Zhou, T., and Lieber, C. M. (2018). Mesh electronics: a new paradigm for tissue-like brain probes. *Curr. Opin. Neurobiol.* 50, 33–41. doi: 10.1016/j.conb.2017.11.007

Jalili, R., Kanneganti, A., Romero-Ortega, M. I., and Wallace, G. G. (2017). Implantable electrodes. *Curr. Opin. Electrochem.* 3, 68–74. doi: 10.1016/j.coelec.2017.07.003

Jeon, M., Cho, J., Kim, Y. K., Jung, D., Yoon, E. S., Shin, S., et al. (2014). Partially flexible mems neural probe composed of polyimide and sucrose gel for reducing brain damage during and after implantation. *J. Micromech. Microeng.* 24:10. doi: 10.1088/0960-1317/24/2/025010

Jorfi, M., Skousen, J. L., Weder, C., and Capadona, J. R. (2015). Progress towards biocompatible intracortical microelectrodes for neural interfacing applications. *J. Neural Eng.* 12:011001. doi: 10.1088/1741-2560/12/1/011001

Karumbaiah, L., Saxena, T., Carlson, D., Patil, K., Patkar, R., Gaupp, E. A., et al. (2013). Relationship between intracortical electrode design and chronic recording function. *Biomaterials* 34, 8061–8074. doi: 10.1016/j.biomaterials.2013.07.016

Kennedy, P. R. (1989). The cone electrode: a long-term electrode that records from neurites grown onto its recording surface. *J. Neurosci. Methods* 29, 181–193. doi: 10.1016/0165-0270(89)90142-8

Kennedy, P. R., Mirra, S. S., and Bakay, R. A. E. (1992). The cone electrode: ultrastructural studies following long-term recording in rat and monkey cortex. *Neurosci. Lett.* 142, 89–94. doi: 10.1016/0304-3940(92)90627-J

Kim, D. H., Wiler, J. A., Anderson, D. J., Kipke, D. R., and Martin, D. C. (2010). Conducting polymers on hydrogel-coated neural electrode provide sensitive neural recordings in auditory cortex. *Acta Biomater.* 6, 57–62. doi: 10.1016/j.actbio.2009.07.034

Klaes, C., Shi, Y., Kellis, S., Minxha, J., Revechkis, B., and Andersen, R. A. (2014). A cognitive neuroprosthetic that uses cortical stimulation for somatosensory feedback. *J. Neural Eng.* 11:56024. doi: 10.1088/1741-2560/11/5/056024

Kozai, T. D. Y., Jaquins-Gerstl, A. S., Vazquez, A. L., Michael, A. C., and Cui, X. T. (2015). Brain tissue responses to neural implants impact signal sensitivity and intervention strategies. *ACS Chem. Neurosci.* 6, 48–67. doi: 10.1021/cn500256e

Kozai, T. D. Y., Vazquez, A. L., Weaver, C. L., Kim, S. G., and Cui, X. T. (2012). In vivo two-photon microscopy reveals immediate microglial reaction to implantation of microelectrode through extension of processes. *J. Neural Eng.* 9:066001. doi: 10.1088/1741-2560/9/6/066001

Lecomte, A., Descamps, E., and Bergaud, C. A. (2018). Review on mechanical considerations for chronically-implanted neural probes. *J. Neural Eng.* 15:031001. doi: 10.1088/1741-2552/aa8b4f

Liu, X., Yue, Z., Higgins, M. J., and Wallace, G. G. (2011). Conducting polymers with immobilised fibrillar collagen for enhanced neural interfacing. *Biomaterials* 32, 7309–7317. doi: 10.1016/j.biomaterials.2011.06.047

Mario Cheong, G. L., Lim, K. S., Jakubowicz, A., Martens, P. J., Poole-Warren, L. A., and Green, R. (2014). A. Conductive hydrogels with tailored bioactivity for implantable electrode coatings. *Acta Biomater.* 10, 1216–1226. doi: 10.1016/j.actbio.2013.12.032

McConnell, G. C., Rees, H. D., Levey, A. I., Gutekunst, C. A., Gross, R. E., and Bellamkonda, R. V. (2009). Implanted neural electrodes cause chronic, local inflammation that is correlated with local neurodegeneration. *J. Neural Eng.* 6:056003. doi: 10.1088/1741-2560/6/5/056003

Michelson, N. J., Vazquez, A. L., Eles, J. R., Salatino, J. W., Purcell, E. K., Williams, J. J., et al. (2018). Multi-scale, multi-modal analysis uncovers complex relationship at the brain tissue-implant neural interface: new emphasis on the biological interface. *J. Neural Eng.* 15:033001. doi: 10.1088/1741-2552/aa9dae

Neumann, H., Kotter, M. R., and Franklin, R. J. M. (2009). Debris clearance by microglia: an essential link between degeneration and regeneration. *Brain* 132, 288–295. doi: 10.1093/brain/awn109

Nguyen, J. K., Park, D. J., Skousen, J. L., Hess-Dunning, A. E., Tyler, D. J., Rowan, S. J., et al. (2014). Mechanically-compliant intracortical implants reduce the neuroinflammatory response. *J. Neural Eng.* 11:056014. doi: 10.1088/1741-2560/11/5/056014

Nolta, N. F., Christensen, M. B., Crane, P. D., Skousen, J. L., and Tresco, P. A. (2015). BBB leakage, astrogliosis, and tissue loss correlate with silicon microelectrode array recording performance. *Biomaterials* 53, 753–762. doi: 10.1016/j.biomaterials.2015.02.081

Polikov, V. S., Tresco, P. A., and Reichert, W. M. (2005). Response of brain tissue to chronically implanted neural electrodes. *J. Neurosci. Methods* 148, 1–18. doi: 10.1016/j.jneumeth.2005.08.015

Purcell, E. K., Seymour, J. P., Yandamuri, S., and Kipke, D. R. (2009). In vivo evaluation of a neural stem cell-seeded prosthesis. *J. Neural Eng.* 6:026005. doi: 10.1088/1741-2560/6/2/026005

Richardson-Burns, S. M., Hendricks, J. L., Foster, B., Povlich, L. K., Kim, D. H., and Martin, D. C. (2007a). Polymerization of the conducting polymer poly(3,4-ethylenedioxythiophene) (pedot) around living neural cells. *Biomaterials* 28, 1539–1552.

Richardson-Burns, S. M., Hendricks, J. L., and Martin, D. C. (2007b). Electrochemical polymerization of conducting polymers in living neural tissue. *J. Neural Eng.* 4, L6–L13. doi: 10.1088/1741-2560/4/2/L02

Sahyouni, R., Chang, D. T., Moshtaghi, O., Mahmoodi, A., Djalilian, H. R., and Lin, H. W. (2017). Functional and histological effects of chronic neural electrode implantation. *Laryngoscope Investig. Otolaryngol.* 2, 80–93. doi: 10.1002/lio2.66

Saito, N., Usui, Y., Aoki, K., Narita, N., Shimizu, M., Hara, K., et al. (2009). Carbon nanotubes: biomaterial applications. *Chem. Soc. Rev.* 38, 1897–1903. doi: 10.1039/b804822n

Saxena, T., Karumbaiah, L., Gaupp, E. A., Patkar, R., Patil, K., Betancur, M., et al. (2013). The impact of chronic blood-brain barrier breach on intracortical electrode function. *Biomaterials* 34, 4703–4713. doi: 10.1016/j.biomaterials.2013.03.007

Scaini, D., and Ballerini, L. (2018). Nanomaterials at the neural interface. *Curr. Opin. Neurobiol.* 50, 50–55. doi: 10.1016/j.conb.2017.12.009

Schendel, A. A., Eliceiri, K. W., and Williams, J. C. (2014a). Advanced materials for neural surface electrodes. *Curr. Opin. Solid State Mater. Sci.* 18, 301–307. doi: 10.1016/j.cossms.2014.09.006

Schendel, A. A., Nonte, M. W., Vokoun, C., Richner, T. J., Brodnick, S. K., Atry, F., et al. (2014b). The effect of micro-ecog substrate footprint on the meningeal tissue response. *J. Neural Eng.* 11:46011. doi: 10.1088/1741-2560/11/4/046011

Schmidt, C. E., and Leach, J. B. (2003). Neural tissue engineering: strategies for repair and regeneration. *Annu. Rev. Biomed. Eng.* 5, 293–347. doi: 10.1146/annurev.bioeng.5.011303.120731

Serruya, M., Harris, J. P., Adewole, D. O., Struzyna, L. A., Burrell, J. C., Petrov, D., et al. (2018). Engineered axonal tracts as 'living electrodes' for synaptic-based modulation of neural circuitry. *Adv. Funct. Mater.* 28: 1701183. doi: 10.1002/adfm.201701183

Seymour, J. P., and Kipke, D. R. (2007). Neural probe design for reduced tissue encapsulation in cns. *Biomaterials* 28, 3594–3607. doi: 10.1016/j.biomaterials.2007.03.024

Shain, W., Spataro, L., Dilgen, J., Haverstick, K., Retterer, S., Isaacson, M., et al. (2003). Controlling cellular reactive responses around neural prosthetic devices using peripheral and local intervention strategies. *IEEE Trans. Neural Syst. Rehabil. Eng.* 11, 186–188. doi: 10.1109/TNSRE.2003.814800

Shen, W., Das, S., Vitale, F., Richardson, A., Ananthakrishnan, A., Struzyna, L. A., et al. (2018). Microfabricated intracortical extracellular matrix-microelectrodes for improving neural interfaces. *Microsyst. Nanoeng.* 4:30. doi: 10.1038/s41378-018-0030-5

Shih, J. J., Krusienski, D. J., and Wolpaw, J. R. (2012). Brain-computer interfaces in medicine. *Mayo Clin. Proc.* 87, 268–279. doi: 10.1016/j.mayocp.2011.12.008

Shoffstall, A. J., and Capadona, J. R. (2018). Bioinspired materials and systems for neural interfacing. *Curr. Opin. Biomed. Eng.* 6, 110–119. doi: 10.1016/j.cobme.2018.05.002

Skousen, J. L., Bridge, M. J., and Tresco, P. A. (2015). A strategy to passively reduce neuroinflammation surrounding devices implanted chronically in brain tissue by manipulating device surface permeability. *Biomaterials* 36, 33–43. doi: 10.1016/j.biomaterials.2014.08.039

Sommakia, S., Lee, H. C., Gaire, J., and Otto, K. J. (2014). Materials approaches for modulating neural tissue responses to implanted microelectrodes through mechanical and biochemical means. *Curr. Opin. Solid State Mater. Sci.* 18, 319–328. doi: 10.1016/j.cossms.2014.07.005

Sridharan, A., Nguyen, J. K., Capadona, J. R., and Muthuswamy, J. (2015). Compliant intracortical implants reduce strains and strain rates in brain tissue in vivo. *J. Neural Eng.* 12:036002. doi: 10.1088/1741-2560/12/3/036002

Sridharan, A., Rajan, S. D., and Muthuswamy, J. (2013). Long-term changes in the material properties of brain tissue at the implant-tissue interface. *J. Neural Eng.* 10:066001. doi: 10.1088/1741-2560/10/6/066001

Stice, P., Gilletti, A., Panitch, A., and Muthuswamy, J. (2007). Thin microelectrodes reduce gfap expression in the implant site in rodent somatosensory cortex. *J. Neural Eng.* 4, 42–53. doi: 10.1088/1741-2560/4/2/005

Struzyna, L. A., Adewole, D. O., Gordián-Vélez, W. J., Grovola, M. R., Burrell, J. C., Katiyar, K. S., et al. (2017). Anatomically inspired three-dimensional micro-tissue engineered neural networks for nervous system reconstruction, modulation, and modeling. *J. Vis. Exp.* 123:e55609. doi: 10.3791/55609

Struzyna, L. A., Browne, K. D., Brodnik, Z. D., Burrell, J. C., Harris, J. P., Chen, H. I., et al. (2018). Tissue engineered nigrostriatal pathway for treatment of parkinson's disease. *J. Tissue Eng. Regen. Med.* 12, 1702–1716. doi: 10.1002/term.2698

Struzyna, L. A., Harris, J. P., Katiyar, K. S., Chen, H. I., and Cullen, D. K. (2015). Restoring nervous system structure and function using tissue engineered living scaffolds. *Neural Regen. Res.* 10, 679–685. doi: 10.4103/1673-5374.156943

Szostak, K. M., Grand, L., and Constandinou, T. G. (2017). Neural interfaces for intracortical recording: requirements, fabrication methods, and characteristics. *Front. Neurosci.* 11:665. doi: 10.3389/fnins.2017.00665

Taub, A. H., Hogri, R., Magal, A., Mintz, M., and Shacham-Diamand, Y. (2012). Bioactive anti-inflammatory coating for chronic neural electrodes. *J. Biomed. Mater. Res. Part A* 100 A, 1854–1858. doi: 10.1002/jbm.a.34152

Thompson, B. C., Richardson, R. T., Moulton, S. E., Evans, A. J., O'Leary, S., Clark, G. M., et al. (2010). Conducting polymers, dual neurotrophins and pulsed electrical stimulation - dramatic effects on neurite outgrowth. *J. Control. Release* 141, 161–167. doi: 10.1016/j.jconrel.2009.09.016

Tresco, P. A., and Winslow, B. D. (2011). The challenge of integrating devices into the central nervous system. *Crit. Rev. Biomed. Eng.* 39, 29–44. doi: 10.1615/CritRevBiomedEng.v39.i1.30

Vitale, F., Shen, W., Driscoll, N., Burrell, J. C., Richardson, A. G., Adewole, O., et al. (2018). Biomimetic extracellular matrix coatings improve the chronic biocompatibility of microfabricated subdural microelectrode arrays. *PLoS One* 13:e0206137. doi: 10.1371/journal.pone.0206137

Vitale, F., Summerson, S. R., Aazhang, B., Kemere, C., and Pasquali, M. (2015). Neural stimulation and recording with bidirectional, soft carbon nanotube fiber microelectrodes. *ACS Nano* 9, 4465–4474. doi: 10.1021/acsnano.5b01060

Webster, T. J., Waid, M. C., McKenzie, J. L., Price, R. L., and Ejiofor, J. U. (2004). Nano-biotechnology: carbon nanofibres as improved neural and orthopaedic implants. *Nanotechnology* 15, 48–54. doi: 10.1088/0957-4484/15/1/009

Winslow, B. D., and Tresco, P. A. (2010). Quantitative analysis of the tissue response to chronically implanted microwire electrodes in rat cortex. *Biomaterials* 31, 1558–1567. doi: 10.1016/j.biomaterials.2009.11.049

Woeppel, K., Yang, Q., and Cui, X. T. (2017). Recent advances in neural electrode–tissue interfaces. *Curr. Opin. Biomed. Eng.* 4, 21–31. doi: 10.1109/EMBC.2014.6945115

Wolpaw, J. R. (2013). *Brain-Computer Interfaces*: *Handbook of Clinical Neurology*, Vol. 110. Amsterdam: Elsevier.

Yu, T., Tutwiler, V. J., and Spiller, K. (2015). "The role of macrophages in the foreign body response to implanted biomaterials," in *Biomaterials in Regenerative Medicine and the Immune System*, ed. L. Santambrogio (Berlin: Springer International Publishing), 17–34. doi: 10.1007/978-3-319-18045-8_2

Zhong, Y., and Bellamkonda, R. V. (2005). Controlled release of anti-inflammatory agent α-msh from neural implants. *J. Control. Release* 106, 309–318. doi: 10.1016/j.jconrel.2005.05.012

Zhong, Y., and Bellamkonda, R. V. (2007). Dexamethasone-coated neural probes elicit attenuated inflammatory response and neuronal loss compared to uncoated neural probes. *Brain Res.* 1148, 15–27. doi: 10.1016/j.brainres.2007.02.024

Zhong, Y., and Bellamkonda, R. V. (2008). Biomaterials for the central nervous system. *J. R. Soc. Interface* 5, 957–975. doi: 10.1098/rsif.2008.0071

Conflict of Interest Statement: DC is a scientific co-founder of INNERVACE, LLC, and Axonova Medical, LLC, which are University of Pennsylvania spin-out companies focused on translation of advanced regenerative therapies to treat nervous system disorders.

The remaining authors declare that the research was conducted in the absence of any commercial or financial relationships that could be construed as a potential conflict of interest.

Copyright © 2019 Adewole, Serruya, Wolf and Cullen. This is an open-access article distributed under the terms of the Creative Commons Attribution License (CC BY). The use, distribution or reproduction in other forums is permitted, provided the original author(s) and the copyright owner(s) are credited and that the original publication in this journal is cited, in accordance with accepted academic practice. No use, distribution or reproduction is permitted which does not comply with these terms.

frontiers in Neuroscience

ORIGINAL RESEARCH
published: 04 April 2019
doi: 10.3389/fnins.2019.00324

Response of Mouse Visual Cortical Neurons to Electric Stimulation of the Retina

Sang Baek Ryu[1,2], *Paul Werginz*[2,3] *and Shelley I. Fried*[1,2]*

[1] *Boston VA Healthcare System, Boston, MA, United States,* [2] *Department of Neurosurgery, Massachusetts General Hospital, Harvard Medical School, Boston, MA, United States,* [3] *Institute for Analysis and Scientific Computing, Vienna University of Technology, Vienna, Austria*

Retinal prostheses strive to restore vision to the blind by electrically stimulating the neurons that survive the disease process. Clinical effectiveness has been limited however, and much ongoing effort is devoted toward the development of improved stimulation strategies, especially ones that better replicate physiological patterns of neural signaling. Here, to better understand the potential effectiveness of different stimulation strategies, we explore the responses of neurons in the primary visual cortex to electric stimulation of the retina. A 16-channel implantable microprobe was used to record single unit activities *in vivo* from each layer of the mouse visual cortex. Layers were identified by electrode depth as well as spontaneous rate. Cell types were classified as excitatory or inhibitory based on their spike waveform and as ON, OFF, or ON-OFF based on the polarity of their light response. After classification, electric stimulation was delivered via a wire electrode placed on the surface of cornea (extraocularly) and responses were recorded from the cortex contralateral to the stimulated eye. Responses to electric stimulation were highly similar across cell types and layers. Responses (spike counts) increased as a function of the amplitude of stimulation, and although there was some variance across cells, the sensitivity to amplitude was largely similar across all cell types. Suppression of responses was observed for pulse rates $\geq$3 pulses per second (PPS) but did not originate in the retina as RGC responses remained stable to rates up to 5 PPS. Low-frequency sinusoids delivered to the retina replicated the out-of-phase responses that occur naturally in ON vs. OFF RGCs. Intriguingly, out-of-phase signaling persisted in V1 neurons, suggesting key aspects of neural signaling are preserved during transmission along visual pathways. Our results describe an approach to evaluate responses of cortical neurons to electric stimulation of the retina. By examining the responses of single cells, we were able to show that some retinal stimulation strategies can indeed better match the neural signaling patterns used by the healthy visual system. Because cortical signaling is better correlated to psychophysical percepts, the ability to evaluate which strategies produce physiological-like cortical responses may help to facilitate better clinical outcomes.

Keywords: primary visual cortex, single unit activity, electrical stimulation, extraocular stimulation, retina

OPEN ACCESS

Edited by:
Jeffrey R. Capadona, Case Western Reserve University, United States

Reviewed by:
Robert Shepherd, The University of Melbourne, Australia
Yongsook Goo, Chungbuk National University, South Korea

***Correspondence:**
Shelley I. Fried
fried.shelley@mgh.harvard.edu

Specialty section:
This article was submitted to Neural Technology, a section of the journal Frontiers in Neuroscience

Received: *04 January 2019*
Accepted: *21 March 2019*
Published: *04 April 2019*

Citation:
Ryu SB, Werginz P and Fried SI (2019) Response of Mouse Visual Cortical Neurons to Electric Stimulation of the Retina. Front. Neurosci. 13:324. doi: 10.3389/fnins.2019.00324

INTRODUCTION

Retinal implants provide a means to restore vision to those blinded by outer retinal degenerative diseases such as retinitis pigmentosa (RP) or age-related macular degeneration (AMRD) (Fujikado et al., 2011; Rizzo, 2011; Zrenner et al., 2011; Humayun et al., 2012; Ayton et al., 2014; Chuang et al., 2014; Shivdasani et al., 2014; Goetz and Palanker, 2016). Blindness results from large-scale degeneration of photoreceptors in the outermost portion of the retina. However, a substantial number of inner retinal neurons remain intact (Santos et al., 1997; Medeiros and Curcio, 2001; Mazzoni et al., 2008), thereby providing a target for electric stimulation from the implant. The activation of surviving retinal neurons leads to transmission of a neural signal to the visual cortex which results in a visual sensation. Clinical tests with existing implants have produced functional vision, e.g., some users can recognize objects and/or letters and some report increased mobility as well (Ahuja et al., 2011; Humayun et al., 2012; Dorn et al., 2013; Stingl et al., 2013, 2015). Although these results are encouraging, the overall performance of these devices remains quite limited.

While many factors are likely to contribute to sub-optimal performance, a key limitation is thought to arise from the inability of the implant to create meaningful patterns of neural activity, e.g., physiological-realistic patterns that are recognizable to downstream visual centers. In the healthy retina, each of at least a dozen different types of retinal ganglion cells (RGCs, retinal output neurons) extract different features of the visual world and use distinct patterns of spiking to convey information to higher visual centers (Baden et al., 2016). For example, ON-Sustained RGCs elicit a burst of spikes that persists for the duration of a bright stimulus while OFF-Transient RGCs remain quiet in response to the same stimulus but spike briefly when the stimulus is turned off. It has proven challenging to re-create this diversity in spiking with electric stimulation and the transmission of non-physiological signals to the brain is likely to be difficult to interpret. Several recent studies suggest however, that novel stimulation strategies may be useful for replicating one or more key elements of physiological signaling, e.g., low-frequency sinusoidal stimulation re-creates the out-of-phase spiking that occurs naturally between ON and OFF RGCs (Freeman et al., 2010; Twyford and Fried, 2016). Other approaches to improve the match to physiological signaling have been reported (Cai et al., 2013; Jepson et al., 2014a,b; Twyford et al., 2014; Lorach et al., 2015; Twyford and Fried, 2016; Ho et al., 2018) with the hope that the re-creation of more "natural" signaling patterns in RGCs will lead to more natural responses in downstream visual centers and ultimately to better clinical outcomes.

Unfortunately, it is not yet possible to produce many of these specialized waveforms with current-generation implants and so the clinical effectiveness of these new strategies remains largely unexplored. The neural response arising in visual cortex is thought to be better correlated to perception (than the neural activity in the retina) (Salzman et al., 1990; Knierim and van Essen, 1992) and so here, as a first step toward determining the efficacy of these new stimulation strategies, we explore the responses of cortical neurons to retinal stimulation. Previous studies that have examined cortical responses arising from electric stimulation of the retina have largely focused on the spatial extent of activation from single channel stimulation, or, on the spatial interactions arising from simultaneous stimulation of two or more neighboring electrodes (Wilms et al., 2003; Sachs et al., 2005; Walter et al., 2005; Eckhorn et al., 2006; Wong et al., 2009; Cicione et al., 2012; Sun et al., 2018). Further, much of this previous work has incorporated measurements of electrically evoked potentials (EEPs) or local field potentials (LFPs), i.e., measurements that reflect population responses from large numbers of cells instead of direct measurements from single cells. Surprisingly, little is known about how neurons that comprise each of the six layers of visual cortex respond to stimulation. Because local computations are transmitted from neurons of layers 4, 2/3, 5, and 6, (Douglas and Martin, 2004), it seems particularly important to understand how the neurons in each of these layers are shaped by the parameters of (retinal) stimulation. It is also important to understand whether stimulation strategies that reproduce key elements of physiological signaling in the retina, e.g., selective activation of ON vs. OFF RGCs (Freeman et al., 2010; Cai et al., 2013; Twyford et al., 2014; Twyford and Fried, 2016) result in better matches to natural signaling in the cortex, e.g., out-of-phase firing in ON vs. OFF cells. This is especially intriguing because better matches to the physiological signaling in cortex could be associated with improved clinical outcomes.

Here, we measured the single unit activity arising in neurons of each layer of mouse visual cortex in response to electrical stimulation of the retina. A 16-channel penetrating microprobe allowed simultaneous recordings from multiple layers of the visual cortex; layers were identified by the depth of penetration as well as by the level of spontaneous activity. Cells were further classified as excitatory or inhibitory according to the shape of their waveform and into ON, OFF, or ON-OFF cells according to the polarity of their response to light. After classification, we investigated responses of individual types as a function of the parameters of stimulation (pulse amplitude and pulse rate). We also explored the efficacy with which physiological-like patterns in the retina are transmitted to cortex.

MATERIALS AND METHODS

Animal Preparation

Experiments were performed on adult (age 2–6 months) male C57BL/6 mice (The Jackson Laboratory, United States). This study was carried out in accordance with the recommendations of all federal and institutional guidelines. The protocol was approved by the Institutional Animal Care and Use Committee of the Massachusetts General Hospital (MGH). The mice were housed in the animal facility of MGH under a 12-h light/dark cycle. Each mouse was anesthetized by an intraperitoneal injection of a mixture of Ketamine (100 mg/kg, Henry Schein Animal Health, United States) and Xylazine (10 mg/kg, Akorn Inc., United States). Body temperature was maintained at 37.5°C by a heating pad. The depth of anesthesia was evaluated every 30–60 min by testing the paw withdrawal reflex, the

eyelid reflex and whisker movements; Ketamine (100 mg/kg, ∼50% of the initial Ketamine-Xylazine dose) was redosed as needed. After completion of all subsequent testing, the mouse was removed from the stereotaxic frame and euthanized via cervical dislocation.

In vivo Electrophysiological Recording

After the mouse was anesthetized, the animal was moved to the recording setup in a darkened room and placed on a stereotaxic frame (SR-9M-HT, Narishige, Japan). Ear bars were positioned into the auditory canals and the scalp was retracted for a craniotomy over primary visual cortex (2-mm diameter); the dura mater within the exposed area was carefully perforated with a thin needle (30 G) and a forceps. Because stimulation was always presented to the right eye (see below), the craniotomy was performed in the left cortical hemisphere. The exposed cortex was rinsed with PBS to clear any residual debris before insertion of the recording electrode. Recordings were made with a 16-channel silicon microprobe (a1x16-3mm50-177, NeuroNexus Technologies, United States); individual electrodes on the microprobe were 15 μm in diameter with 50 μm center-to-center spacing. In some experiments, a single tungsten microelectrode was inserted instead (WE30012.0F3, Microprobes for Life Science, United States). Recording electrodes were oriented orthogonally to the cortical surface and lowered using a micromanipulator (SMM-100, Narshige, Japan) (**Figure 1A**). The position of each electrode within the visual cortex was estimated from the depth readout of the micromanipulator as well as by checking the position of the uppermost electrode and its distance from the cortical surface. The depth of individual cortical layers was based on Olsen et al. (2012) and defined as (in μm): L2/3, 100–350; L4, 350–450; L5, 450–650; and L6 >650. Final calibration of electrode depth was made from the rate of spontaneous firing as measured on individual electrodes (see **Figure 1**): L5 is known to have the highest rate of spontaneous firing (Niell and Stryker, 2008). The recording array typically spanned the full depth of the visual cortex. After the electrode was inserted, the area was covered with 2.5% agarose or PBS to prevent drying and the electrode was allowed to "settle"for 30–45 min before recordings were started. Electrode signals were recorded using an amplifier (Model 3500, A-M Systems, United States) and a data acquisition system (Micro 1401-3, CED, United Kingdom) with software (Spike2, CED, United Kingdom). The extracellular signal was filtered from 100 to 10 kHz and sampled at 25 kHz. All signals were stored on a hard drive and analyzed off-line with custom software written in MATLAB (MathWorks, United States).

Visual and Electrical Stimulation

Visual stimuli consisted of full-field flashes that were generated and controlled by custom software written in LabView (National Instruments, United States) and MATLAB (MathWorks, United States). Each stimulus was delivered at least 30 times (referred to as "repeats"); peristimulus time histograms (PSTHs) were then generated to facilitate the analysis of responses and the classification of cell types. The visual stimulus was displayed on a monitor (Hewlett Packard, HP ZR22w, refresh rate 60 Hz) placed 25 cm from the mouse with a viewing angle of 45° from the center of the monitor (toward the right eye of the mouse).

Electrical stimulation was delivered extraocularly via a platinum-iridium wire (model: 78000, A-M systems, United States); the diameter of the wire was 127 μm, giving an estimated surface area of 12,667 μm^2. The wire was positioned on the surface of the cornea of the right eye using a micromanipulator (SM-25A, Narishige, Japan). The return wire was inserted under the skin behind the neck. Pulse stimuli were generated by a STG8002 stimulator (Multichannel Systems GmbH, Germany) and MC_Stimulus software (Multichannel Systems GmbH, Germany). Stimulus pulses were cathodal-first, biphasic, charge balanced pulses that were rectangular in shape with no interval between the cathodal and anodal phases. Pulse duration was fixed at 2 ms unless otherwise specified. Pulse rate ranged from 1 to 5 pulses per second (PPS) and pulse amplitudes ranged from 20 to 300 μA. For sinusoidal stimulation, frequency ranged from 1 to 5 Hz; the amplitude of all sinusoids was fixed to 100 μA and 20 cycles were delivered regardless of stimulation frequency.

In vitro Electrophysiological Recording

For *in vitro* patch clamp recording, wild type (C57BL/6J) mice were anesthetized with isoflurane and subsequently euthanized by cervical dislocation. Eyeballs were harvested, retinas were dissected from the eyecup and mounted, photoreceptor side down, onto a recording chamber. The retina was subsequently perfused with oxygenated Ames medium (Sigma-Aldrich, United States) at a flow rate of 2–3 ml/min for the duration of the experiment. Temperature was kept at ∼34°C. Small holes were made in the inner limiting membrane in order to obtain access to RGC somata. Spiking responses were obtained using loose (cell-attached) patch recordings. Patch electrode resistance was ∼6–8 MΩ. The visual stimulation was projected from below onto the photoreceptor outer segments using an LCD projector (InFocus, United States). Visual stimulation consisted of bright spots on neutral (gray) background with diameters ranging from 100–1500 μm and presented for 1 s. ON and OFF-α S cells were targeted by their large somata (diameter >15 μm) and identified by their strong sustained light responses. Stimulus control and data acquisition were performed with custom software written in LabView (National Instruments, United States) and Matlab (Mathworks, United States). The electrical stimulation delivered via a 10 kΩ platinum–iridium electrode (MicroProbes, United States); the exposed area at the electrode tip (no Parylene-C insulation) was conical with an approximate height of 125 μm and base diameter of 30 μm, giving a surface area of ∼5,900 μm^2. Stimulating electrodes were positioned 30 μm above the inner limiting membrane; the tip of the electrode was raised by micromanipulator after touching the surface of the inner limiting membrane. Two silver chloride-coated silver wires served as the return; each was positioned ∼8 mm from the targeted cell and ∼6 mm from the other wire. The electric stimuli were applied by a stimulus generator (STG 2004, Multi-Channel Systems MCS GmbH, Germany). For biphasic stimulation, stimulation parameters such as pulse duration (2 ms per phase) and pulse rate (1–5 Hz)

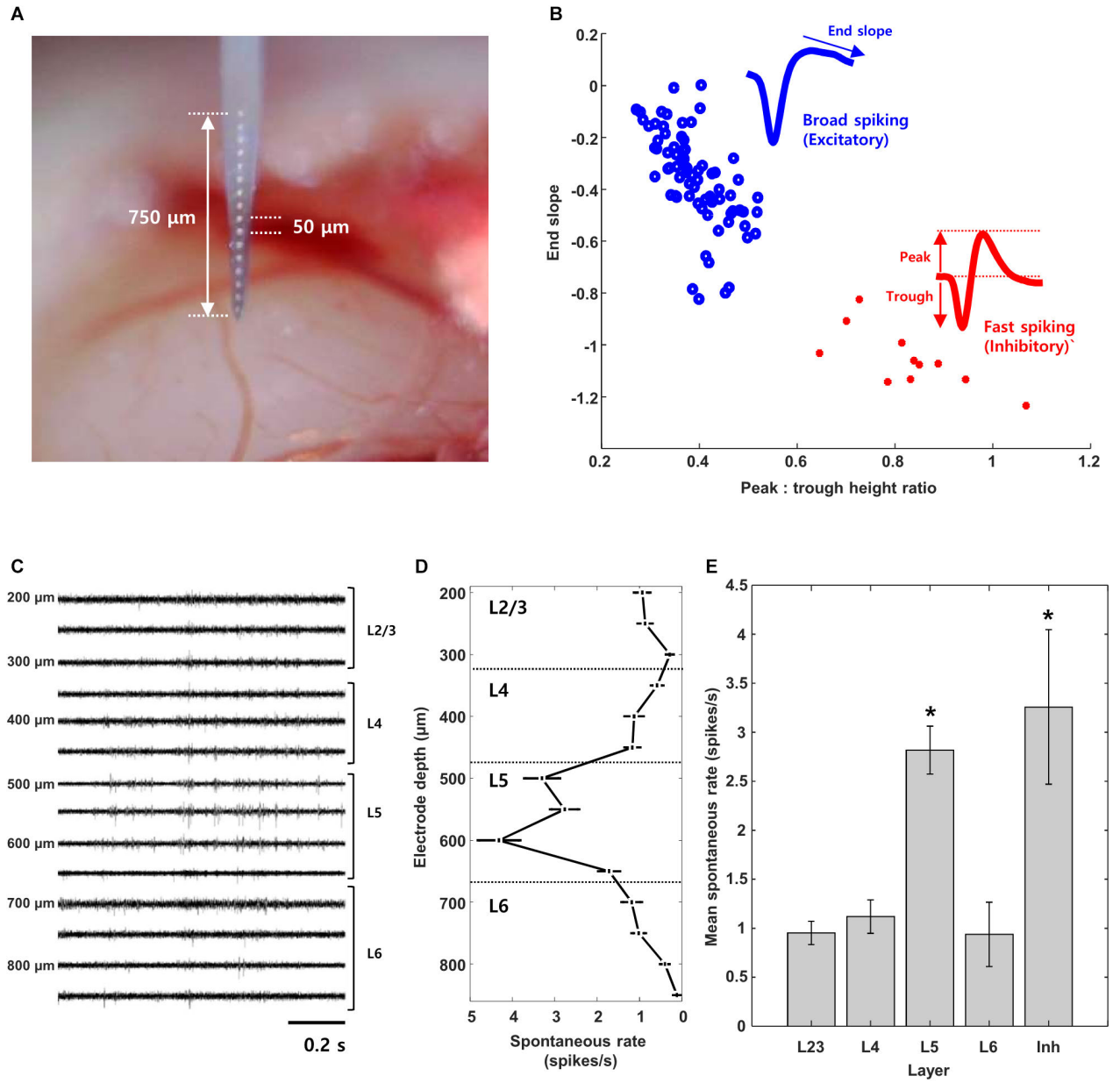

FIGURE 1 | Layer and cell type classification from multisite recording of mouse visual cortex. **(A)** Photograph of the 16-channel linear multisite probe used for insertion into and recording from mouse visual cortex. **(B)** Scatter plot of spike waveform features used to classify cells into excitatory (broad spiking, $n = 74$) and inhibitory (narrow spiking, $n = 11$) types; the average waveforms of broad and fast spiking cells are shown as well. **(C,D)** Raw waveforms and mean spontaneous rate recorded simultaneously from 14/16 channels during a single insertion of the probe. **(E)** Mean spontaneous rate of excitatory cells from each layer and of inhibitory cells pooled across all layers. (L2/3: 15 cells, L4: 18 cells, L5: 29 cells, L6: 16 cells, Inh.: 12 cells), Error bars denote standard error mean (SEM). *indicates $p < 0.05$.

were same with those used for *in vivo* experiment. Stimulation amplitude was fixed at 100 µA. For the electrical sinusoidal stimulation, stimulation frequency from 1 to 5 Hz was used. Pulse and sinusoidal stimuli were controlled by Multi-Channel Systems STG2004 stimulator (Multichannel Systems GmbH, Germany) and MC_Stimulus software (Multichannel Systems GmbH, Germany). Data were recorded using an Axopatch 200B amplifier (Molecular Devices, United States) and digitized by a data acquisition card (PCI-MIO-16E-4, National Instruments, United States). The timing of individual spikes was detected as the depolarization (negative) peak of each spike in the raw trace.

Data Analysis

Spikes were detected by applying a negative threshold to the recorded signal; the timing of individual spikes corresponded to the most negative point of the waveform and therefore, the latency values reported here are ∼0.5 ms slower than actual onsets. Activity from multiple cells was often captured

on a single electrode during the experiment and principal component analysis (PCA) was used for spike sorting (custom software written in MATLAB). Cells were used only if their spike waveforms could be unequivocally separated from other cells on the same electrode. After spike sorting, the average spike waveform was determined for each cell and saved as a template; this allowed verification that the same cell was being consistently recorded throughout an experiment. For example, the average waveform from the spontaneous activity portion of an experiment could be compared to the waveforms from visual stimulation as well as to the responses to electric stimulation. Cells were classified as ON, OFF, or ON-OFF based on their responses to full-field light stimuli.

Features of the extracellular spike waveform were used to distinguish excitatory and inhibitory neurons (see **Figure 1B**) and were based on previous work (Csicsvari et al., 1999; Bruno and Simons, 2002; Andermann et al., 2004; Bartho et al., 2004; Niell and Stryker, 2008; Rummell et al., 2016). In particular, we found consistently good separation using (i) the height of the positive peak relative to the initial negative trough, and, (ii) the slope of the waveform from the first peak to the baseline (Niell and Stryker, 2008). Amplitudes of each average spike waveform were normalized before classification.

The electric artifact was divided into two periods (**Figure 3A**, labeled as periods "i" and "ii"). During the first period which is the actual duration of the stimulation pulse, the amplifiers were saturated and spikes could not be detected. After the first period, the artifact was still prevalent but spikes could nevertheless be observed. The use of an amplitude threshold was not effective for extracting individual spikes and so we utilized a traditional artifact removal technique (Hashimoto et al., 2002) in which a template of the average stimulation artifact waveform is subtracted from the raw waveform in individual traces. Since the artifact size and shape could vary slightly across trials, some residual artifact often remained after subtraction and could result in false positives. As a result, the time period from 0–7 ms after the pulse onset was "flattened" by zero-padding [indicated by (ii) in **Figure 3A**]. Spikes could reliably be detected after 7 ms and their waveforms visually compared to the template waveforms recorded during spontaneous activity and/or visual stimulation (Spike waveforms shown in **Figures 3B–E**).

To quantify the strength of a given electrically elicited response, the number of spikes elicited within 100 ms of the pulse onset was counted and averaged across all repeats of a given stimulus. For statistical analysis, the Student (independent sample) *t*-test was used, $p < 0.05$ was considered as significant (*). In figures presenting the median of data, error bars denote the standard error of the mean.

During patch recordings (the retinal *in vitro* experiments), we record in voltage-clamp mode and so we capture currents (not voltages); with this approach, the polarity of the raw stimulus artifact appears as a negative deflection for anodal stimuli and a positive deflection for cathodal stimuli. This is inverted from typical convention; previous studies that have performed similar experiments (Freeman et al., 2010; Twyford and Fried, 2016), have made note of the anomaly. In the cortical (*in vivo*) experiments, the polarity of the stimulus artifact is not inverted and so the raw waveforms from the two sets of experiments would appear opposite to one another. We felt that this would be confusing in **Figure 8**, where both *in vitro* (Panels A–D) and *in vivo* (Panels E–H) are presented together, i.e., if positive waveforms indicated cathodal stimuli in one part of the figure and negative stimuli in another, it would make the results of the figure difficult to interpret. Therefore, we artificially "inverted" the retinal *in vitro* stimulus waveforms. This was done by low-pass filtering the raw waveform to extract the stimulus waveform, inverting it, and then adding it to a high-pass filtered version of the raw waveform (to capture the spiking responses without the stimulus artifact). While this depicts the same polarity for cathodal and anodal stimuli in both sets of experiments, it has the adverse effect of making the *in vitro* retinal results appear different from earlier work (Freeman et al., 2010; Twyford and Fried, 2016).

RESULTS

A 16-channel implantable microprobe was used to obtain simultaneous recordings of single unit activity from multiple layers of mouse visual cortex. The results below are based on *in vivo* recordings from 126 cortical neurons (L2/3: 24, L4: 32, L5: 37, L6: 33) obtained from 33 adult mice and *in vitro* recordings from 17 RGCs obtained from 5 additional mice.

Layer and Cell Type Classification

Similar to a previous study (Niell and Stryker, 2008), we used the end slope and the peak-to-trough height of measured spikes to classify cells as excitatory vs. inhibitory (Methods, **Figure 1B**); these two parameters resulted in linearly good separability between the two cell types (Andermann et al., 2004; Niell and Stryker, 2008). Similar to previous approaches, cells with broad-spiking waveforms (blue) were classified as excitatory while those with fast-spiking waveforms (red) were classified as inhibitory (Csicsvari et al., 1999; Bruno and Simons, 2002; Andermann et al., 2004; Bartho et al., 2004; Niell and Stryker, 2008; Rummell et al., 2016). Most of the cells we found were excitatory ($n = 113/126$, L2/3: 23/24, L4: 29/32, L5: 33/37, L6: 28/33).

Figure 1C shows a portion of the raw spontaneous activity recorded from 14 channels during a typical experiment. The mean firing rate was calculated for each cell (Methods) and then the average rate of firing across all cells at a given insertion depth was plotted (**Figure 1D**). Insertion depths of 100–350 μm corresponded to layer 2/3 (L2/3) while depths of 350–450, 450–650 and >650 corresponded to layers 4, 5, and 6 (L4, L5, and L6, respectively) (Olsen et al., 2012). The mean rate of activity for cells at depths of 500–650 μm (L5) was higher than that of layers 2/3, 4, or 6 ($p < 0.01$ for all individual comparisons); the higher level of spontaneous activity observed here (L5) is consistent with previous work (Niell and Stryker, 2008). As the number of inhibitory cells found here was limited ($n = 13$), the mean firing rate was pooled from cells across all layers; the mean inhibitory rate was comparable to that from L5 excitatory neurons and significantly different from the mean rate of other layers ($p < 0.05$ for all individual comparisons) (Niell and Stryker, 2008).

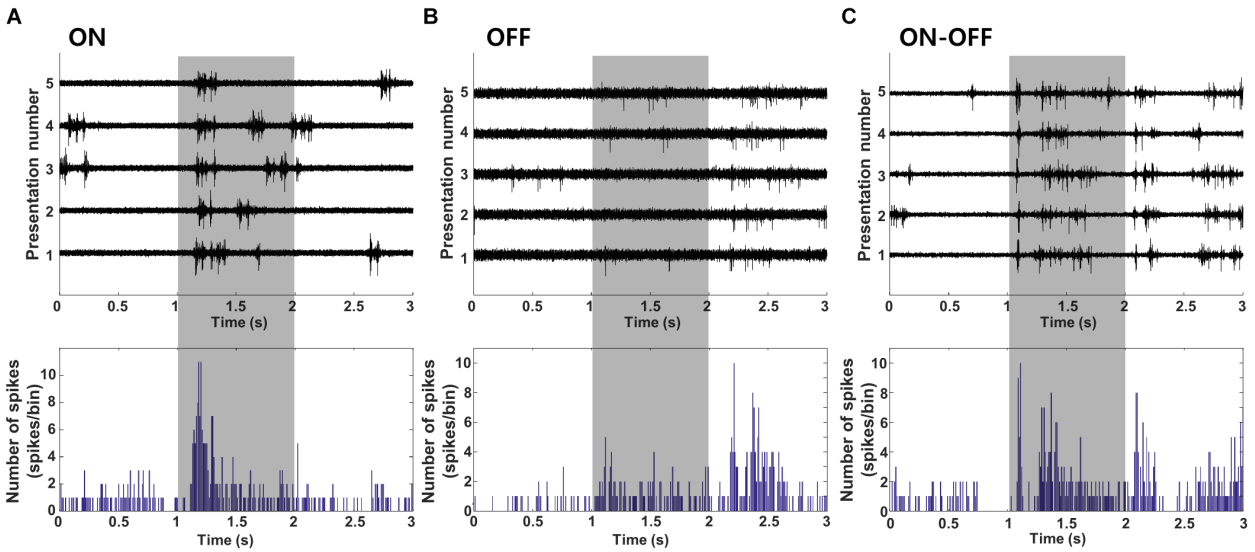

FIGURE 2 | Cell type classification based on visual response. **(A–C)** Cell were classified into ON, OFF, or ON-OFF types based on the polarity of their response to a full-field light stimulus (duration of 1 s indicated by the shaded box). Light stimulation was applied 30 times; raw waveforms for 5 consecutive presentations (out of 30) are shown for a typical cell of each type. PSTHs for all cell types are shown at bottom (time bin = 10 ms).

Most of the V1 neurons we tested showed reliable responses to full field light stimulation (**Figure 2**). Cells responded to either the onset (**Figure 2A**, "ON," $n = 23$, L2/3:7, L4:12, L5: 3, L6:1), the offset (**Figure 2B**, "OFF," $n = 13$, L2/3:5, L4:3, L5:3, L6:2) or both the onset and offset of the stimulus (**Figure 2C**, "ON-OFF," $n = 90$, L2/3:12, L4:17, L5:31, L6:30). Consistent with earlier studies (Weng et al., 2005; Mace et al., 2015; Bae et al., 2018), cells from this third group exhibited considerable variability in the relative proportion of their ON vs. OFF responses. **Table 1** summarizes the complete classification of all cells captured in this study.

Electric Stimulation of the Retina Induces Robust Responses in V1 Neurons

Once cells were classified into layer and type, electric stimulation was delivered to the outer surface of the eye (extraocular stimulation, Methods) and the responses of individual V1 neurons were measured (**Figure 3A**). The stimulus was a biphasic waveform, 2 ms/phase and cathodal first; these type of stimuli have been shown previously to strongly activate RGCs (Jensen and Rizzo, 2008; Lee et al., 2013). Delivery of the stimulus typically saturated the amplifiers for 4–5 ms and the persistence of an electrical artifact hindered our ability to reliably detect spikes for an additional 2–3 ms following the emergence from saturation (**Figure 3A**). Although we could reduce the size of the artifact somewhat by digitally subtracting the mean artifact, averaged over many trials, from each raw recording, the residual artifact often led to false positives. To eliminate the possibility of erroneous spikes, we "zeroed out" the response for the first 7 ms following stimulus onset (**Figure 3A**, bottom trace). After this period, spikes that arose within the remaining portion of the artifact could be reliably captured by our spike detection algorithms (Methods). Spike waveforms detected in response to electric stimulation (**Figure 3B**, overlay at bottom right) were compared to the waveforms from spikes arising spontaneously (**Figure 3D**, overlay at top right) or in response to light (not shown); consistency in waveform shape was used to confirm that electrically elicited spikes were indeed from the same cell, e.g., the small movements of the brain those that occurred routinely during experiments did not result in a shift of the recordings to a different cell.

Responses to electric stimulation typically consisted of a brief burst of spiking that occurred within the first 50 ms following stimulus onset and was followed by a 400–500 ms period during which there was little or no spiking (**Figure 3B**). The elimination of spontaneous activity suggests the presence of a strong inhibitory signal during this period and is consistent with much previous work showing a slow-acting but strong wave of inhibition triggered by electrical and other forms of artificial stimulation (Logothetis et al., 2010). The end of the quiet period was marked by the recovery of spontaneous activity. In a few cells with very low spontaneous rates, it could be difficult to accurately determine the duration of the quiet period (not shown). Responses to electric stimulation were similar in both

TABLE 1 | Classification of all cells captured in this study.

		L2/3	L4	L5	L6
ON	Excitatory	6	12	3	1
	Inhibitory	1	–	–	–
OFF	Excitatory	5	2	1	2
	Inhibitory	–	1	2	–
ON-OFF	Excitatory	12	15	29	25
	Inhibitory	–	2	2	5

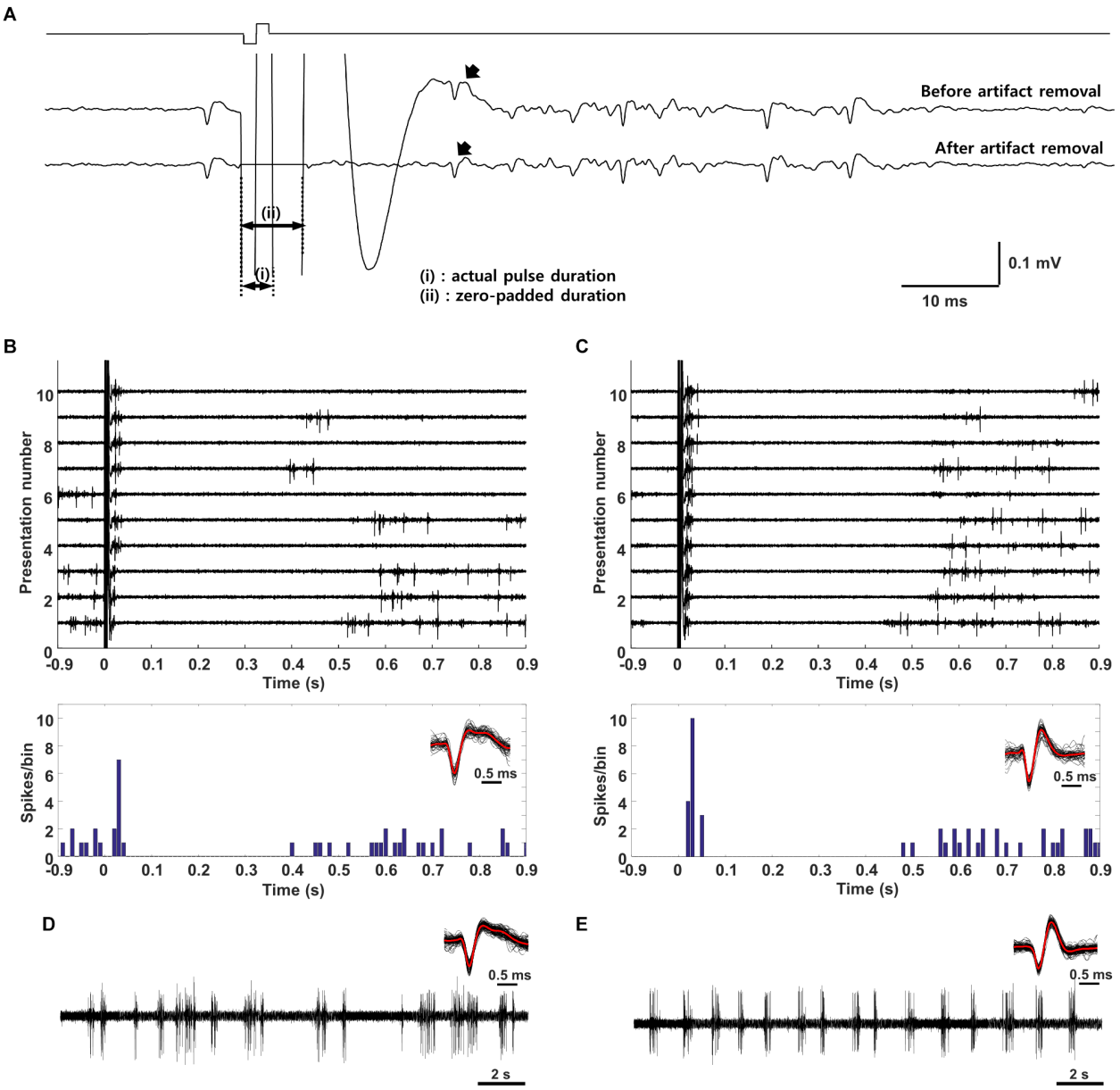

FIGURE 3 | Electric stimulation elicits similar responses in excitatory and inhibitory neurons. **(A)** The stimulus (charge-balanced biphasic pulse, cathodal first, 2 ms/phase, 300 μA) produced an electrical artifact that typically persisted longer than the duration of the stimulus itself. Spikes were sometimes visible within the artifact (top trace, arrow) but were difficult to detect via thresholding (see text); subtraction of the mean artifact from the raw waveform facilitated extraction of such spikes (bottom trace, arrow) but also could result in intermittent false positives during the first 7 ms. To avoid detecting false positives as spikes, this time period was zeroed (bottom trace, period indicated by "ii"). The period labeled as "i" indicates the actual pulse duration. **(B,C)** Raw waveforms (top) and peristimulus time histogram (PSTH) (bottom) of a typical **(B)** L5 excitatory and **(C)** L5 inhibitory neuron. Detected waveforms and their average (red) were overlaid in the inset. (Bottom) **(D,E)** Raw waveforms (spontaneous activity) from the cells in panel **B** and **C**, respectively. The overlay of extracted spikes and the average waveform (red trace) facilitated comparison to electrically and/or visually evoked spikes.

excitatory and inhibitory cells, e.g., compare the responses in **Figures 3B,C**. The timing of the initial burst of spikes in cortical neurons is consistent with the brief, short-latency burst of spikes arising in many different types of RGCs [(Im and Fried, 2015; Werginz et al., 2018), see also **Figure 5**].

Responses to electric stimulation were sensitive to the strength of the stimulus pulse. **Figure 4** shows the responses from a typical L5 excitatory neuron for amplitudes ranging from 60–300 μA. There was some variability across trials, especially for weaker stimuli, e.g., compare responses across the 10 repeats of each stimulus level in panels A–D, but we did not attempt to identify the source of variability. We plotted the average number of spikes elicited within the first 100 ms of each trial (Methods) as a function of stimulus amplitude for each individual cell (dashed

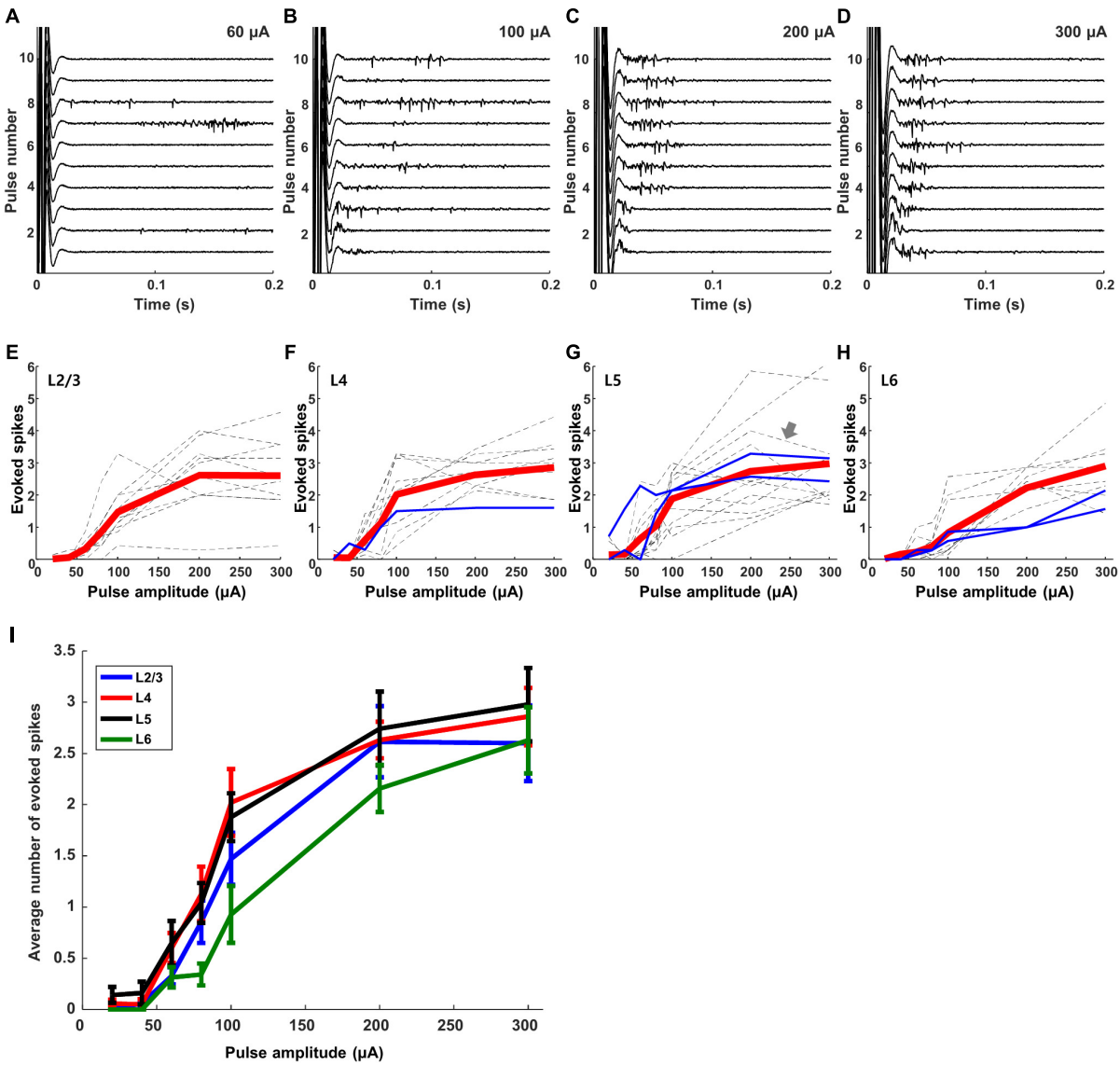

FIGURE 4 | Responses to electric stimulation are sensitive to pulse amplitude. **(A–D)** Raw waveforms recorded in response to electric stimulation from a typical L5 excitatory cell. Each panel shows the response to 10 consecutive pulses; amplitudes are 60, 100, 200, and 300 µA in the 4 panels, respectively. **(E–H)** Dotted gray and blue lines indicate average responses as a function of amplitude from individual excitatory and inhibitory cells, respectively (L2/3: 10 cells, L4: 10 cells, L5: 14 cells, L6: 10 cells). Thick red lines in each graph indicate the average response across all cells within the layer. **(I)** Overlay of the average responses from each layer (the red lines from panels **E–H**).

lines in **Figures 4E–H**; the arrow in **Figure 4G** indicates the cell of panels A–D). Mean responses were generally similar for the cells of a given layer (the average response across all cells in the layer is shown in red.) Overlay of the average responses from all layers (**Figure 4I**) reveals that the sensitivity to amplitude was also similar across layers, including a similar peak level of peak response. The few inhibitory cells that were tested in this experiment (blue lines), exhibited responses that were consistent to those of excitatory cells. We did not observe non-monotonic responses, i.e., responses that increased to the initial increase in stimulus amplitude but then decreased for further increases in amplitude (Barriga-Rivera et al., 2017) (Discussion).

Electrically Elicited Responses Are Suppressed With Increasing Pulse Rate

The prolonged period of inhibition followed each response to electric stimulation (**Figures 3B,C**) suggests that responses to repetitive stimulation may be diminished, at least for rates in which the new stimulus pulse overlaps with the inhibitory signal from the previous pulse. Prior to evaluating the responses of cortical neurons however, we first tested the response of mouse RGCs to increasing rates of stimulation so as to establish the baseline signal leaving the retina. **Figure 5** shows the responses from ON and OFF RGCs in the mouse retinal explant (Methods) to stimulation rates ranging from 1–5 PPS; waveforms were

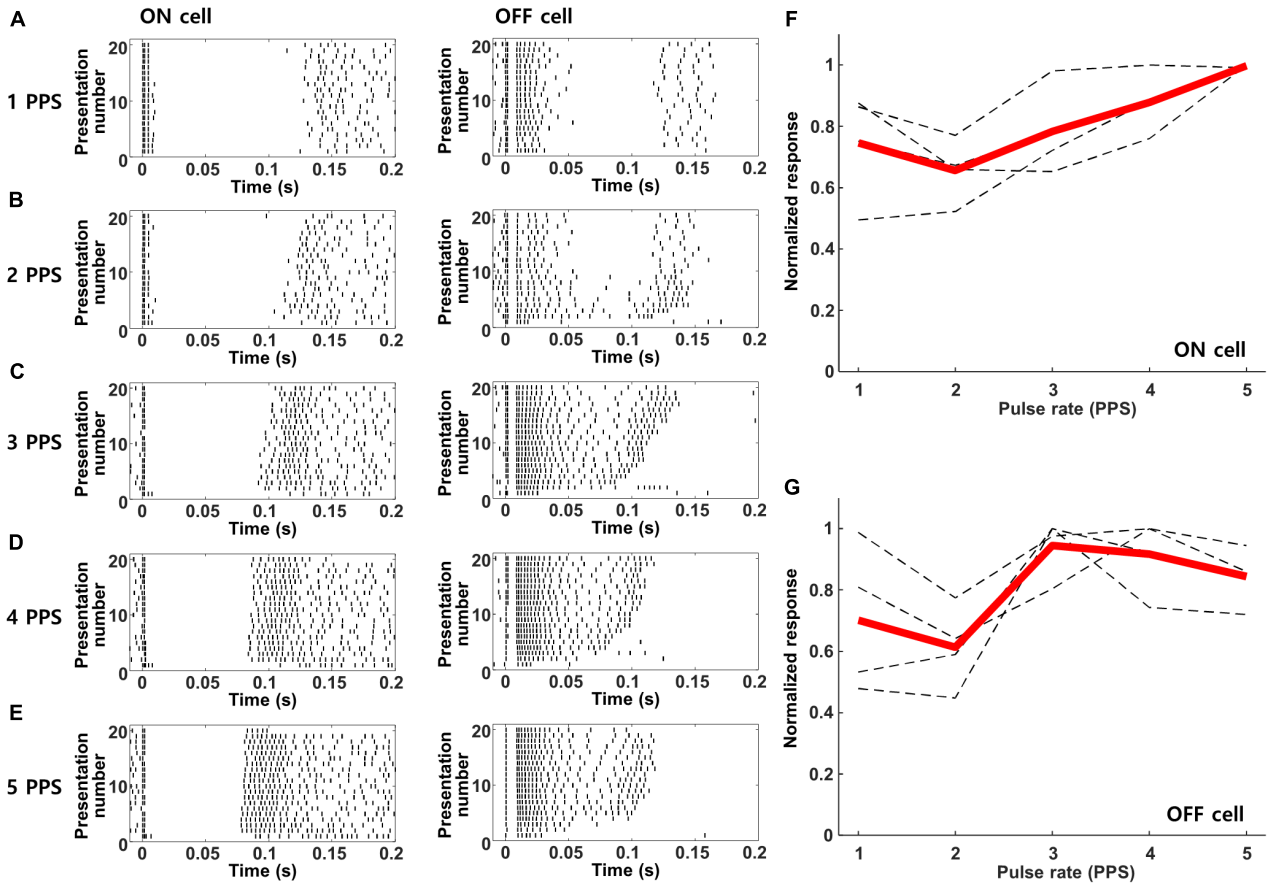

FIGURE 5 | Retinal ganglion cells maintain robust responses to electric stimulation from 1–5 PPS. **(A–E)** Raster plots of a typical ON (left) and OFF (right) RGC in response to pulse rates of 1–5 PPS (biphasic pulse, cathodal first, 2 ms/phase, 100 μA). **(F,G)** Normalized response strength of 4 ON and 4 OFF RGCs, respectively. Dotted gray lines are the response curves from individual RGCs average over 20 repeats; thick red lines indicate the average response of each cell type.

biphasic, cathodal first, and 2 ms/phase). Similar to previous studies (Lee et al., 2013; Im and Fried, 2015; Werginz et al., 2018), responses to these types of relatively long-duration stimuli elicited multiple bursts of spiking that were fairly consistent from trial to trial. As described previously, the onset latencies for bursts were different in ON vs. OFF RGCs (compare burst timing in the left vs. right panels). Individual bursts remained robust and largely consistent as the rate of stimulation was increased from 1 to 5 PPS, although there were some variations in the timing as well as the duration of individual bursts. We counted the number of spikes elicited within the first 200 ms following each stimulus and averaged the results across all ON and OFF cells (**Figures 5F,G**, respectively). The results indicated small variations in the strength of the response across this range of frequencies but there was no systematic reduction in responsiveness with increasing rate, at least up to 5 PPS.

When we delivered the same stimulus extraocularly at 1 PPS and measured the responses of cortical neurons *in vivo*, responses were observed for all 20 pulses (**Figure 6**). The amplitude of stimulation was fixed to 300 μA so as to ensure a strong uniform response across all layers (**Figure 4I**). Similar to the RGC responses, there was some variability across trials in both response strength as well as the timing of individual spikes (**Figure 6A**). When the stimulus rate was increased to 2 PPS however, responses were elicited by the first 13 pulses but not for the subsequent 7 (**Figure 6B**). At even faster rates of stimulation, the number of trials that elicited responses continued to decrease: spikes were elicited for only the first 10 pulses at a rate of 3 PPS (**Figure 6C**) and for only 6 and 7 pulses at rates of 4 and 5 PPS, respectively (**Figures 6D,E**). It is interesting to note that the reduced sensitivity to rates of 3, 4, and 5 PPS arose despite the fact that retinal response levels were not similarly reduced at these same rates (**Figures 5C–E**). Thus the loss of sensitivity in cortical neurons is not due to a corresponding reduction in output signal from the retina, but instead suggests that the loss arises during transmission of the retinal signal to the cortex. Our findings do not reveal the source of this loss in sensitivity, but it is interesting to note that responses in L4 neurons were similar to those from other layers (not shown but see **Figure 6J**), suggesting that the loss occurs prior to arrival at the cortex. It will be interesting in future experiments to record from visual neurons that receive input directly from RGCs (e.g., at the superior colliculus or lateral geniculate nucleus) so as to

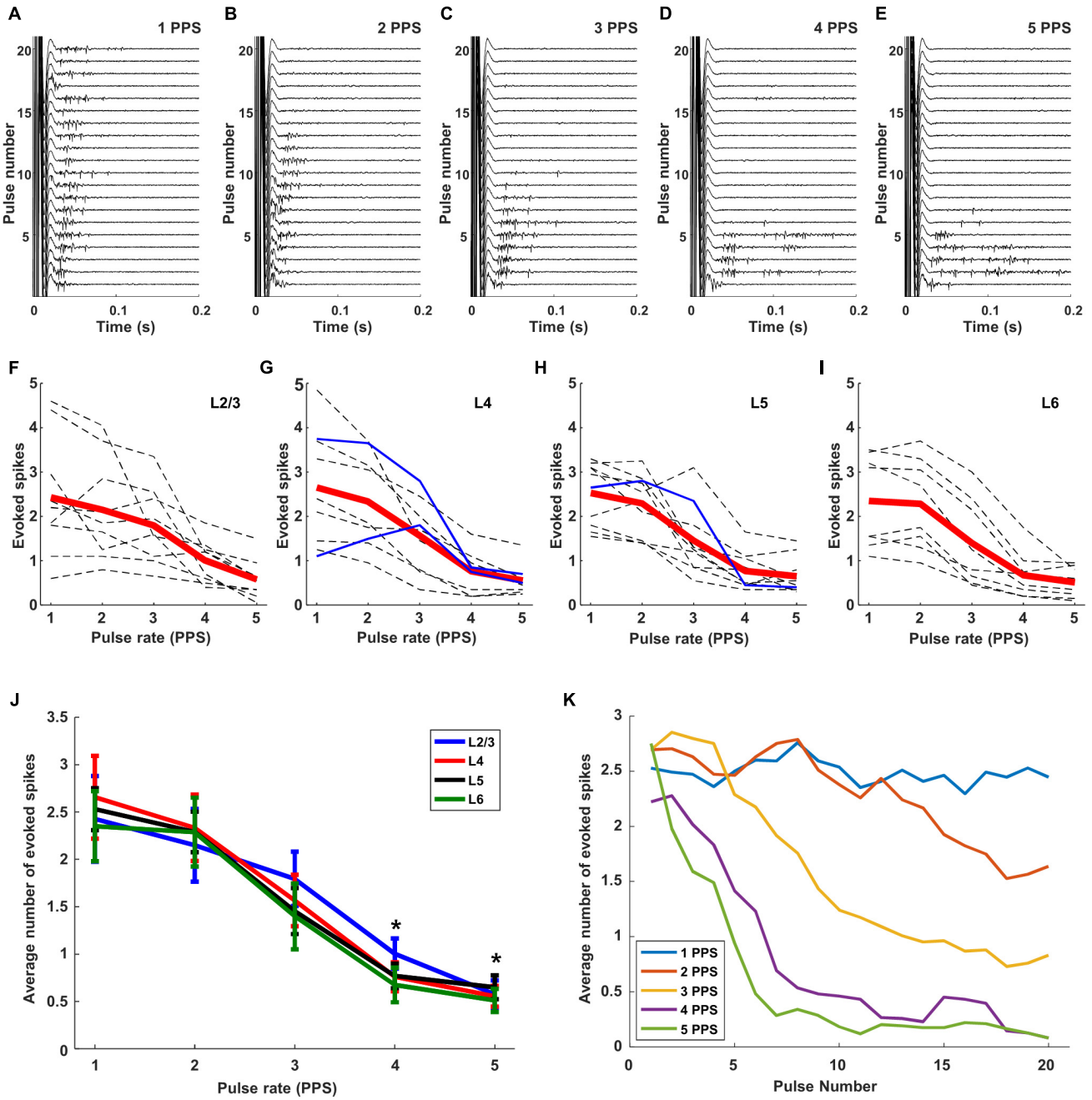

FIGURE 6 | Responses are suppressed by increasing rates of stimulation. **(A–E)** Raw responses from a typical L5 excitatory cell to 20 consecutive pulses at 300 μA; rates of 1, 2, 3, 4, and 5 PPS, respectively, were applied. **(F–I)**. Dotted gray and blue lines are the mean responses from individual excitatory and inhibitory cells, respectively (L2/3: 9 cells, L4: 9 cells, L5: 10 cells, L6: 8 cells). Thick red lines indicate the average response across all cells from the layer. **(J)** Overlay of average response curves from all layers. *indicates $p < 0.05$. **(K)** Response strength versus stimulus number averaged across all layers. Error bars omitted for clarity.

examine their sensitivity to the rate of stimulation; this may help to pinpoint the location at which the sensitivity to higher rates of stimulation is lost. Similar types of suppressive effects have been described in the retina (referred to as desensitization) although they occur at higher rates of stimulation (Jensen and Rizzo, 2007; Freeman and Fried, 2011). Retinal desensitization is thought to be triggered by the strong inhibitory signals that persist longer than the intervals between consecutive stimuli and it is likely that the prolonged inhibitory signal observed in cortical neurons in earlier experiments (**Figure 3**) is similarly tied to the loss of responsiveness seen here. Whereas retinal inhibitory periods persist for <100 ms (Fried et al., 2006), the inhibitory signals seen earlier in cortical neurons (**Figure 3**) persist for several hundred milliseconds and is consistent with the fall-off of sensitivity

at lower-frequencies. To quantify the level of desensitization observed here, we determined the average number of electrically elicited spikes across all 20 repeats for each rate of stimulation. Each dotted line in **Figure 6F** represents the average response from an individual cell in Layer 2/3; the responses from cells in layers 4, 5, and 6 are shown in **Figures 6G–I**, respectively. The red line is the mean response across all cells in the layer. There was a monotonic decrease as stimulus rate increased from 1 to 5 PPS although, once again, there was significant variability across cells. Only three inhibitory cells (two cells in layer 4 and one in layer 5) were tested in this experiment (solid blue lines), their responses were generally similar to those of excitatory neurons.

We overlaid the average plot of response strength vs. pulse rate from each layer (**Figure 6J**) and found that both the overall strength of the response as well as the sensitivity to pulse rate were quite similar across layers. When the mean levels were statistically compared across layers, the responses to 5 PPS stimulation were found to be significantly lower than those to 1 PPS ($p < 0.005$) for all layers. Response strengths at 4 PPS were also significantly lower than those at 1 PPS ($p < 0.05$ for layer 4, $p < 0.005$ for layer 2/3, 5, 6). There was no significant difference in response strength for rates of 1 vs. 2 PPS. A comparison of the response strength as a function of pulse number provided further confirmation that there was minimal desensitization for rates of 1 PPS (**Figure 6K**); as the rate of stimulation increased however, the onset of desensitization occurred earlier, and its effect was stronger. At the fastest rates tested here (5 PPS), desensitization was already evident in the response to the second pulse and responses were almost completely suppressed by the 5th pulse.

We questioned whether the high levels of desensitization seen in these experiments might be arising from the relatively strong stimuli that were used to ensure robust responses from the extraocular stimulus. If so, we reasoned that lower amplitudes might reduce the level of desensitization. Each plot in **Figure 7A** is a raster response to 20 identical stimuli; the rate of stimulation is fixed for each row of plots while the amplitude decreases across columns (from left to right). Consistent with the results of **Figure 6**, responses were consistently robust for a stimulus rate of 1 PPS and a pulse amplitude of 300 μA but they became weaker and less consistent when stimulus strength was reduced to 200 μA and even weaker still at 100 μA. Even with the weaker responses however, there was still a clear reduction in both strength and consistency as the rate of stimulation increased. The persistence of desensitization at weaker stimulus amplitudes suggests that the reductions observed in **Figure 6** were not due to the use of a strong stimulus. At even weaker stimulus levels, e.g., 80 μA, responses were barely detectable, even at 1 PPS, and so it was difficult to assess whether desensitization was present. The response patterns seen in **Figure 7** were highly similar to those from cells in other layers (not shown). Averaging responses across all layers (**Figure 7B**) confirmed that desensitization was strongest for strong stimulus levels but could be observed for any level of stimulation that was strong enough to induce a response. We conclude therefore that the desensitization observed here is not mediated solely by the strength of the stimulus.

Low-Frequency Sinusoids Elicit Out-of-Phase Responses in ON vs. OFF Cells

Low-frequency sinusoidal waveforms activate OFF RGCs during the cathodal phase of the stimulus and ON RGCs during the anodal phase (Freeman et al., 2010; Twyford and Fried, 2016). The ability to reproduce the out-of-phase firing that occurs naturally in RGCs is intriguing and so we questioned whether the out-of-phase firing could be reliably transmitted to cortex, e.g., would ON and OFF cells in cortex exhibit out-of-phase responses? To explore this, we first verified that low-frequency sinusoidal stimulation of mouse retina elicited similar out-of-phase responses to those described previously in rabbit (**Figures 8A–D**). 2 Hz stimulation from a small Pt-Ir electrode (10 kΩ) that was positioned close to the surface of the retinal explant produced burst spiking in ON cells during the peak of the anodal phase of the stimulus (**Figures 8A,B**) but little or no spiking in OFF RGCs at the same time (**Figures 8C,D**). Instead, OFF RGCs responded strongly during the cathodal phase while ON cells were quiet. In subsequent *in vivo* experiments, we delivered electric sinusoidal stimulation at rates of 1–5 Hz extraocularly while measuring the resulting responses in both ON and OFF cells of V1 (**Figures 8E–H**). Low-frequency sinusoids produced robust spiking in both ON and OFF types of cortical neurons (**Figures 8E,G**, respectively) but it was difficult to detect any significant differences from direct observation of the raw waveforms. Converting the timing of elicited spikes to the phase of the stimulus however, revealed that the responses in ON cells indeed occurred during the anodal phase of the stimulus while OFF cells responded during the cathodal phase (PSTHs in **Figures 8F,H**; 13/17 ON cells; 9/9 OFF cells). These recordings suggest that the out-of-phase responses generated artificially in RGCs are indeed faithfully transmitted to higher visual centers. The ability to differentially drive ON vs. OFF channels along the entire visual pathway is intriguing because cortical responses are thought to correlate better to perception and so the ability to selectively target the individual channels offers the hope of higher quality percepts.

DISCUSSION

Our investigation into the response of visual cortical neurons to electrical stimulation of the retina yielded several important insights. First, we found that responses in all cortical neurons were generally brief, persisting for ∼50 ms, and followed by a prolonged period of inhibition (lasting up to a few hundred milliseconds). The relatively short response period was curious given the longer response durations in upstream RGCs. Second, the responses to biphasic pulse stimulation were highly similar across layers and cell types. Third, responses to electric stimulation were highly sensitive to the rate at which stimulation was delivered, e.g., they were significantly reduced for rates as low as 3 PPS. This loss in sensitivity was not mediated within the retinal circuitry as ganglion cell responses remained consistent for rates up to 5 PPS. Finally, selective

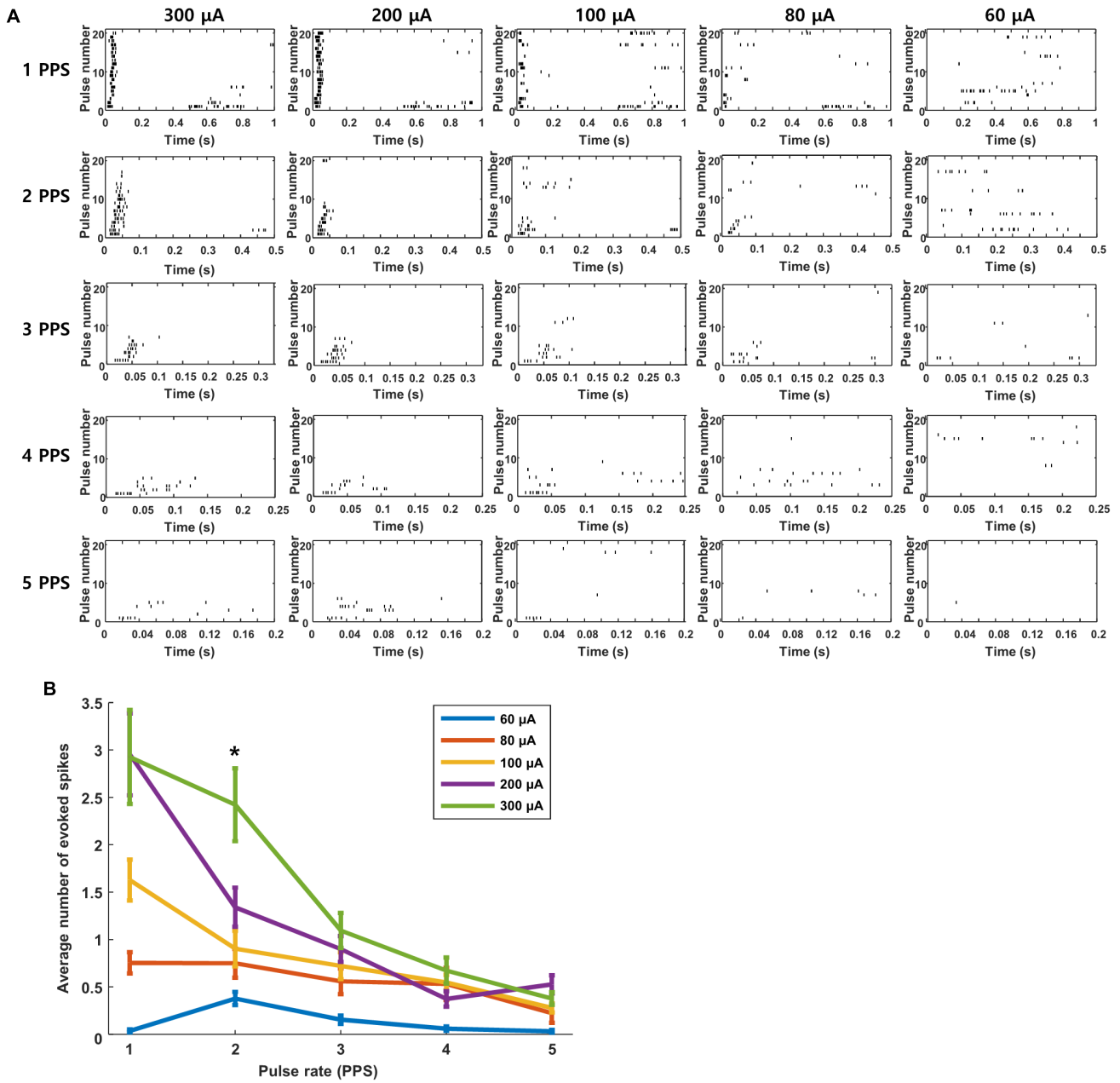

FIGURE 7 | Desensitization is not caused by high stimulus strength. **(A)** Raster responses to electrical stimulation at pulse rates of 1–5 PPS and amplitudes of 60–300 µA in a typical cell. **(B)** Average response strength across all cells as a function of pulse rate; each data point is the average of 11 cells across all layers (L2/3: 2 cells, L4: 2 cells, L5: 4 cells, L6: 3 cells.). *indicates $p < 0.05$.

targeting of ON vs. OFF RGCs (via novel stimulation strategies) led to selective responses in ON vs. OFF cortical neurons, i.e., signaling properties were preserved during propagation to higher visual centers. It is important to note that both ketamine and xylazine can alter cortical responsivity (Bengtsson and Jorntell, 2007; Ordek et al., 2013) but given that anesthesia may not strongly alter the tuning of neurons in primary visual cortex (Lamme et al., 1998; Schanze et al., 2006; Niell and Stryker, 2010), the responses observed here may be representative of those in the awake, behaving animal. Each of these findings is discussed below.

Cortical Responses to Electric Stimulation Are Brief

The responses to pulsatile electrical stimulation were brief, typically persisting for ∼50 ms but always less than 100 ms. While the limited duration is consistent with previous studies

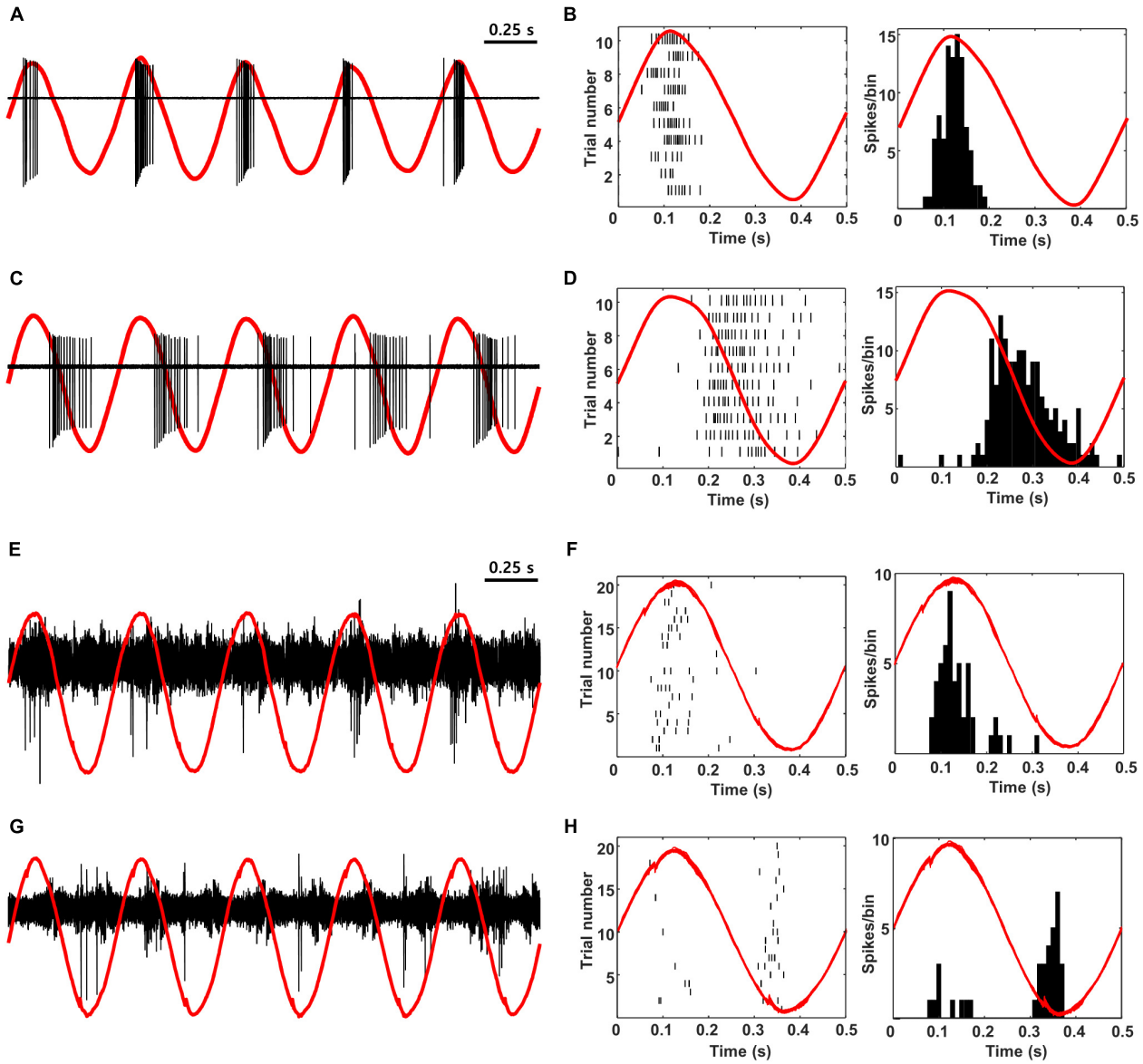

FIGURE 8 | ON vs. OFF selectivity is preserved during propagation from the retina to V1. **(A,C)** Raw *in vitro* response (black) and stimulus waveform (red) from a typical ON and OFF RGC in response to 2-Hz sinusoidal stimulation. **(B,D)** Raster plot (left) and PSTH (right) for the same cells. The red traces are a single period of the stimulus waveform aligned to showing timing of the responses. **(E,G)** Raw response (black) and stimulus waveform (red) from a typical L4 ON cell **(E)** and a typical L2/3 OFF cell **(G)** in response to 2-Hz sinusoidal stimulation (100 μA). **(F,H)** Raster plot (left) and PSTH (right) for the same cells. The red traces are a single period of the stimulus waveform aligned to showing timing of the responses. Note that anodal phases appear as upward and cathodal as downward in all panels (Methods).

(Cicione et al., 2012; Shivdasani et al., 2012; Nimmagadda and Weiland, 2018), they were still somewhat surprising given the prolonged duration in retinal neurons, e.g., spiking responses persisted for ∼150 ms in OFF RGCs and almost 200 ms in ON RGCs (**Figure 5A**). While it is possible that the different durations arise from methodological differences (*in vitro* measurements in the retinal explant utilizing a small stimulating electrode vs. *in vivo* stimulation utilizing a much larger extraocular stimulating electrode), previous studies using a wide range of electrode locations, also report relatively short response durations using smaller, implanted electrodes (Eckhorn et al., 2006; Cicione et al., 2012; Shivdasani et al., 2012; Villalobos et al., 2014). These results suggest that spike bursts with onset latencies >100 ms, e.g., the later bursts in both ON and OFF RGCs (**Figure 5**), do not effectively drive cortical neurons and thus short-latency spike bursts in RGCs are more relevant to cortical responses and probably to psychophysical percepts. Our results do not reveal the reason for the loss of the later bursts but the prolonged period of suppression following the initial burst of spiking in cortical neurons (**Figure 3**) raises

the possibility that subsequent input to cortical neurons is rendered ineffective by the sustained inhibitory signal. Studies in other CNS neurons have described a similar type of sustained inhibitory signal that arises from artificial stimulation (Logothetis et al., 2010).

Similar to earlier studies using both multi-unit recordings (Cicione et al., 2012; Shivdasani et al., 2012; Barriga-Rivera et al., 2017) and EEPs (Chowdhury et al., 2005, 2008), we found that increasing the amplitude of the stimulus pulse resulted in an increase in the number of spikes generated by cortical neurons. The magnitude of RGC responses have also been shown to be sensitive to stimulation strength (Lee et al., 2013) and so it is likely the stronger cortical responses observed here arise directly from stronger responses in RGCs. Cortical responses peaked at 3–4 spikes for even the strongest biphasic pulses we delivered, a level that is comparable to that from a recent report in cat (Barriga-Rivera et al., 2017) although we did not find evidence of non-monotonic responses in some cells as they observed. The similarities in sensitivity to previous reports, including similar magnitudes of overall response strength suggests that our use of extraocular electrodes for stimulation elicits comparable activation of the retina to that from electrodes implanted in the eye. Because we recorded responses with only a single probe, our study does not reveal response variability across different regions of V1 (Cicione et al., 2012) and it is likely that there would be considerable difference if small stimulating electrodes, close to the retina, were compared to the extraocular stimulation used here; it will be useful to perform follow-up studies that incorporate such electrodes in a blind animal model. Testing a chronic implant in an awake behaving animal is also desirable as it will eliminate the potential for response alteration due to anesthesia.

Responses to Electric Stimulation Are Similar Across Cell Types and Layers of V1

We found here that the cortical responses to electric stimulation of the retina were highly consistent across all types of neurons and all layers of the visual cortex (**Figures 4**, **6**). Prior to evaluating the responses to electric stimulation, we first classified cortical neurons into previously established classes. This included (1) the use of visual stimuli to assign cells as ON, OFF, or ON-OFF (**Figure 2**), (2) analysis of the spike waveform to classify cells as excitatory or inhibitory (**Figure 1B**), and (3) correlation of recording channels to cortical depth to assign each cell to a specific layer (**Figures 1C–E**). Our motivation for classifying cells into types was that previous studies repeatedly show that different types of neurons (e.g., RGCs) have different sensitivities to electric stimulation (Im and Fried, 2015); previous studies that have looked at cortical responses to electric stimulation did not similarly classify individual neurons into specific cell types. In general, we found similar distributions of cell types and similar response properties (**Table 1**) to those from previous studies (Chen et al., 2006; Niell and Stryker, 2008). Cortical neurons of different types and from different layers are known to receive synaptic inputs from distinct combinations or (presynaptic) excitatory and inhibitory neurons cells, and, the response properties of the different cell types are shaped by the different inputs they receive (Niell, 2015). Such differences suggested that different cell types might each have a unique response to electric stimulation of the retina. It was therefore somewhat surprising that the different types of cortical neurons had mostly similar responses: a single burst of spiking (that persisted for 40–50 ms (**Figures 3B,C**); the burst has an onset latency of ∼10 ms although we cannot rule out the possibility of earlier spikes that were obfuscated by the artifact. The fact that responses were largely similar suggests that the response differences that arise between different types of RGCs are lost as the neural signal propagates from the retina to V1, at least for the stimulating conditions used here. We cannot rule out the possibility that response differences exist in the lateral direction (Halupka et al., 2017), e.g., beyond the region captured by our single penetrating electrode, and this will be interesting to explore in future studies. The spikes that occurred after the period of inhibition were thought to be the recovery of spontaneous spikes and not an additional phase of the electrically elicited response – this is because cells with a low spontaneous rate did not show spikes at the end of the inhibition period.

V1 Responses Are Suppressed by Stimulation Rates ≥2 PPS

The responses of V1 neurons to electric stimulation were highly sensitive to the rate at which stimulation was delivered. Even at rates of 2 PPS, there was a loss of responsiveness after the first few pulses (**Figures 6A–E**), e.g., robust responses were elicited by the first few pulses in a train but responses stopped completely (no spiking) to subsequent pulses. At higher rates of stimulation, the loss of responsiveness occurred after fewer pulses. This loss of responsiveness was not entirely surprising given the inhibitory signal that persisted for several hundred milliseconds following each pulse (**Figures 3B,C**), i.e., the inhibitory signal from a previous pulse was likely still in effect when the next pulse was delivered. The fact that the first few pulses routinely elicited responses suggests that whatever the source of this inhibitory signal, it does not completely overwhelm the excitatory input arriving from the retina; the inhibitory effect appears to be additive however, and becomes dominant over time. A similar loss of responsiveness to repetitive stimulation has been reported in RGCs *in vitro* (referred to as desensitization) (Jensen and Rizzo, 2007; Freeman and Fried, 2011) although the difference in duration between the RGC (Fried et al., 2006; Im and Fried, 2016) and cortical inhibitory signals makes it unlikely that RGC desensitization was responsible for the decreased sensitivity of cortical neurons observed here. The stable RGC responses observed here for rates up to 5 PPS (**Figure 5**) is also consistent with RGC inhibition having little or no contribution to the inhibitory signal in cortical neurons. It is also worth noting that while some types of RGCs can have complex responses to repetitive stimulation (Im and Fried, 2016), such complexity was not observed in cortical neurons – a single, short burst followed

by a loss of responsiveness after a few pulses was found in all cells tested. Given the difference in sensitivity to repetitive stimulation between retinal and cortical neurons, the loss in sensitivity observed in cortical neurons is likely to arise as the neural signal propagates from the retina to the cortex although our results do not pinpoint the precise location or mechanism.

Some of the loss seen for low rates of stimulation may be attributable to band- or low-pass filtering of the visual pathway. Ridder reported that the amplitude of the VEP began to decrease in response to full field visual stimuli delivered at rates of 3 Hz while the ERG responded to higher frequencies (Ridder and Nusinowitz, 2006). By measuring VEPs from dark-adapted and light-adapted retinas, Ridder also showed that the rod and cone pathways had different sensitivities; the temporal tuning function of dark-adapted VEPs more closely matches the sensitivity to repetitive pulsatile stimulation seen here, raising the possibility that rods (or other retinal neurons that subserve the rod pathway) are activated by the pulses used here. This would not be entirely surprising given the mouse retina is strongly rod-dominated (97% of all photo receptors) (Carter-Dawson and LaVail, 1979; Jeon et al., 1998). Additional studies have shown that the sensitivity to repetitive stimulation varies for different types of visual stimuli, e.g., VEP amplitudes in response to sinusoidal gratings remain consistent at rates up to 5 Hz (Porciatti et al., 1999). This suggests that stimuli that activate spatially confined regions of the retina may result in better responsivity to higher frequencies and thus small, implantable electrodes may have better temporal responsivity than the large extraocular electrodes used here. Similarly, stimuli that preferentially target the cone pathway may also have improved sensitivity to higher rates of stimulation. While the temporal dynamics of the mouse and primate retinas are quite different, clinical reports consistently describe a limitation in the rate at which stimuli can be effectively delivered (Perez Fornos et al., 2012) and thus, the ability to better control the spread of activation and/or the specific cell types activated may help to improve the temporal responsiveness of clinical devices.

It is important to note also that the long-duration stimuli used here (2 ms/phase) were designed to activate outer retinal neurons which in turn activate RGCs (referred to as indirect activation). In addition to producing one or more robust bursts of spiking, this approach also typically results in strong activation of inhibitory neurons that contributes to desensitization. Stimuli that activate RGCs directly (e.g., short-duration pulses), elicit only a single, short-latency spike per pulse. While direct activation can produce very high rates of spiking (Fried et al., 2006; Sekirnjak et al., 2006), we were not able to evaluate whether this approach could improve the temporal responsiveness of cortical neurons. This is because the electrical artifact from short-latency pulses blocked the short-latency responses that we were trying to measure (not shown). The ability to reliably remove the artifact would be of great help for pursuing this line of investigation in the future. This may be possible via the use of small electrodes implanted in the retina as they will greatly reduce the amplitude required for activation. Alternatively, other forms of activation can reduce or eliminate the artifact (Tomita et al., 2010; Nirenberg and Pandarinath, 2012; Lee et al., 2016; Lee and Fried, 2017), thereby allowing unobstructed visualization of all responses.

Sinusoidal Stimulation Creates Temporal Offsets in ON vs. OFF Cells

While the timing of the responses to pulsatile electric stimulation were similar for both ON and OFF neurons in the visual cortex, the use of low frequency sinusoidal stimulation resulted in a temporal offset between the two (**Figure 8**). Consistent with earlier work in the rabbit (Twyford and Fried, 2016), we first showed that ON RGCs in the mouse responded strongly during the anodal phase of low-frequency sinusoidal stimulation while OFF RGCs remained quiet (**Figures 8A–D**). During the cathodal phase OFF cells responded strongly while ON cells were quiet. This temporal offset in response timing is thought to arise because photoreceptors are activated by long, slowly changing stimuli and thus the sign-inverting synapses between photoreceptors and ON bipolar cells alters the sensitivity to stimulus polarity (and timing) for the ON and OFF cell types. When we subsequently recorded from ON and OFF cells in visual cortex, we found a similar offset in phase: OFF cells responded during the cathodal phase of stimulation while ON cells responded during the anodal phase (**Figures 8E–H**). This result is encouraging because it not only indicates that the response timing is maintained as the electrically induced signal propagates from the retina to the visual cortex but also suggests that the use of stimulation strategies that better replicate physiological patterns of spiking in the retina may also lead to patterns of spiking in the cortex that better resemble natural physiology. It is tempting to speculate that because cortical activity better reflects psychophysical percepts (Salzman et al., 1990; Knierim and van Essen, 1992), the use of low-frequency sinusoidal stimulation might improve contrast sensitivity (or other elements of artificial vision). However, it is important to point out that earlier attempts to evoke more natural signaling patterns, e.g., the use of stochastic resonance with cochlear prostheses, did not always lead to improved clinical outcomes unless optimized parameters, such as the level of added noise to enhance detectability, or the information content of a signal (e.g., trains of action potentials) (Moss et al., 2004) were incorporated. Thus, the clinical benefits associated with better matches to retinal signaling, e.g., with low-frequency stimulation will need to be verified in future testing. Also, it is far from certain that strategies that target photoreceptors will be of use in the degenerate retina, although there is some evidence to suggest that parts of photoreceptors can still be harnessed for at least some forms of degeneration (Busskamp et al., 2010). An additional concern is that the low-frequency sinusoidal waveforms described here require a large amount of charge delivery and thus increase the potential for electrochemical damage to the electrode. Any potential benefit of this approach will need to be evaluated in light of this risk. Nevertheless, other stimulation strategies have been proposed to selectively target ON vs. OFF RGCs that do not require intact photoreceptors (Jepson et al., 2014b; Twyford et al., 2014). It will be

interesting to learn whether these strategies similarly result in cortical activity that better matches physiological signaling, and if so, whether they ultimately improve the quality of elicited percepts.

AUTHOR CONTRIBUTIONS

SR and SF conceived and designed the study, analyzed the results, wrote the manuscript, and prepared the figures. SR performed the animal experiments except for the *in vitro* retinal experiments, which was performed by PW.

FUNDING

This work was supported by the Veterans Administration – RR&D (1I01 RX001663) and by the NIH (NINDS U01-NS099700) and Austrian Science Fund (FWF J3947).

REFERENCES

Ahuja, A. K., Dorn, J. D., Caspi, A., McMahon, M. J., Dagnelie, G., Dacruz, L., et al. (2011). Blind subjects implanted with the Argus II retinal prosthesis are able to improve performance in a spatial-motor task. *Br. J. Ophthalmol.* 95, 539–543. doi: 10.1136/bjo.2010.179622

Andermann, M. L., Ritt, J., Neimark, M. A., and Moore, C. I. (2004). Neural correlates of vibrissa resonance; band-pass and somatotopic representation of high-frequency stimuli. *Neuron* 42, 451–463. doi: 10.1016/S0896-6273(04)00198-9

Ayton, L. N., Blamey, P. J., Guymer, R. H., Luu, C. D., Nayagam, D. A., Sinclair, N. C., et al. (2014). First-in-human trial of a novel suprachoroidal retinal prosthesis. *PLoS One* 9:e115239. doi: 10.1371/journal.pone.0115239

Baden, T., Berens, P., Franke, K., Roman Roson, M., Bethge, M., and Euler, T. (2016). The functional diversity of retinal ganglion cells in the mouse. *Nature* 529, 345–350. doi: 10.1038/nature16468

Bae, J. A., Mu, S., Kim, J. S., Turner, N. L., Tartavull, I., Kemnitz, N., et al. (2018). Digital museum of retinal ganglion cells with dense anatomy and physiology. *Cell* 173, 1293.e19–1306.e19. doi: 10.1016/j.cell.2018.04.040

Barriga-Rivera, A., Guo, T., Yang, C. Y., Abed, A. A., Dokos, S., Lovell, N. H., et al. (2017). High-amplitude electrical stimulation can reduce elicited neuronal activity in visual prosthesis. *Sci. Rep.* 7:42682. doi: 10.1038/srep42682

Bartho, P., Hirase, H., Monconduit, L., Zugaro, M., Harris, K. D., and Buzsaki, G. (2004). Characterization of neocortical principal cells and interneurons by network interactions and extracellular features. *J. Neurophysiol.* 92, 600–608. doi: 10.1152/jn.01170.2003

Bengtsson, F., and Jorntell, H. (2007). Ketamine and xylazine depress sensory-evoked parallel fiber and climbing fiber responses. *J. Neurophysiol.* 98, 1697–1705. doi: 10.1152/jn.00057.2007

Bruno, R. M., and Simons, D. J. (2002). Feedforward mechanisms of excitatory and inhibitory cortical receptive fields. *J. Neurosci.* 22, 10966–10975. doi: 10.1523/JNEUROSCI.22-24-10966.2002

Busskamp, V., Duebel, J., Balya, D., Fradot, M., Viney, T. J., Siegert, S., et al. (2010). Genetic reactivation of cone photoreceptors restores visual responses in retinitis pigmentosa. *Science* 329, 413–417. doi: 10.1126/science.1190897

Cai, C., Twyford, P., and Fried, S. (2013). The response of retinal neurons to high-frequency stimulation. *J. Neural Eng.* 10:036009. doi: 10.1088/1741-2560/10/3/036009

Carter-Dawson, L. D., and LaVail, M. M. (1979). Rods and cones in the mouse retina. I. Structural analysis using light and electron microscopy. *J. Comp. Neurol.* 188, 245–262. doi: 10.1002/cne.901880204

Chen, S. J., Mahadevappa, M., Roizenblatt, R., Weiland, J., and Humayun, M. (2006). Neural responses elicited by electrical stimulation of the retina. *Trans. Am. Ophthalmol. Soc.* 104, 252–259.

Chowdhury, V., Morley, J. W., and Coroneo, M. T. (2005). Stimulation of the retina with a multielectrode extraocular visual prosthesis. *ANZ J. Surg.* 75, 697–704. doi: 10.1111/j.1445-2197.2005.03498.x

Chowdhury, V., Morley, J. W., and Coroneo, M. T. (2008). Development of an extraocular retinal prosthesis: evaluation of stimulation parameters in the cat. *J. Clin. Neurosci.* 15, 900–906. doi: 10.1016/j.jocn.2007.08.012

Chuang, A. T., Margo, C. E., and Greenberg, P. B. (2014). Retinal implants: a systematic review. *Br. J. Ophthalmol.* 98, 852–856. doi: 10.1136/bjophthalmol-2013-303708

Cicione, R., Shivdasani, M. N., Fallon, J. B., Luu, C. D., Allen, P. J., Rathbone, G. D., et al. (2012). Visual cortex responses to suprachoroidal electrical stimulation of the retina: effects of electrode return configuration. *J. Neural Eng.* 9:036009. doi: 10.1088/1741-2560/9/3/036009

Csicsvari, J., Hirase, H., Czurko, A., Mamiya, A., and Buzsaki, G. (1999). Oscillatory coupling of hippocampal pyramidal cells and interneurons in the behaving Rat. *J. Neurosci.* 19, 274–287. doi: 10.1523/JNEUROSCI.19-01-00274.1999

Dorn, J. D., Ahuja, A. K., Caspi, A., da Cruz, L., Dagnelie, G., Sahel, J. A., et al. (2013). The detection of motion by blind subjects with the epiretinal 60-electrode (Argus II) retinal prosthesis. *JAMA Ophthalmol.* 131, 183–189. doi: 10.1001/2013.jamaophthalmol.221

Douglas, R. J., and Martin, K. A. (2004). Neuronal circuits of the neocortex. *Annu. Rev. Neurosci.* 27, 419–451. doi: 10.1146/annurev.neuro.27.070203.144152

Eckhorn, R., Wilms, M., Schanze, T., Eger, M., Hesse, L., Eysel, U. T., et al. (2006). Visual resolution with retinal implants estimated from recordings in cat visual cortex. *Vision Res.* 46, 2675–2690. doi: 10.1016/j.visres.2006.01.034

Freeman, D. K., Eddington, D. K., Rizzo, J. F. III, and Fried, S. I. (2010). Selective activation of neuronal targets with sinusoidal electric stimulation. *J. Neurophysiol.* 104, 2778–2791. doi: 10.1152/jn.00551.2010

Freeman, D. K., and Fried, S. I. (2011). Multiple components of ganglion cell desensitization in response to prosthetic stimulation. *J. Neural Eng.* 8:016008. doi: 10.1088/1741-2560/8/1/016008

Fried, S. I., Hsueh, H. A., and Werblin, F. S. (2006). A method for generating precise temporal patterns of retinal spiking using prosthetic stimulation. *J. Neurophysiol.* 95, 970–978. doi: 10.1152/jn.00849.2005

Fujikado, T., Kamei, M., Sakaguchi, H., Kanda, H., Morimoto, T., Ikuno, Y., et al. (2011). Testing of semichronically implanted retinal prosthesis by suprachoroidal-transretinal stimulation in patients with retinitis pigmentosa. *Invest. Ophthalmol. Vis. Sci.* 52, 4726–4733. doi: 10.1167/iovs.10-6836

Goetz, G. A., and Palanker, D. V. (2016). Electronic approaches to restoration of sight. *Rep. Prog. Phys.* 79:096701. doi: 10.1088/0034-4885/79/9/096701

Halupka, K. J., Abbott, C. J., Wong, Y. T., Cloherty, S. L., Grayden, D. B., Burkitt, A. N., et al. (2017). Neural responses to multielectrode stimulation of healthy and degenerate retina. *Invest. Ophthalmol. Vis. Sci.* 58, 3770–3784. doi: 10.1167/iovs.16-21290

Hashimoto, T., Elder, C. M., and Vitek, J. L. (2002). A template subtraction method for stimulus artifact removal in high-frequency deep brain stimulation. *J. Neurosci. Methods* 113, 181–186. doi: 10.1016/S0165-0270(01)00491-5

Ho, E., Smith, R., Goetz, G., Lei, X., Galambos, L., Kamins, T. I., et al. (2018). Spatiotemporal characteristics of retinal response to network-mediated photovoltaic stimulation. *J. Neurophysiol.* 119, 389–400. doi: 10.1152/jn.00872.2016

Humayun, M. S., Dorn, J. D., da Cruz, L., Dagnelie, G., Sahel, J. A., Stanga, P. E., et al. (2012). Interim results from the international trial of Second Sight's visual prosthesis. *Ophthalmology* 119, 779–788. doi: 10.1016/j.ophtha.2011.09.028

Im, M., and Fried, S. I. (2015). Indirect activation elicits strong correlations between light and electrical responses in ON but not OFF retinal ganglion cells. *J. Physiol.* 593, 3577–3596. doi: 10.1113/JP270606

Im, M., and Fried, S. I. (2016). Temporal properties of network-mediated responses to repetitive stimuli are dependent upon retinal ganglion cell type. *J. Neural Eng.* 13:025002. doi: 10.1088/1741-2560/13/2/025002

Jensen, R. J., and Rizzo, J. F. III (2007). Responses of ganglion cells to repetitive electrical stimulation of the retina. *J. Neural Eng.* 4, S1–S6.

Jensen, R. J., and Rizzo, J. F. III (2008). Activation of retinal ganglion cells in wild-type and rd1 mice through electrical stimulation of the retinal neural network. *Vision Res.* 48, 1562–1568. doi: 10.1016/j.visres.2008.04.016

Jeon, C. J., Strettoi, E., and Masland, R. H. (1998). The major cell populations of the mouse retina. *J. Neurosci.* 18, 8936–8946. doi: 10.1523/JNEUROSCI.18-21-08936.1998

Jepson, L. H., Hottowy, P., Mathieson, K., Gunning, D. E., Dabrowski, W., Litke, A. M., et al. (2014a). Spatially patterned electrical stimulation to enhance resolution of retinal prostheses. *J. Neurosci.* 34, 4871–4881. doi: 10.1523/JNEUROSCI.2882-13.2014

Jepson, L. H., Hottowy, P., Weiner, G. A., Dabrowski, W., Litke, A. M., and Chichilnisky, E. J. (2014b). High-fidelity reproduction of spatiotemporal visual signals for retinal prosthesis. *Neuron* 83, 87–92. doi: 10.1016/j.neuron.2014.04.044

Knierim, J. J., and van Essen, D. C. (1992). Neuronal responses to static texture patterns in area V1 of the alert macaque monkey. *J. Neurophysiol.* 67, 961–980. doi: 10.1152/jn.1992.67.4.961

Lamme, V. A., Zipser, K., and Spekreijse, H. (1998). Figure-ground activity in primary visual cortex is suppressed by anesthesia. *Proc. Natl. Acad. Sci. U.S.A.* 95, 3263–3268. doi: 10.1073/pnas.95.6.3263

Lee, S. W., Eddington, D. K., and Fried, S. I. (2013). Responses to pulsatile subretinal electric stimulation: effects of amplitude and duration. *J. Neurophysiol.* 109, 1954–1968. doi: 10.1152/jn.00293.2012

Lee, S. W., Fallegger, F., Casse, B. D., and Fried, S. I. (2016). Implantable microcoils for intracortical magnetic stimulation. *Sci. Adv.* 2:e1600889. doi: 10.1126/sciadv.1600889

Lee, S. W., and Fried, S. I. (2017). Enhanced control of cortical pyramidal neurons with micromagnetic stimulation. *IEEE Trans. Neural Syst. Rehabil. Eng.* 25, 1375–1386. doi: 10.1109/TNSRE.2016.2631446

Logothetis, N. K., Augath, M., Murayama, Y., Rauch, A., Sultan, F., Goense, J., et al. (2010). The effects of electrical microstimulation on cortical signal propagation. *Nat. Neurosci.* 13, 1283–1291. doi: 10.1038/nn.2631

Lorach, H., Goetz, G., Smith, R., Lei, X., Mandel, Y., Kamins, T., et al. (2015). Photovoltaic restoration of sight with high visual acuity. *Nat. Med.* 21, 476–482. doi: 10.1038/nm.3851

Mace, E., Caplette, R., Marre, O., Sengupta, A., Chaffiol, A., Barbe, P., et al. (2015). Targeting channelrhodopsin-2 to ON-bipolar cells with vitreally administered AAV Restores ON and OFF visual responses in blind mice. *Mol. Ther.* 23, 7–16. doi: 10.1038/mt.2014.154

Mazzoni, F., Novelli, E., and Strettoi, E. (2008). Retinal ganglion cells survive and maintain normal dendritic morphology in a mouse model of inherited photoreceptor degeneration. *J. Neurosci.* 28, 14282–14292. doi: 10.1523/JNEUROSCI.4968-08.2008

Medeiros, N. E., and Curcio, C. A. (2001). Preservation of ganglion cell layer neurons in age-related macular degeneration. *Invest. Ophthalmol. Vis. Sci.* 42, 795–803.

Moss, F., Ward, L. M., and Sannita, W. G. (2004). Stochastic resonance and sensory information processing: a tutorial and review of application. *Clin. Neurophysiol.* 115, 267–281. doi: 10.1016/j.clinph.2003.09.014

Niell, C. M. (2015). Cell types, circuits, and receptive fields in the mouse visual cortex. *Annu. Rev. Neurosci.* 38, 413–431. doi: 10.1146/annurev-neuro-071714-033807

Niell, C. M., and Stryker, M. P. (2008). Highly selective receptive fields in mouse visual cortex. *J. Neurosci.* 28, 7520–7536. doi: 10.1523/JNEUROSCI.0623-08.2008

Niell, C. M., and Stryker, M. P. (2010). Modulation of visual responses by behavioral state in mouse visual cortex. *Neuron* 65, 472–479. doi: 10.1016/j.neuron.2010.01.033

Nimmagadda, K., and Weiland, J. D. (2018). Retinotopic responses in the visual cortex elicited by epiretinal electrical stimulation in normal and retinal degenerate rats. *Transl. Vis. Sci. Technol.* 7:33. doi: 10.1167/tvst.7.5.33

Nirenberg, S., and Pandarinath, C. (2012). Retinal prosthetic strategy with the capacity to restore normal vision. *Proc. Natl. Acad. Sci. U.S.A.* 109, 15012–15017. doi: 10.1073/pnas.1207035109

Olsen, S. R., Bortone, D. S., Adesnik, H., and Scanziani, M. (2012). Gain control by layer six in cortical circuits of vision. *Nature* 483, 47–52. doi: 10.1038/nature10835

Ordek, G., Groth, J. D., and Sahin, M. (2013). Differential effects of ketamine/xylazine anesthesia on the cerebral and cerebellar cortical activities in the rat. *J. Neurophysiol.* 109, 1435–1443. doi: 10.1152/jn.00455.2012

Perez Fornos, A., Sommerhalder, J., da Cruz, L., Sahel, J. A., Mohand-Said, S., Hafezi, F., et al. (2012). Temporal properties of visual perception on electrical stimulation of the retina. *Invest. Ophthalmol. Vis. Sci.* 53, 2720–2731. doi: 10.1167/iovs.11-9344

Porciatti, V., Pizzorusso, T., and Maffei, L. (1999). The visual physiology of the wild type mouse determined with pattern VEPs. *Vision Res.* 39, 3071–3081. doi: 10.1016/S0042-6989(99)00022-X

Ridder, W. H. III, and Nusinowitz, S. (2006). The visual evoked potential in the mouse–origins and response characteristics. *Vision Res.* 46, 902–913. doi: 10.1016/j.visres.2005.09.006

Rizzo, J. F. III (2011). Update on retinal prosthetic research: the Boston retinal implant project. *J. Neuroophthalmol.* 31, 160–168. doi: 10.1097/WNO.0b013e31821eb79e

Rummell, B. P., Klee, J. L., and Sigurdsson, T. (2016). Attenuation of responses to self-generated sounds in auditory cortical neurons. *J. Neurosci.* 36, 12010–12026. doi: 10.1523/JNEUROSCI.1564-16.2016

Sachs, H. G., Schanze, T., Wilms, M., Rentzos, A., Brunner, U., Gekeler, F., et al. (2005). Subretinal implantation and testing of polyimide film electrodes in cats. *Graefes Arch. Clin. Exp. Ophthalmol.* 243, 464–468. doi: 10.1007/s00417-004-1049-x

Salzman, C. D., Britten, K. H., and Newsome, W. T. (1990). Cortical microstimulation influences perceptual judgements of motion direction. *Nature* 346, 174–177. doi: 10.1038/346174a0

Santos, A., Humayun, M. S., de Juan, E. Jr., Greenburg, R. J., Marsh, M. J., Klock, I. B., et al. (1997). Preservation of the inner retina in retinitis pigmentosa. A morphometric analysis. *Arch. Ophthalmol.* 115, 511–515. doi: 10.1001/archopht.1997.01100150513011

Schanze, T., Sachs, H. G., Wiesenack, C., Brunner, U., and Sailer, H. (2006). Implantation and testing of subretinal film electrodes in domestic pigs. *Exp. Eye Res.* 82, 332–340. doi: 10.1016/j.exer.2005.07.007

Sekirnjak, C., Hottowy, P., Sher, A., Dabrowski, W., Litke, A. M., and Chichilnisky, E. J. (2006). Electrical stimulation of mammalian retinal ganglion cells with multielectrode arrays. *J. Neurophysiol.* 95, 3311–3327. doi: 10.1152/jn.01168.2005

Shivdasani, M. N., Fallon, J. B., Luu, C. D., Cicione, R., Allen, P. J., Morley, J. W., et al. (2012). Visual cortex responses to single- and simultaneous multiple-electrode stimulation of the retina: implications for retinal prostheses. *Invest. Ophthalmol. Vis. Sci.* 53, 6291–6300. doi: 10.1167/iovs.12-9434

Shivdasani, M. N., Sinclair, N. C., Dimitrov, P. N., Varsamidis, M., Ayton, L. N., Luu, C. D., et al. (2014). Factors affecting perceptual thresholds in a suprachoroidal retinal prosthesis. *Invest. Ophthalmol. Vis. Sci.* 55, 6467–6481. doi: 10.1167/iovs.14-14396

Stingl, K., Bartz-Schmidt, K. U., Besch, D., Braun, A., Bruckmann, A., Gekeler, F., et al. (2013). Artificial vision with wirelessly powered subretinal electronic implant alpha-IMS. *Proc. Biol. Sci.* 280:20130077. doi: 10.1098/rspb.2013.0077

Stingl, K., Bartz-Schmidt, K. U., Besch, D., Chee, C. K., Cottriall, C. L., Gekeler, F., et al. (2015). Subretinal visual implant alpha IMS–clinical trial interim report. *Vision Res.* 111(Pt B), 149–160. doi: 10.1016/j.visres.2015.03.001

Sun, P., Li, H., Lu, Z., Su, X., Ma, Z., Chen, J., et al. (2018). Comparison of cortical responses to the activation of retina by visual stimulation and transcorneal electrical stimulation. *Brain Stimul.* 11, 667–675. doi: 10.1016/j.brs.2018.02.009

Tomita, H., Sugano, E., Isago, H., Hiroi, T., Wang, Z., Ohta, E., et al. (2010). Channelrhodopsin-2 gene transduced into retinal ganglion cells restores functional vision in genetically blind rats. *Exp. Eye Res.* 90, 429–436. doi: 10.1016/j.exer.2009.12.006

Twyford, P., Cai, C., and Fried, S. (2014). Differential responses to high-frequency electrical stimulation in ON and OFF retinal ganglion cells. *J. Neural Eng.* 11:025001. doi: 10.1088/1741-2560/11/2/025001

Twyford, P., and Fried, S. (2016). The retinal response to sinusoidal electrical stimulation. *IEEE Trans. Neural. Syst. Rehabil. Eng.* 24, 413–423. doi: 10.1109/TNSRE.2015.2415811

Villalobos, J., Fallon, J. B., Nayagam, D. A., Shivdasani, M. N., Luu, C. D., Allen, P. J., et al. (2014). Cortical activation following chronic passive implantation of a wide-field suprachoroidal retinal prosthesis. *J. Neural Eng.* 11:046017. doi: 10.1088/1741-2560/11/4/046017

Walter, P., Kisvarday, Z. F., Gortz, M., Alteheld, N., Rossler, G., Stieglitz, T., et al. (2005). Cortical activation via an implanted wireless retinal prosthesis. *Invest. Ophthalmol. Vis. Sci.* 46, 1780–1785. doi: 10.1167/iovs.04-0924

Weng, S., Sun, W., and He, S. (2005). Identification of ON-OFF direction-selective ganglion cells in the mouse retina. *J. Physiol.* 562(Pt 3), 915–923. doi: 10.1113/jphysiol.2004.076695

Werginz, P., Im, M., Hadjinicolaou, A. E., and Fried, S. I. (2018). Visual and electric spiking responses of seven types of rabbit retinal ganglion cells. *Conf. Proc. IEEE Eng. Med. Biol. Soc.* 2018, 2434–2437. doi: 10.1109/EMBC.2018.8512746

Wilms, M., Eger, M., Schanze, T., and Eckhorn, R. (2003). Visual resolution with epi-retinal electrical stimulation estimated from activation profiles in cat visual cortex. *Vis. Neurosci.* 20, 543–555. doi: 10.1017/S0952523803205083

Wong, Y. T., Chen, S. C., Seo, J. M., Morley, J. W., Lovell, N. H., and Suaning, G. J. (2009). Focal activation of the feline retina via a suprachoroidal electrode array. *Vision Res.* 49, 825–833. doi: 10.1016/j.visres.2009.02.018

Zrenner, E., Bartz-Schmidt, K. U., Benav, H., Besch, D., Bruckmann, A., Gabel, V. P., et al. (2011). Subretinal electronic chips allow blind patients to read letters and combine them to words. *Proc. Biol. Sci.* 278, 1489–1497. doi: 10.1098/rspb.2010.1747

Conflict of Interest Statement: The authors declare that the research was conducted in the absence of any commercial or financial relationships that could be construed as a potential conflict of interest.

Copyright © 2019 Ryu, Werginz and Fried. This is an open-access article distributed under the terms of the Creative Commons Attribution License (CC BY). The use, distribution or reproduction in other forums is permitted, provided the original author(s) and the copyright owner(s) are credited and that the original publication in this journal is cited, in accordance with accepted academic practice. No use, distribution or reproduction is permitted which does not comply with these terms.

frontiers in Neuroscience

REVIEW
published: 18 April 2019
doi: 10.3389/fnins.2019.00379

Implantable Direct Current Neural Modulation: Theory, Feasibility, and Efficacy

Felix P. Aplin[1] *and Gene Y. Fridman*[1,2,3]*

[1] Department of Otolaryngology Head and Neck Surgery, Johns Hopkins University, Baltimore, MD, United States, [2] Department of Biomedical Engineering, Johns Hopkins University, Baltimore, MD, United States, [3] Department of Electrical and Computer Engineering, Johns Hopkins University, Baltimore, MD, United States

Implantable neuroprostheses such as cochlear implants, deep brain stimulators, spinal cord stimulators, and retinal implants use charge-balanced alternating current (AC) pulses to recover delivered charge and thus mitigate toxicity from electrochemical reactions occurring at the metal-tissue interface. At low pulse rates, these short duration pulses have the effect of evoking spikes in neural tissue in a phase-locked fashion. When the therapeutic goal is to suppress neural activity, implants typically work indirectly by delivering excitation to populations of neurons that then inhibit the target neurons, or by delivering very high pulse rates that suffer from a number of undesirable side effects. Direct current (DC) neural modulation is an alternative methodology that can directly modulate extracellular membrane potential. This neuromodulation paradigm can excite or inhibit neurons in a graded fashion while maintaining their stochastic firing patterns. DC can also sensitize or desensitize neurons to input. When applied to a population of neurons, DC can modulate synaptic connectivity. Because DC delivered to metal electrodes inherently violates safe charge injection criteria, its use has not been explored for practical applicability of DC-based neural implants. Recently, several new technologies and strategies have been proposed that address this safety criteria and deliver ionic-based direct current (iDC). This, along with the increased understanding of the mechanisms behind the transcutaneous DC-based modulation of neural targets, has caused a resurgence of interest in the interaction between iDC and neural tissue both in the central and the peripheral nervous system. In this review we assess the feasibility of *in-vivo* iDC delivery as a form of neural modulation. We present the current understanding of DC/neural interaction. We explore the different design methodologies and technologies that attempt to safely deliver iDC to neural tissue and assess the scope of application for direct current modulation as a form of neuroprosthetic treatment in disease. Finally, we examine the safety implications of long duration iDC delivery. We conclude that DC-based neural implants are a promising new modulation technology that could benefit from further chronic safety assessments and a better understanding of the basic biological and biophysical mechanisms that underpin DC-mediated neural modulation.

Keywords: direct current, neuromodulation, neural implant, electrical stimulation, neural interface, tDCS, neural block, synaptic remodeling

OPEN ACCESS

Edited by:
Ulrich G. Hofmann, Freiburg University Medical Center, Germany

Reviewed by:
Erika Kristine Ross, Mayo Clinic, United States
Suhrud Rajguru, University of Miami, United States

***Correspondence:**
Gene Y. Fridman
gfridma1@jhmi.edu

Specialty section:
This article was submitted to Neural Technology, a section of the journal Frontiers in Neuroscience

Received: *13 December 2018*
Accepted: *02 April 2019*
Published: *18 April 2019*

Citation:
Aplin FP and Fridman GY (2019) Implantable Direct Current Neural Modulation: Theory, Feasibility, and Efficacy. Front. Neurosci. 13:379. doi: 10.3389/fnins.2019.00379

INTRODUCTION

One of the earliest direct interactions with nervous system was conducted by Luigi Galvani in the late 1700s. In Galvani's experiments, isolated frog leg muscles, and the incoming nerves were depolarized with impulse-like delivery of electrical current. Galvani was confined to using a statically charged rod or metal rods attached with chains to Leyden jar capacitors to evoke a muscular response (Geddes and Hoff, 1971; Piccolino, 1998). Once Alessandro Volta developed a battery in the early 1800's, he tested the effects of delivering ∼50 V of direct current (DC) to neurons by attaching the leads to various parts of his own body, including the ear, eye, and tongue. His famous observations of the sensations are well-known in the field of neuromodulation, with descriptions of crackling, pain, noise, and shocks. While the mechanism of electricity-to-nervous system interaction was not well-understood at the time, one interpretation of these early experiments is that both electrical pulses and direct current can both be used to successfully interact with the nervous system (Guleyupoglu et al., 2013).

The first fully implantable pacemaker was designed and implanted in 1958 by Rune Elmqvist and Åke Senning, at the Karolinska Hospital in Sweden (Aquilina, 2006). This device delivered regularly spaced electrical current to the heart. A 1.5 ms pulse initiated a heart compression, but continued heart activity was self-propagating for another 1 s with no output from the pulse generator. These electrical pulses were delivered to a metal electrode implanted in the heart muscle. The need to deliver a very short duration pulse to depolarize the cardiac tissue of the heart fortuitously coincided with the fact that one could not deliver longer duration electrical current to a metal electrode without creating potentially toxic electrochemical byproducts. The inventors were not necessarily considering this implication during the development process, but the device was safe largely because the pulses were short with long inter-pulse intervals.

The pacemaker was self-contained and battery powered, giving the patient the freedom to move around. In modern terminology, the pacemaker was the first implantable pulse generator (IPG). The invention of this IPG created a precedent that showed us how we could effectively evoke electrical activity in the body safely with a device that delivered short pulses. In the nervous system, pulsatile stimulation was in principle confined to evoking an action potential (AP) in response to a pulse. However, due to the gross spatiotemporal spike rate coding method of the peripheral nervous system, pulsatile stimulation offered such a broad realm of applications that IPG technology dominated the field of neuromodulation for many years and it is still the primary commercial technology for neuromodulation therapies (Loeb, 2018).

DC was nearly abandoned for the purposes of implantable neural stimulation due to the therapeutic success and broad validation of IPGs in various applications, and the technical barrier associated with the challenge of safely delivering electrical current for a prolonged duration to a metal electrode implanted in biological tissue (Merrill et al., 2005). The recent resurgence of this mode of neuromodulation is due to technical innovations that have allowed DC to be delivered for longer durations to neural targets, and the success of experiments conducted through electrodes positioned on the skin where safety concerns could be more easily mitigated (Ruffini et al., 2013; Bikson et al., 2016). The other reason that DC neuromodulation has gained interest in recent years is that the field of neuromodulation has become refined sufficiently to be faced with new challenges that are more difficult to address using pulsatile waveforms. Because DC directly controls membrane potential, it can increase or decrease firing rate, altogether block neural activity, control AP propagation velocity, and modulate synaptic connectivity (Goldberg et al., 1984; Bikson et al., 2004; Vrabec et al., 2017; Strang et al., 2018; Yang et al., 2018). DC also appears to maintain the stochastic properties of AP inter-pulse intervals on each neuron (Goldberg et al., 1984), in contrast to conventional pulsatile stimulation for which an evoked AP in phase with the stimulation pulse is the intended effect.

This review covers the recent technological advances to deliver direct current to neurons, our understanding of how DC electric fields interact with neurons, potential therapeutic applications of DC, and finally the safety considerations associated with delivering DC to neural tissue.

DC ENABLING TECHNOLOGY

The Tissue-Electrode Interface

The interface between an electronic neural implant and biological tissue is called an electrode. One side of the electrode surface is exposed to electrons, while the other is exposed to ions in the body fluids. If the electrons congregate temporarily on one side of this interface, on the other side they cause positive ions to move toward this interface and the negative ions to move away. If they are left there for a longer duration, some of these electrons will cross into the solution, causing a chemical reaction by breaking up or creating molecular bonds. On the opposing electrode, the opposite effect occurs, where lack of electrons will attract an electron from a negative ion in the solution. This general principle is one of the fundamental mechanisms behind electrochemistry (Zoski, 2007). Unless carefully and intentionally controlled, electrochemical reactions occurring at the metal-tissue interface are generally harmful to the body processes, causing pH changes, electrode corrosion with toxic byproducts, and bubble formation due to electrolysis (Brummer et al., 1983; Shannon, 1992; Merrill et al., 2005; Pour Aryan et al., 2014). For this reason, IPG designers are careful to avoid any unwanted electrochemical reactions when using bare metal electrodes to deliver current to the body. This can be accomplished in three ways: by decreasing the amount of time that the electrode is exposed to excess of electrons by reducing pulse duration; by limiting the amplitude of the current pulse that is delivered during this stimulation time and consequently the number of electrons that congregate at the electrode; and by increasing the surface area over which these electrons are distributed to reduce their density. IPGs typically use charge balanced biphasic pulses on the order of microseconds to milliseconds per phase to interact with neurons (Merrill et al., 2005; Pour Aryan et al., 2014). For the typical bare metal Pt electrodes, the safety criterion is 300 $\mu C/cm^2$ (Shannon, 1992; Merrill et al., 2005; Pour Aryan

et al., 2014). This type of safety criterion is referred to as the "charge injection criteria" and it is defined as the charge per electrode area necessary to cause electrolysis.

Improving Charge Injection Criteria

Delivering direct current using a metal-tissue interface designed to function with an IPG is not possible without violating charge injection criteria and thus causing electrochemical reactions at the surface of the electrode. Development of electrode design has focused on improving charge injection limits, either as a means to decrease electrode size and thus improve the resolution of stimulation, or to deliver electrical current for very long durations in applications for which short pulses are not as effective, such neural block (Vrabec et al., 2016, 2017). The gradual evolution of these technologies has helped to enable the development of devices capable of safe DC delivery.

Improvements to the charge injection criteria necessary to enable a decrease in the electrode size have been addressed primarily with improvements in electrode surface treatments that increase the electrode area (Won et al., 2018). Another approach is to coat the electrodes with a dielectric oxide, such as that used for the Ta-Ta^2O^5 electrode, which can be used to prevent electrons from crossing the boundary into the solution without increasing the surface area (Brummer et al., 1983). This benefit comes at the cost of increased voltage needed to deliver the same amount of current, since the capacitance of the electrode drops in proportion to the thickness of the oxide. These treatments are primarily designed to maintain the delivery of charge for a smaller electrode size and they increase charge injection capacity by as much as 4 mC/cm^2 (Guyton and Hambrecht, 1973, 1974).

When the design goal is to deliver current for durations that are much longer than those needed to evoke an action potential (to maintain a neural block for example) the modifications to the electrode design must accommodate several orders of magnitude increase in charge injection criteria. One improvement over the surface treatment method is the use of polymer coatings. This method creates a three-dimensional analog of the two-dimensional electrode surface. These coatings are collectively referred to as hydrogel polymer coatings, with PEDOT:PSS as the most well-known of these (Nyberg et al., 2002; Ferlauto et al., 2018). These polymers conduct electronic current and have the property of absorbing the surrounding electrolyte (e.g., body fluid) that allows for a capacitive interface between ions and electrons to form on a molecular scale throughout the polymer chains. Hydrogel polymer coatings have been able to achieve safe charge injection capacities as high as 34 mC/cm^2 (Nyberg et al., 2002).

Although electrode surface coating can improve charge injection capacities by orders of magnitude, they also introduce new complications. The addition of another material interface can create additional toxicity concerns: for example, carbon nanotube coatings can improve charge injection and impedance properties of metallic electrodes but may also increase cytotoxicity and inflammation at the electrode interface, either due to intrinsic properties of the material (Shvedova et al., 2003; Gilmour et al., 2013) or via chemicals generated as a result of coating deposition (De Volder et al., 2013). Roughened rigid surfaces generate mechanical tissue stress, and along with hydrogel based surfaces are potentially more brittle and thus less stable for chronic implantation (Aregueta-Robles et al., 2014). While none of these limitations are hard barriers to implementation, they prevent a "one-size-fits-all" approach to continued improvement of charge injection capacity in neural implants.

Ionic Direct Current Delivery

Further attempts to increase the duration of current delivery have come in two forms: creating a barrier between the body and the electrochemical byproducts at the electrode, and technology that eliminates or heavily mitigates toxic electrochemical reactions at the electrode while maintaining direct *ionic* current (iDC) flow. Both deliver DC to the tissue under the assumption that the electrochemical toxicity at the metal electrode is avoided for the duration of stimulation and the biological tissue is never exposed to the toxic chemical byproducts.

An electrochemical barrier can be accomplished by physically separating the electrode and the chemical corrosive byproducts with a column of electrolyte or electrolytic gel. One example of such an electrode is the Separated Interface Nerve Electrode (SINE). This concept introduced silicone tubing filled with an electrolyte between a syringe that contained a metal electrode and the target nerve (Ackermann et al., 2011; Vrabec et al., 2016, 2017). It is also possible to gel the electrolyte with Agar to mechanically stabilize it in the column and prevent the electrolyte from potentially leaking (Fridman and Della Santina, 2013a). Other methods involve complex chemical film coatings that "sequester" electrons in a chemical Faradaic reaction, whose products do not diffuse into the solution and are reversible. One example of such interface is activated iridium (Brummer et al., 1983; Beebe and Rose, 1988). In the case of activated iridium, the introduction or removal of an electron results in transitions between Ir^{3+} and Ir^{4+} ionization states within the coating achieve up to 25 mC/cm^2 charge injection capacity at the interface of the coating (Merrill et al., 2005).

In contrast, another approach has been to develop a method by which ionic current can be delivered safely indefinitely (Fridman and Della Santina, 2013a,b; Ou and Fridman, 2017). The principle behind Safe Direct Current Stimulation (SDCS) is to rectify short, biphasic electronic pulses delivered to metal electrodes in the device into direct ionic current at the output of the device. This way the metal electrodes never undergo Faradaic reactions and there are no electrochemical byproducts generated within or external to the device. Conceptually, the SDCS delivers alternating current pulses to electrodes suspended at the opposite ends of a torus filled with ionic solution (termed "saline" in **Figure 1**). With each change in stimulation polarity the valves on either side of each electrode change from open-to-closed and closed-to-open, effectively modulating the path for ionic flow through the valves between low impedance and high impedance. Two extensions connected to the sides of the torus are directed into the body to complete the ionic current circuit. **Figure 1** demonstrates this concept, comparing two states of the apparatus. In both panels of the figure, ionic current flows from left to right through the stimulated tissue. In this way, a

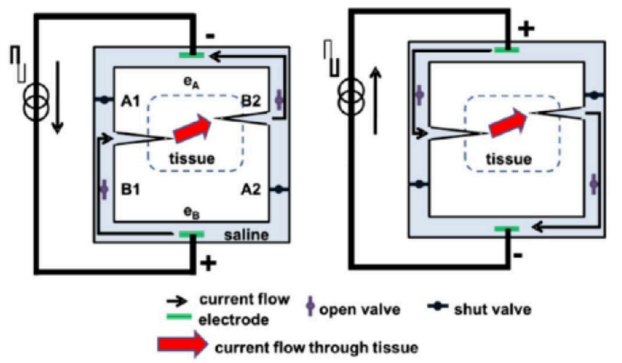

FIGURE 1 | Principle of SDCS operation. The two diagrams indicate two states of the same device. The device converts electronic current delivered between electrodes e_A and e_B to ionic current delivered to the tissue. When the pulse switches current direction, the valves switch states and the ionic current is driven through the alternate paths of the bridge. In both cases the ionic current is driven from left to right. Figures adapted with permission from Fridman and Della Santina (2013a).

continuous AC square wave controlling the apparatus will deliver DC ionic current (iDC) through the tissue from left to right. This system creates a closed-circuit path for the ions to flow, so that the anions that flow into the electrode tube on the right are replaced by the anions that flow out of the electrode tube on the left (Fridman and Della Santina, 2013a).

This concept originated from an attempt to develop a way to maintain endocochlear potential for hearing problems for people suffering from presbycusis, a common age related hearing disorder (Corbett and Clopton, 2004). This disorder disrupts the important ionic balance between endolymph and perilymph in the cochlea. The idea behind the system proposed by Spelman et al. was to create a mechanism by which electronic current delivered in the form of pulses could be rectified into ionic current flow. While this original application therapy was not developed further due to the advances in other treatments of age-related hearing loss, such as improved hearing aids and cochlear implants, this work did serve as an inspiration for developing the SDCS.

The SDCS has gone through several conceptual iterations and technological improvements. The original design shown in **Figures 1**, **2A**, suffered from current flow interruptions due to valve transition timing. During state transitions, the valves would be closed or open simultaneously for a short duration at the same time, causing a short or an open circuit and resulting in interruptions in current flow at the output (Fridman and Della Santina, 2013a). The first solution to the problem of current flow interruption used two SDCS systems that worked in tandem shown in **Figure 2B** (Fridman and Della Santina, 2013b; Ou and Fridman, 2017). The system on the left would deliver the current to the tissue, while the system on the right would switch its valve states; the control of the current flow would switch electronically from the system on the left to the one on the right and the right system would change valve states, and then the process would repeat. Even though this solution solved the problem of current flow interruptions, the system suffered from high power requirements due to the need to operate eight independent valves.

The next design iteration addressed the problem of current flow interruption, and power consumption by reducing the number of valves to just two and requiring only one actuator to control these valves (Fridman, 2017). The basic construction is diagrammed in **Figure 2C**. Conceptually, this construction drives the current through the tissue using one current source, while the second discharges. During the valve switch, both valves are open for a short time, while the current sources ensure the proper amount of DC current flow through the tissue. The microfluidic prototype of this SDCS system is shown in **Figure 2D**. The valves are designed to be controlled on the PDMS chip using a shape memory alloy Nitinol muscle wire. The valves have been shown to operate for over 1 million cycles (Cheng et al., 2017, 2018; Fridman, 2017).

An alternative direction to mitigate electrical/biological interface concerns has been to develop an organic electronic ion pump (OEIP) that can deliver charged molecules directly from a reservoir to neural tissue via electrophoresis (Moulton et al., 2012; Arbring Sjöström et al., 2018). OEIP delivery of neurotransmitters has been shown to modulate neural activity both *in-vitro-* and *in-vivo-* (Isaksson et al., 2007; Simon et al., 2009, 2010, 2015), which could allow for OIEP-mediated neuromodulation to produce a more naturalistic control of neural activity. While OIEPs typically use DC current to drive electrophoresis, OIEPs are typically very low voltage and do not influence the membrane voltage of target neurons via a direct electric field effect, but rather by either the electrophoretic modulation of neurotransmitter or extracellular ionic concentrations (Simon et al., 2010; Larsson et al., 2013; Tarabella et al., 2013; Arbring Sjöström et al., 2018). Given the radically different mechanism of neural interaction that OIEPs employ compared to traditional or even ionic DC electrical stimulation, a full discussion of their mechanisms and potential applications is beyond the scope of this review. However, the reviews cited here discuss the development and function of OIEPs comprehensively (Svennersten et al., 2011; Moulton et al., 2012; Larsson et al., 2013; Arbring Sjöström et al., 2018).

ELECTRICAL STIMULATION—NEURON INTERACTION

With improvements to DC stimulation technology that reduce or even eliminate the safety concerns associated with toxic byproducts at the metal electrode-tissue interface, it becomes important to understand how the resulting focal iDC interacts with neurons. Unless explicitly mentioned, from here-on in the review it should be assumed that we are discussing only the effects of direct ionic current flow through the body and not the effects of undesirable electrochemical reactions at the tissue interface.

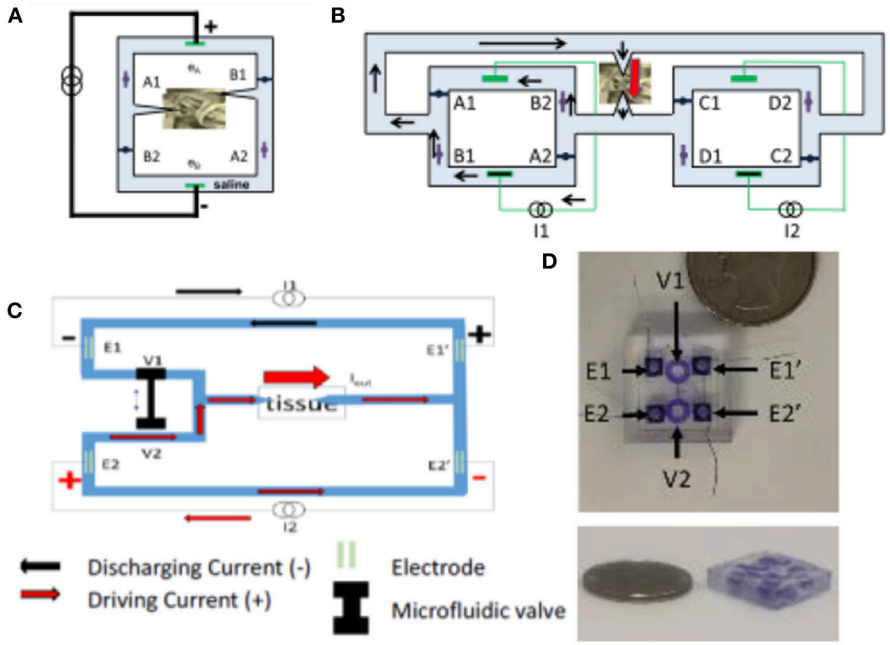

FIGURE 2 | (A) SDCS 1. **(B)** SDCS2 was designed to remove interruptions in current flow observed in SDCS1 construction. **(C)** SDCS3 is designed to remove the current flow interruptions, reduce power consumption and improve reliability. **(D)** SDCS3 microfluidic implementation. Figures adapted with permission from Fridman and Della Santina (2013a) and Fridman (2017).

Current Flow Through Tissue

The electric field associated with current delivered to an electrode in contact with the body depends on the impedance of the tissue through which this current travels. Even though the impedances differ greatly between different types of body tissues (Geddes and Baker, 1967; Pethig, 1987), each individual type of tissue impedance can be loosely modeled as a parallel resistor/capacitor pair, with the capacitance of the tissue modeling the impedance associated with the cell membranes, and the resistive components modeling the interstitial spaces (Gudivaka et al., 1999; Kyle et al., 2004). More accurately, finite element models (FEM) often include realistic morphologies of tissue and electric properties that include both conductivity and permittivity (Grant and Lowery, 2010; Joucla and Yvert, 2012; Wongsarnpigoon and Grill, 2012; Joucla et al., 2014). Capacitive and even dispersive impedances (in which permittivity varies as a function of frequency) are important when current propagation through tissue is pulsed at sub-millisecond duration (Grant and Lowery, 2010). These considerations are simplified for electrical stimuli at low DC-like frequencies, and can be reduced to models of purely resistive current propagation and static electric fields (Plonsey and Heppner, 1967). Just as for pulsatile stimuli, electric field orientations can be modified by introducing multiple electrodes, whose resulting electric fields would add in a standard linear superposition.

Modeling the Effect of Direct Current on Neurons

Whereas, determining the electrical current propagation through the tissue is simpler for DC, the effect of DC electric field on neurons is more complicated when compared to the action potential (AP) evoked by a short biphasic pulse presentation.

The theory governing the effect of an extracellular electrode on neural membrane has been well-described using a compartmental cable equation that relates membrane-voltage to extracellular voltage and time-dependent membrane currents (McNeal, 1976; Rattay, 1986, 1999; Joucla et al., 2014). These equations were originally modeled on Hodgkin-Huxley or Frankenhaeuser-Huxley descriptions (Hodgkin and Huxley, 1952; Frankenhaeuser and Huxley, 1964), but the same compartmental model can be modified to rely on voltage-gated channel dynamics, based on the wealth of latest cellular electrophysiology literature—there are many types of voltage gated sodium and potassium channels, all with different temporal dynamics and expression densities, differentially expressed in the membranes of specific neural types (Vacher et al., 2008; Eijkelkamp et al., 2012; Toloza et al., 2018).

For a monopolar electrode in an isotropic medium such as one diagrammed in **Figure 3A**, that delivers current I_{el} through tissue with resistivity ρ, the extracellular voltage V_n at distance r_n from the electrode is:

$$V_n = \frac{\rho I_{el}}{4\pi r_n}, \quad (1)$$

The relationship that then relates the currents crossing the membrane of the targeted axon depicted in **Figure 3B** is the

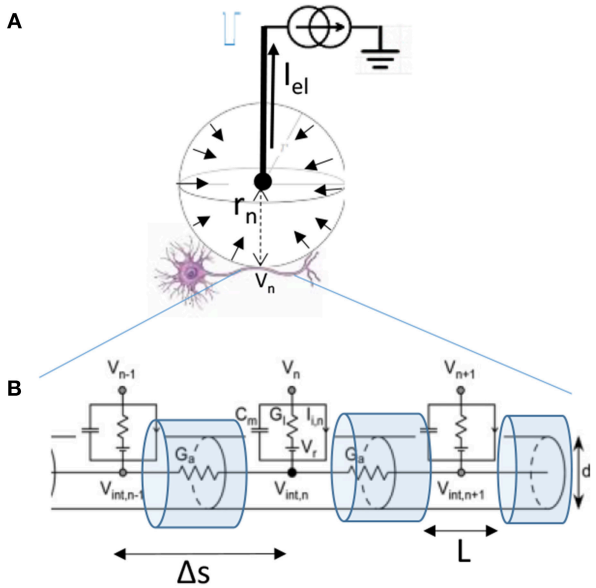

FIGURE 3 | (A) Diagram of the single monopolar electrode distance r_n from the center of the targeted neuron. Because current travels to the electrode from all directions, we can assume that I_{el} is distributed over a sphere indicated by short arrows in an isotropic medium. **(B)** Myelinated axon of diameter d of the targeted neuron is modeled by compartments length Δs between nodes of Ranvier, with L representing the length of exposed membrane. Figure adapted with permission from Joucla and Yvert (2012).

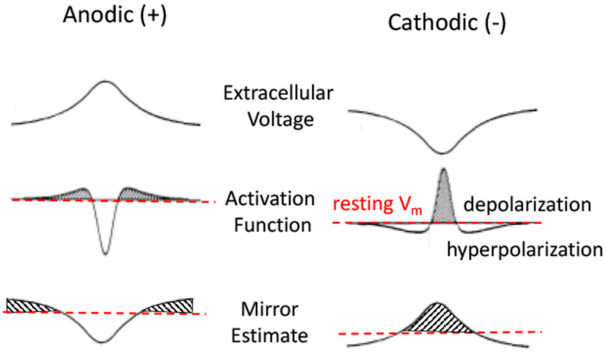

FIGURE 4 | Anodic and cathodic stimulation model approximations. Top row is the extracellular voltage distribution along the fiber. Second and third rows are Activating Function (AF) and Mirror Estimate (ME) approximations of the resulting membrane potential changes. Anodic stimulation delivers a hyperpolarizing center, with short depolarized (shaded) side lobes. Cathodic stimulation delivers a strong depolarization near the electrode and hyperpolarization at the side lobes. The Activation Function is more accurate for short pulses. The Mirror Estimate is more accurate for long duration stimuli.

cable equation:

$$C_m \frac{d\left(V_{int,n} - V_n\right)}{dt} + G_l\left(V_{int,n} - V_n - V_r\right) + I_{i,n} + G_a\left(2V_{int,n} - V_{int,n-1} - V_{int,n+1}\right) = 0 \quad (2)$$

Where the membrane conductances, currents, and capacitances depend on the diameter of the fiber d, the length of the segment Δs, and the exposed length of the membrane L. $C_m = c_m \pi dL$, $G_l = g_l \pi dL$, $G_a = \pi d^2/(4\rho_i \Delta s)$, $I_{i,n} = i_{i,n} \pi dL$. C_m is the compartment membrane capacitance, G_l the membrane leakage conductance, G_a the conductance along the axon, and $I_{i,n}$ the total transmembrane inward current (such as due to voltage gated channels). Membrane voltage (V_m) can be expressed as the difference between the intracellular and the extracellular voltage $V_{m,n} = V_{int,n} - V_n$. For further simplification, we can introduce the time and space constants: $\tau = \frac{C_m}{G_l}$, $\lambda = \Delta s \sqrt{\frac{G_a}{G_l}}$ (Joucla and Yvert, 2012). The equation can now be written as:

$$\tau \frac{dV_{m,n}}{dt} - \lambda^2 \frac{V_{m,n-1} - 2V_{m,n} + V_{m,n+1}}{\Delta s^2} + V_{m,n} + \frac{i_{i,n}}{g_l} = \lambda^2 \frac{V_{n-1} - 2V_n + V_{n+1}}{\Delta s^2} \quad (3)$$

While the actual solution to this equation for a given stimulus is typically obtained by computational means it is possible to intuitively understand of the changes to the membrane potential V_m in response to a pulse presentation. Rattay introduced the concept of an Activating Function (AF) based on the cable equation (Rattay, 1986). For a rapid pulse presentation one can assume a dominant capacitive current across the membrane, negligible intracellular currents, and constant current through membrane channels. Under these conditions, he demonstrated that $V_m \; \alpha \; \frac{\partial^2 V}{\partial s^2}$. That is, the membrane voltage is proportional to the second spatial derivative of the extracellular potential (**Figure 4**, second row). This approximation has been the primary tool used to predict the behavior of neurons in response to extracellular stimulation pulses (McIntyre et al., 2004). The drawback of this approximation is that it provides an intuitive description for the responses to very rapid sub-millisecond pulses, but not for the responses to long-duration stimuli such as those encountered during DC.

An alternative approximation, the Mirror Estimate (ME), was more recently proposed by Joucla and Yvert (2009). This approximation assumes a long-duration stimulus at which the capacitive currents become negligible and the membrane currents have reached a steady state. Using this approximation, it can be shown that the membrane voltage $V_m(s)$ at any point s along the fiber is proportional to the negative of the extracellular potential V offset from its average along the fiber: $V_m(s) \approx \overline{V} - V(s)$. The authors demonstrated this approximation to be more accurate over longer duration stimuli (Joucla and Yvert, 2012). This approximation is more relevant for estimating the effects of DC on the neural membranes.

Figure 4 shows an illustration of the predictions made by AF and ME approximations of the neural membrane response to a pulse presentation. The top row shows the extracellular voltage distribution along the horizontal axon for an electrode positioned in the center above the horizontal axon. The middle row shows the AF approximation (i.e., proportional to the second spatial derivative of the extracellular potential) of the membrane potential in response to a short pulse. The bottom row shows

the ME approximation that is better at estimating the response for a long duration stimulus presentation. While AF and ME approximations of membrane voltage appear similar in shape, the ME has a much wider center, with considerably longer side lobes.

The illustrations for AF provide important intuitive predictions of the neural responses to a short pulse presentation. For example, from the second row, one can predict that a neuron will have a higher threshold for evoking an action potential to an anodic pulse presentation rather than to a cathodic pulse. This prediction is based on the fact that the anodic pulse depolarizes at the side lobes rather than in the center and since the side lobes are much smaller than the center response, one would need a larger amplitude stimulus to evoke an action potential. It is also apparent that the AP will be generated at the side lobes for an anodic stimulus, but it would be generated in the center for a cathodic stimulus. One can also predict that if the cathodic stimulus is large enough, the side lobes of the cathodic response (second row left) would prevent the AP from propagating from the center (Rattay, 1987).

Predicting Neural Responses to Direct Current

Using the equations derived in the previous section, it is possible to make similar intuitive predictions about the types of neural responses generated in response to the long duration (DC-like) current as shown on bottom row of **Figure 4**. Here we present a set of predictions based on our examination of these ME approximations and in the subsequent section we explore the corresponding evidence from the empirical studies for DC effects on neurons. We describe the effects in terms of current amplitude, but these descriptions are equivalent if we describe the effects in terms of distance from the electrode as per Equation 1.

1. (a) When presented with a gradually increasing anodic stimulus, we would expect the membrane potential in the center of the axon to hyperpolarize enough that it would block or reduce the probability of AP propagation from its far distal end. (b) As the anodic stimulus amplitude increases further, we would expect to start depolarizing the side lobes enough to bring those parts of the membrane close to AP generation threshold and start to evoke its own action potentials.
2. (a) When presented with a gradually increasing cathodic stimulus, we would expect the membrane in the center to gradually become more depolarized, moving V_m closer to AP generation threshold, which will start evoking more action potentials from the center. (b) As the stimulus amplitude is further increased, we would expect that the side lobes will become sufficiently hyperpolarized to block or reduce the probability of AP propagation.
3. (a) We would expect the action potential propagation along the neuron to slow down during cathodic DC and (b) to speed up during anodic DC. The AP propagates from one segment (node of Ranvier) along the axon to the next by causing membrane voltage depolarization in the latter segment as a consequence of AP occurring at the previous neighboring segment. During the cathodic stimulus, the chronic hyperpolarization along the side lobes would require a longer time to force the membrane potential at each segment from their now more hyperpolarized state to AP generation threshold potential. The opposite would be expected from an anodic stimulus presentation.
4. In the low-cathodic or high-anodic DC delivery we would expect a more "natural" increase in neural firing rate. Because DC depolarization does not occur as a discrete event like a pulse, but instead creates a gradual persistent change in membrane potential, one would expect the resulting increase in firing rate to maintain the stochastic properties of the neuron's normal firing pattern. That is, for example if the neuron's action potentials are evoked distally as the result of excitatory postsynaptic potentials (EPSPs), we would expect increased AP generation because the new "resting" membrane potential is closer to threshold due to the extracellular DC delivery.
5. Steady state membrane potential should be significantly affected by the behavior of the membrane's ion channels during DC presentation. From this it follows that the specific types and densities of ion membrane channels are important to the membrane voltage change in response to the extracellular DC field. These considerations are typically ignored when the AF is used to predict the AP generation in response to a pulse presentation. This is because the sub-millisecond pulses are shorter than the changes needed to affect membrane channel conductances which occur on the order of milliseconds and longer.

Experimental Observations of DC Neural Interaction

Because DC-based stimulation has not been on the forefront of neuromodulation research, relatively few electrophysiology experiments that assay single fiber responses to DC stimuli have been conducted. There is confirmation that low-anodic DC causes neural block and that low cathodic DC causes excitation. **Figure 5A** shows the anodal block and cathodal excitation at low amplitudes (10's of μA) in support of predictions 1a and 2a (Hopp et al., 1980). In this experiment, DC stimulation was delivered *in-vivo* to the middle of a dog vagal nerve axon while AP propagation was assayed via periodic distal depolarization. Further support for predictions 1a, 2a, and prediction 4 was obtained in a chinchilla vestibular nerve experimental results shown in **Figure 5B** (Goldberg et al., 1984). Vestibular afferents normally maintain spontaneous activity at ∼60–100 spikes/s. In this experiment, vestibular afferents were being recorded during application of chronic DC stimulus. In this plot, the responses of two types of afferents are shown. The regular fiber maintains nearly constant inter-spike intervals (lower stripe), while the irregular fiber (upper stripe) does not. As expected from prediction 2a, cathodic stimulus (black dots) increased the firing rate [shown as decrease in the inter-spike interval (ISI)] of the afferent neuron. Also, in agreement with prediction 1a, Anodic stimulus (open circles) decreases firing rate. Furthermore, illustrating prediction 4, the coefficient of variation (CV) that describes the regularity of inter-spike intervals is maintained during DC stimulation when compared

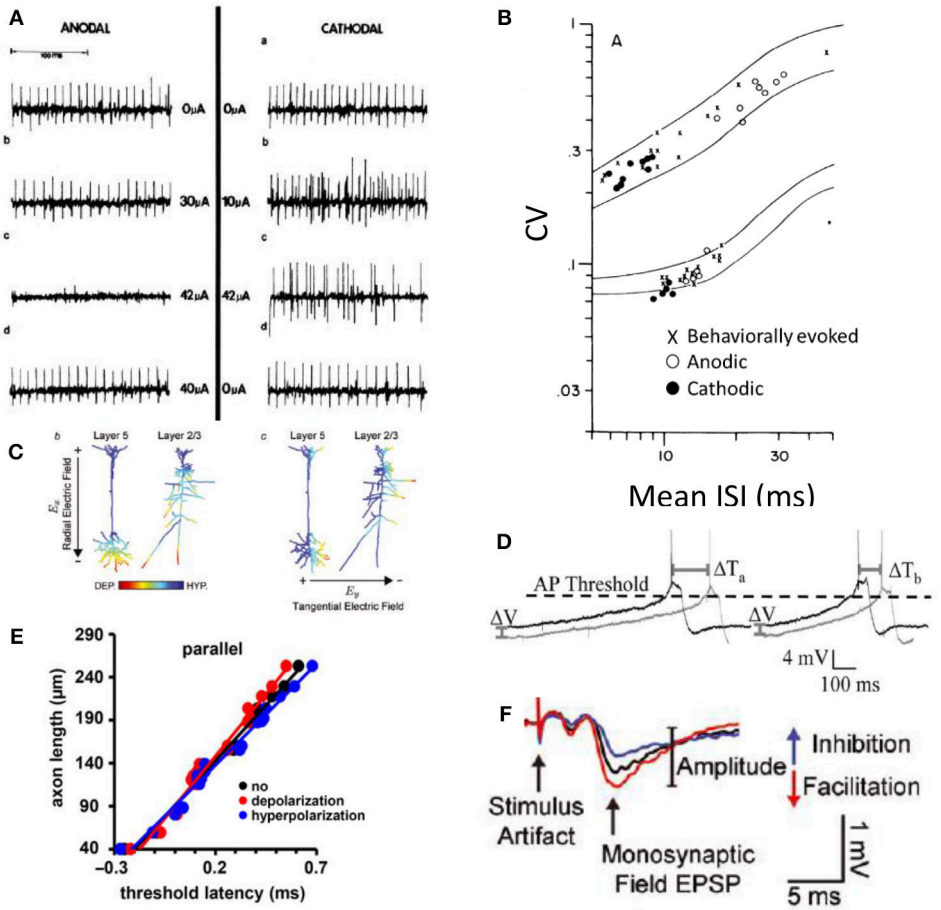

FIGURE 5 | Experimental evidence for the predictions of DC effect on neurons adopted here with permission from the original publications. **(A)** Small cathodic (–) DC excites and small anodic (+) DC suppresses (Hopp et al., 1980). **(B)** Small cathodic DC excites and small anodic DC inhibits and the stochastic properties of each neuron are maintained as shown in the coefficient of variance (CV) measurement during DC for both cathodic and anodic stimuli (Goldberg et al., 1984). **(C)** Cortical neural responses to the direction of the DC field is consistent with a monopolar stimulation effect. Cathodic proximity excites (DEP) and anodic suppresses (HYP) (Rahman et al., 2013). **(D)** The timing of AP generation is affected by the DC field. Dark lines represent voltage changes during the application of the extracellular DC field (Radman et al., 2007). **(E)** Axonal latency of AP propagation plotted when the axon is parallel to the applied DC field. Red is cathodic, blue is an anodic stimulus. Slope of each fitted line corresponds to the conduction velocity in each condition (Chakraborty et al., 2018). **(F)** DC has a clear effect on the potentiation and depression of synapses as assayed here with an excitatory postsynaptic potential (EPSP) after exposure to the corresponding polarity DC fields (Rahman et al., 2013).

to those from behaviorally (not electrically) modulated spike rates (Goldberg et al., 1984).

An increase and decrease of neural activity using correspondingly small cathodic and anodic currents (predictions of 1a and 2a) is further supported by a functional demonstration of DC neuromodulation, also conducted in the vestibular system (Aplin et al., 2018). The results of this work also suggest that DC modulation does not cause entrainment of activity, consistent with prediction 4. Previous experiments implicated phase-locked synchronized multi-neuronal responses to the vestibular nerve pulse-train presentations in the subsequent long-term depression of the synapses in central nervous system (Mitchell et al., 2016, 2017). In contrast to pulsatile train modulation of the nerve, DC modulation did not appear to cause the same depression of sensitivity, although these results are not directly comparable (Aplin et al., 2018).

The effect of anodic and cathodic block on efferent peripheral fibers has been investigated more thoroughly (Bhadra and Kilgore, 2004; Vrabec et al., 2016, 2017), and have concluded that monopolar block can be achieved with both DC polarities in support of predictions 1a and 2b, and 5. A surprising finding in these investigations is that a cathodic block could occur at the center part of the axon closest to the monopolar source, which should be depolarized as seen in **Figure 4** bottom row right. The authors' explanation for how this block could occur is that during cathodic DC application, the voltage gated sodium channels are held in their inactivated states, preventing AP propagation (Bhadra and Kilgore, 2004). This argument is further supported by the investigation of the peripheral afferent cathodic block (Yang et al., 2018).

In agreement with predictions 3a and 3b, the timing and shape of AP generation is affected by DC fields

(Shu et al., 2006; Radman et al., 2007). The timing of action potential propagation is affected with DC fields as shown in **Figures 5D,E**. **Figure 5D** shows the action potential being generated more rapidly due to increased membrane voltage slope affected by the DC field. **Figure 5E** shows the latency associated with AP propagation when anodic or cathodic DC stimulation is applied. The slopes of the lines indicate conduction velocity. Anodic DC increases the speed of AP propagation and cathodic DC decreases it (Chakraborty et al., 2018).

Transcranial direct current stimulation (tDCS) has been shown to have significant clinical implications for psychiatric disorders, epilepsy, stroke, Parkinson's disease, and pain suppression (Jackson et al., 2016). While the mechanisms are not well-understood, it is clear that cortical neurons subjected to typical tDCS electric fields experience only very subtle sub-millivolt changes to their membrane potentials—much lower than the 10 s of millivolts necessary to evoke action potentials. The effects of DC are therefore much more subtle and likely involve synaptic modifications through controlling spike propagation timing and consequently spike-timing dependent plasticity (Radman et al., 2007). Isolated hippocampal slice experiments that exposed neurons to weak directional DC fields identified several important effects of DC on neural signaling. One key finding in these experiments is that orientation of the electric field matters. This field orientation is consistent with the monopolar stimulation concept that we described earlier. The part of the axon closest to the anodic (positive) electrode will be more hyperpolarized than the parts that are farther away (**Figure 5C**). If the electric field is oriented parallel to the fiber, the fiber's response is affected. If it's perpendicular, there's no effect on the fiber's membrane potential (Bikson et al., 2004; Rahman et al., 2013; Jackson et al., 2016; Chakraborty et al., 2018).

When synaptic transmission is occurring, the synaptic connections are potentiated or depressed depending on the orientation of the electric field. The effect of DC fields on synapses is shown in **Figure 5F** with the size of the excitatory postsynaptic potential after cathodic and anodic DC fields are applied to the synapse. If the field is oriented such that the cathode is on the postsynaptic end of the synapse, it will be depressed. Conversely, if the anode is positioned toward the postsynaptic end of the synapse, it will be potentiated (Bikson et al., 2004; Kabakov et al., 2012; Rahman et al., 2013; Jackson et al., 2016).

In support of prediction 5, ionic channel conductances during DC presentation appear to critically influence the neural response (Yang et al., 2018). This was indicated with a neural block experiment in which a cathodic block exhibited different thresholds on different neuronal fiber types, which could not be explained entirely via differences in fiber diameter. Additional evidence for the strong effect of membrane channel dynamics in a DC field comes from an examination of network responses: the modeled effect of DC on neural network responses matches the observed effect only when hyperpolarization activated cation current dynamics (I_h) are included in the model (Magee, 1998; Toloza et al., 2018).

POTENTIAL APPLICATIONS FOR DC MODULATION

As discussed in the previous section and summarized in **Table 1**, DC can increase or decrease firing rate, block AP propagation, potentiate and depress synaptic connections, and increase or decrease neural conduction velocity. The parameters that control how DC interacts with neurons are the position, polarity and the amplitude of the electric field. It is clear that DC modulation offers the ability to interact with the nervous system in many new ways.

In the following discussion we focus on potential applications for DC neuromodulation in systems that can potentially stand to benefit from the unique aspects of DC modulation.

DC for Inhibition/Block of Peripheral Pain

Electrical neuromodulation is a clinical intervention used to treat pain after unsuccessful pharmacological therapy. Although there are multiple approaches to the electrical modulation of pain, typically varying by the location of current delivery, they all rely on pulsatile electric stimuli to disrupt afferent pathways delivering nociceptive information to the brain (Gofeld, 2014; Geurts et al., 2017; Krames et al., 2018). The ultimate aim of neuromodulation of pain is to block undesirable nociceptive input; this is problematic for pulsatile stimulation as it cannot directly suppress neural firing and must indirectly suppress nociceptive circuits via lateral inhibition or disrupt them via the delivery of high-frequency modulation. Trials assessing the efficacy of pulsatile electrical neuromodulation of pain relief have mixed results and report side effects such as undesirable hypersensitivity or somatosensory sensation (Nnoaham and Kumbang, 2008; Geurts et al., 2013, 2017; Shamji et al., 2017). Direct current modulation may hold a potential solution for these issues. DC can suppress or completely block nociceptive fibers directly, in principle foregoing the need for indirect or alternative approaches for suppression of the target neurons (Bhadra and Kilgore, 2004; Vrabec et al., 2017). DC fields may also be able to better target the thin myelinated Aδ fibers and unmyelinated, small-diameter C fibers that are the primary transmitters of the nociceptive signal in the periphery (Yang et al., 2018).

There have been several approaches to the development of DC-mediated pain suppression. Charge balanced DC delivery via an implanted microfluidic device (Fridman and Della Santina, 2013a; Cheng et al., 2017; Ou and Fridman, 2017) could potentially deliver chronic inhibition or block to peripheral nerves (Yang et al., 2018). High capacitance electrodes for sustained DC block and a separated interface system could be used to more efficiently deliver temporary DC pain suppression (Ackermann et al., 2011; Vrabec et al., 2016, 2017). An alternative percutaneous approach has also been developed to both suppress pain and potentially encourage wound healing in traumatic injury (Molsberger and McCaig, 2018). These technologies remain in pre-clinical development but have promising results and are likely to be among the first DC-based neuromodulation therapies to attempt clinical translation.

TABLE 1 | Summary of DC effects on neurons from both intuitive predictions suggested by the Mirror Estimate model and experimental evidence.

Prediction of DC effect on neural signaling	Neurophysiological application importance	Experimental evidence
1a. Low anodic (+): block of AP propagation	Pain propagation block, urinary bladder control, vestibular prosthesis	Hopp et al., 1980; Goldberg et al., 1984; Bhadra and Kilgore, 2004; Vrabec et al., 2017; Aplin et al., 2018
1b. High anodic (++): increased firing rate		
2a. Low cathodic (–): increased firing rate	Vestibular prosthesis, other conventional excitatory neuromodulation paradigms that currently use pulsatile stimuli	Hopp et al., 1980; Goldberg et al., 1984; Aplin et al., 2018
2b. High cathodic (– –): block of AP propagation	Pain propagation block, urinary bladder control	Bhadra and Kilgore, 2004; Vrabec et al., 2017; Yang et al., 2018
3a. Anodic (+): increase of AP conduction velocity	Synaptic connectivity, LTP, LTD, CNS modulation	Radman et al., 2007; Chakraborty et al., 2018
3b. Cathodic (–): decrease of AP conduction velocity	Synaptic connectivity, LTP, LTD, CNS modulation	Radman et al., 2007; Chakraborty et al., 2018
4. Stochastic firing properties are maintained under DC excitation and inhibition	Synaptic connectivity, LTP, LTD, CNS modulation	Goldberg et al., 1984
5. Types and dynamics of ionic conductances play an important role in membrane voltage changes during extracellular DC stimulation	Synaptic connectivity, LTP, LTD, information processing, fiber selectivity, CNS modulation	Shu et al., 2006; Chakraborty et al., 2018; Toloza et al., 2018; Yang et al., 2018

DC for Modulation of the Vestibular Periphery

Another system that could benefit from the ability of DC modulation to inhibit neural activity is the vestibular system. In a normally functioning system, the semicircular canals of the vestibular labyrinth encode the direction and magnitude of head rotational velocity by increasing or decreasing firing rate from a spontaneous baseline of approximately 100 spikes per second in primates (Miles and Braitman, 1980; Sadeghi et al., 2009). In patients with bilateral loss of vestibular function it becomes debilitatingly difficult to maintain stable vision, balance or locomotion (Curthoys and Halmagyi, 1995). Vestibular prostheses modeled on the cochlear implant are in development to address a therapeutic need in patients with vestibular pathologies (Della Santina et al., 2007; Valentin et al., 2013; Hageman et al., 2016; Lewis, 2016). To generate bidirectional encoding of motion, these implants artificially elevate the spontaneous rate of the vestibular afferents via adaptation to a constant pulse rate and then modulate around this increased baseline. This approach has two main limitations: the first is that an increased baseline rate reduces the dynamic range of encodable head rotations (Davidovics et al., 2011, 2012; Lewis, 2016) and the second is that entrained firing of the vestibular nerve (a natural consequence of pulsatile stimuli) is thought to result in long-term depression of post-synaptic neurons in the vestibular nuclei (Lewis, 2016; Mitchell et al., 2016). Direct current can address both of these limitations, as it can both excite and inhibit neural activity as well as deliver "naturalistic" changes in firing rate that retain stochastic variability (Goldberg et al., 1984). iDC modulation using ionic conduits implanted into the semicircular canals of the chinchilla can produce a greater dynamic range of reflexive eye rotations when compared to a pulsatile stimulus, without suppression at higher current baselines (Aplin et al., 2018). Further work will be necessary to test mechanism of action and to demonstrate chronic efficacy and safety of an ionic DC-based vestibular implant.

DC Stimulation for Bladder Control

A common consequence of spinal cord injury is difficulty controlling micturition (urination) reflexes (Krause et al., 2004). Typically, patients suffer from an inability to fully void the bladder, which can lead to severe complications including kidney failure (Krause et al., 2004; Biering-Sørensen et al., 2008). Non-invasive DC modulation of the spinal cord has had some success restoring micturition function in humans (Flamm et al., 1977; Radziszewski, 2013; Stewart et al., 2016; Zhu et al., 2016). The mechanism of action is thought to be subthreshold modulation of spinal circuits rather than the result of DC-evoked spike trains (Kerns et al., 1996; Ahmed and Wieraszko, 2012; Ahmed, 2013, 2017). The current focus has been on non-invasive DC delivery due to the historical inaccessibility of invasive DC delivery. This field might thus stand to benefit from the development of safer DC delivery *in-vivo*-: in the human, non-invasive trans-spinal DC affects a relatively large and non-uniform area (Kuck et al., 2017), while invasive trans-spinal DC has the potential to deliver current to a much more confined target. DC delivery closer to the target tissue could improve effect thresholds and reduce current spread to non-target tissues. Additionally, non-invasive DC still must contend with toxic electrochemical reactions generated at the metal-electrolyte interface, and is typically only delivered therapeutically for relatively short periods (Radziszewski, 2013). An implantable system capable of delivering chronic DC could provide tonic active therapy for cases where short-duration therapy is not efficacious.

Cortical Modulation Using Invasive DC

The potential for non-invasive (trans-cranial) DC to influence cortical firing via diffuse, sub-threshold electric fields has seen a great deal of recent interest and active research (Ruffini et al., 2013; Bikson et al., 2016; Jackson et al., 2016). Invasive DC has the advantage of being able to deliver higher and much more locally directed electric fields, but the use of invasive electrotherapy in the brain is harder to justify given the difficulties and significant safety concerns associated with

invasive penetration into the CNS. As invasive DC technology matures, there may be opportunities to address neural targets within the brain, particularly where pathological conditions occur as a result of hyperexcitability, such as in epilepsy. Locally delivered DC modulation can down-modulate neural activity and has been shown *in-vitro* to suppress epileptiform activity in the rat hippocampus (Lian et al., 2003). Invasive electrotherapy is already used for suppression of epileptic activity when other treatments have failed (Stefan and Lopes da Silva, 2013; Mina et al., 2017) and non-invasive DC is an emerging therapy for epilepsy although the extent of efficacy is controversial (Sanjuan et al., 2015). However, invasive DC modulation will first have to prove significant potential benefit over preexisting non-invasive therapies for epilepsy to be considered as a viable alternative approach.

Another potential cortical target for invasive DC is the treatment of chronic tinnitus. Tinnitus is characterized by persistent auditory illusion and is widespread with limited available treatment options (Møller, 2007b). Etiology in tinnitus is extremely varied, but some forms of the condition are thought to arise due to corruption of auditory processing at the cortex (Møller, 2007a,b; De Ridder et al., 2014). Some of the primary effects of tonic, subthreshold DC fields are changes in excitability and conduction velocity, which can create plastic changes in cortical networks (Radman et al., 2007; Jackson et al., 2016). Non-invasive DC has been explored as a potential therapy for tinnitus, but existing evidence suggests it is not consistently efficacious at reducing symptoms for most patients (Song et al., 2012; Santos et al., 2018). One problem is that neural changes in tinnitus may be highly heterogeneous across local cortical regions (Møller, 2007a; De Ridder et al., 2014). We hypothesize that locally delivered DC has the potential to deliver much more constrained electric fields and thus might provide extra benefit over diffuse non-invasive fields, but studies on animal models of tinnitus will be necessary to test the validity of this hypothesis.

Cochlear Implants

Cochlear implants (CI) are the great success story of the field of neuromodulation. Neuromodulation via CI is now a common treatment for severe hearing loss, with bilateral implantation becoming almost routine. Most people hear with the CI well-enough to talk on the phone in a quiet room. While there's no debate regarding the usefulness of these devices in everyday life, significant hearing deficiencies with the CI in presence of noise, tonal language speech perception (such as Mandarin Chinese), and poor music perception still remain as issues to be addressed (Wilson and Dorman, 2008; Prevoteau et al., 2018).

One potential explanation for the difficulty to convey musical melody is that the cochlear implants typically deliver pulses using some variant of a continuous interleaved stimulation (CIS) paradigm. This method of stimulation delivers pulses in a round-robin sequence to each electrode along the implanted array. With the traditional CIS, each electrode is pulsed at approximately 250–1,000 pps (An et al., 2007; Wilson and Dorman, 2008). Sound information is introduced by varying the amplitude of the delivered pulses proportional to the power of the sound localized by its frequency band. This stimulation method is preferred in cochlear implants because it clearly reduces hearing noise due to channel interaction by allowing targeted populations of neurons to respond without interference from the neighboring channels (Wilson et al., 1991).

In normal hearing, the afferents that carry the sound information to the brain can be divided by their spontaneous activity profile. There are the high spontaneous, and low spontaneous activity neurons. All of these neurons modulate their firing rate depending on the amplitude of the signal within the band. High spontaneous fibers have lower thresholds and sharp rise in firing rate with increased sound amplitude. The low spontaneous fibers have a higher threshold and a very slow-rise linear relationship between firing rate and sound amplitude (Kiang et al., 1976; Liberman, 1978).

From the perspective of neural firing, while the CIS coding scheme recruits different populations of neurons depending on the amplitude of the pulse, recruited neurons all respond in synchrony with high spike rates that correspond to the constant pulse rate delivered from the pulse generator. Thus, the louder the sound within the frequency band, the more neurons fire at high constant spike rate.

This method of stimulation bypasses the linear relationship between firing rate and sound amplitude and compresses the entire range of response to an almost a binary signal for each responding neuron. Using cathodic DC amplitude to encoding sound could reintroduce the more natural recruitment of firing rates in proportion to sound amplitude.

NON-METAL-ELECTRODE BASED DC SAFETY CONSIDERATIONS

As DC-enabling technology progresses toward chronic implantation, it will become increasingly important to characterize how DC fields affect the physiological and electrochemical environment to which they deliver their charge. Emerging technologies provide a potential means to mitigate or eliminate the build-up of toxic electrochemical reactions associated with DC stimulation due to a lack charge recovery at the metal-tissue interface (Ackermann et al., 2011; Fridman and Della Santina, 2013a). However, even charge balanced current delivery is capable of damaging tissue when the total charge or charge-per-phase is large (Brummer and Turner, 1977; McCreery et al., 1990; Merrill et al., 2005; Cogan et al., 2016). Many of the safety limitations for a DC-based implantable device, such as electroporation thresholds, are likely to be a function of total charge delivered (Merrill et al., 2005; Nakauchi et al., 2007; Cogan et al., 2016) and thus similar to those of an IPG-based device. Given that there are already many reviews addressing safe charge densities in IPGs, this section will instead focus on potential safety considerations that have a unique aspect specific to tonic DC delivery.

Temperature

Biological tissue has an impedance associated with it which varies depending on the current path through the tissue (Foster and Schwan, 1989; McAdams and Jossinet, 1995; Gabriel et al.,

1996). When electricity travels through a resistance, some of the energy of the current is converted into heat via a process called joule heating, with power as a function of the resistance and current: $P = I^2R$. Even relatively small changes in temperature can impact neural function (Hodgkin and Katz, 1949) with an increase of 4–5°C resulting in rapid neuronal death (Wang et al., 2014). Like any other device that passes current through the body, implantable DC devices must therefore consider the effect of joule heating on both acute and chronic device safety. It might seem intuitive to consider tDCs safety margins as a close analog to an implantable DC device, but joule heating effects are not comparable between the two methodologies: tDCs must address larger currents and dermal resistances but also benefits from a greater surface area and distance from the target tissue (Datta et al., 2009; Bikson et al., 2016; Gomez-Tames et al., 2016). Implantable devices using DC in the body differ from IPGs due to the lack of phase associated with DC. This has two primary effects: the first is that, for a given current amplitude, DC can potentially deliver a greater charge density, which directly impacts the amount of joule heating produced per unit time. The second effect is that tissue impedances are a function of both the resistance and capacitance of the tissue (typically visualized as a resistor and capacitor in parallel) and, because DC has no frequency, impedances are thus typically higher for DC delivery than for an equivalent high frequency AC waveform (Foster and Schwan, 1989; McAdams and Jossinet, 1995; Faes et al., 1999). In contrast, lower amplitude thresholds for implantable DC devices may offset the higher durations of delivery. For example, a recent comparison of behavioral responses for DC and AC stimulation waveforms of the peripheral vestibular system (Aplin et al., 2018) found that amplitudes for DC waveforms are typically less than for AC waveforms. Similar impedances and peak behavioral responses could be achieved using either 40 μA DC or 420 Hz, ∼175 μA/phase, 400 μs/phase biphasic pulses. The total charge delivered per second for both waveforms is comparable: 40 and 29.4 μC/s for DC and AC waveforms, respectively. As with any electrically active device implanted in tissue, invasive devices that deliver DC will have to show that local thermal changes remain in a range ($< \sim 2$°C) where the effects on neuronal activity are comparatively mild (Wang et al., 2014).

Electroporation

Electroporation is the process of pore formation in the lipid bilayer of cells membranes when subjected to an electric field (Bramlet, 1998). Irreversible electroporation occurs when this process leads to formation of permanent fenestrations in the membrane and subsequent loss of ion homeostasis and cell death (Rubinsky, 2010). Electroporation thresholds are a function of field density with thresholds in the range of 1 kV/cm and can be achieved by both pulsed and DC fields (Bramlet, 1998; Kim et al., 2007). Cell death due to irreversible electroporation can occur as an unintended side-effect of pulsatile electrical stimulation with a threshold relating to both the total charge density and the charge delivered per pulse phase (Butterwick et al., 2007). Electroporation thresholds are typically well above the range of functional IPG stimulation (Merrill et al., 2005; Butterwick et al., 2007; Nakauchi et al., 2007; Boinagrov et al., 2010). There is a non-linear relationship between pulse width and amplitude threshold for electroporation thresholds, with charge delivered over a longer unit time resulting in higher thresholds when compared to the same charge delivered over a short period (Butterwick et al., 2007; Nakauchi et al., 2007; Boinagrov et al., 2010). This may lead to comparatively higher electroporation thresholds for DC because, even though charge delivery per second might be higher, peak charge is much lower.

For example, an implantable DC neuromodulation for pain would be expected to be delivered at a maximum 10 mA (Vrabec et al., 2016, 2017; Yang et al., 2018). The worst-case assumption is that the current is driven in a straight line through a nerve, rather than spread through a homogeneous environment like the brain. Ten milliampere current driven through nerve tissue of 1 kΩcm specific resistance will produce only 10 V potential over a cm of tissue. This voltage is 100 times lower than the typical 1 kV/cm electroporation threshold. It is therefore unlikely that electroporation would result from DC neuromodulation.

pH Changes

IPGs typically only generate transient pH changes (<1 unit) within a small (∼1 μm) radius at the tissue-electrode interface (Ballestrasse et al., 1985; Huang et al., 2001; Chu et al., 2004) and, unless the device is malfunctioning, are not considered to be a significant safety concern (Merrill et al., 2005). While DC electrolysis will, by definition, generate large pH changes between the cathode and anode, proposed DC implantable technologies mitigate this by reversing electrolytic reactions via charge balancing the metal electrodes (Fridman and Della Santina, 2013a) or by chemically and physically buffering the electrode/tissue interface (Ackermann et al., 2011). Ionic DC delivery could still influence pH at the microfluidic/tissue interface as sustained ionic current acts as an ion pump that over time might change the H^+/OH^- concentrations at the tissue/device interface, and a locally sustained electric field can create a pH gradient even in the absence of electrolysis (Macounová et al., 2000; Berkelman, 2005). Given that these effects have historically been masked by pH changes from DC electrolysis there has not yet been an exploration of their significance *in-vivo*. We hypothesize that the theoretical pH gradients generated by ionic DC would be mild and easily compensated for by e.g., natural diffusion and acid-base homeostasis (Hamm et al., 2015) particularly given that neurons are resistant to small (<1 unit) changes in pH (Goldman et al., 1989). Ultimately, the magnitude of potential pH changes in ionic DC fields will have to be confirmed in preclinical safety experiments.

Electrophoresis

Electrophoresis is the movement of charged particles in a fluid as the result of an electric field. In fluids, current is propagated via the physical movement of charged species (ions) through the conductive media. In biological tissue, these species are predominantly Na^+, K^+ and Cl^+, but also any other charged molecule including large protein complexes—this has long been exploited by biologists to separate proteins on the lab bench (Abramson et al., 1942). The movement of ions is dependent

on the size and mass of the ion, the density of the media, the charge of the ion and the strength of the electric field, with typical flow speeds of small ions in the range of ∼100 μm/s for a 100 V/cm field in an unobstructed media. Electrophoresis is not normally a consideration for neural stimulators: during pulsatile stimulation, charge balanced waveforms ensure virtually no net movement of charged molecules. In contrast, DC waveforms are not charged balanced and will cause electrophoretic transport of ions over time. It is known that the body utilizes electrochemical gradients to transport charged proteins (Jaffe, 1977) and it has been proposed that non-invasive DC may have electrophoretic effects on neural tissue (Rae et al., 2013), so there is at least some evidence to suggest that electrophoretic mechanisms should be considered when designing chronically stimulating DC devices. For example, if the ionic composition at the cathode/anode are not identical to the physiologic medium it might be possible to locally deplete a charged protein or ion by "pumping" ions from the microfluidic device to the tissue and displacing preexisting ionic concentrations. This can be mitigated by ensuring that the microfluidic system supplying ionic DC to the tissue has an ionic composition similar to the extracellular medium, and by placing the anode/cathode in locations with similar interstitial ionic concentrations.

TISSUE EFFECTS OF SUSTAINED ELECTRIC FIELDS

Neural tissue is the most electrically active tissue in the body and the typically the primary target for therapies involving electrical stimulation, including those discussed in this review. Endogenous electric fields also occur naturally within other tissues in the body, and these tissues can have electric-field mediated responses, particularly for directing cell migration during development or wound healing (Bramlet, 1998; McCaig et al., 2005). Sustained electric fields may also influence the distribution of charged proteins, membrane potentials and pH gradients in otherwise electrically inactive tissues (Abramson et al., 1942; Jaffe, 1977; Funk, 2015). Locally delivered DC fields via an invasive device may avoid some of these considerations due to a finer control of field distribution, but as the intention may be to deliver chronic DC current over the lifetime of the device, focal effects may be stronger than what might be expected in e.g., tDCs where treatment times are typically very short (5–30 min vs. potentially years or decades for an implanted device). This section briefly outlines several effects of DC electric fields on non-neural tissue and discusses their potential relevance to chronic DC neural stimulation.

Neural Migration and Axonal Growth

Endogenous electric fields are an important mechanism in the developing nervous system to facilitate differentiation and stratification of nervous tissue, and in the mature animal in response to nervous tissue damage (Mccaig and Rajnicek, 1991; McCaig et al., 2005). Artificially generated electric fields have been shown both *in-vivo* and *in-vitro* to direct stem cell migration (Yao and Li, 2016; Feng et al., 2017), axonal growth (Yamashita, 2015), and may also influence stem cell differentiation (Zhao et al., 2015). Typically, in a DC field, axonal growth or cell migration is attracted toward the cathode and repelled away from the anode, although this can vary depending on the neural type and substrate (Mccaig and Rajnicek, 1991). Axonal and cell growth can be influenced *in-vitro* with sustained electric fields on the order of ∼10–100 mV/mm (Mccaig and Rajnicek, 1991).

The effect of polarity-dependent axonal growth is an important consideration for the functional modulation of nervous tissue with DC. If the modulated field is excitatory it might encourage axonal growth near the implantation site (Fehlings et al., 1989). An inhibitory field may have an opposite effect—which could be beneficial if the aim is to reduce overall connectivity in the area but could also potentially cause axonal retraction and thus increased stimulation thresholds. It is difficult to predict how these effects may interact with ongoing degeneration of a neural substrate or the regions of inflammation and glial scar formation that tend to surround implanted neural stimulators *in-vivo* and reduce their efficacy over time (Szarowski et al., 2003; Cicchetti and Barker, 2014; Groothuis et al., 2014). Careful consideration of these effects will be an important component of any long-term histological assessment of implantable DC stimulators aiming to deliver tonic DC fields.

Vascular Changes

Neural tissue is often extensively vascularized due to the high energy requirements of neurons. Externally applied currents can potentially influence ionic movement across the blood-brain barrier via electroporation, electrophoretic or electro-osmotic mechanisms (Bonakdar et al., 2017; Brinton et al., 2018). There has been compelling evidence both *in-vivo* and -*in-vitro* to suggest that both sustained direct current and pulsed electric fields in the brain can transiently modify blood vessel permeability without cell death or electroporation at field strengths relevant to electrical stimulation of neural tissue (Hladovec, 1971; Lopez-Quintero et al., 2010; Brinton et al., 2018). Changes in vascular permeability have been proposed as a possible mechanism contributing to the sustained effects of transcranial DC (Cancel et al., 2018). Locally delivered DC for neural stimulation may output much greater field strengths than in non-invasive DC delivery and proposed uses of invasive DC stimulation involve continuous or near-continuous delivery of DC. Given this, it is important to consider vascular permeability when addressing potential mechanisms for any observed chronic effects of focal DC delivery in the cortex.

Epithelial Migration and Bone Growth

When the body is injured via physical trauma, a complex host of signaling ques inform surviving tissue to direct cell proliferation and orientation (Singer and Clark, 1999; Gurtner et al., 2008). One of these signaling pathways involves endogenous electric fields, that are thought to direct cells to migrate toward the injured site during wound healing (Jaffe and Vanable, 1984; Zhao, 2009). Endogenous field strengths can be relatively strong, ranging from 40 to 140 mV/mm at the wound edge in epithelial tissue (Jaffe and Vanable, 1984; Chiang et al., 1992);

several orders of magnitude larger than in uninjured tissue. These voltages are thought to be generated via ionic currents both as a direct result of the injury (non-ion-specific leakage currents) and as a sustained effect in the surviving tissue, typically via active Na^+/Cl^- transport (Reid et al., 2005; Zhao et al., 2006). The delivery of artificially generated, tonic electric fields at physiologic field strengths could result in an override of endogenous field activity and subsequent cell migration (Zhao et al., 2006).

An invasive device requires a wound for the device to be surgically implanted in the body. Neural implants using DC may also be interfacing with target neural epithelia that has undergone some previous or ongoing degeneration or injury. Given the relative infancy of DC-mediated *in-vivo* neural stimulation there is currently no indication as to the effect of implanted DC stimulation on surrounding tissue response. We might, for example, expect the insertion site of a DC interface to exhibit different tissue responses when it is primarily delivering cathodal vs. anodal constant current. Like with any invasive neural implant, potential tissue reaction will have to be assessed histologically following *in-vivo* implantation and chronic stimulation studies.

Endogenous electric fields also play a similarly important role in bone growth and repair (Fukada and Yasuda, 1957; Konikoff, 1975; McDonald, 1993). Constant current electric stimulation can reliably induce ossification at the cathode, particularly in conjunction with the placement of tissue engineering scaffolds (O'Connor et al., 1969; Buch et al., 1984; Kuzyk and Schemitsch, 2009; Victoria et al., 2009; Griffin and Bayat, 2011; Leppik et al., 2018). DC electric fields are thought to influence ossification primarily via local electrochemical/pH changes at the electrode interface (Brighton et al., 1975; Griffin and Bayat, 2011). Devices that deliver DC for chronic stimulation of neural tissue are unlikely to influence ossification mechanisms as they must mitigate these electrochemical changes in order to function.

CONCLUSION

The development of implantable neuromodulation therapies has been historically constrained by the need to deliver short, biphasic pulses to prevent toxic electrochemical reactions forming at the tissue interface. More recent technological advances have enabled the safe delivery of ionic direct current to neural targets. This method of neuromodulation has the potential to significantly diversify our ability to interact with the nervous system by not only being able to excite neural targets, but also being able to suppress neural activity, control AP conduction velocity, and remodel synaptic connections to affect neural processing. Devices that locally deliver DC modulation could greatly expand the range of applications available to neuromodulation therapies beyond what is achievable with standard IPG waveforms.

While pulsatile neuromodulation methods have been thoroughly investigated for safety limitations, the exploration of DC safety is sparse. This is primarily due to the historic inability to deliver DC in an implantable device without violating charge-injection-criteria. As new technology eliminates the problem of metal-tissue stimulation toxicity for ionic DC delivery, new complications will likely be uncovered.

Future applications could use a combination of DC and pulsatile stimuli to even further enhance our ability to modulate the nervous system. Pulsatile delivery methods have an advantage over DC sources in that pulses can be delivered through very small interfaces such as $\sim$10 μm diameter metal electrodes. DC requires larger interfaces (currently the smallest is 200 μm in diameter). One could therefore envision cortical arrays of DC stimulation ports and pulsatile stimulation and recording probes. DC arrays would create localized electric fields that control synaptic connectivity and information flow and implantable recording and stimulation electrodes would take advantage of the modified neural network connections to record from or convey information to the brain in a more controlled fashion.

While DC neuromodulation must address previously un-encountered safety challenges, it offers an exciting possibility of improving machine-neural interfaces in ways that may be difficult or even impossible to achieve otherwise.

AUTHOR CONTRIBUTIONS

GF wrote the first half of the manuscript and conducted the compilation and final edits. FA wrote the last half of the manuscript and conducted interim edits of the overall manuscript.

FUNDING

We would like to thank the grant sources that provided us with the means to pursue this review. JHU Neurosurgery Pain Research Institute, NIH R01 DC009255, NIH R21 NS081425-01A1, NIH R01 NS092726, and MedEl Corporation.

REFERENCES

Abramson, H. A., Moyer, L. S., and Gorin, M. H. (1942). *Electrophoresis of Proteins and the Chemistry of Cell Surfaces*. New York, NY: Reinhold Publishing Corporation. Available at: https://www.cabdirect.org/cabdirect/abstract/19432202796 (accessed November 18, 2018).

Ackermann, D. M., Bhadra, N., Foldes, E. L., and Kilgore, K. L. (2011). Separated interface nerve electrode prevents direct current induced nerve damage. *J. Neurosci. Methods* 201, 173–176. doi: 10.1016/j.jneumeth.2011.01.016

Ahmed, Z. (2013). Electrophysiological characterization of spino-sciatic and cortico-sciatic associative plasticity: modulation by trans-spinal direct current and effects on recovery after spinal cord injury in mice. *J. Neurosci.* 33, 4935–4946. doi: 10.1523/JNEUROSCI.4930-12.2013

Ahmed, Z. (2017). Effects of cathodal trans-spinal direct current stimulation on lower urinary tract function in normal and spinal cord injury mice with overactive bladder. *J. Neural Eng.* 14:056002. doi: 10.1088/1741-2552/aa76f2

Ahmed, Z., and Wieraszko, A. (2012). Trans-spinal direct current enhances corticospinal output and stimulation-evoked release of glutamate

analog, D-2,3- ^{3}H-aspartic acid. *J. Appl. Physiol.* 112, 1576–1592. doi: 10.1152/japplphysiol.00967.2011

An, S. K., Park, S.-I., Jun, S. B., Lee, C. J., Byun, K. M., Sung, J. H., et al. (2007). Design for a simplified cochlear implant system. *IEEE Trans. Biomed. Eng.* 54, 973–982. doi: 10.1109/TBME.2007.895372

Aplin, F. P., Singh, D., Della Santina, C. C., and Fridman, G. Y. (2018). Ionic direct current modulation for combined inhibition/excitation of the vestibular system. *IEEE Trans. Biomed. Eng.* 66, 775–783. doi: 10.1109/TBME.2018.2856698

Aquilina, O. (2006). A brief history of cardiac pacing. *Images Paediatr. Cardiol.* 8, 17–81. Available online at: http://www.impaedcard.com/

Arbring Sjöström, T., Berggren, M., Gabrielsson, E. O., Janson, P., Poxson, D. J., Seitanidou, M., et al. (2018). A decade of iontronic delivery devices. *Adv. Mater. Technol.* 3:1700360. doi: 10.1002/admt.201700360

Aregueta-Robles, U. A., Woolley, A. J., Lovell, N. H., Poole-Warren, L. A., and Green, R. A. (2014). Organic electrode coatings for next-generation neural interfaces. *Front. Neuroeng.* 7:15. doi: 10.3389/fneng.2014.00015

Ballestrasse, C. L., Ruggeri, R. T., and Beck, T. R. (1985). Calculations of the pH changes produced in body tissue by a spherical stimulation electrode. *Ann. Biomed. Eng.* 13, 405–424. doi: 10.1007/BF02407769

Beebe, X., and Rose, T. L. (1988). Charge injection limits of activated iridium oxide electrodes with 0.2 ms pulses in bicarbonate buffered saline. *IEEE Trans. Biomed. Eng.* 35, 494–495. doi: 10.1109/10.2122

Berkelman, T. (2005). 4 Generation of pH gradients. *Sep. Sci. Technol.* 7, 69–92. doi: 10.1016/S0149-6395(05)80007-8

Bhadra, N., and Kilgore, K. L. (2004). Direct current electrical conduction block of peripheral nerve. *IEEE Trans. Neural Syst. Rehabil. Eng.* 12, 313–324. doi: 10.1109/TNSRE.2004.834205

Biering-Sørensen, F., Craggs, M., Kennelly, M., Schick, E., and Wyndaele, J.-J. (2008). International lower urinary tract function basic spinal cord injury data set. *Spinal Cord* 46, 325–330. doi: 10.1038/sj.sc.3102145

Bikson, M., Grossman, P., Thomas, C., Zannou, A. L., Jiang, J., Adnan, T., et al. (2016). Safety of transcranial direct current stimulation: evidence based update 2016. *Brain Stimul.* 9, 641–661. doi: 10.1016/j.brs.2016.06.004

Bikson, M., Inoue, M., Akiyama, H., Deans, J. K., Fox, J. E., Miyakawa, H., et al. (2004). Effect of uniform extracellular DC electric fields on excitability in rat hippocampal slices *in vitro*. *J. Physiol.* 557 (Pt 1), 175–190. doi: 10.1113/jphysiol.2003.055772

Boinagrov, D., Loudin, J., and Palanker, D. (2010). Strength-duration relationship for extracellular neural stimulation: numerical and analytical models. *J. Neurophysiol.* 104, 2236–2248. doi: 10.1152/jn.00343.2010

Bonakdar, M., Graybill, P. M., and Davalos, R. V. (2017). A microfluidic model of the blood–brain barrier to study permeabilization by pulsed electric fields. *RSC Adv.* 7, 42811–42818. doi: 10.1039/C7RA07603G

Bramlet, R. (1998). Electromanipulation of Cells. *Clin. Nucl. Med.* 23:560. doi: 10.1097/00003072-199808000-00026

Brighton, C. T., Adler, S., Black, J., Itada, N., and Friedenberg, Z. B. (1975). Cathodic oxygen consumption and electrically induced osteogenesis. *Clin. Orthop. Relat. Res.* 107, 277–82. doi: 10.1097/00003086-197503000-00033

Brinton, M., Mandel, Y., Schachar, I., and Palanker, D. (2018). Mechanisms of electrical vasoconstriction. *J. Neuroeng. Rehabil.* 15:43. doi: 10.1186/s12984-018-0390-y

Brummer, S. B., Robblee, L. S., and Hambrecht, F. T. (1983). Criteria for selecting electrodes for electrical stimulation: theoretical and practical considerations. *Ann. N. Y. Acad. Sci.* 405, 159–171. doi: 10.1111/j.1749-6632.1983.tb31628.x

Brummer, S. B., and Turner, M. J. (1977). Electrochemical considerations for safe electrical stimulation of the nervous system with platinum electrodes. *IEEE Trans. Biomed. Eng.* 24, 59–63. doi: 10.1109/TBME.1977.326218

Buch, F., Albrektsson, T., and Herbst, E. (1984). Direct current influence on bone formation in titanium implants. *Biomaterials* 5, 341–346. doi: 10.1016/0142-9612(84)90032-2

Butterwick, A., Vankov, A., Huie, P., Freyvert, Y., and Palanker, D. (2007). Tissue damage by pulsed electrical stimulation. *IEEE Trans. Biomed. Eng.* 54, 2261–7. doi: 10.1109/TBME.2007.908310

Cancel, L. M., Arias, K., Bikson, M., and Tarbell, J. M. (2018). Direct current stimulation of endothelial monolayers induces a transient and reversible increase in transport due to the electroosmotic effect. *Sci. Rep.* 8:9265. doi: 10.1038/s41598-018-27524-9

Chakraborty, D., Truong, D. Q., Bikson, M., and Kaphzan, H. (2018). Neuromodulation of axon terminals. *Cereb. Cortex* 28, 2786–2794. doi: 10.1093/cercor/bhx158

Cheng, C., Nair, A. R., Thakur, R., and Fridman, G. (2018). Normally closed plunger-membrane microvalve self-actuated electrically using a shape memory alloy wire. *Microfluid. Nanofluidics* 22:29. doi: 10.1007/s10404-018-2049-1

Cheng, C., Thakur, R., Nair, A. R., Sterrett, S., and Fridman, G. (2017). "Miniature elastomeric valve design for safe direct current stimulator," in *Proceedings of IEEE Biomedical Circuits and Systems Conference Technology* (Turin). doi: 10.1109/BIOCAS.2017.8325194

Chiang, M., Robinson, K. R., and Vanable, J. W. (1992). Electrical fields in the vicinity of epithelial wounds in the isolated bovine eye. *Exp. Eye Res.* 54, 999–1003. doi: 10.1016/0014-4835(92)90164-N

Chu, A. P., Morris, K., Greenberg, R. J., and Zhou, D. M. (2004). "Stimulus induced pH changes in retinal implants," in *The 26th Annual International Conference of the IEEE Engineering in Medicine and Biology Society* (San Francisco, CA: IEEE), 4160–4162. doi: 10.1109/IEMBS.2004.1404160

Cicchetti, F., and Barker, R. A. (2014). The glial response to intracerebrally delivered therapies for neurodegenerative disorders: is this a critical issue? *Front. Pharmacol.* 5:139. doi: 10.3389/fphar.2014.00139

Cogan, S. F., Ludwig, K. A., Welle, C. G., and Takmakov, P. (2016). Tissue damage thresholds during therapeutic electrical stimulation. *J. Neural Eng.* 13:021001. doi: 10.1088/1741-2560/13/2/021001

Corbett, S., and Clopton, J. (2004). *Apparatus and Method for Treating Strial Hearing Loss*. International Patent No. WO2004041072 (Geneva: World Intellectual Property Organization).

Curthoys, I. S., and Halmagyi, G. M. (1995). Vestibular compensation: a review of the oculomotor, neural, and clinical consequences of unilateral vestibular loss. *J. Vestib. Res.* 5, 67–107. doi: 10.1016/0957-4271(94)00026-X

Datta, A., Elwassif, M., and Bikson, M. (2009). "Bio-heat transfer model of transcranial DC stimulation: comparison of conventional pad versus ring electrode," in *2009 Annual International Conference of the IEEE Engineering in Medicine and Biology Society* (Minneapolis, MN: IEEE), 670–673. doi: 10.1109/IEMBS.2009.5333673

Davidovics, N. S., Fridman, G. Y., Chiang, B., and Della Santina, C. C. (2011). Effects of biphasic current pulse frequency, amplitude, duration, and interphase gap on eye movement responses to prosthetic electrical stimulation of the vestibular nerve. *IEEE Trans. Neural Syst. Rehabil. Eng.* 19, 84–94. doi: 10.1109/TNSRE.2010.2065241

Davidovics, N. S., Fridman, G. Y., and Della Santina, C. C. (2012). Co-modulation of stimulus rate and current from elevated baselines expands head motion encoding range of the vestibular prosthesis. *Exp. Brain Res.* 218, 389–400. doi: 10.1007/s00221-012-3025-8

De Ridder, D., Vanneste, S., Weisz, N., Londero, A., Schlee, W., Elgoyhen, A. B., et al. (2014). An integrative model of auditory phantom perception: tinnitus as a unified percept of interacting separable subnetworks. *Neurosci. Biobehav. Rev.* 44, 16–32. doi: 10.1016/J.NEUBIOREV.2013.03.021

De Volder, M. F., Tawfick, S. H., Baughman, R. H., and Hart, A. J. (2013). Carbon nanotubes: present and future commercial applications. *Science* 339, 535–539. doi: 10.1126/science.1222453

Della Santina, C. C., Migliaccio, A. A., and Patel, A. H. (2007). A multichannel semicircular canal neural prosthesis using electrical stimulation to restore 3-d vestibular sensation. *IEEE Trans. Biomed. Eng.* 54, 1016–1030. doi: 10.1109/TBME.2007.894629

Eijkelkamp, N., Linley, J. E., Baker, M. D., Minett, M. S., Cregg, R., Werdehausen, R., et al. (2012). Neurological perspectives on voltage-gated sodium channels. *Brain* 135, 2585–2612. doi: 10.1093/brain/aws225

Faes, T. J., van der Meij, H. A., de Munck, J. C., and Heethaar, R. M. (1999). The electric resistivity of human tissues (100 Hz-10 MHz): a meta-analysis of review studies. *Physiol. Meas.* 20, R1–R10. doi: 10.1088/0967-3334/20/4/201

Fehlings, M. G., Wong, T. H., Tator, C. H., and Tymianski, M. (1989). Effect of a direct current field on axons after experimental spinal cord injury. *Can. J. Surg.* 32, 188–91.

Feng, J.-F., Liu, J., Zhang, L., Jiang, J.-Y., Russell, M., Lyeth, B. G., et al. (2017). Electrical guidance of human stem cells in the rat brain. *Stem Cell Rep.* 9, 177–189. doi: 10.1016/j.stemcr.2017.05.035

Ferlauto, L., D'Angelo, A. N., Vagni, P., Leccardi, A., Ildelfonsa, M. J., Mor, F. M., et al. (2018). Development and characterization of PEDOT:PSS/alginate soft microelectrodes for application in neuroprosthetics. *Front. Neurosci.* 12:648. doi: 10.3389/fnins.2018.00648

Flamm, J., Kiesswetter, H., and Hufschmidt, H. J. (1977). Treatment of the neurogenic bladder with direct current on the spinal cord (Myelotron). *Urol. Int.* 32, 247–256. doi: 10.1159/000280138

Foster, K. R., and Schwan, H. P. (1989). Dielectric properties of tissues and biological materials: a critical review. *Crit. Rev. Biomed. Eng.* 17, 25–104.

Frankenhaueuser, B., and Huxley, A. F. (1964). The action potential in the myelinated nerve fiber of xenopus laevis as computed on the basis of voltage clamp data. *J. Physiol.* 171, 302–15. doi: 10.1113/jphysiol.1964.sp007378

Fridman, G. (2017). "Safe Direct Current Stimulator design for reduced power consumption and increased reliability," in *Conference Proceedings Annual International Conference of the IEEE Engineering in Medicine and Biology Society* (Seogwipo). doi: 10.1109/EMBC.2017.8037015

Fridman, G. Y., and Della Santina, C. C. (2013a). Safe direct current stimulation to expand capabilities of neural prostheses. *IEEE Trans. Neural Syst. Rehabil. Eng.* 21, 319–328. doi: 10.1109/TNSRE.2013.2245423

Fridman, G. Y., and Della Santina, C. C. (2013b). Safe direct current stimulator 2: concept and design. *Conf Proc IEEE Eng Med Biol Soc.* 2013, 3126–3129. doi: 10.1109/EMBC.2013.6610203

Fukada, E., and Yasuda, I. (1957). On the piezoelectric effect of bone. *J. Phys. Soc.* 12, 1158–1162. doi: 10.1143/JPSJ.12.1158

Funk, R. H. (2015). Endogenous electric fields as guiding cue for cell migration. *Front. Physiol.* 6:143. doi: 10.3389/fphys.2015.00143

Gabriel, S., Lau, R. W., and Gabriel, C. (1996). The dielectric properties of biological tissues: II. Measurements in the frequency range 10 Hz to 20 GHz. *Phys. Med. Biol.* 41, 2251–2269. doi: 10.1088/0031-9155/41/11/002

Geddes, L. A., and Baker, L. E. (1967). The specific resistance of biological material—a compendium of data for the biomedical engineer and physiologist. *Med. Biol. Eng.* 5, 271–293. doi: 10.1007/BF02474537

Geddes, L. A., and Hoff, H. E. (1971). The discovery of bioelectricity and current electricity The Galvani-Volta controversy. *IEEE Spectr.* 8, 38–46. doi: 10.1109/MSPEC.1971.5217888

Geurts, J. W., Joosten, E. A., and van Kleef, M. (2017). Current status and future perspectives of spinal cord stimulation in treatment of chronic pain. *Pain* 158, 771–774. doi: 10.1097/j.pain.0000000000000847

Geurts, J. W., Smits, H., Kemler, M. A., Brunner, F., Kessels, A. G. H., and van Kleef, M. (2013). Spinal cord stimulation for complex regional pain syndrome type I: a prospective cohort study with long-term follow-up. *Neuromodulation Technol. Neural Interface* 16, 523–529. doi: 10.1111/ner.12024

Gilmour, A. D., Green, R. A., and Thomson, C. E. (2013). A low-maintenance, primary cell culture model for the assessment of carbon nanotube toxicity. *Toxicol. Environ. Chem.* 95, 1129–1144. doi: 10.1080/02772248.2013.844429

Gofeld, M. (2014). New horizons in neuromodulation. *Curr. Pain Headache Rep.* 18:397. doi: 10.1007/s11916-013-0397-9

Goldberg, J. M., Smith, C. E., and Fernández, C. (1984). Relation between discharge regularity and responses to externally applied galvanic currents in vestibular nerve afferents of the squirrel monkey. *J. Neurophysiol.* 51, 1236–1256. doi: 10.1152/jn.1984.51.6.1236

Goldman, S. A., Pulsinelli, W. A., Clarke, W. Y., Kraig, R. P., and Plum, F. (1989). The effects of extracellular acidosis on neurons and glia *in vitro*. *J. Cereb. Blood Flow Metab.* 9, 471–477. doi: 10.1038/jcbfm.1989.70

Gomez-Tames, J., Sugiyama, Y., Laakso, I., Tanaka, S., Koyama, S., Sadato, N., et al. (2016). Effect of microscopic modeling of skin in electrical and thermal analysis of transcranial direct current stimulation. *Phys. Med. Biol.* 61, 8825–8838. doi: 10.1088/1361-6560/61/24/8825

Grant, P. F., and Lowery, M. M. (2010). Effect of dispersive conductivity and permittivity in volume conductor models of deep brain stimulation. *IEEE Trans. Biomed. Eng.* 57, 2386–2393. doi: 10.1109/TBME.2010.2055054

Griffin, M., and Bayat, A. (2011). Electrical stimulation in bone healing: critical analysis by evaluating levels of evidence. *Eplasty* 11:e34. Available online at: http://www.eplasty.com/

Groothuis, J., Ramsey, N. F., Ramakers, G. M. J., and van der Plasse, G. (2014). Physiological challenges for intracortical electrodes. *Brain Stimul.* 7, 1–6. doi: 10.1016/j.brs.2013.07.001

Gudivaka, R., Schoeller, D. A., Kushner, R. F., and Bolt, M. J. (1999). Single- and multifrequency models for bioelectrical impedance analysis of body water compartments. *J. Appl. Physiol.* 87, 1087–1096. doi: 10.1152/jappl.1999.87.3.1087

Guleyupoglu, B., Schestatsky, P., Edwards, D., Fregni, F., and Bikson, M. (2013). Classification of methods in transcranial electrical stimulation (tES) and evolving strategy from historical approaches to contemporary innovations. *J. Neurosci. Methods* 219, 297–311. doi: 10.1016/j.jneumeth.2013.07.016

Gurtner, G. C., Werner, S., Barrandon, Y., and Longaker, M. T. (2008). Wound repair and regeneration. *Nature* 453, 314–321. doi: 10.1038/nature07039

Guyton, D. L., and Hambrecht, F. T. (1973). Capacitor electrode stimulates nerve or muscle without oxidation-reduction reactions. *Science* 181, 74–76. doi: 10.1126/science.181.4094.74

Guyton, D. L., and Hambrecht, F. T. (1974). Theory and design of capacitor electrodes for chronic stimulation. *Med. Biol. Eng.* 12, 613–620. doi: 10.1007/BF02477223

Hageman, K. N., Kalayjian, Z. K., Tejada, F., Chiang, B., Rahman, M. A., Fridman, G. Y., et al. (2016). A CMOS neural interface for a multichannel vestibular prosthesis. *IEEE Trans. Biomed. Circuits Syst.* 10, 269–279. doi: 10.1109/TBCAS.2015.2409797

Hamm, L. L., Nakhoul, N., and Hering-Smith, K. S. (2015). Acid-base homeostasis. *Clin. J. Am. Soc. Nephrol.* 10, 2232–2242. doi: 10.2215/CJN.07400715

Hladovec, J. (1971). Experimental arterial thrombosis in rats with continuous registration. *Thromb. Diath. Haemorrh.* 26, 407–10. doi: 10.1055/s-0038-1653690

Hodgkin, A. L., and Huxley, A. F. (1952). A quantitative description of membrane current and its application to conduction and excitation in nerve. *J. Physiol.* 117, 500–44. doi: 10.1113/jphysiol.1952.sp004764

Hodgkin, A. L., and Katz, B. (1949). The effect of temperature on the electrical activity of the giant axon of the squid. *J. Physiol.* 109, 240–249. doi: 10.1113/jphysiol.1949.sp004388

Hopp, F. A., Zuperku, E. J., Coon, R. L., and Kampine, J. P. (1980). Effect of anodal blockade of myelinated fibers on vagal C-fiber afferents. *Am. J. Physiol.* 239, R454–R4R462. doi: 10.1152/ajpregu.1980.239.5.R454

Huang, C. Q., Carter, P. M., and Shepherd, R. K. (2001). Stimulus induced pH changes in cochlear implants: an *in vitro* and *in vivo* study. *Ann. Biomed. Eng.* 29, 791–802. doi: 10.1114/1.1397793

Isaksson, J., Kjäll, P., Nilsson, D., Robinson, N., Berggren, M., and Richter-Dahlfors, A. (2007). Electronic control of Ca^{2+} signalling in neuronal cells using an organic electronic ion pump. *Nat. Mater.* 6, 673–679. doi: 10.1038/nmat1963

Jackson, M. P., Rahman, A., Lafon, B., Kronberg, G., Ling, D., Parra, L. C., et al. (2016). Animal models of transcranial direct current stimulation: methods and mechanisms. *Clin. Neurophysiol.* 127, 3425–3454. doi: 10.1016/j.clinph.2016.08.016

Jaffe, L. F. (1977). Electrophoresis along cell membranes. *Nature* 265, 600–602. doi: 10.1038/265600a0

Jaffe, L. F., and Vanable, J. W. (1984). Electric fields and wound healing. *Clin. Dermatol.* 2, 34–44. doi: 10.1016/0738-081X(84)90025-7

Joucla, S., Glière, A., and Yvert, B. (2014). Current approaches to model extracellular electrical neural microstimulation. *Front. Comput. Neurosci.* 8:13. doi: 10.3389/fncom.2014.00013

Joucla, S., and Yvert, B. (2009). The "Mirror" estimate: an intuitive predictor of membrane polarization during extracellular stimulation. *Biophys. J.* 96, 3495–3508. doi: 10.1016/j.bpj.2008.12.3961

Joucla, S., and Yvert, B. (2012). Modeling extracellular electrical neural stimulation: from basic understanding to MEA-based applications. *J. Physiol.* 106, 146–158. doi: 10.1016/j.jphysparis.2011.10.003

Kabakov, A. Y., Muller, P. A., Pascual-Leone, A., Jensen, F. E., and Rotenberg, A. (2012). Contribution of axonal orientation to pathway-dependent modulation of excitatory transmission by direct current stimulation in isolated rat hippocampus. *J. Neurophysiol.* 107, 1881–1889. doi: 10.1152/jn.00715.2011

Kerns, J. M., Truong, T. T., Walter, J. S., and Khan, T. (1996). Do direct current electric fields enhance micturition in the spinal cat? *J. Spinal Cord Med.* 19, 225–233. doi: 10.1080/10790268.1996.11719438

Kiang, N. Y., Liberman, M. C., and Levine, R. A. (1976). Auditory-nerve activity in cats exposed to ototoxic drugs and high-intensity sounds. *Ann. Otol. Rhinol. Laryngol.* 85, 752–768. doi: 10.1177/000348947608500605

Kim, S. K., Kim, J. H., Kim, K. P., and Chung, T. D. (2007). Continuous low-voltage dc electroporation on a microfluidic chip with polyelectrolytic salt bridges. *Anal. Chem.* 79, 7761–7766. doi: 10.1021/ac071197h

Konikoff, J. J. (1975). Origin of the osseous bioelectric potentials: a review. *Ann. Clin. Lab. Sci.* 5:5.

Krames, E., Peckham, P. H., and Rezai, A. (2018). *Neuromodulation: Comprehensive Textbook of Principles, Technologies, and Therapies*. Cambridge, MA: Academic Press.

Krause, J. S., DeVivo, M. J., and Jackson, A. B. (2004). Health status, community integration, and economic risk factors for mortality after spinal cord injury. *Arch. Phys. Med. Rehabil.* 85, 1764–1773. doi: 10.1016/j.apmr.2004.06.062

Kuck, A., Stegeman, D. F., and van Asseldonk, E. H. F. (2017). Modeling transspinal direct current stimulation for the modulation of the lumbar spinal motor pathways. *J. Neural Eng.* 14:056014. doi: 10.1088/1741-2552/aa7960

Kuzyk, P. R., and Schemitsch, E. H. (2009). The science of electrical stimulation therapy for fracture healing. *Indian J. Orthop.* 43:127. doi: 10.4103/0019-5413.50846

Kyle, U. G., Bosaeus, I., De Lorenzo, A. D., Deurenberg, P., Elia, M., Gómez, J. M., et al. (2004). Bioelectrical impedance analysis—Part I: review of principles and methods. *Clin. Nutr.* 23, 1226–1243. doi: 10.1016/j.clnu.2004.06.004

Larsson, K. C., Kjäll, P., and Richter-Dahlfors, A. (2013). Organic bioelectronics for electronic-to-chemical translation in modulation of neuronal signaling and machine-to-brain interfacing. *Biochim. Biophys. Acta - Gen. Subj.* 9, 4334–4344. doi: 10.1016/j.bbagen.2012.11.024

Leppik, L., Zhihua, H., Mobini, S., Thottakkattumana Parameswaran, V., Eischen-Loges, M., Slavici, A., et al. (2018). Combining electrical stimulation and tissue engineering to treat large bone defects in a rat model. *Sci. Rep.* 8:6307. doi: 10.1038/s41598-018-24892-0

Lewis, R. F. (2016). Vestibular implants studied in animal models: clinical and scientific implications. *J. Neurophysiol.* 116, 2777–2788. doi: 10.1152/jn.00601.2016

Lian, J., Bikson, M., Sciortino, C., Stacey, W. C., and Durand, D. M. (2003). Local suppression of epileptiform activity by electrical stimulation in rat hippocampus *in vitro*. *J. Physiol.* 547, 427–434. doi: 10.1113/jphysiol.2002.033209

Liberman, M. C. (1978). Auditory-nerve response from cats raised in a low-noise chamber. *J. Acoust. Soc. Am.* 63, 442–455. doi: 10.1121/1.381736

Loeb, G. E. (2018). Neural prosthetics: a review of empirical vs. systems engineering strategies. *Appl. Bionics Biomech.* 2018:1435030. doi: 10.1155/2018/1435030

Lopez-Quintero, S. V., Datta, A., Amaya, R., Elwassif, M., Bikson, M., and Tarbell, J. M. (2010). DBS-relevant electric fields increase hydraulic conductivity of *in vitro* endothelial monolayers. *J. Neural Eng.* 7:016005. doi: 10.1088/1741-2560/7/1/016005

Macounová, K, Cabrera, C. R., Holl, M. R., and Yager, P. (2000). Generation of natural pH gradients in microfluidic channels for use in isoelectric focusing. *Anal. Chem.* 72, 3745–3751. doi: 10.1021/AC000237D

Magee, J. C. (1998). Dendritic hyperpolarization-activated currents modify the integrative properties of hippocampal CA1 pyramidal neurons. *J. Neurosci.* 18, 7613–7624. doi: 10.1523/JNEUROSCI.18-19-07613.1998

McAdams, E. T., and Jossinet, J. (1995). Tissue impedance: a historical overview. *Physiol. Meas.* 16, A1–A13. doi: 10.1088/0967-3334/16/3A/001

Mccaig, C. D., and Rajnicek, A. M. (1991). Electrical fields, nerve growth and nerve regeneration. *Exp Physiol.* 76, 473–494. doi: 10.1113/expphysiol.1991.sp003514

McCaig, C. D., Rajnicek, A. M., Song, B., and Zhao, M. (2005). Controlling cell behavior electrically: current views and future potential. *Physiol. Rev.* 85, 943–978. doi: 10.1152/physrev.00020.2004

McCreery, D. B., Agnew, W. F., Yuen, T. G., and Bullara, L. (1990). Charge density and charge per phase as cofactors in neural injury induced by electrical stimulation. *IEEE Trans. Biomed. Eng.* 37, 996–1001. doi: 10.1109/10.102812

McDonald, F. (1993). Electrical effects at the bone surface. *Eur. J. Orthod.* 15, 175–183. doi: 10.1093/ejo/15.3.175

McIntyre, C. C., Grill, W. M., Sherman, D. L., and Thakor, N., V (2004). Cellular effects of deep brain stimulation: model-based analysis of activation and inhibition. *J. Neurophysiol.* 91, 1457–1469. doi: 10.1152/jn.00989.2003

McNeal, D. R. (1976). Analysis of a model for excitation of myelinated nerve. *IEEE Trans. Biomed. Eng.* 23, 329–37. doi: 10.1109/TBME.1976.324593

Merrill, D. R., Bikson, M., and Jefferys, J. G. R. (2005). Electrical stimulation of excitable tissue: design of efficacious and safe protocols. *J. Neurosci. Methods* 141, 171–198. doi: 10.1016/j.jneumeth.2004.10.020

Miles, F. A., and Braitman, D. J. (1980). Long-term adaptive changes in primate vestibuloocular reflex. *II. Electrophysiological observations on semicircular canal primary afferents. J. Neurophysiol.* 43, 1426–1436. doi: 10.1152/jn.1980.43.5.1426

Mina, F., Modolo, J., Recher, F., Dieuset, G., Biraben, A., Benquet, P., et al. (2017). Model-guided control of hippocampal discharges by local direct current stimulation. *Sci. Rep.* 7:1708. doi: 10.1038/s41598-017-01867-1

Mitchell, D. E., Della Santina, C. C., and Cullen, K. E. (2016). Plasticity within non-cerebellar pathways rapidly shapes motor performance *in vivo*. *Nat. Commun.* 7:11238. doi: 10.1038/ncomms11238

Mitchell, D. E., Della Santina, C. C., and Cullen, K. E. (2017). Plasticity within excitatory and inhibitory pathways of the vestibulo-spinal circuitry guides changes in motor performance. *Sci. Rep.* 7:853. doi: 10.1038/s41598-017-00956-5

Møller, A. R. (2007a). The role of neural plasticity in tinnitus. *Prog. Brain Res.* 166, 37–544. doi: 10.1016/S0079-6123(07)66003-8

Møller, A. R. (2007b). Tinnitus: presence and future. *Prog. Brain Res.* 166, 3–16. doi: 10.1016/S0079-6123(07)66001-4

Molsberger, A., and McCaig, C. D. (2018). Percutaneous direct current stimulation—a new electroceutical solution for severe neurological pain and soft tissue injuries. *Med. Devices Evid. Res.* 11, 205–214. doi: 10.2147/MDER.S163368

Moulton, S. E., Higgins, M. J., Kapsa, R. M. I., and Wallace, G. G. (2012). Organic bionics: a new dimension in neural communications. *Adv. Funct. Mater.* 22, 2003–2014. doi: 10.1002/adfm.201102232

Nakauchi, K., Fujikado, T., Kanda, H., Kusaka, S., Ozawa, M., Sakaguchi, H., et al. (2007). Threshold suprachoroidal–transretinal stimulation current resulting in retinal damage in rabbits. *J. Neural Eng.* 4, S50–S57. doi: 10.1088/1741-2560/4/1/S07

Nnoaham, K. E., and Kumbang, J. (2008). "Transcutaneous electrical nerve stimulation (TENS) for chronic pain," in *Cochrane Database of Systematic Reviews*, ed K. E. Nnoaham (Chichester, UK: John Wiley and Sons, Ltd.), CD003222. doi: 10.1002/14651858.CD003222.pub2

Nyberg, T., Inganäs, O., and Jerregård, H. (2002). Polymer hydrogel microelectrodes for neural communication. *Biomed. Microdevices* 4, 43–52. doi: 10.1023/A:1014219828983

O'Connor, B. T., Charlton, H. M., Currey, J. D., Kirby, D. R. S., and Woods, C. (1969). Effects of electric current on bone *in vivo*. *Nature* 222, 162–163. doi: 10.1038/222162a0

Ou, P., and Fridman, G. (2017). "Electronics for a safe direct current stimulator," in *Proceedings of IEEE Biomedical Circuits and Systems Conference Technology* (Turin). doi: 10.1109/BIOCAS.2017.8325191

Pethig, R. (1987). Dielectric properties of body tissues. *Clin. Phys. Physiol. Meas.* 8 (Suppl. A), 5–12. doi: 10.1088/0143-0815/8/4A/002

Piccolino, M. (1998). Animal electricity and the birth of electrophysiology: the legacy of Luigi Galvani. *Brain Res. Bull.* 46, 381–407.

Plonsey, R., and Heppner, D. B. (1967). Considerations of quasi-stationarity in electrophysiological systems. *Bull. Math. Biophys.* 29, 657–64. doi: 10.1007/BF02476917

Pour Aryan, N., Kaim, H., and Rothermel, A. (2014). *Stimulation and Recording Electrodes for Neural Prostheses*. Cham: Springer. doi: 10.1007/978-3-319-10052-4

Prevoteau, C., Chen, S. Y., and Lalwani, A. K. (2018). Music enjoyment with cochlear implantation. *Auris Nasus Larynx* 45, 895–902. doi: 10.1016/j.anl.2017.11.008

Radman, T., Su, Y., An, J. H., Parra, L. C., and Bikson, M. (2007). Spike timing amplifies the effect of electric fields on neurons: implications for endogenous field effects. *J. Neurosci.* 27, 3030–3036. doi: 10.1523/JNEUROSCI.0095-07.2007

Radziszewski, K. (2013). Outcomes of electrical stimulation of the neurogenic bladder: results of a two-year follow-up study. *NeuroRehabilitation* 32, 867–873. doi: 10.3233/NRE-130911

Rae, C. D., Lee, V. H.-C., Ordidge, R. J., Alonzo, A., and Loo, C. (2013). Anodal transcranial direct current stimulation increases brain intracellular pH and modulates bioenergetics. *Int. J. Neuropsychopharmacol.* 16, 1695–1706. doi: 10.1017/S1461145713000084

Rahman, A., Reato, D., Arlotti, M., Gasca, F., Datta, A., Parra, L. C., et al. (2013). Cellular effects of acute direct current stimulation: somatic and synaptic terminal effects. *J. Physiol.* 591, 2563–2578. doi: 10.1113/jphysiol.2012.247171

Rattay, F. (1986). Analysis of models for external stimulation of axons. *IEEE Trans. Biomed. Eng.* 33, 974–977. doi: 10.1109/TBME.1986.325670

Rattay, F. (1987). Ways to approximate current-distance relations for electrically stimulated fibers. *J. Theor. Biol.* 125, 339–49. doi: 10.1016/S0022-5193(87)80066-8

Rattay, F. (1999). The basic mechanism for the electrical stimulation of the nervous system. *Neuroscience* 89, 335–46. doi: 10.1016/S0306-4522(98)00330-3

Reid, B., Song, B., McCaig, C. D., and Zhao, M. (2005). Wound healing in rat cornea: the role of electric currents. *FASEB J.* 19, 379–386. doi: 10.1096/fj.04-2325com

Rubinsky, B. (2010). *Irreversible Electroporation*. Berlin: Springer. doi: 10.1007/978-3-642-05420-4

Ruffini, G., Wendling, F., Merlet, I., Molaee-Ardekani, B., Mekonnen, A., Salvador, R., et al. (2013). Transcranial current brain stimulation (tCS): models and technologies. *IEEE Trans. Neural Syst. Rehabil. Eng.* 21, 333–345. doi: 10.1109/TNSRE.2012.2200046

Sadeghi, S. G., Goldberg, J. M., Minor, L. B., and Cullen, K. E. (2009). Efferent-mediated responses in vestibular nerve afferents of the alert macaque. *J. Neurophysiol.* 101, 988–1001. doi: 10.1152/jn.91112.2008

San-juan, D., Morales-Quezada, L., Orozco Garduño, A. J., Alonso-Vanegas, M., González-Aragón, M. F., Espinoza López, D. A., et al. (2015). Transcranial direct current stimulation in epilepsy. *Brain Stimul.* 8, 455–464. doi: 10.1016/j.brs.2015.01.001

Santos, A., dos, H. M., Santos, A. P. S., Santos, H. S., and da Silva, A. C. (2018). The use of tDCS as a therapeutic option for tinnitus: a systematic review. *Braz. J. Otorhinolaryngol.* 84, 653–659. doi: 10.1016/J.BJORL.2018.02.003

Shamji, M. F., De Vos, C., and Sharan, A. (2017). The advancing role of neuromodulation for the management of chronic treatment-refractory pain. *Neurosurgery* 80, S108–S113. doi: 10.1093/neuros/nyw047

Shannon, R. V. (1992). A model of safe levels for electrical stimulation. *IEEE Trans. Biomed. Eng.* 39, 424–426. doi: 10.1109/10.126616

Shu, Y., Hasenstaub, A., Duque, A., Yu, Y., and McCormick, D. A. (2006). Modulation of intracortical synaptic potentials by presynaptic somatic membrane potential. *Nature* 441, 761–765. doi: 10.1038/nature04720

Shvedova, A. A., Castranova, V., Kisin, E., Schwegler-Berry, D., Murray, A., Gandelsman, V., et al. (2003). Exposure to carbon nanotube material: assessment of nanotube cytotoxicity using human keratinocyte cells. *J. Toxicol. Environ. Heal. Part A.* 66, 1909–1926. doi: 10.1080/713853956

Simon, D. T., Kurup, S., Larsson, K. C., Hori, R., Tybrandt, K., Goiny, M., et al. (2009). Organic electronics for precise delivery of neurotransmitters to modulate mammalian sensory function. *Nat. Mater.* 8, 742–746. doi: 10.1038/nmat2494

Simon, D. T., Larsson, K. C., Berggren, M., and Richter-Dahlfors, A. (2010). Precise neurotransmitter-mediated communication with neurons *in vitro* and *in vivo* using organic electronics. *J. Biomech. Sci. Eng.* 5, 208–217. doi: 10.1299/jbse.5.208

Simon, D. T., Larsson, K. C., Nilsson, D., Burström, G., Galter, D., Berggren, M., et al. (2015). An organic electronic biomimetic neuron enables auto-regulated neuromodulation. *Biosens. Bioelectron.* 71, 359–364. doi: 10.1016/j.bios.2015.04.058

Singer, A. J., and Clark, R. A. F. (1999). Cutaneous wound healing. *N. Engl. J. Med.* 341, 738–746. doi: 10.1056/NEJM199909023411006

Song, J.-J., Vanneste, S., Van de Heyning, P., and De Ridder, D. (2012). Transcranial direct current stimulation in tinnitus patients: a systemic review and meta-analysis. *Sci. World J.* 2012, 1–7. doi: 10.1100/2012/427941

Stefan, H., and Lopes da Silva, F. H. (2013). Epileptic neuronal networks: methods of identification and clinical relevance. *Front. Neurol.* 4:8. doi: 10.3389/fneur.2013.00008

Stewart, F., Gameiro, L. F. F., El Dib, R., Gameiro, M. O. O., Kapoor, A., and Amaro, J. L. L. (2016). Electrical stimulation with non-implanted electrodes for overactive bladder in adults. *Cochrane Database Syst. Rev.* 12:CD010098. doi: 10.1002/14651858.CD010098.pub4

Strang, C. E., Ray, M. K., Boggiano, M. M., and Amthor, F. R. (2018). Effects of tDCS-like electrical stimulation on retinal ganglion cells. *Eye Brain* 10, 65–78. doi: 10.2147/EB.S163914

Svennersten, K., Larsson, K. C., Berggren, M., and Richter-Dahlfors, A. (2011). Organic bioelectronics in nanomedicine. *Biochim. Biophys. Acta Gen. Subj.* 1810, 276–285. doi: 10.1016/j.bbagen.2010.10.001

Szarowski, D. H., Andersen, M. D., Retterer, S., Spence, A. J., Isaacson, M., Craighead, H. G., et al. (2003). Brain responses to micro-machined silicon devices. *Brain Res.* 983, 23–35. doi: 10.1016/S0006-8993(03)03023-3

Tarabella, G., Mahvash Mohammadi, F., Copped,è, N., Barbero, F., Iannotta, S., Santato, C., et al. (2013). New opportunities for organic electronics and bioelectronics: ions in action. *Chem. Sci.* 4:1395. doi: 10.1039/c2sc21740f

Toloza, E. H. S., Negahbani, E., and Fröhlich, F. (2018). Ih interacts with somato-dendritic structure to determine frequency response to weak alternating electric field stimulation. *J. Neurophysiol.* 119, 1029–1036. doi: 10.1152/jn.00541.2017

Vacher, H., Mohapatra, D. P., and Trimmer, J. S. (2008). Localization and targeting of voltage-dependent ion channels in mammalian central neurons. *Physiol. Rev.* 88, 1407–1447. doi: 10.1152/physrev.00002.2008

Valentin, N. S., Hageman, K. N., Chenkai Dai, C., Della Santina, C. C., and Fridman, G. Y. (2013). Development of a multichannel vestibular prosthesis prototype by modification of a commercially available cochlear implant. *IEEE Trans. Neural Syst. Rehabil. Eng.* 21, 830–839. doi: 10.1109/TNSRE.2013.2259261

Victoria, G., Petrisor, B., Drew, B., and Dick, D. (2009). Bone stimulation for fracture healing: what's all the fuss? *Indian J. Orthop.* 43:117. doi: 10.4103/0019-5413.50844

Vrabec, T., Bhadra, N., Van Acker, G., Bhadra, N., and Kilgore, K. (2017). Continuous direct current nerve block using multi contact high capacitance electrodes. *IEEE Trans. Neural Syst. Rehabil. Eng.* 25, 517–529. doi: 10.1109/TNSRE.2016.2589541

Vrabec, T., Bhadra, N., Wainright, J., Bhadra, N., Franke, M., and Kilgore, K. (2016). Characterization of high capacitance electrodes for the application of direct current electrical nerve block. *Med. Biol. Eng. Comput.* 54, 191–203. doi: 10.1007/s11517-015-1385-5

Wang, H., Wang, B., Normoyle, K. P., Jackson, K., Spitler, K., Sharrock, M. F., et al. (2014). Brain temperature and its fundamental properties: a review for clinical neuroscientists. *Front. Neurosci.* 8:307. doi: 10.3389/fnins.2014.00307

Wilson, B. S., and Dorman, M. F. (2008). Cochlear implants: a remarkable past and a brilliant future. *Hear. Res.* 242, 3–21. doi: 10.1016/j.heares.2008.06.005

Wilson, B. S., Finley, C. C., Lawson, D. T., Wolford, R. D., Eddington, D. K., and Rabinowitz, W. M. (1991). Better speech recognition with cochlear implants. *Nature* 352, 236–238. doi: 10.1038/352236a0

Won, S. M., Song, E., Zhao, J., Li, J., Rivnay, J., and Rogers, J. A. (2018). Recent advances in materials, devices, and systems for neural interfaces. *Adv. Mater.* 30:1800534. doi: 10.1002/adma.201800534

Wongsarnpigoon, A., and Grill, W. M. (2012). Computer-based model of epidural motor cortex stimulation: effects of electrode position and geometry on activation of cortical neurons. *Clin. Neurophysiol.* 123, 160–172. doi: 10.1016/J.CLINPH.2011.06.005

Yamashita, M. (2015). Weak electric fields serve as guidance cues that direct retinal ganglion cell axons *in vitro*. *Biochem. Biophys. Rep.* 4, 83–88. doi: 10.1016/j.bbrep.2015.08.022

Yang, F., Anderson, M., He, S., Stephens, K., Zheng, Y., Chen, Z., et al. (2018). Differential expression of voltage-gated sodium channels in afferent neurons renders selective neural block by ionic direct current. *Sci. Adv.* 4:eaaq1438. doi: 10.1126/sciadv.aaq1438

Yao, L., and Li, Y. (2016). The role of direct current electric field-guided stem cell migration in neural regeneration. *Stem Cell Rev. Rep.* 12, 365–375. doi: 10.1007/s12015-016-9654-8

Zhao, H., Steiger, A., Nohner, M., and Ye, H. (2015). Specific intensity direct current (DC) electric field improves neural stem cell migration and enhances differentiation towards βIII-tubulin+ neurons. *PLoS ONE* 10:e0129625. doi: 10.1371/journal.pone.0129625

Zhao, M. (2009). Electrical fields in wound healing—An overriding signal that directs cell migration. *Semin. Cell Dev. Biol.* 20, 674–682. doi: 10.1016/J.SEMCDB.2008.12.009

Zhao, M., Song, B., Pu, J., Wada, T., Reid, B., Tai, G., et al. (2006). Electrical signals control wound healing through phosphatidylinositol-3-OH kinase-γ and PTEN. *Nature* 442, 457–460. doi: 10.1038/nature04925

Zhu, T., Feng, X. J., Zhou, Y., and Wu, J. X. (2016). Therapeutic effects of electrical stimulation on overactive bladder: a meta-analysis. *Springerplus* 5:2032. doi: 10.1186/s40064-016-3737-5

Zoski, C. G. (2007). *Handbook of Electrochemistry*. Amsterdam: Elsevier Science. doi: 10.1016/B978-0-444-51958-0.X5000-9

Conflict of Interest Statement: GF holds the following US patents:
2012 GF, CC Della Santina, "Implantable Vestibular Prosthesis and Methods for Sensing Head Motion and Conveying the Signals Representing Head Movements to the Vestibular Nerve," JHU US Pat. US20120277835.
2012 GF, CC Della Santina, "Artifact Control and Miniaturization of the Safe DC Stimulator for Neural Prostheses," JHU US Pat. US20140364796.
GF has submitted the following pending patents for Johns Hopkins internal review:
2016 GF, "Safe Direct Current Stimulation (SDCS) Self-Curling Nerve Cuff Electrode," JHU C14442.
2017 GF, "Safe Direct Current Stimulator Design for Reduced Power and Increased Reliability," JHU C14620.

The remaining author declares that the research was conducted in the absence of any commercial or financial relationships that could be construed as a potential conflict of interest.

Copyright © 2019 Aplin and Fridman. This is an open-access article distributed under the terms of the Creative Commons Attribution License (CC BY). The use, distribution or reproduction in other forums is permitted, provided the original author(s) and the copyright owner(s) are credited and that the original publication in this journal is cited, in accordance with accepted academic practice. No use, distribution or reproduction is permitted which does not comply with these terms.

frontiers in Neuroscience

ORIGINAL RESEARCH
published: 24 April 2019
doi: 10.3389/fnins.2019.00290

Isolated Murine Brain Model for Large-Scale Optoacoustic Calcium Imaging

Sven Gottschalk[1†], Oleksiy Degtyaruk[1†], Benedict Mc Larney[1,2], Johannes Rebling[1,2,3,4], Xosé Luis Deán-Ben[1,3,4], Shy Shoham[5] and Daniel Razansky[1,2,3,4]*

[1] Institute for Biological and Medical Imaging, Helmholtz Center Munich, Neuherberg, Germany, [2] Faculty of Medicine, Technical University of Munich, Munich, Germany, [3] Faculty of Medicine, Institute of Pharmacology and Toxicology, University of Zurich, Zurich, Switzerland, [4] Institute for Biomedical Engineering and Department of Information Technology and Electrical Engineering, ETH Zurich, Zurich, Switzerland, [5] Tech4Health and Neuroscience Institutes and Department of Ophthalmology, New York University Langone Health, New York, NY, United States

Real-time visualization of large-scale neural dynamics in whole mammalian brains is hindered with existing neuroimaging methods having limited capacity when it comes to imaging large tissue volumes at high speeds. Optoacoustic imaging has been shown to be capable of real-time three-dimensional imaging of multiple cerebral hemodynamic parameters in rodents. However, optoacoustic imaging of calcium activity deep within the mammalian brain is hampered by strong blood absorption in the visible light spectrum as well as a lack of activity labels excitable in the near-infrared window. We have developed and validated an isolated whole mouse brain preparation labeled with genetically encoded calcium indicator GCaMP6f, which can closely resemble *in vivo* conditions. An optoacoustic imaging system coupled to a superfusion system was further designed and used for rapid volumetric monitoring of stimulus-evoked calcium dynamics in the brain. These new imaging setup and isolated preparation's protocols and characteristics are described here in detail. Our new technique captures calcium fluxes as true three-dimensional information across the entire brain with temporal resolution of 10 ms and spatial resolution of 150 μm, thus enabling large-scale neural recording at penetration depths and spatio-temporal resolution scales not covered with any existing neuroimaging techniques.

Keywords: isolated brain, calcium dynamics, optoacoustic neuroimaging, functional neuroimaging, GCaMP6f

OPEN ACCESS

Edited by:
Ulrich G. Hofmann, University Medical Center Freiburg, Germany

Reviewed by:
Mikhail G. Shapiro, California Institute of Technology, United States
Adrian Rodriguez-Contreras, The City College of New York (CUNY), United States

***Correspondence:**
Daniel Razansky
daniel.razansky@uzh.ch

[†] These authors have contributed equally to this work

Specialty section:
This article was submitted to Neural Technology, a section of the journal Frontiers in Neuroscience

Received: *05 October 2018*
Accepted: *12 March 2019*
Published: *24 April 2019*

Citation:
Gottschalk S, Degtyaruk O, Mc Larney B, Rebling J, Deán-Ben XL, Shoham S and Razansky D (2019) Isolated Murine Brain Model for Large-Scale Optoacoustic Calcium Imaging. Front. Neurosci. 13:290. doi: 10.3389/fnins.2019.00290

INTRODUCTION

Each neuron's output in a mammalian brain can be connected to up to 10,000 other neurons, relaying signals between each other via as many as 10^{15} synaptic connections (Azevedo et al., 2009). These highly interconnected basic working units of the brain form specialized neuronal sub-circuits, which functionally connect into a larger network, defining the overall brain architecture (Carpenter and Sutin, 1983). Neuronal activity occurs simultaneously and in a highly coordinated fashion in many different areas across the brain, serving as a fundamental representation of information processing and transmission within the nervous system. Understanding the brain's circuit and network activity and to spatio-temporally map patterns of neuronal activity across large neuronal populations, distributed over the entire brain, is one of the most fundamental goals of neuroscience.

For this, a number of approaches are being explored towards developing imaging systems that allow non-invasive observations of larger neuronal networks with high spatio-temporal resolutions, deep inside the brain.

Blood oxygen-level dependent functional magnetic resonance imaging is one of such functional neuroimaging techniques that detects blood flow and blood oxygenation changes in the brain (Huettel et al., 2004). Such cerebral hemodynamic changes are closely linked to neural activity via neurovascular coupling, (Logothetis et al., 2001) hence fMRI can be used to deduce observations of brain activity. This, however, is also the biggest caveat of fMRI as it can only indirectly assess neuronal activity. Electroencephalography (EEG) is another established method and a valuable tool for research and diagnosis, measuring voltage fluctuations resulting from ionic currents within neurons (Niedermeyer and da Silva, 2005). Non-invasive EEG allows recording of neuronal activity using electrodes placed along the scalp, and boasts millisecond-range temporal resolution (Hämäläinen et al., 1993). A very poor spatial resolution is, however, the critical limitation of EEG, and it can only record signals generated in the superficial layers of the cortex, while neuronal activity from deeper brain areas has far less contributions to the EEG signal (Srinivasan, 1999). A more recently published study also presented a paradigm for pure ultrasound imaging able to visualize stimulus-evoked brain activation in the somatosensory cortex of the rat brain with high spatiotemporal resolution, while also recording data on cerebral blood volume and flow (Macé et al., 2011). The need for an invasive approach using a cranial window and its inability to capture differences in blood oxygenation, however, limit the utility of this ultrasound-based method.

A variety of optical imaging methods that emerged during the last two decades are also becoming alternative approaches to observe the activity of large, distributed neuronal populations (Devor et al., 2012; Adesnik et al., 2014). Among them, macroscopic optical imaging techniques like diffuse optical tomography or near-infrared spectroscopy enable the monitoring of cerebral hemodynamics and measurements of cytochrome redox states across large neuronal populations and whole brains (Durduran et al., 2010). However, these methods again lack the necessary spatio-temporal resolution required for detailed analysis of fast-paced neuronal events. Furthermore, strong light scattering in the brain prevents deep brain imaging and thus only superficial regions can be examined using pure optical methods, preventing observations of deep neural activity (Devor et al., 2012; Liao et al., 2013).

Optoacoustic imaging methods have now emerged as a powerful alternative approach for imaging optical absorption in tissues and in the brain in particular. By combining the benefits of both ultrasound and optical imaging, the optoacoustic approach overcomes the limitations of pure optical methods, allowing for very specific, non-invasive molecular imaging up to several centimeters deep in tissue, picking up at depths where state-of-the-art optical microscopy techniques fail to penetrate (Dean-Ben et al., 2017). Novel optoacoustic imaging systems now also allow the non-invasive acquisition, processing and visualization of five-dimensional optoacoustic data (Dean-Ben and Razansky, 2014; Gottschalk et al., 2017). Functional optoacoustic brain imaging has been shown to deliver real-time, volumetric and spectrally enriched tomography recordings, (Gottschalk et al., 2015b) offering unique imaging performance in comparison to other neuroimaging modalities. Until recently, optoacoustic brain imaging focused on blood oxygenation variations and hemodynamics due to the strong and spectrally distinctive optoacoustic contrast provided by oxygenated and deoxygenated hemoglobin (Yao et al., 2014). The strong intrinsic contrast provided by blood has allowed for label-free visualizations of tissue hemodynamics, (Gottschalk et al., 2015b) stimulus-induced brain function (Liao et al., 2012) and seizure activity in mice (Tsytsarev et al., 2013; Gottschalk et al., 2017). Yet, hemodynamic changes only indirectly reflect neuronal activity.

Genetically encoded calcium indicators (GECIs) that modulate their fluorescence intensity as a function of intracellular calcium concentrations are potent tools for the direct observation of rapid activity in large neuronal networks. Functional optoacoustic neuro-tomography (FONT) has recently been shown capable of imaging fast calcium activity in zebrafish brains labeled with the GCaMP-family of GECI proteins (Deán-Ben et al., 2016). However, GCaMP excitation is usually done at 488 nm wavelength, which cannot be used for imaging deep inside living mammalian brains due to the high absorption by blood and limited light penetration at this wavelength.

In order to demonstrate the fundamental capacity for calcium imaging in whole rodent brains using FONT, we developed and validated an isolated-brain preparation from GCaMP6f-expressing mice and a custom imaging setup continuously perfused with artificial cerebrospinal fluid (ACSF). The model is subsequently shown to closely resemble *in vivo* conditions, exhibiting high viability and functional activity for several hours, while also preserving the indicator responses and a realistic optical light scattering environment. Once cleared from highly absorbing blood background, large-scale optoacoustic neural recording from mouse brains is enabled at penetration depths and spatio-temporal resolution scales not covered with the existing neuroimaging techniques.

RESULTS

Validation of Brain Viability

Swift extraction of an undamaged brain was vital for the viability of the isolated brains. The procedure was performed at 4°C and it took less than 10 min from the beginning of the intracardiac perfusion until commencement of the imaging experiments (**Figure 1**). Neuronal functionality of the isolated brains was first evaluated by intracortically injecting 0.5 μl of 10 kD dextran coupled with Texas red. This is a commonly used neuronal tracer that allows for assessment of both anterograde and retrograde transport and can only be transported by living neurons via a specialized channel (Schmued et al., 1990). The injection was carried out in the cortical area of excised CD-1 mouse brains (**Figure 2**). Clear signs of neuronal uptake in and around the injection site were detected with the Texas red fluorescence. As a negative control, Texas red without dextran was injected in

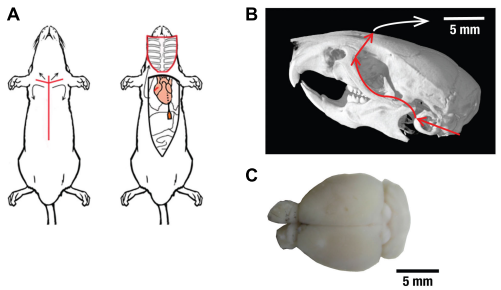

FIGURE 1 | The brain extraction procedure. **(A)** After euthanasia, the surgery began with an incision from the mid abdomen to the sternum (left image). The ventral part of the ribcage was removed to allow unhindered access to the heart. Intracardiac perfusion was then carried out by insertion of a 25G butterfly needle into the left ventricle of the heart followed by an incision to the right atrium. Images are used under the Creative Commons Attribution 3.0 International License from reference (Gage et al., 2012). Incision markers, intestinal outlines and red color around the ribcage were added and images were cropped. **(B)** After decapitation, all tissue and skin surrounding the skull was removed and the skull was rinsed with ice-cold PBS to remove any remaining debris. Using a bone scissor, the skull plate was removed after cutting along the indicated red lines. Skull image from www.digimorph.org adapted with permission from T.B. Rowe. **(C)** Color photograph of an extracted brain after it has been separated from the skull.

another excised CD-1 mouse brain, and no signs of uptake on the cellular level were observed (data not shown). Brains fixated immediately after the injection showed no neuronal transport past the injection site (**Figure 2B**), while those fixated with paraformaldehyde after 1 h of incubation time post-injection revealed structures stained by the tracer up to 2 mm away from the injection site (**Figure 2C**), thus clearly indicating transport of the tracer molecules in the neurons. Notably, the injection location cannot precisely be selected since the commonly used reference point Bregma is no longer available in the isolated brains. However, similar labeling patterns were observed when comparing our results with tracer data from the publicly available mouse connectivity Allen Brain Atlas[1].

To further evaluate the functionality of the neurons in the isolated brain preparation, EEG-recordings during application of the epileptic drug pentylenetetrazol (PTZ) were carried out (**Figure 3**). For this, EEG-data was acquired from the cortex of isolated CD-1 mouse brains and compared to *in vivo* recordings from the cortex of an anesthetized CD-1 mouse. The excised brains were either placed in oxygenated ACSF and immediately measured, or kept in PBS for 1h to ensure brain death and serve as a negative control. **Figures 3B–D** show the recorded EEG signals along with their power spectrum representing the frequency distribution of the brain activity. Low frequency signal variations of 3–7 Hz were most prominent during baseline recordings, corresponding to the anesthetized state of the brain. The noise levels of the EEG-recordings in isolated brains were higher than those in the *in vivo* experiments. The additional background noise can be ascribed to the presence of bubbles produced during

[1]http://connectivity.brain-map.org/

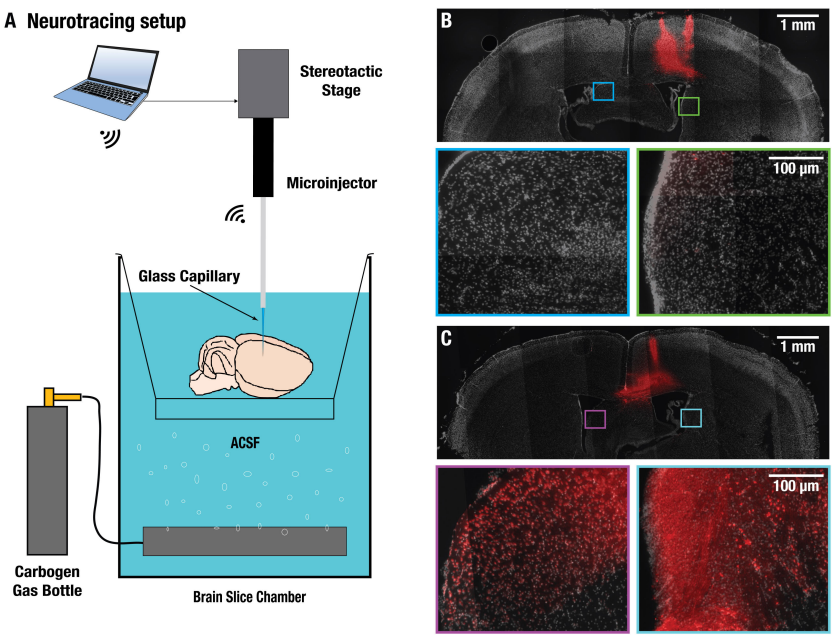

FIGURE 2 | Validation of neural transport in excised brains. **(A)** Experimental setup used for injecting dextran neural tracer coupled to Texas-red directly into the cortex of excised brains under artificial cerebrospinal fluid (ACSF) and oxygen perfusion. For intra-brain injection a wireless robotic injection system with glass micro-capillary was utilized. **(B)** Compound microscopic images of a 50 µm-thick coronal brain slice fixated immediately after the injection showed no neuronal transport past the injection site. No labeled neurons could be detected in the square labeled areas. **(C)** Slice from a brain fixated after 1 h incubation time post-injection revealed structures stained by the tracer up to 2 mm away from the injection site, thus clearly indicating active transport of the tracer molecules in the neurons.

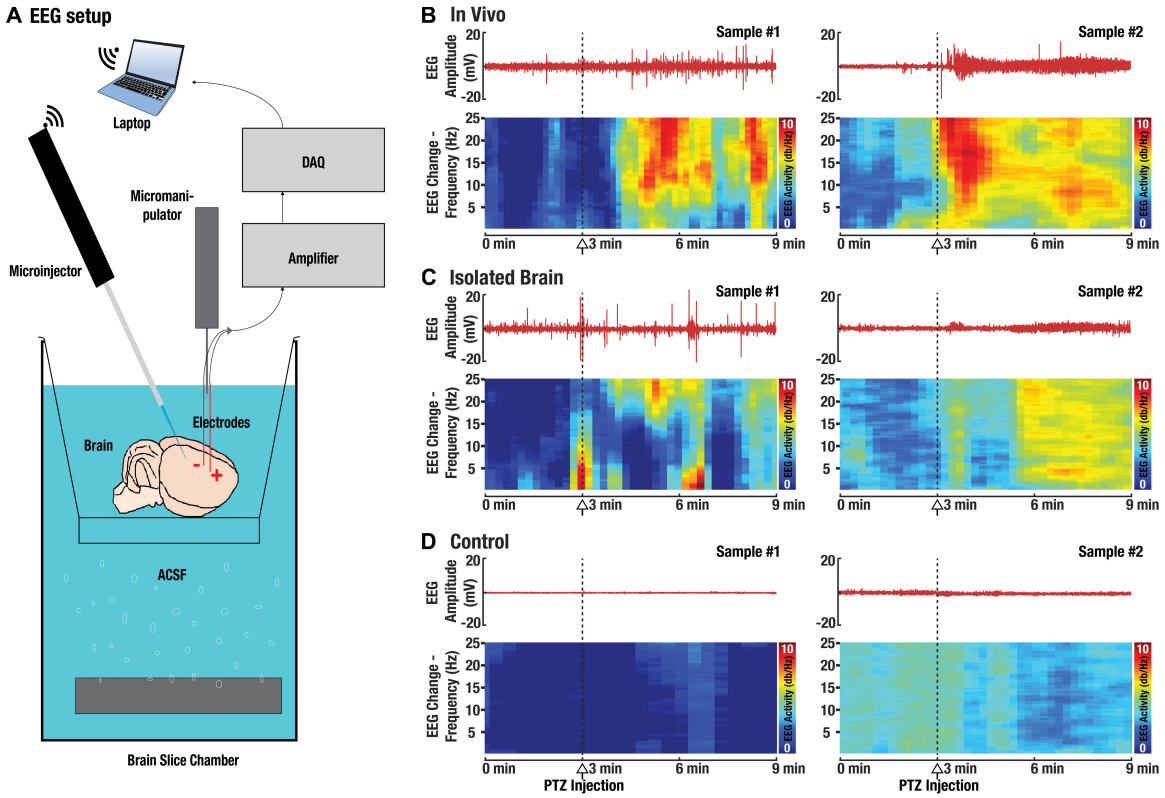

FIGURE 3 | Validation of the isolated brain viability with electroencephalography (EEG) recordings. **(A)** The EEG activity was measured using two custom-made needle electrodes connected to a differential amplifier. In order to induce widespread brain activity, an epileptic agent pentylenetetrazol (PTZ) was injected intraperitoneally. **(B)** EEG signals recorded from mouse brains *in vivo* during injection of PTZ. The signal power spectra represent the frequency distribution of the brain activity. **(C)** The corresponding EEG responses recorded from isolated brains. **(D)** No EEG activity could be detected in negative controls, i.e., brains that were kept in PBS for 1 h to ensure cell death.

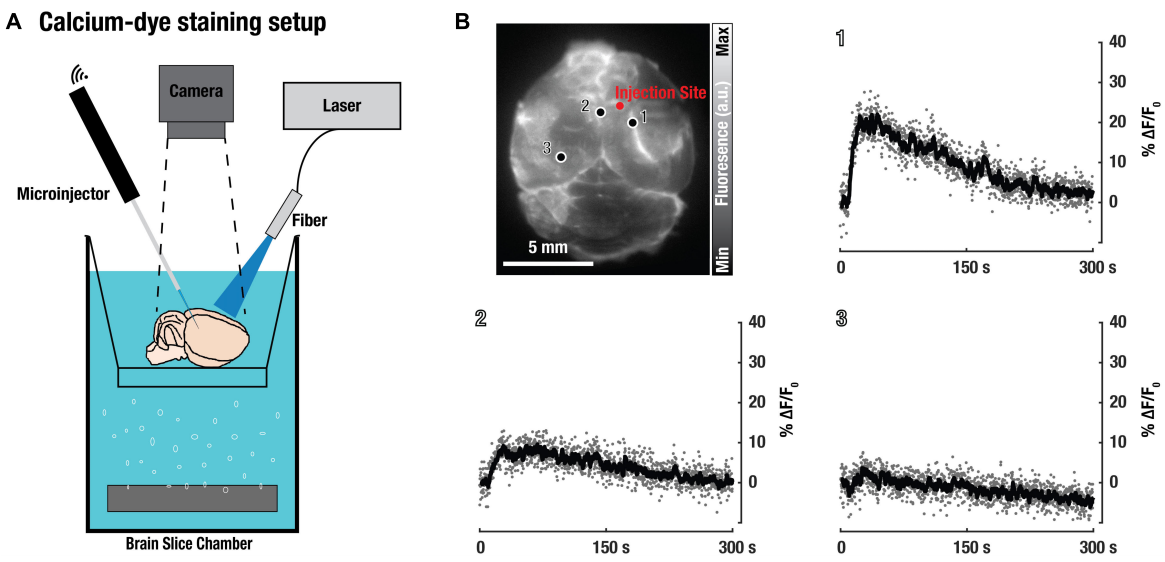

FIGURE 4 | Validation of neuronal functionality based on activity of the calcium-sensitive dye Fluo-3 in the isolated brain preparations. **(A)** Experimental setup used for fluorescence imaging of freshly excised CD-1 mouse brains labeled with the Fluo-3 dye-based calcium indicator. **(B)** Planar (wide-field) fluorescence image of the brain and signal changes in three representative areas show up to 20% increase of the fluorescence intensity following intracortical injection of the epileptic drug pentylenetetrazol.

oxygenation of the ACSF-solution as well as the necessity of placing a grounding electrode inside the isolated brain. Following a baseline recording, neuronal stimulation was induced by PTZ injection (100 μl into the tail vein for the *in vivo* recording and 5 μl of PTZ intracortically for the excised brains). The EEG signal amplitude visibly increased and higher frequency signals in the range of 10–20 Hz appeared in the frequency distribution in both *in vivo* (**Figure 3B**) and isolated brains (**Figure 3C**), while no change could be detected in the negative control (**Figure 3D**). Overall, activity in the EEG-data lasted for up to 30 min in the isolated brain preparations.

Additionally, excised brains were labeled with the calcium-indicator dye Fluo-3 in order to validate neuronal functionality (**Figure 4**). For this, freshly isolated CD-1 mouse brains were stained with Fluo-3-AM and a subsequent intracortical PTZ-injection was used to induce widespread neuronal activity. While only superficial labeling with Fluo-3 was achieved, an increase in calcium-dependent neuronal activity could be observed around the injection site (**Figure 4B**), thus further demonstrating viability and functionality of the isolated brains.

Volumetric FONT Imaging

A schematic of the imaging setup consisting of a spherical array, 3D-printed superfusion chamber and fluorescence camera is displayed in **Figure 5A**. To facilitate imaging experiments and provide appropriate experimental and environmental conditions for the isolated brain, a 3D-printed superfusion chamber was developed, as shown in **Figure 5B**. This allowed for simultaneous planar fluorescence and volumetric optoacoustic imaging of stimulus-evoked brain responses. Nine optical fibers, coupled to an optical parametric oscillator (OPO laser), illuminated the brain from multiple directions to create nearly uniform illumination conditions on its surface. Superfusion inlet and outlet ports were incorporated into the design to establish a physiological environment for the isolated brain by pumping oxygenated ACSF at 37°C around the isolated brain. The spherical ultrasound detection array was designed to provide a field-of-view (FOV) of ∼2 cm^3 efficiently covering the entire mouse brain with nearly isotropic three-dimensional (3D) resolution of ∼150 μm. This corresponds to about one million individual voxels that can be visualized within the FOV at a volumetric imaging rate of 100 Hz (see section "Materials and Methods" for details of the FONT setup).

Figure 6A shows an isolated GCaMP6f-brain as seen under wide-field fluorescence imaging. Naturally, planar fluorescence can only visualize the brain in 2D along the transverse plane. Whilst some anatomical features can be distinguished, the fluorescence images have a very diffuse appearance making it impossible to discriminate signals originating from different depths due to the intense scattering of light in the brain. As a result, quantification of the measurements is severely compromised since the true origin of the signal cannot be accurately determined. In contrast, FONT is readily capable of imaging the entire volume of the isolated brain along the transverse, sagittal and coronal planes, at a high spatial resolution and in 3D (**Figure 6B**). A range of anatomical features can clearly be determined, including complete cortices, the cerebellum, the olfactory bulb and the medulla (**Figure 6C**), thus showcasing the high-resolution volumetric imaging capabilities of FONT and its ability to capture detailed information from the entire isolated brain measuring ∼15 mm along its long axis. **Figure 6D** further shows single transverse slices of the brain further highlighting the high effective penetration depth of FONT not achievable with other optical imaging modalities.

Simultaneous Fluorescence and FONT of Stimulated Calcium Activity

Concurrent fluorescence and FONT imaging of stimulus-evoked calcium activity was used to verify neural activity in the isolated brain model and to validate that signals related to neural calcium dynamics only originate from the GCaMP6f-protein. For this, the neuro-activating agent pentylenetetrazol was injected into the cortex of isolated mouse brains. PTZ is known to interfere with GABAergic signaling thus actuating fast seizure-like activity in the nervous system (Dhir, 2012). Experiments were performed on excised brains from GCaMP6f-expressing mice and CD-1 mice injected with PTZ, with both brains from CD-1 mice injected with PTZ and GCaMP6f-expressing brains injected with PBS, serving as negative controls (**Figures 7A,C,G,I**). Intracortical injection of PTZ resulted in an increase of fluorescence signals of up to 50% over baseline levels in the GCaMP6f-brains (**Figures 7E,F** and **Supplementary Video S1**), while no significant changes could be detected in either of the controls (**Figures 7A–D**). Notably, the time course of the GCaMP6f fluorescence signal is different from Fluo-3 (**Figure 4B**), which can be attributed to the different distribution patterns of the two reporters inside the tissue and cells (Dana et al., 2014a; Johnson and Spence, 2010). The molecular reporter Fluo-3 is also more prone to bleaching when compared to protein-based reporters (Gottschalk et al., 2015a). FONT can be used to three-dimensionally map stimulated calcium activity in the whole isolated mouse brain following PTZ injection (**Figures 7G,H,K,L**). The simultaneously recorded FONT data can directly be compared to the fluorescence results. Injection of PTZ into CD-1 mouse brains (n = 3) and injection of PBS into GCaMP6f-brains (n = 3) resulted in no significant changes in the optoacoustic signals anywhere inside the brain (**Figures 7G–J**). On the other hand, neuronal activation by PTZ and hence calcium changes could readily be observed in the GCaMP6f-expressing brains that were stimulated with PTZ (n = 4, **Figures 7K,L** and **Supplementary Video S1**). Analysis of small volumes of interest (3*3*3 voxels) located 1 mm deep inside the brain again revealed signal increases up to 70% over baseline levels prior to the PTZ injection. Note that the detected OA signal variations were stronger than the corresponding GCaMP6f fluorescence changes, most likely due to the diffuse nature and higher background signal levels of the planar fluorescence modality.

DISCUSSION AND CONCLUSION

Optoacoustic imaging has recently emerged as a new method for functional brain imaging, enabling non-invasive visualization

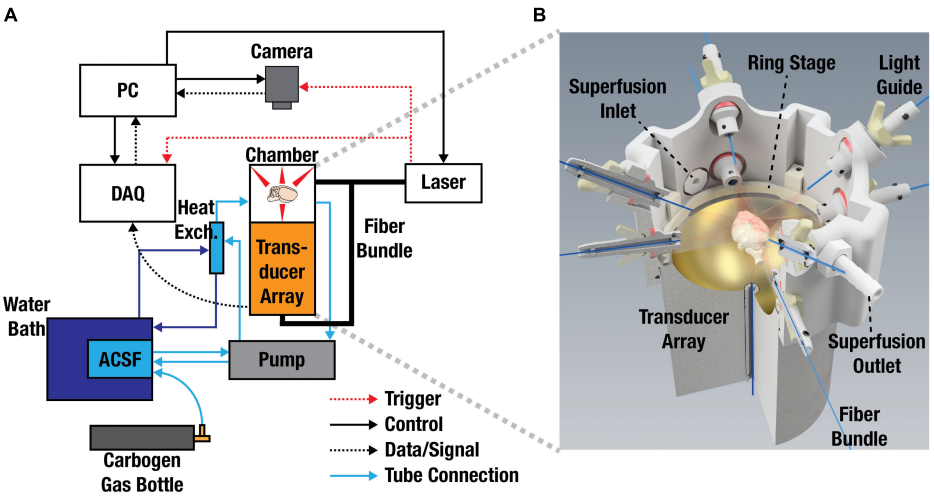

FIGURE 5 | Experimental Layout and system design. **(A)** Layout of the experimental setup used for simultaneous recording of fluorescence and optoacoustic responses from the isolated mouse brains. ACSF, artificial cerebrospinal fluid; DAQ, data acquisition unit; PC, personal computer. **(B)** 3D-rendering of the experimental chamber accommodating the light illumination arrangement, spherical transducer array, superfusion system, and the imaged sample. The isolated brain is placed on top of a transparent polyethylene foil (not shown for simplicity).

and quantification of cerebral hemodynamic changes related to functional activity deep in mammalian brains, inaccessible by common high-resolution optical microscopy methods. Yet, strong absorption of light by hemoglobin remains the main limitation for direct visualization of calcium activity in the whole brain. While other blood-free preparations exist, including cell cultures (Pampaloni et al., 2007; Dana et al., 2014b) or brain slices, (Mainen et al., 1999; Llinás et al., 2002) such models fail to represent long-ranging neuronal interactions and network context at a whole brain level. Our study is the first to demonstrate the possibility and validity of a functional excised mouse brain cleared of blood for direct optoacoustic tracking of calcium dynamics associated with neuronal activity in real time in the whole mammalian brain.

In previously reported studies, guinea-pig brains were isolated and perfused through the cortical vasculature, exhibiting a reaction to electrical stimuli for up to 8 h (Mühlethaler et al., 1993). Smaller isolated zebra-fish brains retained functionality for up to 7 days, as verified by the ability to transport horseradish peroxidase and required no perfusion, relying on diffusion to supply the brain with nutrients (Tomizawa et al., 2001). Another study using excised mouse brains also successfully verified recordings of extracellular field potentials and neuronal tracer transport up to 24 h after extraction without the need for vascular perfusion (Von Bohlen and Halbach, 1999). In our own isolated brain preparation, brain viability was validated by Dextran transport experiments while results of the EEG recordings further indicated the presence of neuronal activity for at least 30 min after brain extraction. Since the total imaging experiment duration did not exceed this time, the data acquired in our experiments can be assumed to reflect *in vivo*-like neuronal functionality.

Considering ethical implications, the use of a ketamine/xylazine mixture is an established form of anesthesia, with sedation lasting up to ∼120 min (Erhardt et al., 1984; Gleed and Ludders, 2001). Ketamine produces anesthetic, dissociative, hallucinogenic, amnesic and analgesic effects in the central nervous system by functioning as an NMDAR antagonist (Kohrs and Durieux, 1998; Quibell et al., 2011). In the current study, by employing relatively high ketamine doses and restricting the total experiment duration to 30 min from the start of perfusion, we ensured the excised brain would remain anesthetized throughout the procedure. At the same time, this could affect neuronal transmission functionality by dampening responses to stimuli and the associated calcium fluxes, the extent of which should be addressed in future experiments. Nonetheless, FONT allowed for an unambiguous detection of calcium fluxes as true high resolution 3D-information not affected by intense light scattering in the brain. In contrast, epi-fluorescence recordings failed to provide high resolution maps of depth-resolved calcium dynamics.

In conclusion, we have developed a novel isolated mouse brain preparation and an accompanying imaging setup to optoacoustically monitor calcium dynamics under blood-free conditions. The developed methodology could readily be adapted to work with future generations of far-red- and near-infrared GECIs. Yet, our current results utilizing GCaMP-proteins in the visible range clearly show that deep brain optoacoustic visualization of activity-related calcium signals is achievable in whole rodent brains.

MATERIALS AND METHODS

Isolated Brain Preparation

CD-1 mice aged between 6 and 36 weeks (Envigo, Rossdorf, Germany) were used in these experiments as well as C57BL/6J-Tg(Thy1-GCaMP6f)GP5.5Dkim/J mice aged between 36 and 68 weeks (The Jackson Laboratory, Bar Harbor, ME,

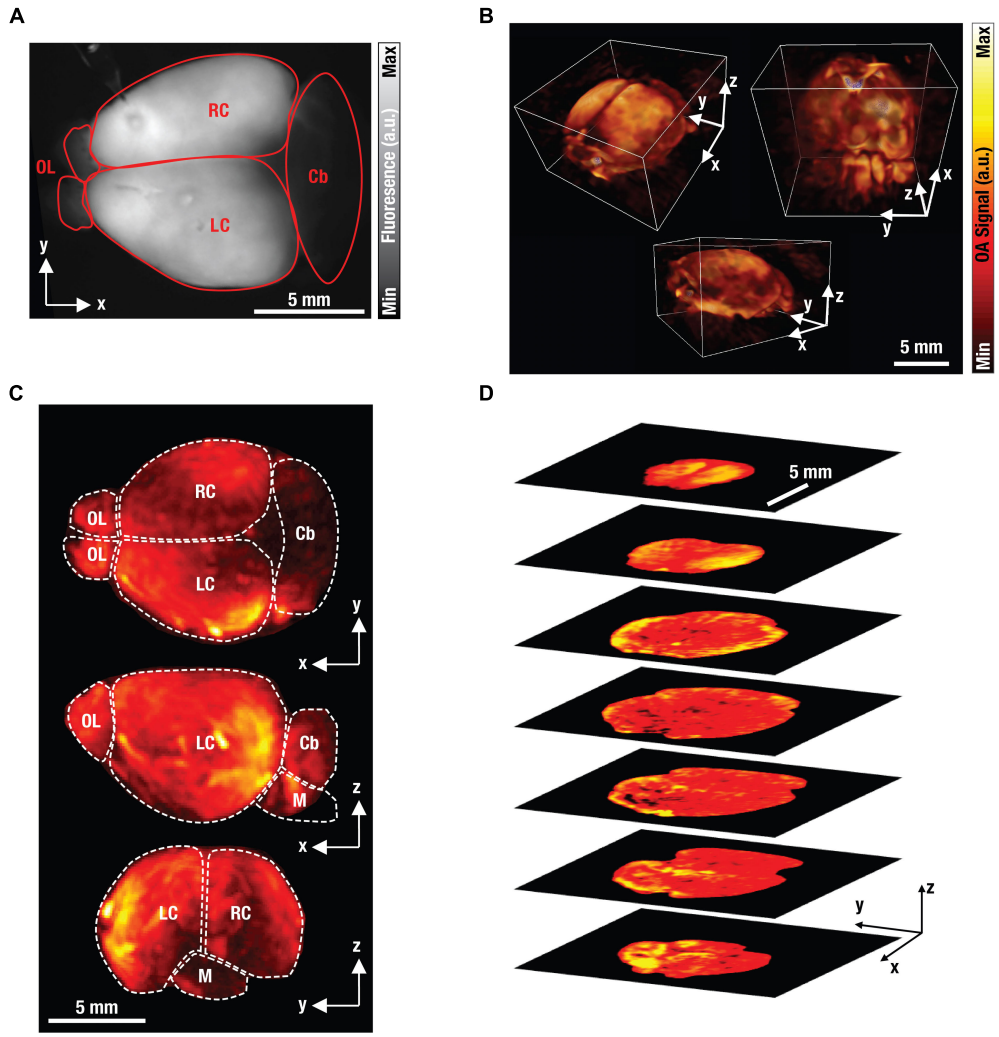

FIGURE 6 | Fluorescence and optoacoustic images of excised brain. **(A)** Planar (wide-field) fluorescence image of an isolated GCaMP6f-labeled mouse brain. For abbreviations see **(C)** below. **(B)** The corresponding volumetric FONT images of the brain. **(C)** Maximum intensity projections of the FONT image. Cb, cerebellum; M, medulla; OL, olfactory bulb; R/LC, right/left cortex. **(D)** Single transverse slices through the brain to highlight the high effective penetration depth of FONT.

United States; stock number 024276) (Dana et al., 2014a). This study was carried out in accordance with the recommendations of the Institute for Biological and Medical Imaging. The protocol was approved by the Government District of Upper Bavaria.

The brain slice chamber (Scientific Products GmbH, Hofheim, Germany) surrounded by ice, was filled with ice-cold oxygenated ACSF and further supplied with freshly oxygenated ACSF (**Figures 2A**, **3A**, **4A**). For cardiac perfusion (**Figure 1A**) ACSF was circulated at a rate of 10 ml/min through a bubble trap and a 25G butterfly infusion set. Mice were anesthetized via a lethal dose of a Ketamine/Xylazine-mixture, administered via an intraperitoneal injection. Surgery commenced once the animal was completely anesthetized as determined by the absence of a toe-pinch reflex at one of the hindpaws. As shown in **Figure 1A**, surgery began with an incision from the mid abdomen to the sternum. The ventral part of the ribcage was removed to allow unhindered access to the heart. Intracardiac perfusion was carried out by the insertion of a 25G butterfly needle into the left ventricle of the heart followed by an incision into the right atrium. A perfusion pump (Cole-Parmer, Vernon Hills, IL, United States) was used to ensure continuous flow and appropriate pressure of blood and perfusion fluid until both the liver and lungs turned white.

At this stage, decapitation was performed. All tissue and skin surrounding the skull was removed and the skull was rinsed with ice-cold PBS to remove any remaining debris. A cut was then made between the skull and the first cervical vertebra exposing the brain stem (**Figure 1B**). Using a bone scissors, a second cut was made on both sides of the skull. This cut extended from the foramen magnum to the external auditory meatus, and then from the molar process up to the lachrymal dorsal aspect of the skull. Using forceps, the upper skull plate along with the brain were separated from the lower skull and placed

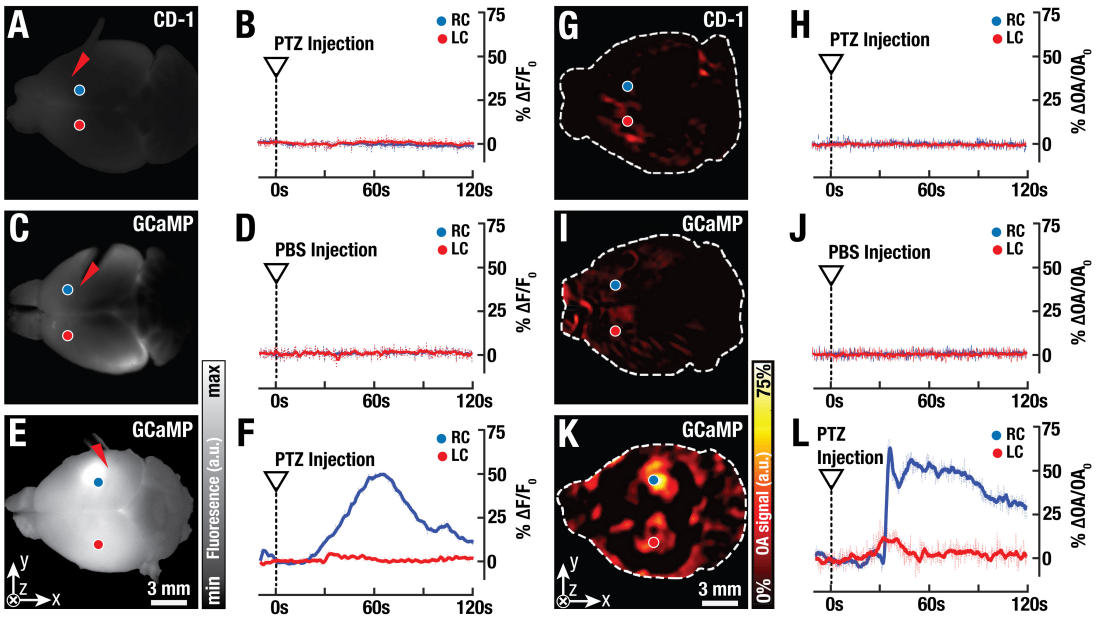

FIGURE 7 | Simultaneously recorded fluorescence and FONT responses in isolated GCaMP6f-brains. **(A)** Planar (wide-field) fluorescence image of an isolated control brain from a CD-1 mouse. **(B)** Normalized time plots from two representative areas of the control brain (20*20 pixels, blue and red circles) reveal no fluorescence activity during injection of the epileptic drug pentylenetetrazol (PTZ) into the brain (injection site indicated by red arrowhead). **(C)** A GCaMP6f-labeled brain exhibits higher background fluorescence levels. **(D)** No activity is detected after injection of phosphate buffered saline (PBS) into the GCaMP6f-labeled brain. **(E)** Planar fluorescence image of a GCaMP6f-labeled brain at ∼40 s post-injection of PTZ. **(F)** The corresponding time trace. **(G)** A 1 mm deep slice of the volumetric FONT image reconstructed from a control CD-1 mouse brain. **(H)** Injection of PTZ into CD-1 mouse brains without GCaMP6f-expression results in no detectable optoacoustic signal variations. **(I)** The FONT slice from a GCaMP6f-expressing brain injected with PBS. **(J)** The corresponding temporal trace reveals no activity. **(K)** Neuronal activation and hence calcium changes are readily observed in the FONT image of GCaMP6f-expressing brains at ∼40 s post PTZ injection. **(L)** Analysis of small volumes of interest in the GCaMP6f-expressing brains (3*3*3 voxels, indicated by blue and red circles) revealed signal increases up to 70% over baseline levels prior to the PTZ injection.

into a Petri dish filled with ice-cold oxygenated ACSF. The brain was separated from the skull using a forceps and placed in a Petri dish filled with fresh ice-cold oxygenated ACSF. Any remaining hair, debris or blood vessels were removed using a fine forceps and pipette. This isolated brain was then directly used for further experiments.

Dextran Tracing

Axonal tracer transport requires intact, functioning neurons and dextran-amines coupled to fluorescent molecules are known for being transported in both the anterograde and retrograde direction (Vercelli et al., 2000). In order to validate the functionality of axonal transport in the isolated brain preparations, 10 kDa dextran coupled to Texas-red (Thermo Fisher Scientific, Waltham, MA, United States) was injected directly into the cortex of excised brains (**Figures 2B,C**). For this, freshly isolated brains were placed in a brain slice chamber (Scientific Products GmbH, Hofheim, Germany) filled with ACSF and with constant supply of a mixture of 95% O_2/5% CO_2 (Carbogen LAB, The Linde Group, Muenchen, Germany) to keep the solution oxygenated. For intra-brain injection a wireless robotic injection system (Neurostar, Tübingen, Germany) using a 15 to 25 μm diameter pulled glass micro-capillary was utilized. Injections of 0.5 μL volumes were made ∼1 mm deep inside the cortex (n = 4). As controls, either PBS or Texas red without Dextran were injected under the same conditions (n = 3). Afterward, the brains were fixated in 4% paraformaldehyde either immediately after injection, or after being kept in oxygenated ACSF at 4°C in the dark for 1 h. For evaluation of axonal transport, fixed brains were then sliced into 50 μm-thick sections. For this, the brains were first dehydrated in a solution of 30% sucrose at 4°C for 48 h, to remove water and to prevent ice-crystal formation during cryoslicing. Subsequently, the brains were embedded into an optimal cutting temperature compound (Tissue-Tek®, Sakura Finetek, Alphen an deen Rijn, Netherlands) and sliced with a CM 1950 Cryo-slicer (Leica Mikrosysteme, Wetzlar, Germany) along the coronal plane. The slices were then mounted onto microscope slides, air-dried for 20 min in the dark and a coverslip was placed on top of the slices and sealed with Vectashield containing DAPI (Vector Laboratories Inc., Burlingame, CA, United States). DAPI stains the DNA and RNA of cells, hence outlining cellular anatomy. Compound brain slice images were captured using an Axio Imager M2 microscope (Carl Zeiss AG, Oberkochen, Germany) fitted with shift-free DAPI and Texas red filter sets (EX TBP 400+495+570, BS FT 410+505+585, EM TBP 460+530+625, Carl Zeiss AG, Oberkochen, Germany). Image acquisition and analysis was done using the Zeiss Zen 2 microscope software.

Electroencephalography Recording

The experimental setup for Electroencephalography (EEG) recordings is depicted in **Figure 3A**. EEG-signals were recorded via two custom-made needle electrodes, connected to a DP-311 differential amplifier (Warner Instruments, LLC, Hamden, CT, United States) and the amplified signals were digitized by means of a PowerLab26T data acquisition module (AD Instruments, Sydney, Australia), controlled through a host PC running the Labchart 8 software (AD Instruments, Sydney, Australia). For comparison, *in vivo* EEG-data of CD-1 mice (n = 3) was also recorded as described previously (Gottschalk et al., 2017). In order to induce widespread brain activity the epileptic drug PTZ was injected intraperitoneally (IP) (Tang et al., 2015). For *in vivo* EEG-recordings the differential amplifier was set to a high pass of 10 Hz, a low pass of 100 Hz and a gain of 100. After baseline recording, 100 μL of PTZ (100 mg/ml in saline) was injected IP and the mouse was euthanized under anesthesia at the end of the experiment. For recordings in isolated brains (n = 3), freshly excised brains were placed in a brain slice chamber (Scientific Products GmbH, Hofheim, Germany) filled with oxygenated ACSF at room temperature (RT). To induce brain activity, 5 μL of PTZ (100 mg/ml in ACSF) was directly injected into the cortex using a pulled glass capillary and a robotic injection system (Neurostar, Tübingen, Germany). For all *ex vivo* EEG-recordings (n = 4 for control), the amplifier settings were the same as for the *in vivo* recordings. The recorded EEG signals were processed using MatLab (MathWorks, Natick, United States) to identify periods of elevated brain activity. For this, the EEG spectrogram was calculated as the short-time Fourier transform with a window of 20 s, sufficient for detecting higher frequency components in the 10–20 Hz range corresponding to seizure-like activity caused by PTZ.

Calcium-Dye Staining

Fluo-3-AM is a fluorescent dye-based calcium indicator that can be used to investigate spatial dynamics of many calcium-dependent signaling processes (Lambert, 2006). Freshly excised CD-1 mouse brains were labeled with Fluo-3 (10 mM Fluo-3-AM and 1 mM Probenecid in oxygenated ACSF) for 20 min in the dark at RT (n = 4). After labeling, the brains were washed twice with ACSF, left to rest in oxygenated ACSF for another 15 min in the dark at RT, and were then placed into the experimental setup for fluorescence imaging, as depicted in **Figure 4A**. A custom-made fiber bundle (CeramOptics GmbH, Bonn, Germany) was used to guide excitation light to the brain from a nanosecond-pulsed optical parametric oscillator laser source (Innolas GmbH, Krailling, Germany). In order to stimulate brain activity, 5 μL of PTZ (100 mg/ml in ACSF) was injected at ∼1 mm depth in the cortex using a pulled glass capillary connected to a robot injection system (Neurostar, Tuebingen, Germany). Fluorescence was recorded during the entire procedure, before and after injection of PTZ.

Imaging Set-Up

A layout of the imaging set-up used for the simultaneous recording of fluorescence and optoacoustic readings of the excised mouse brain is depicted in **Figure 5**. Optoacoustic imaging was performed with a custom-made spherical transducer array (Imasonic SaS, Voray, France) with 40 mm radius consisting of 512 piezocomposite elements covering an angle of 140° (1.3π solid angle). The elements have 2.5 mm diameter, 5 MHz central frequency and 100% −6 dB bandwidth, providing an almost isotropic resolution of 150 μm over an approximate FOV of ∼2 cm^3. The array was held pointing upward via a 3D-printed chamber attached to a X-Y positioning platform (**Figure 5B**). In the experiments, oxygenated ACSF was pumped through an inlet and an outlet in the holder. ACSF is needed for preserving the brain functional and further provides acoustic coupling for the optoacoustically generated ultrasound waves. The whole chamber was made waterproof by smoothening with a sand paper and applying a silicone finish. Further sealing was ensured with the addition of rubber "O-rings" at all openings including two larger "O-rings" surrounding the transducer array. The excised brain was placed approximately at the center of the FOV of the spherical matrix transducer array lying upon a ∼10 μm transparent polyethylene foil glued to a 3D-printed ring stage. Brain illumination was done via a self-developed fiber bundle consisting of nine fibers with a core diameter of 600 μm. One of the fibers was inserted into a cylindrical cavity of the spherical array to illuminate the bottom part of the brain while the other 8 were embedded in apertures in the array holder equally spaced at 90° in azimuth and with polar angles of 5.7° and 37° (**Figure 5B**). The illumination source was an optical parametric oscillator (OPO)-based laser (Innolas GmbH, Krailling, Germany) providing short (<10 ns) pulses at 25 Hz with optical wavelength set to 488 nm. The 512 optoacoustic signals detected by the array elements were simultaneously digitized with a custom-made data acquisition system (Falkenstein Microsystem GmbH, Taufkirchen, Germany) triggered with the Q-switch output of the laser. The digitized signals were transferred to a PC via 1 Gbit/s Ethernet for further processing. A high speed EMCCD camera (Andor Technology Ltd., Belfast, United Kingdom) located on top of the chamber (pointing downward) was used to record the fluorescence responses of the isolated brains being illuminated with the laser source. The camera was equipped with a 105 mm Nikon F mount objective (Nikon, Chiyoda, Tokio, Japan) and a one-inch emission filter with 525 nm center wavelength and 39 nm bandwidth (MF525-39, Thorlabs Inc., Newton, United States). The acquisition time of the camera was set to 200 ms, corresponding to the integration of five laser pulses. The relative positions of the transducer array and the camera were manually adjusted with the X-Y positioning platform holding the transducer array.

Data Analysis and Processing

The relative fluorescence signal changes ($\Delta F/F_0$) were calculated from the recorded images as changes in signal intensity following the PTZ injection. These changes correspond to the calcium responses evoked by neural activity. The baseline fluorescence signal level F_0 was calculated as the average of frames over 5 s

preceding the injection. Volumetric (3D) optoacoustic images were reconstructed from the acquired signals using a graphics processing unit based implementation of a back-projection formula (Dean-Ben et al., 2013). Before reconstruction, the signals were deconvolved with the impulse response of the transducer array elements and a band-pass filter with cut-off frequencies of 0.1 and 6 MHz was applied. The reconstruction of the optoacoustic data was performed on a grid of $150 \times 150 \times 100$ voxels^3 (equivalent to $15 \times 15 \times 10$ mm^3) to match the spatial resolution of the system.

AUTHOR CONTRIBUTIONS

OD performed all experiments. OD, BML, and JR designed and fabricated the 3D-printed chamber. SG, OD, BML, JR, and XLDB analyzed and processed the data. SG, SS, and DR validated the data analysis. SG, SS, and DR designed and led the study. All authors wrote, read, and accepted the manuscript.

FUNDING

The authors acknowledge grant support from the European Research Council under grant agreement ERC-2015-CoG-682379 and the United States National Institutes of Health under grant numbers R21-EY026382 and UF1-NS107680.

SUPPLEMENTARY MATERIAL

The Supplementary Material for this article can be found online at: https://www.frontiersin.org/articles/10.3389/fnins.2019.00290/full#supplementary-material

VIDEO S1 | Video of a concurrent fluorescence and optoacoustic recording of a GCaMP6f-brain. The video shows the changes in fluorescence (planar image) and the optoacoustic signal (MIP, maximum intensity projection) upon injection of the epileptic drug pentylenetetrazol (PTZ, injection at time 0). Clear neuronal activation by PTZ as reflected by calcium changes can be observed in both fluorescence and optoacoustic data. CB, cerebellum; L/RC, left/right cortex; OL, olfactory bulb.

REFERENCES

Adesnik, H., Waller, L., and Shoham, S. (2014). Optics on the brain: OSA's mulitphoton and patterned optogenetics incubator. *Opt. Photonics News* 25, 42–49. doi: 10.1364/OPN.25.4.000042

Azevedo, F. A., Carvalho, L. R. B., Grinberg, L. T., Farfel, J. M., Ferretti, R. E. L., Leite, R. E. P., et al. (2009). Equal numbers of neuronal and nonneuronal cells make the human brain an isometrically scaled-up primate brain. *J. Comp. Neurol.* 513, 532–541. doi: 10.1002/cne.21974

Carpenter, M. B., and Sutin, J. (1983). *Human Neuroanatomy*. Philadelphia, PA: Williams & Wilkins

Dana, H., Chen, T. W., Hu, A., Shields, B. C., Guo, C., Looger, L. L., et al. (2014a). Thy1-GCaMP6 transgenic mice for neuronal population imaging in vivo. *PLoS One* 9:e108697. doi: 10.1371/journal.pone.0108697

Dana, H., Marom, A., Paluch S., Dvorkin, R., Brosh, I., Shoham, S., et al. (2014b). Hybrid multiphoton volumetric functional imaging of large-scale bioengineered neuronal networks. *Nat. Commun.* 5:3997 doi: 10.1038/ncomms4997

Dean-Ben, X. L., Ozbek, A., and Razansky, D. (2013). Volumetric real-time tracking of peripheral human vasculature with GPU-accelerated three-dimensional optoacoustic tomography. *IEEE Trans. Med. Imaging* 32, 2050–2055. doi: 10.1109/TMI.2013.2272079

Dean-Ben, X. L., and Razansky, D. (2014). Adding fifth dimension to optoacoustic imaging: volumetric time-resolved spectrally enriched tomography. *Light Sci. Appl.* 3:e137. doi: 10.1038/lsa.2014.18

Deán-Ben, X. L., Sela, G., Lauri, A., Kneipp, M., Ntziachristos, V., Westmeye, G. G., et al. (2016). Functional optoacoustic neuro-tomography for scalable whole-brain monitoring of calcium indicators. *Light Sci. Appl.* 5:e16201. doi: 10.1038/lsa.2016.201

Dean-Ben, X. L., Gottschalk, S., Mc Larney, B., Shoham, S., and Razansky, D. (2017). Advanced optoacoustic methods for multiscale imaging of in vivo dynamics. *Chem. Soc. Rev.* 46, 2158–2198. doi: 10.1039/C6CS00765A

Devor, A., Sakadžić, S., Srinivasan, V. J., Yaseen, M. A., Nizar, K., Saisan, P. A., et al. (2012). Frontiers in optical imaging of cerebral blood flow and metabolism. *J. Cereb. Blood Flow Metab.* 32, 1259–1276. doi: 10.1038/jcbfm.2011.195

Dhir, A. (2012). Pentylenetetrazol (PTZ) kindling model of epilepsy. *Curr. Protoc. Neurosci.* 58, 9.37.1–9.37.12 doi: 10.1002/0471142301.ns0937s58

Durduran, T., Choe, R., Baker, W., and Yodh, A. (2010). Diffuse optics for tissue monitoring and tomography. *Rep. Prog. Phys.* 73:076701. doi: 10.1088/0034-4885/73/7/076701

Erhardt, W., Hebestedt, A., Aschenbrenner, G., Pichotka, B., and Blümel, G. (1984). A comparative study with various anesthetics in mice (pentobarbitone, ketamine-xylazine, carfentanyl-etomidate). *Res. Exp. Med.* 184, 159–169. doi: 10.1007/BF01852390

Gage, G. J., Kipke, D. R., and Shain, W. (2012). Whole animal perfusion fixation for rodents. *J. Vis. Exp.* 65:e3564. doi: 10.3791/3564

Gleed, R. D., and Ludders, J. (2001). *Recent Advances in Veterinary Anesthesia and Analgesia: Companion Animals*. (Ithaca, NY: International Veterinary Information Service).

Gottschalk, S., Estrada H., Degtyaruk, O., Rebling, J., Klymenko, O., Rosemann, M., et al. (2015a). Short and long-term phototoxicity in cells expressing genetic reporters under nanosecond laser exposure. *Biomaterials* 69, 38–44. doi: 10.1016/j.biomaterials.2015.07.051

Gottschalk, S., Fehm, T. F., Dean-Ben, X. L., and Razansky, D. (2015b). Noninvasive real-time visualization of multiple cerebral hemodynamic parameters in whole mouse brains using five-dimensional optoacoustic tomography. *J. Cereb. Blood Flow Metab.* 35, 531–535. doi: 10.1038/jcbfm.2014.249

Gottschalk, S., Fehm, T. F., Deán-Ben, X. L., Tsytsarev, V., and Razansky, D. (2017). Correlation between volumetric oxygenation responses and electrophysiology identifies deep thalamocortical activity during epileptic seizures. *Neurophotonics* 4:011007 doi: 10.1117/1.NPh.4.1.011007

Hämäläinen, M., Hari, R., Ilmoniemi, R. J., Knuutila, J., and Lounasmaa, O. V. (1993). Magnetoencephalography—theory, instrumentation, and applications to noninvasive studies of the working human brain. *Rev. Mod. Phys.* 65, 413–497. doi: 10.1103/RevModPhys.65.413

Huettel, S. A., Song, A. W., and McCarthy, G. (2004). *Functional Magnetic Resonance Imaging*. Vol. 1, Sunderland: Sinauer Associates

Johnson, I., and Spence, M. T. Z. (2010). Molecular Probes Handbook: A Guide to Fluorescent Probes and Labeling Technologies, 11th Edn. (Carlsbad, CA: Life Technologies).

Kohrs, R., and Durieux, M. E. (1998). Ketamine: teaching an old drug new tricks. *Anesth. Analg.* 87, 1186–1193.

Lambert, D. G. (2006). *Calcium Signaling Protocols*. Vol. 312 (Berlin: Springer Science & Business Media).

Liao L. D., Lin, C. T., Shih, Y. Y., Duong, T. Q., and Lai, H. Y., Wang, P. H. et al. (2012). Transcranial imaging of functional cerebral hemodynamic changes in single blood vessels using in vivo photoacoustic microscopy. *J. Cereb. Blood Flow Metab.* 32, 938–951. doi: 10.1038/jcbfm.2012.42

Liao, L. D., Tsytsarev, V., Delgado-Martínez, I., Li, M. L., Erzurumlu, R., Vipin, A., et al. (2013). Neurovascular coupling: in vivo optical techniques for functional brain imaging. *Biomed. Eng. Online* 12:38. doi: 10.1186/1475-925X-12-38

Llinás, R. R., Leznik, E., and Urbano, F. J. (2002). Temporal binding via cortical coincidence detection of specific and nonspecific thalamocortical inputs:

a voltage-dependent dye-imaging study in mouse brain slices. *Proc. Natl. Acad. Sci. U.S.A.* 99, 449–454. doi: 10.1073/pnas.012604899

Logothetis, N. K., Pauls, J., Augath, M., and Trinath, T., Oeltermann, A. (2001). Neurophysiological investigation of the basis of the fMRI signal. *Nature* 412, 150–157. doi: 10.1038/35084005

Mainen, Z., Maletic-Savatic, M., Shi, S. H., Hayashi, Y., Malinow, R., Svoboda, K., et al. (1999). Two-photon imaging in living brain slices. *Methods* 18, 231–239. doi: 10.1006/meth.1999.0776

Macé, E., Montaldo, G., Cohen, I., Baulac, M., Fink, M., Tanter, M., et al. (2011). Functional ultrasound imaging of the brain. *Nat. Methods* 8, 662–664. doi: 10.1038/nmeth.1641

Mühlethaler, M., Curtis, M., Walton, K., and Llinas, R. (1993). The Isolated and Perfused Brain of the Guinea-pig In Vitro. *Eur. J. Neurosci.* 5, 915-926. doi: 10.1111/j.1460-9568.1993.tb00942.x

Niedermeyer, E., and da Silva, F. L. (2005). *Electroencephalography: Basic Principles, Clinical Applications, and Related Fields*. Philadelphia, PA: Lippincott Williams & Wilkins

Pampaloni, F., Reynaud, E. G., and Stelzer, E. H. (2007). The third dimension bridges the gap between cell culture and live tissue. *Nat. Rev. Mol. Cell Biol.* 8, 839–845. doi: 10.1038/nrm2236

Quibell, R., Prommer, E. E., Mihalyo, M., Twycross, R., and Wilcock, A. (2011). Ketamine. *J. Pain Symptom Manage.* 41, 640–649. doi: 10.1016/j.jpainsymman.2011.01.001

Schmued, L., Kyriakidis, K., and Heimer, L. (1990). In vivo anterograde and retrograde axonal transport of the fluorescent rhodamine-dextran-amine, Fluoro-Ruby, within the CNS. *Brain Res.* 526, 127-134. doi: 10.1016/0006-8993(90)90258-D

Srinivasan, R. (1999). Methods to improve the spatial resolution of EEG. *Int. J. Bioelectromagn.* 1, 102–111.

Tang, J., Xi, L., Zhou, J., Huang, H., Zhang, T., Carney, P. R., et al. (2015). Noninvasive high-speed photoacoustic tomography of cerebral hemodynamics in awake-moving rats. *J. Cereb. Blood Flow Metab.* 35, 1224–1232. doi: 10.1038/jcbfm.2015.138

Tsytsarev, V., Rao, B., Maslov, K. I., Li, L., and Wang, L. V. (2013). Photoacoustic and optical coherence tomography of epilepsy with high temporal and spatial resolution and dual optical contrasts. *J. Neurosci. Methods* 216, 142–145. doi: 10.1016/j.jneumeth.2013.04.001

Tomizawa, K., Kunieda, J. I., and Nakayasu, H. (2001). Ex vivo culture of isolated zebrafish whole brain. *J. Neurosci. Methods* 107, 31–38. doi: 10.1016/S0165-0270(01)00349-1

Vercelli, A., Repici, M., Garbossa, D., and Grimaldi, A. (2000). Recent techniques for tracing pathways in the central nervous system of developing and adult mammals. *Brain Res. Bull.* 51, 11–28. doi: 10.1016/S0361-9230(99)00229-4

Von Bohlen., O., and Halbach, U. (1999). The isolated mammalian brain: an in vivo preparation suitable for pathway tracing. *Eur. J. Neurosci.* 11, 1096–1100. doi: 10.1046/j.1460-9568.1999.00543.x

Yao, L., Xi, L., and Jiang, H. (2014). Photoacoustic computed microscopy. *Sci. Rep.* 4:4960. doi: 10.1038/srep04960

Conflict of Interest Statement: The authors declare that the research was conducted in the absence of any commercial or financial relationships that could be construed as a potential conflict of interest.

Copyright © 2019 Gottschalk, Degtyaruk, Mc Larney, Rebling, Deán-Ben, Shoham and Razansky. This is an open-access article distributed under the terms of the Creative Commons Attribution License (CC BY). The use, distribution or reproduction in other forums is permitted, provided the original author(s) and the copyright owner(s) are credited and that the original publication in this journal is cited, in accordance with accepted academic practice. No use, distribution or reproduction is permitted which does not comply with these terms.

frontiers in Neuroscience

ORIGINAL RESEARCH
published: 24 April 2019
doi: 10.3389/fnins.2019.00380

Using Chronopotentiometry to Better Characterize the Charge Injection Mechanisms of Platinum Electrodes Used in Bionic Devices

Alexander R. Harris[1,2], Carrie Newbold[2,3], Paul Carter[4], Robert Cowan[2,3] and Gordon G. Wallace[1,2]*

[1] ARC Centre of Excellence for Electromaterials Science, Intelligent Polymer Research Institute, University of Wollongong, Wollongong, NSW, Australia, [2] The HEARing CRC, University of Melbourne, Melbourne, VIC, Australia, [3] Department of Audiology and Speech Pathology, University of Melbourne, Melbourne, VIC, Australia, [4] Cochlear, Ltd., Macquarie University, Sydney, NSW, Australia

The safe charge injection capacity and charge density of neural stimulating electrodes is based on empirical evidence obtained from stimulating feline cortices. Stimulation induced tissue damage may be caused by electrochemical or biological mechanisms. Separating these mechanisms requires greater understanding of charge transfer at the electrode-tissue interface. Clinical devices typically use a biphasic waveform with controlled current. Therefore, the charge injection mechanism and charge injection capacity of platinum was assessed on a commercial potentiostat by chronopotentiometry (controlled current stimulation). Platinum is a non-ideal electrode, charge injection by chronopotentiometry can be passed via capacitive and Faradaic mechanisms. Electrodes were tested under a variety of conditions to assess the impact on charge injection capacity. The change in electrode potential (charge injection capacity) was affected by applied charge density, pulse length, pulse polarity, electrode size, polishing method, electrolyte composition, and oxygen concentration. The safe charge injection capacity and charge density could be increased by changing the electrode-solution composition and stimulation parameters. However, certain conditions (e.g., acid polished electrodes) allowed the electrode to exceed the water electrolysis potential despite the stimulation protocol being deemed safe according to the Shannon plot. Multiple current pulses led to a shift or ratcheting in electrode potential due to changes in the electrode-solution composition. An accurate measure of safe charge injection capacity and charge density of an implantable electrode can only be obtained from suitable conditions (an appropriately degassed electrolyte and clinically relevant electrode structure). Cyclic voltammetric measurement of charge storage capacity can be performed on implantable electrodes, but will not provide information on electrode stability to multiple chronopotentiometric pulses. In contrast, chronopotentiometry will provide details on electrode stability, but the minimum time resolution of typical commercial potentiostats (ms range) is greater than used in a clinical stimulator (μs range) so that extrapolation to short stimulation pulses is required. Finally, an impedance

OPEN ACCESS

Edited by:
Jeffrey R. Capadona, Case Western Reserve University, United States

Reviewed by:
Takashi D. Y. Kozai, University of Pittsburgh, United States
Yun Qian, Shanghai Sixth People's Hospital, China

***Correspondence:**
Alexander R. Harris
alexrharris@gmail.com

Specialty section:
This article was submitted to Neural Technology, a section of the journal Frontiers in Neuroscience

Received: *04 December 2018*
Accepted: *02 April 2019*
Published: *24 April 2019*

Citation:
Harris AR, Newbold C, Carter P, Cowan R and Wallace GG (2019) Using Chronopotentiometry to Better Characterize the Charge Injection Mechanisms of Platinum Electrodes Used in Bionic Devices. Front. Neurosci. 13:380. doi: 10.3389/fnins.2019.00380

test is typically used to assess clinical electrode performance. The impedance test is also based on a biphasic chronopotentiometic waveform where the measured potential is used to calculate an impedance value. Here it is shown that the measured potential is a function of many parameters (solution composition, electrode area, and surface composition). Subsequently, impedance test results allow electrode comparison and to indicate electrode failure, but use of Ohm's law to calculate an impedance value is not valid.

Keywords: platinum, chronopotentiometry, cochlear implant, impedance test, charge transfer mechanism

INTRODUCTION

Electrodes are used to stimulate excitable cells in cell culture and in the body (Normann and Fernandez, 2016). Electrical stimulation in humans has been used to: provide sensory input, as in the cochlear implant or bionic eye (Christie et al., 2016; Dhanasingh and Jolly, 2017); control body function, such as deep brain stimulation to reduce body tremor (McIntyre et al., 2015); or to affect or influence behavior, including treatments for depression (Kennedy et al., 2011). Sufficient charge must be ejected from the electrode into tissue to induce the desired clinical outcomes without damaging the electrode or the surrounding tissue. Some issues associated with electrical stimulation include off-target stimulation (Lukins et al., 2014), glial cell or fibrous tissue encapsulation (Niparko et al., 1989) and electrode corrosion (Clark et al., 1983; Robblee et al., 1983). As a result of these factors, implants can induce cell death, show an increase in power usage over time, or fail completely.

The safe stimulation parameters of an electrode are currently defined by the Shannon plot which relates the charge density and charge per phase of an electrical pulse (Shannon, 1992). This is based on electrical stimulation of a feline cortex using platinum or tantalum pentoxide electrodes with a limited stimulation protocol. Clinical electrodes use a variety of stimulation waveforms, typically involving a biphasic reduction and oxidation pulse of varying length, amplitude, repetition rate, and interphase gap that may not be covered by the Shannon plot (McCreery et al., 1992). More recent work has also indicated the Shannon plot may not be valid when applied to microelectrodes (Cogan et al., 2016). The validity of the Shannon plot for different electrode materials and in different tissue also needs to be addressed in more detail. These limitations raise questions about what chemical and biological mechanisms determine safe charge densities, and how safe charge injection capacity and density should be measured and reported.

It is assumed that increasing the charge injection capacity of an electrode will increase its safe charge density by preventing unwanted reactions occurring at the electrode-tissue interface. Significant effort has been spent developing novel electrode materials and geometries to increase the charge injection capacity of an electrode (Wang et al., 2017; Harris and Wallace, 2018). The charge injection capacity of an electrode is typically assessed by electrochemical methods, but with limited theoretical basis, the methods used differ across laboratories and lack sufficient controls. This has resulted in poor correlation between *in vitro* and *in vivo* performance (Prasad and Sanchez, 2012). Subsequently, new materials and geometries demonstrating high charge injection capacities have had poor translation to clinical use. A stronger theoretical understanding of how charge transfer occurs at the electrode-tissue interface is needed to define how electrodes should be tested and what are safe charge densities across different electrode and tissue parameters (Kumsa et al., 2016a). This will reduce concerns of platinum dissolution, changes in pH and generation of gas occurring at the electrode surface (Robblee et al., 1983; Agnew et al., 1986; Merrill et al., 2005). It will also help translate the safe stimulation parameters measured in feline cortex to other devices and tissues such as cochlear implants and the bionic eye.

The safe potential window and charge storage capacity of implantable electrodes are often assessed by cyclic voltammetry. However, stimulation of excitable cells with an electrode requires altering the potential across a cell membrane and is usually achieved with electrical pulsing rather than a potential sweep. When performing electrical pulsing, either the potential or current can be controlled while the other parameter varies with time. The response of a platinum electrode under various biologically relevant conditions during controlled potential pulsing (chronoamperometry) was recently investigated (Harris et al., 2018a). Using chronoamperometric pulsing, the electric field decreases rapidly with distance from the electrode; so the charge delivered may not induce sufficient change in membrane potential to excite a cell. The amount of charge delivery also depends on conditions and decreases rapidly with time. In bionics applications, the electrode is normally used in controlled current mode (chronopotentiometry). For instance, modern cochlear implants use a biphasic waveform composed of a μs timescale chronopotentiometic reduction pulse followed by an interphase gap and oxidation pulse. Using chronopotentiometic pulsing, charge delivery will be constant, but the electrode potential is uncontrolled. Furthermore, the *in vivo* performance of the electrode/tissue interface is often assessed by an impedance test (Newbold et al., 2004, 2010, 2011). This is not to be confused with electrical impedance spectroscopy (EIS), or the unit of impedance (Z). The impedance test also applies a biphasic chronopotentiometic pulse through each electrode measuring the change in potential, which is then used to calculate an impedance value using Ohm's law.

Electrodes used for neural stimulation are often referred to as capacitive (ideally polarizable) or Faradaic (ideally non-polarizable) (Cogan, 2008). When analyzing a

chronopotentiometic measurement, an ideally polarizable electrode only passes current (i_c) through charging of the double-layer capacitance per unit area (C_d) across the electrode surface with area (A) according to

$$i_c = -AC_d(dE/dt) \quad (1)$$

supplying capacitance current requires a constantly changing potential (E) over time (t). An ideally non-polarizable electrode only delivers charge via a Faradaic reaction, in which case the electrode potential would not change with an applied current.

In practice, no electrode is ideal, with current supplied by capacitance and Faradaic reactions at different potentials and mass transport affects the Faradaic current. When mass transport is present, the current of a Faradaic reaction (i_f) is controlled by the flux conditions

$$i_f = nFAD\left(\frac{\partial C}{\partial x}\right)_{x=0} \quad (2)$$

where n is the number of electrons transferred, F is Faraday's constant, D is the diffusion coefficient, C is the concentration and x is the distance from the electrode (for the simple one dimensional case). These conditions are further affected by electrode geometry and the reversibility of the Faradaic reactions. The total current at a non-ideal electrode, $i = i_c + i_f$, therefore has varying proportions of capacitance and Faradaic current over time (De Vries, 1968).

To ensure safe stimulation of cells and to prevent degradation of the electrode, the charge delivery mechanisms must not be damaging or create toxic species. The electrode potential must be kept below levels that would corrode the electrode or cause water electrolysis. However, the composition of the electrode-tissue interface is very complex. An implanted platinum electrode is usually multicrystalline, can have varying amounts of oxide present, and the surrounding fluid is composed of various ions, biomolecules, and cells. Therefore, multiple mechanisms can be involved in charge transfer at the electrode-tissue interface, and the safe charge injection capacity will depend on the local conditions. A systematic analysis of changes in stimulation waveform and electrode-solution composition on the chronopotentiometric response of a platinum electrode under well-controlled conditions will help determine their potential impact on charge delivery mechanisms occurring during *in vivo* electrical stimulation.

To better understand the charge delivery mechanisms occurring during stimulation of excitable cells and the most appropriate way of testing implantable electrodes, this study investigated the use of chronopotentiometry to measure the performance of platinum electrodes under a variety of conditions. The impact of solution composition, oxygen concentration, electrode size, electrode polishing method, and applied potential on the chronopotentiometric response of platinum is reported. The possible charge transfer mechanisms occurring under these conditions and the implications for *in vivo* performance are discussed. The relationship between cyclic voltammetry, chronoamperometry, and chronopotentiometry using commercial potentiostats as methods for investigating implantable electrodes and the implication on impedance testing are explained.

MATERIALS AND METHODS

Chronopotentiometric Waveform and Analysis

Chronopotentiometic experiments were performed with repetitive oxidation and reduction pulses of opposing polarity but equal time and magnitude. This is equivalent to a biphasic pulse with no interphase gap. To investigate the stability of the electrode to repeated pulsing, eight reduction/oxidation (four biphasic) pulses were applied. The charge densities chosen were 3 and 10 $\mu C\ cm^{-2}$, as they are the typical minimum and maximum limits used by modern cochlear implants. The current pulses in a cochlear implant are typically applied for 25 μs, however the shortest pulse achievable on a CH Instruments potentiostat is 5 ms. A 5 ms pulse (10 ms biphasic pulse) is equivalent to 100 pulses per second; doubling the pulse length to 10 ms is equivalent to 50 pulses per second. The applied charge (Q) was calculated by multiplying the charge density by the nominal electrode area (A); the current (i) for the 5 ms time pulse was then calculated from the total charge passed and the time (t), $i = Q/t$. For instance, achieving a current density of 10 $\mu C\ cm^{-2}$ on a 600 μm diameter electrode with a 5 ms pulse, required an applied current of 5.65 μA, resulting in 28.3 nC $phase^{-1}$, this charge density and charge per phase is considered safe according to the Shannon plot (Cogan et al., 2016). The current was adjusted to ensure the same charge density of 10 $\mu C\ cm^{-2}$ was applied for each electrode size. By definition, the larger the change in potential measured during the chronopotentiometric pulse, the smaller is the electrodes charge injection capacity. The stability of the electrode to multiple pulsing was assessed by measuring the change in potential from the end of the second pulse to the end of the last pulse (cumulative six pulses).

Chemicals

Phosphate-buffered saline (PBS: 154 mM NaCl, 10 mM phosphate buffer, pH 7.4), sodium chloride, potassium chloride, sodium bicarbonate, calcium chloride, D-glucose (Sigma-Aldrich), magnesium chloride hexahydrate (Scharlau), monosodium phosphate (Biochemicals) and 98% sulfuric acid (RCI Labscan), were used as received. An artificial perilymph contained 125 mM NaCl, 3.5 mM KCl, 25 mM $NaHCO_3$, 1.2 mM $MgCl_2$, 1.3 mM $CaCl_2$, 0.75 mM NaH_2PO_4, and 5 mM glucose (Salt et al., 2003). Unless indicated, test solutions were degassed with nitrogen for at least 10 min.

Electrodes

Electrodes were 2 mm, 0.6 mm, or 25 μm diameter platinum disks (CH Instruments) or a cochlear implant with 22 half band, 0.3 mm^2 nominal area platinum electrodes (donated by Cochlear, Ltd.). One electrode of each type was tested. The electrodes were freshly polished before every experiment ensuring reproducible starting conditions. Disk electrodes were polished with 0.3 μm

alumina slurry on Microcloth polishing cloth (Buehler), rinsed in deionised water and gently dried (Kimwipe) before use; the cochlear implant was not mechanically polished before use and had not been used for any *in vivo* studies. Acid polishing was achieved by cycling the electrode potential from 1.2 to −0.2 V at 50 mV s^{-1} for 50 cycles in 0.5 M H_2SO_4. Electrodes were tested in a 3-electrode configuration on a CHI660E potentiostat (CH Instruments) using a Ag/AgCl (3 M KCl) as reference electrode and Pt wire as counter electrode. The electrodes were connected to the potentiostat via alligator clips and placed into a beaker of solution.

RESULTS

Varying Chronopotentiometric Waveform

The voltammetric reduction sweep of a platinum electrode in 0.1 M NaCl displays a peak at −85 mV from reduction of platinum oxide and dissolved oxygen and increasing reduction current below −470 mV from hydrogen adsorption (**Figure 1**). On the oxidation sweep, broad peaks are seen around −700 to −400 mV from hydrogen stripping and above 0 V from platinum oxide formation. At potentials above and below the potential window of 800 to −800 mV, water oxidation, and reduction can occur.

When the electrode is first placed into solution, it will be at an open circuit potential (OCP) or resting potential. This is the starting potential at $t = 0$ seen in the chronopotentiometry (**Figure 2**). The OCP varies with electrode and solution properties, but for a mechanically polished electrode in degassed 0.1 M NaCl, it was generally around −50 to −250 mV vs. Ag/AgCl (3 M KCl). Applying a current to the electrode drives electrochemical reactions that changes the electrode potential. A reductive current leads to more negative potentials, an oxidative current to more positive potentials. Increasing the current magnitude results in a larger change in potential.

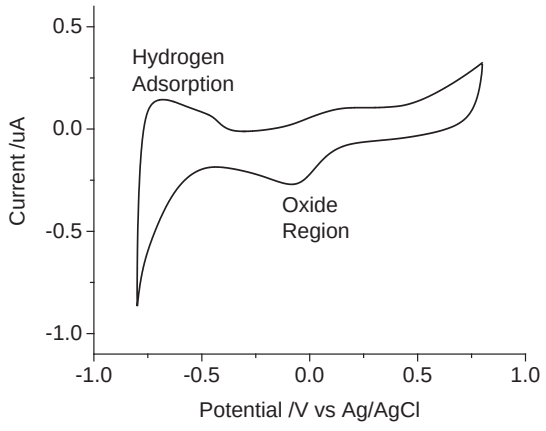

FIGURE 1 | Second cycle of a cyclic voltammogram in degassed 0.1 M NaCl of a mechanically polished 0.6 mm diameter platinum electrode at 100 mV s^{-1}.

Applying a −3 μC cm^{-2} pulse for 5 ms in degassed 0.1 M NaCl, the initial potential was −180 mV, and the final potential was −250 mV (**Figure 2**). The change in potential over time was curved, with decreasing gradient, no plateaus or steps in the curve were seen under any of the conditions tested. On clinical stimulators, a steep rise is seen at the start of the current pulse, called the access voltage, which lasts a few μs (Tykocinski et al., 2005; Mesnildrey et al., 2019), this was not seen on the commercial potentiostat as the minimum sampling time was 10 μs. Increasing the charge density to −10 μC cm^{-2}, the initial potential was −220 mV, shifting to −380 mV after 5 ms. Applying positive current pulses, a 3 μC cm^{-2} charge density had an initial potential at −110 mV, ending at −50 mV. And a charge density of 10 μC cm^{-2} started at −70 mV and finished at 70 mV. This demonstrates the larger change in potential seen with higher applied charge densities.

The first pulse always displayed a smaller and more variable change in potential than subsequent pulses (**Figure 3**). To overcome the variability associated with this initial pulse, the charge injection capacity of the electrode was assessed by measuring the change in potential of the second pulse. A summary of the changes in electrode potential under different conditions is given in **Table 1**.

When applying a reductive current as the first pulse, the electrode potential becomes more negative than the OCP. The subsequent oxidation pulse then increases the electrode potential above the OCP consistent with a non-ideal electrode. At the conclusion of the eight pulses, the final potential had shifted to more positive potentials than at the end of the previous oxidation pulses. When an oxidation current was applied initially, an opposite change in potential direction was seen. As a result, when using an initial reduction current, the electrode potential obtained more negative potentials then with an initial oxidation current.

The current pulse length was set as 5 ms due to the limitations of the potentiostat. To investigate the impact of pulse length on the change in potential, current pulses of 10 ms were applied. To achieve the same charge density of 10 μC cm^{-2}, the applied current was also reduced. The impact of changing the pulse length is shown in **Figure 4** and in **Table 1**. Both the change in potential of the second pulse and the cumulative six pulses were smaller when applying longer current pulses.

Varying Solution Composition

The solution composition was seen to affect the cyclic voltammetric and chronoamperometric response of a platinum electrode (Harris et al., 2018a,b). While electrochemical studies are often undertaken in simple 0.1 M NaCl; cell culture and testing of implantable electrodes are often performed in PBS; while a more accurate model solution for cochlear implants is an artificial perilymph. The OCP of platinum became more positive from 0.1 M NaCl to artificial perilymph to PBS (**Figures 5A,B**). The change in potential of the second pulse and the cumulative six pulses also decreased from 0.1 M NaCl > artificial perilymph > PBS (**Table 1**).

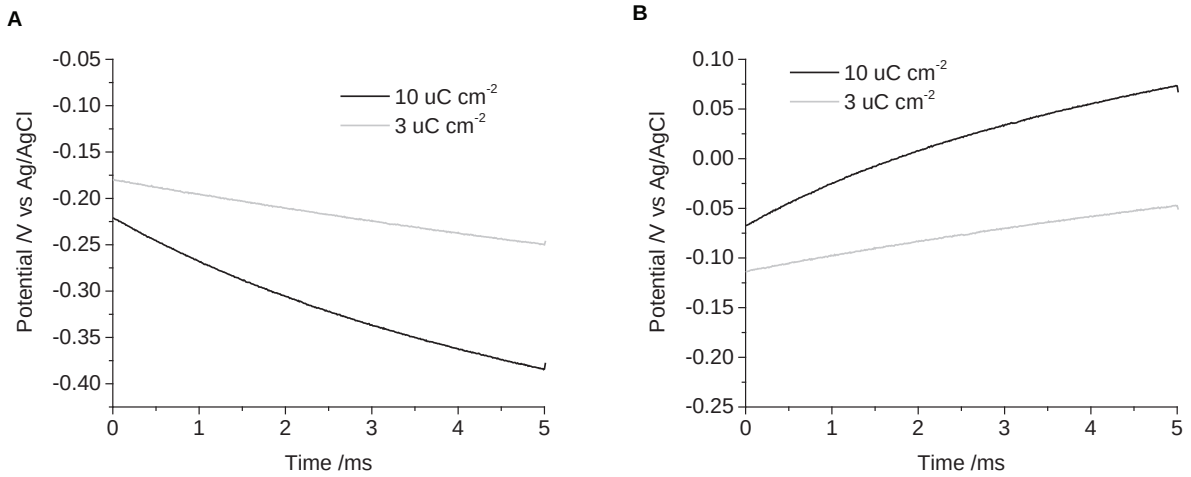

FIGURE 2 | Chronopotentiometric curves of a mechanically polished 0.6 mm diameter platinum electrode in degassed 0.1 M NaCl. **(A)** cathodic pulse, **(B)** anodic pulse. Black curve – current density of 10 μC cm^{-2}, Gray curve – 3 μC cm^{-2}.

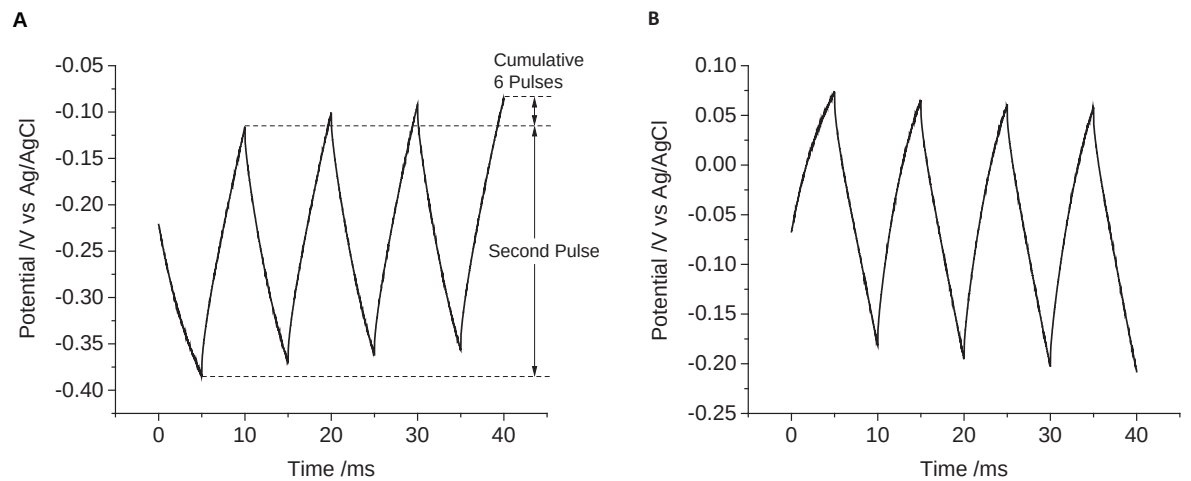

FIGURE 3 | Multiple pulse chronopotentiometry of a mechanically polished 0.6 mm diameter platinum electrode in degassed 0.1 M NaCl. **(A)** Cathodic, **(B)** anodic pulse first with a current density of 10 μC cm^{-2}.

The oxygen tension in the body is low, as it is mostly bound to hemoglobin, but it can vary. A higher oxygen concentration was tested by not degassing the solution with nitrogen before performing current pulsing. The OCP of the electrode without degassing was significantly more positive than after degassing (**Figures 5C,D**). With an initial positive pulse, the change in potential of the second pulse was smaller without degassing, while for an initial negative pulse the change in potential was smaller after degassing (**Table 1**). After multiple pulsing, the change in potential from the cumulative six pulses was smaller without degassing regardless of the initial potential polarity.

Varying Electrode Surface

There were no trends in OCP with electrode size (**Figure 6**). However, there was a significant effect on the change in potential with a decrease in magnitude with decreasing electrode size (**Table 1**).

A mechanically polished electrode has a heterogeneous surface with varying levels of oxide and impurities present and a multicrystalline structure. It is possible to clean the electrode surface by cycling the electrode potential in 0.5 M H_2SO_4 from 1.2 to −0.2 V at 50 mV s^{-1} for 50 cycles. The voltammetry of an acid-cleaned electrode shows more defined redox peaks associated with oxide formation and hydride adsorption (**Figure 7A**). Placing the acid-cleaned electrode straight into 0.1 M NaCl then shows a large change in voltammetric response compared to a mechanically polished electrode (**Figure 7B**). The large reduction peak at −420 mV and oxidation peak at −350 mV are most likely caused by adsorption of chloride to the electrode surface. The chloride

TABLE 1 | Change in potential on a platinum electrode from different chronopotentiometric conditions.

Tested	Electrode Diameter	Polish method	Solution	Degassed	Initial applied charge density (μC cm^{-2})*	Pulse length (ms)	Change in potential (mV)	
Variable							**Second pulse**	**Cumulative six pulses**
Applied waveform	600 μm	Mechanical	0.1 M NaCl	Yes	−3	5	100 (6)	10 (1)
	600 μm	Mechanical	0.1 M NaCl	Yes	3	5	−98 (5)	−8 (0)
	600 μm	Mechanical	0.1 M NaCl	Yes	−10	5	278 (14)	32 (3)
	600 μm	Mechanical	0.1 M NaCl	Yes	10	5	−257 (1)	−25 (1)
	600 μm	Mechanical	0.1 M NaCl	Yes	−10	10	259 (8)	27 (2)
	600 μm	Mechanical	0.1 M NaCl	Yes	10	10	−241 (8)	−20 (1)
Solution composition	600 μm	Mechanical	PBS	Yes	−10	5	207 (40)	23 (1)
	600 μm	Mechanical	PBS	Yes	10	5	−204 (24)	−19 (5)
	600 μm	Mechanical	Artificial perilymph	Yes	−10	5	220 (14)	27 (4)
	600 μm	Mechanical	Artificial perilymph	Yes	10	5	−219 (22)	−20 (1)
	600 μm	Mechanical	0.1 M NaCl	No	−10	5	270 (10)	27 (3)
	600 μm	Mechanical	0.1 M NaCl	No	10	5	−280 (30)	−21 (5)
Electrode surface	2 mm	Mechanical	0.1 M NaCl	Yes	−10	5	397 (6)	46 (4)
	2 mm	Mechanical	0.1 M NaCl	Yes	10	5	−385 (6)	−36 (4)
	25 μm	Mechanical	0.1 M NaCl	Yes	−10	5	12 (1)	−5 (3)
	25 μm	Mechanical	0.1 M NaCl	Yes	10	5	−14 (0)	−7 (3)
	600 μm	Acid	0.1 M NaCl	Yes	−10	5	420 (15)	43 (2)
	600 μm	Acid	0.1 M NaCl	Yes	10	5	−437 (14)	−39 (2)
	Cochlear implant	–	Artificial perilymph	Yes	−10	5	529 (112)$^{+}$	58 (13)$^{+}$
	Cochlear implant	–	Artificial perilymph	Yes	10	5	−575 (109)$^{+}$	−46 (11)$^{+}$

**The initial applied charge density is the magnitude of the first current pulse. Subsequent pulses are of opposing polarity at the same magnitude. $^{+}$Average (standard deviation) of five electrodes.*

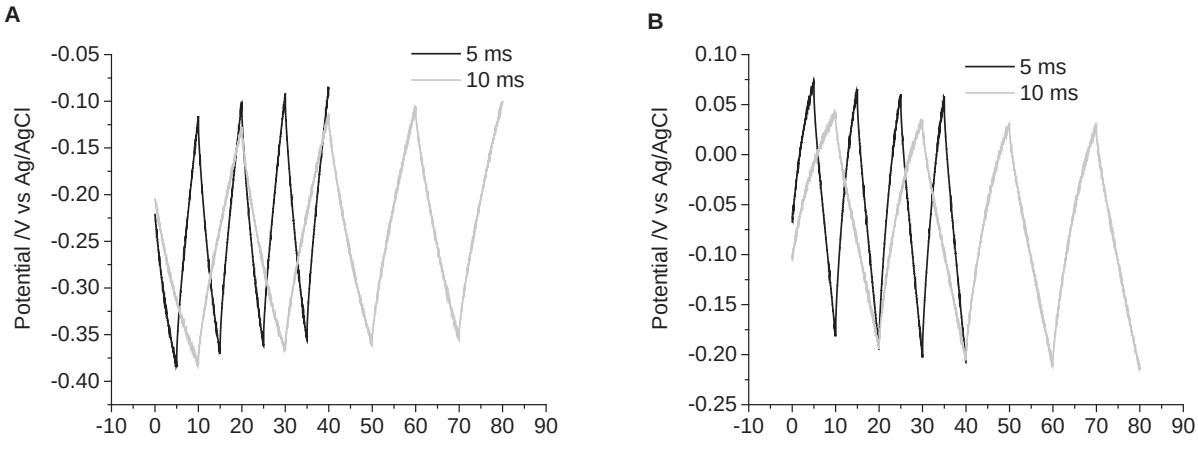

FIGURE 4 | Multiple pulse chronopotentiometry of a mechanically polished 0.6 mm diameter platinum electrode in degassed 0.1 M NaCl. **(A)** Cathodic, **(B)** anodic pulse first with a current density of 10 μC cm^{-2}. Black curve – 5 ms pulse, Gray curve – 10 ms pulse.

adsorption blocks the electrode surface, affecting the Faradaic reactions associated with platinum oxide, hydride, and oxygen (Bagotzky et al., 1970; Li and Lipkowski, 2000; Garcia-Araez et al., 2005). The OCP of the acid-cleaned electrode was significantly more positive than the mechanically polished electrode (**Figures 7C,D**). The change in potential was also significantly larger for the acid-cleaned than mechanically polished electrode (**Table 1**). And when applying a 10 μC cm^{-2}

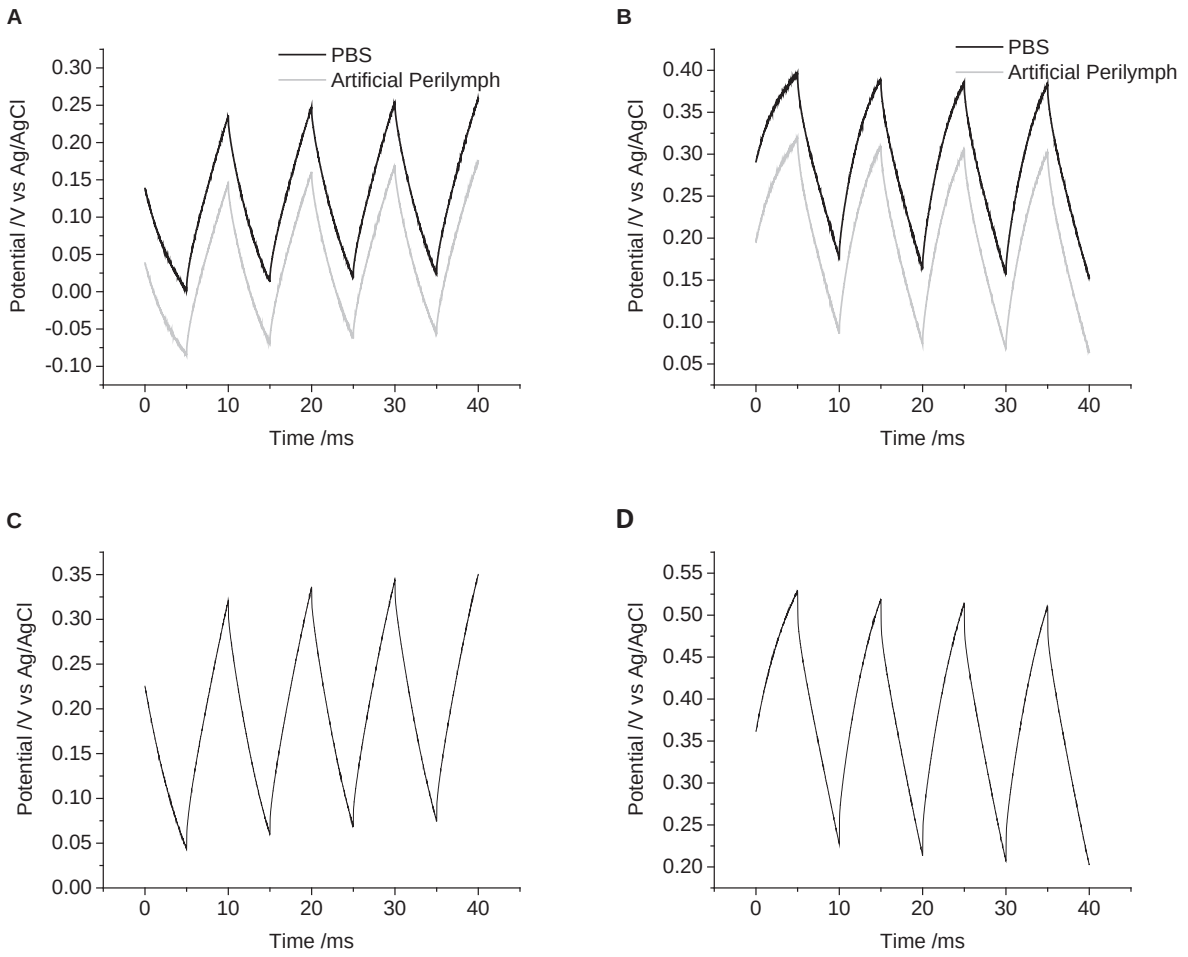

FIGURE 5 | Multiple pulse chronopotentiometry of a mechanically polished 0.6 mm diameter platinum electrode. **(A)** Cathodic, **(B)** anodic pulse first with a current density of 10 μC cm^{-2} in degassed solution. Black curve – PBS, Gray curve – artificial perilymph. **(C)** Cathodic, **(D)** anodic pulse first with a current density of 10 μC cm^{-2} in non-degassed 0.1 M NaCl.

anodic first pulse, the electrode potential was raised to 930 mV, well-above the water oxidation potential.

The change in potential on the cochlear implant electrode in degassed artificial perilymph was larger than an equivalent sized mechanically polished disk electrode (**Figure 8** and **Table 1**). The relatively large standard deviation from five electrodes is most likely due to variations in electrode area and surface properties.

To aid in visualization of reactions mechanisms occurring during chronopotentiometry, a derivative of the potential/time plot can be performed (**Figure 8C**). A capacitance current would then appear as a constant; and a Faradaic current would appear as a sharp dip. The reciprocal of the derivative would then transform any Faradaic current into a sharp peak (**Figure 8D**). The derivative of the cochlear implant chronopotentiometric curve has a larger noise level, but no significant dip in the curve was seen. On the reciprocal derivative curve, the reduction pulses showed an increase over time, while the oxidation current was stable over time; no peaks were seen to indicate a significant variation in the ratio of capacitance and Faradaic current was occurring.

DISCUSSION

Effect of Varying Chronopotentiometric Waveform on the Electrode/Tissue Interface

If chronopotentiometric pulsing of platinum in tissue was an ideally polarizable system, only capacitance current would flow. There would be a linear change in potential over time and increasing the current density would increase the rate of potential change (Eq. 1). During biphasic pulsing, an initial reduction pulse would result in a decrease in electrode potential and the following oxidation pulse of the same charge would return the electrode to the initial potential. Conversely, an initial oxidation pulse would raise the electrode potential,

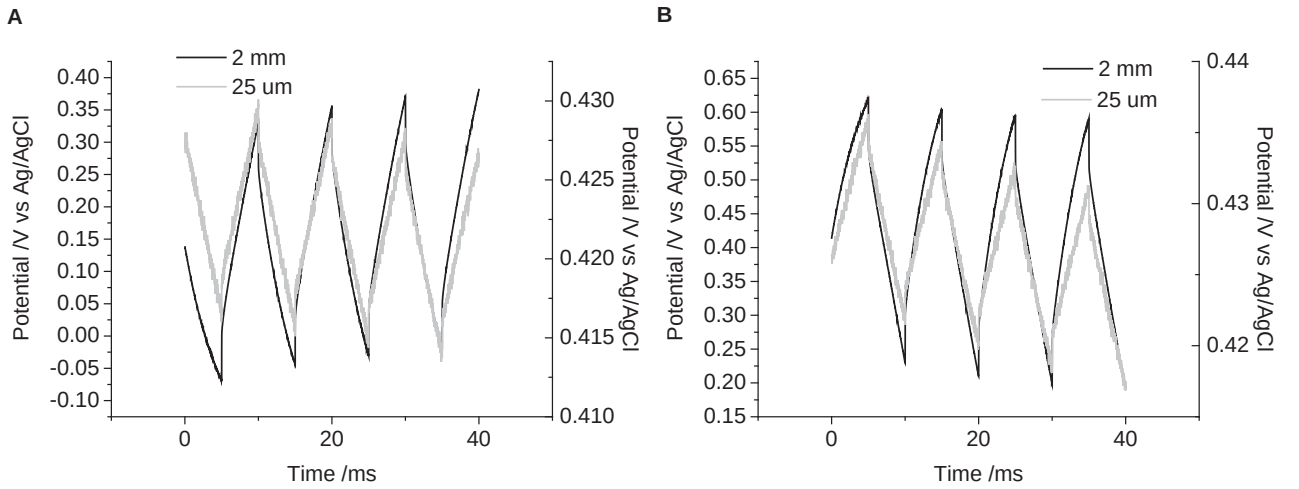

FIGURE 6 | Multiple pulse chronopotentiometry of a mechanically polished platinum electrode in 0.1 M NaCl in degassed 0.1 M NaCl. **(A)** Cathodic, **(B)** anodic pulse first with a current density of 10 μC cm^{-2}. Black curve – 2 mm diameter electrode, Gray curve – 25 μm diameter electrode.

the following reduction pulse returning the electrode to the start potential. A different current magnitude (charge density) could be used for the oxidation and reduction pulses, but by adjusting the pulse length, the same charge could still be passed on each. At a truly ideal electrode, there would be no water electrolysis, and so there would be no defined safe potential limits.

At the other extreme, if chronopotentiometric pulsing at the platinum-tissue interface were ideally non-polarizable, only Faradaic current would flow. A reduction pulse would reduce a redox species and an oxidation pulse would oxidize the redox species. Assuming the concentrations of the oxidized and reduced species were minimally altered from the redox reactions, the electrode potential would not change. The use of a reduction or oxidation pulse initially, increasing the current density, pulse length or the inclusion of an interphase gap would have no impact on the electrode potential. An imbalanced charge from oxidation and reduction pulses would also not lead to a shift in electrode potential.

In reality, the platinum-tissue interface is non-ideal. Charge transfer mechanisms will include capacitance and a range of Faradaic reactions including platinum oxide formation and reduction, deposition and stripping of hydride and reduction of molecular oxygen. Capacitance may not be constant with varying electrode potential, and charge available from a Faradaic reaction may have slow kinetics or be exhausted, either by fully oxidizing or reducing the reactant, or due to mass transport limitations. Changes in current magnitude, polarity, number of pulses, and pulse length were all found to affect the change in electrode potential (**Figures 2–4** and **Table 1**). This will be associated with different amounts of each charge transfer reaction occurring. For instance, a decrease in current pulse length would reduce the diffusion time and limit the amount of charge that can be supplied by a solution phase Faradaic reaction (reduction of oxygen). A reciprocal derivative was applied, but due to the complex platinum-solution interface, it was unable to distinguish specific Faradaic reactions (**Figure 8**). This limits the amount of analysis that can be performed with chronopotentiometry, and so a more general discussion will be made.

The charge transfer mechanisms during a biphasic pulse were affected by initial pulse polarity (**Figure 3**). For instance, in the presence of a redox active species that can be reversibly reduced, an initial reduction pulse could supply charge by capacitance and the Faradaic reaction (i.e., oxygen reduction and platinum oxide reduction). A subsequent oxidation pulse could also pass capacitance and Faradaic charge. However for an initial oxidation pulse, charge may only be supplied by capacitance. On a subsequent reduction pulse, charge could then be supplied by capacitance and the redox reaction. More complicated reaction mechanisms and mass transport conditions may also affect the oxidation and reduction reactions unequally. As a result, the charge transfer mechanisms from oxidation and reduction pulses may not be the same even with charge balanced pulsing. Multiple electrical pulses may then drive large changes in Faradaic reactions, affecting the concentrations of redox species. This can then shift the electrode potential according to the Nernst equation

$$E = E^0 - \frac{kT}{nF} \ln \frac{[\text{Red}]}{[\text{Ox}]} \tag{3}$$

where k is the Boltzmann constant, T is the absolute temperature, [Red] and [Ox] are the concentration of the reduced and oxidized species. Indeed, electrode potential changes were seen with just eight pulses (**Figure 3**) and has been termed ratcheting (Merrill et al., 2005). Ratcheting can lead to large changes in electrode potential, enabling greater platinum dissolution, so changes to the waveform have been attempted to reduce this effect (Kumsa et al., 2016b). This work demonstrates that the

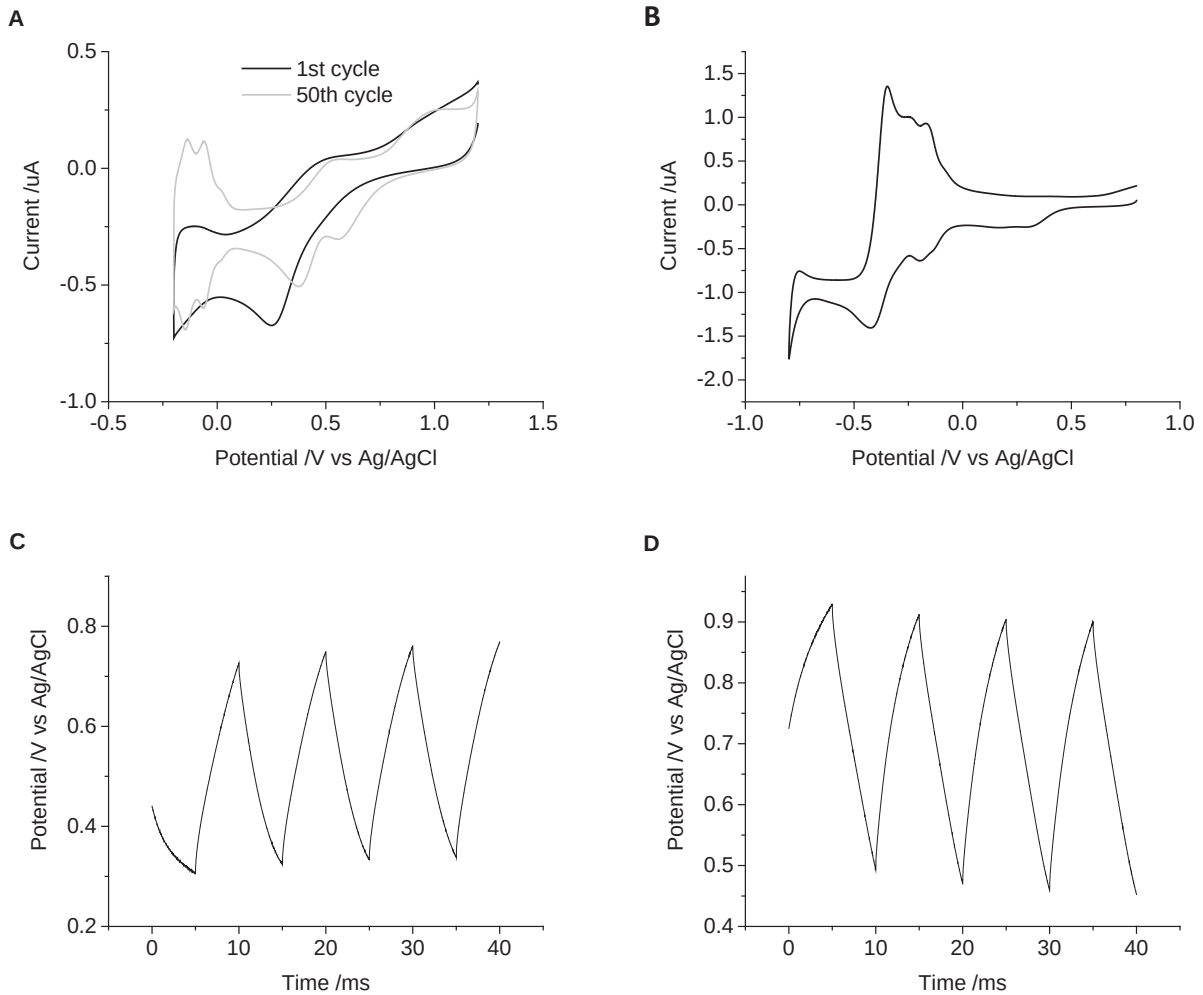

FIGURE 7 | (A) First (black) and fiftieth (gray) cycle of a mechanically polished 0.6 mm diameter platinum electrode in 0.5 M H_2SO_4 at 50 mV s^{-1}. **(B)** First cycle of an acid polished 0.6 mm diameter platinum electrode in degassed 0.1 M NaCl at 100 mV s^{-1}. Multiple pulse chronopotentiometry of an acid polished 0.6 mm diameter platinum electrode in degassed 0.1 M NaCl. **(C)** Cathodic, **(D)** anodic pulse first with a current density of 10 μC cm^{-2}.

ratcheting of the electrode potential can also be controlled by changes to the electrode/solution interface including solution composition (**Figure 5**), electrode size (**Figure 6**), and surface structure (**Figure 7**).

On the cochlear implant (**Figure 8**), an initial reduction pulse will drive the electrode to more negative potentials. Charge will initially be supplied by capacitance and then platinum oxide and oxygen reduction. If the current density is large enough, hydride adsorption and then water reduction may occur. An oxidation pulse would drive hydride desorption, platinum oxide formation, and capacitance with a final potential higher than the original OCP. For an initial oxidation pulse, the electrode would move to more positive potentials with some platinum oxide formation and capacitance before water oxidation and platinum stripping occurred. And the following reduction pulse would drive capacitance and platinum oxide and oxygen reduction. An initial oxidation pulse may result in greater corrosion of the platinum electrode, but platinum dissolution may also occur through reduction of platinum oxide (Mitsushima et al., 2007).

Effect of Varying Solution Composition on the Electrode/Tissue Interface

The composition of the solution affected the change in electrode potential (**Figure 5** and **Table 1**). The electrolyte concentration and composition affect the double layer capacitance. Specific adsorption of ions onto the electrode surface can also occur, such as the adsorption of anions onto platinum at positive potentials. Electrochemical studies are often performed in simple electrolytes such as 0.1 M NaCl and cell culture can be performed in PBS. However, these are poor models of the *in vivo* environment, an artificial perilymph displayed an intermediate change in electrode potential at the same charge densities compared to 0.1 M NaCl and PBS.

The oxygen tension in the body is relatively low as it is mostly bound to hemoglobin, but physical activity and changes

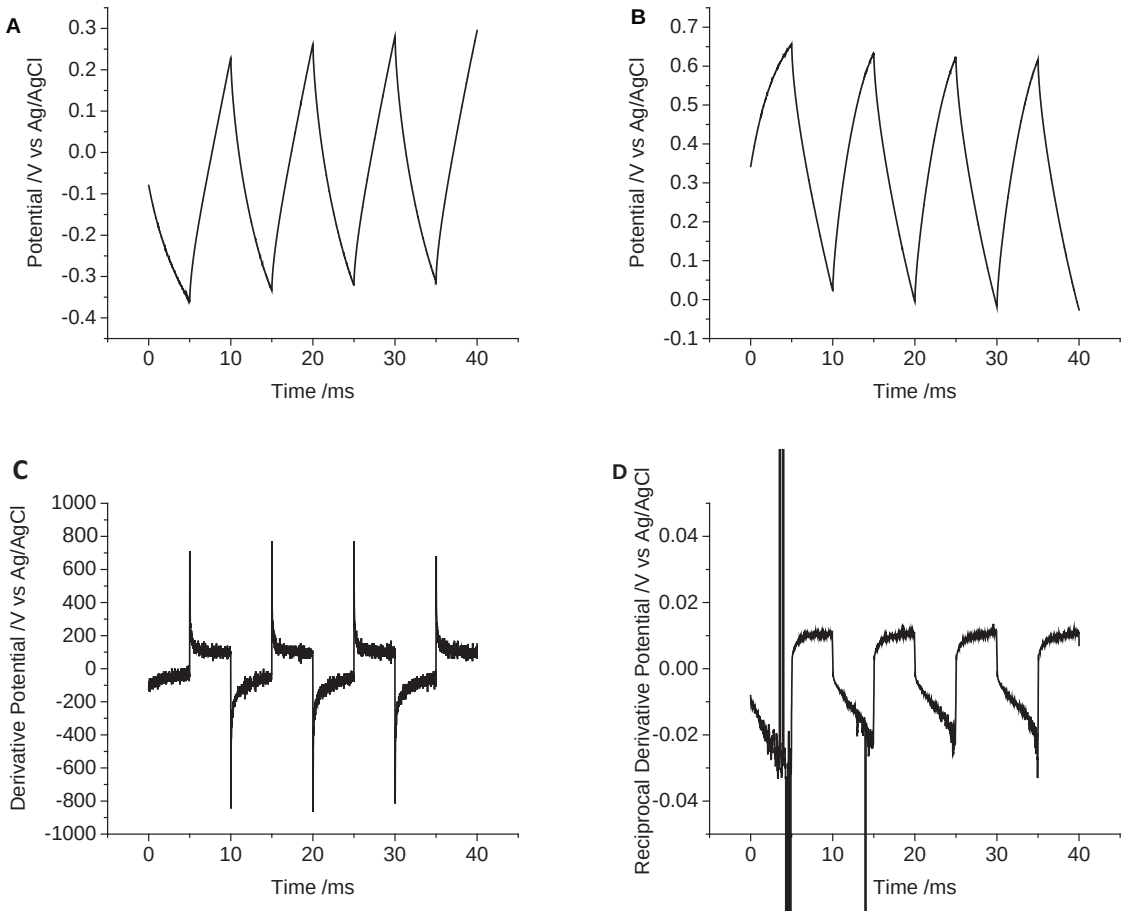

FIGURE 8 | Multiple pulse chronopotentiometry of a non-polished cochlear implant platinum electrode (0.3 mm^2 nominal area) in degassed artificial perilymph. **(A)** Cathodic, **(B)** anodic pulse first with a current density of 10 $\mu C\ cm^{-2}$. **(C)** Derivative and **(D)** reciprocal derivative of curve **(A)**.

in the atmosphere do affect the oxygen tension (Misrahy et al., 1958; Tsunoo and Perlman, 1965. Oxygen can be irreversibly reduced at the electrode surface. The initial potential polarity of a biphasic pulse, charge density and oxygen tension will affect the amount of charge supplied by oxygen reduction (**Figure 5**) (Musa et al., 2011). The presence of other redox active species, including proteins and small organics (e.g., Hemoglobin, dopamine, and amino acids) will also provide sources of Faradaic current. These redox active species will increase the charge injection capacity from a platinum electrode/tissue interface within the water electrolysis window (Donaldson and Donaldson, 1986). An accurate measure of safe charge injection capacity and charge density can only be obtained from an appropriate degassed solution.

Effect of Varying Electrode Surface on the Electrode/Tissue Interface

The nature of the electrode surface was also found to affect the change in electrode potential (**Figures 6**, **7**). The capacitance of an electrode is dependent on its area. Larger electrodes and increased surface roughness can increase the charge available through capacitance (Tykocinski et al., 2001). For a surface confined redox reaction such as the formation and removal of platinum oxide, a larger electrode surface allows greater capacitance and Faradaic charge. Different crystal planes of platinum also allow a higher density of oxide and hydride adsorption. For a solution phase redox reaction, diffusion of the redox species to the electrode surface will be a planar diffusion profile at short times and on large electrodes. At longer times and smaller electrodes, a radial diffusion profile can be obtained. As a result, a microelectrode can pass a higher charge density before reaching the safe charge injection limit. Assessing the safe charge injection capacity and charge density of an implantable electrode must be made with the clinically relevant roughness, crystal plane, geometry, and size.

A highly clean electrode (planar single crystal with no oxide) would provide less capacitance and Faradaic charge, resulting in a lower charge injection capacity than a rough platinum electrode with oxide present. Here it was seen (**Figure 7**) that an acid cleaned electrode could enable its potential to rise above the water oxidation potential even though the applied current was well-below the Shannon limit. As implantable electrodes are not highly clean single crystals, an acid cleaned platinum electrode is a poor

model for understanding *in vivo* charge transfer mechanisms and safe charge injection capacity. Acid cleaning of implantable platinum electrodes should not be performed before assessing their electrochemical properties.

Implications for Using Chronopotentiometry at the Electrode/Tissue Interface

Electrochemical analysis of neural electrodes is undertaken to predict the reaction mechanisms that can occur *in vivo* and define the safe charge injection limits and charge densities. The electrochemical methods can involve potential sweeps (cyclic voltammetry) or electrical pulsing (chronoamperometry of chronopotentiometry). Cyclic voltammetry can assist in determining the reaction mechanisms that can occur and their reversibility. However the charge measured from a cyclic voltmmogram must be made from both forward and backward sweeps, and the stability of the electrode under repeated electrical pulses will not be determined (Harris et al., 2018b). Comparison of electrodes must also be made at the same scan rate and over the same potential window. Chronoamperometry can be used to measure the charge passed with a controlled potential pulse, however the charge flux varies over time and this technique is not typically used *in vivo* (Harris et al., 2018a). Chronopotentiometry is the method typically used for stimulating tissue. The limitations of this technique in understanding the reaction mechanisms and defining safe charge density is discussed below. However, correlations can be made between each of these electrochemical techniques.

The safe charge density measured via cyclic voltammetry is obtained by integrating the current-time plot and dividing the charge by an electrode area. The safe charge density was seen to decrease with increased scan rate and increased electrode area; a higher oxygen concentration increased the reduction charge density and decreased the oxidation charge density; the safe charge density increased from 0.1 M NaCl < artificial perilymph < PBS; and acid cleaning increased the safe charge density. In chronopotentiometry, a larger change in potential is due to a lower charge injection capacity. The charge injection capacity measured by chronopotentiometry was similar to cyclic voltammetry, decreasing with shorter pulse length and larger electrode area; a higher oxygen concentration increased the charge injection capacity of an oxidation pulse and decreased the charge injection capacity of a reduction pulse; the charge injection capacity increased from 0.1 M NaCl < artificial perilymph < PBS; but acid cleaning decreased the charge injection capacity. An increase in charge injection capacity also resulted in less ratcheting of electrode potential during multiple pulses. While there are correlations between voltammetric and chronopotentiometric charge injection capacity and charge density, the specific values obtained were different (Harris et al., 2018b).

The chronopotentiometric experiments performed in this article were undertaken in a three-electrode configuration with a well-defined reference electrode isolated from a simple test solution using a commercial potentiostat. When electrical stimulation is performed *in vivo*, a two-electrode configuration is used and the tissue composition is far more complex. In a two-electrode configuration, the platinum reference electrode also functions as the ground electrode. The composition of the platinum/tissue interface is not well-defined and current passing through the reference/ground electrode will drive capacitance and Faradaic reactions, altering the reference/ground electrode potential. As a result, the potential of the platinum/tissue reference/ground electrode is not defined, so it is also difficult defining a safe potential window. In reality, for most cochlear implants, the reference/ground electrode is many times larger than the stimulating electrode so this effect is minimized.

As soon as the electrode array is inserted into tissue, biofouling processes and glial sheath or fibrous tissue encapsulation will begin (Michelson et al., 2018). This will further affect the reference/ground electrode potential and the reaction mechanisms that occur at the electrode. As a result, defining the working electrode potential to a standard potential is difficult, and it will also impact the *in vivo* safe charge injection limits and charge densities. The impact of biofouling and tissue encapsulation are currently not well-represented in *in vitro* studies and this limits the translation of electrochemical results to electrophysiological performance.

The pulse length of neural stimulators is typically around 25 μs with a shorter interphase gap. Most commercial potentiostats have minimum pulse and sample rates in the ms range, preventing measurement of access voltage (μs timescale). Shorter pulse lengths of the same charge density will also drive more capacitance than Faradaic reactions and ratchet the electrode potential further (**Figure 4** and **Table 1**). So while comparison of safe charge density of different electrodes can be made with a commercial potentiostat, they must be tested under the same conditions (e.g., 5 ms pulse length), and great caution must be used when translating this to safe *in vivo* charge densities.

Overall, an accurate measure of safe charge injection capacity, safe charge density and degree of ratcheting must be made with clinically relevant electrodes and conditions. However, this work also demonstrates increased charge injection capacity and reduced ratcheting can be achieved by decreasing the electrode area, reducing the current magnitude, increasing the pulse length or by adding sources of Faradaic current. More detailed studies comparing the electrochemical, electrophysiological and histological response to electrode stimulation are required to define how much of the Shannon plot is due to electrochemical or biological mechanisms (Cogan et al., 2016; Michelson et al., 2018).

Implications for Impedance Testing of Electrodes

A biphasic chronopotentiometic pulse is also used in an impedance test to provide information on electrode performance. A lower measure from the impedance test should result in lower power usage, $P = I^2Z$, and longer battery life. In a uniform conductor, current, and voltage are related through Ohm's law, $V = IR$. In an AC circuit, Ohm's law must be modified to account for changes in phase, $V = IZ$. The impedance is composed of a

real and imaginary component (amplitude and phase angle)

$$Z = Z_{real} - jZ_{imaginary} \quad (4)$$

where j is used to denote a complex number ($\sqrt{-1}$).

In an electrochemical system, the relationship between current and voltage is complex. The platinum-tissue interface is not a uniform conductor, so Ohm's law can-not be used to calculate an impedance value from the applied current and measured potential (Tykocinski et al., 2005). This article has demonstrated that variations in chronopotentiometic response may be due to changes in electrode area, capacitance, resistance, topography, and chemical functionality; changes to the surrounding fluid including concentration of redox species and cell encapsulation; electrical noise, movement of the electrodes, or anatomical changes. Many of these factors were seen to affect the potential of a biphasic current pulse (**Table 1**), so that use of Ohm's law to calculate an impedance value from the impedance test is not valid. Large variations in response from the impedance test may be caused by insulation failure, electrode shorting or lead wire breakage. Comparisons of impedance over time and across an electrode array may indicate certain mechanisms. However, the complicated nature of the electrode-tissue interface makes it difficult to determine the origins of these effects with just with an impedance test.

CONCLUSION

Implantable electrodes stimulate cells with a constant current while the electrode potential changes over time. Charge is supplied by capacitance and Faradaic reactions, the proportions of each depending on conditions at the electrode-tissue interface. In general, a higher charge storage capacity and charge density measured by integrating a cyclic voltammogram results in a smaller change in potential during a chronopotentiometic pulse. Changes to a biphasic pulse waveform (charge density, pulse length and interphase gap) can also affect the charge transfer mechanisms. The charge injection capacity decreased with shorter pulse length and larger electrode area; a higher oxygen concentration increased the charge injection capacity of an oxidation pulse and decreased the charge injection capacity of a reduction pulse; the charge injection capacity increased from 0.1 M NaCl < artificial perilymph < PBS; acid cleaning decreased the charge injection capacity. An increase in charge injection capacity also resulted in a more stable electrode potential after multiple pulses. Understanding charge transfer at an electrode-tissue interface must be obtained from clinically relevant electrodes and conditions (e.g., a cochlear implant in a degassed artificial perilymph). Safe stimulating limits for the same electrode may vary with location in the body. Modification of stimulating method and conditions can be used to increase the charge injection capacity and reduce the ratcheting of an electrode. An impedance test used to assess electrode function is affected by several parameters, and deconvoluting their impact is difficult.

AUTHOR CONTRIBUTIONS

AH performed all experimental work. All authors were involved in planning and writing of the manuscript.

FUNDING

The authors acknowledge the financial support of the HEARing CRC, established under the Australian Government's Cooperative Research Centres (CRC) Program. The CRC Program supports industry-led collaborations between industry, researchers and the community. Funding from the Australian Research Council Centre of Excellence Scheme (Project Number CE140100012) is gratefully acknowledged.

ACKNOWLEDGMENTS

The authors thank the Materials Node of Australian National Fabrication Facility (ANFF) and acknowledge use of the facilities.

REFERENCES

Agnew, W. F., Yuen, T. G. H., McCreery, D. B., and Bullara, L. A. (1986). Histopathologic evaluation of prolonged intracortical electrical stimulation. *Exp. Neurol.* 92, 162–185. doi: 10.1016/0014-4886(86)90132-9

Bagotzky, V. S., Vassilyev, Y. B., Weber, J., and Pirtskhalava, J. N. (1970). Adsorption of anions on smooth platinum electrodes. *J. Electroanal. Chem. Interfacial Electrochem.* 27, 31–46. doi: 10.1016/S0022-0728(70)80200-5

Christie, B. P., Ashmont, K. R., House, P. A., and Greger, B. (2016). Approaches to a cortical vision prosthesis: implications of electrode size and placement. *J. Neural Eng.* 13:025003. doi: 10.1088/1741-2560/13/2/025003

Clark, G. M., Shepherd, R. K., Patrick, J. F., Black, R. C., and Tong, Y. C. (1983). Design and fabrication of the banded electrode array. *Ann. N. Y. Acad. Sci.* 405, 191–201. doi: 10.1111/j.1749-6632.1983.tb31632.x

Cogan, S. F. (2008). Neural stimulation and recording electrodes. *Annu. Rev. Biomed. Eng.* 10, 275–309. doi: 10.1146/annurev.bioeng.10.061807.160518

Cogan, S. F., Ludwig, K. A., Welle, C. G., and Takmakov, P. (2016). Tissue damage thresholds during therapeutic electrical stimulation. *J. Neural Eng.* 13:021001. doi: 10.1088/1741-2560/13/2/021001

De Vries, W. T. (1968). Distortion of constant-current chronopotentiograms by double-layer charging. *J. Electroanal. Chem. Interfacial Electrochem.* 17, 31–43. doi: 10.1016/S0022-0728(68)80028-2

Dhanasingh, A., and Jolly, C. (2017). An overview of cochlear implant electrode array designs. *Hear. Res.* 356, 93–103. doi: 10.1016/j.heares.2017.10.005

Donaldson, N. D. N., and Donaldson, P. E. K. (1986). Performance of platinum stimulating electrodes mapped on the limitvoltage plane. *Med. Biol. Eng. Comput.* 24, 431–438. doi: 10.1007/BF02442700

Garcia-Araez, N., Climent, V., Herrero, E., Feliu, J., and Lipkowski, J. (2005). Thermodynamic studies of chloride adsorption at the Pt(1 1 1) electrode surface from 0.1 *M HClO*4 solution. *J. Electroanaly. Chem.* 576, 33–41. doi: 10.1016/j.jelechem.2004.10.003

Harris, A. R., Newbold, C., Carter, P., Cowan, R., and Wallace, G. G. (2018a). Charge injection from chronoamperometry of platinum electrodes for bionic devices. *J. Electrochem. Soc.* 165, G3033–G3041. doi: 10.1088/1741-2552/aaba8b

Harris, A. R., Newbold, C., Carter, P., Cowan, R., and Wallace, G. G. (2018b). Measuring the effective area and charge density of platinum electrodes for bionic devices. *J. Neural Eng.* 15:046015. doi: 10.1088/1741-2552/aaba8b

Harris, A. R., and Wallace, G. G. (2018). Organic electrodes and communications with excitable cells. *Adv. Funct. Mater.* 28:1700587. doi: 10.1002/adfm.201700587

Kennedy, S. H., Giacobbe, P., Rizvi, S. J., Placenza, F. M., Nishikawa, Y., Mayberg, H. S., et al. (2011). Deep brain stimulation for treatment-resistant depression: follow-up after 3 to 6 years. *Am. J. Psychiatry* 168, 502–510. doi: 10.1176/appi.ajp.2010.10081187

Kumsa, D. W., Bhadra, N., Hudak, E. M., Kelley, S. C., Untereker, D. F., and Mortimer, J. T. (2016a). Electron transfer processes occurring on platinum neural stimulating electrodes: a tutorial on the i (V e) profile. *J. Neural Eng.* 13:052001. doi: 10.1088/1741-2560/13/5/052001

Kumsa, D. W., Montague, F. W., Hudak, E. M., and Mortimer, J. T. (2016b). Electron transfer processes occurring on platinum neural stimulating electrodes: pulsing experiments for cathodic-first/charge-balanced/biphasic pulses for$0.566 \leq k \leq 2.3$ in oxygenated and deoxygenated sulfuric acid. *J. Neural Eng.* 13:056001. doi: 10.1088/1741-2560/13/5/056001

Li, N., and Lipkowski, J. (2000). Chronocoulometric studies of chloride adsorption at the Pt(111) electrode surface. *J. Electroanal. Chem.* 491, 95–102. doi: 10.1016/S0022-0728(00)00199-6

Lukins, T. R., Tisch, S., and Jonker, B. (2014). The latest evidence on target selection in deep brain stimulation for Parkinson's disease. *J. Clin. Neurosci.* 21, 22–27. doi: 10.1016/j.jocn.2013.05.011

McCreery, D., Agnew, W., Yuen, T., and Bullara, L. (1992). Damage in peripheral nerve from continuous electrical stimulation: comparison of two stimulus waveforms. *Med. Biol. Eng. Comput.* 30, 109–114. doi: 10.1007/BF02446202

McIntyre, C. C., Chaturvedi, A., Shamir, R. R., and Lempka, S. F. (2015). Engineering the next generation of clinical deep brain stimulation technology. *Brain Stimul.* 8, 21–26. doi: 10.1016/j.brs.2014.07.039

Merrill, D. R., Bikson, M., and Jefferys, J. G. R. (2005). Electrical stimulation of excitable tissue: design of efficacious and safe protocols. *J. Neurosci. Methods* 141, 171–198. doi: 10.1016/j.jneumeth.2004.10.020

Mesnildrey, Q., Macherey, O., Herzog, P., and Venail, F. (2019). Impedance measures for a better understanding of the electrical stimulation of the inner ear. *J. Neural Eng.* 16:016023. doi: 10.1088/1741-2552/aaecff

Michelson, N. J., Vazquez, A. L., Eles, J. R., Salatino, J. W., Purcell, E. K., Williams, J. J., et al. (2018). Multi-scale, multi-modal analysis uncovers complex relationship at the brain tissue-implant neural interface: new emphasis on the biological interface. *J. Neural Eng.* 15:033001. doi: 10.1088/1741-2552/aa9dae

Misrahy, G. A., Shinabarger, E. W., and Arnold, J. E. (1958). Changes in cochlear endolymphatic oxygen availability, action potential, and microphonics during and following asphyxia, hypoxia, and exposure to loud sounds. *J. Acoust. Soc. Am.* 30, 701–704. doi: 10.1121/1.1909734

Mitsushima, S., Kawahara, S., Ota, K.-I., and Kamiya, N. (2007). Consumption rate of pt under potential cycling. *J. Electrochem. Soc.* 154, B153–B158. doi: 10.1242/jeb.072587

Musa, S., Rand, D. R., Bartic, C., Eberle, W., Nuttin, B., and Borghs, G. (2011). Coulometric detection of irreversible electrochemical reactions occurring at pt microelectrodes used for neural stimulation. *Anal. Chem.* 83, 4012–4022. doi: 10.1021/ac103037u

Newbold, C., Richardson, R., Huang, C. Q., Milojevic, D., Cowan, R., and Shepherd, R. (2004). An in vitro model for investigating impedance changes with cell growth and electrical stimulation: implications for cochlear implants. *J. Neural Eng.* 1:218.

Newbold, C., Richardson, R., Millard, R., Huang, C., Milojevic, D., Shepherd, R., et al. (2010). Changes in biphasic electrode impedance with protein adsorption and cell growth. *J. Neural Eng.* 7:056011. doi: 10.1088/1741-2560/7/5/056011

Newbold, C., Richardson, R., Millard, R., Seligman, P., Cowan, R., and Shepherd, R. (2011). Electrical stimulation causes rapid changes in electrode impedance of cell-covered electrodes. *J. Neural Eng.* 8:036029. doi: 10.1088/1741-2560/8/3/036029

Niparko, J. K., Altschuler, R. A., Xue, X., Wiler, J. A., and Anderson, D. J. (1989). Surgical implantation and biocompatibility of central nervous system auditory prostheses. *Ann. Otol. Rhinol. Laryngol.* 98, 965–970. doi: 10.1177/000348948909801209

Normann, R. A., and Fernandez, E. (2016). Clinical applications of penetrating neural interfaces and Utah electrode array technologies. *J. Neural Eng.* 13:061003.

Prasad, A., and Sanchez, J. C. (2012). Quantifying long-term microelectrode array functionality using chronic in vivo impedance testing. *J. Neural Eng.* 9:026028. doi: 10.1088/1741-2560/9/2/026028

Robblee, L. S., McHardy, J., Agnew, W. F., and Bullara, L. A. (1983). Electrical stimulation with Pt electrodes. VII. Dissolution of Pt electrodes during electrical stimulation of the cat cerebral cortex. *J. Neurosci. Methods* 9, 301–308. doi: 10.1016/0165-0270(83)90062-6

Salt, A. N., Kellner, C., and Hale, S. (2003). Contamination of perilymph sampled from the basal cochlear turn with cerebrospinal fluid. *Hear. Res.* 182, 24–33. doi: 10.1016/S0378-5955(03)00137-0

Shannon, R. V. (1992). A model of safe levels for electrical stimulation. *Biomed. Eng. IEEE Transact.* 39, 424–426. doi: 10.1109/10.126616

Tsunoo, M., and Perlman, H. B. (1965). Cochlear oxygen tension: relation to blood flow and function. *Acta Oto-Laryngol.* 59, 437–450. doi: 10.3109/00016486509124578

Tykocinski, M., Cohen, L. T., and Cowan, R. S. (2005). Measurement and analysis of access resistance and polarization impedance in cochlear implant recipients. *Otol. Neurotol.* 26, 948–956. doi: 10.1097/01.mao.0000185056.99888.f3

Tykocinski, M., Duan, Y., Tabor, B., and Cowan, R. S. (2001). Chronic electrical stimulation of the auditory nerve using high surface area (HiQ) platinum electrodes. *Hear. Res.* 159, 53–68. doi: 10.1016/S0378-5955(01)00320-3

Wang, M., Mi, G., Shi, D., Bassous, N., Hickey, D., and Webster, T. J. (2017). Nanotechnology and nanomaterials for improving neural interfaces. *Adv. Funct. Mater.* 28:1700905. doi: 10.1002/adfm.201700905

Conflict of Interest Statement: PC was employed by Cochlear, Ltd.

The remaining authors declare that the research was conducted in the absence of any commercial or financial relationships that could be construed as a potential conflict of interest.

Copyright © 2019 Harris, Newbold, Carter, Cowan and Wallace. This is an open-access article distributed under the terms of the Creative Commons Attribution License (CC BY). The use, distribution or reproduction in other forums is permitted, provided the original author(s) and the copyright owner(s) are credited and that the original publication in this journal is cited, in accordance with accepted academic practice. No use, distribution or reproduction is permitted which does not comply with these terms.

frontiers in Neuroscience

ORIGINAL RESEARCH
published: 24 April 2019
doi: 10.3389/fnins.2019.00393

3D Reconstruction of the Intracortical Volume Around a Hybrid Microelectrode Array

*Aparna Nambiar†, Nicholas F. Nolta† and Martin Han**

Department of Biomedical Engineering, University of Connecticut, Storrs, CT, United States

Extensive research using penetrating electrodes implanted in the central and peripheral nervous systems has been performed for many decades with significant advances made in recent years. While penetrating devices provide proximity to individual neurons *in vivo*, they suffer from declining performance over the course of months and often fail within a year. 2D histology studies using serial tissue sections have been extremely insightful in identifying and quantifying factors such as astroglial scar formation and neuronal death around the implant sites that may be contributing to failures. However, 2D histology has limitations in providing a holistic picture of the problems occurring at the electrode-tissue interface and struggles to analyze tissue below the electrode tips where the electrode tracks are no longer visible. In this study, we present 3D reconstruction of serial sections to overcome the limitations of 2D histological analysis. We used a cohort of software: XuvStitch, AutoAligner, and Imaris coupled with custom MATLAB programming to correct warping effects. Once the 3D image volume was reconstructed, we were able to use Imaris to quantify neuronal densities around the electrode tips of a hybrid microelectrode array incorporating Blackrock, Microprobes, and NeuroNexus electrodes in the same implant. This paper presents proof-of-concept and detailed methodological description of a technique which can be used to quantify neuronal densities in future studies of implanted electrodes.

Keywords: serial section, image registration, 3D reconstruction, intracortical microelectrode, histology, foreign body response, confocal microscopy, dewarping

OPEN ACCESS

Edited by:
Jeffrey R. Capadona, Case Western Reserve University, United States

Reviewed by:
Takashi D. Y. Kozai, University of Pittsburgh, United States
Janak Gaire, University of Florida, United States

***Correspondence:**
Martin Han
martin.han@uconn.edu

† These authors have contributed equally to this work

Specialty section:
This article was submitted to Neural Technology, a section of the journal Frontiers in Neuroscience

Received: *18 December 2018*
Accepted: *05 April 2019*
Published: *24 April 2019*

Citation:
Nambiar A, Nolta NF and Han M (2019) 3D Reconstruction of the Intracortical Volume Around a Hybrid Microelectrode Array. Front. Neurosci. 13:393. doi: 10.3389/fnins.2019.00393

INTRODUCTION

Numerous studies have implanted electrodes chronically into the brain to stimulate neurons and record neural activity (Wessberg et al., 2000; Santhanam et al., 2006; Collinger et al., 2013; Downey et al., 2016; McCreery et al., 2018). These studies have produced basic neuroscience discoveries and demonstrated proof-of-concept for brain-machine interfaces such as those restoring upper limb control (Collinger et al., 2013; Downey et al., 2016). However, the electrodes that interface with brain tissue tend to decline in performance over the course of months and in most cases stop recording any single unit action potentials within a year (Liu et al., 1999; Barrese et al., 2013).

Therefore, many investigators have sought to identify the failure modes of microelectrodes in the brain. Breakage of connectors and delamination of insulating materials are significant failure modes, but many failures occur despite a seemingly functional implant, indicating that problems exist on the biological side of the interface as well (Prasad et al., 2012, 2014;

Barrese et al., 2013; Nolta et al., 2015; Black et al., 2018; Cody et al., 2018). Several mechanisms have been proposed including: glial encapsulation increasing the distance and impedance between neurons and electrodes (Edell et al., 1992; Liu et al., 1999; Turner et al., 1999); encapsulation, scarring, tissue loss, or tethering forces causing the electrode to move away from its intended position or to tilt within tissue (Liu et al., 1999; Barrese et al., 2013; Nolta et al., 2015; Cody et al., 2018); and death, degeneration, or rewiring of neurons causing them to become silent (Biran et al., 2005; McCreery et al., 2016; Eles et al., 2018).

The primary tool for testing these hypotheses has been histological analysis of tissue near the electrodes. Typically, tissue is sectioned, immunohistochemically-labeled, and analyzed quantitatively as a series of 2D images (Shain et al., 2003; Biran et al., 2005; McConnell et al., 2009; Kozai et al., 2012; Potter et al., 2012). Even when confocal microscopes are used, the 3D images of individual sections are projected into 2D images before analysis. 2D histological approaches have had some success correlating histological features with chronic performance of individual electrodes on large, multi-electrode devices (Freire et al., 2011; Prasad et al., 2012, 2014; Kozai et al., 2014; Nolta et al., 2015; McCreery et al., 2016); however, in these studies, it was not always possible to determine why a particular electrode failed, and teasing apart multiple confounding failure modes proved challenging.

2D histological analysis has significant limitations. The "recording zone" in which neural action potentials can be detected extends approximately 100 μm from the electrode recording sites (Henze et al., 2000), so in 2D histology, this is taken as a 100-μm-radius circle in a tissue section at a depth corresponding to the recording site. However, the recording zone is actually a 3D sphere, including tissue 100 μm below the recording site in sagittal or coronal view. This means the tissue below the recording site is being ignored. For tip-based microelectrodes, the tissue below is of particular interest since this tissue has been less disrupted by the electrode. This cannot be rectified by simply looking at more sections, because in 2D histology, the location of the recording site is unknown once the electrode track is no longer visible. Hence, some healthy neurons in the tissue below the tip contributing to the recordings may go uncounted, which could lead to inaccurate correlation of neuronal density with recording data. This aspect also has ramifications in stimulation applications because virtually all data related to the Shannon-McCreery curve for safe limits of charge injection were collected based on 2D histology (Shannon, 1992).

Another limitation of 2D histology is the difficulty of visualizing and understanding the large scale, depth-dependent features of the biological response, such as the location or tilt of the device within cortical layers, when looking at a series of 2D images. These changes in location or tilt can be very significant due to the forces exerted by connective tissues and stiff tethering cables (Karumbaiah et al., 2013; Nolta et al., 2015). A holistic, 3D view of these problems could provide new insights.

A few recent studies have conducted 3D analysis of tissue near electrodes. One group cleared, stained, and imaged thick sections with the electrode in place, although the imaging depth was limited to about 300 μm (Woolley et al., 2011, 2013; Lee et al., 2018). 3D regions of tissue loss were reconstructed at low resolution from 2D serial sections (Nolta et al., 2015). Micro-CT has been employed to localize electrodes before sectioning (Cody et al., 2018). Finally, 3D two-photon imaging was used to study the chronic biological response *in vivo*, although this required implanting the device at an oblique angle and installing a cranial window (Kozai et al., 2016; Eles et al., 2018).

An alternative approach would be to use software to reconstruct a 3D dataset from confocal images of every section. This would enable 3D analysis of the full implant area without having to alter established histological procedures, and also allow analysis of already-scanned tissues. The main challenge is in aligning consecutive sections. Fully-automated alignment is possible with advanced software and adequate fiducials (Arganda-Carreras et al., 2010) or if there are fine details that can be correlated between sections (Mathiisen et al., 2010). Unfortunately, in our case, our available fiducials, such as electrode tracks, blood vessels, and brightly-staining regions of tissue, were not recognizable by a professional automatic alignment software package Voloom (Bitplane AG, Zurich, Switzerland). It was also clear that minor blade losses during sectioning and significant deformation of individual sections during processing precluded the use of alternative programs operating on the correlation of fine details between sections. Our strategy instead was to use the electrode tracks as fiducials and perform alignment manually. Our device had electrode sites at the tips of 1-mm-long electrodes, so we were able to reconstruct the tissue above and below the tips of all the 1-mm electrodes using the 2-mm electrodes as fiducials. Our technique was similar to that of a group performing midbrain mapping studies (Markovitz et al., 2012) but different in that it used 3D confocal images, achieved alignment accuracy much better than 100 μm, and did not require adding artificial fiducials. In addition, we developed and employed a simple dewarping algorithm to help reduce the effects of tissue deformation. Finally, we were able to quantify the density of neuronal nuclei in 3D regions around recording sites, which to our knowledge has not yet been accomplished in our field. This work describes our technique in detail and demonstrates its potential to improve the understanding of biological failure modes of chronically implanted electrodes.

MATERIALS AND METHODS

Devices, Surgery, Immunohistochemistry, and Image Acquisition

Raw images were from an unpublished study by our group using "hybrid" electrode arrays in cats. Hybrid electrode arrays (**Figure 1A**) consisting of eight 1 mm long Blackrock electrodes (Blackrock Microsystems, Salt Lake City, UT, United States), four 1.5 mm long planar silicon probes (NeuroNexus, Ann Arbor, MI, United States), and four "short" 1 mm long and four "long" 2 mm long microwires (Microprobes, Gaithersburg, MD, United States) were implanted in the post-cruciate gyri

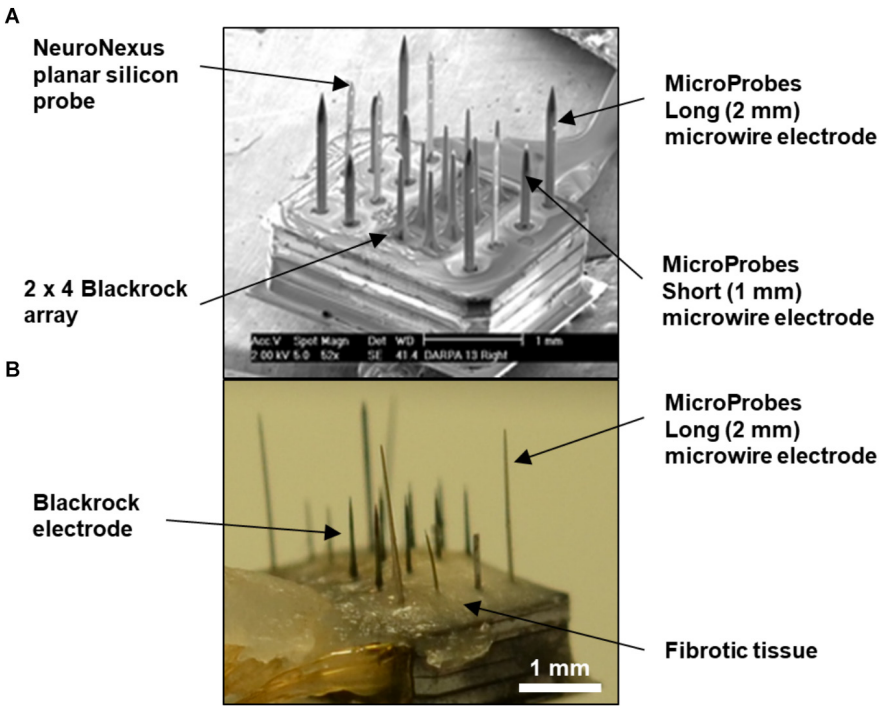

FIGURE 1 | (A) SEM of fully-assembled hybrid array before implantation showing four types of commercial microelectrodes assembled in a mixed fashion. The overall footprint of the array is approximately 1.7 mm × 2.2 mm. **(B)** Photograph of the explanted hybrid array from the animal used in this study. The base of the array was covered with fibrotic tissue, but the majority of the length of the electrodes appeared free of tissue. Also, the long microwire and NeuroNexus probes were tilted at an angle.

of male cats. All electrodes had an active site at 1 mm depth. The implantation duration for the cat whose histological data was analyzed in this study was 371 days, after which the cat was fully anesthetized and transcardially perfused as described previously (Han et al., 2012). After post-fixation, the implanted device was carefully removed (**Figure 1B**), and a tissue block 6 mm × 8 mm × 10 mm was punched out. Horizontal serial sections 50 μm thick were sectioned perpendicular to the electrode shanks to a depth of 3 mm below the brain surface, encompassing the full length of all the electrode shanks, for a total of 60 sections. The tissue sections were stained using immunofluorescence labeling procedures as described previously (Duong and Han, 2013). Briefly, free-floating sections were subjected to 24 h high-intensity LED photoirradiation in citrate buffer to reduce autofluorescence, followed by 1 h antigen retrieval at 83°C, cooling to room temperature, 2 h blocking with 5% normal goat serum, 48 h incubation at 4°C with constant agitation with primary antibodies, then the same incubation for secondary antibodies (Alexa Fluor, Life Technologies, Carlsbad, CA, United States). All tissue sections were multiple-labeled with rabbit anti-IBA-1 (Wako Chemical, Richmond, VA, United States), biotinylated mouse anti-NeuN (EMD Millipore, Billerica, MA, United States), chicken anti-MAP-2 (EMD Millipore, Billerica, MA, United States), rat anti-GFAP (Life Technologies, Carlsbad, CA, United States), and DRAQ-5 nuclear stain (eBioscience, San Diego, CA, United States). IBA-1, MAP-2, GFAP, and DRAQ-5 were used for alignment purposes only. Only NeuN was quantified in this study. Sections were mounted in mounting media on glass slides with 50-μm-thick square-shaped polyimide spacers cut from adhesive film (Product No. 2271K69, McMaster Carr, Los Angeles, CA, United States) placed between the slide and the coverslip to avoid compressing the sections. The slides were imaged using an LSM 510 Meta laser scanning system attached to a Zeiss Axiovert 200 M inverted microscope with an Olympus 20× objective (N.A. = 0.5). A 10 × 10 grid of images spanning about 3.5 mm × 3.5 mm with 10% overlap was obtained at each *z*-depth or "optical slice." All electrode tracks were included in the scanned area. Optical slices were collected from slightly above the top to slightly below the bottom of the section in order to capture all of the tissue. Constant laser power was used. The voxel dimension was 0.89 μm × 0.89 μm × 3 μm. The scan time was approximately 5 h per section. All of the above was carried out at our group's previous institution, Huntington Medical Research Institutes (HMRI), in Pasadena, CA, United States. All procedures involving animals were approved by the HMRI Institutional Animal Care and Use Committee.

Image Processing and 3D Reconstruction

Overview

Figure 2 is a schematic of the steps involved in the 3D reconstruction process. The confocally-scanned images

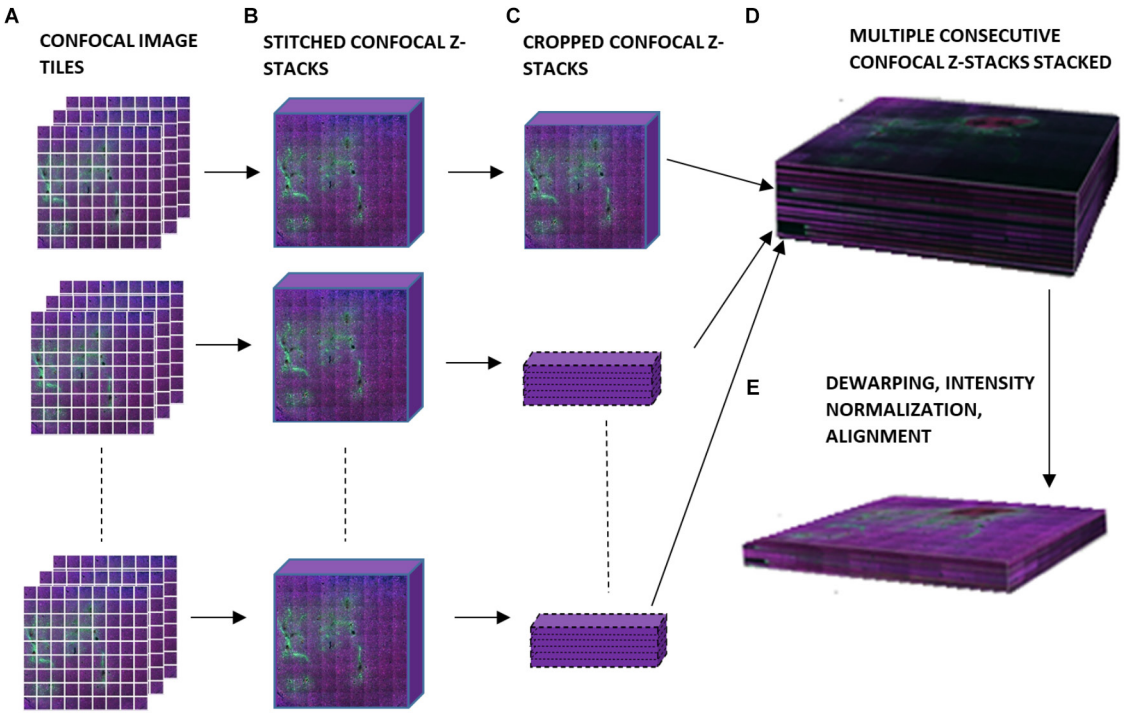

FIGURE 2 | Schematic of workflow for 3D image reconstruction, illustrating **(A)** confocal image tiles, **(B)** stitched confocal *z*-stacks, **(C)** confocal *z*-stacks cropped to the same *x* and *y* dimensions, **(D)** stacked confocal *z*-stacks, and **(E)** the final 3D volume after dewarping, intensity normalization, and alignment.

(**Figure 2A**) were first stitched. This created a 3D stack 50 μm thick for each section (**Figure 2B**). Then, all of these were cropped to the same *x*-*y* size (**Figure 2C**) and stacked consecutively to form one 3D volume (**Figure 2D**). The stacks were not aligned at this point, but putting them in one file streamlined the subsequent steps. Dewarping, intensity normalization, and alignment were then performed to reconstruct the volume of tissue (**Figure 2E**). Finally, electrode tips were drawn, neurons were identified, and quantifications of neuronal density at various distances from the electrode tip were obtained. All these steps are described in detail in the succeeding sections. The computer used was a PC running 64-bit Windows 10 with 176 GB RAM, two quad-core Intel Xeon 2.13 GHz processors, and an ATI FirePro V7800 graphics card.

Stitching, Cropping, and Stacking

Stitching was performed in XuvStitch (Emmenlauer et al., 2009) (**Figures 2A,B**). Individual image tiles were stitched using automatic mode with ten percent overlap and ninety-five percent similarity threshold. Manual stitching was seldomly used only when automatic mode was not adequate. The *x*-*y* size of the largest individual section for stacking was 4553 × 4658 pixels. Differences in the *x* and *y* dimensions of each section were eliminated by cropping them to equal *x* and *y* values, i.e., 4,093 × 4,184 (**Figure 2C**) before stacking them in one 30-GB file (**Figure 2D**). For the dataset shown in this paper, fourteen consecutive physical sections were stacked, because they had all electrode tips and easily-identifiable tracks that could be used later on for alignment. **Figure 3A** shows the image data after cropping and stacking. At this point, the physical sections are totally un-aligned.

Dewarping and Intensity Normalization

Dark bands between sections in the stack were observed (**Figure 3B**). Most of this was from imaging extra optical slices above and below the tissue to ensure that no data was missed, and could be corrected by simply deleting the extra slices. However, many sections were tilted relative to the imaging plane or had significant curvature or wrinkles from mounting, so deleting slices would have resulted in either losing data or including dark areas. To remedy this problem, we developed a custom dewarping program (**Supplementary File 1**) in MATLAB (The MathWorks, Inc., Natick, MA, United States) that interfaced with Imaris (Bitplane AG, Zurich, Switzerland) via the ImarisXT feature. ImarisXT causes MATLAB m-files stored in specific folders to appear as available actions in the Imaris menus. Clicking on one of these actions starts MATLAB and executes the m-file. A Java library provided by Bitplane provides extra functions that can be written into the MATLAB code to perform various operations such as transferring data between the two programs.

When executing the dewarping program, the user is first prompted to input the number of optical slices per section the user wants to keep. We chose sixteen slices per section because the tissue block was sectioned at 50 μm thickness. Each optical slice is 3 μm thick, hence 16 μm × 3 μm = 48 μm (approximately 50 μm).

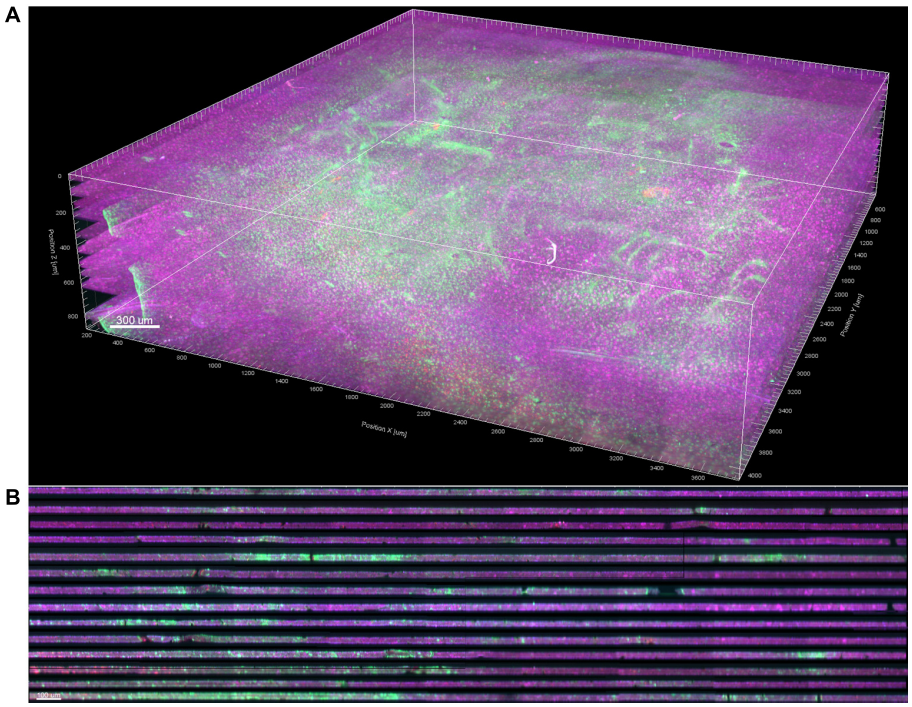

FIGURE 3 | (A) 3D volume rendering of GFAP (green) and NeuN (magenta) after stitching, cropping, and stacking. Dewarping, alignment, and intensity normalization have not yet been performed. **(B)** Vertical cross section through the 3D volume. The dark bands are dark, out-of-focus optical slices above and below the actual tissue in each section.

The algorithm then chooses the brightest contiguous subset of voxels in each *z*-column and retains them, while discarding the low intensity voxels at the top or bottom (**Figure 4**). The dark slices with no useful information encompassing dark, out-of-focus voxels are removed, and because each column of voxels is dealt with separately, any tissue tilt, curvature, or wrinkling is also fixed. The *x*-*y* data are not modified, so there is neither addition nor removal of horizontal distortions, and no alignment is performed at this stage. An additional step of intensity normalization using an in-built function in Imaris was also applied to correct differences in staining intensity from section to section, assisting in qualitative analysis and improving segmentation of nuclei. Intensity-based quantification was not performed in this study, but if it was, the intensity normalization step would have been skipped to avoid introducing systematic error.

Alignment

Next, manual alignment of the stacked, dewarped image dataset was done using AutoAligner (Bitplane AG, Zurich, Switzerland). This software has both automatic and manual alignment mode. However, automatic alignment works best for image data having very large and obvious fiducials, such as the outer boundary of the tissue sample, which we did not have in our dataset. Instead, we applied manual translational and rotational transformations by using the Microprobes and Blackrock electrode tracks that we intended to perform quantification and analysis on as fiducials. The electrode tracks were identified as holes devoid of staining and with characteristic size and arrangement. **Figure 5** shows the alignment process, which involved overlaying the bottom optical slice of one section with the top optical slice of the next vertically-consecutive section in two different colors. By aligning adjacent optical slices, rather than whole sections, the impact of angled or curved fiducials is greatly reduced: horizontal displacement of an angled fiducial will still occur throughout the 16 optical slices of the section, even if it does not occur between the optical slices that are aligned. AutoAligner's manual alignment interface was very useful, but the program crashed when attempting to apply the planned translations and rotations to datasets larger than about 12 GB. Therefore, we created a custom software program in MATLAB that would take saved alignment data (.aln files) from AutoAligner and apply the specified translations and rotations to a dataset in Imaris, using the ImarisXT feature to allow communication between MATLAB and Imaris (**Supplementary File 2**). The program accomplishes the same rotations and translations as AutoAligner, but does not run into file size problems. Briefly, the .aln file must be renamed with the .txt extension, then MATLAB opens and reads the text file, calculates the rotations and translations to be performed in MATLAB (which uses different conventions), orders Imaris to pad (add black space) the margins of its dataset to the exact minimum extent necessary, then loads, rotates, translates, and sends back each optical slice one at a time to Imaris. Sending one slice at a time is necessary because while Imaris and MATLAB have extremely large memory limits, the Java interface handling data transfer does not.

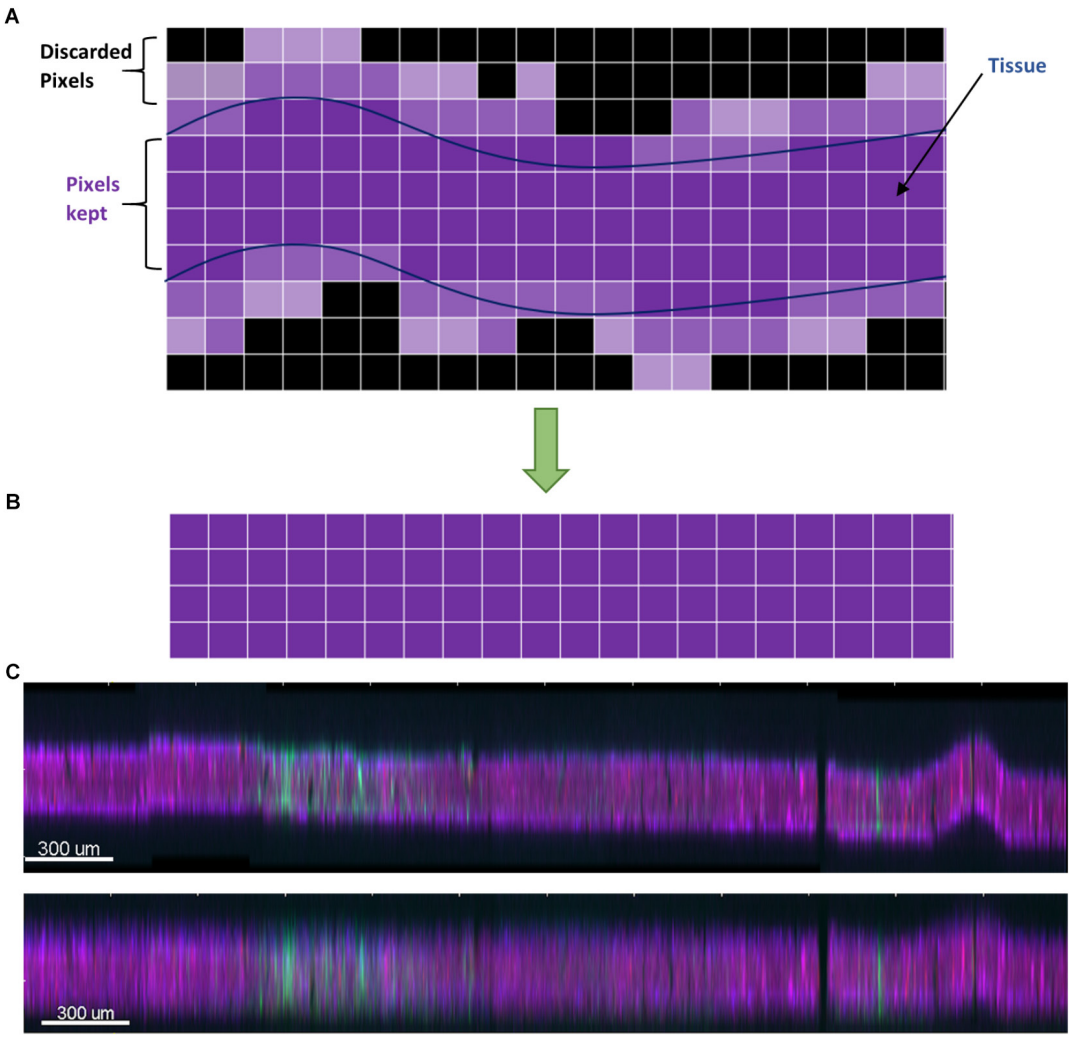

FIGURE 4 | (A) Schematic of the dewarping algorithm. The brightest contiguous subset of voxels in *z* is retained while the rest are discarded, resulting in a flatter section. **(B)** Vertical cross section through a section before dewarping with height scaled 10×. The section is tilted, has a large wrinkle, and has a stitching artifact. **(C)** After dewarping the tissue is nearly flat (height still scaled 10×).

Drawing Recording Sites and Quantification

The data set was first converted from 16-bit to 32-bit and down-sampled by fifty percent before drawing the shanks. This is a requirement for the distance transform in Imaris. Artificial recording sites were manually drawn using the "surfaces" feature in Imaris (**Figure 6**). Electrode tip lengths, i.e., lengths of the active electrode sites, for the Blackrock electrodes and the 1-mm microwire electrodes were previously measured under an optical microscope during device assembly. Using this information, the section where the recording site begun was determined by measuring the distance backward from the deepest point of the electrode track. The "circle" drawing mode was used to draw the recording sites and 100 vertices were chosen to provide smoother zones. Once the contours were drawn on sequential slices, Imaris built the recording site by connecting the contours. Care was taken to ensure that adequate contours were drawn to allow the formation of a smooth surface.

Distance transformations were applied to each shank in Imaris. This computes the distance from each voxel in the image to the nearest point on the shank surface. Then, surfaces were created around the shank to define distance bins in increments of 25 μm up to a distance of 200 μm (**Figure 6A**). These distance bins could be further subdivided by depth, as shown schematically in **Figure 6B**.

The automatic spot detection feature of Imaris was used to identify neurons. Neuronal nuclei are distinguishable as high-intensity spheroids in the NeuN channel having a diameter of about 10 μm. This diameter was obtained by measuring multiple NeuN spheroids in 2D slice views (**Figure 7**). The size requirement also helps avoid double-counting of the same neuron in two vertically-adjacent sections when it is cut in half by the vibratome blade. Intensity mean thresholds were applied to include spots only in a certain range of intensity values. False negatives were manually removed after automatic detection.

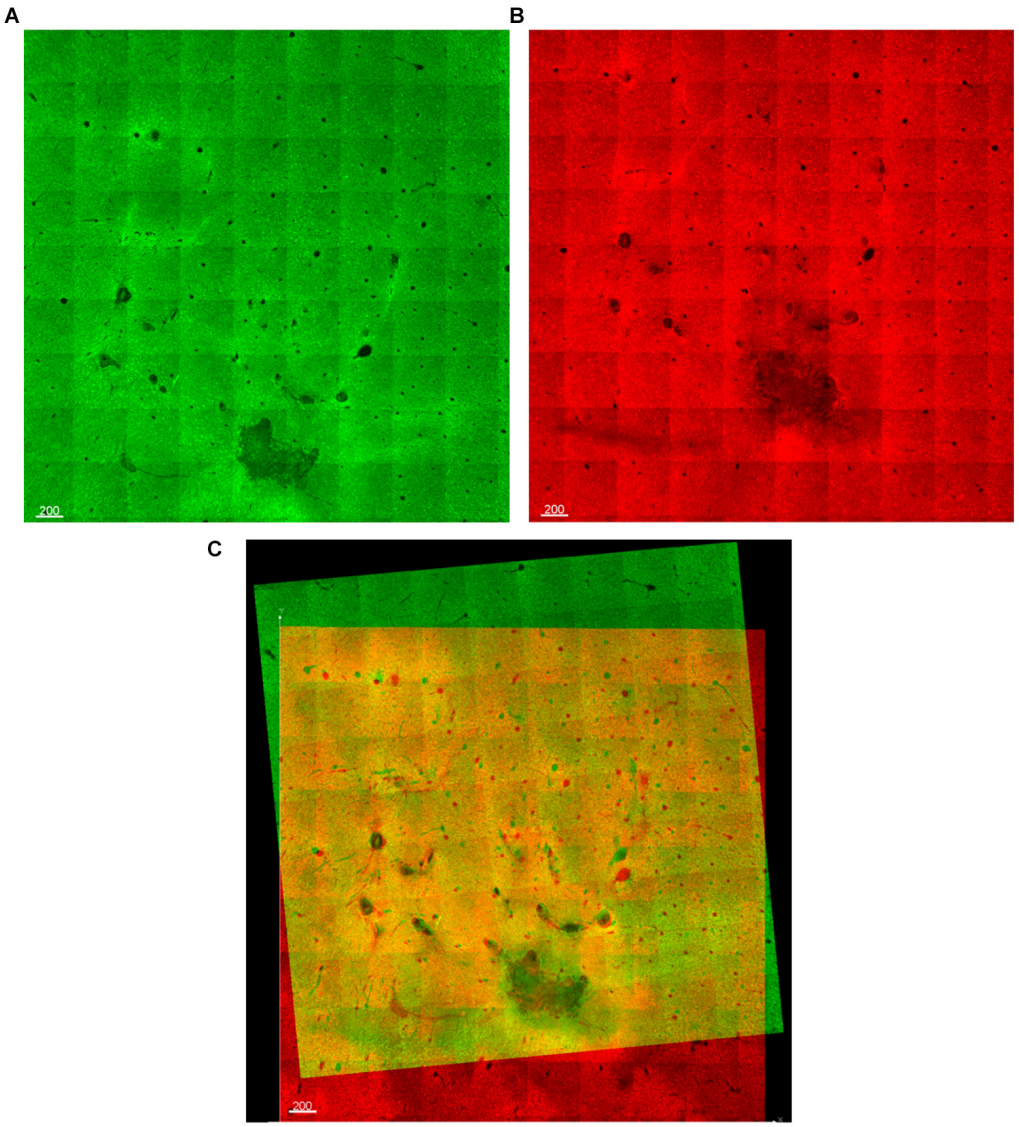

FIGURE 5 | (A,B) Two optical slices from vertically-consecutive sections. One is shown in green, the next in red. **(C)** During alignment, the red and green images are overlaid, allowing fiducials (electrode tracks) to be manually aligned.

Neurons in various distance bins surrounding three Blackrock electrode tips are shown in 3D space in **Figure 8**. Neuron counts were then converted into neuronal density by dividing by the volume of the bin.

RESULTS

Qualitative Analysis of 3D Reconstructed Tissue Volume

A 3D view of the reconstructed tissue volume is shown in **Figure 9**. Several electrode tracks appear as a series of concentric rings (due to inconsistent staining intensity, even after intensity normalization). The quality of alignment was sufficient for large-scale overall viewing as well as close-up viewing and quantification near the electrode tracks. The alignment was within about 40 μm, as shown in **Figure 10**. In order to achieve perfect alignment, local stretching of the image will be necessary to undo the non-uniform stretching, compression, and angling of tissue during immunohistochemistry and mounting.

The 3D reconstruction appeared relatively seamless when viewed from the side except for thin dark bands between sections. It is likely that the thickness of each section during imaging was less than the thickness after sectioning due to shrinkage and/or compression of the section during immunohistochemistry and mounting. In the future this could be corrected by keeping fewer optical slices during dewarping and then scaling the image up to its actual dimensions. This artifact would not affect quantification, however, because the same numbers of neurons are present in each section.

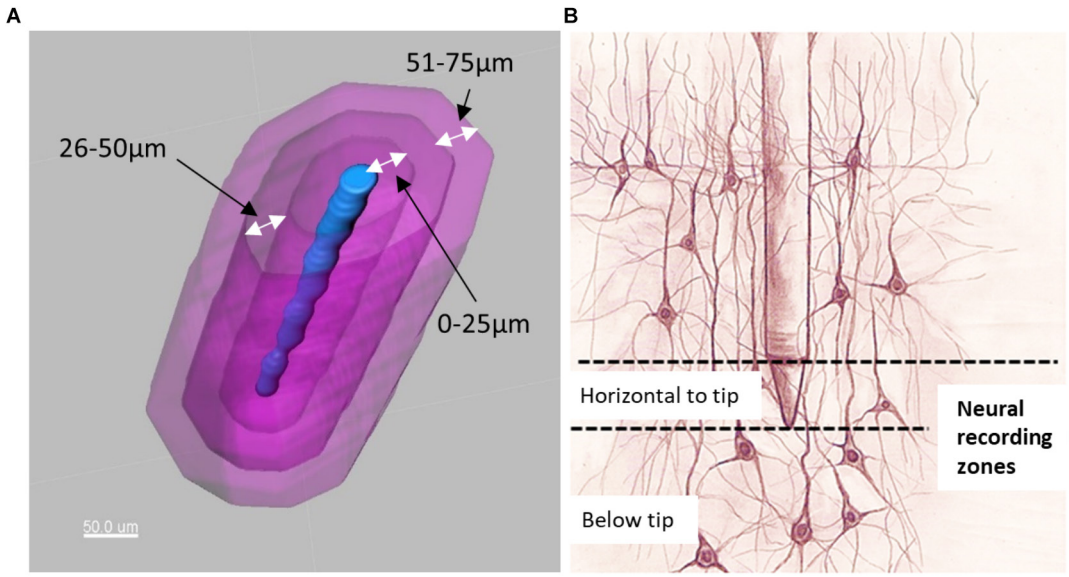

FIGURE 6 | (A) Electrode tip (blue) and distance bins (magenta) for quantification of neurons. **(B)** Illustration of neurons located horizontal to the electrode tip versus those located below the electrode tip.

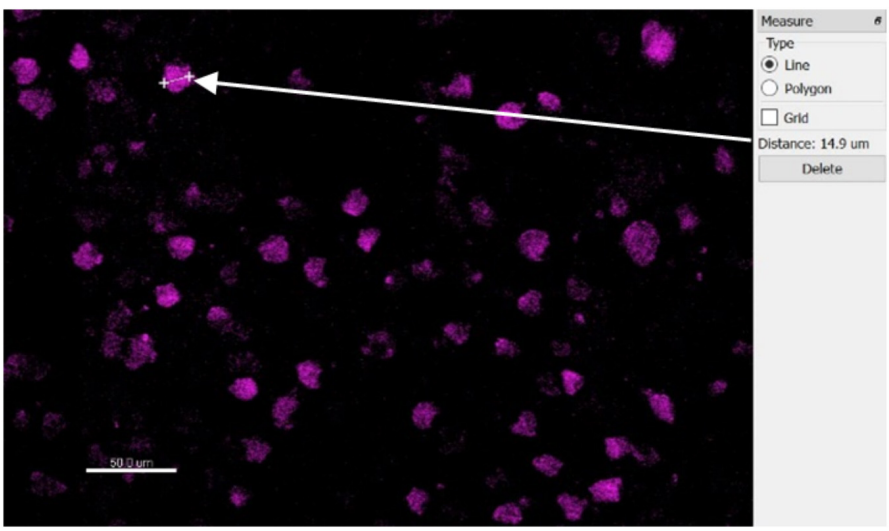

FIGURE 7 | Top-down slice view of NeuN-stained tissue showing one measurement of a typical neuron's diameter.

A significant tilt of the electrodes was observed. Since the tissue punch was inserted perpendicular to the brain surface and the block of tissue was then sectioned horizontally, this observed tilt represents the actual angle of the device in tissue. The device was observed to be tilted and sunken down into cortex at necropsy. Tethering forces and the build-up of fibrotic tissue have been reported to tilt electrodes over time (Barrese et al., 2013; Nolta et al., 2015; Cody et al., 2018). Being able to observe this tilt so clearly is a significant advantage of 3D vs. 2D analysis. It was also noted for this explanted device that the Blackrock and short microwire electrode shanks were still straight while the NeuroNexus and long microwire electrodes had been bent to an angle different from their original position (**Figure 1B**).

The superficial cortex near the base of the array was not included in the reconstruction because the electrode tracks were not visible in this area. As can be seen in **Figure 1B**, fibrotic tissue had encapsulated the base of the array and remained adhered to it during explantation, similar to other reports using Blackrock arrays (Barrese et al., 2013; Cody et al., 2018). However, very little, if any, tissue adhered to most of the length of the shanks, and there were no missing chunks of tissue in the deeper histological sections. Also, the brain did not appear to be torn or stretched as a result of removing the array.

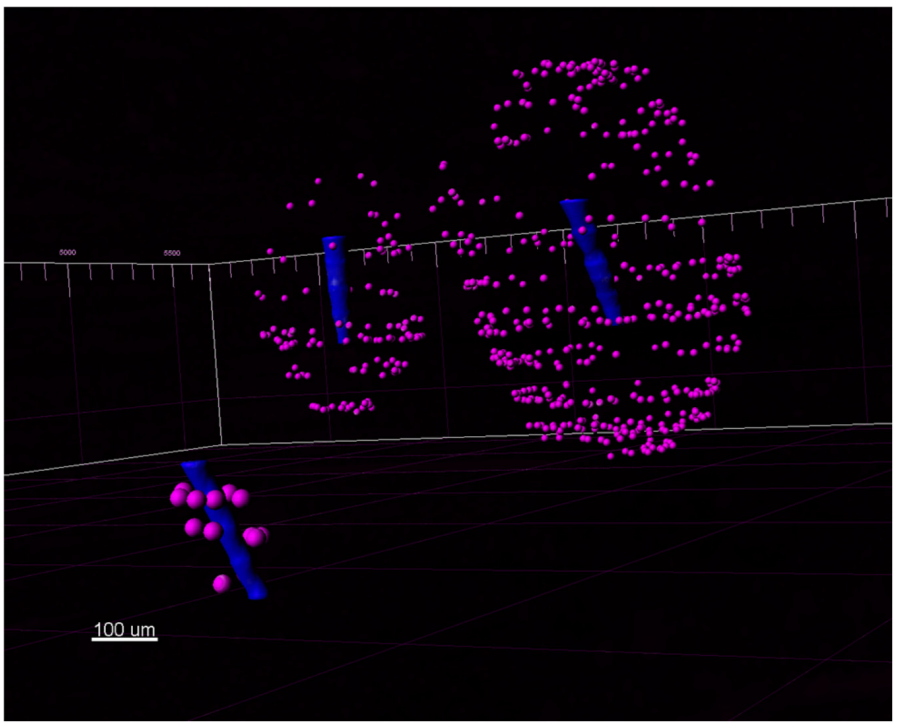

FIGURE 8 | A view of three Blackrock shank tips (blue) with neurons (magenta) detected in the 3D reconstructed volume.

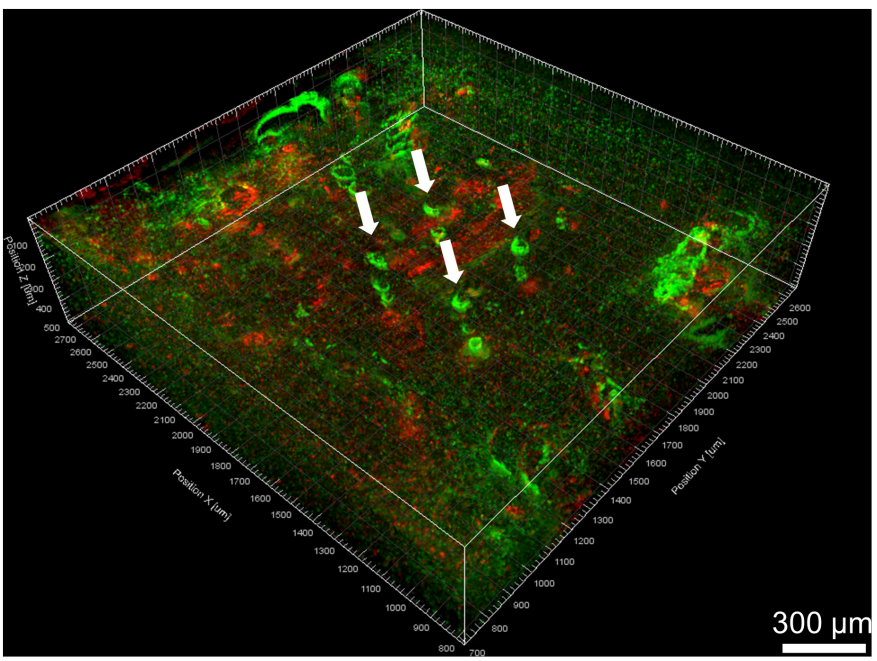

FIGURE 9 | Volume rendering of GFAP (green) and IBA-1 (red) after alignment. Four Blackrock electrode tracks are highlighted with white arrows. The astroglial sheath stained brighter in some sections than others and looks like a series of rings.

To evaluate the consistency of manual alignment across users, the alignment rotations and translations of two users were compared. When each user performed the alignment according to their own judgment, the average absolute difference was 4.4 $\pm$ 4.6° rotation, 170 $\pm$ 81 µm translation in x, and 102 $\pm$ 44 µm in y. When each user was instructed to use the

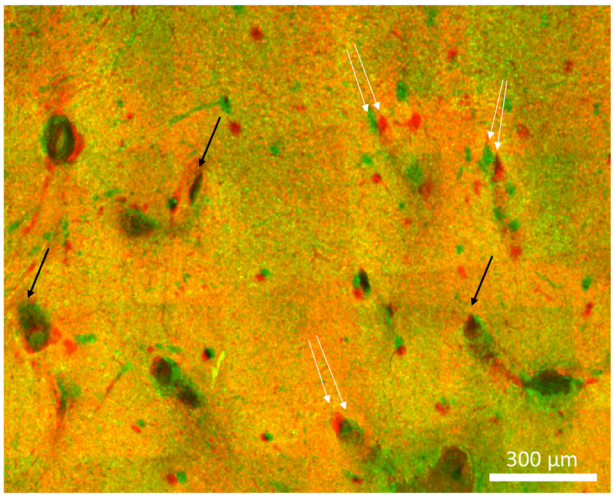

FIGURE 10 | Imperfect alignment of two sections. Black arrows indicate well-aligned fiducials whereas white arrows indicate fiducials that could not be aligned presumably due to distortions in the tissue. The magnitude of the misalignments indicated are 30, 42, and 38 µm.

same set of features as fiducials, the average absolute difference was 0.4 ± 0.6° rotation, 9 ± 16 µm translation in x, and 13 ± 21 µm in y.

Quantitative Analysis of Neuronal Density Near Recording Sites

Manually validating the accuracy of our neuron counting technique for $N = 4$ electrodes showed that automatic neuron counting slightly underestimates the number of neurons in the first 200 µm near an electrode by an average of 2.8%. **Figure 11** shows the numbers counted in each bin manually vs. automatically. As another check on quantification accuracy, and to provide a reference point for neuron quantification near electrode tips, we automatically counted neurons in large regions of healthy neural tissue at the same depth as the electrode tips but far away horizontally. By this method we calculated a density of 48,000 neurons/mm^3 in healthy tissue.

Neuronal density was then quantified for three Blackrock electrodes and one short microwire electrode as a proof-of-concept (**Figure 12**). No statistical inferences were attempted due to the small N. For the Blackrock electrodes, neuronal density was lowest 0–25 µm from the electrode surface, increased by more than two-fold by 76–100 µm, then generally leveled off to a constant value somewhat below healthy tissue by 126–150 µm. Substantial variability was present even in this small sample. Meanwhile, the short microwire electrode had a higher density than the Blackrock electrodes in the first 50 µm, then decreased until it was less than the Blackrock electrodes from 100–200 µm. Future investigations of more microwires will be necessary to elucidate whether this pattern is typical of microwires or was an outlier. Actual neuron counts for the Blackrock electrodes were approximately 10 in the 0–25 µm bin, 200 total in the four bins from 0–100 µm, and 1000 total in the four bins from 100–200 µm.

Finally, we compared counts of neurons found in areas horizontal to the electrode tip (which could have been counted using traditional 2D analysis) versus counts in areas below the electrode tip (which can only be counted using 3D analysis). These regions are shown schematically in **Figure 6B**. **Figure 13** shows the average number of neurons counted around four Blackrock electrode tips in the tissue horizontal to vs. below them. A substantial portion of neurons are found below the electrode tips, especially at farther distances. Combining counts for 0–100 µm, 36% of neurons were found below the tips, and for the whole 0–200 µm, 52% were below the tips.

Total Time Required

For an experienced user performing this analysis on a typical-sized stack (∼15 sections), the process required 2.5 h for stitching, 1 h for cropping, 8 h unattended process time for dewarping, 1.5 h for manual alignment, and 12 h unattended process time to apply the alignment, for a total of 5 h labor plus two overnight steps. For the quantification steps, each electrode tip required 0.5 h to draw the tip, 4 h to create distance bins (mostly unattended process time), and 2.5 h to detect and quantify neurons, for a total of 3 h labor plus 4 h mostly unattended process time. Scaled up to an array of 20 electrodes, the entire process would take 65 h of labor, 80 h mostly unattended process time, and 20 h completely unattended process time.

DISCUSSION

Confocal images of 50 µm serial sections of cat cortex were successfully dewarped, aligned, reconstructed in 3D, and quantified in terms of neuronal density at various distances from electrode tips. To our knowledge, this is the first time that serial sections have been reconstructed around an implanted electrode array. This technique has the advantage of providing a holistic view of the entire implant area and allowing for quantification in more accurate, 3D representations of electrode recording zones. Specifically, electrode tilt was easily visualized (which is not the case in 2D histology) and neurons were quantified below the tips of the electrodes (which is not possible in 2D histology). Within the first 200 µm, 52% of neurons were found below the tips; in 2D histology, these neurons would have been left out. This may have ramifications in correlation of recording quality with tissue response metrics, especially since neurons below the tip are presumably healthier. Our dewarping algorithm and pipeline for manual alignment is not specific for neural electrodes and could also readily be applied to other datasets which require relatively precise alignment of fiducials that are difficult or impossible for software to align automatically.

Our measurement of 48,000 neurons/mm^3 in healthy tissue is plausible. This value is only slightly higher than the average density in the farthest distance bin (175–200 µm) of 39,000 neurons/mm^3, indicating that there may be some loss of neurons 200 µm from the electrode shanks. Alternatively, the brain under the array may have been compressed such

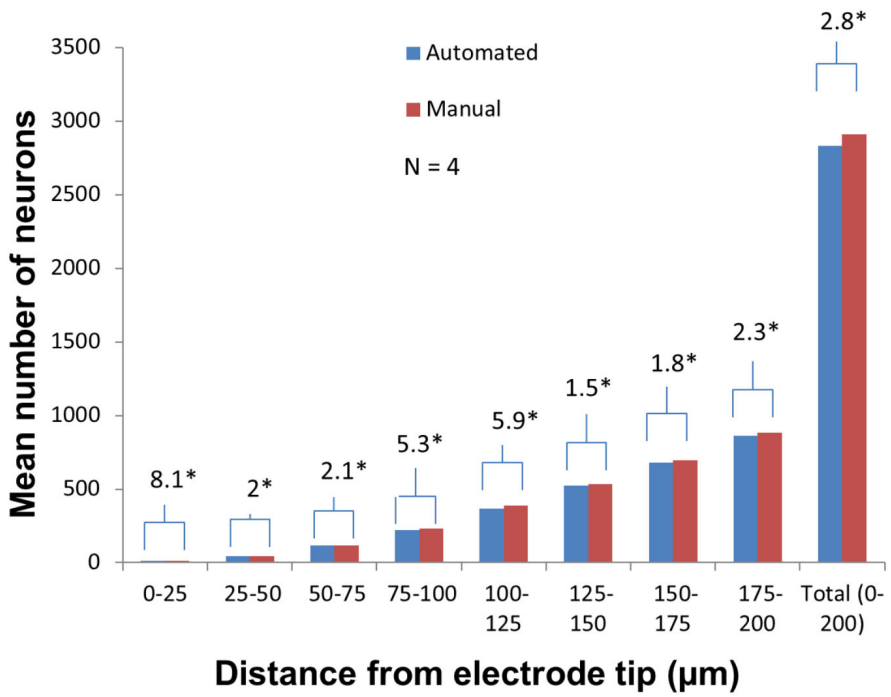

FIGURE 11 | Manual validation of automatic neuron counting protocol. From four electrodes analyzed, on average, manual counting labeled 2.8% more neurons than automatic counting. The greatest errors were seen in the 0–25, 75–100, and 100–125 µm bins. Asterisk denotes statistical significance ($p < 0.05$) using one-tailed paired *t*-tests.

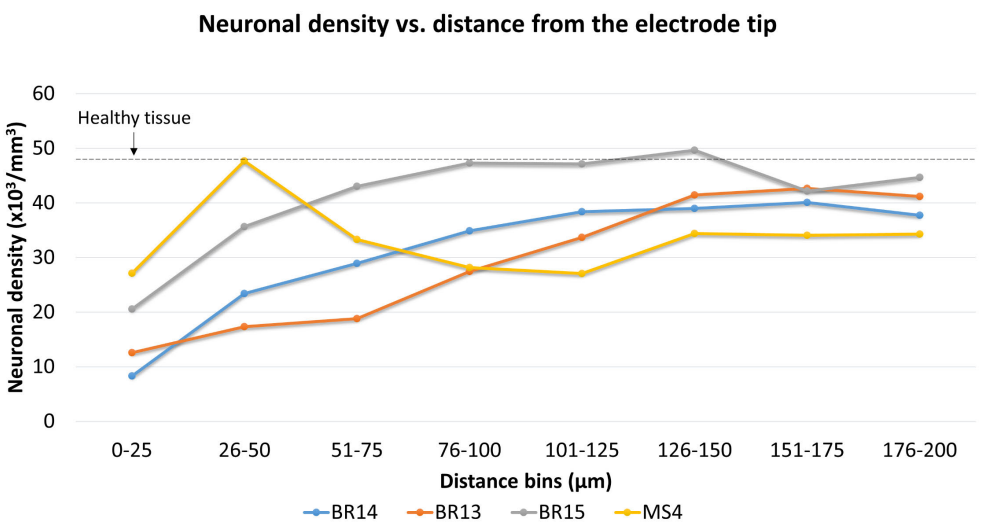

FIGURE 12 | Neuronal density for three Blackrock electrode tips and one short microwire electrode tip. For Blackrock electrodes (BR), neuronal densities increased with distance from the electrode surface. For the microwire electrode (MS), neuronal density was higher than the Blackrock electrodes in the first 50 µm, then decreased until it was less than the Blackrock electrodes from 100–200 µm. Dashed line represents the neuronal density measured in healthy tissue far from the electrode tracks at the same depth.

that the tissue horizontal to the tips was actually a different cortical layer. Neuronal density varies by brain region, cortical depth, and animal species. From an earlier study, averaging the neuronal density of 72 non-stimulating electrode tips in nine cats in the farthest bin (120–150 µm) in the same region of cat cortex (post-cruciate gyrus), one obtains a neuronal

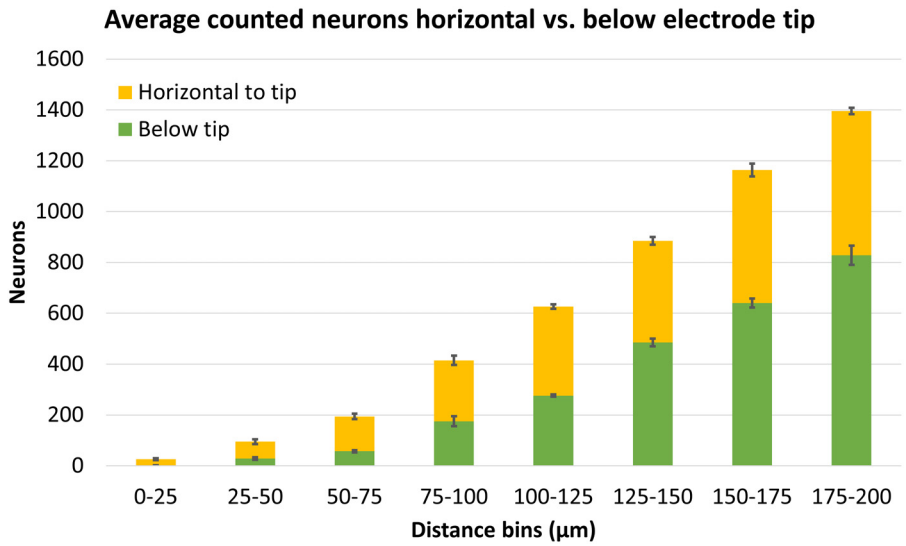

FIGURE 13 | Average neuron counts surrounding four Blackrock electrodes, split in two different depths: horizontal to the electrode tip, or below the electrode tip. Error bars show standard deviation.

density of approximately 570 neurons/mm^2, which can be divided by the thickness (three 7-µm sections) to get an estimate of 27,000 neurons/mm^3 (McCreery et al., 2010). That number is roughly similar but substantially smaller than our measurement, even when compared to the average density we measured in the 125–150 µm in our study, 41,000 neurons/mm^3. Differences in depth (1 mm vs. 1.1–1.2 mm), differences in histological method (free-floating vs. paraffin), or large-scale effects of the devices (hybrid vs. microwire arrays) may explain this discrepancy.

An alternative to using our technique is tissue clearing. Tissue clearing allows staining and imaging of very thick (greater than 1 mm) samples, eliminating the need for digital reconstruction, and eliminating the risk of mishandling/losing one section and having to interpolate its alignment and quantification. However, tissue clearing techniques require specialized equipment (Chung et al., 2013), multi-week processing (Yang et al., 2014), or outsourcing to private companies. Special long-working-distance objectives are also required. In addition, although digital reconstruction introduces minor distortions, clearing can cause major expansion, contraction, reductions in fluorescent signal, or changes in ultrastructure that need to be characterized and troubleshot (Richardson and Lichtman, 2015; Azaripour et al., 2016). This is especially problematic for quantification, where accurate absolute dimensions and consistent staining are important. The presence of electrode tracks, voids, dense fibrotic tissue, or a device left in place may create further complications in achieving uniform dimensions, clearing, and staining. Therefore, for labs that have not yet mastered tissue clearing, the ability to produce 3D reconstructed datasets using standard immunohistochemical methods is still appealing.

There are many areas for improvement in our technique. Neurons near the NeuroNexus probes were not quantified in this study. To do so, it will be necessary to measure backward from the tip of the shank to the known locations of the recording sites. The dewarping algorithm could be improved by using a physical model of the section as an elastic material, so that it is stretched realistically in x and y whenever z is adjusted. Physical models such as thin-plate splines have been used in automatic reconstruction strategies (Anderson et al., 2009; Wang et al., 2014). Even if this is done, distortions may persist due to anisotropic shrinkage or expansion of tissue during immunohistochemistry and mounting. In this case, it may be necessary to allow local stretching and compression during alignment as well. Addressing these distortions would be likely to improve alignment consistency – since the distortions make it impossible to align all fiducials simultaneously, the user has to decide which fiducials to prioritize, leading to high variability in alignment unless the same fiducials are used. Our method could also benefit from making the alignment and tip-drawing steps at least semi-automated to improve consistency and save time. Optimizing the software could also save time. Profiling the execution time of the MATLAB code revealed that the ImarisXT functions passing data between Imaris and MATLAB account for the majority of the code's execution time and cause large files to take several hours to process. A software solution that does not rely on ImarisXT could be much faster. Finally, it is difficult to understand what is happening in complex, multi-channel, 3D histological datasets when they are simply volume rendered and displayed on a flat screen. It may be worthwhile to explore derived data such as intensity averages or use tools to explore the data in virtual reality.

In the future, we intend to analyze the full cohort of cats implanted with hybrid electrode arrays. This cohort has chronic neural recording data and explanted device SEM images, so the correlations and connections between these data sets are likely to provide new insights into chronic failure modes and how they differ among different types of electrodes.

ETHICS STATEMENT

The animal studies were approved by the Animal Care and Use Committee of HMRI and were performed under the guidelines set forth in the Guide to Care and Use of Laboratory Animals.

AUTHOR CONTRIBUTIONS

AN developed the software techniques and processed all data. NN developed the dewarping program and alignment workaround program. MH designed the device, conducted the animal studies, and supervised the study. All the authors wrote the manuscript.

FUNDING

This work was supported by the Defense Advanced Research Projects Agency grant #N66001-11-1-4010, NIH research grants R01DC014044 and R24NS086603, and the University of Connecticut (all to MH).

ACKNOWLEDGMENTS

Edna Smith managed and assisted with the animal surgeries, and we thank her animal care staff for excellent care of the animals. Douglas McCreery supervised the assembly of the hybrid arrays. Yelena Smirnova assembled the hybrid arrays. Haison Duong stained the tissues and collected confocal images. Aloysius Kowalewski fabricated special devices and parts used to assemble the hybrid array.

SUPPLEMENTARY MATERIAL

The Supplementary Material for this article can be found online at: https://www.frontiersin.org/articles/10.3389/fnins.2019.00393/full#supplementary-material

REFERENCES

Anderson, J. R., Jones, B. W., Yang, J. H., Shaw, M. V., Watt, C. B., Koshevoy, P., et al. (2009). A computational framework for ultrastructural mapping of neural circuitry. *PLoS Biol.* 7:e1000074. doi: 10.1371/journal.pbio.1000074

Arganda-Carreras, I., Fernández-González, R., Muñoz-Barrutia, A., and Ortiz-De-Solorzano, C. (2010). 3D reconstruction of histological sections: application to mammary gland tissue. *Microsc. Res. Tech.* 73, 1019–1029. doi: 10.1002/jemt.20829

Azaripour, A., Lagerweij, T., Scharfbillig, C., Jadczak, A. E., Willershausen, B., and Van Noorden, C. J. F. (2016). A survey of clearing techniques for 3D imaging of tissues with special reference to connective tissue. *Prog. Histochem. Cytochem.* 51, 9–23. doi: 10.1016/j.proghi.2016.04.001

Barrese, J. C., Rao, N., Paroo, K., Triebwasser, C., Vargas-Irwin, C., Franquemont, L., et al. (2013). Failure mode analysis of silicon-based intracortical microelectrode arrays in non-human primates. *J. Neural Eng.* 10:066014. doi: 10.1088/1741-2560/10/6/066014

Biran, R., Martin, D. C., and Tresco, P. A. (2005). Neuronal cell loss accompanies the brain tissue response to chronically implanted silicon microelectrode arrays. *Exp. Neurol.* 195, 115–126. doi: 10.1016/j.expneurol.2005.04.020

Black, B. J., Kanneganti, A., Joshi-Imre, A., Rihani, R., Chakraborty, B., Abbott, J., et al. (2018). Chronic recording and electrochemical performance of Utah microelectrode arrays implanted in rat motor cortex. *J. Neurophysiol.* 120, 2083–2090. doi: 10.1152/jn.00181.2018

Chung, K., Wallace, J., Kim, S. Y., Kalyanasundaram, S., Andalman, A. S., Davidson, T. J., et al. (2013). Structural and molecular interrogation of intact biological systems. *Nature* 497, 332–337. doi: 10.1038/nature12107

Cody, P. A., Eles, J. R., Lagenaur, C. F., Kozai, T. D., and Cui, X. T. (2018). Unique electrophysiological and impedance signatures between encapsulation types: an analysis of biological Utah array failure and benefit of a biomimetic coating in a rat model. *Biomaterials* 161, 117–128. doi: 10.1016/j.biomaterials.2018.01.025

Collinger, J. L., Wodlinger, B., Downey, J. E., Wang, W., Tyler-Kabara, E. C., Weber, D. J., et al. (2013). High-performance neuroprosthetic control by an individual with tetraplegia. *Lancet* 381, 557–564. doi: 10.1016/S0140-6736(12)61816-9

Downey, J. E., Weiss, J. M., Muelling, K., Venkatraman, A., Valois, J. S., Hebert, M., et al. (2016). Blending of brain-machine interface and vision-guided autonomous robotics improves neuroprosthetic arm performance during grasping. *J. Neuroeng. Rehabil.* 13:28. doi: 10.1186/s12984-016-0134-9

Duong, H., and Han, M. (2013). A multispectral LED array for the reduction of background autofluorescence in brain tissue. *J. Neurosci. Methods* 220, 46–54. doi: 10.1016/j.jneumeth.2013.08.018

Edell, D. J., Toi, V. V., McNeil, V. M., and Clark, L. D. (1992). Factors influencing the biocompatibility of insertable silicon microshafts in cerebral cortex. *IEEE Trans. Biomed. Eng.* 39, 635–643. doi: 10.1109/10.141202

Eles, J. R., Vazquez, A. L., Kozai, T. D. Y., and Cui, X. T. (2018). In vivo imaging of neuronal calcium during electrode implantation: spatial and temporal mapping of damage and recovery. *Biomaterials* 174, 79–94. doi: 10.1016/j.biomaterials.2018.04.043

Emmenlauer, M., Ronneberger, O., Ponti, A., Schwarb, P., Griffa, A., Filippi, A., et al. (2009). XuvTools: free, fast and reliable stitching of large 3D datasets. *J. Microsc.* 233, 42–60. doi: 10.1111/j.1365-2818.2008.03094.x

Freire, M. A. M., Morya, E., Faber, J., Santos, J. R., Guimaraes, J. S., Lemos, N. A. M., et al. (2011). Comprehensive analysis of tissue preservation and recording quality from chronic multielectrode implants. *PLoS One* 6:e0027554. doi: 10.1371/journal.pone.0027554

Han, M., Manoonkitiwongsa, P. S., Wang, C. X., and McCreery, D. B. (2012). In vivo validation of custom-designed silicon-based microelectrode arrays for long-term neural recording and stimulation. *IEEE Trans. Biomed. Eng.* 59, 346–354. doi: 10.1109/TBME.2011.2172440

Henze, D. A., Borhegyi, Z., Csicsvari, J., Mamiya, A., Harris, K. D., and Buzsaki, G. (2000). Intracellular features predicted by extracellular recordings in the hippocampus in vivo. *J. Neurophysiol.* 84, 390–400. doi: 10.1152/jn.2000.84.1.390

Karumbaiah, L., Saxena, T., Carlson, D., Patil, K., Patkar, R., Gaupp, E. A., et al. (2013). Relationship between intracortical electrode design and chronic recording function. *Biomaterials* 34, 8061–8074. doi: 10.1016/j.biomaterials.2013.07.016

Kozai, T. D., Eles, J. R., Vazquez, A. L., and Cui, X. T. (2016). Two-photon imaging of chronically implanted neural electrodes: sealing methods and new insights. *J. Neurosci. Methods* 258, 46–55. doi: 10.1016/j.jneumeth.2015.10.007

Kozai, T. D., Langhals, N. B., Patel, P. R., Deng, X., Zhang, H., Smith, K. L., et al. (2012). Ultrasmall implantable composite microelectrodes with bioactive surfaces for chronic neural interfaces. *Nat. Mater.* 11, 1065–1073. doi: 10.1038/nmat3468

Kozai, T. D., Li, X., Bodily, L. M., Caparosa, E. M., Zenonos, G. A., Carlisle, D. L., et al. (2014). Effects of caspase-1 knockout on chronic neural recording quality and longevity: insight into cellular and molecular mechanisms of the reactive tissue response. *Biomaterials* 35, 9620–9634. doi: 10.1016/j.biomaterials.2014.08.006

Lee, H. C., Gaire, J., Roysam, B., and Otto, K. J. (2018). Placing sites on the edge of planar silicon microelectrodes enhances chronic recording functionality. *IEEE Trans. Biomed. Eng.* 65, 1245–1255. doi: 10.1109/TBME.2017.2715811

Liu, X., McCreery, D. B., Carter, R. R., Bullara, L. A., Yuen, T. G. H., and Agnew, W. F. (1999). Stability of the interface between neural tissue and chronically implanted intracortical microelectrodes. *IEEE Trans. Rehabil. Eng.* 7, 315–326. doi: 10.1109/86.788468

Markovitz, C. D., Tang, T. T., Edge, D. P., and Lim, H. H. (2012). Three-dimensional brain reconstruction of in vivo electrode tracks for neuroscience and neural prosthetic applications. *Front. Neural Circ.* 6:39. doi: 10.3389/fncir.2012.00039

Mathiisen, T. M., Lehre, K. P., Danbolt, N. C., and Ottersen, O. P. (2010). The perivascular astroglial sheath provides a complete covering of the brain microvessels: an electron microscopic 3D reconstruction. *Glia* 58, 1094–1103. doi: 10.1002/glia.20990

McConnell, G. C., Rees, H. D., Levey, A. I., Gutekunst, C. A., Gross, R. E., and Bellamkonda, R. V. (2009). Implanted neural electrodes cause chronic, local inflammation that is correlated with local neurodegeneration. *J. Neural Eng.* 6:056003. doi: 10.1088/1741-2560/6/5/056003

McCreery, D., Cogan, S., Kane, S., and Pikov, V. (2016). Correlations between histology and neuronal activity recorded by microelectrodes implanted chronically in the cerebral cortex. *J. Neural Eng.* 13:036012. doi: 10.1088/1741-2560/13/3/036012

McCreery, D., Pikov, V., and Troyk, P. R. (2010). Neuronal loss due to prolonged controlled-current stimulation with chronically implanted microelectrodes in the cat cerebral cortex. *J. Neural Eng.* 7:036005. doi: 10.1088/1741-2560/7/3/036005

McCreery, D., Yadev, K., and Han, M. (2018). Responses of neurons in the feline inferior colliculus to modulated electrical stimuli applied on and within the ventral cochlear nucleus; implications for an advanced auditory brainstem implant. *Hear. Res.* 363, 85–97. doi: 10.1016/j.heares.2018.03.009

Nolta, N. F., Christensen, M. B., Crane, P. D., Skousen, J. L., and Tresco, P. A. (2015). BBB leakage, astrogliosis, and tissue loss correlate with silicon microelectrode array recording performance. *Biomaterials* 53, 753–762. doi: 10.1016/j.biomaterials.2015.02.081

Potter, K. A., Buck, A. C., Self, W. K., and Capadona, J. R. (2012). Stab injury and device implantation within the brain results in inversely multiphasic neuroinflammatory and neurodegenerative responses. *J. Neural Eng.* 9:046020. doi: 10.1088/1741-2560/9/4/046020

Prasad, A., Xue, Q. S., Dieme, R., Sankar, V., Mayrand, R. C., Nishida, T., et al. (2014). Abiotic-biotic characterization of Pt/Ir microelectrode arrays in chronic implants. *Front. Neuroeng.* 7:2. doi: 10.3389/fneng.2014.00002

Prasad, A., Xue, Q. S., Sankar, V., Nishida, T., Shaw, G., Streit, W. J., et al. (2012). Comprehensive characterization and failure modes of tungsten microwire arrays in chronic neural implants. *J. Neural Eng.* 9:056015. doi: 10.1088/1741-2560/9/5/056015

Richardson, D. S., and Lichtman, J. W. (2015). Clarifying tissue clearing. *Cell* 162, 246–257. doi: 10.1016/j.cell.2015.06.067

Santhanam, G., Ryu, S. I., Yu, B. M., Afshar, A., and Shenoy, K. V. (2006). A high-performance brain–computer interface. *Nature* 442:195. doi: 10.1038/nature04968

Shain, W., Spataro, L., Dilgen, J., Haverstick, K., Retterer, S., Isaacson, M., et al. (2003). Controlling cellular reactive responses around neural prosthetic devices using peripheral and local intervention strategies. *IEEE Trans. Neural Syst. Rehabil. Eng.* 11, 186–188. doi: 10.1109/TNSRE.2003.814800

Shannon, R. V. (1992). A model of safe levels for electrical stimulation. *IEEE Trans. Biomed. Eng.* 39, 424–426. doi: 10.1109/10.126616

Turner, J. N., Shain, W., Szarowski, D. H., Andersen, M., Martins, S., Isaacson, M., et al. (1999). Cerebral astrocyte response to micromachined silicon implants. *Exp. Neurol.* 156, 33–49. doi: 10.1006/exnr.1998.6983

Wang, C.-W., Ka, S.-M., and Chen, A. (2014). Robust image registration of biological microscopic images. *Sci. Rep.* 4:6050. doi: 10.1038/srep06050

Wessberg, J., Stambaugh, C. R., Kralik, J. D., Beck, P. D., Laubach, M., Chapin, J. K., et al. (2000). Real-time prediction of hand trajectory by ensembles of cortical neurons in primates. *Nature* 408:361. doi: 10.1038/35042582

Woolley, A. J., Desai, H. A., and Otto, K. J. (2013). Chronic intracortical microelectrode arrays induce non-uniform, depth-related tissue responses. *J. Neural Eng.* 10:026007. doi: 10.1088/1741-2560/10/2/026007

Woolley, A. J., Desai, H. A., Steckbeck, M. A., Patel, N. K., and Otto, K. J. (2011). In situ characterization of the brain-microdevice interface using device-capture histology. *J. Neurosci. Methods* 201, 67–77. doi: 10.1016/j.jneumeth.2011.07.012

Yang, B., Treweek, J. B., Kulkarni, R. P., Deverman, B. E., Chen, C. K., Lubeck, E., et al. (2014). Single-cell phenotyping within transparent intact tissue through whole-body clearing. *Cell* 158, 945–958. doi: 10.1016/j.cell.2014.07.017

Conflict of Interest Statement: The authors declare that the research was conducted in the absence of any commercial or financial relationships that could be construed as a potential conflict of interest.

Copyright © 2019 Nambiar, Nolta and Han. This is an open-access article distributed under the terms of the Creative Commons Attribution License (CC BY). The use, distribution or reproduction in other forums is permitted, provided the original author(s) and the copyright owner(s) are credited and that the original publication in this journal is cited, in accordance with accepted academic practice. No use, distribution or reproduction is permitted which does not comply with these terms.

frontiers in Neuroscience

ORIGINAL RESEARCH
published: 26 April 2019
doi: 10.3389/fnins.2019.00397

Multichannel Silicon Probes for Awake Hippocampal Recordings in Large Animals

*Alexandra V. Ulyanova[1], Carlo Cottone[1], Christopher D. Adam[1], Kimberly G. Gagnon[1], D. Kacy Cullen[1,2], Tahl Holtzman[3], Brian G. Jamieson[4], Paul F. Koch[1], H. Isaac Chen[1,2], Victoria E. Johnson[1] and John A. Wolf[1,2]**

[1] Center for Brain Injury and Repair, Department of Neurosurgery, Perelman School of Medicine, University of Pennsylvania, Philadelphia, PA, United States, [2] Corporal Michael J. Crescenz Veterans Affairs Medical Center, Philadelphia, PA, United States, [3] Cambridge NeuroTech, Cambridge, United Kingdom, [4] Scientific & Biomedical Microsystems, Glen Burnie, MD, United States

OPEN ACCESS

Edited by:
Jeffrey R. Capadona, Case Western Reserve University, United States

Reviewed by:
Dmitry Kireev, Julich Research Centre, Germany
Pascale Quilichini, INSERM U1106 Institut de Neurosciences des Systèmes, France

***Correspondence:**
John A. Wolf
wolfjo@pennmedicine.upenn.edu

Specialty section:
This article was submitted to Neural Technology, a section of the journal Frontiers in Neuroscience

Received: *15 January 2019*
Accepted: *08 April 2019*
Published: *26 April 2019*

Citation:
Ulyanova AV, Cottone C, Adam CD, Gagnon KG, Cullen DK, Holtzman T, Jamieson BG, Koch PF, Chen HI, Johnson VE and Wolf JA (2019) Multichannel Silicon Probes for Awake Hippocampal Recordings in Large Animals. Front. Neurosci. 13:397. doi: 10.3389/fnins.2019.00397

Decoding laminar information across deep brain structures and cortical regions is necessary in order to understand the neuronal ensembles that represent cognition and memory. Large animal models are essential for translational research due to their gyrencephalic neuroanatomy and significant white matter composition. A lack of long-length probes with appropriate stiffness allowing penetration to deeper structures with minimal damage to the neural interface is one of the major technical limitations to applying the approaches currently utilized in lower order animals to large animals. We therefore tested the performance of multichannel silicon probes of various solutions and designs that were developed specifically for large animal electrophysiology. Neurophysiological signals from dorsal hippocampus were recorded in chronically implanted awake behaving Yucatan pigs. Single units and local field potentials were analyzed to evaluate performance of given silicon probes over time. EDGE-style probes had the highest yields during intra-hippocampal recordings in pigs, making them the most suitable for chronic implantations and awake behavioral experimentation. In addition, the cross-sectional area of silicon probes was found to be a crucial determinant of silicon probe performance over time, potentially due to reduction of damage to the neural interface. Novel 64-channel EDGE-style probes tested acutely produced an optimal single unit separation and a denser sampling of the laminar structure, identifying these research silicon probes as potential candidates for chronic implantations. This study provides an analysis of multichannel silicon probes designed for large animal electrophysiology of deep laminar brain structures, and suggests that current designs are reaching the physical thresholds necessary for long-term (~1 month) recordings with single-unit resolution.

Keywords: large animals, pigs, multichannel silicon probes, laminar hippocampal electrophysiology, awake chronic recordings, single units, oscillations

INTRODUCTION

Spatiotemporal neuronal ensembles distributed throughout laminar structures in the brain such as the cortex and hippocampus are presumed to be the substrate for cognition and memory. Oscillatory activity and resulting power bands are transmitted throughout the layers of laminar structures as different inputs are driven at different frequencies depending on their area of origin (Buzsáki, 1989, 2015; Bragin et al., 1995a,b; Buzsáki et al., 2003). Laminar analyses of oscillatory activity have proven valuable for elucidating circuit dynamics as well as changes between states in both cortex and hippocampus (Buzsáki et al., 2003; Lewis et al., 2015). Traditionally, single neurons have been analyzed independently on the basis of their tuning to sensory stimuli or movement. Although accuracy of tuning curve approaches is unaffected by growing numbers of simultaneously recorded neurons, newly developed pair-wise interaction models that make predictions based on the activity of the multiple simultaneously recorded neurons become more complex but also more accurate as the number of recorded neurons increases (Stevenson and Kording, 2011). For spike-field entrainment analyses as well as for neuromodulation-based approaches, it is also important to know where inputs that drive the cells originate and how they interact locally. Cell types, dendritic arborization, local and long-range axonal projections are all distributed unevenly across layers, shaping the integration and segregation of neural signals. Ultimately, we must decode laminar information across different structures to understand the spatiotemporal ensembles that represent cognition and memory. Thus, measuring the coordination of spiking activity of large numbers of neurons, and specifically those thought to give rise to distributed functional networks, is critical for understanding neural information processing underlying cognition and behavior (Lewis et al., 2015).

The hippocampus is an example of a deep laminar structure that is highly involved in encoding episodic memory formation presumably via spatiotemporal ensembles of neurons (Carr et al., 2011; Buzsaki and Moser, 2013). Once multichannel silicon probes were developed, they quickly became a standard tool for awake hippocampal neurophysiological recordings in rodents (Vetter et al., 2004). Increasing the density of laminar contacts in deep structures allows researchers to gain more information about these structures and more recently, study the potential effects of neurological disease states on single unit activity (Fernández-Ruiz et al., 2017; Hainmueller and Bartos, 2018; Kee et al., 2018). Although the rodent hippocampus has been studied in great detail, the transition to large animal models has been slower. One of the major obstacles to addressing the research questions and approaches currently accessible in rodents are technical limitations in laminar silicon microelectrodes. While translational models have been actively utilized for neuromodulation studies (Min et al., 2012; Kim et al., 2013; Gibson et al., 2016; Orlowski et al., 2017; Christensen et al., 2018), much of the large animal brain is still inaccessible due to insufficient length of available silicon probes. In large animals and humans, the hippocampus is located sub-cortically and therefore difficult to study electrophysiologically using multi-channel probes. Even many cortical targets cannot be reached with the current technology including those typically utilized for brain machine interface (BMI) such at the Utah electrode. In addition, laminar structure cannot be detected with single wire or tetrode recordings. Existing non-laminar solutions can scale to high density, but have single contacts at the tip, limiting the ability to differentiate single units or localize them within the laminar circuitry (Killian et al., 2012). Therefore, current technology is not suitable for understanding neuronal oscillations and their interaction within and between laminar structures.

Recent advances in high-density linear electrode arrays and wireless recording technology could tremendously enhance translational research studies of large-scale networks in species with large, gyrencephalic brains (Ulyanova et al., 2018). Ideally, the probes for electrophysiological recordings from deep brain structures must resolve laminar local field potentials (LFPs) and provide proper sampling densities to resolve single-units across channels for single unit spike-sorting and minimize damage to the neuro-electric interface (for review, see Kook et al., 2016). For instance, multi-channel silicon probes with many contacts in a linear configuration can isolate units in a 2–300 μm "sphere" around each electrode (Buzsáki, 2004; Blanche et al., 2005). Layer-specific fields can convey information transmitted from other regions, while direct, local spiking activity can be measured simultaneously. Silicon probes also need to be long enough to reach these structures. With little damage to the neural interface, insertion of silicon into multiple brain regions probes could also provide highly detailed information about local and long-range circuit computations (Lewis et al., 2015).

Technology necessary to produce finer features at longer length has only recently became available, including stitching across the dye in the photomask process to utilize smaller feature processes. New multichannel silicon probes designed for large animal electrophysiology allow for simultaneous recordings of fields and spikes from multiple layers of laminar structures such as cortex and hippocampus, and we therefore tested various designs of laminar silicon probes suitable for large animals. Across probe designs, we compared neurophysiological characteristics and biomechanical compatibility based on the variables such as electrode site layout and probe thickness. Current technology in silicon probes appears to have reached the critical size/feature dimension while maintaining insertion stiffness, proving that single units in deep brain structures can be recorded for chronic periods without extensive damage to the neural interface. Further refinement of these probe technologies in combination with chronic drives and wireless technology may usher in a new high-density era for previously unexplored regions of cortex, hippocampus and other non-laminar deep structures in large animals and potentially humans.

MATERIALS AND METHODS

Animals

Male Yucatan miniature pigs were purchased from Sinclair (NSRRC, Catalog # 0012, **RRID:NSRRC_0012** and underwent the current studies at the approximate age of 5–6 months at

a mean weight of 38 ± 3 kg (n = 17, mean ± SEM). At this age Yucatan pigs are considered post-adolescent with near-fully developed brains, while young enough to be of a manageable weight for procedures and behavior (Pampiglione, 1971; Flynn, 1984; Duhaime et al., 2000). All pigs were pair housed when possible, and were always in a shared room with other pigs. All animal procedures were performed in accordance with the University of Pennsylvania animal care committee's regulations, an AALAC accredited institution.

Surgical Procedure

Yucatan miniature pigs were fasted for 16 h then induced with 20 mg/kg of ketamine (Catalog # NDC 0143-9509-01, West-Ward, Eatontown, NJ, United States) and 0.5 mg/kg of midazolam (Catalog # NDC 0641-6060-01, West-Ward, Eatontown, NJ, United States). Animals were intubated with an endotracheal tube and anesthesia was maintained with 2–2.5% isoflurane per 2 liters O_2. Each animal was placed on a ventilator and supplied oxygen at a tidal volume of 10 mL/kg. A catheter was placed in an auricular vein to deliver 0.9% normal saline at 200 mL per hour. Additionally, heart rate, respiratory rate, arterial oxygen saturation, end tidal CO_2 and rectal temperature were continuously monitored, while pain response to pinch was periodically assessed. All of these measures were used to titrate ventilation settings and isoflurane percentage to maintain an adequate level of anesthesia. A forced air warming system was used to maintain normothermia throughout the procedure.

All animals underwent implantation of multi-channel silicon probes under sterile conditions similar to acute implantation procedure described previously (Ulyanova et al., 2018). Briefly, pigs were placed in a stereotactic frame, with the surgical field prepped and draped, and a linear incision was made along the midline. A 13-mm diameter burr hole was centered at 7 mm lateral to the midline and 4.5 mm posterior to bregma, and the bony opening was subsequently expanded using Kerrison punches. Skull screws were placed over the occipital ipsilateral and contralateral cortex as a ground and alternate reference signal. The dura was opened in a cruciate manner and the brain was mapped in the sagittal plane with a tungsten electrode (impedance = 0.5 MΩ, measured at 1 kHz; Catalog # UEWSEGSEBNNM, FHC, Bowdoin, ME, United States), utilizing observed spiking activity to generate a two-dimensional map. Based on this map, a silicon probe was inserted so that the spread of electrode sites would span the laminar structure of the dorsal hippocampus at its maximal thickness in the dorsal–ventral plane, perpendicular to the individual hippocampal layers (Ulyanova et al., 2018). The multichannel silicon probe was stabilized inside the craniectomy using Tisseel (Catalog # 1504514, Baxter Healthcare, Wayne, PA, United States), creating a semi-floating interface between the silicon probe and the animal's skull. The probe cables were fed through the head cap chamber and attached to a custom electrode interface board (EIB) adapter. The head cap chamber, which covered all necessary electronic connections, was attached to the pig skull using anchor screws and secured with Palacos bone cement and Geristore. Once the quality of signals from multichannel silicon depth probes were confirmed, hippocampal signals were first recorded under anesthesia using a QC-72 amplifier and referenced to both internal and skull references. This recording was later used as a baseline for awake recordings and to monitor silicon probe's position over time for possible drift.

Multichannel Silicon Probes

Chronic 32-channel silicon probes for large animal electrophysiology were designed with ATLAS Neuroengineering (Leuven, Belgium) and NeuroNexus (Ann Arbor, MI, United States). In addition, acute 64-channel silicon research probes were developed in a collaboration with SB Microsystems (Glen Burnie, MD, United States) and Cambridge NeuroTech (Cambridge, United Kingdom). Designs of multichannel silicon probes are shown in **Figure 1**. Specific parameters of silicon probes are summarized in **Table 1**.

All multichannel silicon probes were designed with one low-impedance channel placed 1–2 mm above the adjacent proximal channel, which was recorded for use as an internal reference (**Supplementary Figure S1**). For dorsal hippocampal targeting in pigs, this design provides 31 (or 63) channels for intra-hippocampal recordings with the reference channel being positioned within the temporal horn of the lateral ventricle dorsal to the hippocampus. Detailed information on multichannel silicon probes used in the study is as follows:

ATLAS32/TET (Catalog # E32T7-R-275-S01-L25)

32-channel silicon probes had custom designed individual sites arranged in groups of four closely spaced sites or tetrodes (**Figure 1A**). Three electrode sites were added in between groups of tetrodes to cover porcine hippocampal layers of strata radiatum, lacunosum-moleculare and moleculare. The top four tetrodes were designed to be positioned in the pyramidal CA1 layer, with the bottom three tetrodes positioned in the granular cell layer. The top site on each tetrode, along with linear sites were placed 275 μm apart forming 10 equally spaced sites for laminar hippocampal recordings. The total coverage of ATLAS32/TET silicon probe was set to 2,750 μm. The cross-sectional area of the probe, measured at the top site was 21,500 μm^2 (**Figure 1B**). The individual electrode sites of 962 μm^2 were coated with Pt (Maas et al., 2017). The average site impedance, measured at 1 kHz was 1.29 ± 0.21 MΩ (mean ± SEM, n_{sites} = 155).

NN32/TET (Catalog # V1x32-80 mm-275-tet-177-HP32)

32-channel silicon probes had custom designed individual sites arranged in groups of four closely spaced sites or tetrodes (**Figure 1A**). Three electrode sites were added in between groups of tetrodes to cover porcine hippocampal layers of strata radiatum, lacunosum-moleculare and moleculare. The top four tetrodes were designed to be positioned in the pyramidal CA1 layer, with the bottom three tetrodes positioned in the granular cell layer. The top site on each tetrode, along with linear sites were placed 275 μm apart forming 10 equally spaced sites for laminar hippocampal recordings. The total coverage of NN3232/TET silicon probe was set to 2,750 μm. The cross-sectional area of

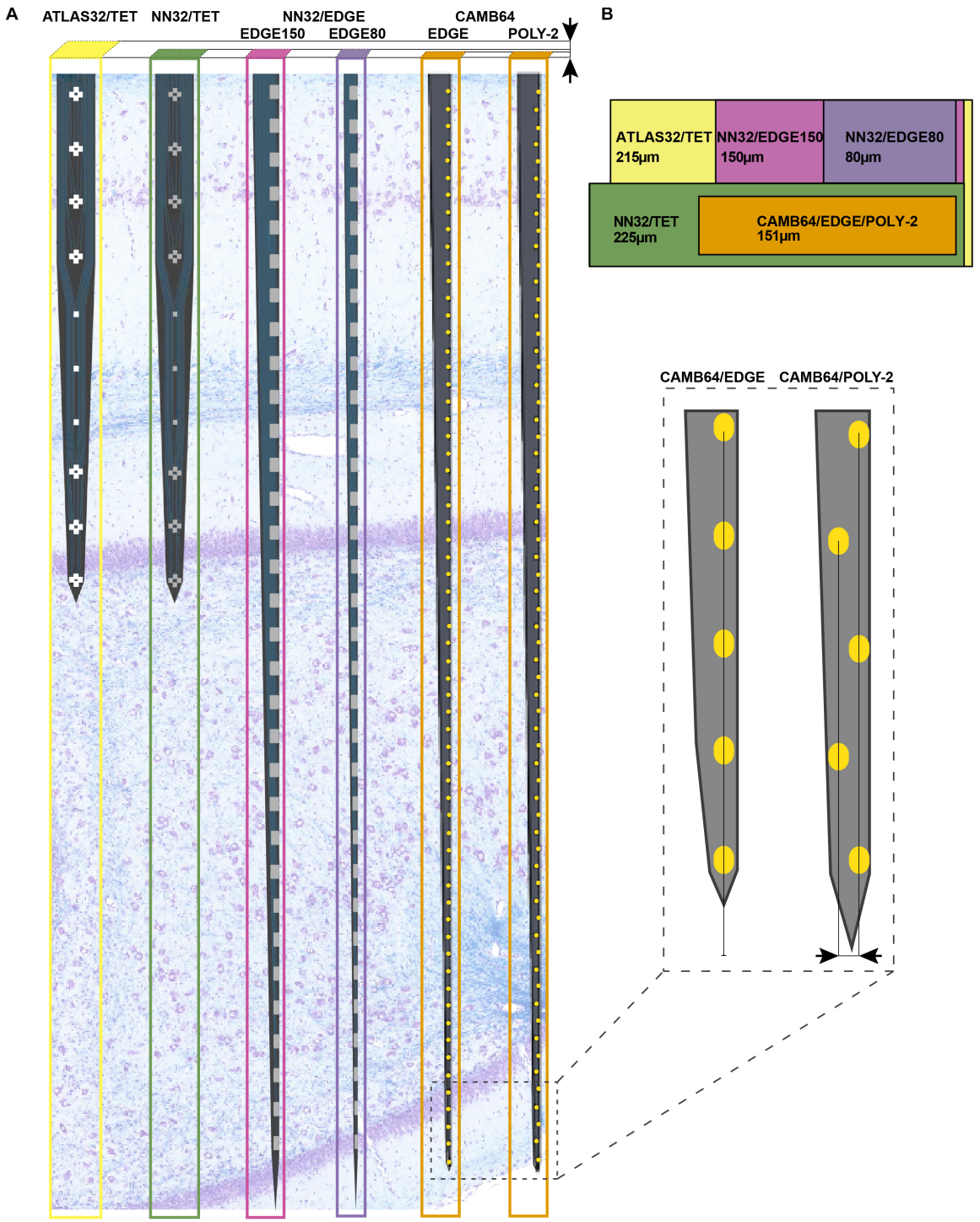

FIGURE 1 | Design of multichannel silicon probes for chronic hippocampal recordings in pigs. **(A)** The arrangement of the individual electrode sites is shown for chronic 32-channel silicon probes [ATLAS32/TET (yellow), NN32/TET (green), NN32/EDGE150 (magenda), and NN32/EDGE80 (purple)] and acute 64-channel silicon probes (CAMB64/EDGE and CAMB64/POLY-2, orange). The vertical offset for CAMB64 silicon probes is also shown magnified (inset). Silicon probes are shown overlaid on a representative sagittal section of dorsal hippocampus stained with LFB/CV to identify individual layers. Cross-sectional area of each silicon probe (measured at the top electrode site) is shown at the top. **(B)** Widths and thicknesses of multichannel silicon probes (also referred to as probe area) are shown overlaid on each other for comparison (colors are the same as in **A**). The corresponding widths are 215 µm for ATLAS32/TET (yellow), 150 µm for NN32/EDGE150 (magenda), 80 µm for NN32/EDGE80 (purple), 225 µm for NN32/TET (green), and 151 µm for CAMB64/EDGE/POLY-2 (orange) silicon probes. NN32/EDGE150 is shown as a continuation of NN32/EDGE80. The thickness of silicon probes is 100 µm for ATLAS32/TET, 50 µm for NN32/EDGE150, NN32/EDGE80, NN32/TET, and 35 µm for both CAMB64/EDGE and CAMB64/POLY-2 probes (orange).

TABLE 1 | Multi-channel silicon probes for chronic hippocampal recordings in pigs.

Silicon probe	Site layout	Site spacing (μm)	Site coating	Site area (μm^2)	Site imp. (MΩ)	Probe thickness (μm)	Probe width (μm)	Probe area (μm^2)	Probe length (μm)
ATLAS32/ TET	Tetrode[1] + linear	275[2]	Pt	962	1.29	100	215	21,500	2,750
NN32/ TET	Tetrode[1] + linear	275[2]	IrOx	312	1.68	50	225	11,250	11,250
NN32/ EDGE150	Edge[3]	200	IrOx	312	1.81	50	150	7,500	7,500
NN32/ EDGE80	Edge[3]	200	IrOx	312	1.81	50	80	4,000	4,000
CAMB64/ EDGE	Edge[3]	100	Au + polymer	165	0.06	35	148	5,180	5,180
CAMB64/ POLY-2	Poly-2[4]	100	Au + polymer	165	0.06	35	154	5,390	5,390

[1]An arrangement of four electrode sites placed close together; [2]spacing between individual tetrodes (at first site) as well as between linear sites; [3]similar to the linear layout, but electrode sites are positioned at the edge of the substrate; [4]similar to the linear layout, but electrode sites are off-set by 21 μm relative to each other.

the probe, measured at the top site was 11,250 μm^2 (**Figure 1B**). The individual electrode sites of 312 μm^2 were coated with IrOx. The average site impedance, measured at 1 kHz was 1.68 ± 0.20 MΩ (mean ± SEM, n_{sites} = 403).

NN32/EDGE150/NN32/EDGE80 (Catalog # V1x32-Edge-10 mm-200-312-Ref)

32-channel silicon probes had a linear site layout, with the electrode sites placed 200 μm apart. The individual electrode sites were also strategically positioned at the edge of the probe (**Figure 1A**). The total coverage of NN32/EDGE150 and NN32/EDGE80 probes was set to 6,200 μm. The cross-sectional area of the probe, measured at the top site was 7,500 μm^2 for NN32/EDGE150 and 4,000 μm^2 for NN32/EDGE80 (**Figure 1B**). The individual electrode sites of 312 μm^2 were coated with IrOx. The average site impedance, measured at 1 kHz was 1.68 ± 0.20 MΩ (mean ± SEM, n_{sites} = 403).

CAMB64/EDGE

64-channel silicon probes had a linear site arrangement, with the individual electrode sites positioned at the edge of the silicon probe (**Figure 1A**). The electrode sites were placed 100 μm apart (**Figure 1A**, inset). The total coverage of CAMB64/EDGE silicon probe was set to 6,300 μm. The cross-sectional area of the probe, measured at the top site was 5,180 μm^2. The individual electrode sites were 165 μm^2 (**Figure 1B**). The individual electrode sites were coated with Au and a conducting organic polymer. The average site impedance, measured at 1 kHz was 0.063 ± 0.001 MΩ (mean ± SEM, n_{sites} = 63).

CAMB64/POLY-2

64-channel silicon probes had individual electrode sites arranged in poly-2 style (**Figure 1A**). The individual electrode sites were placed 100 μm apart, with a 21 μm off-set (**Figure 1A**, inset). The total coverage of CAMB64/POLY-2 silicon probe was set to 6,300 μm. The cross-sectional area of the probe, measured at the top site was 5,390 μm^2. The individual electrode sites were 165 μm^2 (**Figure 1B**). The individual electrode sites were coated with Au and a conducting organic polymer. The average site impedance, measured at 1 kHz was 0.064 ± 0.001 MΩ (mean ± SEM, n_{sites} = 63).

Neural Data Collection and Analysis

Electrophysiological recordings with 32-channel silicon probes (ATLAS32/TET, NN32/TET, NN32/EDGE150, and NN32/EDGE80) were performed in awake behaving animals at various time points at up to 6 months post implantation. Wide bandwidth neural signals were acquired continuously, sampled at 30 kHz with FreeLynx digital acquisition system, amplified and either wirelessly transmitted to Digital Lynx 4SX acquisition system with Cheetah recording and acquisition software during behavioral space recordings or stored to an on-board microSD memory card during home cage recordings (Neuralynx, Inc., Bozeman, MT, United States). Electrophysiological recordings with 64-channel silicon probes (CAMB64/EDGE and CAMB64/POLY-2) were performed acutely under isoflurane anesthesia, with wide band neural signals continuously acquired, sampled at 32 kHz and amplified with Digital Lynx 4SX acquisition system with Cheetah recording and acquisition software (Neuralynx, Inc., Bozeman, MT, United States).

Spike Detection and Analysis

Neural signals acquired from the 32 or 64 channels on the silicon probes were bandpass filtered (0.1 Hz to 9 kHz) in real time prior to sampling. Off-line spike detection and sorting was performed on the wideband signals using the Klusta package[1] (**RRID:SCR_014480**), which was developed for higher density electrodes, and manually refined with KlustaViewa[2], or phy[3] software packages. The Klusta packages are designed to construct putative clusters from all probe channels simultaneously by taking advantage of spike timing and the spatial arrangement of electrode sites (Rossant et al., 2016). After manual refinement, resulting single-unit clusters were then imported into Matlab software, version R2017a for visualization and further analysis using custom and built-in routines (MATLAB, **RRID:SCR_001622**).

Analysis of Local Field Potentials (LFPs)

Acquired wideband LFPs recorded from all channels of the silicon probe were down-sampled to 2 kHz for further analysis. Signals were imported into Matlab software, version R2017a

[1]http://klusta-team.github.io/klustakwik/

[2]https://github.com/klusta-team/klustaviewa

[3]https://github.com/kwikteam/phy

(MATLAB, **RRID:SCR_001622**) and processed using a combination of custom and modified scripts from the freely available Matlab packages FMAToolbox (FMAToolbox, **RRID:SCR_015533**), Chronux (Chronux, **RRID:SCR_005547**), and EEGLAB (EEGLAB, **RRID:SCR_007292**) (Hazan et al., 2006; Mitra and Bokil, 2007).

Tissue Handling and Histological Examinations

Histological analyses were performed to identify electrode tracks on brain tissue from male Yucatan miniature pigs. At the study endpoint, transcardial perfusion was performed under anesthesia using 0.9% heparinized saline followed by 10% neutral buffered formalin (NBF). After further post-fixation for 7 days in 10% NBF at 4°C, the brain was dissected into 5 mm blocks in the coronal plane and processed to paraffin using standard techniques (Johnson et al., 2016, 2018). Eight micrometer sections were obtained at the level of the hippocampus and standard hematoxylin and eosin (H&E) staining was performed on all animals to identify electrode tracks. The following additional stains were performed:

Luxol Fast Blue/Cresyl Violet (LFB/CV) Staining

Tissue sections were dewaxed in xylenes and rehydrated to water via graded ethanols before being immersed in 1% LFB solution (Sigma, S3382) at 60°C for 4 h. Excess stain was then removed by immersion of sections in 95% ethanol. Differentiation was performed via immersion in 0.035% lithium carbonate for 10 s followed by multiple immersions in 70% ethanol until the gray and white matter could be clearly distinguished. Slides were rinsed and counterstained via immersion in preheated 0.1% CV solution (Sigma, C5042) for 5 min at 60°C. After further rinsing, slides were differentiated in 95% ethanol with 0.001% acetic acid, followed by dehydration, clearing in xylenes and cover slipping using cytoseal-60.

Van Gieson's Staining

Tissue sections were dewaxed in xylenes and rehydrated to water via graded ethanols before being immersed in Weigert's Working Hematoxylin solution, prepared by mixing equal parts of Weigert's Iron Hematoxylin A (EMS, Catalog # 26044-05) and Weigert's Iron Hematoxylin B (EMS, Catalog # 26044-15) for 10 min. After rinsing in distilled water, tissue sections were stained for 3 min in Van Gieson's solution (EMS, Catalog # 26046-05). After further rinsing, slides were differentiated in 95% ethanol with 0.001% acetic acid, dehydrated, cleared in xylenes and coverlipped.

Immunohistochemistry (IHC)

Immunohistochemistry (IHC) labeling was performed according to previously published protocols (Johnson et al., 2013, 2016, 2018). Briefly, tissue sections were dewaxed and rehydrated as above, followed by immersion in 3% aqueous hydrogen peroxide for 15 min to quench endogenous peroxidase activity. Antigen retrieval was achieved via microwave pressure cooker at high power for 8 min, submerged in Tris EDTA buffer (pH 8.0). Sections were then incubated overnight at 4°C using antibodies specific for the N-terminal amino acids 66–81 of the amyloid precursor protein (APP) (Millipore, Burlington, MA, United States, clone 22C11 at 1:80K), GFAP (Leica, Biosystems, Buffalo Grove, IL, United States, GA5 clone at 1:10K), and IBA1 (Wako Chemicals USA Inc., Richmond, VA, United States, at 1:7K). Slides were then rinsed and incubated in the relevant species-specific biotinylated universal secondary antibody for 30 min at room temperature. Next, application of the avidin biotin complex (Vector Laboratories, Catalog # PK-6200, Lot # **RRID:AB_2336826**) was performed for 30 min, also at room temperature. Lastly, the 3,3′-diaminobenzidine (DAB) peroxidase substrate kit (Vector Laboratories, Catalog # SK-4100, Lot # **RRID:AB_233638**) was applied according to manufacturer's instructions. All sections were counterstained with hematoxylin, dehydrated in graded ethanols, cleared in xylenes, and cover slipped.

Statistical Analysis

The data was analyzed using Graphpad Prism software, version 7 (GraphPad Prism, **RRID:SCR_002798**). Single unit waveforms recorded with silicon laminar probes are displayed as mean ± SD. Amplitudes of single units are displayed as mean ± SEM. Impedance of silicon probes is shown as mean ± SEM.

RESULTS

Multichannel Silicon Probes Designed for Chronic Implantation in Large Animal

Multichannel silicon probes designed for large animal electrophysiology were evaluated for their ability to continuously record neurophysiological signals (laminar oscillatory and single unit activity) in awake behaving pigs, and for neuropathological changes induced by their placement in the porcine hippocampus over time.

Awake Hippocampal Recordings in Large Animals

Using silicon probes of various designs, the laminar structure of pig dorsal hippocampus was examined electrophysiologically under awake behaving conditions (**Figure 2**). Since the hippocampal region of interest (at our standard recording coordinates in medial-lateral (ML) and anterior-posterior (AP) planes) is about 1,600 μm (see Ulyanova et al., 2018 for more details), silicon probes with 200 μm site spacing provide good coverage for the laminar structure with enough resolution to identify most layers (**Figure 1A**). Oscillatory activity of the porcine hippocampus recorded with NN32/EDGE80 silicon probe is shown in **Figure 2** (Site Spacing = 200 μm, Probe Length = 6,200 μm). Neurophysiological features of the awake porcine hippocampus such as a sharp-wave ripple (SPW-R) and the polarity inversion of the LFPs across stratum radiatum are shown (**Figure 2**). While this silicon probe allowed us to examine the porcine hippocampus in its entirety (including the deeper layers such as hilus), some of the laminar layers (such as L-M) could have easily been poorly sampled using 200 μm resolution (Ulyanova et al., 2018).

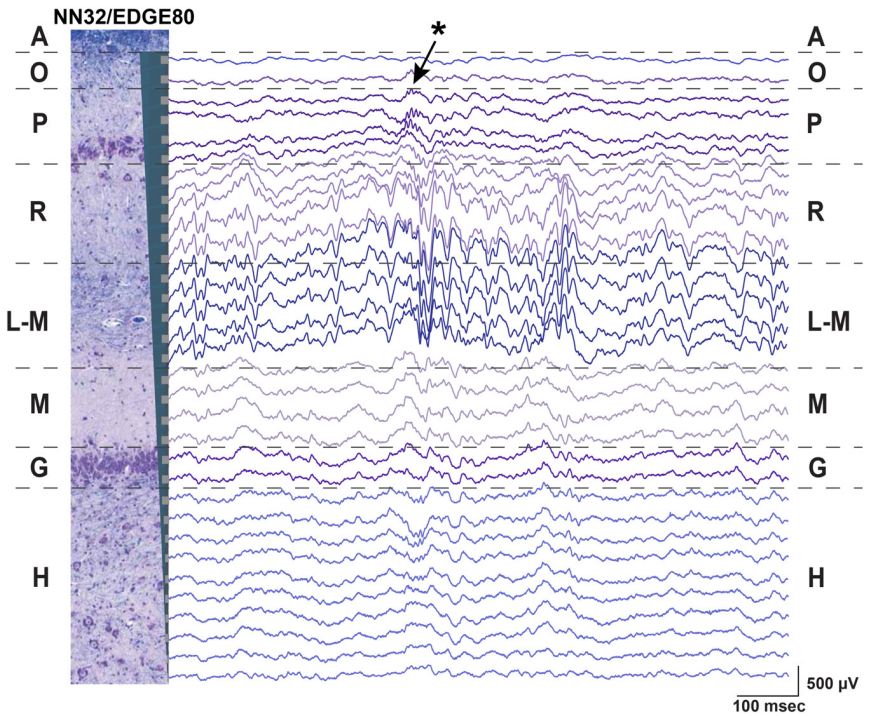

FIGURE 2 | Chronic hippocampal recordings in awake behaving pigs. Hippocampal recording with NN32/EDGE80 silicon probe (site spacing = 200 μm) is shown for an awake behaving animal. The silicon probe was placed in the dorsal hippocampus so that it covers hippocampal layers of stratum oriens (O), pyramidale (P), radiatum (R), lacunosum-moleculare (L-M), moleculare (M), granulosum (G), and hilus (H). A representative hippocampal section stained with LFB/CV is overlaid on laminar oscillatory activity to match representative layers as described previously (Ulyanova et al., 2018). A single sharp-wave ripple event (SPW-R) can be seen in CA1 layer (arrow). The polarity inversion of LFPs across stratum radiatum hippocampal layer can also be seen.

Neurophysiological signals recorded from deep brain structures such as the hippocampus may confer noise from the electrical environment by using an electrically inactive but conductive structure such as the cerebrospinal fluid (CSF) of the ventricle. Designing silicon probes with an internal reference for intra-hippocampal (or other deep brain structures) recordings may help to reduce noise and improve the signal quality over time. We estimated how an introduction of the internal reference affects the noise during awake and anesthetized hippocampal recordings by comparing power of hippocampal oscillations at the level of the pyramidal CA1 layer referenced to either an internal or skull screw reference (**Supplementary Figure S1**). All multichannel silicon probes used in the study were custom-designed to have the top electrode site substituted for a low-impedance reference site (Site Area = 4,200 μm^2) placed 1–2 mm above the most-proximal probe site (depending on the silicon probe design) (**Supplementary Figure S1A**). For dorsal hippocampal targeting in pigs, these designs provide 31 channels for laminar recordings and results in the reference channel being positioned within the temporal horn of the lateral ventricle sitting just above the hippocampus. During awake behaving recordings in pigs, the internal reference eliminated noise associated with movement artifacts (**Supplementary Figures S1B,C**). Under an anesthetized preparation, the internal reference on silicon probes eliminated most of the slow "drift" oscillations as well as the 60 Hz frequency peak, presumably from AC noise during acute recordings, with tether used to record electrophysiological signals (**Supplementary Figure S1D**). The skull screw reference used for large animal awake recordings allows for comparative analysis with the rodent awake behaving literature. In addition, an internal reference may also be beneficial for chronic recordings if a skull screw loses its connection to the CSF due to a growth of the animal's skull over time (months).

Stability of Neuronal Oscillations Over Time

We evaluated the stability of neurophysiological signals recorded from pig hippocampus over time in a sub-sample of these probes. Changes in hippocampal signals were evaluated using power of LFP signals over time (**Figure 3**). Since theta (∼4–10 Hz in pigs) is considered to be a prominent oscillation in the pyramidal CA1 layer of hippocampus, we first calculated the power of theta (at the stratum radiatum) over the first 2 weeks post implantation with NN32/EDGE80 silicon probe (**Figure 3A**). In the first 2 weeks following surgery, chronically implanted silicon probes moved slightly, likely due to recovery effects post-surgery such as swelling (**Figure 3A**). The peak of theta power shifted from channel 8 to channel 5, indicating that NN32/EDGE80 silicon probe moved about 600 μm into the hippocampus, corresponding to a distance between three channels on the NN32/EDGE80 probe with 200 μm site spacing (**Figure 3B**). Overall, all previously characterized hippocampal oscillations (low and high gamma, ripple oscillations) decreased

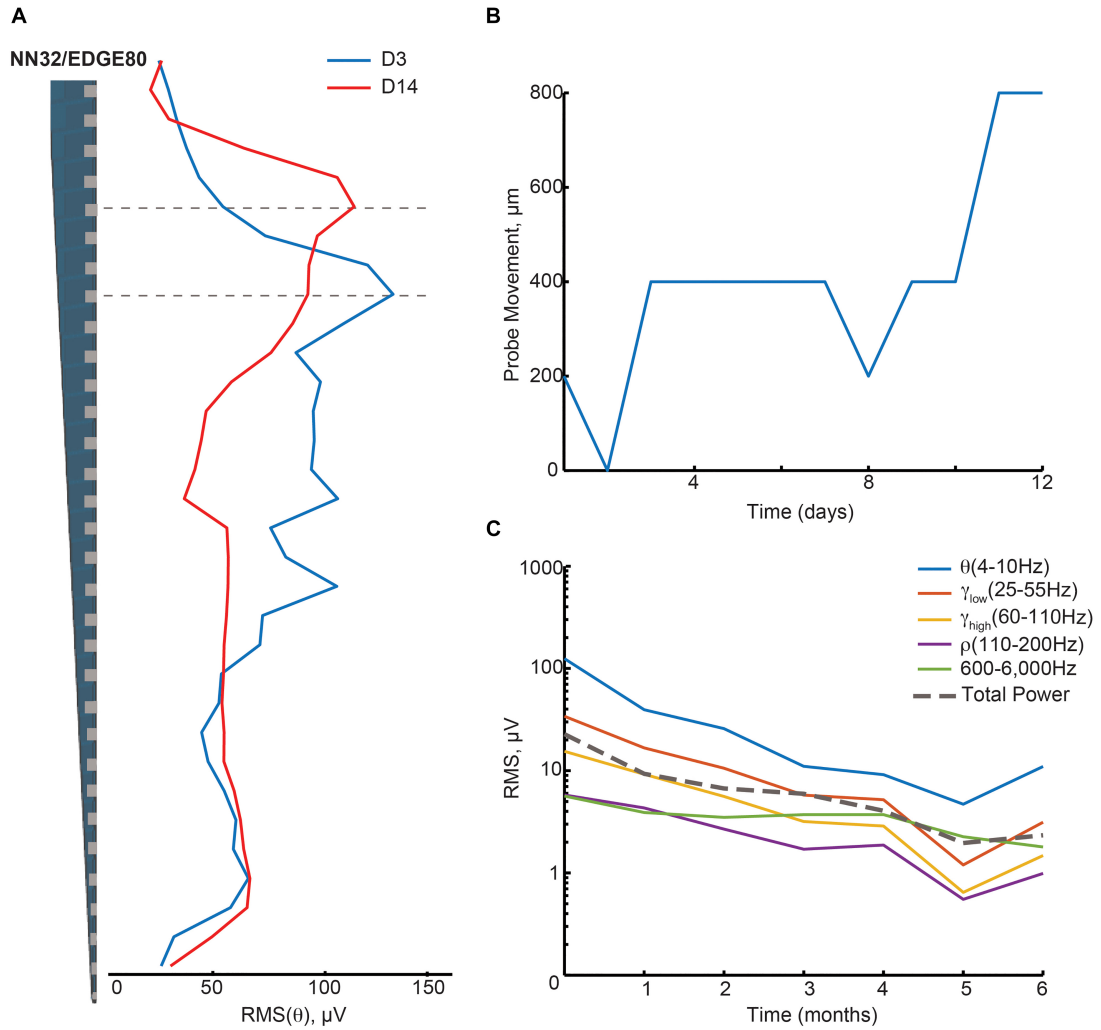

FIGURE 3 | Hippocampal oscillations power decreases over months following chronical implantation. **(A)** Over a period of 2 weeks, a chronically implanted NN32/EDGE80 silicon probe moved deeper into the dorsal hippocampus. One day post- implant, theta oscillation (~4–10 Hz) was maximal at channel 8 (blue trace). Over the course of 2 weeks, the theta peak moved up three electrode sites (red trace). A dotted line indicates the stratum radiatum (gray). **(B)** The silicon probe's drift was calculated for NN/EDGE80 silicon probe as a drift of theta power, which peaks in stratum-radiatum (blue trace). NN/EDGE80 probe moved down into the dorsal hippocampus for 600 μm in a course of 12 days following chronic implantation surgery. **(C)** Overall power of hippocampal oscillations [θ (4–10 Hz), γ_{low} (25–55 Hz), γ_{high} (60–110 Hz), ρ (110–200 Hz), and 600–6,000 Hz] in dorsal hippocampus decreased over months, with significant drop in the first month. The total power is shown with a dotted line.

over months post-surgery, with the largest drop seen in the first month, potentially due to gliosis/scar tissue formation leading to an insulating/filtering effect on the signal (**Figure 3C**).

Stability of Single Units Over Time

Next, we evaluated the amplitude and number of single units recorded from the porcine hippocampus over time (**Figure 4**). Since the 600–6,000 Hz power band representing unit activity decreased over time (**Figure 3C**), we compared the ability of various silicon probes to detect single unit activity during the first month post chronic implantation. Off-line spike detection and sorting was performed on the wideband signals (see "Materials and Methods" section for details), with an example of the raw signal (unfiltered, 0.1–9,000 Hz) recorded with NN32/EDGE80 silicon probes shown in **Supplementary Figure S2A**. In planar silicon probes (ATLAS32/TET and NN32/TET), where the individual electrode sites were placed on the face of the designs, there were no single units recorded after a couple of days post chronic implantation. In an attempt to decrease the damage near electrode sites and increase the exposure of the electrode sites to the parenchyma, we designed NN32/EDGE style probes (**Figure 1A**). The individual electrode sites are strategically positioned on the edge of the substrate, potentially reducing the interference of the insulator with the surrounding signals (Lee et al., 2018).

With NN32/EDGE silicon probes, single units were recorded for up to 3 weeks post implantation (**Figure 4A**). While the average amplitude of single units recorded with NN32/EDGE

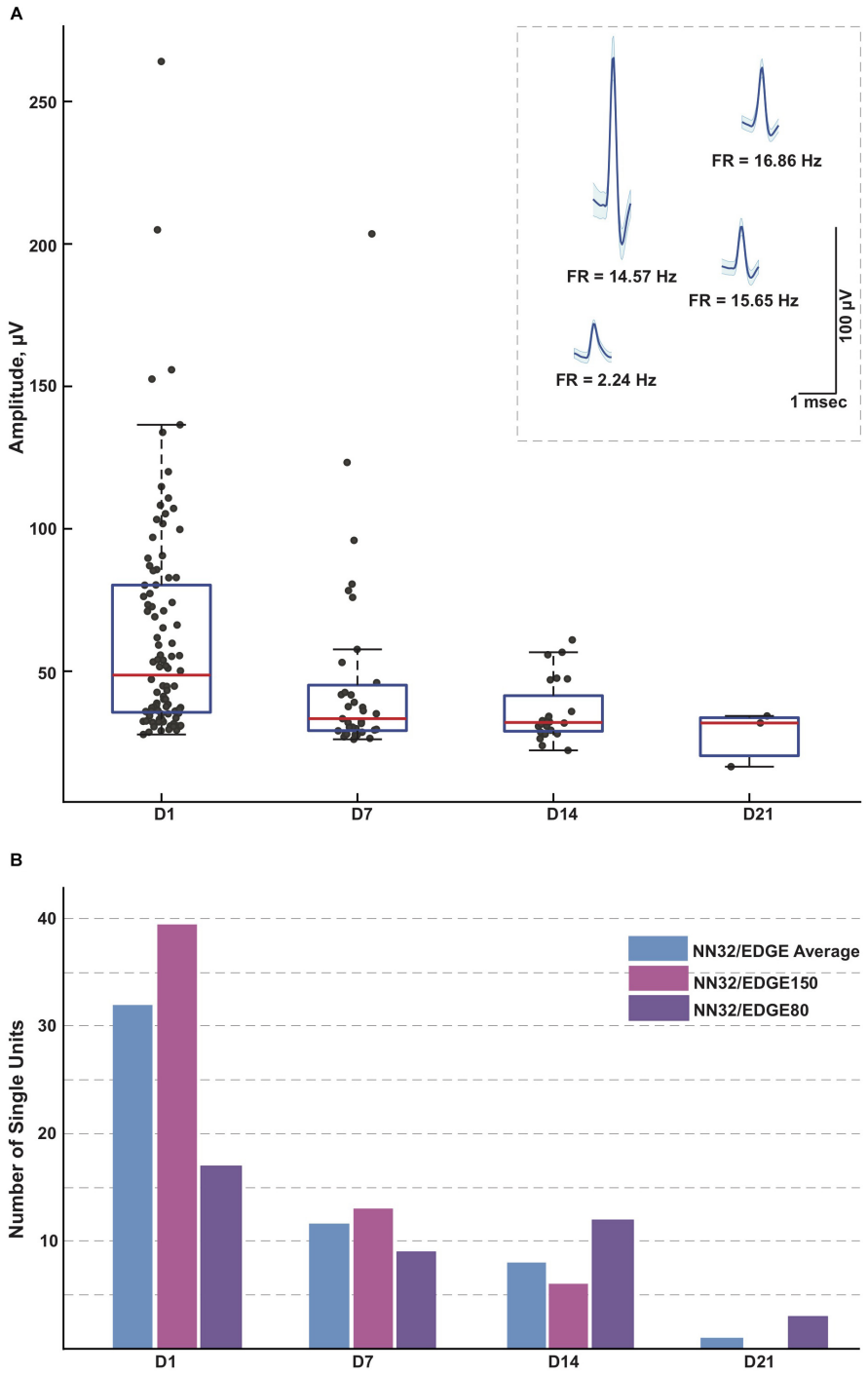

FIGURE 4 | Single units recorded for 3 weeks post implantation. **(A)** Single units were recorded in awake behaving pigs for up to 3 weeks post implantation (n = 3). While the average amplitude of single units recorded with NN32/EDGE silicon probes at D1 post implantation was 63 ± 4 µV (mean ± SEM, range 27–264 µV, $n_{singleunits}$ = 96), it decreased over time to 47 ± 6 µV (mean ± SEM, range 26–204 µV, $n_{singleunits}$ = 35) at D7 and 36 ± 2 µV (mean ± SEM, range 22–61 µV, $n_{singleunits}$ = 29) at D14. In addition, at D21 post implantation, single units were detected only from the narrower design silicon probe (NN32/EDGE80). The average amplitude of single units was 28 ± 6 µV (mean ± SEM, range 16–34 µV, $n_{singleunits}$ = 3), just above the threshold for spike detection. Mean waveform and firing rates (FR) of representative single units are shown at D1 (inset). **(B)** An ability to detect single unit activity was compared for NN32/EDGE150 and NN32/EDGE80 over a 3 week period. NN32/EDGE150 silicon probes ($n_{singleunits}$ = 40, pink, n = 2) had significantly more single units immediately after implantation (D1) than a NN32/EDGE80 ($n_{singleunits}$ = 17, n = 1, purple). However, there were no units recorded with NN32/EDGE150 probes after 3 weeks (D21), while NN32/EDGE80 silicon probes still detected single units ($n_{singleunits}$ = 3, n = 1, purple). Total number of units averaged over time for combined NN32/EDGE style probes is also shown (n = 3, blue).

silicon probes at D1 post implantation was 63 ± 4 μV (mean ± SEM, range 27–264 μV, $n_{singleunits}$ = 96), it decreased over time to 47 ± 6 μV (mean ± SEM, range 26–204 μV, $n_{singleunits}$ = 35) at D7 and 36 ± 2 μV (mean ± SEM, range 22–61 μV, $n_{singleunits}$ = 29) at D14. In addition, at D21 post implantation, single units were detected only from the narrower design of silicon probe (NN32/EDGE80). The average amplitude of single units was 28 ± 6 μV (mean ± SEM, range 16–34 μV, $n_{singleunits}$ = 3), just above the threshold for spike detection (**Figure 4A**). The number of single units recorded with NN32/EDGE style silicon probes also decreased over the period of the first 3 weeks, with 64% of single units disappearing by D7 and additional 31% falling below detection threshold by D14 (**Figure 4B**). Immediately after implantation (D1), the 150 μm wide EDGE-style silicon probe (NN32/EDGE150) had more single units than similar silicon probes of just half the width (NN32/EDGE80, width = 80 μm) (NN32/EDGE150: $n_{singleunits}$ = 40 vs. NN32/EDGE80: $n_{singleunits}$ = 17). However, after 3 weeks (D21), no units were detectable with NN32/EDGE150 silicon probes, while the NN32/EDGE80 still recorded single units ($n_{singleunits}$ = 3), suggesting a greater amount of tissue damage produced by the silicon probe with a larger cross-sectional area (**Figure 4B**).

Chronic Tissue Response to Implantation of Silicon Probes

To test how cross-sectional area of the silicon probe (measured at the top electrode site) affects stability of neurophysiological signals recorded chronically (over time), we histologically evaluated tissue damage in the porcine hippocampus produced by silicon probes of various designs (**Figure 5**). Microscopic examinations performed following acute silicon probe insertions (n = 3, multiple electrode types within 2–5 h) demonstrated (as expected) a degree of tissue disruption with associated hemorrhage around the probe track (**Figure 5A**). In addition, axonal pathology could be identified immediately adjacent to the site of silicon probe placement as evidenced by the pathological accumulation of APP, likely secondary to axonal transection causing acute interruption of transported proteins (**Figure 5B**). While, direct comparisons of chronic histological outcomes of different probe types were not performed, preliminary histological evaluations reveal the nature of the pathological response to silicon probes *in situ* over time in swine. Specifically, at 1.5 months post-implantation (n = 4, multiple electrode types), multiple histological changes were observed surrounding the silicon probe track. Notably, in one case the choroid plexus could be visualized entering the alveus, presumably having been translocated during the insertion as has previously been visualized (see Figure 8 in Skaggs et al., 2007) (**Figure 5C**). Immunostaining revealed both reactive astrocytes, with increased immunoreactivity to GFAP, and IBA-1 positive cells with the morphological appearance of reactive microglia (**Figures 5D–F**). Interestingly, Van Gieson's staining also revealed collagen surrounding the silicon probe track (**Figure 5G**). Notably, these features were also observed even at 6 months post-implantation, regardless of the type of silicon probe (n = 2) (**Figures 5H–K**).

Novel Multichannel Silicon Probes Designed to Improve Outcome of Chronic Implantation in Large Animals

To increase unit yield and to improve longevity of neurophysiological signals (local field oscillations and single unit activity) over time and to reduce pathological tissue response to chronic silicon probe implantations, novel 64-channel flexible silicon probes were developed in a collaboration with SB Microsystems and Cambridge NeuroTech and tested acutely (under anesthesia) in pigs.

Lithography Process Defines Cross-Sectional Area of Chronic Silicon Probes

The lithography and metal etch or liftoff technologies available for a given silicon probe fabrication process determine the size and spacing of the conducting lines, and therefore the device cross sectional area for a given channel count. Based on our experience with chronic probe implants in large animals, probes with cross sectional areas on the order of 10^4 square microns [as is the case for a 100 μm thick and 250 μm wide probes (**Figure 1B**)] are simply too damaging to tissue to reliably record single units on a chronic basis, and most practical recordings are carried out with probes that are 5–10 times slenderer than that. To our knowledge, past efforts at large animal probes have utilized contact lithography that limited interconnect pitch (width of a single conducting trace plus space) to 3–4 microns, leading to a practical upper limit of 32 channels per penetrating shank, given these constraints in cross sectional area. For example, 32-channel silicon probes designed by ATLAS Neuroengineering for large animal recordings (ATLAS32/TET) were 100 μm thick and made of silicon throughout the length of the probe (**Figure 1B**). While 32-channel silicon probes designed by NeuroNexus (NN32/TET, NN32/EDGE150 and NN32/EDGE80) were only 50 μm thick, they became brittle beyond 15 mm. This necessitated a novel interface cable solution whereby a high-density micro-cable was threaded through a 250 μm stainless steel tube and bonded to the contacts at the end of the probe, allowing the probes to be produced in lengths great enough to reach any part of the large animal brain (**Figure 1B**).

To reduce damage to brain tissue caused by insertion and chronic placement of silicon probes in the deep brain structures (hippocampus), we aimed to custom-design novel multichannel silicon probes with minimal cross-sectional area suitable for insertion. The goal was to reduce the profile of the probe, potentially reducing damage to the neural interface and inflammation. Increasing a probe's thickness imparts greater mechanical stiffness of the silicon probe which benefits insertion, but causes a further compliance mismatch between probe and brain tissue, potentially contributing to gliosis and local cell death for chronic implementations. In order to test stiffness/insertion abilities empirically, mock versions of CAMB64 silicon probes were created to have a fixed width of 80 μm, while the thickness of the mock probes varied in a range of 25–100 μm. While 25 μm thick mock silicon probes could be inserted into cortex, they failed to advance to the hippocampal structure. In contrast, mock silicon probes with thickness of >35 μm were capable

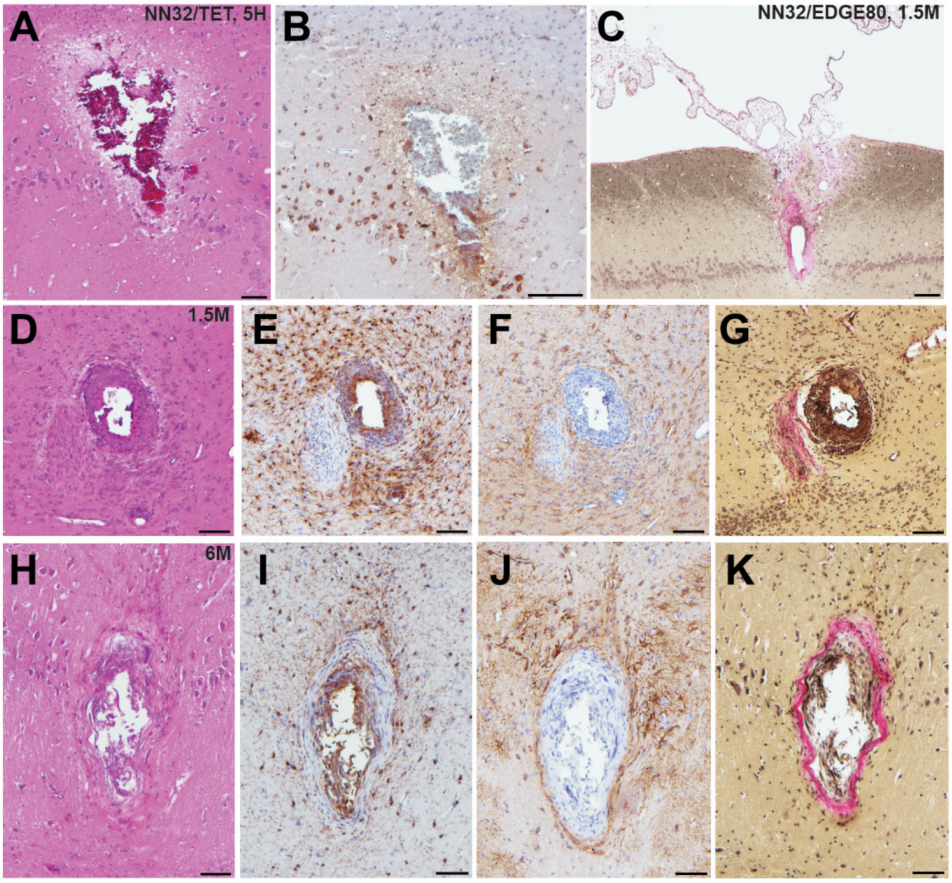

FIGURE 5 | Acute and chronic tissue response to implantation of silicon probes in a large animal. Histopathological responses of multichannel silicon probes were microscopically examined at acute and chronic time points. **(A)** H&E staining showing silicon probe track with associated hemorrhage acutely (<5 h) following insertion of NN32/TET electrode. **(B)** APP immunohistochemistry showing the same region as **(A)**. Note the axonal swellings indicative of axonal transport interruption, likely secondary to axonal transection during insertion. Surrounding pyramidal neurons also show increased APP immunoreactivity. **(C)** Van Gieson stain showing silicon probe track 1.5 months following implantation of NN32/EDGE80 probe where collagen is pink. Notably, there appears to be choroid plexus abnormally located within the alveus. **(D–G)** Neuropathological findings in NN32/TET silicon probe track, 1.5 months following implantation, demonstrating **(D)** lesion with **(E)** IBA-1 positive cells displaying morphological features of activated microglia, **(F)** GFAP immunoreactive cells with features of reactive astrocytes and **(G)** Van Gieson staining demonstrating the presence of collagen (pink). **(H–K)** Silicon probe track 6 months following implantation of NN32/TET, again showing surrounding activation of both microglia **(I)** and astrocytes **(J)**, as well as the presence of collagen **(K)**. Scale bars: **(A,B,D–K)**: 100 μm; **(C)**: 200 μm.

of insertion into the hippocampus. Based on the insertion ability and acute neuropathology, the thickness of 35 μm was selected for production of initial research silicon probes, giving a minimum dimension for the probes as stiffness increases linearly with width.

To potentially reduce tissue damage even further, we aimed to design silicon probes to have a full-length silicon rather than a standard "silicon plus guide tube" design. By reducing the tissue impact during insertion, smaller, less brittle silicon probes may also increase the survival rate of neurons in close proximity to the travel path. In order to produce longer silicon probes without the need for the extension tube, novel research silicon probes were manufactured using projection ("stepper") lithography rather than contact lithography, allowing us produce 0.5 μm resolution features and changing the width/channel count trade-off in our favor. However, the use of projection lithography for these large devices (up to 40 mm in length) meant that the 5X master reticle exceeded the maximum allowed size, and required us to develop a process for stitching multiple exposures of multiple reticles across the process wafer. This novel lithography process allowed for the full length of the probe to be manufactured in silicon. The mock version of these new probes was capable of insertion into the dorsal hippocampus without support of metal guide tubes, which also resulted in less damage to cortical tissue en route to the hippocampus. The new lithography technology used to create novel research silicon probes also allowed for a doubling of the number of sites on the probe, leading to the first 64-channel silicon probes for large animals that are made exclusively from silicon wafer at lengths capable of reaching much of the large animal brain. In addition, the individual electrode sites on CAMB64/EDGE and CAMB64/POLY-2 silicon probes were composed of gold (Au) coated with an organic

polymer, lowering their impedance and decreasing the noise during recordings in comparison to other silicon probes used (**Supplementary Figure S2**).

Multichannel Silicon Probes Designed to Improve Single Unit Isolation

While a linear design is fit for a wide range of applications, isolation of single unit activity may be difficult with only a linear site arrangement. To utilize commercial spike sorting software available at the time (SpikeSort 3D, Neuralynx), individual sites on silicon probes with a linear design had to be artificially grouped into sets of four (tetrodes) in order for single units to be sorted. Previously, single units recorded with 32-channel silicon probes of the earlier designs could not be properly isolated with spike sorting software available at the time, partially due to potential overlap between putative units between the artificial tetrodes.

To address this issue, we initially custom-designed silicon probes (ATLAS32/TET and NN32/TET) to have most of the individual sites arranged in four sites placed close together (tetrodes), allowing for high-quality cell discrimination in hippocampal recordings (**Figure 1A**). Extra electrode sites were added in between groups of tetrodes in order to maintain the laminar analyses. In this configuration, four tetrodes were placed in the pyramidal CA1 hippocampal layer (top part of the probe), while three tetrodes were placed in the granular cell layer (bottom part of the probe). As tetrode-style silicon probes were created with the individual sites arranged closely to form tetrodes, more single units were isolated but cross-over of the units onto neighboring tetrodes were still observed occasionally in the CA1 layer due to the large size and dendritic arbor of these neurons. As modern spike sorting software became available (Klusta and phy software packages), we designed silicon probes with a linear layout of the electrode sites, which also helped to resolve laminar structure of the porcine hippocampus (NN32/EDGE150 and NN32/EDGE80, **Figure 1A**).

The advent of laminar spike-sorting software removed the necessity for specific tetrodes to be recreated in the silicon probes, however, probe geometry is still an important part of the spike-sorting process (Schmitzer-Torbert et al., 2005; Rossant et al., 2016). We therefore designed novel research CAMB64 silicon probes with two arrangements of the individual electrode sites: a linear style CAMB64/EDGE probe (148 μm width) and a poly-2 style CAMB64/POLY-2 probe (154 μm width, electrode sites are off-set by 21 μm), with tip profile of both probes reduced to a minimum (**Figure 1A**, inset). To answer an open question whether vertically offset probe designs are necessary for true resolution of single units using modern sorting algorithms, we compared single-unit separation of a linear vs. a poly-2 CAMB64 silicon probes (**Figure 6**). Again, off-line spike detection and sorting was performed on the wideband signals (see "Materials and Methods" section for details), with an example of the raw signal (unfiltered, 0.1–9,000 Hz) recorded with a CAMB64/POLY-2 silicon probe shown in **Supplementary Figure S2B**. Decreasing spacing between individual electrode sites to 100 μm on both CAMB64/EDGE and CAMB64/POLY-2 style probes helped to sort single units with more precision (**Figure 6A**). The blue unit on the linear (left) or poly-2 (right) style probes could have easily been classified with the red unit had the spacing not revealed the higher amplitude action potentials at the same time stamps. Moreover, the offset geometry of the poly-2 design also appears to better separate single cells compared to the linear design (**Figure 6B**). Many separated clusters from the CAMB64/EDGE recording contained multiple units, which were not well isolated from each other with current spike sorting methods. While some clusters from the CAMB64/POLY-2 probe also contained multiple units, the proportion of multi-unit clusters was less when compared to the linear design (33% and 54% respectively).

DISCUSSION

Silicon multichannel probes designed and used for large animal hippocampal electrophysiology allow for a longer area of coverage in contrast to single site recordings, and reveal laminar structure and correlation of unit activity with field behavior. We have performed a retrospective analysis of chronically implanted pigs from our experiments in order to characterize the differences in electrophysiology over time with various probe sizes and geometries from different manufacturers. In addition, we have examined the neural interface out to 6 months post-implantation in order to assess whether neuropathology in the large animal hippocampus resembles that previously reported in rodents. Differing probe geometries were examined in a new higher density research probe in order to assess their ability for sorting units. Long-length silicon probes may also replace the need for multiple acute insertion experiments if the animal is chronically implanted and/or a drive is utilized.

Our initial attempts at chronic implantations using probes that were developed for acute work and prior to modern spike sorting methods for laminar probes were successful only for field recordings. Units that appeared during the implantation surgery were either not present or were significantly attenuated even 24 h post implantation. Histological examination suggested that the insertion damage to the neural interface, and sometimes even the cytoarchitecture, was significant with these larger dimension probes. In addition, attenuation of unit amplitude over time as well as field power in various frequency ranges is potentially explained by both cellular and collagen encapsulation of the probe as demonstrated at 6 weeks and 6 months post implantation. We therefore redesigned these probes to increase laminar coverage, and plated the electrodes on the edge of the probe in order to take full advantage of the contacts as has previously been described (Lee et al., 2018). This change in dimension and geometry had the effect of increasing unit yields for the initial 2–3 weeks post implantation, with significant attenuation by the third week. Further reduction of the width by almost a factor of two at the top of the active portion of the probe yielded a greater number of units at week 3. It is an open question

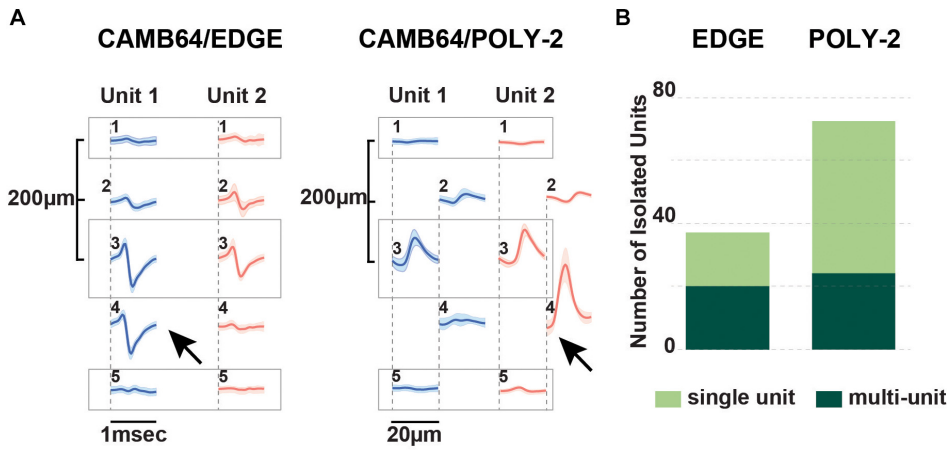

FIGURE 6 | Neurophysiological signals recorded with novel research CAMB64 silicon from pig hippocampus. **(A)** Single units were isolated for a linear and a poly-2 style CAMB64 silicon probes. Decreasing spacing between individual electrode sites to 100 µm on both the CAMB64/EDGE and CAMB64/POLY-2 style probes helped to sort single units with more precision. The blue unit on the linear (left) or poly-2 (right) style probes could have easily been classified with the red unit had the spacing not revealed the higher amplitude action potentials at the same time stamps. **(B)** Spike sorting on a recording with the CAMB64/EDGE silicon probe yielded more multi-units (dark green, *n* = 20) than single units (light green, *n* = 17). While some clusters on the CAMB64/POLY-2 silicon probe contained multiple units (dark green, *n* = 24), two times more single units (light green, *n* = 48) were identified. Also, the proportion of multi-unit clusters for the poly-2 style probe was less when compared to the linear design (33% and 54% respectively).

how much the placement of the edge electrodes increased unit longevity in relationship to the width change, but newer designs with offset spacing may allow for future examination of this relationship by comparing edge electrodes to those offset from the edge. Further detailed quantification of the differences in chronic neuropathology with various probe dimensions is also warranted to examine the potential correlation between these improved results and differences in the chronic neural interface response.

We also tested various designs of silicon probes available from and developed with manufacturers for the ability to separate single units. Linear, tetrode plus linear and poly-2 site arrangement designs were evaluated for single unit vs. multi-unit cluster isolation. Spacing between individual electrode sites played a significant role as 200 µm spacing (as on NN32/EDGE style probes) increased the number of multi-units sorted. This could affect the precision of research studies focused on activity of hippocampal neurons, for example characterization of place cells or interneurons. Interestingly, some CA1 units spanned not two, but three electrodes, suggesting that large putative pyramidal cells that run parallel to the probe can be detected across greater distances than those previously reported, and further suggesting that lateral electrode separation for analysis in these structures may be helpful. Although most of the probes with a linear design site arrangement (NN32/EDGE150, NN32/EDGE80, and CAMB64/EDGE) were able to record neuronal activity of individual neurons, silicon probes with a tetrode (ATLAS32/TET and NN32/TET) and a poly-2 (CAMB64/POLY-2) design site arrangement had better cluster separation with currently available sorting algorithms, as the proportion of single units to multi-units recorded with a given probe increased. Previous acute examinations in large animals have also noted the usefulness of the parallel geometry in isolating units, even prior to the advent of new sorting techniques (Blanche et al., 2005). New sorting techniques, as well as drift associated with the semi-floating chronic preparation, suggest that parallel configurations may be optimal in order to maximize unit detection and separation in large animal laminar structures, and may be helpful as drives are developed for these probes.

Mock probe testing of the CAMB64 25 mm-long probes demonstrated that 35 µm shank thickness for 80 µm wide probes strikes an ideal compromise between ease of tissue penetration and appropriate targeting vs. the need to maintain small device dimensions. This allowed for production and testing of the 30 mm long 64-channel probes described above, which yielded substantially more units in the poly-2 style probe in acute testing. The balance between maximal stiffness, length and electrode density with minimal cross-sectional area in order to reduce damage to the neural interface remains a significant challenge in large animals. Designs such as the NeuroNexus' NN32/EDGE probe and the new CAMB64 probe approach these challenges with different design solutions, but appear to have reached a critical threshold where the full depth can be reached with enough electrodes for sorting, and allowing for single unit detection out to a month post implant without being driven. Future chronic implantation of the CAMB64 probes will further test whether the trade-off of device width for increased channel count increases single unit yield, and for how long. These probes are also not at the minimal feature dimensions for this technique, as electrode yield in the initial testing run was also a consideration. Future dimensions of 80 µm wide, 64-channel probes may also increase yield by reducing damage to the neural interface, but this remains to be tested as well.

Passive laminar silicon probes (as described above) are but one solution to the problem of laminar recordings in large animals (Chen et al., 2017; Rivnay et al., 2017). Other proposed solutions that are either commercially available or being developed are the MicroFlex array and the Neuropixels probes, although the current Neuropixels probe is currently only 10 mm long and therefore cannot reach laminar deep brain structures in large animals such as the pig (Jun et al., 2017). The main benefit of the MicroFlex array is a better biomechanical match to brain properties due to their flexible material, however, the role of insertion trauma from electrodes or their carriers vs. chronic interface trauma due to mismatch in the modulus remains to be resolved. In addition, current reports in large chronically implanted animals have yielded fields, but not stable single units at present which remain to be demonstrated (Talakoub et al., 2019). A future Neuropixels version for large animals would be of limited utility in its current form, as cell densities decrease in laminar structures as you move up on the phylogenetic tree (Ulyanova et al., 2018). In addition, it is not as practical to sample multiple structures along only one axis of a probe in the large animal as it is in rodents, necessitating multiple probes for multi-regional studies. Also, Neuropixels probes designed for chronic implants of a period of 1 year or longer may require different designs or materials to increase long-term biocompatibility (Steinmetz et al., 2018). Neuropixels probes cannot be used for translational research on neurological disorders that require neuromodulation as they are incapable of electrical micro stimulation, a technique also useful for probing the role of neural circuits in perception and cognition (Clark Kelsey et al., 2011).

CONCLUSION

We hope that this study will help to facilitate adoption of novel silicon multi-channel probes suitable for chronic implantations in large animals, by comparing silicon probes available for use in large animal electrophysiology, as well as comparing them to a new design and process. NeuroNexus EDGE style probes (NN32/EDGE80) were determined to yield the largest number of units of the available probes for acute and chronic recordings from laminar structures due a linear edge site arrangement, 6 mm of coverage, and potentially reducing damage to the neural interface upon insertion. In addition, cross-sectional area was found to be one determinant of silicon probes' performance. Novel CAMB64 silicon probes with a poly-2 design were found to have an even better single unit separation and a denser sampling of the laminar structure than existing linear probes. By increasing channel density, we were able to better visualize laminar structure and create offset geometries that enabled better unit sorting. Channel density, site arrangement, and the physical profile of the silicon probe are all important factors to consider when designing probes for acute and chronic implantations to study laminar structures over time in awake behaving animals. We hope these results will lower the threshold for adoption in chronic implantations, by demonstrating consistent yields in laminar electrophysiological recordings in large animals using commercially available probes. We hope that in combination with new wireless technologies allowing for freely moving behavior, this will support new discoveries in both hippocampal and neocortical neurophysiology. In addition, better detection and understanding of laminar circuitry and changes in human disease (i.e., epilepsy, traumatic brain injury) are needed, and therefore viable electrodes need to be tested first in translational large animal models prior to clinical use.

ETHICS STATEMENT

This study was carried out in accordance with the recommendations of the University of Pennsylvania, an AALAC accredited institution. The protocol was approved by the University of Pennsylvania IACUC animal care committee.

AUTHOR CONTRIBUTIONS

AU and JW: conceptualization and visualization. AU, PK, TH, BJ, and JW: methodology. AU, CA, PK, and JW: software. AU, CA, PK, HC, VJ, and JW: validation. AU, CA, CC, and KG: formal analysis. AU, CA, PK, KG, and JW: investigation. DC and JW: resources. AU: data curation and writing-original draft preparation. AU, CA, KG, and JW: writing-review and editing. JW: supervision, project administration, and funding acquisition.

FUNDING

This research was funded by the Department of Veterans Affairs, grant numbers IK2-RX001479, I01-RX002705, and I01-RX001097, the National Institutes of Health, grant numbers NINDS R01-NS-101108-01 and T32-NS043126, CURE Foundation, Taking Flight Award, and DoD ERP CDMRP W81XWH-16-1-0675.

ACKNOWLEDGMENTS

Authors would like to thank Matthew Sergison, Andy Tekriwal, and Maura Weber for their help with the experimental design and execution.

SUPPLEMENTARY MATERIAL

The Supplementary Material for this article can be found online at: https://www.frontiersin.org/articles/10.3389/fnins.2019.00397/full#supplementary-material

FIGURE S1 | Internal reference on multichannel silicon probes reduces artifacts during chronic and acute recordings. **(A)** All multichannel silicon probes used in the study were custom-designed to have a top electrode site substituted for a low-impedance reference site (site area = 4,200 μm^2) placed 1–2 mm above the most-proximal probe site. Schematic diagram of a NN32/EDGE80 silicon probe shows the location of internal reference. **(B,C)** During awake behaving recordings in pigs, the internal reference eliminated movement-associated artifacts. The same 1 s recording segment is shown referenced to a skull screw **(B)** vs. internal reference **(C)**. **(B)** The highlighted areas (gray) show "movement artifacts" detected on all 31 channels during awake recordings (arrows). Note that only 16 out of 31 channels are displayed. **(C)** The noise associated with "movement artifacts" seen in **(B)** is eliminated after neurophysiological signals were re-referenced to the internal reference on the NN32/EDGE80 silicon probe. **(D)** Under the anesthetized preparation, the internal reference on the NN32/EDGE80 silicon probe eliminated most of the slow "drift" oscillations as well as the 60 Hz frequency peak, presumably from AC noise during acute recordings.

FIGURE S2 | Multi-unit activity recorded with multichannel silicon probes designed for large animal electrophysiology. Recording profiles of multichannel silicon probes are displayed for NN32/EDGE80 and CAMB64/EDGE silicon probes. **(A)** Representative traces recorded from a single electrode site on NN32/EDGE80 silicon probe that was located in the pyramidal CA1 layer show raw, unfiltered signal (0.1–9,000 Hz, top trace) and the filtered signal used to identify spiking activity (600–6,000 Hz, bottom trace). Multiunit and oscillatory activity can be seen on both traces. **(B)** Representative traces recorded from a single electrode site on CAMB64/POLY-2 silicon probe that was located in the granular cell layer shows raw, unfiltered signal (0.1–9,000 Hz, top trace) and the filtered signal used to identify spiking activity (600–6,000 Hz, bottom trace).

REFERENCES

Blanche, T. J., Spacek, M. A., Hetke, J. F., and Swindale, N. V. (2005). Polytrodes: high-density silicon electrode arrays for large-scale multiunit recording. *J. Neurophysiol.* 93, 2987–3000. doi: 10.1152/jn.01023.2004

Bragin, A., Jando, G., Nadasdy, Z., Hetke, J., Wise, K., and Buzsaki, G. (1995a). Gamma (40-100 Hz) oscillation in the hippocampus of the behaving rat. *J. Neurosci.* 15(1 Pt 1), 47–60. doi: 10.1523/jneurosci.15-01-00047.1995

Bragin, A., Jando, G., Nadasdy, Z., van Landeghem, M., and Buzsaki, G. (1995b). Dentate EEG spikes and associated interneuronal population bursts in the hippocampal hilar region of the rat. *J. Neurophysiol.* 73, 1691–1705. doi: 10.1152/jn.1995.73.4.1691

Buzsáki, G. (1989). Two-stage model of memory trace formation: a role for "noisy" brain states. *Neuroscience* 31, 551–570. doi: 10.1016/0306-4522(89)90423-5

Buzsáki, G. (2004). Large-scale recording of neuronal ensembles. *Nat. Neurosci.* 7, 446–451. doi: 10.1038/nn1233

Buzsáki, G. (2015). Hippocampal sharp wave-ripple: a cognitive biomarker for episodic memory and planning. *Hippocampus* 25, 1073–1188. doi: 10.1002/hipo.22488

Buzsáki, G., Buhl, D. L., Harris, K. D., Csicsvari, J., Czéh, B., and Morozov, A. (2003). Hippocampal network patterns of activity in the mouse. *Neuroscience* 116, 201–211. doi: 10.1016/s0306-4522(02)00669-3

Buzsaki, G., and Moser, E. I. (2013). Memory, navigation and theta rhythm in the hippocampal-entorhinal system. *Nat. Neurosci.* 16, 130–138. doi: 10.1038/nn.3304

Carr, M. F., Jadhav, S. P., and Frank, L. M. (2011). Hippocampal replay in the awake state: a potential substrate for memory consolidation and retrieval. *Nat. Neurosci.* 14, 147–153. doi: 10.1038/nn.2732

Chen, R., Canales, A., and Anikeeva, P. (2017). Neural recording and modulation technologies. *Nat. Rev. Mater.* 2:16093. doi: NODOI

Christensen, A. B., Sørensen, J. C. H., Ettrup, K. S., Orlowski, D., and Bjarkam, C. R. (2018). Pirouetting pigs: a large non-primate animal model based on unilateral 6-hydroxydopamine lesioning of the nigrostriatal pathway. *Brain Res. Bull.* 139, 167–173. doi: 10.1016/j.brainresbull.2018.02.010

Clark Kelsey, L., Armstrong Katherine, M., and Moore, T. (2011). Probing neural circuitry and function with electrical microstimulation. *Proc. R. Soc. B Biol. Sci.* 278, 1121–1130. doi: 10.1098/rspb.2010.2211

Duhaime, A.-C., Margulies, S. S., Durham, S. R., O'Rourke, M. M., Golden, J. A., Marwaha, S., et al. (2000). Maturation-dependent response of the piglet brain to scaled cortical impact. *J. Neurosurg.* 93, 455–462. doi: 10.3171/jns.2000.93.3.0455

Fernández-Ruiz, A., Oliva, A., Nagy, G. A., Maurer, A. P., Berényi, A., and Buzsáki, G. (2017). Entorhinal-CA3 dual-input control of spike timing in the hippocampus by theta-gamma coupling. *Neuron* 93, 1213.e5–1226.e5. doi: 10.1016/j.neuron.2017.02.017

Flynn, T. (1984). Developmental changes of myelin-related lipids in brain of miniature swine. *Neurochem. Res.* 9, 935–945. doi: 10.1007/bf00964525

Gibson, W. S., Ross, E. K., Han, S. R., Van Gompel, J. J., Min, H.-K., and Lee, K. H. (2016). Anterior thalamic deep brain stimulation: functional activation patterns in a large animal model. *Brain Stimul.* 9, 770–773. doi: 10.1016/j.brs.2016.04.012

Hainmueller, T., and Bartos, M. (2018). Parallel emergence of stable and dynamic memory engrams in the hippocampus. *Nature* 558, 292–296. doi: 10.1038/s41586-018-0191-2

Hazan, L., Zugaro, M., and Buzsáki, G. (2006). Klusters, NeuroScope, NDManager: a free software suite for neurophysiological data processing and visualization. *J. Neurosci. Methods* 155, 207–216. doi: 10.1016/j.jneumeth.2006.01.017

Johnson, V. E., Stewart, J. E., Begbie, F. D., Trojanowski, J. Q., Smith, D. H., and Stewart, W. (2013). Inflammation and white matter degeneration persist for years after a single traumatic brain injury. *Brain* 136, 28–42. doi: 10.1093/brain/aws322

Johnson, V. E., Stewart, W., Weber, M. T., Cullen, D. K., Siman, R., and Smith, D. H. (2016). SNTF immunostaining reveals previously undetected axonal pathology in traumatic brain injury. *Acta Neuropathol.* 131, 115–135. doi: 10.1007/s00401-015-1506-0

Johnson, V. E., Weber, M. T., Xiao, R., Cullen, D. K., Meaney, D. F., Stewart, W., et al. (2018). Mechanical disruption of the blood–brain barrier following experimental concussion. *Acta Neuropathol.* 135, 711–726. doi: 10.1007/s00401-018-1824-0

Jun, J. J., Steinmetz, N. A., Siegle, J. H., Denman, D. J., Bauza, M., Barbarits, B., et al. (2017). Fully integrated silicon probes for high-density recording of neural activity. *Nature* 551:232. doi: 10.1038/nature24636

Kee, S. E., Mou, X., Zoghbi, H. Y., and Ji, D. (2018). Impaired spatial memory codes in a mouse model of Rett syndrome. *eLife* 7:e31451. doi: 10.7554/eLife.31451

Killian, N. J., Jutras, M. J., and Buffalo, E. A. (2012). A map of visual space in the primate entorhinal cortex. *Nature* 491:761. doi: 10.1038/nature11587

Kim, J. P., Min, H.-K., Knight, E. J., Duffy, P. S., Abulseoud, O. A., Marsh, M. P., et al. (2013). Centromedian-parafascicular deep brain stimulation induces differential functional inhibition of the motor, associative, and limbic circuits in large animals. *Biol. Psychiatry* 74, 917–926. doi: 10.1016/j.biopsych.2013.06.024

Kook, G., Lee, W. S., Lee, C. H., Cho, I.-J., and Lee, J. H. (2016). Neural probes for chronic applications. *Micromachines* 7:E179. doi: 10.3390/mi7100179

Lee, H. C., Gaire, J., Roysam, B., and Otto, K. J. (2018). Placing sites on the edge of planar silicon microelectrodes enhances chronic recording functionality. *IEEE Trans. Biomed. Eng.* 65, 1245–1255. doi: 10.1109/TBME.2017.2715811

Lewis, C. M., Bosman, C. A., and Fries, P. (2015). Recording of brain activity across spatial scales. *Curr. Opin. Neurobiol.* 32, 68–77. doi: 10.1016/j.conb.2014.12.007

Maas, A. I. R., Menon, D. K., Adelson, P. D., Andelic, N., Bell, M. J., Belli, A., et al. (2017). Traumatic brain injury: integrated approaches to improve prevention, clinical care, and research. *Lancet Neurol.* 16, 987–1048. doi: NODOI

Min, H.-K., Hwang, S.-C., Marsh, M. P., Kim, I., Knight, E., Striemer, B., et al. (2012). Deep brain stimulation induces BOLD activation in motor and non-motor networks: an fMRI comparison study of STN and EN/GPi DBS in large animals. *Neuroimage* 63, 1408–1420. doi: 10.1016/j.neuroimage.2012.08.006

Mitra, P., and Bokil, H. (2007). *Observed Brain Dynamics*, 1 Edn. Oxford: University Press, 408. doi: NODOI

Orlowski, D., Michalis, A., Glud, A. N., Korshøj, A. R., Fitting, L. M., Mikkelsen, T. W., et al. (2017). Brain tissue reaction to deep brain stimulation—a longitudinal study of DBS in the goettingen minipig. *Neuromodulation* 20, 417–423. doi: 10.1111/ner.12576

Pampiglione, G. (1971). Some aspects of development of cerebral function in mammals. *Proc. R. Soc. Med.* 64, 429–435. doi: NODOI

Rivnay, J., Wang, H., Fenno, L., Deisseroth, K., and Malliaras, G. G. (2017). Next-generation probes, particles, and proteins for neural interfacing. *Sci. Adv.* 3:e1601649. doi: 10.1126/sciadv.1601649

Rossant, C., Kadir, S. N., Goodman, D. F. M., Schulman, J., Hunter, M. L. D., Saleem, A. B., et al. (2016). Spike sorting for large, dense electrode arrays. *Nat Neurosci.* 19, 634–641. doi: 10.1038/nn.4268

Schmitzer-Torbert, N., Jackson, J., Henze, D., Harris, K., and Redish, A. D. (2005). Quantitative measures of cluster quality for use in extracellular recordings. *Neuroscience* 131, 1–11. doi: 10.1016/j.neuroscience.2004.09.066

Skaggs, W. E., McNaughton, B. L., Permenter, M., Archibeque, M., Vogt, J., Amaral, D. G., et al. (2007). EEG sharp waves and sparse ensemble unit activity in the macaque hippocampus. *J. Neurophysiol.* 98, 898–910. doi: 10.1152/jn.00401.2007

Steinmetz, N. A., Koch, C., Harris, K. D., and Carandini, M. (2018). Challenges and opportunities for large-scale electrophysiology with Neuropixels probes. *Curr. Opin. Neurobiol.* 50, 92–100. doi: 10.1016/j.conb.2018.01.009

Stevenson, I. H., and Kording, K. P. (2011). How advances in neural recording affect data analysis. *Nat. Neurosci.* 14:139. doi: 10.1038/nn.2731

Talakoub, O., Sayegh, P. F., Womelsdorf, T., Zinke, W., Fries, P., Lewis, C. M., et al. (2019). Hippocampal and neocortical oscillations are tuned to behavioral state in freely-behaving macaques. *bioRxiv* [Preprint]. doi: 10.1101/552877

Ulyanova, A. V., Koch, P. F., Cottone, C., Grovola, M. R., Adam, C. D., Browne, K. D., et al. (2018). Electrophysiological signature reveals laminar structure of the porcine hippocampus. *eNeuro* 5:ENEURO.0102-18.2018. doi: 10.1523/ENEURO.0102-18.2018

Vetter, R. J., Williams, J. C., Hetke, J. F., Nunamaker, E. A., and Kipke, D. R. (2004). Chronic neural recording using silicon-substrate microelectrode arrays implanted in cerebral cortex. *IEEE Trans. Biomed. Eng.* 51, 896–904. doi: 10.1109/tbme.2004.826680

Conflict of Interest Statement: The authors declare that the research was conducted in the absence of any commercial or financial relationships that could be construed as a potential conflict of interest.

Copyright © 2019 Ulyanova, Cottone, Adam, Gagnon, Cullen, Holtzman, Jamieson, Koch, Chen, Johnson and Wolf. This is an open-access article distributed under the terms of the Creative Commons Attribution License (CC BY). The use, distribution or reproduction in other forums is permitted, provided the original author(s) and the copyright owner(s) are credited and that the original publication in this journal is cited, in accordance with accepted academic practice. No use, distribution or reproduction is permitted which does not comply with these terms.

frontiers in Neuroscience

ORIGINAL RESEARCH
published: 30 April 2019
doi: 10.3389/fnins.2019.00367

Toward a Bidirectional Communication Between Retinal Cells and a Prosthetic Device – A Proof of Concept

*Viviana Rincón Montes[1], Jana Gehlen[2], Stefan Lück[3], Wilfried Mokwa[3], Frank Müller[2], Peter Walter[4] and Andreas Offenhäusser[1]**

[1] Bioelectronics, Institute of Complex Systems-8, Forschungszentrum Jülich, Jülich, Germany, [2] Cellular Biophysics, Institute of Complex Systems-4, Forschungszentrum Jülich, Jülich, Germany, [3] Department of Materials in Electrical Engineering 1, RWTH Aachen University, Aachen, Germany, [4] Department of Ophthalmology, RWTH Aachen University, Aachen, Germany

OPEN ACCESS

Edited by:
Ulrich G. Hofmann,
Freiburg University Medical Center,
Germany

Reviewed by:
Paolo Medini,
Umeå University, Sweden
Gregg Suaning,
University of Sydney, Australia

***Correspondence:**
Andreas Offenhäusser
a.offenhaeusser@fz-juelich.de

Specialty section:
This article was submitted to Neural Technology, a section of the journal Frontiers in Neuroscience

Received: 10 December 2018
Accepted: 01 April 2019
Published: 30 April 2019

Citation:
Rincón Montes V, Gehlen J, Lück S, Mokwa W, Müller F, Walter P and Offenhäusser A (2019) Toward a Bidirectional Communication Between Retinal Cells and a Prosthetic Device – A Proof of Concept. Front. Neurosci. 13:367. doi: 10.3389/fnins.2019.00367

Background: Significant progress toward the recovery of useful vision in blind patients with severe degenerative retinal diseases caused by photoreceptor death has been achieved with the development of visual prostheses that stimulate the retina electrically. However, currently used prostheses do not provide feedback about the retinal activity before and upon stimulation and do not adjust to changes during the remodeling processes in the retina. Both features are desirable to improve the efficiency of the electrical stimulation (ES) therapy offered by these devices. Accordingly, devices that not only enable ES but at the same time provide information about the retinal activity are beneficial. Given the above, a bidirectional communication strategy, in which inner retinal cells are stimulated and the output neurons of the retina, the ganglion cells, are recorded using penetrating microelectrode arrays (MEAs) is proposed.

Methods: Custom-made penetrating MEAs with four silicon-based shanks, each one with three or four iridium oxide electrodes specifically designed to match retinal dimensions were used to record the activity of light-adapted wildtype mice retinas and degenerated retinas from *rd10* mice *in vitro*. In addition, responses to high potassium concentration and to light stimulation in wildtype retinas were examined. Furthermore, voltage-controlled ES was performed.

Results: The spiking activity of retinal ganglion cells (RGCs) was recorded at different depths of penetration inside the retina. Physiological responses during an increase of the extracellular potassium concentration and phasic and tonic responses during light stimulation were captured. Moreover, pathologic rhythmic activity was recorded from degenerated retinas. Finally, ES of the inner retina and simultaneous recording of the activity of RGCs was accomplished.

Conclusion: The access to different layers of the retina with penetrating electrodes while recording at the same time the spiking activity of RGCs broadens the use and the

field of action of multi-shank and multi-site penetrating MEAs for retinal applications. It enables a bidirectional strategy to stimulate inner retinal cells electrically and to record from the spiking RGCs simultaneously (BiMEA). This opens the possibility of a feedback loop system to acknowledge the success of ES carried out by retinal prostheses.

Keywords: retinal implants, intraretinal implants, penetrating microelectrode array, retinal recordings, retinal stimulation, bidirectional communication

INTRODUCTION

The retina harbors not only the photoreceptors but also a neuronal network ("inner retina") that serves for information processing and provides the retinal output neurons, the retinal ganglion cells (RGCs). Degenerative retinal diseases caused by photoreceptor death, such as age-related macular degeneration (AMD) and retinitis pigmentosa (RP), are the third leading cause of blindness in the world (Hartong et al., 2006; Pascolini and Mariotti, 2012). Nowadays it is not possible to restore full vision, yet multiple efforts have been made to treat blind patients with photoreceptors loss. Therapeutic and experimental strategies range from vitamins and pharmacotherapies to transplantation of lost retinal tissue, stem-cell based therapies, gene-replacement, and visual prostheses (Hartong et al., 2006; Mills et al., 2017). The latter consist of devices that perform electrical stimulation (ES) to different locations of the visual pathway, including mainly the visual cortex, the optic nerve, and the retina (Margalit et al., 2002; Lewis et al., 2015). In cases in which photoreceptors are lost but the remaining inner retina is still intact, retinal implants have been used with significant advancements toward the restoration of useful vision in blind patients (Zrenner, 2013; Cheng et al., 2017).

In order to restore the lost function of photoreceptors, commercially available retinal prostheses comprise primarily of a light-sensing device and a microelectrode array (MEA). To capture visual information, a camera together with a signal processor unit can be used to detect and process light stimuli. Likewise, a light-sensitive device such as an array of photodiodes might be used. Following, visual information is transduced into electrical signals and conducted into the retinal tissue by a pulse generator or induced by the same array of photodiodes through a MEA. Thereby, retinal implants activate the remaining circuitry of the visual pathway due to the ES of bipolar and/or RGCs, depending on whether the corresponding MEA is placed between the sclera and the choroid (suprachoroidal), between the choroid and the remaining retinal cells (subretinal), or between the neural layer of the retina and the vitreous body (epiretinal) (Margalit et al., 2002; Zrenner, 2013).

While current retinal prostheses allow the restoration of useful visual percepts to blind patients with RP, they do not automatically adjust to the remodeling processes of the retina that lead to an increase of the stimulation threshold and a reduction of the efficiency of the ES therapy of these devices (Cheng et al., 2017; Haselier et al., 2017). Furthermore, it is not clear how visual signals are being encoded in the visual pathway during stimulation, what becomes even more difficult when retinal areas are being stimulated with large surface area electrodes that allow the stimulation of multiple retinal cells after one stimulation pulse (Cheng et al., 2017). Accordingly, devices that not only enable ES but at the same time provide feedback of the retinal activity are beneficial.

With the aim to facilitate the improvement and adjustment of ES parameters in retinal implants and to provide means to examine in real-time the electrical activity within the retina, a bidirectional communication strategy between retinal cells and a prosthetic device using a penetrating MEA has been proposed (Heil et al., 2014; Brusius, 2015; Walter, 2016). In this way, the possibility for simultaneous recording and stimulation is opened.

In this work, a proof of concept confirming the feasibility of using penetrating MEAs as a dual purpose device that stimulates the inner retina and records local field potentials and spiking activity of retinal ganglion cells (RGCs) is unveiled (see **Figure 1**). Upon photoreceptor degeneration, the thickness of the retina is reduced to approximately 100 μm. Therefore, penetrating devices have to be specifically tailored to match these dimensions. The work presented here shows the design of the probe, its fabrication principles and the application *in vitro* in retinas of normal mice and mice showing a retinal degeneration. Furthermore, the potential field of action of penetrating MEAs in retinal applications is shown. As they allow access to the different retinal layers, a follow-up of a group of neurons corresponding to a same neuronal column is possible.

MATERIALS AND METHODS

The BiMEA Probes

Custom-made penetrating MEAs, here after called BiMEAs, were designed and fabricated at the *Institut für Werkstoffe der Elektrotechnik (IWE-1)*, RWTH Aachen University (Germany) after evaluating the design by Brusius (2015) fabricated by NeuroNexus (Michigan, United States).

Design and Fabrication

The BiMEA probes are penetrating MEAs with four silicon-based shanks, each one containing three or four iridium oxide (IrO_x) electrodes. In total, each penetrating structure contains 12 or 16 electrodes, named 12-BiMEA or 16-BiMEA, respectively. The 12-BiMEAs belong to the first generation of such probes, which have 10–20 μm thick shanks with a width of 100 μm, an inter-shank distance of 150 μm, a total shank length of 1 mm, and rectangular electrodes with a surface area of either 800 μm^2 (12-BiMEA-A) or 1600 μm^2 (12-BiMEA-B) and a vertical inter-electrode distance of 20 μm (**Figures 2A,B**). The 16-BiMEAs have narrower shanks

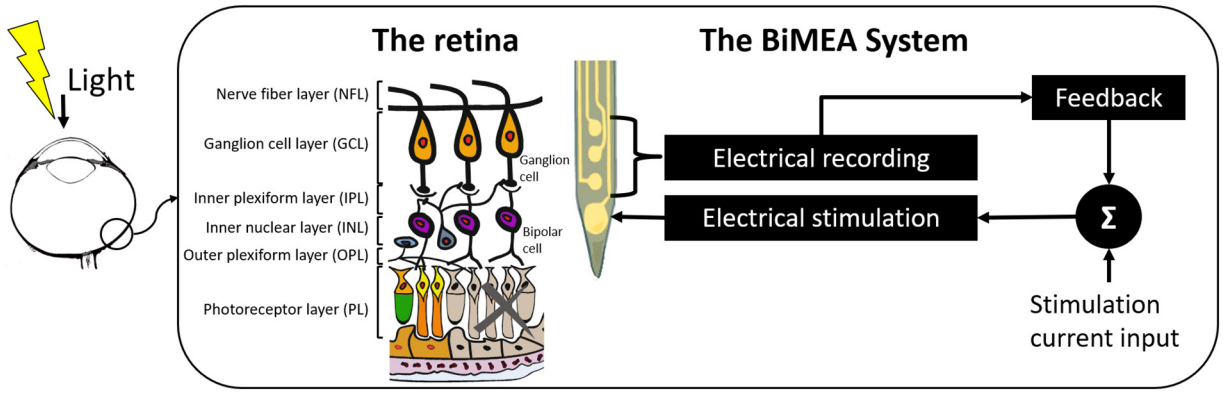

FIGURE 1 | Concept of the BiMEA system. The schematic shows a bidirectional microelectrode array (BiMEA), which consists of a multi-site penetrating MEA, allowing the system to perform electrical stimulation to the inner retina (from the inner plexiform layer to the outer margin of the inner nuclear layer) and to record the electrical activity of retinal ganglion cells (RGCs).

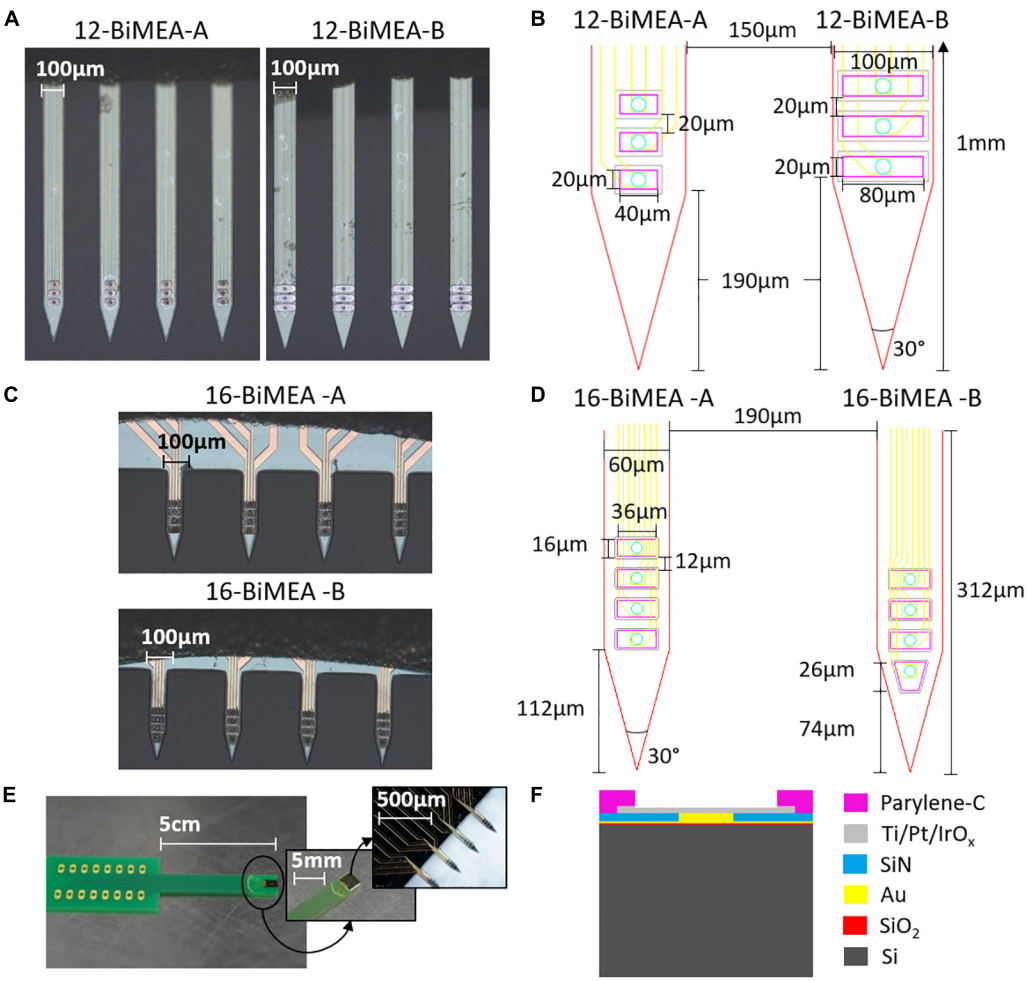

FIGURE 2 | The BiMEA probes. Optical images of the BiMEA probes **(A,C)** bonded to a carrier with a 16-DIP connector **(E)** are shown. The dimensions for both 12-BiMEA shank designs are depicted in **(B)**, which have a distance of 190 µm from the tip to the first electrode (DTE). In contrast, the 16-BiMEAs are displayed in **(D)**, showing a 16-BiMEA-A shank at the left and a 16-BiMEA-B shank at the right with DTEs of 112 µm and 74 µm, respectively. Additionally, the cross-section of a single shank is depicted in **F**.

with a width of 60 μm, a total length of 312 μm, and an inter-shank distance of 190 μm. In contrast to the first design, the 16-BiMEAs have either four rectangular electrodes with a surface area of 576 μm^2 (16-BiMEA-A) or three rectangular electrodes and a bottom trapezoid electrode with the same surface area (16-BiMEA-B) (**Figures 2C,D**). In order to facilitate the insertion of the shanks, both BiMEA designs have a tip angle of 30°. Each silicon (Si) structure is additionally bonded and glued to a carrier with a 16-DIP connector (**Figure 2E**).

Because of the small area of the stimulation sites, the electrode material must fulfill certain features. The necessary charge must be delivered to evoke action potentials therefore a high charge delivery capacity is needed. At the same time the voltage range has to be kept in a safe range to prevent irreversible electrode alterations and electrolysis in the interstitial fluid. Therefore, IrO_x was chosen as the electrode material, as it fulfills all of the aforementioned requirements (Slavcheva et al., 2004, 2006; Wessling et al., 2006; Van Ooyen et al., 2009).

Each Si shank is made of a 20 μm Si substrate, followed by a 300 nm thick layer of oxidized silicon (SiO_2), Titanium/Gold (Ti/Au) feedlines 30/300 nm thick, a first passivation layer of silicon nitride (SiN) 1 μm thick with an opening filled with Au. On top, a stack layer with 30 nm of Ti, 250 nm of platinum (Pt), and 500 nm of IrO_x form the surface area of the electrodes. Afterward, a coating of 3 μm of parylene-C forms a second passivation layer with the corresponding openings to expose the surface area of the IrOx electrodes (**Figure 2F**). For the purpose of this work, the four types of BiMEA probes were used indistinctively during the experiments, however, for direct comparisons between experiments the 16-BiMEAs were used.

To keep track of the recordings corresponding to a same vertical column, the shanks of the BiMEA probes were numbered from 1 to 4 from right to left, and the electrodes were numbered from 1 to 4 from the bottom to the top. Thus, while electrode 1.1 ($E_{1.1}$) corresponds to the bottom electrode of the right-most shank and $E_{1.4}$ to the top electrode, $E_{4.4}$ is the top electrode of the left-most shank.

Electrochemical Properties

The IrO_x electrodes were electrochemically activated using an EG&G 283 Potentiostat/Galvanostat (AMETEK Scientific Instruments) via cyclic voltammetry (CV) with 500 cycles, a scan rate of 100 mV/s, and activation potentials from -0.85 to 0.85 V versus a Silver/Silver Chloride (Ag/AgCl) reference electrode in 0.9% phosphate buffered saline solution (PBS). In addition, the charge delivery capacity (Q_{dc}) was calculated at the last cycle of the CV curve integrating the current density along the electrode potential versus the Ag/AgCl electrode as suggested by Slavcheva et al. (2004). The BiMEA probes showed a Q_{dc} between 239.3 and 552.5 mC/cm^2.

The impedance of the electrodes was evaluated by electrochemical impedance spectroscopy (EIS) using a potentiostat (VSP-300, Bio-Logic Science Instruments SAS) and a three-electrode cell setup prior to the first usage. Each IrOx electrode served as a working electrode and a Ag/AgCl electrode and a platinum (Pt) wire were used as reference and counter electrodes, respectively. The EIS measurements were carried out in 10xPBS applying a 10 mV sinus wave in a range of frequencies between 1 Hz and 100 kHz. The IrO_x electrodes showed a low impedance, which decreased with respect to the increasing electrode surface area (ESA) of the BiMEA electrodes, especially in the frequency range of interest where neuronal spikes are captured (10^2–10^3 Hz). Electrochemical properties showed by the BiMEA probes are summarized in **Table 1**, and the respective impedance and CV plots are shown in **Supplementary Figure 1**.

TABLE 1 | Summary of the electrochemical properties of the BiMEA probes.

BiMEA probes	ESA [μm^2]	|Z| @ 1kHz [kΩ]	Q_{dc} [mC/cm^2]
16-BiMEA	576	33.89 ± 16.09	552.5 ± 9.3
12-BiMEA-A	800	24.24 ± 4.03	243.9 ± 40
12-BiMEA-B	1600	12.26 ± 1.78	239.3 ± 31.5

ESA stands for electrode surface area, |Z| @ 1 kHz refers to magnitude impedance at 1 kHz, and Q_{dc} stands for charge delivery capacity.

Animals

Wildtype animals of the strain C57BL/6 were obtained from Charles River and *rd10* mice were bred locally from breeding pairs obtained from Jackson (strain name: B6CXB1-Pde6brd10/J). In this line the *rd10* mutation was backcrossed onto the C57BL/6J background for five generations before intercrossing to homozygosity. All animals were kept on a 12 h light/dark cycle with food and water *ad libitum*. All experiments were performed in accordance with the German Law for the Protection of Animals and after approval was obtained by the regulatory authorities, the Forschungszentrum Jülich and the Landesamt für Natur, Umwelt, und Verbraucherschutz of the German federal state of North-Rhine Westfalia.

Retina Preparation

Light-adapted retinas from wildtype and *rd10* mice were prepared under ambient light. The animals were deeply anesthetized with isoflurane (Actavis Dtl. GmbH &Co. KG, Germany) and killed by decapitation, followed by the enucleation of the eyeballs, which were immediately transferred into oxygenated Ames' medium (Sigma-Aldrich, Germany) at room temperature. The physiological solution was bubbled with carbogen gas (The Linde Group, Germany) containing 95% O_2 and 5% CO_2 at a pH of 7.4. In order to keep both eyes vital and ensure perfusion during preparation, the eyes were first opened along the *ora serrata*, allowing the removal of the cornea and the lens. Hereafter the procedure that is explained was effected for each eye as the retinal tissue was used for the experiments.

The lens and the vitreous body were carefully removed using fine forceps. Then, the retina was separated from the eyecup and cut into halves. One half was stored in oxygenated Ames' medium until it was used, and the other piece was mounted with the ganglion cell layer (GCL) facing downwards onto a circular piece of nitrocellulose filter paper (Merck KGaA, Germany). The filter served as a carrier for the tissue and had a precut central hole with a diameter of 1.5 mm. Afterward, the filter/retina sandwich was transferred onto a polydimethylsiloxane (PDMS) pillow with the GCL facing up, and the filter paper was fixed to

the PDMS using insect pins. Finally, the tissue was covered with fresh oxygenated medium.

Experimental Setup

The experimental setup was based on Brusius (2015) and consisted of two main components: a data acquisition system (DAQ) and a measurement chamber.

Data Acquisition System

Electrical recordings were performed using the BioMAS (Maybeck et al., 2016), an in-house amplification system with an ES unit that allowed voltage-controlled stimulation of the retina. The system was connected to a 16-channel-headstage that served not only as a pre-amplification stage, but allowed the measurement of the injected current during ES, as it features an internal current measurement circuit that is connected to the respective stimulating electrodes. Moreover, the DAQ provided a digital output for the activation of an LED circuit during light stimulation, and auxiliary channels were used for recording the LED signal, the ES signal, and the current injected to the tissue during ES. Additionally, a high pass filter at 0.1/1 Hz, a sampling rate (F_s) of either 10 or 20 kHz, and a Ag/AgCl reference electrode were used for the electrical recordings.

Measurement Chamber

A Faraday cage was used to shield the measurement setup, including a support for holding the perfusion chamber, the headstage of the BioMAS system, whose front-end facilitated the handling of the BiMEAs, a LED circuit, and a micromanipulator system (Luigs & Neumann, Germany), which enabled the movement of the probes along three different axes (x, y, and z). Furthermore, the perfusion chamber comprised a reservoir with a PDMS pillow to support the retinal tissue and allowed the inflow and outflow of oxygenated Ames' medium at room temperature through a perfusion system with a flow rate between 3 and 4 ml/min, keeping the retina vital during the experiments (see **Figure 3**).

In vitro Electrophysiology

Positioning the BiMEA Inside the Retina

Once the perfusion system was set to run, the BiMEA shanks were driven down slowly with the micromanipulator system onto the epiretinal surface of the tissue until the first peaks or spikes were captured, setting this first position as Z_0. Then, the insertion was carried out stepwise inside the tissue, at intervals of approximately 20–25 μm. In this way, further depths (Z_x) inside the tissue were referenced to the electrode that recorded the first electrical activity.

Treatment With High Potassium Concentration

The extracellular concentration of potassium (K^+) was increased during the perfusion of the tissue to initiate depolarization and increase spiking activity of RGCs. To this effect, potassium bicarbonate ($KHCO_3$) was added to the regular Ames's medium solution to achieve a 20 mM K^+ concentration. The tissue was superfused for 2 min with the high K^+ solution followed by washout with the regular physiological solution.

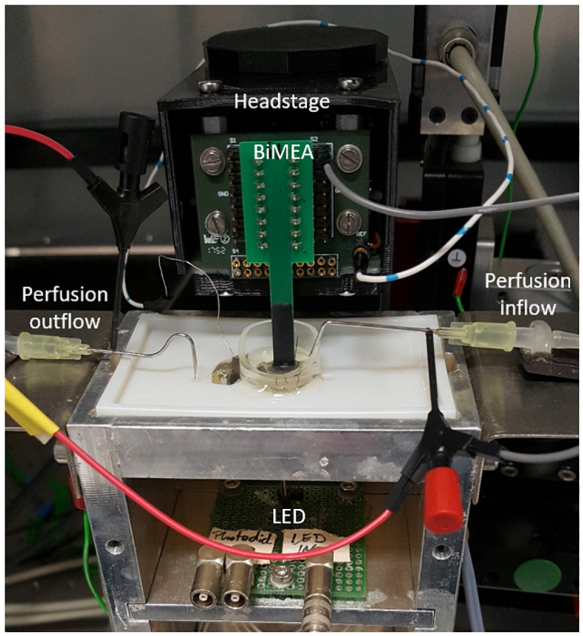

FIGURE 3 | Experimental setup. Inside a Faraday cage, the BioMAS system with a 16-channel-headstage was used for recording the retinal activity and stimulating electrically the retina. The front-end of the headstage and a micromanipulator system were used to place the BiMEA probes inside the tissue. In turn, the retinal tissue was placed inside a perfusion chamber, which had a constant inflow and outflow of oxygenated Ames' medium. Additionally, a light-emitting diode (LED) circuit was employed to perform light stimulation.

Light Stimulation

A 500 ms squared pulse with an intensity of 5 V was generated with the BioMAS system to activate the LED circuit, which consisted of a 5 mm round white LED connected in series to a 61.9 Ω resistor. This configuration allowed an LED current of 34.2 mA that produced a power of 7.96 $\mu W/mm^2$ measured at the position of the retina in the recording chamber. This corresponds to a high photopic light stimulus comparable to broad daylight that effectively activates cone photoreceptors. Single and multiple pulses every 15 s were used to perform optical stimulation of the retina.

Electrical Stimulation

In order to avoid the generation of high voltages that might induce irreversible and undesired reactions like water electrolysis and electrode and tissue damage (Gekeler et al., 2004; Cogan, 2008; Brusius, 2015), a voltage-controlled stimulation was chosen. Moreover, biphasic pulses have been shown to be a good strategy to activate the majority of RGCs, especially in degenerated retinas (Jensen and Rizzo, 2009; Goo et al., 2011b; Celik and Karagoz, 2018). Hence, biphasic squared voltage pulses with an initial cathodic phase followed by an anodic phase were used to carry out ES. Considering the stimulation parameters suggested by different research groups (Walter et al., 2005; Stett et al., 2007; Roessler et al., 2009; Goo et al., 2011b) to perform optimal stimulation of the retina in terms of low charge densities

and evoked potentials, pulses with amplitudes of ±600 and ±800 mV and phase durations between 0.5 and 0.8 ms were tested (ES-1: 0.8 mV – 0.5 ms; ES-2: 0.8 mV – 0.6 ms; ES-3: 0.6 mV – 0.5 ms; ES-4: 0.6 mV – 0.6 ms; ES-5: 0.6 mV – 0.7 ms; ES-6: 0.6 mV – 0.8 ms). When performing ES, only one bottom electrode at a time was selected as the stimulating electrode, which was previously positioned in the inner retina. The latter means that the stimulating electrode was barely recording retinal spikes due to its location within the tissue. To test for reproducibility, the tissue was stimulated with six electrical pulses every 20 s.

In order to assess the efficiency of the ES, an electrical stimulation efficiency ratio (ESE) was calculated by dividing the firing rate in a window of 400 ms after the ES artifact by the firing rate averaged in 8 s before the stimulation pulse as proposed by Haselier et al. (2017). ESE values higher than one indicate an increase of the firing rate after ES, while ESE values lower than one show a decrease of the electrical activity. To avoid artifacts in the filtering phase, ES artifacts with a mean duration of 24.96 ± 1.37 ms were manually segmented from the raw data before applying the band-pass filter and running the spike detection algorithm. Moreover, an ES trial was determined as a significant stimulation, when the firing rate before and after the stimulation along the six stimulation pulses were statistically different. To this effect, data normality was checked with the Kolmogorov–Smirnov test and statistical differences were established applying paired sample *t*-tests with a significance level of 5% using Origin (Microcal Software, United States).

Additionally, the current measurement circuit inside the headstage allowed the measurement of the delivered current during ES (I_{del}), which enabled also the calculation of the injected charge (Q_{inj}) after the time integration of I_{del}, and the calculation of the charge density (Q_d) considering the ESA of the stimulating electrode, which was 576 μm^2, as only 16-BiMEA probes were used during ES experiments. I_{del}, Q_{inj}, and Q_d were then calculated for both cathodic and anodic phases.

Signal Analysis

Raw data were subjected to offline post-processing methods using self-written MATLAB (Mathworks Inc., United States) programs.

Filtering

As suggested by Quian Quiroga (2009), zero-phase filtering stages were used to obtain high and low frequency content. Raw data were filtered using 6th order Butterworth band-pass (high and low pass cutting frequencies of 100 Hz and 3 kHz) and a low-pass (cutting frequency of 100 Hz) filters to extract action potentials and LFP, respectively. Additionally, a Notch filter with a cutting frequency of 50 Hz was applied to the low-pass filtered signals, in order to eliminate the power line noise. Moreover, Fourier analysis was carried out to extract the frequency components of LFPs.

Spikes Analysis

To determine whether or not a peak was an action potential (spike), an algorithm based on the search of spikes whose inter-spike intervals were equal or greater than 3 ms (Rey et al., 2015), whose amplitude would surpass a threshold based on the absolute median deviation of the band-pass filtered signal (Quiroga, 2004), and whose prominence (MATLAB, Mathworks Inc., United States) was at least six times the absolute median deviation was implemented. The firing rate of the detected spikes was computed using histogram bins every 1 s, 500 ms, or 100 ms along the desired recording, thereby obtaining the count of spikes per bin depending on the spike count resolution needed. Such count was then normalized to obtain a firing rate in spikes per seconds, meaning Hz.

RESULTS

Recording With the BiMEA Probes

The feasibility of using the penetrating BiMEAs for recording retinal activity is shown for wildtype and degenerated *rd10* retina.

Recording at Different Depths Inside Wildtype Retina

As a first step in every experiment, the BiMEA electrodes were positioned at different locations inside the tissue, enabling the recording of electrical activity at different depths (Z_x) of the retina. The insertion of the shanks was carried out stepwise: first the shanks were moved close to a position nearby the surface of the retina, then the insertion was continued until the top electrodes of the recording shank had captured spikes. The penetration was performed without the assistance of an optical system, but was assessed by observing the tip of the shanks through the glass ring with naked eyes and the electrical activity recorded by the electrodes. The insertion of the shanks was further confirmed in a dummy experiment (**Figure 4**). Here, the medium was extracted from the perfusion chamber to avoid the refraction of light due to the watery medium, leaving a semi-hydrated retina that was illuminated from beneath, so that a strong contrast between the carrier paper holding the tissue and the shanks was established for imaging.

In all experiments, the retina was penetrated from the nerve fiber layer/ganglion cell layer (NFL/GCL). In this part of the retina, action potentials are generated in somas and axons of RGC, while neurons located in deeper retinal layers do not fire action potentials. While penetrating the tissue, fast voltage deflections in the form of spikes were first recorded at the lowest of the electrodes. Spikes were observed at progressively higher electrodes when shanks were moved deeper into the retina (**Figure 5**). In this manner, the spontaneous activity (SA) of a wildtype retina was followed along a 100 µm trajectory inside the tissue. The electrical activity was first noticed by $E_{1.1}$, which captured low amplitude peaks (≤18 µV), indicating that the bottom electrode of the shank was nearby the retinal surface. In this way, further depths at Z_1 (21.6 µm), Z_2 (39.7 µm), Z_3 (61 µm), Z_4 (80.8 µm), and Z_5 (100.7 µm) corresponded to the position of the bottom electrode ($E_{1.1}$) inside the retina with respect to Z_0 (0 µm).

At Z_1 spikes were detected in all four electrodes, however, the spike amplitude was higher at the bottom electrodes $E_{1.1}$ and $E_{1.2}$, with peak heights of 28.52 ± 5.08 µV and 31.83 ± 3.19 µV accordingly (see **Figure 5** and **Supplementary Table 1**), thereby

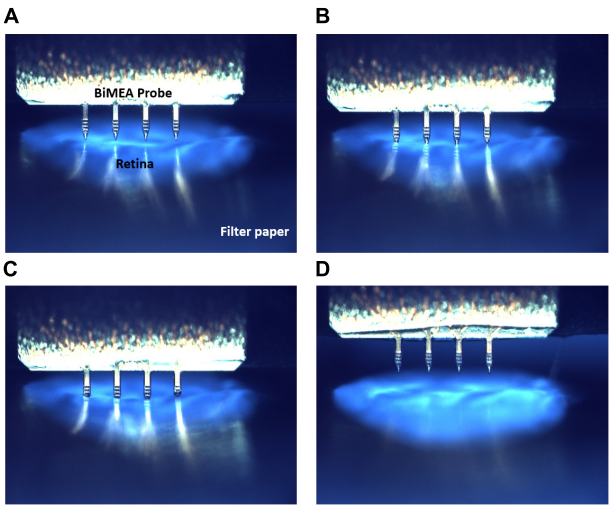

FIGURE 4 | BiMEA insertion into the retina. Optical images showing four different insertion steps. First the BiMEA shanks are at the surface of the tissue before insertion **(A)**, then the tips of the shanks are driven into the tissue **(B)**, followed by the step-wise insertion of the shanks in **C**, and the final retraction of the probes at the end of an experiment in **D**. The tissue was illuminated from beneath, so that a contrast was generated between the filter paper carrying the tissue (dark blue), the retina (light blue), and the BiMEA shanks. A wildtype retina was used during this experiment.

indicating that they were within the NFL and GCL. In such a way, the spike amplitude of the peaks detected by the electrodes increased while they entered the superficial layers of the tissue (NFL and GCL) and decreased as they penetrated deeper inside the retina. In this way, knowing that the distance from the top to the bottom electrode was 100 μm, considering that at Z_3 $E_{1.3}$ and $E_{1.4}$ recorded the spikes with the highest amplitudes (see **Supplementary Table 1**), and taking into account that the summed thickness of the NFL, the GCL, and the inner plexiform layer (IPL) is around 70 μm (Dysli et al., 2015), it was then expected that the two top electrodes ($E_{1.3}$ and $E_{1.4}$) were in between the GCL and the NFL, that $E_{1.2}$ was reaching the IPL, and that the bottom electrode ($E_{1.1}$) was at the end of the IPL and reaching the inner nuclear layer (INL) of the retina (see bottom sketch in **Figure 5**). Consequently, no action potentials were captured with $E_{1.1}$ and $E_{1.2}$ at Z_4, which were expected to be between the outer plexiform layer (OPL) and the INL. In contrast, the upper electrodes $E_{1.3}$ and $E_{1.4}$, which had moved further into the IPL and GCL were still recording spikes. Finally, at Z_5, only low amplitude peaks ($\leq$16 μV) were detected by the upper electrodes, meaning they were already beyond the RGCs.

It is important to notice that in cases when the explanted tissue was not completely flat on the PDMS pillow, the shanks did not contact the tissue at the same depth. The latter can be seen in **Figure 4** and is also observed during the electrical recordings. For example in **Figure 6**, the electrical activity captured by two shanks at Z_2 (42.8 μm) is shown. While the spiking activity of the vertical column in shank one is barely captured by the bottom electrode ($E_{1.1}$) but detected by the upper electrodes ($E_{1.2}$, $E_{1.3}$, and $E_{1.4}$), the bottom electrodes in shank two ($E_{2.1}$ and $E_{2.2}$) are the ones recording the action potentials of RGCs. The latter reveals that even though both shanks were inside the tissue, they were actually at different depths. Thus, when the Z positions were set, these corresponded to the shank whose electrodes captured the first spikes of the recording. Hence, the Z positions for the recordings displayed in **Figure 6**, were taken according to the first shank.

Furthermore, having shanks with multiple recording sites allowed us to follow the activity of a group of cells within a same vertical column inside the tissue. As exhibited in **Figure 6**, the same spikes with different amplitudes were captured by the electrodes of a same shank (depending on how deep inside the tissue they were), what indicates that whenever the bottom electrodes were not detecting any more spikes, it was because they had already passed the GCL, however, the activity of the cells present in that vertical column where the shank was located, was still recorded by the upper electrodes.

Recording Responses to Treatment With High Extracellular Potassium Concentration

In order to confirm that the signals recorded previously indeed reflect physiological activity of RGCs in the form of action potentials, a wildtype retina was subjected to an increased extracellular K^+ concentration, allowing us to observe a physiological retinal response to changes in the extracellular ionic concentration. A recording of one electrode site displaying the spiking activity and the firing rate along a complete experiment is shown in **Figure 7**, where four phases exhibiting the response to the treatment with high K^+ were distinguished. First, regular SA with a firing rate of ∼17 Hz was detected (**Figure 7A**), then after the application of 20 mM K^+ a lag phase was observed, followed by a transient increase in the firing rate with a spike count up to ∼40 Hz (**Figure 7B**) and a spikeless silent phase (**Figure 7C**), which was ended upon washout, thereby permitting the recovery of the spiking activity with a firing rate of ∼23 Hz (**Figure 7D**).

This behavior is in full agreement with our current understanding of how action potentials are generated. The increase in the external K^+ concentration shifted the Nernst potential for K^+ and, therefore, the membrane potential of RGCs to more positive values. This depolarization increased the firing rate of the recorded cells (**Figure 7B**). Continuous depolarization of the cells finally induced a depolarization blockade concomitant with a silence phase (**Figure 7C**), during which no action potentials could be fired because voltage-activated Na^+ channels did not recover from inactivation. Afterward, when the extracellular K^+ concentration was reduced with the perfusion of regular medium, the SA recovered.

Recording Responses to Light Stimulation

In order to confirm that the retinal integrity was preserved upon penetration by BiMEA electrodes, responses of a wildtype retina to optical stimulation were recorded with the penetrating BiMEAs. Light stimuli were 500 ms long and were repeated every 15 s (see **Figure 8**). Light-induced artifacts were observed in the recordings phase-locked with the ON-OFF switching of the light stimuli (pointed with red arrows in **Figure 8A**, but present in all shown examples). In principle, responses to light steps can be ON (increased spike frequency at light onset), OFF (ditto at light

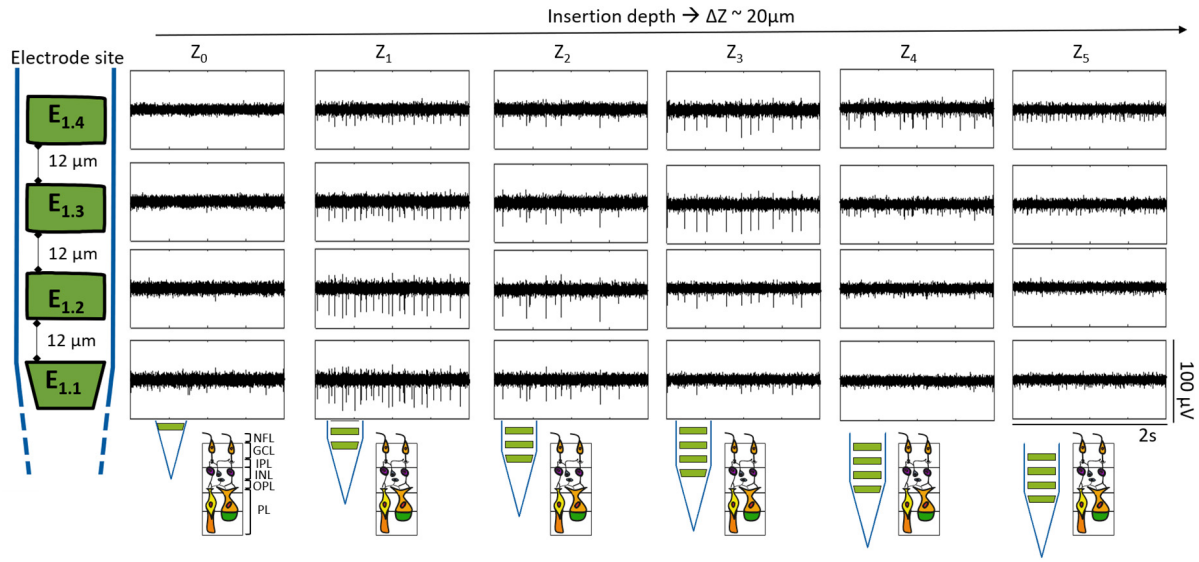

FIGURE 5 | Recording at different depths inside wildtype retina. The boxes display segments of 2 s of the band pass filtered recordings for one shank. Each row corresponds to each one of the four electrodes of the same shank as indicated by the sketch at the left, and each column represents a different insertion depth (Z_{0-5}) inside the retina, corresponding Z_1 to 21.6 µm, Z_2 to 39.7 µm, Z_3 to 61 µm, Z_4 to 80.8 µm, and Z_5 to 100.7 µm in reference to Z_0. The depth difference among each Z (ΔZ) was approximately 20 µm. Likewise, the expected shank position along the different depths within the retina is portrayed at the bottom.

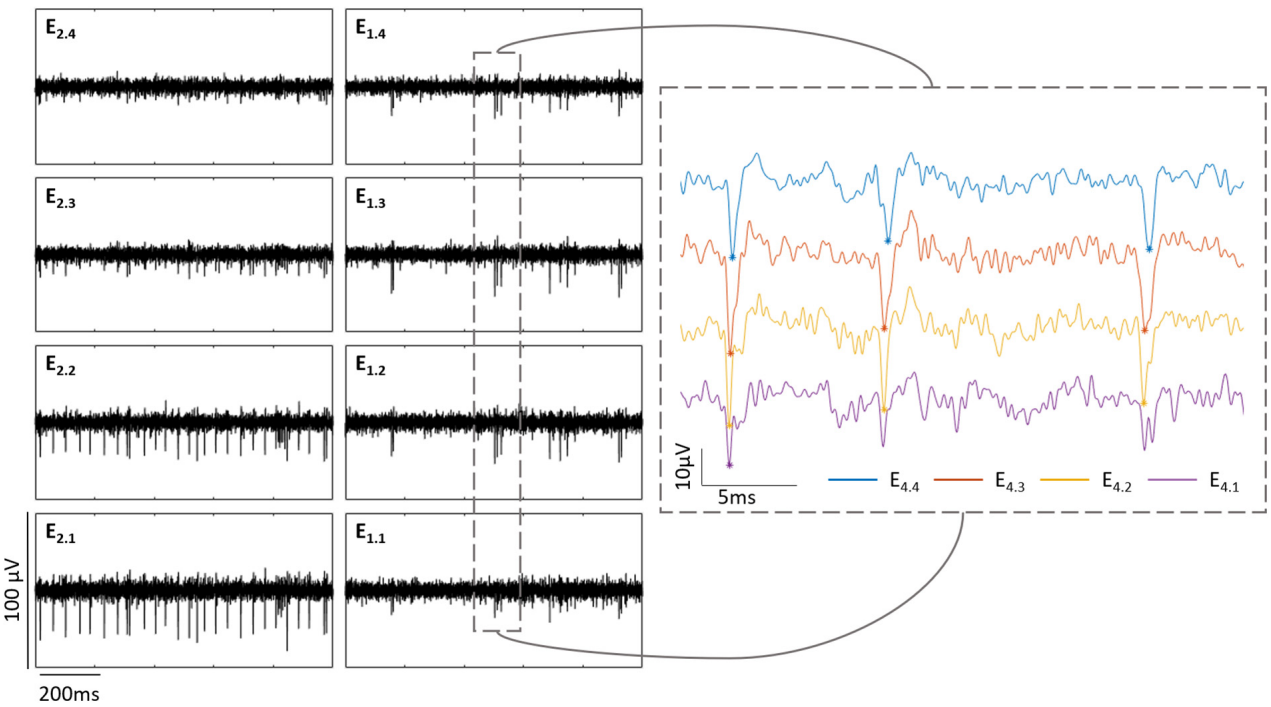

FIGURE 6 | Shanks at different depths inside the retina. The boxes at the left show the electrical activity of a wildtype retina captured by two shanks at Z_2 (42.8 µm) inside the retina. Each column represents each shank and each row an electrode along the shank. The graph at the right zooms the activity captured in shank one, depicting in purple $E_{1.1}$, in yellow $E_{1.2}$, in red $E_{1.3}$, and in blue $E_{1.4}$. The peaks detected as spikes in this extract are marked with an asterisk of the corresponding color.

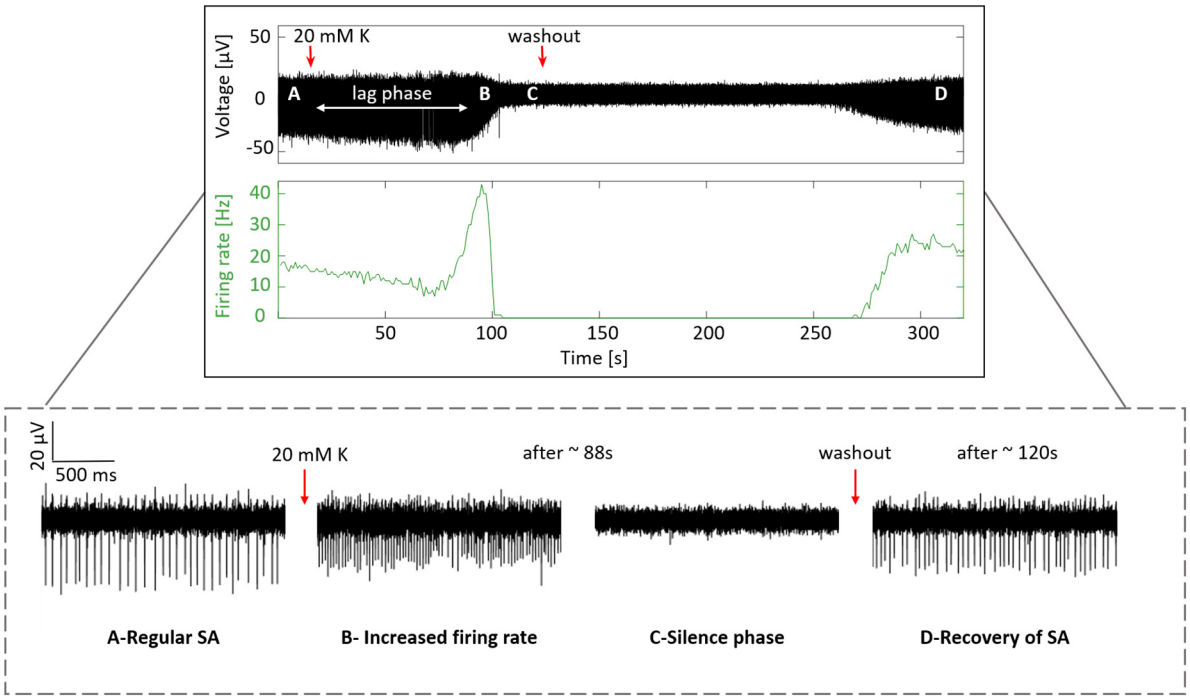

FIGURE 7 | Response to treatment with high potassium. The top box displays the recording of the complete experiment, indicating with red arrows the application time of 20 mM K^+ and the time when the washout with regular medium was started. The second top box shows the firing rate along the experiment with bin counts every second. The four plots inside the dashed box at the bottom show a zoom of the four phases distinguished during the experiment. **(A)** Regular SA captured at the beginning, **(B)** increased firing rate after the application of 20 mM K^+, **(C)** silence phase, and **(D)** recovery of SA upon washout.

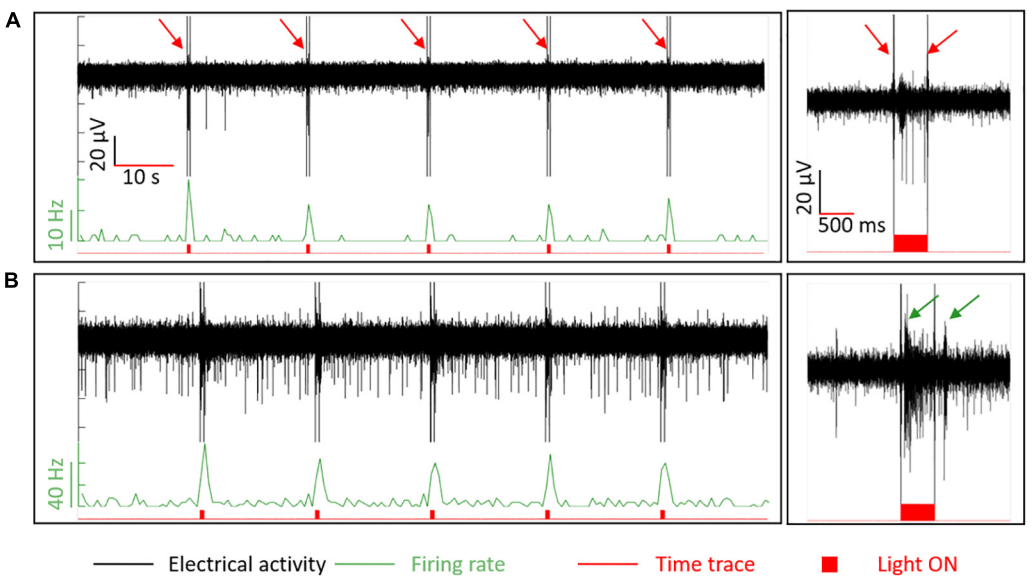

FIGURE 8 | Responses to optical stimulation in wildtype retina. Light stimuli with an ON period of 500 ms every 15 s were used to stimulate the retina optically. In the first column, recordings of ON and OFF responses are shown. Plots at the second column correspond to a 3 s extract of the complete recording shown at the left. In **(A)**, the response of a transient and a sustained ON cell. In **(B)**, the bursting activity of two different cells (ON and OFF cells) are pointed out by the dark green arrows. Traces in black represent the electrical recordings (µV), in light green the firing rate with normalized bin counts every 500 ms [spikes/second (Hz)], and in red the corresponding time trace. The red filled-bumps match the time when the light stimuli were ON. The red arrows in **(A)** point out high amplitude peaks at the onset and offset of the light pulses, which are electrical artifacts induced by light seen in all the recordings when using light.

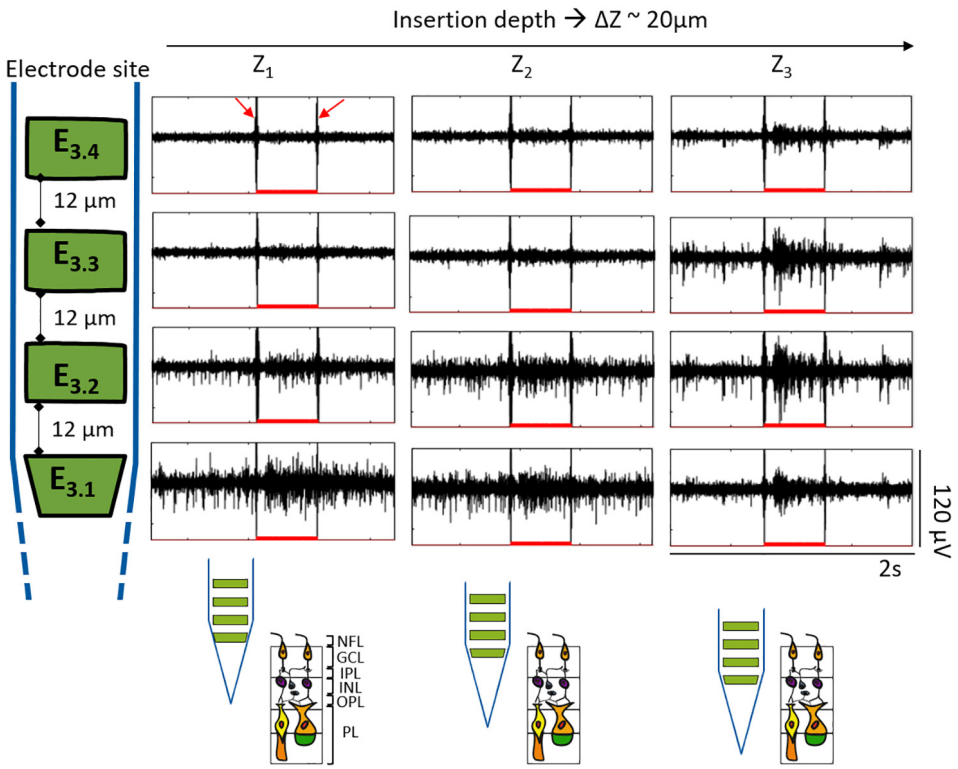

FIGURE 9 | Responses to optical stimulation at different retinal depths. Segments of 2 s showing the electrical recordings during light stimulation. Each row corresponds to each one of the four different electrodes of the same shank as indicated by the shank sketch at the left. Insertion depths from Z_1 to Z_3 correspond to each column. The depth difference among each Z (ΔZ) was approximately 20 µm. The red filled-bumps depict the time where the light stimuli were ON (500 ms). Likewise, the expected shank position along the different depths within the retina is portrayed at the bottom.

offset) or ON-OFF and can be transient or sustained. As retinas were prepared under ambient light and therefore not optimized for recording light responses, we did not attempt to document all response types, but rather show in a few examples that light responses could be recorded with the type of electrodes used here.

The recording in **Figure 8A** shows a low SA (<1 Hz), which was increased up to 20 Hz by a short burst of low amplitude peaks (∼15 µV) and a sequence of higher amplitude spikes (∼38 µV) that lasted until the end of the light stimulus, indicating the presence of a transient and a sustained ON cell recorded by this electrode. In the case of **Figure 8B**, a burst of spikes during the light stimulus (ON cell, first arrow) and a short burst after the offset (OFF cell, second arrow) could be observed. These recordings demonstrate that the retina could still respond to light after the penetration, indicating that tissue damage was minimal.

Responses to light were also used in the experiments to assess the vitality of wildtype retinas while penetrating the tissue, ratifying that the same group of cells at different retinal depths were being recorded. **Figure 9** exhibits an example of the follow-up performed to the ON cells captured in **Figure 8B**, showing the same optical response for Z_1 (20.9 µm), Z_2 (42.5 µm), and Z_3 (63 µm). At Z_1, the reaction to light was evident at the two bottom electrodes, indicating their proximity to the NFL and GCL. At Z_1, the upper recording sites did not capture any action potential but displayed the electrical artifact induced by the stimuli (see red arrows). At Z_2 the spiking activity became more visible for $E_{3.2}$. Finally, at Z_3 the action potentials were diminished in amplitude at $E_{3.1}$, became notorious with higher amplitude peaks at $E_{3.2}$ and $E_{3.3}$, and started to be captured by $E_{3.4}$. Considering the responses to light captured at the upper electrodes, the reduced spikes captured by $E_{3.1}$, and that the latter was at a depth of ∼63 µm inside the retinal tissue, it was an indication that the bottom electrode was entering the next retinal layer, the IPL, and that the retina was still vital. In this way, the BiMEA probes were placed in such a way that the bottom electrode would be located deep inside the retina, where spikes were barely captured or not captured at all, while the upper electrodes were still capable of recording the ongoing activity, so that further experiments, such as ES inside the retina, could be performed.

Recording From Degenerated Retina

Given that it was possible to record the electrical activity of a vital wildtype retina with the penetrating BiMEAs, these were also used to capture the activity of retinas with photoreceptor degeneration. To this end we employed retinas of *rd10* mice, a mouse line that is considered a suitable model for the human disease RP. When positioning the shanks inside the degenerated tissue, a rhythmic activity was recorded (**Figure 10**). This pathological activity is not observed in wildtype retinas. In *rd10*

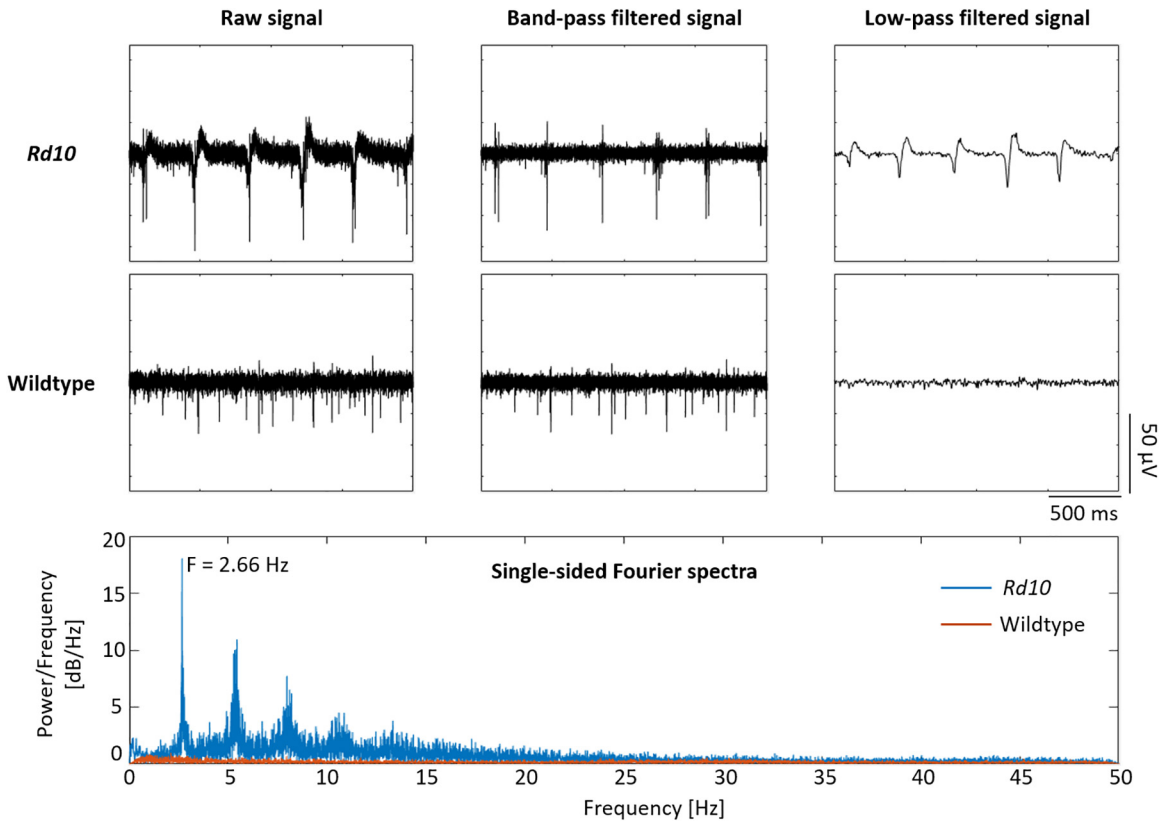

FIGURE 10 | Comparison of wildtype and *rd10* recordings. *Rd10* and wildtype recordings are shown in the first two rows. The raw signal of *rd10* exhibits bursting activity that coincides with the presence of low frequency oscillations, which can be seen in the raw and low-pass filtered signals. Wildtype activity shows only the presence of stochastic spikes. At the bottom box, the single-sided Fourier spectra expose a main frequency component of ∼2.66 Hz for *rd10* LFPs, while none were encountered for the wildtype.

mouse retina, the oscillations are commonly observed (Goo et al., 2011a; Stasheff et al., 2011; Jae et al., 2013; Biswas et al., 2014; Haselier et al., 2017) but may come and go throughout the recording (Biswas et al., 2014). Oscillations can be observed in the raw recording as well as in the low-pass filtered signal, the LFP. Fourier analysis showed a main oscillating frequency of the LFPs around 2.6 Hz, while none were present in the wildtype. Moreover, an inherent bursting activity often phase-locked to the negative deflection of the LFP was observed in comparison to the stochastic spiking activity of a healthy retina (**Figure 10**).

Spike bursts and LFPs with frequencies ranging from 2.6 to 4.3 Hz were also observed at different x-y locations within the same retina (**Figures 11A–C**). These oscillatory frequencies agree well with the typical range of 3–6 Hz reported by Biswas et al. (2014). Moreover, in some *rd10* samples (**Figure 11D**), spike bursts and oscillations were not evident in the LFP, however, the Fourier spectrum revealed an increased power for frequencies ranging between 2.5 and 7 Hz and peak frequencies around 4.3 Hz, showing that an oscillatory component was present in the recorded activity even when not obvious during the live recordings.

We observed some differences between recordings from wildtype and *rd10* retinas. During penetration of the wildtype retina with the shanks, the recording with the highest spike amplitude moved along the shank from the bottom to the top electrode (see e.g., **Figure 5**). A similar effect was observed in *rd10* retina, however, the effect was less pronounced and decent spike recordings could be observed over more penetration steps than in wildtype retina (see **Figures 12A,B** and **Supplementary Tables 2, 3**). Assuming that the highest spike amplitude was recorded by the electrode which was closest to the RGCs, the recordings at Z_8 and Z_3 indicated that the top electrodes $E_{4.4}$ and $E_{3.4}$ were in between the GCL (see **Figures 12A,B** accordingly). At this last depth, the top electrodes captured higher amplitude spikes of 54 ± 11.14 µV and 69.07 ± 23.44 µV, while the bottom electrodes $E_{4.1}$ and $E_{3.1}$ had gone through deeper layers. Considering that the thickness of the retina in adult *rd10* mice is ∼100 µm (Pennesi et al., 2012) and that each bottom electrode had gone through ∼100 µm ($E_{4.1}$ from Z_3) and 81.4 µm ($E_{3.1}$ from Z_2) inside the retina, it was expected that $E_{4.1}$ was reaching the end of the tissue at the outer margin of the INL. While no spikes are generated at this depth, the bottom electrodes captured the same spikes as the upper electrodes, albeit at lower amplitudes of 30 ± 6.81 µV ($E_{4.1}$) and 44.43 ± 9.18 µV ($E_{3.1}$). Finally, the average maximum spike amplitude in wildtype

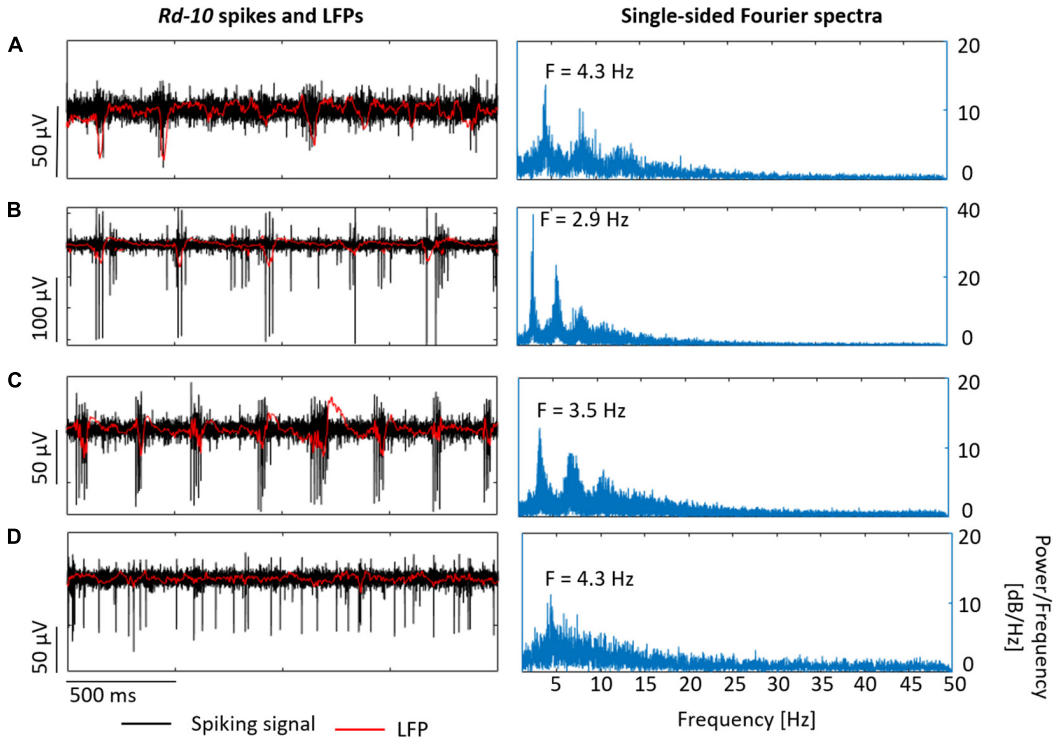

FIGURE 11 | Recording different LFPs in *rd10* retinas. *Rd10* spikes and LFPs in **(A–C)** exhibit the electrical activity of the same retina at different x-y locations, displaying in black the band-pass filtered signal (spiking signal) and in red the low-pass filtered signal (LFP). At the right column, single-sided Fourier spectrum is shown for each case. In the case of **(D)**, which shows the activity of a different sample, the typical *rd10* electrical behavior was not evident, but oscillatory components in the LFPs were exposed by the corresponding Fourier spectrum.

retina was ∼39 µV, while in *rd10* it was ∼100 µV (see **Supplementary Table 4**).

It was possible to do a follow up of the pathologic rhythmic activity of the degenerated *rd10* tissue along different depths. While the typical spike bursts and oscillations were not obvious in the recordings exhibited in **Figure 12A**, Fourier analysis showed an increasing power of oscillatory components ranging between 2.5 and 7 Hz as deeper distances within the retina were achieved, with a peak frequency of 4.3 Hz at Z_8 (see **Supplementary Figures 2A,B**). A clearer behavior was captured when Z steps of ∼40 µm were performed (see **Figures 12B–D**). Here, spike bursts coupled with low frequency waves were noticed from Z_0 until Z_3, with an oscillatory component that increased in power and whose peak frequency was shifted from 3.586 to 4.88 Hz as the electrodes advanced deeper inside the retina (see **Figure 12D**).

Electrical Stimulation and Recording

After validating the feasibility of using the BiMEA probes for recording retinal activity and accessing the different retinal layers for both wildtype and *rd10* retinas, we set out to electrically stimulate neurons of the inner retina with the lowermost electrode while at the same time record activity of RGCs with the upper electrodes. Following the insertion methodology, the shanks of the BiMEA probes were first placed inside the tissue until the recordings of at least one shank would indicate adequate penetration with higher amplitude spikes at the top electrodes and lower amplitude spikes or no spikes at the bottom electrode in deeper layers. Likewise, the vitality of the tissue was assessed by the recording of SA and, in the case of wildtype retinas, responses to light stimulation. Afterward, ES in a voltage-controlled mode was carried out, using the bottom electrode ($E_{X.1}$) of the selected shank as the stimulating electrode, and the rest as recording electrodes. In this way, the shank carrying the stimulating electrode would be referred as the stimulated shank, and the others as non-stimulated shanks. Different sets of stimulation parameters termed ES-1 to ES-6 were chosen and the stimulation efficiency ESE was determined.

ES was first tested in wildtype retinas, which exhibited a burst of spikes when a reaction to an electrical stimulus was present. **Figure 13A** shows an example of a wildtype retina (for vitality of sample and positioning of electrodes see **Supplementary Figure 3A**) stimulated with six ES pulses using ES-3 parameters (0.6 mV – 0.5 ms) every 20 s. The bursting reaction was evoked pulse by pulse, showing a successful stimulation with an activation effect on RGCs, as significant firing rate differences ($p < 0.05$) with ESEs higher than one were revealed for the three recording electrodes ($E_{3.4}$, $E_{3.3}$, and $E_{3.2}$) of the stimulated shank (see recordings inside the green frames in **Figures 13A,B**). Successful stimulation was observed for six different stimulation parameters with ES-3 yielding the highest ESE between 8.04 ± 4.29 and 10.27 ± 6.97 (see **Figure 13B**).

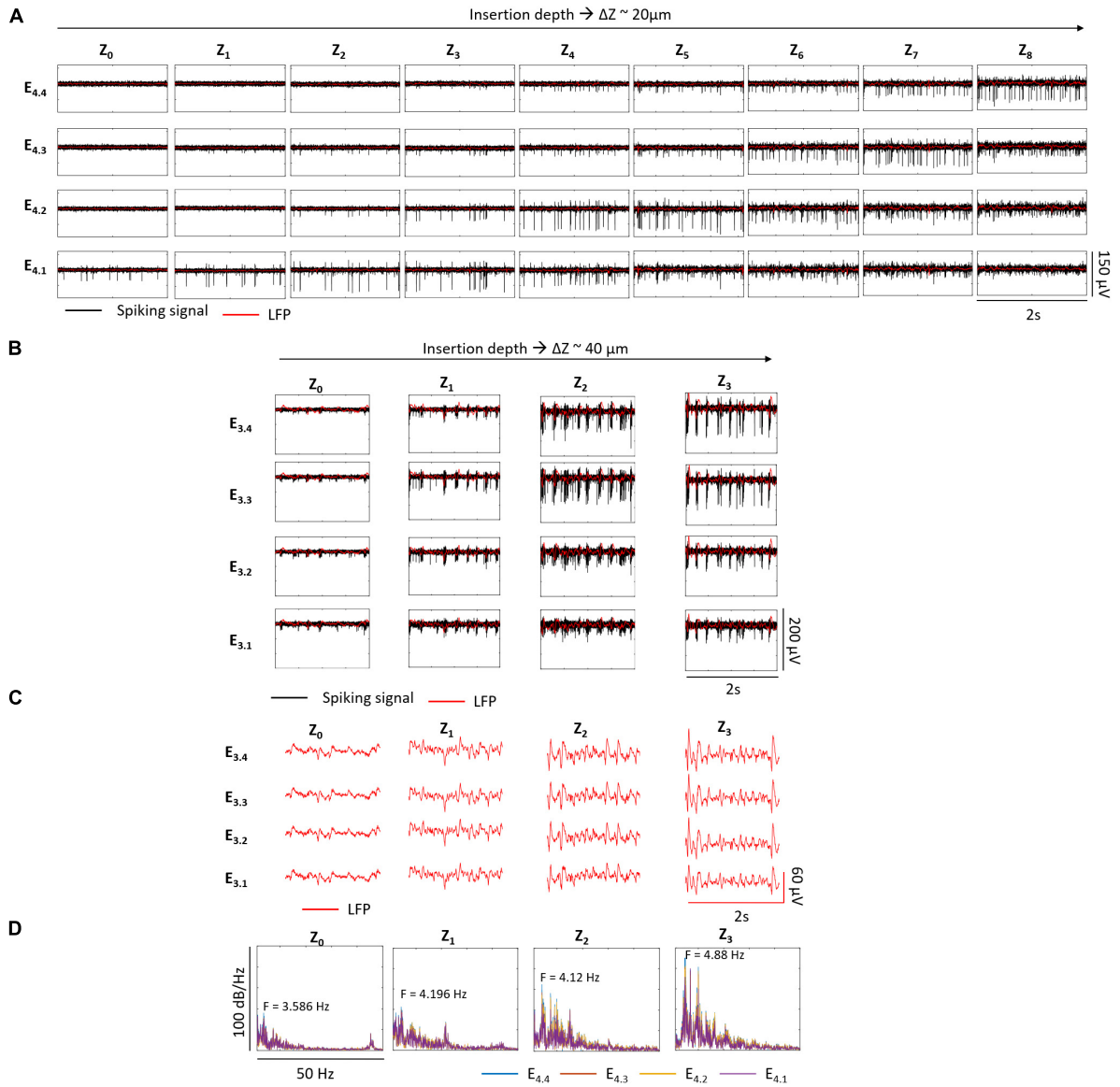

FIGURE 12 | Recording at different depths inside *rd10* retina. In A, the electrical activity of one shank along Z_0–Z_8 with Z steps of ~20 µm, corresponding Z_1 to 21 µm, Z_2 to 42.6 µm, Z_3 to 63.8 µm, Z_4 to 82.3 µm, Z_5 to 101.7 µm, Z_6 to 121.7 µm, Z_7 to 141 µm, and Z_8 to 162.1 µm with respect to Z_0 is shown. Each row corresponds to each one of the four electrodes of the same shank as indicated and each column represents a different insertion depth (Z_x) indicated. B shows the electrical activity of a second *rd10* retina with Z steps of ~40 µm. Z_1 corresponds to 41.5 µm, Z_2 to 80 µm, and Z_3 to 122.9 µm with respect to Z_0. The black traces show the spiking signal and in red the LFPs. In C the LFPs, and in D the corresponding single-sided Fourier Spectra at each depth for all the electrodes of the shank displayed in **B,C**. The peak frequency of the low frequency oscillations range between 3.586 and 4.88 Hz along $Z_{0\text{-}3}$.

Likewise, mean ESEs between 1.26 ± 1.40 and 2.5 ± 2.35 were detected in shank 2, however, the electrical responses captured by the electrodes of this non-stimulated shank were not constant along the six stimuli. In this way, a non-significant stimulation was produced for cells recorded at shank 2, while responses to the stimuli were barely captured from cells recorded by shank 1. Moreover, a significant reduction of the firing rate with ESEs lower than one was also observed during ES-1 (in $E_{2.4}$) and ES-4 (in $E_{2.4}$ and $E_{2.3}$) in recording electrodes of non-stimulated shanks, exposing therewith an inhibition effect after ES (see **Supplementary Table 5**).

Figure 14A exhibits the electrical responses of an *rd10* retina (see SA of sample before ES and positioning of electrodes in **Supplementary Figure 3B**) stimulated with six consecutive pulses every 20 s using ES-2 (0.8 mV and 0.6 ms). Here, the presence of at least two different cells in the recordings of shank 1 was noted, as two different spike amplitudes stood out, exposing thereby responses that comprised a mixture of discontinuous spikes with an increased firing rate and bursts of action potentials.

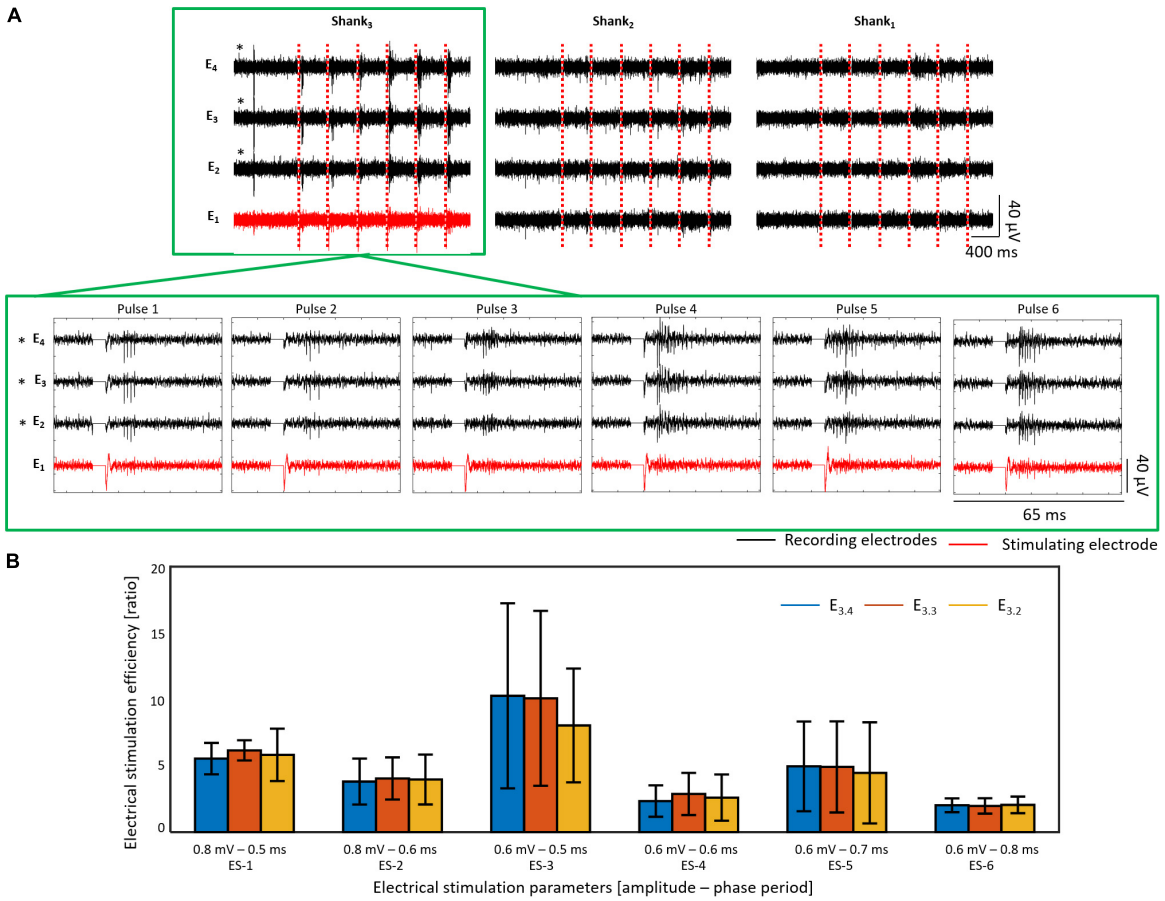

FIGURE 13 | Electrical stimulation and recording in wildtype retina. The electrical activity after six consecutive biphasic pulses (first cathodic) with 0.6 mV in amplitude and a phase period of 0.5 ms (ES-3) every 20 s at E_1 of shank 3 is shown for a wildtype retina in **(A)**. Recording extracts of the first second before electrical stimulation (ES) followed by the electrical activity of the first 400 ms after each electrical stimulus are displayed for each shank (column) and each electrode (row). The ES pulses are represented by red dashed lines, and the activity captured by the recording and stimulating electrodes is displayed in black and red, respectively. Additionally, a zoom of the electrical activity captured 15 ms before and 25 ms after each ES pulse (stimulation artifact shown as a line of 0 V) is shown for the shank of interest, pointed out with a green frame. Electrodes with a significant stimulation ($p < 0.05$) are denoted with an asterisk (*). In **(B)**, the electrical stimulation efficiency (ESE) for six different ES parameters are shown for the same retina used in **(A)**. For this experiment, shank 4 is not shown due to non-working electrodes.

Similarly to wildtype retinas, successful stimulation was observed at the three upper electrodes of the stimulating shank ($p < 0.05$), however, the mean ESEs of the electrodes was lower than in wildtype, between 2.2 and 2.7. Significant stimulations were also obtained using ES-3 and ES-6 on this retinal sample, yet the ESEs were lower than for ES-2, ranging between 1.4 and 2.2 (see **Figure 14B** and **Supplementary Table 6**). Differences in the ESE between wildtype and *rd10* retinas were further confirmed when comparing the average ESE of the stimulated shanks during successful stimulations. In this way, ES-1, ES-2, and ES-3 proved to evoke significantly higher ESEs in wildtype than in *rd10* samples (see **Supplementary Figure 4A**).

Unlike to the electrical responses evoked in wildtype retinas, successful stimulations eliciting the activation of RGCs in the recording electrodes of non-stimulated shanks were detected in *rd10* retinas, as revealed by electrodes $E_{4.4}$, $E_{3.2}$, $E_{2.2}$, and $E_{2.1}$ (see **Figure 14A** and **Supplementary Table 6**). While the recordings before ES suggested that the bottom electrodes of the non-stimulated shanks had reached the GCL ($E_{4.1}$) and the NFL ($E_{3.1}$ and $E_{2.1}$) in the *rd10* sample (see **Supplementary Figure 3B**), electrical responses were also captured in the upper electrodes with low amplitude spikes. The fact that $E_{4.4}$, $E_{3.2}$, and $E_{2.2}$ presented significant firing rate differences can be attributed to the sensitivity of the ESE when a low SA (higher than 0 and lower than 1 Hz) is being captured, since the ratio would calculate an ESE higher than 1 even when one spike is detected after ES, and would rise extremely if the activity before ES is slightly higher than 0 Hz. Nevertheless, consistent and significant electrical responses generating firing rate increases were observed in shank 2 during the three different ES parameters tested on the sample (see **Supplementary Table 6**). Moreover, considering that the inter-shank distance was 190 µm, the stimulation of distant cells with respect to the stimulating electrode was unveiled for *rd10* retinas.

Furthermore, measurements of the delivered current during ES exposed minimum cathodic currents of -4.62 ± 2.92 µA

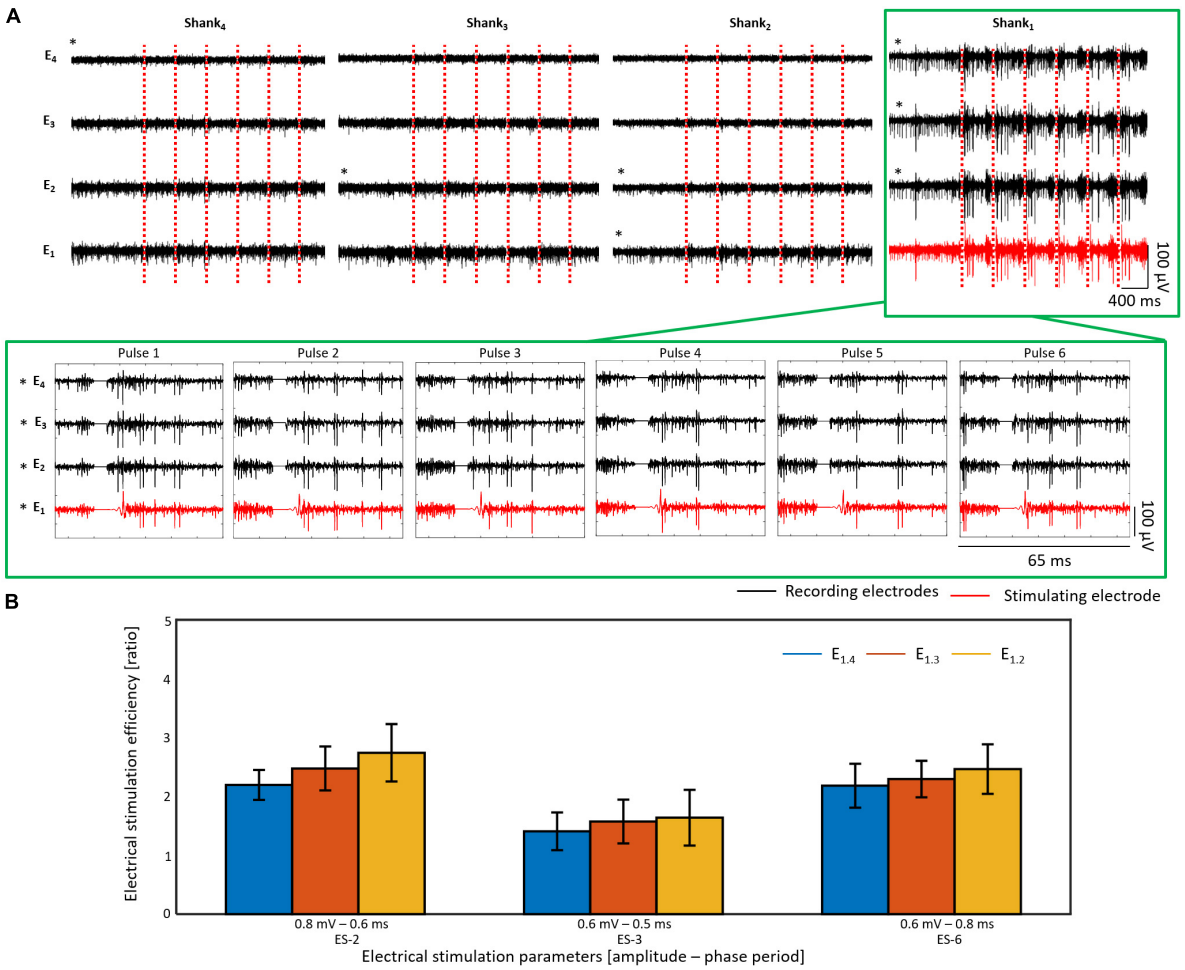

FIGURE 14 | Electrical stimulation and recording in *rd10* retina. In **(A)** the electrical activity after six consecutive biphasic pulses (first cathodic) with 0.8 mV in amplitude and a phase period of 0.6 ms (ES-2) every 20 s is shown for an *rd10* retina. Recording extracts of the first second before electrical stimulation (ES) followed by the electrical activity of the first 400 ms after each electrical stimulus are displayed for each shank (column) and each electrode (row). The ES pulses are represented by red dashed lines, and the activity captured by the recording and stimulating electrodes is displayed in black and red, respectively. Additionally, a zoom of the electrical activity captured 15 ms before and 25 ms after each ES pulse (stimulation artifact shown as a line of 0 V) is shown for the shank of interest, pointed out with a green frame. Electrodes with a significant stimulation ($p < 0.05$) are denoted with an asterisk (*). In **(B)**, the electrical stimulation efficiency (ESE) for three different ES parameters is shown for the same retina used in **A**.

and maximum anodic currents of 6.43 ± 4.04 µA for the generation of successful stimulations on both wildtype and *rd10* samples. Depending on current amplitude and stimulus length, cathodic and anodic charge densities between -686.10 ± 304.16 µC/cm^2 and 555.69 ± 308.41 µC/cm^2, considering an ESA of 576 µm^2 (see **Supplementary Table 7** and **Supplementary Figures 4B,C**) triggered stimulation of cells. Hence, our stimulation parameters lie in the range also employed by other researchers (Stett et al., 2000; Suzuki et al., 2004; Jalligampala et al., 2017; Corna et al., 2018). In addition, despite the higher cathodic but lower anodic charge densities encountered in *rd10* retinas during ES-3 and ES-6, no proportional relationship between higher cathodic currents and higher stimulations efficiencies were found, what can be explained by the high variability of the delivered currents during ES (see **Supplementary Figures 4B,C**).

Finally, reproducibility of the evoked responses was confirmed after testing six different stimulation parameters in three different wildtype retinas, obtaining significant stimulations in two out of three retinas after applying ES-1, ES-2, ES-4, ES-5, and ES-6, and in one retina using ES-3. In contrast, *rd10* retinas showed successful stimulations after ES-1, ES-3, and ES-6 in one out of two retinas, and after ES-2 in two out of two retinas.

DISCUSSION

Multi-Site Penetrating MEAs for Retinal Applications

With the aim to achieve a closer proximity to target neurons and reduce charge densities during ES for retinal implants, penetrating electrodes have been investigated by several research

groups in the form of pillars or protuberant 3D electrodes (Yanovitz et al., 2014; Bendali et al., 2015; González Losada et al., 2017; Flores et al., 2018). In order to amplify and complement such efforts into a bidirectional communication between a prosthetic device and retinal cells, multi-shank and multi-site penetrating MEAs (Michigan-like probes), which have been used mostly as intracortical neural interfaces (Weltman et al., 2016), were tested in this work to prove the feasibility of simultaneous intraretinal electrical recording and stimulation. Penetrating pillars or protuberant electrodes are typically used for unidirectional communication, i.e., ES, while to our knowledge, the application of multi-site penetrating electrodes for a bidirectional communication with simultaneous ES and recording of the retina has not been published before. Even healthy retina is only 200 μm thick, much thinner than the neocortex. Upon photoreceptor degeneration, the remaining retina is only 100 μm in thickness. Hence, in the design of our device we carefully optimized size and distance of the electrodes to match these restrictions.

The use of penetrating shanks with multiple electrode sites made it possible to place the bottom electrodes of the shanks (later on used as stimulating electrodes) in deeper retinal layers, while at least one of the upper electrodes came in close proximity to the GCL, to continuously record the spiking activity of the retina. Recordings of spontaneous electrical activity, as well as meaningful physiological responses to optical stimulation and changes in the extracellular ionic concentrations proved that the recorded spikes originated from RGCs, showing in turn the vitality of the tissue during the intraretinal recordings. Moreover, the penetrating MEAs were also capable of crossing different retinal depths in degenerated *rd10* retinas while recording the typical pathologic rhythmic activity present in *rd10* mice (Goo et al., 2011a; Stasheff et al., 2011; Jae et al., 2013; Biswas et al., 2014; Haselier et al., 2017). After proving the capabilities of the penetrating BiMEAs to access different retinal layers while recording the retinal activity, ES of neurons of the inner retina was carried out using only the bottom electrodes as stimulating electrodes. The upper electrodes of the stimulated shank, located close to the GCL, were then used together with the electrodes of non-stimulated shanks as recording electrodes. In this way, successful electrical responses in both wildtype and *rd10* retinas were captured during simultaneous intraretinal recordings. Bursting reactions to different electrical stimuli were exposed for wildtype retinas, while bursting activity as well as discontinuous spikes were observed for *rd10* retinas. Additionally, lower ESEs were revealed in *rd10* in comparison with wildtype retinas, agreeing with the ES behaviors reported by Haselier et al. (2017) using planar MEAs. While electrical recording and stimulation of retinal neurons can be also achieved with planar MEAs, multi-site penetrating probes allow the possibility to record from the same neuronal column being stimulated. In this way, it was noted that in wildtype retinas ES evoked excitatory responses confined to the neurons within the neuronal column along the stimulated shank. A device that can control the stimulating current and simultaneously record the success of ES could enable a bidirectional communication that provides feedback about the success of ES, capture the presence of abnormal retinal activity, and in principle perform an autonomous calibration of stimulating parameters.

In addition, current measurements during ES exposed injected currents and charge densities within the range of subretinal ES thresholds (100–900 $\mu C/cm^2$) when using small electrode sizes ($\sim$706 μm^2) on *rd10* retinas, as recently reported by Corna et al. (2018). The charge densities revealed here surpass the thresholds reported by Yanovitz et al. (2014) and Bendali et al. (2015) when using penetrating pillar and protuberant electrodes inside the retina. However, optimization of stimulation modes, such as current- and charge-controlled stimulation as well as ES parameters for the BiMEA probes were beyond the scope of the present study and must be addressed in future studies.

We observed some differences between wildtype and *rd10* retina. In wildtype retina using 20 μm steps, we could clearly observe how the electrode that proved optimal for spike registration changed when the shank was inserted deeper into the retina. In *rd10* retina, this was less clear. Mechanical differences between wildtype and *rd10* retinas, such as an increased stiffness (Hamon et al., 2017), might have interfered with the insertion of the penetrating shanks into the *rd10* retina, suggesting that a higher insertion force might be needed when approaching the degenerated tissue. Likewise, in comparison with wildtype retinas, the decreased resistivity in *rd10* retina (Wang and Weiland, 2015) could explain higher spike amplitudes during *rd10* recordings and the presence of retinal spikes at the bottom electrodes when the top electrodes of a shank indicated to be nearby the GCL of the retina. The lower resistivity of the degenerated tissue could also explain the fact that for some stimulation parameters, higher charge densities were achieved in *rd10* retinas in comparison with wildtype, what could have elicited electrical responses in distant neurons. Hence, comparing the results between wildtype and *rd10* retina suggests that the successful stimulation of a narrow group of neurons is possible, however, the stimulation parameters should be tuned for each type of retina.

Design Considerations and Future Penetrating BiMEAs

When compared to planar MEAs, the use of penetrating MEAs is certainly a more invasive method, and this is why efforts must be focused on the optimization of design and materials to minimize the potential damage of a penetrating intraretinal implant.

On one side, the design of such probes must consider the anatomy and microstructure of the retina. The first generation of BiMEA probes (12-BiMEAs) exhibited in this work, had a shank length of 1000 μm, which was reduced to 312 μm in a newer design (16-BiMEAs), coming closer to the total retinal thickness of approximately 200–220 μm in wildtype mice and 100–120 in *rd10* (Pennesi et al., 2012; Dysli et al., 2015; Li et al., 2018). Considering that region of interest for the penetrating MEAs inside the retina comprises from the NFL to the outer margin of the INL ($\sim$100 μm), the shank length of future designs could be further reduced. Similarly, the selection of smaller electrodes (from 80 × 20 μm^2 to 40 × 20 μm^2) lead to the optimization of the shank width, which was reduced from 100 to 60 μm.

Additionally to the reduction of electrode dimension, a geometry modification of the stimulating BiMEA electrode (from rectangular to trapezoidal) helped to reduce the distance from the tip to the bottom electrode, thereby avoiding to pierce completely the retina during positioning of the electrodes. As smaller electrodes could reduce the dimensions of the penetrating shanks and increase spatial resolution, appropriate electrode materials that yield low impedances and high charge delivery capacities, such as IrO_x, PEDOT, or nanostructured Pt (Boehler et al., 2017), should be considered. In addition, different electrode configurations, like the use of a local return electrode, could be tested in order to narrow the scope of the ES (Weiland et al., 2016).

Furthermore, new materials that attenuate the mechanical and biological mismatch between the retinal tissue and the implant should be considered. Current planar retinal implants are based on flexible substrate materials such a polyimide, parylene-C, and silicone rubber (Weiland and Humayun, 2014), however, the growing generation of penetrating probes for retinal applications, including pillar electrodes and the one presented in this work, are mostly based on stiff materials like silicon (Yanovitz et al., 2014; Flores et al., 2018). Considering that the use of stiff materials can lead to glial responses and scar tissues hindering the long term functionality of neuronal implants (Weltman et al., 2016), in the future flexible and compliant penetrating retinal probes must be pursued. Therefore, in order to boost the potential use of bidirectional penetrating MEAs for retinal applications, further tests to investigate the mechanical properties and biological impact of such probes with respect to the retina are needed.

CONCLUSION

This work unveiled the feasibility of using multi-shank and multi-site penetrating MEAs for retinal applications. In this way, different layers of the retina were accessed, offering at the same time the possibility to stimulate the inner retina and to follow-up the electrical activity along the same neuronal column by simultaneous recording of RGCs. Thus, the use of such systems could enable a bidirectional communication that provides feedback about the success of ES, captures the presence of abnormal retinal activity, and in principle could perform an autonomous calibration of stimulating parameters. While this proof of concept opens the door to potential intraretinal implants, it must be taken into account that it is an invasive technique and that the biological impact on the retina has not been established yet. Therefore, future bidirectional penetrating implants must focus on the assessment and reduction of potential damages to the retina, as well as on the development of flexible and complaint penetrating probes.

ETHICS STATEMENT

All experiments were performed in accordance with the German Law for the Protection of Animals and after approval was obtained by the regulatory authorities, the Forschungszentrum Jülich and the Landesamt für Natur, Umwelt und Verbraucherschutz of the German federal state North-Rhine Westfalia.

AUTHOR CONTRIBUTIONS

WM, PW, FM, and AO conceived the idea and designed the experiments. SL fabricated the devices. VRM and JG performed electrical and biological experiments. VRM and SL performed the characterization of the electrodes. The manuscript was written through contributions of all authors. All authors have given approval to the final version of the manuscript.

FUNDING

The study was supported by the DFG grants OF-22/11-3, MO-781/8-3, MU-3036/3-3, and WA-1472/6-3.

ACKNOWLEDGMENTS

We thank all the team of the BiMEA consortium for the research cooperation: Institutes of Bioelectronics (ICS-8) and Cellular Biophysics (ICS-4), Forschungszentrum Jülich, Jülich, Germany; Department of Materials in Electrical Engineering 1 and Department of Ophthalmology, RWTH Aachen University, Aachen, Germany; and Institute of Electronic Components and Circuits, University of Duisburg Essen, Duisburg, Germany.

SUPPLEMENTARY MATERIAL

The Supplementary Material for this article can be found online at: https://www.frontiersin.org/articles/10.3389/fnins.2019.00367/full#supplementary-material

REFERENCES

Bendali, A., Rousseau, L., Lissorgues, G., Scorsone, E., Djilas, M., Dégardin, J., et al. (2015). Synthetic 3D diamond-based electrodes for flexible retinal neuroprostheses: model, production and in vivo biocompatibility. *Biomaterials* 67, 73–83. doi: 10.1016/j.biomaterials.2015.07.018

Biswas, S., Haselier, C., Mataruga, A., Thumann, G., Walter, P., and Müller, F. (2014). Pharmacological analysis of intrinsic neuronal oscillations in rd10 retina. *PLoS One* 9:e0099075. doi: 10.1371/journal.pone.0099075

Boehler, C., Oberueber, F., Schlabach, S., Stieglitz, T., and Asplund, M. (2017). Long-term stable adhesion for conducting polymers in biomedical applications: IrOx and nanostructured platinum solve the chronic challenge. *ACS Appl. Mater. Interfaces* 9, 189–197. doi: 10.1021/acsami.6b13468

Brusius, J. S. (2015). *3-Dimensionale Penetrierende Multi-elektrodenarrays zur Stimulation und Ableitung in der Retina*. Ph.D. thesis, RWTH Aachen, Aachen. doi: NODOI

Celik, M. E., and Karagoz, I. (2018). Comparison of monophasic and biphasic electrical stimulation by using temporal analysis for different inter-electrode

spacings in the hexagonal arrays. *Arab. J. Sci. Eng.* 43, 2889–2898. doi: 10.1007/s13369-017-2918-z

Cheng, D. L., Greenberg, P. B., and Borton, D. A. (2017). Advances in retinal prosthetic research: a systematic review of engineering and clinical characteristics of current prosthetic initiatives. *Curr. Eye Res.* 42, 334–347. doi: 10.1080/02713683.2016.1270326

Cogan, S. F. (2008). Neural stimulation and recording electrodes. *Annu. Rev. Biomed. Eng.* 10, 275–309. doi: 10.1146/annurev.bioeng.10.061807.160518

Corna, A., Herrmann, T., and Zeck, G. (2018). Electrode-size dependent thresholds in subretinal neuroprosthetic stimulation. *J. Neural Eng.* 15:045003. doi: 10.1088/1741-2552/aac1c8

Dysli, C., Enzmann, V., Sznitman, R., and Zinkernagel, M. S. (2015). Quantitative analysis of mouse retinal layers using automated segmentation of spectral domain optical coherence tomography images. *Transl. Vis. Sci. Technol.* 4:9. doi: 10.1167/tvst.4.4.9

Flores, T., Lei, X., Huang, T., Lorach, H., Dalal, R., Galambos, L., et al. (2018). Optimization of pillar electrodes in subretinal prosthesis for enhanced proximity to target neurons. *J. Neural Eng.* 15:036011. doi: 10.1088/1741-2552/aaac39

Gekeler, F., Kobuch, K., Schwahn, H. N., Stett, A., Shinoda, K., and Zrenner, E. (2004). Subretinal electrical stimulation of the rabbit retina with acutely implanted electrode arrays. *Graefes Arch. Clin. Exp. Ophthalmol.* 242, 587–596. doi: 10.1007/s00417-004-0862-6

González Losada, P., Rousseau, L., Grzeskowiak, M., Degardin, J., Berhanu, S., Dubus, E., et al. (2017). Protuberant electrode structures for new retinal implants. *Proceedings* 1:315. doi: 10.3390/proceedings1040315

Goo, Y. S., Ahn, K. N., Song, Y. J., Ahn, S. H., Han, S. K., Ryu, S. B., et al. (2011a). Spontaneous oscillatory rhythm in retinal activities of two retinal degeneration (rd1 and rd10) mice. *Korean J. Physiol. Pharmacol.* 15, 415–422. doi: 10.4196/kjpp.2011.15.6.415

Goo, Y. S., Ye, J. H., Lee, S., and Nam, Y. (2011b). Retinal ganglion cell responses to voltage and current stimulation in wild-type and rd1 mouse retinas. *J. Neural Eng.* 8:035003. doi: 10.1088/1741-2560/8/3/035003

Hamon, A., Masson, C., Bitard, J., Gieser, L., Roger, J. E., and Perron, M. (2017). Retinal degeneration triggers the activation of YAP/TEAD in reactive Müller cells. *Invest. Ophthalmol. Vis. Sci.* 58, 1941–1953. doi: 10.1167/iovs.16-21366

Hartong, D. T., Berson, E. L., Dryja, T. P., and Hamel, C. (2006). Retinitis pigmentosa. *Lancet* 368, 1795–1809. doi: 10.1016/S0140-6736(06)69740-7

Haselier, C., Biswas, S., Rösch, S., Thumann, G., Müller, F., and Walter, P. (2017). Correlations between specific patterns of spontaneous activity and stimulation efficiency in degenerated retina. *PLoS One* 12:e0190048. doi: 10.1371/journal.pone.0190048

Heil, R., Schloesser, M., Offenhäusser, A., Waasen, S. V., and Schieck, M. (2014). Automated electrical stimulation and recording for retina implant research by LabVIEW configured standalone data acquisition device. *Paper Presented at the 2014 Proceedings of the SICE Annual Conference*, Sapporo, 1662–1667. doi: NODOI

Jae, S. A., Ahn, K. N., Kim, J. Y., Seo, J. H., Kim, H. K., and Goo, Y. S. (2013). Electrophysiological and histologic evaluation of the time course of retinal degeneration in the rd10 mouse model of retinitis pigmentosa. *Korean J. Physiol. Pharmacol.* 17, 229–235. doi: 10.4196/kjpp.2013.17.3.229

Jalligampala, A., Sekhar, S., Zrenner, E., and Rathbun, D. L. (2017). Optimal voltage stimulation parameters for network-mediated responses in wild type and rd10 mouse retinal ganglion cells. *J. Neural Eng.* 14:26004. doi: 10.1088/1741-2552/14/2/026004

Jensen, R. J., and Rizzo, J. F. III. (2009). Activation of ganglion cells in wild-type and rd1 mouse retinas with monophasic and biphasic current pulses. *J. Neural Eng.* 6:035004. doi: 10.1088/1741-2560/6/3/035004

Lewis, P. M., Ackland, H. M., Lowery, A. J., and Rosenfeld, J. V. (2015). Restoration of vision in blind individuals using bionic devices: a review with a focus on cortical visual prostheses. *Brain Res.* 1595, 51–73. doi: 10.1016/j.brainres.2014.11.020

Li, Y., Zhang, Y., Chen, S., Vernon, G., Wong, W. T., and Qian, H. (2018). Light-dependent OCT structure changes in photoreceptor degenerative rd 10 mouse retina. *Invest. Ophthalmol. Vis. Sci.* 59, 1084–1094. doi: 10.1167/iovs.17-23011

Margalit, E., Maia, M., Weiland, J. D., Greenberg, R. J., Fujii, G. Y., Torres, G., et al. (2002). Retinal Prosthesis for the Blind. *Survey Ophthalmol.* 47, 335–356. doi: 10.1016/S0039-6257(02)00311-9

Maybeck, V., Schnitker, J., Li, W., Heuschkel, M., and Offenhäusser, A. (2016). An evaluation of extracellular MEA vs optogenetic stimulation of cortical neurons. *Biomed. Phys. Eng. Express* 2:055017. doi: 10.1088/2057-1976/2/5/055017

Mills, J. O., Jalil, A., and Stanga, P. E. (2017). Electronic retinal implants and artificial vision: journey and present. *Eye* 31, 1383–1398. doi: 10.1038/eye.2017.65

Pascolini, D., and Mariotti, S. P. (2012). Global estimates of visual impairment: 2010. *Br. J. Ophthalmol.* 96, 614–618. doi: 10.1136/bjophthalmol-2011-300539

Pennesi, M. E., Michaels, K. V., Magee, S. S., Maricle, A., Davin, S. P., Garg, A. K., et al. (2012). Long-term characterization of retinal degeneration in rd1 and rd10 mice using spectral domain optical coherence tomography. *Invest. Ophthalmol. Vis. Sci.* 53, 4644–4656. doi: 10.1167/iovs.12-9611

Quian Quiroga, R. (2009). What is the real shape of extracellular spikes? *J. Neurosci. Methods* 177, 194–198. doi: 10.1016/j.jneumeth.2008.09.033

Quiroga, R. Q. (2004). Unsupervised spike detection and sorting problem: detect and separate spikes. *Neural Comput.* 16, 1661–1687. doi: 10.1162/089976604774201631

Rey, H. G., Pedreira, C., and Quian Quiroga, R. (2015). Past, present and future of spike sorting techniques. *Brain Res. Bull.* 119, 106–117. doi: 10.1016/j.brainresbull.2015.04.007

Roessler, G., Laube, T., Brockmann, C., Kirschkamp, T., Mazinani, B., Goertz, M., et al. (2009). Implantation and explantation of a wireless epiretinal retina implant device: observations during the epiret3 prospective clinical trial. *Invest. Ophthalmol. Vis. Sci.* 50, 3003–3008. doi: 10.1167/iovs.08-2752

Slavcheva, E., Schnakenberg, U., and Mokwa, W. (2006). Deposition of sputtered iridium oxide — Influence of oxygen flow in the reactor on the film properties. *Appl. Surface Sci.* 253, 1964–1969. doi: 10.1016/j.apsusc.2006.03.073

Slavcheva, E., Vitushinsky, R., Mokwa, W., and Schnakenberg, U. (2004). Sputtered iridium oxide films as charge injection material for functional electrostimulation. *J. Electrochem. Soc.* 151, E226–E237. doi: 10.1149/1.1747881

Stasheff, S. F., Shankar, M., and Andrews, M. P. (2011). Developmental time course distinguishes changes in spontaneous and light-evoked retinal ganglion cell activity in rd1 and rd10 mice. *J. Neurophysiol.* 105, 3002–3009. doi: 10.1152/jn.00704.2010

Stett, A., Barth, W., Weiss, S., Haemmerle, H., and Zrenner, E. (2000). Electrical multisite stimulation of the isolated chicken retina. *Vision Res.* 40, 1785–1795. doi: 10.1016/s0042-6989(00)00005-5

Stett, A., Mai, A., and Herrmann, T. (2007). Retinal charge sensitivity and spatial discrimination obtainable by subretinal implants: key lessons learned from isolated chicken retina. *J. Neural Eng.* 4, S7–S16. doi: 10.1088/1741-2560/4/1/S02

Suzuki, S., Humayun, M. S., Weiland, J. D., Chen, S. J., Margalit, E., Piyathaisere, D. V., et al. (2004). Comparison of electrical stimulation thresholds in normal and retinal degenerated mouse retina. *Jpn. J. Ophthalmol.* 48, 345–349. doi: 10.1007/s10384-004-0084-9

Van Ooyen, A., Topalov, G., Ganske, G., Mokwa, W., and Schnakenberg, U. (2009). Iridium oxide deposited by pulsed dc-sputtering for stimulation electrodes. *J. Micromech. Microeng.* 19:074009. doi: 10.1088/0960-1317/19/7/074009

Walter, P. (2016). Zukünftige entwicklungen bei implantierbaren netzhautprothesen. *Klin. Monbl. Augenheilkd.* 233, 1238–1243. doi: 10.1055/s-0042-115411

Walter, P., Go, M., Alteheld, N., Rossler, G., Stieglitz, T., and Eysel, U. T. (2005). Cortical activation via an implanted wireless retinal prosthesis. *Invest. Ophthalmol. Vis. Sci.* 46, 1780–1785. doi: 10.1167/iovs.04-0924

Wang, B., and Weiland, J. D. (2015). Resistivity profiles of wild-type, rd1, and rd10 mouse retina. *Proc. Annu. Int. Conf. IEEE Eng. Med. Biol. Soc.* 2015, 1650–1653. doi: 10.1109/EMBC.2015.7318692

Weiland, J., and Humayun, M. (2014). Retinal prosthesis. *IEEE Trans. Biomed. Eng.* 61, 1412–1424. doi: 10.1007/9781461452270

Weiland, J. D., Walston, S. T., and Humayun, M. S. (2016). Electrical stimulation of the retina to produce artificial vision. *Annu. Rev. Vis. Sci.* 2, 273–294. doi: 10.1109/IJCNN.2005.1556421

Weltman, A., Yoo, J., and Meng, E. (2016). Flexible, penetrating brain probes enabled by advances in polymer microfabrication. *Micromachines* 7:180. doi: 10.3390/mi7100180

Wessling, B., Mokwa, W., and Schnakenberg, U. (2006). RF-sputtering of iridium oxide to be used as stimulation material in functional. *J. Micromech. Microeng.* 16, S142–S148. doi: 10.1088/0960-1317/16/6/S21

Yanovitz, L., Raz-Prag, D., Eden, K.-O., Saini, R., Hanein, Y., and Gefen, R. (2014). Retinal responses evoked and recorded with 3D electrodes designated for a novel prosthetic device. *Invest. Ophthalmol. Vis. Sci.* 55:1808. doi: NODOI

Zrenner, E. (2013). Fighting blindness with microelectronics. *Sci. Transl. Med.* 5:210s16. doi: 10.1126/scitranslmed.3007399

Conflict of Interest Statement: The authors declare that the research was conducted in the absence of any commercial or financial relationships that could be construed as a potential conflict of interest.

Copyright © 2019 Rincón Montes, Gehlen, Lück, Mokwa, Müller, Walter and Offenhäusser. This is an open-access article distributed under the terms of the Creative Commons Attribution License (CC BY). The use, distribution or reproduction in other forums is permitted, provided the original author(s) and the copyright owner(s) are credited and that the original publication in this journal is cited, in accordance with accepted academic practice. No use, distribution or reproduction is permitted which does not comply with these terms.

frontiers in Neuroscience

ORIGINAL RESEARCH
published: 30 April 2019
doi: 10.3389/fnins.2019.00413

Mediating Retinal Ganglion Cell Spike Rates Using High-Frequency Electrical Stimulation

Tianruo Guo[1†], David Tsai[1,2,3†], Chih Yu Yang[1], Amr Al Abed[1], Perry Twyford[4], Shelley I. Fried[4,5], John W. Morley[6], Gregg J. Suaning[1,7], Socrates Dokos[1] and Nigel H. Lovell[1]*

[1] Graduate School of Biomedical Engineering, UNSW Sydney, Sydney, NSW, Australia, [2] Department of Biological Sciences, Columbia University, New York, NY, United States, [3] Department of Electrical Engineering, Columbia University, New York, NY, United States, [4] VA Boston Healthcare System, Boston, MA, United States, [5] Department of Neurosurgery, Massachusetts General Hospital and Harvard Medical School, Boston, MA, United States, [6] School of Medicine, Western Sydney University, Penrith, NSW, Australia, [7] School of Biomedical Engineering, The University of Sydney, Sydney, NSW, Australia

OPEN ACCESS

Edited by:
Jeffrey R. Capadona, Case Western Reserve University, United States

Reviewed by:
Robert A. Gaunt, University of Pittsburgh, United States
Juan Álvaro Gallego, Northwestern University, United States

***Correspondence:**
Nigel H. Lovell
n.lovell@unsw.edu.au

[†]*Joint first authors*

Specialty section:
This article was submitted to Neuroprosthetics, a section of the journal Frontiers in Neuroscience

Received: *20 December 2018*
Accepted: *11 April 2019*
Published: *30 April 2019*

Citation:
Guo T, Tsai D, Yang CY, Al Abed A, Twyford P, Fried SI, Morley JW, Suaning GJ, Dokos S and Lovell NH (2019) Mediating Retinal Ganglion Cell Spike Rates Using High-Frequency Electrical Stimulation. Front. Neurosci. 13:413. doi: 10.3389/fnins.2019.00413

Recent retinal studies have directed more attention to sophisticated stimulation strategies based on high-frequency (>1.0 kHz) electrical stimulation (HFS). In these studies, each retinal ganglion cell (RGC) type demonstrated a characteristic stimulus-strength-dependent response to HFS, offering the intriguing possibility of focally targeting retinal neurons to provide useful visual information by retinal prosthetics. Ionic mechanisms are known to affect the responses of electrogenic cells during electrical stimulation. However, how these mechanisms affect RGC responses is not well understood at present, particularly when applying HFS. Here, we investigate this issue via an *in silico* model of the RGC. We calibrate and validate the model using an *in vitro* retinal preparation. An RGC model based on accurate biophysics and realistic representation of cell morphology, was used to investigate how RGCs respond to HFS. The model was able to closely replicate the stimulus-strength-dependent suppression of RGC action potentials observed experimentally. Our results suggest that spike inhibition during HFS is due to local membrane hyperpolarization caused by outward membrane currents near the stimulus electrode. In addition, the extent of HFS-induced inhibition can be largely altered by the intrinsic properties of the inward sodium current. Finally, stimulus-strength-dependent suppression can be modulated by a wide range of stimulation frequencies, under generalized electrode placement conditions. *In vitro* experiments verified the computational modeling data. This modeling and experimental approach can be extended to further our understanding on the effects of novel stimulus strategies by simulating RGC stimulus-response profiles over a wider range of stimulation frequencies and electrode locations than have previously been explored.

Keywords: neuromodulation, retinal ganglion cell, high-frequency electrical stimulation, retinal implant, computational modeling, *in vitro* patch-clamp

INTRODUCTION

Extracellular electrical stimulation is extensively used in electro-neural interfaces for the central and peripheral nervous systems (Gybels, 1981; Deep-Brain Stimulation for Parkinson's Disease Study Group et al., 2001; Kilgore and Bhadra, 2004; Guenther et al., 2012). In particular, retinal prosthesis aims to restore functional visual percepts to those suffering from retinal degenerative diseases, by electrically stimulating the surviving neural tissue of the retina (Rizzo and Wyatt, 1997; Palanker et al., 2005; Weiland et al., 2005). In such cases, the aim is to elicit visual percepts by activating the remaining retinal neuronal populations in a controlled spatiotemporal pattern.

Considerable research into high-frequency (defined as being higher than 1.0 kHz) electrical stimulation (HFS) is underway to understand the extent to which neuronal activity can be quantitatively controlled with greater spatiotemporal precision, in order to improve the performance of neuroprostheses. For example, HFS ranging from 2.0 to 20 kHz has been extensively used to block unwanted or unregulated generation of nerve impulses in many disabling conditions (Kilgore and Bhadra, 2004). In addition, the effects of a large range of stimulation frequencies (5–50 kHz) have been investigated to selectively block different types of peripheral nerve fibers (Joseph and Butera, 2011). HFS up to 5 kHz was also reported to generate more stochastic firing in auditory nerve fibers (Litvak et al., 2001, 2003). Finally, recent clinical studies have also begun to assess how HFS might affect the efficacy of neural implants for the cochlear (up to 2.4 kHz) (McKay et al., 2013), the retina (up to 3.33 kHz) (Horsager et al., 2009), and the spinal cord (up to 10 kHz) (Tiede et al., 2013; Van Buyten et al., 2013).

In the retina, recent studies suggest that epiretinal HFS (1.0–6.25 kHz) is able to differentially activate functionally-different retinal ganglion cell (RGC) types (Cai et al., 2013; Twyford et al., 2014; Kameneva et al., 2016; Guo et al., 2018b). The RGC types examined demonstrated a characteristic non-monotonic, stimulus-strength-dependent response during HFS, offering the intriguing possibility of targeting certain functionally-distinct RGC types without simultaneously producing any significant response in other types. Given the promising performances of HFS in retinal and other functional electrical stimulation regimes, it is important to explore the precise mechanisms underlying HFS-induced strength-dependent activation. "What is the main intrinsic property that dominates the response of RGCs to biphasic HFS? and how HFS-induced strength-dependent activation can be modulated across a wide range of stimulus frequencies?"

In answering these questions, we began with *in silico* investigations to gain insights into the mechanisms underlying experimentally-observed non-monotonic stimulus-response profiles during HFS. The model included accurate 3D morphological reconstruction of a single RGC, and its electrical response behavior was optimized against multiple whole-cell recordings from the same cell for accurate biophysics (Guo et al., 2016). Using this model, we identified a correlation between RGC response patterns during HFS and RGC intrinsic properties, in order to elucidate the likely mechanisms underlying neuronal excitation by extracellularly applied HFS. In addition, RGC stimulus-strength-dependent properties over a wide range of stimulation frequencies ranging from 1.0 to 9.0 kHz, were predicted using the computational model. In the second stage, we performed *in vitro* experimentation to verify the mechanisms and results predicted by the computational modeling, for a generalized stimulus electrode placement without a priori knowledge of axon initial segment (AIS) location, a limitation of previous HFS work on RGCs (Cai et al., 2011, 2013; Twyford et al., 2014).

MATERIALS AND METHODS

Morphologically-Realistic and Biophysically-Accurate RGC Model

The RGC model was implemented using the NEURON computational software (Hines and Carnevale, 1997). In order to reconstruct the 3D cellular morphology, an OFF RGC was filled with neurobiotin-Cl using a whole-cell patch pipette. The retina was subsequently fixed in paraformaldehyde, with the filled cell reacted against Streptavidin–Alexa 488, as described previously (Tsai et al., 2012; Guo et al., 2016). The behavior of this RGC model closely replicated published experimental RGC responses to epiretinal electrical stimulation (Twyford et al., 2014; Guo et al., 2018b). Detailed anatomical information of the neuron was included in the model. A compartmentalized axon of 0.94-μm diameter and 1000-μm length was connected to the soma. The axon began with a hillock of 40-μm length, which was reconstructed based on overall measurements from previously published RGC studies (Fohlmeister and Miller, 1997; Fried et al., 2009; Jeng et al., 2011). This was followed by an AIS region of 0.94-μm diameter and 40-μm length. A sufficient number of morphological compartments (>1000) were used for the axon to ensure accurate spatial granularity. All RGC model parameter settings can be found in Guo et al. (2016).

For simulation of extracellular stimulation, we used a circular electrode disk in monopolar configuration. The extracellular potential V at each location was approximated using the following expression (Jeng et al., 2011; Tsai et al., 2012; Barriga-Rivera et al., 2017):

$$V(r,z) = \frac{I_o \rho_e}{2\pi R} \arcsin\left(\frac{2R}{\sqrt{(r-R)^2+z^2}+\sqrt{(r+R)^2+z^2}}\right) \quad (1)$$

where r and z are the radial and axial distances, respectively, from the center of the disk for ($z > 0$), R is the radius of the disk ($R = 15$ μm), I_o is the stimulus current, and ρ_e is the extracellular resistivity as described by Mueller and Grill (2013). The stimulus electrode was placed epiretinally 5 μm above the center of the AIS (**Figure 1B**), unless otherwise stated. RGC responses were recorded at the center of the somatic compartment (**Figure 1C**). The electrical stimulation waveforms and parameters were all adapted from previous HFS experimental studies (Cai et al., 2013; Twyford et al., 2014; Guo et al., 2018b) (see **Figure 1A** and *in vitro* methods for more details of stimulation parameters).

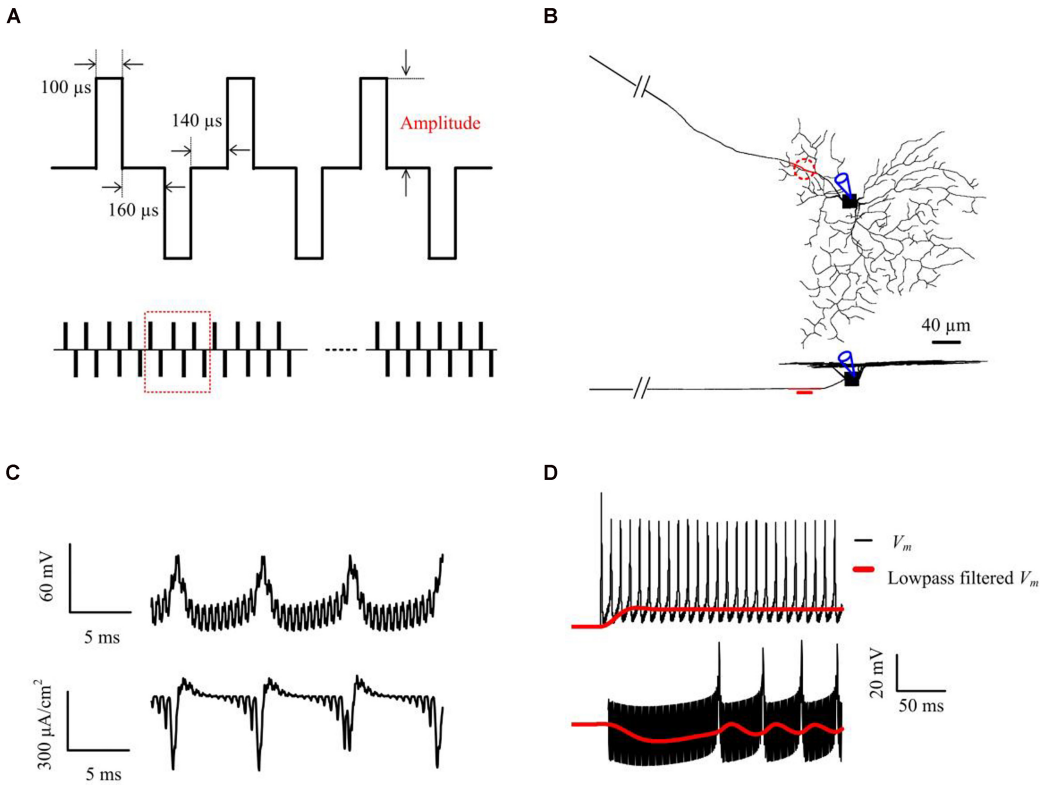

FIGURE 1 | Computational simulations of 2-kHz HFS. **(A)** Applied constant-amplitude stimulation. Stimulus waveforms consisted of biphasic constant-current pulses with a pulse width of 100 µs per phase, and a 160-µs inter-phase interval. The anodal-cathodal inter-phase interval was set to 140 µs (Twyford et al., 2014). The stimulus train amplitude remained constant within each trial but varied across trials. **(B)** Stimulation and measuring locations in the RGC model shown in top- and side-views. The epiretinal stimulus electrode (shown as a red, dashed line, or disk) was placed 5-µm from the AIS center (red compartment) and spiking responses were obtained from the soma. **(C)** An example of simulated somatic membrane potential and total membrane ionic current traces. The stimulus artifact can be seen embedded within the somatic response. **(D)** An example of simulated somatic membrane potential (black) and low-pass filtered membrane potential (red), with 10 µA (upper panel) and 63 µA (lower panel) 2-kHz stimulation. Membrane potential V_m was smoothed by a 3rd order Butterworth 20-Hz low-pass filter. This filtered membrane potential was used to examine the subthreshold (non-spiking) effects of HFS stimulus trains at different stimulus strengths.

To examine the effects of HFS on the (non-spiking) RGC membrane polarization over time, we lowpass-filtered the membrane potential V_m with a 3rd-order Butterworth filter with 20 Hz 3-dB cut-off frequency to remove spiking activities and the stimulus artifacts (e.g., see **Figure 1D**). Membrane depolarization and hyperpolarization induced by HFS was presented by the low-pass filtered membrane potential $V_{m,LP}$ normalized to the resting potential V_{rest} i.e., $V_{m,LP}-V_{rest}$. All processing was performed either offline in Matlab (Mathworks Inc, Natick, MA, United States), or online within NEURON.

Retinal Whole-Mount Preparation and Whole-Cell Patch Clamping

All procedures were approved by the UNSW Animal Care and Ethics Committee and were carried out in compliance with the Australian Code of Practice for the Care and Use of Animals for Scientific Purposes. Wild-type C57BL/6 female or male mice aged 4–8 weeks (purchased from Australian BioResource), were used in the *in vitro* experiments. Details on our whole-mount preparation and patch clamp recording with HFS can be found in Guo et al. (2018b) and Tsai et al. (2009). All elicited spikes were recorded at the soma after application of synaptic blockade, comprising a cocktail of synaptic blockers (in mM) consisting of 0.01 NBQX (2,3-Dioxo-6-nitro-1,2,3,4-tetrahydrobenzo[f]quinoxaline-7-sulfonamide) to block AMPA/kainate receptors, 0.05 D-AP5 [(2R)-amino-5-phosphonovaleric acid) to block NMDA receptors, 0.02 L-AP4 (L-(+)-2-Amino-4-phosphonobutyric acid] to block mGluR6, 0.1 picrotoxin (pic) to block GABAa/c receptors and 0.01 strychnine (stry) to block glycinergic receptors (Yang et al., 2018). The efficacy of the synaptic blockade was confirmed by the absence of RGC light responses.

We delivered HFS using a STG 4002 stimulator (MultiChannel Systems hardware and software, Reutlingen, Germany), with a stimulus duration of 300 ms. We began by stimulating the RGCs with conventional 2-kHz extracellular biphasic pulse trains to investigate RGC stimulus-response profiles. Electrical stimulation waveforms were adapted from Twyford et al. (2014) and Cai et al. (2013). The stimulus waveforms were charge-balanced biphasic with a pulse width of 100 µs per phase and an inter-phase interval of 160 µs. Stimulus amplitudes ranged from 5 to 120 µA, in 5-µA steps. In addition, stimulation

frequencies of 1.0 and 8.33 kHz were chosen to test the influence of stimulation frequency in shaping RGC stimulus-strength-dependent properties. Stimulation waveforms were adapted from Guo et al. (2018b) (see **Figure 7A**). The timing resolution of our STG 4002 stimulator was 20 μs. each pulse width is 40 μs. We provided a range of frequencies (8.33, 6.25, 5.0, 4.17, 3.33, 2.5, 2.0, and 1.67-kHz) of stimulation to investigate the stimulus-frequency-dependency of RGCs. We believe a frequency range up to 8.33 kHz was reasonable in providing a sufficiently large stimulation parameter space for inhibiting RGC response, as well as reasonable stimulation efficacy. In all *in vitro* experiments, each pulse amplitude was delivered three times. The mean spike-stimulus curve was calculated for each cell. For each RGC, we defined a 3D Cartesian (x, y, z) coordinate system, with the soma as the origin, such that the upper surface of the RGC dendritic field was aligned in the x-y plane and the RGC axon was aligned with the y-axis. A platinum-iridium stimulating electrode of 12.5-μm radius was placed at location 0, 0, and −40 μm.

Perfusion Solutions With Different Ionic Concentrations

To characterize the effects of Na^+ reversal potentials on RGC responses to electrical stimulation, extracellular concentrations were custom-made (instead of using Ames' solution) in order to adjust the Na^+ concentration. There are three different $[Na^+]$ solutions. Chemical components and concentrations of each solution are listed in **Table 1**, along with the final Na^+ concentrations and the calculated reversal potentials. In particular, the extracellular Na^+ concentration in the first and second low Na^+ solutions were adjusted to achieve custom Na^+ reversal potentials. Na^+ reversal potentials were calculated by the Goldman equation with $[Na^+]_i$ of 19.5 mM in our internal solution recipe.

$$E_{Na} = \frac{RT}{F} \ln\left(\frac{[Na^+]_o}{[Na^+]_i}\right) \quad (2)$$

where E_{Na} is the reversal potential of Na^+, R is the ideal gas constant (8.314 J mol^{-1} K^{-1}), T is the temperature in kelvin (307 K), F is Faraday's constant (96485 C mol^{-1}). The sequence in which the three solutions were applied was randomly set to avoid possible ordering effects.

TABLE 1 | Extracellular concentration and estimated Na^+ reversal potentials for various $[Na^+]$ solutions.

Chemicals	Control Na^+ solution	1st low Na^+ solution	2nd low Na^+ solution
NaCl	117.41	73.90	43.93
$NaHCO_3$	22.62	22.62	22.62
KCl	3.10	3.10	3.10
KH_2PO_4	0.57	0.57	0.57
$MgSO_4$	1.24	1.24	1.24
$CaCl_2$	1.52	1.52	1.52
Ascorbic acid	0.10	0.10	0.10
Glucose	11.09	12	12
Choline chloride	NA	43.05	73.02
Na^+ external concentration and estimated reversal potential			
$[Na^+]_o$ (mM)	140.0	96.5	66.6
E_{Na} (mV)	52	42	32

RESULTS

Stimulus-Strength-Dependent RGC Responses to Constant-Amplitude 2-kHz HFS

We began by stimulating the model RGC with conventional (fixed-amplitude) 2-kHz extracellular biphasic pulse trains (see **Figure 1A**). The amplitude of the stimulus train remained constant for a given trial but varied across trials ranging from 0 to 120 μA. For each stimulus amplitude, we counted the total number of spikes elicited during the 1-s stimulation period. We then determined the number of evoked spikes as a function of stimulus amplitude. **Figure 2A** shows the simulated membrane potential recorded at stimulation amplitudes of 2, 15, 30, and 60 μA. Elicited spikes were gradually inhibited when the stimulation amplitude was higher than 30 μA, until they were fully suppressed at 70 μA. **Figure 2B** shows spike-stimulus profiles at the soma of the RGC model. At relatively low stimulus magnitudes (i.e., <30 μA), the model RGC spike rate increased with stimulus amplitude. However, as the amplitude increased further (i.e., >30 μA), the number of elicited spikes decreased substantially, thereby creating a non-monotonic response profile as a function of stimulus amplitude, in agreement with recent *in vitro* studies (Cai et al., 2013; Twyford et al., 2014).

Mechanisms Underlying Stimulus-Strength-Dependent Spike Suppression

To investigate possible mechanisms underlying the non-monotonic extracellular response, and how this could be influenced by neuronal biophysical properties, we performed several sets of follow-up simulations and *in vitro* experiments.

In silico Investigation on HFS-Induced Inhibition

Figure 3A demonstrates modeled transient cell membrane voltage across the RGC's dendritic arbor as the stimulus amplitude ranged from 0 to 90 μA for a 1-s duration 2-kHz HFS train shown in **Figure 1A**. We low-pass filtered the membrane potential values, henceforth denoted "slow potential," to better visualize the small-amplitude, long-duration changes induced by the HFS. The slow potential over the entire neuron was examined 40 ms after stimulus onset (i.e., after eighty stimulation pulses). At this time, membrane potential had reached a steady state value. When a small-amplitude stimulus pulse train (2 μA) was delivered, the cellular membrane close to the stimulation site (the AIS region is indicated by the dashed rectangle) was depolarized (yellow). At the same time, a large portion of the peripheral dendritic branches were near their resting potential (green). When a HFS pulse train with 50-μA amplitude was delivered, local hyperpolarization was clearly evident near the AIS region (as indicated in the zoomed subplot). In addition,

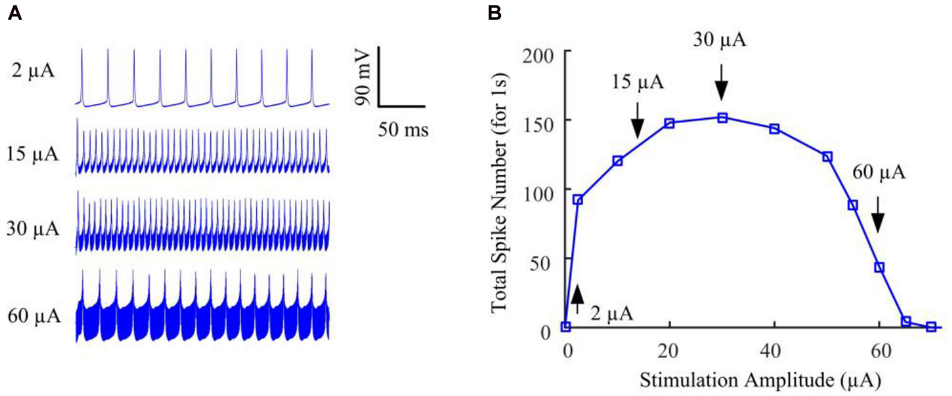

FIGURE 2 | The RGC model exhibited strength-dependent responses to constant-amplitude 2-kHz HFS. **(A)** Somatic voltage recordings for stimulation amplitudes of 2, 15, 30, and 60 μA. Larger stimulation amplitude was accompanied by increasing stimulation artifacts. **(B)** We counted the number of evoked spikes at the soma over a range of stimulus amplitudes. At relatively low stimulus magnitudes (i.e., <30 μA), RGC spiking activity at the soma typically increased with stimulus amplitude. However, as the stimulus strength increased further (i.e., from 30 to 70 μA), the elicited spike count decreased substantially, creating a non-monotonic response profile as a function of stimulus amplitude. Arrows with index numbers correspond to the spiking profiles in panel **A**.

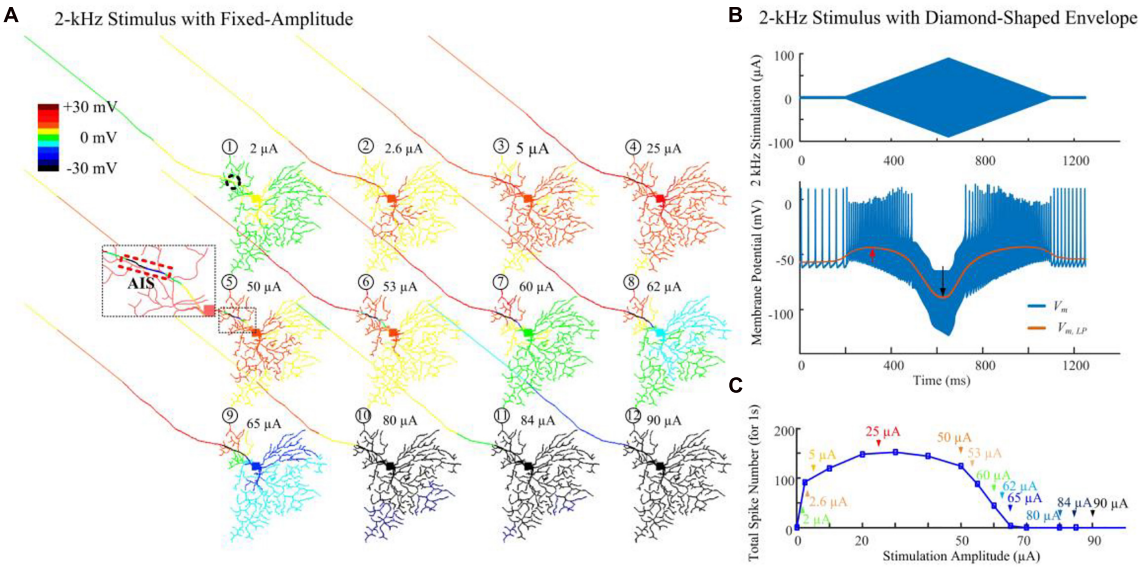

FIGURE 3 | Modeled spike suppression using high-amplitude 2-kHz HFS. **(A)** The relative membrane depolarization and hyperpolarization ($V_{m,LP} - V_{rest}$) induced by constant-amplitude 2-kHz extracellular stimulation immediately following eighty stimulus pulses (40 ms from stimulus onset). Here the membrane potential changes were low-pass filtered to better represent the low-amplitude, long-duration changes during and after HFS. Small amplitude pulses (2 μA) only depolarized neurites near the electrode (dashed circle). When pulses of 50 μA were delivered, local hyperpolarization was apparent at the AIS and neighboring regions (indicated by the zoomed subplot) while the soma and dendrites were still depolarized (region with warm colors). The spatial extent of hyperpolarized regions progressively increased with higher stimulation amplitudes. **(B)** Transient HFS-induced membrane depolarization (red arrow) and hyperpolarization (black arrow) under 2 kHz diamond envelope stimulations (900 ms duration, 2 μA baseline with a peak of 90 μA). **(C)** Number of somatic spikes evoked with a 1-s, 2-kHz HFS over a range of stimulus amplitudes. Index numbers and arrows correspond to each subplot in panel **A**.

proximal neurites were depolarized. As the stimulus strength was increased further, distal neurites began to exhibit progressively stronger hyperpolarization. The index numbers correspond to the arrows in **Figure 3C**.

Figure 3B illustrates an example of slow potential transitions between depolarization (red arrow) and hyperpolarization (black arrow) at the soma during HFS. Here, a 2-kHz stimulus with diamond-shaped envelope (900 ms duration, 2 μA baseline with a peak of 90 μA) was used. With low stimulus amplitudes, the somatic membrane potential became increasingly depolarized (indicated by the red arrow in **Figure 3B**). However, with stronger pulses, membrane hyperpolarization was increasingly evident (indicated by the black arrow in **Figure 3B**).

In another set of simulations, time-dependent membrane behavior was examined when the RGC was stimulated by 2-kHz HFS pulse trains of 10, 50, 62, or 80 μA amplitude. The

slow potentials across the entire cell were plotted at 20, 30, and 40 ms time points (at which steady state was reached) after stimulation onset (**Figure 4**). When 10-μA stimulus pulses were delivered, the membrane potential over the entire cell became increasingly depolarized over time. When stronger (e.g., 50 μA) stimulus pulses were delivered, hyperpolarization was evident in regions juxtaposing the stimulus electrode (indicated by the arrow and the cold colored regions in the zoomed subplot), while all other regions were depolarized. With even stronger stimulus pulses (e.g., 62 and 80 μA), most cellular regions became increasingly hyperpolarized over time. This HFS-induced hyperpolarization, when of sufficient strength, suppressed RGC excitation, contributing to the diminishing RGC spike rates with high-amplitude stimuli. During high-amplitude HFS, membrane potential does not completely recover from the hyperpolarization before the onset of each successive pulse in the train. The hyperpolarization thus increases over time with each successive pulse, eventually causing complete spike suppression.

Hyperpolarization Is Caused by Outward Currents at Neurites Near the Electrode

In **Figure 5A**, local V_e (extracellular voltage) and V_m (transmembrane potential) are recorded below the stimulus electrode as a function of stimulus amplitude. Given low-amplitude stimuli (<10 μA), the intracellular membrane potential (V_i) is the main contributor to V_m due to the low magnitude of V_e. However, with stimulus currents in excess of 20 μA, the magnitude of V_e becomes more dominant and starts exceeding the sodium reversal potential, resulting in the V_m range increasing in proportion to the increasing stimulus amplitude.

For a stimulus amplitude of 20 μA, V_m spanned from −40 to +30 mV at the peaks of the cathodic and anodic phases, respectively. Because V_m is always below the reversal potential of sodium (V_{Na}) activation of sodium channels by the stimuli therefore causes depolarization, and subsequently, action potentials. At stimulus amplitudes >20 μA, V_m begins to exceed V_{Na} (**Figure 5A**, shaded region). Sodium channel activation under such conditions elicits an outward current (**Figure 5B**), causing hyperpolarization. The magnitude of the outward sodium current increases with increasing stimulus strength, hyperpolarizing the affected neurites, thus suppressing spike generation.

In **Figure 5C**, HFS with a ramped amplitude (top panel) is used to demonstrate the transient cell membrane behavior for stimulus amplitudes ramping from 2 to 40 μA. The sodium channel activation (m) and inactivation (h) gating variables start to passively following the extracellular voltage changes with increasing HFS amplitude. At the same time, the outward sodium current becomes increasingly stronger with higher HFS amplitudes (bottom right panel).

Our simulations shown in **Figure 5** indicated that higher stimulation amplitudes can result in a change in the direction of the voltage-gated sodium current, such that the sodium current becomes increasingly outward.

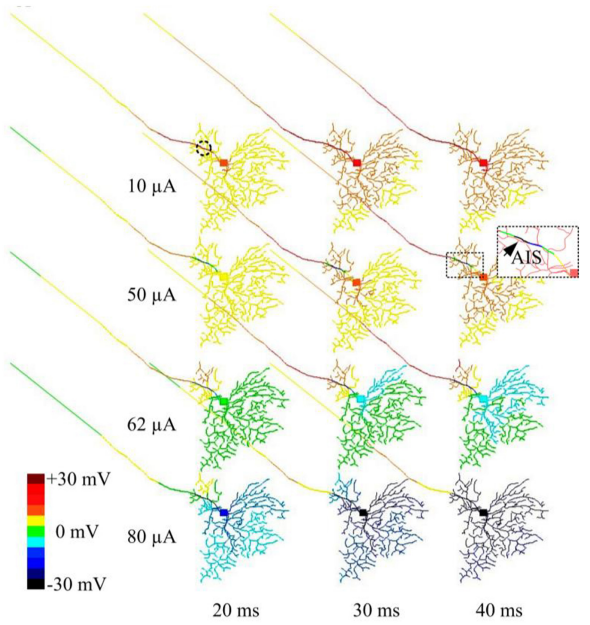

FIGURE 4 | Modeled time-dependent membrane potential suppression with constant-amplitude 2-kHz HFS. The RGC model was stimulated by 10, 50, 62, and 80 μA 2 kHz HFS. At each stimulation level, baseline membrane potential at multiple time points (20, 30, and 40 ms after the stimulation onset) were obtained. At a stimulus amplitude of 10 μA, membrane potential across the whole cell was increasingly depolarized over time. At an amplitude of 50 μA, cumulative local membrane hyperpolarization (indicated by the arrow) was evident near the stimulation electrode (dashed circle). For stimulus pulses of 62 and 80 μA, most cellular regions were increasingly hyperpolarized.

The Stimulus-Strength-Dependent Response Profile Can Be Altered by Sodium Channel Properties

According to the simulated sodium I-V relationship (**Figure 6A**), shifting the sodium reversal potential should advance or postpone the reversal of the sodium current, and consequently influence the non-monotonic response profile. To verify the hypothesis that the stimulus-strength-dependent response profile is influenced by V_{Na}, we progressively altered the sodium (**Figure 6B**) reversal potential throughout the cell, while examining the elicited spikes in response to a range of HFS amplitudes. A stimulus electrode was positioned epiretinally 40-μm above the RGC soma. The *in silico* results suggested that the strength-dependent response profiles observed at the soma were progressively altered by changing the sodium reversal potential. When V_{Na} was shifted to more negative values by changing extracellular sodium concentration, a marked decrease in the width and height of the response curve occurred (**Figure 6B**). Shifting the sodium reversal potential to more positive values resulted in the opposite effect. We also simulated the influence of other ionic currents such as I_K, I_{Ca}, I_h, and I_{CaT}. These currents did not significantly influence the response profile (see **Supplementary Figure S1**), suggesting the important role of sodium channel properties in shaping RGC responses to HFS.

To further validate the computational simulation results, the strength-dependent response profiles were also studied in *in vitro* experiments. In these experiments, we modified V_{Na}

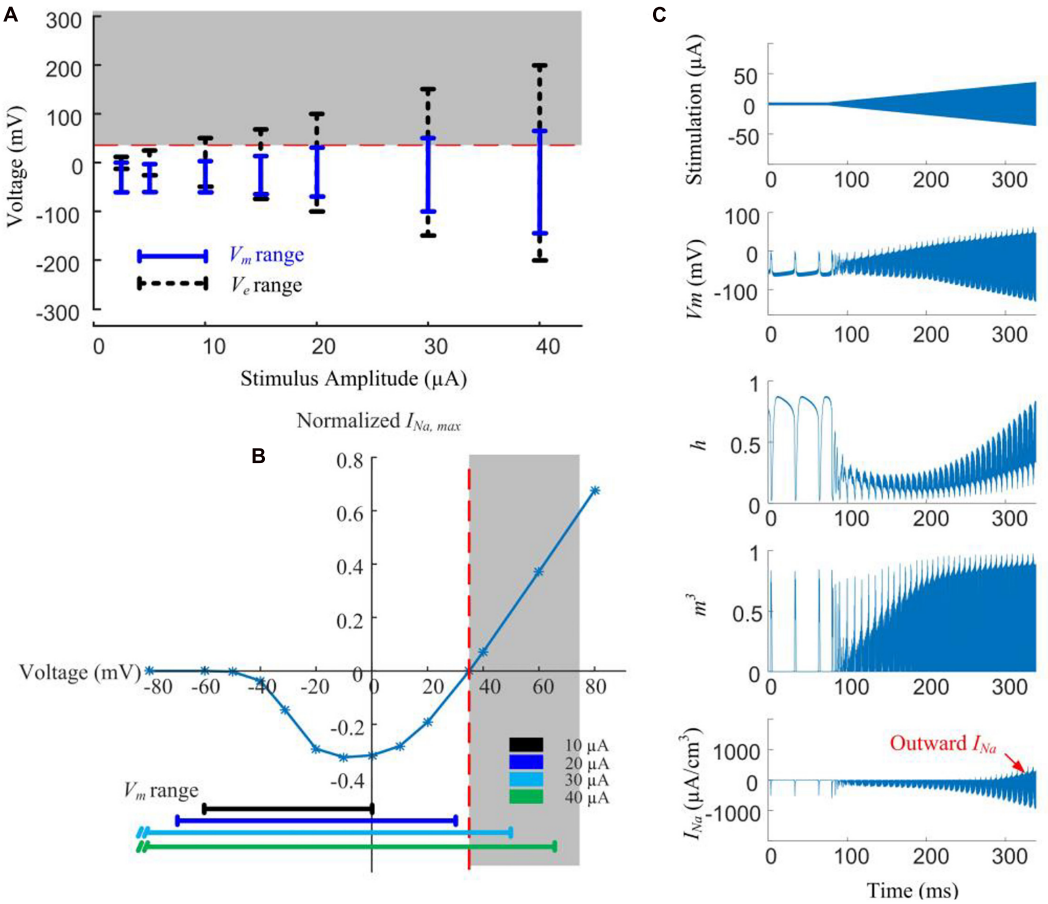

FIGURE 5 | Modeled reversal of sodium current with high-amplitude HFS induces spike inhibition. **(A)** Range of extracellular voltage (V_e) and transmembrane potential (V_m) determined from voltage value differences at cathodal and anodal phase peaks. The shaded region indicates the voltage range (>35 mV) where reversal of sodium current occurs. **(B)** Normalized I-V curve of model RGC peak sodium current. Peak sodium current ($I_{Na,max}$) becomes outward when V_m is above its reversal potential of 35 mV (the shaded region). This reversal occurs when the stimulus amplitude is higher than 20 μA. **(C)** Reversal of sodium current during 2-kHz amplitude-modulated stimulation (250 ms duration, 2 μA baseline ramping to a peak of 40 μA). For HFS amplitudes higher than 30 μA, the activation (*m*) and inactivation (*h*) gating variables of the sodium current (neurites below the electrode) are entrained by the extracellular voltage changes. The sodium current becomes increasingly outward with higher HFS amplitudes (indicated in the bottom right panel).

by altering the extracellular [Na^+] concentration. There are three different [Na^+] solutions, with their chemical components and concentrations listed in **Table 1**, along with the final Na^+ concentrations and calculated reversal potentials. In **Figure 6C**, despite the biological variance across RGCs, the total spikes evoked and the onset of spike suppression (i.e., stimulus amplitude associated with decreasing spike count) increased with increasing sodium reversal potential. In **Figures 6D1,D2**, normalized trends in HFS response curves are plotted as a function of [Na^+] extracellular concentration. *In vitro* and modeled data demonstrated the same trends in the total elicited spike number during all pulse trains, as well as the onset of the falling phase in the spike-stimulus curve, in which the total spike numbers saturate or decline. Both our modeling and *in vitro* results suggested that voltage-gated sodium channel properties can strongly alter the shape of the stimulus-strength-dependent response profile.

Stimulus Induced Spike Inhibition Can Be Maximized With Sufficient Pacing Rate

We conduct *in silico* investigations to explore the ability of HFS to suppress RGC spikes over a wide range of stimulus frequencies (1.0–9.0 kHz, in 0.25-kHz steps). We modified HFS waveforms to generate stimulus frequencies up to 9-kHz. Cathodic-first, charge-balanced biphasic stimuli with a pulse width of 40 μs per phase were used (**Figure 7A**). All pulse trains were 300 ms in duration. A stimulus electrode was positioned epiretinally 40-μm above the RGC soma. The simulated spikes were observed and counted at the soma. As seen in **Figure 7B1**, the model predicts that HFS-induced inhibition could be maximized by increasing HFS pulse train frequency. The RGC model exhibited an increased slope of the rising phase in the spike-stimulus curve (the phase in which spike counts increase with increasing stimulus current) and concomitantly, an earlier onset of the falling phase (in

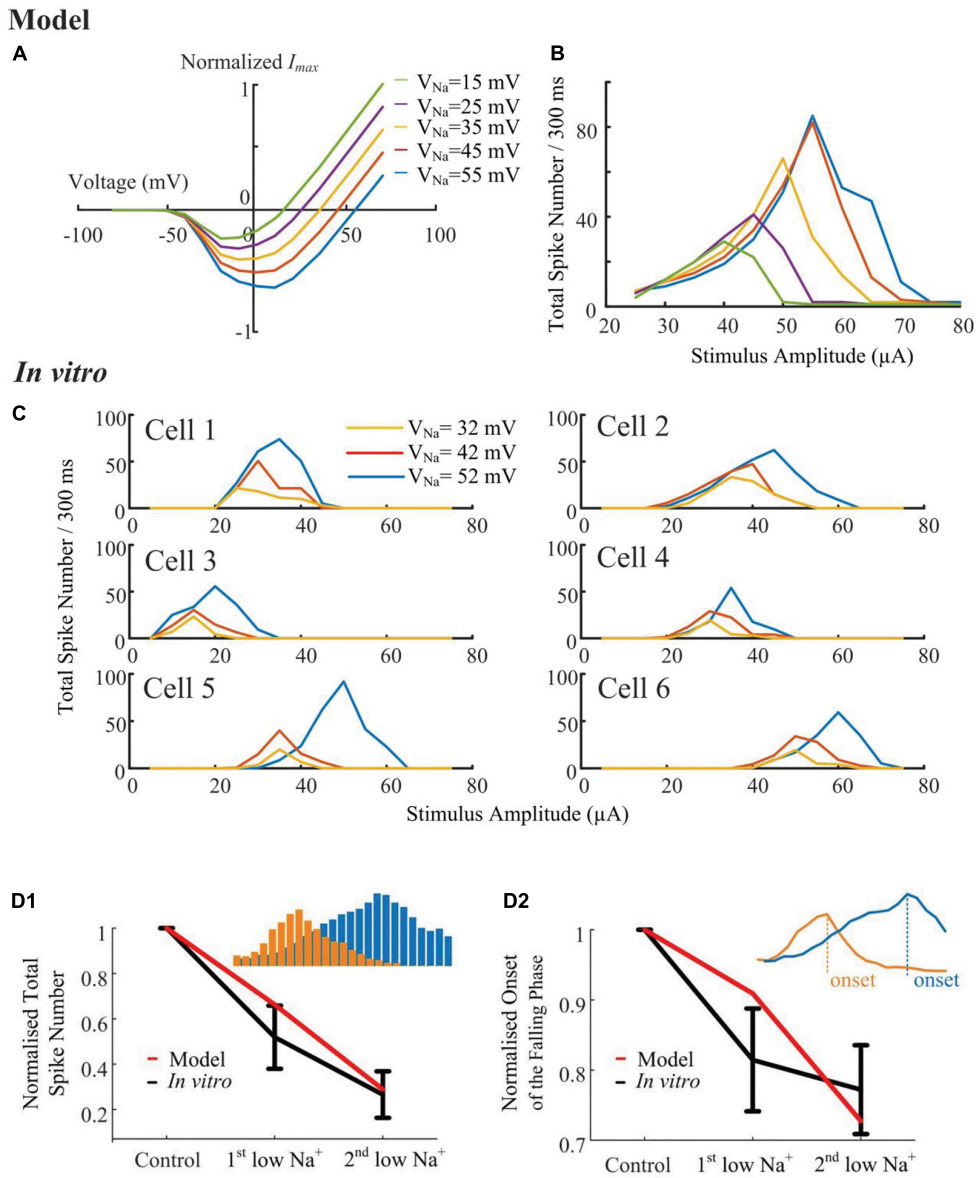

FIGURE 6 | Sodium reversal potentials alter the strength-dependent response. **(A)** Normalized I-V relationship of the model RGC sodium current for various reversal potentials (V_{Na}). Shifting V_{Na} to a more positive value delays the reversal of the sodium current. **(B)** The modeled stimulus-response profile for various V_{Na} values. Shifting V_{Na} to a more positive value increases RGC excitability during HFS, postponing the suppressive effect, and *vice versa*. **(C)** *In vitro* results of HFS response curves with different V_{Na} values (N = 6). The experimentally recorded RGC responses in mouse RGCs generally agree with the simulation results shown in panel B, with respect to the changes in amplitude and width of the response curve. **(D1,D2)** Comparison of model-prediction (red) and experimental data (black) in response to different Na^+ solutions. Model predictions and *in vitro* data exhibited similar normalized trends of the total elicited spike number during all pulse trains (D1), and the normalized onset of the falling phase in the spike-stimulus curve in which the total spike numbers saturated or declined (D2). Examples of total elicited spike number and onset was provided in subplots in D1 and D2, respectively. The error bars indicate standard deviation.

which the averaged total spike numbers saturate or decline). Examples of modeled stimulus-dependent RGC spikes at 1.0 and 8.25 kHz in **Figure 7B2** further indicated the strong frequency-dependent inhibition.

The strength-dependent response profiles at various stimulation frequencies were also observed in *in vitro* experiments. A range of frequencies (6.25, 5.0, 4.17, 3.33, 2.5, 2.0, and 1.67-kHz) of stimulation were used to show the stimulus-frequency-dependent RGC response. **Figure 7C1** shows the averaged (N = 6) stimulus-dependent response curves from 1.0 to 8.33 kHz. Each pulse train was delivered three times. The mean spike-stimulus curve was calculated for each cell and the overall mean was calculated again across all RGCs (N = 6). The standard error of mean (SEM) was calculated to estimate the variability of the estimated mean of population-based RGC spike rates. For comparison, *in vitro* data suggested

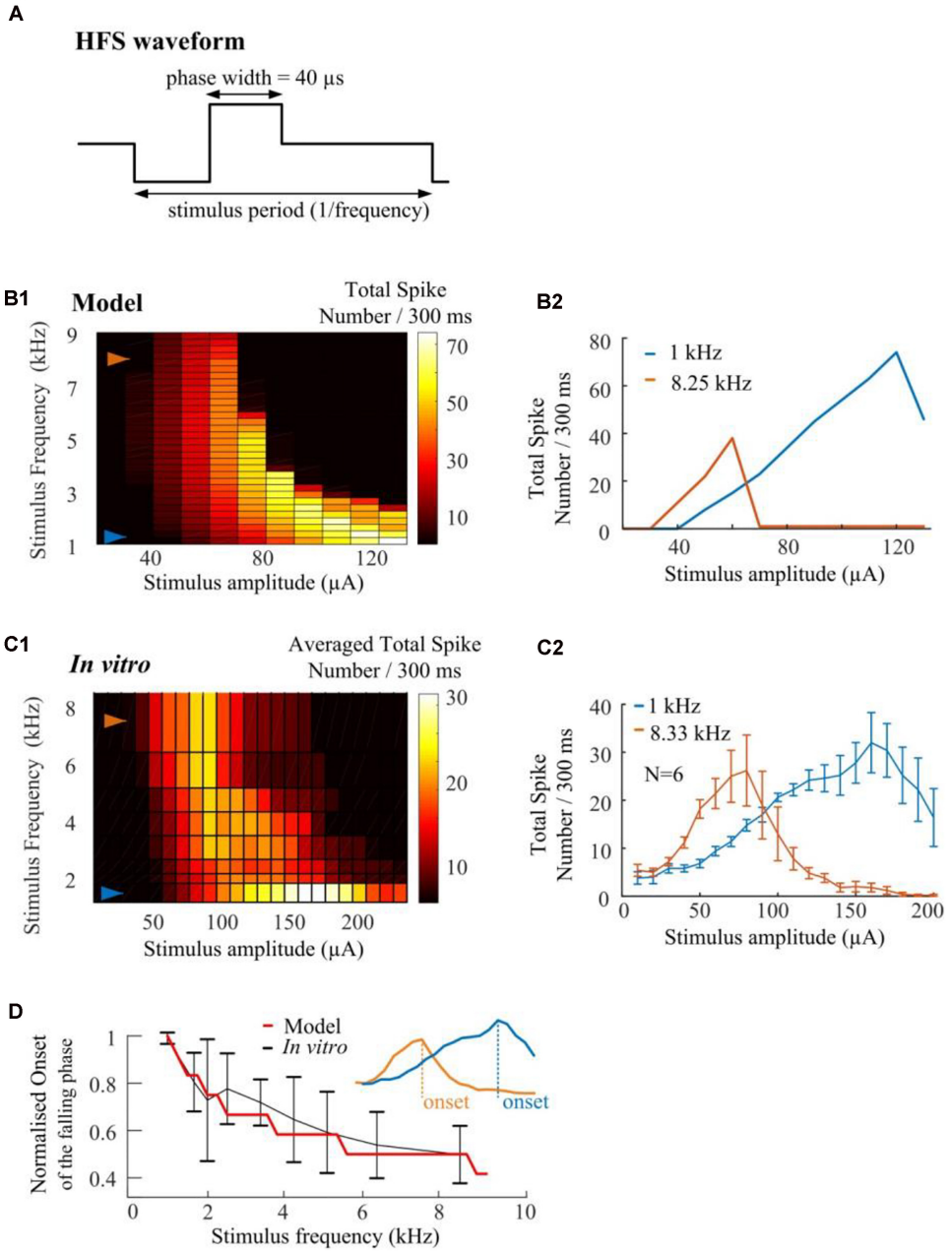

FIGURE 7 | High frequency pulse trains require less amplitude to inhibit spikes in both *in silico* simulations and *in vitro* experiments. **(A)** Cathodic-first, charge-balanced biphasic stimuli with a pulse width of 40 μs per phase were used. Inter-pulse delay was set to be rate-specific (from 1.0 to 9.0 kHz). **(B1)** *In silico* prediction of stimulus-dependent (from 10 to 130 μA) RGC spike behavior in response to a range of stimulus frequencies. All pulse trains were 300 ms in duration. **(B2)** Modeled stimulus-dependent RGC spikes at 1.0 and 8.25 kHz as indicated by arrows in B1. **(C1)** Experimentally-recorded activation map showing the averaged total spike number elicited in six mouse RGCs in response to a range of stimulation amplitudes (from 10 to 240 μA) and frequencies (from 1.0 to 8.33 kHz). Each stimulation pulse train was delivered three times. The mean spike-stimulus curve was calculated for each cell and the overall mean was calculated again across all RGCs. **(C2)** Whole-cell recording of 1-kHz and 8.33-kHz stimulus-dependent RGC spikes for six mouse RGCs with standard error bars. **(D)** Comparison of model-predicted (red) and experimental data (black) in response to multiple stimulus frequencies. Modeled and *in vitro* results demonstrated similar frequency-dependent onset of the falling phase in the spike-stimulus curve. An example of onset was shown in the subplot. The error bars indicate standard deviation.

frequency-dependent inhibition which highly agrees with model predictions (also see our examples of *in vitro* stimulus-dependent RGC spikes at 1.0 and 8.33 kHz in **Figure 7C2**).

In **Figure 7D**, normalized trends in the spike-stimulus curve are plotted as a function of stimulus frequency. *In vitro* and modeled data demonstrated the same trends in the onset

of the falling phase (as indicated in the subplot) in the spike-stimulus curve. In summary, both our modeling and *in vitro* results suggested that other than stimulus-strength dependency, HFS-induced spike suppression is also highly frequency-dependent and can be maximized by modulating stimulation frequencies.

DISCUSSION AND CONCLUSION

The non-monotonic stimulus-strength-dependent response has been previously reported in several retinal studies. Boinagrov et al. (2010) and Boinagrov et al. (2012) demonstrated the existence of an upper stimulus threshold using *in vitro* patch-clamp recording and a spherical model of the soma. In their studies, somatic responses were inhibited when the monophasic stimulation pulse was above a certain amplitude. They suggested that sodium current reversal was the primary reason for the inhibition. Rattay (2014) later conducted *in silico* investigations using a dendrite-soma-axon computational model to propose an anodal block phenomenon, in which an anodic surround of the focal cathodic pulse caused the nerve membrane on the outer wall of a pipette to become hyperpolarized due to current converging toward the tip of the electrode. This upper threshold phenomenon was further studied using charge-balanced biphasic pulses of various amplitude and phase duration (Meng et al., 2018), suggesting that an upper threshold in the soma of RGCs can block axonal excitation only under limited stimulation conditions. However, these studies used electrical stimulation with single monophasic or biphasic pulses. The precise mechanisms underlying HFS-induced strength-dependent activation remain unclear. In this study, we used *in silico* investigations to guide *in vitro* design. We explored the possible mechanisms underlying the HFS-induced non-monotonic spiking response as a function of stimulus amplitude, and how this feature is affected by RGC biophysical properties. Our results indicate that mechanisms underlying the measured strength-dependent response are multifaceted, namely: (1) localized membrane hyperpolarization is generated near the stimulus electrode and subsequently propagates to other neurites to suppress RGC excitation; (2) influence of sodium channel kinetics can strongly alter the shape of the stimulus-strength-dependent response profile; suggesting the important role of sodium channel properties in shaping RGC responses to HFS; (3) the inhibitory effect induced by electric stimulation can be maximized with sufficient stimulation rate. In addition, our results indicate that the non-monotonic RGC response to HFS does not arise through synaptic circuitry, since all *in vitro* results were observed after application of synaptic blockade.

Other Possible Mechanisms Underlying the Non-monotonic Response Profile

Studies in the peripheral nervous system suggest that strong electrical stimulation may induce tonic membrane depolarization, keeping the channels in the inactivated state, thereby increasing activation threshold and preventing further spiking (Kilgore and Bhadra, 2004; Williamson and Andrews, 2005). Bianchi et al. (2012) also explored this "depolarization block" phenomenon during intracellular current injections using a computational model of CA1 pyramidal neurons. More recently, Kameneva et al. (2016) used this phenomenon to explain RGC spike inhibition induced by 2-kHz HFS. In our study, the depolarization block does contribute to RGC spike inhibition at the beginning of the falling phase in the spike-stimulus curve, in which the total spike numbers saturate (see the spike-stimulus curve between 25 and 53 μA in **Figure 3A**). However, at stimulus amplitudes where the total spike numbers begin to decline significantly (>60 μA in **Figure 3A**), progressively stronger hyperpolarization become dominant in inhibiting neuronal activation. Kameneva et al. hypothesized that the HFS-induced stimulus-response pattern is caused by the cell-specific potassium channel density and the size of the axonal sodium channel band. However, to our knowledge, there is no direct experimental evidence showing potassium channel distribution across different retinal neurons. Furthermore, an experimental study revealed that not all RGC types have unique axonal sodium channel band properties (Fried et al., 2009). Therefore, further studies are required to better understand the factors that shape the responses of functionally-distinct retinal neurons to HFS.

The second hypothesis is the inability of neurons to fully recover from their refractory period during HFS (Kilgore and Bhadra, 2004). This was, however, questioned as a possible mechanism underlying high-amplitude and high-frequency stimulations by previous modeling (Kilgore and Bhadra, 2004) and experimental studies (Bowman and McNeal, 1986), which showed that neurons are able to reliably maintain high spike rates during HFS. Since the refractory period is mainly controlled by sodium channel kinetics and our results suggested the importance of sodium channel properties in shaping RGC responses to HFS, we believe that refractory period of a neuron could contribute to HFS-induced RGC inhibition. This possibility, however, is likely dependent on the sodium channel subtype(s) expressed and their distribution in a particular neuronal type. Non-uniform distribution of variable voltage-gated sodium channels has been identified in mammalian RGCs (Fjell et al., 1997; Boiko et al., 2003; Van Wart et al., 2007; O'brien et al., 2008), and these sodium channels may respond differently to identical stimulus frequencies, due to their specific absolute and relative refectory periods. For example, Na(v) 1.2 has been reported to show a greater accumulation of inactivation at higher frequencies of stimulation than Na(v) 1.6 (Rush et al., 2005). Our *in vitro* results shown in **Figure 6** and the results from others (Cai et al., 2011, 2013; Twyford et al., 2014; Guo et al., 2018b) demonstrate the variances of HFS-induced inhibition across different RGCs. Additional modeling studies using a wide range of sodium channel properties will be required to elucidate the mechanisms underlying these recorded variances. A comprehensive model capable of describing RGC intrinsic diversity and their characteristic response to HFS would be a major improvement in this field (Guo et al., 2014, 2018a; Kameneva et al., 2016).

Improving the Quality of Electrical Stimulation

Without knowing how best to stimulate the retina, the vision quality elicited by retinal prosthetic devices will remain poor and unnatural. Previous *in vitro* and modeling studies indicated that appropriate HFS neuromodulation may elicit preferential excitation of different RGCs in a manner similar to RGC responses to light in a healthy retina, i.e., ON and OFF RGCs which respond with an increase in neural spiking activity to an increase or decrease in light intensity, respectively (Cai et al., 2013; Twyford et al., 2014; Guo et al., 2018b). In these studies, to preferentially activate one neuronal type without simultaneously producing substantial responses in another type, the cell types should have different non-monotonic stimulus-strength-dependent responses. Better understanding of mechanisms underlying stimulus-strength-dependent responses may shed light on more sophisticated stimulation strategies to improve the efficacy of retinal prosthetic devices. It remains to be seen if knowledge of RGC mechanisms can be used for practical stimulation strategy design in visual prostheses. For example, further *in vitro* and modeling studies are required to validate the reliability and generalizability of the non-monotonic nature of population-based RGC responses. Moreover, current modeling results are largely limited to somatic simulations, due to the lack of experimental data recorded in other neural processes. Recent modeling studies suggest that inhibition induced by electrical stimulation in the soma may not necessarily occur in the axon (Rattay, 2014; Meng et al., 2018). However, *in vivo* studies indicate that high-amplitude inhibition in the retina could occur at higher visual processing centers (Barriga-Rivera et al., 2017). In our future work, a computational model will be validated by experimental data recorded in RGC axons, to better study spike initiation and propagation. This updated model should shed further insights into the complex mechanisms responsible for HFS-induced inhibition.

Summary

In this study, using previously optimized ionic channel distributions and kinetic parameters for each cellular region and incorporating detailed cell morphology, we were able to predict RGC strength-dependent stimulus response patterns observed experimentally. Our computational modeling approaches allowed us to investigate a wide range of biophysical properties and stimulation settings beyond those recorded in the initial biological dataset, guiding further experimental design. The electric field can be accurately described by mathematical formalisms, and the neurons can be "probed" at resolutions well beyond those achievable by today's state-of-the-art biological techniques, furthering our understanding of the effects of novel stimulus strategies by simulating RGC stimulus-response profiles over a larger stimulation parameter space than have previously been explored.

ETHICS STATEMENT

All procedures were approved by the UNSW Animal Care and Ethics Committee and were carried out in compliance with the Australian Code of Practice for the Care and Use of Animals for Scientific Purposes.

AUTHOR CONTRIBUTIONS

TG, DT, SF, SD, and NL conceived and designed the study. CY, TG, and DT performed the *in vitro* experiments. TG and DT performed the computational simulations. TG, DT, AAA, GS, JM, PT, SF, and NL analyzed the data. All the authors drafted the manuscript and read and approved of the final manuscript.

FUNDING

This research was supported by the Australian National Health and Medical Research Council (RG 1063046, RG 1087224), as well as by the United States Veterans Administration (1I01RX000350), and the NIH (NS-U01099700). DT was supported by an Australian National Health and Medical Research Council CJ Martin Fellowship (APP1054058).

SUPPLEMENTARY MATERIAL

The Supplementary Material for this article can be found online at: https://www.frontiersin.org/articles/10.3389/fnins.2019.00413/full#supplementary-material

FIGURE S1 | Simulated influence of multiple ionic channels in shaping RGC stimulus-strength-dependent properties. **(A)** delayed rectifier potassium channel (IK). **(B)** hyperpolarization-activated non-selective cationic current (Ih). **(C)** L-type Calcium channel (ICa). **(D)** low-threshold voltage-activated calcium current (ICaT). Conductance of each channel was set to be 50, 100, and 150% in the RGC model. Model settings and stimulation parameters are as same as in **Figure 1**.

REFERENCES

Barriga-Rivera, A., Guo, T. R., Yang, C. Y., Al Abed, A., Dokos, S., Lovell, N. H., et al. (2017). High-amplitude electrical stimulation can reduce elicited neuronal activity in visual prosthesis. *Sci. Rep.* 7:42682. doi: 10.1038/srep42682

Bianchi, D., Marasco, A., Limongiello, A., Marchetti, C., Marie, H., Tirozzi, B., et al. (2012). On the mechanisms underlying the depolarization block in the spiking dynamics of CA1 pyramidal neurons. *J. Comput. Neurosci.* 33, 207–225. doi: 10.1007/s10827-012-0383-y

Boiko, T., Van Wart, A., Caldwell, J. H., Levinson, S. R., Trimmer, J. S., and Matthews, G. (2003). Functional specialization of the axon initial segment by isoform-specific sodium channel targeting. *J. Neurosci.* 23, 2306–2313. doi: 10.1523/jneurosci.23-06-02306.2003

Boinagrov, D., Loudin, J., and Palanker, D. (2010). Strength-duration relationship for extracellular neural stimulation: numerical and analytical models. *J. Neurophysiol.* 104, 2236–2248. doi: 10.1152/jn.00343.2010

Boinagrov, D., Pangratz-Fuehrer, S., Suh, B., Mathieson, K., Naik, N., and Palanker, D. (2012). Upper threshold of extracellular neural stimulation. *J. Neurophysiol.* 108, 3233–3238. doi: 10.1152/jn.01058.2011

Bowman, B. R., and McNeal, D. R. (1986). Response of single alpha motoneurons to high-frequency pulse trains. Firing behavior and conduction block phenomenon. *Appl. Neurophysiol.* 49, 121–138. doi: 10.1159/000100137

Cai, C., Twyford, P., and Fried, S. (2013). The response of retinal neurons to high-frequency stimulation. *J. Neural Eng.* 10:036009. doi: 10.1088/1741-2560/10/3/036009

Cai, C. S., Ren, Q. S., Desai, N. J., Rizzo, J. F., and Fried, S. I. (2011). Response variability to high rates of electric stimulation in retinal ganglion cells. *J. Neurophysiol.* 106, 153–162. doi: 10.1152/jn.00956.2010

Deep-Brain Stimulation for Parkinson's Disease Study Group, Obeso, J. A., Olanow, C. W., Rodriguez-Oroz, M. C., Krack, P., Kumar, R., et al. (2001). Deep-brain stimulation of the subthalamic nucleus or the pars interna of the globus pallidus in Parkinson's disease. *N. Engl. J. Med.* 345, 956–963. doi: 10.1056/NEJMoa000827

Fjell, J., Dib-Hajj, S., Fried, K., Black, J., and Waxman, S. (1997). Differential expression of sodium channel genes in retinal ganglion cells. *Brain Res. Mol. Brain Res.* 50, 197–204. doi: 10.1016/s0169-328x(97)00187-3

Fohlmeister, J. F., and Miller, R. F. (1997). Mechanisms by which cell geometry controls repetitive impulse firing in retinal ganglion cells. *J. Neurophysiol.* 78, 1948–1964. doi: 10.1152/jn.1997.78.4.1948

Fried, S. I., Lasker, A. C., Desai, N. J., Eddington, D. K., and Rizzo, J. F. III. (2009). Axonal sodium-channel bands shape the response to electric stimulation in retinal ganglion cells. *J. Neurophysiol.* 101, 1972–1987. doi: 10.1152/jn.91081.2008

Guenther, T., Lovell, N. H., and Suaning, G. J. (2012). Bionic vision: system architectures - a review. *Expert Rev. Med. Dev.* 9, 33–48. doi: 10.1586/Erd.11.58

Guo, T., Tsai, D., Bai, S., Morley, J. W., Suaning, G. J., Lovell, N. H., et al. (2014). Understanding the retina: a review of computational models of the retina from the single cell to the network level. *Crit. Rev. Biomed. Eng.* 42, 419–436. doi: 10.1615/critrevbiomedeng.2014011732

Guo, T., Tsai, D., Morley, J. W., Suaning, G. J., Kameneva, T., Lovell, N. H., et al. (2016). Electrical activity of ON and OFF retinal ganglion cells: a modelling study. *J. Neural Eng.* 13:025005. doi: 10.1088/1741-2560/13/2/025005

Guo, T., Tsai, D., Muralidharan, M., Li, M., Suaning, G. J., Morley, J. W., et al. (2018a). Computational models and tools for developing sophisticated stimulation strategies for retinal neuroprostheses. *Conf. Proc. IEEE Eng. Med. Biol. Soc.* 2018, 2248–2251. doi: 10.1109/EMBC.2018.8512748

Guo, T., Yang, C. Y., Tsai, D., Muralidharan, M., Suaning, G. J., Morley, J. W., et al. (2018b). Closed-loop efficient searching of optimal electrical stimulation parameters for preferential excitation of retinal ganglion cells. *Front. Neurosci.* 12:168. doi: 10.3389/fnins.2018.00168

Gybels, J. (1981). Electrical-stimulation of the nervous-system in the treatment of chronic pain. *Electroen. Clin. Neuro.* 51:86.

Hines, M. L., and Carnevale, N. T. (1997). The NEURON simulation environment. *Neural Comp.* 9, 1179–1209. doi: 10.1162/neco.1997.9.6.1179

Horsager, A., Greenwald, S. H., Weiland, J. D., Humayun, M. S., Greenberg, R. J., McMahon, M. J., et al. (2009). Predicting visual sensitivity in retinal prosthesis patients. *Invest. Ophthalmol. Vis. Sci.* 50, 1483–1491. doi: 10.1167/iovs.08-2595

Jeng, J., Tang, S., Molnar, A., Desai, N. J., and Fried, S. I. (2011). The sodium channel band shapes the response to electric stimulation in retinal ganglion cells. *J. Neural Eng.* 8:036022. doi: 10.1088/1741-2560/8/3/036022

Joseph, L., and Butera, R. J. (2011). High-frequency stimulation selectively blocks different types of fibers in frog sciatic nerve. *IEEE Trans. Neural Syst. Rehabil. Eng.* 19, 550–557. doi: 10.1109/TNSRE.2011.2163082

Kameneva, T., Maturana, M. I., Hadjinicolaou, A. E., Cloherty, S. L., Ibbotson, M. R., Grayden, D. B., et al. (2016). Retinal ganglion cells: mechanisms underlying depolarization block and differential responses to high frequency electrical stimulation of ON and OFF cells. *J. Neural Eng.* 13:016017. doi: 10.1088/1741-2560/13/1/016017

Kilgore, K. L., and Bhadra, N. (2004). Nerve conduction block utilising high-frequency alternating current. *Med. Biol. Eng. Comput.* 42, 394–406. doi: 10.1007/bf02344716

Litvak, L., Delgutte, B., and Eddington, D. (2001). Auditory nerve fiber responses to electric stimulation: modulated and unmodulated pulse trains. *J. Acoust. Soc. Am.* 110, 368–379. doi: 10.1121/1.1375140

Litvak, L. M., Smith, Z. M., Delgutte, B., and Eddington, D. K. (2003). Desynchronization of electrically evoked auditory-nerve activity by high-frequency pulse trains of long duration. *J. Acoust. Soc. Am.* 114(4 Pt 1):20662078.

McKay, C. M., Chandan, K., Akhoun, I., Siciliano, C., and Kluk, K. (2013). Can ECAP measures be used for totally objective programming of cochlear implants? *J. Assoc. Res. Otolaryngol.* 14, 879–890. doi: 10.1007/s10162-013-0417-419

Meng, K., Fellner, A., Rattay, F., Ghezzi, D., Meffin, H., Ibbotson, M. R., et al. (2018). Upper stimulation threshold for retinal ganglion cell activation. *J. Neural Eng.* 15:046012. doi: 10.1088/1741-2552/aabb7d

Mueller, J. K., and Grill, W. M. (2013). Model-based analysis of multiple electrode array stimulation for epiretinal visual prostheses. *J. Neural Eng.* 10:036002. doi: 10.1088/1741-2560/10/3/036002

O'brien, B. J., Caldwell, J. H., Ehring, G. R., Bumsted, O., Brien, K. M., Luo, S., et al. (2008). Tetrodotoxin-resistant voltage-gated sodium channels Nav1.8 and Nav1.9 are expressed in the retina. *J. Comp. Neurol.* 508, 940–951. doi: 10.1002/cne.21701

Palanker, D., Vankov, A., Huie, P., and Baccus, S. (2005). Design of a high-resolution optoelectronic retinal prosthesis. *J. Neural Eng.* 2, S105–S120. doi: 10.1088/1741-2560/2/1/012

Rattay, F. (2014). On the upper threshold phenomenon of extracellular neural stimulation. *J. Neurophysiol.* 112, 2664–2665. doi: 10.1152/jn.00323.2014

Rizzo, J. F., and Wyatt, J. (1997). Prospects for a visual prosthesis. *Neuroscientist* 3, 251–262. doi: 10.1177/107385849700300413

Rush, A. M., Dib-Hajj, S. D., and Waxman, S. G. (2005). Electrophysiological properties of two axonal sodium channels, Na(v)1.2 and Nav1.6, expressed in mouse spinal sensory neurones. *J. Physiol.* 564, 803–815. doi: 10.1113/jphysiol.2005.083089

Tiede, J., Brown, L., Gekht, G., Vallejo, R., Yearwood, T., and Morgan, D. (2013). Novel spinal cord stimulation parameters in patients with predominant back pain. *Neuromodulation* 16, 370–375. doi: 10.1111/ner.12032

Tsai, D., Chen, S., Protti, D. A., Morley, J. W., Suaning, G. J., and Lovell, N. H. (2012). Responses of retinal ganglion cells to extracellular electrical stimulation, from single cell to population: model-based analysis. *PLoS One* 7:e53357. doi: 10.1371/journal.pone.0053357

Tsai, D., Morley, J. W., Suaning, G. J., and Lovell, N. H. (2009). Direct activation and temporal response properties of rabbit retinal ganglion cells following subretinal stimulation. *J. Neurophysiol.* 102, 2982–2993. doi: 10.1152/jn.00545.2009

Twyford, P., Cai, C., and Fried, S. (2014). Differential responses to high-frequency electrical stimulation in ON and OFF retinal ganglion cells. *J. Neural Eng.* 11:025001. doi: 10.1088/1741-2560/11/2/025001

Van Buyten, J. P., Al-Kaisy, A., Smet, I., Palmisani, S., and Smith, T. (2013). High-frequency spinal cord stimulation for the treatment of chronic back pain patients: results of a prospective multicenter european clinical study. *Neuromodulation* 16, 59–66. doi: 10.1111/ner.12006

Van Wart, A., Trimmer, J. S., and Matthews, G. (2007). Polarized distribution of ion channels within microdomains of the axon initial segment. *J. Comp. Neurol.* 500, 339–352. doi: 10.1002/cne.21173

Weiland, J. D., Liu, W., and Humayun, M. S. (2005). Retinal prosthesis. *Annu. Rev. Biomed. Eng.* 7, 361–401. doi: 10.1146/annurev.bioeng.7.060804.100435

Williamson, R. P., and Andrews, B. J. (2005). Localized electrical nerve blocking. *IEEE Trans. Biomed. Eng.* 52, 362–370. doi: 10.1109/Tbme.2004.842790

Yang, C. Y., Tsai, D., Guo, T., Dokos, S., Suaning, G. J., Morley, J. W., et al. (2018). Differential electrical responses in retinal ganglion cell subtypes: effects of synaptic blockade and stimulating electrode location. *J. Neural Eng.* 15:046020. doi: 10.1088/1741-2552/aac315

Conflict of Interest Statement: The authors declare that the research was conducted in the absence of any commercial or financial relationships that could be construed as a potential conflict of interest.

Copyright © 2019 Guo, Tsai, Yang, Al Abed, Twyford, Fried, Morley, Suaning, Dokos and Lovell. This is an open-access article distributed under the terms of the Creative Commons Attribution License (CC BY). The use, distribution or reproduction in other forums is permitted, provided the original author(s) and the copyright owner(s) are credited and that the original publication in this journal is cited, in accordance with accepted academic practice. No use, distribution or reproduction is permitted which does not comply with these terms.

frontiers in Neuroscience

ERRATUM
published: 28 August 2019
doi: 10.3389/fnins.2019.00910

Erratum: Mediating Retinal Ganglion Cell Spike Rates Using High-Frequency Electrical Stimulation

*Frontiers Production Office**

Frontiers Media SA, Lausanne, Switzerland

Keywords: neuromodulation, retinal ganglion cell, high-frequency electrical stimulation, retinal implant, computational modeling, *in vitro* patch-clamp

OPEN ACCESS

Approved by:
Frontiers Editorial Office, Frontiers Media SA, Switzerland

***Correspondence:**
Frontiers Production Office
production.office@frontiersin.org

Specialty section:
This article was submitted to Neuroprosthetics, a section of the journal Frontiers in Neuroscience

Received: *16 August 2019*
Accepted: *16 August 2019*
Published: *28 August 2019*

Citation:
Frontiers Production Office (2019) Erratum: Mediating Retinal Ganglion Cell Spike Rates Using High-Frequency Electrical Stimulation. Front. Neurosci. 13:910. doi: 10.3389/fnins.2019.00910

An Erratum on

Mediating Retinal Ganglion Cell Spike Rates Using High-Frequency Electrical Stimulation
by Guo, T., Tsai, D., Yang, C. Y., Al Abed, A., Twyford, P., Fried, S. I., et al. (2019). Front. Neurosci. 13:413. doi: 10.3389/fnins.2019.00413

Due to a production error, the captions within **Figure 6C** artwork have been incorrectly labeled as "blue (32 mV), red (42 mV), and orange (52 mV)" from top to bottom, instead of "orange (32 mV), red (42 mV), and blue (52 mV)". The corrected **Figure 6** appears below.

The publisher apologizes for this mistake. The original article has been updated.

Copyright © 2019 Frontiers Production Office. This is an open-access article distributed under the terms of the Creative Commons Attribution License (CC BY). The use, distribution or reproduction in other forums is permitted, provided the original author(s) and the copyright owner(s) are credited and that the original publication in this journal is cited, in accordance with accepted academic practice. No use, distribution or reproduction is permitted which does not comply with these terms.

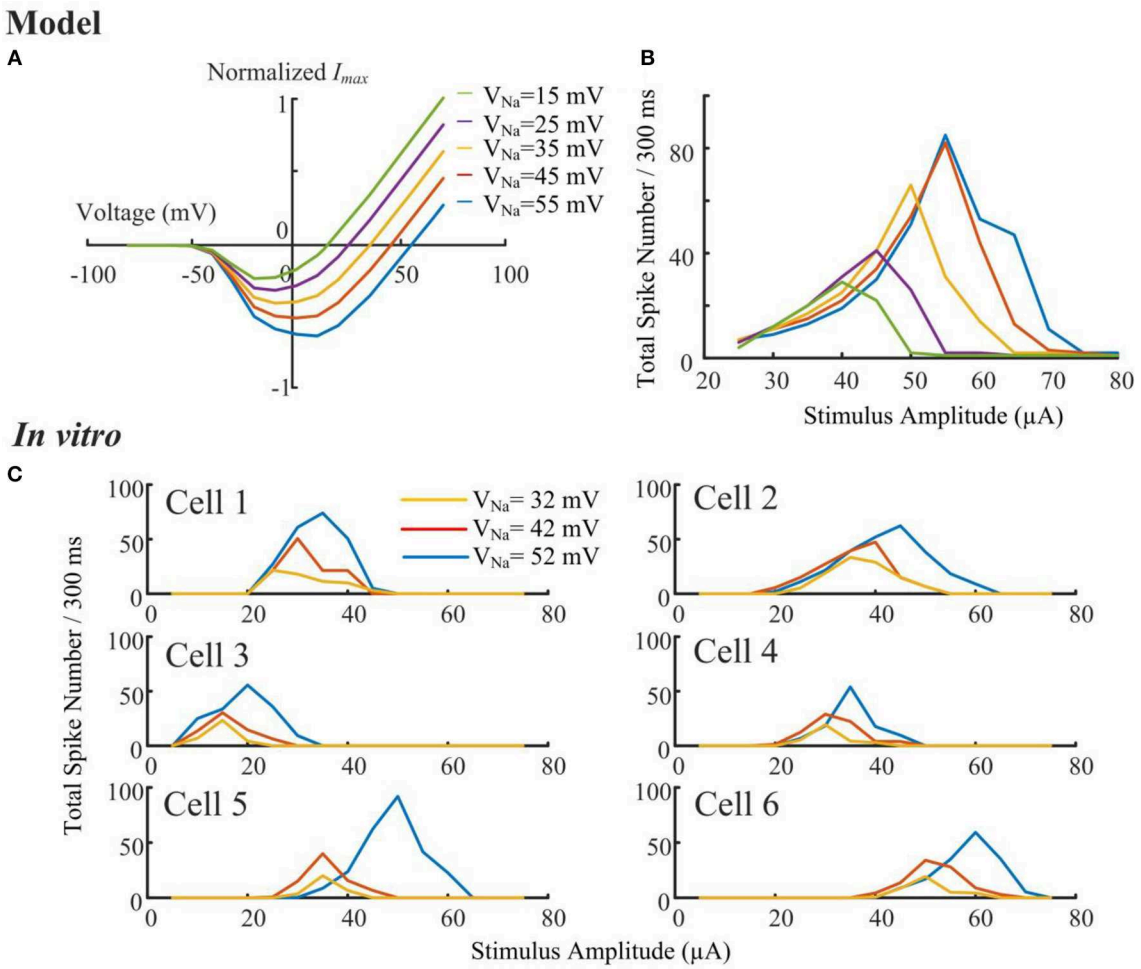

FIGURE 6 | Sodium reversal potentials alter the strength-dependent response. **(A)** Normalized I-V relationship of the model RGC sodium current for various reversal potentials (V_{Na}). Shifting V_{Na} to a more positive value delays the reversal of the sodium current. **(B)** The modeled stimulus-response profile for various V_{Na} values. Shifting V_{Na} to a more positive value increases RGC excitability during HFS, postponing the suppressive effect, and *vice versa*. **(C)** *In vitro* results of HFS response curves with different V_{Na} values ($N = 6$). The experimentally recorded RGC responses in mouse RGCs generally agree with the simulation results shown in panel B, with respect to the changes in amplitude and width of the response curve. **(D1,D2)** Comparison of model-prediction (red) and experimental data (black) in response to different Na^+ solutions. Model predictions and *in vitro* data exhibited similar normalized trends of the total elicited spike number during all pulse trains (D1), and the normalized onset of the falling phase in the spike-stimulus curve in which the total spike numbers saturated or declined (D2). Examples of total elicited spike number and onset was provided in subplots in D1 and D2, respectively. The error bars indicate standard deviation.

frontiers in Neuroscience

ORIGINAL RESEARCH
published: 28 May 2019
doi: 10.3389/fnins.2019.00493

Revealing Spatial and Temporal Patterns of Cell Death, Glial Proliferation, and Blood-Brain Barrier Dysfunction Around Implanted Intracortical Neural Interfaces

*Steven M. Wellman[1,2], Lehong Li[1], Yalikun Yaxiaer[3], Ingrid McNamara[1] and Takashi D. Y. Kozai[1,2,4,5,6]**

[1] Department of Bioengineering, University of Pittsburgh, Pittsburgh, PA, United States, [2] Center for the Neural Basis of Cognition, Pittsburgh, PA, United States, [3] Eberly College of Science, Pennsylvania State University, University Park, PA, United States, [4] Center for Neuroscience, University of Pittsburgh, Pittsburgh, PA, United States, [5] McGowan Institute of Regenerative Medicine, University of Pittsburgh, Pittsburgh, PA, United States, [6] NeuroTech Center, University of Pittsburgh Brain Institute, Pittsburgh, PA, United States

OPEN ACCESS

Edited by:
Ulrich G. Hofmann, University Medical Center Freiburg, Germany

Reviewed by:
Matthias Kirsch, University of Freiburg, Germany
Brent Winslow, Design Interactive, United States

***Correspondence:**
Takashi D. Y. Kozai
tdk18@pitt.edu

Specialty section:
This article was submitted to Neural Technology, a section of the journal Frontiers in Neuroscience

Received: *15 January 2019*
Accepted: *29 April 2019*
Published: *28 May 2019*

Citation:
Wellman SM, Li L, Yaxiaer Y, McNamara I and Kozai TDY (2019) Revealing Spatial and Temporal Patterns of Cell Death, Glial Proliferation, and Blood-Brain Barrier Dysfunction Around Implanted Intracortical Neural Interfaces. Front. Neurosci. 13:493. doi: 10.3389/fnins.2019.00493

Improving the long-term performance of neural electrode interfaces requires overcoming severe biological reactions such as neuronal cell death, glial cell activation, and vascular damage in the presence of implanted intracortical devices. Past studies traditionally observe neurons, microglia, astrocytes, and blood-brain barrier (BBB) disruption around inserted microelectrode arrays. However, analysis of these factors alone yields poor correlation between tissue inflammation and device performance. Additionally, these studies often overlook significant biological responses that can occur during acute implantation injury. The current study employs additional histological markers that provide novel information about neglected tissue components—oligodendrocytes and their myelin structures, oligodendrocyte precursor cells, and BBB -associated pericytes—during the foreign body response to inserted devices at 1, 3, 7, and 28 days post-insertion. Our results reveal unique temporal and spatial patterns of neuronal and oligodendrocyte cell loss, axonal and myelin reorganization, glial cell reactivity, and pericyte deficiency both acutely and chronically around implanted devices. Furthermore, probing for immunohistochemical markers that highlight mechanisms of cell death or patterns of proliferation and differentiation have provided new insight into inflammatory tissue dynamics around implanted intracortical electrode arrays.

Keywords: oligodendrocytes, NG2 glia, pericytes, tissue-electrode interface, neurodegeneration, gliosis, glial cell division, inflammation

INTRODUCTION

Advancements in neural interface technology have provided powerful tools for investigative neuroscience and clinical therapy involving neurodegenerative disease and neurological deficiencies (Schwartz et al., 2006; Kozai et al., 2015b; Iordanova et al., 2018; Michelson and Kozai, 2018; Michelson et al., 2018a; Stocking et al., 2019). Specifically, penetrating intracortical electrodes with high spatial resolution can record and stimulate individual neurons or neuronal

populations locally within the brain (Buzsáki, 2004). However, due to a lack of fundamental knowledge regarding neural and glial circuits, neuromodulatory and stimulating devices experience high variability and unpredictability in their use (Sillay et al., 2010; Cheung et al., 2013; Gittis, 2018). Additionally, these probes are often debilitated by inflammatory tissue reactions that induce neural loss, impairing recording performances (Potter et al., 2012; Kozai et al., 2015c). Overwhelming biological responses to these inserted electrodes need to be addressed in order to improve the quality and robustness of chronically implanted intracortical arrays (Tresco and Winslow, 2011; Wellman et al., 2017, 2018; Wellman and Kozai, 2017). However, attempts at correlating a decline in signal quality with specific inflammatory events have previously proven difficult (Kozai et al., 2014c, 2015a; McCreery et al., 2016; Salatino et al., 2017; Michelson et al., 2018b).

Microglia are one of the first responders to probe insertion injury, polarizing and extending cellular processes within the first hour after implantation in an effort to encapsulate the probe (Kozai et al., 2012b, 2016b; Eles et al., 2017). During the course of implantation, reactive astrocytes mediate gliosis around the device by becoming hypertrophic, expanding and compacting their cellular membranes during scar formation (Szarowski et al., 2003; Polikov et al., 2005; Nolta et al., 2015). The inflammatory milieu secreted by activated glia proximal to the device has been suggested to be a major contributor to the characteristic loss of neurons, resulting in impaired recording performances (Kozai et al., 2015c). However, traditional immunohistochemical analyses involving neurons, microglia, and astrocytes around intracortical devices have not correlated well with recorded electrophysiology, in large part due to intra-animal variability at the electrode-tissue interface (Kozai et al., 2014c; McCreery et al., 2016; Michelson et al., 2018b). For example, tissue demonstrating high neural density and low glial scarring around implanted devices will still demonstrate reduced recording performance, or vice versa (Kozai et al., 2014c; Michelson et al., 2018b). Furthermore, neurons are not the only metabolically active cells susceptible to injury within the parenchyma, nor are microglia and astrocytes the only glial factors that contribute to inflammation during injury (Wellman and Kozai, 2017). Oligodendrocytes maintain important physiological roles mediating neuronal homeostasis via myelin ensheathment while oligodendrocyte precursors, notably NG2 glia, are responsible for replenishing depleted oligodendrocytes and participate in inflammation (Bradl and Lassmann, 2010). Additionally, perivascular pericytes are an essential component of the neurovascular unit and act to regulate blood-brain barrier (BBB) health and maintenance (Winkler et al., 2011). Each of these factors can influence neuronal viability during injury and, as of yet, their dynamics during electrode pathology are unknown.

Oligodendrocytes, a third glial component of the central nervous system, exist predominantly in white matter tracks alongside their myelin fibers but are also present at lower densities within the gray matter cortex (Tomassy et al., 2014). They provide trophic and mechanical support to neurons and promote signal propagation between neural circuits via myelin ensheathment [see review (Wellman et al., 2018)]. Secretion of neuronal growth factors requires oligodendrocytes and their precursors to maintain constant contact with neurons within the parenchyma (Du and Dreyfus, 2002). However, as energy-demanding cells, oligodendrocytes require high metabolic needs in order to produce and maintain the amount of myelin needed to support the central nervous system (McTigue and Tripathi, 2008; Bradl and Lassmann, 2010; Snaidero and Simons, 2017). As a result, oligodendrocytes and their precursors are highly susceptible to ischemic and hypoxic stress events (Dewar et al., 2003; McTigue and Tripathi, 2008). Since electrode insertion can induce stroke-like events, such as BBB disruption and loss of perfusion as well as glial cell activation, mechanical strain, and edema, oligodendrocytes and their precursors are vulnerable to the inflammation sustained from chronic microelectrode implantation (Du et al., 2017; Wellman and Kozai, 2017; Wellman et al., 2018). The only characterization of oligodendrocytes or myelin during electrode-induced inflammation was conducted by Winslow et al. (2010) where they presented evidence of chronic demyelination around an electrode array following 12 weeks of implantation (Winslow and Tresco, 2010). As of yet, oligodendrocyte and myelin pathology have not been thoroughly characterized around acute or chronically implanted devices.

Distributed ubiquitously throughout the central nervous system, oligodendrocyte precursor cells are essential in maintaining physiological support of neurons and act as a reservoir for myelinating oligodendrocytes in the event of oligodendrocyte loss or demyelinating injury (Levine et al., 2001). In regards to glial inflammation, they are known to respond to injury in a similar vein as microglia and react similarly to astrocytes through secretion of axon growth-inhibiting chondroitin sulfate proteoglycans, such as neural/glia antigen 2 (NG2)—thus, they are commonly referred to as NG2 glia (Nishiyama et al., 2005; Tan et al., 2005). NG2 glia also possess the ability to differentiate into reactive astrocytes under specific conditions of injury (Komitova et al., 2011). Using two-photon microscopy, the acute *in vivo* dynamics of microglia (Kozai et al., 2012b) and, more recently, NG2 glia (Wellman and Kozai, 2018) have been observed following microelectrode implantation, revealing a sequence of process extension and cell body migration in a specific spatiotemporal pattern of reactivity. However, beyond acute implantation, the distribution and proliferating patterns of NG2 glia have yet to be characterized around intracortical microelectrode arrays.

Pericytes are mural cells that interface directly between the BBB and parenchyma, mediating cross-talk between the brain and the peripheral circulation (Armulik et al., 2010). Another NG2-expressing cell within the brain, pericytes possess a variety of vascular homeostatic functions such as BBB maintenance, BBB repair, blood flow regulation, angiogenesis, as well as mesenchymal stem cell properties (Sweeney et al., 2016). Pericytes also facilitate neuroinflammatory reactions following injury and have been implicated as targets of interest in a variety of neurodegenerative diseases such as stroke, Alzheimer's disease, multiple sclerosis, and more (Winkler et al., 2011). Many of these studies have correlated a reduction or loss in

pericyte reactivity to occurrences of increased BBB permeability (Lindahl et al., 1997). Blood-brain barrier disruption has recently been recognized as a significant factor of inflammation induced by intracortical electrodes and a potential perpetrator of reduced device performance (Kozai et al., 2010, 2015c). Further investigation of pericyte behavior and reactivity to injury is required to understand how they fit into these sequences of inflammatory events.

In order to fill the gaps in knowledge surrounding these novel cell types of interest, additional immunohistochemical markers were employed (oligodendrocytes, NG2 glia, pericytes) alongside traditional stains (neurons, microglia, and astrocytes) to observe spatiotemporal dynamics following intracortical microelectrode implantation. Markers for cellular apoptosis and proliferation were also used to observe mechanisms of cell death or patterns of division, respectively. Probes were implanted acutely for 1, 3, and 7 days as well as chronically for 28 days post-insertion. These analyses answer critical questions about unknown or understudied parenchymal components during electrode-induced inflammation that can guide future studies to determine mechanistic causes of signal quality degradation or assist in the development of novel therapies to improve device performances.

MATERIALS AND METHODS

Surgical Probe Implantation

Implantation of microelectrode arrays were performed as described previously (Kozai et al., 2014c, 2016c). Prior to surgery, all electrode arrays, surgical tools, and surgical supplies were sterilized using ethylene oxide for 12 h. Single shank non-functional Michigan-style microelectrodes (A16-3 mm-100-703-CM15) were implanted into the left primary monocular visual cortex (V1m) of 8-week old C57BL/6J male mice (Jackson Laboratory, Bar Harbor, ME). Mice were anesthetized using a 7 mg/kg xylazine and 75 mg/kg ketamine cocktail injected intraperitoneally and mounted onto a stereotaxic frame. Eye ointment was administered to keep the eye moisturized and an O_2 line was installed for oxygen delivery. Betadine and alcohol scrubs were administered to sterilize the surgical area prior to removing the scalp and connective tissue from the surface of the skull. A thin layer of Vetbond (3 M) was applied to dry the surface of the skull and provide enhanced adhesion between the skull and dental cement. Three bone screws were drilled into the bone over both motor cortices and the contralateral visual cortex to help secure the headcap. A 1 mm drill-sized craniotomy was formed at 1 mm anterior to lambda and 1.5 mm lateral from the midline using a high-speed dental drill. Saline was periodically administered to prevent overheating of the brain surface. After the craniotomy was removed and brain exposed, gelfoam was used to prevent drying out of the brain prior to implantation. The single shank device was carefully inserted using a stereotaxic manipulator at a speed of ∼2 mm/s until the last electrode contact site was below the surface (∼1600 μm from the pial surface). The inserted probe was sealed using a silicone elastomer (Kwik-sil) and a headcap was secured with UV-curable dental cement (Henry Schein, Melville, NY, United States). Non-steroidal anti-inflammatory ketofen was administered at 5 mg/kg for 2 days post-operatively.

Endpoint Histology

Mice were sacrificed and perfused according to University of Pittsburgh IACUC approved methods at days 1, 3, 7, and 28 days post-insertion (n = 3 per time point). Prior to perfusion, a 7 mg/kg xylazine and 75 mg/kg ketamine cocktail was administered to deeply anesthetize each mouse and a toe-pinch test was used to determine a proper plane of anesthesia. Mice were transcardially perfused (pump pressure: 80–100 mm Hg) using 100 mL of a warm phosphate buffered saline (PBS) flush followed by 100 mL of 4% paraformaldehyde. Following perfusion, mice were decapitated and heads were post-fixed in 4% paraformaldehyde at 4°C overnight. Brains were then removed from the skull and soaked sequentially in 15 and 30% sucrose baths at 4°C for 24 h each. Following this, brains were carefully separated from the device and headcap and soaked in 30% sucrose for another 12–24 h. After sucrose equilibration, brains were blocked and frozen in a 2:1 20% sucrose in PBS:optimal cutting temperature compound (Tissue-Tek, Miles Inc., Elkhart, IN, United States). Samples were sectioned horizontally at a 25 μm slice thickness onto glass slides using a cryostat (Leica Biosystems, Wetzlar, Germany).

In order to minimize variability due to layer-specific differences in cell distribution, sections between a depth of 400–800 μm (layer IV-V) were chosen for immunohistochemical analysis. Additionally, sections free of extraneous tissue holes that could arise during probe extraction, perfusion, or sectioning were chosen for analysis. Prior to staining, sections were re-hydrated with 1× PBS for 30 min. Slides were incubated in 0.01 M sodium citrate buffer (for antigen retrieval) for 30 min at 60°C followed by incubation in a peroxidase blocking solution (10% v/v methanol and 3% v/v hydrogen peroxide) for 20 min on a table shaker at room temperature. Sections were then permeabilized using a solution of 1% triton X-100 with 10% donkey serum in PBS for 30 min at RT. Lastly, sections were blocked with donkey anti-mouse IgG fragment (Fab) or 647 conjugated anti-mouse IgG fragment (Fab) for 2 h at 1:13 or 1:16 dilution at RT.

Following 1× PBS rinses (8 × 4 min), sections were incubated with a primary antibody solution consisting of 10% donkey serum, 1% triton X-100, and antibodies listed in **Table 1** overnight at 4°C. Sections were then rinsed with 1× PBS (3 × 5 min) before being incubated with a secondary antibody solution in 1× PBS (donkey anti-mouse 405, Abcam, and donkey anti-goat 568, Abcam, Cambridge, United Kingdom; donkey anti-mouse IgG 488, Thermo Fisher Scientific, donkey anti-rabbit IgG 568, Thermofisher, and streptavidin, Alexa Fluor 488 conjugate, Thermo Fisher Scientific, Waltham, MA, United States; and donkey anti-chicken IgY 647, Sigma-Aldrich, St. Louis, MO, United States) diluted at 1:500 for 2 h at RT. Following 3× PBS washes for 5 min, sections were incubated with 1:1000 Hoechst 33342 (Invitrogen) for 10 min and then washed one final time with 1× PBS (3 × 5 min) before being coverslipped using Fluoromount-G (Southern Biotech, Birmingham, AL, United States) and sealed with fingernail polish.

TABLE 1 | List of primary antibodies used for immunohistological staining.

Primary antibody	Marker	Supplier	Species	Dilution
Anti-NeuN	Neurons	Sigma-Aldrich (MAB377B)	Ms	1:200
Anti-Iba-1	Microglia	Sigma-Aldrich (MABN92), Fisher (NC9288364)	Ms, Rb	1:200 (Ms), 1:500 (Rb)
Anti-GFAP	Astrocytes	Abcam (AB4674)	Ck	1:500
Anti-CC1	Mature oligodendrocytes	Abcam (AB7474)	Rb	1:400
Anti-Olig2	Immature oligodendrocytes	Sigma (MABN50)	Ms	1:100
Anti-NG2	NG2 glia, pericytes	Sigma (AB5320)	Rb	1:200
Anti-NF-200	Neurofilament	Sigma (MAB5256)	Ms	1:250
Anti-MBP	Myelin basic protein	Abcam (AB7349)	Rt	1:100
Anti-PDGFR-β	Pericytes	R&D Systems (AF1042)	Gt	1:100
Anti-Lectin	Blood vessels	Vector Lab (B-1175)	Tomato	1:250
Anti-Ki67	Proliferation marker Ki67	BD biosciences (550609)	Ms	1:50
Anti-Activated caspase 3	Activated caspase 3	Cell signal (9661S)	Rb	1:400

Samples were imaged at 16-bit (635.9 × 635.9 μm, 1024 × 1024 pixels on FV10-ASW Viewer V4.2) using a confocal microscope (FluoView 1000, Olympus, Inc., Tokyo, Japan) with a 20× oil-immersive objective lens at the Center for Biologic Imaging at the University of Pittsburgh.

Data Analysis

Intensity analyses of immunohistochemical stains (NF-200/MBP/Iba-1/NG2/GFAP) were performed radially around the probe hole using a custom script (INTENSITY Analyzer) written in MATLAB (Mathworks, Natick, MA, United States) developed previously (Kozai et al., 2014b). Bins spaced 10 μm apart up to 300 μm away from the probe hole were generated as concentric rings around the probe hole and the average grayscale intensity was calculated for all pixels above a threshold determined by the intensity of the background noise within each bin. Intensity data was normalized using data from the four corners of each image representing tissue 300 μm or more away from the insertion site. Data was averaged over all animals per time point and per bin and reported as mean ± standard error as a function of distance from the insertion site. Additionally, bar graphs of intensity data averaged over 50 μm away from the probe hole were generated in a separate MATLAB script and reported as mean ± standard error for each time point.

For cell counting (NeuN/CC1/Iba-1/NG2/GFAP/PDGFR-β/Caspase-3/Ki67), the MATLAB script was modified to generate bins spaced 50 μm apart up to 300 μm away from the probe hole. For neuronal and oligodendrocyte density, tissue area was calculated within each bin after excluding tissue "holes" and the density was calculated as total cell count divided by tissue area per bin. Tissue holes were determined by any pixel values that were less than 1 by optimizing image offset during image acquisition. For co-localization analysis, two or more immunohistochemical markers (NeuN/Caspase-3, CC1/Caspase-3, Iba-1/Ki67, NG2/Ki67, GFAP/Ki67, GFAP/Olig2) were merged and quantified in ImageJ (Schindelin et al., 2012). All cell counts were performed against a DAPI stain to confirm the presence of cell nuclei. Similar to the intensity analysis, data was averaged over all animals per time point per bin and reported as mean ± standard error as a function of distance from the probe hole.

Statistics

A two-way ANOVA followed by a *post hoc* Tukey HSD test was used on cell density and fluorescence intensity analysis generated per animal per time point ($n = 3$) to evaluate significant differences between time points of implantation. An unequal variance two-tailed t-test was used to determine significant differences between co-localized cell counts at different time points. A p-value < 0.05 was chosen for significance. Instances of no significance does not mean there is no actual difference between groups, but rather that there is no observable significance given the group size. However, instances in which significant differences are reported demonstrate the robustness of those differences given appropriately applied statistical analysis.

RESULTS

Impact on Neuronal Viability and Axonal Structures Following Microelectrode Implantation

Neuronal cell distribution and axonal integrity were evaluated using markers specific to neuronal nuclei (NeuN) and neurofilament protein (NF-200), respectively, at 1, 3, 7, and 28 days following insertion (**Figure 1A**). Additionally, activated caspase-3 was co-stained to label for cellular degeneration. At regions distal to the probe implant site, NeuN+ cell density was consistent with previously reported values (∼1500 NeuN+ cells/mm^2 at 200–300 μm away from probe hole) affirming the robustness of the histology (Golabchi et al., 2018). While no significant differences were noted, NeuN+ cell density counts revealed a biphasic pattern of reduced neural density occurring at 1 and 28 days and increased neural density at 3 and 7 days post-insertion (**Figure 1B**). Neuronal loss occurred most markedly within 0–50 μm away from the probe hole. To determine mechanistic causes of neuronal loss around the

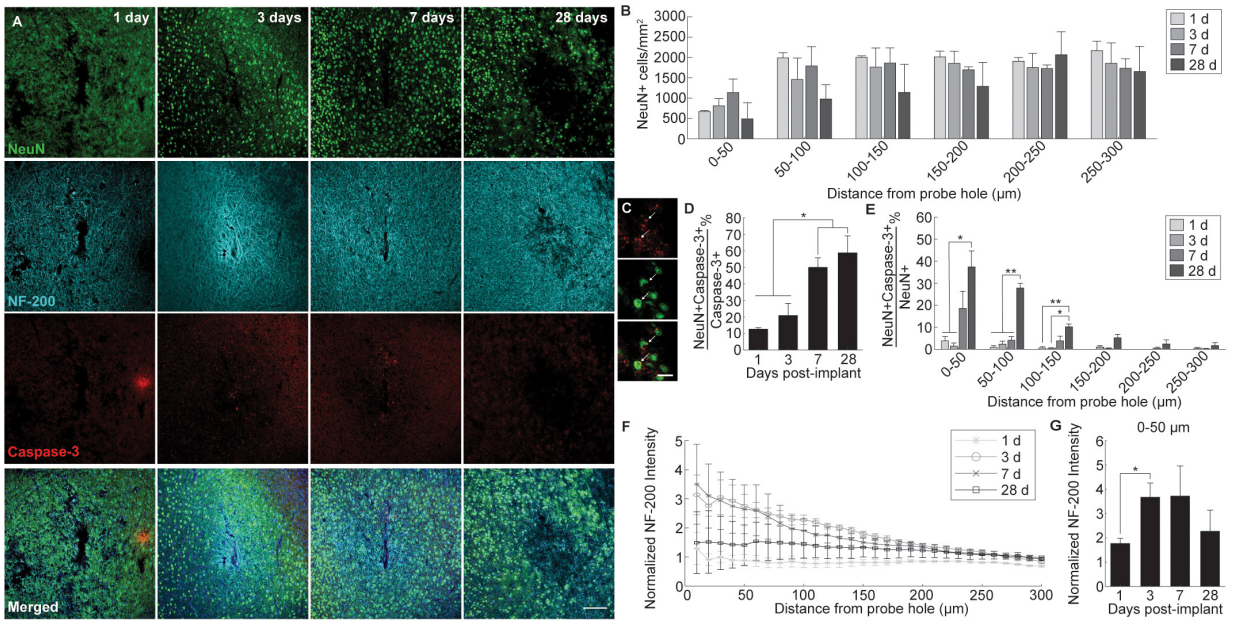

FIGURE 1 | Evaluation of neuronal cell death and axonal preservation around an implanted microelectrode array. Microelectrode implantation induces progressive neuronal loss and degeneration as well as axonal dysfunctional within close proximity of the electrode interface. **(A)** Representative immunohistochemical stain for neurons (NeuN), axons (NF-200), and caspase-3 at 1, 3, 7, and 28 days post-insertion. Scale bar = 100 μm. **(B)** NeuN+ cell counts within 50 μm bins up to 300 μm away from the probe hole demonstrating reduced neural density near the site of probe insertion. Notably, neuronal density is most disrupted within 0–100 μm from the probe hole at each time point. **(C)** Magnified images of Caspase-3+ staining (top), NeuN+ cells (middle), and co-labeled NeuN+Caspase-3+ cells (bottom). White arrows denote co-localized cells. Scale bar = 20 μm. **(D)** Percent of NeuN+Caspase-3+ cells over total Caspase-3+ cells within 300 μm from the probe hole. **(E)** Increases in percent of NeuN+Capase-3+ cells over total NeuN+ cells within 50 micron bins up to 300 μm away from the probe hole demonstrate significant neurodegeneration near the site of implantation. **(F)** Axonal reorganization is presented as normalized NF-200 intensity within 10 μm bins up to 300 μm away from the probe hole. **(G)** Normalized NF-200 intensity averaged over the first 50 μm from the probe hole highlights significant temporal differences in axonal integrity near the site of insertion. Pattern of axonal intensity matches fluctuations in neuronal density over time within 0–50 μm distance from probe hole. * indicates $p < 0.05$. ** indicates $p < 0.01$.

implanted microelectrode array, activated caspase-3 staining was used to observe instances of neurodegeneration (**Figure 1C**). Of the total caspase-3+ cell population observed within 300 μm from the site of device insertion, NeuN+ caspase-3+ cells steadily increased over time from 1 to 28 days post-insertion, with a significant increase in neurodegeneration present at 7 (50 ± 5.7% NeuN+Casp3+/NeuN+) and 28 (58.7 ± 10.3% NeuN+Casp3+/Casp3+) days post-insertion ($p < 0.05$) (**Figure 1D** and **Supplementary Table S1**). To determine the spatial distribution of neurodegeneration, NeuN+ caspase-3+ cells were taken as a proportion of total NeuN+ cells within 50 μm bins up to 300 μm from the probe hole (**Figure 1E** and **Supplementary Table S2**). Within 150 μm from the site of insertion at 28 days post-implantation, the percentage of caspase-3+ cells within the NeuN+ population was significantly increased compared to 1 and 3 days post-insertion ($p < 0.05$). At 100–150 μm away from the probe hole, there was a significant increase at 28 days compared to 1 and 3 days post-insertion ($p < 0.01$). Analysis of axonal structures around the microelectrode array revealed an increase in neurofilament intensity beginning at 3 and 7 days post-insertion before decreasing at 28 days post-insertion (**Figure 1F**). Neurofilament expression was highest with proximity to the implanted device, decreasing to baseline control values further from the site of implantation. Average NF-200 intensity within the first 50 μm from the device demonstrated a significant increase from 1 to 3 days post-insertion ($p < 0.05$) (**Figure 1G** and **Supplementary Table S3**).

Impact on Oligodendrocyte Viability and Myelination Following Microelectrode Implantation

Alterations to oligodendrocyte distribution and myelin organization were evaluated using markers for mature oligodendrocytes (CC1) and myelin basic protein (MBP), respectively, at 1, 3, 7, and 28 days following device implantation (**Figure 2A**). Similar to the neuronal analysis, activated caspase-3 was used to determine the prevalence of induced cellular degeneration in oligodendrocytes. Normalized CC1+ cell density revealed a pattern of oligodendrocyte loss occurring at 3 and 7 days post-insertion (**Figure 2B**). By 28 days post-insertion, an increase in oligodendrocyte population could be observed, however, there was no significant difference reported (**Figure 2B**). Reductions in oligodendrocyte density occurred most heavily within 0–50 μm from the site of insertion, implying decreases in oligodendrocyte viability are in response to the implanted device. The percentage of total

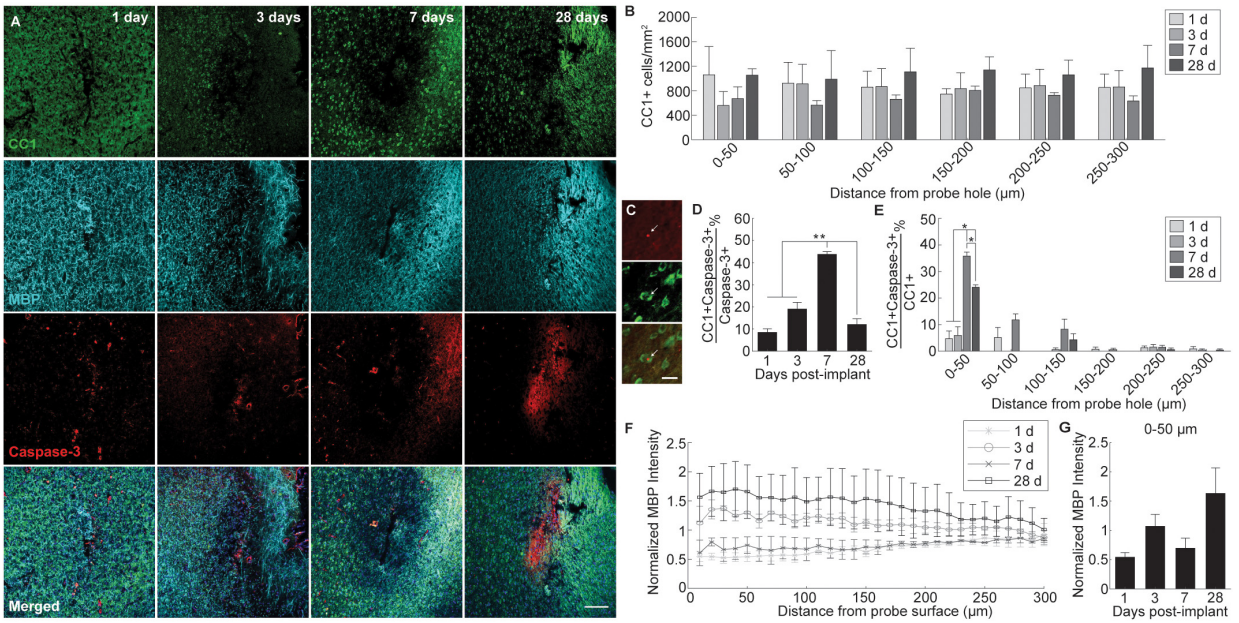

FIGURE 2 | Evaluation of oligodendrocyte cell death and myelin preservation around an implanted microelectrode array. Acute microelectrode implantation compromises oligodendrocyte viability and function, preceding abnormal myelin expression and reorganization around the electrode interface. **(A)** Representative immunohistochemical stain for mature oligodendrocytes (CC1), myelin (MBP), and caspase-3 at 1, 3, 7, and 28 days post-insertion. Scale bar = 100 μm. **(B)** CC1+ cell counts within 50 μm bins up to 300 μm away from the probe hole indicating fluctuations in oligodendrocyte density around the implanted probe. Compared to neurons, oligodendrocyte densities were robust from 1 to 28 days post-insertion, fluctuating between time points but remaining relatively stable over time. **(C)** Magnified images of Caspase-3+ staining (top), CC1+ cells (middle), and co-labeled CC1+Caspase-3+ cells (bottom). White arrows denote co-localized cells. Scale bar = 20 μm. **(D)** Oligodendrocyte degeneration is noted as a percent of CC1+Caspase-3+ cells over total Caspase-3+ cells within 300 μm from the probe hole. *Note*: Peak oligodendrocyte degeneration preceeds peak neuronal degeneration. **(E)** Percent of CC1+Capase-3+ cells over total CC1+ cells within 50 micron bins up to 300 μm away from the probe hole. **(F)** Normalized MBP intensity within 10 μm bins up to 300 μm away from the probe hole. **(G)** Normalized MBP intensity averaged over the first 50 μm from the probe hole demonstrates an increase in myelination around the site of insertion at chronic timepoints. An increase in myelination at 28 days post-insertion coincides with a decrease in oligodendrocyte degeneration, indicating a potential reparative effect. * indicates $p < 0.05$. ** indicates $p < 0.01$.

caspase-3+ cells that were CC1+ within a 300 μm region around the device (CC1+Casp3+/Casp3+) revealed that apoptosis-induced oligodendrocyte cell death occurs most markedly at 7 days post-insertion (43.7 ± 1.3%), significantly increased from 1 (8.45 ± 1.6% CC1+Casp3+/Casp3+) and 3 days (19 ± 3%) following implantation ($p < 0.01$) (**Figures 2C,D** and **Supplementary Table S4**). The proportion of caspase-3+ cells that were CC1+ significantly decreased from 7 to 28 (12 ± 2.6%) days following insertion ($p < 0.01$). Additionally, the percentage of caspase-3+ cells within the total CC1+ population peaked significantly at 7 days post-insertion, specifically within 0–50 μm away from the probe hole indicative of a temporal pattern of oligodendrocyte degeneration around the implanted device (**Figure 2D** and **Supplementary Table S5**). Staining for MBP expression demonstrated a decrease in myelin content proximal to the device at 1 and 7 days post-insertion and an overall increase in myelin intensity at 28 days following implantation (**Figure 2E**). Average MBP intensity within the first 50 μm from the device emphasizes this pattern, with MBP expression increasing 1.5–2 fold by 28 days post-insertion (**Figure 2F**). Notably, instead of reduced or deplete regions of myelin expected of myelin degeneration, MBP appeared with increased intensity near the site of implantation, similar to neurofilament, indicative of an upregulation in myelin basic protein that would occur during reorganization of myelinated axons or remyelination of demyelinated axons following injury. However, no significant differences between each time point were observed.

Pattern of Glial Cell Immunoreactivity and Proliferation Around Implanted Microelectrode Arrays

Glial reactivity to implanted intracortical devices was evaluated by staining for histological markers specific for microglia (Iba-1), astrocytes (GFAP), and NG2 glia (NG2) at 1, 3, 7, and 28 days post-insertion (**Figure 3A**). Iba-1 immunoreactivity was highest proximal to the implant for all time points, decreasing steadily to normalized control levels with distance from the probe hole (**Figure 3B**). When observing directly at the 50 μm region at tissue-device interface, Iba-1 expression increased steadily over time; however, there was no significant difference in fluorescence intensity ($p < 0.05$) (**Figure 3C**). Beginning 3 days after implantation, GFAP fluorescence intensity increased 2–4 fold with proximity to the probe hole showing preferential

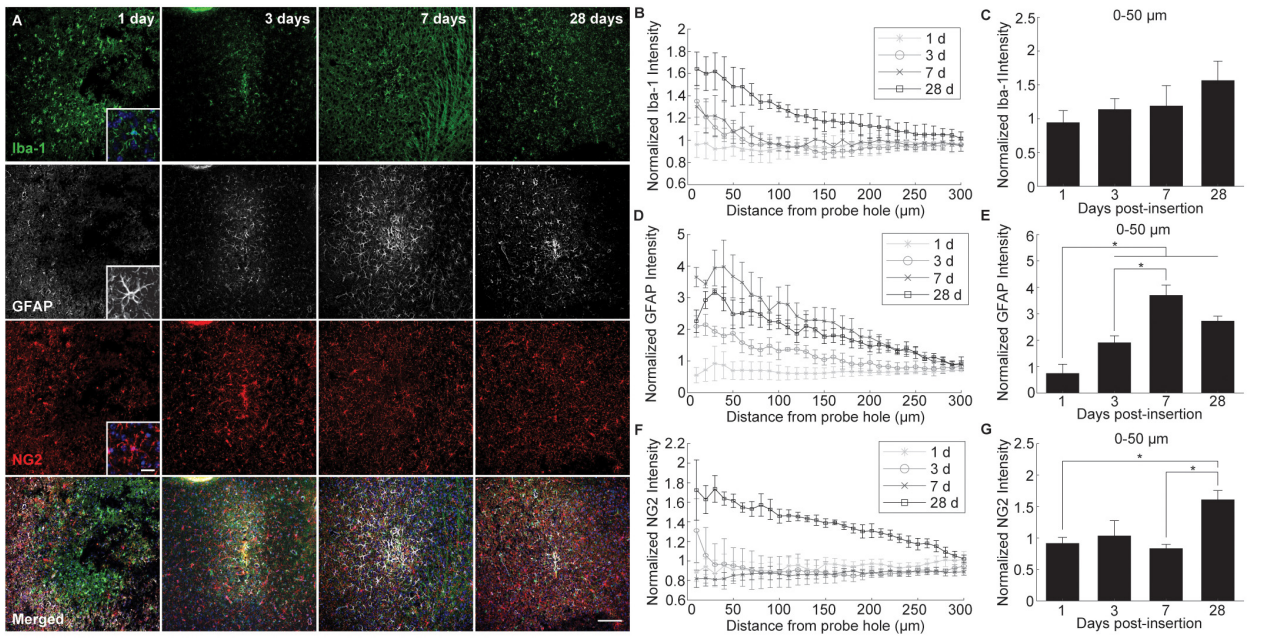

FIGURE 3 | Evaluation of glial cell activation around an implanted microelectrode array. Microelectrode implantation induces distinct spatial and temporal patterns of microglia, astrocyte, and NG2 glia reactivity. **(A)** Representative immunohistochemical stain for microglia (Iba-1), NG2 glia (NG2), and astrocytes (GFAP) at 1, 3, 7, and 28 days post-insertion. Scale bar = 100 μm. Inserts show magnified view of Iba-1+, GFAP+, and NG2+ cells with nuclei stain. Scale bar = 20 μm. **(B)** Normalized Iba-1 intensity within 10 μm bins up to 300 μm away from the probe hole. **(C)** Linear increases in microglia reactivity around the implanted device is depicted as normalized Iba-1 intensity averaged over the first 50 μm from the probe hole. **(D)** Normalized GFAP intensity within 10 μm bins up to 300 μm away from the probe hole. **(E)** Normalized GFAP intensity averaged over the first 50 μm from the probe hole demonstrates temporal patterns in astrocyte scar formation around the implanted device. **(F)** Normalized NG2 intensity within 10 μm bins up to 300 μm away from the probe hole. **(G)** Normalized NG2 intensity averaged over the first 50 μm from the probe hole demonstrates a significant increase in NG2 expression at chronic timepoints. NG2 intensity decreases at 7 days when GFAP intensity peaks. Additionally, NG2 intensity peaks at 28 days as oligodendrocyte degeneration decreases and myelination increases. * indicates $p < 0.05$.

expression around the site of device implantation (**Figure 3D**). GFAP expression was minimal at 1 day post-insertion and the average GFAP fluorescence was significantly increased within the 50 μm region surrounding the device at 3, 7, and 28 days post-implantation ($p < 0.05$) (**Figure 3E** and **Supplementary Table S6**). GFAP intensities reached a maximum at 7 days, and was significantly increased from expression levels at 3 days post-insertion ($p < 0.05$). Interestingly, NG2 expression increased adjacent to the implant at 3 days post-insertion; however, it remained reduced at 1 and 7 days following implantation (**Figure 3F**). Similar to Iba-1 expression, NG2 expression was highest at 28 days post-insertion and was significantly higher within 0–50 μm compared to NG2 fluorescence intensity at 1 and 7 days post-insertion ($p < 0.05$) (**Figure 3G** and **Supplementary Table S7**).

In order to evaluate the extent of dividing glia around the implanted device, Ki67, a marker for cellular proliferation, was co-stained along with Iba-1, GFAP, and NG2 (**Figures 4A–C**). Co-localization of Ki67+ cells with Iba-1+, GFAP+, and NG2+ cells revealed a distinct temporal pattern of division within 300 μm from the site of implantation (**Figure 4D** and **Supplementary Table S8**). At 1 day post-insertion, Iba-1+Ki67+ cells consisted of a significant proportion of Ki67+ cells (72.14 ± 1.5%) compared to GFAP+Ki67+ (13.3 ± 0.8%) and NG2+Ki67+ cells (22.5 ± 11.4%) ($p < 0.05$). By 3 days post-insertion, Iba-1+ cells remained the most co-localized with Ki67+ cells (50.14 ± 11%) compared to GFAP+ (18.6 ± 6.7%) and NG2+ cells (31.7 ± 4.6%); however, there was no significant difference between the three populations. At 7 days post-insertion, GFAP+ cells comprised a significant proportion of Ki67+ cells (57.9 ± 4.8%) compared to NG2+ cells (32.5 ± 3.1%) ($p < 0.05$) but not compared to Iba-1+ cells (19 ± 15.6%). By 28 days post-insertion, NG2+ cells were co-localized significantly with Ki67+ cells (67.6 ± 10.5%) compared to Iba-1+ (22.5 ± 4.7%)and GFAP+ cells (21.2 ± 5.3%) ($p < 0.05$). To observe potential spatial patterns in glial proliferation, co-localized Ki67+ glial cells were taken as a proportion of total Iba-1+, GFAP+, and NG2+ cells counted within 50 μm bins up to 300 μm away from the probe hole. Spatial analysis determined that, for any given time point, the majority of proliferating glia preferentially resided with close proximity to the device with the highest percentage of Ki67+ glia appearing within 50 μm from the probe hole (**Figures 4E–G**). Of the total Iba-1+ population, the proportion of Iba-1+Ki67+ cells was significantly increased at 1 and 3 days post-insertion ($p < 0.05$) (**Figure 4E** and **Supplementary Table S9**). The percentage of Iba-1+Ki67+ cells was reduced at 7 days before significantly increasing by 28 days post-insertion ($p < 0.05$). Within the GFAP+ population, the percentage of Ki67+GFAP+ cells within 50 μm from the site of insertion peaked at

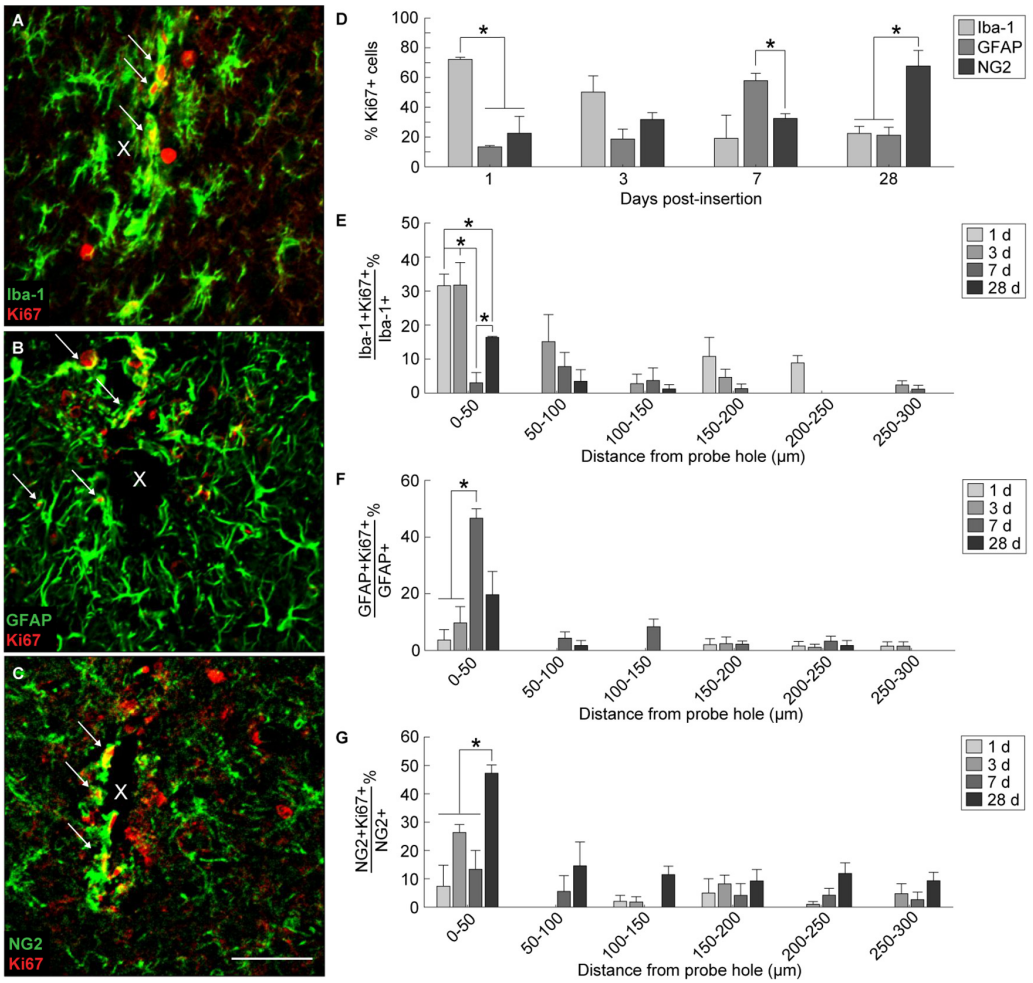

FIGURE 4 | Tracking proliferation of glial cells around an implanted microelectrode array. Microglia, astrocytes, and NG2 glia demonstrate distinct temporal patterns of proliferation following device insertion. Additionally, glial proliferation occurs most prominently at the site of insertion (0–50 μm distance from probe hole). Representative immunohistochemical stain for Iba-1+ **(A)**, GFAP+ **(B)**, and NG2+ **(C)** cells that express the Ki67+ proliferation marker. White arrows denote co-localized cells and indicate glial proliferation. Center of the probe hole is denoted by a white "x." Scale bar = 50 μm. **(D)** Percent of Ki67+ cells within 300 μm from the probe hole which are Iba-1+, GFAP+, or NG2+ at 1, 3, 7, and 28 days post-insertion reveal a distinct temporal pattern of proliferation. **(E)** Percent of Iba-1+Ki67+ cells over total Iba-1+ cells within 50 μm bins up to 300 μm away from the probe hole demonstrate early microglia proliferation around the implanted device. **(F)** Percent of GFAP+Ki67+ cells over total GFAP+ cells within 50 μm bins up to 300 μm away from the probe hole reveal astrocytes as the predominantly dividing glia following microglia. **(G)** The percent of NG2+Ki67+ cells over total NG2+ cells within 50 μm bins up to 300 μm away from the probe hole reveals chronic proliferation of NG2 glia. NG2 proliferation decreases at 7 days when astrocyte proliferation peaks. Additionally, NG2 proliferation peaks at 28 days as oligodendrocyte degeneration decreases and myelination increases. * indicates $p < 0.05$.

7 days post-insertion, significantly increased from 1 and 3 days after implantation ($p < 0.01$) (**Figure 4F** and **Supplementary Table S10**). Finally, the percentage of Ki67+NG2+ cells within 50 μm from the site of insertion was significantly increased at 28 days compared to 1, 3, and 7 days post-insertion (**Figure 4G** and **Supplementary Table S11**).

Appearance of Subpopulation of Olig2+Reactive Astrocytes Around Implanted Microelectrode Arrays

In order to evaluate if oligodendrocyte progenitors near the implant were differentiating into astrocytes, GFAP was co-labeled with the oligodendrocyte transcription factor Olig2. A subpopulation of Olig2+ astrocytes was observed around the implanted microelectrode array at 1, 3, 7, and 28 days post-insertion (**Figure 5A**). GFAP+ astrocytes co-localized with Olig2+ cells proximal to the site of insertion (**Figure 5B**). However, it is worth noting that Olig2+ staining appeared faint in GFAP+Olig2+ cells compared to GFAP-Olig2+ cells, possibly due to astrocyte downregulation of the Olig2 transcription factor. After 3 days post-insertion, the percentage of GFAP+Olig2+ cells out of the total Olig2+ population rose dramatically, significantly increasing between 0–50 μm away from the site of insertion at 7 and 28 days post-insertion and between

100–150 μm away from the site of insertion at 7 days post-insertion ($p < 0.05$) (**Figure 5C** and **Supplementary Table S12**). No significant difference in the percentage of GFAP+Olig2+ cells was noted between 7 and 28 days post-insertion at 100–150 μm away from the site of insertion. On day 1 post-insertion 0–50 μm away from the probe hole, there was an absence of GFAP+Olig2+ cells due to that fact that there was little to no remaining tissue within the 50 μm radius as well as reduced GFAP+ staining to begin with. At 7 and 28 days post-insertion, the percentage of GFAP+Olig2+ cells appeared elevated between 0–150 μm from the probe hole compared to distal regions, indicating a preference for localization close to the implanted device.

PDGFRβ Immunoreactivity and Pattern of Blood-Brain Barrier Leakage Around Implanted Microelectrode Arrays

Microelectrode induced damage specific to the BBB was evaluated by tracking NG2+ perivascular pericytes at 1, 3, 7, and 28 days post-insertion (**Figure 6A**). Pericytes were identified from other NG2+ cells by co-localizing with platelet-derived growth factor receptor β (PDGFR-β), which is absent on NG2+ oligodendrocyte precursor cells (**Figure 6B**). Cell density analysis revealed an initial increase in PDGFR-β+ cells at 3 and 7 days post-insertion, most notably within a 50 μm radius from the site of insertion (**Figure 6C** and **Supplementary Table S13**). By 28 days post-insertion, the density of PDGFR-β+ cells was dramatically decreased around the microelectrode array and significantly different from PDGFR-β+ cell density at 1, 3, and 7 days post-insertion up to 50 μm away from the surface of the probe ($p < 0.01$). Coincidentally, analysis of BBB leakage via immunoglobulin G (IgG) staining revealed a temporal pattern of vascular disruption similar to the observed pericyte reactivity (**Figure 6D**). IgG fluorescence intensity was increased with proximity to the device for all time points, up to 50 μm away from the probe hole at 1, 3, and 7 days post-insertion, and up to 100–150 μm away from the probe hole at 28 days post-insertion (**Figure 6E**). Within the 50 μm region directly adjacent to the probe hole, IgG intensity was highest at 28 days post-insertion, significantly more increased than at 1, 3, and 7 days post-insertion ($p < 0.05$) (**Figure 6F** and **Supplementary Table S14**). Concurrent with reduced PDGFR-β immunoreactivity at chronic time points was a decrease in vascular structures around the implanted device. Tomato lectin staining demonstrated reduced blood vessel distribution around the site of implantation at 28 days post-insertion compared to the contralateral (non-implant) side (**Figure 7**).

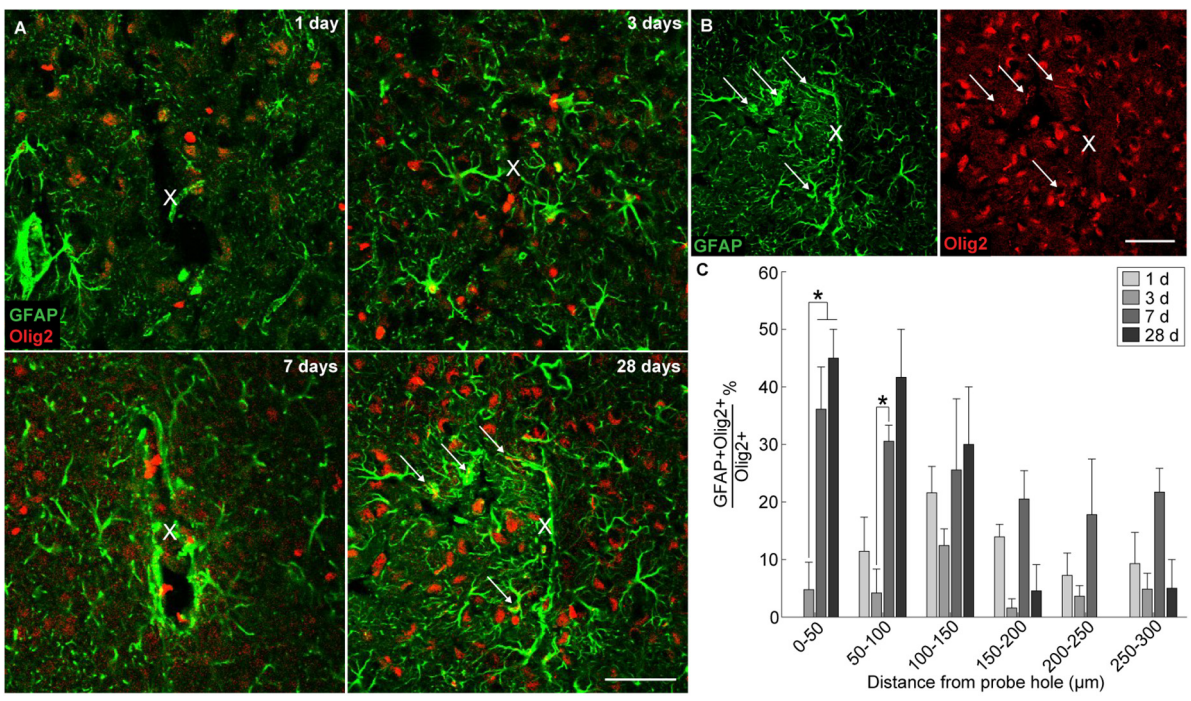

FIGURE 5 | Generation of reactive astrocytes from oligodendrocyte lineage cells around an implanted microelectrode array. Following microelectrode implantation, astrocytes expressed the oligodendrocyte transcription factor Olig2, which may implicate oligodendrocyte lineage cells as a source of astrocytes following injury. **(A)** Representative immunohistochemical stains for GFAP (green) and Olig2 (red) at 1, 3, 7, and 28 days post-insertion revealing a distinct subpopulation of Olig2+GFAP+ astrocytes. White arrows denote co-localized cells. Center of the probe hole is denoted by a white "x." Scale bar = 50 μm. **(B)** Green- and red-only channels for GFAP and Olig2 staining, respectively, at 28 days post-insertion. White arrows denote GFAP+ (left) or Olig2+ (right) cells. Center of the probe hole is denoted by a white "x." Scale bar = 50 μm. **(C)** Percent of GFAP+Olig2+ cells over total Olig2+ cells within 50 μm bins up to 300 μm away from site of insertion suggest preference for Olig2+GFAP+ cells to reside near site of probe implantation. * indicates $p < 0.05$.

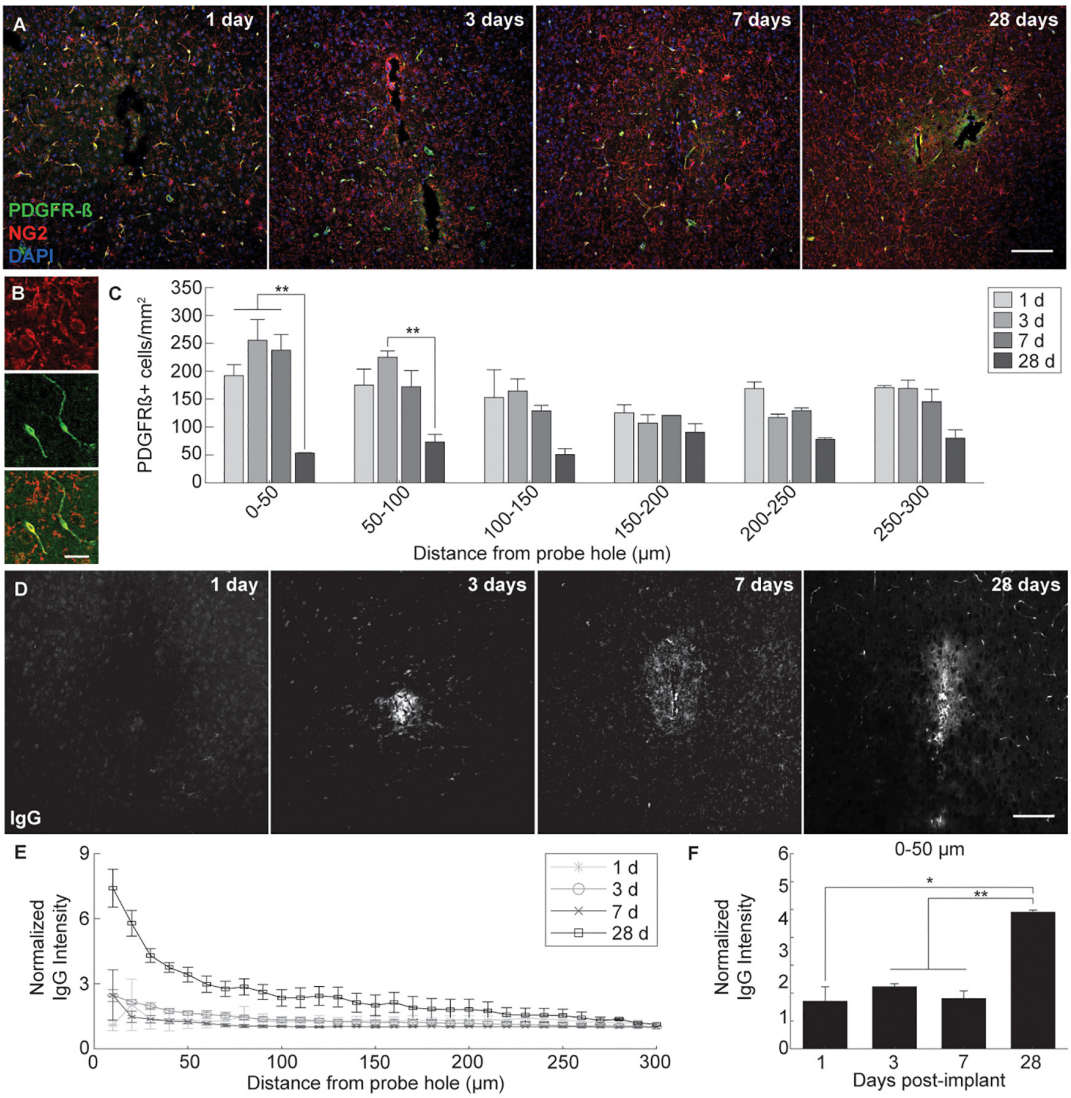

FIGURE 6 | Pericyte dysregulation and blood-brain barrier disruption around an implanted microelectrode array. Microelectrode implantation induces pericyte reactivity and increased BBB leakage within close proximity to the electrode interface, suggesting a progressive dysregulation of the neurovascular unit following injury. **(A)** BBB-associated pericytes were visualized around implanted devices by representative immunohistochemical stains for PDGFR-β (green), NG2 (red), and cell nuclei (blue) at 1, 3, 7, and 28 days post-insertion. Scale bar = 100 μm. **(B)** Magnified images of NG2+ (top), PDGFR-β+ (middle), and NG2+PDGFR-β+ cells (bottom). Scale bar = 20 μm. **(C)** Spatiotemporal patterns of PDGFR-β+ cell density within 50 μm bins up to 300 μm away from the probe hole. **(D)** Temporal patterns of device-induced bleeding revealed by representative immunohistochemical stains for immunoglobulin G at 1, 3, 7, and 28 days post-insertion. **(E)** Normalized IgG intensity within 10 μm bins up to 300 μm away from the probe hole. **(F)** Normalized IgG intensity averaged over the first 50 μm from the probe hole. Increased IgG expression around the probe hole coincides with reduced pericyte densities at 28 days post-insertion. * indicates $p < 0.05$. ** indicates $p < 0.01$.

DISCUSSION

The goal of this study was to evaluate novel histological markers around implanted intracortical probes in order provide further insight on dynamic tissue responses responsible for declining device performances. A more complete basic science knowledge of the tissue response to brain implants may facilitate the identification of novel opportunities for intervention strategies. It is understood that the homeostatic balance of the brain is not governed solely by neurons, microglia, and astrocytes, common targets while studying microelectrode-induced inflammation and injury. Similar to neurons, oligodendrocytes are metabolically active cells which can be considered just as important to brain circuit health given that they provide neurotrophic support and facilitate neuronal signaling via myelin sheath extension (Du and Dreyfus, 2002). Demyelination is a common symptom in many neurodegenerative diseases such as MS, stroke, and dementia, highlighting the susceptibility of oligodendrocytes to injury and their importance for neuronal survival (Dewar et al., 2003; Dulamea, 2017b). Additionally, oligodendrocyte precursors are

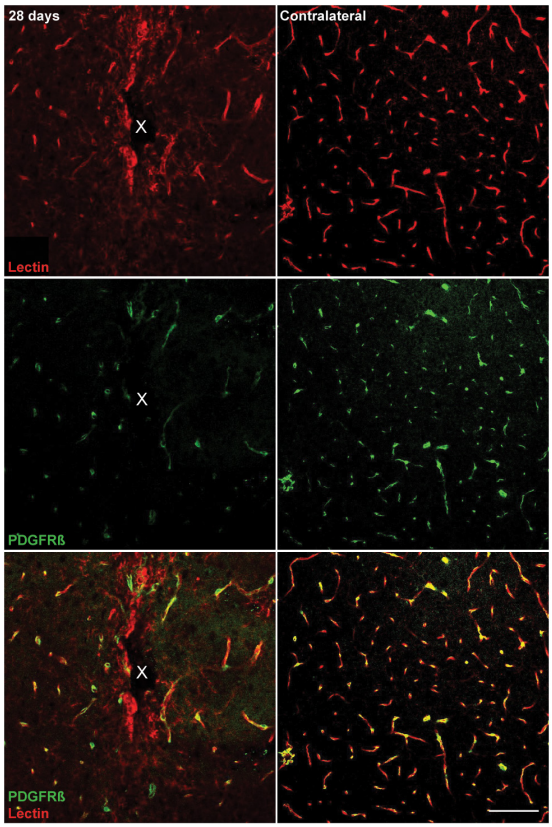

FIGURE 7 | Reduced vascular structures around implanted microelectrode arrays at 28 days post-implantation. Chronic microelectrode implantation reveals specific insult to the endothelial component of the BBB, which may precede pericyte reactivity, vessel permeability, and leakage of plasma components. Blood vessels as well as vessel-bound pericytes are visualized by representative immunohistochemical stains for lectin (red) and PDGFR-β (green) at 28 days post-implantation compared to contralateral (non-implant) side. Center of the probe hole is denoted by a white "x." Scale bar = 100 μm.

versatile cells within the parenchyma, restoring oligodendrocyte populations following injury but are known to contribute to injury-induced inflammation (Dimou and Gallo, 2015). Finally, juxtavascular pericytes have direct associations with BBB health and are an understudied cell type around implanted intracortical devices, despite evidence that they also are implicated in a variety of neurodegenerative disorders (Winkler et al., 2011; Sweeney et al., 2016). Each of these CNS factors play either a direct or indirect role in regulating neuronal homeostasis and their respective dysfunctions following device implantation can affect critical neural circuits, altering recording or stimulating performances of intracortical electrode arrays.

Neuronal Loss and Axonal Structural Changes Following Microelectrode Implantation

Distribution of neuronal cell bodies and axonal organization are significant factors around implanted microelectrode devices considering they are the electrically excitable components of the brain (Eles et al., 2018a). Neuronal cell density was disrupted mostly within the 0–50 μm region from the site of insertion. Within this radius, neuronal densities at 3 and 7 days post-insertion were slightly increased, which could be the result of fluctuations in tissue swelling and displacement around the device. Additionally, alterations in neurofilament intensity matched neural density changes within 50 μm from the probe hole at 1, 3, 7, and 28 days following implantation. Between 1 and 3 days post-insertion, neural density and neurofilament expression increase within 50 μm from the site of implantation. By 28 days post-insertion, a decrease in neurofilament expression within 50 μm away from the probe hole was observed coinciding with a drop in neural density. Gradually, the amount of caspase-3+ neurons increases from 1 to 28 days post-insertion, particularly within the 50 μm region around the device, indicating an increased propensity for these neurons near the device to undergo apoptotic cell death in response to the chronic implantation of a microelectrode array. Both neuronal density and axon neurofilament expression did not return to baseline levels until ∼150 μm away from the site of implantation. Considering that the maximum recordable radius of electrically active cells resides within this 150 μm radius (Buzsáki, 2004), changes to the organization of neurons and axons within this region may significantly influence the quality of device recording performance. However, the exact mechanisms governing this insult on neuronal viability remains unknown (Michelson et al., 2018b).

Microelectrode Implantation Induces Spatial and Temporal Patterns Glial Cell Reactivity and Proliferation

Formation of a glial scar is another significant response to the implantation of a microelectrode array. Microglia and astrocyte glial membranes form a physical barrier between the electrode and neural tissue, which is understood to increase device impedances and directly alter the quality of the recorded signal (Williams et al., 2007; Alba et al., 2015). With specific regard to stimulating devices, gliosis has the potential to increase impedances, alter the material and mechanical properties at the tissue-electrode interface, and widen the distance between the device and the nearest active neuron, requiring higher stimulation thresholds which can pose even further complications to the tissue (Grill and Reichert, 2008; Kozai et al., 2014a; Thomas and Jobst, 2015; Campbell and Wu, 2018). Unlike recording performance, knowledge of stimulation performance suffers from additional parameter spaces and additional variability in performance outcomes (Platia and Brinker, 1986; Mushahwar et al., 2000; Branner et al., 2004; McCreery et al., 2010; Koivuniemi et al., 2011; Gittis, 2018). Reduction in signal-to-noise ratios can be attributed to increases in extracellular noise, which can occur due to the dysregulation of local ionic environments following glial activation. Furthermore, glial-secreted factors that promote inflammation and cell death can compromise neuronal or oligodendrocyte viability and exacerbate further glial activation and BBB disruption around the device (Biran et al., 2005;

Karumbaiah et al., 2012; Prasad et al., 2012, 2014). Therapeutic approaches often attempt to attenuate glial cell activation or scar formation around implanted devices; however, reducing glial cell responses following nervous system injury carries the ability to worsen tissue health (Anderson et al., 2016). Therefore, future analyses focused on understanding glial cell dynamics after injury and their role during inflammation will help better understand wound healing and repair around implanted intracortical devices. Here, Iba-1+ microglia, NG2+ glia, and GFAP+ astrocyte fluorescence intensities were upregulated at different time points around implanted microelectrodes, indicating a temporal pattern of glial cell reactivity during device-induced inflammation.

Microglia are typically the first responders to injury within the CNS, their primary goal being to protect and repair injured tissue (Kawabori and Yenari, 2015). *In vivo* imaging has previously revealed that microglia respond immediately to the implantation of a microelectrode probe (Kozai et al., 2012a, 2016b; Eles et al., 2017). Following the initial response to electrode insertion, microglia begin migrating toward the device after 12 h of insertion (Kozai et al., 2016b; Wellman and Kozai, 2018). Here, Iba-1+ analysis indicated that microglia cells were the most significantly dividing glial cell type at 1 and 3 days post-insertion and that Iba-1+ fluorescence expression steadily increased up to 28 days post-insertion. The activation of microglia is followed by secretion of pro-inflammatory factors such as monocyte chemotactic protein (MCP-1), which induces the recruitment and migration of other immune cells, and tumor necrosis factor-alpha (TNF-α), which induces further glial cell activation and promotes neuron cell death (Biran et al., 2005). However, microglia can also secrete a range of anti-inflammatory cytokines to facilitate wound repair (Cherry et al., 2014). The complex range of microglia activity remains the focus of rigorous research, but these phenotypes can vastly alter the way microglia are viewed as a reactive glial cell type following CNS injury (Ransohoff, 2016; Eles et al., 2018b; Golabchi et al., 2018).

Generation of Heterogeneous Population of Reactive Astrocytes Following Microelectrode Implantation

Following 1 week post-insertion, astrocytes were the dominating proliferative cell type with significantly elevated GFAP expression, indicative of their characteristic encapsulation of intracortical devices during glial scar formation. Of the observed GFAP+ population around implanted microelectrode arrays, GFAP+Olig2+ cells appeared with increasing frequency both as time of implantation progressed and with close proximity to the site of device insertion. The Olig2 marker is an oligodendrocyte transcription factor expressed solely within the central nervous system, responsible for regulating oligodendrocyte differentiation (Zhou et al., 2001). It is a common marker used to identify oligodendrocytes and oligodendrocyte precursors. Olig2 is known to increase following stab wound injury in the cortical gray matter, and the proportion of GFAP+Olig2+ cells within the Olig2+ population was reported between 7–9% at 3 and 7 days post-injury (Buffo et al., 2005). In contrast, this study demonstrates that GFAP+Olig2+ cells make up about 35–45% of the Olig2+ cell population between 3 and 7 days post-insertion, most likely attributed to the chronic presence of an implanted device compared to a transient stab wound injury. Previous studies have suggested that NG2 glia maintain the ability to differentiate into reactive astrocytes following injury (Dimou and Gallo, 2015). Whether these GFAP+Olig2+ cells were previously NG2+Olig2+ oligodendrocyte precursor cells or a separate Olig2+ subpopulation poses an interesting question for tissue injury and repair.

Observing NG2 glia differentiation into astrocytes has previously proven challenging since the *Cspg4* promoter encoding for the NG2 antigen is downregulated during differentiation rendering co-localization using immunohistochemical markers difficult and therefore requires use of retroviral or transgenic manipulations. In the healthy postnatal cortex, it has been shown that local proliferation of astrocytes, not NG2 glia, account for a majority of the astrocyte population (Ge et al., 2012; Ge and Jia, 2016). Previous studies have used Cre-loxP transgenic animals to track the cell fate of NG2 glia following injury *in vivo*. Komitova et al. (2011) determined that NG2 glia are not a significant source of reactive astrocytes following stab wound injury to the cortex, declaring only 8% of reporter-labeled cells who are also labeled GFAP-positive at 10 days post-injury. However, a study conducted by Hackett et al. (2016) observed 25% of NG2 glia express GFAP 7 days following contusive spinal cord injury, indicating that the severity of injury can influence the potential for astrogliogenesis of NG2 glia. Furthermore, a prior study evaluating the extent of NG2-derived astrocytes using transgenic lineage tracing techniques in either spinal cord injury or experimental autoimmune encephalomyelitis (EAE) demonstrated an increased percentage of NG2-differentiated astrocytes in SCI (25–40%) compared to EAE (9%) 4 weeks following injury (Hackett et al., 2018). In the case of microelectrode implantation where inflammation and secondary damage persists due to the chronic presence of the implant, the conversion of NG2 glia into reactive astrocytes could be a major contributor to the gliosis observed around acute and chronically implanted neural probes. The relevance of this phenomenon depends on the origin of reactive astrocytes. For example, astrocytes proliferate readily following 1 week after a stab wound injury to the cortex (Allahyari and Garcia, 2015). This presents two possible sources of origin for reactive astrocytes following device implantation: (1) from existing astrocytes which divide and migrate toward the electrode or (2) from NG2 glia which either (i) differentiate into astrocytes, (ii) proliferate and then differentiate into astrocytes, or (iii) both. Interestingly, NG2 glia intensity and proliferation decreases while astrocyte reactivity and proliferation peaks at 7 days post-insertion, suggesting a transformation of NG2 glia into reactive astrocytes following device implantation. However, the precise contribution from either source remains to be determined and may alter the focus of future research investigating the nature of scar formation following injury.

Robustness of Oligodendrocyte and Oligodendrocyte Precursor Population Following Intracortical Microelectrode Implantation

Oligodendrocyte densities around the microelectrode device revealed a different pattern compared to neuronal distributions. These cells appeared more resistant to the acute and chronic implantation of a microelectrode device compared to neurons, remaining relatively stable in density throughout the time course of implantation. However, oligodendrocyte density was slightly decreased at 3 and 7 days post-insertion. Caspase-3 analysis revealed that oligodendrocyte dysfunction steadily increased up to 7 days post-insertion before decreasing by 28 days. Furthermore, degenerated oligodendrocytes appeared within close proximity to the microelectrode array, indicating a device-induced mechanism of cell death similar to neurons. By 28 days post-insertion, oligodendrocyte densities returned, coinciding with a decrease in apoptosis. Concomitantly, myelin basic protein expression was elevated around the implanted device at 28 days following insertion, suggesting a potential attempt at regeneration of oligodendrocytes and myelination following implantation-induced inflammation and injury. Unlike neurons, oligodendrocytes are supported by a dense and reactive oligodendrocyte precursor population that proliferate and differentiate following injury in order to sustain oligodendrocyte cell numbers (Levine et al., 2001). In some demyelinating diseases such as multiple sclerosis, differentiation of these oligodendrocyte precursor cells is impaired, leading to decreased oligodendrocyte numbers coinciding with increasing neurodegenerative deficits (Dulamea, 2017a). While oligodendrocyte regeneration and remyelination following brain injury is observed, newly formed myelin sheaths can return thinner than normal (Ishii et al., 2012). Although this study did not quantify myelin sheath thickness, integration and health of newly regenerated oligodendrocytes and myelin around implanted devices should be investigated further.

NG2+ cells were most activated at 28 days post-insertion, demonstrating significant proliferation and fluorescent expression of the NG2 antigen around the microelectrode device. It is possible this increase in oligodendrocyte precursor cell population is an attempt to facilitate oligodendrocyte regeneration and remyelination chronically around the device. Pericytes also express the NG2 antigen; however, pericyte reactivity was reduced around chronically implanted microelectrode arrays, therefore, is unlikely that the increase in NG2+ cell proliferation and intensity expression at 28 days post-insertion can be attributed to the pericyte population. Even then, NG2, which is a chondroitin sulfate proteoglycan known for axon growth inhibition within the CNS, can be cleaved and secreted extracellularly, which is why NG2 fluorescence intensity profiles may not be a direct indicator of NG2 glia distribution or behavior. Additional analysis such as chronic *in vivo* experimentation would be needed to determine NG2 glia dynamics around implanted microelectrode arrays. Moreover, thoroughly understanding the behavior of this precursor population following injury will provide future insight on wound repair and regeneration following injury.

Loss of PDGFR-β+ Reactivity and Increased Blood-Brain Barrier Leakage Around Chronically Implanted Microelectrode Arrays

BBB degradation following microelectrode insertion are more frequently becoming a factor in studies concerning biological responses to implanted devices (Bjornsson et al., 2006; Johnson et al., 2007; Kozai et al., 2010, 2015c; Saxena et al., 2013; Nolta et al., 2015; Bedell et al., 2018; Bennett et al., 2019). Insertion of a device through the BBB is inevitable and can be severe depending on the size of the vessel ruptured (Kozai et al., 2010). Bleeding and loss of perfusion due to BBB damage can be detrimental to the viability of metabolically dependent cells such as neurons and oligodendrocytes within the brain (Kozai et al., 2015c; Wellman and Kozai, 2017; Wellman et al., 2018; Baranov et al., 2019). Additionally, inflammatory plasma proteins exposed to the parenchyma and biofouling on the implant surface have the potential to promote glial cell activation and further BBB breakdown (Kozai et al., 2012a). Avoiding or protecting the vasculature during insertion and chronic implantation of a device may potentially improve device performances by reducing inflammation within the brain. However, BBB function is supported by a variety of cells within the brain and each individual component can be influenced separately and distinctly by the chronic implantation of an intracortical electrode array (Muoio et al., 2014). Pericytes, which are gatekeepers to large macromolecules and circulating cells between the brain and the periphery, have many functional roles concerning BBB maintenance (Sweeney et al., 2016). From a tissue regenerative perspective, pericytes can facilitate new vessel formation and BBB repair whereas, during injury, pericytes can demonstrate neuroinflammatory functions and have been implicated in glial scar formation (Sweeney et al., 2016).

In this study, PDGFR-β+ cells were increased within the vicinity of an implanted device at 3 and 7 days following insertion. This increase in pericyte density could be an attempt to repair damaged vessels or mediate angiogenesis around the implanted device. By 28 days post-insertion, PDGFR-β+ cells were dramatically decreased compared to acute implantation. Previously, pericyte deficiencies during injury have been correlated with increased BBB dysfunction (Montagne et al., 2018). Indeed, bleeding was noticeably increased around the implanted device by 28 days post-insertion. However, vascular structures also appeared altered at chronic time points, prompting the question about whether reduced pericyte density is a consequence or effector of BBB disruption around inserted devices. Pericytes are increasingly becoming major cellular targets in neurodegenerative diseases such as Alzheimer's, stroke, MS, and more (Winkler et al., 2011; Sweeney et al., 2016; Iacobaeus et al., 2017; Cheng et al., 2018). Further characterization of their behavior around implanted intracortical devices will help understand

BBB associated inflammation following injury (Kozai et al., 2014c, 2015c; Wellman and Kozai, 2017).

CONCLUSION

Investigation of various aspects of biological inflammation revealed spatiotemporal patterns of cell death, glial proliferation, and BBB-associated pathology around implanted intracortical microelectrode arrays. Neuronal loss was prominent near the site of electrode insertion at acute and chronic time points, coinciding with structural changes to local axons, primarily in an apoptotic-dependent manner. Similarly, apoptosis-induced oligodendrocyte cell death was prevalent at the time of acute implantation prior to a tissue regenerative attempt at restoring oligodendrocyte densities and enhancing myelination at chronic time points. Activation and proliferation of microglia, astrocytes, and NG2 glia were observed preferentially around inserted devices at distinct time points along the course of implantation. Furthermore, a novel subtype of reactive astrocytes was revealed around the site of implantation, potentially derived from a resident oligodendrocyte precursor population. Finally, chronic pericyte deficiency was noted alongside increased vascular dysfunction near inserted devices. This study simultaneously broadens the scope of dynamic tissue events that occur during intracortical device implantation and specifies distinct mechanisms of cell death and reactivity in response to inflammation. Future studies investigating the biological response to electrode-induced injury and inflammation in an attempt to improve device performances will benefit within the context of this newly discovered knowledge.

ETHICS STATEMENT

All procedures and experimental protocols were approved by the University of Pittsburgh, Division of Laboratory Animal Resources, and Institutional Animal Care and Use Committee in accordance with standards for the humane animal case as set by the Animal Welfare Act and the National Institutes of Health Guide for the Care and Use of Laboratory Animals.

AUTHOR CONTRIBUTIONS

SW and TK contributed to conceptualization of the manuscript and developed the original draft of the manuscript. SW and IM performed the experimental surgeries. LL performed the sectioning, staining, and imaging of experimental samples. SW and YY conducted the image processing and analyses of histological data. All authors contributed to review and final edits.

FUNDING

This work was supported by NIH NINDS R01NS094396 and a diversity supplement to this parent grant as well as NIH NINDS R21NS108098.

ACKNOWLEDGMENTS

The authors would like to thank Franca Cambi for expert consultation and interpretation of results and Kelly Maers for valuable discussions regarding histological staining.

SUPPLEMENTARY MATERIAL

The Supplementary Material for this article can be found online at: https://www.frontiersin.org/articles/10.3389/fnins.2019.00493/full#supplementary-material

REFERENCES

Alba, N. A., Du, Z. J., Catt, K. A., Kozai, T. D. Y., and Cui, X. T. (2015). In vivo electrochemical analysis of a PEDOT/MWCNT neural electrode coating. *Biosensors* 5, 618–646. doi: 10.3390/bios5040618

Allahyari, R. V., and Garcia, A. D. R. (2015). Triggering reactive gliosis in vivo by a forebrain stab injury. *J. Vis. Exp.* e52825. doi: 10.3791/52825

Anderson, M. A., Burda, J. E., Ren, Y., Ao, Y., O'Shea, T. M., Kawaguchi, R., et al. (2016). Astrocyte scar formation aids central nervous system axon regeneration. *Nature* 532:195. doi: 10.1038/nature17623

Armulik, A., Genové, G., Mäe, M., Nisancioglu, M. H., Wallgard, E., Niaudet, C., et al. (2010). Pericytes regulate the blood–brain barrier. *Nature* 468:557.

Baranov, S. V., Baranova, O. V., Yablonska, S., Suofu, Y., Vazquez, A. L., and Kozai, T. D. Y. (2019). Mitochondria modulate programmed neuritic retraction. *J. Proc. Natl. Acad. Sci. U.S.A.* 116, 650–659. doi: 10.1073/pnas.1811021116

Bedell, H. W., Hermann, J. K., Ravikumar, M., Lin, S., Rein, A., and Li, X. (2018). Targeting CD14 on blood derived cells improves intracortical microelectrode performance. *Biomaterials* 163, 163–173. doi: 10.1016/j.biomaterials.2018.02.014

Bennett, C., Mohammed, F., Álvarez-Ciara, A., Nguyen, M. A., Dietrich, W. D., and Rajguru, S. M. (2019). Neuroinflammation, oxidative stress, and blood-brain barrier (BBB) disruption in acute Utah electrode array implants and the effect of deferoxamine as an iron chelator on acute foreign body response. *Biomaterials* 188, 144–159. doi: 10.1016/j.biomaterials.2018.09.040

Biran, R., Martin, D. C., and Tresco, P. A. (2005). Neuronal cell loss accompanies the brain tissue response to chronically implanted silicon microelectrode arrays. *Exp. Neurol.* 195, 115–126. doi: 10.1016/j.expneurol.2005.04.020

Bjornsson, C. S., Oh, S. J., Al-Kofahi, Y. A., Lim, Y. J., Smith, K. L., and Turner, J. N. (2006). Effects of insertion conditions on tissue strain and vascular damage during neuroprosthetic device insertion. *J. Neural Eng.* 3, 196–207. doi: 10.1088/1741-2560/3/3/002

Bradl, M., and Lassmann, H. (2010). Oligodendrocytes: biology and pathology. *Acta Neuropathol.* 119, 37–53. doi: 10.1007/s00401-009-0601-5

Branner, A., Stein, R. B., Fernandez, E., Aoyagi, Y., and Normann, R. A. (2004). Long-term stimulation and recording with a penetrating microelectrode array in cat sciatic nerve. *IEEE Trans. Biomed. Eng.* 51, 146–157. doi: 10.1109/TBME.2003.820321

Buffo, A., Vosko, M. R., Ertürk, D., Hamann, G. F., Jucker, M., Rowitch, D., et al. (2005). Expression pattern of the transcription factor Olig2 in response to brain

injuries: implications for neuronal repair. *Proc. Natl. Acad. Sci. U.S.A.* 102, 18183–18188. doi: 10.1073/pnas.0506535102

Buzsáki, G. (2004). Large-scale recording of neuronal ensembles. *Nat. Neurosci.* 7, 446–451. doi: 10.1038/nn1233

Campbell, A., and Wu, C. (2018). Chronically implanted intracranial electrodes: tissue reaction and electrical changes. *Micromachines* 9:430. doi: 10.3390/mi9090430

Cheng, J., Korte, N., Nortley, R., Sethi, H., Tang, Y., and Attwell, D. (2018). Targeting pericytes for therapeutic approaches to neurological disorders. *Acta Neuropathol.* 136, 507–523. doi: 10.1007/s00401-018-1893-0

Cherry, J. D., Olschowka, J. A., and O'Banion, M. K. (2014). Neuroinflammation and M2 microglia: the good, the bad, and the inflamed. *J. Neuroinflam.* 11:98. doi: 10.1186/1742-2094-11-98

Cheung, T., Nuño, M., Hoffman, M., Katz, M., Kilbane, C., Alterman, R., et al. (2013). Longitudinal impedance variability in patients with chronically implanted DBS devices. *Brain Stimul.* 6, 746–751. doi: 10.1016/j.brs.2013.03.010

Dewar, D., Underhill, S. M., and Goldberg, M. P. (2003). Oligodendrocytes and ischemic brain injury. *J. Cereb. Blood Flow Metab.* 23, 263–274. doi: 10.1097/01.wcb.0000053472.41007.f9

Dimou, L., and Gallo, V. (2015). NG2-glia and their functions in the central nervous system. *Glia* 63, 1429–1451. doi: 10.1002/glia.22859

Du, Y., and Dreyfus, C. F. (2002). Oligodendrocytes as providers of growth factors. *J. Neurosci. Res.* 68, 647–654. doi: 10.1002/jnr.10245

Du, Z. J., Kolarcik, C. L., Kozai, T. D. Y., Luebben, S. D., Sapp, S. A., Zheng, X. S., et al. (2017). Ultrasoft microwire neural electrodes improve chronic tissue integration. *Acta Biomater.* 53, 46–58. doi: 10.1016/j.actbio.2017.02.010

Dulamea, A. O. (2017a). "Role of Oligodendrocyte Dysfunction in Demyelination, Remyelination and Neurodegeneration in Multiple Sclerosis," in *Multiple Sclerosis: Bench to Bedside: Global Perspectives on a Silent Killer*, eds A. A. A. Asea, F. Geraci, and P. Kaur (Cham: Springer International Publishing), 91–127. doi: 10.1007/978-3-319-47861-6_7

Dulamea, A. O. (2017b). The contribution of oligodendrocytes and oligodendrocyte progenitor cells to central nervous system repair in multiple sclerosis: perspectives for remyelination therapeutic strategies. *Neural Regenerat. Res.* 12, 1939–1944. doi: 10.4103/1673-5374.221146

Eles, J., Vazquez, A., Kozai, T., and Cui, X. (2018a). In vivo imaging of neuronal calcium during electrode implantation: spatial and temporal mapping of damage and recovery. *Biomaterials* 174, 79–94. doi: 10.1016/j.biomaterials.2018.04.043

Eles, J., Vazquez, A., Kozai, T., and Cui, X. T. (2018b). Meningeal inflammatory response and fibrous tissue remodeling around intracortical implants: an in vivo two-photon imaging study. *Biomaterials* 195, 111–123. doi: 10.1016/j.biomaterials.2018.12.031

Eles, J. R., Vazquez, A. L., Snyder, N. R., Lagenaur, C., Murphy, M. C., Kozai, T. D. Y., et al. (2017). Neuroadhesive L1 coating attenuates acute microglial attachment to neural electrodes as revealed by live two-photon microscopy. *Biomaterials* 113, 279–292. doi: 10.1016/j.biomaterials.2016.10.054

Ge, W. P., and Jia, J. M. (2016). Local production of astrocytes in the cerebral cortex. *Neuroscience* 323, 3–9. doi: 10.1016/j.neuroscience.2015.08.057

Ge, W.-P., Miyawaki, A., Gage, F. H., Jan, Y. N., and Janm, L. Y. (2012). Local generation of glia is a major astrocyte source in postnatal cortex. *Nature* 484:376. doi: 10.1038/nature10959

Gittis, A. (2018). Probing new targets for movement disorders. *Science* 361:462. doi: 10.1126/science.aau4916

Golabchi, A., Wu, B., Li, X., Carlisle, D. L., Kozai, T. D. Y., Friedlander, R. M., et al. (2018). Melatonin improves quality and longevity of chronic neural recording. *Biomaterials* 180, 225–239. doi: 10.1016/j.biomaterials.2018.07.026

Grill, W. M., and Reichert, W. (2008). "Signal considerations for chronically implanted electrodes for brain interfacing," in *Indwelling Neural Implants: Strategies for Contending With the in Vivo Environment*, ed. W. Reichert (Boca Raton FL: CRC Press/Taylor & Francis), 42–58.

Hackett, A. R., D-Lee, H., Dawood, A., Rodriguez, M., Funk, L., Tsoulfas, P., et al. (2016). STAT3 and SOCS3 regulate NG2 cell proliferation and differentiation after contusive spinal cord injury. *Neurobiol. Dis.* 89, 10–22. doi: 10.1016/j.nbd.2016.01.017

Hackett, A. R., Yahn, S. L., Lyapichev, K., Dajnoki, A., D-Lee, H., Rodriguez, M., et al. (2018). Injury type-dependent differentiation of NG2 glia into heterogeneous astrocytes. *Exp. Neurol.* 308, 72–79. doi: 10.1016/j.expneurol.2018.07.001

Iacobaeus, E., Sugars, R. V., Törnqvist Andrén, A., Alm, J. J., Qian, H., and Frantzen, J. (2017). Dynamic changes in brain mesenchymal perivascular cells associate with multiple sclerosis disease duration, active inflammation, and demyelination. *Stem Cells Transl. Med.* 6, 1840–1851. doi: 10.1002/sctm.17-0028

Iordanova, B., Vazquez, A. L., Kozai, T. D. Y., Fukuda, M., and Kim, S. G. (2018). Optogenetic investigation of the variable neurovascular coupling along the interhemispheric circuits. *J. Cereb. Blood Flow Metab.* 38, 627–640. doi: 10.1177/0271678x18755225

Ishii, A., Fyffe-Maricich, S. L., Furusho, M., Miller, R. H., and Bansal, R. (2012). ERK1/ERK2 MAPK signaling is required to increase myelin thickness independent of oligodendrocyte differentiation and initiation of myelination. *J. Neurosci.* 32, 8855–8864. doi: 10.1523/JNEUROSCI.0137-12.2012

Johnson, M. D., Kao, O. E., and Kipke, D. R. (2007). Spatiotemporal pH dynamics following insertion of neural microelectrode arrays. *J. Neurosci. Methods* 160, 276–287. doi: 10.1016/j.jneumeth.2006.09.023

Karumbaiah, L., Norman, S. E., Rajan, N. B., Anand, S., Saxena, T., Betancur, M., et al. (2012). The upregulation of specific interleukin (IL) receptor antagonists and paradoxical enhancement of neuronal apoptosis due to electrode induced strain and brain micromotion. *Biomaterials* 33, 5983–5996. doi: 10.1016/j.biomaterials.2012.05.021

Kawabori, M., and Yenari, M. A. (2015). The role of the microglia in acute CNS injury. *Metab. Brain Dis.* 30, 381–392. doi: 10.1007/s11011-014-9531-6

Koivuniemi, A., Wilks, S. J., Woolley, A. J., and Otto, K. J. (2011). Multimodal, longitudinal assessment of intracortical microstimulation. *Progr. Brain Res.* 194, 131–144. doi: 10.1016/B978-0-444-53815-4.00011-X

Komitova, M., Serwanski, D. R., Richard Lu, Q., and Nishiyama, A. (2011). NG2 cells are not a major source of reactive astrocytes after neocortical stab wound injury. *Glia* 59, 800–809. doi: 10.1002/glia.21152

Kozai, T., Marzullo, T., Hooi, F., Langhals, N., Majewska, A., Brown, E., et al. (2010). Reduction of neurovascular damage resulting from microelectrode insertion into the cerebral cortex using in vivo two-photon mapping. *J. Neural Eng.* 7:046011. doi: 10.1088/1741-2560/7/4/046011

Kozai, T. D. Y., Alba, N. A., Zhang, H., Kotov, N. A., Gaunt, R. A., and Cui, X. T. (2014a). "Nanostructured Coatings for Improved Charge Delivery to Neurons," in *Nanotechnology and Neuroscience: Nano-electronic, Photonic and Mechanical Neuronal Interfacing*, eds M. De Vittorio, L. Martiradonna, and J. Assad (New York, NY: Springer), 71–134. doi: 10.1007/978-1-4899-8038-0_4

Kozai, T. D. Y., Gugel, Z., Li, X., Gilgunn, P. J., Khilwani, R., Ozdoganlar, O. B., et al. (2014b). Chronic tissue response to carboxymethyl cellulose based dissolvable insertion needle for ultra-small neural probes. *Biomaterials* 35, 9255–9268. doi: 10.1016/j.biomaterials.2014.07.039

Kozai, T. D. Y., Li, X., Bodily, L. M., Caparosa, E. M., Zenonos, G. A., Carlisle, D. L., et al. (2014c). Effects of caspase-1 knockout on chronic neural recording quality and longevity: Insight into cellular and molecular mechanisms of the reactive tissue response. *Biomaterials* 35, 9620–9634. doi: 10.1016/j.biomaterials.2014.08.006

Kozai, T. D. Y., Catt, K., Li, X., Gugel, Z. V., Olafsson, V. T., Vazquez, A. L., et al. (2015a). Mechanical failure modes of chronically implanted planar silicon-based neural probes for laminar recording. *Biomaterials* 37, 25–39. doi: 10.1016/j.biomaterials.2014.10.040

Kozai, T. D. Y., Du, Z., Gugel, Z. V., Smith, M. A., Chase, S. M., and Bodily, L. M. (2015b). Comprehensive chronic laminar single-unit, multi-unit, and local field potential recording performance with planar single shank electrode arrays. *J. Neurosci. Methods* 242, 15–40. doi: 10.1016/j.jneumeth.2014.12.010

Kozai, T. D. Y., Jaquins-Gerstl, A. S., Vazquez, A. L., Michael, A. C., and Cui, X. T. (2015c). Brain tissue responses to neural implants impact signal sensitivity and intervention strategies. *ACS Chem. Neurosci.* 6, 48–67. doi: 10.1021/cn500256e

Kozai, T. D. Y., Catt, K., Du, Z., Na, K., Srivannavit, O., Haque, R. M., et al. (2016c). Chronic in vivo evaluation of PEDOT/CNT for stable neural recordings. *IEEE Trans. Biomed. Eng.* 63, 111–119. doi: 10.1109/TBME.2015.2445713

Kozai, T. D. Y., Eles, J. R., Vazquez, A. L., and Cui, X. T. (2016a). Two-photon imaging of chronically implanted neural electrodes: sealing methods and new insights. *J. Neurosci. Methods* 256, 46–55. doi: 10.1016/j.jneumeth.2015.10.007

Kozai, T. D. Y., Jaquins-gerstl, A. S., Vazquez, A. L., Michael, A. C., and Cui, X. T. (2016b). Dexamethasone retrodialysis attenuates microglial response to implanted probes in vivo. *Biomaterials* 87, 157–169. doi: 10.1016/j.biomaterials.2016.02.013

Kozai, T. D. Y., Langhals, N. B., Patel, P. R., Deng, X., Zhang, H., Smith, K. L., et al. (2012a). Ultrasmall implantable composite microelectrodes with bioactive surfaces for chronic neural interfaces. *Nat. Mater.* 11, 1065–1073. doi: 10.1038/nmat3468

Kozai, T. D. Y., Vazquez, A. L., Weaver, C. L., Kim, S.-G., and Cui, X. T. (2012b). In vivo two-photon microscopy reveals immediate microglial reaction to implantation of microelectrode through extension of processes. *J. Neural Eng.* 9:066001. doi: 10.1088/1741-2560/9/6/066001

Levine, J. M., Reynolds, R., and Fawcett, J. W. (2001). The oligodendrocyte precursor cell in health and disease. *Trends Neurosci.* 24, 39–47. doi: 10.1016/s0166-2236(00)01691-x

Lindahl, P., Johansson, B. R., Levéen, P., and Betsholtz, C. (1997). Pericyte loss and microaneurysm formation in PDGF-B-deficient mice. *Science* 277, 242–245. doi: 10.1126/science.277.5323.242

McCreery, D., Cogan, S., Kane, S., and Pikov, V. (2016). Correlations between histology and neuronal activity recorded by microelectrodes implanted chronically in the cerebral cortex. *J. Neural Eng.* 13:036012. doi: 10.1088/1741-2560/13/3/036012

McCreery, D., Pikov, V., and Troyk, P. R. (2010). Neuronal loss due to prolonged controlled-current stimulation with chronically implanted microelectrodes in the cat cerebral cortex. *J. Neural Eng.* 7:036005. doi: 10.1088/1741-2560/7/3/036005

McTigue, D. M., and Tripathi, R. B. (2008). The life, death, and replacement of oligodendrocytes in the adult CNS. *J. Neurochem.* 107, 1–19. doi: 10.1111/j.1471-4159.2008.05570.x

Michelson, N. J., Eles, J. R., Vazquez, A. L., Ludwig, K. A., and Kozai, T. D. J. (2018a). Calcium activation of cortical neurons by continuous electrical stimulation: frequency dependence, temporal fidelity, and activation density. *J. Neurosci. Res.* 97, 620–638. doi: 10.1002/jnr.24370

Michelson, N. J., Vazquez, A. L., Eles, J. R., Salatino, J. W., Purcell, E. K., Williams, J. J., et al. (2018b). Multi-scale, multi-modal analysis uncovers complex relationship at the brain tissue-implant neural interface: new emphasis on the biological interface. *J. Neural Eng.* 15:033001. doi: 10.1088/1741-2552/aa9dae

Michelson, N. J., and Kozai, T. D. Y. (2018). Isoflurane and ketamine differentially influence spontaneous and evoked laminar electrophysiology in mouse V1. *J. Neurophysiol.* 120, 2232–2245. doi: 10.1152/jn.00299.2018

Montagne, A., Nikolakopoulou, A. M., Zhao, Z., Sagare, A. P., Si, G., and Lazic, D. (2018). Pericyte degeneration causes white matter dysfunction in the mouse central nervous system. *Nat. Med.* 24:326. doi: 10.1038/nm.4482

Muoio, V., Persson, P. B., and Sendeski, M. M. (2014). The neurovascular unit – concept review. *Acta Physiol.* 210, 790–798. doi: 10.1111/apha.12250

Mushahwar, V. K., Collins, D. F., and Prochazka, A. (2000). Spinal cord microstimulation generates functional limb movements in chronically implanted cats. *Exp. Neurol.* 163, 422–429. doi: 10.1006/exnr.2000.7381

Nishiyama, A., Yang, Z., and Butt, A. (2005). Astrocytes and NG2-glia: what's in a name? *J. Anat.* 207, 687–693. doi: 10.1111/j.1469-7580.2005.00489.x

Nolta, N. F., Christensen, M. B., Crane, P. D., Skousen, J. L., and Tresco, P. A. (2015). BBB leakage, astrogliosis, and tissue loss correlate with silicon microelectrode array recording performance. *Biomaterials* 53, 753–762. doi: 10.1016/j.biomaterials.2015.02.081

Platia, E. V., and Brinker, J. A. (1986). Time course of transvenous pacemaker stimulation impedance, capture threshold, and electrogram amplitude. *Pacing Clin. Electrophysiol.* 9, 620–625. doi: 10.1111/j.1540-8159.1986.tb05408.x

Polikov, V. S., Tresco, P. A., and Reichert, W. M. (2005). Response of brain tissue to chronically implanted neural electrodes. *J. Neurosci. Methods* 148, 1–18. doi: 10.1016/j.jneumeth.2005.08.015

Potter, K. A., Buck, A. C., Self, W. K., and Capadona, J. R. (2012). Stab injury and device implantation within the brain results in inversely multiphasic neuroinflammatory and neurodegenerative responses. *J. Neural Eng.* 9:046020. doi: 10.1088/1741-2560/9/4/046020

Prasad, A., Xue, Q.-S., Dieme, R., Sankar, V., Mayrand, R., Nishida, T., et al. (2014). Abiotic-biotic characterization of Pt/Ir microelectrode arrays in chronic implants. *Front. Neuroeng.* 7:2. doi: 10.3389/fneng.2014.00002

Prasad, A., Xue, Q. S., Sankar, V., Nishida, T., Shaw, G., Streit, W. J., et al. (2012). Comprehensive characterization and failure modes of tungsten microwire arrays in chronic neural implants. *J. Neural Eng.* 9:056015. doi: 10.1088/1741-2560/9/5/056015

Ransohoff, R. M. (2016). A polarizing question: do M1 and M2 microglia exist? *Nat. Neurosci.* 19:987. doi: 10.1038/nn.4338

Salatino, J. W., Ludwig, K. A., Kozai, T. D. Y., and Purcell, E. K. (2017). Glial responses to implanted electrodes in the brain. *Nature BME* 1, 862–877. doi: 10.1038/s41551-017-0154-1

Saxena, T., Karumbaiah, L., Gaupp, E. A., Patkar, R., Patil, K., Betancur, M., et al. (2013). The impact of chronic blood–brain barrier breach on intracortical electrode function. *Biomaterials* 34, 4703–4713. doi: 10.1016/j.biomaterials.2013.03.007

Schindelin, J., Arganda-Carreras, I., Frise, E., Kaynig, V., Longair, M., Pietzsch, T., et al. (2012). Fiji: an open-source platform for biological-image analysis. *Nat. Methods* 9:676. doi: 10.1038/nmeth.2019

Schwartz, A. B., Cui, X. T., Weber, D. J., and Moran, D. W. (2006). Brain-controlled interfaces: movement restoration with neural prosthetics. *Neuron* 52, 205–220. doi: 10.1016/j.neuron.2006.09.019

Sillay, K. A., Chen, J. C., and Montgomery, E. B. (2010). Long-term measurement of therapeutic electrode impedance in deep brain stimulation. *Neuromodulation* 13, 195–200. doi: 10.1111/j.1525-1403.2010.00275.x

Snaidero, N., and Simons, M. (2017). The logistics of myelin biogenesis in the central nervous system. *Glia* 65, 1021–1031. doi: 10.1002/glia.23116

Stocking, K. C., Vazquez, A. L., and Kozai, T. D. Y. (2019). Intracortical neural stimulation with untethered, ultrasmall carbon fiber electrodes mediated by the photoelectric effect. *IEEE Trans. Biomed. Eng.* 1. doi: 10.1109/TBME.2018.2889832

Sweeney, M. D., Ayyadurai, S., and Zlokovic, B. V. (2016). Pericytes of the neurovascular unit: key functions and signaling pathways. *Nat. Neurosci.* 19:771. doi: 10.1038/nn.4288

Szarowski, D. H., Andersen, M. D., Retterer, S., Spence, A. J., Isaacson, M., Craighead, H. G., et al. (2003). Brain responses to micro-machined silicon devices. *Brain Res.* 983, 23–35. doi: 10.1016/s0006-8993(03)03023-3

Tan, A. M., Zhang, W., and Levine, J. M. (2005). NG2: a component of the glial scar that inhibits axon growth. *J. Anat.* 207, 717–725. doi: 10.1111/j.1469-7580.2005.00452.x

Thomas, G. P., and Jobst, B. C. (2015). Critical review of the responsive neurostimulator system for epilepsy. *Med. Dev.* 8:405. doi: 10.2147/MDER.S62853

Tomassy, G. S., Berger, D. R., Chen, H. H., Kasthuri, N., Hayworth, K. J., Vercelli, A., et al. (2014). Distinct profiles of myelin distribution along single axons of pyramidal neurons in the neocortex. *Science* 344, 319–324. doi: 10.1126/science.1249766

Tresco, P. A., and Winslow, B. D. (2011). The challenge of integrating devices into the central nervous system. *Crit. Rev. Biomed. Eng.* 39, 29–44. doi: 10.1615/critrevbiomedeng.v39.i1.30

Wellman, S. M., Cambi, F., and Kozai, T. D. Y. (2018). The role of oligodendrocytes and their progenitors on neural interface technology: a novel perspective on tissue regeneration and repair. *Biomaterials* 183, 200–217. doi: 10.1016/j.biomaterials.2018.08.046

Wellman, S. M., Eles, J. R., Ludwig, K. A., Seymour, J. P., Michelson, N. J., McFadden, W. E., et al. (2017). A materials roadmap to functional neural interface design. *Adv. Funct. Mater.* 28:1701269. doi: 10.1002/adfm.201701269

Wellman, S. M., and Kozai, T. D. Y. (2017). Understanding the inflammatory tissue reaction to brain implants to improve neurochemical sensing performance. *ACS Chem. Neurosci.* 8, 2578–2582. doi: 10.1021/acschemneuro.7b00403

Wellman, S. M., and Kozai, T. D. Y. (2018). Invivo spatiotemporal dynamics of NG2 glia activity caused by neural electrode implantation. *Biomaterials* 164, 121–133. doi: 10.1016/j.biomaterials.2018.02.037

Williams, J. C., Hippensteel, J. A., Dilgen, J., Shain, W., and Kipke, D. R. (2007). Complex impedance spectroscopy for monitoring tissue responses to inserted neural implants. *J. Neural Eng.* 4, 410–423. doi: 10.1088/1741-2560/4/4/007

Winkler, E. A., Bell, R. D., and Zlokovic, B. V. (2011). Central nervous system pericytes in health and disease. *Nat. Neurosci.* 14:1398. doi: 10.1038/nn.2946

Winslow, B. D., Christensen, M. B., Yang, W. K., Solzbacher, F., and Tresco, P. A. (2010). A comparison of the tissue response to chronically implanted Parylene-C-coated and uncoated planar silicon microelectrode arrays in rat cortex. *Biomaterials* 31, 9163–9172. doi: 10.1016/j.biomaterials.2010.05.050

Winslow, B. D., and Tresco, P. A. (2010). Quantitative analysis of the tissue response to chronically implanted microwire electrodes in rat cortex. *Biomaterials* 31, 1558–1567. doi: 10.1016/j.biomaterials.2009.11.049

Zhou, Q., Choi, G., and Anderson, D. J. (2001). The bHLH transcription factor Olig2 promotes oligodendrocyte differentiation in collaboration with Nkx2. 2. *Neuron* 31, 791–807. doi: 10.1016/s0896-6273(01)00414-7

Conflict of Interest Statement: The authors declare that the research was conducted in the absence of any commercial or financial relationships that could be construed as a potential conflict of interest.

Copyright © 2019 Wellman, Li, Yaxiaer, McNamara and Kozai. This is an open-access article distributed under the terms of the Creative Commons Attribution License (CC BY). The use, distribution or reproduction in other forums is permitted, provided the original author(s) and the copyright owner(s) are credited and that the original publication in this journal is cited, in accordance with accepted academic practice. No use, distribution or reproduction is permitted which does not comply with these terms.

frontiers in Neuroscience

TECHNOLOGY REPORT
published: 04 June 2019
doi: 10.3389/fnins.2019.00518

Design and Development of Microscale Thickness Shear Mode (TSM) Resonators for Sensing Neuronal Adhesion

Massoud L. Khraiche[1]*, *Jonathan Rogul*[2] and *Jit Muthuswamy*[2]

[1] Neural Engineering and Nanobiosensors Group, Biomedical Engineering Program, Maroun Semaan Faculty of Engineering and Architecture, American University of Beirut, Beirut, Lebanon, [2] Neural Microsystems Laboratory, School of Biological and Health Systems Engineering, Arizona State University (ASU), Tempe, AZ, United States

OPEN ACCESS

Edited by:
Ulrich G. Hofmann,
Freiburg University Medical Center,
Germany

Reviewed by:
Ioana Voiculescu,
City College of New York (CUNY),
United States
Liang Guo,
The Ohio State University,
United States

***Correspondence:**
Massoud L. Khraiche
mkhraiche@aub.edu.lb

Specialty section:
This article was submitted to Neural Technology, a section of the journal Frontiers in Neuroscience

Received: 16 February 2019
Accepted: 06 May 2019
Published: 04 June 2019

Citation:
Khraiche ML, Rogul J and Muthuswamy J (2019) Design and Development of Microscale Thickness Shear Mode (TSM) Resonators for Sensing Neuronal Adhesion. Front. Neurosci. 13:518. doi: 10.3389/fnins.2019.00518

The overall goal of this study is to develop thickness shear mode (TSM) resonators for the real-time, label-free, non-destructive sensing of biological adhesion events in small populations (hundreds) of neurons, in a cell culture medium and subsequently *in vivo* in the future. Such measurements will enable the discovery of the role of biomechanical events in neuronal function and dysfunction. Conventional TSM resonators have been used for chemical sensing and biosensing applications in media, with hundreds of thousands of cells in culture. However, the sensitivity and spatial resolution of conventional TSM devices need to be further enhanced for sensing smaller cell populations or molecules of interest. In this report, we focus on key challenges such as eliminating inharmonics in solution and maximizing *Q*-factor while simultaneously miniaturizing the active sensing (electrode) area to make them suitable for small populations of cells. We used theoretical expressions for sensitivity and electrode area of TSM sensors operating in liquid. As a validation of the above design effort, we fabricated prototype TSM sensors with resonant frequencies of 42, 47, 75, and 90 MHz and characterized their performance in liquid using electrode diameters of 150, 200, 400, 800, and 1,200 μm and electrode thicknesses of 33 and 230 nm. We validated a candidate TSM resonator with the highest sensitivity and *Q*-factor for real-time monitoring of the adhesion of cortical neurons. We reduced the size of the sensing area to 150–400 μm for TSM devices, improving the spatial resolution by monitoring few 100–1,000s of neurons. Finally, we modified the electrode surface with single-walled carbon nanotubes (SWCNT) to further enhance adhesion and sensitivity of the TSM sensor to adhering neurons (Marx, 2003).

Keywords: quartz crystal microbalance (QCM), ultrasound, adhesion, neural interfaces, carbon nanotubes, microelectrode, neuron, acoustic sensors

1. INTRODUCTION

The biomechanics of the neuron-implant interface, involving highly localized neuronal adhesion, has a significant impact on intra- and extracellular signal fidelity, signal-to-noise ratio, and the viability of the neural tissue that determines the duration of neuronal recordings *in vitro* or life of an implanted device *in vivo*. Neurons change shape and realign their cytoskeleton to adhere to foreign substrates in their proximity. The complexity and dynamic nature of the adhesion process presents a challenge for studying this phenomenon using state-of-the-art end point imaging techniques such as fluorescent and electron microscopy. Electrical impedance-based methods lack the sensitivity required to capture changes in focal adhesion complexes (protein cytoskeletal anchor points at cell/substrate) since the measured current flows through the entire cell. Piezoelectric transducers have widely been used for sensing cellular adhesion due to their ease of use, low cost and high sensitivity. Quartz crystals are the most commonly used piezoelectric material for building transducers due to their desirable mechanical, thermal, chemical and electrical properties (Sauerbrey, 1959; Ferreira et al., 2009). AT-cut quartz produces bulk transverse shear waves with particle displacements parallel to the surface of the crystal and its electrodes. These AT-cut quartz oscillators are commonly termed thickness shear mode (TSM) resonators. When a small mass is deposited on the surface of a quartz crystal oscillator, the oscillator's resonance frequency decreases in direct proportion to the deposited mass as described by the classic Sauerbrey equation:

$$\Delta f_o = \frac{2f_o^2}{(\rho_Q \mu_Q)^{1/2}} \frac{\Delta m}{A} \tag{1}$$

where f_o is the fundamental resonant frequency of the quartz crystal, A is the surface area of the piezoelectric area of the crystal, μ_Q and ρ_Q are the shear modulus and the density of quartz (Sauerbrey, 1959). The stability of AT-cut quartz under temperature change has led to a wide range of applications involving measurement of mass deposition in vacuum. TSM devices can operate in liquid and have been used for a variety of chemical or biosensor applications which include detection and analysis of proteins (serum, neurotransmitters) (Wang and Muthuswamy, 2008), antibodies as well as DNA (Ferreira et al., 2009; Li et al., 2011), self-assembled monolayer (SAMs) (Seker et al., 2016), lipids and cells (neurons, fibroblast, blood cells, neutrophils, bacteria) (Khraiche et al., 2003, 2005; Da-Silva et al., 2012; Khraiche and Muthuswamy, 2012; Zhou et al., 2012; Westas et al., 2015). The first attempts to study adhesion of cells using TSM sensors involved platelet adhesion (Matsuda, 1992). In the above report, Matsuda et al. concluded that the time dependent response of the acoustic sensor to cell attachment was not just due to the number of cells attaching but also to the adhesion state of the cells. In addition, work done by Gryte et al. (1993) showed that resonant frequency of the TSM sensor recovers to baseline when the pH was changed drastically causing the cells to detach from the sensor surface. Additionally, adding nonadherent beads to the sensor surface showed no change in resonant frequency. These early findings demonstrating the specificity of the changes in resonant frequency of the TSM sensors to cellular adhesion events opened the door to multiple studies using TSM sensors for monitoring adhesion (Khraiche et al., 2005; Khraiche and Muthuswamy, 2012; Lee et al., 2012; Saitakis and Gizeli, 2012; Da-Silva et al., 2013). Although the use of TSM resonators as biosensors encompasses a large number of applications, the commonly used dimensions of the electrodes and resonant frequencies of the crystal in most studies have a narrow range between 5 and 7 mm for electrode diameters, 200 nm for electrode thickness and 5–10 MHz resonant frequencies for the quartz crystal (Kosslinger et al., 1995). The above parameters of TSM resonators result in sensitivity (using Equation 1) and sensing area that is typically suitable for measurements of biological events in tens or hundreds of thousands of cells. Their performance therefore falls short of other comparable biosensing modalities such as surface plasmon resonance (SPR) (Su et al., 2005; Fang et al., 2015). In this study, we aim to develop a TSM sensor that can monitor biological adhesion in tens or hundreds of neurons *in vitro*. If successful, the natural advantages of TSM sensors such as label-free, non-destructive and real-time monitoring capabilities can be used to monitor the biomechanics of neurophysiology with much higher spatial resolution in a countable number of cells. Besides playing a key role in neuronal function and dysfunction in several pathologies, neuronal adhesion to a brain implant *in vivo* is also an important part of the immune response to the implants. Therefore, the proposed approach has potential *in vivo* applications in the future. The focus of this study is to investigate the effect of resonant frequency of TSM sensors and electrode dimensions (active sensing area) on sensitivity and *Q*-factor in the context of sensing neuronal adhesion. As indicated by Equation (1), the sensitivity of TSM sensors operating in air or vacuum is directly proportional to the square of the resonant frequency. But the fundamental resonant frequency in the bulk of the TSM sensor is limited by the thickness (wavelength of the fundamental is twice the thickness as indicated in Equation 2) of the quartz substrate. For instance, to fabricate a TSM sensor with 100 MHz resonant frequency, the thickness of the substrate needs to be approximately 16 μm which pose challenges to fabrication, handling and packaging. Furthermore, for sensing neuronal adhesion in biological media, two critical aspects of TSM sensor operation-inharmonic modes and the quality factor (*Q*-factor) need to be optimized. Inharmonic modes or spurious modes are standing waves in the quartz substrate with frequencies different from the resonant frequency and its harmonics. These unwanted inharmonics reduce acoustic energy trapping and, if the frequency separation between the harmonic and inharmonic modes is not sufficient, adjacent resonant peaks interfere with each other, resulting in mode coupling or frequency jumps. The *Q*-factor is considered a critical metric for sensor sensitivity as it determines the minimal frequency change detectable and is affected by dielectric, acoustic and electric losses within the TSM sensor. In this study, we specifically minimize inharmonic modes and maximize *Q*-factor and develop a design framework that serves as a guide for increasing sensitivity and spatial resolution of TSM sensors operating in a liquid environment.

2. THEORY

2.1. Harmonic and Inharmonic Waves

The application of an electric field across the thickness of AT-cut quartz leads to particle movement, which in turn results in two types of standing waves-a transverse wave in the thickness direction referred to as the thickness shear TS1 wave and a wave traveling in the radial direction known as the thickness twist TT3 wave. The path length of TS1 waves is the quartz plate thickness with nodes along the diameter of the plate, while the path length for TT3 is the electrode radius with concentric nodal lines along the center of the quartz plate. When the length of the path is an integral number of wavelengths, a standing wave occurs and results in resonance (Shockley et al., 1967). The fundamental resonant frequency of AT-cut quartz is a result of the TS1 standing wave and is the most reliable and largest wave of this type of acoustic systems. TT3 waves are considered unwanted inharmonic waves that, if present, can interfere with the correct measurements of the resonant frequency.

2.2. Energy Trapping

The theory of energy trapping is based on the principle that waves traveling in a piezoelectric substrate must have a frequency higher than a certain "cutoff frequency," defined as the fundamental frequency of the system, which is the frequency predicted based on the thickness of the quartz substrate (hs).

$$f_0 = \frac{\sqrt{\mu_Q/\rho_Q}}{2h_s} \tag{2}$$

where f_o is the fundamental resonant frequency of the quartz crystal, A is the surface area of the piezoelectric area of the crystal, μ_Q and ρ_Q are the shear modulus and the density of quartz (Ferreira et al., 2009).

When electrodes are applied to an AT-cut quartz plate they create two regions of different frequencies as illustrated in **Figure 1A** (plated and unplated) where a cross section of the TSM sensor is shown. The two regions are formed due to the mass of the electrodes on the plated region "e." resulting in the cutoff frequency (f_s) of the unplated "s" region being slightly higher than the cutoff frequency (f_e) of the plated region "e." These two regions give rise to three different scenarios for the propagation of a wave (frequency f_t) within the quartz. For waves having frequencies f_t where $f_e < f_t < f_s$, these waves can propagate within the "e" region but not the "s" region, and total internal reflection occurs at the boundary between the two regions. Waves in the plated "e" region with frequencies below f_e (i.e., $f_t < f_e$) cannot propagate in the plated region, "e" or into the unplated region, "s" and get attenuated within the plated "e" region. For waves with frequency, f_t higher than f_s ($f_t > f_s$) vibration energy generated in plated region "e" will propagate away resulting in a loss of energy and, therefore, will not contribute to a localized standing wave response. The latter is desirable for unwanted waves.

2.3. Eliminating Inharmonic Waves

Based on the energy trapping theory, the frequency of the inharmonic waves needs to be higher than the cut-off frequency of the unplated region in order to eliminate the inharmonic

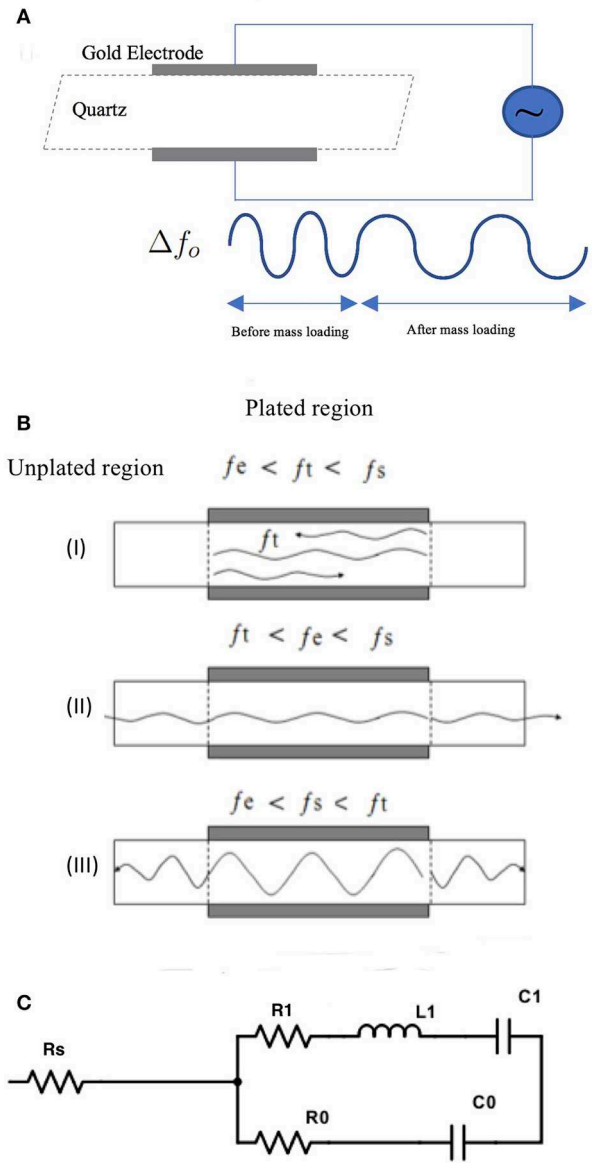

FIGURE 1 | (A) Illustration of theory of operation of TSM devices. **(B)** Shows three scenarios for propagation of waves within the quartz crystal in a TSM sensor. For illustration, the waves are shown in a cross-section of the TSM sensor, where metalized electrodes over the quartz create two distinct regions with different cut-off frequencies for the propagated waveforms -unplated region "s" with a cutoff frequency f_s and plated region "e" with a cutoff frequency f_e with $f_s > f_e$ due to the weight of the electrode. This gives rise to three different scenarios for propagation of waves of frequency f_t in the plated quartz substrate. (I) when f_t is between f_e and f_s, waves can propagate within the "e" region but not into the "s" region, and total internal reflection occurs at the boundary between the two regions (II) when f_t is below f_e, waves cannot propagate into "s" region but get attenuated within the "e" region III) when f_t is higher than f_s, vibration energy generated in region "e" will propagate into the "s" region, resulting in loss of energy and therefore will not contribute to a localized standing wave response. **(C)** The BVD electrical model consists of three series components modified by the mass and viscous loading of the crystal where R1 is the dissipation of the oscillation, C1 corresponds to the stored energy in the oscillation, L1 (inductor) corresponds to the inertial component of the oscillation. The BVD model can be modified to a five-element model, in which a series resistor (RS) is added.

modes. This will cause the inharmonic to travel in the unplated region without creating a standing wave in the crystal (Bottom, 1982). The eigen frequency of a clamped resonator f_{nmk} with a circular electrode can be calculated from the following equation;

$$f_{nmk} = f_{n01}(1 + 2\frac{X_{mk}h_s}{n\pi d}) \quad (3)$$

X_{mk} is the kth root of the Bessel function of order m, f_{n01}- the frequency of the nth harmonic mode, d is the diameter of the electrodes and hs is the thickness of the quartz. As mentioned earlier, if the first inharmonic is larger than the cut-off frequency of the unplated region, the inharmonic will propagate into the unplated region and will not result in a standing wave. So, our design should consider the following;

$$nf_0 < f_{nmk}$$

where f_0 is the fundamental resonant frequency. Given that X_{11}=3.832 and substituting Equation (3) we have;

$$\Delta f_{pb} < f_{n01}\frac{2.98}{n^2}(\frac{h_s}{d})^2 \quad (4)$$

We refer to Δf as the plate-back. From Equation (4), we find a design guide for eliminating the inharmonic modes. We assume that the change in mass by adding electrodes is equivalent to the plate-back, which will allow us to equate plate-back to the Sauerbrey equation and substituting n=1 (first inharmonic), we get the following equation;

$$h_e < \frac{9.38X10^8 m^3 s^{-3}}{f_0^3 d^2} \quad (5)$$

Where the term h_e is thickness of the electroded region of the crystal (electrode + quartz). This equation provides a guide to designing a resonator while avoiding all inharmonic modes.

2.4. Liquid Load

However, when the sensor is operated under liquid loading, Equation (4) becomes inaccurate in predicting the presence of the inharmonics, due to the impact of viscoelastic loading on the QCM sensor under liquid load. Kanazawa et al used the velocity distribution of the crystal oscillation in fluid to describe how the viscosity and density of the fluid affects the oscillation. The result of that work was an expression describing the frequency change induced by immersing one face of a quartz resonator in a liquid as a function of the viscosity as well as the density of the liquid (Kanazawa and Gordon, 1985).

$$\Delta f = -f_0^{\frac{3}{2}}(\frac{\rho_l \eta_l}{\pi \rho_q \mu_q})^{\frac{1}{2}} \quad (6)$$

where η_l is the viscosity of the liquid and ρ_l is the liquid's density, ρ_q and μ_q are the density and shear modulus of the quartz. The net change in resonant frequency is therefore the summation of the mass loading effects described by Sauerbrey and the viscosity effects described by Kanazawa's equations. If we assume that plate-back is equivalent to the change in frequency from both of these mass loadings, we have

$$\Delta f = \frac{-2f_0^2 \Delta m}{v_q \rho_q A} - f_0^{\frac{3}{2}}\sqrt{\frac{\eta_l \rho_l}{\pi \mu_q \rho_q}} \quad (7)$$

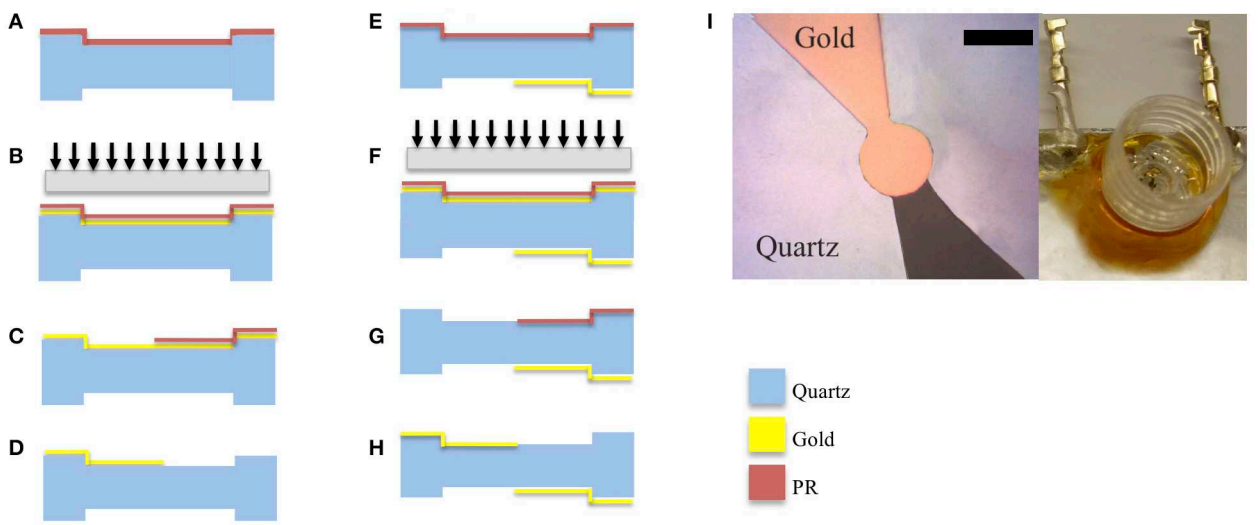

FIGURE 2 | Schematic of the fabrication process involving deposition of gold electrodes on quartz substrates with inverted mesa-like out-of-plane structures. Figures on the left-hand column correspond to the patterning of the topside of the quartz plate. **(A)** gold was vapor deposited on the quartz surface. **(B)** photoresist (PR) patterned on gold and pattern exposed. **(C)** solvent used to wash away exposed PR. **(D)** gold etchant used to expose electrode. Figures on the right-hand column correspond to patterning of the bottom side of the quartz plate. The quartz wafer was flipped to expose the bottom side, **(E)** photoresist coated on quartz **(F)** photoresist (PR) patterned on gold and pattern exposed using backside alignment. **(G)** solvent used to wash away exposed PR; **(H)** gold is evaporated to form the electrode on the bottom side. **(I)** Micrograph of the resulting pattern of gold electrodes on 50 Hz quartz (scale bar 150 μm) along with a picture of the cell culture well toping the crystal with interconnects.

And

$$\Delta f = \frac{-2f_0^2 \Delta m}{v_q \rho_q A} - f_0^{\frac{3}{2}} \sqrt{\frac{\eta_l \rho_l}{\pi \mu_q \rho_q}} < f_{n01} \frac{2.98}{n^2} \left(\frac{h_s}{d}\right)^2 \quad (8)$$

The equation can be rearranged to;

$$h_e < \frac{2.98 \mu_q v_q}{16 n^2 f_0^3 d^2 \rho_e} - f_0^{\frac{3}{2}} \sqrt{\frac{\eta_l \rho_l}{\pi \mu_q \rho_q}} \frac{v_q \rho_q}{4 f_0^2 \rho_e} \quad (9)$$

$$h_e < \frac{2.98 \mu_q v_q}{16 n^2 f_0^3 d^2 \rho_e} - \sqrt{\frac{\eta_l \rho_l \rho_q}{\pi \mu_q f_0}} \frac{v_q}{4 \rho_e} \quad (10)$$

Assuming that the liquid is water at 20^{o}C with a viscosity of 1.0022×10^{-3} Pa.s [or kg/(m.s)] and a density of 998.2 kg/m^3, then the equation further reduces to:

$$h_e < \frac{9.38X10^8 m^3 s^{-3}}{f^3 d^2} - \sqrt{\frac{5.32X10^{11} m^2 s^{-1}}{f_0}} \quad (11)$$

2.5. *Q*-Factor

The quality factor (*Q*-factor) for resonators is the ratio between energy stored and the energy dissipated per cycle. This quantity is a metric for sensor efficiency and stability and can be calculated based on material properties. The following equation relates the *Q*-factor to the resonant frequency of the quartz (Mason, 1956);

$$Q = 1.6X10^{13} \frac{1}{f_0} \quad (12)$$

The *Q*-factor value calculated in Equation (12) is not reached in experimental prototypes. This is due to two types of losses in TSM oscillators-electrical losses and acoustic losses. The electrical losses stem from the electrical properties of the electrodes sandwiching the quartz crystal in the TSM sensor and the associated leads. As for the acoustic losses, it includes internal losses due to defects, scattering and losses due to acoustic boundaries between thin films in the oscillator. In addition, for TSM sensors operating in fluid, the acoustic energy is dissipated in the fluid by viscous mechanisms resulting in a decrease in the quality factor. While a thin solid film will only cause a change in resonant frequency, a Newtonian liquid will cause a simultaneous shift in the resonant frequency and the decrease of the quality factor. That being said, a more accurate estimate of the *Q*-factor can be obtained from the BVD (Butterworth van dyke) model. The classic BVD model consists of a series of R_1 , L_1, and C_1 components modified by the mass and viscous loading of the crystal where R_1 is the dissipation of the oscillation, C_1 corresponds to the stored energy in the oscillation, L_1 corresponds to the inertial component of the oscillation. The BVD model can be further modified to better describe the crystal, and the losses impacting the *Q*-factor, as a six-element model, in which a series resistor (R_S) and acoustic leakage resistance Ro is added (**Figure 1C**). The addition of RS accounts for losses due to the electrode electrical properties. Past

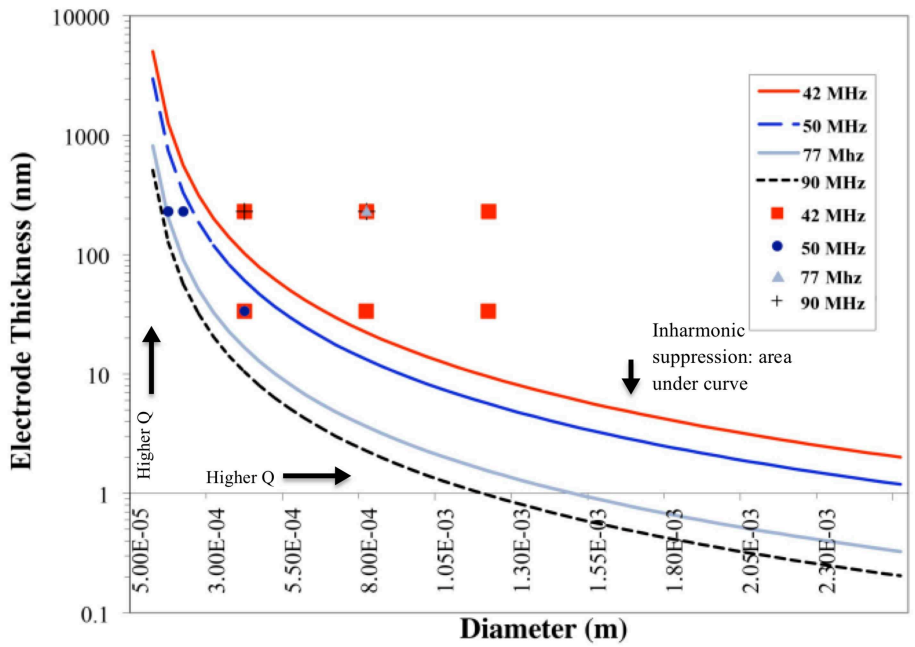

FIGURE 3 | Plate-back characteristics for suppressing the unwanted inharmonic modes in air demonstrate the theoretical relation between electrode thickness and electrode diameter for any given resonant frequency (inversely proportional to the thickness of the quartz crystal). The lines correspond to the specific resonant frequency of the quartz crystal. The region under each curve indicates possible combinations of electrode thicknesses and diameters that will suppress inharmonic modes of vibration.

work has shown that this modified BVD model improves *Q*-factor estimates and relates electrode conductivity to *Q*-factor changes (Larson et al., 2000). In addition, the *Q*-factor's impact on TSM sensor sensitivity can be determined by considering the smallest detectable resonant frequency, which is governed largely by the *Q*-factor and can be calculated from the following (Lakin et al., 1993; Weber et al., 2008);

$$\Delta f_o = \frac{1}{2} f_o \frac{\Delta \phi_{min}}{Q} \tag{13}$$

The previous equation relates the smallest detectable change in the resonant frequency by TSM sensors to the *Q*-factor and ϕ (phase resolution of the acquisition system). Using Equation (1) we can rewrite Equation (13) for sensitivity in terms of the smallest change in mass per unit area:

$$\frac{\Delta m_{min}}{A} = \frac{1}{2} \frac{\sqrt{\rho_Q \mu_Q} \Delta \phi_{min}}{f_o Q} \tag{14}$$

2.6. Motional Resistance and Viscoelastic Changes

Through an electromechanical analogy of the quartz crystal, Muramatsu et al. derived a relationship between the motional resistance R_1 and the density and viscosity of the liquid that is shown below in Equation (15):

$$R_1 = \frac{(2\pi f_0 \rho_l \eta_l)^{\frac{1}{2}} A}{\kappa^2} \tag{15}$$

Where A is the active electrode area of the sensor, ρ_l is the density and η_L is the absolute viscosity of the liquid, κ an electromechanical coupling factor (Kanazawa and Gordon, 1985; Muramatsu and Kimura, 1992). A plot of ΔR_1 vs. Δf_s has then been used to describe the mechanical changes in the deposited thin film on the sensor surface (Zhou and Muthuswamy, 2004). The term $(\rho_L \eta_L)$ appears in both Equations (6) and (14) and the ratio of both equations resulting in a straight line in the case of pure viscous liquid contacting the sensor surface. The relationship of ΔR_1 vs. Δf_s provides insights into viscoelastic changes in the thin layer adhering to the sensor, where changes in frequency only (without a corresponding change in ΔR_1), are due to rigid mass deposition (elastic changes) and changes in viscosity of the adhering layer only, will result in changes along a line of unit slope in the ΔR_1 vs. Δf_s plot (energy dissipation). This type of plot was introduced by Muramatsu et al (Muramatsu and Kimura, 1992; Kang et al., 2008) and was later used by Marx et al in studying thin film deposition and cells (Marx, 2003).

3. MATERIALS AND METHODS

3.1. Sensor Fabrication

High frequency polished quartz crystals were obtained from Xeco, Cedar City, UT, USA. The crystals had an inverted mesa structure that provided a thick outer frame for handling while having a thin inner membrane. Photoresist was used to adhere the quartz to glass slides that were used as chips carrier. A metallization layer of chrome/gold was then deposited by thermal evaporation as illustrated in **Figure 2**. PR (AZ4620) was spun coated on the crystal without the ramp step to reduce beading

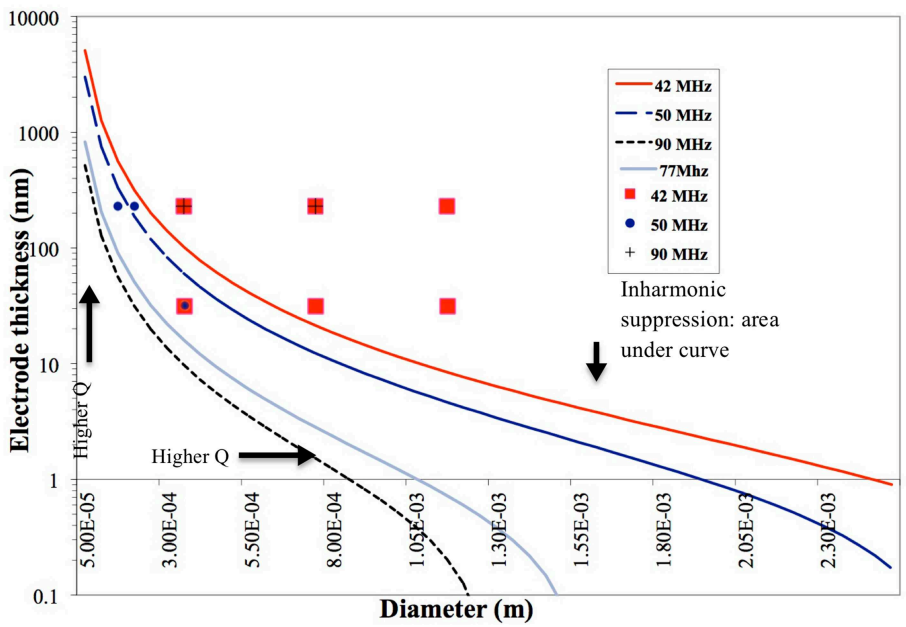

FIGURE 4 | Plate-back characteristics for suppressing the unwanted inharmonic modes in liquid operation demonstrate the theoretical relation between electrode thickness and electrode diameter for any given resonant frequency (inversely proportional to the thickness of the quartz crystal). The region under each curve (corresponding to a specific resonant frequency of the quartz crystal) indicates possible combinations of electrode thicknesses and diameters that will suppress inharmonic modes of vibration.

on the crystal edge. Using a photomask, the edge beading was removed from the crystal by overexposing the edges and developing it in 400T developer for 2 min at 1:3 concentrations. The pattern of the first side was exposed using a laser aligner (EVG620) at 700 mJ/cm^2 and developed in 300 MIF for 2 min. Gold etchant was used to etch away the exposed gold, revealing the pattern on the crystals. The quartz wafers were then removed from the glass slides using acetone, cleaned and remounted with the new pattern facing down. A layer of photoresist (PR) AZ4620 was spin-coated on the crystal at 5,000 rpm without a ramp-up

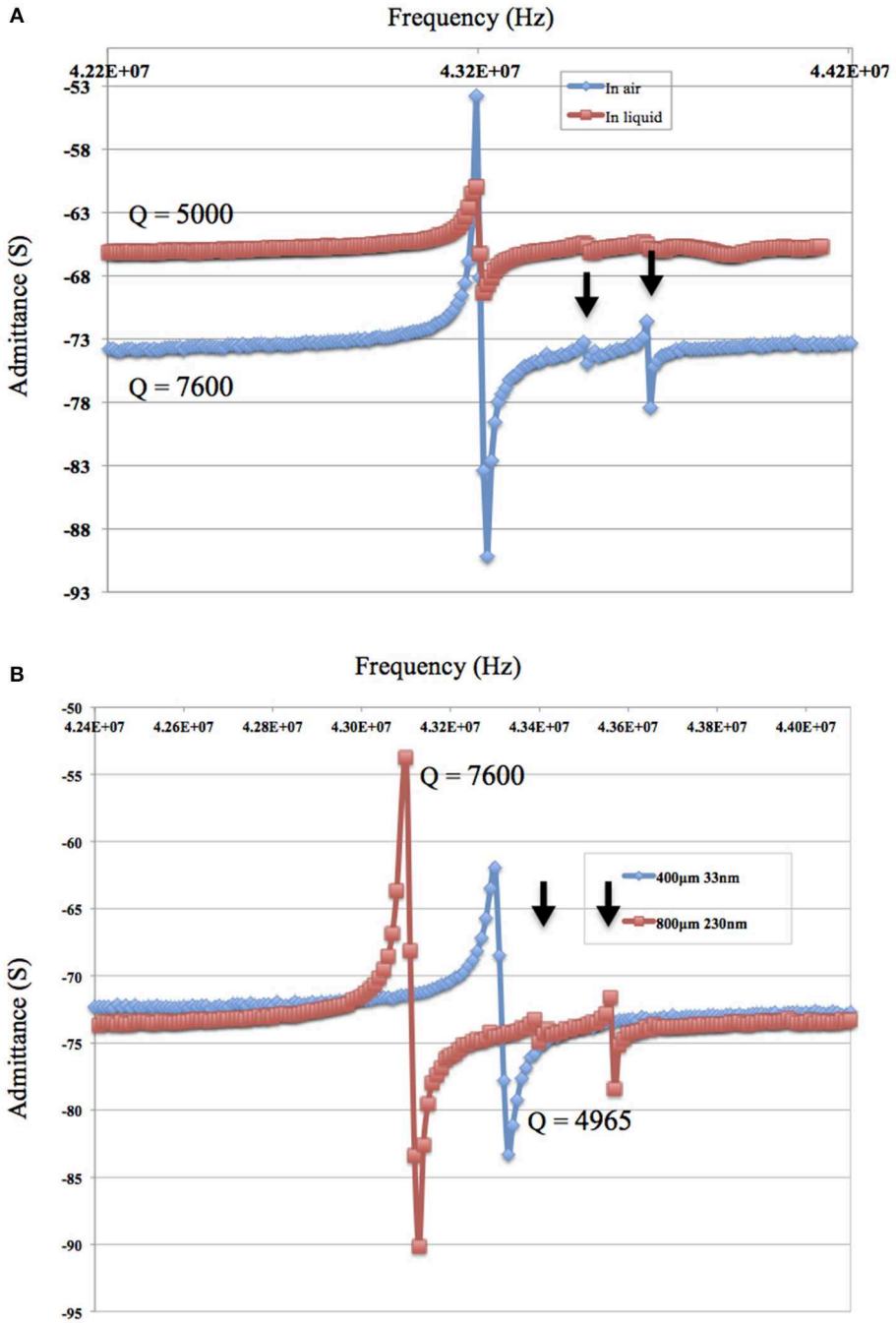

FIGURE 5 | (A) The admittance spectrum of the 42 MHz TSM resonator in air and in phosphate buffered saline (PBS) show that inharmonics are more suppressed under liquid due to the liquid loading. The admittance of the TSM sensor at the most significant inharmonic is 1/6th the impedance at resonant frequency in air vs. 1/30th in PBS. **(B)** The admittance spectrum in air of 42 MHz and a gold electrode of 800 μm diameter and a thickness of 230 μm (in red) and the admittance spectrum of 42 MHz and a gold electrode of 400 μm diameter and a thickness of 33 nm (in blue).

step and the crystal was baked at 100^{o}C for 2 min. The pattern of the second side was exposed after being aligned with the bottom side using a laser aligner (EVG620) at 700 mJ/cm^2 and was developed in 300 MIF for 2 min. Gold was then deposited on the exposed areas. The next step involved washing away the gold that was deposited on the PR and exposing the top pattern resulting in overlapped electrodes on each side of the crystal (**Figure 2I**).

3.2. Device Cleaning and Post-processing

To remove organic deposits from the surface of the devices, the quartz crystal and gold electrode were cleaned using piranha solution (H_2O_2 + H_2SO_4) 3:1 v/v) for 5 min, then rinsed with DI (de-ionized water) water and dried in air for 15 min. The crystal was then treated with 1 M NaOH for 20 min, then rinsed with DI water (Khraiche and Muthuswamy, 2012).

3.3. Surface Modification Using Carbon Nanotubes (CNTs) to Enhance Sensitivity

Single walled carbon nano tubes have excellent properties for sensing including high conductivity, high surface to volume ratio which results in high surface roughness on the nanoscale [31–33]. The increase surface roughness of TSM electrodes has been shown to increase the absolute change in resonant frequency and subsequent sensitivity of TSM sensors (Daikhin and Michael Urbakh, 1997; Du and Johannsmann, 2004; Rechendorff et al., 2007). This increase in Δf is due to interfacial slip between the solid and liquid phase, where there is an abrupt change in velocities at the interface. Several attempts have been made to understand this phenomenon and a model was developed to predict the impact on Δf by deriving a term that can be added to the Kanazawa's expressions listed earlier (where no slip condition is assumed) (Equation 6):

$$\frac{\Delta f}{f^2\rho} = -\frac{1}{\sqrt{\rho_0\mu_0}}(\pi^{1/2}\frac{w^2}{\xi} + R\delta) \tag{16}$$

Where w is the surface roughness, ξ is the correlation length of the roughness, R is a roughness factor and δ decay length. When surface roughness is equal to zero (smooth surface), then Equation (16) reduces to Equation (6). Single walled carbon nano tubes (SWNT) were purchased from Sigma Aldrich. The procedure of depositing SWNT was as previously reported (Gabriel et al., 2009). The SWNT were made into a black suspension by mixing 10 mg of pure SWNT with 10 ml of dimethyl formamide (DMF). The solution was placed under ultrasonic agitation for 50 min. Several drops were placed on the microelectrodes typically 5-10 μl and allowed to evaporate at 100^{o}C. After the solution evaporated, the MEA was rinsed with DI water and wiped with clean room wipes. The steps were repeated 4–5 times until the microelectrodes appeared black. After mechanical polishing the carbon nanotubes (CNT) stayed only on the gold microelectrodes.

3.4. Data Acquisition

A network analyzer HP E5100A (Agilent Technologies, USA) connected to a PC was used to acquire and record the impedance spectrum via a custom LabVIEW^{TM} program. The network analyzer was equipped with a passive π-network fixture where the leads to the crystals were directly connected. Admittance spectrum was collected with 201 points around the center

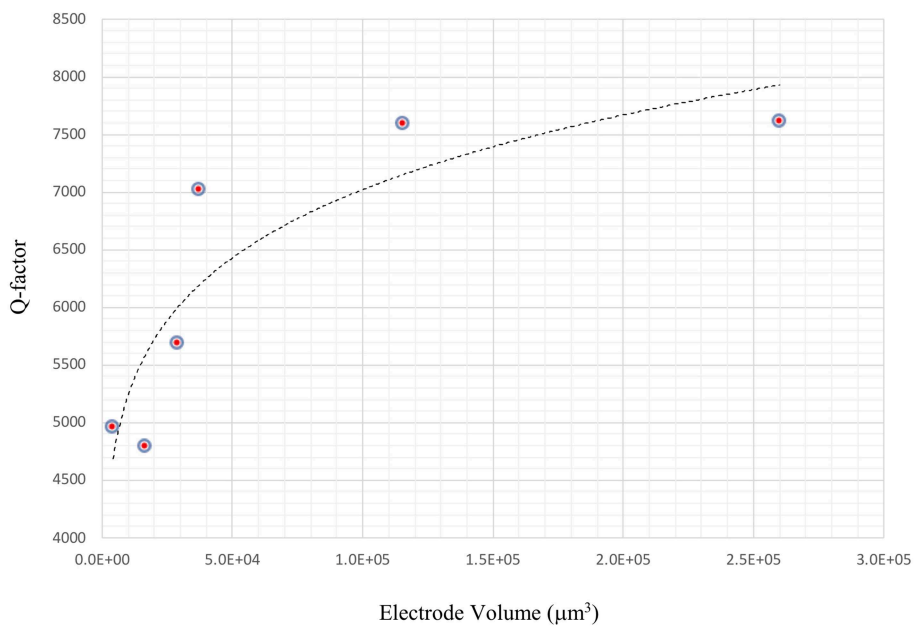

FIGURE 6 | Improvement in *Q*-factor with increasing electrode thickness. Increasing electrode thickness increases the conductivity of the electrodes and reduces the resistance, which results in a higher *Q*-factor.

resonant frequency, at 200 KHz bandwidth and 0.5 dBm with an incident power of 1 mW.

3.5. Cell Culture

Neurons were extracted from cortical slices from embryonic day-18 Sprague-Dawley rats obtained from BrainBits (Springfield, IL). Slices arrived in Hibernate-E media. Mechanical titration was used to break down the slices, and the supernatant was spun for 1 min at 1,100 rpm and suspended in ActiveNB neuron growth media with B27, 25 μM glutamic acid and 0.5 mM l-glutamine. Cells were added in suspension to a sensor surface in 20 μl and left for 20 min to adhere before adding more growth media and before the start of the resonant frequency measurements. Prior to neuron seeding, the resonator surface was coated with laminin (20 ml of 1 mg/ml laminin diluted in 1 ml of growth medium) and PEI (.1% in borate buffer). Fabricated TSM devices were topped with wells that hold 1.5 ml of media (**Figure 2**, top right) and sealed with a fluorinated ethylene-propylene (FEP Teflon® film), a transparent, oxygen permeable and water impermeable membrane. The whole setup was then placed in a cell culture incubator (controlled CO2 and 98% humidity) for the duration of the experiment, and media levels were monitored constantly. After 7 days in culture, neural cell culture viability was checked using live/dead fluorescence assay and by measuring single unit activity. All experiments were conducted according to standard biosecurity and institutional safety procedures of Arizona State University, Tempe, AZ.

3.6. SEM Protocol

Growth media was rinsed off with PBS wash (three times). Samples were then fixed in 2.5% glutaraldehyde in 0.1 M cacodylate buffer at pH = 7.4 and left for a 1 h at room temperature. This was followed by a wash in PBS (three times)

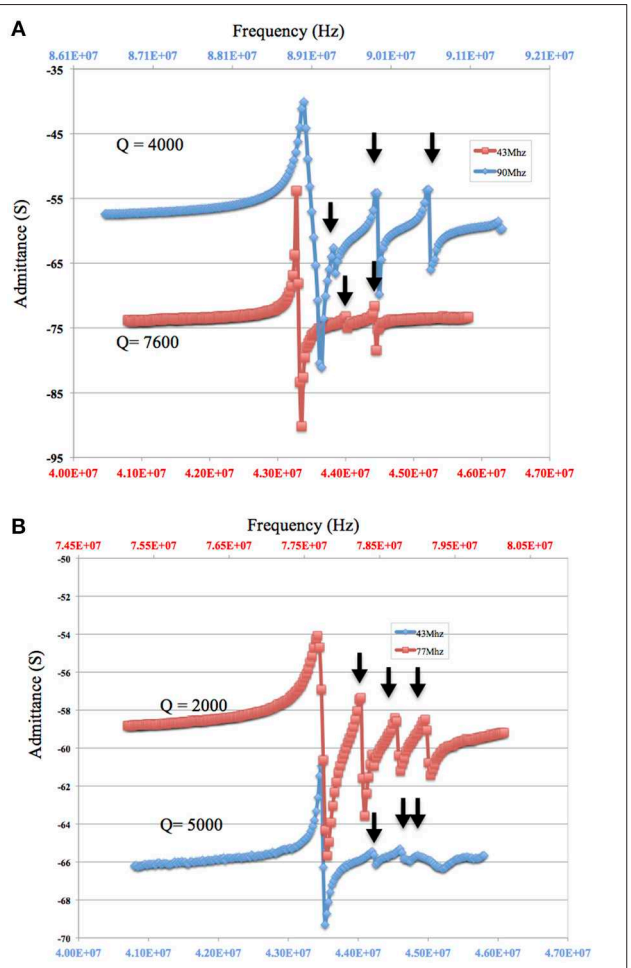

FIGURE 7 | (A,B) Decreasing *Q*-factor and larger inharmonic modes with increasing resonant frequency of the quartz substrate. The admittance spectrum of two microresonators with a resonant frequency of approximately 90 MHz and an electrode of 800 μm diameter and a thickness of 33 nm (in blue) and a second with a resonant frequency of approximately 42 MHz and a gold electrode of 800 μm diameter and a thickness of 33 nm (in red) are shown (**A**: in air and **B**: in fluid with 90 MHz resonator replaced by a 77 MHz resonator). Arrow points to the inharmonic.

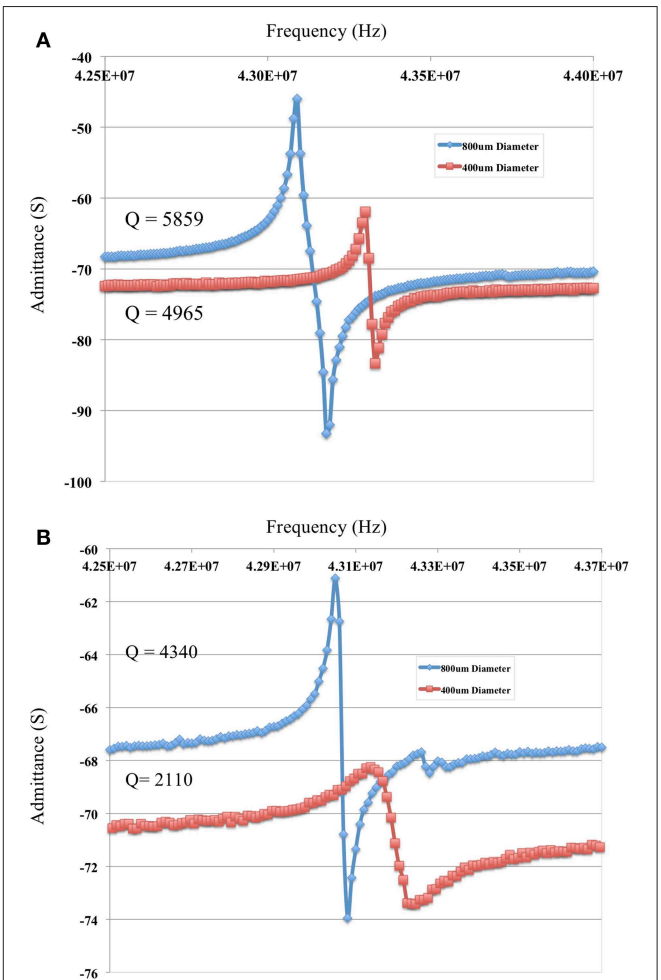

FIGURE 8 | (A,B) Increasing electrode diameter improves the *Q*-factor of the micro-resonator. The admittance spectrum of two microresonators with a resonant frequency of approximately 42 MHz and an electrode of 400 μm diameter and a thickness of 33 nm (in red) and a second with a gold electrode of 800 μm diameter and a thickness of 33 nm (in blue) are shown **(A)** in air and **(B)** in fluid.

and the sample was left in PBS for 5 min after each rinse. The next step included adding PBS solution containing 1% osmium tetroxide to the sample for 1 h at room temperature to improve the contrast in imaging, followed by washing in distilled water (three times). Dehydration: The samples underwent a serial dehydration in 30, 50, 70, and 90% (10 min. each) and three times with 100% ethanol (within 15 min). Critical point drying: Samples were placed in a critical point dryer for 10–15 min and imaged afterward (Liu et al., 2017).

4. RESULTS AND DISCUSSION

4.1. Plate-Back

Results plotted in **Figure 3** represent the theoretical plate-back characteristics relating electrode thicknesses and electrode diameters for TSM resonators operating in air. Traces corresponding to 42, 50, 75 and 90 MHz are shown in **Figure 3** along with points that correspond to the quartz TSM prototypes fabricated and tested in this study. The plate-back characteristics for suppressing the unwanted inharmonic modes change between operations in liquid (**Figure 4**) vs. air (**Figure 3**). Changes in admittance spectrum in response to TSM operation in air vs. liquid are shown in **Figure 5A**. Comparing the performance of the TSM resonator in air vs. liquid in **Figure 5A**, the inharmonics are more suppressed under liquid operation due to liquid loading. The admittance at the most significant inharmonic is 1/6th the admittance at the resonant frequency in air, compared to 1/30th in liquid. The usefulness of **Figure 3** can be enhanced for biosensor design when we account for frequency changes due to the dampening effects of fluid loading or even target analyte (cells proteins). By incorporating Kanazawa's equation, that accounts for the density and viscosity of water at 20^{o}C in the plate-back equations for eliminating inharmonics (Equation 10), **Figure 4** is obtained as a guide for sensor design. When comparing **Figure 3** with **Figure 4**, we found notable differences in the design space for suppressing inharmonics in TSM sensors operating in air vs. TSM sensors operating in liquid, for larger diameter electrodes. This relationship was based on the density and viscosity of water. This is especially evident for higher frequency resonators. If the sensor is to operate in a different medium, necessary changes to Equation 10 need to be made (Kanazawa and Gordon, 1985; Kanazawa, 2002). In order to suppress unwanted inharmonic modes based on the relationship defined by Equation 11, the region under the curve represents ideal resonator designs where the frequency of the first inharmonic is larger than the cut-off frequency of the unplated region of the sensor resulting in inharmonic suppression (as predicted by the plate-back Equation 11). An example of this is the admittance spectrum plots in **Figure 5B** of two 42 MHz sensors, one with a 400 μm diameter electrode and 33 nm of gold thickness (blue trace in **Figure 5B**) that corresponds to a point below the plate-back characteristics of 42 MHz sensor in **Figure 4**, while the second 42 MHz TSM sensor with 800 μm diameter electrode and 230 nm of gold thickness (red trace in **Figure 5B**) lies above the plate-back characteristics in **Figure 4**. Inharmonic frequencies are only observed in the trace corresponding to the second TSM sensor (in red; inharmonic modes indicated by arrows) and not the first. This result is consistent with Equation (11), where increasing the electrode thickness will increase the left side of the inequality resulting in more inharmonics.

4.2. Increasing Electrode Thickness

The impact of electrode thickness on TSM sensor performance is not immediately apparent. The impedance spectra of two TSM sensors in **Figure 5A** (in air) and **Figure 5B** (in water) reveal a higher *Q*-factor for the TSM sensor with 230 nm of gold thickness compared to the sensor with 33 nm of gold thickness. Changes in the thickness of deposited gold electrodes lead to changes in the electrical resistance. The dependence of the *Q*-factor of TSM devices on the resistivity can be better understood from the modified BVD model of a resonator. Adding a resistor in series with the BVD model for a bulk acoustic resonator accounts for changes in *Q*-factor and improves the accuracy of the model. Increasing electrode thickness increases the conductivity of the electrodes and reduces the resistance, which results in a higher *Q*-factor as shown also in **Figure 6** as the *Q*-factor increases with increasing electrode volume.

4.3. Sensor Frequency

When considering sensor design, sensitivity requirements determine the choice of the fundamental resonant frequency of the TSM sensor and ultimately the choice of the thickness of the quartz. Increasing the resonant frequency of TSM sensors increases sensor sensitivity as shown by the Sauerbrey equation (Equation 1). On the other hand, increasing the resonant frequency of the TSM sensor lowers the *Q*-factor (Equation 12). This relationship is evident in the impedance sweep in **Figure 7A** showing two TSM prototypes with different resonant frequencies (90 MHz shown in blue and 42 MHz shown in red) but with the same electrode dimensions (800 μm diameter and 33 nm thickness of gold). The *Q*-factor for the TSM sensor with a resonant frequency of 42 MHz is 7,000 compared to 4,000 for the one with a resonant frequency of 90 MHz. The impact of frequency on the *Q*-factor has implications when operating

TABLE 1 | Summary of prototypes designs and their corresponding *Q*-factors.

Δm (ng/mm2)	Freq (MHz)	Diameter	Electrode thickness (nm)	Q-factor
0.54	42	1.2 mm	33	7,020
0.49	42	1.2 mm	230	7,620
0.22	42	800 μm	230	7,600
0.35	42	800 μm	33	4,800
0.073	42	400 μm	230	5,695
0.084	42	400 μm	33	4,965
0.081	50	400 μm	33	4,340
0.023	50	200 μm	230	3,800
0.016	50	150 μm	230	3,000
0.182	77	800 μm	230	5,000
0.049	90	400 μm	230	4,000
0.13	90	800 μm	230	6,000
70.13	10	8 mm	230	10,000

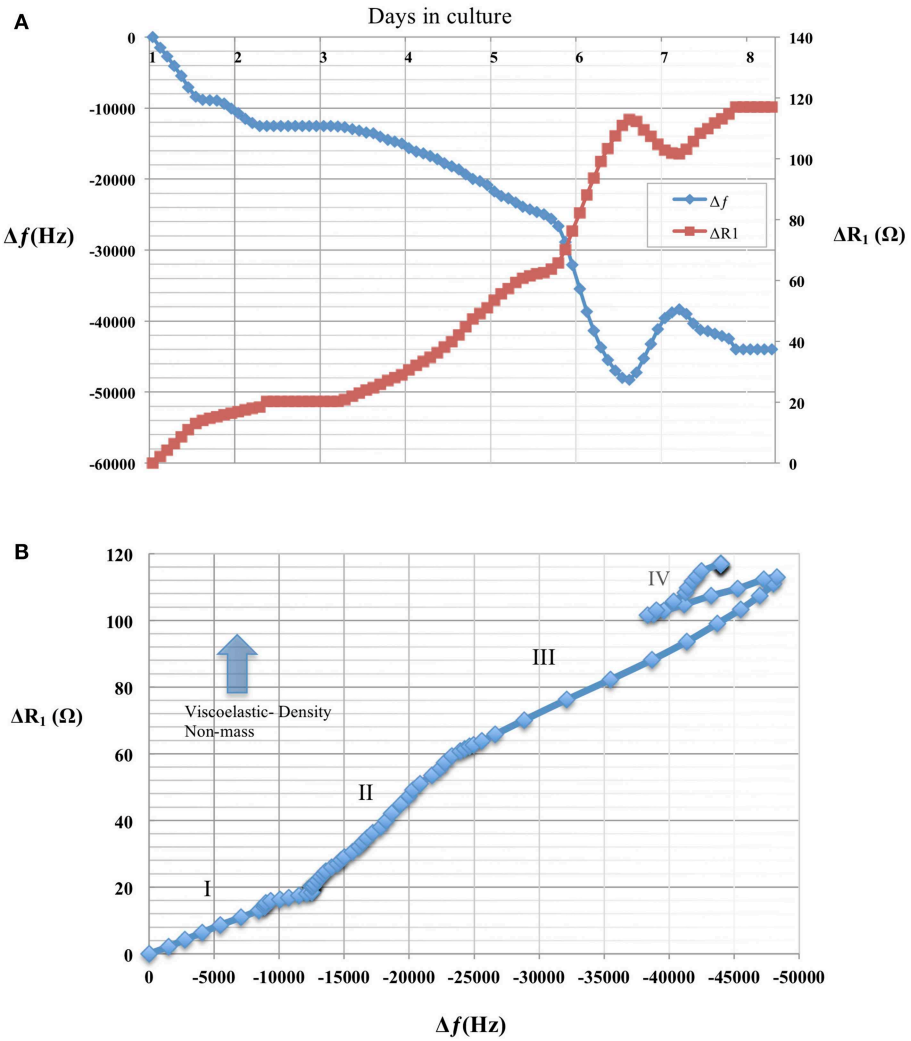

FIGURE 9 | (A) Changes in resonant frequency and motional resistance of the TSM sensor are plotted in response to neuronal adhesion over a period of 8 days in culture for a TSM resonator with resonant frequency of 90 MHz and an electrode diameter of 400 μm. **(B)** Plot shows ratio of ΔR_1 vs. Δf_S, Increase in the slope of the curve indicates increase in viscoelastic-density (non-mass) changes in the adhering layer. The plot shows mechanical changes in adhering cell layer over the course of

(Continued)

FIGURE 9 | 8 days. Phase I shows a linear behavior indicating both mass and viscoelastic changes in the adhering layer. Phase II shows a slope increase due to increase in the contributing of the viscoelastic changes of the adhering layer. Phase III shows a return to linear behavior and an equal contribution from mass and viscoelastic changes to the curve. Phase IV: shows cell layer exhibits changes in both viscoelastic and mass contributions. **(C)** Live/Dead assay as described of neural culture 7 days after seeding. Live cells are identified by green calcein fluorescence. Arrows in the image are indicating electrode edge.

in liquid, as the quartz undergoes hydrostatic dampening and dampening due to the viscous medium, both of which lead to a further reduction in the *Q*-factor (**Figure 7B**).

As for the impact of sensor fundamental resonant frequency on the inharmonic frequencies, plate-back characteristics in **Figures 3**, **4** indicate that the higher the resonant frequency of the quartz, the lower the inharmonic suppression, which has an adverse impact on the operation of the crystal. In **Figure 7A**, the first inharmonic appears to be larger and closer to the resonant frequency for the TSM sensor with a resonant frequency of 90 MHz compared to the resonant frequency of the 42 MHz resonator. Referring back to **Figure 3**, the point corresponding to the 90 MHz micro-resonator with its electrode diameter and thickness shown in **Figure 7**, lies farther above the plate-back characteristics of 90 MHz in comparison with the point corresponding to the 42 MHz micro-resonator, relative to its corresponding curve in **Figure 3**. Therefore, the 90 MHz micro-resonator profiled in **Figure 7** is expected to generate significantly larger inharmonic modes than the 42 MHz resonator, and the results shown in **Figure 7A** confirms the presence of these modes.

4.4. Changing Electrode Diameter

For bio-sensing applications, electrode size of TSM devices determines the sensing area and impacts sensitivity as demonstrated by Sauerbrey's Equation (1) and subsequently Equation (14). The plot in **Figure 4** shows that reducing electrode size allows for designing TSM sensors without inharmonic waves. This relationship is due to the fact that reducing electrode size increases f_e and reduces the range of frequencies that lie between f_e and f_s, leading to less inharmonic waves (**Figure 1A**). On the other hand, as we have discussed in the previous section, increasing electrode resistance (due to reduced electrode size) reduces the *Q*-factor as explained by the modified BVD model. The admittance spectrum of TSM sensors with two different electrode diameters is shown in **Figures 8A,B**, where the *Q*-factor for the sensor with 800 μm diameter electrode is higher than the sensor with 400 μm diameter. Therefore, reduction in diameter of the electrodes, to increase the spatial resolution of the TSM sensor, reduces the *Q*-factor, which in turn has the effect of decreasing the sensitivity. Simultaneously, the decrease in electrode sensing area (proportional to the square of the diameter) also has the effect of increasing the sensitivity as shown in Equation 14, which compensates for the loss in sensitivity due to lower *Q*-factor.

4.5. Cell Adhesion

The advantages offered by TSM sensors that include real-time monitoring of adhering masses have been of interest in the study of mechanics of cell adhesion to artificial substrates. For a long time, the adhesion phenomenon has been investigated using bright field or fluorescence methods that do not easily lend themselves to real-time quantitative assessment of adhesion dynamics. Studies using TSM to track cell adhesion have been extended to a variety of cell lines and pharmacological manipulation of cell cytoskeletal mechanics (Khraiche et al., 2003; Wang and Muthuswamy, 2008). This interest in studying large populations of cells, has even led to the availability of commercial systems to study cell adhesion using TSM sensors. However, the electrode size (in the order of 5–8 millimeters) of commercially available TSM sensors limits these studies to large cell populations (tens or hundreds of thousands of cells). Therefore from **Table 1**, we chose a sensor prototype that had a large *Q*-factor at the highest resonant frequency (90 MHz) with an electrode diameter of 400 μm (that can accommodate hundreds of cells) that can achieve the highest sensitivity according to Equation (14). Data in **Figure 9** shows a mostly monotonic decrease in resonant frequency of a TSM device in response to neuronal adhesion tracked over a period of 8 days. The average standard deviation in the resonant frequencies of these TSM sensors in liquid over a 5-h period, before the addition of neurons, was 31 Hz, demonstrating long-term stability of the TSM sensors in liquid. In addition, the mechanical properties of the adhering cell layer can be tracked in real-time by considering changes in the ratio of ΔR_1 to Δf_s (Silva and Khraiche, 2013). The data in **Figure 9B** show a plot of ΔR_1 vs Δf_s where an increase in the slope of the curve indicates non-mass changes such as viscoelastic density in the adhering layer. The adhesion process typically involves dramatic changes in the cytoskeleton that translates to changes in cell shape, mechanical properties, and cell spreading. These changes are typically difficult to monitor and quantify in real-time using conventional techniques, but it has been shown that TSM sensors are very effective in monitoring such mechanical changes in cells. Additionally, their ability to differentiate between adhering and non-adhering mass makes them ideal for antigen-based cell capture (Khraiche et al., 2005). This performance characteristic is due to the affective lateral sensing layer that extends only a few 100 nm into the solution, which enables TSM sensors to monitor adhered thin films, without being affected by the rest of the medium. This feature offers an advantage when using TSM sensors compared to competing technologies such as EIS (electrochemical impedance spectrum) that typically monitors cell adhesion via a current flow between two neighboring electrodes which can be susceptible to changes in conductivity of the medium and non-adhering cells. In comparison with conventional, commercial TSM sensors, whose electrode diameters are 5–8 mm and a resonant frequency of 5–10 MHz, the electrode diameters of the microscale TSM resonators reported in this current study are at least an order of magnitude smaller, with resonant frequencies at least an order of magnitude larger. Data in **Table 1** shows the impact of sensor design parameters on sensitivity as represented by

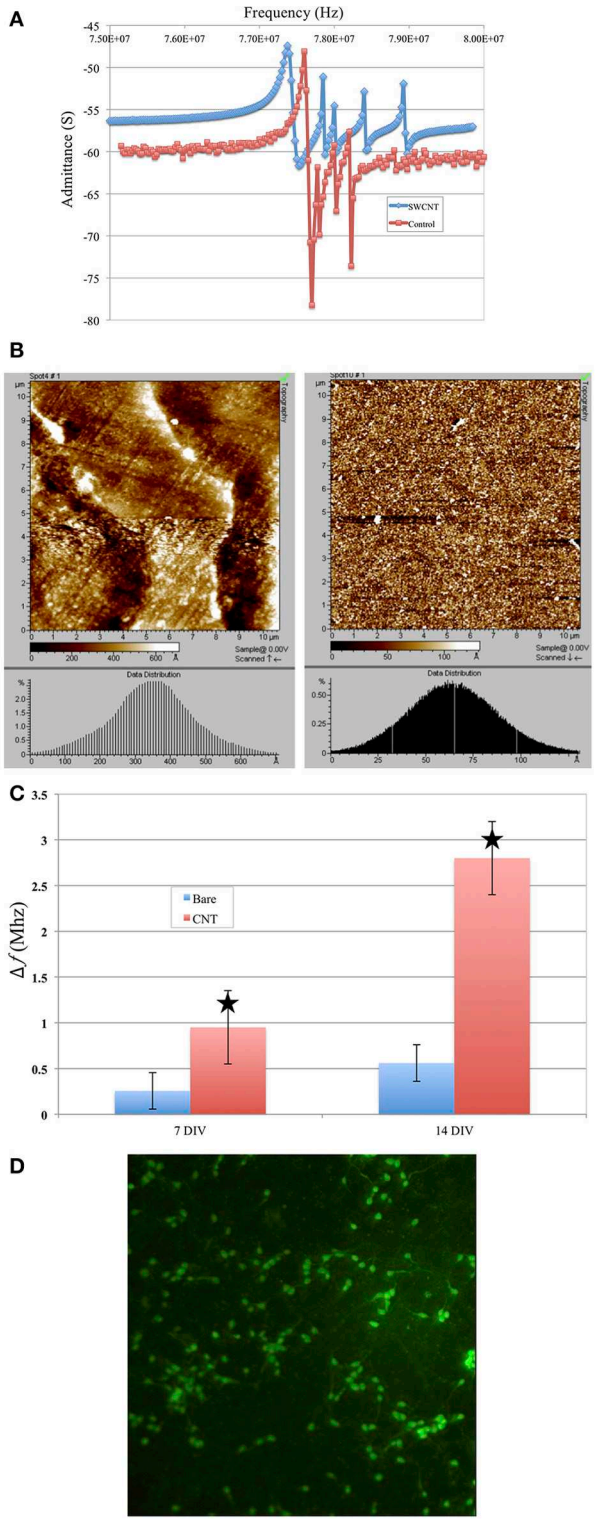

FIGURE 10 | (A) Coating top gold electrode with SWCNT reduced the *Q*-factor. Plot in red shows the admittance spectrum before and plot in blue shows admittance spectrum after SWCNT coating. **(B)** Results from AFM scanning of the surface of the coated TSM (Right) electrode vs. the noncoated surface (left). The histogram shows an average surface roughness of 35–40 nm for SWCT coated electrodes vs. 6–7 nm for noncoated. **(C)** Change in resonant frequency of TSM devices after cells are added to sensor surface. Bars in red indicated frequency change due to cells added to TSM electrodes coated with SWCNT. Blue bars indicate frequency due to uncoated (control) TSM surfaces. Overall, the SWCNT sensors show higher resonant frequency drop for cells at similar seeding densities compared to the control (uncoated) surfaces. The star shows the predicted change in resonant frequency for higher surface roughness electrodes. **(D)** Live/dead assay of neurons at day 7 grown on SWCNT.

(Continued)

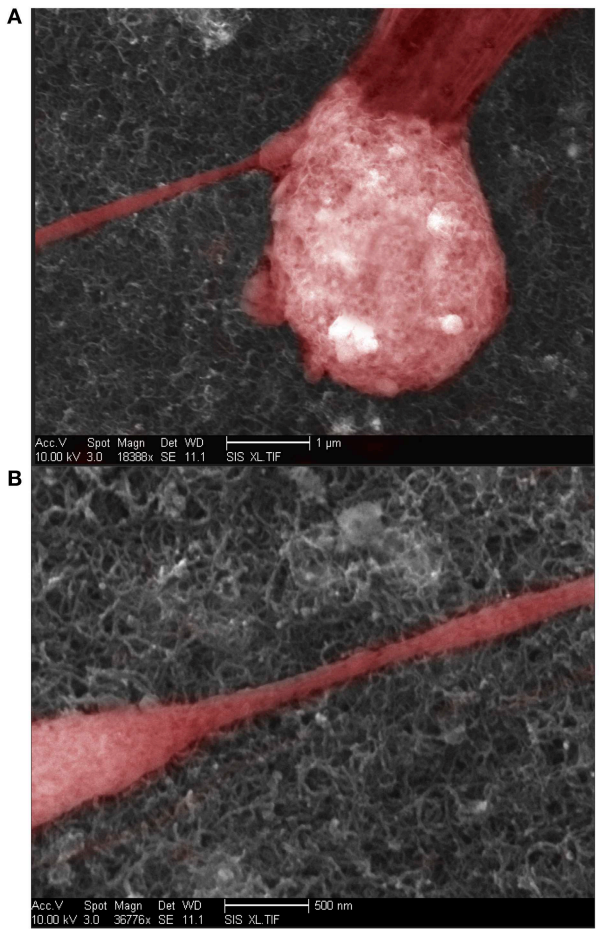

FIGURE 11 | (A) Scanning Electron Microscope image of neuron growing over a SWCNT coated surface. **(B)** Scanning electron microscope image of neural processes growing over a SWCNT coated surface.

the smallest detectable mass calculated in column 1. The smaller electrode diameters will result in a proportionate decrease in the number of cells on the electrode surface. In principle, an order of magnitude increase in resonant frequency will translate into an increase in sensitivity by two orders of magnitude since the sensitivity is proportional to the square of the resonant frequency. Furthermore, an order of magnitude decrease in the electrode diameter translates into two orders of magnitude increase in sensitivity, since sensitivity is inversely proportional to the square of the electrode diameters.

4.6. Neuron Adhesion to SWCNT Coated TSMs

We investigated the effect of surface roughness on the performance of TSM electrodes by coating the gold electrodes on the quartz with SWCNT (single walled carbon nanotube). The choice of SWCNT is due to their excellent properties for sensing, including high conductivity and high surface to volume ratio. Additionally, nanotopography of SWCNT is of great interest for studying cell adhesion to nano-substrates (McHale and Newton, 2004; Ballerini, 2008; Khraiche et al., 2009; Hecht et al., 2011). We coated the gold electrodes with SWCNT via drop-casting which resulted in almost 4-fold increase in surface roughness measured via AFM (**Figure 10B**). Results in **Figure 10A** shows the *Q*-factor is reduced for the TSM device coated with SWCNT. Acoustic losses reduce the *Q*-factor due to defects, scattering and losses at the acoustic boundaries (**Figure 10A**) (Heitmann and Wegener, 2007). In addition, the presence of high surface roughness leads to slip conditions between the solid and liquid phases as the TSM sensor is operated in liquid, leading to an increase in Δf. Furthermore, TSM sensors have been shown to be capable of tracking cell adhesion quantitatively in real-time under various chemical and surface treatments (Mindlin and Deresiewicz, 1954; Khraiche et al., 2005; Sapper et al., 2006; Khraiche and Muthuswamy, 2012). In the final section of this work, we investigated TSM sensor response (change in resonant frequency) to cell adhesion on SWCNT modified electrodes over a period of 14 days. Measurement time points were chosen to collect data well past the typical maturity of disassociated neurons, as indicated by an advanced state of axonal growth and spreading. This experiment allowed us to quantify the adhesion response of neurons on gold vs. SWCNT. The data in **Figure 10C** shows that TSM sensors coated with SWCNT have a significantly larger change in resonant frequency to the same density of adhering cells at two time points (7 and 14 days *in vitro*). The increase in TSM response correlates with observations of enhanced adhesion of neurons on CNTs and was consistent with the predicted Δf in Equation 16 (**Figure 10D**). Scanning electron micrographs (SEM) in **Figure 11** show adhesion of individual processes of neurons grown on SWCNT.

5. CONCLUSION

Thickness shear mode piezoelectric sensors have shown great promise in bio-sensing applications but currently fall short in the sensitivity and detection area as compared to competing sensing modalities such as surface plasmon resonance (SPR). This report highlights key design principles for improving sensitivity and lowering the detection area for TSM sensors operating in liquids, for the purposes of monitoring cell adhesion in real time. The theoretical predictions have been validated with fabricated prototypes operating in liquid. The plate-back equation first derived by Mindlin et al. was used to eliminate unwanted inharmonic standing waves that interfere with the correct prediction of the sensor's resonant frequency (Mindlin and Deresiewicz, 1954). We added a new term to include the effect of liquid and higher density and viscosity coatings on inharmonic suppression which changes the design space previously suggested for inharmonic suppression. We also used the prototypes with the highest sensitivity and smallest sensing area to monitor neuronal adhesion. In addition, we used TSM sensors to probe cell responses to SWCNT. Finally, reducing the size of the sensing area to a 150–400 μm for TSM devices, improves the spatial resolution by monitoring 100–1,000s of neurons. This technology remains an important tool in studying cell adhesion as they provide real-time, label-free information and hold many advantages over competing technologies such as EIS for monitoring cell adhesion. The theoretical guidelines in this work lay out the interplay among sensor design parameters, such as sensing area, frequency of the quartz, and thickness of the electrode, and how they affect sensor performance. The design of TSM sensors should be application driven so as to set the expectation of one or more aspects of the design specification while tuning the rest of the parameters to produce the desired performance.

DATA AVAILABILITY

The datasets generated for this study are available on request to the corresponding author.

AUTHOR CONTRIBUTIONS

MK, JR, and JM contributed to the conceptualization and design of the TSM sensors. MK fabricated and tested the TSM sensor prototypes and performed the *in vitro* and bench top experiments. MK and JM also contributed to the experimental design and writing of the manuscript.

ACKNOWLEDGMENTS

The authors would like to thank the Center for Solid State Electronic Research (CSSER) at Arizona State University, Tempe for enabling the microfabrication of the TSM sensors.

REFERENCES

Ballerini, L. (2008). Interfacing cultured brain circuits and carbon nanotubes: impact on spontaneous and stimulation-induced neuronal signaling. *J. Neurochem.* 104:72. doi: 10.1523/JNEUROSCI.1051-07.2007

Bottom, V. E. (1982). *Introduction to Quartz Crystal Unit Design*. New York, NY: Van Nostrand Reinhold.

Daikhin, L., and Michael Urbakh, A. (1997). Influence of surface roughness on the quartz crystal microbalance response in a solution new configuration for qcm studies. *Faraday Discus.* 107, 27–38. doi: 10.1039/a703124f

Da-Silva, A. C., Rodrigues, R., Rosa, L. F., de Carvalho, J., Tome, B., and Ferreira, G. N. (2012). Acoustic detection of cell adhesion on a quartz crystal microbalance. *Biotechnol. Appl. Biochem.* 59, 411–419. doi: 10.1002/bab.1041

Da-Silva, A. C., Soares, S. S., and Ferreira, G. N. (2013). Acoustic detection of cell adhesion to a coated quartz crystal microbalance-implications for studying the biocompatibility of polymers. *Biotechnol. J.* 8, 690–898. doi: 10.1002/biot.201200320

Du, B., and Johannsmann, D. (2004). Operation of the quartz crystal microbalance in liquids: derivation of the elastic compliance of a film from the

ratio of bandwidth shift and frequency shift. *Langmuir* 20, 2809–2812. doi: 10.1021/la035965l

Fang, J. J., Ren, C. L., Zhu, T., Wang, K. Y., Jiang, Z. Y., and Ma, Y. Q. A. (2015). Comparison of the different responses of surface plasmon resonance and quartz crystal microbalance techniques at solid-liquid interfaces under various experimental conditions. *Analyst* 140, 1323–1336. doi: 10.1039/C4AN01756K

Ferreira, G. N. M., Da-Silva, A. C., and Tome, B. (2009). Acoustic wave biosensors: physical models and biological applications of quartz crystal microbalance. *Trends Biotechnol.* 27, 689–697. doi: 10.1016/j.tibtech.2009.09.003

Gabriel, G., Gómez, R., Bongard, M., Benito, N., Fernández, E., and Villa, R. (2009). Easily made single-walled carbon nanotube surface microelectrodes for neuronal applications. *Biosens. Bioelectron.* 24, 1942–1948. doi: 10.1016/j.bios.2008.09.036

Gryte, D. M., Ward, M. D., and Hu, W. S. (1993). Real-time measurement of anchorage-dependent cell-adhesion using a quartz crystal microbalance. *Biotechnol. Progr.* 9, 105–108. doi: 10.1021/bp00019a016

Hecht, D. S., Hu, L., and Irvin, G. (2011). Emerging transparent electrodes based on thin films of carbon nanotubes, graphene, and metallic nanostructures. *Biotechnol. Progr.* 23, 1482–1513. doi: 10.1002/adma.201003188

Heitmann, V., and Wegener, J. (2007). Monitoring cell adhesion by piezoresonators: impact of increasing oscillation amplitudes. *Anal. Chem.* 79, 3392–3400. doi: 10.1021/ac062433b

Kanazawa, K. K. (2002). Steady state and transient qcm solutions at the metal | solution interface. *J. Electroanal. Chem.* 524–525:103–109. doi: 10.1016/S0022-0728(02)00752-0

Kanazawa, K. K., and Gordon, J. G. (1985). Frequency of a quartz microbalance in contact with liquid. *Anal. Chem.* 57, 1770–1771. doi: 10.1021/ac00285a062

Kang, H.-W., Ida, K., Yamamoto, Y., and Muramatsu, H. (2008). Monitoring of morphology and physical properties of cultured cells using a micro camera and a quartz crystal with transparent indium tin oxide electrodes after injections of glutaraldehyde and trypsin. *Anal. Chim. Acta* 624, 154–161. doi: 10.1016/j.aca.2008.06.037

Khraiche, M., and Muthuswamy, J. (2012). Multi-modal biochip for simultaneous, real-time measurement of adhesion and electrical activity of neurons in culture. *Lab. Chip* 12, 2930–2941. doi: 10.1039/c2lc40190h

Khraiche, M. L., Jackson, N., and Muthuswamy, J. (2009). Early onset of electrical activity in developing neurons cultured on carbon nanotube immobilized microelectrodes. *Conf. Proc. IEEE Eng. Med. Biol. Soc.* 2009, 777–780. doi: 10.1109/IEMBS.2009.5333590

Khraiche, M. L., Zhou, A., and Muthuswamy, J. (2003). "Acoustic sensors for monitoring neuronal adhesion in real-time," in *Proceedings of the 25th Annual International Conference of the Ieee Engineering in Medicine and Biology Society, Vols 1-4*, Vol. 25 (Cancun), 2186–2188.

Khraiche, M. L., Zhou, A., and Muthuswamy, J. (2005). Acoustic sensor for monitoring adhesion of neuro-2a cells in real-time. *J. Neurosci. Methods* 144, 1–10. doi: 10.1016/j.jneumeth.2004.09.029

Kosslinger, C., Uttenthaler, E., Drost, S., Aberl, F., Wolf, H., Brink, G., et al. (1995). Comparison of the qcm and the spr method for surface studies and immunological applications. *Sens. Actuators B Chem.* 24, 107–112. doi: 10.1016/0925-4005(95)85023-6

Lakin, K. M., Kline, G. R., and McCarron, K. T. (1993). High-q microwave acoustic resonators and filters. *IEEE Trans. Microw. Theory Tech.* 41, 2139–2146. doi: 10.1109/22.260698

Larson, J. D., I., Bradley, R. C., Wartenberg, S., and Ruby, R. C. (2000). "Modified butterworth-van dyke circuit for fbar resonators and automated measurement system," in in *Ultrasonics Symposium, 2000 IEEE*, Vol. 1 (San Juan), 863–868.

Lee, C.-F., Yan, T.-R., and Wang, T.-H. (2012). Long-term monitoring of caco-2 cell growth process using a qcm-cell system. *Sens. Actuators B Chem.* 166–167:165–171. doi: 10.1016/j.snb.2012.02.027

Li, D., Wang, J., Wang, R., Li, Y., Abi-Ghanem, D., Berghman, L., et al. (2011). A nanobeads amplified qcm immunosensor for the detection of avian influenza virus h5n1. *Biosen. Bioelectron.* 26, 4146–4154. doi: 10.1016/j.bios.2011.04.010

Liu, R., Chen, R., Elthakeb, A. T., Lee, S. H., Hinckley, S., Khraiche, M. L., et al. (2017). High density individually addressable nanowire arrays record intracellular activity from primary rodent and human stem cell derived neurons. *Nano Lett.* 17, 2757–2764. doi: 10.1021/acs.nanolett.6b04752

Marx, K. A. (2003). Quartz crystal microbalance: a useful tool for studying thin polymer films and complex biomolecular systems at the solution-surface interface. *Biomacromolecules* 4, 1099–1120. doi: 10.1021/bm020116i

Mason, W. P. (1956). Physical acoustics and the properties of solids. *J. Acoust. Soc. Am.* 28, 1197–1206. doi: 10.1121/1.1908593

Matsuda, T. (1992). Novel instrumentation monitoring in situ platelet adhesivity with a quartz crystal microbalance. *Asaio J.* 38, 171–173. doi: 10.1097/00002480-199207000-00012

McHale, G., and Newton, M. I. (2004). Surface roughness and interfacial slip boundary condition for quartz crystal microbalances. *J. Appl. Phys.* 95, 373–380. doi: 10.1063/1.1630373

Mindlin, R., and Deresiewicz, H. (1954). Thickness-shear and flexural vibrations of a circular disk. *J. Appl. Phys.* 25, 1329–1332. doi: 10.1063/1.1721554

Muramatsu, H., and Kimura, K. (1992). Quartz crystal detector for microrheological study and its application to phase transition phenomena of langmuir-blodgett films. *Anal. Chem.* 64:2502. doi: 10.1021/ac00045a008

Rechendorff, K., Hovgaard, M. B., Foss, M., and Besenbacher, F. (2007). Influence of surface roughness on quartz crystal microbalance measurements in liquids. *J. Appl. Phys.* 101, 114502. doi: 10.1063/1.2735399

Saitakis, M., and Gizeli, E. (2012). Acoustic sensors as a biophysical tool for probing cell attachment and cell/surface interactions. *Cell. Mol. Life Sci.* 69, 357–371. doi: 10.1007/s00018-011-0854-8

Sapper, A., Wegener, J., and Janshoff, A. (2006). Cell motility probed by noise analysis of thickness shear mode resonators. *Anal. Chem.* 78, 5184–5191. doi: 10.1021/ac060094g

Sauerbrey, G. (1959). The use of quartz crystal oscillators for weighing thin layers and for microweighing applications. *Z. Phys.* 155, 206–222. doi: 10.1007/BF01337937

Seker, S., Elcin, A. E., and Elcin, Y. M. (2016). Real-time monitoring of mesenchymal stem cell responses to biomaterial surfaces and to a model drug by using quartz crystal microbalance. *Artif. Cells Nanomed. Biotechnol.* 44, 1722–1732. doi: 10.3109/21691401.2015.1089255

Shockley, W., Curran, D. R., and Koneval, D. J. (1967). Trapped-energy modes in quartz filter crystals. *J. Acoust. Soc. Am.* 41, 981. doi: 10.1121/1.1910453

Silva, G. A., and Khraiche, M. L. (2013). Nanotechnologies for stimulating and recording excitable events in neurons and cardiomyocytes. *Discov. Med.* 15, 357–365.

Su, X., Wu, Y. J., and Knoll, W. (2005). Comparison of surface plasmon resonance spectroscopy and quartz crystal microbalance techniques for studying dna assembly and hybridization. *Biosen. Bioelectron.* 21, 719–726. doi: 10.1016/j.bios.2005.01.006

Wang, T., and Muthuswamy, J. (2008). Immunosensor for detection of inhibitory neurotransmitter gamma-aminobutyric acid using quartz crystal microbalance. *Anal. Chem.* 80, 8576–8582. doi: 10.1021/ac801463a

Weber, J., Link, M., Primig, R., Pitzer, D., Wersing, W., and Schreiter, M. (2008). Investigation of the scaling rules determining the performance of film bulk acoustic resonators operating as mass sensors. *IEEE Trans. Ultrason.* 54, 405–412. doi: 10.1109/TUFFC.2007.254

Westas, E., Svanborg, L. M., Wallin, P., Bauer, B., Ericson, M. B., Wennerberg, A., et al. (2015). Using qcm-d to study the adhesion of human gingival fibroblasts on implant surfaces. *J. Biomed. Mater. Res. A* 103, 3139–3147. doi: 10.1002/jbm.a.35458

Zhou, A., and Muthuswamy, J. (2004). Acoustic biosensor for monitoring antibody immobilization and neurotransmitter gaba in real-time. *Sens. Actuat. B Chem.* 101, 8–19. doi: 10.1016/j.snb.2004.02.015

Zhou, T., Marx, K. A., Dewilde, A. H., McIntosh, D., and Braunhut, S. J. (2012). Dynamic cell adhesion and viscoelastic signatures distinguish normal from malignant human mammary cells using quartz crystal microbalance. *Anal. Biochem.* 421, 164–171. doi: 10.1016/j.ab.2011.10.052

Conflict of Interest Statement: The authors declare that the research was conducted in the absence of any commercial or financial relationships that could be construed as a potential conflict of interest.

Copyright © 2019 Khraiche, Rogul and Muthuswamy. This is an open-access article distributed under the terms of the Creative Commons Attribution License (CC BY). The use, distribution or reproduction in other forums is permitted, provided the original author(s) and the copyright owner(s) are credited and that the original publication in this journal is cited, in accordance with accepted academic practice. No use, distribution or reproduction is permitted which does not comply with these terms.

frontiers in Neuroscience

MINI REVIEW
published: 14 June 2019
doi: 10.3389/fnins.2019.00600

Mechanics of Brain Tissues Studied by Atomic Force Microscopy: A Perspective

*Prem Kumar Viji Babu and Manfred Radmacher**

Institute of Biophysics, University of Bremen, Bremen, Germany

Tissue morphology and mechanics are crucial to the regulation of organ function. Investigating the exceptionally complex tissue of the brain at the sub-micron scale is challenging due to the complex structure and softness of this tissue, despite the large interest of biologists, medical engineers, biophysicists, and others in this topic. Atomic force microscopy (AFM) both as an imaging and as a mechanical tool provides an excellent opportunity to study soft biological samples such as live brain tissues. Here we review the principles of AFM, the performance of AFM in tissue imaging and mechanical mapping of cells and tissues, and finally opening the prospects and challenges of probing the biophysical properties of brain tissue using AFM.

Keywords: tissue morphology, tissue mechanics, atomic force microscopy (AFM), tissue imaging, mechanical mapping

OPEN ACCESS

Edited by:
Jeffrey R. Capadona,
Case Western Reserve University,
United States

Reviewed by:
Mitchel J. Doktycz,
Oak Ridge National Laboratory (DOE),
United States
Brent Winslow,
Design Interactive, United States

***Correspondence:**
Manfred Radmacher
radmacher@uni-bremen.de

Specialty section:
This article was submitted to Neural Technology, a section of the journal Frontiers in Neuroscience

Received: *12 February 2019*
Accepted: *27 May 2019*
Published: *14 June 2019*

Citation:
Viji Babu PK and Radmacher M (2019) Mechanics of Brain Tissues Studied by Atomic Force Microscopy: A Perspective. Front. Neurosci. 13:600. doi: 10.3389/fnins.2019.00600

INTRODUCTION

Brain tissue combines an ensemble of different cells such as neurons and glia cells and the extracellular matrix, the latter is mainly made from filamentous proteins such as collagen, fibronectin, elastin, and others like proteoglycans and polysaccharides. Tissue mechanics results from the mechanical properties of the cells and the extracellular mechanics interacting with each other. So far, brain tissue mechanics has been investigated by various techniques such as atomic force microscopy (AFM) (Bouchonville et al., 2016), magnetic resonance elastography (MRE) (Mariappan et al., 2010), and ultrasound elastography (Gennisson et al., 2013). Among all, AFM has the advantage of allowing simultaneous imaging, mapping the mechanics with high resolution (nanometer scale precision), and force sensitivity (piconewton precision) of most tissues (brain, blood vessel, lung, cartilage, tendon) in either fluids or physiologically relevant environments (Mao et al., 2009; Chan et al., 2010; Liu and Tschumperlin, 2011; Marturano et al., 2013; Iwashita et al., 2014). The advent of AFM to capture the live actions of biomolecules at high spatial and temporal resolutions has been enabled by techniques such as high-speed AFM (Ando, 2018; Heath and Scheuring, 2019). AFM-based recognition imaging and force spectroscopy enables unbinding force mapping of receptors–ligand interaction sites on a lipid membrane at the single molecule level (Koehler et al., 2019). Not only a surface-imaging tool, but also a force–distance (FD) curve-based AFM has been used in different modes such as ringing (Dokukin and Sokolov, 2017), tapping (Zhong et al., 1993), multifrequency (Garcia and Herruzo, 2012), and contact resonance (Stan et al., 2014) mode to measure nanoscale mechanical (viscoelastic) properties of cells, biopolymers, and tissues. At the cellular level, single-cell force spectroscopy (SCFS)-based AFM adds extra information and is increasingly used to study cell mechanics (Lekka et al., 1999; Rianna and Radmacher, 2017; Viji Babu et al., 2018), cell–cell interaction (Benoit et al., 2000),

and cell–ECM interaction (Friedrichs et al., 2010). Similarly, AFM has been used as an imaging and spectroscopic [single-molecule force spectroscopy (SMFS)] tool in investigating bio-molecular structures (Shibata et al., 2017) and their intra- and inter-molecular interactions (Florin et al., 1994; Neuman and Nagy, 2008). Not only restricted to their ability to measure forces and displacements accurately and precisely, AFM cantilevers which act as a spring were also used as a motion micro-sensor to detect nanoscale vibrations of various prokaryotic and eukaryotic cells (Kasas et al., 2015). From single-molecule to single-cell manipulation, AFM becomes a multifunctional toolbox to observe and measure various biophysical parameters of cellular and subcellular assemblies and machineries. Remarkably, AFM can be used in cell or biomolecule physiological conditions and also does not require elaborated or specific sample preparation. AFM provides a technology that can also be integrated with other microscopic and spectroscopic techniques such as laser scanning confocal (Staunton et al., 2016), Total Internal Reflection Fluorescence (TIRF) (Ramachandran et al., 2014), STimulated Emission Depletion (STED) (Harke et al., 2012), and Förster Resonance Energy Transfer (FRET) (He et al., 2012). These correlative approaches offer a wide spatial (nm) and high temporal (ms) resolution to study cellular and molecular biophysics. Currently, AFM has gained a lot of attention in the field of biomedical engineering, especially in investigating the mechanical properties of tissues. Researchers take advantage of the simple sample preparation in AFM, which allows studying the living samples surface through imaging and mechanical mapping at the same time. In cancerology, AFM has been extensively used as an innovative diagnostic tool to explore the effects of cytotoxic drugs (Pillet et al., 2014). With simple setup and principle, AFM probes the tissue dynamics at the nano-scale.

The presence of different types of cells and their correlated functions including ECM synthesis, remodeling, and degradation (mainly fibroblasts) makes a tissue (connective tissue) unique within an organ. So far, biochemical properties of tissues have provided a large amount of information about the presence of tissue or cell specific biomarkers. These biomarkers reveal the distinction between the healthy and diseased state of a tissue, which may help in synthesizing specifically targeted drugs. Cell mechanics has now become a potential biomarker to discriminate between the different physiological and pathological states of cells (Rianna and Radmacher, 2016). Similarly, investigating tissue mechanics opens up a new platform in the biomedical field to diagnose pathological states of different tissues.

Generally speaking, brain tissue has three distinct parts: the cerebrum, cerebellum, and the brainstem. Each part has its own unique function in governing the different functions of the human body. As the central nervous system (CNS) for the whole body, brain tissues mainly contain neuronal and glia cells which interact through electric and ionic signaling and neurotransmitters. The mechanical properties of neurons and glia cells play a key role in neuronal growth and development (Spedden and Staii, 2013). Studying local and global brain topography and mechanics noninvasively can lead to a better understanding of the development of various diseases such as neurodegenerative diseases and cancer. Previous rheological studies on brain tissues were mostly conducted non-destructively on a macroscopic scale of centimeter to millimeter. Investigation into micro- and nano-scale range regions of living brain samples may allow distinguishing between cell and ECM properties and their correlation.

The main goal of this mini review is to introduce readers to the working principle of AFM and its application in tissue imaging and the mapping of mechanical properties of tissues. Finally, we discuss the possibility of using AFM in brain tissue biomechanics.

AFM – WORKING PRINCIPLE – IMAGING AND MECHANICAL MAPPING

Atomic force microscopy is conceptually a simple technique, employing the interaction between a tip whose shape can be tuned according to the application (sharp tips for high resolution imaging and pyramidal or spherical tips for mechanical mapping) attached to a soft cantilever spring and the sample. There are four main components (**Figure 1A**) in AFM: a cantilever, which acts as a spring with an integrated tip; a laser beam focused onto the very end of the cantilever where the tip is attached; a position-sensitive photo-detector to detect the reflected laser beam, which can measure the horizontal and vertical deflection of the cantilever; and finally, a xyz piezo scanner for moving the sample or the cantilever in all three directions. In our example schematics, the piezo scanner setup has been designed in such a way that the z piezo controls the cantilever movement in the z-direction and the xy piezo controls the sample movement in the xy-direction.

Different imaging modes such as contact (DC) and non-contact tapping (AC) modes are used in AFM to measure the sample topography. In contact mode, the AFM tip is brought into physical contact with the sample and the cantilever deflection is measured. In the constant height mode, the sample is kept at a constant height while the tip raster scans the sample. The topographic information is inferred from the deflection of the cantilever as the tip scans over areas of different heights. This particular mode is generally used for flat and rigid samples, since, due to the deflection of the cantilever the loading force will change. For soft biological samples, especially for cells, this mode will damage the cells as they will be exposed to large loading forces. In order to image soft samples, a feedback is introduced to adjust the z height such that the deflection, and therefore the loading force, is held constant. This mode is called a constant force or constant deflection mode. **Figure 1B** shows the height and error signal images of the extracellular matrix topography of the decellularized dermal matrix. In constant deflection mode, the output of the feedback corresponds to the height signal image which shows the overall sample topography. Since the feedback will react with a finite response time, the main time limiting factor will be the piezo transducers used in AFM, there are some residual changes in deflection, which are not perfectly compensated. In control theory this behavior is called the error (of the feedback loop); therefore, in AFM the phrase error signal image is also often used. To reduce lateral forces exerted to the

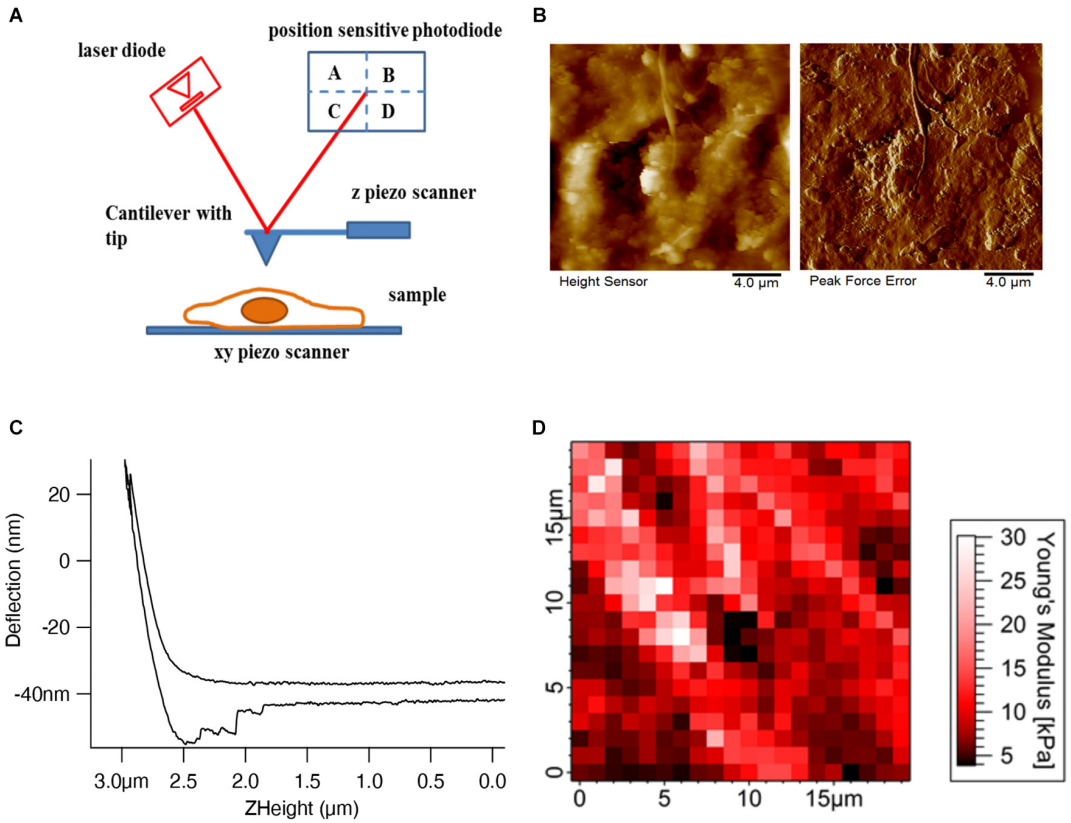

FIGURE 1 | AFM setup and tissue imaging. **(A)** AFM consists of four important components – cantilever with an AFM tip, laser diode, position-sensitive photodetector, and xyz-piezo scanner. **(B)** Height and deflection images show the decellularized dermal matrix which shows the collagen fibers running along other matrix components (Rianna et al., 2018). **(C)** Deflection (nm) vs. Z height (µm) shows the approach and retract curve (Viji Babu et al., 2018). **(D)** Force maps show the elastic modulus values of mouse skin tissue in a respective color scale (Pa) (Joshi et al., 2017).

sample in contact mode, which can be substantial and destroy or detach samples, the tip is periodically retracted from the sample and the cantilever height is modulated at the cantilever's resonance frequency. This mode is called the tapping mode and is used largely in imaging biomolecules such as DNA, proteins, and lipids. Like in contact deflection mode, tapping mode produces two images: a height and an amplitude error image. A novel variant of the tapping mode, the peak force mode, where the data during one oscillation cycle are captured and analyzed online to control the maximum force, seems to be favorable for cell imaging (**Figure 1B**; Schillers et al., 2016).

In a force curve (**Figure 1C**) the interaction forces between the tip and sample are measured while the tip is approached and retracted from the sample. This can be performed over a region of interest of the sample, generating a force map or force volume (**Figure 1D**) in which each pixel in the map represents a force curve. Both the approach and retract curves reflect information on the mechanical, or more precise viscoelastic properties of the sample, as well as adhesion properties between the tip and sample, e.g., a cell or the ECM. The elastic properties of the sample can be inferred by fitting the data with an appropriate geometric model of the tip and sample to yield the Young's modulus. Different models are used from continuum mechanics depending on the shape of the AFM tip. In most cases, the AFM tip shapes are pyramidal, conical, and spherical. According to the tip geometry, the Hertz model (Hertz, 1882) for spherical indenters, Sneddon model (Sneddon, 1965) for conical indenters, and Sneddon extended model (Rico et al., 2005) for pyramidal indenters are used to describe the elastic behavior of the biological samples. The force can be calculated by Hooke's law from the deflection of the cantilever, if the spring constant is known. The sample indentation is calculated from the z movement of the z piezo and the cantilever deflection.

TISSUE IMAGING AND MECHANICAL MAPPING IN AFM

The simplicity of the working principle of AFM allows users to obtain the fine microstructures of biological tissue with good resolution. Biological tissues are comprised of different cells and ECM, whose interplay facilitates tissue dynamics and maintains homeostasis. Investigating biomechanical properties and imaging of cells and ECM are studied individually and cells are mostly cultured in hydrogels, matrigels, or three-dimensional (3D) matrices in order to evaluate the substrate

stiffness or composition-dependent cell elastic properties. Whereas decellularized ECM is evaluated for the ECM component arrangement and stiffness. Intracellular actin cytoskeleton arrangement and dynamics reveal that the cell stiffness and actin stress fibers interact with and transmit mechanical information to the ECM through the transmembrane protein focal adhesion complex. This adhesion complex consists of the transmembrane protein integrin, whose extracellular domain binds to the RGD (Arg-Gly-Asp) sequence of any of the ECM proteins and its intracellular domain binds to the adaptor proteins which further bind to the actin cytoskeleton. This combined complex transfers both the extracellular and intracellular force generated by respective ECM protein fibers and actin stress fibers in the cells, resulting in signaling in both directions: from the cell to the ECM environment and back from the environment into the cells (Discher et al., 2005). ECM imaging and biomechanical properties are so far performed in decellularized tissue samples. The surface topology of acellular ECM scaffolds provides information on the ECM protein fibers' orientation, spacing, diameter, and also records mechanical maps which enable their stiffness and surface roughness. Collagen fibers are mostly dominant and abundant in these decellularized tissue samples and sometimes the collagen fibers are also seen with other ECM proteins. AFM measurement can be combined with fluorescence microscopy in order to study different ECM proteins by tagging them with different fluorophores which make them easier to visualize in conducting decellularized ECM imaging and mechanics (Jorba et al., 2017).

Ensemble investigations of cells and ECM at the tissue or sub-tissue level provide information on the cell–ECM mechanical crosstalk and disease-related alterations in tissue morphology and mechanics. The AFM sample preparation for tissue investigation starts with the immobilization of tissue blocks which is quite challenging. Tissues are normally immobilized to a coverslip or any other suitable support in several ways. Tissue adhesives such as Histoacryl tissue glue (Stolz et al., 2009; Plodinec et al., 2010) or ethyl cyanoacrylate (Chan et al., 2010) are mostly used and care has been taken so that adhesives do not make contact with the investigated region. Nevertheless, this immobilization procedure will have some effect on the tissue as substances released from the adhesives may diffuse, either through the surrounding air or water, or directly through the neighboring tissue. Sectioned tissue specimens are often immobilized to microscope glass slides coated with poly-lysine (Stolz et al., 2004; Grant et al., 2012). This procedure is a good option but only for thin tissue sections. The main aim of immobilization of tissues is to avoid sample movement while recording images or mechanical maps. An alternative to adhesives is using Thermanox coverslips punctured in the center and used for holding down the sample in such a way that the tissue can be accessed by the AFM tip. The edge of the Thermanox coverslip can then be glued to the support (**Figure 2A**; Morgan et al., 2014). This setup avoids contact of tissue and glue or any other adhesive materials and serves as a better way to immobilize tissue samples. This approach paves way for investigating the topographical and mechanical changes of the mouse skin tissue. **Figure 2B** shows the presence of thick ECM fibers in mouse skin tissue before and after the addition of collagenase, which leads to the disappearance of fibers and correlatively decreases their elastic properties (Joshi et al., 2017). Biological tissues, cells and the ECM, are composed mainly of water (around 70% for the cytosol), even though for the biological function usually only macromolecules such as proteins or small organic and inorganic molecules are discussed. Therefore, it is very important to study tissues in a hydrated environment such as selecting the suitable medium which brings the utmost native environment to tissues that affect their topography and mechanical properties. It was reported (Zhu and Fang, 2012) that hydration and dehydration of cartilage affects the collagen fiber distribution and its roughness. Standardizing the tissue immobilization protocol and selecting the correct liquid medium are simple to set up and efficient in measuring the morphological and mechanical alteration in the tissues. Tissue samples are normally very soft. As a consequence, they are very difficult to cut into thin slices in their native state even with state of the art vibratomes; therefore, they are often frozen to prepare thin sections (cryosectioning). Normally thin tissue sections of 5–50 μm in thickness are generated for imaging and recording mechanical maps in AFM studies. However, the cryo-procedure not only decreases the cell viability dramatically, but also changes ECM and cell mechanics. Thus, the interplay of cell and ECM mechanics will be difficult or even impossible to investigate. A recent report (Xu et al., 2016) demonstrated the ability to show the difference in mechanical properties of vibratome and cryotome tissue sections. Vibratomed tissue sections show good cell viability and in mechanical maps, cell and ECM regions can be distinguished. Thus, in vibratomed sections nearly all the properties of the living tissue sample are preserved, e.g., for AFM measurements. In contrast, in mechanical maps recorded from cryotomed sections, cell and ECM regions could not be distinguished, because the freezing process increased the stiffness of the entire tissue, possibly because cells were not viable anymore.

For AFM imaging, cryotomed tissue sections or samples chemically fixed in paraformaldehyde are mostly used. Both preparations increase sample stiffness and decrease adhesion to the cantilever tip (Joshi et al., 2017), which makes them suitable only for imaging; mechanical data from chemically fixed samples will be strongly affected by this sample preparation and show no resemblance with the mechanical data of live cells or tissue (Braet et al., 1998). Tissue sample preparation, immobilization, and hydration procedures are important for imaging and for obtaining mechanical maps of native samples by AFM. In a pioneering work it has been demonstrated that AFM can be used for *in vivo* nanomechanical imaging in living mammals by capturing real-time changes in nanomechanical properties during vasodilation and vasoconstriction in blood vessels (Mao et al., 2009). Although it is not clear how this could be adopted to other applications, especially in humans, it clearly demonstrates the potential of AFM directly following dynamics in living mammalian tissues. AFM was also used for capturing ultrastructural high-resolution imaging of native biomolecules, specifically intracellular organelles and extracellular matrix structures in mammalian connective tissue cryo-sections (Graham et al., 2010). AFM nanoindentation experiments

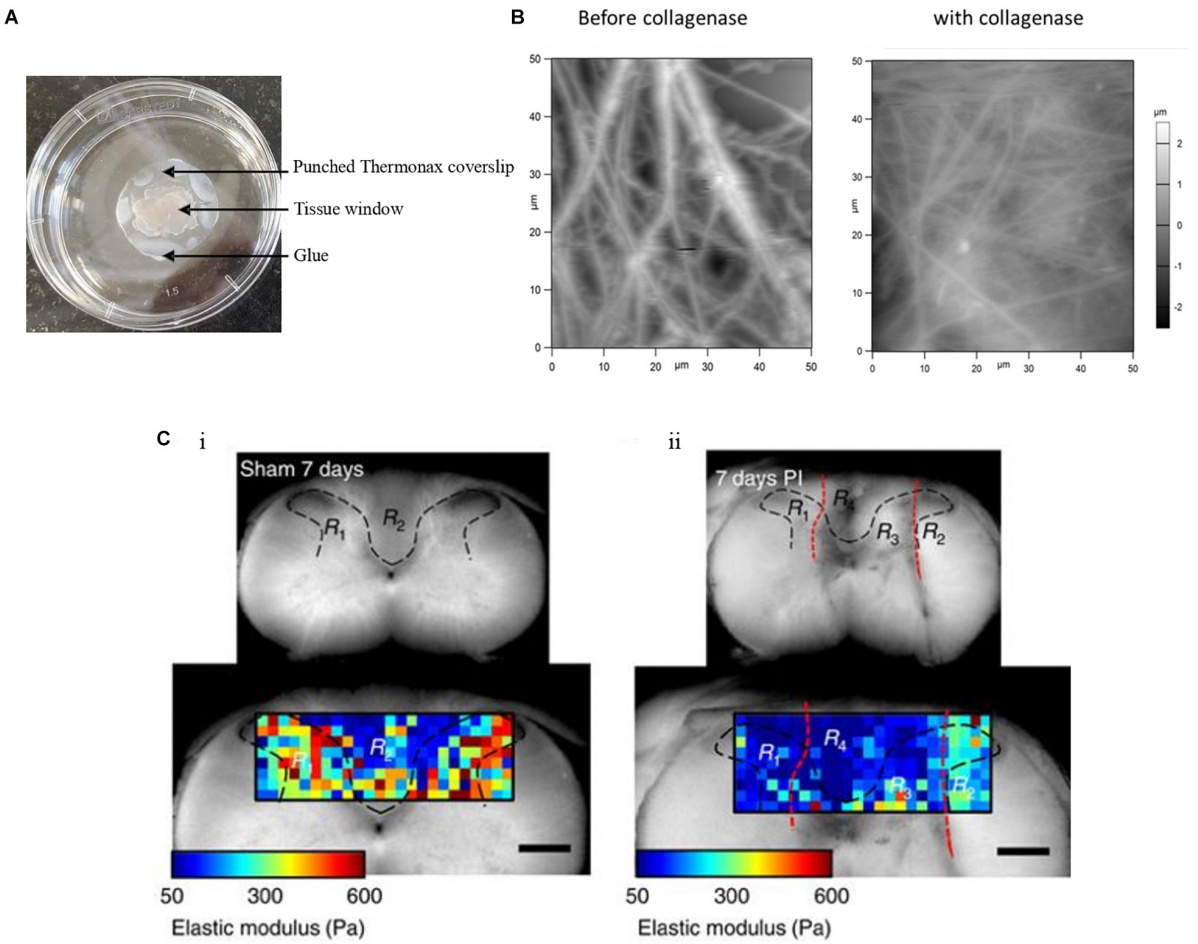

FIGURE 2 | Tissue sample immobilization and AFM imaging of mouse skin tissue sample. **(A)** Tissue samples are immobilized with punched Thermanox coverslips, glued to the Petri dish at their borders, thus avoiding direct contact of tissue with glue. AFM tip accesses the sample through the tissue window. **(B)** AFM height images show the presence of thick and rich ECM fibers in the mouse skin tissue matrix before addition of collagenase and after the addition of thick fibers, after which disappeared and decreased ECM fibers are seen (Joshi et al., 2017). **(C)** The gray (R_1 and R_3 in both i and ii) and white (R_2 and R_4 in both i and ii) matter are indicated within the area (black dashed lines) of the transverse spinal cord section of a sham control and of an animal with a dorsal column crush lesion at 7 days post-injury. The elastic moduli values are represented by means of a color map. In ii, the injured areas are identified by the red dashed lines (Reprinted with the permission from Moeendarbary et al., 2017 and this work is licensed under a Creative Commons Attribution 4.0 International License. To view the copy of this license, visit http://creativecommons.org/licenses/by/4.0/).

are able to characterize the stiffness and elastic modulus of soft tissue scaffolds such as collagen–chitosan biopolymers (Zhu et al., 2011). 3D mechanical properties of the skin epidermis and dermis at the nanoscale resolution are measured using AFM nanoindentation (Kao et al., 2016). By selecting the right AFM probes and by standardizing tissue section preparation and immobilization, one can measure the morphological and biomechanical changes in the tissue of any animal.

AFM IN NEUROBIOLOGY – PROSPECTS AND CHALLENGES

Here we discuss some of the reports where AFM was used in neurobiology, concentrating on neuronal and glial cells' biomechanics, including also brain tissue mechanics. For a detailed review on AFM usage in neuron biomechanics, readers are pointed to this review (Spedden and Staii, 2013). In neuronal growth and development, both neuronal cells and ECM function in a very coordinated manner. For example, the intracellular actin cytoskeleton helps neuronal growth cone movements. During development, neuronal growth cones are found at the apex of each axon and move in a direct way toward the target cell through the detection of extracellular signals. High resolution imaging and by studying the mechanical properties of these neuronal growth cones using AFM show varying protein motilities between different growth cone regions (Grzywa et al., 2006). AFM imaging of neurons grown on laminin micropatterns shows the laminin-guided neurite growth and the role of actin cytoskeleton in growth cone dynamics (Xing et al., 2010). AFM combined with confocal fluorescence microscopy have been used to analyze the morphology of neuronal growth cones of

rat dorsal root ganglia (Laishram et al., 2009). 3D imaging from AFM and confocal evaluates the 3D architecture of living chick dorsal root ganglia and sympathetic ganglia (McNally et al., 2005). 3D AFM imaging of neurons and glia cells provides a wealth of information on 3D cell structures and sub-cellular structures of organelles such as the mitochondria or the nucleus (Parpura et al., 1993). Viscoelastic properties of individual neuronal and glial cells in the CNS show a large mechanical heterogeneity because of the distribution of cell organelles. Generally, both cell types are very soft compared to other eukaryotic cells (Lu et al., 2006). This work also reveals that glial cells do not serve as a structural support or as a glue cell for neuronal cells. In all the reports mentioned above, chemically fixed or living cells are used for AFM imaging and mechanical measurements.

The discussion of AFM application in brain cells opens up the possibility of mechanical characterization of brain tissues using AFM. Before we further discuss this topic, the focus on tissue sample preparation for such application has to be elaborated on as this provides varied techniques along with their advantages and disadvantages. Tissue extraction, embedding, and slice preparations largely fall into deformations, due to the loss of the native environment and dehydration. This causes global shrinkage from the earlier primary and secondary deformations and greatly affects the tissue structures (Dauguet et al., 2007). This demands a unique embedding and slice preparation method to maintain the brain tissue integrity. Concerning 2D brain tissue preparation, conventional slice preparation methods for AFM investigation largely alter the tissue structure. Therefore, agar embedded tissue blocks were used for slide preparation which maintains the tissue structure and helps in carrying out mechanical measurements (Iwashita et al., 2014). Regarding 2D tissue section mechanical preservation, AFM mechanical characterization of living tissues showed cryotomed sections preventing the mechanical measurements of cells in the tissues. Comparatively, vibratomed sections are able to distinguish between the cell and ECM regions in the AFM-generated sub-micron resolution mechanical maps (Xu et al., 2016). As brain tissues are much softer than other tissues, their sectioning preparation by vibratome in a standardized fashion is quite challenging. Earlier, our lab tried to prepare cancer tissue sections from vibratome and due to the softness of the cancer tissue, we could not succeed in obtaining reproducible and useful results. The preparation of brain tissues from techniques other than cryotome may be advantageous to measure living tissue's mechanical properties.

Sub-tissue level nanomechanical imaging of both cells and ECM could possibly demonstrate the elastic properties as well as fine details of biomolecular structures of different brain regions. AFM measurements of the hippocampal and cortex regions of a rat brain show mechanical heterogeneity in subregions and also age-dependent tissue stiffness correlation (Elkin et al., 2007; Elkin et al., 2010). AFM indentation, with a spherical indenter, shows significant mechanical differences between white and gray matter of the rat cerebellum (Christ et al., 2010). AFM spatiotemporal tissue mechanical profiling shows the gradual stiffness increase in ventricular and subventricular zones of a mouse brain during embryonic development (Iwashita et al., 2014). Spatial mechanical mapping of the living guinea pigs' retinae, using scanning force microscopy, determines the elastic modulus of retinal regions and finds the contribution of neuronal cell bodies to the mechanical properties of inner retina (Franze et al., 2011). At the microscale, AFM time lapse *in vivo* imaging was performed in a live *Xenopus laevis* embryo in order to follow their local stiffness, which changes during embryonic brain development. This change in brain local stiffness is largely due to brain cell proliferation (Thompson et al., 2019). This time-resolved stiffness measurement can be conducted in other tissue development and is able to capture the tissue dynamics in varying temporal resolutions. Other than following embryonic brain development, AFM mechanical maps show the mechanical heterogeneity in a mouse primary somatosensory cortex and their age-dependent increase in tissue stiffness. Furthermore, AFM topographical imaging of thin sections of the different layers of the sensory cortex at different ages (weaning to adulthood) shows the continuing smoothing of the cortex surfaces (Smolyakov et al., 2018). AFM is a useful tool that can elucidate stiffness maps which correlate to brain development and many neurodegenerative diseases. AFM mechanical measurement shows Alzheimer's disease associated reduced brain tissue stiffness in mice comparatively to their wild type in both normoxia and hypoxia conditions (Menal et al., 2018). The molecular mechanism of amyloid beta (Aβ) fibril formation and toxicity in Alzheimer's disease is well characterized by AFM imaging (Moores et al., 2011). Pathological conditions such as acidosis stiffens the cerebellar gray matter when brain tissue is exposed to CO_2 thus decreasing the pH (Holtzmann et al., 2016). Comparative to other mammalian tissues, CNS tissue softens after injury. The glial intermediate filaments and ECM composition such as laminin and collagen IV contribute to the rat brain neocortex tissue softening assessed by AFM micro-indentation experiments (Moeendarbary et al., 2017). The elastic modulus color maps from gray and white matter regions show a decrease in elastic modulus values in the 7 days post-injured area, as compared to the control (**Figure 2C**). AFM mechanical characterization of a rat brain subjected to thromboembolic focal vertebral ischemia shows a decreased Young's modulus compared to the wild type (Michalski et al., 2015). Lewy bodies from postmortem brain tissue samples of Parkinson's disease human patients were imaged by AFM. These images show the aggregated fibrillary nanostructures in Lewy bodies and also show disconnected neurons which are located in the substantia nigra (Tercjak et al., 2014). The mechanical fingerprint of human glioblastoma and meningothelial meningioma tissues was measured by AFM mechanical maps. These potential applications of AFM in brain development and diseased tissue characterization help to better understand the sub-tissue level mechanosensitivity and its implications in the cells and ECM mechanical interactions. The recent advancement in AFM makes it an ideal tool to understand the role of mechanical cues in brain tissues and to correlate these cues to histopathological features. Further advancement in brain tissue sample preparation methods, together with AFM bioimaging techniques, widely covers the neuroscientific

network by using AFM for diagnosing and analyzing neurodegenerative diseases.

CONCLUSION

We reviewed the application of AFM bio-imaging and mechanical mapping of soft tissue samples like brain tissue and discussed the ability of AFM to work under near physiological conditions, which is essential for mechanical mapping. With the simple working principle, scientists from different disciplines can solve arising questions in tissue biology with the aid of AFM. The challenges in tissue sample immobilization, using the right liquid medium and tissue sectioning for AFM experiments were also discussed. As outlined and reviewed, medical engineers and scientists have to keep the challenges mentioned above in mind, and design experiments accordingly to study different tissues of varying animals. Concerning the brain tissue, there is great demand to use AFM in brain tissue imaging to visualize the micro scale arrangements of cells together with ECM. Additionally, obtaining mechanical maps of different regions of the brain enables one to study varying stiffness within brain tissues.

AUTHOR CONTRIBUTIONS

PV performed the AFM experiments, data analysis, and manuscript preparation. MR designed the content and was involved in data analysis and preparation of the manuscript.

ACKNOWLEDGMENTS

We thank the Bruker Nano Incorporation for their support and helpful discussion. The AFM probes were a kind gift from the Bruker Nano Incorporation, Santa Barbara, CA, United States.

REFERENCES

Ando, T. (2018). High-speed atomic force microscopy and its future prospects. *Biophys. Rev.* 10, 285–292. doi: 10.1007/s12551-017-0356-355

Benoit, M., Gabriel, D., Gerisch, G., and Gaub, H. E. (2000). Discrete interactions in cell adhesion measured by single-molecule force spectroscopy. *Nat. Cell Biol.* 2, 313–317. doi: 10.1038/35014000

Bouchonville, N., Meyer, M., Gaude, C., Gay, E., Ratel, D., and Nicolas, A. (2016). AFM mapping of the elastic properties of brain tissue reveals kPa μm-1gradients of rigidity. *Soft Matter* 12, 6232–6239. doi: 10.1039/c6sm00582a

Braet, F., Rotsch, C., Wisse, E., and Radmacher, M. (1998). Comparison of fixed and living liver endothelial cells by atomic force microscopy. *Appl. Phys. A* 66, S575–S578. doi: 10.1007/s003390051204

Chan, S., Neu, C., DuRaine, G., Komvopoulos, K., and Reddi, A. (2010). Atomic force microscope investigation of the boundary-lubricant layer in articular cartilage. *Osteoarthritis Cartilage* 18, 956–963. doi: 10.1016/j.joca.2010.03.012

Christ, A. F., Franze, K., Gautier, H., Moshayedi, P., Fawcett, J., Franklin, R. J., et al. (2010). Mechanical difference between white and gray matter in the rat cerebellum measured by scanning force microscopy. *J. Biomechan.* 43, 2986–2992. doi: 10.1016/j.jbiomech.2010.07.002

Dauguet, J., Delzescaux, T., Condé, F., Mangin, J.-F., Ayache, N., Hantraye, P., et al. (2007). Three-dimensional reconstruction of stained histological slices and 3D non-linear registration with in-vivo MRI for whole baboon brain. *J. Neurosci. Methods* 164, 191–204. doi: 10.1016/j.jneumeth.2007.04.017

Discher, D. E., Janmey, P., and Wang, Y. L. (2005). Tissue cells feel and respond to the stiffness of their substrate. *Science* 310, 1139–1143. doi: 10.1126/science.1116995

Dokukin, M. E., and Sokolov, I. (2017). Nanoscale compositional mapping of cells, tissues, and polymers with ringing mode of atomic force microscopy. *Sci. Rep.* 7:11828. doi: 10.1038/s41598-017-12032-z

Elkin, B. S., Azeloglu, E. U., Costa, K. D., and Morrison, B. III (2007). Mechanical heterogeneity of the rat hippocampus measured by atomic force microscope indentation. *J. Neurotrauma* 24, 812–822. doi: 10.1089/neu.2006.0169

Elkin, B. S., Ilankovan, A., and Morrison, B. III (2010). Age-dependent regional mechanical properties of the rat hippocampus and cortex. *J. Biomech. Eng.* 132:011010. doi: 10.1115/1.4000164

Florin, E., Moy, V., and Gaub, H. (1994). Adhesion forces between individual ligand-receptor pairs. *Science* 264, 415–417. doi: 10.1126/science.8153628

Franze, K., Francke, M., Günter, K., Christ, A. F., Körber, N., Reichenbach, A., et al. (2011). Spatial mapping of the mechanical properties of the living retina using scanning force microscopy. *Soft Matter* 7:3147. doi: 10.1039/c0sm01017k

Friedrichs, J., Helenius, J., and Muller, D. J. (2010). Quantifying cellular adhesion to extracellular matrix components by single-cell force spectroscopy. *Nat. Protoc.* 5, 1353–1361. doi: 10.1038/nprot.2010.89

Garcia, R., and Herruzo, E. T. (2012). The emergence of multifrequency force microscopy. *Nat. Nanotech.* 7, 217–226. doi: 10.1038/nnano.2012.38

Gennisson, J.-L., Deffieux, T., Fink, M., and Tanter, M. (2013). Ultrasound elastography: principles and techniques. *Diagn. Interv. Imaging* 94, 487–495. doi: 10.1016/j.diii.2013.01.022

Graham, H. K., Hodson, N. W., Hoyland, J. A., Millward-Sadler, S. J., Garrod, D., Scothern, A., et al. (2010). Tissue section AFM: in situ ultrastructural imaging of native biomolecules. *Matrix Biol.* 29, 254–260. doi: 10.1016/j.matbio.2010.01.008

Grant, C., Twigg, P., and Tobin, D. (2012). Static and dynamic nanomechanical properties of human skin tissue using atomic force microscopy: effect of scarring in the upper dermis. *Acta Biomaterialia* 8, 4123–4129. doi: 10.1016/j.actbio.2012.06.042

Grzywa, E. L., Lee, A. C., Lee, G. U., and Suter, D. M. (2006). High-resolution analysis of neuronal growth cone morphology by comparative atomic force and optical microscopy. *J. Neurobiol.* 66, 1529–1543. doi: 10.1002/neu.20318

Harke, B., Chacko, J. V., Haschke, H., Canale, C., and Diaspro, A. (2012). A novel nanoscopic tool by combining AFM with STED microscopy. *Opt. Nanoscopy* 1:3. doi: 10.1186/2192-2853-1-3

He, Y., Lu, M., Cao, J., and Lu, H. P. (2012). Manipulating protein conformations by single-molecule AFM-FRET nanoscopy. *ACS Nano* 6, 1221–1229. doi: 10.1021/nn2038669

Heath, G. R., and Scheuring, S. (2019). Advances in high-speed atomic force microscopy (HS-AFM) reveal dynamics of transmembrane channels and transporters. *Curr. Opin. Struct. Biol.* 57, 93–102. doi: 10.1016/j.sbi.2019.02.008

Hertz, H. (1882). Über die Berührung fester elastischer Körper. *J. Reine Angew. Mathematik* 92, 156–171.

Holtzmann, K., Gautier, H. O., Christ, A. F., Guck, J., Káradóttir, R. T., and Franze, K. (2016). Brain tissue stiffness is a sensitive marker for acidosis. *J. Neurosci. Methods* 271, 50–54. doi: 10.1016/j.jneumeth.2016.07.002

Iwashita, M., Kataoka, N., Toida, K., and Kosodo, Y. (2014). Systematic profiling of spatiotemporal tissue and cellular stiffness in the developing brain. *Development* 141, 3793–3798. doi: 10.1242/dev.109637

Jorba, I., Uriarte, J. J., Campillo, N., Farré, R., and Navajas, D. (2017). Probing micromechanical properties of the extracellular matrix of soft tissues by atomic force microscopy. *J. Cell. Physiol.* 232, 19–26. doi: 10.1002/jcp.25420

Joshi, S., Rianna, C., Mirastschijski, U., and Radmacher, M. (2017). "Measuring the mechanical properties of living neonatal mouse skin tissue by atomic force microscopy," in *Physics of Cancer: Interdisciplinary Problems and*

Clinical Applications : Proceedings of the International Conference on Physics of Cancer: Interdisciplinary Problems and Clinical Applications (PC IPCA'17) Tomskes, (Melville, NY: AIP Publishing LLC), doi: 10.1063/1.5001607

Kao, A. P., Connelly, J. T., and Barber, A. H. (2016). 3D nanomechanical evaluations of dermal structures in skin. *J. Mech. Behav. Biomed. Mater.* 57, 14–23. doi: 10.1016/j.jmbbm.2015.11.017

Kasas, S., Ruggeri, F. S., Benadiba, C., Maillard, C., Stupar, P., Tournu, H., et al. (2015). Detecting nanoscale vibrations as signature of life. *Proc. Natl. Acad. Sci. U.S.A.* 112, 378–381. doi: 10.1073/pnas.1415348112

Koehler, M., Fis, A., Gruber, H. J., and Hinterdorfer, P. (2019). AFM-based force spectroscopy guided by recognition imaging: a new mode for mapping and studying interaction sites at low lateral density. *Methods Protoc.* 2:6. doi: 10.3390/mps2010006

Laishram, J., Kondra, S., Avossa, D., Migliorini, E., Lazzarino, M., and Torre, V. (2009). A morphological analysis of growth cones of DRG neurons combining atomic force and confocal microscopy. *J. Struct. Biol.* 168, 366–377. doi: 10.1016/j.jsb.2009.09.005

Lekka, M., Laidler, P., Gil, D., Lekki, J., Stachura, Z., and Hrynkiewicz, A. Z. (1999). Elasticity of normal and cancerous human bladder cells studied by scanning force microscopy. *Eur. Biophys. J.* 28, 312–316. doi: 10.1007/s002490050213

Liu, F., and Tschumperlin, D. J. (2011). Micro-mechanical characterization of lung tissue using atomic force microscopy. *J. Vis. Exp.* 54:2911. doi: 10.3791/2911

Lu, Y.-B., Franze, K., Seifert, G., Steinhauser, C., Kirchhoff, F., Wolburg, H., et al. (2006). Viscoelastic properties of individual glial cells and neurons in the CNS. *Proc. Natl. Acad. Sci. U.S.A.* 103, 17759–17764. doi: 10.1073/pnas.0606150103

Mao, Y., Sun, Q., Wang, X., Ouyang, Q., Han, L., Jiang, L., et al. (2009). In vivo nanomechanical imaging of blood-vessel tissues directly in living mammals using atomic force microscopy. *Appl. Phys. Lett.* 95:013704. doi: 10.1063/1.3167546

Mariappan, Y. K., Glaser, K. J., and Ehman, R. L. (2010). Magnetic resonance elastography: a review. *Clin. Anat.* 23, 497–511. doi: 10.1002/ca.21006

Marturano, J. E., Arena, J. D., Schiller, Z. A., Georgakoudi, I., and Kuo, C. K. (2013). Characterization of mechanical and biochemical properties of developing embryonic tendon. *Proc. Natl. Acad. Sci. U.S.A.* 110, 6370–6375. doi: 10.1073/pnas.1300135110

McNally, H. A., Rajwa, B., Sturgis, J., and Robinson, J. P. (2005). Comparative three-dimensional imaging of living neurons with confocal and atomic force microscopy. *J. Neurosci. Methods* 142, 177–184. doi: 10.1016/j.jneumeth.2004.08.018

Menal, M. J., Jorba, I., Torres, M., Montserrat, J. M., Gozal, D., Colell, A., et al. (2018). Alzheimer's disease mutant mice exhibit reduced brain tissue stiffness compared to wild-type mice in both normoxia and following intermittent hypoxia mimicking sleep apnea. *Front. Neurol.* 9:1. doi: 10.3389/fneur.2018.00001

Michalski, D., Härtig, W., Krueger, M., Hobohm, C., Käs, J. A., and Fuhs, T. (2015). A novel approach for mechanical tissue characterization indicates decreased elastic strength in brain areas affected by experimental thromboembolic stroke. *Neuroreport* 26, 583–587. doi: 10.1097/wnr.0000000000000395

Moeendarbary, E., Weber, I. P., Sheridan, G. K., Koser, D. E., Soleman, S., Haenzi, B., et al. (2017). The soft mechanical signature of glial scars in the central nervous system. *Nat. Commun.* 8:14787. doi: 10.1038/ncomms14787

Moores, B., Drolle, E., Attwood, S. J., Simons, J., and Leonenko, Z. (2011). Effect of surfaces on amyloid fibril formation. *PLoS One* 6:e25954. doi: 10.1371/journal.pone.0025954

Morgan, J. T., Raghunathan, V. K., Thomasy, S. M., Murphy, C. J., and Russell, P. (2014). Robust and artifact-free mounting of tissue samples for atomic force microscopy. *Biotechniques* 56, 40–42. doi: 10.2144/000114126

Neuman, K. C., and Nagy, A. (2008). Single-molecule force spectroscopy: optical tweezers, magnetic tweezers and atomic force microscopy. *Nat. Methods* 5, 491–505. doi: 10.1038/nmeth.1218

Parpura, V., Haydon, P. G., and Henderson, E. (1993). Three-dimensional imaging of living neurons and glia with the atomic force microscope. *J. Cell Sci.* 104, 427–432.

Pillet, F., Chopinet, L., Formosa, C., and Dague, É. (2014). Atomic force microscopy and pharmacology: from microbiology to cancerology. *Biochim. Biophys. Acta* 1840, 1028–1050. doi: 10.1016/j.bbagen.2013.11.019

Plodinec, M., Loparic, M., and Aebi, U. (2010). Imaging articular cartilage tissue using atomic force microscopy (AFM). *Cold Spring Harb. Protoc.* 2010:db.rot5499. doi: 10.1101/pdb.prot5499

Ramachandran, S., Arce, F. T., Patel, N. R., Quist, A. P., Cohen, D. A., and Lal, R. (2014). Structure and permeability of ion-channels by integrated AFM and waveguide TIRF microscopy. *Sci. Rep.* 4:4424. doi: 10.1038/xsrep04424

Rianna, C., Kumar, P., and Radmacher, M. (2018). The role of the microenvironment in the biophysics of cancer. *Semin. Cell Dev. Biol.* 73, 107–114. doi: 10.1016/j.semcdb.2017.07.022

Rianna, C., and Radmacher, M. (2016). "Cell mechanics as a marker for diseases: Biomedical applications of AFM," in *Proceedings of the AIP Conference Proceedings*, (Melville, NY: AIP Publishing LLC), doi: 10.1063/1.4960276

Rianna, C., and Radmacher, M. (2017). Influence of microenvironment topography and stiffness on the mechanics and motility of normal and cancer renal cells. *Nanoscale* 9, 11222–11230. doi: 10.1039/c7nr02940c

Rico, F., Roca-Cusachs, P., Gavara, N., Farré, R., Rotger, M., and Navajas, D. (2005). Probing mechanical properties of living cells by atomic force microscopy with blunted pyramidal cantilever tips. *Phys. Rev.* E72:021914. doi: 10.1103/physreve.72.021914

Schillers, H., Medalsy, I., Hu, S., Slade, A. L., and Shaw, J. E. (2016). PeakForce tapping resolves individual microvilli on living cells. *J. Mol. Recognit.* 29, 95–101. doi: 10.1002/jmr.2510

Shibata, M., Nishimasu, H., Kodera, N., Hirano, S., Ando, T., Uchihashi, T., et al. (2017). Real-space and real-time dynamics of CRISPR-Cas9 visualized by high-speed atomic force microscopy. *Nat. Commun.* 8:1430. doi: 10.1038/s41467-017-01466-8

Smolyakov, G., Dague, E., Roux, C., Seguelas, M. H., Galés, C., Senard, J. M., et al. (2018). Nanoscale structural mapping as a measure of maturation in the murine frontal cortex. *Brain Struct. Funct.* 223, 255–265. doi: 10.1007/s00429-017-1486-z

Sneddon, I. N. (1965). The relation between load and penetration in the axisymmetric boussinesq problem for a punch of arbitrary profile. *Int. J. Eng. Sci.* 3, 47–57. doi: 10.1016/0020-7225(65)90019-14

Spedden, E., and Staii, C. (2013). Neuron biomechanics probed by atomic force microscopy. *IJMS* 14, 16124–16140. doi: 10.3390/ijms140816124

Stan, G., Solares, S. D., Pittenger, B., Erina, N., and Su, C. (2014). Nanoscale mechanics by tomographic contact resonance atomic force microscopy. *Nanoscale* 6, 962–969. doi: 10.1039/c3nr04981g

Staunton, J. R., Doss, B. L., Lindsay, S., and Ros, R. (2016). Correlating confocal microscopy and atomic force indentation reveals metastatic cancer cells stiffen during invasion into collagen I matrices. *Sci. Rep.* 6:19686. doi: 10.1038/srep19686

Stolz, M., Gottardi, R., Raiteri, R., Miot, S., Martin, I., Imer, R., et al. (2009). Early detection of aging cartilage and osteoarthritis in mice and patient samples using atomic force microscopy. *Nat. Nanotech.* 4, 186–192. doi: 10.1038/nnano.2008.410

Stolz, M., Raiteri, R., Daniels, A., Van Landingham, M. R., Baschong, W., and Aebi, U. (2004). Dynamic elastic modulus of porcine articular cartilage determined at two different levels of tissue organization by indentation-type atomic force microscopy. *Biophys. J.* 86, 3269–3283. doi: 10.1016/s0006-3495(04)74375-1

Tercjak, A., Bergareche, A., Caballero, C., Tuñon, T., and Linazasoro, G. (2014). Lewy bodies under atomic force microscope. *Ultrastructural Pathol.* 38, 1–5. doi: 10.3109/01913123.2013.825689

Thompson, A. J., Pillai, E. K., Dimov, I. B., Foster, S. K., Holt, C. E., and Franze, K. (2019). Rapid changes in tissue mechanics regulate cell behaviour in the developing embryonic brain. *eLife* 8:e39356. doi: 10.7554/elife.39356

Viji Babu, P. K., Rianna, C., Belge, G., Mirastschijski, U., and Radmacher, M. (2018). Mechanical and migratory properties of normal, scar, and Dupuytren's fibroblasts. *J. Mol. Recognit.* 31:e2719. doi: 10.1002/jmr.2719

Xing, S., Liu, W., Huang, Z., Chen, L., Sun, K., Han, D., et al. (2010). Development of neurons on micropatterns reveals that growth cone responds to a sharp change of concentration of laminin. *Electrophoresis* 31, 3144–3151. doi: 10.1002/elps.201000133

Xu, X., Li, Z., Cai, L., Calve, S., and Neu, C. P. (2016). Mapping the nonreciprocal micromechanics of individual cells and the surrounding matrix within living tissues. *Sci. Rep.* 6:24272. doi: 10.1038/srep24272

Zhong, Q., Inniss, D., Kjoller, K., and Elings, V. (1993). Fractured polymer/silica fiber surface studied by tapping mode atomic force microscopy. *Surface Sci. Lett.* 290, L688–L692. doi: 10.1016/0167-2584(93)90906-y

Zhu, P., and Fang, M. (2012). Nano-morphology of cartilage in hydrated and dehydrated conditions revealed by atomic force microscopy. *J. Phys. Chem. Biophys.* 2:1. doi: 10.4172/2161-0398.1000106

Zhu, Y., Dong, Z., Wejinya, U. C., Jin, S., and Ye, K. (2011). Determination of mechanical properties of soft tissue scaffolds by atomic force microscopy nanoindentation. *J. Biomechan.* 44, 2356–2361. doi: 10.1016/j.jbiomech.2011.07.010

Conflict of Interest Statement: The authors declare that the research was conducted in the absence of any commercial or financial relationships that could be construed as a potential conflict of interest.

Copyright © 2019 Viji Babu and Radmacher. This is an open-access article distributed under the terms of the Creative Commons Attribution License (CC BY). The use, distribution or reproduction in other forums is permitted, provided the original author(s) and the copyright owner(s) are credited and that the original publication in this journal is cited, in accordance with accepted academic practice. No use, distribution or reproduction is permitted which does not comply with these terms.

frontiers in Neuroscience

REVIEW
published: 05 July 2019
doi: 10.3389/fnins.2019.00689

Tissue Response to Neural Implants: The Use of Model Systems Toward New Design Solutions of Implantable Microelectrodes

*Maurizio Gulino[1,2,3], Donghoon Kim[4], Salvador Pané[4], Sofia Duque Santos[1,2] and Ana Paula Pêgo[1,2,3,5]**

[1] i3S – Instituto de Investigação e Inovação em Saúde, Universidade do Porto, Porto, Portugal, [2] INEB – Instituto de Engenharia Biomédica, Universidade do Porto, Porto, Portugal, [3] FEUP – Faculdade de Engenharia, Universidade do Porto, Porto, Portugal, [4] Multi-Scale Robotics Lab (MSRL), Institute of Robotics and Intelligent Systems (IRIS), ETH Zurich, Zurich, Switzerland, [5] ICBAS – Instituto de Ciências Biomédicas Abel Salazar, Universidade do Porto, Porto, Portugal

The development of implantable neuroelectrodes is advancing rapidly as these tools are becoming increasingly ubiquitous in clinical practice, especially for the treatment of traumatic and neurodegenerative disorders. Electrodes have been exploited in a wide number of neural interface devices, such as deep brain stimulation, which is one of the most successful therapies with proven efficacy in the treatment of diseases like Parkinson or epilepsy. However, one of the main caveats related to the clinical application of electrodes is the nervous tissue response at the injury site, characterized by a cascade of inflammatory events, which culminate in chronic inflammation, and, in turn, result in the failure of the implant over extended periods of time. To overcome current limitations of the most widespread macroelectrode based systems, new design strategies and the development of innovative materials with superior biocompatibility characteristics are currently being investigated. This review describes the current state of the art of *in vitro*, *ex vivo*, and *in vivo* models available for the study of neural tissue response to implantable microelectrodes. We particularly highlight new models with increased complexity that closely mimic *in vivo* scenarios and that can serve as promising alternatives to animal studies for investigation of microelectrodes in neural tissues. Additionally, we also express our view on the impact of the progress in the field of neural tissue engineering on neural implant research.

Keywords: neural tissue response, microelectrodes, foreign body reaction, brain slice cultures, neural tissue engineering, deep brain stimulation

OPEN ACCESS

Edited by:
Jeffrey R. Capadona, Case Western Reserve University, United States

Reviewed by:
Abhishek Prasad, University of Miami, United States
Takashi D. Y. Kozai, University of Pittsburgh, United States
Janak Gaire, University of Florida, United States

***Correspondence:**
Ana Paula Pêgo
apego@i3s.up.pt;
apego@ineb.up.pt

Specialty section:
This article was submitted to Neural Technology, a section of the journal Frontiers in Neuroscience

Received: *15 February 2019*
Accepted: *18 June 2019*
Published: *05 July 2019*

Citation:
Gulino M, Kim D, Pané S, Santos SD and Pêgo AP (2019) Tissue Response to Neural Implants: The Use of Model Systems Toward New Design Solutions of Implantable Microelectrodes. Front. Neurosci. 13:689. doi: 10.3389/fnins.2019.00689

IMPLANTABLE ELECTRODES IN NEUROLOGICAL AND NEUROPSYCHIATRIC DISORDERS

Clinical Applications

Recent technological progress in the field of brain-machine interfaces boosted the development of innovative tools and electrodes for neurophysiological research and neurostimulation applications to treat neuro disability-related conditions.

Deep brain stimulation (DBS) is an invasive neurosurgical operation consisting in the delivery of electrical impulses to specific areas of the brain by means of implantable electrodes connected to a pulse generator. The concept of DBS is the generation of action potentials resulting in beneficial neurochemical effects, such as the recovery of disrupted neural circuits and physiological brain function. For specific applications, DBS is a U. S. "Food and Drug Administration" (FDA) approved technique which is already applied in the clinic for a vast number of neurological dysfunctions (Coenen et al., 2015; Revell, 2015). In patients affected by Parkinson's disease, DBS at the level of the globus pallidus or subthalamic nucleus is able to reduce bradykinesia, dystonia, as well as walking problems, allowing for substantial improvements in the quality of life (Ramirez-Zamora and Ostrem, 2018). In patients affected by dystonia, globus pallidus DBS has been shown to reduce tremors and involuntary motor contraction, with persistent effects after several years (Meoni et al., 2017). For essential tremors, the principal targets for DBS to reduce tremors with lower stimulation amplitudes and fewer side effects than previous treatments are the posterior subthalamic area and the zona incerta (Holslag et al., 2017; Barbe et al., 2018). In patients with medically refractory epilepsy, long-term DBS at the level of the anterior nucleus of the thalamus is an U. S. FDA-approved therapy that is able to reduce epileptic episodes and ensure perdurable improvements in the quality of life for years (Salanova, 2018). For the treatment of chronic and neuropathic pain, DBS is a supported therapy in Europe, although not currently approved by the U. S. FDA. Several clinical studies report a reduction of pain in patients with amputations, post-stroke pain, cranial and facial pain (Farrell et al., 2018). DBS was also found to be a valid therapeutic approach for the treatment of psychiatric disorders. Ventral capsule/ventral striatum DBS is another U. S. FDA-approved treatment under a humanitarian device exemption for patients affected by obsessive-compulsive disorder (Karas et al., 2019). A relevant efficacy of DBS has been also observed for the treatment of refractory depression. Clinical application of DBS in patients non-responsive to anti-depressant treatments reported a remission of depression after chronic stimulation of various brain targets, with a decrease in negativity and sadness, reduction of cerebral blood flow at the level of the limbic-cortical circuitry, and improvements in memory and motor function (Dandekar et al., 2018; Drobisz and Damborská, 2019).

Spinal cord stimulation (SCS) has shown to be an effective strategy for the treatment of different diseases. SCS is being successfully used to treat angina pectoris pain, low back, and leg pain and peripheral limb ischemia (Song et al., 2014). Clinical studies reported beneficial effects of SCS combined with activity-based training in the recovery of motor function and muscle activation patterns in patients that suffered spinal cord injury (Rejc et al., 2017).

Besides the applications described above, the use of implantable electrodes for neurostimulation therapy is continuing to expand toward many other medical conditions. DBS has been recently proposed for the treatment of pain, dystonia and motor symptoms in post-stroke, although additional investigations are necessary to identify specific brain districts to improve the effectiveness of the treatment (Elias et al., 2018). In a study involving patients affected by Tourette syndrome, DBS of the anterior and posterior globus pallidus, centromedian thalamus and anterior limb of internal capsule showed common positive results after 1 year of treatment in the reduction of motor tic symptoms (Martinez-Ramirez et al., 2018). Partial improvements have been described in clinical trials involving patients affected by Alzheimer's disease, with positive effects in cognition, reversal of memory and reduction of altered glucose metabolism (Mao et al., 2018).

As seen above, the progress in neurostimulation technology and the increased knowledge of the neurophysiology of the central nervous system (CNS) opened the way to new therapeutic approaches for the treatment of a vast number of neurological disorders and neuropsychiatric conditions. Although well established and approved for some diseases, additional trials and experimental work need to be conducted to better define the ideal brain targets, stimulation variables, and electrode design in order to ameliorate the clinical outcomes. Due to the impact of the inflammatory response and tissue encapsulation elicited by traditional DBS macroelectrodes, the field of neuroengineering is progressing toward the employment of implantable microelectrodes (Daniele and Bragato, 2014). Traditional DBS electrodes present several drawbacks such as the rigidity of the materials employed for fabrication as well as a high size which exacerbate the neuroinflammatory response and tissue damage. Although they have a higher activation radius compared to microelectrodes, macroelectrode implantation is often associated to a wrong positioning in the interested area causing a decrease in therapeutic efficacy of DBS (Kloc et al., 2017; Morishita et al., 2017). In the case of small target areas, the reduced dimensions of microelectrodes can provide a better targeting accuracy ensuring an increased therapeutic efficacy of DBS and tissue integration for chronic applications (Desai et al., 2012; Du et al., 2017; Ganji et al., 2017). These miniaturized devices offer additional advantages such as reduced tissue damage and impedance, increased signal-to-noise ratio and neuronal activation compared to traditional electrodes (Desai et al., 2014). A key component contributing to microelectrode design and, ultimately, to clinical performance is the selection of the materials for the device. Such materials should not only satisfy the mechanical and the structural requirements for the efficient electrochemical performance but also provide a durable and biocompatible interface with the brain tissue. In the following section, the current materials used in microelectrode fabrication are presented.

Current Materials for Microelectrode Fabrication

For the long-lasting efficient microelectrodes, the material should not only function properly *in vivo* but also be biocompatible and durable for the protection of both the patient and the device (Szostak et al., 2017). As different materials show dissimilar behavior in the tissue environment the choice of the implant material is crucial. To mitigate foreign body

reactions and corrosion/degradation of the structures, electrical, chemical, and mechanical properties of materials, such as chemical composition, crystallinity, surface morphology, the electrode microstructure, and Young's modulus (a measurement of elasticity) need to be carefully considered (Cogan, 2008; Williams, 2008, 2009). With the advance of the micro-fabrication techniques, silicon and polymers have been widely employed as the substrate materials, while metals, carbon nanotubes, conductive polymers as electrode site materials (Samba et al., 2015; Yi et al., 2015; Antensteiner and Abidian, 2017).

Typical microelectrodes are designed to have either an array of microwires or micro-electromechanical system (MEMS) arrays. Microwires are generally composed of metals such as gold, tungsten, and stainless-steel, coated with insulators. Two different types of silicon substrate-based MEMS micro-machined electrodes, i.e., the Utah array (Normann and Fernandez, 2016; Wendelken et al., 2017) and the Michigan array (Kipke et al., 2008; Kiss et al., 2015), have been significantly exploited for decades. However, a huge mechanical mismatch between hard metals/silicon (E $\sim$ 10 to 100 GPa) and soft brain tissue (0.4–15 kPa) results in substantial strain at the tissue-electrode interface, causing local physical damage that result in inflammation and neural degeneration (Polikov et al., 2005; Harris et al., 2011; Merrill, 2014). The inflammatory process may hinder the stimulation of neuronal cells, as well as it may contribute to device failure as a result of electrode degradation (Kozai et al., 2015a; McCreery et al., 2016). However, it must be highlighted that not all the microelectrode types exhibit the same degradation profile or that there is a direct correlation between electrode failure and the acute inflammatory response (Gaire et al., 2018a). Several efforts have been reported to overcome the drawbacks from the mechanical mismatch between electrode and tissue by implementing materials with lower Young's modulus, e.g., flexible and biocompatible polymer substrates (Trevathan et al., 2019). Polyimide- (Lai et al., 2012) and parylene-based MEMS (Hess et al., 2011) electrodes have been heavily investigated for their improved mechanical properties, easy access to fabricate, and capability to introduce bioactive molecules at the interface to facilitate long-term interaction with the tissue. As chronic stimulation electrode site materials, metals including tungsten, platinum, iridium, tantalum pentoxide, and titanium nitride have been extensively used for their electrical charge-injection properties and biocompatibility (Cogan, 2008; Fattahi et al., 2014; Meijs et al., 2015). For its remarkably increased charge storage and injection capacity and high corrosion resistivity, iridium oxide has been also widely utilized as a coating material (Meyer et al., 2001; Hasenkamp et al., 2009) to enhance the performance and the durability of the electrode. Carbon nanotubes (Jiang et al., 2011; Schmidt et al., 2013) and conducting polymers such as poly(3,4-ethylene dioxythiophene) (PEDOT) and poly(styrene sulfonate) (PSS) (Cui and Martin, 2003; Pranti et al., 2018) are attracting considerable attention as alternatives to the metal electrodes and coatings for their biocompatibility and tunable electrical properties.

An important challenge in microelectrode fabrication for neural stimulation is the identification of smart materials that are able to provide enhanced biocompatibility. So far, all the current microelectrodes are recognized, in the long run, as foreign bodies by the nervous tissue. As the difference in Young's modulus between the electrode and tissue is the main factor that causes damage and inflammation, most research is focused on using materials with low Young's modulus for both substrates and electrode sites. However, it should be also taken into account that mechanical strain from the motion artifacts, such as bending of conducting material, can cause changes in resistance or capacitance of materials. As a result, this can affect the electrical signals of the electrode and can result in unintended performance (Michelson et al., 2019). Thus, the balance between Young's modulus and the electrical properties need to be carefully considered in designing microelectrodes for neural stimulation.

FOREIGN BODY RESPONSE AS A CAUSE OF IMPLANT FAILURE

The nervous tissue response to implantable microelectrodes is a complex process characterized by a cascade of biochemical alterations and chemical reactions occurring at the level of the tissue-material interface. These biochemical and chemical alterations may culminate in an undesired foreign body response. Additionally, changes in the inherent properties of the electrode after long-term implantation, for example due to corrosion, may further impair its tissue compatibility and durability. Body fluids and tissues are highly corrosive environments characterized by an elevated presence of oxygen, saline electrolytes, macromolecules and dissolved ions that can cause the electrochemical detachment of microelectrode surface. Once surgically implanted, microelectrodes must remain intact for several years to ensure the efficacy of the therapy and device functionality. To provide successful integration, reliability, and durability once implanted in the brain tissue, microelectrodes must fulfill the following requirements:

- Biocompatibility: the surface of the microelectrode must be non-toxic for neural cells without causing any adverse effects to the surrounding tissues.
- Biomimicry: the surface has to mimic the physicochemical and mechanical characteristics of the extracellular matrix (ECM) in order to promote neurite outgrowth toward the electrode surface and to avoid activation and recruitment of glial cells and fibroblasts that can contribute to the encapsulation of the electrodes.
- Biostability: microelectrodes need to maintain their physical integrity, electrochemical stability, and functionality, and resist the highly corrosive tissue microenvironment without undergoing any structural modification.

Microelectrode implantation causes unavoidable damage to the tissue, triggering a series of neuroinflammatory reactions, which are part of the natural wound healing process that can seriously affect the stimulating site integrity and hamper the electrochemical performance in long-term implantations (Salatino et al., 2018). The complexity of such a process can be described by dividing it into two coupled factors: biotic factors, represented by the effects of cells and tissue reactions occurring

at the surface; and the abiotic factors, related to the characteristic of the material itself.

Biotic factors include the blood-brain barrier (BBB) rupture, protein absorption at the material surface, immune cells and fibroblast recruitment, increased production of radical ions, cell death and the formation of the insulating glial scar around the electrode surface, which hampers blood supply and ionic equilibrium at the injury site. The abiotic factors are represented by the physicochemical surface modifications such as the dissolution of passive films, material-related impedance, the failure of the stimulating site integrity, the formation of electrochemical cells at the level of the surface that can evolve in crevices or pits. Biotic and abiotic factors cannot be considered as two separated processes, as they are strictly dependent and occur simultaneously interacting in different manners during the lifetime of the electrode. The complexity of such a process is not totally understood and further research is needed to clarify whether the contributions of these interrelated factors occur and what are the most effective intervention strategies.

In this section, we will provide a description of the main cascade of biochemical and cellular events occurring upon brain microelectrode implantation with a focus on the biotic reactions.

The process that leads to glial scar formation due to implantation and can culminate in the encapsulation of an implant can be divided into two phases (**Figure 1**). An acute phase that starts immediately after device implantation and characterized by BBB dysfunction and glial cell activation, followed by a chronic phase characterized by an immune response and the development of a glial scar around the implant.

The first and one of the most critical events occurring during device implantation is the rupture of the BBB. The implantation causes a break at the level of the endothelial vessels, with a reduction of blood flow and oxygen supply, accumulation of plasma proteins and pro-inflammatory factors, and myeloid cell infiltration (Kozai et al., 2015b). Cell membrane damage by mechanical stress causes an increase in Ca^{2+} concentration either by its release through the pores in the cell membrane and by disturbances in the electrochemical potential of Na^{+} channels, which lead to membrane depolarization (Eles et al., 2018; Salatino et al., 2019). Membrane depolarization, in turn, leads to the increase in intracellular Ca^{2+}, neurotransmitters release from presynaptic terminations (Eles et al., 2018), resulting in excessive production of reactive oxygen species (ROS) due to mitochondrial damage (Ereifej et al., 2018). The BBB breach has been shown to be crucial in the triggering of biochemical pathways responsible for neuronal degeneration and glial activation (Saxena et al., 2013). Some plasma proteins such as globulins, fibrinogen, thrombin, plasmin, and albumin can accumulate at the injury site through the BBB gap and can be adsorbed at the electrode surface.

Microglia

Glial activation represents the main cellular event involved in the neuroinflammatory response. As the resident macrophage cells of the brain, microglia are ubiquitous in the CNS, and they become activated to carry out their neuroprotective functions immediately after electrode implantation. Once activated, they act as principal effectors of the neuroinflammatory response and can orchestrate the process through cross-talk with astrocytes and oligodendrocytes. It is already been accepted that microglia exist in "pro-inflammatory" and "anti-inflammatory" phenotypes. The former is the "classical activation" phenotype, in which cells secrets pro-inflammatory cytokines and contribute to neuronal injury; in the case of the latter phenotype cells secret anti-inflammatory cytokines and contribute to tissue remodeling and repair, phagocytosis of cell debris, as well as antagonize pro-inflammatory activity. In the early hours post-implantation, pro-inflammatory microglia secrete pro-inflammatory cytokines and chemokines such as interleukins IL-1α, IL-1β, IL-6, tumor necrosis factor (TNF-α), monocyte chemoattractant protein 1 (MCP-1) (Sawyer et al., 2014), ROS and reactive nitrogen species (RNS), determining massive immune cell recruitment and additional cytokine production (Hermann et al., 2018a). The lack of oxygen redox homeostasis acts directly on microglia, astroglia and endothelial cells causing activation of metalloproteinase, downregulation of tight junctions and adherens junction genes in the first hours after BBB injury (Bennett et al., 2018), facilitating the entrance of infiltrating macrophages, which will also have a crucial role in neurodegeneration (Ravikumar et al., 2014).

Astrocytes

Astrocytes are another type of neuroglia that is very affected after implantation. Astrocytes perform many functions, including biochemical support of endothelial cells that form the BBB, supplying of nutrients to the nervous tissue, maintenance of extracellular ion balance, having a key role in the repair and scarring process of the brain. In analogy to microglia, astrocytes exist in a pro-inflammatory phenotype and an anti-inflammatory phenotype. Pro-inflammatory astrocytes are activated by pro-inflammatory microglia and secret neurotoxins creating a hostile environment for neuronal and oligodendrocytes regeneration. Pro-inflammatory astrocytes are activated by Il-1β, TNF-α and complement component 1q (C1q) from microglia, responding immediately to electrode implantation and changes in neuronal activity, accumulating in the vicinity of the microelectrode during the first week after implantation (Liddelow et al., 2017). At this level, astrocytes alter the neuronal viability causing neuronal loss, reduction of fiber density and overexpression of glial fibrillary protein (GFAP) and vimentin, which are critical for their change in morphology and extension of the protrusions at the injury site (Woolley et al., 2013; Moeendarbary et al., 2017).

Neurons

The neuronal loss also occurs immediately after implantation. The mechanical stress caused by electrode entry into the tissue leads to axonal morphological changes, neuronal membrane disruption with the formation of axonal blebs as an indication of neuronal damage. Oxidative stress in neurons is caused by the increase in intracellular calcium through glutamate-N-methyl-D-aspartate receptor (NMDA) activation, as well as by ROS and RNS produced by microglia and astrocytes, causing mitochondrial dysfunction. Neuronal degeneration and neuroinflammation are exacerbated by the persistent secretion

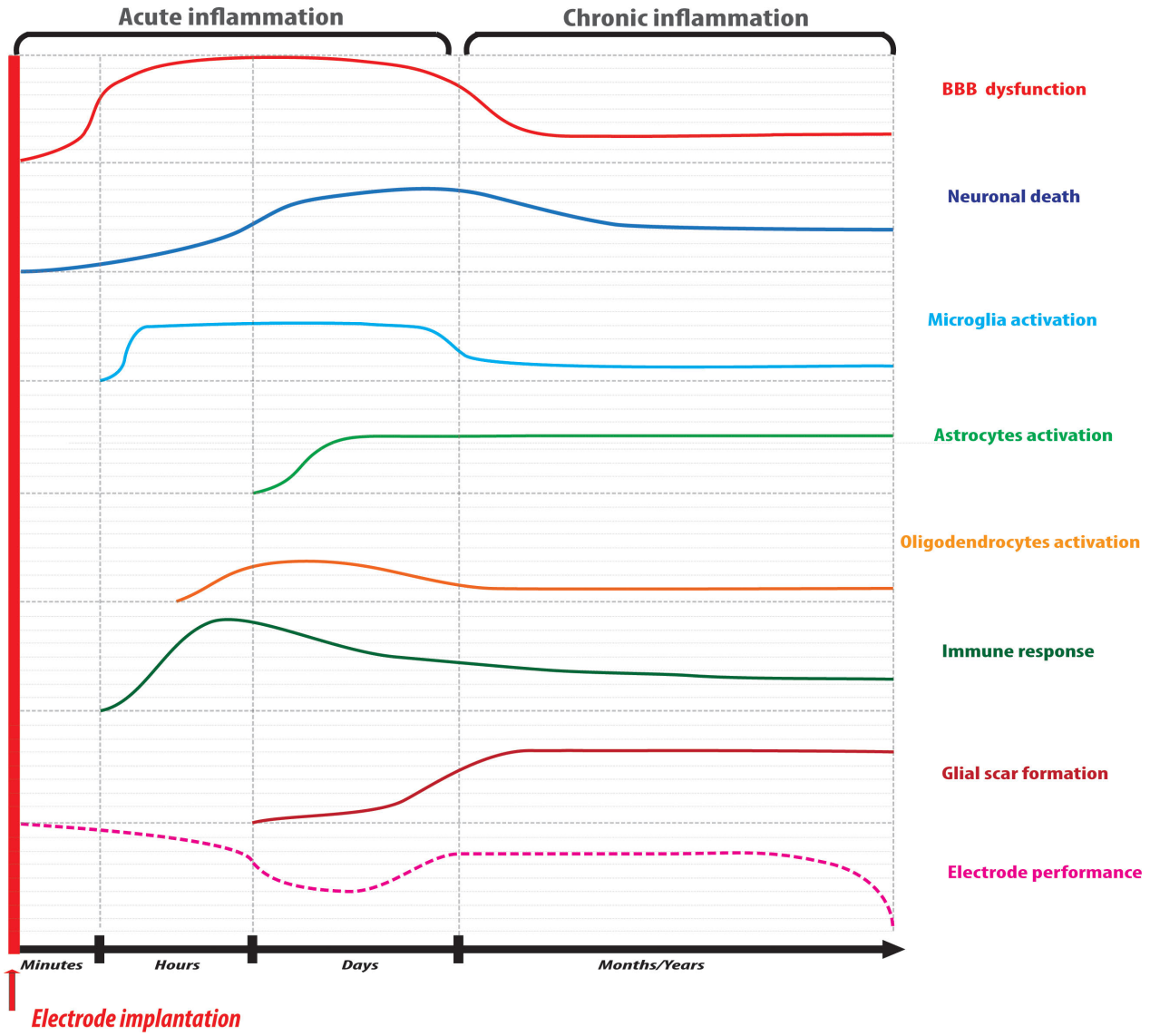

FIGURE 1 | Schematic timeline representation of the reactions involved in the process of neural tissue response to implantable microelectrodes. The acute phase of inflammation is characterized by BBB disruption and neuronal death due to mechanical insult followed by glial activation and immune cell recruitment at the injury site. Microelectrode performance may be hampered at this level due to mechanical mismatch with the tissue accompanied by a temporary recovery. In the chronic phase of inflammation, a glial fibrotic scar surrounds the microelectrode impeding material and stimulating site integrity that, ultimately, may result in implant failure.

of proinflammatory cytokines and glial fibrillary proteins deposition by microglia and astrocytes, finally forming the glial scar (**Figure 1**). As a consequence of this neuronal death at the tissue-electrode interface, the distance between electrode and synapses grows in time, hampering electrical stimulation performance.

Oligodendrocytes

Oligodendrocyte cell death will also occur at the implantation site. Either due to cell membrane damage or as a result of neuronal cell death or axonal degeneration. Oligodendrocytes play the important function of ensuring axonal support and myelin production and maintenance. In the acute phase of foreign body reaction, oligodendrocytes become highly sensitive to oxidative stress by ROS and RNS as well as excitotoxic damage by glutamate oversignaling. Apoptosis of oligodendrocytes leads to demyelination and can also culminate in neuronal death depending on the extent of the event. In the adult brain, one can find not only myelinating oligodendrocytes but also cells in the form of neuron-glia antigen 2-expressing glial cells (NG2) precursors, which are present from development to the adult phase, denominated oligodendrocyte progenitor cells. *In vivo* studies showed that new NG2 precursors become activated by proinflammatory factors secreted by reactive microglia and can be seen migrating to the injury site 12 h post-implantation (Wellman and Kozai, 2018). But there, NG2

precursors preferentially differentiate to astrocytes and further move toward the implant participating in the formation of the glial scar, not contributing to the turnover of new myelinating oligodendrocytes (Wellman et al., 2018a).

The Glial Scar

Over 2 weeks post-implantation, in the chronic phase of the process, it has been observed that astrocytes and microglia have their protrusions extended toward the material surface creating a non-permeable barrier between the implant and the tissue over 2 weeks post-implantation (Wellman and Kozai, 2017). At this stage, fibroblasts have reached the inflammation core from meninges and secret ECM proteins such as fibronectin, type IV collagen, laminin, and chondroitin sulfate proteoglycans, also contributing to the formation of the glial scar and the encapsulation of the microelectrode at the parenchymal level (Dias and Göritz, 2018). This insulating barrier constitutes a hostile environment that hampers electrophysiological performance due to the absence of contact between microelectrode and neurons, leading to the failure of the implant over extended periods of time (**Figure 1**).

Despite all the efforts that have been carried out to study the dynamics of glial scar in injury and disease, additional investigations are required to understand the specificities of the foreign body response in the context of electrode implantation, to uncover the most effective intervention strategies to promote microelectrode integration in the CNS (Salatino et al., 2018). Besides, it is important to take in consideration that other aspects can influence glial scar heterogeneity, such as the type of microelectrode material used, the cerebral anatomical district of implantation, as well as the pathological context in which it is applied. Hence, the use of modeling systems that can mimic specific *in vivo* pathological conditions is a great opportunity to move toward the establishment of innovative approaches on which to base future microelectrode design.

EXPERIMENTAL MODELS TO STUDY FOREIGN BODY RESPONSE TO NEURAL IMPLANTS

Despite the great advances achieved in neural interface technology, some questions related to the molecular and cellular events involved in nervous tissue response to implantable microelectrodes remain unanswered. Several *in vivo* studies have been performed to identify critical aspects and design solutions to inhibit glial encapsulation in chronic applications. However, due to their cost, time consumption and complexity *in vivo* models are not ideal systems to investigate the detailed cues of tissue-electrode interactions. With this purpose, substantial research has been focused on the development of relevant *in vitro* biological platforms of increased complexity to test new materials and biosurfaces, which can offer a controlled and reproducible platform for high-throughput screenings. In the following paragraphs, we provide an overview of the current *in vitro*/*ex vivo*/*in vivo* models employed in microelectrode research, as well as a description of new promising 3D *in vitro* technologies with increased complexity that can be of added value to future investigations in this field (**Figure 2**).

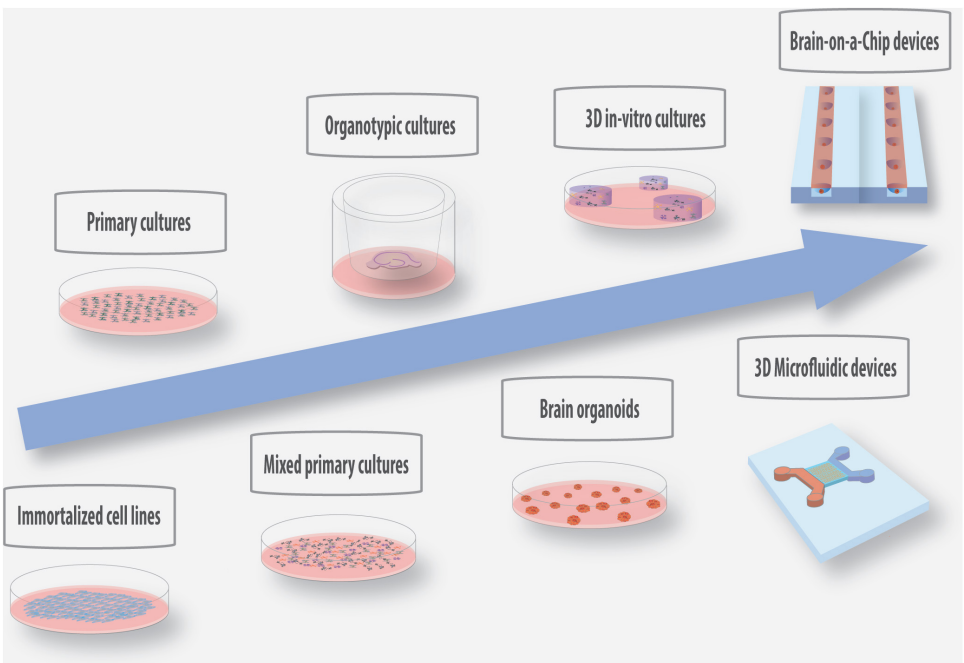

FIGURE 2 | Schematic representation of the current and promising *in vitro*/*ex vivo* models with increased physiological relevance for the screening of materials and coatings for the development of implantable microelectrodes.

In vitro Models

One of the main goals in the design and testing of new materials as well as coatings for microelectrodes is to reduce glial cell activation while allowing/inducing neuronal synaptic activity. *In vitro* 2D cultures represent the simplest model to investigate the impact of materials properties on the cellular response (**Table 1**).

Immortalized Cell Line Cultures

The use of relevant immortalized cell lines can provide significant insights regarding material biocompatibility and can contribute to the study of cell-microelectrode material interactions. The experimental conditions are controlled in terms of cell identity, adaptability, and reproducibility. Immortalized cell lines are simple to culture, can be grown for indefinite periods of time, maintaining genotypic stability and allowing the readily generation of large amounts of cells for analysis. Fibroblasts are one of the most well-characterized cell types to study the biocompatibility and the cell-adhesion properties of metals and coatings for biomedical devices. These cells play a critical role in the formation of the fibrotic scar in the late phases of inflammation. The modulation of their adhesion and interactions with the implants is crucial for ensuring a stable device performance. Fibroblast cell lines such as L929 and NIH/3T3 have been widely used to conduct standard material biocompatibility and cytotoxicity testing in accordance with the International Organization for Standardization (ISO) norm 10993-5. The latter defines a series of test methods employing cell monolayers in contact with the material or with material extracts to assess toxicity. In particular, the mouse embryonic NIH/3T3 fibroblasts are a well-characterized cell type used by FDA for biocompatibility testing of materials and coatings for neural devices. Namely, these were employed to assess surface properties of various preparations of polymeric conductive materials for neural devices applications (Mantione et al., 2016; Rejmontová et al., 2016; Hadler et al., 2017; Morin and He, 2017; Wang J. et al., 2018).

Given their central role in orchestrating nervous tissue response to microelectrodes, glial cell were also employed to investigate the effects of new surfaces and designs on cell adhesion, morphology and activation (Persheyev et al., 2011; Ereifej et al., 2013b; Lee et al., 2014). Bérces et al. (2018) employed the immortalized murine microglial cell line BV-2 to investigate the effects of nanotopography on silica and platinum surfaces and compared their behavior with neural stem cells. They showed that while BV-2 cells grew indifferently on nanostructured and non-coated samples, neural stem cells grown on nanostructured surfaces displayed a decrease in cell viability, adhesion and a tendency to adhere to each other instead of to the surface. C6 glioma cells were employed to investigate the biocompatibility of Pt-grown carbon nanofibers coatings for enzymatic glutamate biosensors and compared to Ni-grown nanofibers, showing that cells exhibit different cell adhesion and morphology at different dimensions of nanofibers (Isoaho et al., 2018). Several studies have been conducted to investigate the biocompatibility and the effect of surface properties, like roughness and topography, on neuronal cells. Rat pheochromocytoma PC12 neuronal cell lines are the most used to study the ability of new biomaterials to promote neuronal adhesion and neurite outgrowth (Klymov et al., 2015; Li et al., 2015). Wandiyanto et al. (2018) have recently shown that PC12 cells grown on anti-bactericidal titanium nanostructures displayed enhanced proliferation, differentiation and neurite outgrowth compared to non-nanostructured surfaces. Tasnim et al. (2018) recently investigated, using the SH-SY5Y cell line, the biocompatibility of graphene oxide coating for commercially available 316 stainless steel. They showed that graphene oxide coating enables cell adhesion, proliferation and viability, as well as reduces ROS production compared to bare 316 stainless steel. Nissan et al. (2017) also employed SH-SY5Y to investigate the nanotopographical effects of silver nanoline coatings, showing that cells positively respond by increasing neurite outgrowth and branching points compared to unmodified silica wafers.

While immortalized cell lines are a versatile and readily available tool in the early phases of material testing (**Table 1**), these do not have the same biological relevance and response of their primary counterparts or even. Immortalized cell lines display evident phenotypic and physiological differences from the cell type of origin. These differences can be due to the cell source (many times tumor samples), immortalization process, the propagation and differentiation protocols, as well as the culture conditions and medium composition (Kaur and Dufour, 2012; Lorsch et al., 2014). Consequently, despite being from a similar cell type, immortalized cells can display different viability, metabolic and adhesive properties, as well as different expression profiles and cytotoxic responses to materials. In the context of neurophysiological investigations, they can display different electrophysiological responses to stimulations/recordings, thus they are not the best candidates to serve as models to recapitulate the pathophysiology of diseases (Xicoy et al., 2017). Therefore, results obtained with these cells require validation and comparison with more relevant experimental models. Primary cell lines are a more reliable cell type as they do not have a tumor origin or were not manipulated, and, therefore, more closely recapitulate the characteristics of neural cells *in vivo*.

Primary Cell Cultures

Primary cells represent the most used and reliable cell type for *in vitro* studies because they are similar to cells involved in the tissue response *in vivo* (**Table 1**). These cultures are not always the first choice due to experimental constraints, like ethics and economic issues. However, they are an excellent tool to study cell behavior prior to *in vivo* studies. CNS neural primary cells are obtained by dissociation of excised CNS tissue explants and subsequent isolation and plating. For *in vitro* studies, CNS primary cells are most commonly obtained from animal models like rat and mouse, as one has very limited access to human CNS biopsies. With the recent advances in neuronal cell derivation from (human) pluripotent stem cells, neuronal cultures derived from these cell sources are emerging as a powerful tool for *in vitro* modeling (Song et al., 2016; Chen W. et al., 2018).

In vitro primary neuronal cultures are widely employed in microelectrode research for the testing of new surface modified materials with improved biocompatibility and to investigate the

TABLE 1 | Current and novel models explored for the study of biocompatibility of materials for neural applications and assessment of electrochemical performance and durability of implantable microelectrodes.

Model	Specifics	Purpose of the study	References
Immortalized cell cultures	BV-2 mouse microglia cell line	Cellular responses to nanotextured silicon surfaces	Persheyev et al., 2011
	C6 rat astrocytoma cell line	Effect of nanopatterned poly(methyl methacrylate) surfaces on astrocyte reactivity	Ereifej et al., 2013b
	PC-12 rat pheochromocytoma cell line	Biocompatibility of polyurethane/poly(vinyl alcohol) hydrogel coatings	Li et al., 2015
	SH-SY5Y human neuroblastoma cell line	Cytotoxicity of nanostructured Pt-coatings	Boehler et al., 2015
	NIH/3T3 mouse embryonic fibroblast cell line	Cytocompatibility of polyaniline surfaces	Rejmontová et al., 2016
	L929 mouse fibroblast cell line	Cytotoxicity of poly(3,4-ethylenedioxythiophene): glycosaminoglycan (PEDOT:GAG)	Mantione et al., 2016
	NIH/3T3 mouse embryonic fibroblast cell line	Biocompatibility of hydrophilic copolymers	Hadler et al., 2017
Primary cell cultures	Primary microglia	Cellular responses to nanostructured titanium oxide surfaces	De Astis et al., 2013
	Primary rat microglia	Response of microglia to P(TMC-CL)	Pires et al., 2015
	Primary mouse hippocampal neurons	Effects of nanotopography on neuronal cell signaling	Onesto et al., 2017
	Primary rat hippocampal neurons	Biocompatibility of poly(3,4-ethylenedioxythiophene) doped with poly(styrene sulfonate) MEAs	Koutsouras et al., 2017
	Primary human dermal fibroblasts	Study of surface nano-topography and chemistry on collagen I and III production	Bachhuka et al., 2017
	Primary rat cortical neurons	Development of a MEA-based *in vitro* model for drug screening	Bradley et al., 2018
	Primary rat cortical and spinal cord Astrocytes	Response of astrocytes to fiber surface nanotopography	Johnson et al., 2018
2D mixed cell cultures	Primary rat mixed microglia, astrocytes and oligodendrocytes	2D *in vitro* glial scar assay to test biocompatibility of insulating silicone polymer coatings	Achyuta et al., 2010
	Primary rat astrocytes derived from neurospheres and rat embryonic spinal cord cells	2D *in vitro* model of spinal cord injury for drug screening	Boomkamp et al., 2012
	Primary rat mixed neurons, microglia, astrocytes and oligodendrocytes	2D *in vitro* glial scar assay to test cellular responses of dip-coated PEG films	Sommakia et al., 2014
	Rat primary astrocytes and dorsal root ganglia neurons	2D *in vitro* model of spinal cord injury to study isotropic-to-anisotropic cellular transitions	Zuidema et al., 2015
	Primary cortical neurons and astrocytes	Cellular responses to nanoporous gold surfaces	Chapman et al., 2016
3D *in vitro* cultures	Primary rat microglia and astrocytes	Hyaluronic-based hydrogel as a 3D model to test electrode biocompatibility	Jeffery et al., 2014
	Primary mouse mixed neurons, microglia, astrocytes and oligodendrocytes	Alvetex membrane scaffold as a 3D culture for high-throughput screening	Smith et al., 2015
	Primary rat cortical neurons and astrocytes	Alginate-based hydrogel as a 3D model of glial scar	Rocha et al., 2015
	Primary rat mixed neurons, microglia, astrocytes and oligodendrocytes	Type I collagen-based hydrogel as a 3D model of glial scar	Spencer et al., 2017a
	Primary rat mixed microglia, astrocytes and oligodendrocytes	Hyaluronic acid-based hydrogel as a 3D model of glial scar	Koss et al., 2017
	PC-12, C6, human iPSC and rat primary dorsal root ganglia neurons	Type I collagen-based 3D hydrogel for high-throughput study of neurodegeneration	O'Rourke et al., 2017
Organotypic cultures	Rat organotypic hippocampal slices	Biocompatibility of silicon-based electrode arrays	Kristensen et al., 2001

(Continued)

TABLE 1 | Continued

Model	Specifics	Purpose of the study	References
	Rat organotypic brain slices	Biocompatibility of nanopatterned polydimethylsiloxane	Ereifej et al., 2013a
	Mouse organotypic spinal cord slices	Characterization of the ability of 3D meshed-carbon nanotubes to support neurite regrowth	Usmani et al., 2016
	Chicken embryo organotypic brain and liver slices	Cyto-biocompatibility of thin-film transistors	Leclerc et al., 2017
Brain organoids	Human induced pluripotent stem cells (hiPSC) derived organoids	Model of autosomal recessive primary microcephaly	Gabriel and Gopalakrishnan, 2017
	Human embryonic stem cells (hESCs) derived organoids	Testing functionalized borosilicate glass capillaries for glutamate detection	Nasr et al., 2018
	Human primary microvascular endothelial cells, perycites, and astrocytes, mixed iPSC derived oligodendrocytes, microglia and neural stem cells	3D spheroid model of BBB for High-Throughput neurotoxicity screening and disease modeling	Nzou et al., 2018
Microfluidics	hiPSC-derived neurons and astrocytes	High-throughput screening of neurotoxic compounds	Wevers et al., 2016
	Ventral spinal cord motoneurons, rat primary meningeal fibroblasts and astrocytes	*In vitro* model of glial scar	Li et al., 2017
	Pre-differentiated hiPSC lines derived from skin fibroblasts	Brain organoids on chip for the study of impaired neurogenesis induced by cadmium	Yin et al., 2018
In vivo models	Unilateral 6-OHDA injection in adult rats to model nigrostriatal degeneration of Parkinson's disease	Analysis of c-fos expression after DBS of the pedunculopontine tegmental nucleus	Saryyeva et al., 2011
	Unilateral 6-OHDA injection Adult rats to model nigrostriatal degeneration of Parkinson's disease	Analysis of subthalamic nucleus-DBS on behavioral performance	Badstuebner et al., 2017
	Rat model of retinitis pigmentosa	Analysis of a fully organic retinal prosthesis to treat degenerative blindness	Maya-vetencourt et al., 2017
	Induction of status epilepticus through injection of pilocarpine in adult rats	Study of long-term DBS of the anterior thalamic nucleus	Ferreira et al., 2018

BV-2, mouse microglia cell line (CVCL_0182); C6, rat astrocytoma cell line (CVCL_0194); DBS, deep brain stimulation; C-fos, transcription factor subunit (OMIM: 164810); hESCs, human embryonic stem cells; hiPSC, human induced pluripotent stem cells; L929, mouse fibroblast cell line (CVCL_AR58); MEA, multi-electrode array; NIH/3T3, mouse embryonic fibroblast cell line (CVCL_0594); 6-OHDA, 6-hydroxidopamine (5-(2-aminoethyl)benzene-1,2,4-triol); PEDOT:GAG, poly(3,4-ethylenedioxythiophene): glycosaminoglycan; PEG, poly(ethylene glycol); PC-12, rat pheochromocytoma cell line (CVCL_F659); P(TMC-CL), poly(trimethylene carbonate-co-epsilon-caprolactone); SH-SY5Y, human neuroblastoma cell line (CVCL_0019).

effects of surface topographies in the enhancement of neuronal adhesion, neurite outgrowth and electrochemical performance (Chapman et al., 2016; Catt et al., 2017; Seyock et al., 2017; Zöndör and Thoumine, 2017).

The use of single isolated cell types, despite being useful for the investigation of specific biochemical and morphological responses once in contact with a surface, excludes the possibility to study cell interaction with the material in the presence of the glial and neuronal cells crosstalk. A common approach to improve the *in vitro* assays is the use of mixed glial cultures with neuronal cells, obtained in a single isolation procedure, as a strategy to mimic the environmental characteristics and cellular events involved in astrogliosis. The use of mixed glial cells allowed to increase the physiological relevance of *in vitro* testing and to monitor the neuroinflammatory process and microelectrode modifications under manageable and reproducible conditions. Mixed glial and neuronal cultures were used as an efficient *in vitro* glial scar model for the screening of new design coatings for microelectrodes (Achyuta et al., 2010; Sommakia et al., 2014) (see **Table 1** for examples). However, despite useful and cost-effective if compared to *in vivo* studies, primary neural cell cultures also present limitations. The isolation procedures are challenging and require appropriate expertise (Uysal et al., 2018). In addition, primary cell lines do not divide (as in the case on neurons) or do not divide indefinitely as immortalized cell lines, hence the number of cells obtained for each isolation is substantially reduced, limiting the number of experiments and the amount of sample for molecular studies (Gordon et al., 2014). Besides the difficulty in their manipulation, primary neural cells, are isolated in early stages of development, therefore they can result unapt for the study of processes that are only observed in the adult or lead to unaccurate results, as some cellular responses can only be observed in early stages of development. The neural differentiation protocols, including for embryonic stem cells (ESCs) or induced pluripotente stem cells (iPSCs), are also laborious and expensive and can lead to different maturation properties (Verpelli et al., 2013; Engel et al., 2016).

Common to conventional immortalized and primary cell cultures conducted in 2D substrates, is the loss of the ECM composition and structure, cell-ECM and cell-cell interactions (namely, the neuronal network), and cell mechanics of the tissue of origin, which, inevitably, results in a different cell behavior compared to *in vivo* (Tekin et al., 2018). Thus, conventional cell cultures cannot provide detailed information about the interactions of electrode materials with the neural tissue in the initial phases of acute injury or the process of foreign body response in pathological environments. Whence, the necessity of developing complementary models in order to properly study the host reaction to microelectrodes.

3D *in vitro* Cell Cultures

With progress in the field of tissue engineering, one is observing an increase in the number of reports of mixed culture systems conducted in 3D scaffolds (**Table 1**). The use of 3D matrices provides additional dynamics to the application of *in vitro* platforms for glial scar modeling, offering a valid and reproducible system to implement microelectrode research prior to *in vivo* studies. Several types of 3D scaffolds for neural cultures have been developed. These engineered scaffolds can be based on natural or synthetic materials (mostly polymers). These constitute a great improvement for *in vitro* studies in terms of increase in complexity and open the way to a vast window of applications in nervous system modeling (Ko and Frampton, 2016). Jeffery et al. (2014) developed a photocrosslinkable and tunable hyaluronic acid-based hydrogel scaffold for mixed glial cultures and high throughput screening of microelectrode materials. A commercially available synthetic polystyrene scaffold was shown to support neuronal cell growth and differentiation. It has been already tested for the development of a 3D model of neuroinflammation employing embryonic primary cortical neurons that are able to grow, interact and form networks possessing electrical activity in the presence of mixed glial cultures (Smith et al., 2015). We have proposed the use of a alginate-based simple and reproducible astrocyte 3D culture system that mimics many features of astrogliosis (Rocha et al., 2015). Using this platform, we established the ECM mechanical properties as a key modulator of astrogliosis. Spencer and coworkers developed a type-1 collagen gel with mixed primary embryonic neural cultures as an *in vitro* model of glial scar to investigate the effects of micromotion around neural implants (Spencer et al., 2017a). Koss et al. (2017) recently developed a hyaluronic acid-based 3D hydrogel model to study the process of glial scar formation in response to implantable microelectrodes. The biocompatibility of this system allows the encapsulation of primary oligodendrocytes, microglia and astrocytes and has shown to reproduce the typical features of the *in vivo* glial scar process.

The additional advantage of using 3D systems is the possibility to manipulate and tune scaffold composition through the incorporation of different matrix components and bioactive factors to promote cell survival, migration, and differentiation in a 3D context. The objective is to generate 3D structures with mechanical and structural properties as similar as possible to the ones of the CNS tissue (see **Table 1** for examples). Despite the great advances in this field, these systems still present some constraints. Some biomaterials used for scaffold production are characterized by a high modulus compared to the neural tissue and can lead to altered cell viability, proliferation, and differentiation. Conversely, soft biomaterials are more difficult to handle. The design of matrices with a nanosized microstructure and topographical cues that fully mimic the one found in the nervous tissue was still not attained. The procedures of cell extraction for molecular analysis after testing, scaffold processing, and imaging become more challenging in 3D, limiting high-throughput studies. Additional complications are related to the cell culture conditions: 3D scaffolds can constitute a physical barrier that limits oxygen perfusion, nutrient supply and accumulation of toxic compounds that can cause cellular alterations or apoptosis. Optimizations are still required to ensure a versatile cell encapsulation for different cell types and controlled culture conditions as close as possible to the *in vivo* environment. This is even more challenging in the context of disease modeling, where cells must be induced to display specific pathological profiles.

It is expectable in the future that the continuous progresses attained in the tissue engineering field, particularly related to improved scaffolds/matrices development, will allow the development of better *in vitro* systems that recapitulate neural tissue architecture, in an effort to minimize the gap between *in vitro* and *in vivo* experiments.

Ex vivo Models

The development of 3D *in vitro* models of brain tissue, as stated above, represents an attractive tool for researchers working in the neurosciences field and their use in microelectrode research would have a great impact on the screening of new biomaterials for biomedical applications. However, additional optimizations are still required to allow a consistent application in neuroscientific research. A potential alternative that enables researchers to get closer to *in vivo* conditions is the use of *ex vivo* excised brain/spinal cord tissues.

Organotypic Cultures

Tissue explants can be extracted from euthanized animals or obtained from human biopsies and cultured *in vitro*. The great advantage of organotypic cultures compared to artificial *in vitro* systems is the preservation of the native cytoarchitecture with the maintenance of intact neuronal networks. Although several types of *ex vivo* models have been described in literature (Mii et al., 2013; Nery et al., 2015; Jones et al., 2016; Neville et al., 2018), brain slice cultures from rodents are the most established and widely used as a system of election for neurophysiological investigations, neuropharmacology and as a model of disease. The procedure consists in the isolation of specific districts from the whole brain, their dissection in slices and incubation under controlled conditions. The possibility to obtain several slices from a single animal constitutes an additional advantage in terms of reduction of the number of animals for experiment and of related costs.

Brain slice cultures have been well established from different brain regions (**Table 2**). Two types of brain slices preparations exist: acute slices from the adult brain, with a short life and

TABLE 2 | Organotypic cultures as a model of neurological and neurodegenerative diseases.

Disease	Type of organotypic slice	Induction of disease	References
Parkinson's disease	Parasagittal nigrostriatal slices	Slices incubation with 6-hydroxydopamine (6-OHDA)	Kearns et al., 2006
	Organotypic midbrain slices	Transfection with truncatedα-synuclein (A53T)	Zach et al., 2007
	Nigrostriatal organotypic slices	Mechanical cutting of dopaminergic fibers from substantia nigra to striatum	Cavaliere et al., 2010
	Ventral mesencephalon organotypic slices	Unilateral microinjection of 6-hydroxydopamine (6-OHDA)	Stahl et al., 2011
	Sagittal nigrostriatal slices	mechanical transection of the medial forebrain bundle	Daviaud et al., 2014
	Coronal nigrostriatal slices	Injection of rotenone	Ullrich and Humpel, 2009
	Cerebellar nigrostriatal slices	Slices incubation with 1-methyl-4-phenylpyridinium (MPP+)	Chong et al., 2015
Epilepsy	Organotypic hippocampal slices	Slices incubation with Kainic acid	Järvelä et al., 2011; Jung et al., 2013
	Organotypic hippocampal slices	Slices incubation with kainic acid or n-methyl di-aspartate	Prasad Tripathi and Ayyannan, 2017
	Organotypic hippocampal slices	Slices incubation in a Neurobasal/B27 serum-free medium	Magalhães et al., 2018
Alzheimer disease	Organotypic hippocampal slices	P301S Alzheimer disease mouse model	Mewes et al., 2012
	Organotypic coronal brain slices	Co-transfection with amyloid precursor protein cDNA or human tau4R0N cDNA	Van Kanegan et al., 2016
	Organotypic hippocampal slices	APPsdl mouse model	Penazzi et al., 2017
	Organotypic hippocampal slices	3xTg-AD mouse model	Croft and Noble, 2018; Jang et al., 2018
Traumatic brain injury	Organotypic hippocampal slices	Focal mechanical trauma at the CA1 region	Schoeler et al., 2012; Krings et al., 2016
	Organotypic hippocampal slices	Tissue deformation by mechanical stretching	Choo et al., 2013; Lamprecht et al., 2017
Stroke	Organotypic coronal brain slices	Exposure to oxygen glucose deprivation	Wang et al., 2006;
	Organotypic hippocampal slices	Exposure to oxygen glucose deprivation	Hall et al., 2009
Spinal cord injury	Organotypic spinal cord slices	Exposure to hypoxic condition	Kim H.M. et al., 2010
	Organotypic spinal cord slices	Slices incubation with kainic acid	Mazzone and Nistri, 2014
	Organotypic spinal cord slices	Mechanical damage using weight drop model of injury	Labombarda et al., 2013; Pandamooz et al., 2019

APPsdl, amyloid precursor protein gene mutation; A53T, point mutation human α-synuclein protein; CA1, "Cornu Ammonis" 1 hippocampal region; MPP+, (1-Methyl-4-phenylpyridin-1-ium); 6-OHDA, 6-hydroxidopamine [5-(2-aminoethyl)benzene-1,2,4-triol]; P301S, microtubule associated protein Tau (OMIM 157140 genetic mutation); tau4R0N, human microtubule associated protein tau, transcript variant 3, mRNA; 3xTg-AD, transgenic Alzheimer disease mouse model.

mainly used for electrophysiological recordings, and organotypic slices from neonatal animals. The latter are the most diffused *ex vivo* platforms for the study of many physiological and pathological conditions, thanks to the possibility to reproduce, by external intervention, the hallmarks of diseases that occur *in vivo* (Magalhães et al., 2018). The great success of this system is due to the simplicity of the procedure and manipulation by mechanical or pharmacological treatment, as well as the possibility to perform electrophysiological recordings on bioelectric activity. Based on these features, organotypic cultures can constitute an ideal model for the long-term assessment of the complex host reaction to microelectrodes or for high-throughput biocompatibility studies of new materials and surfaces. Nevertheless, few works can be found in the open literature (Kristensen et al., 2001; Huuskonen et al., 2005; Ereifej et al., 2013a; Usmani et al., 2016; Leclerc et al., 2017). A possible explanation for this fact could be related to the preferential use of *in vivo* models as the gold standard for microelectrode testing. Although necessary for the translation of new materials to the clinic, *in vivo* experiments have ethical issues, they are expensive, time-consuming and unapt for screening studies due to their complexity. The great advances achieved by *in vitro*/*ex vivo* systems can be the successful strategy to accelerate microelectrode research prior to *in vivo* testing. The controllable and reproducible conditions make them suitable to identify strategies to mitigate neuroinflammation, to prevent the early biochemical and corrosion-related events at the interface electrode-neural tissue and to impair foreign body response. Nevertheless, although organotypic cultures maintain the 3D cytoarchitecture, slice preparation causes an unavoidable axotomy of the brain tissue and neuronal death. This physical damage is accompanied by loss of blood flow, and consequently jeopardize oxygen perfusion and nutrient supply. As occurs in primary neural cultures, organotypic cultures are derived from animals in early stages of development and require extensive periods of culture for their maturation

for use in post-developmental studies and assessment of pathophysiological processes. Another important caveat is the lack of the BBB and circulating immune cells. In the context of testing materials for neural devices, we previously showed that these factors play a crucial role in the process of foreign body response. BBB dysfunction and cell infiltration are also associated with several neuropathological processes. This can limit the physiological relevance of organotypic cultures for disease modeling (Humpel, 2016). Hence, researchers are developing innovative approaches combining microfluidic technologies with cellular vascular structures to mimic BBB microarchitecture and improve culture conditions for long term studies (Xu et al., 2016). These authors proposed a new and dynamic in vivo-like three-dimensional microfluidic system to replicate the BBB *in vivo*. Despite these limitations, organotypic cultures are still one of the most relevant models and can represent a fascinating tool to reduce the differences between *in vitro* and *in vivo* studies (some examples are present in **Tables 1**, **2**).

Finally, as a duty of each and every scientist, the use of *in vitro*/*ex vivo* models must be encouraged in order to improve the ethical acceptability of research in the fulfillment of the principles of Replacement, Reduction, and Refinement (3R's) (Lossi and Merighi, 2018).

In vivo Models

Different types of *in vivo* studies have been carried out in microelectrode research to evaluate therapeutic efficacy, durability and safety of microelectrodes. In this type of studies rats and mice are the most common model of choice. The animal disease models that are used to assess the efficacy of neurostimulation therapies are several (**Table 1**). The main categories are represented by animal models of neurodegenerative disease such as Parkinson's disease (Badstuebner et al., 2017; Musacchio et al., 2017), Alzheimer's disease (Leplus et al., 2018), epilepsy (Desai et al., 2016), sensory-motor deficits due to spinal cord injury (Capogrosso et al., 2018), blindness (Tang et al., 2018), hearing loss conditions (Allitt et al., 2016) and ischemic models (Yang et al., 2017). Large animals such as cats, dogs, sheep, pigs, and non-human primates, are used for chronic studies on the efficacy and safety of neural stimulators. They concern the analysis of both biotic and abiotic reactions on the tissue-electrode interface in long-term experiments (Shepherd et al., 2018). The employment of large animals for these types of investigations is recommended because their anatomy perfectly mimics the environment in which microelectrodes will be applied, allowing the use of all the device components in their real size. Moreover, the full inflammatory component is present *in vivo* as opposed to *in vitro*/*ex vivo* models. The surgical procedure in *in vivo* experiments generally consists in the exposition of the skull in a deeply anesthetized animal, the production of one or more drills in the vicinity of the target region, the insertion of the neural implant in a specific site and fixation of the plugs with dental cement, followed by continuous monitoring to assess the recovery of the animal, integrity of device and/or efficacy of the therapy (Fluri et al., 2015). Besides the damage caused by electrode implantation, the majority of *in vivo* experiments are carried out by tethering the animal to an external component through cables, causing severe discomfort. To overcome this, new wireless microstimulation technologies were developed to ensure better freedom of movement, allowing the reduction of distress (Fluri et al., 2017; Pinnell et al., 2018). Besides the use of animal models of disease, chimeric mice models have found great utility for answering important biological questions concerning the role of different cell types in the process of foreign body response. Chimeras are animal models with two or more different genotypes experimentally obtained by transplanting cells or organs from another organism. Bone marrow chimeric mice were employed to investigate the contributions of different cells in the mechanism of foreign body response (Ravikumar et al., 2014). Sawyer et al. (2014) generated chimera mice between wild type and MCP-1 knock out mice, assessed the key-role of MCP-1 in the enhancement of neuronal loss and showed that its inhibition can be an effective strategy to prolong the lifetime of implantable microelectrodes. Bedell and co-workers recently developed chimeric mice lacking cluster of differentiation 14 (CD-14) genes in myelinating cells and blood-derived macrophages. They demonstrated that targeting CD-14 in blood-derived macrophages improved microelectrode performance in long term experiments (Bedell et al., 2018a). Genetically engineered animal models are another successful tool in microelectrode research. Mice lacking specific genes involved in neuroinflammation and immunity were employed to investigate the biochemical pathways involved in the foreign body response, the identification of pharmacological targets (Kozai et al., 2014; Bedell et al., 2018b; Hermann et al., 2018a,b) and material testing (Lee et al., 2017). Mice carrying cell specific fluorescent tags have been shown to provide great advantages in the study of the contribution of different cells in a single animal as well as a valuable alternative to immunostaining steps (Sunshine et al., 2018; Eles et al., 2019). Gaire and colleagues recently developed a quadruple-labeled mouse with specific fluorescent tags for oligodendrocytes, microglia, neurons, and astrocytes and investigate the process of nervous tissue response to "Michigan" array silicon microelectrodes (Gaire et al., 2018b).

Substantial improvements have been implemented in the quality and quantity of *in vivo* investigations: new bio-imaging tools were applied in microelectrode research to make *in vivo* works more explanatory. Two-photon laser scanning microscopy allows imaging of living animals with elevated resolution. It has been used to investigate the nervous tissue response to new electrode coatings (Eles et al., 2017), glial cells characterization (Wellman and Kozai, 2018) or live calcium imaging (Kondo et al., 2017). Optical coherence tomography is a minimally invasive technique that has been proposed to be used in combination with two-photon laser scanning microscopy to provide high resolution angiography of damaged tissues around microelectrodes (Hammer et al., 2016). As an alternative to laborious histological and staining procedures on sectioned brains, x-ray micro CT scanning has been proposed as a high-resolution, time and cost saving procedure that allows a 3D x-ray scanning of the entire brain to quantify and characterize the lesions caused by electrode implantation (Masís et al., 2018).

The growing scientific interest in neural interfaces in the last decades is confirmed by the multitude of *in vivo* works focused on the testing of new and fully biocompatible coatings (Du et al., 2017; Spencer et al., 2017b; Shen et al., 2018; Vitale et al., 2018), less invasive implantation strategies (Tawakol et al., 2016; Shoffstall et al., 2018b) and new designs with improved electrical performance (Ferlauto et al., 2018; Xu et al., 2018) and with longer durability.

Despite being considered the ultimate model to test microelectrode prior clinical tests, *in vivo* models present some important drawbacks as previously mentioned. An important aspect to consider is the elevated costs and time required for animal experiments, as well as the resulting ethical constraints. *In vivo* experiments are complex and demand adequate facilities and technical expertise. As discussed above, transgenic mice offer great advantages, however, they have an extremely high cost due to their production and maintenance. More importantly, the effects of such modifications can lead to altered phenotypes that depart from the real scenario. In the context of device testing, *in vivo* experiments are quite laborious and require long periods of time to assess the long-term performance of microelectrodes or the biological and behavioral effects of specific neurostimulation therapies. The complexity and invasiveness of the experimental techniques do not always enable scientists to identify the early biochemical and material-related events at the interface electrode-neural tissue and the strategies to mitigate neuroinflammation.

Despite these weaknesses, *in vivo* studies constitute the gold-standard for the investigations on neural implants, where the results obtained by previous *in vitro* testing find their effective validation. They represent the final step in the long process of microelectrode design and testing before the application in the clinic. A rigorous progression along all the steps determines the success of new technologies. This is even more important in the case of new materials or designs, where a careful preclinical assessment is necessary to minimize the risk of failure once applied to human patients.

FUTURE PERSPECTIVES

Increasing Complexity

Preclinical studies are paramount in the development and testing of new materials for neural implants. As a consequence, the demand for more reliable *in vitro*/*ex vivo* models is growing to satisfy the need for assessing of the increasing number of new materials being proposed for this application, improve the quality of device testing and reduce the time between prototyping and commercialization of new products. As discussed in the previous section, several *in vitro* models and new platforms have been described in the literature (**Table 1**), but they still need to be explored, tested and eventually adapted for microelectrode research.

The use of *ex vivo* platforms from tissue explants can represent a valuable solution that fits perfectly these purposes. Brain organotypic cultures have been widely used in the last years as an excellent model for a great number of applications. They were employed to study physiological (Svensson and Chen, 2018), and pathological conditions (Tan et al., 2017) or for the screening of new therapeutics (Minami et al., 2017). Furthermore, several organotypic cultures have been established as models of neurological and neurodegenerative diseases (**Table 2**), for which neural implants have been proposed as therapeutic strategies. This places organotypic models that mimic a pathological environment in a privileged position to serve as platforms for microelectrode testing and a potential strategy to move closer to the *in vivo* scenario. Moreover, thanks to the preservation of intact neural circuitry, organotypic cultures are particularly suitable to perform electrophysiological studies, analyze microelectrode performance and assess astrogliosis.

Developments in the stem cell biology field have also contributed to the establishment of new *in vitro* models of human disease, aiming at an increase of complexity to reach the relevance of the *in vivo* environment, while maintaining the controllability and manageability of *in vitro* systems. Organoids, self-organized 3D tissue cultures derived from stem cells, are currently leading these technologies and have already been developed for the majority of human tissues, including the brain. More recently, the advances in hiPSC reprogramming techniques are also contributing to a better performance of organoid platforms in mimicking human disease and serve as testing platforms for personalized medicine (Perkhofer et al., 2018). Lancaster and Knoblich (2014) the preparation of cerebral organoids prepared from hiPSC. The described methodology allows cell aggregates cultured in Matrigel to mimic native brain tissue, originating different developing brain regions, namely, cerebral cortex, ventral telencephalon and retinal, among others, within 1 to 2 months. iPSC derived organoids represent an innovation in the field of *in vitro* disease modeling, offering a great opportunity to investigate pathophysiological mechanisms of neurological diseases with elevated reliability (Ho et al., 2018; LaMarca et al., 2018; Sun et al., 2018) and can also contribute to the field of implantable microelectrodes. In fact, Ormel et al. (2018) demonstrated that organoids can innately develop microglia and have a response to inflammatory stimuli that recapitulates neurons-glia interactions *in vivo*. This is an important aspect since glial cells, particularly microglia, are involved in a great variety of pathophysiological mechanisms.

Great advances *in vitro* modeling have been also achieved thanks to the application of microfluidics combined with 3D *in vitro* cultures (Rocha et al., 2016). Microfluidic platforms consist of polymer-based platforms for *in vitro* culture of cells that allow control and manipulation of microenvironment and fluids (see **Figure 3** for relevant examples). The use of these microdevices brings *in vitro* models to a whole new level, thanks to the possibility of modifying spatial organization by isolating specific districts and simulate 3D tissue architecture of the native tissue. These systems allow the continuous control of external conditions, conferring an added value to *in vitro* technology, and giving the possibility to reproduce new biological features that are not possible to achieve with conventional culture systems (as discussed in section "Organotypic Cultures" for the case of the BBB). Wang and colleagues developed an

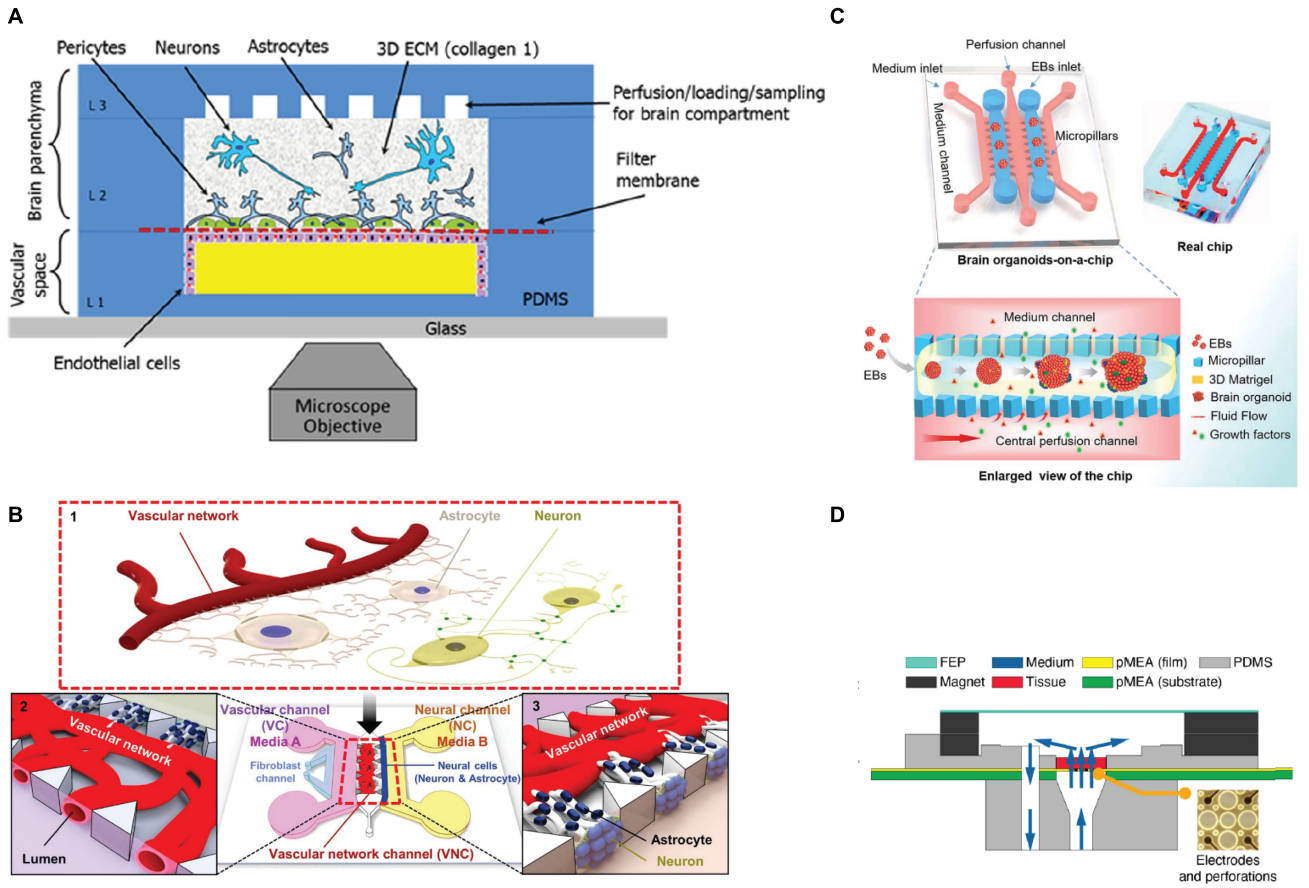

FIGURE 3 | Schematic representations of 3D microfluidic systems. **(A)** Schematic view of a microfluidic device for 3D cell culture composed by a vascular channel (VC) for primary human brain-derived microvascular endothelial cells (hBMVEC), and a brain chamber for primary cell-derived human neurons, pericytes and astrocytes culture in a type I collagen matrix. Reprinted from Brown et al. (2015) with the permission of AIF publishing. **(B)** 3D microfluidic platform for the establishment of a neurovascular unit (NVU) including blood-brain barrier (BBB). The NVU is characterized by a VC composed by a co-culture of HUVEC and Primary human lung fibroblasts, and a secondary NC composed by a co-culture of neurons and astrocytes. Adapted with permission from Bang et al. (2017). **(C)** Organ-on-a-chip device for 3D culture and differentiation of brain organoids, showing an enlarged view of the component parts and a flow chart showing the development stages of hiPSCs-derived brain organoids (Wang Y. et al., 2018) published by the Royal Society of Chemistry. **(D)** Vertical cross-section view of a perforating multi-electrode array (MEA) integrated in a PDMS device for long-term culture, live imaging, recording and stimulation of brain tissues and 3D cultures (Killian et al., 2016).

organ-on-a-chip system for long-term culture of brain organoids under controlled conditions. Brain organoids were cultured on Matrigel scaffolds with a sided channel for the culture medium supply and a central perfusion channel, allowing a continuous culture medium flow and providing an improved proliferation and neural differentiation compared to static culture conditions (Wang Y. et al., 2018). Liu et al. (2018) combined multielectrode array technology with a microfluidic perfusion system for organotypic hippocampal slices as a platform for high throughput drug discovery. Microfluidic vascular models have been developed and applied to brain-on-a-chip platforms, enabling scientists to improve the quality of culture conditions and get even more close to *in vivo* dynamics (Osaki et al., 2018; Wang, 2018). New microfluidic devices that model the BBB were fabricated and tested on 2D and 3D cultures, showing that BBB integrity and permeability simulates *in vivo* characteristics (Chin and Goh, 2018). Adriani et al. (2017) developed a 3D neurovascular chip composed by a central hydrogel co-culture of rat primary neurons and astrocytes, and two lateral channels hosting human umbilical vein endothelial cells and human cerebral microvascular endothelial cells. Bang et al. (2017) developed a 3D microfluidic BBB platform with a vascular channel (VC) composed by a co-culture of human umbilical vein endothelial cells and primary human lung fibroblasts directly interfacing with a neural channel (NC) composed by a co-culture of primary rat neurons and astrocytes to simulate the neurovascular unit. They showed that this platform displayed permeability, cellular contacts and synaptic structures comparable to the *in vivo* BBB, suggesting its great potential for the drug screening for neurological diseases. Microfluidic technology can conduct *in vitro* culture system to a more complex and realistic level providing many advantages and details that cannot be extracted with conventional *in vivo* models, such as the easy manipulation, low cost, and the

possibility to investigate more intimately key mechanisms of diseases. These characteristics perfectly fit with ideal biological platforms for the testing of microelectrode materials developed in the last decades. 3D microfluidic systems can eliminate some of the limitations of 3D *in vitro* technology, creating new high-fidelity throughput systems that can improve the testing performance and reduce the cost and time for pre-clinical assessment. An additional advantage is the possibility to induce specific pathological features by external treatment for long-term experiments, offering the possibility to investigate in advance microelectrode performance and nervous tissue response under disease conditions.

Design Solutions and New Materials for the Improvement of Microelectrode Durability and Biocompatibility

Despite remarkable developments in implantable microelectrodes for neuroprosthetics and DBS, additional investigations are still required to address the biocompatibility

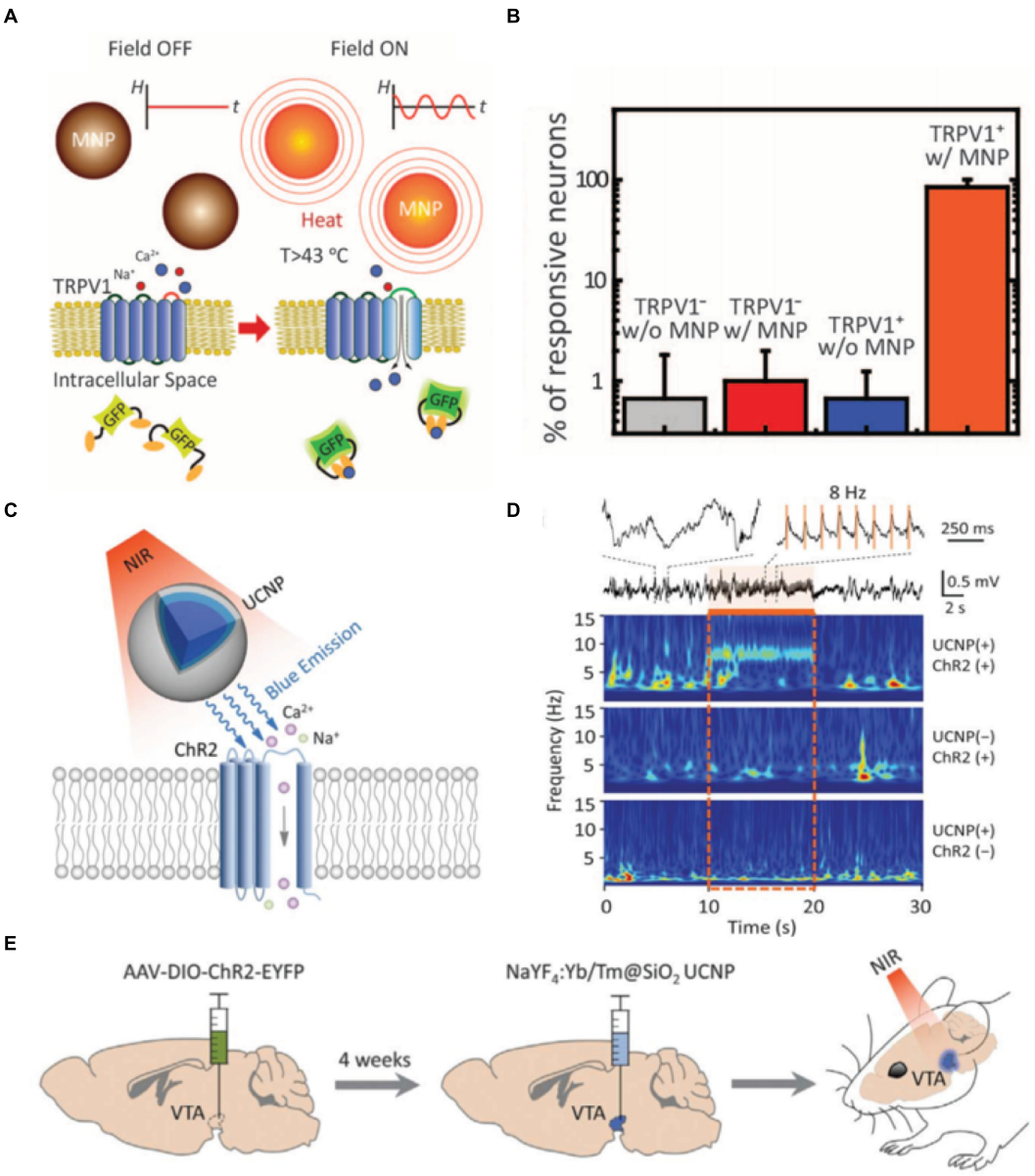

FIGURE 4 | New strategies for deep brain stimulation using functional nanoparticles. **(A)** A schematic description of magnetothermal effect on transient receptor potential cation channel subfamily V member 1 (TRPV1) cells. **(B)** Comparison of the neuron reactivity under different conditions. Figures from Chen et al. (2015), reprinted with permission from AAAS. **(C)** A schematic description of nanoparticle-mediated near infrared (NIR) upconversion optogenetics. **(D)** Hippocampal local field potential response under NIR stimulation under different conditions. **(E)** *In vivo* experimental description of NIR stimulation of the ventral tegmental area of mice. Figures from Chen S. et al. (2018), reprinted with permission from AAAS.

and the long-term durability issues. A critical issue is reducing the physical stress, local inflammation and electrode degradation caused by the reaction between electrode and tissue interface while maintaining the electrical sensitivity of the electrode (Prodanov and Delbeke, 2016). To tackle these issues, multiple material-based strategies regarding this problem have been suggested, including (i) chemical modification of the electrode materials, (ii) new design of electrode structures, and (iii) non-invasive and wireless approach using functional nanoparticles.

Biological and non-biological electrode modifications, especially through the surface coating of substrates and electrode sites, are the most commonly used strategies to improve interfacial mechanical mismatch (Aregueta-Robles et al., 2014). Advances in fabrication approaches for integrating conductive polymers (Kim et al., 2018), shape-memory polymers (Shoffstall et al., 2018a), hydrogels (Crompton et al., 2007; Frampton et al., 2007) and carbon nanotubes (Baranauskas et al., 2011; Bareket-Keren and Hanein, 2012) onto complex electrode structures, provide not only a chronically stable neural interface, but also an improvement in the electrode performance. The reduced surface area combined with low impedance and sensitivity provided by such materials make them suitable for either stimulation and recording applications (Vitale et al., 2015; Du et al., 2017; Pancrazio et al., 2017; Wang et al., 2019).

The additional advantage is that the bioactive molecules can be attached to the coating surfaces to increase stimulating/recording sensitivity. Employing composite materials for electrodes and coatings has also emerged as a promising strategy for upgrading electrode functionalities and biocompatibility. Heo et al. (2016) have reported improved biocompatibility in polyimide-based microelectrodes by coating them with PEG hydrogels containing Poly lactic-glycol acid (PGLA) microspheres loaded with the anti-inflammatory drug. On the other hand, Zhou et al. (2013) proposed a carbon nanotube doped PEDOT composite coating material onto the Pt electrode. They showed that this coating makes the electrode more stable with enhanced charge transfer capacity and tissue-electrode interaction. While chemical modification of materials is still being suggested as an efficient way of protecting both electrode and brain tissue, the long-term stability issue caused by the degradation and delamination of coating materials still remains as the challenge that needs to be overcome (Green et al., 2008).

Another attempt to reduce the immune response while enhancing functionality is to introduce new microelectrode designs. The development of the fabrication techniques of soft materials has enabled the production of ultrasoft and ultrathin electrodes with complex designs that minimize the mechanical mismatch of the electrode-tissue interface (Weltman et al., 2016). Recently, Kim et al. have fabricated ultrathin polyimide-based polymer electrodes covered by bioresorbable silk film. They successfully demonstrated the integration of the ultrathin electrodes with a complex structure by allowing the silk to be dissolved and resorbed. This procedure encouraged the spontaneous wrapping process driven by the capillary effect at the material-tissue interface, generating greatly improved biocompatibility (Kim D.H. et al., 2010). Carbon nanotube-based soft fiber microelectrodes have also proved to have low impedance and effective therapeutic stimulation along with single-neuronal-unit signal detectable resolution, owing to their high surface area and electrical conductivity (Vitale et al., 2015). Compared to the similar dimension and surface environment, ultra-soft and ultra-thin electrodes have a great potential to significantly reduce inflammatory tissue response in the long-term scale (Du et al., 2017). However, as mentioned earlier, the balance between flexibility/softness and the electrical performance should be carefully considered when designing these type of electrodes (Wellman et al., 2018b). Implementing functional nanoparticles are attracting increasing attention as a non-invasive and remotely controllable method. Chen et al. (2015) succeeded in utilizing the magnetothermal effect of nanoparticles for DBS (**Figures 4A,B**). They injected Fe_3O_4 magnetic nanoparticles in the ventral tegmental area of mice and exposed them to the external magnetic field. When magnetic nanoparticles are exposed to the AC magnetic field, stimulation of neurons at the targeted brain region was triggered by the dissipated heat from the magnetothermal effect. Wireless neural stimulation was successfully performed 1 month after injection. Moreover, lower glial activation, less macrophage accumulation and neuronal loss have been reported compared to a stainless steel implant. Chen S. et al. (2018) recently proposed optogenetic treatment by shining near infrared light to molecular tailored upconversion nanoparticles (**Figures 4C–E**). They injected nanoparticles into the ventral tegmental area of the brain to stimulate deep neurons and successfully demonstrated that light treatment on upconversion nanoparticles can induce dopamine release from dopaminergic neurons, activation of inhibitory neurons, inhibition of hippocampal excitatory cells, and memory recall. Magnetoelectric nanoparticles are another great candidate for neural stimulation. It has been already proven that the piezoelectric materials can generate electric signals under the acoustic wave and can induce neural cell differentiation (Chen et al., 2019). As ferromagnetism and ferroelectricity are coupled to each other, applied external magnetic field can induce variation in electric polarization of nanoparticles, causing a change of the electronic structure at the particle surface and therefore facilitating stimulation of the tissue deep inside the brain (Kargol et al., 2012; Guduru et al., 2015). As a non-invasive stimulating method, implementing magnetoelectric material is attracting significant attention. While these approaches using nanoparticles have great potential, biocompatibility and cellular uptake of these functional particles still remain as a problem to be solved (Adjei et al., 2014; Behzadi et al., 2017).

CONCLUDING REMARKS

The field of the brain-machine interface is exponentially growing and comprises an important source of progress in many aspects of neurosciences. The application of bionic systems, neural prosthetics and neurostimulation for restoring/treating severe neuro-debilitating conditions and neurological diseases has attracted the interest of many researchers and clinicians. All these technologies require the use of implantable microelectrodes

to interface with the CNS. They represent an essential tool that serves as a link between the electronic components and the neuronal networks, in order to ensure a stable electrochemical communication over time. Great success has been achieved by the clinical application of neural prosthetics in the improvement of the quality of life of patients that suffer from sensory-motor deficits. DBS has become a treatment of choice for movement disorders and neuropsychiatric diseases and is proving to be a relevant alternative for a multitude of other pathological conditions.

The recent progress in microfabrication techniques made possible the development of microelectrodes capable of simultaneous recording and stimulation with improved cell selectivity and spatial resolution. Despite the improvements in device fabrication, biocompatibility and electrochemical performance for long-term applications, unfavorable nervous tissue response and microelectrode failure are still significant limitations. The process of nervous tissue response to microelectrodes has been described by an acute and chronic phase. The acute phase represents the most critical step characterized by a series of pathological reactions triggered by BBB dysfunction and glial activation. The persistence of this neuroinflammation is responsible for the immune response and the formation of the glial scar in the chronic phase, which may lead to microelectrode failure. A better understanding of the signaling pathways involved in the acute and chronic responses is required in order to develop new design strategies to mitigate neuroinflammation and promote a successful integration. Several surface modified microelectrodes have been designed to provide minimal damage and establish a minimally reactive interaction with the brain tissue. However, additional studies are necessary to comprehend some of the key-cellular mechanisms implicated in the process of the glial scar formation around microelectrodes that remain to be elucidated. An important aspect in which research must be focused on is the binary role of the glial scar: several studies report a neuroprotective function of the glial scar in many pathological conditions, and its modulation has been suggested as a therapeutic approach to improve neuronal recovery and tissue regeneration. In the case of chronically implanted microelectrodes, the participation of the various glial subtypes to the nervous tissue response and how their activation states can be influenced to soften tissue damage and avoid rejection are still unclear aspects. Toward this end, the use of appropriate experimental models can provide significant advantages in the development and testing of biocompatible and durable neural devices.

In this review, we provide an overview of the current and potential experimental *in vitro*, *ex vivo*, and *in vivo* models to investigate the mechanisms of foreign body response to implantable microelectrodes. The progress in 3D tissue engineering and disease modeling opened the way toward the development of *in vitro* biological platforms with increased complexity and physiological relevance to be used for high-throughput studies before moving to *in vivo* animals. Organotypic culture systems are widely established *ex vivo* platforms which offer the possibility to simulate several pathological conditions and to isolate specific cerebral regions, ensuring the preservation of tissue architecture and synaptic organization for electrophysiological studies. While the use of organotypic culture systems as screening platforms for novel microelectrodes is still limited, their application is expected to grow in the near future, not only for the reasons mentioned earlier but also because these systems can contribute to significantly minimize the use of animal models. Additional implementations have been also achieved *in vivo* studies. Despite being considered the gold-standard for microelectrode safety and efficacy studies, the principal limitation of *in vivo* experiments is the difficulty to monitor tissue response in the initial phases of injury. New advanced neuroimaging techniques open a new window of opportunities to improve the relevance of *in vivo* assessment thanks to the possibility to study biochemical processes, cell behavior and structural modifications in real time with elevated resolution. The advent of iPSC technology has enabled to simulate more closely the pathophysiological cues that occur in human diseases, offering the relevant advantage to recapitulate molecular and biological characteristics of the human brain. Success is also being achieved by the use of microfluidic systems combined with 3D cell cultures and/or iPSC-derived organoids, which allowed for integrating mechanical and physiological dynamics to simulate organ-like functions and responses. They represent a cost-effective compromise between the versatility of *in vitro* models and physiological relevance of *in vivo* models, offering the possibility to model pathophysiological cues under simulated conditions.

In conclusion, researchers have now a great variety of relevant models that can be adopted to improve microelectrode research in all the phases of development and to address the scientific unknowns related to the nervous tissue response to microelectrodes. Ultimately, with further improvements of these *in vitro* models, one can expect the creation of optimal milieus, which can substantially replace animal experimentation for large scale studies.

AUTHOR CONTRIBUTIONS

All authors listed have made a substantial, direct and intellectual contribution to the work, and approved it for publication.

FUNDING

This work was financially supported by the Projects NORTE-01-0145-FEDER-000008 and NORTE-01-0145-FEDER-000012, supported by the Norte Portugal Regional Operational Programme (NORTE 2020), under the PORTUGAL 2020 Partnership Agreement, through the European Regional Development Fund (ERDF) and FEDER - Fundo Europeu de Desenvolvimento Regional funds through the COMPETE 2020 – Operacional Programme for Competitiveness and Internationalisation (POCI), Portugal 2020, and by Portuguese funds through FCT/MCTES in the framework of the project "Institute for Research and Innovation in Health Sciences" (POCI-01-0145-FEDER-007274).

ACKNOWLEDGMENTS

SP acknowledges funding from a Consolidator Grant from the European Research Council (ERC) under the European Union's Horizon 2020 Research and Innovation Programme (Grant Agreement No. 771565). MG and DK acknowledge their Ph.D. grants in the framework of the project mCBEEs funded by the European Union's Horizon 2020 Research and Innovation Programme under the Marie Skłodowska-Curie grant agreement No. 764977. SS would like to acknowledge national funds through the FCT – Fundação para a Ciência e a Tecnologia, I.P., provided by the contract program and according to numbers 4, 5, and 6 of art. 23 of Law No. 57/2016 of 29th August, as amended by Law No. 57/2017 of 19th July. AP and SP would like to acknowledge the contribution of the COST Action CA16122.

REFERENCES

Achyuta, A. K. H., Polikov, V. S., White, A. J., Pryce Lewis, H. G., and Murthy, S. K. (2010). Biocompatibility assessment of insulating silicone polymer coatings using an in vitro glial scar assay. *Macromol. Biosci.* 10, 872–880. doi: 10.1002/mabi.200900451

Adjei, I., Sharma, B., and Labhasetwar, V. (2014). Nanoparticles: cellular uptake and cytotoxicity. *Adv. Exp. Med. Biol.* 811, 73–91. doi: 10.1007/978-94-017-8739-0_5

Adriani, G., Ma, D., Pavesi, A., Kamm, R. D., and Goh, E. L. K. (2017). A 3D neurovascular microfluidic model consisting of neurons, astrocytes and cerebral endothelial cells as a blood–brain barrier. *Lab Chip* 17, 448–459. doi: 10.1039/c6lc00638h

Allitt, B. J., Harris, A. R., Morgan, S. J., Clark, G. M., and Paolini, A. G. (2016). Thin-film micro-electrode stimulation of the cochlea in rats exposed to aminoglycoside induced hearing loss. *Hear. Res.* 331, 13–26. doi: 10.1016/j.heares.2015.10.003

Antensteiner, M., and Abidian, M. R. (2017). Tunable nanostructured conducting polymers for neural interface applications. *Conf. Proc. IEEE Eng. Med. Biol. Soc.* 2017, 1881–1884. doi: 10.1109/EMBC.2017.8037214.Tunable

Aregueta-Robles, U. A., Woolley, A. J., Poole-Warren, L. A., Lovell, N. H., and Green, R. A. (2014). Organic electrode coatings for next-generation neural interfaces. *Front. Neuroeng.* 7:15. doi: 10.3389/fneng.2014.00015

Bachhuka, A., Hayball, J. D., Smith, L. E., and Vasilev, K. (2017). The interplay between surface nanotopography and chemistry modulates collagen I and III deposition by human dermal fibroblasts. *ACS Appl. Mater. Interfaces* 9, 5874–5884. doi: 10.1021/acsami.6b15932

Badstuebner, K., Gimsa, U., Weber, I., Tuchscherer, A., and Gimsa, J. (2017). Deep brain stimulation of hemiparkinsonian rats with unipolar and bipolar electrodes for up to 6 weeks: behavioral testing of freely moving animals. *Parkinsons Dis.* 2017:5693589. doi: 10.1155/2017/5693589

Bang, S., Lee, S., Ko, J., Son, K., and Tahk, D. (2017). A low permeability microfluidic blood-brain barrier platform with direct contact between perfusable vascular network and astrocytes. *Sci. Rep.* 7:8083. doi: 10.1038/s41598-017-07416-0

Baranauskas, G., Maggiolini, E., Castagnola, E., Ansaldo, A., Mazzoni, A., Angotzi, G. N., et al. (2011). Carbon nanotube composite coating of neural microelectrodes preferentially improves the multiunit signal-to-noise ratio. *J. Neural Eng.* 8:066013. doi: 10.1088/1741-2560/8/6/066013

Barbe, M. T., Reker, P., Hamacher, S., Franklin, J., Kraus, D., Dembek, T. A., et al. (2018). DBS of the PSA and the VIM in essential tremor. *Neurology* 91, e543–e550. doi: 10.1212/WNL.0000000000005956

Bareket-Keren, L., and Hanein, Y. (2012). Carbon nanotube-based multi electrode arrays for neuronal interfacing?: progress and prospects. *Front. Neural Circuits* 6:122. doi: 10.3389/fncir.2012.00122

Bedell, H. W., Hermann, J. K., Ravikumar, M., Lin, S., Rein, A., Li, X., et al. (2018a). Targeting CD14 on blood derived cells improves intracortical microelectrode performance. *Biomaterials* 163, 163–173. doi: 10.1016/j.biomaterials.2018.02.014

Bedell, H. W., Song, S., Li, X., Molinich, E., Lin, S., Stiller, A., et al. (2018b). Understanding the effects of both CD14-mediated innate immunity and device / tissue mechanical mismatch in the neuroinflammatory response to intracortical microelectrodes. *Front. Neurosci.* 12:772. doi: 10.3389/fnins.2018.00772

Behzadi, S., Serpooshan, V., Tao, W., Hamaly, M. A., Alkawareek, M. Y., Dreaden, E. C., et al. (2017). Cellular uptake of nanoparticles: journey inside the cell. *Chem. Soc. Rev.* 46, 4218–4244. doi: 10.1039/c6cs00636a

Bennett, C., Samikkannu, M., Mohammed, F., Dietrich, W. D., Rajguru, S. M., and Prasad, A. (2018). Blood brain barrier (BBB)-disruption in intracortical silicon microelectrode implants. *Biomaterials* 164, 1–10. doi: 10.1016/j.biomaterials.2018.02.036

Bérces, Z., Pomothy, J., Horváth, Á. C., Kōhidi, T., Benyei, É., Fekete, Z., et al. (2018). Effect of nanostructures on anchoring stem cell-derived neural tissue to artificial surfaces. *J. Neural Eng.* 15:056030. doi: 10.1088/1741-2552/aad972

Boehler, C., Stieglitz, T., and Asplund, M. (2015). Nanostructured platinum grass enables superior impedance reduction for neural microelectrodes. *Biomaterials* 67, 346–353. doi: 10.1016/j.biomaterials.2015.07.036

Boomkamp, S. D., Riehle, M. O., Wood, J., Olson, M. F., and Barnett, S. C. (2012). The development of a rat in vitro model of spinal cord injury demonstrating the additive effects of Rho and ROCK inhibitors on neurite outgrowth and myelination. *Glia* 60, 441–456. doi: 10.1002/glia.22278

Bradley, J. A., Luithardt, H. H., Metea, M. R., and Strock, C. J. (2018). In vitro screening for seizure liability using microelectrode array technology. *Toxicol. Sci.* 163, 240–253. doi: 10.1093/toxsci/kfy029

Brown, J. A., Pensabene, V., Markov, D. A., Allwardt, V., Neely, M. D., Shi, M., et al. (2015). Recreating blood-brain barrier physiology and structure on chip: a novel neurovascular microfluidic bioreactor. *Biomicrofluidics* 9:054124. doi: 10.1063/1.4934713

Capogrosso, M., Wagner, F. B., Gandar, J., Moraud, E. M., Wenger, N., Milekovic, T., et al. (2018). Configuration of electrical spinal cord stimulation through real-time processing of gait kinematics. *Nat. Protoc.* 13, 2031–2061. doi: 10.1038/s41596-018-0030-9

Catt, K., Li, H., and Cui, X. T. (2017). Poly (3,4-ethylenedioxythiophene) graphene oxide composite coatings for controlling magnesium implant corrosion. *Acta Biomater.* 48, 530–540. doi: 10.1016/j.actbio.2016.11.039

Cavaliere, F., Vicente, E. S., and Matute, C. (2010). An organotypic culture model to study nigro-striatal degeneration. *J. Neurosci. Methods* 188, 205–212. doi: 10.1016/j.jneumeth.2010.02.008

Chapman, C. A. R., Chen, H., Stamou, M., Lein, P. J., and Seker, E. (2016). Mechanisms of reduced astrocyte surface coverage in cortical neuron-glia co-cultures on nanoporous gold surfaces. *Cell. Mol. Bioeng.* 9, 433–442. doi: 10.1007/s12195-016-0449-4

Chen, R., Romero, G., Christiansen, M. G., Mohr, A., and Anikeeva, P. (2015). Wireless magnetothermal deep brain stimulation. *Science* 347, 1477–1480. doi: 10.1126/science.1261821

Chen, S., Weitemier, A. Z., Zeng, X., He, L., Wang, X., Tao, Y., et al. (2018). Near-infrared deep brain stimulation via upconversion nanoparticle – mediated optogenetics. *Science* 359, 679–684. doi: 10.1126/science.aaq1144

Chen, W., Han, S., Qian, W., Weng, S., Yang, H., Sun, Y., et al. (2018). Nanotopography regulates motor neuron differentiation of human pluripotent stem cells. *Nanoscale* 10, 3556–3565. doi: 10.1039/c7nr05430k

Chen, X.-Z., Liu, J.-H., Dong, M., Müller, L., Chatzipirpiridis, G., Hu, C., et al. (2019). Magnetically driven piezoelectric soft microswimmers for neuron-like cell delivery and neuronal differentiation. *Mater. Horiz.* doi: 10.1039/C9MH00279K

Chin, E., and Goh, E. (2018). Blood–brain barrier on a chip. *Methods Cell Biol.* 146, 159–182. doi: 10.1016/bs.mcb.2018.06.003

Chong, C., Ma, D., Zhao, C., Franklin, R. J. M., Zhou, Z., Ai, N., et al. (2015). Discovery of a novel neuroprotectant, BHDPC, that protects against MPP^+/MPTP-induced neuronal death in multiple experimental models. *Free Radic. Biol. Med.* 89, 1057–1066. doi: 10.1016/j.freeradbiomed.2015.08.013

Choo, A. M., Miller, W. J., Chen, Y., Nibley, P., Patel, T. P., Goletiani, C., et al. (2013). Antagonism of purinergic signalling improves recovery from traumatic brain injury. *Brain* 136, 65–80. doi: 10.1093/brain/aws286

Coenen, V. A., Amtage, F., Volkmann, J., and Schläpfer, T. E. (2015). Deep brain stimulation in neurological and psychiatric disorders. *Dtsch. Arztebl. Int.* 112, 519–526. doi: 10.3238/arztebl.2015.0519

Cogan, S. F. (2008). Neural stimulation and recording electrodes. *Annu. Rev. Biomed. Eng.* 10, 275–308. doi: 10.1146/annurev.bioeng.10.061807.160518

Croft, C. L., and Noble, W. (2018). Preparation of organotypic brain slice cultures for the study of Alzheimer's disease. *F1000Res.* 7:592. doi: 10.12688/f1000research.14500.2

Crompton, K. E., Goud, J. D., Bellamkonda, R. V., Gengenbach, T. R., Finkelstein, D. I., Horne, M. K., et al. (2007). Polylysine-functionalised thermoresponsive chitosan hydrogel for neural tissue engineering. *Biomaterials* 28, 441–449. doi: 10.1016/j.biomaterials.2006.08.044

Cui, X., and Martin, D. C. (2003). Electrochemical deposition and characterization of poly (3,4-ethylenedioxythiophene) on neural microelectrode arrays. *Sens. Actuators B* 89, 92–102. doi: 10.1016/s0925-4005(02)00448-3

Dandekar, M. P., Fenoy, A. J., Carvalho, A. F., Soares, J. C., and Quevedo, J. (2018). Deep brain stimulation for treatment-resistant depression: an integrative review of preclinical and clinical findings and translational implications. *Mol. Psychiatry* 23, 1094–1112. doi: 10.1038/mp.2018.2

Daniele, S., and Bragato, C. (2014). "From macroelectrodes to microelectrodes: theory and electrode properties BT," in *Environmental Analysis by Electrochemical*, eds L. M. Moretto and K. Kalcher (New York, NY: Springer Science+Business Media), 373–401. doi: 10.1007/978-1-4939-0676-5_15

Daviaud, N., Garbayo, E., Lautram, N., Franconi, F., Lemaire, L., Perez-Pinzon, M., et al. (2014). Modeling nigrostriatal degeneration in organotypic cultures, a new ex vivo model of Parkinson's disease. *Neuroscience* 256, 10–22. doi: 10.1016/j.neuroscience.2013.10.021

De Astis, S., Corradini, I., Morini, R., Rodighiero, S., Tomasoni, R., Lenardi, C., et al. (2013). Nanostructured TiO_2 surfaces promote polarized activation of microglia, but not astrocytes, toward a proinflammatory profile. *Nanoscale* 5, 10963–10974. doi: 10.1039/c3nr03534d

Desai, S. A., Gutekunst, C., Potter, S. M., and Gross, R. E. (2014). Deep brain stimulation macroelectrodes compared to multiple microelectrodes in rat hippocampus. *Front. Neuroeng.* 7:16. doi: 10.3389/fneng.2014.00016

Desai, S. A., Gutekunst, C. A., Potter, S. M., and Gross, R. E. (2012). Analyzing neuronal activation with macroelectrode vs. microelectrode array stimulation. *Conf. Proc. IEEE Eng. Med. Biol. Soc.* 2012, 4144–4147. doi: 10.1109/EMBC.2012.6346879

Desai, S. A., Rolston, J. D., Mccracken, C. E., Potter, S. M., and Gross, R. E. (2016). Asynchronous distributed multielectrode microstimulation reduces seizures in the dorsal tetanus toxin model of temporal lobe epilepsy. *Brain Stimul.* 9, 86–100. doi: 10.1016/j.brs.2015.08.008

Dias, D. O., and Göritz, C. (2018). Fibrotic scarring following lesions to the central nervous system. *Matrix Biol.* 68–69, 561–570. doi: 10.1016/j.matbio.2018.02.009

Dougherty, D. D. (2018). Deep brain stimulation: clinical applications. *Psychiatr. Clin. North Am.* 41, 385–394. doi: 10.1016/j.psc.2018.04.004

Drobisz, D., and Damborská, A. (2019). Deep brain stimulation targets for treating depression. *Behav. Brain Res.* 359, 266–273. doi: 10.1016/j.bbr.2018.11.004

Du, Z. J., Kolarcik, C. L., Kozai, T. D. Y., Luebben, S. D., Sapp, S. A., Sally, X., et al. (2017). Ultrasoft microwire neural electrodes improve chronic tissue integration. *Acta Biomater.* 53, 46–58. doi: 10.1016/j.actbio.2017.02.010

Eles, J. R., Vazquez, A. L., Kozai, T. D. Y., and Cui, X. T. (2018). In vivo imaging of neuronal calcium during electrode implantation: spatial and temporal mapping of damage and recovery. *Biomaterials* 174, 79–94. doi: 10.1016/j.biomaterials.2018.04.043

Eles, J. R., Vazquez, A. L., Kozai, T. D. Y., and Cui, X. T. (2019). Meningeal inflammatory response and fibrous tissue remodeling around intracortical implants: an in vivo two-photon imaging study. *Biomaterials* 195, 111–123. doi: 10.1016/j.biomaterials.2018.12.031

Eles, J. R., Vazquez, A. L., Snyder, N. R., Lagenaur, C., Matthew, C., Kozai, T. D. Y., et al. (2017). Neuroadhesive L1 coating attenuates acute microglial attachment to neural electrodes as revealed by live two-photon microscopy. *Biomaterials* 113, 279–292. doi: 10.1016/j.biomaterials.2016.10.054

Elias, G. J. B., Namasivayam, A. A., and Lozano, A. M. (2018). Deep brain stimulation for stroke: current uses and future directions. *Brain Stimul.* 11, 3–28. doi: 10.1016/j.brs.2017.10.005

Engel, M., Do-Ha, D., Munoz, S. S., and Ooi, L. (2016). Common pitfalls of stem cell differentiation: a guide to improving protocols for neurodegenerative disease models and research. *Cell. Mol. Life Sci.* 73, 3693–3709. doi: 10.1007/s00018-016-2265-3

Ereifej, E. S., Cheng, M. M., Mao, G., and Vandevord, P. J. (2013a). Examining the inflammatory response to nanopatterned polydimethylsiloxane using organotypic brain slice methods. *J. Neurosci. Methods* 217, 17–25. doi: 10.1016/j.jneumeth.2013.04.023

Ereifej, E. S., Matthew, H. W., Newaz, G., Mukhopadhyay, A., Auner, G., Salakhutdinov, I., et al. (2013b). Nanopatterning effects on astrocyte reactivity. *J. Biomed. Mater. Res. A* 101, 1743–1757. doi: 10.1002/jbm.a.34480

Ereifej, E. S., Rial, G. M., Hermann, J. K., Smith, C. S., Meade, S. M., Rayyan, J. M., et al. (2018). Implantation of neural probes in the brain elicits oxidative stress. *Front. Bioeng. Biotechnol.* 6:9. doi: 10.3389/fbioe.2018.00009

Farrell, S. M., Green, A., and Aziz, T. (2018). The current state of deep brain stimulation for chronic pain and its context in other forms of neuromodulation. *Brain Sci.* 8:E158. doi: 10.3390/brainsci8080158

Fattahi, P., Departments, C. E., State, P., Yang, G., and Kim, G. (2014). A review of organic and inorganic biomaterials for neural interfaces. *Adv. Mater.* 26, 1846–1885. doi: 10.1002/adma.201304496.A

Ferlauto, L., D'Angelo, A. N., Vagni, P., Leccardi, M. J. I. A., Mor, F. M., Cuttaz, E. A., et al. (2018). Development and characterization of PEDOT:PSS/alginate soft microelectrodes for application in neuroprosthetics. *Front. Neurosci.* 12:648. doi: 10.3389/fnins.2018.00648

Ferreira, E. S., Vieira, G., Moraes, D. M., Amorim, B. O., Malheiros, J. M., Hamani, C., et al. (2018). Long-term effects of anterior thalamic nucleus deep brain stimulation on spatial learning in the pilocarpine model of temporal lobe epilepsy. *Neuromodulation* 21, 160–167. doi: 10.1111/ner.12688

Fluri, F., Bieber, M., Volkmann, J., and Kleinschnitz, C. (2015). Microelectrode guided implantation of electrodes into the subthalamic nucleus of rats for long-term deep brain stimulation. *J. Vis. Exp.* 104:53066. doi: 10.3791/53066

Fluri, F., Mützel, T., Schuhmann, M. K., Krstić, M., Endres, H., and Volkmann, J. (2017). Development of a head-mounted wireless microstimulator for deep brain stimulation in rats. *J. Neurosci. Methods* 291, 249–256. doi: 10.1016/j.jneumeth.2017.08.024

Frampton, J. P., Hynd, M. R., Williams, J. C., Shuler, M. L., and Shain, W. (2007). Three-dimensional hydrogel cultures for modeling changes in tissue impedance around microfabricated neural probes. *J. Neural Eng.* 4, 399–409. doi: 10.1088/1741-2560/4/4/006

Gabriel, E., and Gopalakrishnan, J. (2017). Generation of iPSC-derived human brain organoids to model early neurodevelopmental disorders. *J. Vis. Exp.* 122:55372. doi: 10.3791/55372

Gaire, J., Lee, H. C., Hilborn, N., Ward, R., Regan, M., and Otto, K. J. (2018a). The role of inflammation on the functionality of intracortical microelectrodes. *J. Neural Eng.* 15:066027. doi: 10.1088/1741-2552/aae4b6

Gaire, J., Lee, H. C., Ward, R., Currlin, S., Woolle, A. J., Coleman, J. E., et al. (2018b). PrismPlus: a mouse line expressing distinct fluorophores in four different brain cell types. *Sci. Rep.* 8:7182. doi: 10.1038/s41598-018-25208-y

Ganji, M., Tanaka, A., Gilja, V., Halgren, E., and Dayeh, S. A. (2017). Scaling effects on the electrochemical stimulation performance of Au, Pt, and PEDOT:PSS electrocorticography arrays. *Adv. Funct. Mater.* 27:1703019. doi: 10.1002/adfm.201703019

Gordon, J., Amini, S., and White, M. K. (2014). General overview of neuronal cell culture. *Methods Mol. Biol.* 1078, 1–8. doi: 10.1007/978-1-62703-640-5_1

Green, R. A., Lovell, N. H., Wallace, G. G., and Poole-warren, L. A. (2008). Conducting polymers for neural interfaces: challenges in developing an effective long-term implant. *Biomaterials* 29, 3393–3399. doi: 10.1016/j.biomaterials.2008.04.047

Guduru, R., Liang, P., Hong, J., Rodzinski, A., Hadjikhani, A., Horstmyer, J., et al. (2015). Magnetoelectric 'spin' on stimulating the brain. *Nanomedicine* 10, 2051–2061. doi: 10.2217/nnm.15.52

Hadler, C., Wissel, K., Brandes, G., Dempwolf, W., Reuter, G., Lenarz, T., et al. (2017). Photochemical coating of Kapton® with hydrophilic polymers for the improvement of neural implants. *Mater. Sci. Eng. C* 75, 286–296. doi: 10.1016/j.msec.2017.02.020

Hall, A. A., Leonardo, C. C., Collier, L. A., Rowe, D. D., Willing, A. E., and Pennypacker, K. R. (2009). Delayed treatments for stroke influence neuronal death in rat organotypic slice cultures subjected to oxygen glucose deprivation. *Neuroscience* 164, 470–477. doi: 10.1016/j.neuroscience.2009.08.051

Hammer, D. X., Kim, D.-H., Lozzi, A., Boretsky, A., Ye, M., and Welle, C. (2016). *Imaging the Response to Long-Term Neural Implants*. Bellingham, WA: SPIE. doi: 10.1117/2.1201601.006321

Harris, J. P., Capadona, J. R., Miller, R. H., Healy, B. C., Shanmuganathan, K., Rowan, S. J., et al. (2011). Mechanically adaptive intracortical implants improve the proximity of neuronal cell bodies. *J. Neuroeng. Rehabil.* 8:066011. doi: 10.1088/1741-2560/8/6/066011

Hasenkamp, W., Musa, S., Alexandru, A., Eberle, W., and Bartic, C. (2009). Electrodeposition and characterization of iridium oxide as electrode material for neural recording and stimulation. *IFMBE Proc.* 25, 472–475. doi: 10.1007/978-3-642-03889-1_126

Heo, D. N., Song, S., Kim, H., Jae, Y., Ko, W., Jin, S., et al. (2016). Multifunctional hydrogel coatings on the surface of neural cuff electrode for improving electrode-nerve tissue interfaces. *Acta Biomater.* 39, 25–33. doi: 10.1016/j.actbio.2016.05.009

Hermann, J. K., Lin, S., Soffer, A., Wong, C., Srivastava, V., Chang, J., et al. (2018a). The role of toll-like receptor 2 and 4 innate immunity pathways in intracortical microelectrode-induced neuroinflammation. *Front. Bioeng. Biotechnol.* 6:113. doi: 10.3389/fbioe.2018.00113

Hermann, J. K., Ravikumar, M., Shoffstall, A., Ereifej, E., Kovach, K., Chang, J., et al. (2018b). Inhibition of the cluster of differentiation 14 innate immunity pathway with IAXO-101 improves chronic microelectrode performance. *J. Neural Eng.* 15:025002. doi: 10.1088/1741-2552/aaa03e

Hess, A. E., Capadona, J. R., Shanmuganathan, K., Hsu, L., Rowan, S. J., Weder, C., et al. (2011). Development of a stimuli-responsive polymer nanocomposite toward biologically optimized, MEMS-based neural probes. *J. Micromech. Microeng.* 21:054009. doi: 10.1088/0960-1317/21/5/054009

Ho, B. X., Pek, N. M. Q., and Soh, B. S. (2018). Disease modeling using 3D organoids derived from human induced pluripotent stem cells. *Int. J. Mol. Sci.* 19:E936. doi: 10.3390/ijms19040936

Holslag, J. A. H., Neef, N., Beudel, M., Drost, G., Oterdoom, D. L. M., Kremer, N. I., et al. (2017). Deep brain stimulation for essential tremor: a comparison of targets. *World Neurosurg.* 110, e580–e584. doi: 10.1016/j.wneu.2017.11.064

Humpel, C. (2016). Organotypic brain slice cultures: a review. *Neuroscience* 305, 86–98. doi: 10.1016/j.neuroscience.2015.07.086

Huuskonen, J., Suuronen, T., Miettinen, R., van Groen, T., and Salminen, A. (2005). A refined in vitro model to study inflammatory responses in organotypic membrane culture of postnatal rat hippocampal slices. *J. Neuroinflammation* 2:25.

Isoaho, N., Peltola, E., Sainio, S., Koskinen, J., and Laurila, T. (2018). Pt-grown carbon nanofibers for enzymatic glutamate biosensors and assessment of their biocompatibility. *RSC Adv.* 8, 35802–35812. doi: 10.1039/c8ra07766e

Jang, S., Kim, H., Kim, H. J., Lee, S. K., Kim, E. W., Namkoong, K., et al. (2018). Long-term culture of organotypic hippocampal slice from old 3xTg-AD mouse: an ex vivo model of Alzheimer's disease. *Psychiatry Investig.* 15, 205–213. doi: 10.30773/pi.2017.04.02

Järvelä, J. T., Ruohonen, S., Kukko-Lukjanov, T. K., Plysjuk, A., Lopez-Picon, F. R., and Holopainen, I. E. (2011). Kainic acid-induced neurodegeneration and activation of inflammatory processes in organotypic hippocampal slice cultures: treatment with cyclooxygenase-2 inhibitor does not prevent neuronal death. *Neuropharmacology* 60, 1116–1125. doi: 10.1016/j.neuropharm.2010.09.024

Jeffery, A. F., Churchward, M. A., Mushahwar, V. K., Todd, K. G., and Elias, A. L. (2014). Hyaluronic acid-based 3D culture model for in vitro testing of electrode biocompatibility. *Biomacromolecules* 15, 2157–2165. doi: 10.1021/bm500318d

Jiang, C., Li, L., and Hao, H. (2011). Carbon nanotube yarns for deep brain stimulation electrode. *IEEE Trans. Neural Syst. Rehabil. Eng.* 19, 612–616. doi: 10.1109/TNSRE.2011.2165733

Johnson, C. D., D'Amato, A. R., Puhl, D. L., Wich, D. M., Vesperman, A., and Gilbert, R. J. (2018). Electrospun fiber surface nanotopography influences astrocyte-mediated neurite outgrowth. *Biomed. Mater.* 13:054101. doi: 10.1088/1748-605X/aac4de

Jones, R. S. G., da Silva, A. B., Whittaker, R. G., Woodhall, G. L., and Cunningham, M. O. (2016). Human brain slices for epilepsy research: pitfalls, solutions and future challenges. *J. Neurosci. Methods* 260, 221–232. doi: 10.1016/j.jneumeth.2015.09.021

Jung, N. Y., Lee, K. H., Won, R., and Lee, B. H. (2013). Neuroprotective effects of α-tocotrienol on kainic acid-induced neurotoxicity in organotypic hippocampal slice cultures. *Int. J. Mol. Sci.* 14, 18256–18268. doi: 10.3390/ijms140918256

Karas, P. J., Lee, S., Jimenez-Shahed, J., Goodman, W. K., Viswanathan, A., and Sheth, S. A. (2019). Deep brain stimulation for obsessive compulsive disorder: evolution of surgical stimulation target parallels changing model of dysfunctional brain circuits. *Front. Neurosci.* 12:998. doi: 10.3389/fnins.2018.00998

Kargol, A., Malkinski, L., and Caruntu, G. (2012). "Biomedical applications of multiferroic nanoparticles," in *Advanced Magnetic Materials*, ed. L. Malkinski (London: InTech Publishing), 89–118. doi: 10.5772/39100

Kaur, G., and Dufour, J. M. (2012). Cell lines: valuable tools or useless artifacts. *Spermatogenesis* 2, 1–5. doi: 10.4161/spmg.19885

Kearns, S. M., Scheffler, B., Goetz, A. K., Lin, D. D., Baker, H. D., Roper, S. N., et al. (2006). A method for a more complete in vitro Parkinson's model: slice culture bioassay for modeling maintenance and repair of the nigrostriatal circuit. *J. Neurosci. Methods* 157, 1–9. doi: 10.1016/j.jneumeth.2006.03.020

Killian, N. J., Vernekar, V. N., Potter, S. M., and Vukasinovic, J. (2016). A device for long-term perfusion, imaging, and electrical interfacing of brain tissue in vitro. *Front. Neurosci.* 10:135. doi: 10.3389/fnins.2016.00135

Kim, D. H., Viventi, J., Amsden, J. J., Xiao, J., Vigeland, L., Kim, Y., et al. (2010). Dissolvable films of silk fibroin for ultrathin conformal bio-integrated electronics. *Nat. Mater.* 9, 511–517. doi: 10.1038/nmat2745

Kim, H. M., Lee, H. J., Lee, M. Y., Kim, S. U., and Kim, B. G. (2010). Organotypic spinal cord slice culture to study neural stem/progenitor cell microenvironment in the injured spinal cord. *Exp. Neurobiol.* 19, 106–113. doi: 10.5607/en.2010.19.2.106

Kim, S., Kim, N., Kim, Y., Baik, M., Yoo, M., Kim, D., et al. (2018). High-performance, polymer-based direct cellular interfaces for electrical stimulation and recording. *NPG Asia Mater.* 10, 255–265. doi: 10.1038/s41427-018-0014-9

Kipke, D. R., Shain, W., Buzsaki, G., Fetz, E., Henderson, J. M., Hetke, J. F., et al. (2008). Advanced neurotechnologies for chronic neural interfaces: new horizons and clinical opportunities. *J. Neurosci.* 28, 11830–11838. doi: 10.1523/JNEUROSCI.3879-08.2008

Kiss, M., Foldesy, P., and Fekete, Z. (2015). Optimization of a Michigan-type silicon microprobe for infrared neural stimulation. *Sens. Actuators B Chem.* 224, 676–682. doi: 10.1016/j.snb.2015.10.084

Kloc, M., Kosutzka, Z., Steno, J., and Valkovic, P. (2017). Prevalent placement error of deep brain stimulation electrode in movement disorders (technical considerations). *Bratisl. Med. J.* 118, 647–653. doi: 10.4149/BLL

Klymov, A., Rodrigues Neves, C. T., te Riet, J., Agterberg, M. J. H., Mylanus, E. A. M., Snik, A. F. M., et al. (2015). Nanogrooved Surface-Patterns induce cellular organization and axonal outgrowth in neuron-like PC12-Cells. *Hear. Res.* 320, 11–17. doi: 10.1016/j.heares.2014.12.009

Ko, K. R., and Frampton, J. P. (2016). Developments in 3D neural cell culture models: the future of neurotherapeutics testing? *Expert Rev. Neurother.* 16, 739–741. doi: 10.1586/14737175.2016.1166053

Kondo, M., Kobayashi, K., Ohkura, M., Nakai, J., and Matsuzaki, M. (2017). Two-Photon calcium imaging of the medial prefrontal cortex and hippocampus without cortical invasion. *eLife* 6:e26839. doi: 10.7554/eLife.26839

Koss, K. M., Churchward, M. A., Jeffery, A. F., Mushahwar, V. K., Elias, A. L., and Todd, K. G. (2017). Improved 3D hydrogel cultures of primary glial cells for in vitro modelling of neuroinflammation. *J. Vis. Exp.* 130:e56615. doi: 10.3791/56615

Koutsouras, D. A., Hama, A., Pas, J., Gkoupidenis, P., Hivert, B., Faivre-Sarailh, C., et al. (2017). PEDOT:PSS microelectrode arrays for hippocampal cell culture electrophysiological recordings. *MRS Commun.* 7, 259–265. doi: 10.1557/mrc.2017.34

Kozai, T. D. Y., Catt, K., Li, X., Gugel, Z. V., Olafsson, V. T., Vazquez, A. L., et al. (2015a). Mechanical failure modes of chronically implanted planar silicon-based neural probes for laminar recording. *Biomaterials* 37, 25–39. doi: 10.1016/j.biomaterials.2014.10.040

Kozai, T. D. Y., Jaquins-Gerstl, A. S., Vazquez, A. L., Michael, A. C., and Cui, X. T. (2015b). Brain tissue responses to neural implants impact signal sensitivity and intervention strategies. *ACS Chem. Neurosci.* 6, 48–67. doi: 10.1021/cn500256e

Kozai, T. D. Y., Li, X., Bodily, L. M., Caparosa, E. M., Zenonos, G. A., Carlisle, D. L., et al. (2014). Effects of caspase-1 knockout on chronic neural recording quality and longevity: insight into cellular and molecular mechanisms of the reactive tissue response. *Biomaterials* 35, 9620–9634. doi: 10.1016/j.biomaterials.2014.08.006.Effects

Krings, M., Höllig, A., Liu, J., Grüsser, L., Rossaint, R., and Coburn, M. (2016). Desflurane impairs outcome of organotypic hippocampal slices in an *in vitro* model of traumatic brain injury. *Med. Gas Res.* 6, 3–9. doi: 10.4103/2045-9912.179338

Kristensen, B. W., Noraberg, J., Thiébaud, P., Koudelka-Hep, M., and Zimmer, J. (2001). Biocompatibility of silicon-based arrays of electrodes coupled to organotypic hippocampal brain slice cultures. *Brain Res.* 896, 1–17. doi: 10.1016/s0006-8993(00)03304-7

Labombarda, F., Ghoumari, M. A., Liere, P., De Nicola, A. F., Schumacher, M., and Guennoun, R. (2013). Neuroprotection by steroids after neurotrauma in organotypic spinal cord cultures: a key role for progesterone receptors and steroidal modulators of GABA(A) receptors. *Neuropharmacology* 71, 46–55. doi: 10.1016/j.neuropharm.2013.03.010

Lai, H., Liao, L., Lin, C., Hsu, J., He, X., Chen, Y.-Y., et al. (2012). Design, simulation and experimental validation of a novel flexible neural probe for deep brain stimulation and multichannel recording. *J. Neural Eng.* 9:036001. doi: 10.1088/1741-2560/9/3/036001

LaMarca, E. A., Powell, S. K., Akbarian, S., and Brennand, K. J. (2018). Modeling neuropsychiatric and neurodegenerative diseases with induced pluripotent stem cells. *Front. Pediatr.* 6:82. doi: 10.3389/fped.2018.00082

Lamprecht, M. R., Elkin, B. S., Kesavabhotla, K., and Crary, J. F. (2017). Strong correlation of genome-wide expression after traumatic brain injury in vitro and in vivo implicates a role for SORLA. *J. Neurotrauma* 34, 97–108. doi: 10.1089/neu.2015.4306

Lancaster, M. A., and Knoblich, J. A. (2014). Generation of cerebral organoids from human pluripotent stem cells. *Nat. Protoc.* 9, 2329–2340. doi: 10.1038/nprot.2014.158

Leclerc, E., Duval, J. L., Egles, C., Ihida, S., Toshiyoshi, H., and Tixier-Mita, A. (2017). In vitro cyto-biocompatibility study of thin-film transistors substrates using an organotypic culture method. *J. Mater. Sci. Mater. Med.* 28:4. doi: 10.1007/s10856-016-5815-1

Lee, C., Cheng, Y., and Huang, G. S. (2014). Topographical control of cell-cell interaction in C6 glioma by nanodot arrays. *Nanoscale Res. Lett.* 9:250. doi: 10.1186/1556-276X-9-250

Lee, H. C., Ejserholm, F., Gaire, J., Currlin, S., Schouenborg, J., Wallman, L., et al. (2017). Histological evaluation of flexible neural implants; flexibility limit for reducing the tissue response? *J. Neural Eng.* 14:036026. doi: 10.1088/1741-2552/aa68f0

Leplus, A., Lauritzen, I., Melon, C., Kerkerian-Le Goff, L., Fontaine, D., and Checler, F. (2018). Chronic fornix deep brain stimulation in a transgenic Alzheimer's rat model reduces amyloid burden, inflammation, and neuronal loss. *Brain Struct. Funct.* 224, 363–372. doi: 10.1007/s00429-018-1779-x

Li, M., Zhou, H. H., Li, T., Li, C. Y., Xia, Z. Y., and Duan, Y. Y. (2015). Polyurethane/poly(Vinyl alcohol) hydrogel coating improves the cytocompatibility of neural electrodes. *Neural Regen. Res.* 10, 2048–2053. doi: 10.4103/1673-5374.172325

Li, Y., Chen, Y., Tan, L., Lin, J. P. W., Wu, J., Hu, W., et al. (2017). RNAi-mediated ephrin-B2 silencing attenuates fibrotic scar formation and improves spinal cord axon growth. *CNS Neurosci. Ther.* 23, 779–789. doi: 10.1111/cns.12723

Liddelow, S. A., Guttenplan, K. A., Clarke, L. E., Bennett, F. C., Bohlen, C. J., Schirmer, L., et al. (2017). Neurotoxic reactive astrocytes are induced by activated microglia. *Nature* 541, 481–487. doi: 10.1038/nature21029

Liu, J., Sternberg, A. R., Ghiasvand, S., and Berdichevsky, Y. (2018). Epilepsy-on-a-chip system for antiepileptic drug discovery. *IEEE Trans. Biomed. Eng.* 66, 1231–1241. doi: 10.1109/TBME.2018.2871415

Lorsch, B. J. R., Collins, F. S., and Lippincott-schwartz, J. (2014). Fixing problems with cell lines. Technologies and policies can improve authentication. *Science* 346, 1452–1453. doi: 10.1126/science.1259110

Lossi, L., and Merighi, A. (2018). The use of ex vivo rodent platforms in neuroscience translational research with attention to the 3Rs philosophy. *Front. Vet. Sci.* 5:164. doi: 10.3389/fvets.2018.00164

Magalhães, D. M., Pereira, N., Rombo, D. M., Beltrão-Cavacas, C., Sebastião, A. M., and Valente, C. A. (2018). Ex vivo model of epilepsy in organotypic slices – a new tool for drug screening. *J. Neuroinflammation* 15:203. doi: 10.1186/s12974-018-1225-2

Mantione, D., del Agua, I., Schaafsma, W., Diez-garcia, J., Castro, B., Sardon, H., et al. (2016). Poly(3,4-ethylenedioxythiophene):Glycosamino-glycan aqueous dispersions: toward electrically conductive bioactive materials for neural interfaces. *Macromol. Biosci.* 16, 1227–1238. doi: 10.1002/mabi.201600059

Mao, Z. Q., Wang, X., Xu, X., Cui, Z. Q., Pan, L. S., Ning, X. J., et al. (2018). Partial improvement in performance of patients with severe Alzheimer's disease at an early stage of fornix deep brain stimulation. *Neural Regen. Res.* 13, 2164–2172. doi: 10.4103/1673-5374.241468

Martinez-Ramirez, D., Jimenez-Shahed, J., Leckman, J. F., Porta, M., Servello, D., Meng, F. G., et al. (2018). Efficacy and safety of deep brain stimulation in tourette syndrome: the international tourette syndrome deep brain stimulation public database and registry. *JAMA Neurol.* 75, 353–359. doi: 10.1001/jamaneurol.2017.4317

Masís, J., Mankus, D., Wolff, S. B. E., Guitchounts, G., Joesch, M., and Cox, D. D. (2018). A micro-CT-based method for quantitative brain lesion characterization and electrode localization. *Sci. Rep.* 8:5184. doi: 10.1038/s41598-018-23247-z

Maya-vetencourt, J. F., Ghezzi, D., Antognazza, M. R., Colombo, E., Mete, M., Feyen, P., et al. (2017). A fully organic retinal prosthesis restores vision in a rat model of degenerative blindness. *Nat. Mater.* 16, 681–689. doi: 10.1038/nmat4874.A

Mazzone, G., and Nistri, A. (2014). S100β as an early biomarker of excitotoxic damage in spinal cord organotypic cultures. *J. Neurochem.* 130, 598–604. doi: 10.1111/jnc.12748

McCreery, D., Cogan, S., Kane, S., and Pikov, V. (2016). Correlations between histology and neuronal activity recorded by microelectrodes implanted chronically in the cerebral cortex. *J. Neural Eng.* 13:036012. doi: 10.1088/1741-2560/13/3/036012

Meijs, S., Fjorback, M., Jensen, C., Sørensen, S., Rechendorff, K., and Rijkhoff, N. J. M. (2015). Electrochemical properties of titanium nitride nerve stimulation electrodes: an in vitro and in vivo study. *Front. Neurosci.* 9:268. doi: 10.3389/fnins.2015.00268

Meoni, S., Fraix, V., Castrioto, A., Benabid, A. L., Seigneuret, E., Vercueil, L., et al. (2017). Pallidal deep brain stimulation for dystonia: a long term study. *J. Neurol. Neurosurg. Psychiatry* 88, 960–967. doi: 10.1136/jnnp-2016-315504

Merrill, D. R. (2014). Materials considerations of implantable neuroengineering devices for clinical use. *Curr. Opin. Solid State Mater. Sci.* 18, 329–336. doi: 10.1016/j.cossms.2014.07.002

Mewes, A., Franke, H., and Singer, D. (2012). Organotypic brain slice cultures of adult transgenic P301S mice — a model for tauopathy studies. *PLoS One* 7:e45017. doi: 10.1371/journal.pone.0045017

Meyer, R. D., Cogan, S. F., Nguyen, T. H., and Rauh, R. D. (2001). Electrodeposited iridium oxide for neural stimulation and recording electrodes. *IEEE Trans. Neural Syst. Rehabil. Eng.* 9, 2–11. doi: 10.1109/7333.918271

Michelson, N. J., Eles, J. R., Vazquez, A. L., Ludwig, K. A., and Kozai, T. D. Y. (2019). Calcium activation of cortical neurons by continuous electrical stimulation: frequency dependence, temporal fidelity, and activation density. *J. Neurosci. Res.* 97, 620–638. doi: 10.1002/jnr.24370

Mii, S., Uehara, F., Yano, S., Tran, B., Miwa, S., Hiroshima, Y., et al. (2013). Nestin-expressing stem cells promote nerve growth in long-term 3-dimensional gelfoam-supported histoculture. *PLoS One* 8:e67153. doi: 10.1371/journal.pone.0067153

Minami, N., Maeda, Y., Shibao, S., Arima, Y., Ohka, F., Kondo, Y., et al. (2017). Organotypic brain explant culture as a drug evaluation system for malignant brain tumors. *Cancer Med.* 11, 2635–2645. doi: 10.1002/cam4.1174

Moeendarbary, E., Weber, I. P., Sheridan, G. K., Koser, D. E., Soleman, S., Haenzi, B., et al. (2017). The soft mechanical signature of glial scars in the central nervous system. *Nat. Commun.* 8:14787. doi: 10.1038/ncomms14787

Morin, E. A., and He, W. (2017). In vitro study of central nervous system foreign body response towards hydrogel particle modified planar substrate. *J. Biomed. Mater. Res. A* 105, 3242–3250. doi: 10.1002/jbm.a.36180

Morishita, T., Hilliard, J. D., Okun, M. S., Neal, D., Nestor, K. A., Peace, D., et al. (2017). Postoperative lead migration in deep brain stimulation surgery: incidence, risk factors, and clinical impact. *PLoS One* 12:e0183711. doi: 10.1371/journal.pone.0183711

Musacchio, T., Rebenstorff, M., Fluri, F., Brotchie, J. M., Volkmann, J., Koprich, J. B., et al. (2017). Subthalamic nucleus deep brain stimulation is

neuroprotective in the A53T α-synuclein Parkinson's disease rat model. *Ann. Neurol.* 81, 825–836. doi: 10.1002/ana.24947

Nasr, B., Chatterton, R., Yong, J. H. M., Jamshidi, P., D'Abaco, G. M., Bjorksten, A. R., et al. (2018). Self-organized nanostructure modified microelectrode for sensitive electrochemical glutamate detection in stem cells-derived brain organoids. *Biosensors* 8:E14. doi: 10.3390/bios8010014

Nery, F. C., da Hora, C. C., Yaqub, U., Zhang, X., McCarthy, D. M., Bhide, P. G., et al. (2015). New methods for investigation of neuronal migration in embryonic brain explants. *J. Neurosci. Methods* 239, 80–84. doi: 10.1016/j.jneumeth.2014.09.028

Neville, K. E., Bosse, T. L., Klekos, M., Mills, J. F., Weicksel, S. E., Waters, J. S., et al. (2018). A novel ex vivo method for measuring whole brain metabolism in model systems. *J. Neurosci. Methods* 296, 32–43. doi: 10.1016/j.jneumeth.2017.12.020

Nissan, I., Schori, H., Kumar, B., Passig, A., Shefi, O., and Gedanken, A. (2017). Topographical impact of silver nanolines on the morphology of neuronal SH-SY5Y cells. *J. Mater. Chem. B* 5, 9346–9353. doi: 10.1039/c7tb02492d

Normann, R. A., and Fernandez, E. (2016). Clinical applications of penetrating neural interfaces and Utah Electrode Array technologies. *J. Neural Eng.* 13:061003. doi: 10.1088/1741-2560/13/6/061003

Nzou, G., Wicks, R. T., Wicks, E. E., Seale, S. A., Sane, C. H., Chen, A., et al. (2018). Human cortex spheroid with a functional blood brain barrier for high-throughput neurotoxicity screening and disease modeling. *Sci. Rep.* 8:7413. doi: 10.1038/s41598-018-25603-5

Onesto, V., Cancedda, L., Coluccio, M. L., Nanni, M., Pesce, M., Malara, N., et al. (2017). Nano-topography enhances communication in neural cells networks. *Sci. Rep.* 7:9841. doi: 10.1038/s41598-017-09741-w

Ormel, P., Vieira de Sa, R., Hol, E., and Pasterkamp, R. J. (2018). Microglia innately develop within cerebral organoids. *Nat. Commun.* 9:4167. doi: 10.1038/s41467-018-06684-2

O'Rourke, C., Lee-reeves, C., Drake, R. A. L., Cameron, G. W. W., Loughlin, A. J., and Phillips, J. B. (2017). Adapting tissue-engineered in vitro CNS models for high-throughput study of neurodegeneration. *J. Tissue Eng.* 8:204173141769792. doi: 10.1177/2041731417697920

Osaki, T., Sivathanu, V., and Kamm, R. D. (2018). Vascularized microfluidic organ-chips for drug screening, disease models and tissue engineering. *Curr. Opinin. Biotechnol.* 52, 116–123. doi: 10.1016/j.copbio.2018.03.011

Pancrazio, J. J., Deku, F., Ghazavi, A., Stiller, A. M., Rihani, R., Frewin, C. L., et al. (2017). Thinking small: progress on microscale neurostimulation technology. *Neuromodulation* 20, 745–752. doi: 10.1111/ner.12716

Pandamooz, S., Saied, M., Ismail, M., and Safari, A. (2019). Tissue and Cell Modeling traumatic injury in organotypic spinal cord slice culture obtained from adult rat. *Tissue Cell* 56, 90–97. doi: 10.1016/j.tice.2019.01.002

Penazzi, L., Lorengel, J., Sündermann, F., Golovyashkina, N., Marre, S., Mathis, C. M. B., et al. (2017). DMSO modulates CNS function in a preclinical Alzheimer's disease model. *Neuropharmacology* 113, 434–444. doi: 10.1016/j.neuropharm.2016.10.020

Perkhofer, L., Frappart, P.-O., Muller, M., and Kleger, A. (2018). Importance of organoids for personalized medicine. *Per. Med.* 15, 461–465. doi: 10.2217/pme-2018-0071

Persheyev, S., Fan, Y., Irving, A., and Rose, M. J. (2011). BV-2 microglial cells sense micro-nanotextured silicon surface topology. *J. Biomed. Mater. Res. Part A* 99, 135–140. doi: 10.1002/jbm.a.33159

Pinnell, R. C., de Vasconcelos, A. P., Cassel, J. C., and Hofmann, U. G. (2018). A miniaturized, programmable deep-brain stimulator for group-housing and water maze use Richard. *Front. Neurosci.* 12:231. doi: 10.3389/fnins.2018.00231

Pires, L. R., Rocha, D. N., Ambrosio, L., Pe, A. P., and Pe, A. P. (2015). The role of the surface on microglia function: implications for central nervous system tissue engineering. *J. R. Soc. Interface* 12:20141224. doi: 10.1098/rsif.2014.1224

Polikov, V. S., Tresco, P. A., and Reichert, W. M. (2005). Response of brain tissue to chronically implanted neural electrodes. *J. Neurosci. Methods* 148, 1–18. doi: 10.1016/j.jneumeth.2005.08.015

Pranti, A. S., Schander, A., Bödecker, A., and Lang, W. (2018). PEDOT: PSS coating on gold microelectrodes with excellent stability and high charge injection capacity for chronic neural interfaces. *Sens. Actuators B Chem.* 275, 382–393. doi: 10.1016/j.snb.2018.08.007

Prasad Tripathi, R. K., and Ayyannan, S. R. (2017). Anticonvulsant activity, organotypic hippocampal neuroprotection assay and in-silico sodium channel blocking potential of 2-amino-6-nitrobenzothiazole derived semicarbazones. *Biomed. Pharmacother.* 95, 1451–1460. doi: 10.1016/j.biopha.2017.09.070

Prodanov, D., and Delbeke, J. (2016). Mechanical and biological interactions of implants with the brain and their impact on implant design. *Front. Neurosci.* 10:11. doi: 10.3389/fnins.2016.00011

Ramirez-Zamora, A., and Ostrem, J. L. (2018). Globus pallidus interna or subthalamic nucleus deep brain stimulation for Parkinson disease: a review. *JAMA Neurol.* 75, 367–372. doi: 10.1001/jamaneurol.2017.4321

Ravikumar, M., Sunil, S., Black, J., Barkauskas, D. S., Haung, A. Y., Miller, R. H., et al. (2014). The roles of blood-derived macrophages and resident microglia in the neuroinflammatory response to implanted Intracortical microelectrodes. *Biomaterials* 35, 8049–8064. doi: 10.1016/j.biomaterials.2014.05.084

Rejc, E., Angeli, C. A., Atkinson, D., and Harkema, S. J. (2017). Motor recovery after activity-based training with spinal cord epidural stimulation in a chronic motor complete paraplegic. *Sci. Rep.* 7:13476. doi: 10.1038/s41598-017-14003-w

Rejmontová, P., Capáková, Z., Mikušová, N., Maráková, N., Kašpárková, V., Lehocký, M., et al. (2016). Adhesion, proliferation and migration of NIH/3T3 cells on modified polyaniline surfaces. *Int. J. Mol. Sci.* 17:E1439. doi: 10.3390/ijms17091439

Revell, M. A. (2015). Deep brain stimulation for movement disorders. *Nurs. Clin. North Am.* 50, 691–701. doi: 10.1016/j.cnur.2015.07.014

Rocha, D. N., Carvalho, E. D., and Pêgo, A. P. (2016). High-throughput platforms for the screening of new therapeutic targets for neurodegenerative diseases. *Drug Discov. Today* 21, 1355–1366. doi: 10.1016/j.drudis.2016.05.005

Rocha, D. N., Ferraz-Nogueira, J. P., Barrias, C. C., Relvas, J. B., and Pêgo, A. P. (2015). Extracellular environment contribution to astrogliosis—lessons learned from a tissue engineered 3D model of the glial scar. *Front. Cell. Neurosci.* 9:377. doi: 10.3389/fncel.2015.00377

Salanova, V. (2018). Deep brain stimulation for epilepsy. *Epilepsy Behav.* 88, 21–24. doi: 10.1016/j.yebeh.2018.06.041

Salatino, J. W., Kale, A. P., and Purcell, E. K. (2019). Alterations in ion channel expression surrounding implanted microelectrode arrays in the brain. *bioRxiv* [Preprint]. doi: 10.1101/518811

Salatino, J. W., Ludwig, K. A., Kozai, T. D. Y., and Purcell, E. K. (2018). Glial responses to implanted electrodes in the brain. *Nat. Biomed. Eng.* 1, 862–877. doi: 10.1038/s41551-017-0154-1.Glial

Samba, R., Herrmann, T., and Zeck, G. (2015). PEDOT–CNT coated electrodes stimulate retinal neurons at low voltage amplitudes and low charge densities. *J. Neural Eng.* 12:016014. doi: 10.1088/1741-2560/12/1/016014

Saryyeva, A., Nakamura, M., Krauss, J. K., and Schwabe, K. (2011). C-Fos expression after deep brain stimulation of the pedunculopontine tegmental nucleus in the rat 6-hydroxydopamine Parkinson model. *J. Chem. Neuroanat.* 42, 210–217. doi: 10.1016/j.jchemneu.2011.08.003

Sawyer, A. J., Tian, W., Saucier-sawyer, J. K., Rizk, P. J., Saltzman, W. M., Bellamkonda, R. V., et al. (2014). The effect of inflammatory cell-derived MCP-1 loss on neuronal survival during chronic neuroinflammation. *Biomaterials* 35, 6698–6706. doi: 10.1016/j.biomaterials.2014.05.008

Saxena, T., Karumbaiah, L., Gaupp, E. A., Patkar, R., Patil, K., Betancur, M., et al. (2013). The impact of chronic blood-brain barrier breach on intracortical electrode function. *Biomaterials* 34, 4703–4713. doi: 10.1016/j.biomaterials.2013.03.007

Schmidt, A. C., Wang, X., Zhu, Y., and Sombers, L. A. (2013). Carbon nanotube yarn electrodes for enhanced detection of neurotransmitter dynamics in live brain tissue. *ACS Nano* 24, 7864–7873. doi: 10.1021/nn402857u

Schoeler, M., Loetscher, P. D., Rossaint, R., Fahlenkamp, A. V., Eberhardt, G., Rex, S., et al. (2012). Dexmedetomidine is neuroprotective in an in vitro model for traumatic brain injury. *BMC Neurol.* 12:20. doi: 10.1186/1471-2377-12-20

Seyock, S., Maybeck, V., Scorsone, E., Rousseau, L., Bergonzo, P., and Offenhhausser, A. (2017). Interfacing neurons on carbon nanotubes covered with diamond. *RSC Adv.* 7, 153–160. doi: 10.1039/C6RA20207A

Shen, W., Das, S., Vitale, F., Richardson, A., Ananthakrishnan, A., Struzyna, L. A., et al. (2018). Microfabricated intracortical extracellular matrix-microelectrodes for improving neural interfaces. *Microsyst. Nanoeng* 4:30. doi: 10.1038/s41378-018-0030-5

Shepherd, R. K., Villalobos, J., Burns, O., and Nayagam, D. A. X. (2018). The development of neural stimulators: a review of preclinical safety and efficacy studies. *J. Neural Eng.* 15:041004. doi: 10.1088/1741-2552/aac43c

Shoffstall, A. J., Ecker, M., Danda, V., Joshi-imre, A., Stiller, A., Yu, M., et al. (2018a). Characterization of the neuroinflammatory response to thiol-ene shape memory polymer coated intracortical microelectrodes. *Micromachines* 9:E486. doi: 10.3390/mi9100486

Shoffstall, A. J., Srinivasan, S., Willis, M., Stiller, A. M., Ecker, M., Voit, W. E., et al. (2018b). A mosquito inspired strategy to implant microprobes into the brain. *Sci. Rep.* 8:122. doi: 10.1038/s41598-017-18522-4

Smith, I., Haag, M., Ugbode, C., Tams, D., Rattray, M., Przyborski, S., et al. (2015). Neuronal-glial populations form functional networks in a biocompatible 3D scaffold. *Neurosci. Lett.* 609, 198–202. doi: 10.1016/j.neulet.2015.10.044

Sommakia, S., Rickus, J. L., and Otto, K. J. (2014). Glial cells, but not neurons, exhibit a controllable response to a localized inflammatory microenvironment in vitro. *Front. Neuroeng.* 7:41. doi: 10.3389/fneng.2014.00041

Song, J. J., Popescu, A., and Bell, R. L. (2014). Present and potential use of spinal cord stimulation to control chronic pain. *Pain Physician* 17, 235–246.

Song, L., Wang, K., Li, Y., and Yang, Y. (2016). Nanotopography promoted neuronal differentiation of human induced pluripotent stem cells. *Colloids Surf. B Biointerfaces* 148, 49–58. doi: 10.1016/j.colsurfb.2016.08.041

Spencer, K. C., Sy, J. C., Falcòn-Banchs, R., and Cima, M. J. (2017a). Three dimensional in vitro glial scar model to investigate local strain effects from micromotion around neural implants. *Lab Chip* 17, 795–804. doi: 10.1039/c6lc01411a

Spencer, K. C., Sy, J. C., Ramadi, K. B., Graybiel, A. M., Langer, R., and Cima, M. J. (2017b). Characterization of mechanically matched hydrogel coatings to improve the biocompatibility of neural implants. *Sci. Rep.* 7:1952.

Stahl, K., Mylonakou, M. N., Skare, Ø., Amiry-Moghaddam, M., and Torp, R. (2011). Cytoprotective effects of growth factors: BDNF more potent than GDNF in an organotypic culture model of Parkinson's disease. *Brain Res.* 1378, 105–118. doi: 10.1016/j.brainres.2010.12.090

Sun, A. X., Ng, H. H., and Tan, E. K. (2018). Translational potential of human brain organoids. *Ann. Clin. Transl. Neurol.* 5, 226–235. doi: 10.1002/acn3.505

Sunshine, M. D., Streeter, K. A., Gaire, J., Otto, K. J., and Fuller, D. D. (2018). Cervical spinal cord injury in a transgenic mouse expressing fluorophores in neurons, microglia, astrocytes, and oligodendrocytes. *FASEB J.* 32:625.9. doi: 10.1096/fasebj.2018.32.1_supplement.625.9

Svensson, M., and Chen, P. (2018). Novel models to study stromal cell-leukocyte interactions in health and disease. *Adv. Exp. Med. Biol.* 1060, 131–146. doi: 10.1007/978-3-319-78127-3_8

Szostak, K. M., Grand, L., and Constandinou, T. G. (2017). Neural interfaces for intracortical recording: requirements, fabrication methods, and characteristics. *Front. Neurosci.* 11:665. doi: 10.3389/fnins.2017.00665

Tan, G. A., Furber, K. L., Thangaraj, M. P., Sobchishin, L., Doucette, J. R., and Nazarali, A. J. (2017). Organotypic cultures from the adult CNS: a novel model to study demyelination and remyelination ex vivo. *Cell. Mol. Neurobiol.* 38, 317–328. doi: 10.1007/s10571-017-0529-6

Tang, J., Qin, N., Chong, Y., Diao, Y., Yiliguma, Wang, Z., et al. (2018). Nanowire arrays restore vision in blind mice. *Nat. Commun.* 9:786. doi: 10.1038/s41467-018-03212-0

Tasnim, N., Kumar, A., and Joddar, B. (2018). Attenuation of the in vitro neurotoxicity of 316L SS by graphene oxide surface coating. *Mater. Sci. Eng. C Mater. Biol. Appl.* 73, 788–797. doi: 10.1016/j.msec.2016.12.123

Tawakol, O., Bredeson, S. D., and Troyk, P. R. (2016). Preparation of a neural electrode implantation device for in-vivo surgical use. *Proc. Annu. Int. Conf. IEEE Eng. Med. Biol. Soc.* 2016, 4507–4510. doi: 10.1109/EMBC.2016.7591729

Tekin, H., Simmons, S., Cummings, B., Gao, L., Adiconis, X., Hession, C. C., et al. (2018). Effects of 3D culturing conditions on the transcriptomic profile of stem-cell-derived neurons. *Nat. Biomed. Eng.* 2, 540–554. doi: 10.1038/s41551-018-0219-9

Trevathan, J. K., Baumgart, I. W., Nicolai, E. N., Gosink, B. A., Asp, A. J., Settell, M. L., et al. (2019). A truly injectable neural stimulation electrode made from an in-body curing polymer/metal composite. *bioRxiv* [Preprint]. doi: 10.1101/584995

Ullrich, C., and Humpel, C. (2009). Rotenone induces cell death of cholinergic neurons in an organotypic co-culture brain slice model. *Neurochem. Res.* 34, 2147–2153. doi: 10.1007/s11064-009-0014-9

Usmani, S., Aurand, E. R., Medelin, M., Fabbro, A., Scaini, D., Laishram, J., et al. (2016). 3D meshes of carbon nanotubes guide functional reconnection of segregated spinal explants. *Sci. Adv.* 2:e1600087. doi: 10.1126/sciadv.1600087

Uysal, O., Sevimli, T., Sevimli, M., Gunes, S., and Sariboyaci, A. E. (2018). "Chapter 17 - cell and tissue culture: the base of biotechnology," in *Omics Technologies and Bio-Engineering*, eds D. Barh and V. Azevedo (Cambridge, MA: Academic Press), 391–429.

Van Kanegan, M. J., Dunn, D. E., Kaltenbach, L. S., Shah, B., He, D. N., Mccoy, D. D., et al. (2016). Dual activities of the anti-cancer drug candidate PBI-05204 provide neuroprotection in brain slice models for neurodegenerative diseases and stroke. *Sci Rep.* 6:25626. doi: 10.1038/srep25626

Verpelli, C., Carlessi, L., Bechi, G., Poli, E. F., Orellana, D., Heise, C., et al. (2013). Comparative neuronal differentiation of self-renewing neural progenitor cell lines obtained from human induced pluripotent stem cells. *Front. Cell. Neurosci.* 7:175. doi: 10.3389/fncel.2013.00175

Vitale, F., Shen, W., Driscoll, N., Burrell, J. C., Richardson, A. G., Adewole, O., et al. (2018). Biomimetic extracellular matrix coatings improve the chronic biocompatibility of microfabricated subdural microelectrode arrays. *PLoS One* 13:e0206137. doi: 10.1371/journal.pone.0206137

Vitale, F., Summerson, S. R., Aazhang, B., Kemere, C., and Pasquali, M. (2015). Neural stimulation and recording with bidirectional, soft carbon nanotube fiber microelectrodes. *ACS Nano* 9, 4465–4474. doi: 10.1021/acsnano.5b01060

Wandiyanto, J. V., Linklater, D., Perera, P. G. T., Orlowska, A., Truong, V. K., Thissen, H., et al. (2018). Pheochromocytoma (PC12) cell response on mechanobactericidal titanium surfaces. *Materials* 11:E605. doi: 10.3390/ma11040605

Wang, H. (2018). Modeling neurological diseases with human brain organoids. *Front. Synaptic Neurosci.* 10:15. doi: 10.3389/fnsyn.2018.00015

Wang, J., Loye, A. M., Ketkaew, J., Schroers, J., and Kyriakides, T. R. (2018). Hierarchical micro- and nanopatterning of metallic glass to engineer cellular responses. *ACS Appl. Bio Mater.* 1, 51–58. doi: 10.1021/acsabm.8b00007

Wang, Y., Wang, L., Guo, Y., Zhu, Y., and Qin, J. (2018). Engineering stem cell-derived 3D brain organoids in a perfusable organ-on-a-chip system. *RSC Adv.* 8, 1677–1685. doi: 10.1039/c7ra11714k

Wang, J. K. T., Portbury, S., Thomas, M. B., Barney, S., Ricca, D. J., Morris, D. L., et al. (2006). Cardiac glycosides provide neuroprotection against ischemic stroke: discovery by a brain slice-based compound screening platform. *Proc. Natl. Acad. Sci. U.S.A.* 103, 10461–10466. doi: 10.1073/pnas.0600930103

Wang, K., Frewin, C. L., Esrafilzadeh, D., Yu, C., Wang, C., Pancrazio, J. J., et al. (2019). High-performance graphene-fiber-based neural recording microelectrodes. *Adv. Mater.* 31:180586. doi: 10.1002/adma.201805867

Wellman, S. M., Cambi, F., and Kozai, T. D. (2018a). The role of oligodendrocytes and their progenitors on neural interface technology: a novel perspective on tissue regeneration and repair. *Biomaterials* 183, 200–217. doi: 10.1016/j.biomaterials.2018.08.046

Wellman, S. M., Eles, J. R., Ludwig, K. A., Seymour, J. P., Michelson, N. J., McFadden, W. E., et al. (2018b). A materials roadmap to functional neural interface design. *Adv. Funct. Mater.* 28:1701269. doi: 10.1002/adfm.201701269

Wellman, S. M., and Kozai, T. D. Y. (2017). Understanding the inflammatory tissue reaction to brain implants to improve neurochemical sensing performance. *ACS Chem. Neurosci.* 8, 2578–2582. doi: 10.1021/acschemneuro.7b00403

Wellman, S. M., and Kozai, T. D. Y. (2018). In vivo spatiotemporal dynamics of NG2 glia activity caused by neural electrode implantation. *Biomaterials* 164, 121–133. doi: 10.1016/j.biomaterials.2018.02.037

Weltman, A., Yoo, J., and Meng, E. (2016). Flexible, penetrating brain probes enabled by advances in polymer microfabrication. *Micromachines* 7:180. doi: 10.3390/mi7100180

Wendelken, S., Page, D. M., Davis, T., Wark, H. A. C., Kluger, D. T., Duncan, C., et al. (2017). Restoration of motor control and proprioceptive and cutaneous sensation in humans with prior upper-limb amputation via multiple Utah Slanted Electrode Arrays (USEAs) implanted in residual peripheral arm nerves. *J. Neuroeng. Rehabil.* 14:121. doi: 10.1186/s12984-017-0320-4

Wevers, N. R., VanVught, R., Wilschut, K. J., Nicolas, A., Chiang, C., Lanz, H. L., et al. (2016). High-throughput compound evaluation on 3D networks of neurons and glia in a microfluidic platform. *Sci. Rep.* 6:38856. doi: 10.1038/srep38856

Williams, D. F. (2008). On the mechanisms of biocompatibility. *Biomacromolecules* 29, 2941–2953. doi: 10.1016/j.biomaterials.2008.04.023

Williams, D. F. (2009). On the nature of biomaterials. *Biomaterials* 30, 5897–5909. doi: 10.1016/j.biomaterials.2009.07.027

Woolley, A. J., Desai, H. A., and Otto, K. J. (2013). Chronic intracortical microelectrode arrays induce non-uniform, depth-related tissue responses. *J. Neural Eng.* 10:026007. doi: 10.1088/1741-2560/10/2/026007

Xicoy, H., Wieringa, B., and Martens, G. J. M. (2017). The SH-SY5Y cell line in Parkinson's disease research: a systematic review. *Mol. Neurodegener.* 12:10. doi: 10.1186/s13024-017-0149-0

Xu, H., Li, Z., Yu, Y., Sizdahkhani, S., Ho, W. S., Yin, F., et al. (2016). A dynamic in vivo-like organotypic blood-brain barrier model to probe metastatic brain tumors. *Sci. Rep*. 6:36670. doi: 10.1038/srep36670

Xu, J., Guo, H., Nguyen, A. T., Lim, H., and Yang, Z. (2018). A bidirectional neuromodulation technology for nerve recording and stimulation. *Micromachines* 9:E538. doi: 10.3390/mi9110538

Yang, J., Liu, L., Li, T., and Li, C. (2017). Array focal cortical stimulation enhances motor function recovery and brain remodeling in a rat model of ischemia. *J. Stroke Cerebrovasc. Dis.* 26, 658–665. doi: 10.1016/j.jstrokecerebrovasdis.2016.11.009

Yi, W., Chen, C., Feng, Z., Xu, Y., Zhou, C., Masurkar, N., et al. (2015). A flexible and implantable microelectrode arrays using high-temperature grown vertical carbon nanotubes and a biocompatible polymer substrate. *Nanotechnology* 26:125301. doi: 10.1088/0957-4484/26/12/125301

Yin, F., Zhu, Y., Wang, Y., and Qin, J. (2018). Engineering brain organoids to probe impaired neurogenesis induced by cadmium. *ACS Biomater. Sci. Eng.* 4, 1908–1915. doi: 10.1021/acsbiomaterials.8b00160

Zach, S., Bueler, H., Hengerer, B., and Gillardon, F. (2007). Predominant neuritic pathology induced by viral overexpression of α-synuclein in cell culture. *Cell. Mol. Neurobiol.* 27, 505–515. doi: 10.1007/s10571-007-9141-5

Zhou, H., Cheng, X., Rao, L., Li, T., and Duan, Y. Y. (2013). Poly(3,4-ethylenedioxythiophene)/multiwall carbon nanotube composite coatings for improving the stability of microelectrodes in neural prostheses applications. *Acta Biomater.* 9, 6439–6449. doi: 10.1016/j.actbio.2013.01.042

Zöndör, K., and Thoumine, O. (2017). Synaptogenic assays using neurons cultured on micropatterned substrates. *Methods Mol. Biol.* 1538, 29–44. doi: 10.1007/978-1-4939-6688-2_3

Zuidema, J. M., Desmond, G. P., Rivet, C. J., Kearns, K. R., Thompson, D. M., and Gilbert, R. J. (2015). Nebulized solvent ablation of aligned PLLA fibers for the study of neurite response to anisotropic-to-isotropic fiber/film transition (AFFT) boundaries in astrocyteneuron co-cultures. *Biomaterials* 46, 82–94. doi: 10.1016/j.biomaterials.2014.12.046

Conflict of Interest Statement: The authors declare that the research was conducted in the absence of any commercial or financial relationships that could be construed as a potential conflict of interest.

Copyright © 2019 Gulino, Kim, Pané, Santos and Pêgo. This is an open-access article distributed under the terms of the Creative Commons Attribution License (CC BY). The use, distribution or reproduction in other forums is permitted, provided the original author(s) and the copyright owner(s) are credited and that the original publication in this journal is cited, in accordance with accepted academic practice. No use, distribution or reproduction is permitted which does not comply with these terms.

frontiers in Neuroscience

MINI REVIEW
published: 17 July 2019
doi: 10.3389/fnins.2019.00737

Insights From Dynamic Neuro-Immune Imaging on Murine Immune Responses to CNS Damage

*R. Dixon Dorand[1], Bryan L. Benson[2], Lauren F. Huang[3], Agne Petrosiute[2,3,4] and Alex Y. Huang[2,3,4]**

[1] Department of Medicine, Vanderbilt University Medical Center, Nashville, TN, United States, [2] Department of Pathology, Case Western Reserve University School of Medicine, Cleveland, OH, United States, [3] Department of Pediatrics, Case Western Reserve University School of Medicine, Cleveland, OH, United States, [4] Angie Fowler Adolescent & Young Adult (AYA) Cancer Institute/University Hospitals (UH) Rainbow Babies & Children's Hospital, Cleveland, OH, United States

Evolving technologies and increasing understanding of human physiology over the past century have afforded our ability to intervene on human diseases using implantable bio-materials. These bio-electronic devices present a unique challenge through the creation of an interface between the native tissue and implantable bio-materials: the generation of host immune response surrounding such devices. While recent developments in cancer immunology seek to stimulate the immune system against cancer, successful long-term application of implantable bio-material devices need to durably minimize reactive immune processes at involved anatomical sites. Peripheral immune system response has been studied extensively for implanted bio-materials at various body sites. Examples include tooth composites (Gitalis et al., 2019), inguinal hernia repair (Heymann et al., 2019), and cardiac stents and pacemaker leads (Slee et al., 2016). Studies have also been extended to less well-studied immune reactivity in response to CNS neural-electronic implant devices. Recent technological advances in 2-Photon Laser Scanning Microscopy (2P-LSM) have allowed novel insights into *in vivo* immune response in a variety of tissue microenvironments. While imaging of peripheral tissues has provided an abundance of data with regards to immune cell dynamics, central nervous system (CNS) imaging is comparatively complicated by tissue accessibility and manipulation. Despite these challenges, the results of dynamic intravital neuro-immune imaging thus far have provided foundational insights into basic CNS biology. Utilizing a combination of intravital and *ex vivo* 2P-LSM, we have observed novel pathways allowing immune cells, stromal cells, cancer cells and proteins to communicate between the CNS parenchyma and peripheral vasculature. Similar to what has been reported in the intestinal tract, we have visualized myeloid cells extend dendritic processes across the blood brain barrier (BBB) into pial blood vessels. Furthermore, transient vessel leaks seen during systemic inflammation provide opportunities for cellular protein to be exchanged between the periphery and CNS. These insights provide new, visual information regarding immune surveillance and antigen presentation within the CNS. Furthermore, when combining intravital 2P-LSM and microfluidic devices complexed with mathematical modeling, we are gaining new insights into the intravascular behavior

OPEN ACCESS

Edited by:
Ulrich G. Hofmann, University Medical Center Freiburg, Germany

Reviewed by:
Naoto Kawakami, Ludwig Maximilian University of Munich, Germany
Renaud Blaise Jolivet, Université de Genève, Switzerland

***Correspondence:**
Alex Y. Huang
alex.y.huang@case.edu

Specialty section:
This article was submitted to Neural Technology, a section of the journal Frontiers in Neuroscience

Received: *15 February 2019*
Accepted: *02 July 2019*
Published: *17 July 2019*

Citation:
Dorand RD, Benson BL, Huang LF, Petrosiute A and Huang AY (2019) Insights From Dynamic Neuro-Immune Imaging on Murine Immune Responses to CNS Damage. Front. Neurosci. 13:737. doi: 10.3389/fnins.2019.00737

of circulating immune cells. This new knowledge into the basic mechanisms by which cells migrate to and interact with the CNS provide important considerations for the design of neuro-electronic biomaterials that have the potential to connect the peripheral-neural microenvironments into a unique, artificial interface.

Keywords: two-photon microscopy, microglia, CNS, immune response, innate and adaptive immunity, tissue microenvironment, blood-brain-barrier, vascular crawling

INTRODUCTION

The use of implantation devices dates back to ancient Egypt with archeological discovery of a toe prosthesis (Nerlich et al., 2000; Brier et al., 2015). More recently, technological advances have allowed clinical application of implantable electronic devices such as pacemakers and deep brain stimulators, once thought to belong to the realm of science fiction, to become routine in clinical practice. These devices have advantages due to their macroscopic scale and relatively large output voltages, which allow them to overpower the potential negative functional effects of tissue fibrosis and host immune reactions in response to the presence of foreign substances.

Meanwhile, challenges remain in the field of implantable neural devices, whether in applying fine sensor arrays for recording neural activity, or in reconstituting neural activities into motor commands to circumvent deficits resulting from spinal cord injury or stroke. Numerous factors contribute to this ongoing challenge, but two are classically identified as being of major importance: tissue stiffness mismatch and breakdown of blood-brain barrier (BBB). Critically, both of these issues interrupt normal neural physiology, implying that simple strategies to prevent tissue fibrosis, such as scavenging of cytokines like TGF-β, will not be sufficient. Such an approach may reduce impedance from tissue fibrosis, but would result in faithfully reporting deranged neural activity.

First and foremost, these devices do not match tissue stiffness of the brain, an organ with the lowest stiffness second only to blood. The importance of tissue stiffness is underscored by the broad success of bony prostheses dating back before recorded history, whereas for blood, the most pliable tissue, even state-of-the art intravascular devices such as extracorporeal membrane oxygenation remain plagued by tissue reaction. This issue is well established in neural technology and extensively reviewed elsewhere (Lotti et al., 2017; Salatino et al., 2017; Campbell and Wu, 2018).

Second, and unique to brain tissue, device implantation invariably disrupts the BBB. This disruption leads to dramatic alterations in the function of all intra-parenchymal cells, whose physiology is predicated on residing within an environment separated from the intravascular milieu. Microglia, astrocytes, neurons, pericytes, and brain endothelial cells are all known to trigger inflammatory programs in response to serum proteins present within the brain parenchyma. In turn, this leads to further inflammation as intra-parenchymal cytokine release promotes further increase in BBB permeability, resulting in accumulation of peripheral blood immune cells such as monocytes, a cell type that is typically excluded from the immune-privileged brain parenchyma. This inflammation occurs via the coordinated synergistic efforts of multiple mechanisms, most of which follow patterns well established in other tissues.

FAILURE OF NEURO-ELECTRONIC DEVICES

In a quest to restore function to damaged neuronal circuits resulting from trauma, stroke, or neurodegenerative processes, implantable neuro-electronic devices have shown some efficacy. However, the success of these neuro-electronic devices have been limited by inflammatory responses, scarring, and associated neuronal cell death in response to immune cell activation, leading to a progressive neurodegenerative state and ultimate failure of device function (McConnell et al., 2009). In one study, of 78 silicon microelectrode arrays (MEA) implanted in 27 non-human primates, 56% of devices failed within 1 year with a mean recording duration of 387 days. Approximately 15% of devices failed due to the development of a dense, fibrous meningeal encapsulation with extrusion of the device from the cortex (Barrese et al., 2013). Additional studies demonstrated that CCL2- and TNFα-secreting $CD68^{+}$ cells were responsible for MEA device failure that was associated with the destruction of neuronal circuits in close proximity to the implanted biomaterials (Biran et al., 2005). More recently, peripheral blood-derived monocytes bearing surface CD14 antigen has been implicated as a dominant innate immune cell population that could potently mediate neurodegenerative pathologies associated with microelectrode implantation (Ravikumar et al., 2014b), and serve as a potential therapeutic target to alleviate this problem (Bedell et al., 2018; Hermann et al., 2018). Further review of the acute and chronic tissue response to electrode implantation is reviewed elsewhere (Fernandez et al., 2014; Kozai et al., 2015).

IMMUNE CELLS IN THE CNS

It is critical to decipher which cell types are responsible for generating and potentiating immune responses in the CNS in order to potentially address the issue of immune-mediated device failure. In peripheral tissues, dendritic cells (DCs) and circulating monocytes serve as the major source of antigen presenting cells (APCs), which recognize damage-associated molecular patterns (DAMPs) or pathogen-associate molecular patterns (PAMPs), while presenting processed antigenic peptides in the draining lymph nodes (Itano and Jenkins, 2003).

However, in the CNS, APCs are made up of both CNS-resident microglia and blood-derived DCs (Ransohoff and Cardona, 2010). Microglia, characterized as $CX_3CR_1^+$/$Ly6C^{lo}$/$CD45^{lo}$/Iba-1^+, serve as resident phagocytes and immune sentinels of the non-inflamed CNS parenchyma, as they utilize their dendritic extensions to survey the entire CNS multiple times per day (Nimmerjahn et al., 2005). Microglia are present in both white and gray matter in varying densities and may possess different activation states based on their anatomic location (Lawson et al., 1990; Mittelbronn et al., 2001). Microglia have been shown to play a functional role in enhancing the activity of neuronal synapses through physical contacts. Disruption of these synapses by inflammatory stimuli could result in dis-synchronization of neural networks (Akiyoshi et al., 2018). Because of these important Microglial functions, understanding microglia physiology is essential as they are major contributors to the success or failure of implantable bio-materials. Microglia begin to show morphologic changes from as far as 130 microns from probe insertion sites in as soon as 6 h post implantation (Kozai et al., 2012b), implying that these immune cells' reactivity may extend beyond direct physical contact.

STRATEGIES FOR MODIFYING MICROGLIA FUNCTION

Since microglia play an integral role in the CNS immune response, both biological interference and mechanical device design play a central role in manipulating the neuro-electronic interface. For example, anti-Parkinson's disease monoamine oxidase B inhibitors have been shown to dampen the inflammatory response of microglia by regulating voltage-gated sodium channels, reducing the neuro-inflammatory reaction to MPTP (Hossain et al., 2018). Another novel target includes the THIK-1 potassium channel, which was recently shown to play an integral role in microglia ramification, surveillance, and was shown to be necessary for IL-1b release. Injection of tetrapentylammonium reduced microglia surveillance by 60% (Madry et al., 2018). Additionally, coating electrodes with neuronal adhesive molecules can help dampen the acute effects of the innate immune response by 80% (Eles et al., 2017). Lastly, reducing electrode size and enhancing their mechanical compliance with brain tissue also reduces the immune response to implanted bio-materials, as evidenced by diminished microglia and astrocyte activation (Kozai et al., 2012a). Whether these methods of immune suppression will lead to overall improved device longevity and decreased scar formation remains to be seen. Nevertheless, these and other approaches certainly bear further investigation.

PERIPHERAL-DERIVED MYELOID CELLS

Another important immune cell type to consider is the $CX_3CR_1^+$/$Ly6C^+$/$CD45^{hi}$/$CCR2^+$ blood derived macrophages that can be found in the perivascular and parameningeal spaces and can sample cerebrospinal fluid (CSF) in the arachnoid and Virchow-Robin spaces (McMahon et al., 2006; D'Agostino et al., 2012). Peripheral monocytes can be further divided into an inflammatory subset (CX_3CR_1loCCR2hiGR1+Ly6Chi) that are short-lived and home to inflamed tissue, or a patrolling subset (CX_3CR_1hiCCR2loGR1-Ly6Clo) that are long-lived and are recruited to non-inflamed tissue (Geissmann et al., 2003). Common to microglia and both monocyte subsets is the surface expression of CD14, a glycosylphosphatidyl-inositol-anchored protein notable for its role as a co-adaptor protein for toll-like receptor 2 (TLR-2), toll-like receptor 4 (TLR-4), and damage-associated molecular patterns (DAMPS) including heat shock protein 70 (hsp70) and S100A9 (Haziot et al., 1988; Yang et al., 1999; Asea et al., 2000; Beschorner et al., 2002; He et al., 2016). Using bone marrow chimera approach to distinguish the contribution of brain-resident microglia versus bone marrow-derived infiltrating monocytes, we observed that blood-derived monocyte/macrophages, not CNS-resident microglia, dominated the infiltrating cell population following microelectrode implantation site at 2 and 16 weeks post implantation, and their densities correlated with neuron loss at the microelectrode-tissue interface (Ravikumar et al., 2014b). In particular, functional CD14 on blood-derived monocytes and the presence of endotoxin contamination on intracortical microelectrode devices contribute to the decline in overall device performance (Ravikumar et al., 2014a; Bedell et al., 2018), so much so that specific inhibition of CD14 signaling pathway were shown to improve long-term performance of the implanted microelectrode (Hermann et al., 2018).

APPLICATION OF INTRAVITAL 2P-LSM TO STUDY THE CNS

As host immune response is a dynamic process involving the recruitment, retention, and functional differentiation of highly motile immune cells to damaged CNS tissue sites, traditional static histologic examinations often do not fully capture the evolution of the inflammatory process. To this end, 2P-LSM allows for the visualization of fluorescently tagged structures deep within undisturbed living tissues in a time-resolved, dynamic fashion (Denk et al., 1990). Two photon excitation also enables second harmonic generation to illuminate ordered structures such as collagen and myosin without exogenous fluorescence probes, thus allowing for morphologic observation in collagen-rich structures within tissues such as the lymph node and the brain (Campagnola et al., 2002; Williams et al., 2005; Kawakami and Flugel, 2010). While the field of immunology has taken advantage of two photon technology in the past two decades (Germain et al., 2012), neuroscientists first began using this technology in the late 1990s to monitor calcium flux in organotypic brain slice cultures (Yuste and Denk, 1995). Since the early 2000s, intravital CNS imaging in the brain has flourished and scientists have been able to capture a variety of biological processes including but not exclusively: astrocyte reactivity, dendritic spine

turnover, formation of plaques in Alzheimer disease, microglial dynamics, and immune cell trafficking. Using intravital 2-photon laser scanning microscopy (2P-LSM), our group has identified three additional mechanisms of immune surveillance in various physiological and pathological states that may have unique implications for brain tissue reactivity to intracortical implantation devices.

For the remainder of this review, we will focus on these novel insights provided by a combination of disease models and application of intravital 2P-LSM to reveal synergistic mechanisms that maintain BBB disruption and promote ongoing inflammation within the brain parenchyma. First, similar to what has been reported in the intestinal tract, we have visualized inflamed myeloid cells extending dendritic processes across the BBB into pial blood vessels. Second, we have demonstrated that cytokine-induced BBB permeability increase is temporal-spatially heterogenous and includes prominent but transient vessel leaks. Third, we have demonstrated that geometric changes to the pial vasculature in response to inflammation promote the arrest of peripheral blood immune cells, promoting their recruitment into the brain. We propose that these additional mechanisms must be addressed to achieve faithful, fail-safe and durable recording and control by neural implants.

INTRAVASCULAR DENDRITIC PROJECTIONS BY MYELOID CELLS THROUGH INTACT BBB

Recently, we described a unique mechanism whereby microglia extend their dendritic processes through the basement membrane and endothelium into the surrounding pial vessels, thereby providing a new potential avenue for immune cell interactions (Barkauskas et al., 2013). While extending dendritic processes between distinct anatomic compartments is not unique to the CNS (Niess et al., 2005; Girard et al., 2012), this is the first-time microscopy has captured this type of interaction between the immune privileged CNS and peripheral tissues. Using electron microscopy, we were able to confirm astrocyte end feet on either side of the extension, indicating that the astrocytes are actively participating in this breach of the BBB. At baseline in the gray matter of the cortex, we found a density of 175 $CX_3CR_1^+$ cell projections per mm^2 of vessel wall surface compared with only 75 projections in the dorsal column white matter in the spinal cord. Using three distinct pathologic models, we compared the frequency of projections in different inflammatory states. During the induction phase of experimental autoimmune encephalomyelitis (EAE), we found that the number of extensions doubled in the cortex by day 9 of induction and doubled in the spine by day 12, even though clinical symptoms usually only appear by day 12. In the cortex, projections could be seen in vessels of both small and large caliber, while in the spinal cord, they were only seen in association with small caliber vessels. In contrast to this EAE model, studies of traumatic spinal cord injury showed a 40% reduction in projections that slowly recovered to 85% of baseline by day 8 after injury. Projections in spinal cord injury were associated with both large and small caliber vessels. Of interest, in a third model of primary CNS malignancy in the gray matter of the cortex, we observed dendritic extensions into the tumor neo-vasculature with a frequency of less than half of baseline ($73/mm^2$ vs. $175/mm^2$). These intriguing observations required further investigations in order to understand the molecular and cellular signaling between microglia, surrounding CNS parenchyma, and endothelial tissues that regulate this behavior under physiological and different disease states.

Differential contribution of resident microglia and blood-derived monocytes/macrophages to neuron loss during CNS trauma was also demonstrated by direct intravital observation by 2P-LSM. Using a traumatic spinal crush injury model, we investigated the role of inflammatory monocytes in the process of post-traumatic axonal dieback (Evans et al., 2014). Immediately after crush injury, CX_3CR_1+ cells extravasated from blood vessels into the lesion and increased their abundance by six-fold in 5 days. Parenchymal microglia, on the other hand, did not accumulate at the injury site. While imaging animals on days 2, 5, and 8 post-injury, we observed axon-macrophage contacts that were associated with morphologic changes of the axon, ultimately resulting in either thinning of the axon or destruction within an hour.

TRANSIENT CNS VESSEL LEAK AND DC ACCUMULATION

Peripheral monocytes can also differentiate into DCs, characterized as CD11c+, and have the potential to stimulate CD8+ T-cells (Geissmann et al., 2003). Using an EAE model, we utilized intravital 2P-LSM to elucidate the initiating events in EAE and found that in fact multiple cell types are required to induce durable immune responses. First, we found transient focal blood vessel leaks from post-capillary venule junctions that occur within hours to days immediately following EAE induction before any clinically evidence symptoms can be appreciated. These leaks lasted as long as 30 min and where rapidly cleared by CSF flow near the pial surfaces but persisted when vessel contents leaked into the parenchyma. We visualized CX_3CR_1 microglia phagocytose blood vessel contents, which lead to their activation in the first 3 days following induction of EAE. The phagocytic CX_3CR_1+ microglia were then associated with an increase in CD11c+ DCs by day 6 post induction, which was then followed by infiltration and accumulation of antigen-specific T cells by day 9. Both antigen-specific T-cells and DCs congregated around areas of previous vessel leak, forming immune clusters within the CNS parenchyma. Following these observations of immune clusters, clinical EAE symptoms then started around day 10–12. Of interest, treatment with hydroxyzine ultimately decreased microglia activation and phagocytic capacity by day 3 and resulted in decreased accumulation of peripheral immune cells by day 6 (Barkauskas et al., 2015).

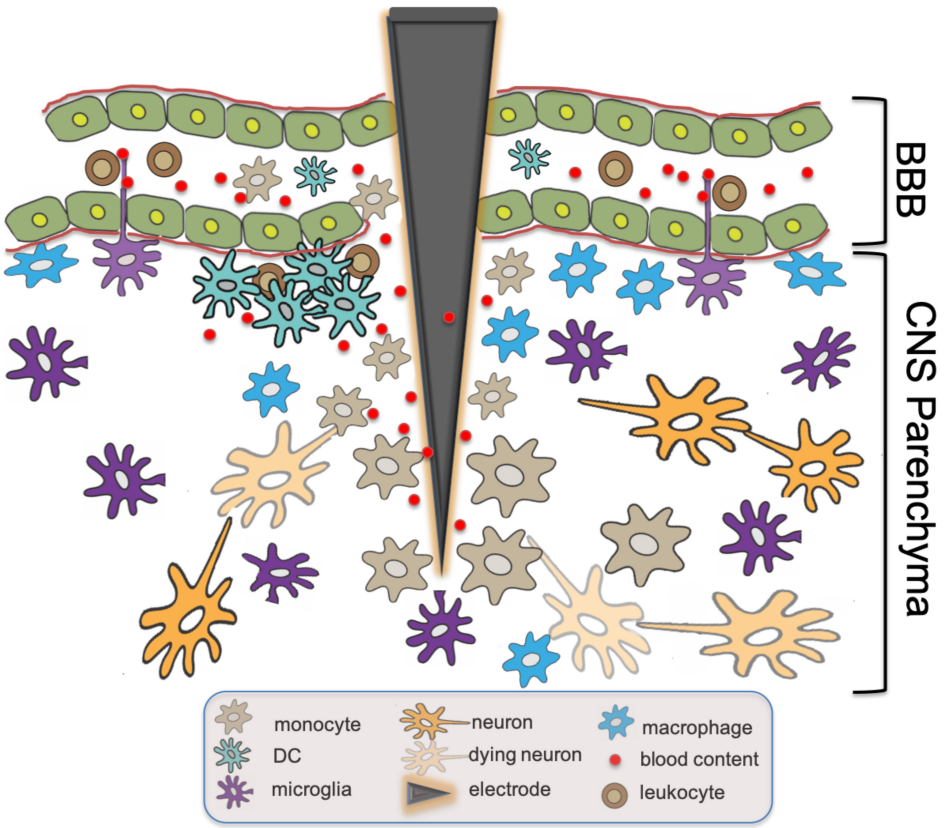

FIGURE 1 | Innate immune responses at intracortical electrode implantation sites. BBB Breach resulting from trauma associated with the insertion of intracortical electrodes causes leakage of blood content into CNS parenchyma. Subsequent tissue inflammatory response includes the recruitment of monocytes expressing CD14,the accumulation of DCs and macrophages, as well as the activation of microglia with intravascular dendritic protrusions that potentially participate in the further recruitment of circulating immune effector cells. The presence of DAMPs activates these innate immune cells via molecular signaling cascades including CD14, resulting in the eventual neuron loss and failure of the electronic device over time.

BBB Permeability has been implicated in the progression of multiple pathologic processes including Alzheimer's disease (AD), psychosis, and systemic lupus erythematosus (Bowman et al., 2007; Hirohata et al., 2018; Pollak et al., 2018). Indeed, an inverse correlation has also been demonstrated between CNS electronic implant performance and the severity and frequency of BBB breach (Saxena et al., 2013; Fernandez et al., 2014). Histamine, bradykinin, fibrin, and clotting pathways have all been implicated in modulating BBB permeability (Ryu and McLarnon, 2009; Passos et al., 2013; Chen et al., 2017). In fact, the accumulation of CNS infiltrating DCs was further demonstrated recently in a murine model of Alzheimer's disease, a process that was directly related to plasma Factor XII. Reduction in Factor XII correlated with reduced inflammation, neuronal damage, and improved cognitive function in the early stages of AD (Chen et al., 2017). Utilizing intravital 2P-LSM in these disease models would be helpful in establishing whether similar vessel leaks as observed in our EAE studies (Barkauskas et al., 2015) could also serve as a primary mechanism of cell accumulation in these other models of neurodegenerative diseases. **Figure 1** summarizes the above-mentioned findings regarding the functional roles of $CD14^+$ monocytes, DC, macrophages and microglia in traumatic CNS injury and associated BBB breach such as intracortical electrode implantation.

INTRAVASCULAR CELLULAR DYNAMICS

While our understanding of the role of different immune subsets involved in implantable bio-material device failure will continue to evolve, one constant parameter is the absolute requirement for circulating cells to successfully navigate the vast vasculature as they traverse and home to sites of insult; either in the periphery or in the CNS. When combining 2P-LSM with resonance scanning, we were able to visualize cellular flow within post-capillary venules in the CNS in real time (Benson et al., 2018). Our initial intravital observations revealed that cellular arrest was most prominent in areas of sudden vasculature volume expansion. As such, we designed biomimetic microfluidic devices that allowed efficient modeling of the CNS vasculature with different characteristic widths. Once coupled with a physiologic hematocrit, purified leukocytes exhibited slow rolling and adhesion that was dependent on

Intracellular adhesion molecule-1 (ICAM-1). The modeling of CNS vasculature with microfluidic devices and microscopy allowed us to demonstrate the critical importance of dynamic vessel geometry changes in promoting recruitment of peripheral blood leukocytes. This is likely to critically influence the early response to device implantation, since vessel dilatation is seen as an early response to implantation (Wellman and Kozai, 2018; Eles et al., 2019). Parallel work in suppressing vascular remodeling in lung inflammation suggests angiopoietin 2 (Ang2) as a potential additional target for this process (Le et al., 2015), in addition to TNF which is already known to contribute to gliosis and neuronal death after implantation.

ADDITIONAL CONSIDERATIONS

Several recent studies have implicated a potential new role for the deep cervical lymph nodes in regulating CNS immunity (de Vos et al., 2002; Furtado et al., 2008; Hatterer et al., 2008). Until recently, it was believed that the CNS lacked an overt lymphatic system. However, confocal, electron, and intravital 2P-LSM microscopy have now been used to validate the presence and functionality of lymphatic vessels running along the venous sinuses to the deep cervical lymph nodes (Louveau et al., 2015). This knowledge may impact our ongoing investigation into CNS tissue response to injury and repair, which is an issue critical to the field of neuro-electronic interface, device designs and clinical applications. Whether these lymphatic vessels work alone or in concert with other proposed mechanisms of antigen and solute drainage remains to be seen (Bradbury et al., 1981; Walter et al., 2006; Carare et al., 2008; Jessen et al., 2015). Deeper understanding of the newly discovered lymphatic flow within the CNS may inform future decisions as to how neuro-electronic devices should be implanted for best long-term clinical outcome by avoiding immune-mediated tissue repair and inflammatory responses that tend to diminish device functionality over time *in vivo* (McConnell et al., 2009).

CONCLUSION

The above insights from 2P-LSM intravital imaging provide several key characteristics to consider for proper design and insertion of implantable bio-materials that could preserve functional integrity without interference from intrinsic host tissue-derived immune response. First, the possibility that resident microglia can participate in direct antigen presentation by extending their processes into intact blood vessels provides a potential mechanism for recruiting and mediating additional peripheral immune cell-CNS parenchyma contact. This argues that while coating of electrodes with non-immunogenic materials and rationale device design may decrease local inflammation, the addition of systemic therapy aimed at reducing inflammatory co-factors in the peripheral circulation may provide added benefit in prolonging device longevity. Additionally, considering that microglia are more concentrated in white matter (Mittelbronn et al., 2001), surgical planning for device insertion through tracks that reduce contact with these immune cells may prove useful in preventing acute and chronic device-associated inflammation. Second, our direct visualization of CNS blood vessel leaks provides a new challenge to consider within the realm of BBB integrity preservation during neuro-electronic device insertion. Understanding regulation of blood vessel leaks and phagocyte activation in damaged CNS microenvironment is critical for future electrode design, as well as our basic understanding of CNS pathology. Our research suggests that treating patients with anti-histamines, i.e., hydroxyzine, may help quench these initial leaks and restrain the initial immune reaction during device implantation. Additionally, recent studies demonstrated that reducing specific clotting factors and bradykinin have beneficial effects in AD. Therefore, a multimodal approach should be considered. For example, administration of icatibant, a bradykinin antagonist approved to treat hereditary angioedema, may be beneficial in the perioperative period. These observations could be extrapolated to basic medication management. For example, ACE inhibitors, with their bradykinin increasing effects, should be avoided in patients with AD or other bio-material implants. Lastly, our new insights from studies using microfluidic devices lend support for treatment with antibodies or small molecules blocking adhesion (ICAM-1) or vessel remodeling (TNF and Ang2) in the perioperative period, as such approaches may have the potential to limit device immunogenicity.

As tissue reactions and immune responses are highly sensitive to tissue trauma within the CNS, care must be taken in conducting experiments where disruption of CNS tissues is involved [such as insertion of glass guide tubing following cortical tissue removal for deep tissue imaging (Barretto et al., 2011; Barretto and Schnitzer, 2012a,b)] in order to allow unbiased interpretation of data. Simple acts of thinning the skull or creation of cranial windows can lead to substantial immune activation and BBB disruption (Dorand et al., 2014). New imaging modalities that allows reduced invasiveness of the CNS tissue, such super-long-wave two-photon microscopy (Kondo et al., 2017), 3-photon microscopy (Liu et al., 2019a,b) or a combination of both techniques (Weisenburger et al., 2019) may offer advantages and opportunities in this regard. As our knowledge of CNS immunology continues to develop, further strategies for limiting immunogenicity of implantable bio-materials could be developed to enhance and sustain their long-term viability. While we continue to advance our knowledge into the world of CNS neuro-immunology, ongoing collaborations with immunologists and neuroscientists will be crucial to optimize future device performance and patient outcome.

AUTHOR CONTRIBUTIONS

All authors listed have made a substantial, direct and intellectual contribution to the work, and approved it for publication.

FUNDING

The authors are grateful for the support from the following sources: NIH R03CA219725, NIH R21CA281790, NIH R03CA230840, Theresia G. and Stuart F. Kline Family

Foundation, Char and Chuck Fowler Family Foundation, Keira Kilbane Foundation, St. Baldrick's Foundation, Pediatric Cancer Research Foundation, Hyundai Hope-on-Wheels Program, Bear Necessities Pediatric Cancer Foundation, Steven G. AYA Cancer Research Fund, Errol's Cancer Discovery Fund, Risman Family Fund, Alex's Lemonade Stand Foundation, VeloSano Pilot Funds, Gabrielle's Angel Foundation, and Case Comprehensive Cancer Center Pilot Funds.

REFERENCES

Akiyoshi, R., Wake, H., Kato, D., Horiuchi, H., Ono, R., Ikegami, A., et al. (2018). Microglia enhance synapse activity to promote local network synchronization. *eNeuro* 5:ENEURO.88-18.2018. doi: 10.1523/ENEURO.0088-18.2018

Asea, A., Kraeft, S. K., Kurt-Jones, E. A., Stevenson, M. A., Chen, L. B., Finberg, R. W., et al. (2000). HSP70 stimulates cytokine production through a CD14-dependant pathway, demonstrating its dual role as a chaperone and cytokine. *Nat. Med.* 6, 435–442. doi: 10.1038/74697

Barkauskas, D. S., Dixon Dorand, R., Myers, J. T., Evans, T. A., Barkauskas, K. J., Askew, D., et al. (2015). Focal transient CNS vessel leak provides a tissue niche for sequential immune cell accumulation during the asymptomatic phase of EAE induction. *Exp. Neurol.* 266, 74–85. doi: 10.1016/j.expneurol.2015.02.018

Barkauskas, D. S., Evans, T. A., Myers, J., Petrosiute, A., Silver, J., and Huang, A. Y. (2013). Extravascular CX3CR1+ cells extend intravascular dendritic processes into intact central nervous system vessel lumen. *Microsc. Microanal.* 19, 778–790. doi: 10.1017/S1431927613000482

Barrese, J. C., Rao, N., Paroo, K., Triebwasser, C., Vargas-Irwin, C., Franquemont, L., et al. (2013). Failure mode analysis of silicon-based intracortical microelectrode arrays in non-human primates. *J. Neural. Eng.* 10:066014. doi: 10.1088/1741-2560/10/6/066014

Barretto, R. P., Ko, T. H., Jung, J. C., Wang, T. J., Capps, G., Waters, A. C., et al. (2011). Time-lapse imaging of disease progression in deep brain areas using fluorescence microendoscopy. *Nat. Med.* 17, 223–228. doi: 10.1038/nm.2292

Barretto, R. P., and Schnitzer, M. J. (2012a). In vivo microendoscopy of the hippocampus. *Cold Spring Harb. Protoc.* 2012, 1092–1099. doi: 10.1101/pdb.prot071472

Barretto, R. P., and Schnitzer, M. J. (2012b). In vivo optical microendoscopy for imaging cells lying deep within live tissue. *Cold Spring Harb. Protoc.* 2012, 1029–1034. doi: 10.1101/pdb.top071464

Bedell, H. W., Hermann, J. K., Ravikumar, M., Lin, S., Rein, A., Li, X., et al. (2018). Targeting CD14 on blood derived cells improves intracortical microelectrode performance. *Biomaterials* 163, 163–173. doi: 10.1016/j.biomaterials.2018.02.014

Benson, B. L., Li, L., Myers, J. T., Dorand, R. D., Gurkan, U. A., Huang, A. Y., et al. (2018). Biomimetic post-capillary venule expansions for leukocyte adhesion studies. *Sci. Rep.* 8:9328. doi: 10.1038/s41598-018-27566-z

Beschorner, R., Nguyen, T. D., Gozalan, F., Pedal, I., Mattern, R., Schluesener, H. J., et al. (2002). CD14 expression by activated parenchymal microglia/macrophages and infiltrating monocytes following human traumatic brain injury. *Acta Neuropathol.* 103, 541–549. doi: 10.1007/s00401-001-0503-7

Biran, R., Martin, D. C., and Tresco, P. A. (2005). Neuronal cell loss accompanies the brain tissue response to chronically implanted silicon microelectrode arrays. *Exp. Neurol.* 195, 115–126. doi: 10.1016/j.expneurol.2005.04.020

Bowman, G. L., Kaye, J. A., Moore, M., Waichunas, D., Carlson, N. E., and Quinn, J. F. (2007). Blood-brain barrier impairment in Alzheimer disease: stability and functional significance. *Neurology* 68, 1809–1814. doi: 10.1212/01.wnl.0000262031.18018.1a

Bradbury, M. W., Cserr, H. F., and Westrop, R. J. (1981). Drainage of cerebral interstitial fluid into deep cervical lymph of the rabbit. *Am. J. Physiol.* 240, F329–F336.

Brier, B., Vinh, P., Schuster, M., Mayforth, H., and Johnson Chapin, E. (2015). A radiologic study of an ancient Egyptian mummy with a prosthetic toe. *Anat. Rec.* 298, 1047–1058. doi: 10.1002/ar.23135

Campagnola, P. J., Millard, A. C., Terasaki, M., Hoppe, P. E., Malone, C. J., and Mohler, W. A. (2002). Three-dimensional high-resolution second-harmonic generation imaging of endogenous structural proteins in biological tissues. *Biophys. J.* 82, 493–508. doi: 10.1016/s0006-3495(02)75414-3

Campbell, A., and Wu, C. (2018). Chronically implanted intracranial electrodes: tissue reaction and electrical changes. *Micromachines* 9:E430. doi: 10.3390/mi9090430

Carare, R. O., Bernardes-Silva, M., Newman, T. A., Page, A. M., Nicoll, J. A., Perry, V. H., et al. (2008). Solutes, but not cells, drain from the brain parenchyma along basement membranes of capillaries and arteries: significance for cerebral amyloid angiopathy and neuroimmunology. *Neuropathol. Appl. Neurobiol.* 34, 131–144. doi: 10.1111/j.1365-2990.2007.00926.x

Chen, Z. L., Revenko, A. S., Singh, P., MacLeod, A. R., Norris, E. H., and Strickland, S. (2017). Depletion of coagulation factor XII ameliorates brain pathology and cognitive impairment in Alzheimer disease mice. *Blood* 129, 2547–2556. doi: 10.1182/blood-2016-11-753202

D'Agostino, P. M., Gottfried-Blackmore, A., Anandasabapathy, N., and Bulloch, K. (2012). Brain dendritic cells: biology and pathology. *Acta Neuropathol.* 124, 599–614. doi: 10.1007/s00401-012-1018-0

de Vos, A. F., van Meurs, M., Brok, H. P., Boven, L. A., Hintzen, R. Q., van der Valk, P., et al. (2002). Transfer of central nervous system autoantigens and presentation in secondary lymphoid organs. *J. Immunol.* 169, 5415–5423. doi: 10.4049/jimmunol.169.10.5415

Denk, W., Strickler, J. H., and Webb, W. W. (1990). Two-photon laser scanning fluorescence microscopy. *Science* 248, 73–76. doi: 10.1126/science.2321027

Dorand, R. D., Barkauskas, D. S., Evans, T. A., Petrosiute, A., and Huang, A. Y. (2014). Comparison of intravital thinned skull and cranial window approaches to study CNS immunobiology in the mouse cortex. *Intravital* 3:e29728. doi: 10.4161/intv.29728

Eles, J. R., Vazquez, A., Kozai, T. D. Y., and Cui, X. T. (2019). Meningeal inflammatory response and fibrous tissue remodeling around intracortical implants: an in vivo two-photon imaging study. *Biomaterials* 195, 111–123. doi: 10.1016/j.biomaterials.2018.12.031

Eles, J. R., Vazquez, A. L., Snyder, N. R., Lagenaur, C., Murphy, M. C., Kozai, T. D., et al. (2017). Neuroadhesive L1 coating attenuates acute microglial attachment to neural electrodes as revealed by live two-photon microscopy. *Biomaterials* 113, 279–292. doi: 10.1016/j.biomaterials.2016.10.054

Evans, T. A., Barkauskas, D. S., Myers, J. T., Hare, E. G., You, J. Q., Ransohoff, R. M., et al. (2014). High-resolution intravital imaging reveals that blood-derived macrophages but not resident microglia facilitate secondary axonal dieback in traumatic spinal cord injury. *Exp. Neurol.* 254, 109–120. doi: 10.1016/j.expneurol.2014.01.013

Fernandez, E., Greger, B., House, P. A., Aranda, I., Botella, C., Albisua, J., et al. (2014). Acute human brain responses to intracortical microelectrode arrays: challenges and future prospects. *Front. Neuroeng.* 7:24. doi: 10.3389/fneng.2014.00024

Furtado, G. C., Marcondes, M. C., Latkowski, J. A., Tsai, J., Wensky, A., and Lafaille, J. J. (2008). Swift entry of myelin-specific T lymphocytes into the central nervous system in spontaneous autoimmune encephalomyelitis. *J. Immunol.* 181, 4648–4655. doi: 10.4049/jimmunol.181.7.4648

Geissmann, F., Jung, S., and Littman, D. R. (2003). Blood monocytes consist of two principal subsets with distinct migratory properties. *Immunity* 19, 71–82. doi: 10.1016/s1074-7613(03)00174-2

Germain, R. N., Robey, E. A., and Cahalan, M. D. (2012). A decade of imaging cellular motility and interaction dynamics in the immune system. *Science* 336, 1676–1681. doi: 10.1126/science.1221063

Girard, J. P., Moussion, C., and Forster, R. (2012). HEVs, lymphatics and homeostatic immune cell trafficking in lymph nodes. *Nat. Rev. Immunol.* 12, 762–773. doi: 10.1038/nri3298

Gitalis, R., Zhou, L., Marashdeh, M. Q., Sun, C., Glogauer, M., and Finer, Y. (2019). Human neutrophils degrade methacrylate resin composites and tooth dentin. *Acta Biomater.* 88, 325–331. doi: 10.1016/j.actbio.2019.02.033

Hatterer, E., Touret, M., Belin, M. F., Honnorat, J., and Nataf, S. (2008). Cerebrospinal fluid dendritic cells infiltrate the brain parenchyma and target the cervical lymph nodes under neuroinflammatory conditions. *PLoS One* 3:e3321. doi: 10.1371/journal.pone.0003321

Haziot, A., Chen, S., Ferrero, E., Low, M. G., Silber, R., and Goyert, S. M. (1988). The monocyte differentiation antigen, CD14, is anchored to the cell membrane by a phosphatidylinositol linkage. *J. Immunol.* 141, 547–552.

He, Z., Riva, M., Bjork, P., Sward, K., Morgelin, M., Leanderson, T., et al. (2016). CD14 Is a Co-Receptor for TLR4 in the S100A9-Induced Pro-Inflammatory Response in Monocytes. *PLoS One* 11:e0156377. doi: 10.1371/journal.pone.0156377

Hermann, J. K., Ravikumar, M., Shoffstall, A. J., Ereifej, E. S., Kovach, K. M., Chang, J., et al. (2018). Inhibition of the cluster of differentiation 14 innate immunity pathway with IAXO-101 improves chronic microelectrode performance. *J. Neural. Eng.* 15:025002. doi: 10.1088/1741-2552/aaa03e

Heymann, F., von Trotha, K. T., Preisinger, C., Lynen-Jansen, P., Roeth, A. A., Geiger, M., et al. (2019). Polypropylene mesh implantation for hernia repair causes myeloid cell-driven persistent inflammation. *JCI Insight* 4:e123862. doi: 10.1172/jci.insight.123862

Hirohata, S., Sakuma, Y., Matsueda, Y., Arinuma, Y., and Yanagida, T. (2018). Role of serum autoantibodies in blood brain barrier damages in neuropsychiatric systemic lupus erythematosus. *Clin. Exp. Rheumatol* 36, 1003–1007.

Hossain, M. M., Weig, B., Reuhl, K., Gearing, M., Wu, L. J., and Richardson, J. R. (2018). The anti-parkinsonian drug zonisamide reduces neuroinflammation: role of microglial Nav 1.6. *Exp. Neurol.* 308, 111–119. doi: 10.1016/j.expneurol.2018.07.005

Itano, A. A., and Jenkins, M. K. (2003). Antigen presentation to naive CD4 T cells in the lymph node. *Nat. Immunol.* 4, 733–739. doi: 10.1038/ni957

Jessen, N. A., Munk, A. S., Lundgaard, I., and Nedergaard, M. (2015). The glymphatic system: a beginner's guide. *Neurochem. Res* 40, 2583–2599. doi: 10.1007/s11064-015-1581-6

Kawakami, N., and Flugel, A. (2010). Knocking at the brain's door: intravital two-photon imaging of autoreactive T cell interactions with CNS structures. *Semin. Immunopathol.* 32, 275–287. doi: 10.1007/s00281-010-0216-x

Kondo, M., Kobayashi, K., Ohkura, M., Nakai, J., and Matsuzaki, M. (2017). Two-photon calcium imaging of the medial prefrontal cortex and hippocampus without cortical invasion. *eLife* 6:e26839. doi: 10.7554/eLife.26839

Kozai, T. D., Jaquins-Gerstl, A. S., Vazquez, A. L., Michael, A. C., and Cui, X. T. (2015). Brain tissue responses to neural implants impact signal sensitivity and intervention strategies. *ACS Chem. Neurosci.* 6, 48–67. doi: 10.1021/cn500256e

Kozai, T. D., Langhals, N. B., Patel, P. R., Deng, X., Zhang, H., Smith, K. L., et al. (2012a). Ultrasmall implantable composite microelectrodes with bioactive surfaces for chronic neural interfaces. *Nat. Mater.* 11, 1065–1073. doi: 10.1038/nmat3468

Kozai, T. D., Vazquez, A. L., Weaver, C. L., Kim, S. G., and Cui, X. T. (2012b). In vivo two-photon microscopy reveals immediate microglial reaction to implantation of microelectrode through extension of processes. *J. Neural. Eng.* 9:066001. doi: 10.1088/1741-2560/9/6/066001

Lawson, L. J., Perry, V. H., Dri, P., and Gordon, S. (1990). Heterogeneity in the distribution and morphology of microglia in the normal adult mouse brain. *Neuroscience* 39, 151–170. doi: 10.1016/0306-4522(90)90229-w

Le, C. T., Laidlaw, G., Morehouse, C. A., Naiman, B., Brohawn, P., Mustelin, T., et al. (2015). Synergistic actions of blocking angiopoietin-2 and tumor necrosis factor-alpha in suppressing remodeling of blood vessels and lymphatics in airway inflammation. *Am. J. Pathol.* 185, 2949–2968. doi: 10.1016/j.ajpath.2015.07.010

Liu, H., Wang, J., Zhuang, Z., He, J., Wen, W., Qiu, P., et al. (2019a). Visualizing astrocytes in the deep mouse brain in vivo. *J. Biophotonics.* 12:e201800420. doi: 10.1002/jbio.201800420

Liu, H., Zhuang, Z., He, J., Tong, S., He, C., Deng, X., et al. (2019b). High-energy polarized soliton synthesis and its application to deep-brain 3-photon microscopy in vivo. *Opt. Express* 27, 15309–15317. doi: 10.1364/OE.27.015309

Lotti, F., Ranieri, F., Vadala, G., Zollo, L., and Di Pino, G. (2017). Invasive intraneural interfaces: foreign body reaction issues. *Front. Neurosci.* 11:497. doi: 10.3389/fnins.2017.00497

Louveau, A., Smirnov, I., Keyes, T. J., Eccles, J. D., Rouhani, S. J., Peske, J. D., et al. (2015). Structural and functional features of central nervous system lymphatic vessels. *Nature* 523, 337–341. doi: 10.1038/nature14432

Madry, C., Kyrargyri, V., Arancibia-Carcamo, I. L., Jolivet, R., Kohsaka, S., Bryan, R. M., et al. (2018). microglial ramification, surveillance, and interleukin-1beta release are regulated by the two-pore Domain K(+) Channel THIK-1. *Neuron* 97, 299–312.e6. doi: 10.1016/j.neuron.2017.12.002

McConnell, G. C., Rees, H. D., Levey, A. I., Gutekunst, C. A., Gross, R. E., and Bellamkonda, R. V. (2009). Implanted neural electrodes cause chronic, local inflammation that is correlated with local neurodegeneration. *J. Neural. Eng.* 6:056003. doi: 10.1088/1741-2560/6/5/056003

McMahon, E. J., Bailey, S. L., and Miller, S. D. (2006). CNS dendritic cells: critical participants in CNS inflammation? *Neurochem. Int.* 49, 195–203. doi: 10.1016/j.neuint.2006.04.004

Mittelbronn, M., Dietz, K., Schluesener, H. J., and Meyermann, R. (2001). Local distribution of microglia in the normal adult human central nervous system differs by up to one order of magnitude. *Acta Neuropathol.* 101, 249–255.

Nerlich, A. G., Zink, A., Szeimies, U., and Hagedorn, H. G. (2000). Ancient Egyptian prosthesis of the big toe. *Lancet* 356, 2176–2179. doi: 10.1016/s0140-6736(00)03507-8

Niess, J. H., Brand, S., Gu, X., Landsman, L., Jung, S., McCormick, B. A., et al. (2005). CX3CR1-mediated dendritic cell access to the intestinal lumen and bacterial clearance. *Science* 307, 254–258. doi: 10.1126/science.1102901

Nimmerjahn, A., Kirchhoff, F., and Helmchen, F. (2005). Resting microglial cells are highly dynamic surveillants of brain parenchyma in vivo. *Science* 308, 1314–1318. doi: 10.1126/science.1110647

Passos, G. F., Medeiros, R., Cheng, D., Vasilevko, V., Laferla, F. M., and Cribbs, D. H. (2013). The bradykinin B1 receptor regulates Abeta deposition and neuroinflammation in Tg-SwDI mice. *Am. J. Pathol.* 182, 1740–1749. doi: 10.1016/j.ajpath.2013.01.021

Pollak, T. A., Drndarski, S., Stone, J. M., David, A. S., McGuire, P., and Abbott, N. J. (2018). The blood-brain barrier in psychosis. *Lancet Psychiatry* 5, 79–92. doi: 10.1016/S2215-0366(17)30293-6

Ransohoff, R. M., and Cardona, A. E. (2010). The myeloid cells of the central nervous system parenchyma. *Nature* 468, 253–262. doi: 10.1038/nature09615

Ravikumar, M., Hageman, D. J., Tomaszewski, W. H., Chandra, G. M., Skousen, J. L., and Capadona, J. R. (2014a). The effect of residual endotoxin contamination on the neuroinflammatory response to sterilized intracortical microelectrodes. *J. Mater. Chem. B* 2, 2517–2529. doi: 10.1039/c3tb21453b

Ravikumar, M., Sunil, S., Black, J., Barkauskas, D. S., Haung, A. Y., Miller, R. H., et al. (2014b). The roles of blood-derived macrophages and resident microglia in the neuroinflammatory response to implanted intracortical microelectrodes. *Biomaterials* 35, 8049–8064. doi: 10.1016/j.biomaterials.2014.05.084

Ryu, J. K., and McLarnon, J. G. (2009). A leaky blood-brain barrier, fibrinogen infiltration and microglial reactivity in inflamed Alzheimer's disease brain. *J. Cell Mol. Med.* 13, 2911–2925. doi: 10.1111/j.1582-4934.2008.00434.x

Salatino, J. W., Ludwig, K. A., Kozai, T. D. Y., and Purcell, E. K. (2017). Glial responses to implanted electrodes in the brain. *Nat. Biomed. Eng.* 1, 862–877. doi: 10.1038/s41551-017-0154-1

Saxena, T., Karumbaiah, L., Gaupp, E. A., Patkar, R., Patil, K., Betancur, M., et al. (2013). The impact of chronic blood-brain barrier breach on intracortical electrode function. *Biomaterials* 34, 4703–4713. doi: 10.1016/j.biomaterials.2013.03.007

Slee, J. B., Alferiev, I. S., Nagaswami, C., Weisel, J. W., Levy, R. J., Fishbein, I., et al. (2016). Enhanced biocompatibility of CD47-functionalized vascular stents. *Biomaterials* 87, 82–92. doi: 10.1016/j.biomaterials.2016.02.008

Walter, B. A., Valera, V. A., Takahashi, S., and Ushiki, T. (2006). The olfactory route for cerebrospinal fluid drainage into the peripheral lymphatic system. *Neuropathol. Appl. Neurobiol.* 32, 388–396. doi: 10.1111/j.1365-2990.2006.00737.x

Weisenburger, S., Tejera, F., Demas, J., Chen, B., Manley, J., Sparks, F. T., et al. (2019). Volumetric Ca(2+) imaging in the mouse brain using hybrid multiplexed sculpted light microscopy. *Cell* 177, 1050–1066.e14. doi: 10.1016/j.cell.2019.03.011

Wellman, S. M., and Kozai, T. D. Y. (2018). In vivo spatiotemporal dynamics of NG2 glia activity caused by neural electrode implantation.

Biomaterials 164, 121–133. doi: 10.1016/j.biomaterials.2018.02.037

Williams, R. M., Zipfel, W. R., and Webb, W. W. (2005). Interpreting second-harmonic generation images of collagen I fibrils. *Biophys. J.* 88, 1377–1386. doi: 10.1529/biophysj.104.047308

Yang, R. B., Mark, M. R., Gurney, A. L., and Godowski, P. J. (1999). Signaling events induced by lipopolysaccharide-activated toll-like receptor 2. *J. Immunol.* 163, 639–643.

Yuste, R., and Denk, W. (1995). Dendritic spines as basic functional units of neuronal integration. *Nature* 375, 682–684. doi: 10.1038/375682a0

Conflict of Interest Statement: This work was supported in part by a Sponsored Research Agreement from Biogen Idec.

Copyright © 2019 Dorand, Benson, Huang, Petrosiute and Huang. This is an open-access article distributed under the terms of the Creative Commons Attribution License (CC BY). The use, distribution or reproduction in other forums is permitted, provided the original author(s) and the copyright owner(s) are credited and that the original publication in this journal is cited, in accordance with accepted academic practice. No use, distribution or reproduction is permitted which does not comply with these terms.

frontiers in Neuroscience

ORIGINAL RESEARCH
published: 31 July 2019
doi: 10.3389/fnins.2019.00759

Viral-Mediated Optogenetic Stimulation of Peripheral Motor Nerves in Non-human Primates

Jordan J. Williams[1], *Alan M. Watson*[2,3], *Alberto L. Vazquez*[4,5] *and Andrew B. Schwartz*[1,5,6]*

[1] Department of Neurobiology, Systems Neuroscience Institute, University of Pittsburgh, Pittsburgh, PA, United States, [2] Center for Biologic Imaging, University of Pittsburgh, Pittsburgh, PA, United States, [3] Department of Cell Biology, University of Pittsburgh, Pittsburgh, PA, United States, [4] Department of Radiology, University of Pittsburgh, Pittsburgh, PA, United States, [5] Department of Bioengineering, University of Pittsburgh, Pittsburgh, PA, United States, [6] Department of Neurobiology, University of Pittsburgh, Pittsburgh, PA, United States

Objective: Reanimation of muscles paralyzed by disease states such as spinal cord injury remains a highly sought therapeutic goal of neuroprosthetic research. Optogenetic stimulation of peripheral motor nerves expressing light-sensitive opsins is a promising approach to muscle reanimation that may overcome several drawbacks of traditional methods such as functional electrical stimulation (FES). However, the utility of these methods has only been demonstrated in rodents to date, while translation to clinical practice will likely first require demonstration and refinement of these gene therapy techniques in non-human primates.

Approach: Three rhesus macaques were injected intramuscularly with either one or both of two optogenetic constructs (AAV6-hSyn-ChR2-eYFP and/or AAV6-hSyn-Chronos-eYFP) to transduce opsin expression in the corresponding nerves. Neuromuscular junctions were targeted for virus delivery using an electrical stimulating injection technique. Functional opsin expression was periodically evaluated up to 13 weeks post-injection by optically stimulating targeted nerves with a 472 nm fiber-coupled laser while recording electromyographic (EMG) responses.

Main Results: One monkey demonstrated functional expression of ChR2 at 8 weeks post-injection in each of two injected muscles, while the second monkey briefly exhibited contractions coupled to optical stimulation in a muscle injected with the Chronos construct at 10 weeks. A third monkey injected only in one muscle with the ChR2 construct showed strong optically coupled contractions at 5 ½ weeks which then disappeared by 9 weeks. EMG responses to optical stimulation of ChR2-transduced nerves demonstrated graded recruitment relative to both stimulus pulse-width and light intensity, and followed stimulus trains up to 16 Hz. In addition, the EMG response to prolonged stimulation showed delayed fatigue over several minutes.

Significance: These results demonstrate the feasibility of viral transduction of peripheral motor nerves for functional optical stimulation of motor activity in non-human primates,

OPEN ACCESS

Edited by:
Jeffrey R. Capadona, Case Western Reserve University, United States

Reviewed by:
Amy L. Orsborn, University of Washington, United States
Andres Canales, Massachusetts Institute of Technology, United States

***Correspondence:**
Andrew B. Schwartz
abs21@pitt.edu

Specialty section:
This article was submitted to Neuroprosthetics, a section of the journal Frontiers in Neuroscience

Received: *30 November 2018*
Accepted: *08 July 2019*
Published: *31 July 2019*

Citation:
Williams JJ, Watson AM, Vazquez AL and Schwartz AB (2019) Viral-Mediated Optogenetic Stimulation of Peripheral Motor Nerves in Non-human Primates. Front. Neurosci. 13:759. doi: 10.3389/fnins.2019.00759

a variable timeline of opsin expression in a animal model closer to humans, and fundamental EMG response characteristics to optical nerve stimulation. Together, they represent an important step in translating these optogenetic techniques as a clinically viable gene therapy.

Keywords: optogenetics, neural prosthetics, peripheral nerve stimulation, functional optical stimulation, neurostimulation, muscle control, tissue clearing

INTRODUCTION

Disease states such as severe spinal cord injuries (SCIs) are often accompanied by muscle paralysis and loss of motor function. In these cases, restoration of native muscle and motor function is the ultimate goal of therapeutic interventions. Brain-Machine Interfaces (BMIs), which attempt to reroute control signals from an intact brain to a motor effector and effectively bypass the site of injury, have made great strides toward achieving this goal over the last several decades. Motor BMIs have progressed from simple control of a computer cursor (Serruya et al., 2002; Taylor et al., 2002; Leuthardt et al., 2004; Revechkis et al., 2015) to high-dimensional control of a robotic arm (Hochberg et al., 2012; Collinger et al., 2013; Wodlinger et al., 2015). While these systems provide an excellent intermediate step and can restore a significant degree of independence to patients that they may not have experienced for many years, they do not address the desired goal of native limb reanimation.

The traditional approach to reanimating paralyzed limbs is to electrically stimulate muscles or their nerves. This approach, often referred to as Functional Electrical Stimulation (FES), was previously coupled to residual movements or muscle activity to control the electrical stimulation of paralyzed muscles (Peckham et al., 2002; Kilgore et al., 2008). More recently, intramuscular FES has been coupled with BMI control signals by several groups to produce brain-controlled modulation of native muscle activity and limb movements in both non-human primates (NHPs) (Moritz et al., 2008; Ethier et al., 2012) and human subjects (Bouton et al., 2016; Ajiboye et al., 2017; Biasiucci et al., 2018). While these studies demonstrate restoration of volitional control over previously paralyzed muscles and can convey a significant increase in independence to a patient, the control offered by these systems is far from ideal naturalistic control. For example, in the study by Ajiboye et al. (2017), a C4-level SCI patient implanted with intracortical microelectrode arrays regained some volitional control over paralyzed arm muscles after pairing FES of those muscles with intracortical control signals. This scheme allowed the subject to reclaim certain daily functions such as feeding himself, but these movements were quite slow, taking several tens of seconds for tasks that most people would complete in a second or two. FES-mediated movements in this study also required additional hardware to support the arm against gravity. These studies demonstrate that the current state-of-the art for muscle stimulation necessitates major technological advances to approach practical relevance or even approach the performance level of other BMI-driven effectors such as robotic arms.

The difficulties highlighted by that study may be due to several inherent drawbacks of FES. These potentially include a non-physiological, random or reverse recruitment order of muscle fibers (Henneman, 1957; Fang and Mortimer, 1991; Singh et al., 2000; Lertmanorat and Durand, 2004; Gregory and Bickel, 2005; Bickel et al., 2011), a poorly graded, steeply sigmoidal recruitment curve making controlled stimulation of intermediate force values difficult to achieve, and early fatigue of muscle contractions (Gregory and Bickel, 2005). These factors have limited the use of FES for reanimation of paralyzed muscle.

A potential alternative to FES that may circumvent some of these shortcomings is the use of peripheral optogenetic techniques to elicit muscle activity through Functional Optical Stimulation (FOS). In this approach, light sensitive ion channels, i.e., "opsins," are inserted into the motor nerve axonal membrane, allowing the nerve to be depolarized using light stimulation. FOS experiments in rodents have suggested that this approach may hold several advantages over FES by overcoming the drawbacks of FES discussed above. In an initial study, Llewellyn et al. demonstrated in transgenic mice expressing the blue-light sensitive channelrhodopsin (ChR2) that optically stimulating motor nerves elicits a natural recruitment of muscle fibers; small diameter muscle fibers are recruited first with low-amplitude stimulation, and larger fibers are recruited with increasing stimulation intensities (Llewellyn et al., 2010). This combination of fiber activation produced a wide dynamic range of forces from fine to gross. This differs from the recruitment order of muscle fibers observed with FES. Related to these observations of natural recruitment order, Llewellyn et al. also found that muscle activation leads to decreased muscle fatigue, delaying the onset of muscle fatigue to repetitive optical stimulation for several minutes vs. only a few tens of seconds with electrical stimulation (Llewellyn et al., 2010). Additionally, viral transduction of opsins sensitive to different wavelengths of light makes it possible to selectively target only nerve fibers innervating a desired muscle. Conversely, FES is relatively non-selective in stimulating axons to individual muscles at proximal nerve sites. For example, electrically stimulating the sciatic nerve will activate contractions of the gastrocnemius, tibialis anterior, and other lower leg muscles non-specifically. However, Towne et al. have demonstrated selective activation of a single viral-targeted tibialis anterior muscle with optical stimulation at a common proximal sciatic nerve location (Towne et al., 2013). Although selective electrical stimulation can be accomplished to a degree, it typically requires complex spatial activation patterns or deforming the nerve (Tyler and Durand, 2002). Finally, although optical stimulation can cause photoelectric artifacts

if shone directly on an electrode (Kozai and Vazquez, 2015), it does not cause electromyographic (EMG) artifacts to arise from distant optical stimulation, unlike the volume-conducted artifact associated with electrical stimulation of a muscle or nerve. This artifact-free stimulation could simplify signal processing in closed-loop stimulation schemes that rely on EMG or intraneural feedback (Yeom and Chang, 2010; Bruns et al., 2013). Overall, these potential advantages may make peripheral optogenetic stimulation a viable alternative to FES for muscle activation in neuroprosthetic applications.

To date, peripheral optogenetic activation of muscle activity displaying these potential benefits has only been demonstrated in rodents. Across these studies, several methods have been used to label motor nerves with stimulating opsins. Llewellyn et al. used a transgenic mouse line to express ChR2 in neurons in the peripheral nervous systems (PNS) under the Thy1 promoter, allowing the authors to elicit muscle activity through optical stimulation of peripheral motor nerve axons (Llewellyn et al., 2010). While use of transgenic mouse lines of this nature is useful for testing the neurophysiological characteristics of optogenetic stimulation, this type of germ-line manipulation is impractical for human applications. Bryson et al. demonstrated optical control of muscle in wild-type mice after transplanting motor neurons expressing ChR2 derived from embryonic stem cells into a nerve graft site (Bryson et al., 2014). A more common approach in line with genetic manipulation used in other systems and disease models (Asokan et al., 2012) is the utilization of adeno-associated virus (AAV) vectors to enable optical modulation of muscle activity. These include expression of ChR2 in rat peripheral motor nerves following muscle injection of an AAV vector (Towne et al., 2013; Maimon et al., 2017) or expression directly in mouse skeletal muscle tissue following systemic injection (Bruegmann et al., 2015). While direct optical modulation of muscle tissue is feasible, it would require individual light sources for each targeted muscle, and implanting optical stimulation hardware could be difficult in smaller or deep muscles such as intrinsic hand muscles. Conversely, viral transduction of opsins in motor nerve axons offers the potential to independently control multiple muscles from a single proximal nerve location more amenable to light source implantation, making it an appealing approach over muscle transduction.

While the rodent studies above are an important step in exploring the potential of peripheral optogenetic stimulation, translating these techniques to NHPs prior to human trials remains largely unexplored. Indeed, even the development of optogenetic techniques for NHPs in the central nervous system (CNS) has proven challenging with examples of successful viral transduction studies slowly beginning to accumulate. Multiple cortical studies have demonstrated optogenetic perturbation of local cortical network dynamics but did not report appreciable alteration of behavior (Han et al., 2009; Diester et al., 2011; Yazdan-Shahmorad et al., 2016). However, a small number of examples have demonstrated an effect of optogenetic modulation on behavior such as those related to reward (Stauffer et al., 2016), vision (Jazayeri et al., 2012), salience (Dai et al., 2014), eye movements (Cavanaugh et al., 2012; El-Shamayleh et al., 2017), and somatosensation (May et al., 2014). Notably, reports of optogenetic modulation of somatomotor behavior are still lacking. Outside of the brain, a handful of studies have demonstrated viral transduction of peripheral neuromuscular tissue with fluorescent proteins in NHP models (Towne et al., 2009; Okada et al., 2013), but optogenetic modulation of peripheral neural activity in primates similar to the aforementioned rodent studies has not been reported to date. With the difficulties in translating rodent-proven optogenetic techniques to primates, it is likely that similar challenges will be faced in translating peripheral motor optogenetic techniques due to the PNS's greater exposure to the immune system, the differences in rodent vs. primate immune responses, and sheer scale difference.

Given the potential benefits of FOS over current FES approaches for neuroprosthetic applications and the current gap regarding peripheral optogenetic modulation of motor activity in higher-order animal models, the current study examined the feasibility of virally mediated optogenetic modulation of motor activity in a macaque model. We explored the utility of an AAV vector, used successfully in prior rodent FOS studies, to transduce macaque motor nerves with commonly used opsins (ChR2 and Chronos) and drive PNS motor activity in an NHP model. To overcome some of the aforementioned translational challenges, we delivered the virus using a stimulating muscle injection technique to target and deliver virus locally near neuromuscular junctions. We then used optical stimulation of targeted nerves and EMG recordings to functionally assess opsin expression. We next examined the relationships between optical stimulation variables and elicited EMG activity for comparison with previous observations in rodents. Finally, we examined whole tissue imaging of opsin expression to correlate expression variability with observations of functional optical sensitivity in nerve samples. The results presented will not only help to address the feasibility of peripheral viral gene therapy and FOS in BMI applications, but may also help to identify further virus, opsin, and hardware development needed prior to clinical translation.

METHODS

Subjects

For the main focus of this study, three male rhesus macaques (Macaca mulatta), Monkeys M, O, and P, weighing 7–9 kg were used in these experiments. All animal procedures were approved and conducted in accordance with the University of Pittsburgh's Institutional Animal Care and Use Committee.

Viral Constructs

Two high-titer AAV6-based viral vectors were obtained from Virovek, Inc. (Hayward, CA) for use in these experiments. The first vector, AAV6-hSyn-ChR2(H134R)-eYFP, was produced at a titer of 1.04×10^{14} vp/mL. This construct was previously used for AAV-mediated transduction of excitatory opsins in peripheral motor nerves (Towne et al., 2013; Maimon et al., 2017), and has been reported at a range of viral titers. The second construct tested in these experiments replaced the well-studied

opsin, ChR2(H134R), with the more recently developed Chronos (Klapoetke et al., 2014). Chronos has faster kinetics and increased sensitivity over ChR2, but its utility has not been demonstrated in the periphery to date. The AAV6-hSyn-Chronos-eYFP construct was produced by Virovek at a titer of 1.00×10^{14} vp/mL.

Virus Injections

Aseptic techniques were used for all virus injection surgeries. Prior to virus injection, each monkey was sedated with a cocktail of ketamine (20 mg/kg) and xylazine (0.5 mg/kg). For each target muscle, a skin incision was made to expose the muscle while leaving the surrounding fascia intact. Following virus injection procedures as described below, all skin incisions were closed with subcuticular stitches. Injected animals received a 5 day course of antibiotics and were returned to their home cage to recover for at least 3 weeks before evaluation expression.

Monkeys M, O, and P received injections of AAV-based constructs in two, four, and one muscle(s), respectively, as shown in **Figure 1** with injection parameters summarized in **Table 1**. Monkey M was injected in two muscles with the AAV6-hSyn-ChR2(H134R)-eYFP construct. The tibialis anterior (TA) muscle of each leg was injected with construct diluted to relatively low or high titer. The right TA ("high" titer leg) was injected with 160 μL of virus (1.66×10^{13} vp) diluted in hypertonic saline to a total volume of 2 mL (8.32×10^{12} vp/mL). The left TA ("low" titer) was injected with 20 μL of virus (2.08×10^{12} vp) diluted with hypertonic saline to a volume of 2 mL (1.04×10^{12} vp/mL). Ten individual injections were made per muscle with approximately 200 μL of virus solution injected per site.

At each injection site, low-threshold electrical stimulation was used to localize potential motor endplates to minimize the distance virus would have to diffuse before uptake at the neuromuscular junction. A 30 gauge monopolar injectable needle (Technomed, Netherlands) was attached to a tuberculin syringe filled with virus solution, while a metal hub needle attached to a ground lead was inserted through the skin edge. A biphasic waveform (200 μs at 0.25 mA, 400 μs at −0.125 mA) was applied between the needle tip and ground electrode via an analog stimulus isolator (A-M Systems, Model 2200). As electrical stimulation was applied, the needle was slowly advanced into the muscle by hand while monitoring muscle twitches. After finding a needle insertion position facilitating maximum contraction, stimulation was paused and 200 μL of virus was injected over ∼1 min. The needle was held in place for an additional minute before slowly withdrawing it. This process was repeated for each injection site. Injections were aimed at the presumed line of neuromuscular junctions approximately 1/3 of the muscle length away from the proximal end of the muscle. Needle insertions were aimed in both proximal-to-distal and distal-to-proximal fashions toward this zone, and were spaced laterally across the muscle surface.

Monkey O received injections of both the ChR2 and Chronos viral constructs. Four muscles groups (two flexor/extensor pairs) were targeted. In the right leg, we injected the TA muscle with the AAV6-hSyn-ChR2-eYFP construct, and we injected the lateral gastrocnemius (GN) with AAV6-hSyn-Chronos-eYFP. In the left forearm, we injected the extensor digitorum (ED) with the ChR2 construct, and we injected both flexor carpi radialis (FCR) and pronator teres (PT) muscles with the Chronos solution. For each muscle, 100 μL of stock virus was diluted with hypertonic saline to 2 mL total volume (5.02×10^{12} vp/mL for ChR2, 5.0×10^{12} vp/mL for Chronos). The Chronos solution was split evenly between the FCR and PT muscles in the forearm (∼1 mL per muscle over 4–5 sites). Targeting of the muscle endplates and muscle injections were performed in a similar fashion to those described for Monkey M.

Monkey P was injected with the AAV6-ChR2 construct in the right TA muscle. One-hundred microliters of stock virus (1.04×10^{13} vp) was diluted to a total volume of 1 mL with hypertonic saline at a slightly higher concentration (1.04×10^{13} vp/mL) than the highest used in Monkey M. Stimulating injections targeting neuromuscular junctions were used to deliver 900 μL of virus solution to the muscle over 5 sites. The deep peroneal (DP) nerve innervating the TA muscle was also exposed near its insertion into the TA via blunt separation of fibers of the overlying biceps femoris muscle. One-hundred microliters of virus solution was injected directly into the DP nerve over 3 sites.

Expression Evaluation

Each monkey was periodically evaluated for opsin expression over the course of 8–13 weeks. During an evaluation surgery, the monkey was anesthetized, and a previously injected muscle was re-exposed. Blunt dissection was used to separate fascia from the muscle and to expose the innervating nerve. Electrical stimulation of the nerve using a pair of bipolar hook electrodes (Cadwell Laboratories, Kennewick, WA) was used to confirm the identity of the desired nerve. Optical stimulation was delivered using a 400 μm diameter core multimode fiber (ThorLabs, Newton, NJ) connected to a 150 mW, 472 nm fiber-coupled laser (LaserGlow Technologies, Toronto, Ontario). Maximum laser output at the fiber tip was typically around 110 mW. While moving the fiber tip manually along the length of the nerve, optical stimulation trains of 15–20 ms pulses at 2.5 Hz and 100 mW were delivered to scan the nerve for areas sensitive to optical stimulation. A pair of the injectable electrode needles (same model as used for stimulation during muscle injection) was inserted into the muscle belly to measure EMG activity with a metal hub needle in the skin edge serving as electrical ground. EMG electrodes were connected to a low-impedance differential headstage with 20x gain (RA16LI-D, Tucker Davis Technologies (TDT), Alachua, FL). A TDT neurophysiology recording system (RZ-2) was used to coordinate optical stimulation waveforms with EMG recordings. All waveforms were sampled at 24 kHz.

Following periodic evaluations of nerve expression, any retracted muscle and fascia overlying target nerves were sutured in layers with absorbable suture. Skin incisions were closed with subcuticular stitches, and the animal was returned to its cage to recover.

Perfusion, Tissue Clearing, and Imaging

Following final evaluation of opsin expression, each animal was perfused transcardially with 1X phosphate buffer solution (PBS)

TABLE 1 | Virus injection summary.

Monkey	Muscle	Virus injection	Viral concentration (vp/mL)	Total viral load injected (vp)	Visible contractions	Week of sensitivity
M	R. Tibialis Anterior	AAV6-hSyn-ChR2-eYFP	8.32E + 12	1.66E + 13	Yes	8
	L. Tibialis Anterior	AAV6-hSyn-ChR2-eYFP	1.04E + 12	2.08E + 12	Yes	8
O	R. Tibialis Anterior	AAV6-hSyn-ChR2-eYFP	5.02E + 12	1.04E + 13	No	N/A
	R. Gastrocnemius	AAV6-hSyn-Chronos-eYFP	5.00E + 12	1.00E + 13	No	N/A
	L. Extensor Digitorum	AAV6-hSyn-ChR2-eYFP	5.02E + 12	1.04E + 13	No	N/A
	L. Flexor Carpi Radialis/Pronator Teres	AAV6-hSyn-Chronos-eYFP	5.00E + 12	1.00E + 13	Yes (PT)	10
P	R. Tibialis Anterior	AAV6-hSyn-ChR2-eYFP	1.04E + 13	1.04E + 13	Yes	5.5

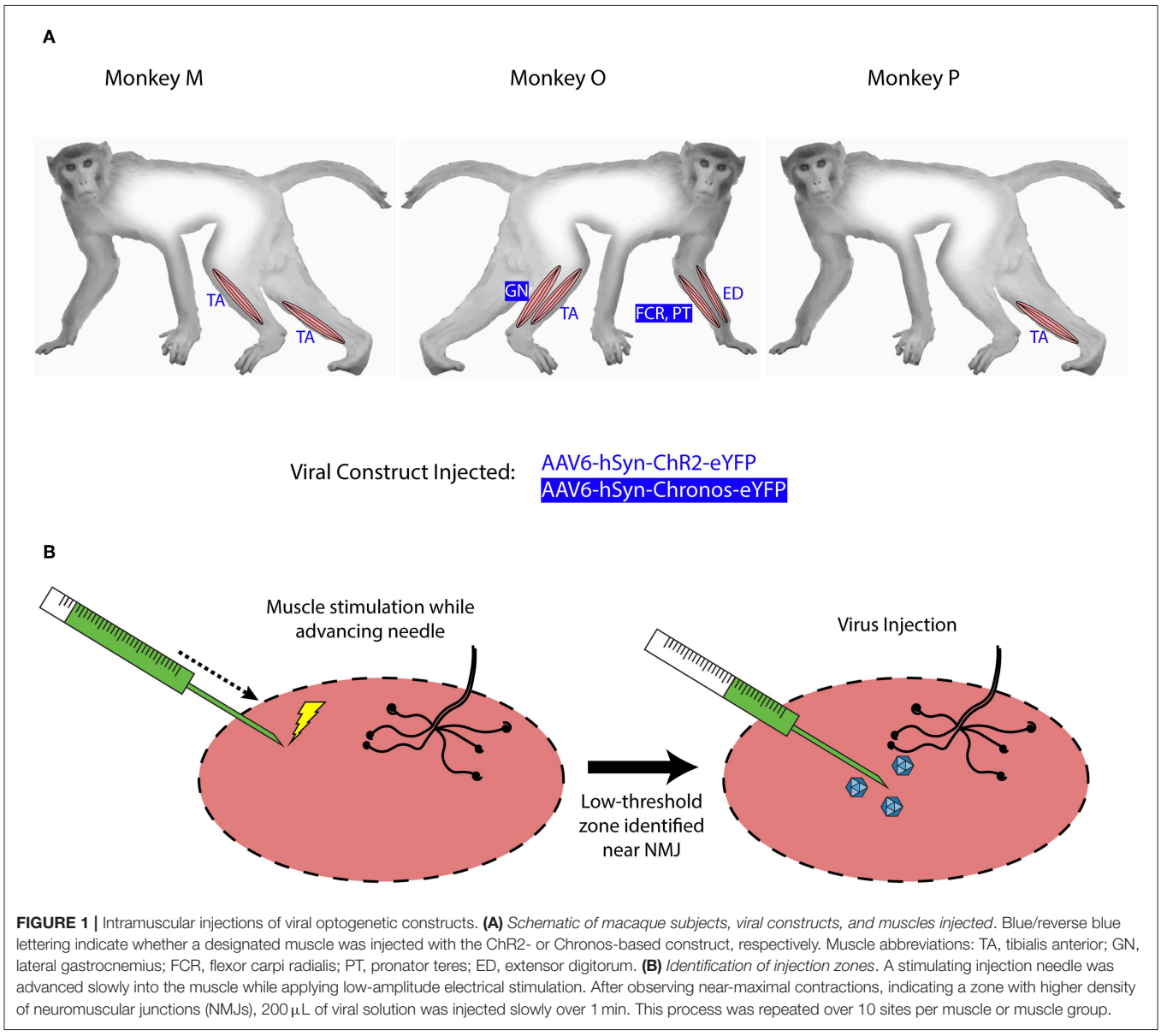

FIGURE 1 | Intramuscular injections of viral optogenetic constructs. **(A)** *Schematic of macaque subjects, viral constructs, and muscles injected*. Blue/reverse blue lettering indicate whether a designated muscle was injected with the ChR2- or Chronos-based construct, respectively. Muscle abbreviations: TA, tibialis anterior; GN, lateral gastrocnemius; FCR, flexor carpi radialis; PT, pronator teres; ED, extensor digitorum. **(B)** *Identification of injection zones*. A stimulating injection needle was advanced slowly into the muscle while applying low-amplitude electrical stimulation. After observing near-maximal contractions, indicating a zone with higher density of neuromuscular junctions (NMJs), 200 μL of viral solution was injected slowly over 1 min. This process was repeated over 10 sites per muscle or muscle group.

followed by 4% paraformaldehyde (PFA). Sections of targeted nerves were harvested and post-fixed in 4% PFA overnight, after which they were stored in 0.02% sodium azide solution in PBS at 4°C while awaiting processing for tissue clearing. Several nerve samples from each animal were reserved for tissue clearing and whole sample imaging. 5–10 mm long sections

of nerve were excised from the main nerve branch directly innervating virus targeted muscles. Nerve samples were cleared using the polyethylene glycol (PEG)-associated solvent system (PEGASOS) passive immersion protocol (Jing et al., 2018). Briefly, following tissue fixation in 4% PFA, tissues were first passively bathed in a 25% Quadrol to decolor the tissue step, followed by gradient solutions (30, 50, 70%) of tert-Butanol (tB) at 37° over 2 days for delipidation and dehydration. Samples were further dehydrated in a solution composed of 70% tB, 27% PEG methacrylate M_n 500 (PEGMMA500), and 3% Quadrol for 2 days. Finally tissues were cleared for at least 1 day in a solution of BB-PEG formed by mixing 75% benzyl benzoate (BB) and 25% PEGMMA500 supplemented with 3% Quadrol until tissues reached transparency. Following clearing, samples were preserved in the BB-PEG clearing medium at room temperature.

Following tissue clearing, whole nerve samples were mounted in BB-PEG and sealed between two rounded cover glass. Tissues were imaged using the RS-G4 ribbon scanning confocal microscope (Caliber I.D., Rochester, NY) (Watson et al., 2017) equipped with an iChrome MLE laser engine (Toptica Photonics, Munich Germany). Large-area mosaic images were captured using the Olympus XLPLN25XWMP2, 25x, 1.05NA, water immersion objective with a scan zoom of 1.7 and lateral resolution of 0.295 microns. Z-steps were acquired at 1.52 microns. Fluorescence from eYFP was detected by using 488 nm excitation and 520/44 nm emission filters. The tissue was imaged from bottom to top with the 488-laser power interpolated linearly through Z from 15% (top) to 30% (bottom). Mosaic images were stitched and assembled by the microscope software.

To facilitate analysis, mosaic images were processed in MATLAB R2017b by first flattening the image and then subtracting background. A unique background filter was calculated for each image by applying a gaussian filter with a standard deviation of 6 and then a morphologic opening with a disk structuring element of radius 200 pixels. A flattening filter was produced by taking the mean of the background filter divided by the background filter:

$$filter_{flattening} = \frac{mean\left(filter_{background}\right)}{filter_{background}}$$

First the flattening filter was applied to both the RAW image and the background filter by multiplying the two images. The flattened background filter was subtracted from the resulting image:

$$Image_{final} = \left(Image_{RAW} \times filter_{flattening}\right) - \left(filter_{background} \times filter_{flattening}\right)$$

Flattened and background-subtracted images were then assembled into volumes using the Imaris File Converter and analyzed using Imaris v9.2.1 (Bitplane). Models of eYFP expressing nerve axon segments were built using the Imaris Surpass surface tool. Manual cleaning of the surface rendering was performed to ensure that labeled regions represented eYFP expressing nerves. Volume and position data for eYFP model surface elements were exported from the surface tool to Matlab where expression volume was binned as a function of longitudinal (Y) position.

RESULTS

Time Course of Expression

Each monkey was tested for expression in targeted nerves intermittently between the injection surgery and final terminal evaluation surgery. Injection results are summarized in **Table 1**. Monkey M was tested at 3 (right TA), 4 (left TA), and 8 weeks (both legs). During evaluation time points at weeks 3 and 4, neither leg showed visible contractions or EMG deflections upon laser stimulation at full power. The deep peroneal (DP) nerve innervating the TA muscle was exposed for stimulation but was not aggressively dissected to avoid permanently damaging the nerve. At week 8, both targeted nerves were re-exposed and tested. Initial optical stimulation along the length of the superficial (anterior) portion of the left DP nerve again did not suggest overt expression of ChR2. However, stimulation of the posteriolateral aspect of the nerve at a single proximal site demonstrated visible contraction of the TA muscle. Optical stimulation of the anterior aspect of the nerve at this location or proximal/distal to it did not elicit muscle contractions. However, following this initial display of sensitivity, the DP was dissected distally to its insertion into the TA muscle where it branches out. At this point, optical stimulation of the nerve and muscle activity became more consistent with several branches showing sensitivity. Evaluation of the DP nerve of the right leg proceeded in a similar fashion with dispersed sensitive spots along the nerve proximal to the muscle, and more consistent sensitivity where the nerve branched out close to the muscle.

Expression of optogenetic transduction in Monkey O was tested at 5, 10, and 13 weeks post-injection. We first tested expression in the nerves leading to the TA and lateral GN muscles of the right leg at 5 weeks. No visible muscle contractions were elicited with optical stimulation of either nerve. At 10 weeks, we tested all targeted nerves in the right leg and left forearm. Neither nerve branch in the leg nor in the nerve supplying the ED muscle of the forearm demonstrated optically sensitivity. A branch of the median nerve supplying the PT muscle in the left forearm (injected with the Chronos vector) did facilitate brisk contraction of the PT when stimulated optically with the fiber-coupled laser. Upon observing optical sensitivity, we further dissected the nerve to accommodate placement of an LED nerve cuff intended for chronic stimulation of the nerve. After initial placement of the cuff, the nerve no longer initiated PT contractions when stimulated with blue light from the cuff or optical fiber. We suspected the nerve may have become irritated by prolonged exposure or irritation during the LED cuff placement, so we removed the cuff, re-sutured all nerve and muscle exposures, and returned the monkey to its home cage. At 13 weeks, we re-tested each targeted nerve. During this experiment, no nerves (including the previously sensitive branch to the PT muscle) exhibited optical sensitivity. Electrical stimulation of the PT muscle's nerve elicited brisk contractions, suggesting that the nerve was healthy.

The DP nerve of Monkey P innervating the injected right TA muscle was tested at 5 ½ weeks and 9 weeks post-injection. At the first checkpoint, optical stimulation of the exposed nerve resulted in small contractions visible through the skin. Optical sensitivity was more consistent along the exposed portion of the nerve than in Monkeys M and O with no obvious insensitive portions of nerve. After returning to check the nerve at the 9 week time point, no visual or EMG evidence of sensitivity to optical stimulation of the target nerve was present.

Visually Observed Responses to Optical Stimulation

Visible contractions to optical stimulation of targeted nerves were observed in all three monkeys. In monkey M, contractions of the TA muscle were clearly visible in both legs (**Supplementary Movie 1**). Additionally, contractions of different portions of the muscle could be observed when different fascicles were stimulated at the branch-out location of the nerve near insertion into the muscle. However, even at full power stimulation (>100 mW, 30 ms pulse duration), optical stimulation along the nerve did not produce functional movement of the lower leg (i.e., dorsiflexion of the foot). For the short period of time that we observed optical sensitivity in monkey O, optical stimulation of a branch of the median nerve produced brisk contractions of the PT muscle similar to those observed in monkey M. Again, although clearly visible, these contractions did not result in pronation of the forearm. Finally, optical stimulation of the right DP nerve in Monkey P resulted in contractions of the TA that could be seen through the skin before further exposing the muscle belly.

As a set of visual checks that opsin expression was limited to nerve tissue innervating the target muscle, no muscle contractions were observed when the injected muscle was directly stimulated with blue light. In addition, optical stimulation of nearby non-injected muscles and their corresponding nerves did not induce visible contractions or EMG activity.

Individual Optical Pulses Elicit Graded EMG Responses to Pulse Duration and Intensity

After observing visual responses to optical stimulation in monkey M, we recorded the EMG response of each TA muscle to variations in several optical stimulation parameters. First, the pulse duration was varied from 1 to 30 ms (100 mW). The delay from the onset of the optical pulse to a deflection in EMG activity was consistent across muscles at approximately 12 ms. As shown in **Figure 2A**, the length of the evoked EMG waveform stays

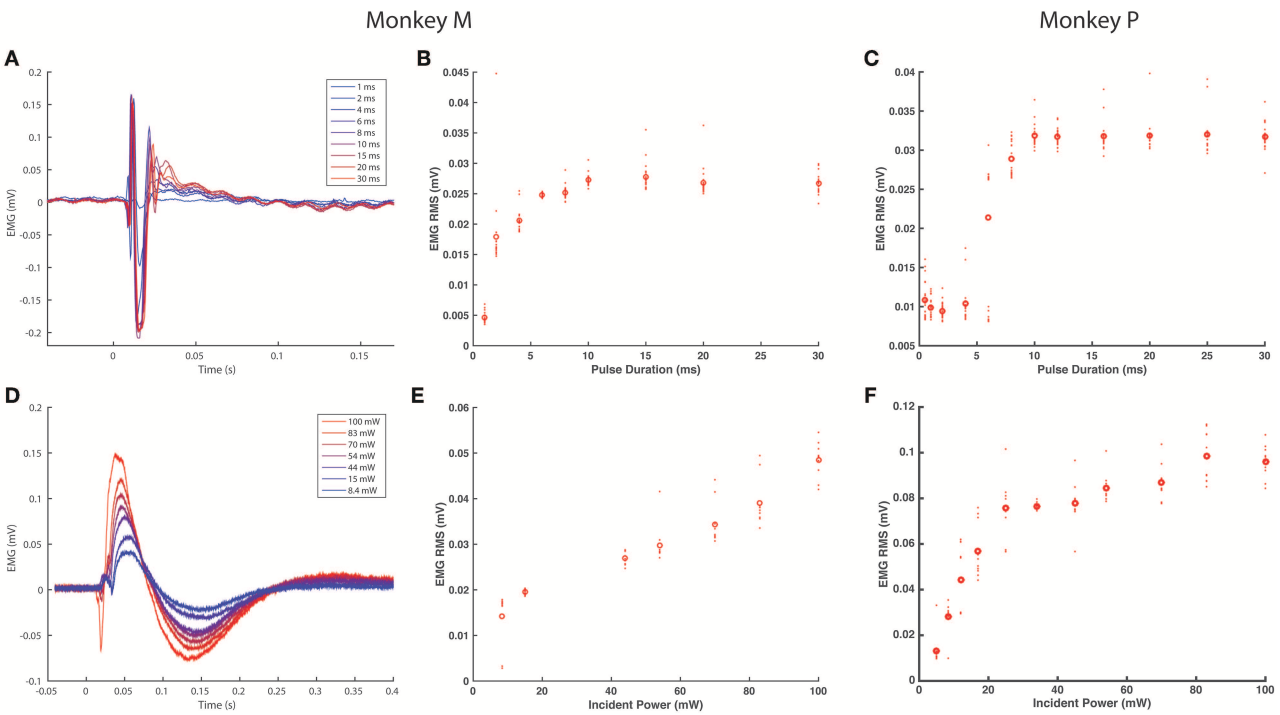

FIGURE 2 | EMG response characteristics to optogenetic stimulation. **(A–C)** *EMG response to varying optical pulse duration*. **(A)** shows stimulus averaged EMG traces from the right TA muscle of monkey M, color-coded by optical pulse duration varying from 1 to 30 ms (20 pulses, 2.5 Hz trains), while **(B)** shows the corresponding distributions of RMS values. **(C)** shows the corresponding EMG vs. optical pulse duration curve from monkey P. **(D–F)** *EMG response to varying optical power*. **(D)** depicts stimulus-averaged EMG waveforms from the left TA muscle of monkey M, color-coded by optical power measured at the output of the optical fiber. Stimulus trains consisted of 20 pulses of 20 ms duration at 2.5 Hz. **(E)** illustrates the corresponding trend in EMG RMS vs. optical power, while **(F)** displays similar data from monkey P. Open circles in **(B–E)** and **(D)** indicate mean RMS values while dots indicate RMS responses for individual optical pulses.

relatively constant while the peak amplitude and RMS of EMG activity (**Figure 2B**) increases gradually with pulse duration until plateauing at pulse durations above 10 ms. We then measured the evoked EMG activity as a function of the incident intensity of optical stimulation. **Figure 2D** shows that the magnitude of the EMG waveform changed with varying optical intensity, while **Figure 2E** depicts a near-linear monotonic increase of EMG activity with optical intensity within the range studied. Results from Monkey P showed similar trends with a plateau in elicited EMG activity near 10 ms and a linear increase in EMG with light intensity (**Figures 2C,F**). These trends are consistent with results from previous studies in rodents utilizing AAV6 and ChR2 (Llewellyn et al., 2010; Towne et al., 2013), and support the notion that optogenetic stimulation offers graded recruitment of muscle activity.

As we injected each TA muscle in monkey M with different viral loads approximately an order of magnitude apart (1.66×10^{13} vp in the right TA vs. 2.08×10^{12} vp in the left TA), we examined whether viral load impacted viral transduction and optically elicited muscle activity. We compared the EMG RMS activity in each leg elicited by similar trains (20 ms pulses, 100 mW, 2.5 Hz). Although visual observation did not suggest distinct differences in the magnitude of muscle contractions, the EMG recorded from each leg showed appreciable differences in the shape and duration of the stimulus-averaged waveform. The right TA demonstrated a sharp, transient spike lasting <100 ms (**Figure 2A**) while the left TA demonstrated a waveform lasting 250 ms (**Figure 2C**). Counterintuitive to the trend expected with respect to viral load, these waveforms correspond to EMG RMS values of 0.027 and 0.051 mV, respectively. As we observed above that optical sensitivity was not consistent along a nerve, these differences could arise due to the accessibility of labeled fibers at a given location as opposed to the total number of transduced nerve fibers. In general, however, the range of viral loads injected in this study did not appear to directly correlate with differences in optically stimulated EMG activity.

EMG Response to Optical Pulse Trains

After measuring basic EMG responses of optogenetically labeled nerves to single pulses of varying duration and intensity, we then examined the response to longer trains. EMG activity was measured over 10 s blocks of continuous stimulation (20 ms, 100 mW) at increasing pulse frequencies from 2 to 30 Hz. The train of responses within a frequency block (RMS value of 600 sample/24.6 ms window following the onset of each light pulse) was then normalized to the response of the block's first stimulus pulse to assess how well the nerve and corresponding muscle activation could track the optical stimulus. As shown in **Figures 3A,B**, EMG responses in Monkey M tracked optical stimulation relatively well for pulse frequencies below 16 Hz, retaining EMG responses near 50% of their maximum initial response. Between 16 and 20 Hz, however, stimulus tracking appears to suffer as the normalized response drops precipitously. At 20 Hz, occasional EMG responses near 50% are interspersed throughout the train from 2 to 10 s, but these are dominated by weak EMG spikes as the nerve/muscle fail to recover. Monkey P demonstrated a similar frequency response with a noticeable dropoff in EMG-optical stimulus coupling between 12 and 16 Hz (see **Figures 3C,D**). These results suggest a functional maximum stimulation frequency below 20 Hz, similar to reports of the frequency response of ChR2 in neuronal culture (Nagel et al., 2003; Boyden et al., 2005; Mattis et al., 2012).

EMG Shows Delayed Decay With Prolonged Optical Stimulation

Finally, we assessed for any decay in optical sensitivity following optical stimulation in a transduced nerve in Monkey M. The right DP nerve was stimulated continuously via the blue laser at maximum power with a 10 Hz, 20 ms optical pulse train for 2 min. **Figures 4A,B** depicts the raw EMG trace from monkey M's right TA muscle as well as the normalized RMS response to stimulation over time. The normalized response falls to 70% of maximum within a few seconds and then levels off similar to traces above 12 Hz in **Figure 3**. However, after 40 s, the muscle response again trends gradually downward over the next 80 s before approaching 40% of the initial EMG RMS response at the end of stimulation. Optical stimulation of the right DP nerve of Monkey P showed a similar profile with an initial drop in EMG rms after the initial few pulses followed by a sustained, consistent EMG activity for the rest of the 2 min (see **Figures 4C,D**). The slow decline observed in this study is again consistent with the delayed time course of muscle fatigue with optical stimulation observed in rodent studies (Llewellyn et al., 2010).

Whole Tissue Imaging Demonstrates Variable Opsin Expression

After final evaluation of functional expression, nerve samples were harvested, cleared, and imaged as whole samples using ribbon confocal microscopy to examine opsin expression patterns. **Figure 5A** depicts native eYFP fluorescence of an intact whole nerve sample from the right DP nerve of Monkey M, while no similar fluorescence of fiber tracts was observed in a control nerve from an uninjected muscle as seen in **Figure 5B**. Imaris software was used to trace the eYFP expression in **Figure 5A** and approximate a longitudinal profile of expression. 3D surfaces corresponding to positive eYFP expression were first computed using a built-in local background signal subtraction algorithm and manual removal of noisy features, with the resulting surfaces highlighted in **Figure 5C**. The volume of these surfaces was then binned as a function of distance along the length of the nerve (200 μm bins), and the resulting longitudinal profile of opsin/eYFP expression was plotted in **Figure 5D**. As seen from **Figures 5C,D**, expression of the viral gene product was not uniform along the nerve as patches of expression would emerge and disappear along the nerve. This finding corroborated the previously described variability in the nerve's sensitivity to optical stimulation (section Time Course of Expression) as well as similar observations in some of our parallel rodent pilot experiments (Williams et al., 2016). Nerves that had demonstrated optical sensitivity at some point during an animal's experimental timeline but were insensitive by the terminal checkpoint (i.e., right median nerve branch to the PT muscle of Monkey O, right DP nerve to the right TA muscle of Monkey

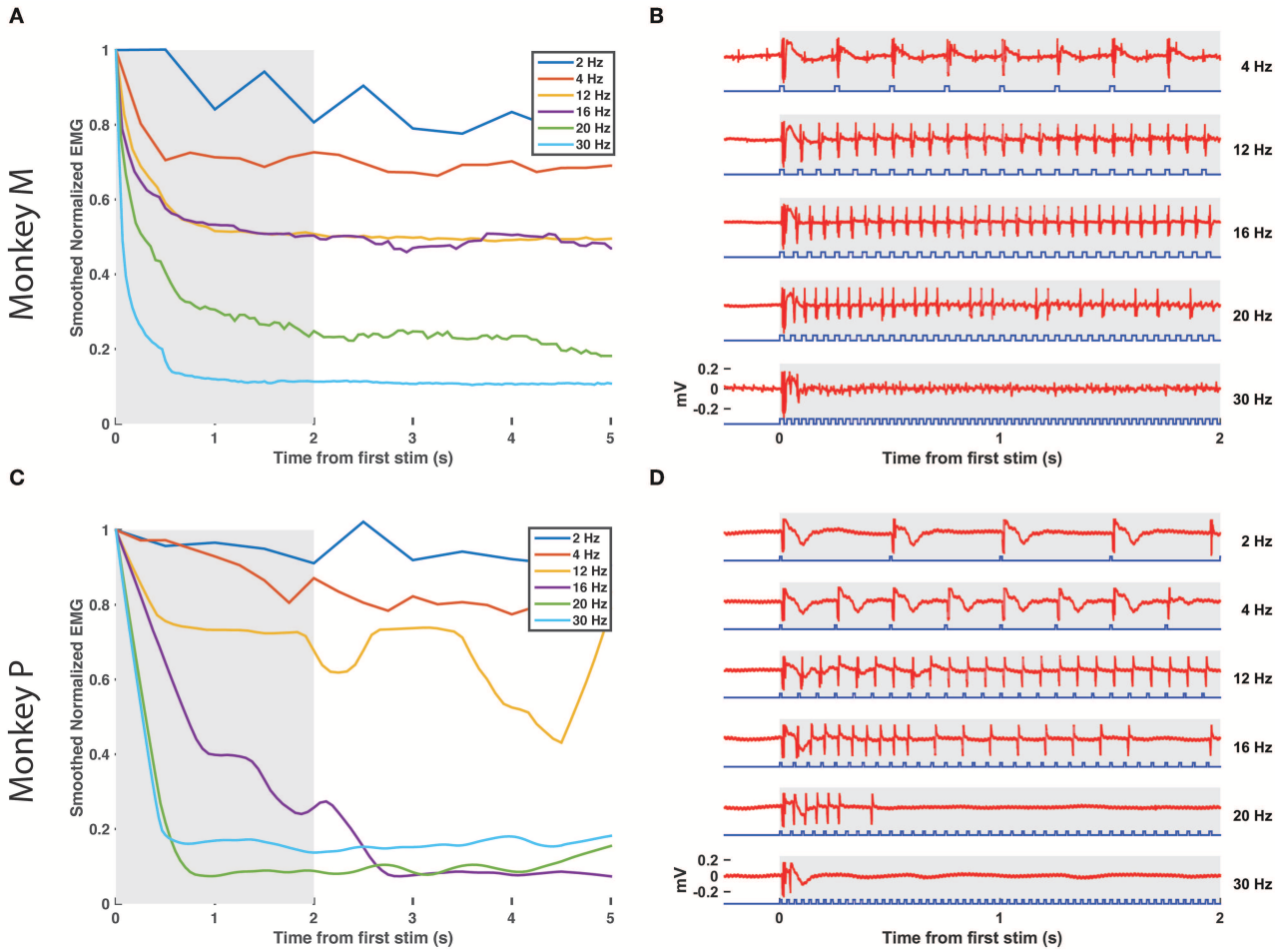

FIGURE 3 | EMG tracking of optical stimulation trains. **(A,B)** The right DP nerve of monkey M was stimulated with trains of varying frequency (2–30 Hz, 20 ms pulse width, 100 mW) for 10 s while recording EMG from the corresponding TA muscle. The RMS value of the EMG activity elicited by each stimulus pulse (24.6 ms window following pulse onset) was calculated and normalized by the RMS elicited by the first pulse in the train. **(A)** depicts the smoothed EMG response to prolonged optical stimulation at various frequencies, while **(B)** depicts the first 2 s of raw EMG responses from the shaded window in **(A)**. Although a significant drop in elicited EMG activity within the first 1–2 s is present at each frequency, stimulus trains below 16 Hz are able to maintain normalized EMG activity at or above 50% of first stimulus magnitude. Between 16 and 20 Hz, however, elicited EMG waveforms become more erratic as some spikes are missed. EMG responses to stimulus trains above 20 Hz drop off precipitously to below 20% of first stimulus response magnitude. **(C,D)** Similar experimental analysis and results as in **(A,B)** from the right DP nerve and TA muscle of monkey P.

P) were cleared and imaged similarly to the nerves in **Figure 5**. Reporter expression in these nerves at the time of perfusion was grossly absent or indistinguishable from background suggesting that loss of optical sensitivity was related to loss of opsin expression along the nerve (see **Supplementary Figure S1**).

DISCUSSION

This study represents a critical step in translating the potential of virally mediated peripheral optogenetics to a clinical therapy capable of alleviating a number of motor diseases or injuries. We have demonstrated that the AAV6-hSyn-ChR2 vector previously shown to be efficacious in transducing peripheral motor axons in rodents following muscle injection (Towne et al., 2013; Maimon et al., 2017) is also a viable vector for peripheral expression of light-sensitive opsins in non-human primates. Our results also exhibit several of the suggested benefits of peripheral optogenetic stimulation over electrical stimulation of muscle activity including graded muscle activation and delayed muscle fatigue. Finally, the correlation of EMG responses to basic optical stimulation parameters lays a foundation from which to approach the design of functional optical stimulation paradigms. Although this study is an important proof-of-concept demonstration, our results also highlight several of the necessary hurdles to be addressed prior to clinical viability as well as new potential avenues of investigation.

Time Course of Opsin Expression

Because we employed a novel longitudinal study of nerve expression in Rhesus monkeys with periodic checks of optical

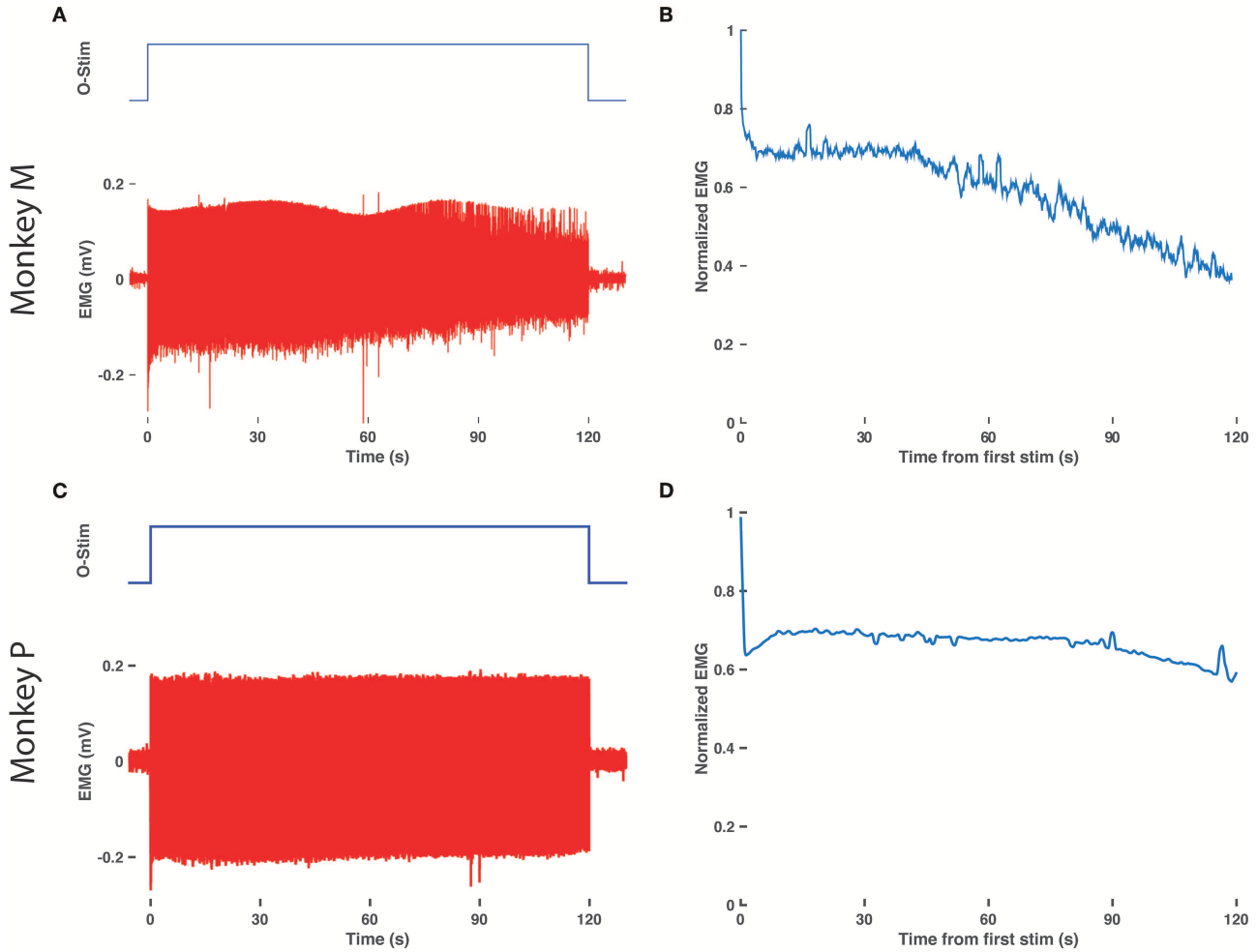

FIGURE 4 | Delay in EMG decay with prolonged optical stimulation. **(A)** Raw EMG traces (bottom, red) from the right TA muscle of monkey M in response to 2 min of optical stimulation (top blue trace, duration of train of 20 ms pulses at 10 Hz). **(B)** Normalized EMG response over time. The RMS response to each optical stimulation pulse was calculated over a 600 sample/24.6 ms window following the onset of each pulse and then normalized to the response to the first pulse of the 2 min train. **(C,D)** Same as in **(A,B)**, repeated for the right TA muscle of monkey P.

sensitivity, we were able to construct a gross timeline of expression in each animal for comparison with other studies and species. Towne et al. utilized a 4–6 week incubation period prior to assessing expression of ChR2 following intramuscular virus injection in rats (Towne et al., 2013). Similarly, a 4 week incubation period was utilized prior to evaluating the expression of eGFP in the spinal cord following intramuscular injection of AAV6-CMV-eGFP in African green monkeys (Towne et al., 2009). However, a recent study utilizing transdermal stimulation of ChR2-labeled nerves mediated by AAV6 (Maimon et al., 2017) suggests that peak transgene expression may occur later in rats, between 5 and 8 weeks, although even these gross time points of peak sensitivity showed considerable variability. Our findings agree with this variable and potentially extended time course of expression as optical sensitivity was observed initially at 5 ½, 8, and 10 weeks post-injection. In the case of monkey P, although expression was evident relatively early at 5 ½ weeks, optical sensitivity had disappeared by the next check at 9 weeks. As we did not test each injected muscle during earlier evaluations in the first two monkeys in order to minimize surgical manipulations at a given site, we cannot rule out that some sites may have demonstrated optical sensitivity at earlier time points similar to Monkey P. Additionally, the focal sensitivity observed along the left DP nerve of monkey M raises the possibility we did not fully expose or probe one of these focal "hotspots" of sensitivity during our earlier assessments while attempting to leave the surrounding tissue grossly intact. Once we more aggressively exposed the DP nerve and its insertion into the TA muscle, stimulation of one of these hotspots likely became more probable. In any case, the time course of expression, as well as differences between species, remains a critical yet poorly understood process.

One potential confound in our experimental design is the multiple surgical procedures utilized to test nerves for optical sensitivity. The variable timeline of functional expression

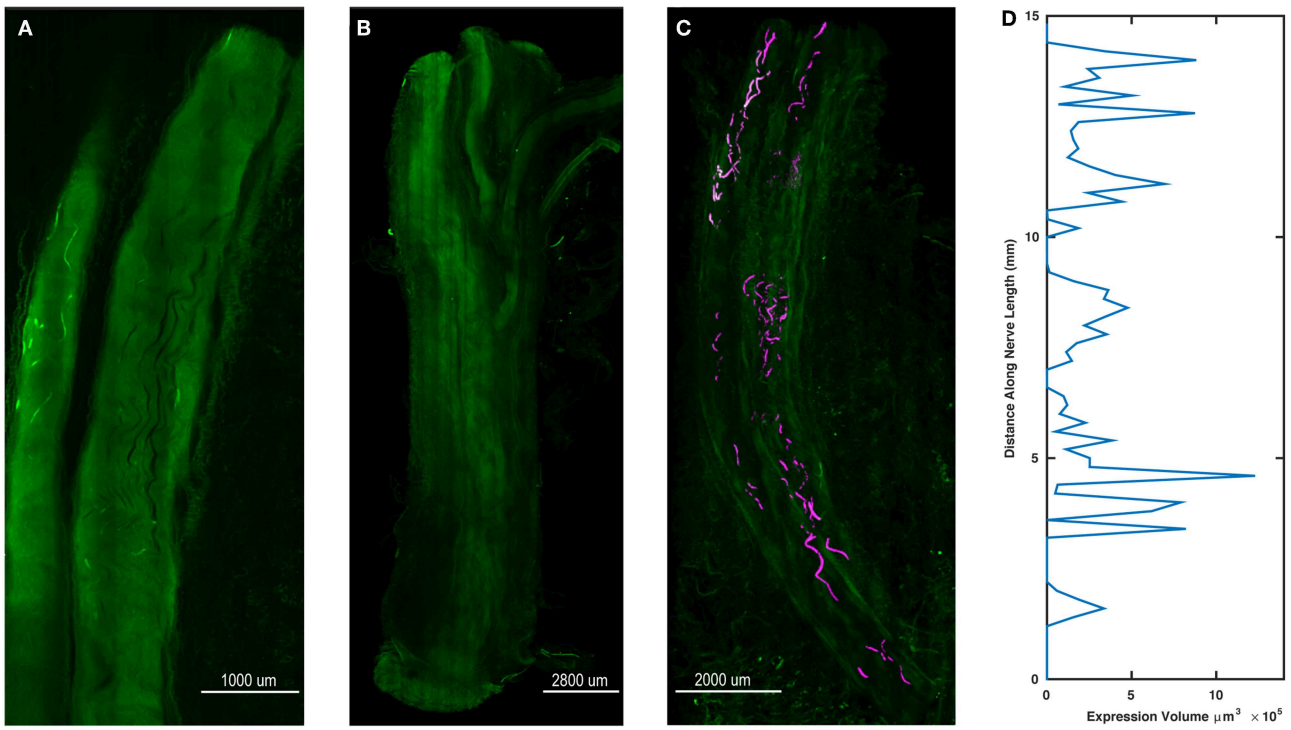

FIGURE 5 | Spatial variability of transgene expression in cleared whole nerve sections. **(A)** Native eYFP fluorescence observed in a cleared nerve section from the right DP nerve of Monkey M using ribbon confocal microscopy. Fluorescent labeling of individual axonal fibers appears to fade in and out within the displayed segment. **(B)** Control nerve from non-injected muscle. In contrast to **(A)**, no distinct patterns of increased fluorescence along individual axons are discernable. **(C)** Maximum intensity projection zoomed-out view of the cleared nerve segment in **(A)** with expression sites marked. eYFP positive axon segments were labeled in software as 3D surfaces (purple) to highlight the variable labeling of axons along the length of the nerve segment. **(D)** Volume of eYFP expression (horizontal axis) as a function of longitudinal distance (vertical axis) along the nerve in **(A,C)**. The dependent variable axis (distance along nerve length) has been rotated to the vertical axis to roughly align with the nerve in **(C)** and displays how viral expression varies along the length of the nerve.

observed in this study supports testing at several time points so as not to miss a window of expression as opposed to using a single checkpoint and perfusion at 6 or 8 weeks as is often employed in similar studies (Towne et al., 2009). However, it is possible that each surgical manipulation of the muscle and nerve could cause an inflammatory or immune response that could interfere with future expression and optical sensitivity. Whereas transdermal illumination of targeted nerves offers a non-invasive approach to probe functional expression in rodents (Maimon et al., 2017), the scattering of blue light caused by additional tissue thickness between skin and nerve in a macaque makes this approach ill-suited to evaluating expression in large primates. Chronically implanted light sources (e.g., LED cuff or fiber) would offer the possibility of evaluating sensitivity over time without additional surgical events, but it is very likely that a device implanted around the nerve could induce a foreign body response that might also compromise expression or efficient light delivery. In the current study, the nerve, muscle, and surrounding fascia did not typically display significant scar tissue buildup between evaluation surgeries, and functional expression was observed in nerves that had already been exposed in a prior evaluation surgery. Thus, we hypothesize that our surgical protocol had minimal impact on opsin expression and offered a reasonable approach to grossly evaluate optical sensitivity over an uncertain timeline compared to unproven alternatives.

Considerations for Chronic Optical Stimulation

Our results also bring forth several considerations for chronic FOS. As one potential application of this gene therapy is to restore volitional control of paralyzed muscle activity through a hybrid optogenetic-BMI, optical nerve stimulation hardware such as chronic LED or fiber optic nerve cuffs must be able to consistently stimulate opsin-labeled axons over a period of years. A potential benefit of using chronically implanted optical nerve cuffs on virally targeted nerves would be the ability to assess the time course of expression without additional surgical procedures. However, the variable expression and sensitivity pattern of ChR2 observed in monkey M in **Figure 5** and some of our parallel rat studies (Williams et al., 2016) suggests that proper placement of stimulation hardware for either of these applications may be more challenging than initially anticipated. Correct temporal assessment of opsin expression patterns would require blind, accurate placement of nerve cuffs soon after injection over high expression zones on the nerve. Similarly, to provide consistent

chronic optical stimulation capabilities in a rehabilitation setting would require (1) an additional evaluation surgery following the virus incubation period to properly place optical cuffs, (2) securing the cuff such that it does not move relative to the hotspot of expression on the nerve, and (3) stability of expression/low turnover at the hotspot. It is possible that the variable optical sensitivity and fluorescent expression observed in this study is due in part to poor expression and trafficking of opsins to the axonal membrane, although another likely contributor may be the immune system through a piecemeal recognition and degradation of opsins by an immune response. Elucidating the underlying cause of this problem could then direct further development of opsins or promoters (Chaffiol et al., 2017) with better expression and trafficking characteristics vs. development of injection techniques (Favre et al., 2000; Burger et al., 2005; Harris et al., 2012; Tosolini and Morris, 2016; Williams et al., 2016), recombinant viruses (Bartel, 2011; Tervo et al., 2016) to increase the efficiency and total number of axons transduced within a nerve, or immunosuppressive approaches to maintain expressed opsins.

Transduction as a Function of Viral Load

As we contemplate potential approaches to improve opsin expression along the nerve, we must also examine the results of this study with respect to viral load delivered to the muscle. As a first pass study, we used a range of viral loads grossly spanning approximately an order of magnitude ($\sim 10^{12}$-10^{13} vp per muscle) between the three monkeys with no obvious trend in expression. The lower end of this range is consistent with a previous study by Towne et al. in African green monkeys (Towne et al., 2009). However, the range of viral loads per kilogram of bodyweight used in this study (9.24×10^{11}-1.84×10^{12} vp/kg) is an order of magnitude lower than the high titer intramuscular injections used by Maimon et al. in rats ($1.5–2.5 \times 10^{13}$ vp/kg) (Maimon et al., 2017). Assuming that the mass and volume of the muscles targeted in these studies scale approximately with total body weight, a lack of functional limb movement from optical stimulation in this study could be explained by an insufficient dose of viral particles delivered to muscles with much greater volume compared to prior mouse and rat models. The limited sample size afforded by early NHP studies such as this often precludes the systematic examination of factors such as viral load, but based on rodent studies, it is possible that doses on the order of 10^{14} vp per muscle might be necessary to yield consistent opsin expression that is functional for eliciting limb movements in primates.

Virus Delivery Approaches

The differences in viral load as a function of body weight across animal models highlights another difficulty in scaling this gene therapy approach up to humans. Because the volume of muscle and corresponding zone of neuromuscular junctions targeted for viral uptake increases dramatically from rodent to primate, efficient delivery of viral particles to the entire motor end plate may become both expensive and technically challenging. Our first attempt to address this challenge was to simply increase the volume of viral solution injected with hypertonic saline to be on the same order of magnitude used in rodent studies ($\sim$200 μL/kg bodyweight vs. 100 μL/kg bodyweight in Maimon et al., 2017) with the potential ramifications discussed above. Our second approach was to attempt to localize zones of high neuromuscular junction density near the motor end plate using electrical stimulation. Previous rodent studies have demonstrated that targeting muscle injections along motor endplates greatly enhances motor neuron transduction (Tosolini et al., 2013; Tosolini and Morris, 2016). Targeting of the motor end plate as in these studies requires prior histological mapping of the motor end plate in a given muscle *in situ* followed by visual alignment of anatomical landmarks in the subject to be injected. Conversely, our approach uses electrophysiological responses to map the end plate and potentially account for anatomical variability between animals. A third injection approach that we employed in Monkey P that may be promising for scaling up injections with animal size was to inject virus directly into the nerve branch of interest. Our experience with this technique has shown that intraneural injections near the insertion of the nerve into the muscle may effectively utilize the nerve sheath to contain and funnel the virus toward the motor end plate as the nerve branches out within the muscle (Williams et al., 2016). Therefore, virus that does not directly enter nerve axons upon injection but instead resides in the connective tissue perineurium may still be guided back down to the muscle where it may have a greater probability of uptake at neuromuscular junctions. Utilization of nerve injections in this manner could significantly reduce the volume of virus needed for effective motor neuron transduction in larger animals such as the macaque. Intraneural injections at sites more proximal to the spinal cord such as the sciatic nerve do hold the possibility of transducing unwanted sensory neurons. However, injecting the nerve closer to the target muscle would likely minimize unrelated sensory transduction or limit it to proprioceptive fibers that could be utilized for feedback. Alternatively, future muscle injection approaches may seek to incorporate advancements utilized in convection enhanced delivery (CED) currently used to deliver drugs and gene therapy in the brain (Yazdan-Shahmorad et al., 2016).

Viral Vector Design

In addition to the load and route of viral particles delivered to motor nerves, the composition of the viral construct itself holds great potential for improvement of motor nerve transduction. The mechanisms by which AAV vectors undergo uptake at the neuromuscular junction and traffic to the spinal cord are not completely understood, but presumably it is a receptor-mediated process facilitated by domains on the viral capsid which confer tissue tropism to various serotypes. A better fundamental understanding of these uptake and transport processes could inform the design of viral vectors for peripheral motor gene therapies. An alternative approach recently taken by several groups is "directed evolution" or high-throughput screening and selection of recombinant AAV variants for a desired trait (Dalkara et al., 2013; Choudhury et al., 2016; Tervo et al., 2016). Similarly, the hSyn promoter has been commonly used for peripheral nerve transduction

due to its specificity for neural tissues yet relatively strong expression. Using a promoter restricting expression to specific nerve fiber types (e.g., slow/fast fatiguable motor units, proprioceptive fibers, etc.) would enable selective modulation of efferent or afferent activity as well as an approach to artificially specify the recruitment order of motor unit types. However, in general, more specific promoters result in weaker expression in the target tissues, so this tradeoff of nerve optical sensitivity vs. fiber type specificity would have to be addressed.

Immune Response to AAV and Gene Products

AAV6 was chosen as the gene delivery vehicle in this study due to AAV's safety profile and low immunogenicity (Calcedo and Wilson, 2013) as well as its previously demonstrated success in transducing peripheral motor nerves in non-human primates (Towne et al., 2009). However, a considerable proportion of both humans and macaques naturally exhibit pre-existing neutralizing antibodies (NAbs) to a variety of AAV serotypes (Boutin et al., 2010; Hurlbut et al., 2010; Calcedo and Wilson, 2013). Even at low NAb levels, transgene expression may be significantly inhibited in non-human primates (Jiang et al., 2006; Hurlbut et al., 2010). We did not assess the status of preexisting NAbs to AAV6 in our subjects, so its role regarding differences in expression between monkeys in this study is unclear. Nevertheless, several transient immunosuppression strategies such as those used for organ transplants have shown efficacy in maintaining AAV6-mediated transgene expression in canine models (Shin et al., 2012; Wang et al., 2012) as well as non-human primate models examining AAV8 (Jiang et al., 2006). Employing such regimens may not only increase transduction efficiency and prolong transgene expression, it could also enable separate viral injections of multiple muscle groups over several surgeries without decreased efficacy after an initial viral exposure (Riviere et al., 2006).

In addition to the viral vector, a recent rodent study has strongly suggested that opsins expressed along a peripheral nerve may also elicit a strong immune response and is likely to be a primary factor for the decay of optical sensitivity over time (Maimon et al., 2018). Indeed, results from the aforementioned rodent study and a preliminary study from our group in non-human primates (Williams et al., 2019) have demonstrated that opsin expression and functional sensitivity can be prolonged with the use of chronic immunosuppression similar to regimens used for organ transplants. However, an alternative approach to this problem would be to engineer the opsin itself, screening opsin variants for those that might be minimally immunogenic. Use of such an opsin for expression through a viral vector might preclude the need for subjects to endure long or potentially lifelong courses of immunosuppression.

Optical Stimulation Parameters and Opsin Selection

The results from this study provide baseline practical guidelines for optical stimulation parameters. EMG responses were modulated with pulse widths up to 10 ms, above which responses appeared to plateau. From a frequency response perspective, EMG responses tracked optical stimulation trains up 16 Hz, suggesting an upper bound for use in FOS stimulation schemes. This limit is relatively low compared to the frequency of stimulus trains commonly used for FES, often ranging from 20 to 50 Hz for clinical applications (Doucet et al., 2012). However, due to the previously discussed differences in recruitment order between optical and electrical stimulation, further study is required to elucidate how these optical stimulation parameters translate to functional force production and how to optimize modulation strategies for neuroprosthetic driven movements.

The EMG relation to optical stimulation parameters explored here was only characterized for the opsin ChR2. Although its use in this and similar prior studies in rodents as a first line of investigation is warranted by ChR2's well-characterized behavior and consistent expression patterns in a wide array of neural systems, other recently developed opsins may hold properties beneficial to peripheral motor stimulation. Indeed, we injected several muscles in our second monkey with a construct using the opsin Chronos to exploit its increased sensitivity and faster kinetics to (1) lower the light intensity and consequently power requirements for implantable optical stimulation hardware, and (2) increase the frequency range of pulsed stimulation trains to at least comparable levels used for FES. Recent studies have supported the fast temporal advantages of Chronos over ChR2 in the central auditory pathway (Guo et al., 2015; Hight et al., 2015). Although this study demonstrated a novel use of Chronos in the motor periphery, the brief period during which we were able to observe its response left us unable to fully examine whether these purported benefits extend to the peripheral motor system. However, preliminary data from our parallel rat studies (Williams et al., 2016) suggest that Chronos does have a better frequency response for light stimulus-EMG coupling in the periphery than ChR2. Other opsins which may prove beneficial for peripheral applications include red-shifted variants such as Chrimson (Klapoetke et al., 2014). The use of longer stimulation wavelengths would allow greater tissue penetration that could prove highly desirable when scaling stimulation hardware up to target primate nerves several millimeters in diameter.

Finally, the stimulus response characteristics referenced above may be influenced by both the level of expression within a given axon as well as the number of axons transduced within a given nerve in addition to the basic channel properties of the opsin. As there was a disconnect between the window of functional expression and the time of perfusion for histological evaluation in two of the three monkeys, we were unable to evaluate any such trends in the current study. However, based on our own experience with stimulation of transgenic mice expressing ChR2 in peripheral nerves and virally transduced rats similar to previous rodent studies (Llewellyn et al., 2010; Towne et al., 2013), the EMG frequency response characteristics are unlikely to appreciably change with expression levels while the magnitude of EMG responses will likely show a stronger correlation with expression. How these relationships scale with animal and nerve size is a question worthy of further investigation.

Comparison With Spinal Electrical Stimulation Approaches

Our main goal in this study was to introduce peripheral optogenetic stimulation as an alternative to FES in BMI applications. FES is typically associated with electrical stimulation of muscles directly or through nerve stimulation. However, several groups have used brain-controlled electrical intraspinal (Zimmermann and Jackson, 2014) or epidural spinal (Capogrosso et al., 2016) stimulation in NHPs for grasping and hindlimb locomotion, respectively. This mode of stimulation elicits muscle activation patterns either directly by stimulating pools of alpha motoneurons or indirectly by inducing motor patterns through interneurons following stimulation of dorsal roots. Thus, our peripheral FOS approach may not be directly comparable to electrical stimulation approaches at the spinal level. Nonetheless, it is possible that the potential benefits of FOS observed in the periphery may also extend to analogous optical stimulation of the spinal cord as has been recently investigated (Mondello et al., 2018).

Peripheral Optogenetics Relevance to Motor Behavior

As discussed in the introduction, success in using viral optogenetics to alter behavior has been difficult to achieve in non-human primates, especially regarding direct modulation of somatomotor activity. The current study represents an early success toward this goal. Although the muscle activity elicited by optical stimulation in this study was likely small compared to those typically elicited during normal locomotion, it did produce an easily observable change in the activity of the target effector. Even small optically induced contractions could potentially be used in perturbation studies of natural movements, while larger scales of virus expression and induced muscle contractions will likely be necessary to be therapeutically useful. A primary difference between the success achieved in this study and past unsuccessful attempts at optogenetic modulation of somatomotor behavior in the brain (Diester et al., 2011) may lie in the proximity of targeted opsin expression to the desired output. While even a small cortical volume transduced by a single virus injection may result in transfection of multiple downstream effector pathways, injection of a vector such as AAV into a single desired end effector (e.g., muscle) virtually guarantees that only the desired effector will be optically activated without upstream transmission. This simplicity in targeting and stimulating desired effector pathways further supports the role of this approach in motor disease therapy.

CONCLUSIONS

In summary, the viral transduction and functional expression of opsins for peripheral optical modulation of muscle activity in non-human primates is a step toward effective reanimation of movement in paralyzed subjects. The introduction of neuromuscular junction targeting for virus injection is a useful technique for increasing the likelihood of virus uptake. In addition, the EMG response characteristics to optical stimulation parameters described here serve as an important base upon which to build future primate studies and FOS algorithms.

While the jump from rodent to primate is important in itself, this study also highlights problems due to differences in scale and species that may not have been as pronounced in prior rodent studies. Potential variability in both the timeline and spatial profile of expression, the immune system's probable role in this variability, and effectiveness of the virus as well as light delivery in much larger target muscles/nerves are all challenges that must be addressed before FOS may become a clinically viable approach to restoring lost motor function.

ETHICS STATEMENT

This study was carried out in accordance with the recommendations of the University of Pittsburgh's Institutional Animal Care and Use Committee. The protocol was approved by the University of Pittsburgh's Institutional Animal Care and Use Committee.

AUTHOR CONTRIBUTIONS

JW, AV, and AS contributed to study conception and experimental design. JW performed all surgeries and experiments. AW performed tissue clearing and imaging while JW and AW analyzed imaging data. JW wrote the first draft of the manuscript. All authors contributed to manuscript revision, read, and approved the submitted version.

FUNDING

This work was funded in part by the DARPA Grant W911NF1420107, Brain Control Optical Stimulation of Muscles, as well as Chair in Systems Neuroscience funds from the University of Pittsburgh.

ACKNOWLEDGMENTS

We would like to thank Chris Towne for his consultation regarding peripheral optogenetic techniques. We thank Richard Dum, Jean-Alban Rathelot, and Peter Strick for their guidance and expertise with primate virus injections, Doug Weber for his aid with EMG recordings, and Bistra Iordanova for her help with histology. Finally, we would like to thank Kathy Hansell-Prigg, Scott Kennedy, Hongwei Mao, Steve Suway, Rex Tien, and Sally Zheng for their assistance with surgeries and experiments.

Note: A version of this manuscript was previously released as a pre-print (Williams et al., 2018) to the bioRxiv server hosted by the Cold Spring Harbor Laboratory.

SUPPLEMENTARY MATERIAL

The Supplementary Material for this article can be found online at: https://www.frontiersin.org/articles/10.3389/fnins.2019.00759/full#supplementary-material

REFERENCES

Ajiboye, A. B., Willett, F. R., Young, D. R., Memberg, W. D., Murphy, B. A., Miller, J. P., et al. (2017). Restoration of reaching and grasping movements through brain-controlled muscle stimulation in a person with tetraplegia: a proof-of-concept demonstration. *Lancet* 389, 1821–1830. doi: 10.1016/S0140-6736(17)30601-3

Asokan, A., Schaffer, D. V., and Jude Samulski, R. (2012). The AAV vector toolkit: poised at the clinical crossroads. *Mol. Ther.* 20, 699–708. doi: 10.1038/mt.2011.287

Bartel, M. (2011). Enhancing the clinical potential of AAV vectors by capsid engineering to evade pre-existing immunity. *Front. Microbiol.* 2:204. doi: 10.3389/fmicb.2011.00204

Biasiucci, A., Leeb, R., Iturrate, I., Perdikis, S., Al-Khodairy, A., Corbet, T., et al. (2018). Brain-actuated functional electrical stimulation elicits lasting arm motor recovery after stroke. *Nat. Commun.* 9:2421. doi: 10.1038/s41467-018-04673-z

Bickel, C. S., Gregory, C. M., and Dean, J. C. (2011). Motor unit recruitment during neuromuscular electrical stimulation: a critical appraisal. *Eur. J. Appl. Physiol.* 111, 2399–2407. doi: 10.1007/s00421-011-2128-4

Boutin, S., Monteilhet, V., Veron, P., Leborgne, C., Benveniste, O., Montus, M. F., et al. (2010). Prevalence of serum IgG and neutralizing factors against adeno-associated virus (AAV) types 1, 2, 5, 6, 8, and 9 in the healthy population: implications for gene therapy using AAV vectors. *Hum. Gene Ther.* 21, 704–712. doi: 10.1089/hum.2009.182

Bouton, C. E., Shaikhouni, A., Annetta, N. V., Bockbrader, M. A., Friedenberg, D. A., Nielson, D. M., et al. (2016). Restoring cortical control of functional movement in a human with quadriplegia. *Nature* 533, 247–250. doi: 10.1038/nature17435

Boyden, E. S., Zhang, F., Bamberg, E., Nagel, G., and Deisseroth, K. (2005). Millisecond-timescale, genetically targeted optical control of neural activity. *Nat. Neurosci.* 8, 1263–1268. doi: 10.1038/nn1525

Bruegmann, T., van Bremen, T., Vogt, C. C., Send, T., Fleischmann, B. K., and Sasse, P. (2015). Optogenetic control of contractile function in skeletal muscle. *Nat. Commun.* 6:7153. doi: 10.1038/ncomms8153

Bruns, T. M., Wagenaar, J. B., Bauman, M. J., Gaunt, R. A., and Weber, D. J. (2013). Real-time control of hind limb functional electrical stimulation using feedback from dorsal root ganglia recordings. *J. Neural Eng.* 10:026020. doi: 10.1088/1741-2560/10/2/026020

Bryson, J. B., Machado, C. B., Crossley, M., Stevenson, D., Bros-Facer, V., Burrone, J., et al. (2014). Optical control of muscle function by transplantation of stem cell–derived motor neurons in mice. *Science* 344, 94–97. doi: 10.1126/science.1248523

Burger, C., Nguyen, F. N., Deng, J., and Mandel, R. J. (2005). Systemic mannitol-induced hyperosmolality amplifies rAAV2-mediated striatal transduction to a greater extent than local co-infusion. *Mol. Ther.* 11, 327–331. doi: 10.1016/j.ymthe.2004.08.031

Calcedo, R., and Wilson, J. M. (2013). Humoral immune response to AAV. *Front. Immunol.* 4:341. doi: 10.3389/fimmu.2013.00341

Capogrosso, M., Milekovic, T., Borton, D., Wagner, F., Moraud, E. M., Mignardot, J.-B., et al. (2016). A brain–spine interface alleviating gait deficits after spinal cord injury in primates. *Nature* 539, 284–288. doi: 10.1038/nature20118

Cavanaugh, J., Monosov, I. E., McAlonan, K., Berman, R., Smith, M. K., Cao, V., et al. (2012). Optogenetic inactivation modifies monkey visuomotor behavior. *Neuron* 76, 901–907. doi: 10.1016/j.neuron.2012.10.016

Chaffiol, A., Caplette, R., Jaillard, C., Brazhnikova, E., Desrosiers, M., Dubus, E., et al. (2017). A new promoter allows optogenetic vision restoration with enhanced sensitivity in macaque retina. *Mol. Ther.* 25, 2546–2560. doi: 10.1016/j.ymthe.2017.07.011

Choudhury, S. R., Fitzpatrick, Z., Harris, A. F., Maitland, S. A., Ferreira, J. S., Zhang, Y., et al. (2016). *In vivo* selection yields AAV-B1 capsid for central nervous system and muscle gene therapy. *Mol. Ther.* 24, 1247–1257. doi: 10.1038/mt.2016.84

Collinger, J. L., Wodlinger, B., Downey, J. E., Wang, W., Tyler-Kabara, E. C., Weber, D. J., et al. (2013). High-performance neuroprosthetic control by an individual with tetraplegia. *Lancet* 381, 557–564. doi: 10.1016/S0140-6736(12)61816-9

Dai, J., Brooks, D. I., and Sheinberg, D. L. (2014). Optogenetic and electrical microstimulation systematically bias visuospatial choice in primates. *Curr. Biol.* 24, 63–69. doi: 10.1016/j.cub.2013.11.011

Dalkara, D., Byrne, L. C., Klimczak, R. R., Visel, M., Yin, L., Merigan, W. H., et al. (2013). *In vivo*–directed evolution of a new adeno-associated virus for therapeutic outer retinal gene delivery from the vitreous. *Sci. Transl. Med.* 5:189ra76. doi: 10.1126/scitranslmed.3005708

Diester, I., Kaufman, M. T., Mogri, M., Pashaie, R., Goo, W., Yizhar, O., et al. (2011). An optogenetic toolbox designed for primates. *Nat. Neurosci.* 14, 387–397. doi: 10.1038/nn.2749

Doucet, B. M., Lam, A., and Griffin, L. (2012). Neuromuscular electrical stimulation for skeletal muscle function. *Yale J. Biol. Med.* 85, 201–215.

El-Shamayleh, Y., Kojima, Y., Soetedjo, R., and Horwitz, G. D. (2017). Selective optogenetic control of purkinje cells in monkey cerebellum. *Neuron* 95, 51–62.e4. doi: 10.1016/j.neuron.2017.06.002

Ethier, C., Oby, E. R., Bauman, M. J., and Miller, L. E. (2012). Restoration of grasp following paralysis through brain-controlled stimulation of muscles. *Nature* 485, 368–371. doi: 10.1038/nature10987

Fang, Z.-P., and Mortimer, J. T. (1991). Selective activation of small motor axons by quasitrapezoidal current pulses. *IEEE Trans. Biomed. Eng.* 38, 168–174. doi: 10.1109/10.76383

Favre, D., Cherel, Y., Provost, N., Blouin, V., Ferry, N., Moullier, P., et al. (2000). Hyaluronidase enhances recombinant adeno-associated virus (rAAV)-mediated gene transfer in the rat skeletal muscle. *Gene Ther.* 7, 1417–1420. doi: 10.1038/sj.gt.3301256

Gregory, C. M., and Bickel, C. S. (2005). Recruitment patterns in human skeletal muscle during electrical stimulation. *Phys. Ther.* 85, 358–364. doi: 10.1093/ptj/85.4.358

Guo, W., Hight, A. E., Chen, J. X., Klapoetke, N. C., Hancock, K. E., Shinn-Cunningham, B. G., et al. (2015). Hearing the light: neural and perceptual encoding of optogenetic stimulation in the central auditory pathway. *Sci. Rep.* 5:10319. doi: 10.1038/srep10319

Han, X., Qian, X., Bernstein, J. G., Zhou, H., Franzesi, G. T., Stern, P., et al. (2009). Millisecond-timescale optical control of neural dynamics in the nonhuman primate brain. *Neuron* 62, 191–198. doi: 10.1016/j.neuron.2009.03.011

Harris, J. A., Wook Oh, S., and Zeng, H. (2012). Adeno-associated viral vectors for anterograde axonal tracing with fluorescent proteins in nontransgenic and cre driver mice. *Curr. Protoc. Neurosci.* 59, 20.1–1.20.18. doi: 10.1002/0471142301.ns0120s59

Henneman, E. (1957). Relation between size of neurons and their susceptibility to discharge. *Science* 126, 1345–1347.

Hight, A. E., Kozin, E. D., Darrow, K., Lehmann, A., Boyden, E., Brown, M. C., et al. (2015). Superior temporal resolution of Chronos versus channelrhodopsin-2 in an optogenetic model of the auditory brainstem implant. *Hear. Res.* 322, 235–241. doi: 10.1016/j.heares.2015.01.004

Hochberg, L. R., Bacher, D., Jarosiewicz, B., Masse, N. Y., Simeral, J. D., Vogel, J., et al. (2012). Reach and grasp by people with tetraplegia using a neurally controlled robotic arm. *Nature* 485, 372–375. doi: 10.1038/nature11076

Hurlbut, G. D., Ziegler, R. J., Nietupski, J. B., Foley, J. W., Woodworth, L. A., Meyers, E., et al. (2010). Preexisting immunity and low expression in primates highlight translational challenges for liver-directed AAV8-mediated gene therapy. *Mol. Ther.* 18, 1983–1994. doi: 10.1038/mt.2010.175

Jazayeri, M., Lindbloom-Brown, Z., and Horwitz, G. D. (2012). Saccadic eye movements evoked by optogenetic activation of primate V1. *Nat. Neurosci.* 15, 1368–1370. doi: 10.1038/nn.3210

Jiang, H., Couto, L. B., Patarroyo-White, S., Liu, T., Nagy, D., Vargas, J. A., et al. (2006). Effects of transient immunosuppression on adenoassociated, virus-mediated, liver-directed gene transfer in rhesus macaques and implications for human gene therapy. *Blood* 108, 3321–3328. doi: 10.1182/blood-2006-04-017913

Jing, D., Zhang, S., Luo, W., Gao, X., Men, Y., Ma, C., et al. (2018). Tissue clearing of both hard and soft tissue organs with the PEGASOS method. *Cell Res.* 28, 803–818. doi: 10.1038/s41422-018-0049-z

Kilgore, K. L., Hoyen, H. A., Bryden, A. M., Hart, R. L., Keith, M. W., and Peckham, P. H. (2008). An implanted upper-extremity neuroprosthesis using myoelectric control. *J. Hand Surg.* 33, 539–550. doi: 10.1016/j.jhsa.2008.01.007

Klapoetke, N. C., Murata, Y., Kim, S. S., Pulver, S. R., Birdsey-Benson, A., Cho, Y. K., et al. (2014). Independent optical excitation of distinct neural populations. *Nat. Methods* 11, 338–346. doi: 10.1038/nmeth.2836

Kozai, T. D. Y., and Vazquez, A. L. (2015). Photoelectric artefact from optogenetics and imaging on microelectrodes and bioelectronics: new challenges and opportunities. *J. Mater. Chem. B* 3, 4965–4978. doi: 10.1039/C5TB00108K

Lertmanorat, Z., and Durand, D. M. (2004). Extracellular voltage profile for reversing the recruitment order of peripheral nerve stimulation: a simulation study. *J. Neural Eng.* 1, 202–211. doi: 10.1088/1741-2560/1/4/003

Leuthardt, E. C., Schalk, G., Wolpaw, J. R., Ojemann, J. G., and Moran, D. W. (2004). A brain-computer interface using electrocorticographic signals in humans. *J. Neural Eng.* 1, 63–71. doi: 10.1088/1741-2560/1/2/001

Llewellyn, M. E., Thompson, K. R., Deisseroth, K., and Delp, S. L. (2010). Orderly recruitment of motor units under optical control *in vivo*. *Nat. Med.* 16, 1161–1165. doi: 10.1038/nm.2228

Maimon, B. E., Diaz, M., Revol, E. C. M., Schneider, A. M., Leaker, B., Varela, C. E., et al. (2018). Optogenetic peripheral nerve immunogenicity. *Sci. Rep.* 8:14076. doi: 10.1038/s41598-018-32075-0

Maimon, B. E., Zorzos, A. N., Bendell, R., Harding, A., Fahmi, M., Srinivasan, S., et al. (2017). Transdermal optogenetic peripheral nerve stimulation. *J. Neural Eng.* 14:034002. doi: 10.1088/1741-2552/aa5e20

Mattis, J., Tye, K. M., Ferenczi, E. A., Ramakrishnan, C., O'Shea, D. J., Prakash, R., et al. (2012). Principles for applying optogenetic tools derived from direct comparative analysis of microbial opsins. *Nat. Methods* 9, 159–172. doi: 10.1038/nmeth.1808

May, T., Ozden, I., Brush, B., Borton, D., Wagner, F., Agha, N., et al. (2014). Detection of optogenetic stimulation in somatosensory cortex by non-human primates - towards artificial tactile sensation. *PLoS ONE* 9:e114529. doi: 10.1371/journal.pone.0114529

Mondello, S. E., Sunshine, M. D., Fischedick, A. E., Dreyer, S. J., Horwitz, G. D., Anikeeva, P., et al. (2018). Optogenetic surface stimulation of the rat cervical spinal cord. *J. Neurophysiol.* 120, 795–811. doi: 10.1152/jn.00461.2017

Moritz, C. T., Perlmutter, S. I., and Fetz, E. E. (2008). Direct control of paralysed muscles by cortical neurons. *Nature* 456, 639–642. doi: 10.1038/nature07418

Nagel, G., Szellas, T., Huhn, W., Kateriya, S., Adeishvili, N., Berthold, P., et al. (2003). Channelrhodopsin-2, a directly light-gated cation-selective membrane channel. *Proc. Natl. Acad. Sci. U. S. A.* 100, 13940–13945. doi: 10.1073/pnas.1936192100

Okada, H., Ishibashi, H., Hayashita-Kinoh, H., Chiyo, T., Nitahara-Kasahara, Y., Baba, Y., et al. (2013). Robust long-term transduction of common marmoset neuromuscular tissue with rAAV1 and rAAV9. *Mol. Ther. Nucleic Acids* 2:e95. doi: 10.1038/mtna.2013.21

Peckham, P. H., Kilgore, K. L., Keith, M. W., Bryden, A. M., Bhadra, N., and Montague, F. W. (2002). An advanced neuroprosthesis for restoration of hand and upper arm control using an implantable controller. *J. Hand Surg.* 27, 265–276. doi: 10.1053/jhsu.2002.30919

Revechkis, B., Aflalo, T. N. S., Kellis, S., Pouratian, N., and Andersen, R. A. (2015). Parietal neural prosthetic control of a computer cursor in a graphical-user-interface task. *J. Neural Eng.* 12:019601. doi: 10.1088/1741-2560/12/1/019601

Riviere, C., Danos, O., and Douar, A. M. (2006). Long-term expression and repeated administration of AAV type 1, 2 and 5 vectors in skeletal muscle of immunocompetent adult mice. *Gene Ther.* 13, 1300–1308. doi: 10.1038/sj.gt.3302766

Serruya, M. D., Hatsopoulos, N. G., Paninski, L., Fellows, M. R., and Donoghue, J. P. (2002). Instant neural control of a movement signal. *Nature* 416, 141–142. doi: 10.1038/416141a

Shin, J.-H., Yue, Y., Srivastava, A., Smith, B., Lai, Y., and Duan, D. (2012). A simplified immune suppression scheme leads to persistent micro-dystrophin expression in duchenne muscular dystrophy dogs. *Hum. Gene Ther.* 23, 202–209. doi: 10.1089/hum.2011.147

Singh, K., Richmond, F. J., and Loeb, G. E. (2000). Recruitment properties of intramuscular and nerve-trunk stimulating electrodes. *IEEE Trans. Rehabil. Eng.* 8, 276–285. doi: 10.1109/86.867869

Stauffer, W. R., Lak, A., Yang, A., Borel, M., Paulsen, O., Boyden, E. S., et al. (2016). Dopamine neuron-specific optogenetic stimulation in rhesus macaques. *Cell 166*, 1564–1571.e6. doi: 10.1016/j.cell.2016.08.024

Taylor, D. M., Tillery, S. I., and Schwartz, A. B. (2002). Direct cortical control of 3D neuroprosthetic devices. *Science* 296, 1829–1832. doi: 10.1126/science.1070291

Tervo, D. G. R., Hwang, B.-Y., Viswanathan, S., Gaj, T., Lavzin, M., Ritola, K. D., et al. (2016). A Designer AAV variant permits efficient retrograde access to projection neurons. *Neuron* 92, 372–382. doi: 10.1016/j.neuron.2016.09.021

Tosolini, A. P., Mohan, R., and Morris, R. (2013). Targeting the full length of the motor end plate regions in the mouse forelimb increases the uptake of fluoro-gold into corresponding spinal cord motor neurons. *Front. Neurol.* 4:58. doi: 10.3389/fneur.2013.00058

Tosolini, A. P., and Morris, R. (2016). Targeting motor end plates for delivery of adenoviruses: an approach to maximize uptake and transduction of spinal cord motor neurons. *Sci. Rep.* 6:33058. doi: 10.1038/srep33058

Towne, C., Montgomery, K. L., Iyer, S. M., Deisseroth, K., and Delp, S. L. (2013). Optogenetic control of targeted peripheral axons in freely moving animals. *PLoS ONE* 8:e72691. doi: 10.1371/journal.pone.0072691

Towne, C., Schneider, B. L., Kieran, D., Redmond, D. E., and Aebischer, P. (2009). Efficient transduction of non-human primate motor neurons after intramuscular delivery of recombinant AAV serotype 6. *Gene Ther.* 17, 141–146. doi: 10.1038/gt.2009.119

Tyler, D. J., and Durand, D. M. (2002). Functionally selective peripheral nerve stimulation with a flat interface nerve electrode. *IEEE Trans. Neural Syst. Rehabil. Eng.* 10, 294–303. doi: 10.1109/TNSRE.2002.806840

Wang, Z., Storb, R., Halbert, C. L., Banks, G. B., Butts, T. M., Finn, E. E., et al. (2012). Successful regional delivery and long-term expression of a dystrophin gene in canine muscular dystrophy: a preclinical model for human therapies. *Mol. Ther.* 20, 1501–1507. doi: 10.1038/mt.2012.111

Watson, A. M., Rose, A. H., Gibson, G. A., Gardner, C. L., Sun, C., Reed, D. S., et al. (2017). Ribbon scanning confocal for high-speed high-resolution volume imaging of brain. *PloS ONE* 12:e0180486. doi: 10.1371/journal.pone.0180486

Williams, J. J., Vazquez, A. L., and Schwartz, A. B. (2019). "Prolonged functional optical sensitivity in non-human primate motor nerves following Cyclosporine-based immunosuppression and rAAV2-retro mediated expression of ChR2," in *Proceedings of the 9th International IEEE EMBS Conference on Neural Engineering* (San Francisco, CA).

Williams, J. J., Vazquez, A. L., Wirblich, C., Schnell, M. J., and Schwartz, A. B. (2016). "Virus, opsin, and immunomodulation selection for optogenetic control of peripheral motor function," in *2016 Neuroscience Meeting Planner* (San Diego, CA). Available online at: http://www.abstractsonline.com/pp8/#!/4071/presentation/15933 (accessed September 27, 2017).

Williams, J. J., Watson, A. M., Vazquez, A. L., and Schwartz, A. B. (2018). Viral-mediated optogenetic stimulation of peripheral motor nerves in non-human primates. *bioRxiv* 261925. doi: 10.1101/261925

Wodlinger, B., Downey, J. E., Tyler-Kabara, E. C., Schwartz, A. B., Boninger, M. L., and Collinger, J. L. (2015). Ten-dimensional anthropomorphic arm control in a human brain-machine interface: difficulties, solutions, and limitations. *J. Neural Eng.* 12:016011. doi: 10.1088/1741-2560/12/1/016011

Yazdan-Shahmorad, A., Diaz-Botia, C., Hanson, T. L., Kharazia, V., Ledochowitsch, P., Maharbiz, M. M., et al. (2016). A large-scale interface for optogenetic stimulation and recording in nonhuman primates. *Neuron* 89, 927–939. doi: 10.1016/j.neuron.2016.01.013

Yeom, H., and Chang, Y.-H. (2010). Autogenic EMG-controlled functional electrical stimulation for ankle dorsiflexion control. *J. Neurosci. Methods* 193, 118–125. doi: 10.1016/j.jneumeth.2010.08.011

Zimmermann, J. B., and Jackson, A. (2014). Closed-loop control of spinal cord stimulation to restore hand function after paralysis. *Front. Neurosci.* 8:87. doi: 10.3389/fnins.2014.00087

Conflict of Interest Statement: The authors declare that the research was conducted in the absence of any commercial or financial relationships that could be construed as a potential conflict of interest.

Copyright © 2019 Williams, Watson, Vazquez and Schwartz. This is an open-access article distributed under the terms of the Creative Commons Attribution License (CC BY). The use, distribution or reproduction in other forums is permitted, provided the original author(s) and the copyright owner(s) are credited and that the original publication in this journal is cited, in accordance with accepted academic practice. No use, distribution or reproduction is permitted which does not comply with these terms.

frontiers in Neuroscience

ORIGINAL RESEARCH
published: 06 August 2019
doi: 10.3389/fnins.2019.00691

Computational Simulation Expands Understanding of Electrotransfer-Based Gene Augmentation for Enhancement of Neural Interfaces

Amr Al Abed[1], Jeremy L. Pinyon[2], Evelyn Foster[1], Frederik Crous[1], Gary J. Cowin[3], Gary D. Housley[2] and Nigel H. Lovell[1]*

[1] Graduate School of Biomedical Engineering, University of New South Wales, Sydney, NSW, Australia, [2] Translational Neuroscience Facility, Department of Physiology, School of Medical Sciences, University of New South Wales, Sydney, NSW, Australia, [3] National Imaging Facility, Centre for Advanced Imaging, University of Queensland, Brisbane, QLD, Australia

The neural interface is a critical factor in governing efficient and safe charge transfer between a stimulating electrode and biological tissue. The interface plays a crucial role in the efficacy of electric stimulation in chronic implants and both electromechanical properties and biological properties shape this. In the case of cochlear implants, it has long been recognized that neurotrophins can stimulate growth of the target auditory nerve fibers into a favorable apposition with the electrode array, and recently such arrays have been re-purposed to enable electrotransfer (electroporation)-based neurotrophin gene augmentation to improve the "bionic ear." For both this acute bionic array-directed electroporation and for chronic conventional cochlear implant arrays, the electric fields generated in target tissue during pulse delivery are central to efficacy, but are challenging to map. We present a computational model for predicting electric fields generated by array-driven DNA electrotransfer in the cochlea. The anatomically realistic model geometry was reconstructed from magnetic resonance images of the guinea pig cochlea and an eight-channel electrode array embedded within this geometry. The model incorporates a description of both Faradaic and non-Faradaic mechanisms occurring at the electrode-electrolyte interface with frequency dependency optimized to match experimental impedance spectrometry measurements. Our simulations predict that a tandem electrode configuration with four ganged cathodes and four ganged anodes produces three to fourfold larger area in target tissue where the electric field is within the range for successful gene transfer compared to an alternate paired anode-cathode electrode configuration. These findings matched *in vivo* transfection efficacy of a green fluorescent protein (GFP) reporter following array-driven electrotransfer of the reporter-encoding plasmid DNA. This confirms utility of the developed model as a tool to optimize the safety and efficacy of electrotransfer protocols for delivery of neurotrophin growth factors, with the ultimate aim of using gene augmentation approaches to improve the characteristics of the electrode-neural interfaces in chronically implanted neurostimulation devices.

Keywords: electroporation, electric field, cochlea, computational modeling, field mapping, electrode impedance

OPEN ACCESS

Edited by:
Ulrich G. Hofmann, University Medical Center Freiburg, Germany

Reviewed by:
Waldo Nogueira, Hannover Medical School, Germany
Jit Muthuswamy, Arizona State University, United States

****Correspondence:***
Amr Al Abed
amra@unsw.edu.au

Specialty section:
This article was submitted to Neural Technology, a section of the journal Frontiers in Neuroscience

Received: *15 January 2019*
Accepted: *18 June 2019*
Published: *06 August 2019*

Citation:
Al Abed A, Pinyon JL, Foster E, Crous F, Cowin GJ, Housley GD and Lovell NH (2019) Computational Simulation Expands Understanding of Electrotransfer-Based Gene Augmentation for Enhancement of Neural Interfaces. Front. Neurosci. 13:691. doi: 10.3389/fnins.2019.00691

INTRODUCTION

The neural interface can be considered as the predominant factor limiting further advancement of chronic neurostimulation technologies such as the cochlear implant. Deterioration of the neural interface, due to surgical implant procedure, fibrosis, and strong foreign body responses among other reasons, leads to poor coupling of implanted multi-electrode arrays to target neurons. In the case of cochlear implants, inadequate neural selectivity due to high excitation thresholds and resulting current spread prevents the improvement of positional recruitment – based pitch perception and speech perception outcomes in implant recipients (O'Leary et al., 2009).

Attempts to improve the cochlear implant neural interface have included delivery of neurotrophic factors through a variety of approaches to regenerate nerve fibers, reducing the distance between target neuron processes and the electrode array (Pettingill et al., 2008; Richardson et al., 2009; Wise et al., 2010; Atkinson et al., 2012). Within this context, close field electroporation (CFE) has shown promising potential for the electrotransfer of gene constructs to cells within localized tissue region. Because CFE utilizes the cochlear implant electrode array itself to drive transfection with highly specific localization proximal to the array, CFE is able to achieve meaningful tropism in the context of enhancement of the bionic ear interface (Pinyon et al., 2014). This potentially provides superiority to alternate approaches such as those that are cell-based, viral-based or through direct protein infusion, which do not provide cochlear implant-guided tropic support. An effect that was successfully demonstrated by transfecting localized regions of mesenchymal cells within the cochlea surrounding the electrode array. When these cells produce recombinant neurotrophic factors, a concentration gradient is established, directing regrowth of the cochlear neuron peripheral processes directly toward the transfected mesenchymal cells and thus the electrodes of the cochlear implant array. Furthermore, changing the configuration of active and return electrodes used for gene electrotransfer in an eight-channel array can affect the number of cells transfected both *in vitro* using cultured human embryonic kidney-293 (HEK293) cells and *in vivo* in the guinea pig cochlea (Pinyon et al., 2014; Browne et al., 2016).

It is hypothesized that successful electrotransfer of gene constructs is correlated to the strength of electric fields generated by the electroporation pulses in target tissue (Browne et al., 2016). While electric field mapping has been carried out *in vitro* (Browne et al., 2016), electric field density and the resulting transfection patterns produced within the cochlea are not well understood due to the difficulty of mapping electric fields in a complex geometry such as the cochlea. Knowledge of optimal stimulation parameters for targeted gene electrotransfer is needed to achieve high efficiency and enable spatial control of the transfected region.

To address this knowledge gap, in this study we develop an anatomically realistic computational model of the guinea pig cochlea to enable simulation of electroporation pulses produced by array-driven stimulation. We hypothesize that the electric fields predicted by our computational model are correlated to transfection localization and density observed experimentally. The validated model can then be utilized to design electrode configurations for CFE that optimize acute targeted gene electrotransfer in the cochlea, facilitating broad improvement of chronically implanted neural interfaces in the cochlea.

MATERIALS AND METHODS

Electrode Impedance Characterization

Electrochemical impedance spectrometry (EIS) was conducted on an eight channel Pt electrode array (part no. Z60276; Cochlea, Australia). The array consisted of eight platinum electrodes with diameter 350 μm, length 300 μm, and spacing of 300 μm.

The electrode array was immersed in 40 mL of Dulbecco's phosphate-buffered saline (DPBS) and measurements were conducted using an EA 163 three electrode potentiostat (eDAQ, Australia). The collecting/return electrode was chosen to be a piece of platinum scrap with dimensions significantly larger than the cochlea working electrodes. The reference electrode was a Ag/AgCl electrode. To ensure that distances between electrodes remained constant, all three electrodes ran into the solution parallel to the axis of the beaker. The cochlea electrode array and return and reference electrodes were vertically aligned and submerged to approximately the mid-level of the solution. Electrodes were positioned so that the reference electrode was in the midline between the working electrode (cochlear electrode array) and the return electrode. The electrode system was placed within a Faraday cage to minimize electrical interference.

The ERZ100 software (eDAQ, Australia) provided the functionality to perform the EIS measurements. It contains a function generator which provided the stimulation waveform as well as a frequency response analyzer that determined impedance magnitude and phase angle. Each of the eight electrodes on the cochlea array was analyzed individually, with order being randomized. For each electrode, frequency was swept in the 0.1–10 kHz range with AC amplitude of 30 mV.

In vivo Electroporation

All experimental procedures were conducted in accordance with the NSW Animal Research Act 1985, NSW Animal Research Regulations 2010, and Australian Code for the Care and Use of Animals for Scientific Purposes 8th Edition 2013, and were approved by the University of New South Wales Animal Care and Ethics Committee (ACEC approval number 10/81A).

The data on cochlear mesenchymal cell transfection with green fluorescence protein reporter (GFP) expression – encoding plasmid DNA used in this study to validate the cochlear implant array computational modeling was derived from the initial report of close-field electroporation (Pinyon et al., 2014). The methodology is further expanded in Browne et al. (2016) and Pinyon et al. (2019). Briefly, colored guinea pigs of both

sexes 300–900 g in weight were anesthetized using isoflurane. GFP reporter plasmid DNA incorporating a cytomegalovirus promoter [2 μg/μl in Tris(hydroxymethyl)aminomethane (Tris) buffered saline] was delivered to the cochlea via the round window at a rate of 20 μl per 40 s using a Narishige IM-1 microdrive pump (Narishige, Japan). A pre-clinical research cochlear implant electrode array (part no. Z60276; Cochlea, Australia) was then inserted into the basal turn of the scala tympani via the round window. Prior to electroporation the total impedance of the system was determined using the resistance-measuring mode of a CUY21 square wave electroporator (Nepa Gene, Japan). For electroporation, constant voltage pulses were delivered via the electrode array in either of two electrode configurations: "alternate" whereby alternating electrodes in the array were set as anode and cathode (n = 4), or "tandem" whereby four neighboring electrodes were set as the anode and the next four as cathode (n = 7). In selected experiments, as a no electrotransfer, the array was inserted but the electroporation pulse train was not applied (n = 2). The cochlear implant array was removed within 5 min of the DNA electrotransfer and the surgical field was closed. The guinea pigs were euthanized after 3–4 days and following fixation with 4% paraformaldehyde (PFA), the cochlea was removed and decalcified in 8% ethylenediaminetetraacetic acid (EDTA) in 0.1 M sodium phosphate buffer at 4°C for 2–3 weeks. The nuclear-localized GFP reporter signal in the target mesenchymal cell area adjacent to the electrode array was visualized using a NLO710 confocal laser scanning microscope (Zeiss, Germany). Fluorescence was excited at 488 nm using an argon laser and emissions collected at 492–548 nm wavelengths.

MRI and Image Reconstruction

For high resolution magnetic resonance imaging (MRI) to delineate the spatial features of the cochlea, a 500 g male guinea pig was euthanized via intraperitoneal injection of pentobarbital and then cardiac perfused using 50 ml of saline containing 0.5% sodium nitroprusside, followed by fixation with 100 ml of phosphate buffered 4% PFA. The cochleae were removed and further fixed overnight at 4°C. Magnetic resonance images of the guinea pig cochlea were obtained using a 16.4T AV700 MRI system at the National Imaging Facility, Australia, with a 12.5 μm × 12.9 μm × 12.5 μm spatial resolution, and averaging of four repeats and the following image sequence parameters: 3D gradient echo, Fast Low Angle Shot (FLASH), TR = 40, TE = 5.5, pulse = 35°. The total acquisition time was 22.5 h. The soft tissue, cochlear canals and nerve tissue were segmented and 3D masks reconstructed in Mimics v19.0 (Materialise, Belgium) using standard thresholding and morphological filters as well as tracing tools (**Figure 1**). Further smoothing and morphological filtering was conducted to define the Reissner's membrane boundary (between scala vestibuli and scala media) and the basilar membrane boundary (between scala media and scala tympani).

The geometry for the electrode array was created in SolidWorks 2016 (Dassault Systèmes, France) as a spiral with variable radius and uniform pitch. The curvature was defined based on anatomical measurements to ensure that the electrode array would fit within the scala tympani (**Figure 1**). The positioning within the scala tympani structure was achieved by manual rotation and translation in 3-Matic v11.0 (Materialise, Belgium). Meshes for anatomical structures and the electrode array were generated, smoothed and assembled in 3-Matic v11.0 (Materialise, Belgium) before export to COMSOL Multiphysics v5.3a (COMSOL AB, Sweden) for further refinement.

Finite Element Modeling

A computational model was built to simulate array-driven electroporation in the reconstructed cochlea using the finite-element solver software COMSOL Multiphysics.

The cochlea geometry with electrode array embedded was meshed using tetrahedral volumetric elements (1,368,698) and triangular boundary elements (125,799). The average element skewness was 0.67, on a scale from 0 to 1 with 1 being a perfect equilateral tetrahedron or triangle.

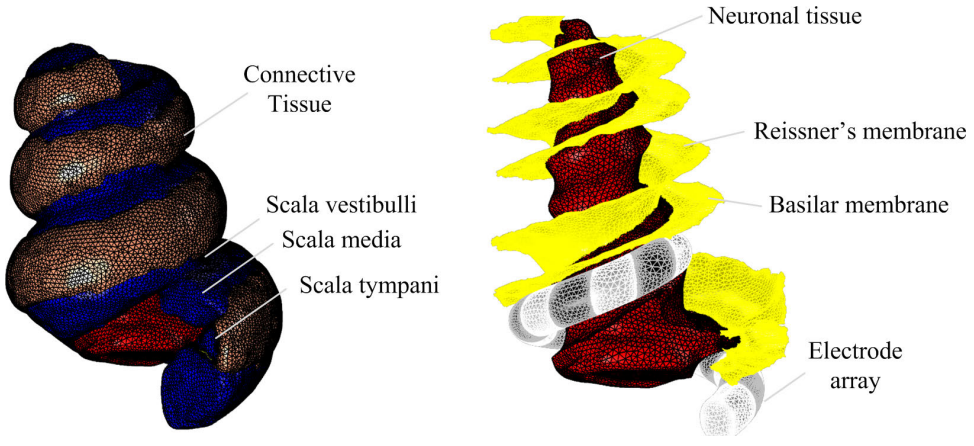

FIGURE 1 | 3D reconstruction of guinea pig cochlea.

The cochlea was assumed to be electrically passive, with each anatomical structure having an isotropic specific conductivity σ (S.m^{-1}) (**Table 1** for values) with the extracellular voltage distribution V (V) governed by Poisson's equation:

$$\nabla \cdot (-\sigma \nabla V) = 0$$

The basilar membrane and Reissner's membranes were modeled as boundaries assigned with numerical thicknesses (d_s) of 90 μm and 20 μm, respectively, representing contact impedances:

$$\hat{n}.\overrightarrow{J_1} = \frac{\sigma}{d_s}(V_1 - V_2)$$

$$\hat{n}.\overrightarrow{J_2} = \frac{\sigma}{d_s}(V_2 - V_1)$$

where $\hat{n}$ is the unit vector normal to the boundary, V_1 and V_2 are the electric potentials on either side of the boundary, and $\overrightarrow{J_1}$ and $\overrightarrow{J_2}$ the current fluxes (A.m^{-2}) across the boundary in either direction.

Electroporation pulses were modeled as a time-varying electric potential boundary condition on each of the electrode boundaries in contact with the surrounding scala tympani. The voltage waveform outputted by the circuited analysis of the electrode-tissue interface was applied as a Dirichlet boundary condition. To estimate the total resistivity of the tissue for the cases of tandem and alternate electrode configurations, a constant voltage stimulus of 1 V was applied as the Dirichlet boundary condition and the current measured at the boundaries. A Neumann boundary condition (zero flux) was used to model all other boundaries.

The finite element model was solved using an iterative conjugate gradient stationary linear system solver with an algebraic multigrid preconditioner using a successive over-relaxation (SOR) pre-smoother and a backward SOR (SORU) post-smoother algorithm. A backward differentiation formula adaptive time stepping routine was used with a maximum time step of 100 μs. The relative tolerance was set at 10^{-2}. The number of degrees of freedom (DOF) was 1,930,229. Quadratic Lagrange basis functions were applied irrespective of the mesh element type. To capture both rapid changes in electric potential as well as steady state values, simulation results were sampled at adaptive intervals ranging between 10 μs and 1 ms.

TABLE 1 | Conductivity values for various anatomical structures in the finite element model.

Tissue	Specific conductivity (S.m^{-1})	Assumption and references
Scala tympani, scala vestibule, and scala media	1.5000	Body fluid (Andreuccetti et al., 2017)
Soft tissue surrounding the cochlear ducts	0.25092	Tendon (Andreuccetti et al., 2017)
The cochlear partition, including the organ of Corti	0.017126	Nerve tissue (Andreuccetti et al., 2017)
Basilar and Reissner's membranes	0.2904	Thorne et al., 2004

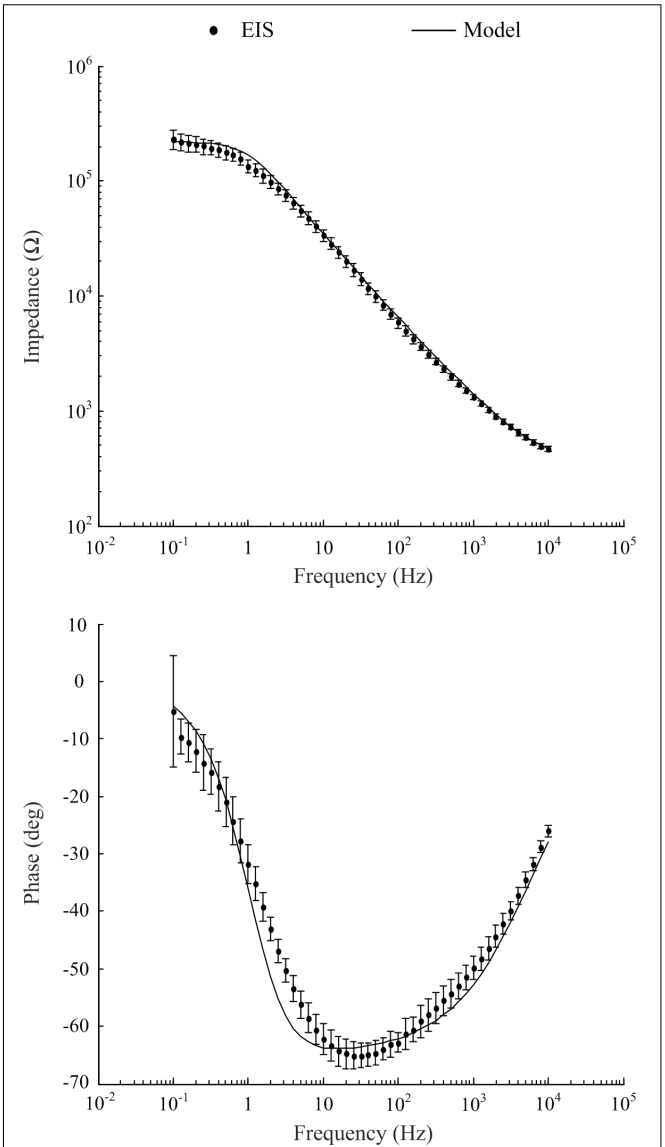

FIGURE 2 | Electrochemical impedance spectrometry characterization of electrodes of the eight channel cochlea array and optimized model to match experimental EIS data (mean ± standard deviation).

RESULTS

Electrode Impedance Characterization

Typical of electrodes in electrolytes, impedance was frequency dependent (refer to **Figure 2**). All eight electrodes displayed a decrease in impedance magnitude as frequency increased and approached a common value at higher frequencies. The standard deviation at 0.1 Hz was 42.3 kΩ and at 10 kHz the standard deviation was 24.17 Ω. The impedance values fell within two standard deviations of the mean. The phase angle peaked at approximately 65° at 12 Hz, with no values falling outside two standard deviations of the mean (refer to **Figure 2**, bottom panel).

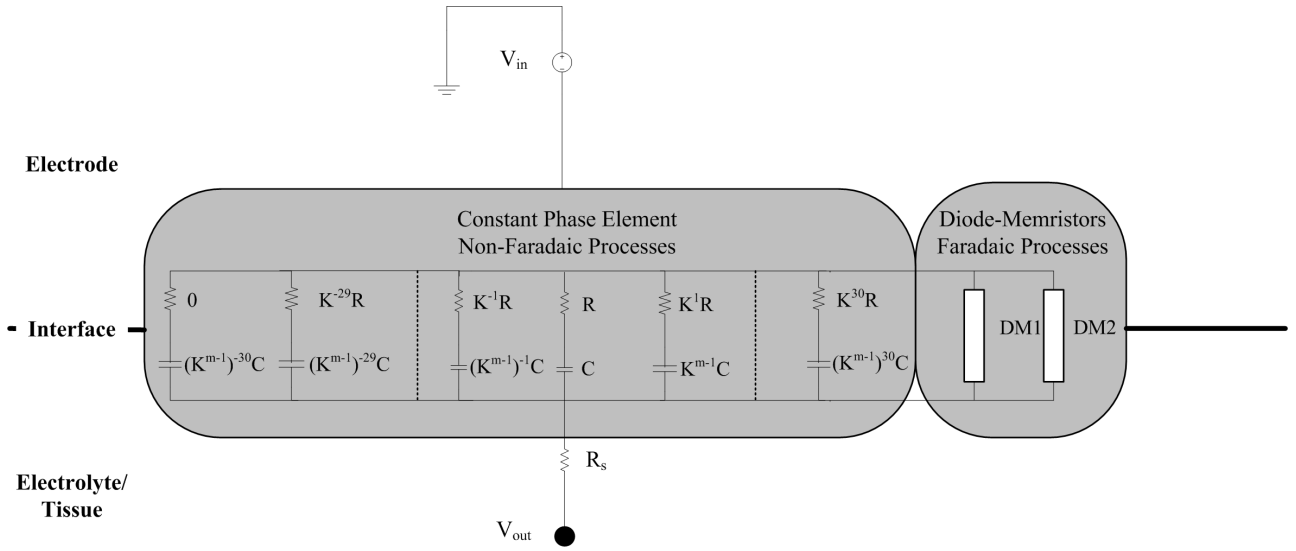

FIGURE 3 | Schematic of the circuit implementation of the electrode-tissue interface. The non-Faradaic processes are modeled as 61 RC branches representing a constant phase element. After selection of the initial R and C values for the middle branch, the resistance and capacitance of all the other branches can be calculated using the m and k parameters. R_S is a spreading resistance that represents the contact between the interface and the bulk solution or tissue. Stimulus is provided by a grounded voltage source (V_{in}) and delivered, via the interface, to the tissue (V_{out}).

TABLE 2 | Parameters of the constant phase element model of electrodes in the cochlea array.

Constant phase angle (θ_{CPE})	**65.3°**
Density of RC branches (k)	1.18
Number of RC circuits in network	61
Serial resistance (R_S)	297 Ω

Parameter values were optimized to reproduce experimental impedance measurements.

A Circuit Description of the Electrode-Tissue Interface

The electrode-electrolyte can be considered as a constant phase element (CPE), which we modeled as a network of series resistor-capacitor (RC) branches in parallel to allow for simulation of frequency dependency in the time domain. The time constant of each series-RC branch covers a particular frequency such that the entire network spans the 0.1–10 kHz bandwidth analyzed during EIS measurements. This circuit is coupled with a spreading resistance, representing the contact between the electrode-electrolyte bilayer, and the bulk solution or tissue. Scott and Single (2014) provided a method for determining the necessary parameters of the RC network based on work from Morrison (1959) who provided the mathematical basis of building up the RC network to represent a CPE. **Figure 3** shows the topography of the required RC network.

Producing a model with good correlation to the experimental EIS measurements required iterative adjustment of variables. Briefly, to calculate the resistance and capacitance of each branch two parameters are required: the density of RC branches in the network (k), and m the average value of the argument of the CPE.

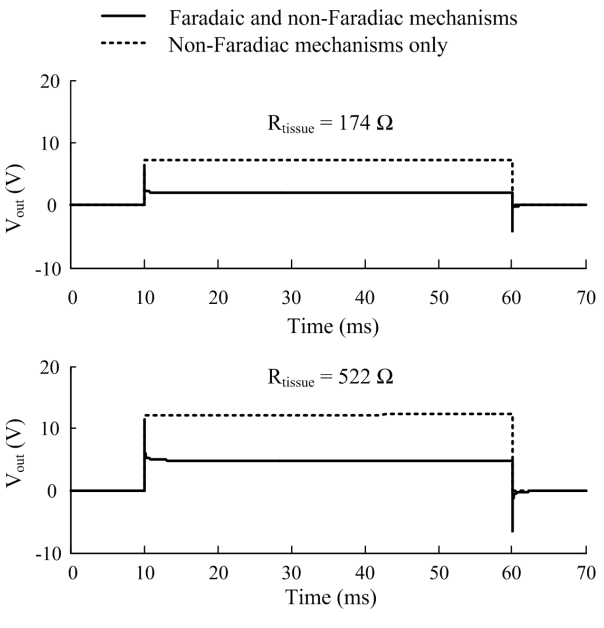

FIGURE 4 | The effect of including Faradaic mechanisms in the electrode-tissue interface model. Two tissue resistance cases are illustrated corresponding to stimulation applied in the alternate and tandem configurations, respectively, in the cochlea. Responses of the interface circuit to a pulse stimulus (20 V, 50 ms, 10 μs rise and fall times) as simulated in LTSpice (1 μs maximum time step size). Faradaic currents were modeled by diode-memristors circuits.

Parameter m is calculated by

$$m = \frac{\pi}{2\theta_{CPE}}$$

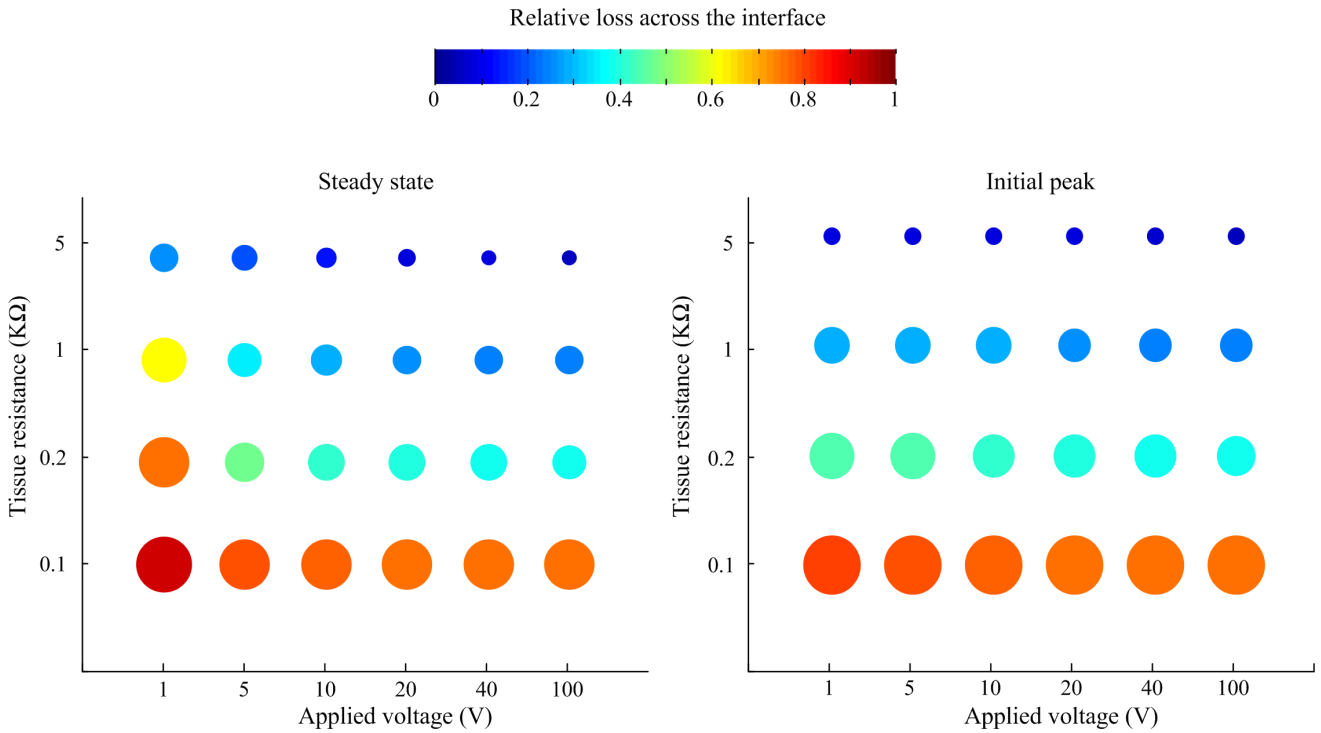

FIGURE 5 | Relative loss of applied voltage across the interface predicted by the LTSpice model. For all cases, the applied rectangular pulse had a width of 50 ms and rise and fall times of 10 μs. The loss was measured at the steady state at the end of the pulse and the initial peak.

where θ_{CPE} is the phase angle. Model parameters were manually adjusted in the following order to obtain best fit for the impedance magnitude and phase data: number of RC circuits, k, θ_{CPE}, and finally R_s. Optimized model parameters are listed in **Table 2** and the values of R and C for each branch are provided in the **Supplementary Material**.

The CPE represents the non-Faradaic mechanisms occurring at the electrode-electrolyte bilayer. To solve the frequency dependent model in the time domain, the 61-branch circuit was implemented as a SPICE model using LTSpice XVII (Analog Devices, United States). The CPE response is characterized by rapid peaks at the onset and termination of voltage pulses and a non-zero steady state of the output potential during the plateau of the pulse (**Figure 4**), the magnitude of both peaks and steady state are dependent on the resistance of the tissue in contact with the electrode.

A pair of diode-memristor branches was added to phenomenologically represent Faradaic redox reactions occurring at the electrode-electrolyte interface (Scott and Single, 2014) (refer to **Supplementary Material** for the full circuit diagram). At a stimulus pulse magnitude of 20 V and duration 50 ms, this addition had the effect of increasing the electric potential output across the electrode-tissue interface and masking the CPE peaks at the onset and termination of the stimulus pulse (**Figure 4**).

A sensitivity study was conducted to systematically investigate the relationship of tissue impedance and applied pulse amplitude on the potential output of the electrode-tissue interface. Using pulses of 50 ms duration and 10 μs rise and fall times, the response of the interface was simulated in LTSpice. The loss in peak and steady-state electric potential across the interface relative to applied voltage is plotted in **Figure 5**. In general, the relative loss decreased with applied voltage and tissue resistance, although the effect of tissue resistance was more pronounced, especially when considering the initial peak response.

Finite Element Simulations of Electroporation in the Cochlea

The tissue impedance was predicted *in silico* by applying a constant 1 V stimulus in the alternate and tandem configurations and solving the computational model using a stationary solver. The tissue impedance was predicted to be 174 and 522 Ω for the alternate and tandem configurations compared to 200 and 600 Ω measured experimentally *in vivo*.

These *in silico* predicted tissue impedances were used to calculate the voltage drop across the electrode-tissue interface using the circuit model (**Figure 4**) in response to 20 V, 50 ms monophasic electroporation pulses for both the alternate and tandem configuration (note that the rise and fall times were increased to 1 ms to facilitate numerical convergence in the following step). The predicted voltage waveforms (V_{out} in **Figure 4**) were subsequently applied in the cochlea FE model to examine the electric field distribution during electroporation. The cochlea experienced electric potentials of ±7 and ±12 V at the cathode/anode electrodes for the alternate and tandem configurations, respectively. The differences between tandem and

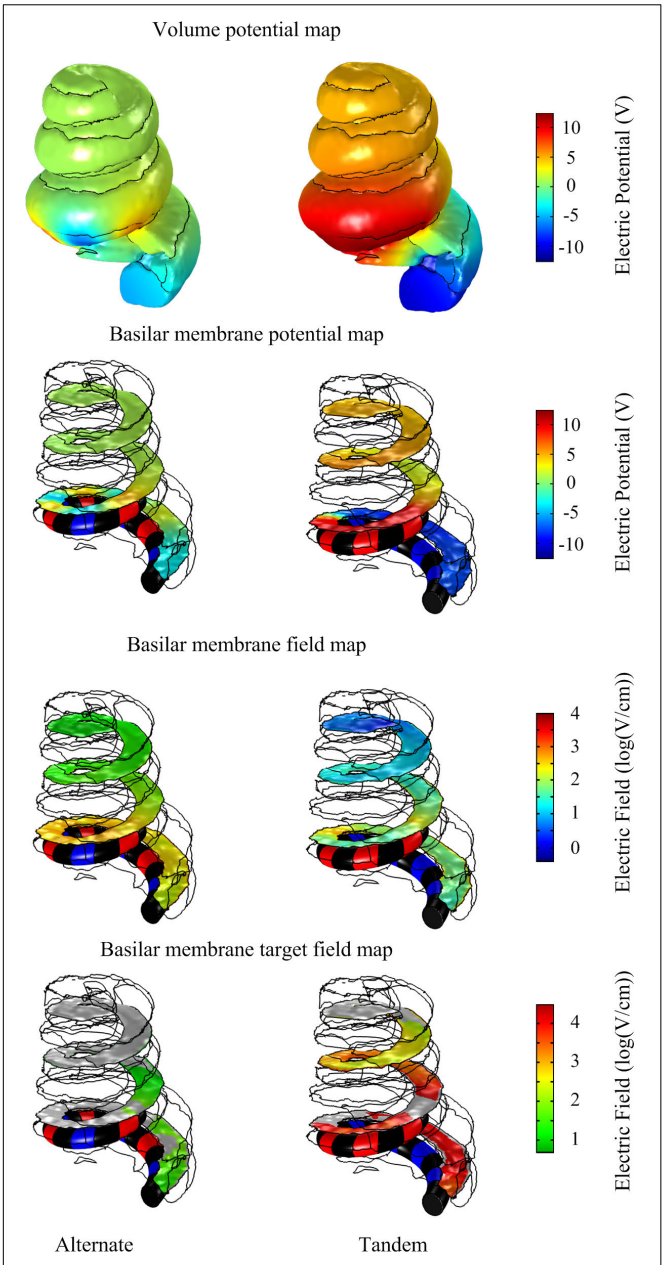

FIGURE 6 | Comparison of electric potential and field maps predicted by a computational finite element model of array-driven electroporation in the guinea pig cochlea. For both alternate and tandem electrode configurations a 20 V, 50 ms pulse was applied with 1 ms rise and fall times. Electric potential and field maps were plotted on the surface representing the basilar membrane.

alternate configurations in terms of both electric potentials and fields are illustrated in **Figure 6**.

To quantify differences in the electric fields at the target tissue, namely the basilar membrane, we grouped the electric fields at various levels of interest and calculated the areas of target tissue subject to electric field strengths over each range (**Figure 7**). It is worth noting the spread of areas subject to the electric field within the target range beyond the insertion point of the electrode array.

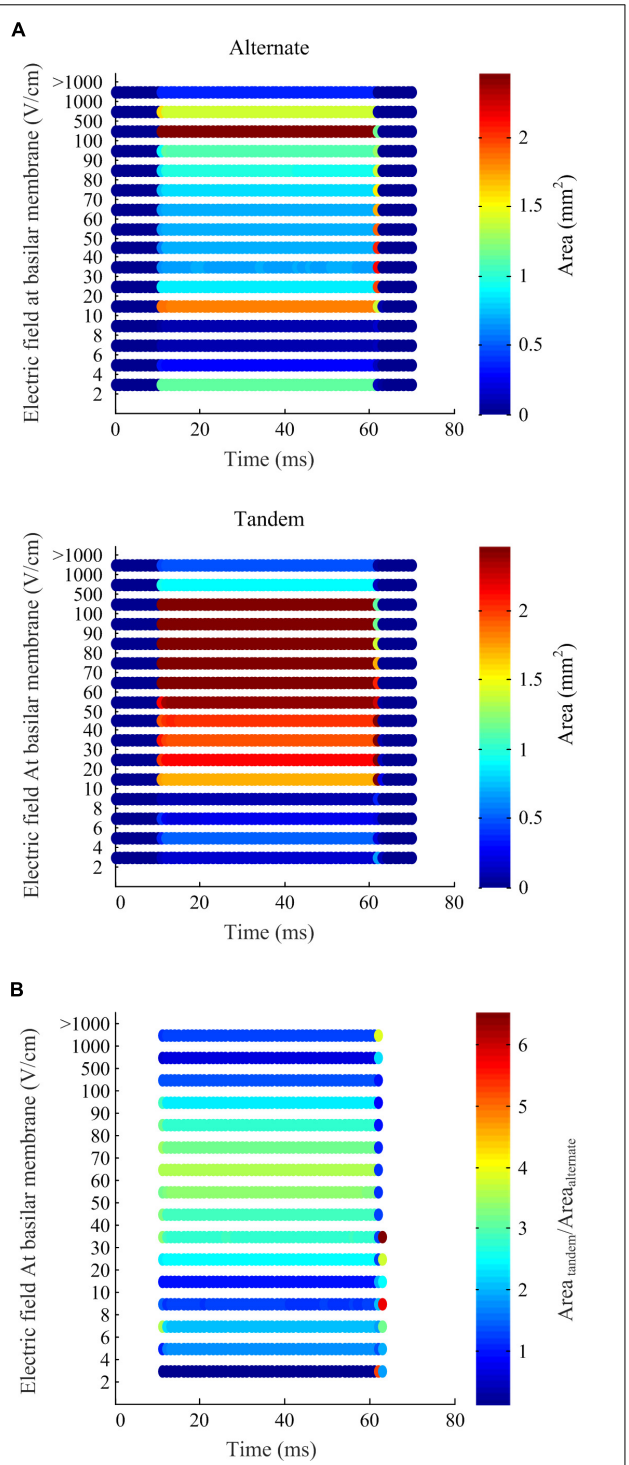

FIGURE 7 | Electric field levels predicted at the basilar membrane by the computational simulation of array-driven electroporation in the guinea pig cochlea. **(A)** The electric field is categorized into different levels and the area on the basilar membrane subjected fallen within each level is plotted at each sample time point. Two electrode configurations are considered: alternate and tandem, and in both cases a single 20 V, 50 ms pulse was applied with 1 ms rise and fall times. **(B)** A comparison of the areas at each electric field level obtained using the tandem electroporation configuration relative to the alternate configuration.

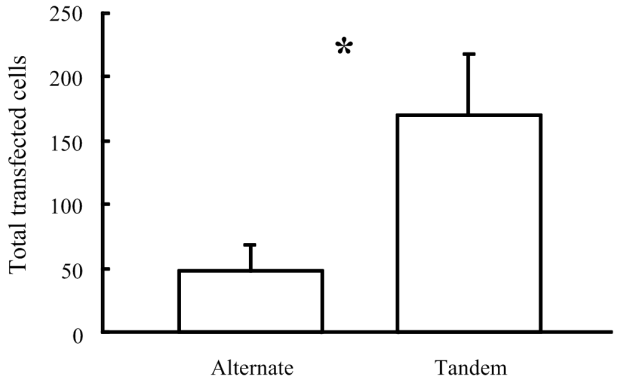

FIGURE 8 | Comparison of the number of cells transfected *in vivo* in the Guinea pig cochlea following electroporation using 40 V pulses delivered by two electrode configurations (*p = 0.035).

The area of the basilar membrane subjected to electric fields in the 20–100 V.cm^{-1} during array-driven electroporation using the tandem configuration was about three to fourfold that predicted for the alternate configuration (**Figure 7**). In the 4–8 V.cm^{-1} range an approximately twofold increase in the area in the tandem configuration compared to alternate can be also noted. Also noteworthy is that the alternate configuration generated a large area of target tissue subject to electric fields in the much higher 500–1000 V.cm^{-1} range.

In vivo Gene Electrotransfer

As described by Pinyon et al. (2014), using five × 50 ms constant-voltage pulses of 20 V in the tandem array configuration achieved much greater DNA electrotransfer efficiency than equivalent pulses using the alternating electrode configuration. Five × 50 ms pulses of 20 V were the most efficient electroporation parameters tested using the tandem array, while with the alternating array configuration, increasing pulse number to 20 and voltage to 40 V improved electrotransfer efficiency. However, even using these increased parameters with the alternating configuration, the mean number of transfected cells was still greater using the tandem configuration (mean = 169.1 ± 47.9, n = 7) compared to the alternating configuration (mean = 47.4 ± 21.5, n = 5), One-tailed P-value = 0.035 (**Figure 8**).

DISCUSSION

In contrast to chronic electrical stimulation in neural prostheses where cell or tissue excitability can be related to charge injection and strength-duration curves, hypotheses to explain the novel acute application of bionic array based electric field focusing underlying electroporation based gene delivery (Browne et al., 2016; Housley et al., 2016; Abed et al., 2018) are less established; naked plasmid DNA electrotransfer appears less dependent on membrane pore formation and resealing, than processes of endocytosis (Escoffre et al., 2011). However, both modalities share the premise that efficacy is tied to the strength of the electric field at the target cell or tissue. Therefore it is imperative to be able to map the electric field at target sites *in situ*. For the consideration here of the DNA electrotransfer application, electric fields have been mapped in saline baths *in vitro* and contributed to understanding the improved efficiency of GFP expression using a tandem as opposed to an alternating electrode configuration in HEK293 cell monolayers (Browne et al., 2016). However, the utilized methodology of measuring electric potentials using a microelectrode limits *in vivo* application, and the computational modeling approach is most informative.

In this study, the computational simulation has predicted the electric fields around the complex target tissues within the guinea pig cochlea. Combining electrochemical impedance characterization and modeling of electrodes and anatomically realistic reconstruction of target geometry we simulated array driven electroporation of the cochlea and predicted the electric fields generated at the basilar membrane for both alternate and tandem electrode array configurations. The model's predictions were verified by comparing and closely matching *in posteriori* differences quantified by imaging of transfected marker proteins following *in vivo* electroporation during similar stimulation protocols.

Finite element computational modeling of electrical stimulation in the cochlea has been the subject of many investigations for over 30 years (Finley et al., 1987; Finley, 1989; Finley et al., 1990). More recent models based on image reconstructions (Ceresa et al., 2014; Kalkman et al., 2015; Kang et al., 2015; Malherbe et al., 2016; Tachos et al., 2016; Teal and Ni, 2016; Wong et al., 2016; Cakir et al., 2017; Schafer et al., 2018) or simplified geometries (Briaire and Frijns, 2000, 2006; Hanekom, 2001; Rattay et al., 2001; Goldwyn et al., 2010; Saba et al., 2014; Nogueira et al., 2016) of the cochlea have been applied to predict electric potential and field distributions following electric stimulation by electrode arrays of cochlear implants.

Our 3D finite element electric model is a novel application of computational modeling to study electroporation in the cochlea (**Figure 9**). The incorporation of time-domain representation of both Faradaic and non-Faradaic mechanisms occurring at the electrode-tissue interface enables simulation of the relatively large-amplitude voltage pulses applied during gene electrotransfer.

The utility of computational modeling to predict generated electric fields during electric stimulation or electroporation pulses is especially demonstrated in cases with complex anatomical and electrode geometries. The helical structure of the cochlea and the winding insertion of the electrode array is a case in point. Our simulations predicted extension of target regions in the cochlea structure distal to the insertion point of the electrode array. This unanticipated finding would have been unattainable by simple analytical calculation of electric fields in tissue between two parallel plate electrodes. Other approaches for estimating electric fields in target tissue or cells include MRI or impedance-based methods (Kranjc et al., 2011). However, these still cannot match the spatial or temporal resolution of computational models.

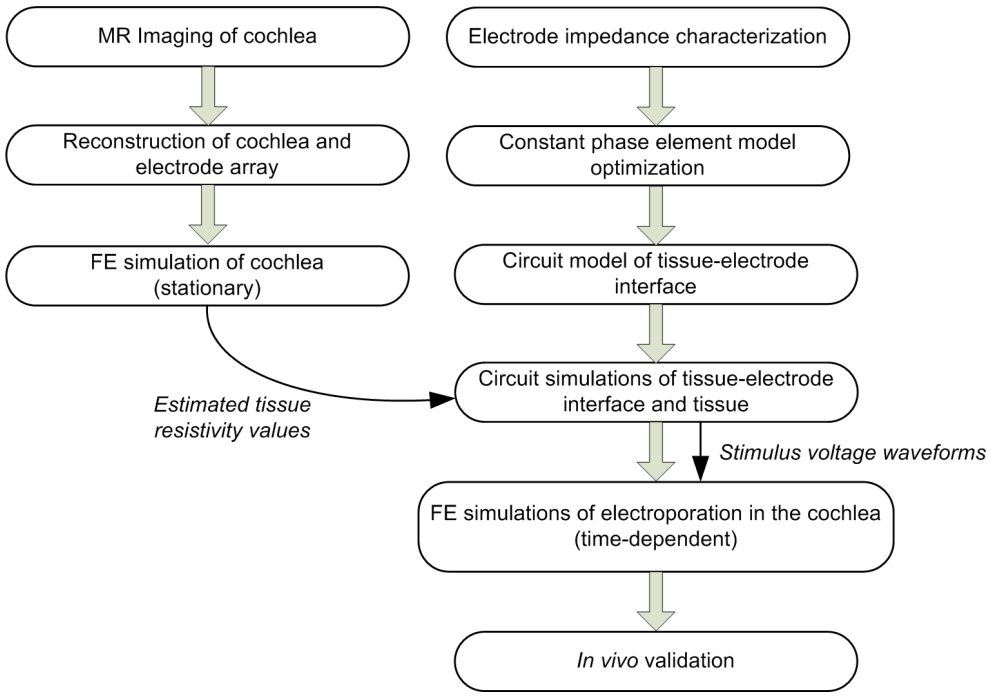

FIGURE 9 | Modeling workflow.

Impedance of the electrodes, more specifically the electrode-tissue bilayer, is one critical factor in neural interfacing. For stimulating electrodes, an extensive research effort has been targeted toward characterization of impedance with the aim of developing materials and fabrication techniques to reduce the interface impedance and improve long-term biocompatibility. Electrochemical impedance spectrometry has motivated development of mathematical and circuit models of the electrode-electrolyte bilayer that could capture the frequency dependency of interface impedance. This has posed a challenge for developers of computational models of neuroprostheses, whom rely on transient analysis to simulate the responses of tissue to electrical stimulation delivered by the prosthesis. In most 3D finite element cases, the interface has simply been ignored, or replaced by a simple RC circuit that fails to capture frequency-dependency behavior. For small offset potentials, that is non-Faradaic stimulation (Franks et al., 2005; Pham et al., 2010) or the use of recording electrodes (Al Abed et al., 2018), the voltage drop across the interface has been modeled using a cosh function based on the Gouy-Chapman-Stern capacitances (Gouy, 1910; Chapman, 1913; Stern, 1924).

Based on the work by Scott and Single (2014) and Morrison (1959) our electrode-tissue interface model includes formulations for both Faradaic mechanisms, optimized to match experimental EIS measures, and non-Faradaic mechanisms occurring at the bilayer and therefore allows simulation of high voltage pulses typical of electroporation that would most likely drive oxidation and reduction of chemical species at the interface. This is a significant advancement on published computational studies of electroporation that use a voltage boundary condition to model application of pulses to target tissue (e.g., Sel et al., 2007; Corovic et al., 2008; Suzuki et al., 2015). On the other hand, our approach can replicate the voltage drop across the electrode-tissue interface and therefore enables more accurate prediction of the effective electric fields generated in the target tissue.

Our sensitivity analysis predicts that for relatively long voltage pulses (50 ms) the relative loss of applied voltage across the interface decreases with tissue resistance and applied pulse amplitude. In chronically implantable neuroprotheses, development of tissue fibrosis around the implanted electrodes is a major issue reducing the long-term efficacy of implants. Our analysis demonstrates that the impact of fibrosis is complex, for voltage-based stimuli. The voltage drop across the electrode-neural interface will be reduced but at the expense of a higher loss across the extracellular space due to the presence of fibrotic tissue.

It appears that predictions from *in silico* simulations of the cochlea underestimate the tissue impedance for alternate and tandem configurations (174 and 522 Ω for the alternate and tandem compared to 200 and 600 Ω). However, it should be noted that impedance measurements conducted during *in vivo* experiments are measures of total system impedance including the interface impedance. We have shown in circuit simulations that for voltage stimulation the tissue resistance affects the interface impedance and hence the differences in tissue impedance values are expected.

Gene Electrotransfer in the Cochlea

Cochlear implants can be considered one of the most clinically successful neuroprostheses, with more than 500,000 devices

implanted to aid in the restoration of functional hearing in patients. Electroporation facilitated transfection of neurotrophic factors is a methodology that could allow for improving the efficacy of electrical stimulation in cochlear implants (O'Leary et al., 2009; Pinyon et al., 2014, 2019; Browne et al., 2016; Housley et al., 2016; Abed et al., 2018). Even though the model was developed with electroporation as the primary application in this paper, the inclusion of anatomically realistic geometry and EIS-based electrode-electrolyte model makes it well suited to predict electric potentials and fields generated by shorter pulses typically used in cochlear implants for electrical stimulation of the auditory nerve. However, it is notable that current cochlear implant devices cannot produce the sustained current pulses required for CFE due to limitations on rail voltage (∼10 V) and the inductive power supply which is matched to typically low tens of μs pulse durations at kHz frequencies which are effective for auditory nerve fiber excitation, switching dynamically between individual electrodes.

Model Shortcomings and Limitations

As in all computational simulations studies our model takes a compromise between simplicity of assumptions and accuracy. The model's description of Faradaic mechanisms at the tissue-electrode interface is purely phenomenological, with no details included for the electrochemical reactions per chemical species at the interface. If knowledge of changes in concentration of ions is required, say for example to predict changes in pH associated with exceeding the water window, an alternative approach that is more focused on the electrochemistry is required. For simplicity we approximated likely tissue damage by identifying target regions subject to high electric field intensities. Based on this we postulate that the alternate configuration yields larger areas with higher electric fields, potentially leading to a higher percentage of cell death.

Another limitation is that the parameters of the diode-memristor circuit representing the Faradaic mechanism at the electrode-tissue interface are taken from Scott and Single (2014) who also used a platinum electrode array in their study albeit of a different size and structure. Future work could include optimizing these parameters for our particular experiments and electrode array.

ETHICS STATEMENT

This study was carried out in accordance with the NSW Animal Research Act 1985, NSW Animal Research Regulations 2010, and Australian Code for the Care and Use of Animals for Scientific Purposes 8th Edition 2013, and were approved by the University of New South Wales Animal Care and Ethics Committee (ACEC approval number 10/81A).

AUTHOR CONTRIBUTIONS

FC and AA conducted the EIS measurements. JP and GH conducted the *in vivo* electroporation experiments. GC conducted the MR imaging of the cochlea. FC developed the constant phase element model. AA developed the full electrode–tissue interface LTSpice model. EF segmented and reconstructed the cochlea geometry as well as the electrode array, and generated the 3D mesh. AA and EF developed the computational model. AA drafted the manuscript. AA, JP, GH, and NL designed and coordinated the study. All authors reviewed the manuscript.

FUNDING

This research was supported by the Australian Research Council (Grant Nos. LP140101008 and DP151014754) and the Australian National Imaging Facility.

ACKNOWLEDGMENTS

We thank Benedict Dupree for the introduction to and stimulating discussions on the compact non-linear CPE approach to modeling the electrode-electrolyte bilayer and Peter Single from the Saluda Medical Ltd., for sharing his LTSpice implementation of the diode-memristor circuit.

SUPPLEMENTARY MATERIAL

The Supplementary Material for this article can be found online at: https://www.frontiersin.org/articles/10.3389/fnins.2019.00691/full#supplementary-material

REFERENCES

Abed, A. A., Foster, E., Pinyon, J. L., Li, C. H., Cowin, G. J., Housley, G. D., et al. (2018). Computational simulation of array-based electroporation in the cochlea. *Conf. Proc. IEEE Eng. Med. Biol. Soc.* 2018, 2462–2465. doi: 10.1109/EMBC.2018.8512808

Al Abed, A., Srinivas, H., Firth, J., Ladouceur, F., Lovell, N. H., Silvestri, L., et al. (2018). A biopotential optrode array: operation principles and simulations. *Sci. Rep.* 8:2690. doi: 10.1038/s41598-018-20182-x

Andreuccetti, D., Fossi, R., and Petrucci, C. (2017). *Dielectric Properties Of Body Tissues*. Florence: Italian National Research Council.

Atkinson, P. J., Wise, A. K., Flynn, B. O., Nayagam, B. A., Hume, C. R., O'Leary, S. J., et al. (2012). Neurotrophin gene therapy for sustained neural preservation after deafness. *PLoS One* 7:e52338. doi: 10.1371/journal.pone.0052338

Briaire, J. J., and Frijns, J. H. (2000). Field patterns in a 3D tapered spiral model of the electrically stimulated cochlea. *Hear. Res.* 148, 18–30. doi: 10.1016/s0378-5955(00)00104-0

Briaire, J. J., and Frijns, J. H. (2006). The consequences of neural degeneration regarding optimal cochlear implant position in scala tympani: a model approach. *Hear. Res.* 214, 17–27. doi: 10.1016/j.heares.2006.01.015

Browne, C. J., Pinyon, J. L., Housley, D. M., Crawford, E. N., Lovell, N. H., Klugmann, M., et al. (2016). Mapping of bionic array electric field focusing in plasmid DNA-based gene electrotransfer. *Gene. Ther.* 23, 369–379. doi: 10.1038/gt.2016.8

Cakir, A., Dwyer, R. T., and Noble, J. H. (2017). Evaluation of a high-resolution patient-specific model of the electrically stimulated cochlea. *J. Med. Imaging* 4:025003. doi: 10.1117/1.JMI.4.2.025003

Ceresa, M., Lopez, N. M., Velardo, H. D., Herrezuelo, N. C., Mistrik, P., and Kjer, H. M. (2014). Patient-specific simulation of implant placement and function for cochlear implantation surgery planning. *Med. Image Comput. Comput. Assist. Interv.* 17, 49–56. doi: 10.1007/978-3-319-10470-6_7

Chapman, D. (1913). A contribution to the theory of electrocapillarity. *Philos. Mag.* 25, 475–481.

Corovic, S., Al Sakere, B., Haddad, V., Miklavcic, D., and Mir, L. M. (2008). Importance of contact surface between electrodes and treated tissue in electrochemotherapy. *Technol. Cancer Res. Treat* 7, 393–399. doi: 10.1177/153303460800700507

Escoffre, J. M., Portet, T., Favard, C., Teissie, J., Dean, D. S., and Rols, M. P. (2011). Electromediated formation of DNA complexes with cell membranes and its consequences for gene delivery. *Biochim. Biophys. Acta* 1808, 1538–1543. doi: 10.1016/j.bbamem.2010.10.009

Finley, C., Wilson, B., and White, M. (1987). "A finite-element model of bipolar field patterns," in *Proceedings of the 9th IEEE Annual International Conference on Electrically Stimulated Cochlea: a Two Dimensional Approximation and EMBS*, (Seattle, WA: IEEE), 1901–1903.

Finley, C. C. (1989). "A finite-element model of radial bipolar field patterns in the electrically stimulated cochlea-two and three dimensional approximations and tissue parameter sensitivities, engineering in medicine and biology society, 1989," in *Proceedings of the Annual International Conference of the IEEE Engineering Images of the Twenty-First Century*, (Seattle, WA: IEEE), 1059–1060.

Finley, C. C., Wilson, B. S., and White, M. W. (1990). Models of neural responsiveness to electrical stimulation, in *Cochlear Implants*, eds J.M. Miller, F.A. Spelman, eds (New York, NY: Springer), 55–96.

Franks, W., Schenker, I., Schmutz, P., and Hierlemann, A. (2005). Impedance characterization and modeling of electrodes for biomedical applications. *IEEE Trans. Biomed. Eng.* 52, 1295–1302. doi: 10.1109/tbme.2005.847523

Goldwyn, J. H., Bierer, S. M., and Bierer, J. A. (2010). Modeling the electrode-neuron interface of cochlear implants: effects of neural survival, electrode placement, and the partial tripolar configuration. *Hear. Res.* 268, 93–104. doi: 10.1016/j.heares.2010.05.005

Gouy, M. (1910). Sur la constitution de la charge électrique à la surface d'un électrolyte. *J. Phys. Theor. Appl.* 9, 457–468. doi: 10.1051/jphystap:019100090045700

Hanekom, T. (2001). Three-dimensional spiraling finite element model of the electrically stimulated cochlea. *Ear Hear.* 22, 300–315. doi: 10.1097/00003446-200108000-00005

Housley, G. D., Browne, C. J., Crawford, E. N., Klugmann, M., Lovell, N. H., Pinyon, J. L., et al. (2016). "Cochlear implant close-field electroporation," in *Handbook of Electroporation*, ed. D. Miklavcic (NewYork, NY: Springer International Publishing), 1–20. doi: 10.1007/978-3-319-26779-1_59-1

Kalkman, R. K., Briaire, J. J., and Frijns, J. H. (2015). Current focussing in cochlear implants: an analysis of neural recruitment in a computational model. *Hear. Res.* 322, 89–98. doi: 10.1016/j.heares.2014.12.004

Kang, S., Chwodhury, T., Moon, I. J., Hong, S. H., Yang, H., Won, J. H., et al. (2015). Effects of electrode position on spatiotemporal auditory nerve fiber responses: a 3D computational model study. *Comput. Math. Methods Med.* 2015:934382. doi: 10.1155/2015/934382

Kranjc, M., Bajd, F., Sersa, I., and Miklavcic, D. (2011). Magnetic resonance electrical impedance tomography for monitoring electric field distribution during tissue electroporation. *IEEE Trans. Med. Imaging* 30, 1771–1778. doi: 10.1109/TMI.2011.2147328

Malherbe, T. K., Hanekom, T., and Hanekom, J. J. (2016). Constructing a three-dimensional electrical model of a living cochlear implant user's cochlea. *Int. J. Numer. Method Biomed. Eng.* 32:e02751. doi: 10.1002/cnm.2751

Morrison, R. (1959). RC constant-argument driving-point admittances. in *Proceedings of the IRE Transact. Circuit Theory*, Piscataway, NJ.

Nogueira, W., Schurzig, D., Buchner, A., Penninger, R. T., and Wurfel, W. (2016). Validation of a cochlear implant patient-specific model of the voltage distribution in a clinical setting. *Front. Bioeng. Biotechnol.* 4:84. doi: 10.3389/fbioe.2016.00084

O'Leary, S. J., Richardson, R. R., and McDermott, H. J. (2009). Principles of design and biological approaches for improving the selectivity of cochlear implant electrodes. *J. Neural. Eng.* 6:055002. doi: 10.1088/1741-2560/6/5/055002

Pettingill, L. N., Minter, R. L., and Shepherd, R. K. (2008). Schwann cells genetically modified to express neurotrophins promote spiral ganglion neuron survival in vitro. *Neuroscience* 152, 821–828. doi: 10.1016/j.neuroscience.2007.11.057

Pham, P., Scapola, R., Rubeck, C., and Dupont, F. (2010). "Search for a suitable numerical model for electrical stimulation: from the electric double layer to electrokinetics, confrontation with impedance measurements," in *Proceedings of the Technical Papers and Presentations COMSOL Conference*, Paris

Pinyon, J. L., Klugmann, M., Lovell, N. H., and Housley, G. D. (2019). Dual-Plasmid bionic array-directed gene electrotransfer in hek293 cells and cochlear mesenchymal cells probes transgene expression and cell fate. *Hum. Gene Ther.* 30, 211–224. doi: 10.1089/hum.2018.062

Pinyon, J. L., Tadros, S. F., Froud, K. E., Ac, Y. W., Tompson, I. T., and Crawford, E. N. (2014). Close-field electroporation gene delivery using the cochlear implant electrode array enhances the bionic ear. *Sci. Transl. Med.* 6:233ra54. doi: 10.1126/scitranslmed.3008177

Rattay, F., Leao, R. N., and Felix, H. (2001). A model of the electrically excited human cochlear neuron. II. influence of the three-dimensional cochlear structure on neural excitability. *Hear. Res.* 153, 64–79. doi: 10.1016/s0378-5955(00)00257-4

Richardson, R. T., Wise, A. K., Thompson, B. C., Flynn, B. O., Atkinson, P. J., and Fretwell, N. J. (2009). Polypyrrole-coated electrodes for the delivery of charge and neurotrophins to cochlear neurons. *Biomaterials* 30, 2614–2624. doi: 10.1016/j.biomaterials.2009.01.015

Saba, R., Elliott, S. J., and Wang, S. (2014). Modelling the effects of cochlear implant current focusing. *Cochlear Implants Int.* 15, 318–326. doi: 10.1179/1754762814Y.0000000081

Schafer, F., Enke, J., Bohnke, F., Hemmert, W., and Bai, S. (2018). Influence of the cochlear implant electrode array placement on the current spread in the cochlea. *Conf. Proc. IEEE Eng. Med. Biol. Soc.* 2018, 6145–6148. doi: 10.1109/EMBC.2018.8513666

Scott, J., and Single, P. (2014). Compact nonlinear model of an implantable electrode array for spinal cord stimulation (SCS). *IEEE Trans. Biomed. Circuits Syst.* 8, 1932–4545. doi: 10.1109/TBCAS.2013.2270179

Sel, D., Lebar, A. M., and Miklavcic, D. (2007). Feasibility of employing model-based optimization of pulse amplitude and electrode distance for effective tumor electropermeabilization. *IEEE Trans. Biomed. Eng.* 54, 773–781. doi: 10.1109/tbme.2006.889196

Stern, O. (1924). Zur theorie der elektrolytischen doppelschicht (the theory of the electrolytic double-layer). *Zeitschrift für Elektrochemie und Angewandte Physikalische Chemie* 30, 508–516.

Suzuki, D. O., Anselmo, J., de Oliveira, K. D., Freytag, J. O., Rangel, M. M., Marques, J. L., et al. (2015). Numerical model of dog mast cell tumor treated by electrochemotherapy. *Artif. Organs* 39, 192–197. doi: 10.1111/aor.12333

Tachos, N. S., Sakellarios, A. I., Rigas, G., Isailovic, V., Ni, G., Bohnke, F., et al. (2016). Middle and inner ear modelling: from microCT images to 3D reconstruction and coupling of models. *Conf. Proc. IEEE Eng. Med. Biol. Soc.* 2016, 5961–5964. doi: 10.1109/EMBC.2016.7592086

Teal, P. D., and Ni, G. (2016). Finite element modelling of cochlear electrical coupling. *J. Acoust. Soc. Am.* 140:2769. doi: 10.1121/1.4964897

Thorne, P. R., Munoz, D. J., and Housley, G. D. (2004). Purinergic modulation of cochlear partition resistance and its effect on the endocochlear potential in the guinea pig. *J. Assoc. Res. Otolaryngol.* 5, 58–65. doi: 10.1007/s10162-003-4003-4

Wise, A. K., Hume, C. R., Flynn, B. O., Jeelall, Y. S., Suhr, C. L., and Sgro, B. E. (2010). Effects of localized neurotrophin gene expression on spiral ganglion neuron resprouting in the deafened cochlea. *Mol. Ther.* 18, 1111–1122. doi: 10.1038/mt.2010.28

Wong, P., George, S., Tran, P., Sue, A., Carter, P., and Li, Q. (2016). Development and validation of a high-fidelity finite-element model of monopolar stimulation in the implanted guinea pig cochlea. *IEEE Trans. Biomed. Eng.* 63, 188–198. doi: 10.1109/TBME.2015.2480601

Conflict of Interest Statement: Patents filings associated with this research are managed via New South Innovations, the commercialization arm of University of New South Wales.

The authors declare that the research was conducted in the absence of any commercial or financial relationships that could be construed as a potential conflict of interest.

Copyright © 2019 Al Abed, Pinyon, Foster, Crous, Cowin, Housley and Lovell. This is an open-access article distributed under the terms of the Creative Commons Attribution License (CC BY). The use, distribution or reproduction in other forums is permitted, provided the original author(s) and the copyright owner(s) are credited and that the original publication in this journal is cited, in accordance with accepted academic practice. No use, distribution or reproduction is permitted which does not comply with these terms.

frontiers in Neuroscience

ORIGINAL RESEARCH
published: 09 August 2019
doi: 10.3389/fnins.2019.00745

High Density, Double-Sided, Flexible Optoelectronic Neural Probes With Embedded μLEDs

*Jay W. Reddy[1], Ibrahim Kimukin[1], Luke T. Stewart[2], Zabir Ahmed[1], Alison L. Barth[2,3], Elias Towe[1] and Maysamreza Chamanzar[1,3]**

[1] Department of Electrical and Computer Engineering, Carnegie Mellon University, Pittsburgh, PA, United States, [2] Department of Biological Sciences, Carnegie Mellon University, Pittsburgh, PA, United States, [3] Carnegie Mellon Neuroscience Institute, Carnegie Mellon University, Pittsburgh, PA, United States

Optical stimulation and imaging of neurons deep in the brain require implantable optical neural probes. External optical access to deeper regions of the brain is limited by scattering and absorption of light as it propagates through tissue. Implantable optoelectronic probes capable of high-resolution light delivery and high-density neural recording are needed for closed-loop manipulation of neural circuits. Micro-light-emitting diodes (μLEDs) have been used for optical stimulation, but predominantly on rigid silicon or sapphire substrates. Flexible polymer neural probes would be preferable for chronic applications since they cause less damage to brain tissue. Flexible μLED neural probes have been recently implemented by flip-chip bonding of commercially available μLED chips onto flexible substrates. Here, we demonstrate a monolithic design for flexible optoelectronic neural interfaces with embedded gallium nitride μLEDs that can be microfabricated at wafer-scale. Parylene C is used as the substrate and insulator due to its biocompatibility, compliance, and optical transparency. We demonstrate one-dimensional and two-dimensional individually-addressable μLED arrays. Our μLEDs have sizes as small as 22 × 22 μm in arrays of up to 32 μLEDs per probe shank. These devices emit blue light at a wavelength of 445 nm, suitable for stimulation of channelrhodopsin-2, with output powers greater than 200 μW at 2 mA. Our flexible optoelectronic probes are double-sided and can illuminate brain tissue from both sides. Recording electrodes are co-fabricated with μLEDs on the front- and backside of the optoelectronic probes for electrophysiology recording of neuronal activity from the volumes of tissue on the front- and backside simultaneously with bi-directional optical stimulation.

Keywords: neural probe, micro-LED, Parylene C, microfabrication, optogenetics

OPEN ACCESS

Edited by:
Ulrich G. Hofmann, Freiburg University Medical Center, Germany

Reviewed by:
Eric Klein, Albert Ludwigs Universität Freiburg, Germany
Patrick Degenaar, Newcastle University, United Kingdom

***Correspondence:**
Maysamreza Chamanzar
mchamanzar@cmu.edu

Specialty section:
This article was submitted to Neural Technology, a section of the journal Frontiers in Neuroscience

Received: *18 February 2019*
Accepted: *05 July 2019*
Published: *09 August 2019*

Citation:
Reddy JW, Kimukin I, Stewart LT, Ahmed Z, Barth AL, Towe E and Chamanzar M (2019) High Density, Double-Sided, Flexible Optoelectronic Neural Probes With Embedded μLEDs. Front. Neurosci. 13:745. doi: 10.3389/fnins.2019.00745

1. INTRODUCTION

Optical methods have been widely used for stimulation and functional imaging of neural circuits (Delbeke et al., 2017; Yang and Yuste, 2017). In particular, optogenetics has been used as a powerful tool for selective excitation or inhibition of specific cell types using light of different wavelengths (Chen et al., 2017; Zhao, 2017). To isolate details of neural circuit functions at different stages of health and disease, it is desirable to stimulate or inhibit a subset of neurons that express the same light-sensitive proteins. This requires delivering patterns of light into brain tissue with high spatial

resolution. Conventional methods based on external optics for light delivery are limited to superficial layers of the tissue because of absorption and scattering (Ntziachristos, 2010). Moreover, in the context of closed-loop optogenetic experiments, recording electrodes must be integrated on an optical neural probe to enable simultaneous electrical recording and optical stimulation. Recently, optoelectronic probes using either integrated μLEDs or passive optical waveguides have been introduced to enable light delivery in deep tissue (Kim et al., 2013; McAlinden et al., 2013; Wu et al., 2013; Hoffman et al., 2015; Schwaerzle et al., 2017; Shin et al., 2017; Noh et al., 2018; Zhao et al., 2018). Probes based on μLED arrays can potentially provide a higher device density for individual optical output ports. Waveguide-based optical neural probes are limited in density because each waveguide needs to be independently routed through the probe shank. Moreover, packaging of commercially-available light sources at the backend further limits the number of independently addressable channels in waveguide-based probes.

To understand the neural basis of brain function and dysfunction, it is essential to perform chronic experiments over a long period of time. Flexible polymer neural probes have recently been shown to reduce chronic damage to the brain by minimizing the tethering force on the tissue and the associated glial scarring (Biran et al., 2007; Lind et al., 2013; Moshayedi et al., 2014; Kozai et al., 2015; Spencer et al., 2017; Wurth et al., 2017). Therefore, such flexible neural probes are potential candidates for long-term chronic neural recording. Adding optical functionality to these polymer neural probes is highly desirable to allow simultaneous stimulation and recording of neural circuits. We have recently demonstrated integration of passive polymer optical waveguides with flexible neural probes to enable simultaneous electrical recording and optical stimulation (Reddy and Chamanzar, 2018a,b). Optoelectronic neural probes consisting of arrays of micro-light-emitting-diodes (μLEDs) operating at optogenetic wavelengths (450–680 nm) with integrated recording electrodes have also been demonstrated by others, but mostly on rigid substrates such as sapphire or silicon (McAlinden et al., 2015; Wu et al., 2015; Shin et al., 2017). Dense integration of μLEDs on flexible substrates remains challenging. Polymer neural probes have been realized based on flip-chip bonding of μLED chips onto a probe shank (Kim et al., 2013; Schwaerzle et al., 2015). This type of integration technique is limited to μLED chips that are separately fabricated and must then be flip-chip bonded onto a flexible substrate. This serial packaging approach of individual μLEDs limits manufacturing throughput. Recently, microfabricated μLEDs were realized on Polyimide or epoxy resin cables by transferring μLEDs from a sapphire substrate using specialized laser processing techniques (Goßler et al., 2014; Klein et al., 2018; Noh et al., 2018). Additionally, 2D arrays of μLEDs have been fabricated on sapphire substrate and bonded to a silicon wafer to take advantage of wafer-scale trace routing on silicon (Klein et al., 2017; Scharf et al., 2018).

Here, we demonstrate fabrication of μLEDs in gallium nitride (GaN)-based heterostructures grown on a silicon wafer, monolithically integrated and encapsulated in a flexible polymer that includes interconnects. The polymer and electrical interconnects are realized on top of the wafer during the fabrication process to encapsulate linear or 2D arrays of GaN μLEDs. The monolithic flexible stack is then released from the silicon substrate at the end of the fabrication process. We demonstrate wafer-scale, high-throughput microfabrication processes to implement μLED neural probes, consisting of monolithically integrated arrays of GaN μLEDs and recording electrodes on a flexible Parylene C polymer substrate. Although GaN-based μLEDs grown on silicon substrates have a low emission efficiency compared to similar devices fabricated on sapphire substrates, the fabrication process is scalable and is based on commonly-used microfabrication techniques. This process allows for a dense integration of optical stimulation and electrical recording functionalities on a unified platform for realizing high-resolution, minimally invasive neural interfaces that can be made available to a wide user base.

2. DEVICE ARCHITECTURE

Our flexible optoelectronic neural probe architecture allows simultaneous optical and electrical access to the brain, while minimizing tethering force and tissue damage inherent to rigid probe implementations. A schematic of the probe architecture is shown in **Figure 1A**. The backend of the probe, which stays outside the brain, is designed to interface with the control and signal processing electronic circuit boards (**Figure 1B**). The frontend of the probe (i.e., the probe shank), shown in **Figure 1C**, contains dense arrays of collocated μLEDs and recording electrodes. Each layer is lithographically defined, allowing for flexibility in designing the layout of the electrodes and μLEDs along the probe shank.

2.1. μLED Light Sources

Arbitrary sizes and shapes of lithographically-defined GaN μLEDs can be realized in our optoelectronic neural probes. As an example, a linear array of μLEDs with a pitch of 60 μm and 30×30 μm active area is shown in **Figure 1**. Two-dimensional arrays with any desired arrangement of light sources and recording electrodes can also be designed in our platform.

The GaN μLED mesas are encapsulated in Parylene C on the top and sides of the mesa, and by insulating undoped GaN and (Al,Ga)N on the bottom surface (**Figure 1D**). Parylene C is optically transparent at the emission wavelength of our GaN μLEDs (i.e., $\lambda = 445$ nm). As opposed to optical neural probes realized on opaque substrates, our μLEDs can emit light from both the front- and backside surfaces for stimulating surrounding neurons on both sides.

2.2. Integrated Recording Electrodes

To enable experiments in which neural activity may be monitored and stimulated at the same time, our optoelectronic neural probe platform features collocated recording electrodes and light sources. Recording electrodes and associated interconnects are realized on the same layer as the metal traces for powering the μLEDs. The traces and interconnects are insulated with a second layer of Parylene C. The recording electrodes are then exposed by etching the Parylene C layer covering the electrode sites. The monolithic fabrication process and lithographic patterning of

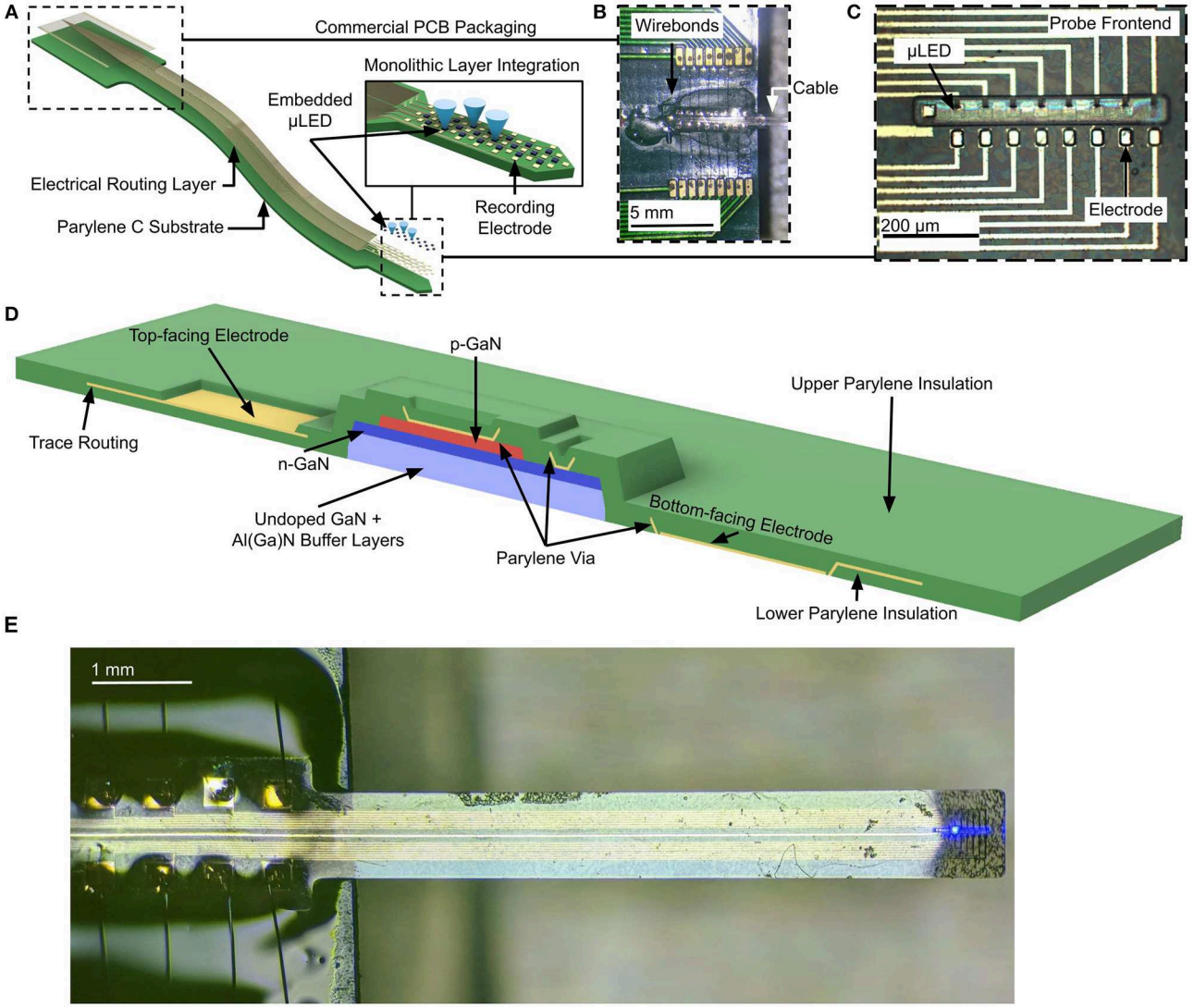

FIGURE 1 | (A) Schematic illustration of the probe architecture with a flexible Parylene C cable routing electrical traces from the device backend to the probe active region, containing µLEDs and recording electrodes, **(B)** Packaging of probe backend with consumer PCB via wirebonding, **(C)** Active region of probe, featuring GaN µLED array alongside backside recording electrodes, **(D)** Schematic cross-section of active region showing GaN µLED mesa embedded in Parylene C insulation. The metal trace layer is entirely embedded in Parylene C; front- and backside electrodes are exposed by patterning the top or bottom layer of Parylene C. Traces are connected to GaN *p*-type and *n*-type contacts with vias though the Parylene C insulation. **(E)** Packaged neural probe with linear array active region and 7-mm cable, packaged with a consumer PCB and showing emission from GaN µLED.

features in each layer of the neural probe enable us to create customizable recording electrode arrangements. In our design, recording electrodes may be fabricated either on the front- or backside of the probe, allowing for directional recording from both sides (**Figure 1D**). This capability, along with the bidirectional light emission from individual µLEDs, is a unique feature of our design that maximizes the yield of neural recording from volumes of neural tissue on both sides of the probe.

An example of our optoelectronic neural probes is shown in **Figure 1E** with the active region near the tip of the 7 mm long probe cable.

2.3. Monolithic Neural Probes With High Channel Counts

To maximize the read/write bandwidth to and from the brain using a neural probe, a high density of light sources and recording electrodes is essential. In some cases, closely spaced electrodes and light sources may interface with overlapping populations of neurons in the brain, which may result in redundant or overlapping information. However, since the mechanisms of neural encoding at the network-level are not well-understood, it is highly advantageous to stimulate and sample neuronal activity in the brain with high spatio-temporal resolution in multiple distinct regions simultaneously (Buzsáki, 2004; Buzsáki et al.,

2015). A rather serious challenge in the design of high-density neural probes is the trade-off between the compactness of the neural probe to minimize damage to tissue, and the need to increase the number of channels in a probe. This trade-off is fundamental and is rooted in the planar fabrication processes, where each recording electrode and each μLED requires a dedicated electrical path that must be routed along the probe cable. As a result of this trade-off, the number of electrical traces scales linearly with the number of additional device channels (optical or electrical), which in the end becomes a major bottleneck to maintaining a narrow width of the probe shank (**Figure 2A**). Under this circumstance, the width of the probe is determined by the number of traces that must be routed along the cable to the probe shank, i.e., (n_t) and the trace pitch (p) (Equation 1).

$$W = p \times n_t. \tag{1}$$

In our current design, we used a conservative trace width of 10 μm for ease of fabrication. However, in our previous work we have demonstrated that traces can be made as small as 300 nm (Chamanzar et al., 2015). In principle, advanced nanofabrication techniques can be employed to implement electrical traces with very narrow widths using high-resolution electron-beam or deep-UV lithography (Shobe et al., 2015; Jun et al., 2017). In general however, specialized lithographic processes are not easily scalable, require dedicated lithography equipment, and are costly to implement. Furthermore, there is a fundamental limitation to the density of traces. As traces become narrower, the electrical resistance increases, although this also depends on the trace thickness. Increasing the trace resistance results in a larger voltage drop on the lines that power μLEDs and also increases the associated thermal noise, decreasing the signal-to-noise ratio for recording electrodes. Therefore, when scaling down the size of traces, resistance must be carefully considered. Reduced spacing between traces also leads to crosstalk between channels. Scaling is only practical to a point through improved lithography resolution. Consequently, an architecture that reduces the number of necessary traces is needed to enable continued future scaling of the number of device channels. In this work, we report an architecture that enables massive scaling of μLEDs on a single neural probe shank, even with large trace widths.

Considering the case of the μLEDs, one notes that each device requires a *p*-type and an *n*-type ohmic contact interconnect. In a naive routing scheme, where each contact trace is routed individually (**Figure 2B**), the total probe width would be given as

$$W = p \times 2N, \tag{2}$$

where N is the number of μLED devices. In such a scheme, a probe shank with 200 traces would support a maximum of 100 μLED devices. This scheme can be improved through use of a shared common *n*-type contact in linear arrays (**Figure 2C**), thus reducing the width of the shank to

$$W = p \times (N + 1), \tag{3}$$

since each μLED now requires only one trace for each contact to the *p*-type layer, and all devices share a common trace for the *n*-type contact. In this shared *n*-type contact scheme, a probe shank that can accommodate 200 traces would support a maximum of 199 μLEDs.

To allow for a massive scaling of the number of μLED devices per probe shank, we can design a network of interconnects such that the traces for the *p*-type and the *n*-type contacts are shared among μLEDs in an individually-addressable grid (**Figure 2D**). Such a scheme would reduce the required probe width to

$$W = p \times 2\sqrt{N} \tag{4}$$

in a square device array. In this design, a probe shank capable of accommodating 200 traces would support 10,000 μLEDs, which is a significant improvement over other routing schemes. However, this type of architecture would be precluded by the 2D nature of our planar microfabrication process since perpendicular traces defined in a single layer would cross each other and cause short-circuits. Although multilayer routing schemes are possible, these greatly complicate the fabrication process and reduce yield. Instead, we offer an alternative novel approach to achieving optimal electrical routing without the need for additional trace insulation or routing layers.

Our technique takes advantage of the lithographic definition of each layer of the μLED mesa structure. Since the *p*-type and *n*-type GaN layers are defined in separate lithography steps, they may be formed with arbitrary shapes. In this case, we etch individual *p*-type mesas in a rectangular grid, and etch *n*-type mesas in horizontal strips along the axis of the grid. The routing of each *n*-type "row" of the grid is accomplished by the *n*-type contacts on the GaN mesa itself (**Figure 2E**), forming a "bridge." Electrical traces running in vertical "columns" join the *p*-type contacts vertically. The *n*-type layer is separated from the electrical traces by SiO_2 and Parylene C passivation, providing two separate layers for routing without additional processing steps. This architecture is only possible when the GaN mesas and neural probe cable routing are monolithically integrated, since it requires the geometry in the mesa structures to complement the overall probe routing and architecture.

To demonstrate the feasibility of this monolithically integrated architecture, we have created dense 2D arrays with a pitch of 60 μm along the y-axis and 40 μm along the x-axis. Individual GaN μLEDs have an active area of 22 × 22 μm. Our devices are the first to demonstrate the full 2D implementation of the shared-contact routing scheme. Two-dimensional indexing of μLEDs has been previously suggested by Goßler et al. (2014). The unique feature of our design, which obviates the need for an extra layer of traces in a 2D indexing scheme, is that we use the *n*-type mesa to access μLEDs in each row.

In this architecture, each μLED may be powered and individually addressed by supplying current to the proper trace for the *p*-type contacts and grounding the related trace for *n*-type contacts (**Figure 2F**). Although arbitrary patterns of μLEDs may not be simultaneously illuminated, arbitrary patterns of neural stimulation are still possible through time-division multiplexing of the μLED channels. In general, GaN optoelectronics can switch

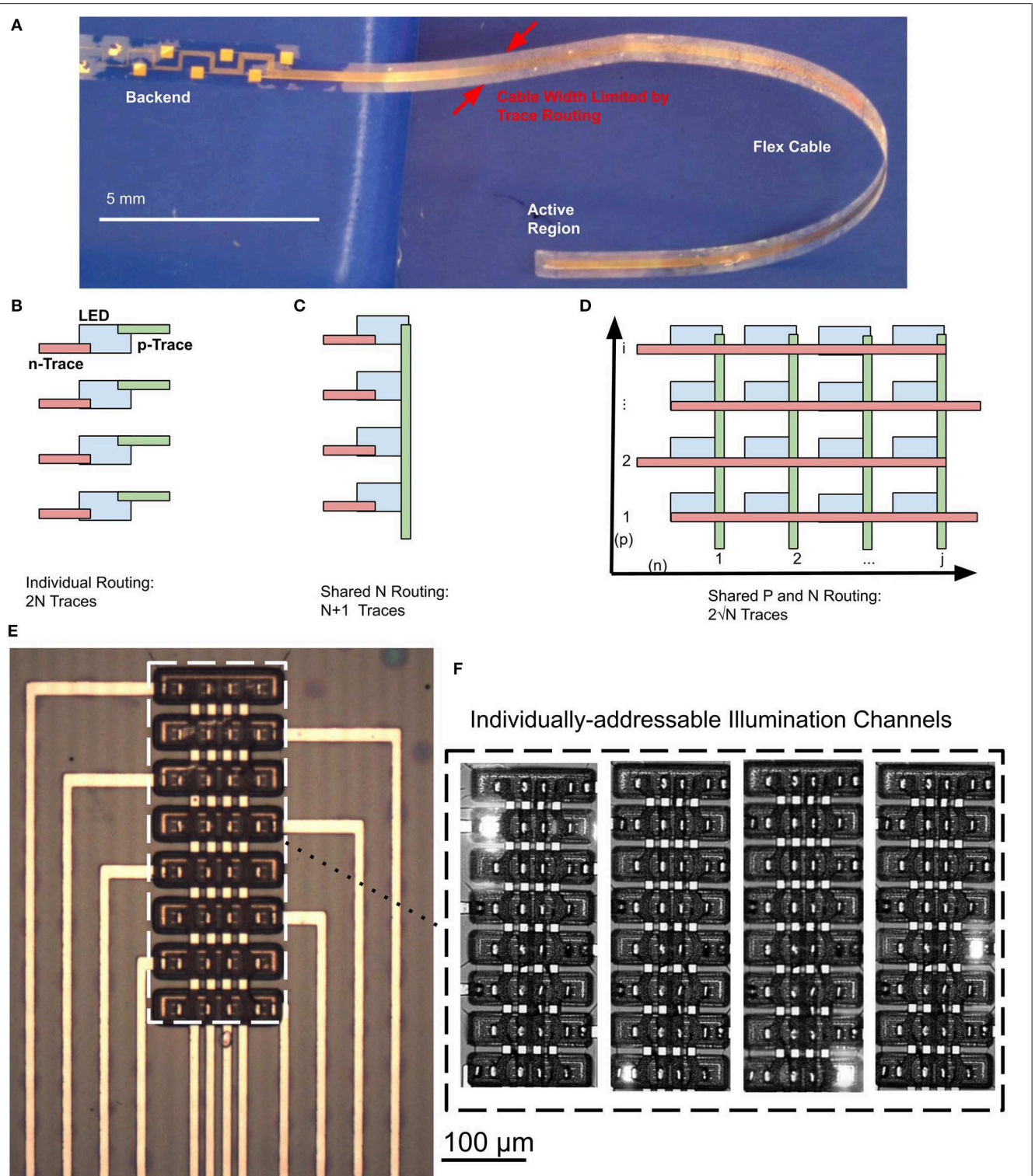

FIGURE 2 | (A) Released, flexible 2.1-cm Parylene C cable with embedded µLEDs. Cable dimensions are constrained by the number of traces that needs to be routed in a single layer. **(B)** Trace routing scheme when each µLED has a dedicated electrical trace for the *p*-type and *n*-type contacts, resulting in 2N total traces. **(C)** Trace routing scheme where a linear array of µLEDs share *n*-type contacts, resulting in N + 1 total traces. **(D)** Trace routing scheme where a 2D array of µLEDs share traces for *p*-type and *n*-type contacts, resulting in only $2\sqrt{N}$ traces. This routing scheme cannot be achieved in a single routing layer, as trace intersections will short the *p*-type and *n*-type traces. **(E)** Microscope image of 2D µLED array. **(F)** Illumination patterns of µLED array showing individual addressability in the 2D routing scheme.

at speeds that are several orders of magnitude faster than the relevant time constants of neural activity. For example, GaN LEDs with sizes comparable to our devices, operating at an emission wavelength of 450 nm, can be modulated faster than 300 MHz (Kelly et al., 2012), while the time constants of neuron membrane potentials are at the scale of kHz. Thus, rapid time-division multiplexing between μLED elements would appear as simultaneous stimulation to neurons.

3. METHODS

3.1. Fabrication Methods

We have designed a scalable, wafer-level fabrication process for high-throughput manufacturing of the optoelectronic neural probes. Fabrication is performed on commercially-available GaN-on-Si epitaxial wafers (Suzhou Innovo China). The substrate is a 2-inch, 1.5-mm thick Si (111) wafer; from the substrate up, the layer structure consists of 900 nm of an (Al,Ga)N buffer layer, 400 nm of an undoped GaN layer, 3,200 nm of an *n*-type doped GaN layer, a 250 nm active region comprised of multiple quantum wells, and a 150 nm *p*-type doped GaN ohmic contact layer. The fabrication process is schematically illustrated in **Figure 3A**. In the following sections, we will discuss the details of the process.

3.1.1. Lithographically-Defined GaN μLED Mesas

To fabricate GaN μLEDs, the process is as follows: first, metal contacts (17 nm Ni/150 nm Au) are deposited and patterned on the top *p*-type GaN layer of the device structure using an electron beam evaporator (Kurt J. Lesker PVD 75). The contacts are formed using a lift-off process (**Figure 3Ab**). The *p*-type GaN mesa is then lithographically defined and dry-etched (**Figure 3Ac**) in chlorine gas chemistry using an inductively-coupled plasma reactive-ion etching (ICP RIE) process (PlasmaTherm Versaline). The etching process was calibrated and timed to etch the *p*-type GaN layer and to stop at the *n*-type layer well below the active multiple quantum well and (Al,Ga)N cladding layers. Metal contacts (17 nm Ni/ 150 nm Au) are then deposited on the exposed *n*-type GaN layer using an electron beam evaporation and lift-off process (**Figure 3Ac**). The *n*-type layer is then lithographically patterned to define the overall μLED mesa structure. In this process, the *n*-type GaN and (Al,Ga)N layers are etched to the Si substrate (**Figure 3Ad**) using the chlorine ICP RIE process (PlasmaTherm Versaline). This process requires a thick photoresist layer (10 μm, AZ4620). During the etching process, the backside of the wafer was cooled by the chuck and the etching was cycled in 2-min intervals to prevent substrate heating and reflow of the photoresist.

3.1.2. Parylene C Cables and Vias

To passivate the mesa structures, a 300-nm film of SiO_2 was deposited on the mesa sidewalls using a plasma-enhanced chemical vapor deposition (PECVD) method in a Trion Orion II PECVD machine (**Figure 3Ae**). The SiO_2 was then removed from the μLED contacts and the probe outline using a CHF_3 RIE process in a PlasmaTherm 790 RIE machine. During this etching step, openings for the backside electrodes are patterned so that the electrode will be exposed when the wafer is released. The SiO_2 layer under the cable region of the probe was intentionally left intact as an etch-stop layer during the release process. A 5-μm thick layer of Parylene C was then deposited (SCS Labcoter-2) to form the neural probe substrate and lower trace insulation. An adhesion promoter (A174 Silane) was applied prior to the deposition of Parylene C to prevent its premature delamination during processing (**Figure 3Af**).

The Parylene C deposition is conformal and covers the entire wafer surface. Vias in the Parylene C insulation layer are required for routing traces to the *p*-type and *n*-type ohmic contacts of the μLED, as well as to the backside recording electrodes. Due to the poor selectivity (1:1) of the etching process for photoresist, Parylene C is typically etched using an oxygen plasma RIE process with a hardmask instead of a photoresist mask. Although it provides superior etch selectivity, patterning Parylene C with a hardmask yields steep sidewalls. Such steep sidewalls prevent a continuous metallization layer across the vias, resulting in discontinuous electrical traces and hence poor device yield. To address this issue, we developed an optimized lithography process using a biased mask design with deliberate underexposure to pattern sloped sidewalls in a thick photoresist mask (8 μm), which are then transferred to the Parylene C through oxygen plasma etching (Trion Phantom II RIE). This process creates sloped sidewalls in Parylene C, suitable for realizing vias (**Figure 3B**). The average sidewall angle was measured to be 70.3° using a combination of top-down scanning electron micrograph (SEM) imaging and step height measurement using a profilometer (KLA Tencor P-15). The sloped sidewalls create process variance in the exact dimensions of the Parylene C openings for contacts, creating larger features than defined on the mask. In practice, this can sometimes lead to shorts between the p-GaN and n-GaN layers when the enlarged contact would overlap with the n-GaN mesa. The precise definition of the contact opening in the SiO_2 passivation in a separate lithographic step prevents enlarged Parylene C openings from causing shorts between the p-GaN and n-GaN. This technique is highly repeatable and leads to, on average, a device yield of >90% for the continuity of electrical interconnects. During this step, backside recording electrodes are also defined by patterning and etching the lower Parylene C insulation layer all the way to the surface of the Si substrate. The backside electrodes are exposed after the device is released from the silicon substrate.

To further ensure a contiguous electrical connection through vias, a thick metal layer stack (15 nm Pt, 400 nm Au, 15 nm Pt) is deposited using an electron beam evaporation process (Kurt J. Lesker PVD 75) (**Figure 3Ag**). Platinum is used as the adhesion layer to Parylene C. It also exhibits favorable electrochemical properties for the recording electrodes, including biocompatibility and low electrochemical impedance (Geddes and Roeder, 2003). To perform the lift-off of such a thick metal stack, we used the polydimethylglutarimide-based photoresist-type known as LOR 5B as the lift-off resist. We note that Parylene C has low temperature processing requirements (glass transition temperature 170 °C). However, Parylene C can usually withstand significantly higher temperatures (300 °C) in the

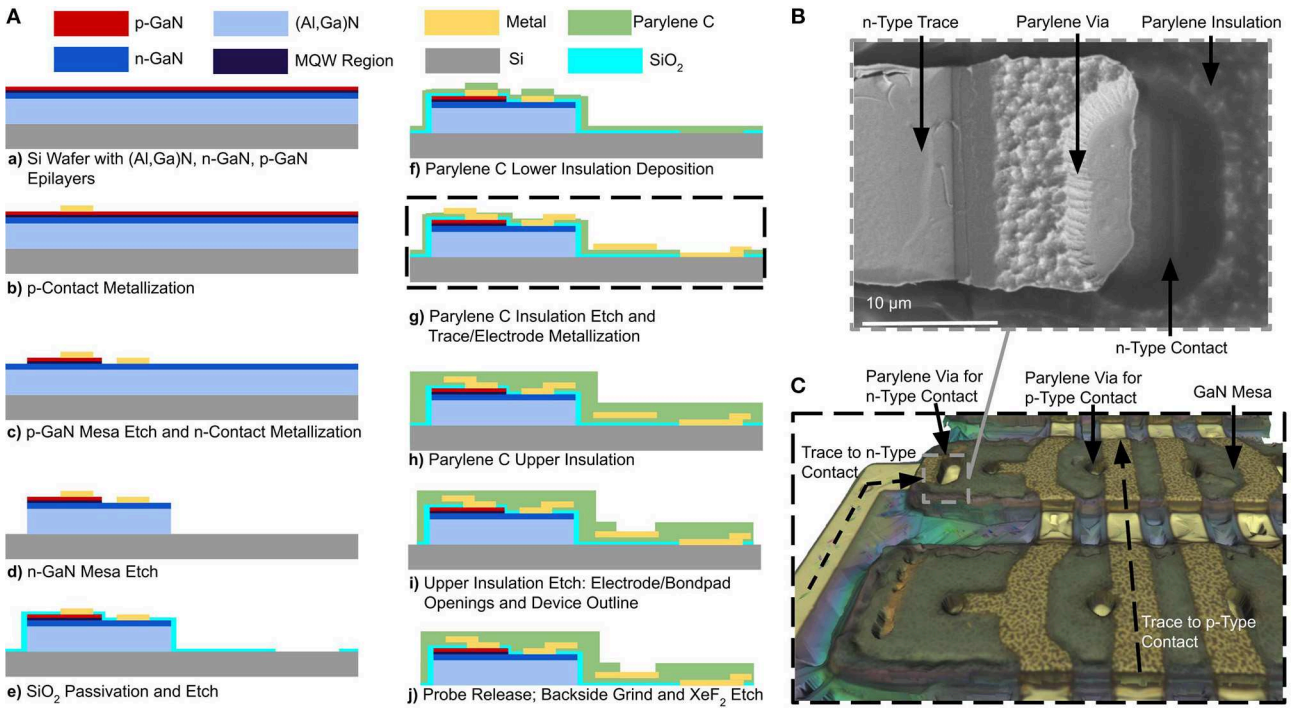

FIGURE 3 | (A) Schematic process flow for a µLED neural probe, **(B)** Top-down SEM photomicrograph image of a Parylene C via formed with a sidewall from a photoresist underexposure process. This image is taken perpendicular to the surface; the sloped edge is evident due to the width of the edge. Metal deposited via evaporation is continuous from the top surface of the Parylene C to the µLED contact. **(C)** 3D optical microscope image of GaN mesa structure during fabrication step (g). Traces for *p*-type contacts run orthogonally to the mesas and connect to the *p*-type GaN contacts through Parylene C vias. Traces for the *n*-type contacts are routed through a via on the edge of the GaN mesa and are connected to *n*-type contacts which are patterned along the mesa in the *n*-type GaN layer.

absence of oxygen (von Metzen and Stieglitz, 2013). To perform the required 180 °C bake step for LOR 5B resist, an oven with nitrogen atmosphere was used for the bake process. Traces were patterned with a 10 µm width and spacing. The mesa topography and metal interconnects are shown in **Figure 3C** as a reconstructed 3D microscope image (InfiniteFocus, Alicona Imaging GmbH).

To insulate the metal traces, a second layer of Parylene C is deposited (SCS Labcoter-2) to a thickness of 5 µm (**Figure 3Ah**). To expose the frontside recording electrodes and bond-pads, the top layer of the Parylene C must be etched. To singulate the neural probe, the top and bottom layers of the Parylene C (which have a total thickness of 10 µm) need to be patterned and etched around the outline of the device. To pattern such a thick layer of Parylene C, we used a 100-nm chromium (Cr) hardmask. The thin film stress in the Cr hardmask layer can sometimes result in the formation of cracks in the Parylene C film. To alleviate this issue, a customized sputtering process (CVC Connexion) was carefully optimized for the deposition of the Cr hardmask layer in order to minimize the thin film stress by adjusting the chamber pressure during the deposition. We found that cracking of the Parylene C was prevented when the Cr thin film stress was less than 1 GPa. Our optimized deposition process yielded a final stress of 600 MPa, providing a safe margin for achieving crack-free Parylene C films. We patterned the Cr hardmask using wet etching (Cr 1020 Etchant, Microchem GmbH). Parylene C was then etched using oxygen plasma (Trion Phantom II). At an etch depth of 5 µm, the bond-pads and frontside electrodes are exposed. The etch is continued to a depth of 10 µm in order to define the probe outline through the top and bottom layers of Parylene C. We observed that over-etching of the electrode and bond-pad sites removes Parylene C residue from the surface. The Cr hardmask is stripped away using a wet etch step in Cr etchant (Cr 1020 Etchant, Microchem GmbH). Following this step, the optoelectronic probes are finally realized on the wafer (**Figure 3Ai**). The next step is to remove the silicon handle layer and release the probes.

3.1.3. A Grind-and-Etch Release Process to Release Fully Flexible Devices

To release the flexible devices from the Si substrate, the wafer is first ground down from the backside to a thickness of about 100 µm from its initial thickness of 1.5 mm (Grinding Dicing Services, Inc. San Jose, CA). The remaining silicon is then isotropically etched using XeF_2. The wafer is first mounted on a quartz carrier substrate upside-down using a CrystalBond adhesive and then etched using XeF_2 (Xactix e2) from the backside. The Parylene C cable is protected by the 300-nm SiO_2 passivation layer. Once the Si layer is completely removed, the bottom-facing electrodes are exposed. Finally, the probes may be released from the carrier wafer by dissolving the CrystalBond adhesive by soaking the samples for 4 h in Acetone (**Figure 3Aj**).

The SiO_2 sacrificial layer along the probe cable is removed by dipping the backend in a 49% HF acid solution, leaving only the flexible Parylene C cable.

3.1.4. Released and Packaged Optoelectronic Probes With Electronic Circuit Boards

The released optoelectrodes are packaged with printed circuit boards (PCBs) that connect with a commercial neural recording amplifier through a recording headstage (Intan Inc.) using Omnetics connectors. The PCB adaptor also connects with custom-designed electronic control circuitry for driving individual μLEDs. This electronic control circuitry utilizes a switching network of commercial metal-oxide-semiconductor field-effect transistors to route current to the appropriate traces. A commercial Keithley 2401 Sourcemeter, (Keithley Instruments) with a precise (±100 nA) current control capability, was used as a current source to prevent accidental breakdown of the μLEDs.

To package the released optoelectronic probes with the PCB, we developed a die attach technique using Epotek 301 epoxy to affix the flexible probes to the adapter PCB. We were then able to electrically connect the bond-pads on the backend of the flexible polymer substrate to the PCB using an aluminum wedge-bonder.

3.2. Electrophysiology Methods

3.2.1. Brain Slice Preparation

Brain slices recordings were obtained from p22 somatostatin (SST)-Cre/Ai32 mice (SST-Cre, stock: 013044; Ai32(RCL-ChR2(H134R)/YFP), stock: 024109; Jackson Laboratory; Bar Harbor, ME). 350 μm thick coronal slices were cut in ice-cold artificial cerebrospinal fluid (ACSF) containing (in mM): 119 NaCl, 2.5 $CaCl_2$, 1 NaH_2PO_4, 26.2 $NaHCO_3$, 11 glucose on a VT1200S vibrating blade microtome (Leica Biosystems Inc., Buffalo Grove, IL). Slices were recovered for >45 min and maintained at room temperature for 4–6 h under continuous oxygenation (95% O_2 5% CO_2).

3.2.2. Electrophysiology

Visualized juxtacellular and whole cell current clamp recordings were performed on an Olympus BX43 Light Microscope (Tokyo, Japan) using an Axon Instruments MultiClamp 700B microelectrode amplifier (San Jose, USA). Recordings were made from the somata of neocortical ChR2-yellow fluorescent protein (YFP) expressing SST interneurons targeted using FITC optical filter (Olympus-Lifescience, Center Valley, PA) using borosillicate glass electrodes, resistance 6–10 MΩ. Recordings were carried out in modified ACSF containing (in mM): 119 NaCl, 5 KCl, 0.5 $MgSO_4$, 1 $CaCl_2$, 1 NaH_2PO_4, 26.2 $NaHCO_3$, 11 glucose. Upon reaching juxtacellular configuration (20–30 MΩ), neurons were stimulated with a 5 pulse train of blue light LED stimulation (10 ms duration, 80 ms interstimulus interval).

3.2.3. Neural Data Analysis

Neural data were acquired using a custom-written IgorPRO software. To eliminate electronic interference from the neural recordings, data were filtered during analysis. Notch filters were applied to eliminate 60 Hz harmonics. Additionally, a bandpass filter from 400 Hz to 5 kHz was applied. The filtering was performed using Python 3.7.2 and Scipy 1.2.1.

4. RESULTS

4.1. Spectral Intensity of a μLED Suitable for Neural Stimulation

The μLED neural probe in this work was designed for spectral overlap with commonly used channelrhodopsin variants that have peak absorption at $\lambda = 450$ nm. Our μLED emission peak is at $\lambda = 445$ nm, with a narrow spectral bandwidth of 20 nm; this is the full-width-at-half-maximum (FWHM) (**Figure 4A**). Optical device characterization was performed using a fiber spectrometer (Flame-S, OceanOptics) equipped with an integrating sphere.

The optical power and wall-plug efficiency for individual (22 × 22 μm) μLEDs were measured using a calibrated power meter from the top and bottom surfaces of the device across a range of drive currents (**Figures 4B,C**). The peak wall plug efficiency of 6.5% agrees with the previously reported results for GaN μLEDs grown on silicon substrate (Wu et al., 2015). The peak efficiency drive current of 8.5 μA corresponds to 540 nW of optical power from the top surface of the probe and 1.3 μW of optical power from the bottom surface. The difference in intensity between top and bottom measurements is due to the reflection of emitted light from the topside U-shaped metal contacts.

4.2. Probes With Front- and Backside Recording Electrodes

We characterize the electrodes of our devices using electrochemical impedance spectroscopy (EIS). Measurements were performed in a 3-electrode configuration in potentiostatic mode (PSGSTAT202N, Metrohm Autolab) in a phosphate-buffered saline (PBS) solution. The electrochemical impedance of the electrode was characterized from 0.1 Hz to 10 kHz with a sinusoidal signal whose peak amplitude was 50 mV at an open circuit potential configuration. A silver/silver chloride (Ag/AgCl) reference electrode (MF-2052, BASI Inc.) and a platinum wire counter electrode (MW-1032, BASI Inc.) were used.

Front- and backside electrodes (25 × 35 μm) were fabricated alongside the GaN μLEDs in our architecture. The frontside electrode performance is shown in **Figure 4D**, while the backside electrode performance is shown in **Figure 4E**. Both electrodes exhibit a similar electrochemical impedance of ≈1.0 MΩ at 1 kHz, which is typical for electrodes of this size and suitable for neural recording (Ahuja et al., 2008; Neto et al., 2018). The ability to record from both sides of the probe shank, along with the bidirectional emission of the μLED is a unique feature of our design that enables stimulation and recording from a much larger volume compared to the usual single-sided probes.

4.3. Thermal and Optical Modeling

4.3.1. Thermal Model

A common concern of implantable μLEDs probes is tissue heating during operation. Due to the low conversion efficiency from electrical to optical power (6.5% peak efficiency demonstrated here), the majority of device power is dissipated

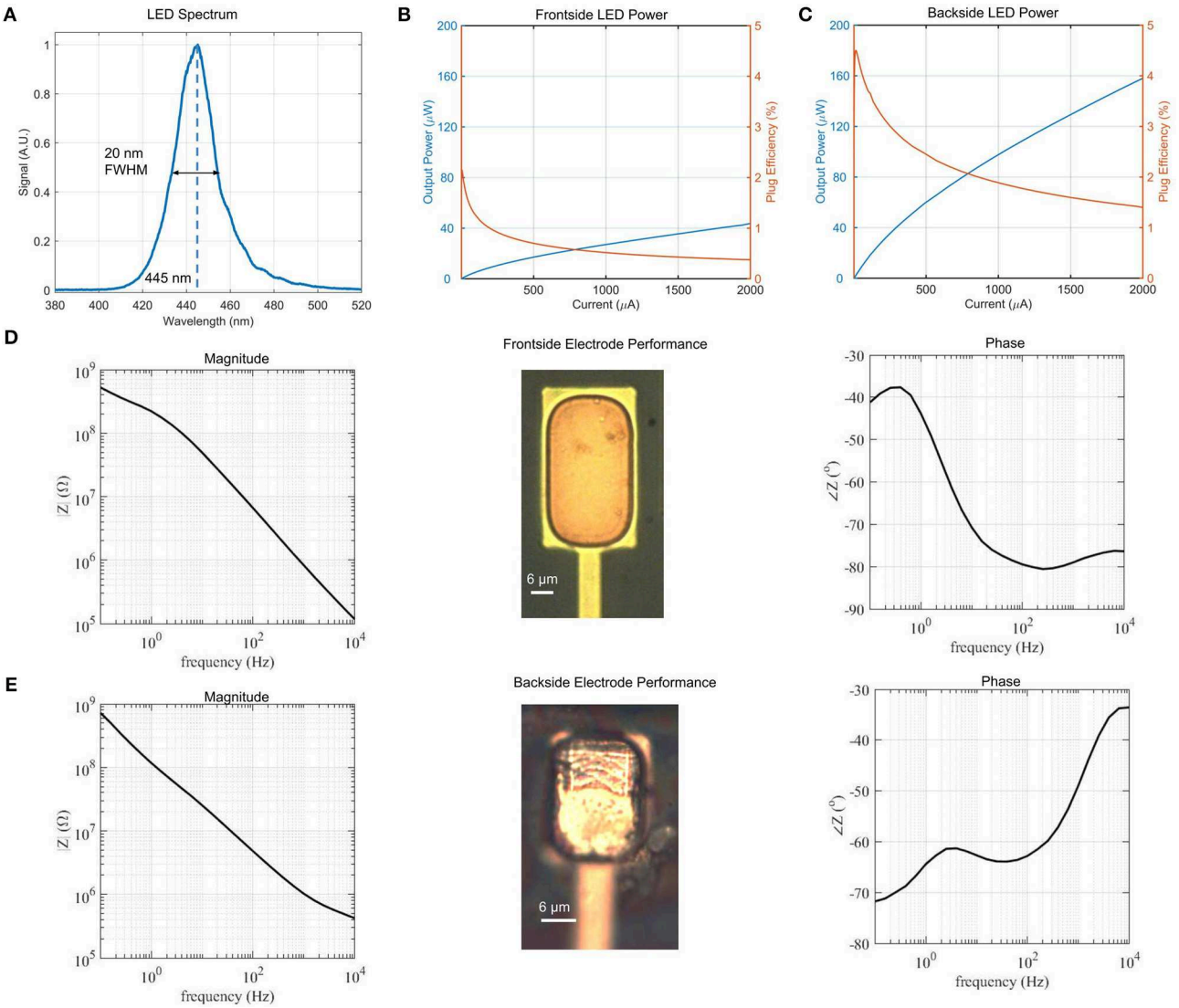

FIGURE 4 | (A) Micro-LED spectrum with peak intensity at λ = 445 nm and spectral linewidth of 20 nm FWHM, **(B)** Frontside and **(C)** Backside μLED power and efficiency vs. drive current. Backside emission is approximately 4 times higher due to reflection from the topside metal contacts. Total efficiency of the μLED structure for a given current is the sum of the frontside and backside efficiencies. Peak efficiency is therefore 6.5%. **(D)** Magnitude and phase plots of electrochemical impedance in the relevant frequency range of neural recordings for frontside electrodes. Inset image shows frontside electrode surface. **(E)** Magnitude and phase plots of electrochemical impedance for backside electrodes. Inset image shows backside electrode surface.

as heat into the surrounding medium. We adopt the Pennes bio-heat transfer model in COMSOL Multiphysics (COMSOL Inc.) to demonstrate the threshold of safe operation of the device in tissue (Wu et al., 2015; Dong et al., 2018). The probe geometry was modeled exactly using dimensions from the photomask design files and layer thicknesses measured during the fabrication process. The GaN μLED mesas, metal traces, and Parylene C insulation were included in the model. The relevant material properties are listed in **Table 1**. Blood perfusion rate, density, and heat capacity are taken from Wu et al. (2015).

Thermal simulations show the effects of local heating in the μLED structure on the surrounding tissue. The front- and backsides of the probe experience different local heating due to the difference in thermal conductivity of the Parylene C insulation on the top surface and the GaN mesa on the bottom. **Figure 5A** shows the heating profile at the μLED/tissue interface.

TABLE 1 | Material properties for thermal simulations.

Material	k (W/(m*K))	ρ (kg/m^3)	C_p (J/(kg*K))
Brain Tissue (Dong et al., 2018)	0.6	1,057	3,600
GaN (Dong et al., 2018)	200	6,150	485
Parylene C	0.084	1,110	712
Gold	317	19,300	129

The tissue in contact with the GaN mesa experiences significantly more heating than the upper Parylene C interface. The heat distribution on a top-view cross-section of the device is shown in **Figure 5B**. Due to the higher thermal conductivity of the GaN mesa and traces compared to Parylene C and surrounding tissue, heat spreads preferentially throughout the GaN mesa structure and through traces to the adjacent mesas.

To simulate worst-case heating performance, we performed analysis on the forwardmost μLED mesa, which has only one adjacent mesa. The temperature of Parylene C/Tissue and GaN/Tissue interfaces on front- and backside of the probe, directly over the center of the active μLED were monitored in a time-dependent study (**Figure 5C**). To remain below the standard safety limit of 1 °C temperature increase in tissue, a 5 ms pulse of 90 μA was found to be the limit. This drive current corresponds to a topside optical power of 4.82 μW and a backside power of 14.3 μW. The heat is quickly dissipated in the tissue, and after 10 ms following stimulation offset, the temperature in the surrounding area is less than 0.05 °C above initial temperature (37 °C).

4.3.2. Optical Model

To enable high-resolution interrogation of individual neural circuits, dense two-dimensional arrays of GaN μLEDs may be individually modulated to create independent stimulation voxels in tissue. Analytical and Monte Carlo methods have been developed to describe light scattering in tissue (Wang et al., 1995; Bernstein et al., 2008), with the latter being necessary to accurately model light penetration beyond 200 μm, as light enters the multiple scattering regime (Al-Juboori et al., 2013).

The attenuation of light due to scattering and absorbing media is described via the Kubelka-Monk model, depending on the scattering coefficient, μ_s, and absorption coefficient, μ_a of tissue. These coefficients vary throughout the brain and also with the wavelength. We adopt values from previously reported measurements at 450 nm, which is the closest wavelength to our emission wavelength (445 nm). The model parameters are $\mu_s = 19.96\,\mathrm{mm}^{-1}$ (Al-Juboori et al., 2013), and $\mu_a = 0.14\,\mathrm{mm}^{-1}$ (Yaroslavsky et al., 2002).

We experimentally measured the relative light intensity from multiple angles using a low-NA microscope (NA = 0.10) equipped with a CCD camera on a rotating stage to obtain the μLED emission profile (**Figure 5D**). Our measured emission profile closely resembled an analytical Lambertian profile (**Figure 5D**). Therefore, we used an analytical model for the light spread in tissue (Foutz et al., 2012), assuming a Lambertian emission from the μLED.

This model allows for the rapid estimation of penetration depth and light spread for a given optical power. A plot of optical power density spread for 4.8 μW of emitted optical power, which corresponds to frontside emission at our maximum thermally-safe (less than 1 °C) tissue heating threshold, is shown in **Figure 5E**. A penetration depth of ∼40 μm for 0.1 $\mathrm{mW/mm}^2$ optical power density is observed, with a lateral spread of less than 20 μm. Thus, the stimulation volumes of adjacent high-density μLEDs are independent at this distance.

During chronic implantation, glial encapsulation and reduced local neuron density can hinder the effectiveness of a neural probe, requiring greater depth of penetration to reach healthy cells. Greater depth of penetration can be achieved by increasing the μLED power up to 200 μW. **Figure 5F** shows the spatial intensity decay of light from the μLED at several ranges of operating power predicted by our model. To stimulate further from the device, multiple μLEDs may be operated as one larger LED to achieve greater overall optical power and penetration depth.

4.4. Neuronal Spikes and Synaptic Network Activation Elicited by μLED Illumination

To test and validate the efficacy of the μLEDs to elicit evoked activity in channelrhodopsin-expressing neurons, μLED arrays were used to stimulate acute brain slices while simultaneous electrophysiological recordings were conducted. We elected to test μLED array efficacy in driving spikes in a specific subtype of inhibitory neuron, somatostatin-expressing (SST) inhibitory neurons, since these cells typically rest at moderately depolarized potentials (Urban-Ciecko et al., 2018) and it might be easier to drive them to spike in our experimental preparation than pyramidal neurons. The μLED probes were affixed to the bottom of the recording chamber, and brain slices were placed over the probe. SST-targeted recordings were carried out using fluorescence signal from a YFP-tagged channelrhodopsin genetically expressed in these cells, and were selected from the top-surface of the brain slice, above the μLED array (**Figure 6A**). Upon delivery of a 5-pulse train from μLEDs (10 ms pulse duration, 80 ms inter-pulse interval), ChR2/YFP-expressing neuron showed an increase in evoked spiking, indicating photoactivation (**Figure 6B**). Onset and offset stimulation artifacts from the μLED were observed with opposite polarity and synchronized with stimulation timings. Due to their highly stereotyped amplitude and waveforms, they are visually distinct from natural spikes. Following μLED illumination, the tissue was subjected to conventional full-field 470 nm light stimulation through a 40x immersion objective lens positioned above the slice using the same pulse train parameters (**Figure 6C**, top trace). Importantly, full-field optical stimulation elicited more spikes per pulse, likely due to comparatively larger recruitment of the target cell neurites. To test μLED activation of SST-mediated inhibitory synaptic networks, whole-cell current clamp recordings were carried out in neocortical pyramidal neurons (non-ChR2/YFP expressing neurons) from SST-Cre/Ai32 mice. Micro-LED stimulation resulted in inhibition of spontaneous pyramidal neuron firing (**Figure 6D**, top trace), showing a consistent pause in spiking during μLED pulse train (**Figure 6D**, mid/bottom). Stimulation was once again changed to conventional full-field 470 nm light stimulation through the 40x objective (**Figure 6E**, top trace), and a similar synchronized pause in spiking during light pulse train was observed. In contrast to μLED stimulation, conventional full-field illumination elicited distinct optically activated inhibitory postsynaptic potentials (IPSPs), suggesting a more broad activation of local SST interneurons than obtained

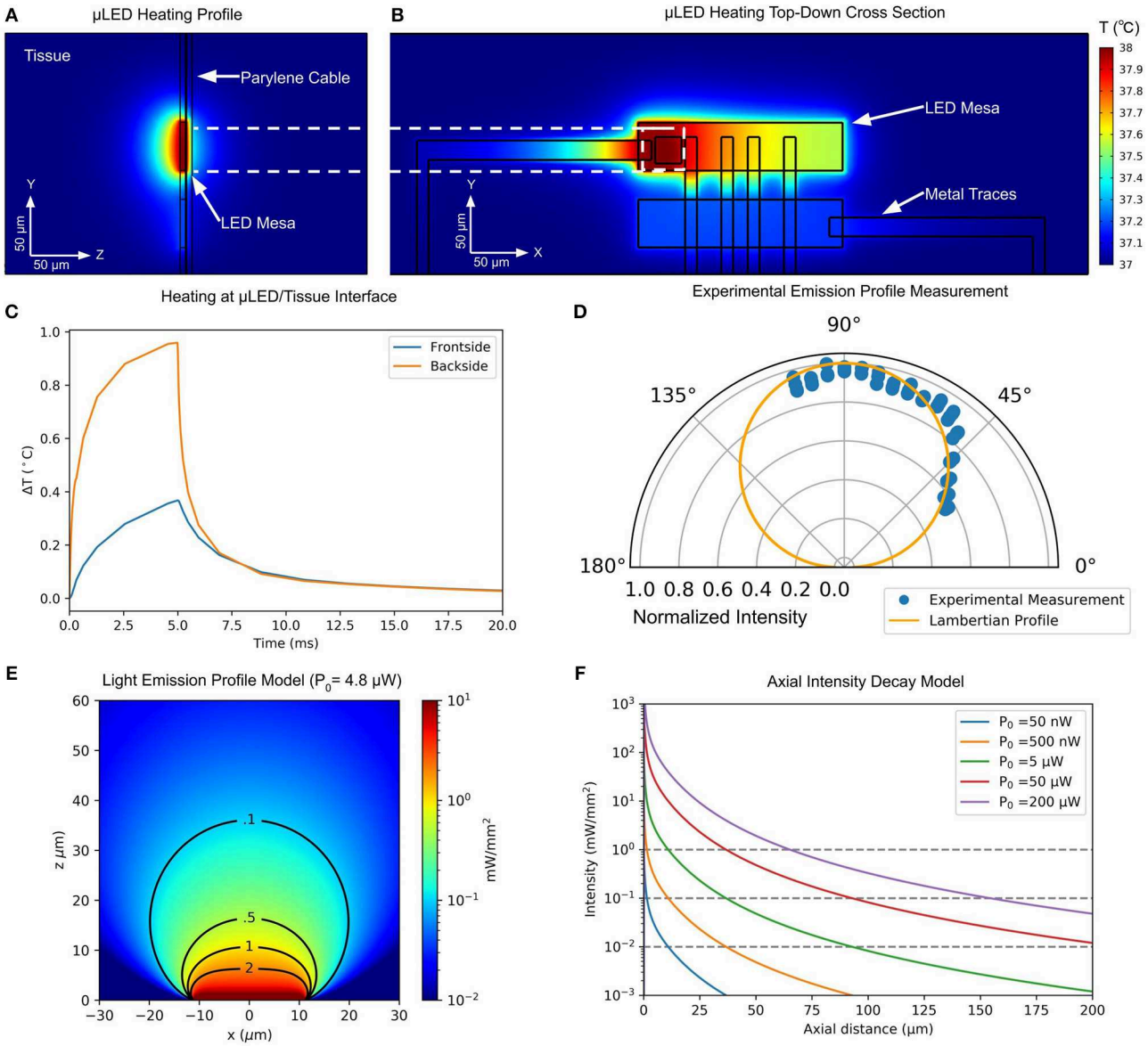

FIGURE 5 | (A) Profile of simulated tissue heating using Pennes bio-heat model at 90 μA of μLED drive current. Due to the difference in thermal conductivity between GaN and Parylene C, front- and backside of the probe experience different amounts of tissue heating. **(B)** Top-down cross section of heat spread in μLED device structure at 90 μA of μLED drive current. Thermal conduction in GaN mesa and along metal traces can be observed. **(C)** Tissue heating plot at front- and backside probe/tissue interfaces for 5-ms, 90-μA pulse. **(D)** Experimental measurement of directional μLED intensity profile and comparison to ideal Lambertian source. **(E)** Analytical model of light intensity in tissue from a Lambertian source with 4.8 μW of optical power. **(F)** Analytical model of axial intensity profile in tissue for various optical powers.

with the μLED array. Thus, μLED stimulation can both directly activate ChR2-expressing neurons and also indirectly engage feedforward inhibitory networks in acute brain slices.

5. DISCUSSION

Our optoelectronic neural probe platform monolithically combines μLEDs and recording electrodes in a flexible Parylene C substrate. The scalable wafer-level fabrication process introduced in this paper greatly increases the process throughput and yield compared to serial packaging processes such as flip-chip bonding. Unlike manual assembly processes, which are limited by the alignment accuracy of the available device bonders and increased fabrication time with the number of devices, lithographic definition of the electrical and photonic devices in our design results in much higher precision, allowing for high-throughput realization of an arbitrary number of devices in parallel. Because we utilize standard microfabrication techniques, our optoelectronic probes can be manufactured with high yield and volume and made available to a wide user base.

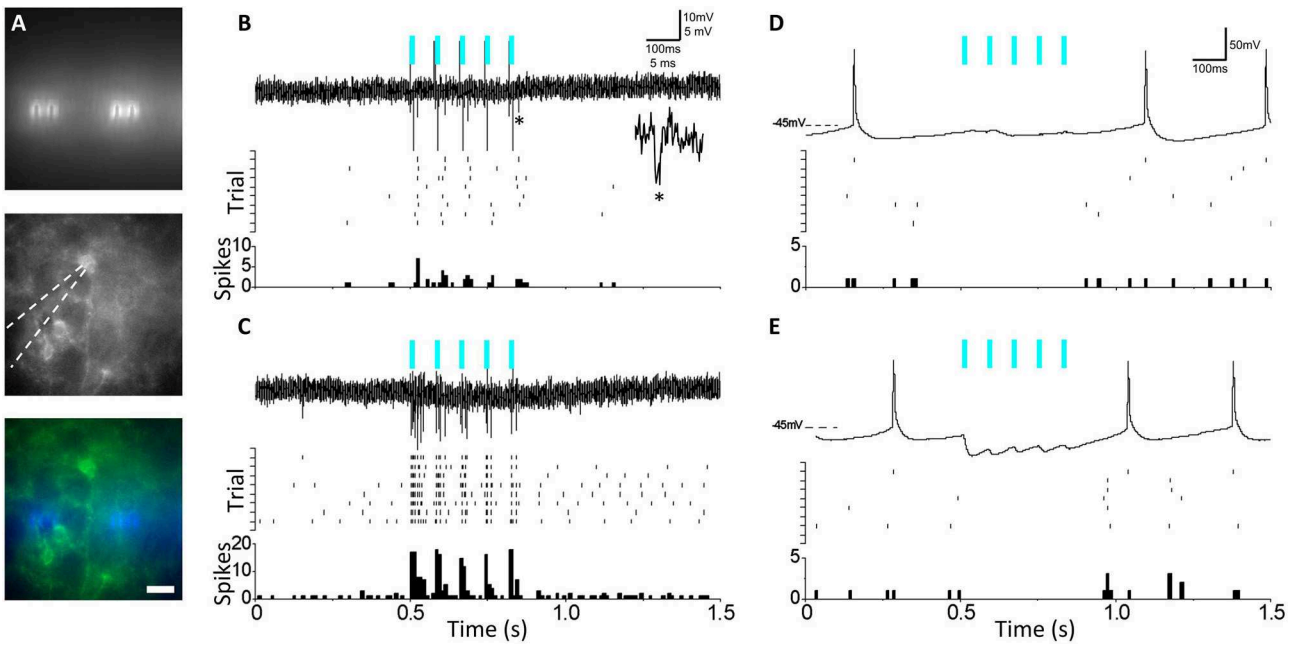

FIGURE 6 | (A) Top: Activation of micro-LED (μLED) array embedded beneath recording chamber prior to slice positioning. Center: Targeted recordings from fluorescent ChR2-expressing SST interneurons above array. Bottom: overlay. (Scale = 22 μm). **(B)** Top: Juxtacellular recording showing μLED activation (blue bars) of channelrhodopsin-expressing SST interneuron. *Shown as inset, single μLED evoked spike. Center: Multi-trial spike rasters from the same neuron aligned to μLED activation. Bottom: Peri-stimulus time histograms (PSTH) from the above. **(C)** As in **(B)** but with full-field LED activation of SST interneuron (lower trace) **(D)** Top: As in **(B)** but for whole-cell current clamp recording of neocortical pyramidal neuron showing feedforward inhibition during μLED activation of SST interneurons, with suppression of spontaneous pyramidal neuron firing activity. **(E)** As in **(D)** but using full-field LED activation. IPSPs are larger than with μLED activation and visible as inward currents as $V_{rest} > E_{Cl}$.

This approach could conceivably become the standard way for making this type of neural probe for closed-loop interfacing with neural circuits.

Once released, the μLED probe is supported by a flexible Parylene C substrate, which can significantly help with reducing the foreign body response in tissue. However, flexible neural interfaces incur difficulty during implantation since they lack the rigidity to penetrate brain tissue. The flexible neural interfaces need to be temporarily stiffened so that they can be feasibly implanted. This can be carried out by coating the probes with bioresorbable materials such as polyethylene glycol or silk or by attaching them to a stiff shuttle for implantation (Weltman et al., 2016).

The transparency of Parylene C combined with the process-enabled light emission from both facets of the GaN μLEDs, makes it possible to use light in the tissue from the frontside as well as the backside of the device. This new feature means that having only frontside recording electrodes may be inadequate for recording signatures originating from the entire stimulated volume. The design of our platform allows the integration of backside recording electrodes for simultaneous recording and stimulation from both sides of the probe. The emission profiles from the front and back surfaces in this device are asymmetric due to reflections from the metal contacts of the top surface. Symmetric emission profiles could be achieved using thin or transparent contact materials such as indium tin oxide (Kim et al., 2001).

Electrodes on both sides exhibit electrochemical impedances suitable for neural recording. Electrodes are implemented in separate fabrication steps, etching the top Parylene C insulation layer to expose the topside electrodes, and deposition of the metal films for the electrodes through Parylene C vias on the silicon substrate surface, which is eventually etched off during the release process to expose the backside electrodes. These fabrication differences are believed to be responsible for the different phase characteristics of the impedance of the front- and backside electrodes, either because of Parylene C or silicon debris that remains on the surface or a surface modification of the electrode from exposure to the etching gasses.

Furthermore, the monolithic fabrication process described in our work allows for customizable arrangement of recording electrodes and light sources through patterning of individual layers. Unlike traditional flip-chip bonding processes that utilize pre-fabricated μLED chips, we have the flexibility to design complementary structures in various device layers. We leverage this flexibility to enable an individually-addressable 2D grid of devices. By patterning the *n*-type GaN to form connected rows, we are able to use the μLED mesa as an additional layer for electrical routing. This allows creation of arbitrary 2D grids of devices without a second electrical trace routing layer that would complicate the fabrication process. In this particular scheme, the number of traces scales as the square root of the number of devices, as opposed to traditional routing schemes where the number of required electrical traces scales linearly with the

number of μLEDs. Therefore, our scheme allows a significant increase in the number of devices that can be realized in a given probe footprint with a single trace routing layer.

Here, we have demonstrated dense arrays of μLEDs with a single n-GaN mesa "bridge" forming the n-layer routing. However, for long linear arrays, the stiffness of the n-GaN layer would quickly compromise the flexibility of the probe. It would be preferable to have many small "floating" GaN mesas at optical stimulation sites connected by polymer cable interconnects. This approach is adopted by Goßler et al. (2014) and Klein et al. (2018), who use two routing layers to separate *p*-type and *n*-type traces. However, multiple routing layers are only necessary where *p*-type and *n*-type traces intersect. We have shown a high-yield method of fabricating Parylene C vias, combined with two-layer routing on the GaN μLED mesa itself. Thus, the 2D grid that we demonstrate could be made sparse, with GaN μLED mesas only at the nodes of the trace matrix, forming a collection of optical stimulators floating in a polymer "web." Furthermore, additional routing layers may be incorporated in our architecture for linear scaling of cable density, through additional planar layers of Parylene C insulation and vias. We have demonstrated, however, that the fabrication complexity incurred by additional routing layers is not necessary for a 2D routing scheme.

Here, the shank of our demonstration device is very large (570 μm active region), which would be highly damaging during *in-vivo* implantation despite the flexibility of the substrate. This is primarily limited by the conservative trace pitch (16 μm). As previously discussed (Device Architecture Section), the overall size of the device is determined by the lithography resolution and number of required traces. Our 2D routing scheme allows for a significant reduction in the number of traces, and can be combined with high-resolution lithography to create extremely compact, high-density devices.

Our routing scheme also allows for each μLED device in the array to be individually indexed. However, it does not allow for arbitrary patterns of simultaneous illumination. Each μLED device can be indexed in the array by the trace number for the *p*-type and *n*-type contacts: (p, n). To activate a given μLED, the indexing *p*-type electrical trace is connected to a current source, and the *n*-type trace to a current sink. Multiple devices may be powered simultaneously by sourcing power to traces for multiple *p*-type and *n*-type contacts. This scheme powers specific sets of devices. For example, devices $(1, 1)$ and $(2, 2)$ may not be powered without activating devices $(1, 2)$ and $(2, 1)$. The set of indexed devices is the cartesian product of the sets of active *p*-type and *n*-type contacts. In this scheme, entire rows of μLEDs may be powered simultaneously.

Although arbitrary patterns of simultaneous illumination are not possible, arbitrary patterns of simultaneous neural stimulation can be achieved through time-division multiplexing. The temporal response of ion channels, which mediates the generation and propagation of action potentials, is generally on the order of milliseconds (kHz); the light sources in our platform, on the other hand, can be modulated at frequency rates in the range of MHz (Kelly et al., 2012). This means time-division multiplexing on these timescales would be indistinguishable to a neuron from continuous illumination. This way, one may generate arbitrary patterns of neural stimulation by rapidly time-division multiplexing sets of μLEDs. Using this method, the average delivered power to neural tissue is reduced since it is split between various μLEDs, providing an ultimate limit to the number of simultaneous optical stimulation sites that can be achieved. Since the maximum output power of our μLEDs is well above the threshold for optical stimulation, still many devices may be multiplexed. Additional research into the behavior of these devices at short pulse durations is needed to ascertain the total number of simultaneous active light sources that could ultimately be possible.

Our devices emit at a center wavelength of 445 nm, which is typical of GaN LEDs widely used in optogenetics. Although this wavelength overlaps well with the peak absorption of channelrhodopsin, shorter wavelengths increase the risk of photochemical damage in tissue, especially in the context of retinal implants (Wu et al., 2006; Soltan et al., 2018). Thus, a longer wavelength which also overlaps with channelrhodopsin absorption, such as 470 nm, may be preferred. The emission wavelength depends on the exact composition of the (Al,Ga)N/GaN or (In,Ga)N/GaN quantum structure in the active region of the device, and emission wavelengths up to 526 nm have been demonstrated (Alhassan et al., 2016). The process described here may be used with any epitaxial GaN-based structure, and thus is generalizable to longer wavelengths with the appropriate composition of the (Al,Ga)N/GaN or (In,Ga)N/GaN active quantum-well region of the GaN-based device structure.

Similarly, the low device conversion efficiency, which raises concerns about tissue heating, is currently limited by the small number of commercial GaN-on-silicon device wafers. In general, GaN-on-sapphire devices are more efficient than ones grown on silicon substrates because of increased lattice mismatch and thermal mismatch issues on silicon. However, silicon-based μLED neural probes offer significant advantages in micromachining such as isotropic XeF_2 etching, used here, which has been developed for the release of MEMS structures. As a standard microfabrication process, XeF_2 etching is more widely available and less expensive than laser lift-off (LLO) of GaN on sapphire. Furthermore, the fabrication process discussed in this paper may also be combined with LLO processing of GaN μLEDs fabricated on sapphire substrates.

With our presented conversion efficiencies, the devices may be used in a pulsed mode for high temporal-resolution optogenetic stimulation. We demonstrate a stimulation scheme of 5-ms pulses which leads to the emission of 4.82 μW of optical power from the probe frontside and 14.3 μW from the probe backside, while inducing less than 1 °C temperature increase in surrounding tissue. Such high power may not be necessary *in-vivo*, as Wu et al. have shown robust induced spiking with only 60 nW of optical power (Wu et al., 2015).

The required power depends on the distance between healthy neurons and the optical stimulator after implantation. Acute and chronic damage to tissue by the neural implant reduces neuron density around the implantation site. Although the flexible platform presented here is intended to reduce chronic damage, a "dead zone" around the implant is unavoidable. In this case, higher optical power will be necessary to stimulate neurons, inducing more local heating. However, heating above

1 °C is not a concern in dead tissue. Thus, a higher power stimulation paradigm, where sufficient optical power extends beyond the "dead zone", but heating above 1 °C is localized, can be envisioned. Since the extent of tissue damage around the neural probe is difficult to predict, the stimulation paradigm for the probe will need to be calibrated after implantation by slowly increasing optical power until robust evoked activity is observed. We showed that our μLEDs, individually driven at 625 μA can stimulate neurons that express channelrhodopsin through a 350-μm thick mouse brain slice.

6. CONCLUSION

To the best of our knowledge, our neural probe platform is the first to monolithically integrate GaN μLEDs and recording electrodes on a flexible polymer substrate using a process that can be achieved in standard microfabrication facilities. This architecture allows the manufacture of extremely high density of μLEDs in 2D arrays. Since each device layer is lithographically defined in the fabrication process, we are able to use the *n*-type GaN mesa as an additional routing layer to create a 2D grid without multiple layers of metal traces. This novel routing scheme enables realization of ultra-compact, high-density, optoelectronic neural probes with correspondingly compact shanks and cables. The overall scheme enables arbitrary patterns of neuronal stimulation. Furthermore, through an optimized wafer-scale fabrication process and post-fabrication packaging, we can achieve a high-throughput manufacturing process to produce a large number of these neural probes. Arbitrary patterns of optical stimulation can be generated using our optoelectrodes. The collocation of recording electrodes and μLEDs enables simultaneous electrophysiology recording and optogenetic stimulation of the brain to study neural circuits with high spatio-temporal resolution.

DATA AVAILABILITY

The datasets generated for this study will be made available upon reasonable request to the corresponding author.

ETHICS STATEMENT

All experimental procedures involving animals were conducted in accordance with the NIH guidelines and were approved by the Institutional Animal Care and Use Committee at Carnegie Mellon University.

AUTHOR CONTRIBUTIONS

JR designed the devices, performed microfabrication, characterization, modeling, and prepared the manuscript. IK designed the devices, performed microfabrication and characterization, and reviewed the manuscript. LS performed electrophysiology and prepared the manuscript. ZA performed EIS measurements and reviewed the manuscript. AB and ET Co-PI, designed and supervised the research, and reviewed the manuscript. MC PI, conceived the idea, designed the research, and prepared the manuscript.

FUNDING

This work was partially supported by a BrainHUB ProSEED grant from the Carnegie Mellon University (MC, AB, and ET), the National Science Foundation under Grant No. 1512794 (MC) and NIH R01 NS088958 (AB). JR was supported by the Carnegie Mellon University Ben Cook Presidential Graduate Fellowship and the Carnegie Mellon University Richard King Mellon Foundation Presidential Fellowship in the Life Sciences.

REFERENCES

Ahuja, A., Behrend, M., Whalen, J., Humayun, M., and Weiland, J. (2008). The dependence of spectral impedance on disc microelectrode radius. *IEEE Trans. Biomed. Eng.* 55, 1457–1460. doi: 10.1109/TBME.2007.912430

Alhassan, A. I., Farrell, R. M., Saifaddin, B., Mughal, A., Wu, F., DenBaars, S. P., et al. (2016). High luminous efficacy green light-emitting diodes with AlGaN cap layer. *Opt. Express* 24:17868. doi: 10.1364/OE.24.017868

Al-Juboori, S. I., Dondzillo, A., Stubblefield, E. A., Felsen, G., Lei, T. C., and Klug, A. (2013). Light scattering properties vary across different regions of the adult mouse brain. *PLoS ONE* 8:e67626. doi: 10.1371/journal.pone.0067626

Bernstein, J. G., Han, X., Henninger, M. A., Ko, E. Y., Qian, X., Talei Franzesi, G., et al. (2008). *Prosthetic Systems for Therapeutic Optical Activation and Silencing of Genetically Targeted Neurons*, Vol. 6854. San Jose, CA: International Society for Optics and Photonics.

Biran, R., Martin, D. C., and Tresco, P. A. (2007). The brain tissue response to implanted silicon microelectrode arrays is increased when the device is tethered to the skull. *J. Biomed. Mater. Res. Part A* 82A, 169–178. doi: 10.1002/jbm.a.31138

Buzsáki, G. (2004). Large-scale recording of neuronal ensembles. *Nat. Neurosci.* 7, 446–451. doi: 10.1038/nn1233

Buzsáki, G., Stark, E., Berényi, A., Khodagholy, D., Kipke, D., Yoon, E., et al. (2015). Tools for probing local circuits: high-density silicon probes combined with optogenetics. *Neuron* 86, 92–105. doi: 10.1016/J.NEURON.2015.01.028

Chamanzar, M., Denman, D. J., Blanche, T. J., and Maharbiz, M. M. (2015). "Ultracompact optoflex neural probes for high-resolution electrophysiology and optogenetic stimulation," in *2015 28th IEEE International Conference on Micro Electro Mechanical Systems (MEMS)* (Estoril: IEEE), 682–685.

Chen, R., Canales, A., and Anikeeva, P. (2017). Neural recording and modulation technologies. *Nat. Rev. Mater.* 2:16093. doi: 10.1038/natrevmats.2016.93

Delbeke, J., Hoffman, L., Mols, K., Braeken, D., and Prodanov, D. (2017). And then there was light: perspectives of optogenetics for deep brain stimulation and neuromodulation. *Front. Neurosci.* 11:663. doi: 10.3389/fnins.2017.00663

Dong, N., Berlinguer-Palmini, R., Soltan, A., Ponon, N., O'Neil, A., Travelyan, A., et al. (2018). Opto-electro-thermal optimization of photonic probes for optogenetic neural stimulation. *J. Biophotonics* 11:e201700358. doi: 10.1002/jbio.201700358

Foutz, T. J., Arlow, R. L., and McIntyre, C. C. (2012). Theoretical principles underlying optical stimulation of a channelrhodopsin-2 positive pyramidal neuron. *J. Neurophysiol.* 107, 3235–3245. doi: 10.1152/jn.00501.2011

Geddes, L. A., and Roeder, R. (2003). Criteria for the selection of materials for implanted electrodes. *Ann. Biomed. Eng.* 31, 879–890. doi: 10.1114/1.1581292

Goßler, C., Bierbrauer, C., Moser, R., Kunzer, M., Holc, K., Pletschen, W., et al. (2014). GaN-based micro-LED arrays on flexible substrates for optical cochlear implants. *J. Phys. D Appl. Phys.* 47:205401. doi: 10.1088/0022-3727/47/20/205401

Hoffman, L., Welkenhuysen, M., Andrei, A., Musa, S., Luo, Z., Libbrecht, S., et al. (2015). "High-density optrode-electrode neural probe using SixNy photonics for *in vivo* optogenetics," in *2015 IEEE International Electron Devices Meeting (IEDM)* (Washington, DC: IEEE), 1–29.

Jun, J. J., Steinmetz, N. A., Siegle, J. H., Denman, D. J., Bauza, M., Barbarits, B., et al. (2017). Fully integrated silicon probes for high-density recording of neural activity. *Nature* 551, 232–236. doi: 10.1038/nature24636

Kelly, A. E., McKendry, J. J. D., Zhang, S., Massoubre, D., Rae, B. R., Green, R. P., et al. (2012). "High-speed GaN micro-LED arrays for data communications," in *2012 14th International Conference on Transparent Optical Networks (ICTON)* (Coventry: IEEE), 1–5.

Kim, B. J., Kuo, J. T. W., Hara, S. A., Lee, C. D., Yu, L., Gutierrez, C. A., et al. (2013). 3D Parylene sheath neural probe for chronic recordings. *J. Neural Eng.* 10:045002. doi: 10.1088/1741-2560/10/4/045002

Kim, D., Sung, Y., Park, J., and Yeom, G. (2001). A study of transparent indium tin oxide (ITO) contact to p-GaN. *Thin Solid Films* 398–399, 87–92. doi: 10.1016/S0040-6090(01)01368-2

Klein, E., Gossler, C., Paul, O., and Ruther, P. (2018). High-density μLED-based optical cochlear implant with improved thermomechanical behavior. *Front. Neurosci.* 12:659. doi: 10.3389/fnins.2018.00659

Klein, E., Gossler, C., Paul, O., Schwarz, U. T., and Ruther, P. (2017). "High-yield indium-based wafer bonding for large-area multi-pixel optoelectronic probes for neuroscience," in *2017 IEEE 30th International Conference on Micro Electro Mechanical Systems (MEMS)* (Las Vegas, NV: IEEE), 452–455.

Kozai, T. D. Y., Jaquins-Gerstl, A. S., Vazquez, A. L., Michael, A. C., and Cui, X. T. (2015). Brain tissue responses to neural implants impact signal sensitivity and intervention strategies. *ACS Chem. Neurosci.* 6, 48–67. doi: 10.1021/cn500256e

Lind, G., Linsmeier, C. E., and Schouenborg, J. (2013). The density difference between tissue and neural probes is a key factor for glial scarring. *Sci. Rep.* 3:2942. doi: 10.1038/srep02942

McAlinden, N., Gu, E., Dawson, M. D., Sakata, S., and Mathieson, K. (2015). Optogenetic activation of neocortical neurons *in vivo* with a sapphire-based micro-scale LED probe. *Front. Neural Circuits* 9:25. doi: 10.3389/fncir.2015.00025

McAlinden, N., Massoubre, D., Richardson, E., Gu, E., Sakata, S., Dawson, M. D., et al. (2013). Thermal and optical characterization of micro-LED probes for *in vivo* optogenetic neural stimulation. *Opt. Lett.* 38:992. doi: 10.1364/OL.38.000992

Moshayedi, P., Ng, G., Kwok, J. C., Yeo, G. S., Bryant, C. E., Fawcett, J. W., et al. (2014). The relationship between glial cell mechanosensitivity and foreign body reactions in the central nervous system. *Biomaterials* 35, 3919–3925. doi: 10.1016/J.BIOMATERIALS.2014.01.038

Neto, J. P., Baião, P., Lopes, G., Frazão, J., Nogueira, J., Fortunato, E., et al. (2018). Does impedance matter when recording spikes with polytrodes? *Front. Neurosci.* 12:715. doi: 10.3389/fnins.2018.00715

Noh, K. N., Park, S. I., Qazi, R., Zou, Z., Mickle, A. D., Grajales-Reyes, J. G., et al. (2018). Miniaturized, battery-free optofluidic systems with potential for wireless pharmacology and optogenetics. *Small* 14:1702479. doi: 10.1002/smll.201702479

Ntziachristos, V. (2010). Going deeper than microscopy: the optical imaging frontier in biology. *Nat. Methods* 7, 603–614. doi: 10.1038/nmeth.1483

Reddy, J., and Chamanzar, M. (2018a). Parylene photonic waveguide arrays: a platform for implantable optical neural implants. in *Conference on Lasers and Electro-Optics* (Washington, DC: OSA), AM3P.6.

Reddy, J. W., and Chamanzar, M. (2018b). Low-loss flexible Parylene photonic waveguides for optical implants. *Opt. Lett.* 43:4112. doi: 10.1364/OL.43.004112

Scharf, R., Reiche, C., McAlinden, N., Cheng, Y., Xie, E., Sharma, R., et al. (2018). "A compact integrated device for spatially-selective optogenetic neural stimulation based on the Utah Optrode Array," in *Optogenetics and Optical Manipulation 2018*, Vol. 10482, eds S. K. Mohanty, N. V. Thakor, and E. D. Jansen (San Francisco, CA: SPIE), 15.

Schwaerzle, M., Paul, O., and Ruther, P. (2017). Compact silicon-based optrode with integrated laser diode chips, SU-8 waveguides and platinum electrodes for optogenetic applications. *J. Micromech. Microeng.* 27:065004. doi: 10.1088/1361-6439/aa6ad4

Schwaerzle, M., Pothof, F., Paul, O., and Ruther, P. (2015). "High-resolution neural depth probe with integrated 460 NM light emitting diode for optogenetic applications," in *2015 Transducers - 2015 18th International Conference on Solid-State Sensors, Actuators and Microsystems (TRANSDUCERS)* (Anchorage, AK: IEEE), 1774–1777.

Shin, G., Gomez, A. M., Al-Hasani, R., Jeong, Y. R., Kim, J., Xie, Z., et al. (2017). Flexible near-field wireless optoelectronics as subdermal implants for broad applications in optogenetics. *Neuron* 93, 509–521. doi: 10.1016/J.NEURON.2016.12.031

Shobe, J. L., Claar, L. D., Parhami, S., Bakhurin, K. I., and Masmanidis, S. C. (2015). Brain activity mapping at multiple scales with silicon microprobes containing 1,024 electrodes. *J. Neurophysiol.* 114, 2043–2052. doi: 10.1152/jn.00464.2015

Soltan, A., Barrett, J. M., Maaskant, P., Armstrong, N., Al-Atabany, W., Chaudet, L., et al. (2018). A head mounted device stimulator for optogenetic retinal prosthesis. *J. Neural Eng.* 15:065002. doi: 10.1088/1741-2552/aadd55

Spencer, K. C., Sy, J. C., Falcón-Banchs, R., and Cima, M. J. (2017). A three dimensional *in vitro* glial scar model to investigate the local strain effects from micromotion around neural implants. *Lab Chip* 17, 795–804. doi: 10.1039/c6lc01411a

Urban-Ciecko, J., Jouhanneau, J.-S., Myal, S. E., Poulet, J. F., and Barth, A. L. (2018). Precisely timed nicotinic activation drives SST inhibition in neocortical circuits. *Neuron* 97, 611–625. doi: 10.1016/J.NEURON.2018.01.037

von Metzen, R. P., and Stieglitz, T. (2013). The effects of annealing on mechanical, chemical, and physical properties and structural stability of Parylene C. *Biomed. Microdevices* 15, 727–735. doi: 10.1007/s10544-013-9758-8

Wang, L., Jacques, S. L., and Zheng, L. (1995). MCML–Monte Carlo modeling of light transport in multi-layered tissues. *Comput. Methods Programs Biomed.* 47, 131–146. doi: 10.1016/0169-2607(95)01640-F

Weltman, A., Yoo, J., Meng, E., Weltman, A., Yoo, J., and Meng, E. (2016). Flexible, penetrating brain probes enabled by advances in polymer microfabrication. *Micromachines* 7:180. doi: 10.3390/mi7100180

Wu, F., Stark, E., Im, M., Cho, I.-J., Yoon, E.-S., Buzsáki, G., et al. (2013). An implantable neural probe with monolithically integrated dielectric waveguide and recording electrodes for optogenetics applications. *J. Neural Eng.* 10:056012. doi: 10.1088/1741-2560/10/5/056012

Wu, F., Stark, E., Ku, P.-C., Wise, K. D., Buzsáki, G., and Yoon, E. (2015). Monolithically integrated μLEDs on silicon neural probes for high-resolution optogenetic studies in behaving animals. *Neuron* 88, 1136–1148. doi: 10.1016/j.neuron.2015.10.032

Wu, J., Seregard, S., and Algvere, P. V. (2006). Photochemical damage of the retina. *Survey Ophthalmol.* 51, 461–481. doi: 10.1016/J.SURVOPHTHAL.2006.06.009

Wurth, S., Capogrosso, M., Raspopovic, S., Gandar, J., Federici, G., Kinany, N., et al. (2017). Long-term usability and bio-integration of polyimide-based intra-neural stimulating electrodes. *Biomaterials* 122, 114–129. doi: 10.1016/j.biomaterials.2017.01.014

Yang, W. and Yuste, R. (2017). *In vivo* imaging of neural activity. *Nat. Methods* 14, 349–359. doi: 10.1038/nmeth.4230

Yaroslavsky, A. N., Schulze, P. C., Yaroslavsky, I. V., Schober, R., Ulrich, F., and Schwarzmaier, H.-J. (2002). Optical properties of selected native and coagulated human brain tissues *in vitro* in the visible and near infrared spectral range. *Phys. Med. Biol.* 47:305. doi: 10.1088/0031-9155/47/12/305

Zhao, H. (2017). Recent progress of development of optogenetic implantable neural probes. *Int. J. Mol. Sci.* 18: E1751. doi: 10.3390/ijms18081751

Zhao, H., Soltan, A., Maaskant, P., Dong, N., Sun, X., and Degenaar, P. (2018). A scalable optoelectronic neural probe architecture with self-diagnostic capability. *IEEE Trans. Circuits Syst. I Regul Pap.* 65, 2431–2442. doi: 10.1109/TCSI.2018.2792219

Conflict of Interest Statement: The authors declare that the research was conducted in the absence of any commercial or financial relationships that could be construed as a potential conflict of interest.

Copyright © 2019 Reddy, Kimukin, Stewart, Ahmed, Barth, Towe and Chamanzar. This is an open-access article distributed under the terms of the Creative Commons Attribution License (CC BY). The use, distribution or reproduction in other forums is permitted, provided the original author(s) and the copyright owner(s) are credited and that the original publication in this journal is cited, in accordance with accepted academic practice. No use, distribution or reproduction is permitted which does not comply with these terms.

frontiers in Neuroscience

ORIGINAL RESEARCH
published: 27 August 2019
doi: 10.3389/fnins.2019.00885

Protuberant Electrode Structures for Subretinal Electrical Stimulation: Modeling, Fabrication and *in vivo* Evaluation

*Pedro González Losada[1], Lionel Rousseau[1], Marjorie Grzeskowiak[1], Manon Valet[2], Diep Nguyen[2], Julie Dégardin[2], Elisabeth Dubus[2], Serge Picaud[2] and Gaelle Lissorgues[1]**

[1] Laboratory ESYCOM, University Paris Est-ESIEE-MLV, Noisy-le-Grand, France, [2] INSERM, CNRS, Institut de la Vision, Sorbonne Université, Paris, France

OPEN ACCESS

Edited by:
Ulrich G. Hofmann,
University Medical Center Freiburg, Germany

Reviewed by:
Daniel Llewellyn Rathbun,
Henry Ford Health System, United States
Kazutaka Takahashi,
The University of Chicago, United States

***Correspondence:**
Gaelle Lissorgues
gaelle.lissorgues@esiee.fr

Specialty section:
This article was submitted to Neuroprosthetics, a section of the journal Frontiers in Neuroscience

Received: 16 December 2018
Accepted: 07 August 2019
Published: 27 August 2019

Citation:
Losada PG, Rousseau L, Grzeskowiak M, Valet M, Nguyen D, Dégardin J, Dubus E, Picaud S and Lissorgues G (2019) Protuberant Electrode Structures for Subretinal Electrical Stimulation: Modeling, Fabrication and in vivo Evaluation. Front. Neurosci. 13:885. doi: 10.3389/fnins.2019.00885

Many neural interfaces used for therapeutic applications are based on extracellular electrical stimulation to control cell polarization and thus functional activity. Amongst them, retinal implants have been designed to restore visual perception in blind patients affected by photoreceptor degeneration diseases, such as age-related macular degeneration (AMD) or retinitis pigmentosa (RP). While designing such a neural interface, several aspects must be taken into account, like the stimulation efficiency related to the current distribution within the tissue, the bio-interface optimization to improve resolution and tissue integration, and the material biocompatibility associated with long-term aging. In this study, we investigate the use of original microelectrode geometries for subretinal stimulation. The proposed structures combine the use of 3D wells with protuberant mushroom shaped electrode structures in the bottom, implemented on a flexible substrate that allows the *in vivo* implantation of the devices. These 3D microelectrode structures were first modeled using finite element analysis. Then, a specific microfabrication process compatible with flexible implants was developed to create the 3D microelectrode structures. These structures were tested *in vivo* to check the adaptation of the retinal tissue to them. Finally, preliminary *in vivo* stimulation experiments were performed.

Keywords: retinal prostheses, microfabrication, 3D microelectrode, FEM, subretinal, electrical stimulation

INTRODUCTION

Many neural interfaces used for therapeutic applications are based on extracellular electrical stimulation to control cell polarization and thus functional activity. Common examples range from deep brain stimulators for Parkinson's disease to sensory prostheses such as cochlear implants (Deuschl et al., 2006; Schwalb and Hamani, 2008; Eshraghi et al., 2012). More recently, retinal implants have been designed to restore some visual perception in blind patients affected by photoreceptor degeneration diseases, such as age-related macular degeneration (AMD) and retinitis pigmentosa (RP). Depending on the chosen surgery, the implant may be placed at different locations to intervene at different levels in the visual system: (i) into the subretinal space where

the electrode array is located between the inner nuclear layer and the retinal pigment epithelium to replace the lost photoreceptors like Alpha-AMS (Edwards et al., 2018) and Pixium PRIMA® (Hornig et al., 2017) devices, (ii) on the epiretinal position close to the ganglion cell layer as the Argus-II prosthesis (Luo and da Cruz, 2016) *or the Pixium IRIS®*. In the case of subretinal implantation, the electrical stimulation is expected to activate the surviving retinal bipolar cells, which transfers the artificial visual information coded as spike signals to the ganglion cells and the optic nerve whereas epiretinal implants aim at direct activation of retinal ganglion cells.

While designing such a neural interface, several aspects must be taken into account: (i) the stimulation efficiency related to the current distribution within the tissue, (ii) the bio-interface optimization to improve resolution and tissue integration, (iii) the material biocompatibility and long-term aging.

Return electrodes in form of grids surrounding the stimulating electrodes could greatly increase the spatial contrast, and in specific cases also the spatial resolution, of electrical stimulation (Joucla and Yvert, 2009; Flores et al., 2016). A photovoltaic retinal implant with a ground grid has also shown the possibility to generate a high spatial resolution *in vivo* (Wang et al., 2012). 3D structures could further increase the spatial resolution with or without a ground grid by confining neurons in a stimulating area (Djilas et al., 2011) or bringing the electrode in the vicinity of the targeted neurons (Mathieson et al., 2012*)*. Using such 3D geometries, we have previously demonstrated that the remaining retinal tissue of blind rats can mold into 3D wells such that bipolar cells can be isolated in regular columns for a selective stimulation (Djilas et al., 2011). Others have proposed protuberant structures to induce a selective stimulation of retinal cells (Koo et al., 2006; Kim et al., 2008). In parallel mushroom shapes have been used in rigid Micro Electrode Arrays to improve the interaction between cells and the electronic device (Huys et al., 2008; Sasso et al., 2010; Fendyur and Spira, 2012).

We here investigated the possibility to combine 3D wells with the presence of protuberant mushroom electrodes on a flexible retinal implant. This study aimed at modeling the resulting current densities in the tissue and developing in parallel a simple microfabrication process compatible with the production of flexible implants having protuberant structures previously produced by others on rigid substrates such as silicon (Butterwick et al., 2009). Finally, using these prototypes, we investigated how the retinal tissue can interface properly with these new 3D complex structures with protuberant mushrooms in a well.

MATERIALS AND METHODS

FEM Simulation

A finite element model (FEM) was developed using COMSOL®Multiphysics Version 5.2, Grenoble, France. The studied model consisted of a protuberant metallic electrode embedded in an insulating substrate and surrounded by a liquid environment with an electrical conductivity which represents the physiological environment, i.e., the retinal tissue. The interface between the insulating substrate and the liquid bio-environment is classically modeled using insulating boundaries described by Equation 1. For the electrode-electrolyte interface, Robin boundary condition described by Equation 2 is used as previously defined by Joucla et al. (2014). The conductivity values σ for the different materials were considered homogeneous and isotropic, and they are summarized in **Table 1**.

$$\nabla Vn = 0 \tag{1}$$

$$\sigma \nabla Vn = g\,(V_{metal} - V) \tag{2}$$

Three types of structures were modeled for comparison (**Figure 1**): a flat electrode in a cavity surrounded by a top ground plane, a single protuberant electrode in a cavity surrounded by a top ground plane, and a double protuberant structure embedded in the same cavity and with the same DC voltage being applied to the electrodes. For the three geometries the other parameters such as the cavity depth, width and length, the electrode diameter, or the pillar base diameter were constant, allowing the exact surface of the electrodes to be considered in each case.

Microfabrication

The fabrication technology is based on the existing planar implant technology developed in our laboratory, to which new steps were added to introduce the protuberant electrodes into the 3D shaped wells. The fabrication process for the soft implants on a silicon wafer is summarized in **Figure 2**. (Step 1) A sacrificial layer composed of sputtered titanium (100 nm) and aluminum (500 nm) was deposited on a silicon wafer. (Step 2) 10 μm of polyimide (PI 2611 from HD MicroSystems) were spin coated and baked to create the substrate of the implant. (Step 3) A layer of titanium (100 nm) and gold (500 nm) was deposited by sputtering and patterned using photolithography to simultaneously define the electrodes, tracks and pads. (Step 4) SU8 2002 (from MicroChem) was spin-coated to form a 2 μm encapsulation layer to protect the metallic parts and, using a second photolithography step, openings were created on the pads and electrodes. (Step 5) Finally, 500 nm of aluminum were sputtered and patterned using an additional photolithography step followed by wet etching to create a mask to define the shape of the implant. The polymer was etched to pattern the shape of the implant by means of reactive ion etching (RIE), using a gas mixture of argon (Ar) and oxygen (O_2) at 120 W and under a controlled flow rate. The aluminum layer acts as a stop layer for the polymer etching and it is chemically removed once the process is finished.

The fabrication process of the 3D structures on the flexible implant is summarized in **Figure 3**. Indeed the process continues

TABLE 1 | Parameters used for the simulation.

Material	Conductivity σ (S/m)	Relative Permittivity
Physiological liquid	$1.47e^{-2}$	81
Insulating material	$1.31e^{-18}$	3.4
Conductive material	$45.6e^{6}$	–

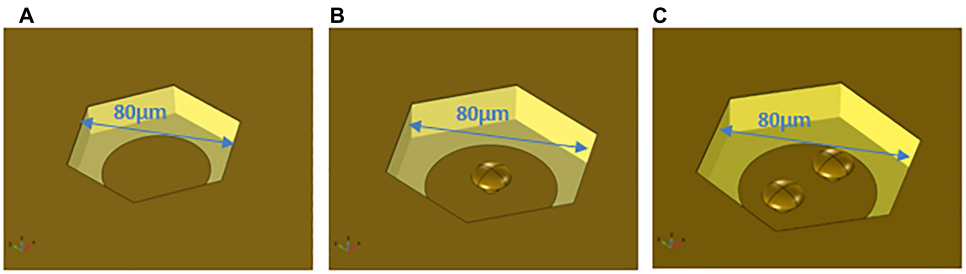

FIGURE 1 | Different geometries modeled. **(A)** Cavity with a planar electrode in the bottom; **(B)** cavity with a planar electrode and one protuberance; **(C)** cavity with a planar electrode and two protuberances.

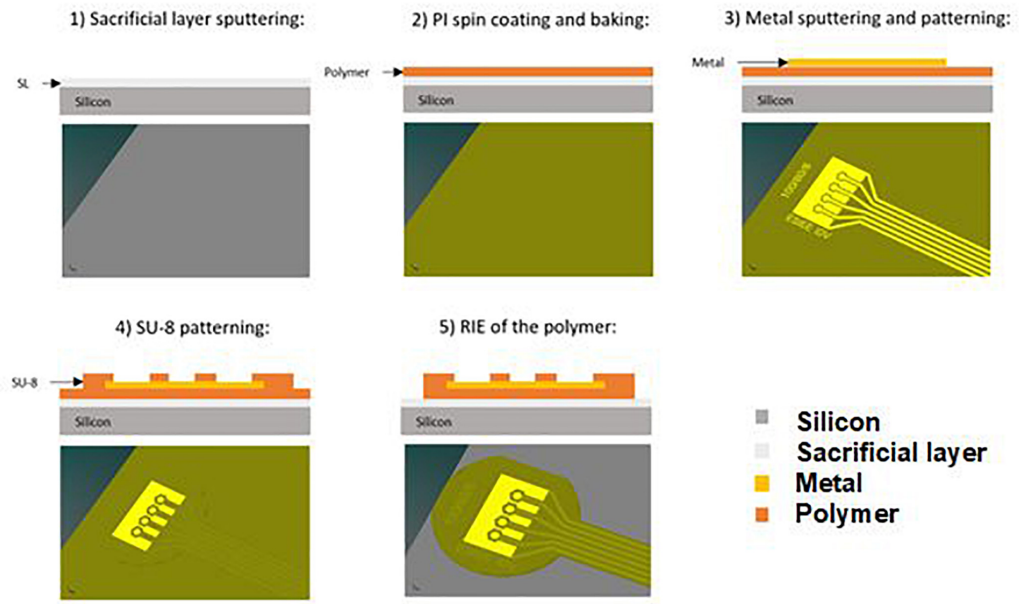

FIGURE 2 | Fabrication process of the planar flexible implant.

after the patterning of the implant shape to produce the requested 3D structures (top ground grid and pillars at the bottom).

Initially, the 3D structures were fabricated in copper and then encapsulated in parylene to avoid any contact between the tissue and the copper. Copper electroplating is a well-known process in microfabrication technologies, which allowed us to fabricate the first prototypes fast and in a reliable way. Once the technology was established and consolidated, we were able to do *in vivo* experiments to assess its feasibility. Then, we transferred the technology to a biocompatible metal that does not need to be encapsulated i.e., gold.

(Step 1) On the whole wafer, we deposited a thin seed layer consisting of 50 nm titanium and 150 nm of either copper or gold, depending on the material used for the 3D structures. (Step 2) A photoresist (SIPR 3.0 or 6.0 from ShinEtsuMicroSi) was deposited and patterned to create the mold for protuberant electrodes. (Step 3) The wafer was placed in a copper or gold solution and a constant current (100 mA for copper and 0.1 mA for gold) was applied to electrodeposit the metal, thus creating the protuberances. The first photoresist was cleaned in solvent. (Step 4) A new thick photoresist (15 µm) layer was used to create the ground plane mold. (Step 5) Once the photolithography step was completed, the wafer was placed for a second time in the electrodeposition solution under the same growth conditions to obtain the ground plane. Then wafers were cleaned, and the initial seed layer etched. (Last step – not represented on **Figure 3**) A thin photoresist protection was applied before peeling off the implants to protect the electrodes and contacts from any corrosion. To peel off the implants from the silicon wafer, the aluminum layer below the implant was dissolved by electro erosion.

After cleaning, in the case of the copper devices only, an additional thin layer of parylene C (2 µm) was used to encapsulate the whole structure and ensure biocompatibility.

In vivo Histology

The 3D structures have been implanted in sub retinal position in blind rats (P23H) to check the structural plasticity of the retina. Indeed, P23H rats (Machida et al., 2000) are considered

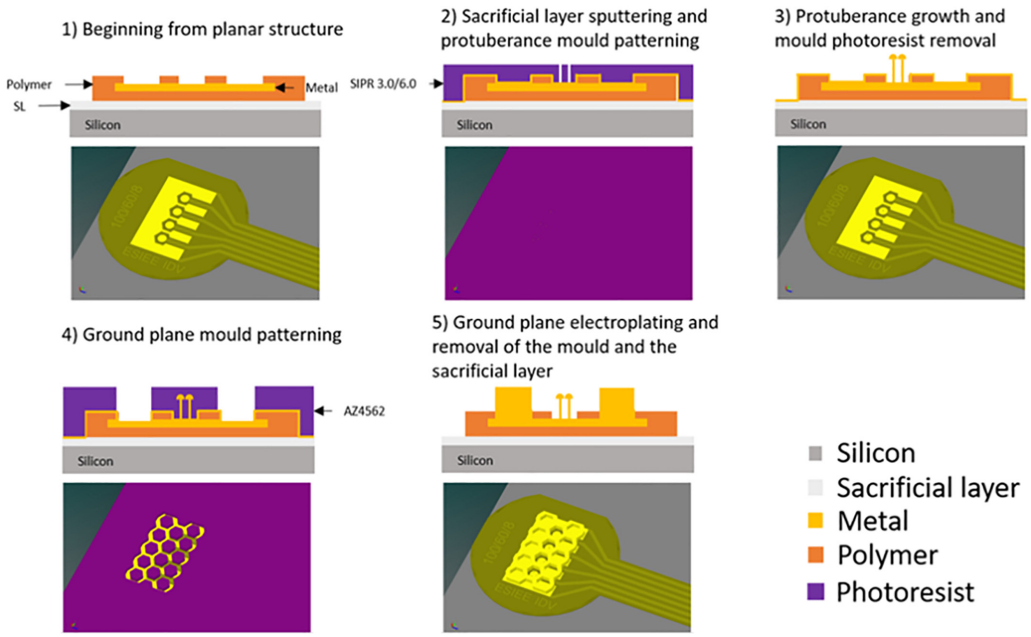

FIGURE 3 | Fabrication process of the 3D structures on the flexible implant – Due to the small size of the holes compared to the implant, the software was unable to produce an image where such features can be appreciated while keeping the large view of the whole implant.

as a reference model for retinis pigmentosa degeneration, since the rods' degeneration is comparable to clinical cases observed on patients progressively losing their photoreceptors. The correct position of the implant is monitored by optical coherence tomography (OCT), immediately after surgery, and regularly every week.

The implant is explanted after 12 weeks *in vivo* and animal sacrifice and cell labeling is done for confocal analysis. The eyes are removed and placed in phosphate-buffered saline (PBS, 0.1 M, pH 7.4). The implanted area is isolated using a 3 mm biopsy punch. This fragment is fixed by incubation overnight at 4°C in paraformaldehyde in PBS (4% wt/vol) and then rinsed in PBS. For immunolabelling, retinal fragments are incubated in a blocking solution [10% bovine serum albumin (Sigma, St. Quentin Fallavier, France), 2% Triton X-100 (Sigma), 0.5% Tween 20 (Sigma) and 0.1 g/l Thimerosal (Sigma) in PBS] for 1 h at room temperature. They are then incubated for 3 days at 4°C (with slow stirring), followed by incubation at room temperature for 2 h with primary antibodies in blocking solution. The antibodies used are polyclonal antibodies directed against Chicken anti Glial Fibrillary Acidic Protein (1:100, LifeSpan Biosciences, Seattle, WA, United States), Rabbit anti Iba1 (1:500, Wako Sobioda, MONTBONNOT St. Martin, France) and a monoclonal antibody directed against mouse Goα (1:200, Merck-Millipore, Darmstadt, Allemagne). The fragments are rinsed and then incubated with secondary antibodies: goat anti-Chicken IgY Alexa 647, goat anti-rabbit IgG Alexa 488, and goat anti-mouse IgG Alexa 594 (1:500, Molecular Probes, Invitrogen, Eugene, Oregon) for 2 days at 4° followed by incubation at room temperature for 1 h. The implant/retina ensemble is rinsed and mounted, in permanent mounting medium (MM France, Brignais, France), on a microscope slide, for viewing under an upright confocal microscope from Olympus (FV1000 laser-scanning confocal microscope). 4′,6-diamidino-2-phenylindole (DAPI) counterstaining, AlexaFluor-488 and AlexaFluor-594 and AlexaFluor-647 can be detected by excitation with a 405 nm laser diode, a 488 nm argon ion laser, and 559 and 635 nm laser diode lines, respectively.

Thanks to this cell labeling technique, it is possible to count in which well we find bipolar cells compared to glial cells, and to proceed to a statistical analysis, typically to estimate the ratio of bipolar cells over total cell number, depending on the geometry and shape of the electrode. We need to keep in mind the limited number of *in vivo* experiments we can do. So we decided to focus on the largest cavities (80 μm) with more results available as small cavities are more difficult to fill.

All experiments were carried out in accordance with the recommendations of the European Community Council Directives (86/609/EEC) and with the ARVO (Association for Research in Vision and Ophthalmology) statement for the use of animals in ophthalmic and visual research. The protocol was approved by the French "Comité National de Réflexion Ethique sur l'Expérimentation Animale" under the reference #15258 2018052811521506 v1 in October 2018. The surgical procedure used to implant the prototypes has been described in detail elsewhere (Bendali et al., 2015).

Statistical Analysis

Among the implants studied, some of the cavities could not be exploited because of difficulties to determine the number of remaining protuberances. Indeed, after surgery, some protuberances were broken (although we only implanted

implants of good quality after fabrication, removing those with missing protuberances). For the determination of the influence of the cavity width, 16 cavities of 100 μm in diameter were exploited, 8 of 80 μm, and 3 of 60 μm. In the case of the influence of the number of protuberances, 12 cavities without protuberant structures were analyzed, 7 cavities with one protuberance, 9 with two protuberances, 9 with three protuberances, and 7 with four protuberances. The average number of total cells per implant is recorded using the explanted retina with previously described labeling technique.

In vivo Physiology

As it is difficult to physically stabilize the 3D implants in the subretinal space, we demonstrate influence of the protuberant structures in acute conditions. Implantation is done just before the stimulation experiments and the retinal tissue does not have time to fully conform the 3D shapes compared to studies where the implant remained for several weeks. For this reason and in order to reduce the mismatch between the retinal tissue and the stimulating electrodes, a set of implants consisting of electrodes with protuberances but without cavities were fabricated for these tests. The idea is also to mimic in a short time a situation close to what is expected after long implantation when the retinal cells move into the wells. The employed device consists of four microelectrodes where one of them is planar, the second one has one protuberant structure, the third one has two protuberances and the fourth one has three three-dimensional structures. The size of the planar electrode is 60 μm and the height of the protuberances is around 7 μm.

The active site of the connected implant was acutely placed in the subretinal space of a 12 weeks old healthy Long Evans rat (Janvier Labs, France) while the flexible shank and base is placed on an adjacent platform. The healthy model enables a positive control of evoked potential via light stimulation to be compared with electrical stimulation. A craniotomy on the contralateral visual cortex is made to allow electrophysiological recordings. Initial anesthesia is provided through a 5% isofluorane induction for several minutes. Fixed anesthesia for the surgery and recording was done using intraperitoneal injection of ketamine 1000 (40 mg/kg, Axience, France) and domitor (0.14 mg/kg, Vétoquinol, France). Anesthesia is maintained with 1/3 initial dosage every 45 min. The animal is placed on a stereotaxic frame with body temperature maintained at 35°C. A sagittal incision is made from the ears to the eyes. Tissue is pushed aside to reveal the cranium. A craniotomy is achieved through drilling a window and removing the parietal bone and the dura mater. Gel foam soaked in cortex buffer is maintaining the integrity of the brain during the implantation.

The implant head was placed in the nasal hemisphere of the subretinal space contralateral to the craniotomy. Surgical microscope verified that the implant is placed in the subretinal position. Tropicamide (5%) was used for eye dilation while oxybuprocaïne provided a local anesthesia. A small sclerotomy was made on the dorsal sclera and a 1 mm incision gives access. Retinal detachment was achieved using basic saline solution as previously described (Roux et al., 2016). Immediately after the device implantation, the recording electrode array is descended into the monocular region of the primary visual cortex (V1M) contralateral to the implanted eye. Electrophysiolgy recording lasted about 3 h after the surgery and the animal was euthanized through intracardiac injection of pentobarbital (dolethal 1 mL).

Full field natural stimulation is provided by a white LED (Thorlabs, United States) having an intensity of 2.2 mW/cm^2. Current controlled microelectrical stimulation is delivered using a stimulus generator (Multichannel Systems, Germany) with a stainless-steel needle as a counter electrode is placed subcutaneously on the lower back of the animal. Recording on the primary visual cortex is done using a 16-channel linear MEA (NeuroNexus) connected to a 16-channel amplifier (Multichannel System).

Intracortical recordings are taken while stimulation is delivered at the eye at a rate of 1 Hz and repeated 100 times to be averaged. Light stimulation lasted for 10–100 ms as usually used in brain light stimulation or optogenetics. Electrical stimulation is delivered to individual electrodes on the subretinal implant. Delivered electrical stimulation waveforms have a symmetrical charge balanced biphasic pulse of 1 ms at each phase and an interpulse interval of 1 ms. The 3 ms waveform of is repeated three times to match the duration of stimulations delivered by light and obtain a total of 10 ms stimulation. Variation of stimulus intensity, duration, cathodic vs. anodic, are compared to determine the response effect of the different geometrical configurations. Raw data has been sampled at 25 kHz and is analyzed for evoked potential. The signal is always bandpass filtered from 1 to 100 Hz and averaged over the 100 repetitions aligned by the trigger onset. The results compare the averaged response amplitude and latency of each acquisition.

RESULTS

FEM Simulation

To assess the impact of introducing protuberant structures into a well on current distributions, **Figure 4** illustrates the cross-sectional view of the current densities in a color code for the different conditions. The maximum and minimum values of current densities, corresponding respectively to upward and downward black triangles, depend on the computational meshing and so are slightly different, but the color scale is kept the same (dark blue – 0 to dark red – 30). These conditions have a ground plane on the superior part of the implant, a stimulation electrode centered at the bottom surface of the well for the planar geometry (G0) and protuberant mushrooms with an electrode on their surface (G1 and G2). In the planar geometry, a border effect is identified both at the border of the stimulating electrode in the well and the border of the ground plane: most of the current penetrates the liquid in this region of the electrode. In the protuberant geometries we appreciate a redistribution of the current density as higher current density is observed between the mushrooms and the ground plane.

Curve graphs show the comparison of the current density through a line over three different positions: over the cavity (line A), in the height of the ground plane (line B) and inside the cavity (line C). In the case of the measurement inside the cavity (line C),

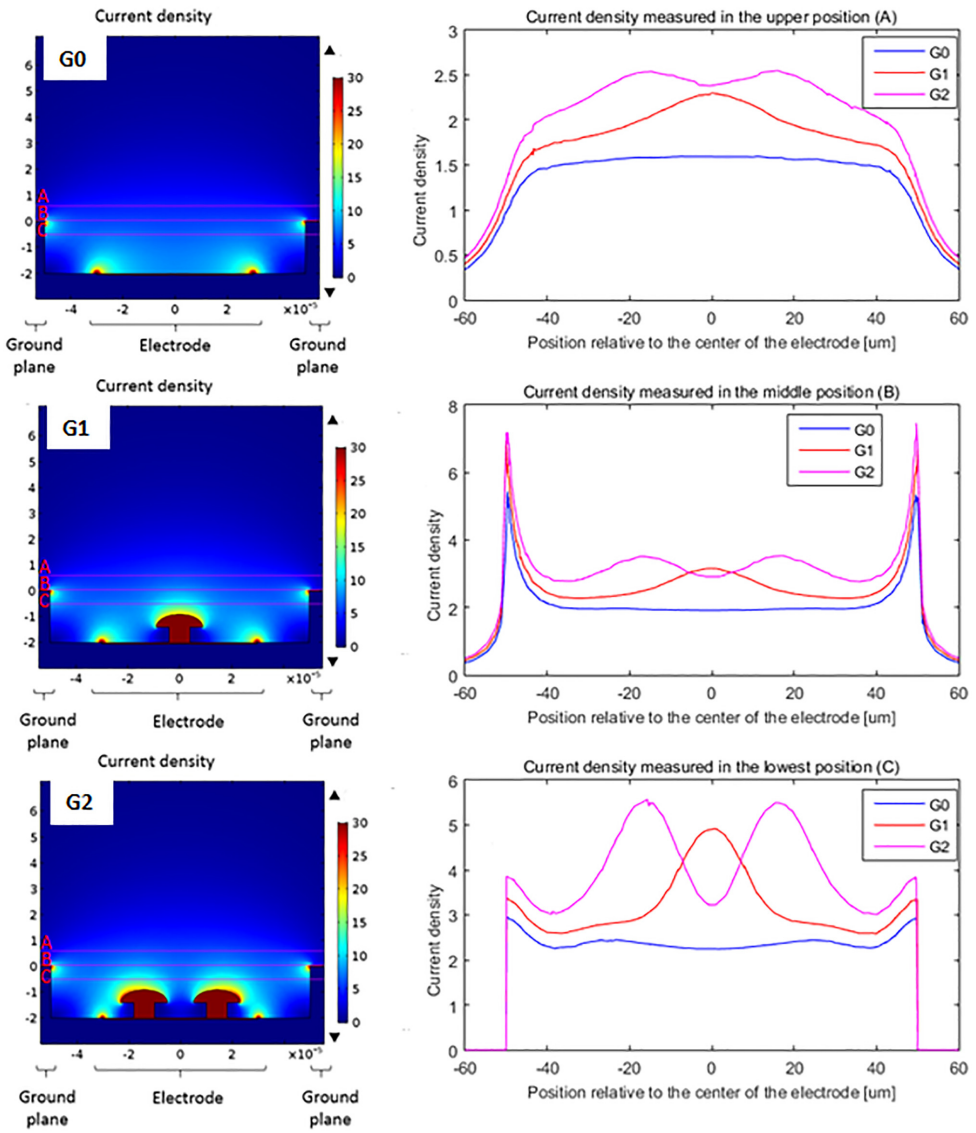

FIGURE 4 | Comparison of the current density delivered by a flat electrode **(G0)**, a single protuberant **(G1)** and a double protuberant geometry **(G2)** in a two level configuration: ground plane and flat electrode plane are not at the same level – but same color scale (dark blue 0 to dark red 30 – units arbitrary here, as simulations done with a normalized applied voltage of 1V). Right side curves show the current density in A/m^2 along the lines placed over the cavity (line A), at the ground plane level (line B) and inside the cavity (line C).

the protuberant structures change the distribution of the current density adding one (G1) or two (G2) peaks while the planar geometry (G0) shows two small peaks due to the edge effect of the planar electrode. Measurements done further from the electrode (line A and B) still show this effect but attenuated because of the distance. In the case of the line B measurements, the edge effect of the ground plane is also shown by the peaks in the edges, as line B corresponds to the top of the ground plane.

In addition, **Figure 5** shows the derivatives of the current density along the depth (Z axis) and the width of the well (Y axis) which is more representative of the current variations. We clearly see that the introduction of the mushroom pillars into the cavities concentrates the current variations inside the cavity where the bipolar cells are expected to be located. This spatial variation of the current density, according to the work activating function theory, should be responsible of neuron activation. Hence, neurons having moved into the well between the mushroom pillars and the ground plane would therefore be better activated.

Microfabrication

The size of the hexagonal cavities was varied from 100 to 60 μm and the diameter of the base of the protuberances from 12 to 6 μm. The number of protuberances was also varied from 0 to 4 in every cavity in order to study the adaptation of the tissue according to the number of protuberances. **Figure 6**

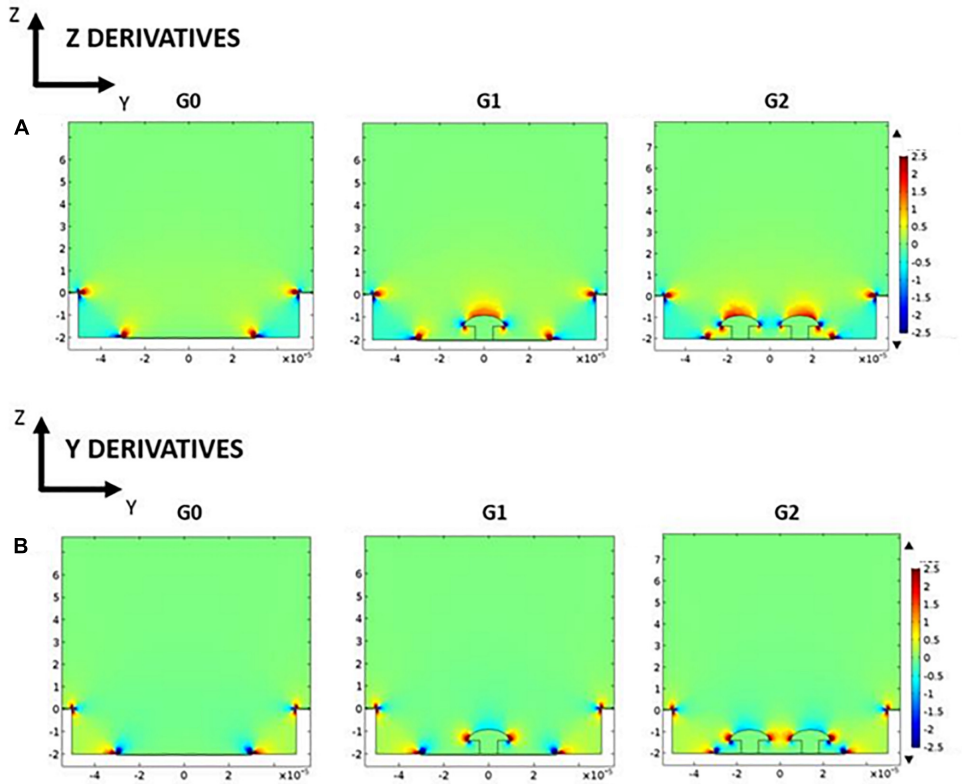

FIGURE 5 | Potential derivatives along depth *Z* axis **(A)** and width *Y* axis **(B)** for the three studied geometries: G0, G1, and G2 (arbitrary color scale – from low value, blue, to high value, red).

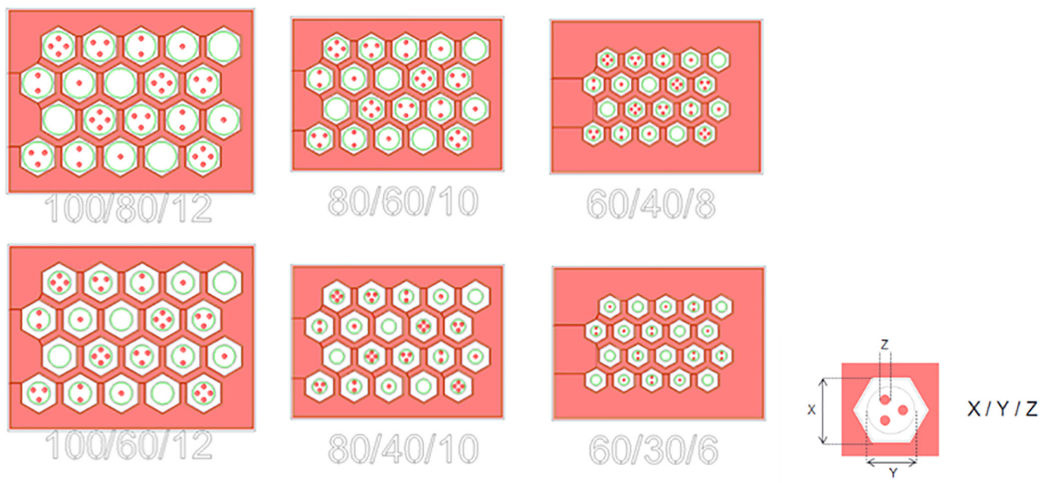

FIGURE 6 | Mask of the six different configurations fabricated.

summarizes the different geometries resulting in the combination of different sizes of well and protuberances. Every implant has an identification code composed of one letter and three configuration numbers that represent the size of the different parts of the structure: X stands for well length, Y for planar electrode diameter and Z for protuberance base diameter. An additional letter was used to differentiate implants sharing a single configuration.

Previous work in our group focused on the fabrication and *in vivo* characterization of cavities by means of silicon molding (Bendali et al., 2015). The main drawbacks of this technique are the time consumption required to create the silicon mold and

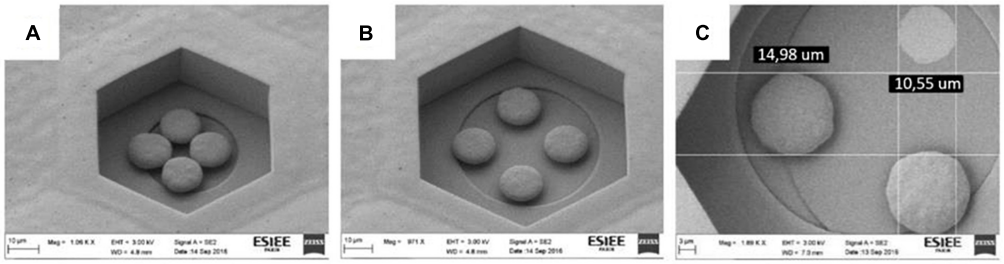

FIGURE 7 | SEM picture of the four protuberant pillars made in copper in a 60/40/8 **(A)** – scale bar 10 μm – and a 80/60/10 **(B)** – scale bar 10 μm – structures. Detail of the diameter of a 3 protuberances structure with one of the protuberances detached in a 100/80/12 **(C)**, showing the base diameter of the pillar – scale bar 3 μm – For dimensions in **(C)**, 14.98 μm represents the diameter of the top of the mushroom while 10.55 μm represents the base of the pillar of similar mushroom.

the impossibility to obtain straight edges due to the isotropic (KOH) etching of the mold. Conversely, the electroplating method allows the control of the structure thickness by adjusting the time and the current in the bath during electroplating, and the well cavities can be defined with perpendicular walls at 90 degrees (**Figure 7**). In addition, the shapes have been defined to be compatible with other families of implants, like those based on photovoltaic effects (Mathieson et al., 2012; Wang et al., 2012).

As explained, devices were initially fabricated in copper due to its common use in microelectronics and its low cost compared to other techniques. However, copper is not a biocompatible material and it was covered with a layer of parylene (2 μm) to avoid any contact with the retinal tissue. Then a second rendition was fabricated using electroplated gold for the 3D structures. Growth conditions are different between copper and gold, leading to small changes in the mushroom's shape. Optical (**Figure 8A**) and SEM (**Figure 8B**) images show the implant fabricated in gold (large view A with the implant's head diameter being 1 mm and zoom on electrodes B with a base of 10 μm and the top of the mushroom of 17.5 μm).

In vivo Histology

Previous studies in our group have already shown that retinal tissue is capable of adapting to and filling the cavities of a subretinal implant (Bendali et al., 2015). However, the cavities tested before were offering an angle of 54.7° due to KOH etching during mold creation, which may change the adhesion of the tissue compared to the vertical walls (90°) of the new devices described here.

Optical coherence tomography (OCT) and eye fundus observation were used to verify the position of the implant during the 12 weeks of implantation (**Figure 9**). The results showed that the implant was stable in time over 3 months, did not cause retinal detachment, and did not damage the retina. In addition, OCT allowed us to visualize an absence of inflammation in presence of the implant under the retina.

Data from implants ranging from a well length of 100 to 60 μm (X dimension) and without protuberances inside were exploited. For comparison purposes, since the size of the cavities and the space occupied by the protuberances inside was different, the number of bipolar, glial and other types of cells has been counted for every cavity and then normalized regarding the total number of cells in the cavity.

The first relevant aspect is the influence of the diameter of the cavity on the molding of the retina onto the 3D structures. **Figure 10** represents the percentage of cells of every type in the different cavities. The graphic shows a direct relation between the number of bipolar cells and the width of the cavity: 60 μm width cavities have an 18.75 ± 10.10% of bipolar cells which increases to 66.29 ± 8.67% for the 80 μm and to 84.10 ± 9.77% for the 100 μm ones. On the contrary, the number of other cells contained in the cavities is inversely proportional: for the 60 μm width cavities, there is a 76.59 ± 7.25% of other cells, 26.16 ± 9.75% for the 80 μm ones and 10.79 ± 10% for the 100 μm ones. We also observe that the number of glial cells almost remains constant for the three different cavity sizes: 4.66 ± 4.25% for the 60 μm, 7.55 ± 3.59% for the 80 μm and 5.11 ± 4.48% for the 100 μm.

This, again, demonstrates that the residual retina is structurally plastic enough to mold itself into the vertical 3D implant cavities for a cavity of minimal width above 80 μm in diameter, as confirmed with the confocal images (**Figure 11**).

The second aspect to study is the influence of the protuberances on the adaptation of the retinal tissue to the bottom of the cavity. For this purpose and considering the results of the influence of the cavity size, data from the 100 μm cavities are studied. **Figure 12** shows the comparison of the mean percentage of every type of cells for the different structures contained in the 100/80/12 implants studied. Unlike in the case of cavity width, the number of cells of every type does not experience a significant variation for the different configurations. In the case of the bipolar cells the value for the cavities without protuberances is 86.64 ± 10.00% while for the opposite case of four protuberances it is 76.98 ± 13.63%. The average percentage of other cells also does not experience a significant variation being 7.88 ± 9.98% for the case of empty cavities, 13.18 ± 12.45% for the intermediate case of two protuberances and 13.62 ± 12.51% for the extreme case of four protuberances. As in the case of the different cavity width, the percentage of glial cells remains stable ranging from values of 4.13 ± 1.40% for the case of two protuberant structures to 5.47 ± 4.31% in the case of no protuberant structures, with the

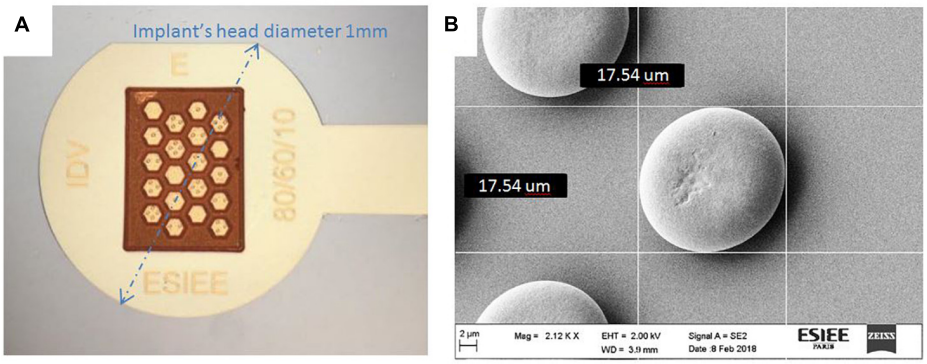

FIGURE 8 | Device fabricated in gold: optical microscope image **(A)** SEM image of protuberances **(B)**; we observe small variations in the mushroom's shape between **Figure 7** and **Figure 8**, as electroplating parameters in copper and gold are different leading to different growth results.

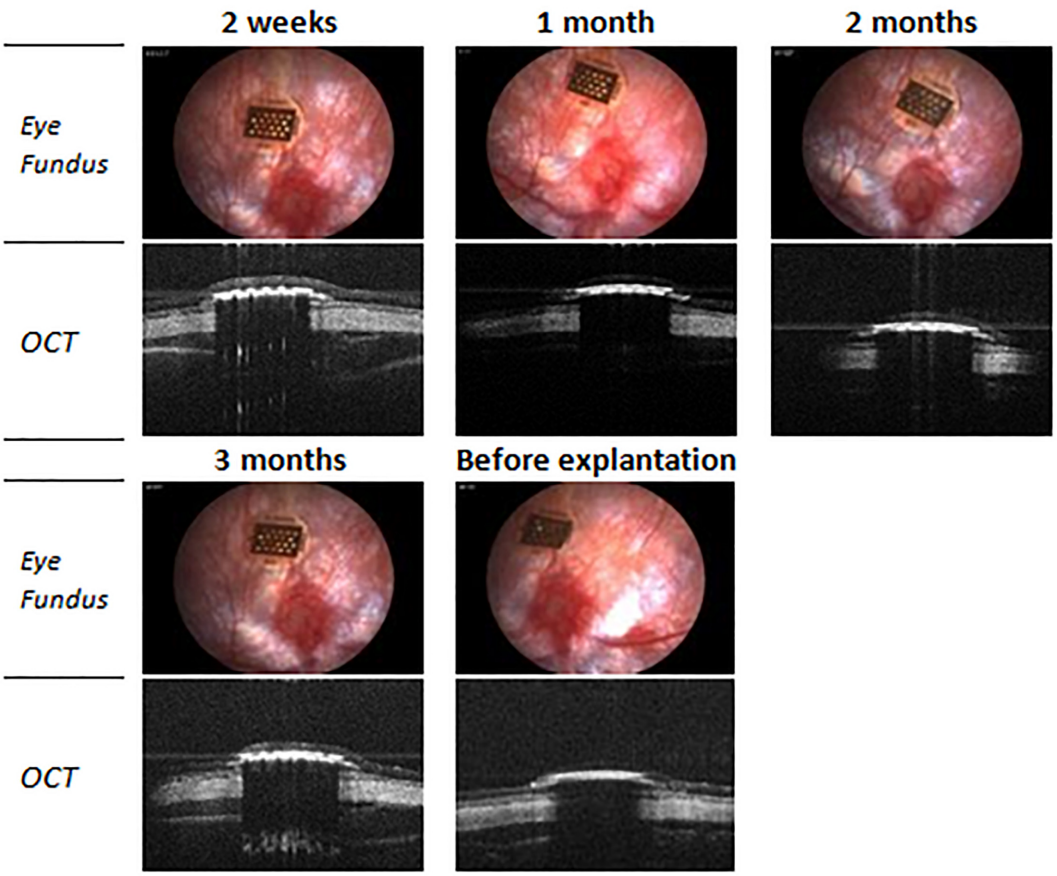

FIGURE 9 | Optical coherence tomography (OCT) and eye fundus images of a 100/80/12 implant in subretinal position during the implantation period.

exception of the four protuberances cavities that has a value of 9.41 ± 4.65%.

In vivo Physiology

Electrophysiological recording at the visual cortex of the brain allows for the observation of responses to light and electrical stimulation at the retinal. The general set-up is presented on **Figure 13**. Stimulation was delivered using pulses of 10 ms at 1 Hz with each recording lasting for 100 trials. Three stimulation electrodes were tested for comparison: classic planar electrode and two protuberant electrodes consisting of either one mushroom or two mushroom electrodes. Light stimulation delivered at the retina with different durations and a fixed intensity of 2.2 mW/cm^2 was done to evaluate the cortical

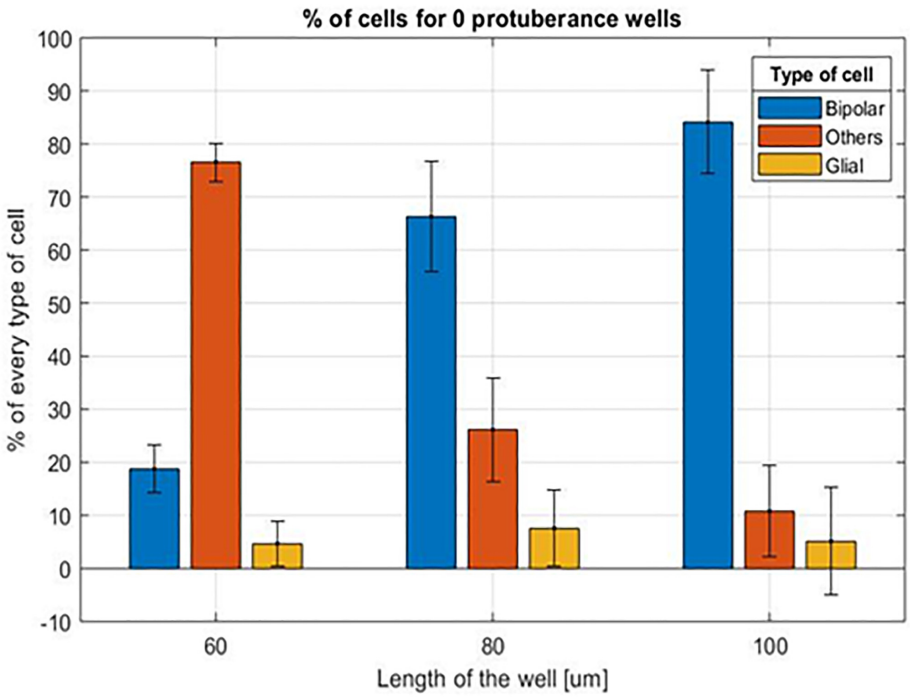

FIGURE 10 | Mean percentage of cells for the different cavity sizes without protuberances inside.

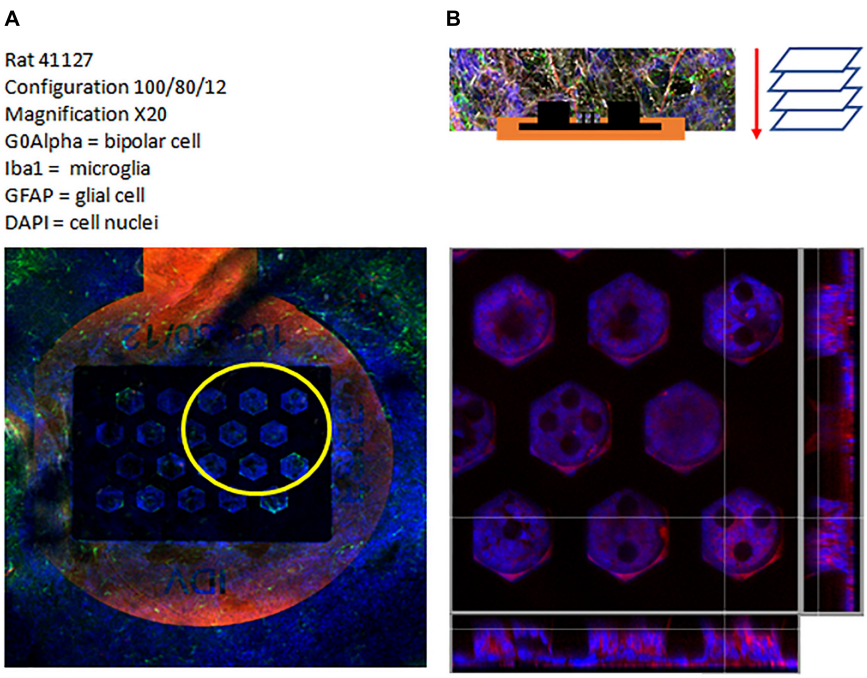

FIGURE 11 | Confocal image of a 100/80/12 implant: general view of the implant **(A)**, top view and cross section view of the 3D region **(B)**. Labeling: G0Alpha (red), Iba1 (green), GFAP (brown) and Dapi (Blue).

measured response. **Figure 14A** shows the cortical response to light stimuli at different duration measured by the recording electrode that had measured the largest response.

Electrical stimulation protocol consists of progressively increasing the current amplitude that is delivered at the different electrodes within the implant while recording at

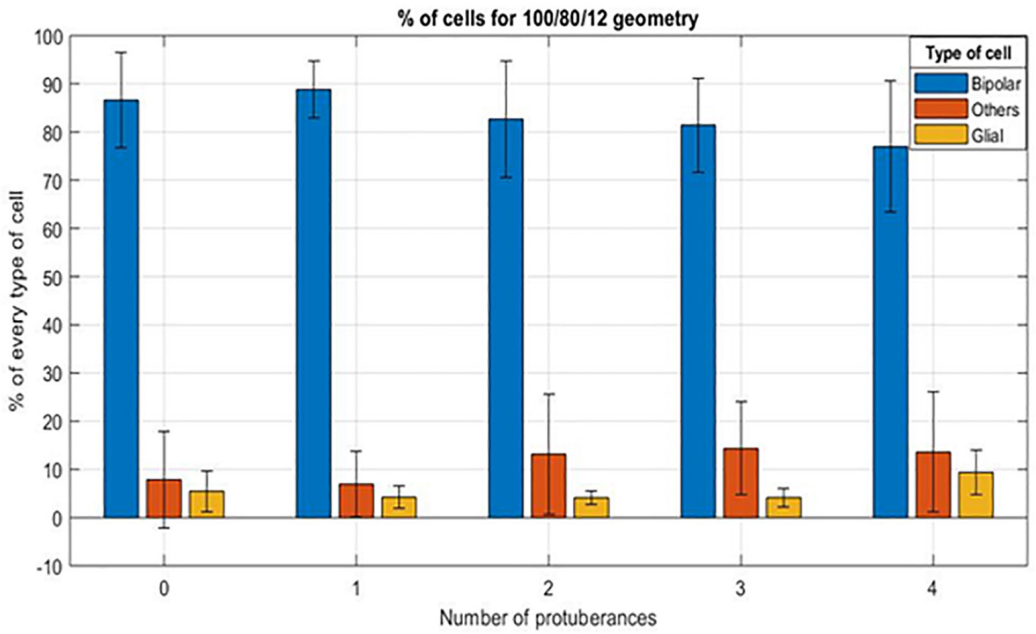

FIGURE 12 | Mean percentage of cells for a 100/80/12 implant, depending on the number of protuberant structures (from 0 to 4).

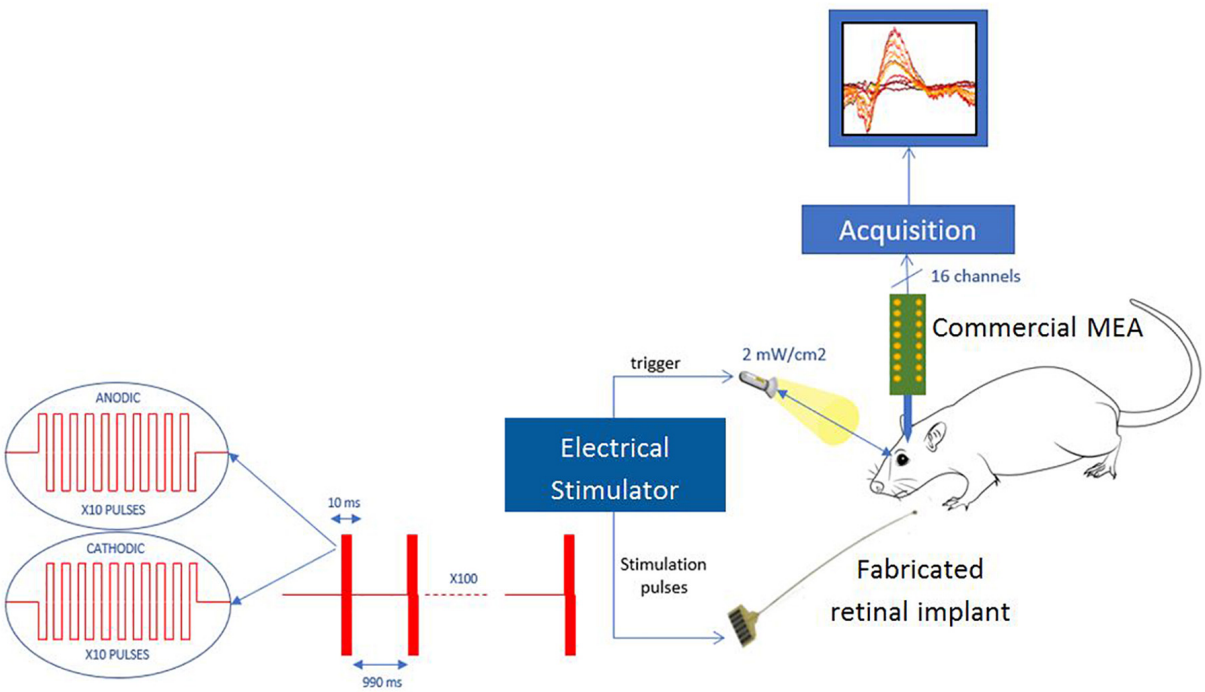

FIGURE 13 | Measurement set-up for *in vivo* experiments.

the same exact location in the visual cortex. **Figure 14B** shows the comparison among the measured responses to the stimulation of the three tested electrodes for the four highest current amplitudes: 64, 128, 192, and 256 μA. Our study did not show a difference in the local field potential response between stimulation waveforms that had started with cathodic or anodic first (data not shown). The plots in **Figure 14B** show that a threshold of current intensity must be reached in order to result an evoked potential similar to that elicited by light stimulation. This effect may be due to

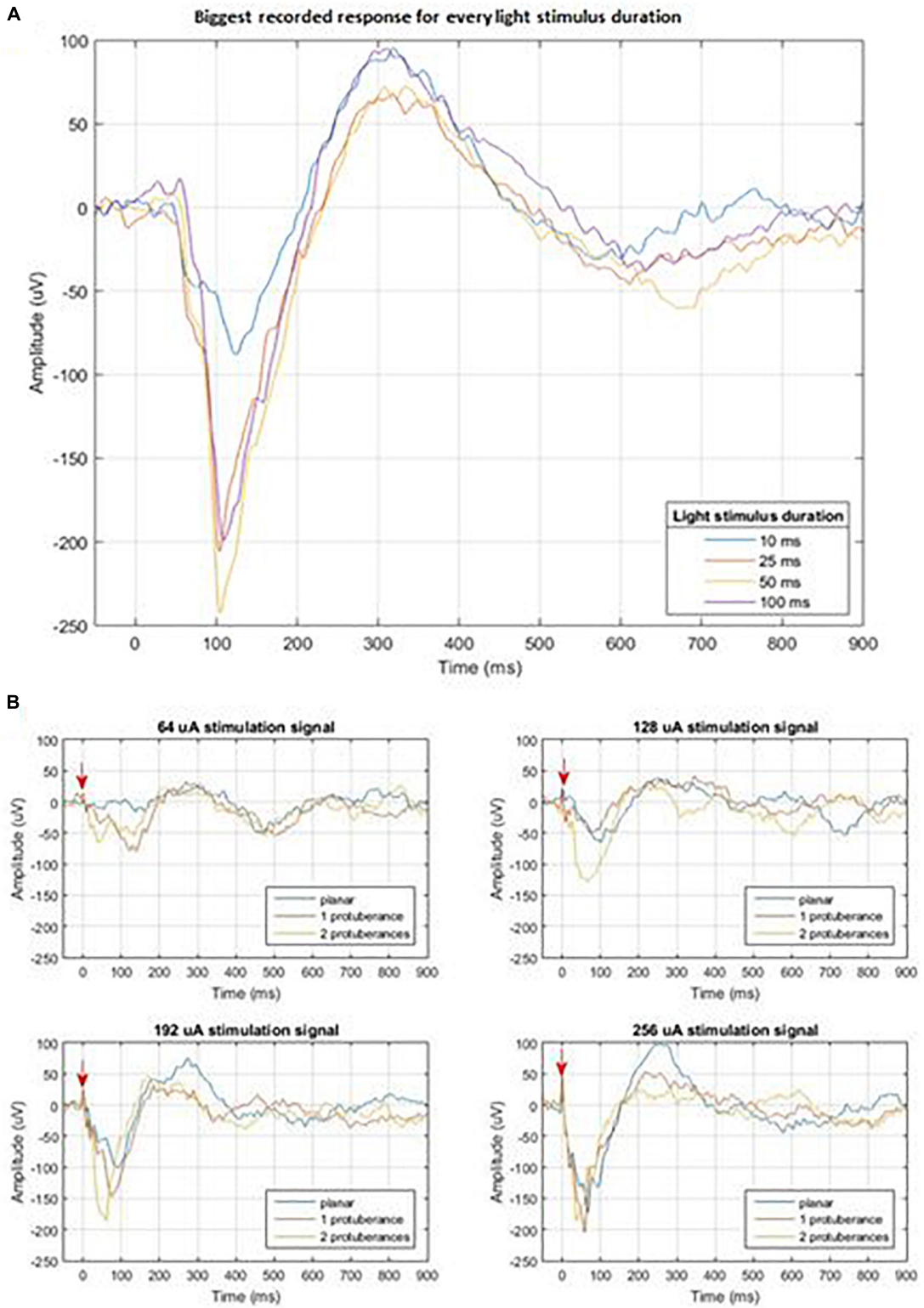

FIGURE 14 | (A) Cortical measured response to light stimulus of different durations; **(B)** Cortical measured response of the three different stimulation electrodes for four different stimulation amplitudes: 64, 128, 192, and 256 μA. The red arrow indicates the moment of electrical stimulation.

the smaller distance between the retina and the stimulating electrodes in the case of the protuberant ones and may be enhanced by the mismatch between the three-dimension geometries and the tissue.

DISCUSSION

In order to assess the influence of the microelectrode geometry on the current distribution, a finite element model of the microelectrode was developed, and three different geometries were modeled for comparison purposes.

Current density cross view and current density line graphs show that a high spatial variation of the current density is obtained by the introduction of protuberant structures on the top of the flat electrode. This spatial variation of the current density has been shown to have an influence on the neural activation. Hence, we expect that neurons having moved into the well between the mushrooms and the ground plane would therefore become highly activated. In addition, the use of cavities and a ground plane surrounding the stimulating microelectrode keeps the current in its vicinity, thus reducing the probability of activating other neurons.

Simulation results showed the interest of fabricating protuberant structures embedded into a cavity. To implant these structures in the retina and study their performance and the acceptance of the tissue to them, they should be preferably fabricated on a flexible polymeric substrate like polyimide or parylene for example. Two major techniques exist to create 3D structures: etching the silicon substrate or growing the structures by electroplating means. The electroplating method was chosen for its compatibility with soft implantable substrates.

The use of a microelectronics standard technique as copper electroplating allowed a fast development of the microfabrication process and the possibility of assessing the compatibility of these structures with the retinal tissue. Histological results showed that there is a direct relation between the size of the cavity and the number of bipolar cells that can enter in the cavity: cavities smaller than 80 μm are not suitable. Possible limitations of these results may come from the parylene used to encapsulate the metallic protuberant structures that might play a role due to its hydrophobic behavior.

Moreover, we tried to evaluate the influence of the number of protuberances for the same cavity size. For this purpose, 20 cavities per implant were defined, equally divided in five groups: cavities without protuberant structures, with one, with two, three, and four protuberant structures. All cavities were distributed in a manner to keep a constant separation of 16 μm among them. In order to maximize the number of electrodes per implant, this distance should be reduced, but a tradeoff is required to avoid sharp edges that could damage the retinal tissue. Therefore the results obtained in this first study can be exploited in a future study to optimize this parameter.

Another aspect that could have influenced is the distance between the cavities, which could prevent bipolar cells to descent into the cavities. Additional experiments would be needed to verify this hypothesis. These results also showed that the number of protuberances per cavity does not have a big influence on the rate of bipolar cells descending to the cavity.

Finally, after adapting the fabrication technique to use gold as microelectrode material, a preliminary *in vivo* stimulation experiment with these structures was conducted. Due to the surgical limitation of chronically fastening the flexible shank and base of the implant to the animal while maintaining the active site in the retina, an acute approach was taken. The results of this experiment showed that the implant is functional, and that electrodes with both protuberant and planar surfaces are capable of stimulating retinal tissue and evoking a response in the visual cortex. Recorded signals show that a smaller current is needed to generate a response when using protuberant electrodes. However, these results cannot be considered fully conclusive since the *in vivo* experiment was performed in only one animal and factors such as the position of the implant may play an important role.

Additional experiments must be conducted in the future to corroborate these preliminary results. Furthermore, in order to evaluate the 3D structures originally designed, a chronic implantation of the connected device must be achieved in order to ensure a reattachment of the retina to the device and that cells of the retina can occupy the 3D surface as in the biocompatibility results.

CONCLUSION

The work presented in this article intends to address one of the problems of the retinal electrical stimulation devices: the specificity of the stimulation. For this, we propose the use of a novel microelectrode geometry that includes three main elements: cavities, protuberant microelectrode structures and a ground plane around the microelectrode structures.

The finite element simulation of the proposed structures showed that a redistribution of the current density is obtained around the protuberances. This redistribution of the current density may increase the probability of activating the neurons in its vicinity.

Considering the results of the simulation and their interest for retinal stimulation, a microfabrication process was developed to create these microelectrode structures on flexible substrates to create implantable devices. These devices were implanted on animals to perform a histological study and assess the feasibility of using these structures in a real retina. Results showed that a minimum width of 80 μm must be used for the cavities and that the number of protuberances per cavity does not have an important influence on the rate of bipolar cells.

Finally, a preliminary *in vivo* electrical stimulation experiment was performed. Considering that this experiment was performed only in one animal and it is not statistically significant, the results showed that the device is able to stimulate the retina.

In order to determine the performance of the presented microelectrode structures, more *in vivo* stimulation experiments should be conducted in the close future.

ETHICS STATEMENT

All experiments were carried out in accordance with the European Community Council Directives (86/609/EEC) and with the ARVO (Association for Research in Vision and Ophthalmology) statement for the use of animals in ophthalmic and visual research.

AUTHOR CONTRIBUTIONS

PL developed the modeling part in collaboration with MG, and fabricated the devices in collaboration with LR. GL supervised and coordinated the first part of the research. MV, JD, and ED were in charge of the implantation procedures and image analysis. DN performed the *in vivo* stimulation experiments in collaboration with PL. SP supervised and coordinated the second part of the research.

FUNDING

This work was partly supported by the French Research Agency under grant number 15-CE19-006-04-NEUROMEDDLE, and by the laboratory ESYCOM through the doctoral funding of the Ph.D. student PL in doctoral school MSTIC of University Paris Est.

ACKNOWLEDGMENTS

The authors are willing to thank both the Institute of Vision and ESIEE Paris clean room facilities for their support during this work.

REFERENCES

Bendali, A., Rousseau, L., Lissorgues, G., Scorsone, E., Djilas, M., Dégardin, J., et al. (2015). Synthetic 3D diamond-based electrodes for flexible retinal neuroprostheses: model, production and in vivo biocompatibility. *Biomaterials* 67, 73–83. doi: 10.1016/j.biomaterials.2015.07.018

Butterwick, A., Huie, P., Jones, B. W., Marc, R. E., Marmor, M., and Palanker, D. (2009). Effect of shape and coating of a subretinal prosthesis on its integration with the retina. *Exp. Eye Res.* 88, 22–29. doi: 10.1016/j.exer.2008.09.018

Deuschl, G., Schade-Brittinger, C., Krack, P., Volkmann, J., Schäfer, H., Bötzel, K., et al. (2006). A randomized trial of deep-brain stimulation for Parkinson's disease. *N. Eng. J. Med.* 355, 896–908. doi: 10.1056/NEJMoa060281

Djilas, M., Oles, C., Lorach, H., Bendali, A., Degardin, J., Dubus, E., et al. (2011). Three-dimensional electrode arrays for retinal prostheses: modeling, geometry optimization and experimental validation. *J. Neural Eng.* 8:046020. doi: 10.1088/1741-2560/8/4/046020

Edwards, T. L., Cottriall, C. L., Xue, K., Simunovic, M. P., Ramsden, J. D., Zrenner, E., et al. (2018). Assessment of the electronic retinal implant alpha AMS in restoring vision to blind patients with end-stage retinitis pigmentosa. *Ophthalmology* 2018, 432–443. doi: 10.1016/j.ophtha.2017.09.019

Eshraghi, A. A., Nazarian, R., Telischi, F. F., Rajguru, S. M., Truy, E., and Gupta, C. (2012). The cochlear implant: historical aspects and future prospects. *Anat. Rec.* 295, 1967–1980. doi: 10.1002/ar.22580

Fendyur, A., and Spira, M. E. (2012). Toward on-chip, in-cell recordings from cultured cardiomyocytes by arrays of gold mushroom-shaped microelectrodes. *Front. Neuroeng.* 5:21. doi: 10.3389/fneng.2012.00021

Flores, T., Goetz, G., and Palanker, D. (2016). Optimization of return electrodes in neurostimulating arrays. *J. Neural Eng.* 13:036010. doi: 10.1088/1741-2560/13/3/036010

Hornig, R., Drapper, M., Le Joliff, E., Hill, R., Ishaque, K., Posch, C., et al. (2017). "Pixium vision: first clinical results and innovative developments," in *Artificial Vision*, ed. V. Gabel, (Cham: Springer).

Huys, R., Braeken, D., Van Meerbergen, B., Winters, K., Eberle, W., Loo, J., et al. (2008). Novel concepts for improved communication between nerve cells and silicon electronic devices. *Solid. State. Electron* 52, 533–539. doi: 10.1016/j.sse.2007.10.025

Joucla, S., Glière, A., and Yvert, B. (2014). Current approaches to model extracellular electrical neural microstimulation. *Front. Comput. Neurosci.* 8:13. doi: 10.3389/fncom.2014.00013

Joucla, S., and Yvert, B. (2009). improved focalization of electrical microstimulation using microelectrode arrays: a modeling study. *PLoS One* 4:e4828. doi: 10.1371/journal.pone.0004828

Kim, E. T., Seo, J. M., Woo, S. J., Zhou, J. A., Chung, H., and Kim, S. J. (2008). Fabrication of pillar shaped electrode arrays for artificial retinal implants. *Sensors* 8, 5845–5856. doi: 10.3390/s8095845

Koo, K., Chung, H., Yu, Y., Seo, J., Park, J., Ling, J.-M., et al. (2006). Fabrication of pyramid shaped three-dimensional 8 × 8 electrodes for artificial retina. *Sensors Actuators A Phys.* 130–131, 609–615. doi: 10.1016/j.sna.2005.11.070

Luo, Y. H. L., and da Cruz, L. (2016). The argus® II retinal prosthesis system. *Prog. Retin. Eye Res.* 50, 89–107. doi: 10.1016/j.preteyeres.2015.09.003

Machida, S., Kondo, M., Jamison, J. A., Khan, N. W., Kononen, L. T., Sugawara, T., et al. (2000). P23H rhodopsin transgenic rat: correlation of retinal function wih histopathology. *Invest. Ophthalmol. Vis. Sci.* 41, 3200–3209.

Mathieson, K., Loudin, J., Goetz, G., Huie, P., Wang, L., Kamins, T., et al. (2012). Photovoltaic retinal prosthesis with high pixel density. *Nature Photonics* 6, 391–397. doi: 10.1038/nphoton.2012.104

Roux, S., Matonti, F., Dupont, F., Hoffart, L., Takerkart, S., Picaud, S., et al. (2016). Probing the functional impact of sub-retinal prosthesis. *eLife* 5:e12687. doi: 10.7554/eLife.12687

Sasso, L., Vazquez, P., Vedarethinam, I., Castillo-León, J., Emnéus, J., and Svendsen, W. E. (2010). Conducting polymer 3D microelectrodes. *Sensors* 10, 10986–11000. doi: 10.3390/s101210986

Schwalb, J. M., and Hamani, C. (2008). The history and future of deep brain stimulation. *Neurotherapeutics* 5, 3–13. doi: 10.1016/j.nurt.2007.11.003

Wang, L., Mathieson, K., Kamins, T. I., Loudin, J. D., Galambos, L., Goetz, G., et al. (2012). Photovoltaic retinal prosthesis: implant fabrication and performance. *J. Neural Eng.* 9:046014. doi: 10.1088/1741-2560/9/4/046014

Conflict of Interest Statement: The authors declare that the research was conducted in the absence of any commercial or financial relationships that could be construed as a potential conflict of interest.

Copyright © 2019 Losada, Rousseau, Grzeskowiak, Valet, Nguyen, Dégardin, Dubus, Picaud and Lissorgues. This is an open-access article distributed under the terms of the Creative Commons Attribution License (CC BY). The use, distribution or reproduction in other forums is permitted, provided the original author(s) and the copyright owner(s) are credited and that the original publication in this journal is cited, in accordance with accepted academic practice. No use, distribution or reproduction is permitted which does not comply with these terms.

frontiers in Neuroscience

ORIGINAL RESEARCH
published: 10 January 2020
doi: 10.3389/fnins.2019.01367

Chronically Implanted Microelectrodes Cause *c-fos* Expression Along Their Trajectory

*Patrick Pflüger[1,2], Richard C. Pinnell[1,2], Nadja Martini[1,2] and Ulrich G. Hofmann[1,2]**

[1] Section for Neuroelectronic Systems, Clinic for Neurosurgery, Medical Center – University of Freiburg, University of Freiburg, Freiburg im Breisgau, Germany, [2] Faculty of Medicine, University of Freiburg, Freiburg im Breisgau, Germany

When designing electrodes and probes for brain–machine interfaces, one of the challenges faced involves minimizing the brain-tissue response, which would otherwise create an environment that is detrimental for the accurate functioning of such probes. Following the implantation process, the brain reacts with a sterile inflammation response and resulting astrocytic glial scar formation, potentially resulting in neuronal cell loss around the implantation site. Such alterations in the naïve brain tissue can hinder both the quality of neuronal recordings, and the efficacy of deep-brain stimulation. In this study, we chronically implanted a glass-supported polyimide microelectrode in the dorsolateral striatum of Sprague–Dawley rats. The effect of high-frequency stimulation (HFS) was investigated using *c-fos* immunoreactivity techniques. GFAP and ED1 immunohistochemistry were used to analyze the brain-tissue response. No changes in *c-fos* expression were found for either the acute or chronic stimulus groups; although a *c-fos* expression was found along the length of the implantation trajectory, following chronic implantation of our stiffened polyimide microelectrode. Furthermore, we also observed the formation of a glial scar around the microelectrode, with an accompanying low number of inflammation cells. Histological and statistical analysis of NeuN-positive cells did not demonstrate a pronounced "kill zone" with accompanying neuronal cell death around the implantation site, neither on the polymer side, nor on the glass side of the PI-glass probe.

Keywords: *c-fos*, NeuN, GFAP, inflammation, striatum, brain implant, ED1, polymer probe

OPEN ACCESS

Edited by:
Yen-Chung Chang,
National Tsing Hua University, Taiwan

Reviewed by:
Kevin J. Otto,
University of Florida, United States
Michael Thomas Lippert,
Leibniz Institute for Neurobiology (LG), Germany

***Correspondence:**
Ulrich G. Hofmann
ulrich.hofmann@uniklinik-freiburg.de;
ulrich.hofmann@coregen.uni-freiburg.de

Specialty section:
This article was submitted to Neural Technology, a section of the journal Frontiers in Neuroscience

Received: *15 July 2019*
Accepted: *03 December 2019*
Published: *10 January 2020*

Citation:
Pflüger P, Pinnell RC, Martini N and Hofmann UG (2020) Chronically Implanted Microelectrodes Cause c-fos Expression Along Their Trajectory. Front. Neurosci. 13:1367. doi: 10.3389/fnins.2019.01367

INTRODUCTION

When an electrode is implanted into the brain, numerous mechanisms are involved in the wound-healing process (Polikov et al., 2005; Biran et al., 2007). Microglia act as "*first responders*" and form the main cellular components in this acutely disturbed environment (Davalos et al., 2005). Their roles involve the removal of blood, debris, and pathogens from the implantation site through cytotoxic means (Polikov et al., 2005), and later during the chronic response, the formation of the glial scar (Röhl et al., 2007). Activated astrocytes are later involved with the reactive gliosis representing a frustrated phagocytosis to remove the foreign body (Reier, 1986; Turner et al., 1999; Polikov et al., 2005; Biran et al., 2007; Leach et al., 2010).

While the functionality of recording and stimulating electrodes are generally favorable in the short term, a degradation in the signal can occur during chronic timescales due to both the neuronal cell loss (the so-called "kill zone") and the encapsulation of the implant by a glial scar formation (Edell et al., 1992; Liu et al., 1999; Biran et al., 2005). This process may be prolonged, depending

on various factors including the initial tissue injury, and the long-term stability of the electrode (Campbell and Wu, 2018).

To alleviate the brain-tissue response, numerous approaches have been made, including alterations in the electrode design (Hofmann et al., 2006), material (Csicsvari et al., 2003; Kipke et al., 2003), coating (Ludwig et al., 2006; He et al., 2007), and implantation techniques (Kim et al., 2004; Wise et al., 2004). To this end, we have conducted a study aimed at examining both the effects of high-frequency stimulation (HFS) in the dorsolateral striatum using microelectrodes and the brain-tissue response in rodents for up to 10 weeks. The targeted brain area features somatotopically organized corticostriatal connections (Voorn et al., 2004) and has already served as model region to highlight the neurochemical effects of HFS (Hiller et al., 2007; Xie et al., 2014). Post-mortem immunohistochemistry was used to probe neuronal (using NeuN as a neuronal marker) activation by the expression of *c-fos* (Dragunow and Faull, 1989; Bullitt, 1990; Herrera and Robertson, 1996; Wilson et al., 2002; Shehab et al., 2014), astrocytic activity by glial fibrillary acidic protein (GFAP), and microglia activity by anti-CD68 (ED1), in order to determine the inflammatory reaction to the chronic implantation of the microelectrode (Turner et al., 1999; Grill et al., 2009; McConnell et al., 2009a; Beck et al., 2010).

MATERIALS AND METHODS

Ethics Statement

All procedures involving animals and their care were conducted in conformity with relevant institutional guidelines in compliance with the guidelines of the German Council on Animal Protection. Protocols were approved by the Animal Care Committee of the University of Freiburg under supervision of the Regierungspräsidium Freiburg (approval G13/97) in accordance with the guidelines of the European Union Directive 2010/63/UE.

Electrode Assembly

A 12-μm-thick, 380-μm-wide polyimide microelectrode (IMTEK; Freiburg University) as described in Böhm et al. (2019) was superglued (Renfert Dental, Hilzingen, Germany) to a 125-μm glass rod prior to implantation to provide accurate positioning and rigidity to the otherwise flexible probe (Richter et al., 2013). The probe's shaft contains 12 recording sites (15 μm × 15 μm) and four stimulation sites (50 μm × 50 μm). A large circular aperture, surrounded by a 300-nm-thick platinum ring forms the tip of the shaft.

Handling, Surgery, and Recovery

Prior to surgery, all rats underwent several days of handling in order to familiarize them with the experimenter and test apparatus (see **Figure 1** for an experimental timeline).

Female Sprague–Dawley rats (290–330 g; n = 15) were anesthetized with oxygen (0.15 L/min) and isoflurane (AbbVie, United States); the latter of which was initially set to 4% and gradually lowered to 1.5% after placing the animal into the stereotaxic frame (David Kopf, United States). Animal breathing, reflexes and level of anesthesia were monitored throughout the duration of the surgery.

During surgery, animals were implanted with the electrode-glass assemblies in the left dorsolateral striatum (AP: +0.4, ML: +3.6; from Bregma, DV: -3.7 from dura mater) (Paxinos et al., 1985). For this process, a hole was drilled at the electrode site, after which dura was resected using a fine needle. The electrode was subsequently lowered manually at a rate of approximately 200 μm/s, and the skull aperture around the implanted electrode was filled with bone wax. Once in place, the electrode was fixed to a nearby stainless-steel screw anchor (0–80 × 1/8; Plastics One) using a two-compound dental cement (Palapress; Heraeus Holding GmbH; Germany). An additional four screw anchors were used to attach a 3D-printed headstage socket around the electrode assembly (Pinnell et al., 2016) using five stainless steel screws (0–80 × 1/8; Plastics One). An upward-facing Omnetics connector was attached to the electrode assembly, and the headstage was filled with dental cement.

Following surgery, animals were pair-housed, utilizing a sealable headsocket (Pinnell et al., 2016), and were given 13–15 days recovery. Animals were allowed access to food and water *ad libitum*, and were housed under a 12-h light–dark cycle, at 22°C and 40% humidity.

Stimulation

Following recovery, all animals underwent two stimulation sessions each, which were spaced apart by 6–7 weeks. The first (chronic) stimulation session took place over six consecutive days, and the second (acute) stimulation session took place 3 h before the animals were euthanized (**Figure 1**); this approach was made for the purposes to obtain a stable *c-fos* expression Dragunow and Faull, 1989). Animals were divided into four groups, on the basis of having received stimulation or sham stimulation at either of these sessions (see **Table 1**). The stimulation parameters were set to the following: 130 Hz biphasic rectangular pulses, 60 μs pulse width/phase, 400 μA constant current intensity, and 5-min duration using a tethered stimulation system (AlphaLab SNR System, Alpha Omega GmbH, Germany). The geometrical area of stimulating iridium-oxide microelectrode contacts (Mottaghi et al., 2015) was 2500 μm^2, yielding a charge per stimulating phase of 24 nC/ph and a total stimulating charge of 960 $\mu C/cm^2$. Sham-stimulated animals had underwent the same procedure as their stimulated counterparts (attachment of tether, etc.), but with the absence of electrical stimulation.

Euthanasia and Histology

Following testing, chronically implanted rats were euthanized with an overdose of isoflurane and perfused transcardially with 4% formaldehyde solution (PFA in phosphate buffer). Their brains were removed, post-fixed in PFA for 7 days, and stored in 30% sucrose until cutting them in coronal sections (20 μm) along the probe's implantation trajectory with a cryostat. The sections were collected on glass and stored at −20°C until further processing.

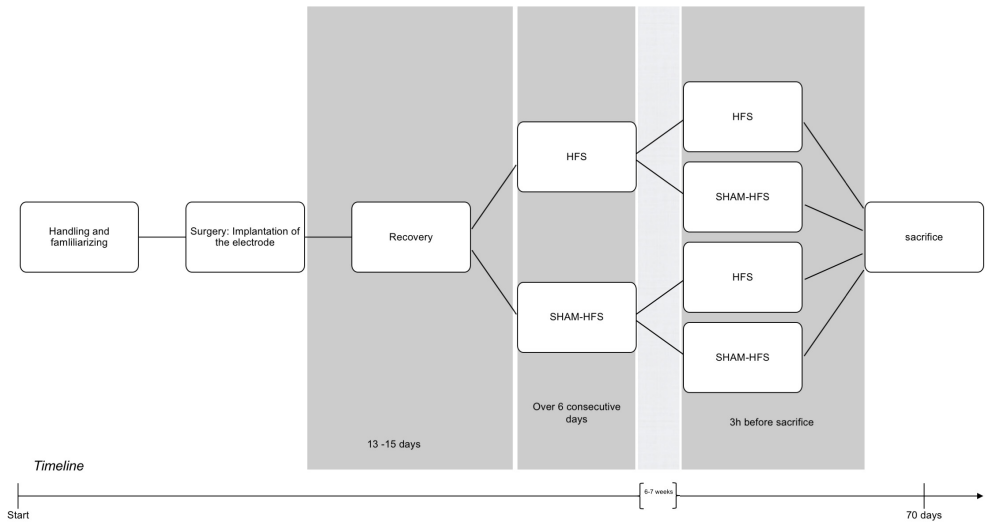

FIGURE 1 | Graphical depiction of the experimental period, including handling, surgery, recovery, and the chronic/acute stimulation sessions.

TABLE 1 | Organization of animal groups.

	Acute session	Chronic session
$n = 4$	STIM	STIM
$n = 3$	SHAM	STIM
$n = 5$	STIM	SHAM
$n = 3$	SHAM	SHAM

c-fos and NeuN Immunofluorescence Staining

The *c-fos* immunoreactivity was visualized using a double-label immunofluorescent staining for *c-fos* and neuronal nuclei (NeuN). Coronal brain sections were processed and incubated overnight with a polyclonal rabbit anti-*c-fos* antibody (sc-52, Santa Cruz Biotechnology, Santa Cruz, CA, United States, diluted 1:100) (Shehab et al., 2014). After rinsing in phosphate-buffered saline (PBS), sections were incubated with a fluorescent donkey anti-rabbit IgG conjugated with Alexa Fluor 647 (Abcam, Burlingame, CA, United States, diluted 1:1000). Sections were rinsed again in PBS, blocked with 10% normal donkey serum (NDS), and incubated for 3 h with a polyclonal mouse anti-NeuN antibody (Anti-NeuN, Millipore Cooperation, Burlington, MA, United States, diluted 1:100) (Mullen et al., 1992). After rinsing in PBS, sections were incubated with a fluorescent donkey anti-mouse IgG conjugated with Alexa Fluor 488 (Abcam, Burlingame, CA, United States, diluted 1:1000). Finally, sections were rinsed again in PBS, mounted with DAPI-Fluoromount G (Southern Biotechnology Associates, Inc., Birmingham, AL, United States) and stored at 4°C.

Counting of *c-fos*/NeuN-Positive Cells

For quantitative analysis, six sections from each animal were used for counting the *c-fos*/NeuN+ cells along the implantation trajectory. Images of stained sections were taken using a Zeiss microscope equipped with a ProgRes camera, along with ProgRes CapturePro 2.7 software (Carl Zeiss, Germany, Jenoptik, Germany). We created composites of the coronal sections using the ImageJ plugin "stitching" (Preibisch et al., 2009), while the brightness and contrast were adjusted as necessary. Using the ImageJ software "cellcounter," we first quantified the number of NeuN+ cells per box (**Figure 3**) (100 μm × 100 μm) and, in the next step from the colocalized NeuN und *c-fos* sections, the number of *c-fos*/NeuN+ cells (**Figure 8**). The mean cell counts of the ipsilateral (stimulated) sides of the coronal sections were compared between groups. For statistical analysis of the NeuN+ cells, we compared their means in the region from 0 to 100 μm to numbers in the background within one group. As such, we calculated the difference between those two means and used its 95% CI as significance marker. The same analysis was performed for double-stained *c-fos*/NeuN+ cells. Insignificant differences revealed themselves by a 95% CI value overlapping 0 ($p > 0.05$). A 95% CI not including 0 was taken as a sign of significant differences between close by and background tissue ($p < 0.05$).

For a secondary comparison between groups, we used the software JMP (JMP 13.1.0, SAS Institute Inc., SAS Campus Drive, Cary, NC, United States) and applied a one-way ANOVA and the Scheffé method for *post hoc* testing. We defined a level of $p < 0.05$ as statistical significance.

GFAP and ED1 Immunofluorescence Staining

To visualize the glial cell and microglial response, we also performed a double-label immunofluorescence staining for GFAP (**Figure 4**) and anti-CD68 (ED1, **Figure 7**). The coronal brain sections were processed and incubated for 3 h with polyclonal mouse anti-rat-CD68-antibody (AbD Serotec, United Kingdom, diluted 1:100). After rinsing in PBS, sections were incubated with a fluorescent donkey anti-mouse IgG conjugated with Alexa Fluor 488 (Abcam, Burlingame,

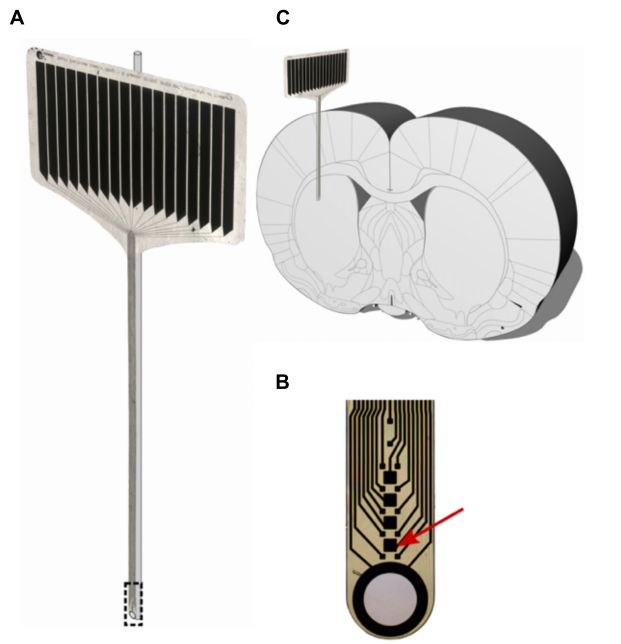

FIGURE 2 | (A) 16-contact polyimide micro probe (IMTEK; Freiburg University) with glass rod. **(B)** Magnified tip of the micro probe, with the red arrow pointing at one stimulating contact (50 μm × 50 μm). **(C)** Stiffened probes were implanted parallel to the rat brain's midline with the polymer facing laterally and the glass rod medially.

CA, United States, diluted 1:1000). For visualizing GFAP immunoreactivity, sections were rinsed again in PBS, blocked with 10% NDS, and incubated for 3 h with a polyclonal rabbit anti-GFAP antibody (GFAP, Millipore Cooperation, Burlington, MA, United States, diluted 1:1000). After rinsing in PBS, sections were incubated with a fluorescent donkey anti-rabbit IgG conjugated with Alexa Fluor 647 (Abcam, Burlingame, CA, United States, diluted 1:1000). Finally, sections were rinsed again in PBS, mounted with DAPI-Fluoromount G (Southern Biotechnology Associates, Inc., Birmingham, AL, United States) and stored at 4°C.

GFAP and ED1 Analysis

Four coronal sections along the trajectory of each animal were used to quantify the GFAP and ED1 immunoreactivity. Images of stained sections were taken using a Zeiss microscope equipped with a ProgRes camera with ProgRes CapturePro 2.7 software (Carl Zeiss, Germany, Jenoptik, Germany). Due to the low microglial (ED1) response to the chronic implantation of the microelectrode, we could not apply a numerical analysis, and a representative picture is shown as an example (**Figure 7**). For quantifying the GFAP-immunoreactivity, we used ImageJ "PlotProfile" and collected several profiles for each region (cortex, corpus callosum, and striatum), separated in both medial and lateral planes of one section. We calculated the means of one region and site, and subtracted the background immunofluorescence intensities from at least 600 μm away from the scar's rim (=background-corrected immunofluorescence intensity). The profiles of background-corrected immunofluorescence intensities of the different groups are shown in **Figures 5**, **6**. Furthermore, we calculated the full widths at half maximum (FWHM) to quantify the expansion of the glial scar. For statistical analysis, we compared the FWHM between groups. We applied one-way ANOVA and following significant ANOVA, the Scheffé method for *post hoc* testing using the software JMP (JMP 13.1.0, SAS Institute Inc., SAS Campus Drive, Cary, NC, United States). We defined a level of $p < 0.05$ as statistical significance.

RESULTS

Effects of the Chronic Implantation of a Microelectrode on NeuN Expression

Among all treatment groups, NeuN-positive cells could be found along the trajectory. They could be seen with a high density in the cortical areas as compared to the striatum (**Figure 3A**). Statistical analysis of NeuN+ cells in the region of 0–100 μm from the scar's rim, the tentative former location of the implant, in comparison to a region of 400–500 μm away, showed for group 1 a 95% CI of [0.37;1.16]; group 2, [0.14;0.93]; group 3, [1.27;2.56]; and group 4, [0.37;0.95]. Thus, in all four groups, the number of NeuN+ cells in the vicinity of the tentative microelectrode was not significantly reduced as compared to background ($p < 0.05$).

Effects of the Chronic Implantation of a Microelectrode on GFAP and ED1 Immunoreactivity

All groups had expressed GFAP alongside the former trajectory of the microelectrode, as illustrated in **Figure 4A**. Astrocytes agglomerated and built a dense glial layer proximal to the implant trajectory, while their typical star shape can be observed further away (**Figure 4B**). In **Figure 5A**, the background-corrected mean fluorescence intensities are illustrated as a function of distance to the implantation lesion. The highest GFAP immunoreactivity is found within a distance up to 100 μm of the scar's rim (peak background-corrected fluorescence intensity) and decreases with increasing distance from the trajectory. The calculation of the FWHM (full width at half maximum) indicated a mean scar thickness from all groups of 129 ± 10 μm, whereas group 1 had the thickest (150 μm) and group 3 the thinnest (113 μm) FWHM (**Figure 5B**). Statistical analysis of the FWHM showed no significant difference between groups ($p = 0.8826$). Thus, the chronic implantation of a stiffened polyimide microelectrode leads to a reactive astrocytosis, with the formation of a glial scar with an extent of about 130 μm.

Please note in **Figure 4A** a fine example of a disruption of a glial sheath in the center of the picture – presumably caused by removing the implant from the wound prior to slicing.

As the polymer microelectrode was glued single sided and flat to the glass fiber support, we had essentially two different surfaces exposed back to back to the brain's environment: polymer on the one side and silicon oxide (glass) on the other. However, when analyzing GFAP immunoreactivity with

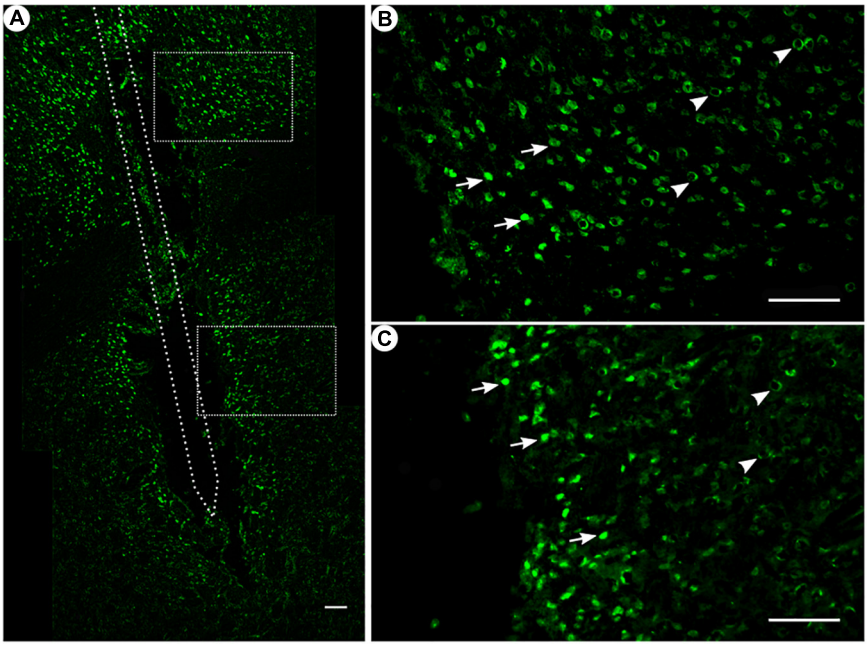

FIGURE 3 | NeuN immunoreactivity. **(A)** Overview of an exemplary corticostriatal area as composite of a series of coronal sections. **(B,C)** Corresponding magnified pictures from panel **(A)**, with white arrows pointing at high NeuN immunoreactivity, and white arrowheads pointing at low NeuN immunoreactivity. Scale bar = 100 μm.

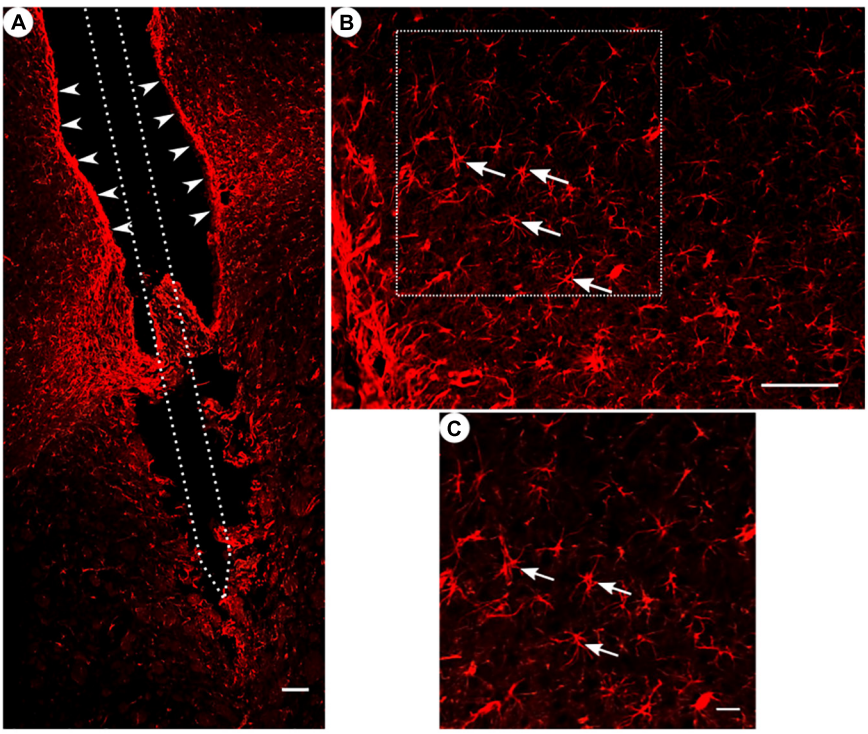

FIGURE 4 | GFAP immunoreactivity. **(A)** Overview of a corticostriatal area as composite of a series of coronal sections, with arrowheads pointing at a dense glial layer at the brain tissue/microelectrode interface. Scale bar = 100 μm. **(B)** Corresponding magnified picture from panel **(A)**, white arrows pointing at GFAP+ star-shaped cells (astrocytes). Scale bar = 100 μm. **(C)** Corresponding magnified picture from panel **(B)**, with white arrows pointing at GFAP+, star-shaped cells (astrocytes). Scale bar = 25 μm.

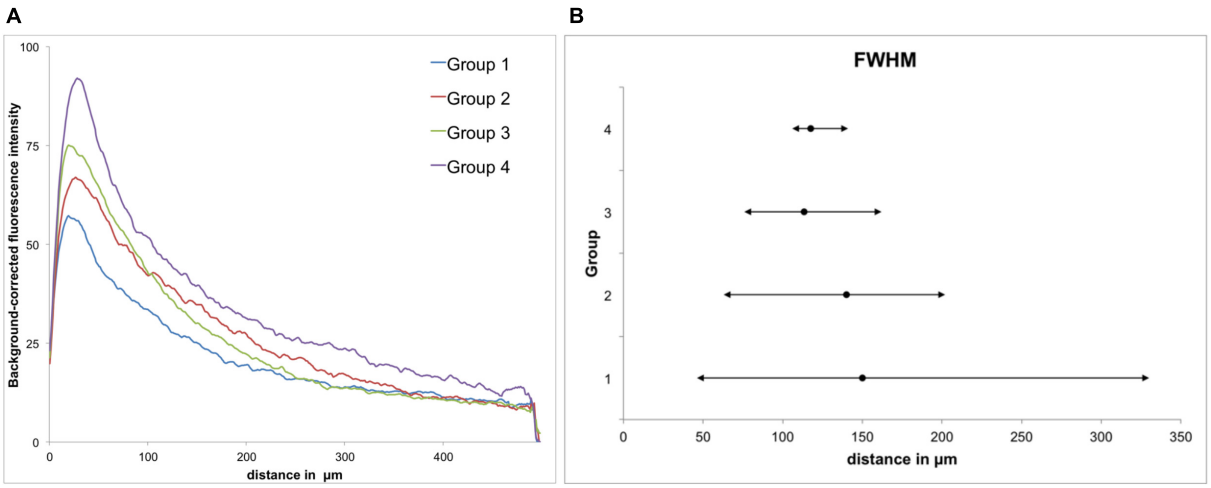

FIGURE 5 | GFAP immunoreactivity. **(A)** Background-corrected mean GFAP fluorescence intensities illustrated as a function of distance from the scar's rim for each group. **(B)** Full widths at half maximum (FWHM) of groups 1–4. Mean + maximum/minimum.

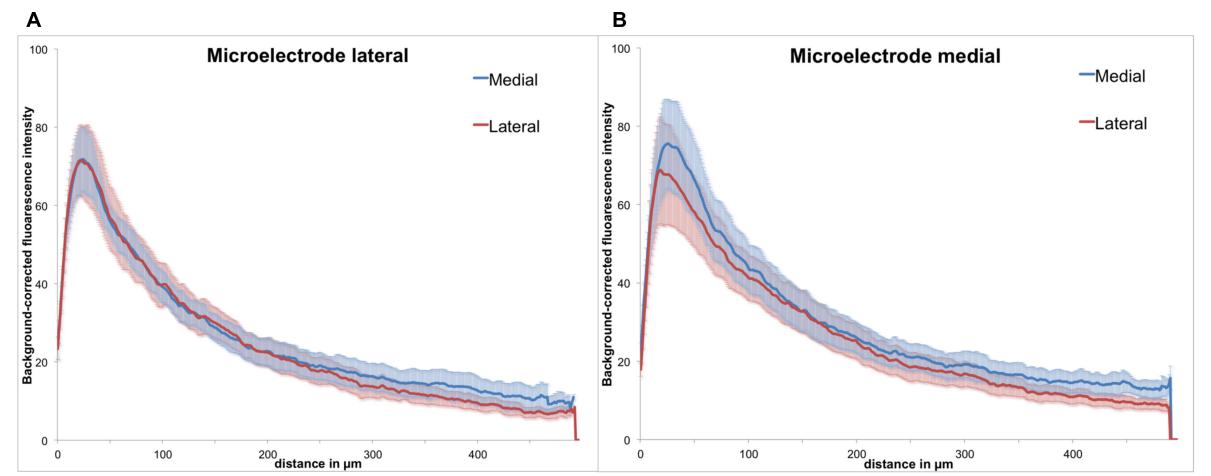

FIGURE 6 | Background-corrected GFAP immunoreactivity relative to the microelectrode assembly. **(A)** Lateral from assembly. **(B)** Medial from assembly, Means ± SE.

regard to the implant's orientation, we found no discernible difference between both materials. **Figure 6** illustrates the background-corrected fluorescence intensities separated in the medial and lateral directions, for both electrode materials [lateral = polymer (A), medial = glass (B)]. The results demonstrate no difference between the lateral and medial GFAP expression, with astrocytic reaction seemingly independent from the utilized material.

While ED1 expression was generally present (**Figure 7**), ED1-positive cells were found to form agglomerates on the scar's edges, and could not be readily distinguished from one another.

Effects of the Chronic Implantation of a Microelectrode on *c-fos* Expression

All animal groups, independent of their stimulation paradigm, had displayed colocalized *c-fos*/NeuN+ cells along the microelectrode trajectory. **Figure 8** displays the colocalization of the *c-fos*-labeled cells to NeuN-labeled neurons. Statistical analysis of *c-fos*/NeuN+ cells in the region of 0–100 µm from the scar's rim, in comparison to the region of 400–500 µm, showed for group 1 a 95% CI of [12.43;31.46]; group 2, [38.24;66.21]; group 3, [45.27;77.61]; and group 4, [27.63;66.93]. Thus, in all four groups, the number of *c-fos*/NeuN+ cells in the vicinity of the implant's scar was significantly higher than that of the background ($p < 0.05$). This result corroborates that a chronic implantation of a stiff microelectrode for 10 weeks can cause *c-fos* expression in neurons along the implant trajectory and thus presumably indicates neuronal activation. No *c-fos*/NeuN+ cells were found contralaterally, as there was no implant (histology not shown). The relative frequency distribution of the *c-fos*/NeuN+ cells along a full trajectory is displayed by heatmaps in **Figure 9**.

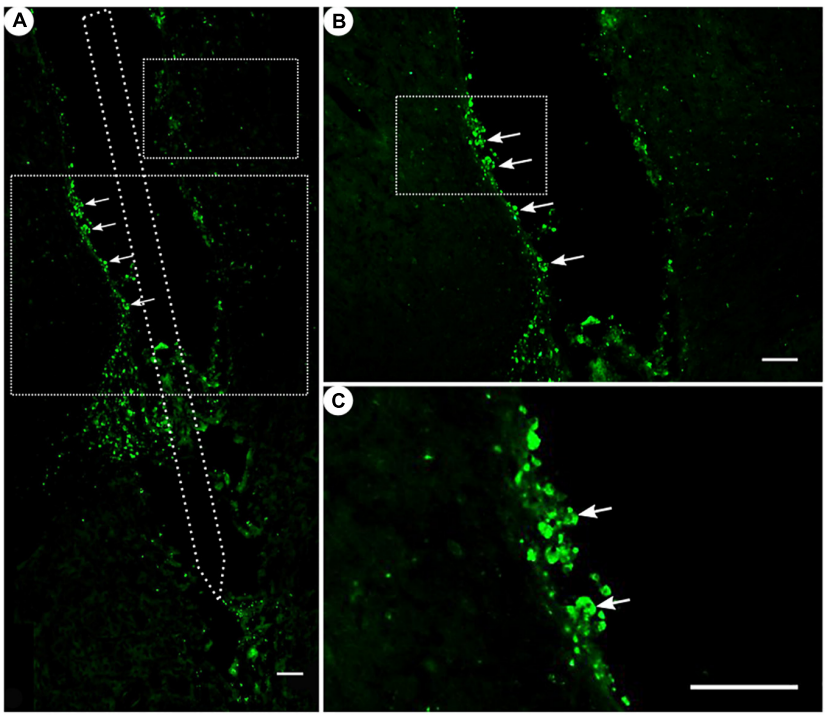

FIGURE 7 | ED1 immunoreactivity. **(A)** Overview of a corticostriatal area as composite of a series of coronal sections, with arrows pointing at ED1+ cells at the tentative brain tissue/microelectrode interface. Scale bar = 100 μm. **(B)** Corresponding magnified picture from panel **(A)**, with white arrows pointing at ED1+ cells (microglia). Scale bar = 100 μm. **(C)** Corresponding magnified picture from panel **(B)**, with white arrows pointing at agglomerated ED1+ cells in the lumen. Scale bar = 25 μm.

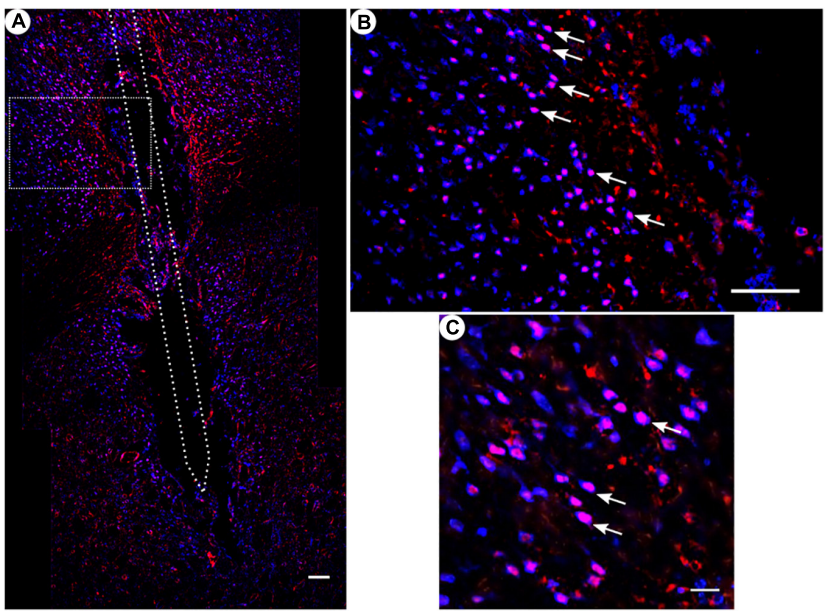

FIGURE 8 | *c-fos* and NeuN immunoreactivity: **(A)** Overview of corticostriatal area as composite of a series of coronal sections, The merged image shows the colocalization of *c-fos*-labeled nuclei (red) with respect to NeuN (blue). This indicates that the induced *c-fos* activity is situated in neurons [white arrows in panels **(B,C)**]. **(B)** Corresponding magnified picture from panel **(A)**. Scale bar = 100 μm. **(C)** Further magnification from panel **(A)**. Scale bar = 25 μm.

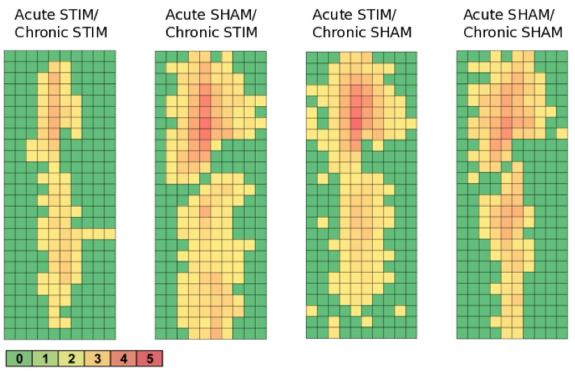

FIGURE 9 | Heatmaps of *c-fos*/NeuN+ cells along the implant trajectory relative to the scar's rim. Group 1 (Acute STIM/Chronic STIM) $n = 4$, Group 2 (Acute SHAM/Chronic STIM). $n = 3$, Group 3 (Acute STIM/Chronic SHAM) $n = 5$, Group 4 (Acute SHAM/Chronic SHAM) $n = 3$. Lookup table showing number of *c-fos*/NeuN+ cells per box (100 μm × 100 μm). See **Supplementary Figure S1** for illustration.

Effects of Chronic High-Frequency Stimulation of the Dorsolateral Striatum on *c-fos* Expression

Chronic HFS of the dorsolateral striatum did not change the neuronal *c-fos* expression in close vicinity to the tentative microelectrode trajectory. Statistical analysis of neurons expressing *c-fos* showed no significantly reduced or higher number of *c-fos*/NeuN+ cells in the ipsilateral striatal ($p = 0.99$) and cortical ($p = 0.12$) areas. Group 1 (Acute STIM/Chronic STIM), however, did exhibit the lowest number of *c-fos*/NeuN+ cells in comparison to the other three groups (**Figure 10**).

DISCUSSION

The chronic implantation of a stiffened polyimide microelectrode assembly leads to the formation of a glial scar and an accumulation of microglia cells at the trajectory–brain interface.

In our study, we used polyimide microelectrodes glued to a 125-μm glass rod in order to achieve a precise targeting of electrical microstimulation in the dorsolateral striatum (**Figure 2**). After a mean implantation time of 70 days, we detected an accumulation of astrocytes (high GFAP expression) alongside the implant trajectory. The highest GFAP intensities were found within 100 μm from the scar's rim, with a mean glial width of 130 μm, whereas the density of GFAP+ cells decreased as the distance to the implant lesion increased (**Figure 5**). The GFAP expression had provided no indication for a material-dependent astrocytic reaction, as the fluorescence distribution was similar in both medial and lateral directions, respectively, to PI or glass (**Figure 6**). Astrocytes represent 30–65% of the glial cell population in the CNS and are essential for maintaining a proper neuronal environment (Nathaniel and Nathaniel, 1981; Kimelberg et al., 1993). Following chronic implantation of an electrode, astrocytes are thought to build an encapsulation (glial scar) (Turner et al., 1999). Our findings are in accordance with reports suggesting a formation of an astrocytic boundary around the lesion, building up a tightly connected network of hyperfilamentous astrocytes, surrounded by an extracellular matrix (Bush et al., 1999; Fawcett and Asher, 1999; Faulkner et al., 2004; Seifert et al., 2006).

A significant neuronal cell loss in the vicinity of the scar's rim was not observed. However, as can be seen in **Figure 4A**, the removal of the implant prior to histological preparation may have a strong detrimental impact on the integrity of the true implant/brain boundary. In fact, we recognize a strong and almost pristine appearing glial sheath in the upper, cortical part of the slice. Whereas the subthalamic region doesn't show a closed glial sheath and instead appears ruptured. Particularly revealing seems the transition region between both, as here the structure resembles the cross-section of an inside-out turned glove's finger, presumed to be a consequence from probe extraction.

The ED1 immunoreactivity as a result of activated monocytes and macrophages had shown a hard-to-quantify signal. Monocytes and macrophages are usually one of the first

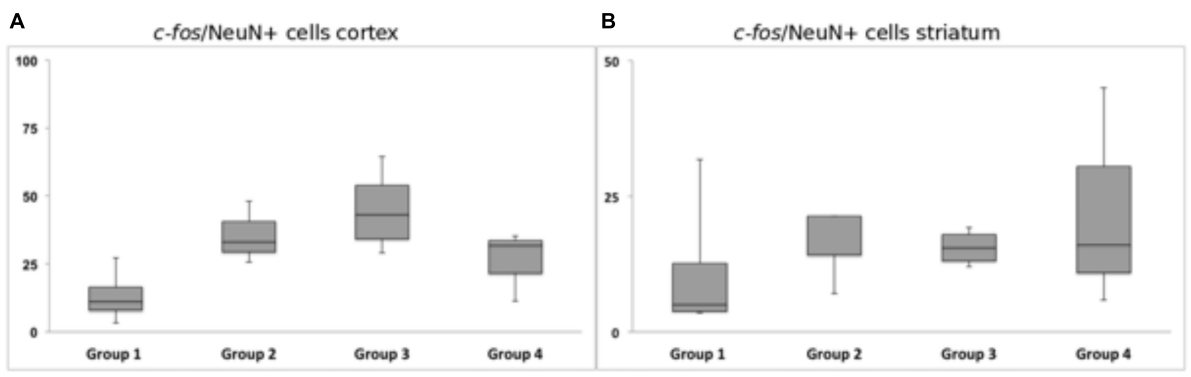

FIGURE 10 | Response of *c-fos* immunoreactivity to chronic high-frequency stimulation of the dorsolateral striatum. **(A)** *c-fos*/NeuN+ cells in cortical area in a distance of 100 μm from the scar's rim. **(B)** *c-fos*/NeuN+ cells in the striatal area in a distance of 100 μm from the scar's rim. Whiskers showing maximum and minimum.

responders after an injury or lesion of the CNS and react to it by their activation (Kreutzberg, 1996). Activated monocytes begin to proliferate and change their morphology to a more "amoeboid" shape (Polikov et al., 2005). Proliferation was not observed with the residuals of the ED1+ cells (**Figure 7**), which were located at the tentative electrode–brain interface, the scar's rim. Over time, the microglia's activity and thus the acute foreign body reaction may have faded as is expected by a mean implantation time of 10 weeks (Potter et al., 2012).

The vitality of the surrounding neurons is essential for a stable signal transmission between electrode and CNS (Biran et al., 2005). The foreign body reaction, following an electrode implantation, might very well lead to neuronal cell loss and the resulting formation of a "kill zone" (Edell et al., 1992; McConnell et al., 2009a). The extent of this "kill zone" can reach up to 100 μm (Polikov et al., 2005). In our study, we could not detect a significant kill zone or neuronal cell loss in the vicinity of the trajectory's rim. This could be either due to a weak foreign body reaction with a low ED1 expression (McConnell et al., 2009b) or simply due to a negative artifact by the destruction of the pristine probe/brain interface when removing the probe.

While *c-fos* immunochemistry is widely used as a marker for neuronal activation (Dragunow and Faull, 1989; Bullitt, 1990; Herrera and Robertson, 1996; Wilson et al., 2002), *c-fos* expression has to be considered quite unspecific regarding its mechanism of activation. *c-fos* is reported to be induced by chemical, physical, or electrical stress, and has even been found expressed in various brain regions (Greenberg and Ziff, 1984; Morgan and Curran, 1989; Hughes et al., 1992; Herrera and Robertson, 1996; Arcot-Desai et al., 2014). However, in our study, the highest density of activated neurons was located alongside the trajectory and declined with increasing distance from the implantation track (**Figures 8**, **9**). This observation indicates that the *c-fos* expression is most likely caused by the implanted foreign body and is further supported by the low basal *c-fos* expression in the contralateral brain region. Furthermore, statistical analysis had verified the elevated number of *c-fos*/NeuN-positive cells in the vicinity of the microelectrode track, demonstrating that the implanted microelectrode resulted in an activation of the surrounding neurons. One possible explanation of this effect could be that the CNS injury caused by the implantation leads to a release of cytokines and growth factors, resulting in a modified cellular state of action (Polikov et al., 2005; He et al., 2007; Pineau and Lacroix, 2007). The cells involved in the foreign body reaction, particularly microglia and astrocytes, change their state of action in response to the trauma, and subsequently release cytokines, growth factors, enzymes, and other neuroactive substances (Eddleston and Mucke, 1993; Fawcett and Asher, 1999; Loane and Byrnes, 2010; Benarroch, 2013). Furthermore, previous evidence has demonstrated that a cortical brain injury can cause an elevated *c-fos* expression in the surrounding neurons, as a response to release of excitatory amino acids (Faden et al., 1989; Herrera and Robertson, 1990; Sharp et al., 1990). Recent studies utilizing Fast Cyclic Voltammetry (FCV) during human DBS implantations have demonstrated this "microthalamotomy" dubbed release of adenosine (Bennet et al., 2016).

Long-term HFS of the dorsolateral striatum seemed unable to significantly change the number of *c-fos*/NeuN-positive cells in the stimulated area along the lower end of the trajectory. This is surprising, as several studies report on positive effects of neuronal activation upon electrical stimulation (Krukoff et al., 1992; McKitrick et al., 1992; Arcot-Desai et al., 2014; Neyazi et al., 2016). However, differing to our HFS stimulation paradigm, the mentioned studies stimulated with low frequencies (20–40 Hz, LFS) in other regions of the brain and may thus have used a different mode of operation. Given that our chosen stimulation parameters (60 μs pulse width) coincide with known chronaxy values for neuronal fibers, but not somata, we would rather expect an axonal stimulation than a somal one (Holsheimer et al., 2000a,b; McIntyre et al., 2004; Löffler and Lujàn, 2016). As such, one would not expect a local *c-fos* expression due to electrical HFS, but rather a change in activation in fiber-connected cells. Considering the broad somatotopically organized cortico-striatal connections (Voorn et al., 2004), we looked at the *c-fos* expression of cortical neurons as well. Group 1 (Acute STIM/Chronic STIM) had shown the lowest number of *c-fos*/NeuN-positive cells, when compared to the other groups. HFS of the dorsolateral striatum might result in a suppression of the activity of cortical neurons, by means of an antidromic axonal stimulation that would affect the facilitatory GABAergic autoreceptors (Li et al., 2007; Feuerstein et al., 2011). This might help to explain an apparent reduction in *c-fos*, given that GABA acts as an inhibitory transmitter and is insensitive to *c-fos* expression (Faden et al., 1989; Hughes and Dragunow, 1995).

To conclude, our study has shown evidence that sole chronic implantation of a stiffened polyimide microelectrode (groups 1–4), and even an absence of electrical stimulation (group 4), leads to a *c-fos* expression along its trajectory.

DATA AVAILABILITY STATEMENT

The datasets generated for this study are available on request to the corresponding author.

ETHICS STATEMENT

The animal study was reviewed and approved by the Animal Care Committee of the University of Freiburg under supervision of the Regierungspräsidium Freiburg (approval G13/97).

AUTHOR CONTRIBUTIONS

PP: experiments, formal analysis, visualization, methodology, and writing. RP: conceptualization, experiments, supervision,

and writing. NM: methodology. UH: conceptualization, resources, supervision, funding acquisition, validation, and writing – review and editing.

ACKNOWLEDGMENTS

Part of this study was supported by a FRIAS/USIAS stipend to RP and the Cluster of Excellence Brainlinks-Braintools (EXC 1086).

SUPPLEMENTARY MATERIAL

The Supplementary Material for this article can be found online at: https://www.frontiersin.org/articles/10.3389/fnins.2019.01367/full#supplementary-material

FIGURE S1 | Artistic sketch demonstrating one exemplary composite *c-fos*/NeuN+ IHC with an approximated 100ţm counting grid on top. Count results from these grids are shown in **Figure 9** heatmaps. The sketch includes the targeted coordinate in the striatum (red cross) and the corresponding excerpt from the rat atlas (Paxinos and Watson, 2007).

REFERENCES

Arcot-Desai, S., Gutekunst, C.-A., Potter, S. M., and Gross, R. E. (2014). Deep brain stimulation macroelectrodes compared to multiple microelectrodes in rat hippocampus. *Front. Neuroengin.* 7:16. doi: 10.3389/fneng.2014.00016

Beck, K. D., Nguyen, H. X., Galvan, M. D., Salazar, D. L., Woodruff, T. M., and Anderson, A. J. (2010). Quantitative analysis of cellular inflammation after traumatic spinal cord injury: evidence for a multiphasic inflammatory response in the acute to chronic environment. *Brain* 133(Pt 2), 433–447. doi: 10.1093/brain/awp322

Benarroch, E. E. (2013). Microglia Multiple roles in surveillance, circuit shaping, and response to injury. *Neurology* 81, 1079–1088. doi: 10.1212/WNL.0b013e3182a4a577

Bennet, K. E., Tomshine, J. R., Min, H.-K., Manciu, F. S., Marsh, M. P., Paek, S. B., et al. (2016). A diamond-based electrode for detection of neurochemicals in the human brain. *Front. Hum. Neurosci.* 10:102. doi: 10.3389/fnhum.2016.00102

Biran, R., Martin, D. C., and Tresco, P. A. (2005). Neuronal cell loss accompanies the brain tissue response to chronically implanted silicon microelectrode arrays. *Exp. Neurol* 195, 115–126. doi: 10.1016/j.expneurol.2005.04.020

Biran, R., Martin, D. C., and Tresco, P. A. (2007). The brain tissue response to implanted silicon microelectrode arrays is increased when the device is tethered to the skull. *J. Biomed. Mater. Res.* 82, 169–178. doi: 10.1002/jbm.a.31138

Böhm, T., Joseph, K., Kirsch, M., Moroni, R., Hilger, A., Manke, I., et al. (2019). Quantitative synchrotron X-ray tomography of the material-tissue interface in rat cortex implanted with neural probes. *Sci. Rep.* 9:7646. doi: 10.1038/s41598-019-42544-9

Bullitt, E. (1990). Expression of c-fos-like protein as a marker for neuronal activity following noxious stimulation in the rat. *J. Comp. Neurol.* 296, 517–530. doi: 10.1002/cne.902960402

Bush, T. G., Puvanachandra, N., Horner, C. H., Polito, A., Ostenfeld, T., Svendsen, C. N., et al. (1999). Leukocyte infiltration, neuronal degeneration, and neurite outgrowth after ablation of scar-forming, reactive astrocytes in adult transgenic mice. *Neuron* 23, 297–308. doi: 10.1016/s0896-6273(00)80781-3

Campbell, A., and Wu, C. (2018). Chronically implanted intracranial electrodes: tissue reaction and electrical changes. *Micromachines* 9:E430. doi: 10.3390/mi9090430

Csicsvari, J., Henze, D. A., Jamieson, B., Harris, K. D., Sirota, A., Barthó, P., et al. (2003). Massively parallel recording of unit and local field potentials with silicon-based electrodes. *J. Neurophysiol.* 90, 1314–1323. doi: 10.1152/jn.00116.2003

Davalos, D., Grutzendler, J., Yang, G., Kim, J. V., Zuo, Y., Jung, S., et al. (2005). ATP mediates rapid microglial response to local brain injury in vivo. *Nat. Neurosci.* 8, 752–758. doi: 10.1038/nn1472

Dragunow, M., and Faull, R. (1989). The use of c-fos as a metabolic marker in neuronal pathway. *J. Neurosci.* 29, 261–265. doi: 10.1016/0165-0270(89)90150-7

Eddleston, M., and Mucke, L. (1993). Molecular profile of reactive astrocytes—implications for their role in neurologic disease. *Neuroscience* 54, 15–36. doi: 10.1016/0306-4522(93)90380-x

Edell, D. J., Toi, V., McNeil, V. M., and Clark, L. (1992). Factors influencing the biocompatibility of insertable silicon microshafts in cerebral cortex. *IEEE Trans. Biomed. Eng.* 39, 635–643. doi: 10.1109/10.141202

Faden, A. L., Demediuk, P., Panter, S. S., and Vink, R. (1989). The role of excitatory amino acids and NMDA receptors in traumatic brain injury. *Science* 244, 798–800. doi: 10.1126/science.2567056

Faulkner, J. R., Herrmann, J. E., Woo, M. J., Tansey, K. E., Doan, N. B., and Sofroniew, M. V. (2004). Reactive astrocytes protect tissue and preserve function after spinal cord injury. *J. Neurosci.* 24, 2143–2155. doi: 10.1523/jneurosci.3547-03.2004

Fawcett, J. W., and Asher, R. A. (1999). The glial scar and central nervous system repair. *Brain Res. Bull.* 49, 377–391. doi: 10.1016/s0361-9230(99)00072-6

Feuerstein, T. J., Kammerer, M., Lucking, C. H., and Moser, A. (2011). Selective GABA release as a mechanistic basis of high-frequency stimulation used for the treatment of neuropsychiatric diseases. *Naunyn Schmiedebergs Arch. Pharmacol.* 384, 1–20. doi: 10.1007/s00210-011-0644-8

Greenberg, M. E., and Ziff, E. B. (1984). Stimulation of 3T3 cells induces transcription of the c-fos proto-oncogene. *Nature* 311, 433–438. doi: 10.1038/311433a0

Grill, W. M., Norman, S. E., and Bellamkonda, R. V. (2009). Implanted neural interfaces: biochallenges and engineered solutions. *Annu. Rev. Biomed. Eng.* 11, 1–24. doi: 10.1146/annurev-bioeng-061008-124927

He, W., McConnell, G. C., Schneider, T. M., and Bellamkonda, R. V. (2007). A novel anti-inflammatory surface for neural electrodes. *Adv. Mater.* 19, 3529–3533. doi: 10.1002/adma.200700943

Herrera, D., and Robertson, H. (1990). Application of potassium chloride to the brain surface induces the c-fos proto-oncogene: reversal by MK-801. *Brain Res.* 510, 166–170. doi: 10.1016/0006-8993(90)90747-y

Herrera, D. G., and Robertson, H. A. (1996). Activation of c-fos in the brain. *Prog. Neurobiol.* 50, 83–107.

Hiller, A., Loeffler, S., Haupt, C., Litza, M., Hofmann, U., and Moser, A. (2007). Electrical high frequency stimulation of the caudate nucleus induces local GABA outflow in freely moving rats. *J. Neurosci. Methods* 159, 286–290. doi: 10.1016/j.jneumeth.2006.07.023

Hofmann, U. G., Folkers, A., Mosch, F., Malina, T., Menne, K. M., Biella, G., et al. (2006). A novel high channel-count system for acute multisite neuronal recordings. *IEEE Trans. Biomed. Eng.* 53, 1672–1677. doi: 10.1109/tbme.2006.877807

Holsheimer, J., Demeulemeester, H., Nuttin, B., and De Sutter, P. (2000a). Identification of the target neuronal elements in electrical deep brain stimulation. *Euro. J. Neurosci.* 12, 4573–4577. doi: 10.1111/j.1460-9568.2000.01306.x

Holsheimer, J., Dijkstra, E. A., Demeulemeester, H., and Nuttin, B. (2000b). Chronaxie calculated from current–duration and voltage–duration data. *J. Neurophysiol.* 97, 45–50. doi: 10.1016/s0165-0270(00)00163-1

Hughes, P., and Dragunow, M. (1995). Induction of immediate-early genes and the control of neurotransmitter-regulated gene expression within the nervous system. *Pharmacol. Rev.* 47, 133–178.

Hughes, P., Lawlor, P., and Dragunow, M. (1992). Basal expression of Fos. Fos-related, Jun, and Krox 24 proteins in rat hippocampus. *Mol. Brain Res.* 13, 355–357. doi: 10.1016/0169-328x(92)90219-2

Kim, Y.-T., Hitchcock, R. W., Bridge, M. J., and Tresco, P. A. (2004). Chronic response of adult rat brain tissue to implants anchored to the skull. *Biomaterials* 25, 2229–2237. doi: 10.1016/j.biomaterials.2003.09.010

Kimelberg, H., Jalonen, T., and Walz, W. (1993). "Regulation of the brain microenvironment: transmitters and ions," in *Astrocytes: Pharmacology and*

Function, ed. S. Murphy, (Cambridge, MA: Academic Press), 193–228. doi: 10.1016/b978-0-12-511370-0.50013-8

Kipke, D. R., Vetter, R. J., Williams, J. C., and Hetke, J. F. (2003). Silicon-substrate intracortical microelectrode arrays for long-term recording of neuronal spike activity in cerebral cortex. *IEEE Trans. Neural Syst. Rehabil. Eng.* 11, 151–155. doi: 10.1109/tnsre.2003.814443

Kreutzberg, G. W. (1996). Microglia: a sensor for pathological events in the CNS. *Trends Neurosci.* 19, 312–318. doi: 10.1016/0166-2236(96)10049-7

Krukoff, T. L., Morton, T. L., Harris, K. H., and Jhamandas, J. H. (1992). Expression of c-fos protein in rat brain elicited by electrical stimulation of the pontine parabrachial nucleus. *J. Neurosci.* 12, 3582–3590. doi: 10.1523/jneurosci.12-09-03582.1992

Leach, J., Achyuta, A. K. H., and Murthy, S. K. (2010). Bridging the divide between neuroprosthetic design, tissue engineering and neurobiology. *Front. Neuroeng.* 2:18. doi: 10.3389/neuro.16.018.2009

Li, S., Arbuthnott, G. W., Jutras, M. J., Goldberg, J. A., and Jaeger, D. (2007). Resonant antidromic cortical circuit activation as a consequence of high-frequency subthalamic deep-brain stimulation. *J. Neurophysiol.* 98, 3525. doi: 10.1152/jn.00808.2007

Liu, X., McCreery, D. B., Carter, R. R., Bullara, L. A., Yuen, T. G., and Agnew, W. F. (1999). Stability of the interface between neural tissue and chronically implanted intracortical microelectrodes. *IEEE Trans. Rehabil. Eng.* 7, 315–326. doi: 10.1109/86.788468

Loane, D. J., and Byrnes, K. R. (2010). Role of microglia in neurotrauma. *Neurotherapeutics* 7, 366–377. doi: 10.1016/j.nurt.2010.07.002

Löffler, S., and Lujàn, J. L. (2016). "Biophysical fundamentals of neural excitations," in *Deep Brain Stimulation - Indications and Applications*, Vol. 1, eds K. H. Lee, P. S. Duffy, and A. J. Bieber, (Singapore: Pan Stanford Publishing.), 486.

Ludwig, K. A., Uram, J. D., Yang, J., Martin, D. C., and Kipke, D. R. (2006). Chronic neural recordings using silicon microelectrode arrays electrochemically deposited with a poly (3, 4-ethylenedioxythiophene)(PEDOT) film. *J. Neural Eng.* 3, 59–70. doi: 10.1088/1741-2560/3/1/007

McConnell, G. C., Butera, R. J., and Bellamkonda, R. V. (2009a). Bioimpedance modeling to monitor astrocytic response to chronically implanted electrodes. *J. Neural Eng.* 6:055005. doi: 10.1088/1741-2560/6/5/055005

McConnell, G. C., Rees, H. D., Levey, A. I., Gutekunst, C.-A., Gross, R. E., and Bellamkonda, R. V. (2009b). Implanted neural electrodes cause chronic, local inflammation that is correlated with local neurodegeneration. *J. Neural Eng.* 6:056003. doi: 10.1088/1741-2560/6/5/056003

McIntyre, C. C., Savasta, M., Walter, B. L., and Vitek, J. L. (2004). How does deep brain stimulation work? Present understanding and future questions. *J. Clin. Neurophysiol.* 21, 40–50. doi: 10.1097/00004691-200401000-00006

McKitrick, D. J., Krukoff, T. L., and Calaresu, F. R. (1992). Expression of c-fos protein in rat brain after electrical stimulation of the aortic depressor nerv. *Brain Res.* 599, 215–222. doi: 10.1016/0006-8993(92)90394-o

Morgan, J. I., and Curran, T. (1989). Stimulus-transcription coupling in neurons: role of cellular immediate-early genes. *Trends Neurosci.* 12, 459–462. doi: 10.1016/0166-2236(89)90096-9

Mottaghi, S., Pinnell, R. C., and Hofmann, U. G. (2015). "A 16-bit high-voltage digital charge-control electrical stimulator," in *Proceedings of the IFMBE*, ed. D. A. Jaffray (Toronto: IFMBE: World Congress on Medical Physics and Biomedical Engineering), 1208–1212.

Mullen, R. J., Buck, C. R., and Smith, A. M. (1992). NeuN, a neuronal specific nuclear protein in vertebrates. *Development* 116, 201–211.

Nathaniel, E. J., and Nathaniel, D. R. (1981). The reactive astrocyte. *Adv. Cell. Neurobiol.* 2, 249–301. doi: 10.1016/b978-0-12-008302-2.50012-2

Neyazi, B., Schwabe, K., Alam, M., Krauss, J. K., and Nakamura, M. (2016). Neuronal expression of c-Fos after epicortical and intracortical electric stimulation of the primary visual cortex. *J. Chem. Neuroanat.* 77, 121–128. doi: 10.1016/j.jchemneu.2016.06.004

Paxinos, G., and Watson, C. (2007). *The Rat Brain in Stereotaxic Coordinates: 6th Edn Hard Cover Edition*. Amsterdam: Elsevier Science & Technology.

Paxinos, G., Watson, C., Pennisi, M., and Topple, A. (1985). Bregma, lambda and the interaural midpoint in stereotaxic surgery with rats of different sex, strain and weight. *J. Neurosci. Methods* 13, 139–143. doi: 10.1016/0165-0270(85)90026-3

Pineau, I., and Lacroix, S. (2007). Proinflammatory cytokine synthesis in the injured mouse spinal cord: multiphasic expression pattern and identification of the cell types involved. *J. Comp. Neurol.* 500, 267–285. doi: 10.1002/cne.21149

Pinnell, R. C., Almajidy, R. K., and Hofmann, U. G. (2016). Versatile 3D-printed headstage implant for group housing of rodents. *J. Neurosci. Methods* 257, 134–138. doi: 10.1016/j.jneumeth.2015.09.027

Polikov, V. S., Tresco, P. A., and Reichert, W. M. (2005). Response of brain tissue to chronically implanted neural electrodes. *J. Neurosci. Methods* 148, 1–18. doi: 10.1016/j.jneumeth.2005.08.015

Potter, K. A., Buck, A. C., Self, W. K., and Capadona, J. R. (2012). Stab injury and device implantation within the brain results in inversely multiphasic neuroinflammatory and neurodegenerative responses. *J. Neural Eng.* 9:046020. doi: 10.1088/1741-2560/9/4/046020

Preibisch, S., Saalfeld, S., and Tomancak, P. (2009). Globally optimal stitching of tiled 3D microscopic image acquisitions. *Bioinformatics* 25, 1463–1465. doi: 10.1093/bioinformatics/btp184

Reier, P. J. (1986). Gliosis following CNS injury: the anatomy of astrocytic scars and their influences on axonal elongation. *Astrocytes* 3, 263–324. doi: 10.1016/b978-0-12-250453-2.50014-1

Richter, A., Xie, Y., Schumacher, A., Löffler, S., Kirch, R. D., Al-Hasani, J., et al. (2013). A simple implantation method for flexible, multisite microelectrodes into rat brains. *Front. Neuroeng.* 6:6. doi: 10.3389/fneng.2013.00006

Röhl, C., Lucius, R., and Sievers, J. (2007). The effect of activated microglia on astrogliosis parameters in astrocyte cultures. *Brain Res.* 1129, 43–52. doi: 10.1016/j.brainres.2006.10.057

Seifert, G., Schilling, K., and Steinhäuser, C. (2006). Astrocyte dysfunction in neurological disorders: a molecular perspective. *Nat. Rev. Neurosci.* 7, 194–206. doi: 10.1038/nrn1870

Sharp, J. W., Sagar, S. M., Hisanaga, K., Jasper, P., and Sharp, F. R. (1990). The NMDA receptor mediates cortical induction of fos and fos-related antigens following cortical injury. *Exp. Neurol.* 109, 323–332. doi: 10.1016/s0014-4886(05)80023-8

Shehab, S., D'Souza, C., Ljubisavljevic, M., and Redgrave, P. (2014). High-frequency electrical stimulation of the subthalamic nucleus excites target structures in a model using c-fos immunohistochemistry. *Neuroscience* 270, 212–225. doi: 10.1016/j.neuroscience.2014.04.016

Turner, J., Shain, W., Szarowski, D., Andersen, M., Martins, S., Isaacson, M., et al. (1999). Cerebral astrocyte response to micromachined silicon implants. *Exp. Neurol.* 156, 33–49. doi: 10.1006/exnr.1998.6983

Voorn, P., Vanderschuren, L. J., Groenewegen, H. J., Robbins, T. W., and Pennartz, C. M. (2004). Putting a spin on the dorsal-ventral divide of the striatum. *Trends Neurosci.* 27, 468–474. doi: 10.1016/j.tins.2004.06.006

Wilson, Y., Nag, N., Davern, P., Oldfield, B. J., McKinley, M. J., Greferath, U., et al. (2002). Visualization of functionally activated circuitry in the brain. *Proc. Natl. Acad. Sci. U.S.A.* 99, 3252–3257. doi: 10.1073/pnas.042701199

Wise, K. D., Anderson, D., Hetke, J., Kipke, D., and Najafi, K. (2004). Wireless implantable microsystems: high-density electronic interfaces to the nervous system. *Proc. IEEE* 92, 76–97. doi: 10.1109/jproc.2003.820544

Xie, Y., Heida, T., Stegenga, J., Zhao, Y., Moser, A., Tronnier, V., et al. (2014). High frequency electrical stimulation suppresses cholinergic accumbens interneurons in acute rat brain slices through GABAB receptors. *Europ. J. Neurosci.* 40, 3653–3662. doi: 10.1111/ejn.12736

Conflict of Interest: The authors declare that the research was conducted in the absence of any commercial or financial relationships that could be construed as a potential conflict of interest.

Copyright © 2020 Pflüger, Pinnell, Martini and Hofmann. This is an open-access article distributed under the terms of the Creative Commons Attribution License (CC BY). The use, distribution or reproduction in other forums is permitted, provided the original author(s) and the copyright owner(s) are credited and that the original publication in this journal is cited, in accordance with accepted academic practice. No use, distribution or reproduction is permitted which does not comply with these terms.

frontiers in Neuroscience

METHODS
published: 07 July 2020
doi: 10.3389/fnins.2020.00095

Second Harmonic Generation Imaging of Collagen in Chronically Implantable Electrodes in Brain Tissue

*Corinne R. Esquibel[1], Kristy D. Wendt[1], Heui C. Lee[2,3], Janak Gaire[4], Andrew Shoffstall[5,6], Morgan E. Urdaneta[4], Jenu V. Chacko[1], Sarah K. Brodnick[1], Kevin J. Otto[3,4], Jeffrey R. Capadona[5,6], Justin C. Williams[1] and K. W. Eliceiri[1,7,8]**

[1] Laboratory for Optical and Computational Instrumentation, Department of Biomedical Engineering, University of Wisconsin, Madison, WI, United States, [2] Weldon School of Biomedical Engineering, Purdue University, West Lafayette, IN, United States, [3] J. Crayton Pruitt Family Department of Biomedical Engineering, University of Florida, Gainesville, FL, United States, [4] Department of Neuroscience, University of Florida, Gainesville, FL, United States, [5] Department of Biomedical Engineering, Case Western Reserve University, Cleveland, OH, United States, [6] Advanced Platform Technology Center, Louis Stokes Cleveland Department of Veterans Affairs Medical Center, Cleveland, OH, United States, [7] Morgridge Institute for Research, Madison, WI, United States, [8] Department of Medical Physics, University of Wisconsin, Madison, WI, United States

OPEN ACCESS

Edited by:
Jessica O. Winter,
The Ohio State University,
United States

Reviewed by:
Xiaoqin Zhu,
Fujian Normal University, China
Brent Winslow,
Design Interactive, United States

***Correspondence:**
K. W. Eliceiri
eliceiri@wisc.edu

Specialty section:
This article was submitted to Neural Technology, a section of the journal Frontiers in Neuroscience

Received: 15 July 2019
Accepted: 23 January 2020
Published: 07 July 2020

Citation:
Esquibel CR, Wendt KD, Lee HC, Gaire J, Shoffstall A, Urdaneta ME, Chacko JV, Brodnick SK, Otto KJ, Capadona JR, Williams JC and Eliceiri KW (2020) Second Harmonic Generation Imaging of Collagen in Chronically Implantable Electrodes in Brain Tissue. Front. Neurosci. 14:95. doi: 10.3389/fnins.2020.00095

Advances in neural engineering have brought about a number of implantable devices for improved brain stimulation and recording. Unfortunately, many of these micro-implants have not been adopted due to issues of signal loss, deterioration, and host response to the device. While glial scar characterization is critical to better understand the mechanisms that affect device functionality or tissue viability, analysis is frequently hindered by immunohistochemical tissue processing methods that result in device shattering and tissue tearing artifacts. Devices are commonly removed prior to sectioning, which can itself disturb the quality of the study. In this methods implementation study, we use the label free, optical sectioning method of second harmonic generation (SHG) to examine brain slices of various implanted intracortical electrodes and demonstrate collagen fiber distribution not found in normal brain tissue. SHG can easily be used in conjunction with multiphoton microscopy to allow direct intrinsic visualization of collagen-containing glial scars on the surface of cortically implanted electrode probes without imposing the physical strain of tissue sectioning methods required for other high resolution light microscopy modalities. Identification and future measurements of these collagen fibers may be useful in predicting host immune response and device signal fidelity.

Keywords: second harmonic generation, collagen, glial scar, imaging, implantable device

INTRODUCTION

Multiphoton microscopy is now a widely adopted brain imaging method, and can be used to monitor *in vivo* neural activity with single spine resolution (Knott et al., 2006; Svoboda and Yasuda, 2006; Kerr and Denk, 2008; Holtmaat et al., 2009; Ozbay et al., 2018). As a non-linear modality, multiphoton offers spatial confinement to the focal region in scattering brain tissue and allows deep, high-resolution optical sectioning of live brain or thick sections

in vitro (Kobat et al., 2011). Multiphoton microscopy can generate both fluorescence and second harmonic generation (SHG) as simultaneous contrast mechanisms, which provide complementary information regarding tissue structure and function, as well as orientation, polarization, and symmetry properties of chiral proteins (Zoumi et al., 2002; Belluscio, 2005; Provenzano et al., 2010; Chen et al., 2012). SHG generates its intrinsic contrast from the interaction of light with non-centrosymmetric structures such as collagen I, collagen II, and myosin (Roth and Freund, 1979; Plotnikov et al., 2006; Chen et al., 2012). SHG is a coherent optical process during which two photons combine and emit a single photon with visible light. As such, SHG imaging offers many of the same benefits of traditional multiphoton microscopy. SHG can be used for high resolution, deep imaging of tissues, allowing a depth penetration of up to ∼500 μm. The triple-helix structure of fibrillar collagen permits visualization up to 0.2–0.3 μm resolution with little to no tissue damage, and does not require the use of fluorescent labels, stains, or genetically modified species (Williams et al., 2005; Li et al., 2011; Chen et al., 2012; Mostaço-Guidolin et al., 2017). While the current study was performed in *ex vivo* brain slices, SHG can also be used *in vivo* to observe changes over time (Zoumi et al., 2002; Dilipkumar et al., 2019). Though the phenomenon of SHG was first demonstrated in biological tissues over three decades ago, and is easily observed with the appropriate filter, it remains an underutilized modality by those already using multiphoton microscopy to image brain-implanted devices *in vivo* and *in vitro* (Freund and Deutsch, 1986; Chen et al., 2012). One factor might be that the most common application for SHG imaging is examining fibrillar collagen and the role of collagen in the brain is still emerging (Shearer and Fawcett, 2001; Heck et al., 2003).

Extracellular matrix (ECM) molecules in the unwounded brain occupy up to 20% of adult brain volume and are characterized by long, linear polysaccharide glycosaminoglycans such as chondroitin sulfate and hyaluronan, while fibrillar collagen is notably absent (Syková and Nicholson, 2008; Miyata and Kitagawa, 2017). Brain ECM exists in diffuse forms found throughout the neuropil and perisynaptic spaces and condensed forms called perineuronal nets (PNNs) that form lattice-like structures around subpopulations of neurons (Miyata and Kitagawa, 2017). While glycosaminoglycans in brain ECM were previously considered non-specific physical barriers to neural regeneration, recent studies have proposed that ECM molecules actively regulate neuronal function through specific interactions with their binding partners (Miyata and Kitagawa, 2017). Though non-fibrillar types of collagen have been observed in healthy brain tissue and have been shown to be necessary for proper function (Seppänen et al., 2007; Hubert et al., 2009; Su et al., 2010) the brain does not typically show the same patterns or abundance of fibrillar collagen (Rauch, 2007; Fox, 2008). However, early experiments suggest the existence of fibroblasts and fibrillar collagens of types I, III, IV, and V within wound areas in the brain (Berry et al., 1983; Maxwell et al., 1984, 1990).

When a penetrating lesion is made in the adult rat cerebral hemisphere, the initial hemorrhagic reaction is followed by invasion of blood-borne macrophages and fibroblasts from the adjacent connective tissue into the lesion lumen, resulting in collagen fibril and basement membrane formation (Berry et al., 1983; Maxwell et al., 1984). The first responders after electrode insertion are microglia, the macrophage lineage cells of the brain, which begin their activation within minutes of injury and show increased density within 24 h (Davalos et al., 2005; Nimmerjahn et al., 2005; Kozai et al., 2015). Reactive astrocytes peak within the first week following injury, and within approximately three to 4 weeks form a compact, collagen-containing sheath around any foreign bodies that remain (Biran et al., 2005). Glial scar formation around chronically implanted electrodes is a reactive, cellular process with rapidly changing cell population dynamics that include perivascular-derived fibroblasts, pericytes, ependymal cells, and phagocytic macrophages (Adams and Gallo, 2018). Immunohistological labeling of various populations of activated fibroblasts and astrocytes surrounding the lesion core requires histological sectioning, a process that frequently causes artifactual damage to electrodes and surrounding tissue under analysis. While others have reported that the fibrotic scar is replete with collagen (Shearer and Fawcett, 2001), the advantages it offers as an endogenous marker of glial scar formation imageable by SHG is largely unrecognized even by those already characterizing rodent brain tissue around chronically implanted electrodes by multiphoton microscopy.

Established histological methods for identifying collagen in tissue include immunohistochemical staining for collagen types I and II as well as non-specific anionic dye procedures such as Van Gieson's stain, Masson's Trichrome, and Sirius Red. Anionic dyes stain collagen by reacting acid groups with the basic groups of collagen, and standard method protocols specify tissue section thicknesses of 5 μm in paraffin sections to permit dye penetration into the tissue. In Sirius Red staining, the elongated axis of dye molecules are attached parallel to the collagen fiber, resulting in enhanced birefringency and specificity when combined with polarized light detection methods. A traditional transmission pathology microscope fitted with linear polarizers or more specialized instrumentation such as the liquid crystal based PolScope perform optimally with standard histological tissue section thicknesses between 5 and 10 μm, so that light can effectively pass through the specimen for phase-shift contribution to contrast in the final image.

Ischemia of a resected specimen before fixation for immunohistochemistry can result in degradation of protein, RNA, and DNA as well as activation of tissue enzymes and autolysis, and small variations in ischemic time can be a crucial factor affecting IHC results. Thick tissue sections can produce higher background signals as can frozen sections, and soluble antigen may be diffused out during the process of IHC prior to fixation. Immunohistochemical protocols for the anticollagens I and II antibodies specify 30–40 μm thick frozen tissue sections, and instruct cutting thinner sections for greater permeation of antibody. These methods typically result in electrode shattering or tearing and separation of the electrode from the tissue for industry standard silicon-based NeuroNexis probes with thicknesses of 15 μm or greater.

None of the methods for imaging collagen described above offer the depth (100s of microns) and non-invasiveness of

SHG to image implanted electrode surfaces in histological thick sections 300–500 μm as described in this experiment. SHG is highly specific to the non-centrosymmetric structure of fibrillar collagen, offers high resolution, good signal-to-noise ratio, and ability to work non-destructively on stained and unstained tissues. Unlike fluorescence, SHG suffers no inherent photobleaching or toxicity and does not require exogenous labels. Unlike polarization microscopy, SHG provides intrinsic confocality and deep sectioning in complex tissues.

Previous antibody-based studies have shown collagen I deposition around penetrating neural implants (Kim et al., 2004). However, label-free, high resolution SHG based imaging of the collagenic scar around implanted neural electrodes has not been demonstrated. In this method validation study, multiple penetrating electrodes types harvested at different times post-implantation were imaged post-mortem by SHG to confirm the presence of collagen fiber deposition around the device. We demonstrate collagen fibrils associated with implanted tissue not found in normal brain tissue. Label-free measures of collagen fibers around intact implanted electrodes may be useful in predicting host immune response to various electrode device designs and may also predict signal fidelity of the device.

MATERIALS AND METHODS

Ex vivo SHG images of brain slices in the backward direction were collected through a Nikon 20× water-dipping objective (1.0 NA) at 890 nm excitation. A dichroic cube filter set (Chroma Technologies, Bellow Falls, VT, United States) containing two band-pass emission filters SHG (445/40 nm) and flavin adenine dinucleotide (FAD) (592/100 nm) were used in an imaging system consisting of a multialkali photomultiplier detector (Hamamatsu, Shizuoka, Japan) on a Bruker Ultima IV (Bruker FM, Middleton, WI, United States) multiphoton microscope equipped with an Insight ultrafast laser (Spectra Physics, Santa Clara, CA, United States). A motorized stage was used to automatically collect images at tiled x/y locations throughout the brain sections. Tiled images were stitched together using FIJI's grid/collection stitching plugin (Preibisch et al., 2009).

The power at the back aperture of the objective was ∼7 mW. For 890 nm, 1.0NA, at these powers the lateral resolution is 380 nm and axial resolution ∼4 um. Imaging parameters were optimized by starting with low Pockels cell values using a range check LUT to display intensity scale for an image to ensure optimal saturation to prevent photobleaching and phototoxicity. The images from the Ultima are digitized to 12 bits, which means that the input channel data intensity scale ranges from 0 (no signal) to 4095 (saturated signal). In a black and white LUT, values of 0 are usually represented as pure black and values of 4095 are usually represented as pure white. Since the computer only has 256 gray levels, a function or LUT is used to define the display intensity scale. If these 256 display gray levels are used to display the full range of 4096 intensity levels then each display gray level is equal to 16 PMT data intensity levels. Photomultiplier tube values on multialkali PMTs were 650–700.

To help validate the SHG based observations, antibody staining on a horizontal electrode was done. Primary antibody staining was done with 1:750 Chicken anti-GFAP (EMD Millipore, AB5541) and 1:300 Rabbit anti-Collagen I (Novus Biologicals, NB600-408). Secondary antibodies used were 1:500 Goat Anti-Rabbit IgG H&L (FITC) (Abcam, AB6717) and 1:1000 Alexa-fluor-633 goat anti-chicken (Invitrogen). The samples were mounted with Vectashield mounting medium with DAPI (Vector Laboratories, Burlingame, CA, United States) and imaged on a Leica DMi8 fluorescence microscope (Leica Microsystems, Wetzlar, Germany) with a 10x 0.4 NA air immersion dry objective (Leica Microsystems, Wetzlar, Germany) and the following filter cubes CFP (Ex. 426–446, Em. 435–485), GFP (Ex. 450–490, Em. 500–550) and Y3/RFP (Ex. 532–558, Em. 570–640). The fluorescence images were registered with the SHG images from the same slide with fine-structures registration approach (BUNWARPJ, FIJII). A mask from SHG was used to see if all the pixels are co-registered.

Off-stoichiometry thiol-enes-epoxy (OSTE+) polymer probes were fabricated in the laboratory of Marting Bengtsson at Lund University, implanted in mice and harvested as previously described by Lee et al. (2017) following Institutional Animal Care and Usage Committee (IACUC) guidelines at the University of Florida. OSTE+ Hard, OSTE+ Soft, polyimide, and silicon electrodes had dimensions of 250 μm wide and 3 mm long with a tapered tip of approximately 18° in angle. Thicknesses were: 21.3 ± 1.0 μm (polyimide), 23.5 ± 2.1 μm (OSTE+Hard), and 22.4 ± 2.1 μm (OSTE+Soft) (mean ± standard deviation, $N = 15$). Probes were cortically implanted in mice and harvested at 4 and 6 weeks respectively. Mouse brains were lightly embedded with optimum cutting temperature (OCT) compound (Sakura Finetek, Netherlands) and sliced into 25 μm horizontal sections with the retained probes. More common varieties of NeuroNexus silicon probes from implanted rat brains were imaged at various time points as previously described (Woolley et al., 2013). Intact single shank NeuroNexus probes (249 μm width, 15 μm thickness, $N = 3$; 132 μm width, 15 μm thickness, $N = 2$), single shank bare silicon probes (132 μm width, 15 μm thickness, $N = 3$), and quadruple shank bare silicon probes (132 μm width, 15 μm thickness, $N = 2$) were collected within coronal slices of rat brain harvested between 53 and 177 days prior to sacrifice using the device capture technique described by Woolley et al. (2013) and sectioned between 350 and 450 μm.

RESULTS

We report the direct observation of high-resolution collagen fibers encapsulating intact, indwelling silicon NeuroNexus neural devices in thickly sectioned (350–450 μm) rat coronal slices ($N = 10$ for all varieties of NeuroNexus probes) that contrasts with the absence of non-fibrillar collagen in the unwounded brain (**Figures 1**, **2**). In **Figure 2**, abundant collagen fibers within a substantial glial scar are shown with SHG imaging (890 nm

excitation 445/40 nm emission) of a NeuroNexus silicon device, implanted for 8 weeks, sectioned at 400 μm, and captured within a coronal slice of rat brain tissue. Collagen fibers on the surface of the silicon device are shown in Panels A and B. Panel C magnifies a 500 μm × 200 μm segment of the image, clearly showing fibers encircling the device as well as extending along the length of the device. When the depth of the collagen within the imaged z-stack is encoded as color (shallow z-depth, surface of tissue slice = white; deep z-depth, interior of tissue slice = indigo), circumferential fibers can be observed both above and below longitudinal fibers. Collagen fibers that match the geometry of implanted silicon NeuroNexus devices (time of implantation ranged from 53 to 177 days) can be observed with SHG imaging independent of probe size and shank number (**Figure 3**). Imaging 25 μm histological sections of mouse brain tissue harvested at 4 and 8-week timepoints proved more difficult due to the artifacts induced by tissue processing required by the criteria of that study (Lee et al., 2017). In these

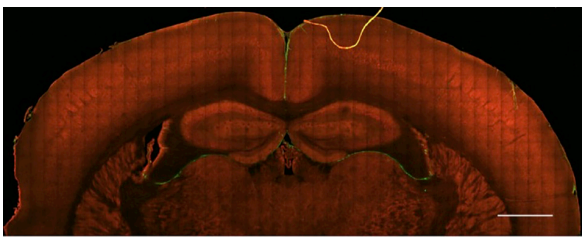

FIGURE 1 | Healthy brain tissue is largely devoid of fibrillar collagen. Second Harmonic Generation (SHG) imaging of mouse brain tissue shows virtually no fibrillar collagen (green, 890 nm excitation 445/40 nm emission) within the parenchyma. Collagen fibers can be seen surrounding the cortex and within and between ventricles. Multiphoton induced autofluorescence (red, 890 nm excitation, 592/100 nm emission, likely FAD) was recorded to observe gross anatomical features of the tissue. Scale bar = 1 mm.

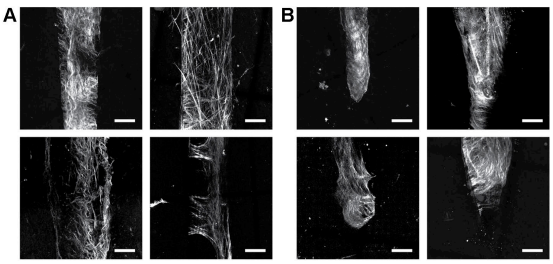

FIGURE 3 | Collagen fibers observed with SHG imaging match the geometry of implanted neural devices independent of probe size/type in silicon NeuroNexus probes. Although the manifestation of fibrillar collagen varied, fibers consistently conformed to the implant shape, encompassing both the **(A)** shank and the **(B)** tip of the device. Electrodes were implanted between 53 and 177 days prior to sacrifice. Scale bar = 50 um.

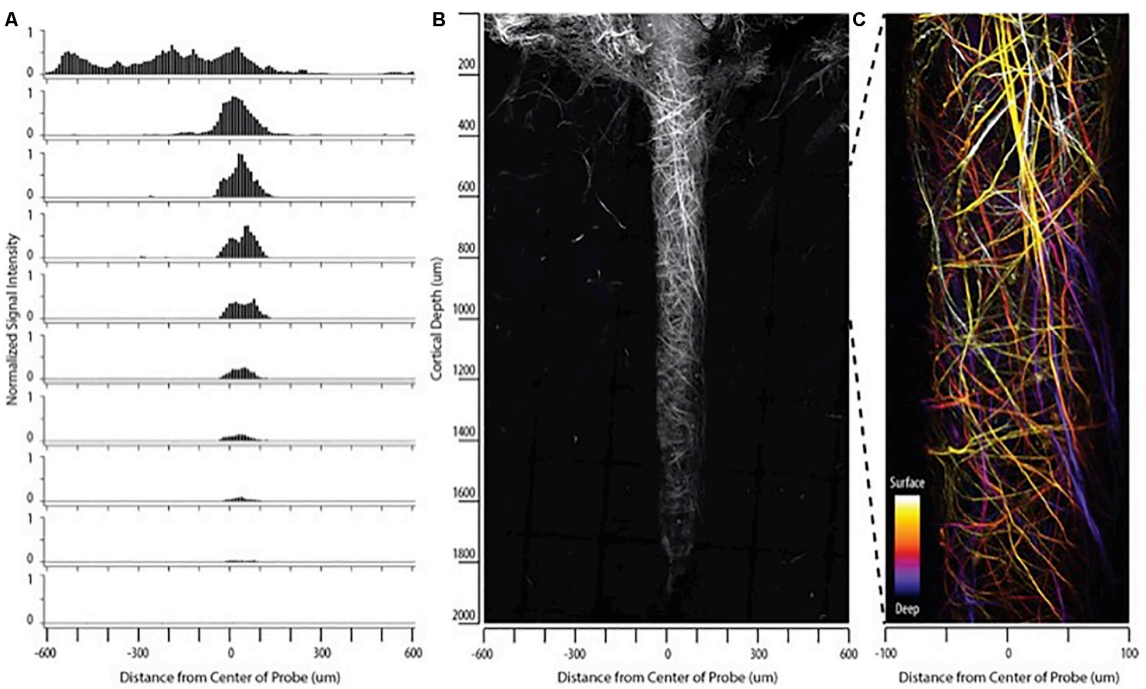

FIGURE 2 | Collagen fibers encapsulate indwelling neural devices. Abundant collagen fibers are shown with SHG imaging (890 nm excitation 445/40 nm emission) of a 132 um NeuroNexus silicon device, implanted for 56 days, captured within a coronal slice of rat brain tissue. **(A,B)** Quantify and visualize, respectively, that collagen fibers are only observed on the surface of the device, not in the surrounding parenchyma. **(C)** Magnifies a 500 um × 200 um segment of the image, clearly showing fibers encircling the device as well as extending along the length of the device. When the depth of the collagen within the imaged z-stack is encoded as color (shallow z-depth, surface of tissue slice = white; deep z-depth, interior of tissue slice = indigo), circumferential fibers can be observed both above below longitudinal fibers.

samples, the softer electrodes were physically cross-sectioned by the 25 μm sectioning processing method. Though collagen fibers were still observable, the degree of apparent collagen deposition was decreased in samples processed in this manner (**Figure 4**). When tissue from animals implanted with silicon probes was cross-sectioned at 25 μm, the probes shattered and pulled away from the tissue, disallowing observation of collagen fibers. Given the fragile nature of the tissue and electrodes it was challenging to do any sort of antibody validation on most of these samples, few survived the process. However, we were able to take one of the horizontal electrodes and stain it for collagen I and GFAP (**Figure 5**). We used a mask from SHG to see if all the pixels are co-registered. We found 88% of the SHG pixels belong to the collagen 1 antibody staining.

DISCUSSION

Understanding glial scar formation is fundamental to improving biocompatibility of chronic implanted electrodes. Scar borders are formed primarily by newly proliferated astrocytes and glia that surround and recruit inflammatory and fibrotic cells into discrete areas that are separated from adjacent tissue containing viable neurons (Wanner et al., 2013). Our observations of fibrillar collagen on the surface and perimeter of chronically implanted electrode probes in rat and mouse, correspond with the glial scar and suggest a correlative signal that may be used to assess and quantify wounding in the brain caused by chronically implanted electrodes. This signal can be evaluated in both *in vivo* and thickly sectioned post-mortem coronal sections, without the addition of extrinsic stains or fluorescence. This study offers a new method to assess and potentially quantify scarring around a chronically implanted electrode. While fibrillar collagen has not been previously reported on the surface of electrodes in conjunction with glial scar formation, it appears to coincide with glial scar location.

Glial scars provide a biochemical and mechanical barrier to neuronal generation and result in tissue softening in the cortex after injury (Moeendarbary et al., 2017). Blood brain barrier (BBB) leakage, astrogliosis, and tissue remodeling correlate with a reduction in silicon microelectrode array recording performance, increases in microelectrode impedance and loss of neuronal recording attributed to the encapsulating brain tissue response (Nolta et al., 2015). Changes to the tissue microenvironment

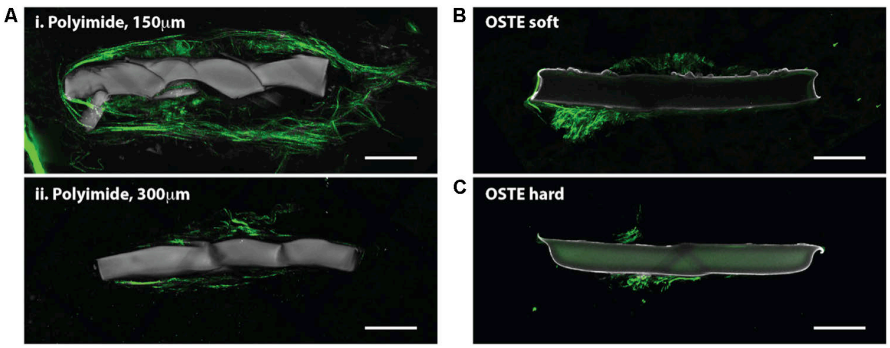

FIGURE 4 | Horizontal slices through implanted probes show collagen deposition. SHG imaging (green, 890 nm excitation 445/40 nm emission) shows collagen fibers around neural probes, independent of the indwelling device material. Multiple slices through the same polyimide device show that the collagen fibers are most abundant close to the cortical surface **(Ai)** but are still observable in deeper cortical regions **(Aii)** Collagen fibers were also observed on and around neural probes made of OSTE soft **(B)** and OSTE hard **(C)** materials. Autofluorescence from the implanted device is shown in gray (890 nm excitation, both 445/40 and 592/100 nm emission). Scale bar = 50 microns.

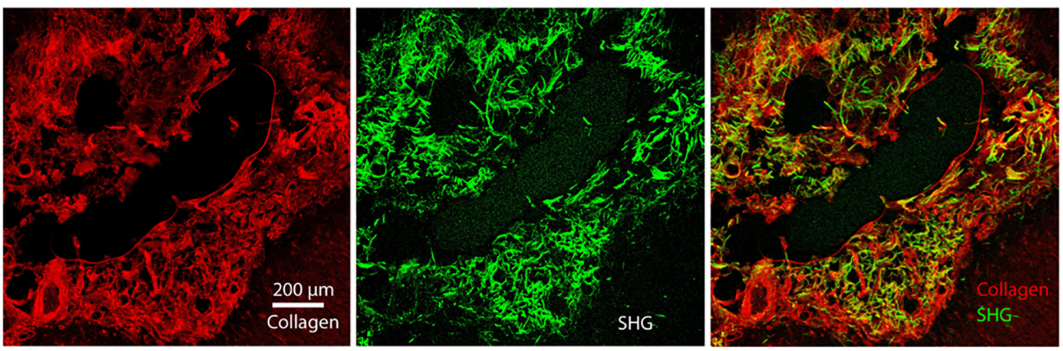

FIGURE 5 | Immunohistochemistry of Collagen I overlaid with GFAP of the astrocytic glial scar in chronic horizontal slices. We re-registered the two files with fine-structures registration (BUNWARPJ, FIJI). We used a mask from SHG to see if all the pixels are co-registered. We found 88% of the SHG pixels belong to the collagen 1 antibody staining. Scale bar = 200 microns.

surrounding the device can dramatically impact electrochemical and electrophysiological signal sensitivity and stability over time (Williams et al., 1999). Glial cells form tight junctions with each other to create a glial sheath, which in combination with collagen along the length of the electrode can form a diffusion barrier that limits transmission of ions as well as overflow of neurotransmitters through the extracellular space (Roitbak and Syková, 1999). In general, this increase in impedance is observed over the first 2 weeks following insertion, before stabilizing (Williams et al., 1999; Kozai et al., 2014). Furthermore, neuronal cell death and degeneration of neurites can occur within 150 μm of the device over the first 4 weeks (Biran et al., 2005; Kozai et al., 2014, 2015). The long-term utility of neural devices depends on the severity of this tissue reaction, with chronically implanted devices becoming less reliable over time (Williams et al., 1999; Polikov et al., 2005; Barrese et al., 2013; Sommakia et al., 2014).

Research also suggests that a mechanical mismatch between the softer brain tissue and industry standard silicon electrodes may induce cellular sheath formation, particularly near the tip and edges of the probe where the highest elevated local strains occur (Lee et al., 2017). Strain–stress caused by neural implant rigidity and the brain's micromotion may exacerbate the foreign body response (FBR). Flexible nanocomposite probes (12 MPa) induce significantly less neuroinflammatory response than standard silicon probes and polyvinyl acetate (PVAc)-coated silicon probes (Harris et al., 2011; Nguyen et al., 2014) and flexible penetrating devices have been shown to have comparatively long-term electrophysiological characteristics in the CNS. Lee et al. (2017) observed a significant reduction in the fluorescence intensity of biomarkers for activated microglia/macrophages and BBB leakiness around three types of soft polymer probes compared to silicon probes at 4 and 8 weeks post-implantation, suggesting that the mechanical compliance of neural probes can mediate the degree of FBR.

Reactive astrocytes are believed to be the main contributors of the molecular cues that drive glial scar formation in the wounded brain (Ridet et al., 1997; Heck et al., 2003). When astrocytic cell lines were developed with a range of abilities to promote or inhibit neurite outgrowth, the most inhibitory of these cell lines, Neu7, was correlated with fibrillar collagen production (Heck et al., 2003). The glial scar may impede electrophysiology measurements by directly altering the impedance or ionic microenvironment, or by simply increasing the physical distance between the neurons and the recording contacts. Identifying and modulating potentially inhibitory molecules or physical barriers in the ECM will be critical to developing interventions that allow axons to regenerate beyond the glial scar (Silver and Miller, 2004; Fitch and Silver, 2008; Cregg et al., 2014).

SHG can penetrate 100s of microns in brain tissues, making it an appropriate technique for imaging without risking shattering the sample or tearing the tissue during sectioning as occurred in the brain samples harvested in mice for Lee et al. (2017). The most commonly used laser for SHG imaging offers average performance for multiphoton imaging in the brain, the Nd:YVO4 (532 nm; 5–18 W) pumped Ti:sapphire oscillator, that has tuning ranges of ∼700–1,000 nm, repetition rates of ∼80 MHz, average powers of 1–2 W and pulse widths of ∼100 fs, which correspond to a bandwidth of about 10 nm full width at half-maximum (FWHM) (Chen et al., 2012). SHG is not a resonant process, and the choice of excitation wavelength in terms of signal intensity is thus not crucial (Chen et al., 2012). 900-nm excitation is a good compromise between imaging depth, viability and Ti:sapphire performance (Chen et al., 2012). A short wave pass (SWP) dichroic mirror following the laser is necessary for background-free SHG detection, as residual pump (532 nm) can co-propagate with Ti:sapphire through the entire microscope path to the detectors.

SHG can be used to visualize collagen to improve our understanding of how ECM components impact and participate in the foreign body response to implanted neural devices. While this study demonstrated that collagen coincides with glial scar location, a true comparison of the FBR in electrode material will require normalized distribution of tissue processing methods, electrode types, and rodent species. We demonstrate high-resolution, in-depth imaging of fibrillar collagen on the surface of the implants coinciding with glial scar location in intact electrodes in thickly sectioned samples (350–450 μm) without artifacts typically induced by histological sectioning. Future studies should investigate whether the material type or composition of the electrode affects the collagen response. This imaging tool could enable rapid evaluation of new probe designs and therapies aimed at reducing the formation of the glial scar to ultimately improve the chronic performance of implanted neural devices.

DATA AVAILABILITY STATEMENT

All datasets generated for this study are included in the article/supplementary material.

ETHICS STATEMENT

The animal study was reviewed and approved by University of Wisconsin at Madison.

AUTHOR CONTRIBUTIONS

CE, KW, JG, HL, AS, MU, and JC carried out the measurements. JW, CE, and KE conceived the experiment and KE supervised the project. All authors participated in designing the research and writing the manuscript.

FUNDING

We acknowledge funding from the National Institutes of Health (NIH NIBIB 1R01EB009103-01, NIH NIBIB 2R01EB000856-06, 1U01NS099700-01, and NIH NIBIB 1T32EB011434-01A1) and the Defense Advanced Research Projects Agency (DARPA RCI #N66001-12-C-4025, DARPA HIST

#N66001-11-1-4013). We also acknowledge Career Development Award-1 #1IK1RX002492-01A2 (Shoffstall) from the United States (US) Department of Veterans Affairs Rehabilitation Research and Development Service.

ACKNOWLEDGMENTS

We acknowledge useful discussion and manuscript feedback from Dr. Kip Ludwig and Dr. Ellen Arena.

REFERENCES

Adams, K. L., and Gallo, V. (2018). The diversity and disparity of the glial scar. *Nat. Neurosci.* 21, 9–15. doi: 10.1038/s41593-017-0033-9

Barrese, J. C., Rao, N., Paroo, K., Triebwasser, C., Vargas-Irwin, C., Franquemont, L., et al. (2013). Failure mode analysis of silicon-based intracortical microelectrode arrays in non-human primates. *J. Neural Eng.* 10:066014. doi: 10.1088/1741-2560/10/6/066014

Belluscio, L. (2005). Two-photon imaging in live rodents. *Curr. Protoc. Neurosci.* 32, 2.9.1–2.9.14. doi: 10.1002/0471142301.ns0209s32

Berry, M., Maxwell, W. L., Logan, A., Mathewson, A., McConnell, P., Ashhurst, D. E., et al. (1983). Deposition of scar tissue in the central nervous system. *Acta Neurochir. Suppl. (Wien)* 32, 31–53. doi: 10.1007/978-3-7091-4147-2_3

Biran, R., Martin, D. C., and Tresco, P. A. (2005). Neuronal cell loss accompanies the brain tissue response to chronically implanted silicon microelectrode arrays. *Exp. Neurol.* 195, 115–126. doi: 10.1016/j.expneurol.2005.04.020

Chen, X., Nadiarynkh, O., Plotnikov, S., and Campagnola, P. J. (2012). Second harmonic generation microscopy for quantitative analysis of collagen fibrillar structure. *Nat. Protoc.* 7, 654–669. doi: 10.1038/nprot.2012.009

Cregg, J. M., DePaul, M. A., Filous, A. R., Lang, B. T., Tran, A., and Silver, J. (2014). Functional regeneration beyond the glial scar. *Exp. Neurol.* 253, 197–207. doi: 10.1016/j.expneurol.2013.12.024

Davalos, D., Grutzendler, J., Yang, G., Kim, J. V., Zuo, Y., Jung, S., et al. (2005). ATP mediates rapid microglial response to local brain injury in vivo. *Nat. Neurosci.* 8, 752–758. doi: 10.1038/nn1472

Dilipkumar, A., Al-Shemmary, A., Kreiß, L., Cvecek, K., Carlé, B., Knieling, F., et al. (2019). Label-free multiphoton endomicroscopy for minimally invasive in vivo imaging. *Adv. Sci. (Weinh)* 6:1801735. doi: 10.1002/advs.201801735

Fitch, M. T., and Silver, J. (2008). CNS injury, glial scars, and inflammation: inhibitory extracellular matrices and regeneration failure. *Exp. Neurol.* 209, 294–301. doi: 10.1016/j.expneurol.2007.05.014

Fox, M. A. (2008). Novel roles for collagens in wiring the vertebrate nervous system. *Curr. Opin. Cell Biol.* 20, 508–513. doi: 10.1016/j.ceb.2008.05.003

Freund, I., and Deutsch, M. (1986). Second-harmonic microscopy of biological tissue. *Opt. Lett.* 11:94. doi: 10.1364/ol.11.000094

Harris, J. P., Capadona, J. R., Miller, R. H., Healy, B. C., Shanmuganathan, K., Rowan, S. J., et al. (2011). Mechanically adaptive intracortical implants improve the proximity of neuronal cell bodies. *J. Neural Eng.* 8:066011. doi: 10.1088/1741-2560/8/6/066011

Heck, N., Garwood, J., Schütte, K., Fawcett, J., and Faissner, A. (2003). Astrocytes in culture express fibrillar collagen. *Glia* 41, 382–392. doi: 10.1002/glia.10184

Holtmaat, A., Bonhoeffer, T., Chow, D. K., Chuckowree, J., De Paola, V., Hofer, S. B., et al. (2009). Long-term, high-resolution imaging in the mouse neocortex through a chronic cranial window. *Nat. Protoc.* 4, 1128–1144. doi: 10.1038/nprot.2009.89

Hubert, T., Grimal, S., Carroll, P., and Fichard-Carroll, A. (2009). Collagens in the developing and diseased nervous system. *Cell. Mol. Life Sci.* 66, 1223–1238. doi: 10.1007/s00018-008-8561-9

Kerr, J. N. D., and Denk, W. (2008). Imaging in vivo: watching the brain in action. *Nat. Rev. Neurosci.* 9, 195–205. doi: 10.1038/nrn2338

Kim, Y. T., Hitchcock, R. W., Bridge, M. J., and Tresco, P. A. (2004). Chronic response of adult rat brain tissue to implants anchored to the skull. *Biomaterials* 25, 2229–2237. doi: 10.1016/j.biomaterials.2003.09.010

Knott, G. W., Holtmaat, A., Wilbrecht, L., Welker, E., and Svoboda, K. (2006). Spine growth precedes synapse formation in the adult neocortex in vivo. *Nat. Neurosci.* 9, 1117–1124. doi: 10.1038/nn1747

Kobat, D., Horton, N. G., and Xu, C. (2011). In vivo two-photon microscopy to 1.6-mm depth in mouse cortex. *J. Biomed. Opt.* 16:106014. doi: 10.1117/1.3646209

Kozai, T. D. Y., Gugel, Z., Li, X., Gilgunn, P. J., Khilwani, R., Ozdoganlar, O. B., et al. (2014). Chronic tissue response to carboxymethyl cellulose based dissolvable insertion needle for ultra-small neural probes. *Biomaterials* 35, 9255–9268. doi: 10.1016/j.biomaterials.2014.07.039

Kozai, T. D. Y., Jaquins-Gerstl, A. S., Vazquez, A. L., Michael, A. C., and Cui, X. T. (2015). Brain tissue responses to neural implants impact signal sensitivity and intervention strategies. *ACS Chem. Neurosci.* 6, 48–67. doi: 10.1021/cn500256e

Lee, H. C., Ejserholm, F., Gaire, J., Currlin, S., Schouenborg, J., Wallman, L., et al. (2017). Histological evaluation of flexible neural implants; flexibility limit for reducing the tissue response? *J. Neural Eng.* 14:036026. doi: 10.1088/1741-2552/aa68f0

Li, C., Hall, G., Zeng, X., Zhu, D., Eliceiri, K., and Jiang, H. (2011). Three-dimensional surface profiling and optical characterization of liquid microlens using a Shack-Hartmann wave front sensor. *Appl. Phys. Lett.* 98:171104. doi: 10.1063/1.3583379

Maxwell, W. L., Duance, V. C., Lehto, M., Ashurst, D. E., and Berry, M. (1984). The distribution of types I, III, IV and V collagens in penetrant lesions of the central nervous system of the rat. *Histochem. J.* 16, 1215–1229. doi: 10.1007/BF01003445

Maxwell, W. L., Follows, R., Ashhurst, D. E., and Berry, M. (1990). The response of the cerebral hemisphere of the rat to injury. I. The mature rat. *Philos. Trans. R. Soc. Lond. B Biol. Sci.* 328, 479–500. doi: 10.1098/rstb.1990.0121

Miyata, S., and Kitagawa, H. (2017). Formation and remodeling of the brain extracellular matrix in neural plasticity: roles of chondroitin sulfate and hyaluronan. *Biochim. Biophys. Acta Gen. Subj.* 1861, 2420–2434. doi: 10.1016/j.bbagen.2017.06.010

Moeendarbary, E., Weber, I. P., Sheridan, G. K., Koser, D. E., Soleman, S., Haenzi, B., et al. (2017). The soft mechanical signature of glial scars in the central nervous system. *Nat. Commun.* 8:14787. doi: 10.1038/ncomms14787

Mostaço-Guidolin, L., Rosin, N. L., and Hackett, T. L. (2017). Imaging collagen in scar tissue: developments in second harmonic generation microscopy for biomedical applications. *Int. J. Mol. Sci.* 18:1772. doi: 10.3390/ijms18081772

Nguyen, J. K., Park, D. J., Skousen, J. L., Hess-Dunning, A. E., Tyler, D. J., Rowan, S. J., et al. (2014). Mechanically-compliant intracortical implants reduce the neuroinflammatory response. *J. Neural Eng.* 11:056014. doi: 10.1088/1741-2560/11/5/056014

Nimmerjahn, A., Kirchhoff, F., and Helmchen, F. (2005). Resting microglial cells are highly dynamic surveillants of brain parenchyma in vivo. *Science* 308, 1314–1318. doi: 10.1126/science.1110647

Nolta, N. F., Christensen, M. B., Crane, P. D., Skousen, J. L., and Tresco, P. A. (2015). BBB leakage, astrogliosis, and tissue loss correlate with silicon microelectrode array recording performance. *Biomaterials* 53, 753–762. doi: 10.1016/j.biomaterials.2015.02.081

Ozbay, B. N., Futia, G. L., Ma, M., Bright, V. M., Gopinath, J. T., Hughes, E. G., et al. (2018). Three dimensional two-photon brain imaging in freely moving mice using a miniature fiber coupled microscope with active axial-scanning. *Sci. Rep.* 8, 1–14. doi: 10.1038/s41598-018-26326-3

Plotnikov, S. V., Millard, A. C., Campagnola, P. J., and Mohler, W. A. (2006). Characterization of the myosin-based source for second-harmonic generation from muscle sarcomeres. *Biophys. J.* 90, 693–703. doi: 10.1529/biophysj.105.071555

Polikov, V. S., Tresco, P. A., and Reichert, W. M. (2005). Response of brain tissue to chronically implanted neural electrodes. *J. Neurosci. Methods* 148, 1–18. doi: 10.1016/j.jneumeth.2005.08.015

Preibisch, S., Saalfeld, S., and Tomancak, P. (2009). Globally optimal stitching of tiled 3D microscopic image acquisitions. *Bioinformatics* 25, 1463–1465. doi: 10.1093/bioinformatics/btp184

Provenzano, P. P., Eliceiri, K. W., Inman, D. R., and Keely, P. J. (2010). Engineering three-dimensional collagen matrices to provide contact guidance during 3D cell migration. *Curr. Protoc. Cell Biol.* 47, 10.17.1–10.17.11. doi: 10.1002/0471143030.cb1017s47

Rauch, U. (2007). Brain matrix: structure, turnover and necessity. *Biochem. Soc. Trans.* 35(Pt 4), 656–660. doi: 10.1042/BST0350656

Ridet, J. L., Malhotra, S. K., Privat, A., and Gage, F. H. (1997). Reactive astrocytes: cellular and molecular cues to biological function. *Trends Neurosci.* 20, 570-577.

Roitbak, T., and Syková, E. (1999). Diffusion barriers evoked in the rat cortex by reactive astrogliosis. *Glia* 28, 40–48. doi: 10.1002/(SICI)1098-1136(199910)28:1<40::AID-GLIA5<3.0.CO;2-6

Roth, S., and Freund, I. (1979). Second harmonic generation in collagen. *J. Chem. Phys.* 70, 1637–1643. doi: 10.1063/1.437677

Seppänen, A., Suuronen, T., Hofmann, S. C., Majamaa, K., and Alafuzoff, I. (2007). Distribution of collagen XVII in the human brain. *Brain Res.* 1158, 50–56. doi: 10.1016/j.brainres.2007.04.073

Shearer, M. C., and Fawcett, J. W. (2001). The astrocyte/meningeal cell interface – a barrier to successful nerve regeneration? *Cell Tissue Res.* 305, 267–273. doi: 10.1007/s004410100384

Silver, J., and Miller, J. H. (2004). Regeneration beyond the glial scar. *Nat. Rev. Neurosci.* 5, 146–156. doi: 10.1038/nrn1326

Sommakia, S., Gaire, J., Rickus, J. L., and Otto, K. J. (2014). Resistive and reactive changes to the impedance of intracortical microelectrodes can be mitigated with polyethylene glycol under acute in vitro and in vivo settings. *Front. Neuroeng.* 7:33. doi: 10.3389/fneng.2014.00033

Su, J., Gorse, K., Ramirez, F., and Fox, M. A. (2010). Collagen XIX is expressed by interneurons and contributes to the formation of hippocampal synapses. *J. Comp. Neurol.* 518, 229–253. doi: 10.1002/cne.22228

Svoboda, K., and Yasuda, R. (2006). Principles of two-photon excitation microscopy and its applications to neuroscience. *Neuron* 50, 823–839. doi: 10.1016/j.neuron.2006.05.019

Syková, E., and Nicholson, C. (2008). Diffusion in brain extracellular space. *Physiol. Rev.* 88, 1277–1340. doi: 10.1152/physrev.00027.2007

Wanner, I. B., Anderson, M. A., Song, B., Levine, J., Fernandez, A., Gray-Thompson, Z., et al. (2013). Glial scar borders are formed by newly proliferated, elongated astrocytes that interact to corral inflammatory and fibrotic cells via STAT3-dependent mechanisms after spinal cord injury. *J. Neurosci* 33, 12870–12886. doi: 10.1523/JNEUROSCI.2121-13.2013

Williams, J. C., Rennaker, R. L., and Kipke, D. R. (1999). Long-term neural recording characteristics of wire microelectrode arrays implanted in cerebral cortex. *Brain Res. Protoc.* 4, 303–313. doi: 10.1016/S1385-299X(99)00034-3

Williams, R. M., Zipfel, W. R., and Webb, W. W. (2005). Interpreting second-harmonic generation images of collagen I fibrils. *Biophys. J.* 88, 1377–1386. doi: 10.1529/biophysj.104.047308

Woolley, A. J., Desai, H. A., and Otto, K. J. (2013). Chronic intracortical microelectrode arrays induce non-uniform, depth-related tissue responses. *J. Neural Eng.* 10:026007. doi: 10.1088/1741-2560/10/2/026007

Zoumi, A., Yeh, A., and Tromberg, B. J. (2002). Imaging cells and extracellular matrix in vivo by using second-harmonic generation and two-photon excited fluorescence. *Proc. Natl. Acad. Sci. U.S.A.* 99, 11014–11019. doi: 10.1073/pnas.172368799

Disclaimer: The contents of this paper do not represent the views of the U.S. Department of Veterans Affairs or the United States Government.

Conflict of Interest: The authors declare that the research was conducted in the absence of any commercial or financial relationships that could be construed as a potential conflict of interest.

Copyright © 2020 Esquibel, Wendt, Lee, Gaire, Shoffstall, Urdaneta, Chacko, Brodnick, Otto, Capadona, Williams and Eliceiri. This is an open-access article distributed under the terms of the Creative Commons Attribution License (CC BY). The use, distribution or reproduction in other forums is permitted, provided the original author(s) and the copyright owner(s) are credited and that the original publication in this journal is cited, in accordance with accepted academic practice. No use, distribution or reproduction is permitted which does not comply with these terms.

Advantages of publishing in Frontiers

OPEN ACCESS
Articles are free to read for greatest visibility and readership

FAST PUBLICATION
Around 90 days from submission to decision

HIGH QUALITY PEER-REVIEW
Rigorous, collaborative, and constructive peer-review

TRANSPARENT PEER-REVIEW
Editors and reviewers acknowledged by name on published articles

Frontiers
Avenue du Tribunal-Fédéral 34
1005 Lausanne | Switzerland

Visit us: www.frontiersin.org
Contact us: info@frontiersin.org | +41 21 510 17 00

REPRODUCIBILITY OF RESEARCH
Support open data and methods to enhance research reproducibility

DIGITAL PUBLISHING
Articles designed for optimal readership across devices

FOLLOW US
@frontiersin

IMPACT METRICS
Advanced article metrics track visibility across digital media

EXTENSIVE PROMOTION
Marketing and promotion of impactful research

LOOP RESEARCH NETWORK
Our network increases your article's readership